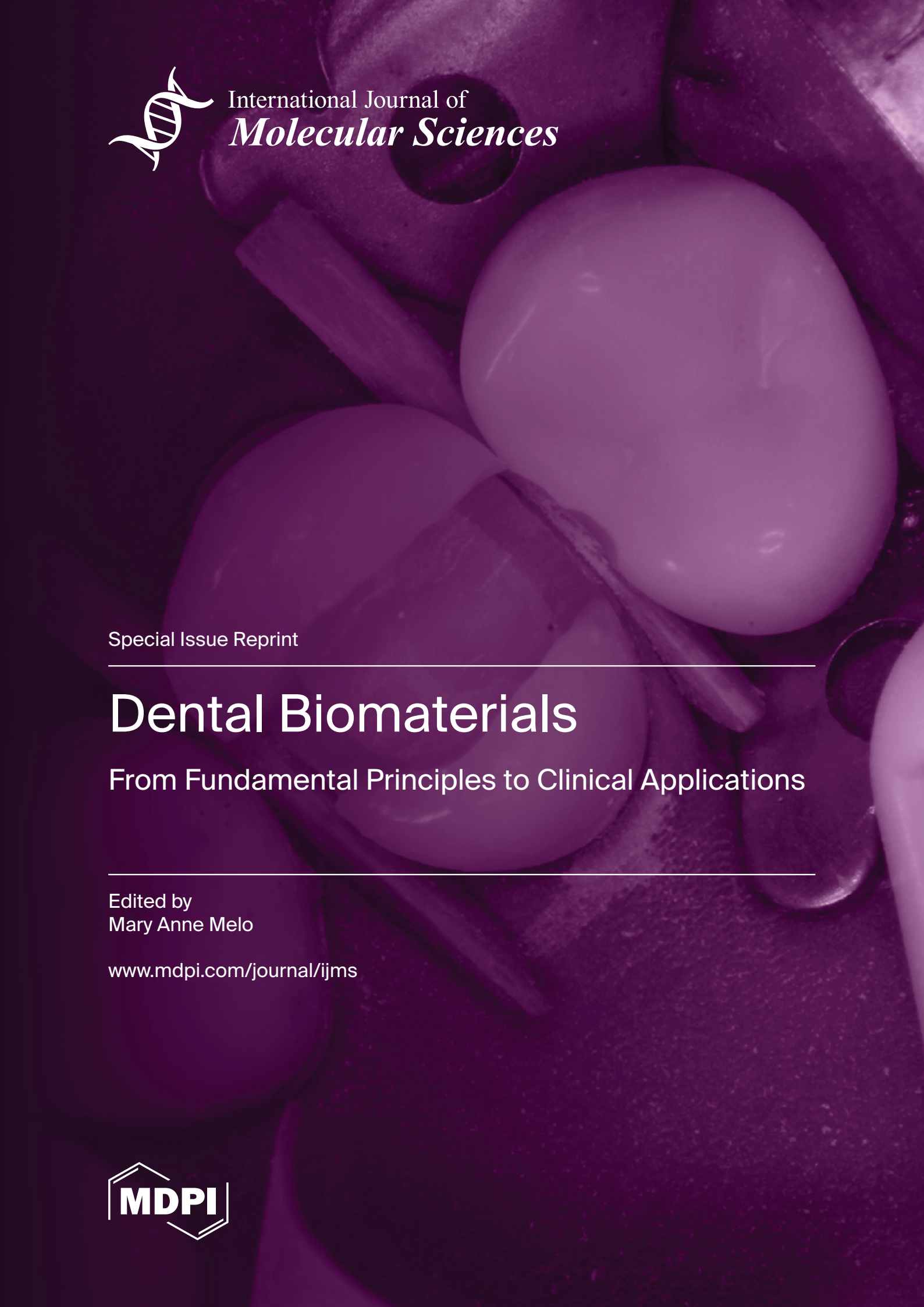


International Journal of
Molecular Sciences

Special Issue Reprint

Dental Biomaterials

From Fundamental Principles to Clinical Applications

Edited by
Mary Anne Melo

www.mdpi.com/journal/ijms

MDPI

Dental Biomaterials: From Fundamental Principles to Clinical Applications

Dental Biomaterials: From Fundamental Principles to Clinical Applications

Editor

Mary Anne Melo

MDPI • Basel • Beijing • Wuhan • Barcelona • Belgrade • Manchester • Tokyo • Cluj • Tianjin



Editor
Mary Anne Melo
General Dentistry
University of Maryland
School of Dentistry
Baltimore
United States

Editorial Office
MDPI
St. Alban-Anlage 66
4052 Basel, Switzerland

This is a reprint of articles from the Special Issue published online in the open access journal *International Journal of Molecular Sciences* (ISSN 1422-0067) (available at: www.mdpi.com/journal/ijms/special_issues/noveldental_materials).

For citation purposes, cite each article independently as indicated on the article page online and as indicated below:

Lastname, A.A.; Lastname, B.B. Article Title. *Journal Name* **Year**, *Volume Number*, Page Range.

ISBN 978-3-0365-7725-8 (Hbk)
ISBN 978-3-0365-7724-1 (PDF)
doi.org/10.3390/books978-3-0365-7724-1

Cover image courtesy of Mary Anne Melo

© 2024 by the authors. Articles in this book are Open Access and distributed under the Creative Commons Attribution (CC BY) license. The book as a whole is distributed by MDPI under the terms and conditions of the Creative Commons Attribution-NonCommercial-NoDerivs (CC BY-NC-ND) license.

Contents

About the Editor . . . . . **ix**

Preface to "Dental Biomaterials: From Fundamental Principles to Clinical Applications" . . . **xi**

Dmitry I. Grachev, Evgeny A. Chizhmakov, Dmitry Yu. Stepanov, Dmitry G. Buslovich, Ibragim V. Khulaev and Aslan V. Deshev et al.
Dental Material Selection for the Additive Manufacturing of Removable Complete Dentures (RCD)
Reprinted from: *Int. J. Mol. Sci.* **2023**, *24*, 6432, doi:10.3390/ijms24076432 . . . . . **1**

Irina Nica, Florin Nedeff, Valentin Nedeff, Cristina Popa, Ștefan Lucian Toma and Maricel Agop et al.
The Cracking Behavior of Two Dental Composite Materials Validated through Multifractal Analyzes
Reprinted from: *Int. J. Mol. Sci.* **2023**, *24*, 6493, doi:10.3390/ijms24076493 . . . . . **21**

Matko Oguić, Marija Čandrlić, Matej Tomas, Bruno Vidaković, Marko Blašković and Ana Terezija Jerbić Radetić et al.
Osteogenic Potential of Autologous Dentin Graft Compared with Bovine Xenograft Mixed with Autologous Bone in the Esthetic Zone: Radiographic, Histologic and Immunohistochemical Evaluation
Reprinted from: *Int. J. Mol. Sci.* **2023**, *24*, 6440, doi:10.3390/ijms24076440 . . . . . **39**

Bernd Sigusch, Stefan Kranz, Andreas Clemm von Hohenberg, Sabine Wehle, André Guellmar and Dorika Steen et al.
Histological and Histomorphometric Evaluation of Implanted Photodynamic Active Biomaterials for Periodontal Bone Regeneration in an Animal Study
Reprinted from: *Int. J. Mol. Sci.* **2023**, *24*, 6200, doi:10.3390/ijms24076200 . . . . . **53**

Matej Tomas, Matej Karl, Marija Čandrlić, Marko Matijević, Martina Juzbašić and Olga Cvijanović Peloza et al.
A Histologic, Histomorphometric, and Immunohistochemical Evaluation of Anorganic Bovine Bone and Injectable Biphasic Calcium Phosphate in Humans: A Randomized Clinical Trial
Reprinted from: *Int. J. Mol. Sci.* **2023**, *24*, 5539, doi:10.3390/ijms24065539 . . . . . **71**

Chien-Chou Lin, Li-Hsuan Chiu, Walter H. Chang, Cheng-An J. Lin, Ruei-Ming Chen and Yuan-Soon Ho et al.
A Non-Invasive Method for Monitoring Osteogenesis and Osseointegration Using Near-Infrared Fluorescent Imaging: A Model of Maxilla Implantation in Rats
Reprinted from: *Int. J. Mol. Sci.* **2023**, *24*, 5032, doi:10.3390/ijms24055032 . . . . . **91**

Agata Szczesio-Wlodarczyk, Izabela M. Barszczewska-Rybarek, Marta W. Chrószcz-Porebska, Karolina Kopacz, Jerzy Sokolowski and Kinga Bociong
Can Modification with Urethane Derivatives or the Addition of an Anti-Hydrolysis Agent Influence the Hydrolytic Stability of Resin Dental Composite?
Reprinted from: *Int. J. Mol. Sci.* **2023**, *24*, 4336, doi:10.3390/ijms24054336 . . . . . **101**

Min-Kyung Ji, Seon-Ki Lee, Hee-Seon Kim, Gye-Jeong Oh, Hoonsung Cho and Hyun-Pil Lim
Assessment of Inhibition of Biofilm Formation on Non-Thermal Plasma-Treated TiO_2 Nanotubes
Reprinted from: *Int. J. Mol. Sci.* **2023**, *24*, 3335, doi:10.3390/ijms24043335 . . . . . **119**

Sanako Makishi, Taisuke Watanabe, Kotaro Saito and Hayato Ohshima
Effect of Hydroxyapatite/-Tricalcium Phosphate on Osseointegration after Implantation into Mouse Maxilla
Reprinted from: *Int. J. Mol. Sci.* **2023**, *24*, 3124, doi:10.3390/ijms24043124 . . . . . **133**

Anastasia Beketova, Emmanouil-Georgios C. Tzanakakis, Evangelia Vouvoudi, Konstantinos Anastasiadis, Athanasios E. Rigos and Panagiotis Pandoleon et al.
Zirconia Nanoparticles as Reinforcing Agents for Contemporary Dental Luting Cements: Physicochemical Properties and Shear Bond Strength to Monolithic Zirconia
Reprinted from: *Int. J. Mol. Sci.* **2023**, *24*, 2067, doi:10.3390/ijms24032067 . . . . . **147**

Toshikatsu Suzumura, Takanori Matsuura, Keiji Komatsu and Takahiro Ogawa
A Novel High-Energy Vacuum Ultraviolet Light Photofunctionalization Approach for Decomposing Organic Molecules around Titanium
Reprinted from: *Int. J. Mol. Sci.* **2023**, *24*, 1978, doi:10.3390/ijms24031978 . . . . . **167**

Andreas Wiessner, Torsten Wassmann, Johanna Maria Wiessner, Andrea Schubert, Bernhard Wiechens and Tristan Hampe et al.
In Vivo Biofilm Formation on Novel PEEK, Titanium, and Zirconia Implant Abutment Materials
Reprinted from: *Int. J. Mol. Sci.* **2023**, *24*, 1779, doi:10.3390/ijms24021779 . . . . . **185**

Marta W. Chrószcz-Porebska, Izabela M. Barszczewska-Rybarek and Grzegorz Chladek
Physicochemical Properties of Novel Copolymers of Quaternary Ammonium UDMA Analogues, Bis-GMA, and TEGDMA
Reprinted from: *Int. J. Mol. Sci.* **2023**, *24*, 1400, doi:10.3390/ijms24021400 . . . . . **197**

Denver P. Linklater, Phuc H. Le, Arturo Aburto-Medina, Russell J. Crawford, Shane Maclaughlin and Saulius Juodkazis et al.
Biomimetic Nanopillar Silicon Surfaces Rupture Fungal Spores
Reprinted from: *Int. J. Mol. Sci.* **2023**, *24*, 1298, doi:10.3390/ijms24021298 . . . . . **211**

Zdravko Schauperl, Luka Ivanković, Leonard Bauer, Sanja Šolić and Marica Ivanković
Effects of Different Surface Treatments of Woven Glass Fibers on Mechanical Properties of an Acrylic Denture Base Material
Reprinted from: *Int. J. Mol. Sci.* **2023**, *24*, 909, doi:10.3390/ijms24020909 . . . . . **227**

Erika Dunavári, Gergely Berta, Tamás Kiss, József Szalma, Márk Fráter and Katalin Böddi et al.
Effect of Pre-Heating on the Monomer Elution and Porosity of Conventional and Bulk-Fill Resin-Based Dental Composites
Reprinted from: *Int. J. Mol. Sci.* **2022**, *23*, 16188, doi:10.3390/ijms232416188 . . . . . **239**

Takanori Matsuura, Keiji Komatsu and Takahiro Ogawa
N-Acetyl Cysteine-Mediated Improvements in Dental Restorative Material Biocompatibility
Reprinted from: *Int. J. Mol. Sci.* **2022**, *23*, 15869, doi:10.3390/ijms232415869 . . . . . **259**

Shih-Kai Lin, Yi-Fan Wu, Wei-Jen Chang, Sheng-Wei Feng and Haw-Ming Huang
The Treatment Efficiency and Microbiota Analysis of *Sapindus mukorossi* Seed Oil on the Ligature-Induced Periodontitis Rat Model
Reprinted from: *Int. J. Mol. Sci.* **2022**, *23*, 8560, doi:10.3390/ijms23158560 . . . . . **275**

Lohitha Kalluri and Yuanyuan Duan
Parameter Screening and Optimization for a Polycaprolactone-Based GTR/GBR Membrane Using Taguchi Design
Reprinted from: *Int. J. Mol. Sci.* **2022**, *23*, 8149, doi:10.3390/ijms23158149 . . . . . **289**

Marjan Kheirmand Parizi, Katharina Doll, Muhammad Imran Rahim, Carina Mikolai, Andreas Winkel and Meike Stiesch
Antibacterial and Cytocompatible: Combining Silver Nitrate with Strontium Acetate Increases the Therapeutic Window
Reprinted from: *Int. J. Mol. Sci.* **2022**, *23*, 8058, doi:10.3390/ijms23158058 . . . . . **303**

Noala Vicensoto Moreira Milhan, William Chiappim, Aline da Graça Sampaio, Mariana Raquel da Cruz Vegian, Rodrigo Sávio Pessoa and Cristiane Yumi Koga-Ito
Applications of Plasma-Activated Water in Dentistry: A Review
Reprinted from: *Int. J. Mol. Sci.* **2022**, *23*, 4131, doi:10.3390/ijms23084131 . . . . . **321**

Fabien Kawecki, Jessica Jann, Michel Fortin, François A. Auger, Nathalie Faucheux and Julie Fradette
Preclinical Evaluation of BMP-9-Treated Human Bone-like Substitutes for Alveolar Ridge Preservation following Tooth Extraction
Reprinted from: *Int. J. Mol. Sci.* **2022**, *23*, 3302, doi:10.3390/ijms23063302 . . . . . **347**

Filip Kuśmierczyk, Aleksandra Fiołek, Alicja Łukaszczyk, Agnieszka Kopia, Maciej Sitarz and Sławomir Zimowski et al.
Microstructure and Selected Properties of Advanced Biomedical n-HA/ZnS/Sulfonated PEEK Coatings Fabricated on Zirconium Alloy by Duplex Treatment
Reprinted from: *Int. J. Mol. Sci.* **2022**, *23*, 3244, doi:10.3390/ijms23063244 . . . . . **365**

Sung-Un Kang, Chul-Ho Kim, Hee-Kyung Kim, Ye-Won Yoon, Yu-Kwon Kim and Seung-Joo Kim
Effect of the Plasma Gas Type on the Surface Characteristics of 3Y-TZP Ceramic
Reprinted from: *Int. J. Mol. Sci.* **2022**, *23*, 3007, doi:10.3390/ijms23063007 . . . . . **387**

Marcel Ferreira Kunrath and Christer Dahlin
The Impact of Early Saliva Interaction on Dental Implants and Biomaterials for Oral Regeneration: An Overview
Reprinted from: *Int. J. Mol. Sci.* **2022**, *23*, 2024, doi:10.3390/ijms23042024 . . . . . **401**

About the Editor

Mary Anne Melo

Mary Anne Melo (DDS, MSc, Ph.D., Fellow ADM) is a Clinical Professor at the University of Maryland School of Dentistry and currently serves as Chair of the Department of General Dentistry. Dr. Melo applies her experience as a dentist and dental materials researcher to advance the development of smart and bioactive restorative materials. Her clinical areas of interest focus on minimally invasive dentistry, the management of patients with high-risk caries, and esthetic dentistry. Her research has focused chiefly on anticaries approaches for caries-inhibiting, antibacterial, or remineralization functionalities. Her research group has pioneered the investigation of antibacterial and remineralizing dental adhesives and resin composites. Dr. Melo is a current member of the Academy of Operative Dentistry, the International Association for Dental Research, the American Academy of Cariology, and the American Academy of Cosmetic Dentistry. Dr. Melo is a co-inventor on two patents, has edited three books, and has published more than 200 papers in the area of dental materials. Several grants support her research. She lectures nationally and internationally on diverse topics in restorative dentistry.

Preface to ”Dental Biomaterials: From Fundamental Principles to Clinical Applications”

Despite significant advancements in dental biomaterials, there are still unmet needs in the field of dentistry. The oral environment is highly complex, requiring dental materials to perform effectively under diverse physiological conditions. Therefore, it is crucial to establish methods for evaluating the performance of these materials in physiologically intricate environments that simulate real-world intraoral conditions.

Furthermore, the evolution of preventive and therapeutic strategies aimed at enhancing oral health outcomes is an ongoing process. Innovative approaches are being developed to prevent and treat common oral diseases, such as dental caries, periodontitis, and oral cancer. Researchers are also exploring the potential applications of biomaterials in regenerative dentistry, including stimulating bone growth and repairing damaged oral tissues.

Collectively, continuous research and development in dental materials and biomaterials offer promising prospects for enhancing oral health outcomes. However, it is essential to sustain ongoing research efforts to fully capitalize on their potential and effectively address the unmet needs within the dental field.

In the Special Issue titled “Dental Biomaterials: From Fundamental Principles to Clinical Applications,“ a range of valuable findings have emerged from diverse sources, including in vitro experiments and clinical trials. These insights have deepened our understanding of the biology of oral diseases, leading to the development of innovative treatment approaches such as targeted drug delivery systems and gene therapy. Clinical trials have also provided evidence regarding the efficacy and safety of these novel treatment options.

Overall, these technological and treatment advancements offer hope for improved management of oral diseases. However, it is crucial to emphasize the necessity for ongoing research and development to fully harness the potential of these innovations and make substantial progress in enhancing oral health outcomes.

Mary Anne Melo
Editor

International Journal of
Molecular Sciences

MDPI

Article

Dental Material Selection for the Additive Manufacturing of Removable Complete Dentures (RCD)

Dmitry I. Grachev [1], Evgeny A. Chizhmakov [2], Dmitry Yu. Stepanov [3], Dmitry G. Buslovich [4], Ibragim V. Khulaev [5], Aslan V. Deshev [6], Levon G. Kirakosyan [1], Anatoly S. Arutyunov [2], Svetlana Yu. Kardanova [5], Konstantin S. Panin [7] and Sergey V. Panin [3,*]

1 Digital Dentistry Department, A.I. Yevdokimov Moscow State University of Medicine and Dentistry, 127473 Moscow, Russia
2 Prosthodontics Technology Department, A.I. Yevdokimov Moscow State University of Medicine and Dentistry, 127473 Moscow, Russia
3 Laboratory of Mechanics of Polymer Composite Materials, Institute of Strength Physics and Materials Science of Siberian Branch of Russian Academy of Sciences, 634055 Tomsk, Russia
4 Laboratory of Nanobioengineering, Institute of Strength Physics and Materials Science of Siberian Branch of Russian Academy of Sciences, 634055 Tomsk, Russia
5 Institute of Dentistry and Maxillofacial Surgery, Kabardino-Balkarian State University Named after H.M. Berbekov, 360004 Nalchik, Russia
6 Laboratory of Digital Dentistry, Kabardino-Balkarian State University Named after H.M. Berbekov, 360004 Nalchik, Russia
7 Department of Chemical Physics, Institute for Laser and Plasma Technologies, National Research Nuclear University MEPhI, 115409 Moscow, Russia
* Correspondence: svp@ispms.ru

Abstract: This research addresses the development of a formalized approach to dental material selection (DMS) in manufacturing removable complete dentures (RDC). Three types of commercially available polymethyl methacrylate (PMMA) grades, processed by an identical Digital Light Processing (DLP) 3D printer, were compared. In this way, a combination of mechanical, tribological, technological, microbiological, and economic factors was assessed. The material indices were calculated to compare dental materials for a set of functional parameters related to feedstock cost. However, this did not solve the problem of simultaneous consideration of all the material indices, including their significance. The developed DMS procedure employs the extended VIKOR method, based on the analysis of interval quantitative estimations, which allowed the carrying out of a fully fledged analysis of alternatives. The proposed approach has the potential to enhance the efficiency of prosthetic treatment by optimizing the DMS procedure, taking into consideration the prosthesis design and its production route.

Keywords: PMMA; additive manufacturing (AM); material selection; analytic hierarchy process (AHP); VIKOR; multicriteria decision-making (MCDM); material index; ranking

Citation: Grachev, D.I.; Chizhmakov, E.A.; Stepanov, D.Y.; Buslovich, D.G.; Khulaev, I.V.; Deshev, A.V.; Kirakosyan, L.G.; Arutyunov, A.S.; Kardanova, S.Y.; Panin, K.S.; et al. Dental Material Selection for the Additive Manufacturing of Removable Complete Dentures (RCD). *Int. J. Mol. Sci.* **2023**, *24*, 6432. https://doi.org/10.3390/ijms24076432

Academic Editor: Lia Rimondini

Received: 28 February 2023
Revised: 20 March 2023
Accepted: 27 March 2023
Published: 29 March 2023

Copyright: © 2023 by the authors. Licensee MDPI, Basel, Switzerland. This article is an open access article distributed under the terms and conditions of the Creative Commons Attribution (CC BY) license (https://creativecommons.org/licenses/by/4.0/).

1. Introduction

Material selection is a relevant issue that is solved in various branches of science and technology, inter alia dental treatment (for example, manufacturing RCD). In this case, components are calculated according to the strength criterion (by the finite element method [1], as an example) and assigned margin factors. Therefore, reference data (primarily, manufacturers' data sheets) should be taken into account. Typically, the most appropriate materials have to be selected for various functional applications. For this purpose, (i) the elastic modulus is considered to ensure a required stiffness level, (ii) crack resistance is controlled by fracture toughness, and (iii) corrosion resistance can be characterized either qualitatively or quantitatively according to the parameters measured by strictly regulated industrial standards, etc. In addition to physical and mechanical characteristics, designers consider

(i) the material manufacturability (including the possibility of 3D printing, CAD milling, etc.), (ii) the variation of properties under heat treatment (for example, annealing)/post-build processing (additional polymerization, as an example), and (iii) machinability with various types of tools (grinding), etc. [2].

DMS with such a formalized approach can be solved if several required (target) characteristics are considered, among them: (a) physical and mechanical; (b) biological; (c) functional (color, polishability, roughness, etc.); (d) technological (processing methods, machinability, warpage); (e) cost, etc. Nevertheless, medical treatment tactics for the use of (temporal) dental prosthetics are a multifactorial problem. Therefore, the mission of DMS, including prosthesis manufacturing methods, becomes more complex. In practice, it is greatly affected by the mostly subjective relationships in the group "dentist–dental technician–patient" [3].

Despite the necessity of using temporary dentures, the attitude of maxillo-facial surgeons, dentists and patients to such structures is rather dismissive. To this end, breakdowns and complications are frequent due to medical and technical errors. In practical dentistry, there is a need for enduring polymer prostheses in the treatment of complex dental pathologies that requires an accurate and long-term examination. In particular, this is relevant for diagnosing gnathic problems, especially in cases of muscular–articular dysfunction. Therefore, such therapeutic and prophylactic orthopedic constructions play an important role in first-stage rehabilitation measures. These include periods of (i) temporary filling of a defect in the dentition, (ii) programming a new occlusion, (iii) osseointegration of dental implants, etc. [4–6]. Hence, the practice of using temporary dentures remains very important.

The State of the Art in the Additive Manufacturing of RDC

RCDs for edentulous patients are typically made of PMMA [7]. However, a high concentration of free monomer (methyl methacrylate) and the possible development of allergic stomatitis is a significant drawback of this material [8].

Up-to-date CAD/CAE/CAM systems are frequently implemented into dental practice. They provide (i) great shape and dimensional accuracy, (ii) reproducibility, (iii) minimization of medical and technical routine work, (iv) cost reduction, and therefore (v) the availability of highly efficient dentures and facial epithesis [9,10]. However, additive manufacturing (AM) demands novel classes of polymers. In addition, the CAM process (as a subtractive method) possesses the following drawbacks: (i) material waste due to grinding and milling, (ii) wear of cutting tools and expensive equipment, (iii) restrictions on the sizes of the blanks (in the form of blocks) which does not allow the fabrication, for example, of volumetric jaw prostheses-obturators [11].

In this way, 3D printing is an actual trend in dental practice. Studies of physical–mechanical characteristics and aesthetics of such volumetric structures are highly controversial when polymeric prostheses or medical devices must be designed for long-term use (for example, in the case of parafunctional phenomena, or when an occlusion is to be reprogrammed) [12]. The quality of the AM structures depends on 3D printing parameters, building accuracy, shape, and dimensions of a virtual model, among many others [13]. Currently, a wide variety of 3D printers are available, including various physical principles of layer-by-layer deposition. To this end, prosthesis accuracy is a tangible drawback [14,15]. However, the prospects of AM in dentistry are beyond dispute [16].

Laser stereolithography apparatus (SLA) employs liquid photopolymers that are cured with a laser beam or an ultraviolet (UV) source of a certain wavelength. Product quality is affected by the dimensions of a prototype, the angle of the 3D-printed object related to the platform, the locations of supports, etc. Besides economic efficiency, such procedures are convenient for planning surgical operations with parts of a complex shape and structure [17].

The durability of (temporary) RDC depends on their design features, physical–chemical nature of the structural materials, and production routes [18]. Karaokutan et al. studied the influence of manufacturing techniques for provisional PMMA-based crowns on their

strength characteristics [19]. The authors reported that computer-controlled milling improves the strength of the temporary RDC, compared to those fabricated by a direct manufacturing method. Alt et al. presented a comparative study of the strength characteristics of temporary polymer bridges made by conventional and digital technologies and concluded that the manufacturing methods substantially affect their values [20].

Dikova showed that high dimensional accuracy and surface smoothness of fixed dentures can be achieved when the vertical axis of teeth coincides with the *Z* axis of a platform [21]. At the same time, the number of supports should be increased (at least four per tooth) to reduce warpage in 3D printing and post-build polymerization. Thus, to ensure a high-quality product in designing and planning the process, it is important to consider the following: (i) printer characteristics, (ii) model placement, (iii) number of supports, and (iv) dimensional variation during and after polymerization.

Li suggested that the high-quality manufacture of temporary polymer prostheses be provided by the SLA method based on temperature-controlled layer-by-layer deposition in 3D printing (TCMIP-SL) [22]. The TCMIP-SL process contributes to the deposition of high-viscosity polymers with excellent accuracy at high speeds.

Based on the above, it can be stated that searching for dental AM materials with improved quality has moved into the phase of developing optimal dental technologies that use industrial polymers and help to minimize fabrication process disruptions that deteriorate a product's characteristics.

This paper addresses the development of a formalized approach for DMS and the additive manufacturing of RCD. This issue was solved using a decision-making methodology. Rational ranking was illustrated on examples of three types of commercially available PMMA grades processed by the identical DLP method. The paper is structured as follows. Section 2 describes the 3D printing method and techniques for evaluating the key properties of the AM blanks. Section 3 contains the measurement results for various characteristics of dental materials; the calculation of the material indices is also provided. Section 4 proposes the approach to multicriteria optimization in DMS and examples of their ranking as well. Section 5 discusses the obtained data. The authors proposed, based on examples of certain industrially produced brands, an approach to (or the tool for) brand ranking; the variability of the results was emphasized. Recommendations to use one or another brand of dental materials remain for individual consideration.

2. Materials and Methods

2.1. Three-dimensional Printing (Materials and Equipment)

The test samples were fabricated in two stages: modeling and 3D printing. Virtual master models were created using the ExoCad Gateway 3.0 software (Align Technology, San Jose, CA, USA). The final files of the completed sample models (in the "*.STL" format) were imported into the (slicer) software package for the 3D printing preparation. Then, (i) the models were positioned relative to the plane of the 3D printer platform, (ii) the supports were placed, (iii) the models were divided into layers, and (iv) the 3D printing parameters were adjusted in line with recommendations of the feedstock manufacturers (Table 1).

Table 1. The data on the 3D printing materials and methods.

Material	FreePrint, Temp 385, A2	Nolatech	Dental Sand, A1–A2
Designation in the text	FP	NT	DS
Manufacturer	DETAX GmbH & Co. KG (Germany)	Nolatech (Russia)	Harz Labs (Russia)
3D printer		NextDent 5100; (3DSystem, USA)	
Software for constructing digital models		3DSprint (3DSystem, USA)	
3D printing technology		Digital Light Processing (DLP)	
Thickness of a single printed layer		50 μm	
Post-build processing	Anycubic Wash & Cure 2.0 (Cleaning with 70% isopropyl alcohol for 3 min, UV curing)		

2.2. Property Evaluation Methods

Comparative studies of the mechanical, tribological, technological, biological, and economic characteristics of dental materials were performed. Mechanical tests were carried out for tension, compression, and three-point bending. In this paper, only the three-point bending data are reported, since they are more informative for the dental materials [23]. The key parameters to be evaluated are flexural strength, flexural modulus, and flexural strain.

2.2.1. Three-Point Bending Tests

The samples took the form of rectangular plates with dimensions of 25 × 2 × 2 mm following the Russian State Standard GOST 31574-2012. An "Instron 5982" electromechanical testing machine (Illinois Tool Works Inc., Glenview, IL, USA) was used with a crosshead speed of 0.75 mm/min. The force gauge had an upper measurement limit of ± 5000 N (series 2580–108). The span was 20 mm. Before testing, the samples were conditioned in distilled water at a temperature of 37 ± 1 °C for 24 h. The tests were carried out until the sample failure.

2.2.2. Impact Strength Tests

The a_n Charpy impact strength of specimens without a notch was measured with a "KM-5" pendulum impact tester ("ZIP" LLC, Ivanovo, Russia). Their sizes were 80 × 10 × 4 mm according to the Russian State Standard GOST 4647-2015. There were four specimens of each material. After the tests, the average a_n values were calculated.

2.2.3. Biological Tests

For biological tests, the samples were in the form of disks 5 mm in diameter and 1 mm thick. The attachment points for supports were finished with the polishes of various abrasiveness in the following sequence: 9400.204.030, 9401.204.030, 9402.204.030 (Komet, Gebr. Brasseler GmbH & Co. KG, Germany). The time lag from sample fabrication to the biological tests did not exceed 72 h. Immediately before the start of the in vitro experiment, the samples were cleaned in an ultrasonic bath for 15 min, after they were treated with 70% ethanol.

To carry out the process of the primary adhesion of microorganisms, the samples were placed in test tubes with a suspension of the test strains of the corresponding species at a standard concentration. We used the optical turbidity standard of 0.5 U McFarland, which corresponded to 10^9 colony-forming units (CFU)/mL for bacterial cultures and 10^8 CFU/mL for yeast ones. After quantitative inoculation, bacteria were cultivated under anaerobic conditions at a temperature of 37 °C for 7 days, and fungi—at room temperature (25 °C) for 2 days. Adhesion indices were determined as a ratio of the decimal logarithm of the number of CFU obtained after sonication of the test samples to the decimal logarithm of the CFU of the initial microbial suspension. The authors described the experimental technique in detail in their previous paper [7].

2.2.4. Tribological Tests

In the point tribological contact according to the "ball-on-disk" scheme, the dry sliding friction tests were carried out at a load (P) of 5 N and a sliding speed (V) of 0.3 m/s. A "CH 2000" tribometer (CSEM, Neuchâtel, Switzerland) was used following ASTM G99. The tribological tests were conducted using a ceramic counterpart (a ball made of the ZrO_2) with a diameter of 6 mm and the R_a surface roughness of 0.02 μm. The latter was assessed with the "New View 6200" optical interferential profilometer (Zygo Corporation, Middlefield, CT, USA). The testing distance was 1 km and the tribological track radius was 10 mm.

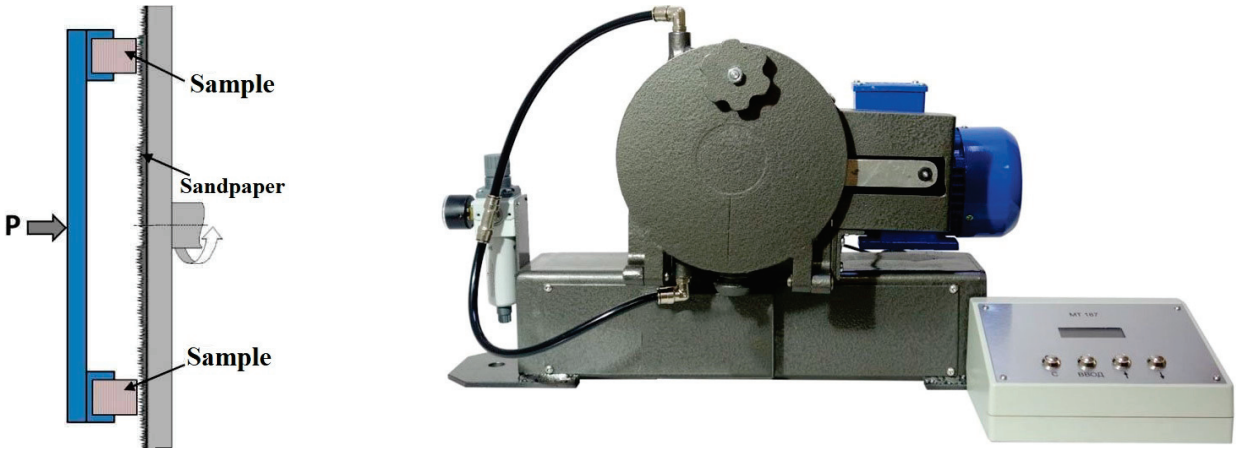
In the linear tribological contact according to the "block-on-ring" scheme, dry sliding friction tests were performed using a "2070 SMT-1" friction testing machine (Tochpribor Production Association, Ivanovo, Russia). A load (P) was 60 N, while a sliding speed (V) was 0.3 m/s. A ceramic counterpart was made of an Al_2O_3 ring with a diameter of

35 mm and a width of 11 mm. The R_a surface roughness was 0.20 µm. The counterpart temperatures were assessed with the "CEM DT-820" non-contact infrared (IR) thermometer (Shenzhen Everbest Machinery Industry Co., Ltd., Shenzhen, China).

WR levels were determined by measuring the width and depth of wear tracks according to a stylus profilometry (KLA-Tencor, Milpitas, CA, USA), followed by multiplication by their length. They were calculated taking into account load and distance values:

$$\text{Wear rate } = \frac{\text{volume loss } (\text{mm}^3)}{\text{load } (\text{N}) \times \text{sliding distance } (\text{m})} \quad (1)$$

In the flat tribological contact, abrasion wear tests were conducted. The "MI-2" abrasion testing machine (Metroteks LLC, Moscow, Russia) was used to determine the weight loss values at abrasion by fixed particles, according to the "polymer pin-on-abrasive disk" scheme (Figure 1b), regulated by the Russian State Standard GOST 426-77. The dimensions of the samples were 8 × 10 × 8 mm. The average grain size of an abrasive paper (P1000) was ~17 µm. The angular sliding velocity was 40 rpm, and the load was 10 N. The test scheme is shown in Figure 1a.



(**a**) (**b**)

Figure 1. A scheme of the abrasive wear tests (**a**) and the "MI-2" abrasion testing machine (**b**).

Weight loss was determined every 5 min during the total test duration of 20 min. The samples were weighed using the "Sartogosm LV 120-A" (Sartogosm LLC, Saint Petersburg, Russia) with an accuracy of 0.1 mg.

2.2.5. Polishability (via Roughness)

The protocol for grinding and polishing in the sample preparation procedure is presented below.

1. Surface treatment with a carbide cutter for polymers until the required configuration or shape.
2. Surface treatment with a carbide cutter for polymers to remove surface irregularities.
3. Sanding with 180–220 grit sandpaper for extra fine finishing.
4. Finishing with a felt and a moistened polishing powder.
5. Brushing with a grinder using a coarse bristle and a moistened polishing powder for a smooth surface.
6. Processing with a grinder using a thread brush and a fine-grained polishing paste to a mirror finish.

The R_a surface roughness was assessed with the "New View 6200" optical interferential profilometer (Zygo Corporation, Middlefield, CT, USA).

3. Results

3.1. Mechanical Properties

The mechanical properties of the SLA 3D-printed PMMA samples, registered in the three-point bending tests, are presented in Table 2. For the Dental Sand (DS), the flexural strength and strain values exceed by ~10 % and two times the corresponding characteristics for Free Point (FP), as well as by 2.5 and 3.6 times for Nolatech (NT), respectively. For all the studied PMMA grades, the flexural modulus values were at the same level of about 2.7 ± 0.1 GPa.

Table 2. The mechanical properties of the 3D printed PMMA of the studied grades.

No.	Material	Flexural Modulus, GPa	Flexural Strength, MPa	Flexural Strain, %
1	FP	2.7 ± 0.6	90.7 ± 5.9	2.7 ± 0.6
2	NT	2.8 ± 0.1	41.7 ± 4.5	1.5 ± 0.1
3	DS	2.6 ± 0.3	104.2 ± 2.7	5.4 ± 1.2

Since PMMA RCD could experience impact in use (for example, being accidentally dropped on ceramic tiles), their impact strength could be an important performance characteristic. The conducted Charpy impact tests showed that a_n values were 0 J/cm^2 at the minimum applied impact energies regardless of the PMMA grade. Thus, it was impossible to differentiate the materials by this parameter. Please note that an increase in impact strength could be achieved by loading PMMA with fibers or nanoparticles in various concentrations, but this would change the manufacturability of the materials, including the possibility of their AM processing [24–26].

3.2. Biological Properties

The adhesion indices (AIs) of the normal, periodontopathogenic, and fungal microbiota to the studied materials are presented in Table 3. In the normal microbiota case, no differences were found between the FP (0.55 ± 0.06) and the NT (0.56 ± 0.06). For the DS, a value of 0.43 ± 0.06 was noticeably lower than those for the other two materials. For the periodontopathogenic microbiota, an AI value of 0.42 ± 0.05 for the NT was noticeably higher than those for the DS and the FP, for which no significant differences were found (AI = 0.34 ± 0.05). In the fungal microbiota case, some variations were observed for all the materials. The maximum level was typical for the NT (AI = 0.49 ± 0.05), and the minimum was detected for the DS (AI = 0.34 ± 0.05).

Table 3. The adhesion indices of the normal, periodontopathogenic, and fungal microbiota to the materials under study.

No.	Material	Normal	Periodontopathogenic	Fungal
1	FP	0.55 ± 0.06	0.34 ± 0.05	0.43 ± 0.02
2	NT	0.56 ± 0.06	0.42 ± 0.05	0.49 ± 0.05
3	DS	0.43 ± 0.06	0.34 ± 0.05	0.34 ± 0.05

3.3. Tribological Properties

3.3.1. The Point Tribological Contact

The point tribological contact involved a local impact of the ceramic ball on the polymer sample (in the form of a disk) under dry sliding friction conditions. Table 4 presents the values of the tribological properties of the materials under study. The FP and DS had the lowest coefficient of friction (CoF) values (0.276 and 0.271, respectively), while it was higher by 10 % (0.303) for the NT (Figure S1). The wear rate (WR) levels were also evaluated. For the FP, it was half that for the NT and DS. Roughness on the wear friction track surfaces was approximately at the same level of 0.19 μm regardless of the PMMA grade.

Table 4. The tribological properties of the PMMA dental materials in the point tribological contact.

No.	Material	Coefficient of Friction, CoF	Wear Rate, WR, $mm^3/N \cdot m$, 10^{-5}	Wear Track Roughness, Ra, μm
1	FP	0.276 ± 0.019	13.52 ± 1.01	0.191 ± 0.030
2	NT	0.303 ± 0.025	26.97 ± 0.91	0.204 ± 0.026
3	DS	0.271 ± 0.022	28.29 ± 0.98	0.179 ± 0.015

3.3.2. The Linear Tribological Contact

In the linear tribological contact, the ring-shaped ceramic counterpart slid relative to the stationary polymer samples, along the "non-renewable" surface of the wear tracks. Therefore, the specific pressure was noticeably lower compared to that in the point tribological contact. As a result, the average CoF values were lower by ~3 times for all the studied materials (0.131, 0.096, and 0.122, respectively, according to Table 5). The NT had the lowest WR level of 0.078×10^{-6} $mm^3/N \cdot m$, which was 2.3 times lower compared to that for the DS and 1.5 times than that for the FP (Figure S2). In contrast to the point tribological contact, the WR values were an order of magnitude lower (10^{-5} and 10^{-6}, respectively).

Table 5. The tribological properties of the PMMA dental materials in the linear tribological contact.

No.	Material	Coefficient of Friction CoF	Wear Rate, WR, $mm^3/N \cdot m$, 10^{-6}	Temperature, °C
1	FP	0.131 ± 0.018	0.120 ± 0.007	31.43 ± 1.50
2	NT	0.096 ± 0.016	0.078 ± 0.013	33.31 ± 0.21
3	DS	0.122 ± 0.018	0.176 ± 0.017	36.59 ± 0.99

3.3.3. The Flat Tribological Contact, Abrasive Wear

Since PMMA prostheses could be worn out by hard particles, abrasive wear tests were conducted according to the "polymer pin-on-abrasive disk" scheme. It was shown that the least wear (weight loss) was observed for the FP (0.12 mg) after 20 min of testing (with abrasive particles fixed on the non-renewable surface of the abrasive counterpart), which was 1.6 times less compared to that for the DS (0.19 mg) and 2.0 times less compared to the NT (0.25 mg) (Figure S3).

Table 6 summarizes the data on the WR values in the point, linear, and flat tribological contacts used to calculate the material indices.

Table 6. The summarized data on the WR values in the point, linear, and flat tribological contacts.

No.	Material	WR, Point Contact, $mm^3/N \cdot m$, 10^{-5}	WR, Linear Contact, $mm^3/N \cdot m$, 10^{-6}	(Abrasive) Weight Loss, Flat Contact, Δm, gr
1	FP	13.52 ± 1.01	0.120 ± 0.007	0.121 ± 0.01
2	NT	26.97 ± 0.91	0.078 ± 0.013	0.255 ± 0.01
3	DS	28.29 ± 0.98	0.176 ± 0.017	0.193 ± 0.01

3.4. Technological Properties

A significant number of the parameters could be qualified as "technological properties". Since the study deals with DMS concept development, to simplify the process, the authors limited themselves to only three ones (Table 7).

Table 7. The technological properties of 3D-printed PMMA materials.

No.	Material	Average Duration of 3D Printing and Post-Polymerization Processing, min	Roughness after Standard Polishing, Ra, μm	Warpage after 3D Printing (Quality)
1	FP	33 + 30 = 63	0.048 ± 0.005	–(0)
2	NT	33 + 50 = 88	0.049 ± 0.007	+(1)
3	DS	80 + 30 = 110	0.051 ± 0.003	–(0)

The first parameter was determined by the average duration of 3D printing and post-build polymerization processing. Its minimum value was typical for the FP (t = 63 min), while the maximum for the DS was (t = 110 min).

The second parameter was polishability, which was related to the ability of the 3D-printed PMMA products to achieve the required degree of gloss, determined by the surface roughness. In general, all the studied materials could be considered to be similar in terms of their values (R_a ~ 0.048–0.051 μm).

The third parameter was shape distortion (warpage) [27]. This was assessed qualitatively, being associated with the ability of a 3D-printed product to retain its shape after cooling. From this point of view, the NT was the only material characterized by warpage after 3D printing and post-build polymerization processing. To use these data as a quantitative criterion, this parameter was assigned at a level of 0 in the absence of the shape distortion, and otherwise it was 1.

3.5. Economic Indicator (Cost)

The financial aspects of manufacturing PMMA prostheses via 3D printing could also be assessed by numerous criteria, including costs of logistics, purchasing licenses, deployment of a particular type of 3D printer and its maintenance, and many others. Nevertheless, the authors implemented the only criterion, namely the feedstock cost, for simplification (since the sample fabrication was carried out with the same 3D printer). Quantitative data are given in Table 8 for all the materials under study.

Table 8. The price for the dental material feedstocks (February 2023).

No.	Material	Price for 1 kg, US Dollar
1	FP	USD 381
2	NT	USD 203
3	DS	USD 404

3.6. Ranking Materials by Indices

The following parameters were introduced in the study according to the concept of the material indices proposed by Ashby [2] (as a ratio of the data presented in Tables 2–7 to the feedstock costs in Table 8). The charts of the material indices are shown in Figure 2. Their values were obtained by dividing the factors by the feedstock costs and multiplying by 100, they are:

- M1 is the ratio of the mechanical properties to the feedstock cost (namely flexural modulus, flexural strength, and flexural strain);
- M2 is the ratio of the biological properties to the feedstock cost (all three types of the studied microbiota were considered);
- M3 is the ratio of the tribological properties to the feedstock cost (a wear resistance for all three schemes of the tribological tests);
- M4 is the ratio of the technological properties to the feedstock cost (the average duration of 3D printing and post-build polymerization processing, roughness after standard polishing, and warpage after 3D printing).

To this end, the use of the concept of material indices (Tables S1–S4) offered a clear tool for quantitative comparison of the dental materials in the case under study. Moreover, it was possible to choose (from the point of view of a user or an expert) a more or less significant one. However, the significance factor was very subjective, so the analysis had to be carried out either by considering the data in a multilevel space or using multicriteria optimization approaches [28].

In the first case, an efficient method could be implemented to reduce the dimension of the analyzed data space, e.g., down to two [29–32]. The solution using the second approach is introduced in the next section.

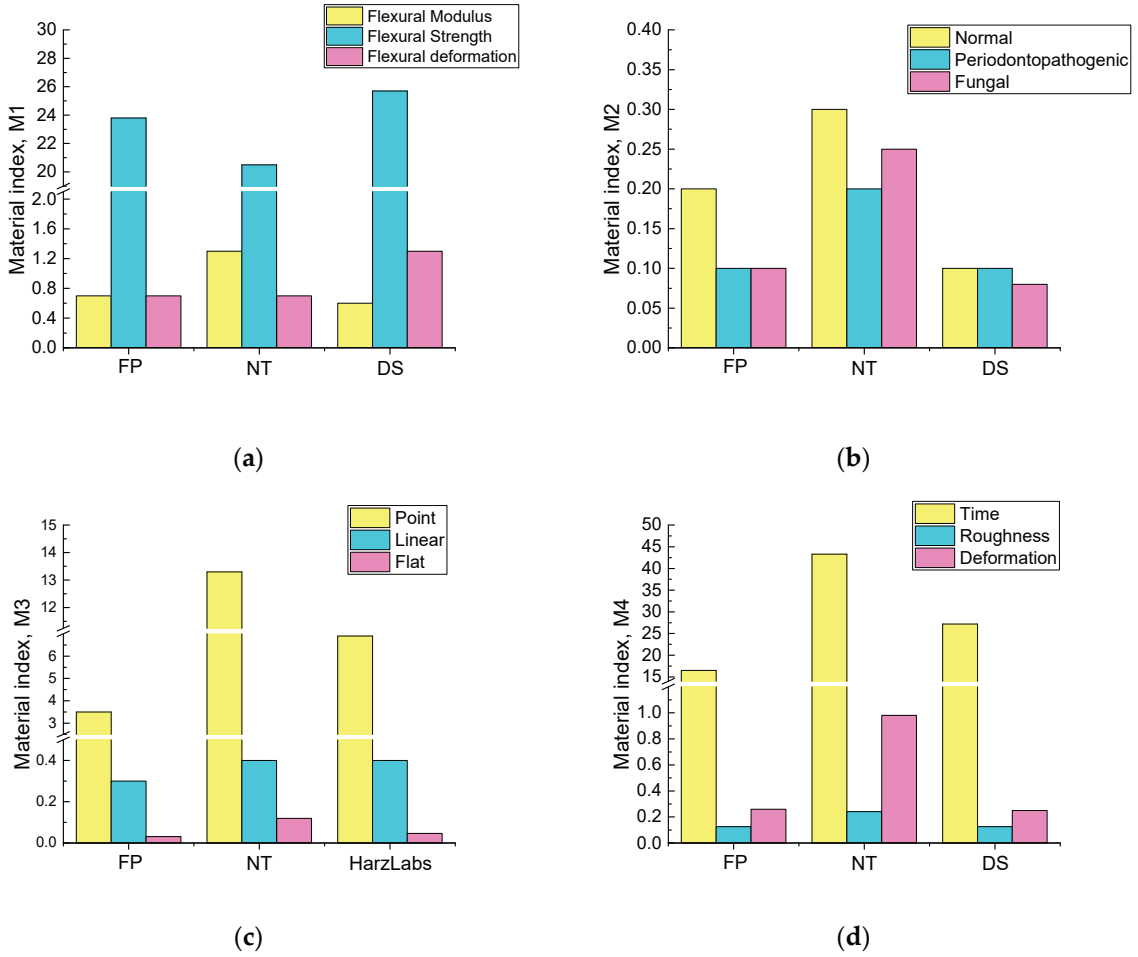


Figure 2. The material indices of the studied dental materials: M1 is the ratio of the mechanical properties to the feedstock cost (**a**), M2 is the ratio of the biological properties to the feedstock cost (**b**), M3 is the ratio of the tribological properties to the feedstock cost (**c**), M4 is the ratio of the technological properties to the feedstock cost (**d**).

4. Data Interpretation—The Combined AHP–Extended VIKOR Methods

In this section, some methods for DMS were compared, taking into account their production routes, which provided a trade-off between requirements for a set of mechanical, tribological, technological, biological, and economic criteria. The authors used informal subjective assessments of experts in the field of dental prosthetics, 3D printing, and the manufacture of CRD by subtractive and additive methods (primarily at A.I. Yevdokimov Moscow State University of Medicine and Dentistry, Russia).

4.1. The Problem Statement and Methods

Within the decision-making theory framework, the studied dental materials were qualified as decision alternatives with their designation as A_i. The factors characterizing each alternative were quantitative assessments and qualitative indicators. Based on the factors, if the criteria of (i) quality, (ii) usefulness, (iii) reliability, etc. were put forward, then the alternatives could be compared. The problem of choosing an alternative arose when there was a contradiction between the results of comparison or the absence of an alternative with the best indicators of the factors (an ideal combination of the characteristics) [33]. In this case, the problem of multicriteria optimization arose, namely the choice of a rational alternative from the available finite set, i.e., an alternative that was closest to an "ideal" option.

To date, a large number of methods for solving multicriteria optimization problems are known [34,35], i.e., Multicriteria Decision-Making (MCDM) methods. They include the

Analytic Hierarchy Process (AHP), Technique for Order of Preference by Similarity to Ideal Solution (TOPSIS), VIKOR, ÉLimination Et Choix Traduisant la REalité (ELECTRE), Preference Ranking for Organization Method for Enrichment Evaluation (PROMETHEE), etc. The key difference between these methods lies in the algorithms bringing different-scale, often qualitative, data into a single normalized space and the subsequent choice of a metric inside it. Examples of MCDM can be found both in tribology [36] and medicine [37–39], as well as in other areas [40,41]. Recently, MCDM, based on interval estimates, has been developed. For example, extended both TOPSIS and VIKOR methods were described, [42,43] while their advantages and drawbacks were reported in [44–46]. In this paper, the authors consider the possibility to implement the AHP and VIKOR ones for solving the problem of the DMS (PMMA-based) for manufacturing RCD (including the temporary ones).

4.2. Initial Data Analysis

All the data were divided into groups according to their physical meanings (Table 9). The mechanical, tribological, technological, biological, and economic groups included the experimental data in the form of interval quantitative estimations with different scales. The remaining groups were described by point quantitative values (in contrast to the interval ones). The exception was the "Warpage after 3D printing" technological factor. It was qualitative (binary) in nature and could be coded as "0" ("no warpage"), and as "1" ("might be distorted") in this case. Since the "Roughness after polishing" technological factor turned out to be identical for all the materials, it was not used in analysis and decision-making.

Table 9. The alternatives, their factors, and the criteria for the initial data analysis.

Group	Factor	Criterion	Alternative		
			A_1 FP	A_2 NT	A_3 DS
Mechanical	Flexural modulus, GPa	1	2.7 ± 0.6	2.8 ± 0.1	2.6 ± 0.3
	Flexural strength, MPa	1	90.7 ± 5.9	41.7 ± 4.5	104.2 ± 2.7
	Flexural strain, %	1	2.7 ± 0.6	1.5 ± 0.1	5.4 ± 1.2
Tribological	Wear rate, point contact, WR, $mm^3/N{\cdot}m$, 10^{-5}	–1	13.52 ± 1.01	26.97 ± 0.91	28.29 ± 0.98
	Wear rate, linear contact, WR, $mm^3/N{\cdot}m$, 10^{-6}	–1	0.120 ± 0.007	0.078 ± 0.013	0.176 ± 0.017
	(Abrasive) weight loss, flat contact, Dm, gr	–1	0.121 ± 0.01	0.255 ± 0.01	0.193 ± 0.01
Technological	Average duration of 3D printing and post-build polymerization processing, min.	–1	63	88	110
	Roughness after standard polishing, Ra, μm	–1	0.05 ± 0.00	0.05 ± 0.00	0.05 ± 0.00
	Warpage after 3D printing (quality)	–1	0	1	0
Biological	Normal, c.u.	–1	0.55 ± 0.06	0.56 ± 0.06	0.43 ± 0.06
	Periodontopathogenic, c.u.	–1	0.34 ± 0.05	0.42 ± 0.05	0.34 ± 0.05
	Fungal, c.u.	–1	0.43 ± 0.02	0.49 ± 0.05	0.34 ± 0.05
Economic	Price for 1 kg of feedstock, USD.	–1	USD 381	USD 203	USD 404

The material assessment criteria were selected separately for each factor and coded according to two principles: (+1) was the "utility" principle ("the more, the better") and (–1) was the "cost" one ("the less, the better").

4.3. Determination of Criteria Weights by the AHP Method

The AHP method was implemented to determine the weights (significance) of the criteria [47]. It referred to ones for supporting selection from a small number of alternatives based on pairwise comparisons. In this case, the formation of a matrix of the pairwise significance of the criteria was performed by an expert, and the calculation of the weights of the criteria was carried out by searching for the eigenvalues of this matrix. Due to the large number of the criteria and their different nature, the analysis of their pairwise significance was conducted within the groups, first, and between them, second. The following scale was used to assess the pairwise significance:

1—the criteria were the same;

3—the first criterion was slightly more important than the second one;

5—the first criterion was much more important than the second one;

7—the first criterion was undeniably more important than the second one, it was confirmed not only by experts but also in practice;

9—the first criterion was of absolutely greater importance than the second one.

Tables of the pairwise comparison within the groups were filled by experts from the respective fields. Therefore, despite such an assessment being subjective, the spread of opinions within the groups was low and not of interest to the research. The results of the pairwise comparison and the calculation of the weights are presented in Tables 10–13.

Table 10. The data on the paired comparison and the weights. Mechanical factors.

Criterion	Flexural Modulus	Flexural Strength	Flexural Strain	Weight
Flexural modulus	1.00	1.50	1.50	0.43
Flexural strength	0.67	1.00	1.00	0.29
Flexural strain	0.67	1.00	1.00	0.29

Table 11. The data on the paired comparison and the weights. Tribological factors.

Criterion	Wear Rate, Point Contact	Wear Rate, Linear Contact	(Abrasive) Weight Loss, Flat Contact	Weight
Wear rate, point contact	1	1	1	0.33
Wear rate, linear contact	1	1	1	0.33
(Abrasive) weight loss, flat contact	1	1	1	0.33

Table 12. The data on the paired comparison and the weights. Technological factors.

Criterion	Average Duration of 3D Printing and Post-Polymerization Processing	Warpage after 3D Printing (Quality)	Weight
Average duration of 3D printing and post-build polymerization processing	1	0.33	0.25
Warpage after 3D printing (quality)	3	1	0.75

Table 13. The data on the paired comparison and the weights. Biological factors.

Criterion (Microbiota)	Normal	Periodontopathogenic	Fungal	Weight
Normal	1	0.11	0.20	0.06
Periodontopathogenic	9	1	5	0.72
Fungal	5	0.20	1	0.22

4.4. Determination of the Criteria Weights by the VIKOR Method

To rank alternatives, the authors used the extended VIKOR method for the interval estimation [42]. The VIKOR method was based on the L_p metric for normalized functions [42,46]:

$$L_{pi} = \left\{ \sum_{j=1}^{n} \left[w_j \frac{f_j^* - f_{ij}}{f_j^* - f_j^-} \right]^p \right\}^{\frac{1}{p}} \quad (2)$$

where f_{ij} is a value of the j-th criterion for i-th alternative; f_j^* is the best value of j-th criterion among all the alternatives; f_j^- is the worst value of j-th criterion among all the alternatives; w_j is the weight of the j-th criterion. In calculations, two special cases of this metric (2) were applied:

$$\text{at } p = 1 \; S_i = \sum_{j=1}^{n} w_j \left[\frac{f_j^* - f_{ij}}{f_j^* - f_j^-} \right] \quad (3)$$

was the weighted Manhattan distance to the ideal alternative consisting of the "best" factor values,

$$\text{at } p = \infty \; R_i = \max_j w_j \left[\frac{f_j^* - f_{ij}}{f_j^* - f_j^-} \right] \quad (4)$$

was the weighted Chebyshev distance.

Additionally, a weighted and normalized value was introduced as an intermediate one of the above metrics:

$$Q_i = v \frac{S_i - S^*}{S^- - S^*} + (1 - v) \frac{R_i - R^*}{R^- - R^*} \quad (5)$$

where $S^* = \min_i S_i$, $S^- = \max_i S_i$, $R^* = \min_i R_i$, $R^- = \max_i R_i$, v is the weight of the "the majority of criteria" strategy.

The S, R, and Q values (3–5), could be referred to as the pessimistic, optimistic, and rational assessments of the alternative position in the set, respectively. Their values were in the range of 0 to 1. For the S, R, and Q values, their equality to zero was the ideal combination, while the equality to 1 was the worst option.

Ranking of the alternatives was carried out by ordering Q_i values and comparing their difference with the $\frac{1}{(m-1)}$ level, where m was the number of alternatives.

For the interval values of the factors, distances were assessed according to their boundaries [42]: $S_i = [S_{i1}, S_{i2}]$, $R_i = [R_{i1}, R_{i2}]$, $Q_i = [Q_{i1}, Q_{i2}]$. The calculation results are presented in Table S5. Figures 3 and 4 show the values of Q_1 and Q_2 at v = 0.5. The analysis of the lower boundary of the Q rational option reflected that the NT turned out to be the worst alternative, since it had the best factors only in the "economic" group out of the five ones. Both the FP and DS possessed the best factors in the two groups (Figure 3). However, there was no obvious advantage of the DS over the NT considering the Q top boundary (Figure 4).

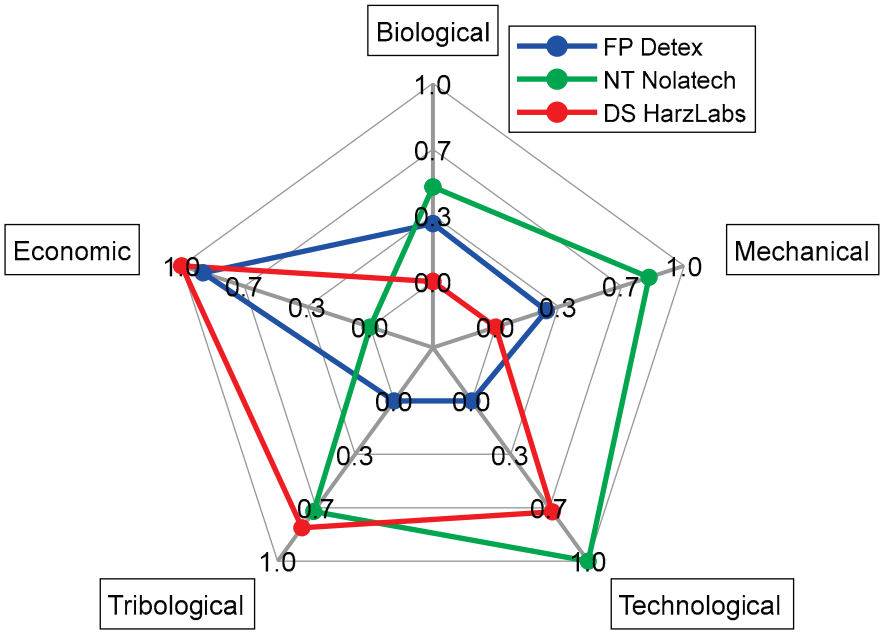


Figure 3. A radial diagram of Q_1 calculation by the groups of the factors.

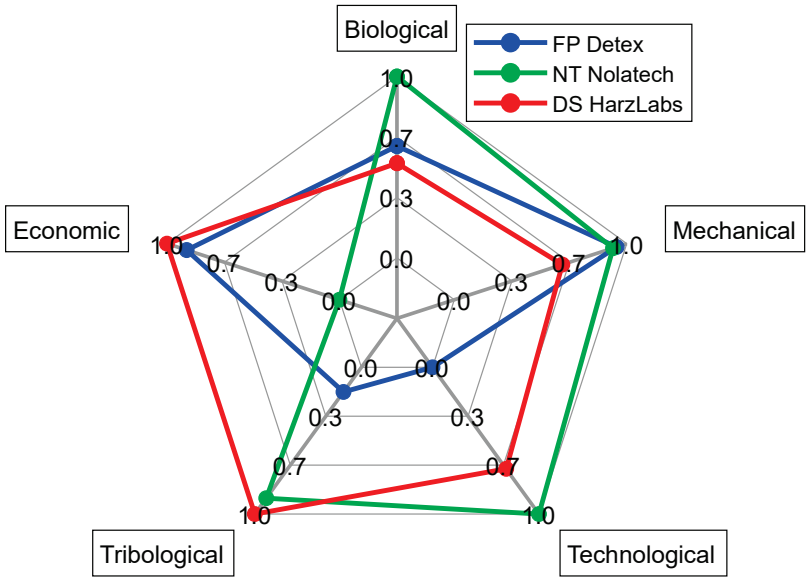


Figure 4. A radial diagram of Q_2 calculation by the groups of the factors.

4.5. Ranking Analysis for All Criteria

The stage of the paired comparison of the groups was the most subjective phase of the analysis. As a result, there can be achieved a coordinated decision of several experts from different subject areas at once or a single decision maker. In the latter case, the preference for the advantage of a characteristics group of a final product could be determined, for example, by the price-to-quality ratio. If the first four groups of the factors and the criteria corresponding to them characterized the product quality, then the quantitative expression of the price-to-quality indicator in the table of the pairwise comparison of the groups is proposed to express in the form of the following preference options (Table 14):

- Preference #1. The group equivalence assumption.
- Preference #2. The small advantage assumption for the "economic" group over all the others.
- Preference #3. The "economic" group was considered less significant relative to all the others.

Table 14. The paired comparison of the groups. Preference #1/Preference #2/Preference #3.

Group	Mechanical	Tribological	Technological	Biological	Economic
Mechanical	1/1/1	1/1/1	1/1/1	1/1/1	1/0.33/3
Tribological	1/1/1	1/1/1	1/1/1	1/1/1	1/0.33/3
Technological	1/1/1	1/1/1	1/1/1	1/1/1	1/0.33/3
Biological	1/1/1	1/1/1	1/1/1	1/1/1	1/0.33/3
Economic	1/3/0.33	1/3/0.33	1/3/0.33	1/3/0.33	1/1/1

Table 15 summarizes the results of the calculation of the weights by the AHP method of pairwise comparison for all the studied cases. As expected,

- the preference variability for the "economic" group affected the weight of the economic factor from the first rank (of importance) to the last one;
- the criteria of those factors (excluding the "economic" ones) recognized as the most significant within their groups had the highest weights. In this example, they were (i) the "periodontopathogenic" parameter from the "biological" group, (ii) the "warpage after 3D printing" from the "technological" group, and (iii) the "flexural modulus" from the "mechanical" group.

Table 15. Criteria weights.

Group	Factor	Preference #1		Preference #2		Preference #3	
		Weight	Order	Weight	Order	Weight	Order
Mechanical	Flexural modulus	0.085	4	0.090	4	0.074	5
	Flexural strength	0.076	6	0.081	6	0.066	7
	Flexural strain	0.076	6	0.081	6	0.066	7
Tribological	Wear rate, point contact	0.079	5	0.083	5	0.068	6
	Wear rate, linear contact	0.079	5	0.083	5	0.068	6
	(Abrasive) weight loss, flat contact	0.079	5	0.083	5	0.068	6
Technological	Average duration of 3D printing and post-build polymerization processing	0.074	7	0.078	7	0.064	8
	Warpage after 3D printing (quality)	0.091	2	0.096	2	0.078	3
Biological	Normal	0.067	8	0.071	8	0.058	9
	Periodontopathogenic	0.129	1	0.135	1	0.113	2
	Fungal	0.086	3	0.091	3	0.075	4
Economic	Price for 1 kg of feedstock	0.079	5	0.028	9	0.203	1

For all three preferences, the *S*, *R*, and *Q* values were calculated using both the VIKOR and the extended VIKOR methods [42,46]. The obtained results and the ranking data are presented in Table 16. According to the preferences:

- under the assumption of the equivalence of the groups, the extended VIKOR method did not reveal any obvious advantage of the alternatives, while the VIKOR one recognized the equal advantage of the FP and NT over the DS.
- under the assumption of the importance of the "economic" factors, the FP was recognized as a rational alternative according to the VIKOR method, but it was the NT according to the extended VIKOR one.
- under the assumption of the significance of all groups over the "economic" factors, both methods recognized the FP and DS as rational alternatives, but the NT was the worst one.

Table 16. The ranks according to the criteria of all groups. Preference #1/Preference #2/Preference #3.

No.	Alternative	S	R	Q (v = 0.5)	Rank	
					VIKOR	extVIKOR
A_1	FP	[0.2294, 0.5132] /[0.3211, 0.5479] /[0.1966, 0.4728]	[0.0596, 0.1285] /[0.1803, 0.1803] /[0.0512, 0.0904]	[0.0000, 0.7666] /[0.4074, 0.7323] /[0.0000, 0.4566]	1/1/1	1/2/1
A_2	NT	[0.5811, 0.7617] /[0.4964, 0.6702] /[0.6065, 0.8172]	[0.0829, 0.0907] /[0.0782, 0.1129] /[0.0958, 0.1348]	[0.4996, 0.7258] /[0.2510, 0.6381] /[0.5970, 1.0000]	1/2/2	1/1/2
A_3	DS	[0.3591, 0.6200] /[0.4331, 0.6607] /[0.3097, 0.5864]	[0.0788, 0.1071] /[0.2035, 0.2035] /[0.0781, 0.0833]	[0.2613, 0.7115] /[0.6604, 0.9863] /[0.2519, 0.5060]	2/3/1	1/3/1

Comparing the ranks for all the preferences, it should be noted that the subjective phase of determining the significance of the criteria made a significant contribution, but the variability of the factors was no less important. As follows from Table 16, a large spread of the measured interval factors (Table 9) caused a great dispersion of S, R, and Q interval estimations and, accordingly, predetermined a lower "resolving capacity" of the extended VIKOR method (Table 16) at a few alternatives. Under MCDM resolving capacity, the authors meant the ability of the method to compare the alternatives and differentiate them [48].

5. Discussion

The photopolymerization process is well studied and widely used in industry [49–57]. SLA is based on the photopolymerization phenomenon as well. In particular, when the photoinitiator absorbs UV, the molecule splits into two radicals. The latter combines with monomers to form new radicals that group with other monomers. This reaction forms polymer chains to transform liquid photopolymerized resin into a solid state [58].

In dentistry, one of the challenges in the 3D printing of acrylate resins is residual monomers. After material curing, dental acrylates release various amounts of potentially toxic substances into saliva, where they dissolve and affect tissues of the mouth and the human body as a whole. The substances include unpolymerized, unreacted components of a chemical system, as well as secondary polymerization products. At high concentrations, they are very toxic, but their amount dissolved in the saliva is negligible when using dentures, depending on the possibility of their diffusion from the material. However, these substances may significantly affect a patient's well-being due to individual intolerance, since acrylates are cytotoxic substances.

It is generally accepted that the residual monomers (MMA, BuMA, EMA, and UDMA) and the crosslinkers (EGDMA, IBMA, etc.), which have not fully polymerized in the material curing procedure, are responsible for the toxic and allergenic effects of the acrylates. The amount of a monomer released into the patient's oral cavity is proportional to its total residual quantity in the matrix of the acrylates. The residual monomer diffuses rather quickly from the polyacrylate surface layer (it is released into saliva during the first day

of using a denture). However, its certain amount remains "locked" inside polyacrylate for a long time, continuing to slowly diffuse outwards. The amount of the released MMA becomes stable two weeks on from the denture installation.

According to ISO 1567:1999, the maximum allowable residual MMA contents are 2.2% and 4.5% for thermal and cold-cured dental acrylates, respectively. The residual monomer amount can be reduced by post-curing (additional thermal polymerization in boiling water or a microwave oven) and extraction (immersion and holding of dentures in a water bath or sonication in water). Using microwave post-curing procedures, the residual monomer amount can be lowered by 25% (due to its polymerization and/or evaporation). According to the authors, the most promising method for its decreasing is preliminary polymerization under the action of ultraviolet or microwave radiation. In addition, new initiating systems (polymerizable monomers) should be developed.

The authors assume that the above aspect is very relevant from the standpoint of DMS and should be considered when developing such procedures. In the present research, this aspect was neglected for objective reasons. Nevertheless, it will be analyzed in a forthcoming paper by the authors, including the addition of appropriate quantitative indicators to the matrix for comparing the functional properties.

Dental materials used for the manufacture of RCD (for temporary use) must have a wide range of functional properties, which include bio-inertness; anti-allergenicity; specific color palette (including stability of shades and surface textures); physical and mechanical characteristics; good polishability; no negative reaction to hygiene products; manufacturability (simplicity and ease of processing; short duration); economic viability, etc. [59]. Some of these parameters can be characterized quantitatively, and some only qualitatively. Moreover, the achievement of the required level of some properties may be accompanied by the unattainability of those for others. Thus, the issue of DMS is very complicated and carried out empirically in most cases. This contributes to a great risk of errors, transforming into complications and aggravation of the patient's conditions, which is confirmed by the long-term practice of doctors, reflected in the literature [60,61]. Presently, the importance of production routes is a fact that significantly affects the quality characteristics of the fabrication of dental products.

Even though most of the study was devoted to the analysis of the properties of the dental materials and their ranking based on the assessment of their characteristics, it should be noted that they were mainly determined by the structure formed during the 3D-printing process. With this method and the applied conditions for AM, the achievement of the key mechanical and tribological properties was determined by the PMMA molecular structure and the pattern of macromolecule arrangement. For this reason, the revealed difference in the properties between the three types of the studied dental materials was not associated mostly with some variations in the feedstock compositions, but with the specifics of their polymerization during the 3D printing process (taking into account high rates of the product fabrication). In addition, the important influencing factors were:

- compositions of processing additives (trade secrets of the manufacturers);
- recommended time-depended modes of 3D printing and post-build polymerization processing (differed for the studied PMMA grades);
- degrees of residual monomer contents, implemented in 3D printing and post-build polymerization processing;
- residual stresses, characterized by strains of the 3D printed samples, etc.

The mathematical algorithm implementation could contribute to the consideration of structural characteristics in the DMS. However, this would complicate the approach (tool) applied in this research, which was based on the materials' ranking over the integral and experimentally determined characteristics (interval, quantitative or qualitative).

DMS was highly case-sensitive, depending on the preferences of an expert. Nevertheless, the proposed approach (with proper tuning) was rigorous and enabled the obtaining of quite weighted estimations. It could be effectively used for solving related problems, such as digital milling from blanks. The key aspects remained as follows:

- correct selection of the factors (groups of factors);
- ensuring the accuracy of their measurement and reducing errors (dispersions of the experimental data);
- ensuring the most representative expert assessment;
- if the risk of making a wrong decision remains informalized, the only way to minimize it is to form the right attitude of the decision maker toward expressing his/her preferences.

Note, in this research, the evaluation of the tribological performance was carried out according to the standards intended for testing structural materials (without taking into account the specifics of existing regulations for dental ones). This was not critical from the standpoint of developing an approach to DMS. However, the authors will be careful to follow the standard requirements for testing dental materials.

It should be also noted that presently the issue of DMS is solved in a very subjective way. It depends on a large number of factors: the dentist's experience, price, patients' budget, time availability, and particular values of a variety of functional properties. The papers proposed a concept that considers the factors formulated by experienced long-term practicing dentists. The developed approach presumes an option to make flexible corrections. In addition, it can be easily adapted for solving the DMS issue for dental implants as well. The paper illustrated it over the ranking of three commercially available PMMAs. The significance of the study concludes in attracting the mathematical tools for solving real problems of practicing dentists with a low amount of subjectivity in making a decision.

By way of summarizing, the following might be concluded. We have employed the AHP method for ranking the factors, i.e., more or less important. Furthermore, a compromise is possible to be found over the set of alternatives with the VIKOR method. The proposed approach (the tool) is of great promise to enhance the efficiency of prosthetic treatment by optimizing the DMS procedure, taking into account the prosthesis design and its production route.

6. Conclusions

The formalized approach to a rational ranking of dental materials aimed at RCD additive manufacturing was proposed within the framework of the multicriteria optimization algorithm. It was tested through three types of commercially available PMMAs, processed by the DLP. For this purpose, the combination of mechanical, tribological, technological, microbiological, and economic factors was assessed. The following results were obtained, and conclusions were drawn.

1. The calculation of the material indices was carried out to compare the studied dental materials for a set of functional parameters related to feedstock cost. However, this did not solve the problem of simultaneous consideration of all the material indices, inter alia their significance.
2. For the 3D printing of RCD, the problem of the DMS could be solved as a multicomponent optimization. This study solved the problem by combining the AHP and extended VIKOR methods with interval estimation.
3. It was shown that the formulated preferences by experts exerted a significant impact on the decision-making results under the conflict of the adopted criteria. The proposed method of grouping the factors according to the expert competencies allowed the reduction of subjectivity, at least at the stage of ranking within the groups. However, uncertainty arose for all criteria at the stage of alternative analysis.
4. The implementation of the extended VIKOR method, based on the analysis of interval quantitative estimations, allowed the carrying out of a fully fledged analysis of the alternatives. Its results were rather plausible. However, it was characterized by a lower "resolving capacity", i.e., the ability to separate the alternatives.

As an outlook, the authors consider it necessary to note the following. The AHP method was employed to rank the factors over the degree of importance. Furthermore, a compromise is possible over the set of alternatives with the VIKOR method. The proposed approach is targeted at enhancing the efficiency of prosthetic treatment by optimizing the DMS procedure if the prosthesis design and its production route are taken into account. The development of the proposed approach correlates with the attraction of the MCDM, which takes the experts' uncertainty in decision-making (estimation) into account. The methods based on fuzzy logic theory are among them [41,62,63].

Supplementary Materials: The following supporting information can be downloaded at: https://www.mdpi.com/article/10.3390/ijms24076432/s1.

Author Contributions: Conceptualization, S.V.P. and D.Y.S.; methodology, S.V.P. and D.Y.S.; software, D.Y.S.; validation, D.Y.S. and S.V.P.; formal analysis, S.V.P.; investigation, D.I.G., E.A.C. and L.G.K.; resources, I.V.K., A.V.D., A.S.A. and S.Y.K.; data curation, D.G.B.; writing—original draft preparation, S.V.P., L.G.K., D.G.B. and K.S.P.; writing—review and editing, S.V.P.; visualization, D.Y.S. and D.G.B.; supervision, S.V.P.; project administration, S.V.P.; funding acquisition, I.V.K., A.V.D., A.S.A. and S.Y.K. All authors have read and agreed to the published version of the manuscript.

Funding: S.V.P. and D.G.B. acknowledge support from the project FWRW-2021-0010 through the government research assignment for ISPMS SB RAS.

Institutional Review Board Statement: Not applicable.

Informed Consent Statement: Not applicable.

Data Availability Statement: The data presented in this study are available on request from the corresponding author.

Acknowledgments: The authors express great gratitude to the head of the Digital Dentistry Department Professor Sergey D. Arutyunov (A.I. Yevdokimov Moscow State University of Medicine and Dentistry) for inspiring this research and for multiple fruitful discussions of the results. His administrative and technical support is also acknowledged.

Conflicts of Interest: The authors declare no conflict of interest.

References

1. Grachev, D.I.; Ruzuddinov, N.S.; Arutyunov, A.S.; Akhmedov, G.D.; Dubova, L.V.; Kharakh, Y.N.; Panin, S.V.; Arutyunov, S.D. Algorithm for Designing a Removable Complete Denture (RCD) Based on the FEM Analysis of Its Service Life. *Materials* **2022**, *15*, 7246. [CrossRef]
2. Ashby, M.F. *Materials Selection in Mechanical Design*, 5th ed.; Butterworth-Heinemann: Oxford, UK, 2016; p. 660. ISBN 9780081006108.
3. Afrashtehfar, K.I.; Assery, M.K.A.; Bryant, S.R. Patient Satisfaction in Medicine and Dentistry. *Int. J. Dent.* **2020**, *29*, 6621848. [CrossRef] [PubMed]
4. Orthlieb, J.D.; Deroze, D.; Lacout, J.; Maniere-Ezvan, A. Pathogenic occlusion and functional occlusion definition of completion. *Orthod. Fr.* **2006**, *77*, 451–459. [CrossRef] [PubMed]
5. Kress, B.; Schmitter, M. Temporomandibulargelenk: MRT-Diagnostik. *Radiologe* **2005**, *45*, 790–796. [CrossRef]
6. Arutyunov, S.D.; Krasheninnikov, S.V.; Levchenko, I.M.; Orjonikidze, R.Z.; Sadovskaya, N.V.; Kirakosyan, L.G.; Kharakh, Y.N. Monitoring of changes in physicochemical and clinical characteristics of the dental polymer materials used in additive manufacturing of dental prostheses. *Georgian Med. News* **2018**, *285*, 37–41.
7. Arutyunov, S.; Kirakosyan, L.; Dubova, L.; Kharakh, Y.; Malginov, N.; Akhmedov, G.; Tsarev, V. Microbial Adhesion to Dental Polymers for Conventional, Computer-Aided Subtractive and Additive Manufacturing: A Comparative In Vitro Study. *J. Funct. Biomater.* **2022**, *13*, 42. [CrossRef] [PubMed]
8. Astudillo-Rubio, D.; Delgado-Gaete, A.; Bellot-Arcís, C.; Montiel-Company, J.M.; Pascual-Moscardó, A.; Almerich-Silla, J.M. Mechanical Properties of Provisional Dental Materials: A Systematic Review and Meta-Analysis. *PLoS ONE* **2018**, *13*, e0193162. [CrossRef]
9. Marchesi, G.; Camurri Piloni, A.; Nicolin, V.; Turco, G.; Di Lenarda, R. Chairside CAD/CAM Materials: Current Trends of Clinical Uses. *Biology* **2021**, *10*, 1170. [CrossRef]
10. Kurbad, A.; Reichel, K. CAD/CAM-manufactured restorations made of lithium disilicate glass ceramics. *Int. J. Comput. Dent.* **2005**, *4*, 337–348.
11. Lankes, V.; Reymus, M.; Liebermann, A.; Stawarczyk, B. Bond strength between temporary 3D printable resin and conventional resin composite: Influence of cleaning methods and air-abrasion parameters. *Clin. Oral Investig.* **2023**, *27*, 31–43. [CrossRef]

12. Digholkar, S.; Madhav, V.N.V.; Palaskar, J. Evaluation of the Flexural Strength and Microhardness of Provisional Crown and Bridge Materials Fabricated by Different Methods. *J. Indian Prosthodont. Soc.* **2016**, *16*, 328–334. [CrossRef] [PubMed]
13. Maximov, J.; Dikova, T.; Duncheva, G.; Georgiev, G. Influence of Factors in the Photopolymerization Process on Dental Composites Microhardness. *Materials* **2022**, *15*, 6459. [CrossRef] [PubMed]
14. Nguyen, P.; Stanislaus, I.; McGahon, C.; Pattabathula, K.; Bryant, S.; Pinto, N.; Jenkins, J.; Meinert, C. Quality assurance in 3D printing: A dimensional accuracy study of patient-specific 3D printed vascular anatomical models. *Front. Med. Technol.* **2023**, *5*, 1097850. [CrossRef] [PubMed]
15. Dorweiler, B.; Baqué, P.E.; Chaban, R.; Ghazy, A.; Salem, O. Quality Control in 3D Printing: Accuracy Analysis of 3D Printed Models of Patient-Specific Anatomy. *Materials* **2021**, *14*, 1021. [CrossRef] [PubMed]
16. Reymus, M.; Lümkemann, N.; Stawarczyk, B. 3D printed material for temporary restorations: Impact of print layer thickness and post-curing method on degree of conversion. *Int. J. Comput. Dent.* **2019**, *9*, 231–237.
17. Holmer, H.; Bekele, A.; Hagander, L.; Harrison, E.M.; Kamali, P.; Ng-Kamstra, J.S.; Khan, M.A.; Knowlton, L.; Leather, A.J.M.; Marks, I.H.; et al. Evaluating the Collection, Comparability and Findings of Six Global Surgery Indicators. *Br. J. Surg.* **2019**, *106*, e138–e150. [CrossRef]
18. Christensen, G.J. The Fastest and Best Provisional Restorations. *J. Am. Dent. Assoc.* **2003**, *134*, 637–639. [CrossRef]
19. Karaokutan, I.; Sayin, G.; Kara, O. In Vitro Study of Fracture Strength of Provisional Crown Materials. *J. Adv. Prosthodont.* **2015**, *7*, 27–31. [CrossRef]
20. Alt, V.; Hannig, M.; Wöstmann, B.; Balkenhol, M. Fracture Strength of Temporary Fixed Partial Dentures: CAD/CAM versus Directly Fabricated Restorations. *Dent. Mater.* **2011**, *27*, 339–347. [CrossRef]
21. Dikova, T. Production of High-Quality Temporary Crowns and Bridges by Stereolithography. *Scr. Sci. Med. Dent.* **2019**, *5*, 33. [CrossRef]
22. Li, X.; Xie, B.; Jin, J.; Chai, Y.; Chen, Y. 3D Printing Temporary Crown and Bridge by Temperature Controlled Mask Image Projection Stereolithography. *Procedia Manuf.* **2018**, *26*, 1023–1033. [CrossRef]
23. Yamaguchi, S.; Li, H.; Imazato, S. Materials informatics for developing new restorative dental materials: A narrative review. *Front. Dent. Med.* **2023**, *4*, 1123976. [CrossRef]
24. Dikbas, I.; Gurbuz, O.; Unalan, F.; Koksal, T. Impact Strength of Denture Polymethyl Methacrylate Reinforced with Different Forms of E-Glass Fibers. *Acta Odontol. Scand.* **2013**, *71*, 727–732. [CrossRef] [PubMed]
25. Alhotan, A.; Yates, J.; Zidan, S.; Haider, J.; Silikas, N. Assessing Fracture Toughness and Impact Strength of PMMA Reinforced with Nano-Particles and Fibre as Advanced Denture Base Materials. *Materials* **2021**, *14*, 4127. [CrossRef]
26. Beketova, A.; Tzanakakis, E.-G.C.; Vouvoudi, E.; Anastasiadis, K.; Rigos, A.E.; Pandoleon, P.; Bikiaris, D.; Tzoutzas, I.G.; Kontonasaki, E. Zirconia Nanoparticles as Reinforcing Agents for Contemporary Dental Luting Cements: Physicochemical Properties and Shear Bond Strength to Monolithic Zirconia. *Int. J. Mol. Sci.* **2023**, *24*, 2067. [CrossRef] [PubMed]
27. Huynh, T.T.; Nguyen, T.V.; Nguyen, Q.M.; Nguyen, T.K. Minimizing warpage for macro-size fused deposition modeling parts. *Comput. Mater. Contin.* **2021**, *68*, 2913–2923. [CrossRef]
28. Emovon, I.; Oghenenyerovwho, O.S. Application of MCDM method in material selection for optimal design: A review. *Results Mater.* **2020**, *7*, 100115. [CrossRef]
29. Jamroz, D.; Niedoba, T.; Surowiak, A.; Tumidajski, T.; Szostek, R.; Gajer, M. Application of Multi-Parameter Data Visualization by Means of Multidimensional Scaling to Evaluate Possibility of Coal Gasification. *Arch. Min. Sci.* **2017**, *62*, 445–457. [CrossRef]
30. Jamroz, D.; Niedoba, T. Comparison of Selected Methods of Multi-Parameter Data Visualization Used for Classification of Coals. *Physicochem. Probl. Miner. Process.* **2015**, *51*, 769–784. [CrossRef]
31. Niedoba, T. Multi-parameter data visualization by means of principal component analysis (PCA) in qualitative evaluation of various coal types. *Physicochem. Probl. Miner. Process.* **2014**, *50*, 575–589.
32. Bondarev, A.E.; Galaktionov, V.A. Multidimensional data analysis and visualization for time-dependent CFD problems. *Program. Comput. Softw.* **2015**, *41*, 247–252. [CrossRef]
33. Wang, C.-N.; Yang, F.-C.; Vo, N.T.M.; Nguyen, V.T.T. Wireless Communications for Data Security: Efficiency Assessment of Cybersecurity Industry—A Promising Application for UAVs. *Drones* **2022**, *6*, 363. [CrossRef]
34. Osintsev, N.A. Multi-Criteria Decision-Making Methods in Green Logistics. *World Transp. Transp.* **2021**, *19*, 105–114. [CrossRef]
35. Guitouni, A.; Martel, J. Tentative guidelines to help choosing an appropriate MCDA method. *Eur. J. Oper. Res.* **1998**, *109*, 501–521. [CrossRef]
36. Shinde, D.; Öktem, H.; Kalita, K.; Chakraborty, S.; Gao, X.-Z. Optimization of Process Parameters for Friction Materials Using Multi-Criteria Decision Making: A Comparative Analysis. *Processes* **2021**, *9*, 1570. [CrossRef]
37. Ozsahin, I.; Ozsahin, D.U.; Uzun, B. (Eds.) *Applications of Multi-Criteria Decision-Making Theories in Healthcare and Biomedical Engineering*; Elsevier Inc.: Amsterdam, The Netherlands, 2021. [CrossRef]
38. Kumar, R.; Dubey, R.; Singh, S.; Singh, S.; Prakash, C.; Nirsanametla, Y.; Królczyk, G.; Chudy, R. Multiple-Criteria Decision-Making and Sensitivity Analysis for Selection of Materials for Knee Implant Femoral Component. *Materials* **2021**, *14*, 2084. [CrossRef]
39. Singh, T.; Goswami, C.; Patnaik, A.; Lendvai, L. Optimal Design of Ceramic Based Hip Implant Composites Using Hybrid AHP-MOORA Approach. *Materials* **2022**, *15*, 3800. [CrossRef] [PubMed]

40. Pramanik, P.K.D.; Biswas, S.; Pal, S.; Marinković, D.; Choudhury, P. A Comparative Analysis of Multi-Criteria Decision-Making Methods for Resource Selection in Mobile Crowd Computing. *Symmetry* **2021**, *13*, 1713. [CrossRef]
41. Fuse, K.; Dalsaniya, A.; Modi, D.; Vora, J.; Pimenov, D.Y.; Giasin, K.; Prajapati, P.; Chaudhari, R.; Wojciechowski, S. Integration of Fuzzy AHP and Fuzzy TOPSIS Methods for Wire Electric Discharge Machining of Titanium (Ti6Al4V) Alloy Using RSM. *Materials* **2021**, *14*, 7408. [CrossRef]
42. Sayadi, M.K.; Heydari, M.; Shahanaghi, K. Extension of VIKOR method for decision making problem with interval numbers. *Appl. Math. Model.* **2009**, *33*, 2257–2262. [CrossRef]
43. Pan, X.-H.; He, S.-F.; Wang, Y.-M.; Martínez, L. A novel interval-valued three-way decision theory under multiple criteria environment. *Knowl.-Based Syst.* **2022**, *253*, 109522. [CrossRef]
44. Samal, S.; Dash, R. An Empirical Comparison of TOPSIS and VIKOR for Ranking Decision-Making Models. In *Intelligent and Cloud Computing*; Mishra, D., Buyya, R., Mohapatra, P., Patnaik, S., Eds.; Smart Innovation, Systems and Technologies; Springer: Singapore, 2022; Volume 286. [CrossRef]
45. Taşabat, S.E.; Özkan, T.K. TOPSIS vs. VIKOR: A Case Study for Determining Development Level of Countries. In *Multi-Criteria Decision Analysis in Management*; IGI Global: Hershey, PA, USA, 2020. [CrossRef]
46. Opricovic, S.; Tzeng, G.H. Compromise solution by MCDM methods: A comparative analysis of VIKOR and TOPSIS. *Eur. J. Oper. Res.* **2004**, *156*, 445–455. [CrossRef]
47. Saaty, T.L. The analytic hierarchy process—What it is and how it is used. *Math. Model.* **1987**, *9*, 161–176. [CrossRef]
48. Larichev, O.I. *Verbal Decision Making*; Institute of System of Russian Academy of Sciences: Moscow, Russia, 2006; p. 181. (In Russian)
49. Yagci, Y.; Jockusch, S.; Turro, N.J. Photoinitiated Polymerization: Advances, Challenges, and Opportunities. *Macromolecules* **2010**, *43*, 6245–6260. [CrossRef]
50. Quan, H.; Zhang, T.; Xu, H.; Luo, S.; Nie, J.; Zhu, X. Photo-Curing 3D Printing Technique and Its Challenges. *Bioact. Mater.* **2020**, *5*, 110–115. [CrossRef] [PubMed]
51. Bártolo, P. *Stereolithography: Materials, Processes and Applications*; Springer: New York, NY, USA, 2011.
52. Bagheri, A.; Jin, J. Photopolymerization in 3D Printing. *ACS Appl. Polym. Mater.* **2019**, *1*, 593–611. [CrossRef]
53. Wendel, B.; Rietzel, D.; Kühnlein, F.; Feulner, R.; Hülder, G.; Schmachtenberg, E. Additive Processing of Polymers. *Macromol. Mater. Eng.* **2008**, *293*, 799–809. [CrossRef]
54. Layani, M.; Wang, X.; Magdassi, S. Novel Materials for 3D Printing by Photopolymerization. *Adv. Mater.* **2018**, *30*, 1–7. [CrossRef]
55. Zhang, J.; Xiao, P. 3D Printing of Photopolymers. *Polym. Chem.* **2018**, *9*, 1530–1540. [CrossRef]
56. De Leon, A.C.; Chen, Q.; Palaganas, N.B.; Palaganas, J.O.; Manapat, J.; Advincula, R.C. High Performance Polymer Nanocomposites for Additive Manufacturing Applications. *React. Funct. Polym.* **2016**, *103*, 141–155. [CrossRef]
57. Gordeev, E.G.; Ananikov, V.P. Widely accessible 3D printing technologies in chemistry, biochemistry and pharmaceutics: Applications, materials and prospects. *Russ. Chem. Rev.* **2020**, *89*, 1507. [CrossRef]
58. Available online: https://blog.fabweaver.com/3d-printing-principle-sla-resin-photopolymerization-process-0 (accessed on 20 March 2023).
59. Zafar, M.S. Prosthodontic Applications of Polymethyl Methacrylate (PMMA): An Update. *Polymers* **2020**, *12*, 2299. [CrossRef]
60. Chander, N.G. Polymethyl metha acrylate denture base: An overview. *J. Indian Prosthodont. Soc.* **2018**, *18*, 87–88. [CrossRef] [PubMed]
61. Kostić, M.; Igić, M.; Gligorijević, N.; Nikolić, V.; Stošić, N.; Nikolić, L. The Use of Acrylate Polymers in Dentistry. *Polymers* **2022**, *14*, 4511. [CrossRef] [PubMed]
62. Dang, T.-T.; Nguyen, N.-A.-T.; Nguyen, V.-T.-T.; Dang, L.-T.-H. A Two-Stage Multi-Criteria Supplier Selection Model for Sustainable Automotive Supply Chain under Uncertainty. *Axioms* **2022**, *11*, 228. [CrossRef]
63. Gul, M.; Celik, E.; Aydin, N.; Gumus, A.T.; Guneri, A.F. A state of the art literature review of VIKOR and its fuzzy extensions on applications. *Appl. Soft Comput.* **2016**, *46*, 60–89. [CrossRef]

Disclaimer/Publisher's Note: The statements, opinions and data contained in all publications are solely those of the individual author(s) and contributor(s) and not of MDPI and/or the editor(s). MDPI and/or the editor(s) disclaim responsibility for any injury to people or property resulting from any ideas, methods, instructions or products referred to in the content.

International Journal of
Molecular Sciences

MDPI

Article

The Cracking Behavior of Two Dental Composite Materials Validated through Multifractal Analyzes

Irina Nica [1], Florin Nedeff [2,*], Valentin Nedeff [3], Cristina Popa [4], Ștefan Lucian Toma [5], Maricel Agop [6,7,*] and Decebal Vasincu [8]

1 Department of Odontology-Periodontology, Fixed Prosthesis, Faculty of Dental Medicine, Grigore T. Popa University of Medicine and Pharmacy, 700115 Iasi, Romania
2 Department of Environmental Engineering and Mechanical Engineering, Faculty of Engineering, Vasile Alecsandri University of Bacău, 600115 Bacău, Romania
3 Department of Industrial Systems Engineering and Management, Faculty of Engineering, Vasile Alecsandri University of Bacău, 600115 Bacău, Romania
4 Department of Oral Pathology, Faculty of Dental Medicine, Grigore T. Popa University of Medicine and Pharmacy, 700115 Iasi, Romania
5 Department of Materials Engineering and Industrial Security, Faculty of Materials Science and Engineering, Gheorghe Asachi Technical University of Iasi, 700050 Iasi, Romania
6 Department of Physics, Faculty of Machine Manufacturing and Industrial Management, Gheorghe Asachi Technical University of Iasi, 700050 Iasi, Romania
7 Academy of Romanian Scientists, 050094 Bucharest, Romania
8 Department of Biophysics, Faculty of Dental Medicine, Grigore T. Popa University of Medicine and Pharmacy, 700115 Iasi, Romania
* Correspondence: florin_nedeff@ub.ro (F.N.); magop@tuiasi.ro (M.A.)

Abstract: The aim of this in vitro study was to analyze, both experimentally and theoretically, the mechanical behavior of two types of composite materials used in restoring dental integrity. The samples of each composite resin, namely Filtek Supreme XT (3M ESPE, St. Paul, MN, USA) and Filtek Z250 (3M ESPE, St. Paul, MN, USA), were experimentally analyzed by determining their compressive strength and fracture behavior. The fractured fragments of the samples were subjected to surface evaluation by scanning electron microscopy. The compressive stress—compressive strain dependencies revealed stronger cracking of the Filtek Supreme XT composite than Filtek Z250 prior to fracture. Theoretically, the evaluation was made by means of holographic implementations of such types of composite materials. A Hooke-type equation in a differential form is presented, which links the proposed theoretical model with the experimentally obtained data.

Keywords: dental composite material; compression; non-linear behaviors; multifractality

Citation: Nica, I.; Nedeff, F.; Nedeff, V.; Popa, C.; Toma, Ș.L.; Agop, M.; Vasincu, D. The Cracking Behavior of Two Dental Composite Materials Validated through Multifractal Analyzes. *Int. J. Mol. Sci.* **2023**, *24*, 6493. https://doi.org/10.3390/ijms24076493

Academic Editor: Mary Anne Melo

Received: 28 February 2023
Revised: 25 March 2023
Accepted: 28 March 2023
Published: 30 March 2023

Copyright: © 2023 by the authors. Licensee MDPI, Basel, Switzerland. This article is an open access article distributed under the terms and conditions of the Creative Commons Attribution (CC BY) license (https://creativecommons.org/licenses/by/4.0/).

1. Introduction

The choice of materials for direct restorations is challenging, as they are subject to masticatory forces, sometimes harmful, that can lead to cracks or fractures in final restorations. In this context, mechanical properties play a central role in assessing the longevity of restorations. The diverse types of stresses during masticatory processes make it necessary to determine several mechanical characteristics of restorative composites: bending strength, radial and longitudinal compressive strength, tensile strength, etc. Among these, compressive strength is essential for the durability of restorations [1,2].

On the other hand, the usual physical models used in describing the dynamics of dental composite materials are based on the hypothesis of the differentiability of the physical quantities used to describe their evolution. Therefore, the validity of these models must be understood gradually in areas where differentiability and integrability are still functional [3–5]. However, when discussing nonlinearity and chaoticity in the dynamics of dental composite materials, differentiable and integrable mathematical procedures are of

little use. Thus, to correctly show dental composite materials dynamics, we must add scale resolution for physical variables and fundamental equations controlling the dynamics [3–5].

Accepting the above affirmation, any physical variable (used in the description of dental composite materials dynamics) will depend on the usual mathematical procedures on spatial and time coordinates and on a scale resolution. Specifically, instead of working with a single physical variable (a strictly non-differentiable mathematical function), it is possible to operate only with approximations of this mathematical function, resulting in averaging it at different scale resolutions. Thus, any physical variable used to describe the dynamics of dental composite materials will operate as the limit of a family of mathematical functions, the function being non-differentiable for zero scale resolution and differentiable for non-zero scale resolution [6–8].

This way of describing the dynamics of dental composite materials obviously implies the development of both new geometric structures and physical theories consistent with these geometric structures, for which the laws of motion, invariant to time coordinate transformations, are also invariant to transformations with respect to scale resolution. Such a geometric structure is based on the concept of the fractal/multifractal and the corresponding physical model described in the Scale Relativity Theory (SRT) [6–8]. From this perspective, the holographic implementation in the description of the dynamics of dental composite materials will be explicitly made based on the description of the dynamics of the structural units of any dental composite materials by continuous but non-differentiable curves (fractal/multifractal curves).

The present study aimed to analyze, both experimentally and theoretically, the mechanical behavior of two types of composite materials used for direct restorations: experimentally, by determining their compressive strength and fracture behavior to make a more accurate choice of composite in relation to the position of the tooth on the arch and the degree of overloading of the fillings and theoretically, using holographic implementations of such types of composite materials.

2. Results

The compressive stress (in MPa) was determined by relating the applied force (N) to the surface area of the base of the specimen analyzed and the relative deformation by relating its length to its initial value. Shown below are the variations of compressive strain (%) with compressive stress (MPa) for a series of specimens, Filtek Supreme XT (Figure 1) and Filtek Z250 (Figure 2), which were subjected to compression at a feed rate of 1 mm/min. The specimens did not initially show surface cracks.

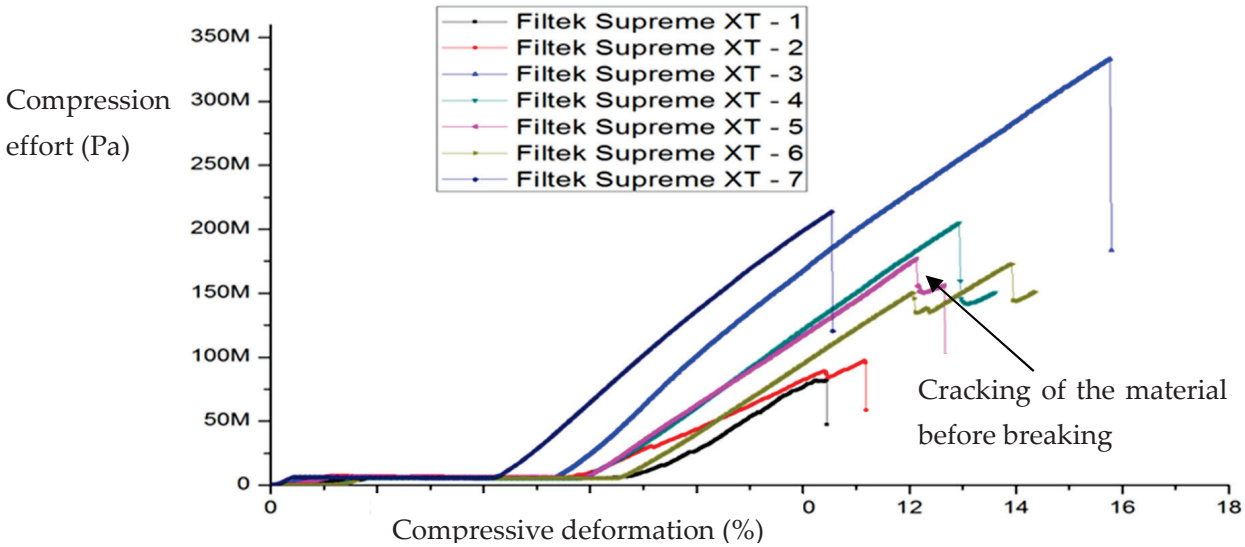


Figure 1. Variation of compressive strain with compressive stress for Filtek Supreme XT composite specimens.

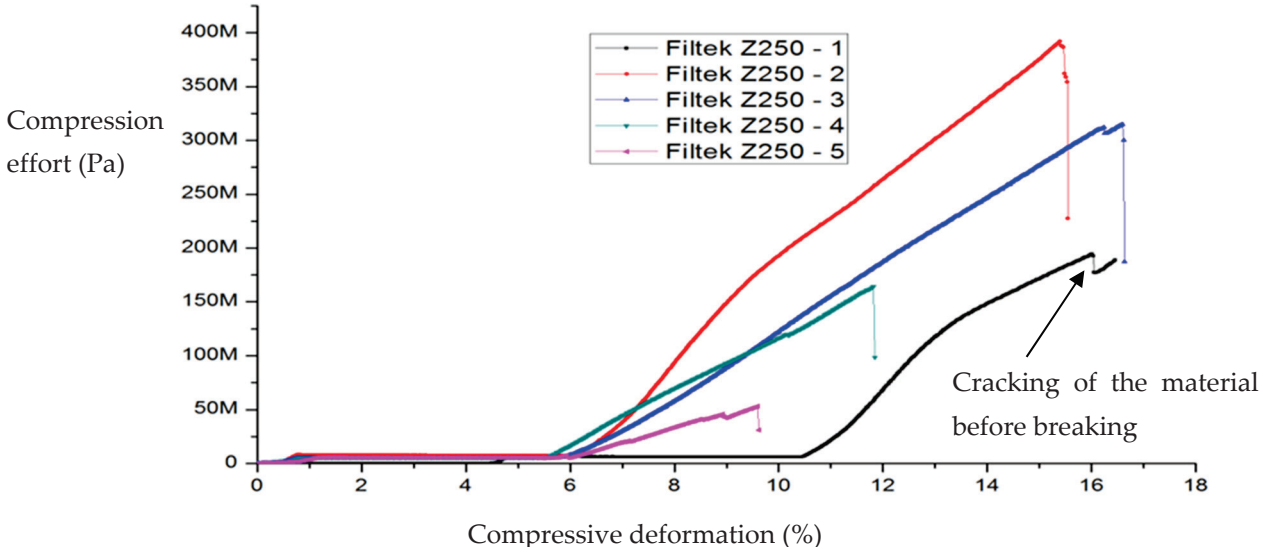


Figure 2. Variation of compressive strain with compressive stress for Filtek Z250 composite specimens.

All the samples showed high compressive strength; the experimental values obtained are shown in Table 1, reaching maximum forces in the order of thousands of newtons.

Table 1. Experimental values of shear strain and compressive strength for Filtek Supreme XT and Filtek Z250 composite specimens.

No. crt.	Sample	Ultimate Compressive Strain (%)	Ultimate Compressive Strength (MPa)
1	Filtek Supreme XT-1	10.45	82
2	Filtek Supreme XT-2	11.18	97.41
3	Filtek Supreme XT-3	15.79	333.12
4	Filtek Supreme XT-4	13.61	205.19
5	Filtek Supreme XT-5	12.66	177.18
6	Filtek Supreme XT-6	14.35	172.83
7	Filtek Supreme XT-7	10.55	213.81
8	Filtek Z250-1	16.45	194.58
9	Filtek Z250-2	15.54	392
10	Filtek Z250-3	16.63	314.72
11	Filtek Z250-4	11.84	164.39
12	Filtek Z250-5	9.62	53.08

3. Discussion

3.1. Analysis of the Experimental Data

Table 1 shows that there are widely dispersed values for both types of material. This is because the existence of internal defects in the materials can lead to the formation of micro voids that weaken the compressive strength. Thus, it was found that very good pressing prior to light curing in the fluid state leads to compact specimens with high strength. In this context, we will note only the maximum values obtained by us, 333 MPa for Filtek Supreme XT and the higher 392 MPa for Filtek Z250. We also note that at the test speeds used, 0.5, 1, and 1.5 mm/min, no significantly different results were obtained.

Comparing with the data indicated by the manufacturer, (360±5) MPa for Filtek Supreme XT, respectively (410±20) MPa for Filtek Z250, it can be seen that our maximum data falls within these ranges.

Although the data given in the literature for compressive strength vary within very wide limits, it is unanimously accepted that all mechanical properties (compressive strength, diametral strength, flexural strength) are better for Filtek Z250 hybrid composite than for Filtek Supreme XT nanocomposite [9–12]. Both materials have the same polymer matrix

and similar particle loadings but different particle sizes. Therefore, a possible explanation for these properties lies in the different propagation mechanisms of microcracks during deformation. Thus, it can be seen that the micrometer particles of the Filtek Z250 block crack propagation and reflection, while the nanometer particles allow it. In fact, the curves in Figures 1 and 2, through the regions marked with dotted lines, indicate stronger cracking of Filtek Supreme XT composite than Filtek Z250 composite before breakage.

In order to highlight this tendency of microcrack blocking on micrometric particles, the surface of the material in fracture was studied by SEM microscopy.

Figure 3 shows microstructural details of the Filtek Supreme XT-2 sample at various magnification powers.

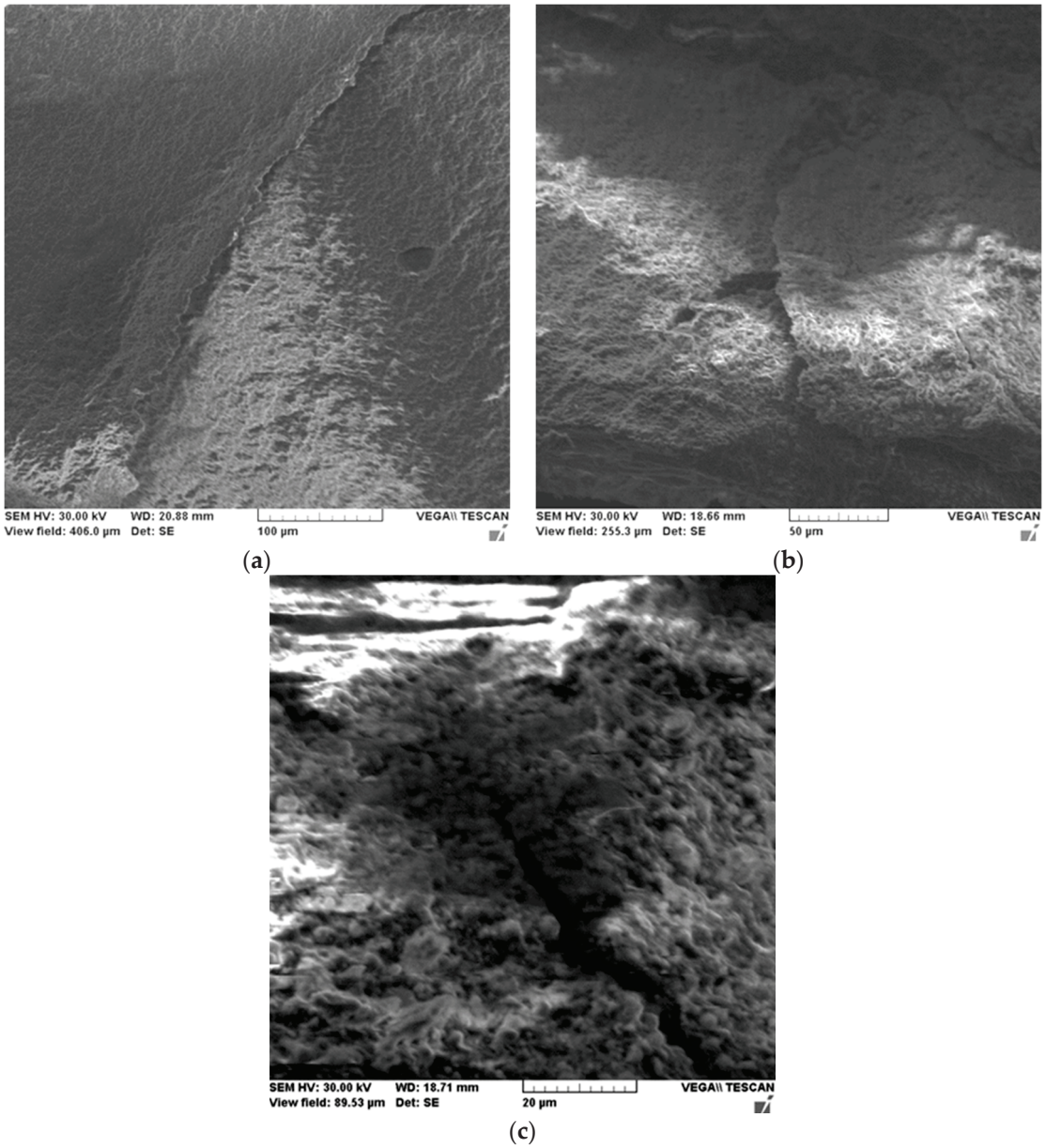
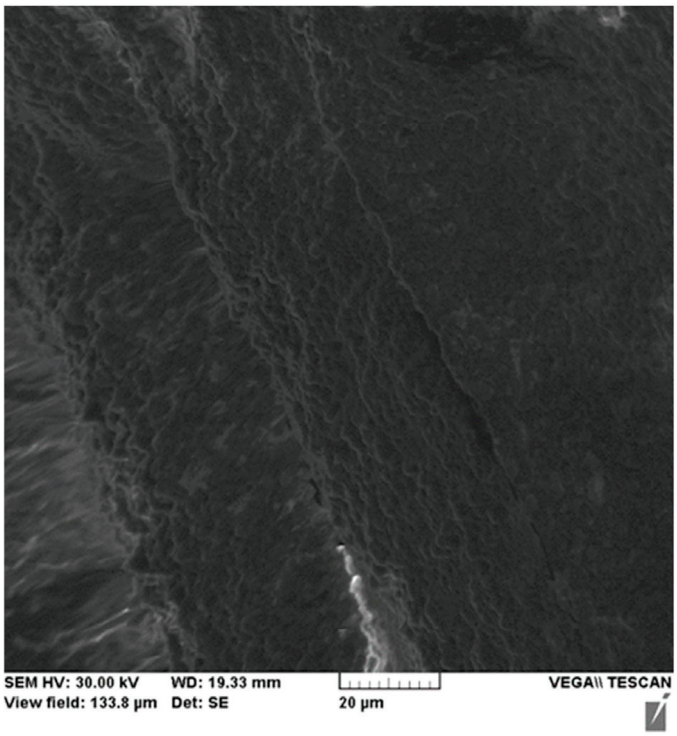


Figure 3. SEM microscopies of the Filtek Supreme XT-2 sample at various magnification powers: 700× (**a**), 1100× (**b**) and 3200× (**c**).

Fracture surface analysis of Filtek Supreme XT material under compressive stress shows brittle fracture of the material with the propagation of microcracks along the fracture planes. It is observed from the micrographs the direction of material pull-out is character-

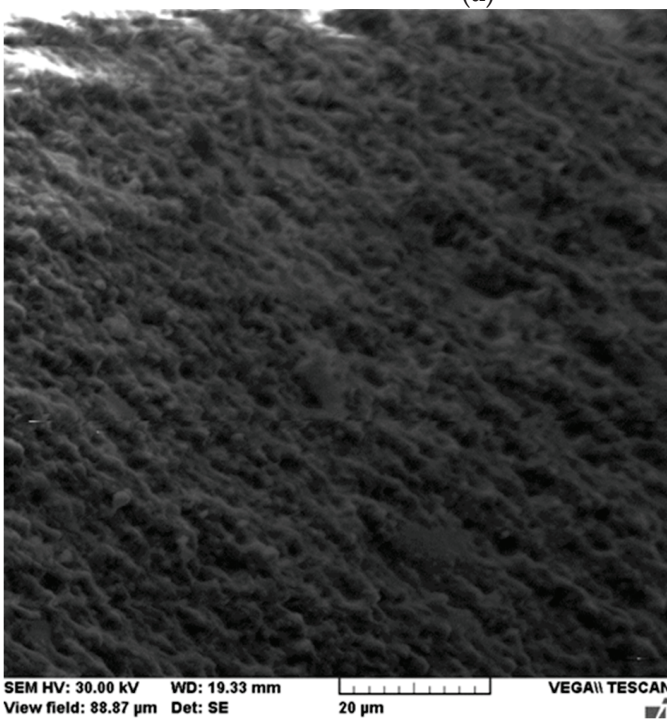
ized by overlapping planes of the material, major cracks oriented along the same direction, and areas with effective micro filler pull-outs.

Detailing a microcrack, Figure 4a shows its linear propagation through micro clusters of nanometer particles and adjacent areas of unaffected material are shown in Figure 4b.



Microcracking area

(**a**)



(**b**)

Figure 4. SEM microscopy of the Filtek Supreme XT-4 sample with propagation of a microcrack between nanometer particle clusters (**a**) and an unaffected area (**b**).

Figure 5 shows the microstructure of the Filtek Z250 composite in fracture at different scales of magnification. The characteristic of this material is the existence of microgules caused by the pulling out of the micrometer filler particles from the base matrix in which they were embedded, which could not be observed for the Filtek Supreme XT nanocomposite.

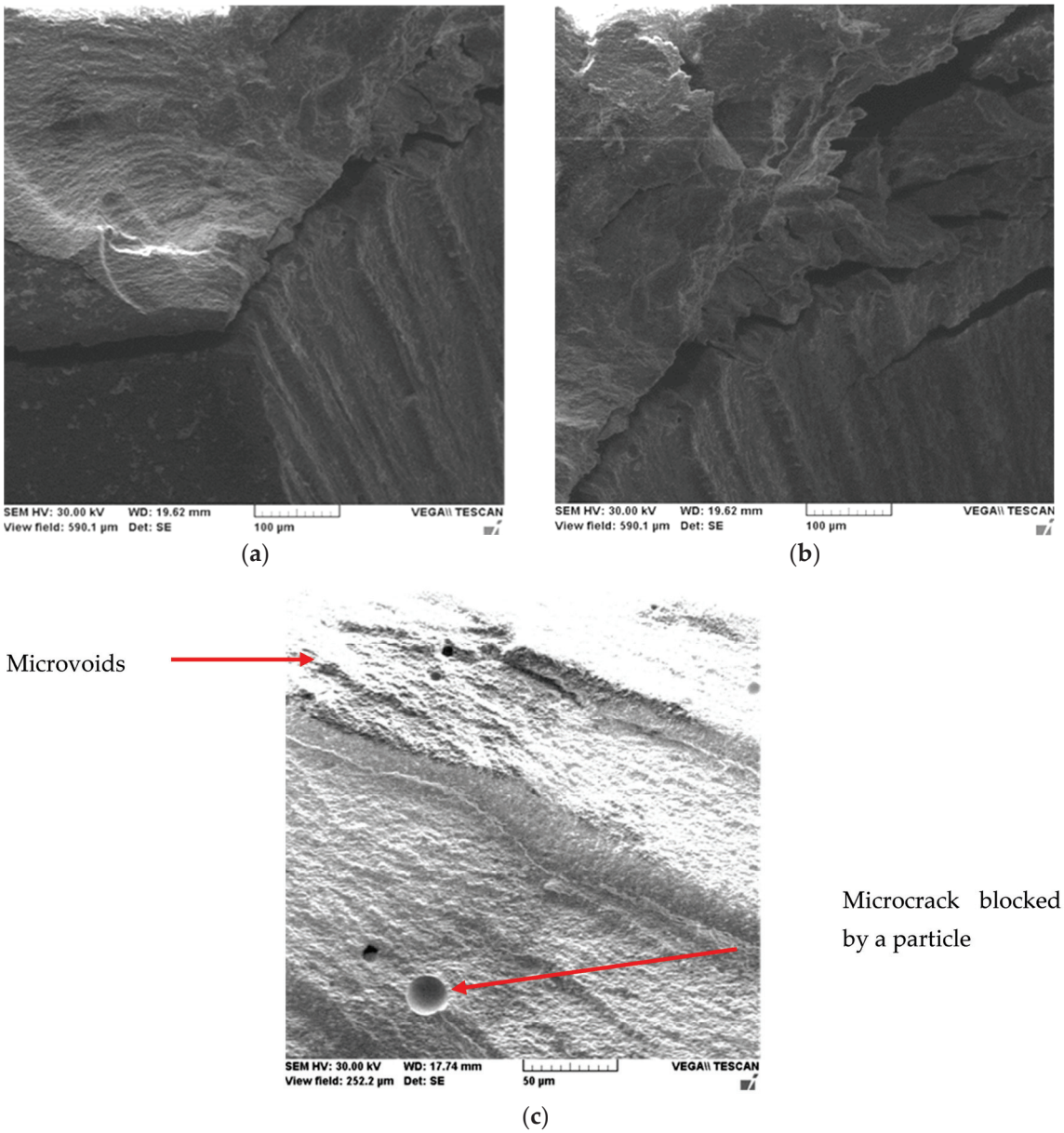


Figure 5. SEM microscopy of the Filtek Z250—1 sample at various magnifications 500× (**a**,**b**), 1150× (**c**) showing some micro voids resulting from the pulling out of the filler particles.

The previously assumed mechanism of microparticle blocking of microcracks in the Filtek Z250 hybrid composite is highlighted in Figure 6. We can see a microcrack of about 150 µm, which, on reaching a relatively large particle of about 40 µm, is stopped in its advance through the material. In fact, this detail can also be seen at the bottom of Figure 5c in the marked area. We conclude that this mechanism may explain the superior properties of the Filtek Z250 hybrid composite compared to the Filtek Supreme XT nanocomposite. However, we must consider the other advantages of using nanoparticles for reinforcement: a lower viscosity in the unpolymerized state, and preservation of surface gloss over time, which are particularly important in dental restoration practice [13–16].

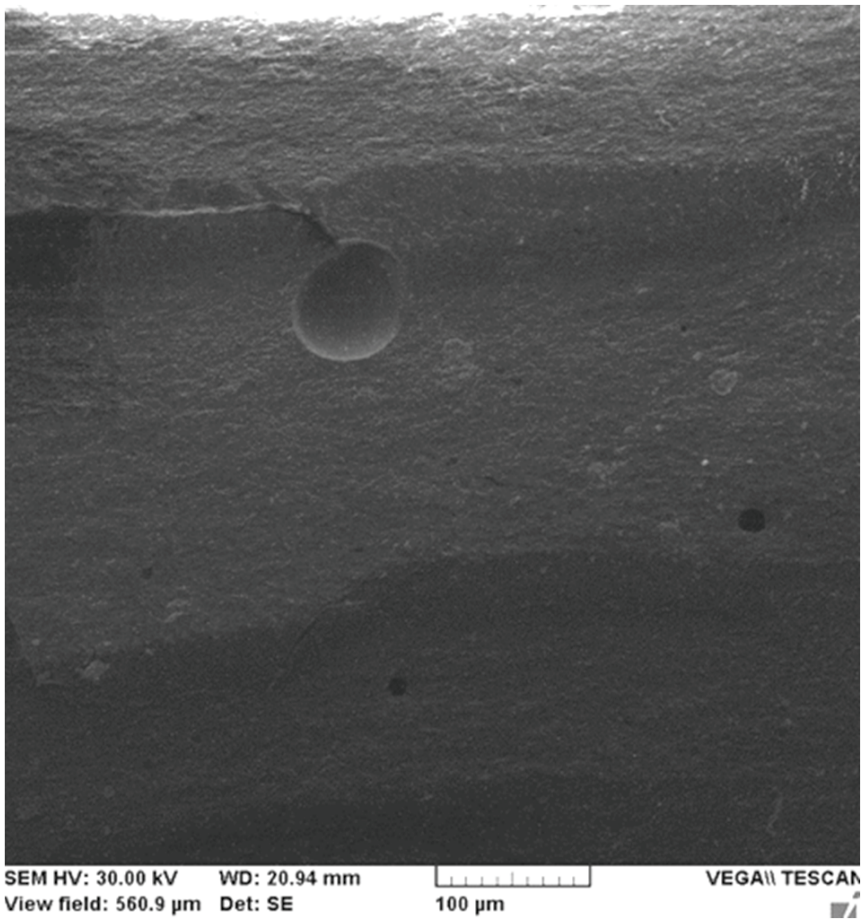


Figure 6. SEM microscopy of Filtek Z250-4 sample with microcrack blocked by a micrometer particle and areas with effective micro filler pull-outs.

3.2. Theoretical Design Considerations

3.2.1. Types of Scenarios in the Description of Dental Composite Materials Dynamics

It is a known fact that the mechanical behaviors of composite dental materials are described through material constitutive laws. For the most part, these are empirical laws that depend on the nature of the dental composite material. Moreover, the variables that describe the mechanical behaviors of said materials and play a role in these material constitutive laws can be expressed through continuous and differentiable functions. Because in time, during mastication, dental composite materials are subjected to various "efforts" (mechanical wearing, chemical wearing, etc.), they will suffer both structural and functional "transformations" (see, for example, the subsequent surface analyzes following various mechanical "efforts"). Such situations cannot be described unless using variables expressed through continuous and non-differentiable mathematical functions (fractal/multifractal functions) [6–8], variables that operate in the context of the SRT. Within the framework of SRT, two description scenarios are proposed to describe the mechanical behavior of dental composite materials: the Schrödinger-type scenario and the Madelung-type scenario. The two scenarios are not mutually exclusive; rather, they are complementary.

In the Schrödinger-type scenario [6–8], the dynamics of dental composite materials are described through the multifractal Schrödinger equation:

$$\lambda^2 (dt)^{\left[\frac{4}{f(\alpha)}\right]-2} \partial_l \partial^l \Psi + i\lambda (dt)^{\left[\frac{2}{f(\alpha)}\right]-1} \partial_t \Psi = 0, \quad (1)$$

where

$$\partial_t = \frac{\partial}{\partial_t}, \partial_l = \frac{\partial}{\partial x^l}, \partial_l \partial^l = \frac{\partial^2}{\partial x_l^2}. \tag{2}$$

In the above relations, Ψ is the states function, dt is the scale resolution, x^l is the multifractal spatial coordinate, t is the non-multifractal temporal coordinate with the role of an affine parameter of the motion curves, λ is a parameter associated to the fractal/multifractal-non-fractal/non-multifractal scale transition, $f(\alpha)$ is the singularity spectrum with a singularity index of order $\alpha = \alpha(D_F)$ and D_F is the fractal dimension of the motion curves [17–19].

On the other hand, by choosing Ψ of the form:

$$\Psi = \sqrt{\rho} e^{is} \tag{3}$$

where $\sqrt{\rho}$ is the amplitude and s is the phase, and introducing the real velocity fields (V_D^i- differentiable velocity field, V_F^i-non-differentiable velocity field):

$$V_D^i = 2\lambda (dt)^{[\frac{2}{f(\alpha)}]-1} \partial^i s \tag{4}$$

$$V_F^i = i\lambda (dt)^{[\frac{2}{f(\alpha)}]-1} \partial^i \ln \rho \tag{5}$$

and the multifractal Schrödinger equation is reduced to the multifractal hydrodynamic equation system—the Madelung-type scenario:

$$\partial_t V_D^i + V_D^l \partial_l V_D^i = -\partial^i Q \tag{6}$$

$$\partial_t \rho + \partial_l \left(\rho V_D^l \right) = 0 \tag{7}$$

with Q the multifractal specific potential:

$$Q = -2\lambda^2 (dt)^{[\frac{4}{f(\alpha)}]-2} \frac{\partial^l \partial_l \sqrt{\rho}}{\sqrt{\rho}} = -V_F^i V_F^i - \frac{1}{2} \lambda (dt)^{[\frac{2}{f(\alpha)}]-1} \partial_l V_F^l. \tag{8}$$

Equation (6) corresponds to the multifractal specific momentum conservation law, while Equation (7) corresponds to the multifractal state density conservation law. The multifractal specific potential (8) implies the multifractal specific force:

$$F^i = -\partial^i Q = -2\lambda^2 (dt)^{[\frac{4}{f(\alpha)}]-2} \partial^i \frac{\partial^l \partial_l \sqrt{\rho}}{\sqrt{\rho}} \tag{9}$$

which is a measure of the multifractality of the motion curves of the dynamics.

From the Equations (6)–(8) the following meanings result:

- Any dental composite materials structural units are in permanent contact with a multifractal medium through the multifractal specific force;
- The multifractal medium can be assimilated with a multifractal fluid whose dynamics are characterized by the multifractal hydrodynamic equation system;
- The velocity field V_F^i is absent from the multifractal states density conservation laws. In such a context, it induces non-manifest dental composite materials dynamics facilitating the transmission of multifractal specific momentum and multifractal energy of focus;
- In dental composite materials dynamics, the "self-aspect" of the multifractal specific momentum, transfer the reversibility, and existence of eigenstates are guaranteed by the conservation of multifractal energy and multifractal momentum. Using the tensor:

$$\hat{\tau}^{il} = 2\lambda^2 (dt)^{[\frac{4}{f(\alpha)}]-2} \rho \partial^i \partial^l \ln \rho \tag{10}$$

Equation (9) takes the form of a multifractal equilibrium equation:

$$\rho \partial^i Q = \partial_l \hat{\tau}^{il} \tag{11}$$

Moreover, since the tensor $\hat{\tau}^{il}$ can also be written in the form:

$$\hat{\tau}^{il} = \eta \left(\partial_l V_F^i + \partial_i V_F^l \right) \tag{12}$$

with:

$$\eta = \lambda (dt)^{[\frac{2}{f(\alpha)}]-1} \rho \tag{13}$$

a multifractal linear constitutive equation for a multifractal "viscous fluid", becomes functionally offering at the same time the reason for an original interpretation of coefficient η as a multifractal dynamic viscosity of the multifractal fluid.

3.2.2. Material Constitutive Laws

The previous relations, which are considered constitutive equations for deformable viscous solids of multifractal type, allow us to analyzedental composite materials behavior both in terms of compression and stretching. Then, both the multifractal tension tensor $\widehat{\sigma_{il}}$, and the deformation tensor $\widehat{\varepsilon_{il}}$, are characterised by the following:

$$\sigma^3 - I_1 \sigma^2 + I_2 \sigma - I_3 = 0 \tag{14}$$

for multifractal tension, and:

$$\varepsilon^3 - J_1 \varepsilon^2 + J_2 \varepsilon - J_3 = 0 \tag{15}$$

for multifractal deformation. Of these, I_1, I_2 and I_3 are multifractal invariants of $\widehat{\sigma_{il}}$, and J_1, J_2 along with J_3 are multifractal invariants of $\widehat{\varepsilon_{il}}$. Now let us define their functional dependency with the relation:

$$\hat{\sigma} = \hat{\sigma}(\hat{\varepsilon}) \tag{16}$$

which implies correlations between the invariants mentioned above. These correlations can be explained through the homographic transformation [20,21]:

$$\varepsilon_k = \frac{\alpha \sigma_k + \beta}{\gamma \sigma_k + \delta}, k = 1, 2, 3 \tag{17}$$

where σ_k and ε_k are the roots of the previously mentioned equations. The coefficients α, β, γ, and δ gain the status of material parameters, while the matrix:

$$\hat{M} = \begin{pmatrix} \alpha & \beta \\ \gamma & \delta \end{pmatrix} \tag{18}$$

given by Equation (17) becomes fundamental in generating the material constitutive laws through the differential geometry associated with this matrix.

In such a context, we will obtain a relation between the matrix and an ensemble of values of σ for which σ' remains constant. From a geometric perspective, this means to find the ensemble $(\alpha, \beta, \gamma, \delta)$ which corresponds unequivocally to σ. Using Equation (16) the problem proves to be reducible to solving the Riccati-type differential equation [20,21]:

$$d\sigma + \omega_1 \sigma^2 + \omega_2 \sigma - \omega_3 = 0 \tag{19}$$

where the following notations were used:

$$\omega_1 = \frac{\gamma d\alpha - \alpha d\gamma}{\Delta}, \omega_2 = \frac{\delta d\alpha - \alpha d\delta + \gamma d\beta - \beta d\gamma}{\Delta}, \omega_3 = \frac{\delta d\beta - \beta d\gamma}{\Delta} \tag{20}$$

$$\Delta = \alpha\delta - \beta\gamma. \tag{21}$$

It is possible to see that the metric:

$$ds^2 = \left(\frac{\delta d\alpha - \alpha d\delta + \gamma d\beta - \beta d\gamma}{\Delta}\right)^2 - \frac{d\alpha d\delta - d\beta d\gamma}{\Delta} \tag{22}$$

is in direct relation to the discriminant of Equation (18):

$$ds^2 = \frac{1}{4}\left({\omega_2}^2 - 4\omega_1\omega_3\right). \tag{23}$$

The three differential 1-forms of Equation (19) constitute a coframe in any point of absolute space. This allows the translation of geometric properties of the absolute space into algebraic properties of Equation (18). The simplest of these refers to dynamics over the geodesics of the metrics of Equation (22), which can be translated directly to statistical properties, given that we discuss multifractalization through stochasticity. In this situation, the 1-forms ω_1, ω_2, and ω_3 are exact differentials of the same parameter, which is the length of the arc of the geodesic. Let us note it with s. Explicitly, we obtain:

$$\omega_1 = a_1 ds, \omega_2 = a_2 ds, \omega_3 = a_3 ds \tag{24}$$

where a_1, a_2 and a_3 are constants which characterize a certain geodesic of the given family. Along this geodesic, Equation (18) becomes a differential equation of the type:

$$\frac{d\sigma}{ds} = a_1\sigma^2 + 2a_2\sigma + a_3 \tag{25}$$

Equation (24) admits a direct integration, giving the following solutions:

$$\sigma(s) = -\frac{\alpha_2}{\alpha_1} + \frac{\sqrt{\Delta}}{\alpha_1}\tan\left[\sqrt{\Delta}(s - s_0)\right] \; for \; \Delta > 0 \tag{26a}$$

$$\sigma(s) = \frac{as + b}{cs + d} \; for \; \Delta = 0 \tag{26b}$$

$$\sigma(s) = -\frac{\alpha_2}{\alpha_1} + \frac{\sqrt{\Delta}}{\alpha_1}\coth\left[\sqrt{\Delta}(s - s_0)\right] \; for \; \Delta < 0 \tag{26c}$$

with:

$$\Delta = a_1 a_3 - {a_2}^2, a_2 = \sqrt{\Delta}\tan\left(\sqrt{\Delta}s_0\right) \tag{27}$$

Furthermore, s_0, a, b, c, d are constants, not all of them are arbitrary.

Any of Equation (26) describes a deformation process for constant tensions. A similar procedure can be applied to $\widehat{\varepsilon_{il}}$. Then, the following equation is satisfied:

$$\frac{d\varepsilon}{d\tau} = \overline{a_1}\varepsilon^2 + 2\overline{a_2}\varepsilon + \overline{a_3} \tag{28}$$

these constants characterize a certain geodesic of the family and τ the length of the arc. Equation (27) admits direct integration, which yields three possibilities:

$$\varepsilon(\tau) = -\frac{\overline{\alpha_2}}{\overline{\alpha_1}} + \frac{\sqrt{\overline{\Delta}}}{\overline{\alpha_1}}\tan\left[\sqrt{\overline{\Delta}}(\tau - \tau_0)\right] \; for \; \overline{\Delta} > 0 \tag{29a}$$

$$\varepsilon(\tau) = \frac{\overline{a}\tau + \overline{b}}{\overline{c}\tau + \overline{d}} \; for \; \overline{\Delta} = 0 \tag{29b}$$

$$\varepsilon(\tau) = -\frac{\overline{\alpha_2}}{\overline{\alpha_1}} + \frac{\sqrt{\overline{\Delta}}}{\overline{\alpha_1}}\coth\left[\sqrt{\overline{\Delta}}(\tau - \tau_0)\right] \; for \; \overline{\Delta} < 0. \tag{29c}$$

Here, $\overline{\Delta}$ and τ_0 are given through the relations:

$$\overline{\Delta} = \overline{a_1 a_3} - \overline{a_2}^2, \overline{a_2} = \sqrt{\overline{\Delta}}\tan\left(\sqrt{\overline{\Delta}}\tau_0\right). \tag{30}$$

However, these constants are not necessarily arbitrary. Now, if both $\sigma(s)$ and $\tau(\varepsilon)$ follow the same manifold, which implies:

$$a_1 = \overline{a_1}, a_2 = \overline{a_2}, a_3 = \overline{a_3}, \tau = \frac{s}{E}, E = const. \tag{31}$$

then from Equations (24) and (27) the following differential relation is obtained:

$$d\sigma = Ed\varepsilon. \tag{32}$$

From Equation (31), the Young-type differential elasticity modulus results:

$$E = \frac{d\sigma}{d\varepsilon}. \tag{33}$$

This equation can also present negative values, $E = \frac{d\sigma}{d\varepsilon} < 0$, which might specify self-structuring phenomena through pattern formation. Now, if we admit the particular case:

$$a_1 = -f, 2a_2 = f, a_3 = 0. \tag{34}$$

Equation (24) is reduced to a logistic-type equation [17,18]:

$$\frac{d\sigma}{ds} = f\sigma(1 - \sigma) \tag{35}$$

thus, the growth of σ is limited by the finite matrix effect. The solution of Equation (34) is:

$$\sigma = \frac{1}{1 - \left(1 - \frac{1}{\sigma_0}\right)e^{(-fs)}} \tag{36}$$

where σ_0 is an integration constant. A similar mathematical procedure can be applied to Equation (27), which implies:

$$\varepsilon = \frac{1}{1 - \left(1 - \frac{1}{\varepsilon_0}\right)e^{(-\Omega\tau)}} \tag{37}$$

where ε_0 is an integration constant. Such a result is possible if, in Equation (27), we admit the identifications:

$$\overline{a_1} = -\Omega, 2\overline{a_2} = \Omega, \overline{a_3} = 0. \tag{38}$$

It is possible to highlight the otherwise well-known fact of nonlinear dynamics [17,18] that the increase in the logistic map parameter after 3.56995 leads to chaos. This means that between roughly 3.6 and 4, there are complex chaotic dynamics; in our case, it means that the variation of f between 3.6 and 4 leads to repeated ordered-chaotic dynamics transition for $\frac{d\sigma}{ds}$. Practically, because of the nature of this mapping, there are order-disorder transitions in dental composite materials dynamics, wherein f is the control parameter (see Figure 7).

In order to further investigate the dental composite materials dynamics of this system, it is also possible to rewrite Equation (19) as:

$$\dot{w} - \frac{1}{M}w^2 + 2\frac{R}{M}w - K = 0. \tag{39}$$

It is important to find the most general solution of this equation. For our current needs, it is enough to note that the complex number roots of the quadratic polynomial of Equation (39):

$$w_0 \equiv R + iM\Omega, w_0^* \equiv R - iM\Omega; \Omega^2 = \frac{K}{M} - \left(\frac{R}{M}\right)^2 \tag{40}$$

are constant solutions of the equation, thus their derivative is zero. Let us perform the homographic transformation:

$$z = \frac{w - w_0}{w - w_0^*} \tag{41}$$

and now it can easily be seen by direct calculation that z is a solution of the linear and homogeneous equation of the first order:

$$\dot{z} = 2i\Omega z \ \therefore \ z(t) = z(0)e^{2i\Omega t}. \tag{42}$$

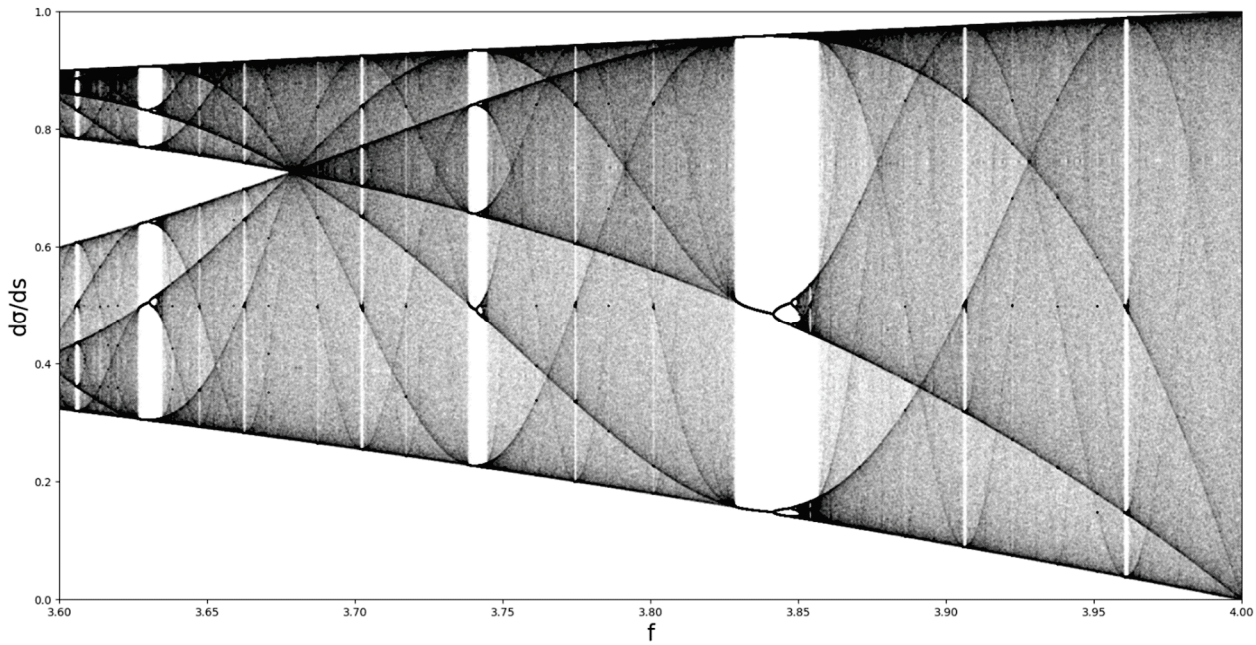


Figure 7. Representation of Equation (35) in the same manner as the logistic map; chaotic region with areas of stability.

Therefore, if we conveniently express the initial condition $z(0)$, we can give the general solution of the Equation (39) by simply inverting the transformation in Equation (41), with the result:

$$w = \frac{w_0 + re^{2i\Omega(t-t_r)}w_0^*}{1 + re^{2i\Omega(t-t_r)}} \tag{43}$$

where r and t_r are two real constants that characterize the solution. Using Equation (40), we can put this solution in real terms, which highlights a frequency modulation through what we would call a Stoler transformation [20,21] which leads us to a complex form of this parameter. Furthermore, if we make the notation:

$$r \equiv \coth\tau \tag{44}$$

the real term becomes:

$$z = R + M\Omega h \tag{45}$$

where h is given by:

$$h = -i\frac{\cosh\tau - e^{-2i\Omega(t-t_m)}\sinh\tau}{\cosh\tau + e^{-2i\Omega(t-t_m)}\sinh\tau}. \tag{46}$$

The meaning of this complex parameter will become clear later. For the moment, let it be noted that any dynamic process appears here as a frequency modulation process using a gauge invariance of a Riccati-type.

In these figures, Real (h) (the amplitude at various scale resolutions given by the maximum value of Ω) is represented as functions of t and Ω for r = 0.5.

As is observed in Figures 8a–d and 9a-d, the natural transition of dental composite materials dynamics passes through various states, such as self-modulation and period doubling. The dental composite materials dynamics never reach a chaotic state, but they permanently evolve towards that state.

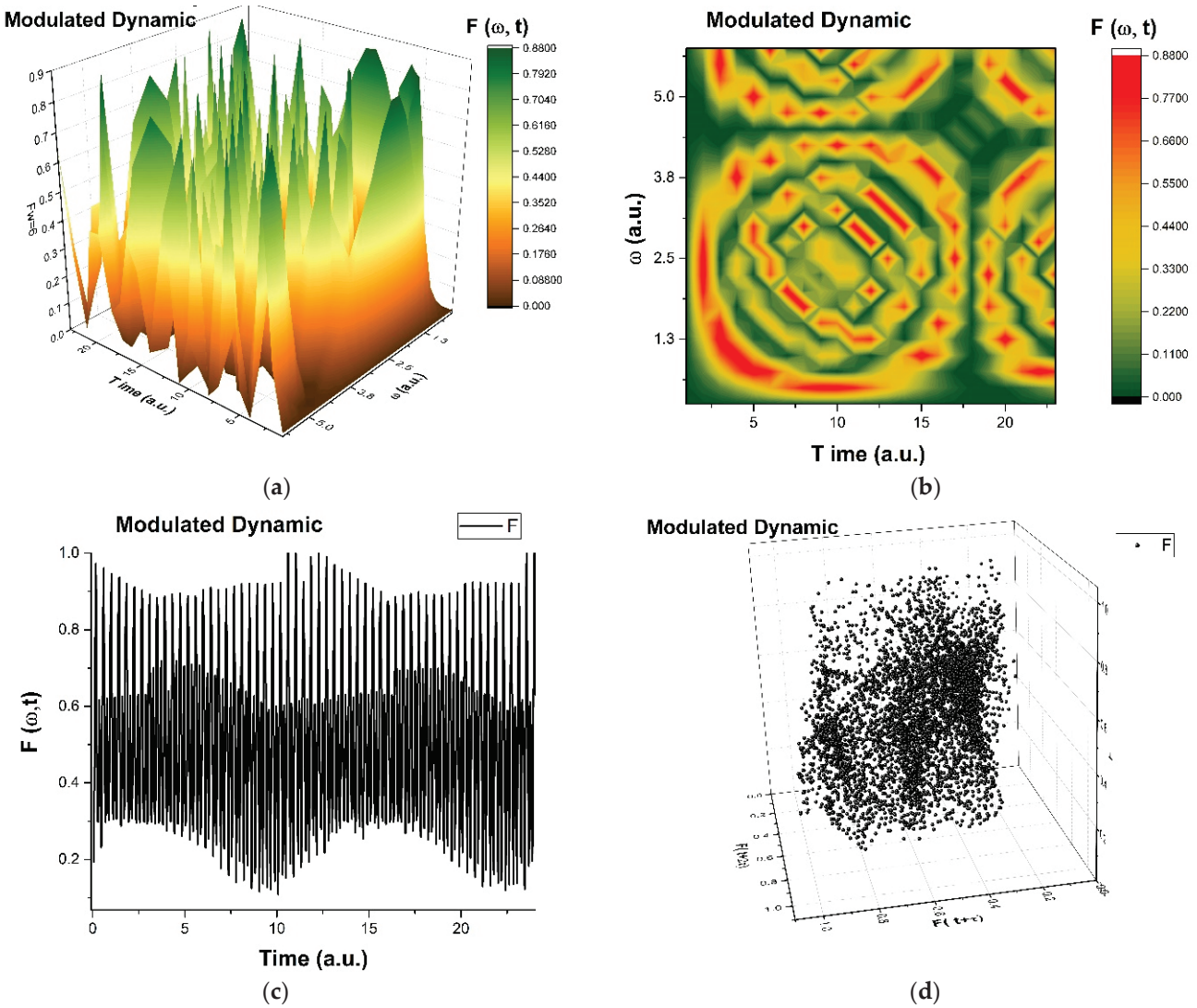


Figure 8. (**a**–**d**): The "modulated dynamic modes" in mastication of the structural units of dental composite materials dynamics are presented: (**a**)—3D diagram, (**b**)—contour diagram, (**c**)—time series and (**d**)—reconstituted attractor for scale resolutions given by Ω_{max}.

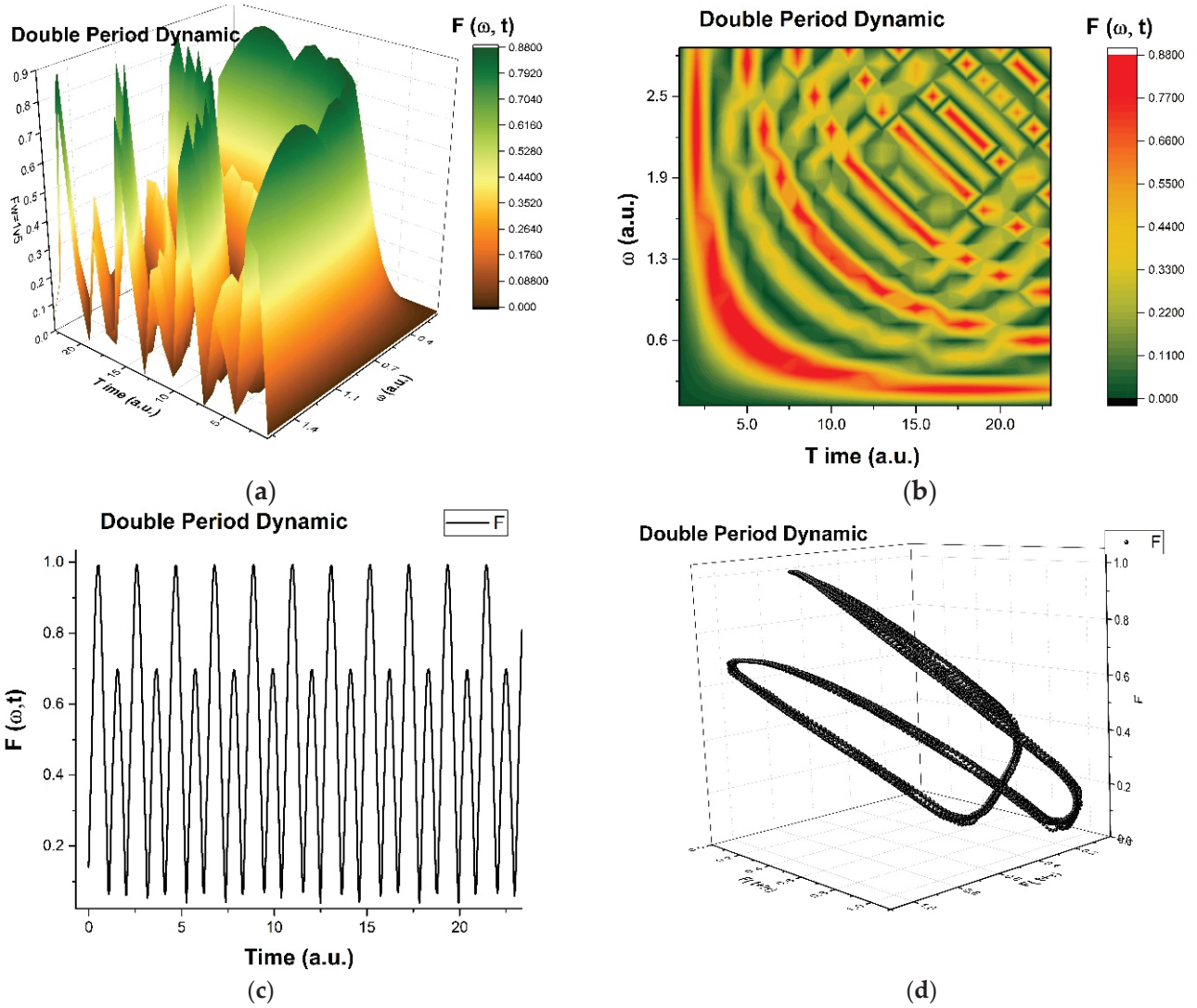
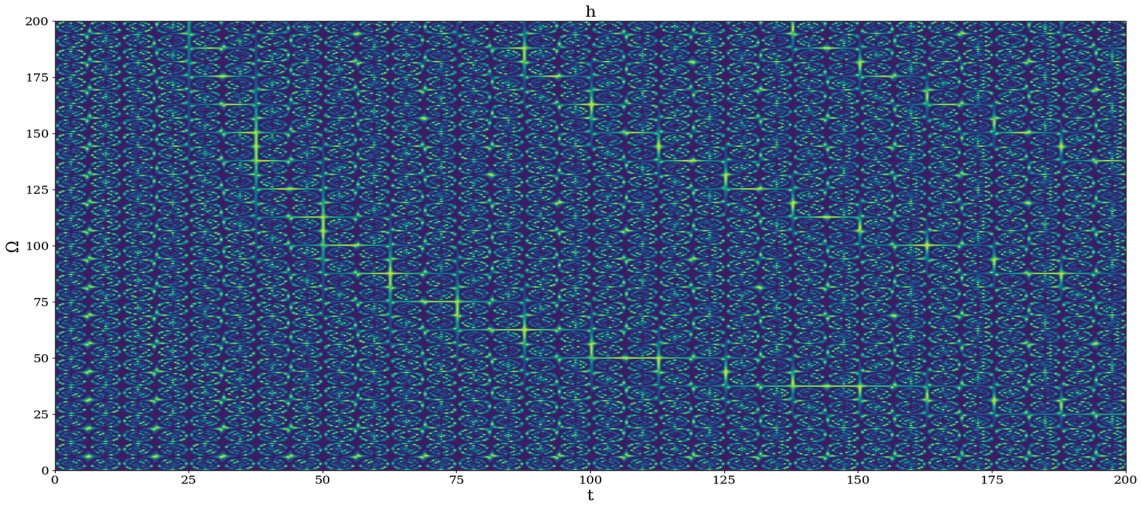


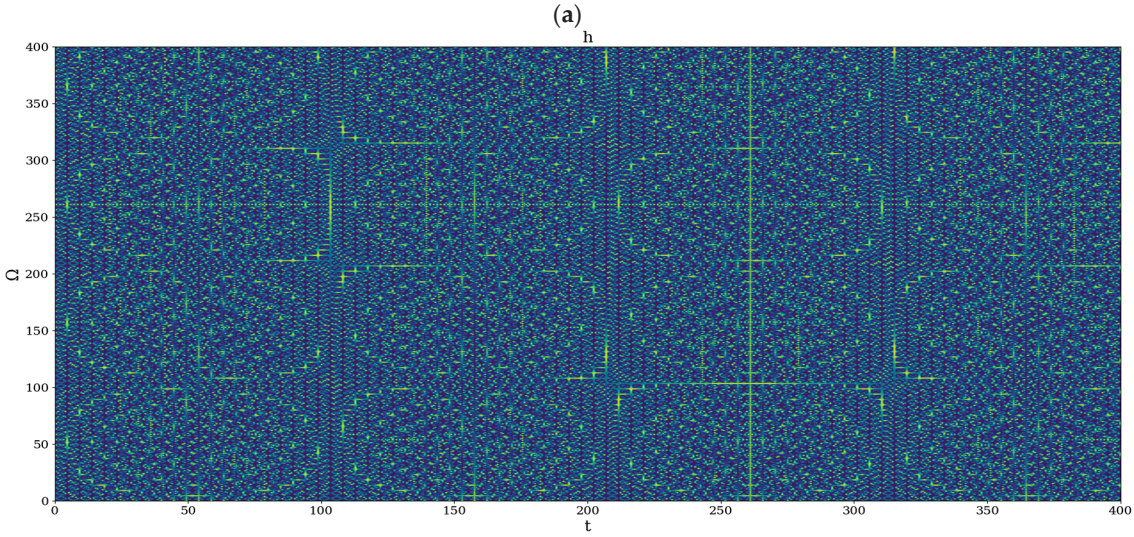
Figure 9. (**a**–**d**): The "double period dynamic modes" in mastication of the structural units of dental composite materials dynamics are presented: (**a**)—3D diagram, (**b**)—contour diagram, (**c**)—time series and (**d**)—reconstituted attractor for scale resolutions given by Ω_{max}.

Let it be noted that the mathematical formalism of the SRT naturally implies various operational procedures (invariance groups, harmonic mappings, groups isomorphism, embedding manifolds, etc.) with several applications incomposite materials dynamics [7,8]. Interestingly, plotting h in dimensionless parameters again highlights certain temporal self-similar properties, with the multifractal structures being contained into similar multifractal structures at much higher scales (Figure 10a–c). This behavior is quite difficult to represent because of the complicated balance between choosing an adequate number of plot points and manifesting self-similarity. Still, it shows how the small-scale behavior of the system ripples and manifests itself at higher scales, which is exactly what we would expect from a multifractal system.

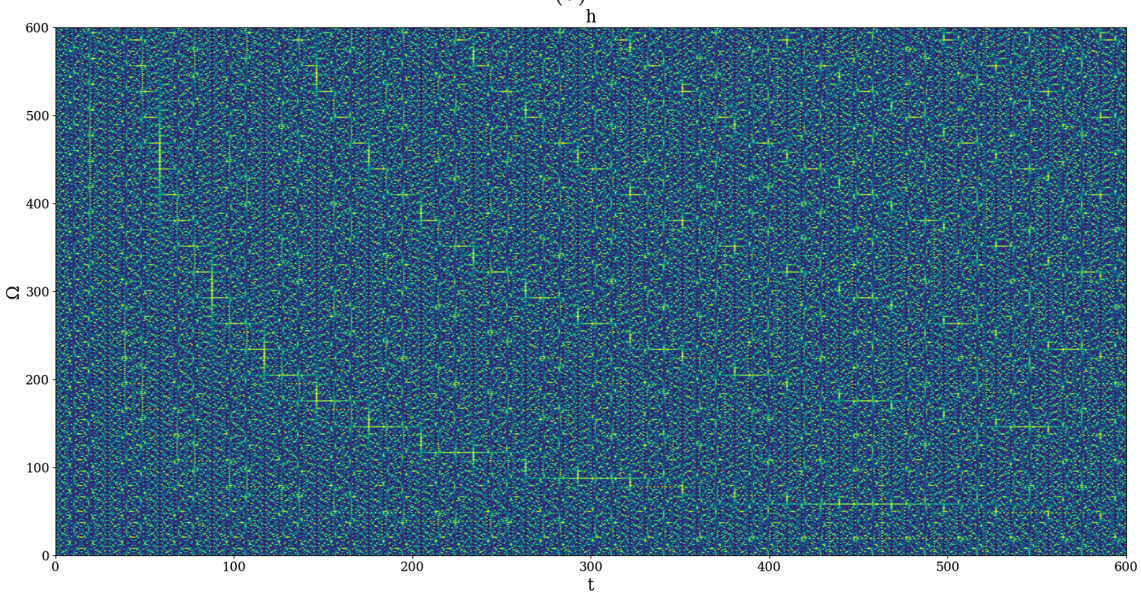
In such a context, the transitions from the patterns presented in Figures 8b and 9b through Figure 10a–c can be made through compression. Figure 9a–c illustrates fracture patterns due to compressive stresses. Moreover, the phenomenon can be explained through a mathematical equation that governs it.



(**a**)



(**b**)



(**c**)

Figure 10. (**a**): Example of 2D plot fracture patterns by means of $h(\Omega, t)$, maximum at 200; $\Phi = 2.35$. (**b**): Example of 2D plot fracture patterns by means of $h(\Omega, t)$, maximum at 400; $\Phi = 2.35$. (**c**): Example of 2D plot fracture patterns by means of $h(\Omega, t)$, maximum at 600; $\Phi = 2.35$.

Thus, an analytical expression is given for the nonlinear range of $\sigma - \varepsilon$ curves under compression and is as follows (see Equation (33), through a convenient choice of the parameters and considering that the dental composite materials dynamics manifest on the same manifold, which implies $s \equiv \tau$):

$$\sigma = E_0\varepsilon(1 + \alpha\varepsilon) \tag{47}$$

where E_0 is the initial tangent at zero (corresponding to the elastic modulus for purely linear elastic behavior). For example, for fused silica, the elastic material parameters are commonly known and need no further elaboration. The used (linear) elastic modulus is E_0 = 70 GPa. Elastic volume compressibility is expressed by the Poisson ratio with ν = 0.17. In the equation, the experimental data provided the coefficient α = 3 for the nonlinear behavior. Such a law, in dimensionless coordinates (for various fractal dimensions and scale resolutions), can very well describe the experimental curves obtained in Figures 1 and 2. Let it be noted that such scenarios were employed before in the description of mechanical behaviors of various materials. For example, in [22], a Schrödinger type scenario was used for the description of the hysteresis-type behavior of shape memory alloys.

4. Materials and Methods

Experimental Design

The equipment for tensile/compression testing of dental composite materials is the INSTRON 3382 USA servo-hydraulic type. It is characterized by the following technical parameters:

- load capacity of 100 kN with a maximum speed of 500 mm/min, minimum speed of 5×10^{-3} mm/min;
- maximum force at maximum speed: 50 kN;
- maximum speed at maximum force: 250 mm/min;
- return speed: 600 mm/min;
- Blue hill® Lite software;
- INSTRON climatic enclosure with a possible temperature range of −70 °C to +350 °C;
- INSTRON 3-point bending device, 100kN, and a compression device.

The equipment, connected and controlled by a computer, can develop different compression speeds of materials, in this case, dental composites to follow their behavior in different compression phases.

The composite resin tested in the present study and their structure are presented in Table 2. The samples from the two materials were made into cylindrical molds with a length of 9 mm and a diameter of 4.5 mm, i.e., with a length/diameter (l/d) ratio of 2:1, which is standard for this type of mechanical test. They were subjected to compression tests at different working speeds of the mechanical equipment, of 0.5, 1, and 1.5 mm/min. The tests were carried out at a room temperature of 27 °C.

Table 2. Structure of the two materials.

Material	Manufacturer	Type/Shade	Matrix	Filler
Filtek Supreme XT Universal Restorative	3MESPE, St. Paul, MN, USA	Nanocomposite/A2	Bis-GMA, Bis-EMA, TEGDMA UDMA	Non-agglomerated/non-aggregated 20 nm silica particles, Non-agglomerated/non-aggregated 4 to 11 nm zirconia particles, Aggregated zirconia/silica cluster filler (comprised of 20 nm silica and 4 to 11 nm zirconia particles) 78.5 wt % 63.3 vol%
Filtek Z250 Universal Restorative	3MESPE, St. Paul, MN, USA	Microhybrid/A2	Bis-GMA, Bis-EMA, TEGDMA UDMA	Silica and zirconia particles 0.01–3.5 μm, average size 0.6 μm 84.5 wt% 60 vol%

After the mechanical tests were completed, the resulting fragments from the samples were investigated by SEM microscopy in order to identify the causes of breakage and the mode of propagation of the microcracks.

Samples made from the two materials were machined into cylindrical form with a length of 9 mm and a diameter of 4.5 mm, i.e., with a length/diameter (l/d) ratio of 2:1, which is standard for this type of mechanical test. They were subjected to compression tests at different working speeds of the mechanical equipment of 0.5, 1, and 1.5 mm/min. The tests were carried out at room temperature, 27 °C.

After the mechanical tests, the samples were investigated by SEM microscopy to identify the causes of breakage and the mode of propagation of microcracks. Such experimental studies have been performed on other materials and employed other types of mechanical "efforts" (see, for example, [23,24]).

5. Conclusions

The main conclusions of the present paper are the following:

Regarding the experimental design, the compressive strength of the Filtek Supreme XT composite was obtained as 332.14 MPa, lower than that of the Filtek Z250 material, 392 MPa, values in agreement with those specified by the manufacturer and the literature. However, this parameter depends on the samples' compaction before light curing. Analysisof the compressive stress—compressive strain dependencies revealed stronger cracking of the Filtek Supreme XT composite than Filtek Z250 prior to fracture, which has important clinical implications for ensuring the integrity of dental restorations. SEM microscopy results of the two materials showed microcracks produced upon compression and, in the case of Filtek Z250, the existence of micro gaps produced by the detachment of micrometer filler particles. A crack-blocking mechanism by the filler microparticles of Filtek Z250 has been revealed. This may explain its superior mechanical properties compared to the Filtek Supreme XT nanocomposite, where cracks bypass the nanometer particles.

Regarding the theoretical design, in Schrödinger-type and Madelung-type scenarios, the descriptions of dental composite materials dynamics are highlighted. The existence of an SL(2R) type symmetry allows the generation of material constitutive laws. In such a context, through gauge invariances of Riccati-type, various non-linear behaviors are established: double period and modulated dynamics regimes. A material constitutive law of Hooke-type in differential form was obtained, which was explained for compression-type behaviors. In such a context, an explicit form of the law was highlighted, which was correlated with the experimental data.

Author Contributions: Conceptualization, I.N., F.N. and M.A.; methodology, C.P., D.V. and Ș.L.T.; software, F.N.; validation, I.N., M.A. and V.N.; formal analysis, C.P. and D.V.; investigation, Ș.L.T. and I.N.; resources, F.N., M.A. and V.N.; data curation, F.N. and D.V.; writing—original draft preparation, I.N. and M.A.; writing—review and editing, V.N. and C.P.; visualization, D.V.; supervision, I.N. and M.A.; project administration, M.A. and V.N. All authors have read and agreed to the published version of the manuscript.

Funding: This research recieved no external funding.

Institutional Review Board Statement: Not applicable.

Informed Consent Statement: Not applicable.

Data Availability Statement: Research data is available upon request.

Conflicts of Interest: The Authors declare no conflict of interest.

Abbreviations

List of abbreviations:

SRT	Scale Relativity Theory
Bis-GMA	bisphenol A-glycidyl methacrylate
bis-EMA	bisphenol A-ethoxylateddimethacrylate
TEGDMA	triethyleneglycoldimethacrylate
UDMA	urethane dimethacrylate,

References

1. Miletic, V. *Dental Composite Materials for Direct Restorations*; Springer International Publishing: Cham, Switzerland, 2018.
2. Brenna, F. *Restorative Dentistry: Treatment Procedures and Future Prospects*; Elsevier/Saunders: St. Louis, MO, USA, 2012.
3. Mitchell, M. *Complexity: A Guided Tour*; Oxford University Press: Oxford, UK, 2009.
4. Badii, R. *Complexity: Hierarchial Structures and Scaling in Physics*; Cambridge University Press: Cambridge, UK, 1997.
5. Bar-Yam, Y. *Dynamics of Complex Systems*; The Advanced Book Program; Addison-Wesley: Reading, MA, USA, 1997.
6. Nottale, L. *Scale Relativity and Fractal Space-Time: A New Approach to Unifying Relativity and Quantum Mechanics*; Imperial College Press: London, UK, 2011.
7. Merches, I.; Agop, M. *Differentiability and Fractality in Dynamics of Physical Systems*; World Scientific: Hackensack, NJ, USA, 2016.
8. Agop, M.; Paun, V.-P. *On the New Perspectives of Fractal Theory. Fundaments and Applications*; Romanian Academy Publishing House: Bucharest, Romania, 2017.
9. Moezzyzadeh, M. Evaluation of the compressive strength of hybrid and nanocomposites. *J. Dent. Sch.* **2012**, *1*, 24–29.
10. Mohandesi, J.A.; Rafiee, M.A.; Barzegaran, V. Compressive fatigue behavior of dental restorative composites. *Dent. Mater. J.* **2007**, *26*, 827–837. [CrossRef] [PubMed]
11. Pradeep, K.; Ginjupalli, K.; Kuttappa, M.A.; Kudva, A.; Butula, R. In vitro Comparison of Compressive Strength of Bulk-fill Composites and Nanohybrid Composite. *World J. Dent.* **2016**, *7*, 119–122. [CrossRef]
12. Gamen, A.; Iovan, G.; Stoleriu, S.; Pancu, G.; Nica, I.; Georgescu, A.; Taraboanta, I.; Andrian, S. Evaluation of Mechanical Parameters at Compression Test for Different Restorative Composite Resins. *Mater. Plast.* **2019**, *56*, 592–595. [CrossRef]
13. Rakhee, R.; Jayasree, S.; Ramesh, K.; Prashant, B.; Rajeesh, M.K.; Abdu Semeer, P. Comparative Evaluation of Compressive And Flexural Strength of Newer Nanocomposite Materials with Conventional Hybrid Composites-An Invitro Study. *IOSR-JDMS* **2017**, *16*, 65–69.
14. Meenakumari, C.; Manohar Bhat, K.; Bansal, R.; Singh, N. Evaluation of Mechanical Properties of Newer Nanoposterior Restorative Resin Composites: An In vitro Study. *Contemp. Clin. Dent.* **2018**, *9*, 142–146. [CrossRef] [PubMed]
15. Stoleriu, S.; Andrian, S.; Nica, I.; Sandu, A.V.; Pancu, G.; Murariu, A.; Iovan, G. Evaluation of Adhesive Capacity of Universal Bonding Agents Used in Direct Composite Resins Repair. *Mater. Plast.* **2017**, *54*, 574. [CrossRef]
16. Ghiorghe, C.A.; Iovan, G.; Topoliceanu, C.; Sandu, A.V.; Andrian, S. Comparative Study Regarding the Colorimetric Changes of Two Composite Resins after Immersion in Several Beverages and One Antibacterial Mouthwash. *Rev. Chem.* **2013**, *64*, 1436–1440.
17. Jackson, E.A. *Perspectives of Nonlinear Dynamics*; Cambridge University Press: New York, NY, USA, 1993; Volume 1–2.
18. Cristescu, C.P. *Nonlinear Dynamics and Chaos. Theoretical Fundaments and Applications*; Romanian Academy Publishing House: Bucharest, Romania, 2008.
19. Mandelbrot, B.B. *The Fractal Geometry of Nature*; W.H. Freeman and Company: San Francisco, CA, USA, 1982.
20. Mazilu, N.; Agop, M. *At the Crossroads of Theories. Between Newton and Einstein—The Barbilian Universe*; ArsLonga Publishing House: Iasi, Romania, 2010. (In Romanian)
21. Mazilu, N.; Agop, M. *Skyrmions: A Great Finishing Touch to Classical Newtonian Philosophy, World Philosophy Series*; Nova: New York, NY, USA, 2012.
22. Plăcintă, C.; Stanciu, S.; Panainte-Lehadus, M.; Mosnegutu, E.; Nedeff, F.; Nedeff, V.; Tomozei, C.; Petrescu, T.-C.; Agop, M. Theoretical and Experimental Designs on Several Mechanical Properties of Cu–Al–Zn Shape Memory Alloys Used in the Processing Industry. *Materials* **2023**, *16*, 1441. [CrossRef] [PubMed]
23. Schauperl, Z.; Ivankovi'c, L.; Bauer, L.; Šolić, S.; Ivankovic, M. Effects of Different Surface Treatments of Woven Glass Fibers on Mechanical Properties of an Acrylic Denture Base Material. *Int. J. Mol. Sci.* **2023**, *24*, 909. [CrossRef] [PubMed]
24. Beketova, A.; Tzanakakis, E.G.C.; Vouvoudi, E.; Anastasiadis, K.; Rigos, A.E.; Pandoleon, P.; Bikiaris, D.; Tzoutzas, I.G.; Kontonasaki, E. Zirconia Nanoparticles as Reinforcing Agents for Contemporary Dental Luting Cements: Physicochemical Properties and Shear Bond Strength to Monolithic Zirconia. *Int. J. Mol. Sci.* **2023**, *24*, 2067. [CrossRef] [PubMed]

Disclaimer/Publisher's Note: The statements, opinions and data contained in all publications are solely those of the individual author(s) and contributor(s) and not of MDPI and/or the editor(s). MDPI and/or the editor(s) disclaim responsibility for any injury to people or property resulting from any ideas, methods, instructions or products referred to in the content.

International Journal of
Molecular Sciences

MDPI

Article

Osteogenic Potential of Autologous Dentin Graft Compared with Bovine Xenograft Mixed with Autologous Bone in the Esthetic Zone: Radiographic, Histologic and Immunohistochemical Evaluation

Matko Oguić [1,2,†], Marija Čandrlić [3,†], Matej Tomas [3], Bruno Vidaković [3], Marko Blašković [4,5], Ana Terezija Jerbić Radetić [6], Sanja Zoričić Cvek [6], Davor Kuiš [3,7,8,*] and Olga Cvijanović Peloza [6,*]

1 Doctoral School of Biomedicine and Health, Faculty of Medicine, University of Rijeka, 51 000 Rijeka, Croatia
2 Dental Clinic Rident, 51 000 Rijeka, Croatia
3 Department of Dental Medicine, Faculty of Dental Medicine and Health Osijek, J.J. Strossmayer University of Osijek, 31 000 Osijek, Croatia
4 Private Practice, 51 000 Rijeka, Croatia
5 Department of Oral Surgery, Faculty of Dental Medicine Rijeka, University of Rijeka, 51 000 Rijeka, Croatia
6 Department of Anatomy, Faculty of Medicine, University of Rijeka, 51 000 Rijeka, Croatia
7 Department of Periodontology, Faculty of Dental Medicine Rijeka, University of Rijeka, 51 000 Rijeka, Croatia
8 Clinical Hospital Center Rijeka, 51 000 Rijeka, Croatia
* Correspondence: kuisdavor@gmail.com (D.K.); olga.cvijanovic@uniri.hr (O.C.P.)
† These authors contributed equally to this work.

Abstract: This prospective, randomized, controlled clinical trial reports clinical, radiographic, histologic and immunohistochemical results of autologous dentin graft (ADG) and its comparison with a mixture of bovine xenograft with autologous bone (BX+AB). After tooth extraction in the esthetic zone of maxilla, the alveolar ridge of 20 patients in the test group was augmented with ADG, while 17 patients in the control group received the combination of BX+AB. Cone beam computed tomography (CBCT) was performed before tooth extraction and after 4 months when a total of 22 bone biopsies were harvested and subjected to histological and immunohistochemical analysis. Radiological analysis showed comparable results of bone dimension loss in both groups. Quantitative histologic analysis showed comparable results with no statistically significant differences between the groups. Immunohistochemical staining with TNF-α and BMP-4 antibodies revealed immunopositivity in both groups. A statistically significant difference between the groups was found in the intensity of TNF-α in the area of newly formed bone ($p = 0.0003$) and around remaining biomaterial particles ($p = 0.0027$), and in the intensity of BMP-4 in the area around biomaterial particles ($p = 0.0001$). Overall, ADG showed biocompatibility and achieved successful bone regeneration in the esthetic zone of the maxilla similar to BX+AB.

Keywords: guided bone regeneration; alveolar ridge preservation; autologous dentin; bovine xenograft; CBCT; histology; BMP-4; TNF-α

Citation: Oguić, M.; Čandrlić, M.; Tomas, M.; Vidaković, B.; Blašković, M.; Jerbić Radetić, A.T.; Zoričić Cvek, S.; Kuiš, D.; Cvijanović Peloza, O. Osteogenic Potential of Autologous Dentin Graft Compared with Bovine Xenograft Mixed with Autologous Bone in the Esthetic Zone: Radiographic, Histologic and Immunohistochemical Evaluation. *Int. J. Mol. Sci.* **2023**, *24*, 6440. https://doi.org/10.3390/ijms24076440

Academic Editor: Mary Anne Melo

Received: 24 February 2023
Revised: 22 March 2023
Accepted: 28 March 2023
Published: 29 March 2023

Copyright: © 2023 by the authors. Licensee MDPI, Basel, Switzerland. This article is an open access article distributed under the terms and conditions of the Creative Commons Attribution (CC BY) license (https://creativecommons.org/licenses/by/4.0/).

1. Introduction

Tooth extraction is one of the most common procedures in dentistry. Scientific studies have clearly shown that the loss of a tooth significantly alters the size of the alveolar ridge, which may be unfavorable for the placement of dental implants [1]. Although bone resorption after tooth extraction is a long-term process, statistically, the greatest loss occurs in the first month after tooth extraction. In the first six months after tooth extraction, horizontal alveolar bone loss ranges from 29% to 63% and vertical alveolar bone loss ranges from 11% to 22% [2]. According to a study conducted by Chappuis et al. [3], an alveolus with a buccal wall thickness of 1 mm or less loses 7.5 mm in height two months after

tooth extraction, while an alveolus with a buccal wall thickness of 1 mm or more loses 1 mm in vertical dimension. All of the aforementioned dimensional changes have negative effects on the patient's ability to receive prosthetic or implant-supported rehabilitation, including altered alveolar ridge morphology, atrophy, and complete disappearance of the alveolar ridge bone [2–4]. Due to the specific structure of the maxilla, where trabecular bone dominates, this procedure can be particularly challenging in the anterior region of this bone. Therefore, the maxilla is less resistant to resorption processes than the mandible, which is predominantly composed of cortical bone [5,6]. In addition, the anterior maxilla is also the esthetic zone, making soft and hard tissue reconstruction more challenging to meet the esthetic expectations of patients and professionals [7].

To prevent the loss of bone volume, a method known as alveolar ridge preservation is used [8]. Bone volume preservation is possible with various surgical procedures such as guided bone regeneration (GBR), with the goal of achieving successful bone regeneration according to the principles of osteogenesis, osteoinduction, and osteoconduction [9,10]. A variety of graft materials has been used to preserve the dimensions of the alveolar ridge, including autologous bone grafts, xenografts, allografts, and alloplast [11,12].

Compared to other bone graft substitutes, autologous bone is the only material that has osteogenic, osteoinductive, and osteoconductive effects [10,13]. Autologous bone is therefore the "gold standard" for augmentation of various alveolar bone defects [14,15]. However, the use of autologous bone is associated with a number of potential complications related to morbidity at the harvest or placement site, sometimes unpredictable and rapid resorption, and limited availability [15]. The incidence of complications has been reported in the literature to range from 0.5% to 10.5%, with a lower incidence of complications associated with intraoral autologous graft retrieval. Rapid resorption of autologous bone is an unpredictable and relatively common complication with an incidence ranging from 5 to 28% [16]. To reduce resorption, mixing autologous bone with bovine xenograft and using a GBR membrane is recommended, which can reduce autologous graft resorption by 50% [17].

Xenograft is a bone substitute material derived from a species different from that of the recipient. These grafts are primarily made from the inorganic portion of animal bone tissue using chemical and/or mechanical processes that remove the organic components of the bone and produce hydroxyapatite granules that resemble the human mineralized bone matrix. Xenografts have been reported to have osteoconductive properties, are hydrophilic, and biocompatible; however, bovine-derived graft biomaterials may inherently carry the risk of transmitting prion diseases to patients [18–21]. One of the most commonly used xenografts for alveolar ridge preservation today is cerabone® (botiss biomaterials, Zossen, Germany). It is made from trabecular bovine bone under a a high temperature treatment (>1200 °C), which contributes to its safety and special physical properties. It has a granular structure with high porosity, which allows for good penetration of blood vessels and the formation and reorganization of newly formed bone tissue [22].

A relatively new graft material for bone regeneration is autologous dentin. In 1967, Yeomans and Urist demonstrated the presence of bone morphogenetic proteins (BMPs) in dentin, providing the first known evidence of the osteoinductive potential of the demineralized dentin matrix [23]. The only signaling molecules that can independently induce de novo bone formation at orthotopic and heterotopic sites are BMPs, and their presence in dentin distinguishes it from xenogeneic biomaterials that do not contain proteins [24,25]. Due to the development of technologies that facilitate the clinical application of dentin, it has been increasingly used as an augmentation material since 2008 [26]. The osteoconductive and osteoinductive properties of autologous dentin were determined in studies using an experimental animal model that demonstrated osteoconduction, integration and resorption of autologous dentin [27–29]. The use of autologous dentin in combination with platelet-rich fibrin was evaluated radiographically with cone beam computed tomography (CBCT) analysis [30]. A recent clinical study compared the clinical and histologic outcomes of augmentation of alveolar bone defects with autologous dentin and bovine xenograft [31].

Nevertheless, there is a knowledge gap regarding the osteogenic potential of autologous dentin, especially regarding the expression of inflammatory and osteoinductive factors in bone tissue after the application of autologous dentin in the alveolar socket. Therefore, the aim of this randomized controlled clinical trial was to investigate the clinical and radiographic efficacy, as well as the histological and immunohistochemical properties, of autologous dentin in alveolar ridge preservation and to compare it with bovine xenograft mixed with autologous bone.

2. Results

2.1. Clinical Evaluation

A total of 37 patients met the inclusion criteria for participation in the clinical trial. The demographic characteristics of the population and the distribution of extraction sites are shown in the tables below (Tables 1 and 2). For each participant, only one extraction site in the esthetic zone (maxillary incisors, canines, and premolars) was considered.

Table 1. Participants' demographic information.

	ADG [1]	BX+AB [2]
Gender		
Female	7 (35%)	12 (70.5%)
Male	13 (65%)	5 (29.5%)
n	20	17
Age (years)		
Mean	52.4	55.9
SD	10.8	8.8
Min	26	38
Max	71	74

[1] Autologous dentin graft, [2] bovine xenograft + autologous bone.

Table 2. Distribution of maxillary extraction sites.

	Incisor	Canine	Premolar	Total
ADG [1]	12	3	5	20
BX+AB [2]	13	3	1	17
Total	25	6	6	37

[1] Autologous dentin graft, [2] bovine xenograft + autologous bone.

The healing was uneventful. Only five patients in the test group and three patients in the control group reported moderate discomfort, pain, and swelling. Patients did not report exposed wounds or leakage of biomaterial into the oral cavity. All patients participated in regular check-ups and CBCT scans and transitioned to implant therapy after four months. At the four-month follow-up, the oral mucosa and underlying bone had completely healed in all patients.

2.2. Histological Results

A total of 22 bone biopsies were obtained for histologic analysis, 12 from the test group and 10 from the control group. New bone (NB) formation was noted in both groups, extending from the apical to the coronal part of each specimen. The NB had lamellar organization and was filled with many osteocytes embedded in lacunae. Residual biomaterial (BM) was detected in close contact with NB in both groups. Many fibroblasts were present in the soft tissue (ST). No inflammatory reaction was observed in any group (Figure 1). Histomorphometric analysis revealed no statistically significant differences between the groups in the percentage of NB, BM, and ST (Table 3).

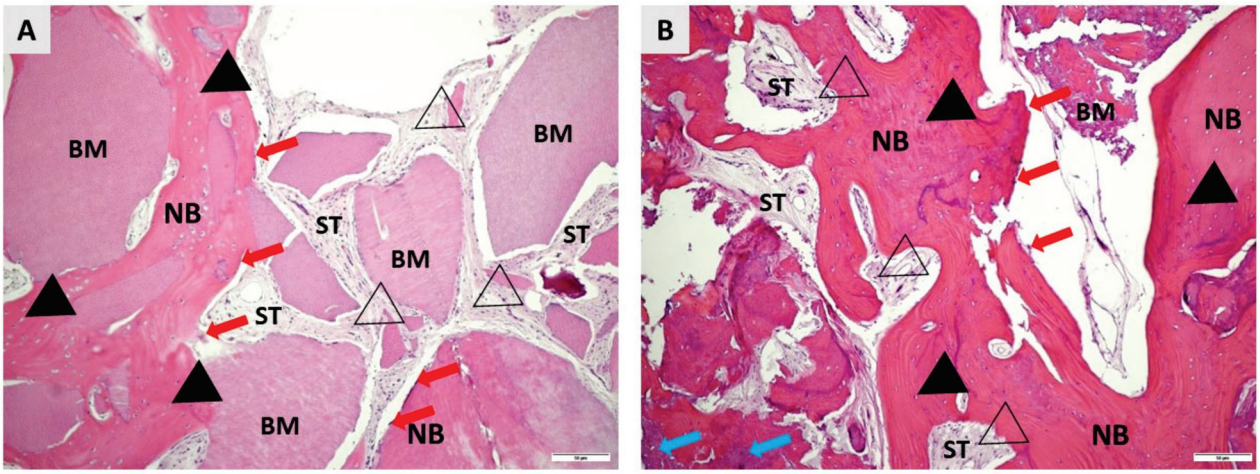


Figure 1. Representative photomicrographs of biopsies taken four months after alveolar ridge preservation. (**A**) shows details of the bone augmented with autologous dentin graft (ADG), whereas (**B**) shows details of bovine xenograft mixed with autologous bone. In both groups, the remaining biomaterial particles (BM and blue arrows in (**B**)) are in close contact with the newly formed bone (NB). NB has a regular, lamellar appearance in both groups and is filled with osteocytes (black fill triangles) embedded in lacunae. Osteoblasts (red arrows) are clearly visible at the margins of NB. The soft tissue areas (ST) are rich in cells, especially fibroblasts (no fill triangles). No inflammatory tissue reaction was detected in either group (hematoxylin-eosin, 100× magnification).

Table 3. Histomorphometrical results.

	Newly Formed Bone (NB)	Residual Biomaterial (BM)	Soft Tissue (ST)
ADG [1]	72.55 ± 12.14%	10.61 ± 5.37%	16.84 ± 9.18%
BX+AB [2]	69.61 ± 13.53%	12.31 ± 7.83%	18.07 ± 6.93%
p-value *	0.613	0.570	0.742

[1] Autologous dentin graft, [2] bovine xenograft + autologous bone; * two-tailed *t* Test.

Immunohistochemical analysis revealed TNF-α- and BMP-4-positive cells in the area of the new bone formation (Figure 2). Expression of TNF-α and BMP-4 was observed in both osteocytes embedded in the newly formed bone and in osteoblasts located at the bone surface. In addition, the intensity of immunohistochemical detection of TNF-α and BMP-4 was measured in the areas of newly formed bone and around the remaining biomaterial particles. A statistically significant difference in the intensity of TNF-α in the area of newly formed bone ($p = 0.0003$) and around the remaining biomaterial particles ($p = 0.0027$) and in the intensity of BMP-4 in the area around biomaterial particles ($p = 0.0001$) was observed between the test and control groups (Table 4).

Table 4. Immunohistochemical intensity score results.

	Mean Value ADG [1] ± SD [2]	Mean Value BX+AB [3] ± SD	*p* Value *
TNF-α around biomaterial	140.89 ± 4.92	149.96 ± 6.64	0.0027
TNF-α new bone area	77.49 ± 3.61	88.72 ± 7.1	0.0003
BMP-4 around biomaterial	131.26 ± 9.1	171.75 ± 10.5	0.0001
BMP-4 new bone area	108.76 ± 7.54	108.66 ± 8.2	0.9761

[1] Autologous dentin graft, [2] standard deviation, [3] bovine xenograft + autologous bone; * Student's *t* test.

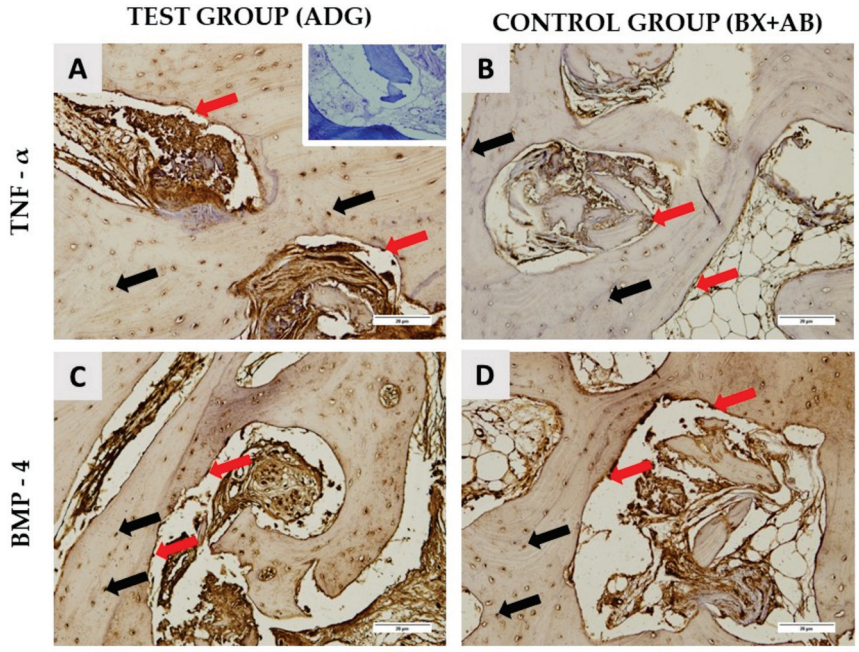


Figure 2. TNF-α and BMP-4 immunohistochemical staining of representative samples from the test group (**A**,**C**) and the control groups (**B**,**D**). The negative control is shown in the right upper corner of the (**A**). Red arrows indicate TNF-α- and BMP-4-positive osteoblasts located in the contact area of newly formed bone and autologous dentin graft (ADG) (**A**,**C**) or bovine xenograft mixed with autologous bone (BX+AB) (**B**,**D**). Black arrows indicate strong expression of TNF-α and BMP-4 in osteocytes embedded in the newly formed bone (**A**–**D**) (200× magnification).

2.3. Cone Beam Computed Tomography (CBCT) Results

A total of 37 CBCT scans were analyzed for radiographic evaluation, 20 from the test group and 17 from the control group. The measurements of alveolar ridge width before tooth extraction and 4 months after alveolar ridge preservation revealed no statistical differences in dimensional changes between the test and control groups (Table 5).

Table 5. CBCT analysis of alveolar ridge dimensional changes.

	Width before Extraction	Width after Extraction	Net Change
ADG [1]	8.06 ± 1.34 mm	7.18 ± 1.48 mm	−0.88 ± 0.76
BX+AB [2]	7.88 ± 1.08 mm	6.64 ± 0.85 mm	−1.24 ± 0.99
p-value *	0.654	0.172	0.219

[1] Autologous dentin graft, [2] bovine xenograft + autologous bone; * two-tailed *t* test.

3. Discussion

The purpose of alveolar ridge preservation is to minimize alveolar ridge resorption after extraction [32]. Alveolar ridge preservation after tooth extraction according to guided bone regeneration (GBR) principles has been shown to be a reliable method of preventing alveolar ridge volume loss during healing [8,33]. Autologous bone is considered the gold standard among bone graft substitutes; however, due to the reported possible complications associated with its use, the focus has shifted to the development of alternatives. With this in mind, bone biopsies harvested 4 months after alveolar ridge preservation with autologous dentin graft (ADG) and bovine xenograft mixed with autologous bone (BX+AB) were examined radiographically, histologically, and immunohistochemically. To our knowledge, this is one of the first immunohistochemical reports on the use of ADG in humans, as well as the first comparison of clinical, radiographic and histologic results with the well-known and commonly used combination BX+AB. Both biomaterials were found to be effective in terms

of osteoconduction and osteoinduction, and no inflammatory tissue reaction was observed. Histomorphometric and radiological results were comparable between the biomaterials, but quantitative immunohistochemical analysis examination showed statistically significant differences in TNF-α and BMP-4 expression between the analyzed biomaterials.

Depending on the preparation protocol and degree of mineralization, three types of ADG can be distinguished: demineralized dentin matrix, partially demineralized dentin matrix, and undermineralized dentin [34,35]. In this clinical study, we used a protocol that results in a demineralized dentin matrix (DDM) [36]. DDM has been shown to be superior in bone regeneration due to its irregular surface and exposed collagen fibers leading to better osteoblasts adhesion [36]. Because of the great heterogeneity of studies regarding the use of ADG and to present our results as objectively as possible, we compared them with the results of studies in which DDM was used.

The osteoinductive and osteoconductive capabilities of ADG were examined histologically in studies using an experimental animal model. ADG was found to be fully integrated into newly formed bone [29]. The studies carried out by Kim and Lee on an experimental animal model also demonstrated the ability of ADG to promote bone growth, which was related to the presence of minerals such as hydroxyapatite (HA) and tricalcium phosphate (TCP) in dentin [27,28]. In addition, studies on animal models showed that these changes began on day 14 of healing, when ADG started to be integrated into the newly formed bone [37,38]. Similar qualitative histologic observations were found in human studies [31,32]. The qualitative histologic analysis in our study revealed close contact between NB and BM, indicating successful bone regeneration and thus the osteoconductive potential of the grafts. Furthermore, no inflammatory reaction was observed in either the control or the test groups, suggesting the biocompatibility of the grafted biomaterials and the surrounding tissue. We reported that the histomorphometric result of new bone formation in the test group was 72.55 ± 12.14%. This is in accordance with findings from a recent clinical study, which exclusively examined bone tissue histomorphometrically after the use of autologous dentin, and reported 63% newly formed bone and 25% residual biomaterial 7 months after guided bone regeneration [39]. There are only few clinical studies comparing xenogeneic biomaterials with ADG. In our study, the histomorphometrical examination revealed no significant differences in the percentages of newly formed bone, residual biomaterial and soft tissue between groups. Furthermore, the results of alveolar ridge preservation with bovine xenograft BioOss® and ADG were compared by Pang et al. [31], and it was found that there was no statistically significant difference in the volume of bone tissue preserved, which is in accordance with our findings.

More than 15 types of BMPs belonging to the TGF-β family have been discovered, but only three stimulate bone formation at the graft site, namely BMP-2, BMP-4, and BMP-7. Their presence stimulates mesenchymal cells to differentiate into osteoblasts, which it is strong evidence of osteoinductive properties [40]. The presence of proinflammatory cytokines such as TNF-α is essential for the initiation of bone healing, as it plays a role in the differentiation of osteoprogenitor cells into preosteoblasts [10]. Moreover, TNF-α along with RANKL plays an essential role in bone remodeling and their expression has been shown to correlate with the dynamics of bone turnover. Namely, TNF-alpha can indirectly stimulate osteoclast differentiation by itself or via RANK signaling [41,42]. In conditions of bone homeostasis, bone resorption is the most important prerequisite for bone formation. It may be that the presence of xenogeneic biomaterial in the alveolar socket caused a stronger inflammatory reaction than dentin, which was visible from the higher expression of the TNF-α immunostaining; however, it did not affect the physiology of the bone remodeling, as was evident from the achieved percentages of the newly formed bone (Table 3). Previous studies in animal models showed immunopositivity of BMP-2 and BMP-4 in the first days of bone healing after augmentation with DDM, supporting evidence of osteoinduction [29]. The immunohistochemical examination in our study revealed TNF-α and BMP-4 immunopositivity in the area surrounding biomaterial particles and the area of the newly formed bone 4 months after alveolar ridge preservation in both

groups, which was confirmed by the quantitative results. These results demonstrate the osteoinductive potential in both groups. The immunopositivity in the ADG group is of additional significance because the dentin was treated with ethylenediaminetetraacetic acid (EDTA), proving that dentin can still maintain its osteoinductivity after that procedure. Interestingly, TNF-α immunopositivity around biomaterial particles and in the area of the newly formed bone was significantly higher in the BX+AB group compared to the ADG group (TNF-α ADG vs. BX+AB around BM $p = 0.0027$; TNF-α ADG vs. BX+AB around NB $p = 0.0003$) and BMP-4 immunopositivity around the biomaterial particles was significantly higher in the BX+AB group (BMP-4 ADG vs. BX+AB around BM $p = 0.0001$). This finding may be related to the presence of a bovine xenograft in the BX+AB group, which may elicit a stronger immune response, that is a common reaction to all types of substitutes and it is essential for bone healing [43].

Radiographic studies of ADG performance in the alveolar ridge are characterized by very high heterogeneity. The study by Li et al. [44] showed comparable results of marginal bone resorption at 6 and 18 months after alveolar ridge preservation using ADG and BX Pohl et al. [30] investigated dimensional changes in the alveolar ridge after socket preservation with ADG and platelet-rich fibrin (PRF). The study found that the mean changes in alveolar ridge width of 1 mm, 3 mm, and 5 mm below the crest were -1.38 ± 1.24 mm, -0.82 ± 1.13 mm, and -0.43 ± 0.89 mm, respectively. We measured the alveolar ridge at the most prominent bone points buccally and orally; therefore, an objective comparison between the aforementioned studies and our study was not possible.

From a clinical point of view, ADG shows some additional advantages compared to BX+AB. The surgical procedure (chair time) is shorter since the preparation of ADG is performed by the dental assistant during the surgery. There is also no need for additional autologous bone harvesting, which prolongs the procedure and may cause more morbidity and postoperative complications for the patient. Finally, the cost of the procedure is lower since there is no extra material used other than autologous dentin from the patient.

It should be noted that the sample size of the analyzed CBCTs and bone biopsies is small. However, we only studied the anterior part of the maxilla, which is also known as the esthetic zone and includes exclusively maxillary incisors, canines and premolars; thus, a smaller sample size is justified. In addition, this is one of the first studies to investigate TNF-α and BMP-4 expression in human alveolar bone, making this study an important demonstration of the osteogenic potential of ADG.

In conclusion, according to this study, ADG is biocompatible and has been shown to have osteoconductive and osteoinductive properties comparable to those of commonly used BX+AB (in radiological and histological comparison). The significantly higher expression of BMP-4 in the BX+AB group indicates good osteoinductive properties, due to the addition of the autologous bone. The significantly higher expression of TNF-α in the same group indicates an active bone remodeling, which has resulted in a high percentage of newly formed bone. This statistically significant difference should be further investigated and be the focus of future clinical studies.

4. Materials and Methods

4.1. Selection Criteria and Preoperative Assessment

The study was conducted in accordance with the Declaration of Helsinki. The Ethics Committee of the Faculty of Medicine of the University of Rijeka (Class: 003-08/21-01/20, No. 2170-24-04-3-21-6) and the Clinical Hospital Centre Rijeka (Class: 003-05/20-1/151, No. 2170-29-02/1-20-2) approved the conduct of the study on human participants willing to sign inform consent.

Participants were consecutive individuals referred for extraction of at least one hopeless tooth in anterior maxilla followed by implant treatment. A total of 42 patients underwent the screening process; finally, 37 patients met the inclusion criteria and provided written consent to participate in clinical trial (Figure 3).

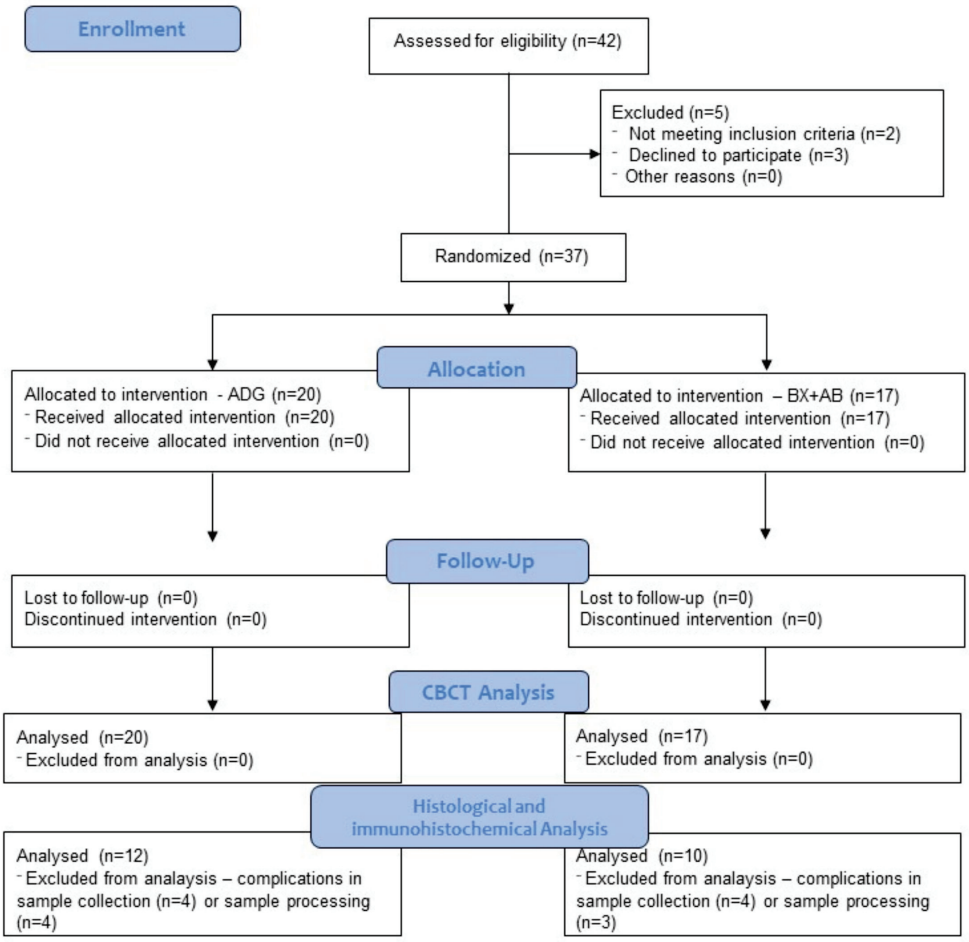


Figure 3. CONSORT flowchart.

All participants were older than 18 years, healthy, and had no health problems that would exclude them from dental implants. Smokers (>10 cigarettes per day), patients with uncontrolled systemic diseases, patients who had received therapeutic radiation to the head or neck, and pregnant and lactating patients were excluded from the study. They were all treated by the same surgeon (M. O.) at the dental clinic in Rijeka, Croatia, between June 2020 and March 2022.

Before the procedure, patients underwent periodontal treatment to remove plaque and calculus and received detailed oral hygiene instructions. One hour before the procedure, patients received an appropriate antibiotic (875 mg penicillin + 125 mg clavulanic acid or 600 mg clindamycin in case of allergy). Preoperatively, 0.2% clorhexidine was used for mouth rinsing.

4.2. Surgical Procedure and Postoperative Follow-Up

The local anesthetic Ubistesin forte (3M, Neuss, Germany) was used to anesthetize the area around the teeth. After a painless and atraumatic tooth extraction, the inflammatory material in the alveolus was curetted and a probe (15 UNC Colour-Coded, Hu-Friedy, Chicago, IL, USA) was used to check the integrity of all bone walls of the alveolus. Only alveoli with three intact bone walls were included in this study. After extraction and curettage, a full-thickness soft tissue flap was elevated with Curette Lucas 2.5 mm (Helmut Zepf, Seit-ingen-Oberflacht, Germany), and a resorbable collagen membrane (Biogide®, Geistlich Pharma, Wolhusen, Switzerland) was placed under the buccal flap. Patients were then randomized into two groups using a free randomization tool available at https://www.randomizer.org/ (accessed on 30 July 2022). Finally, in the test group, patients received an autologous dentin graft, and in the control group, they received bovine xenograft

(cerabone®, botiss biomaterials, Zossen, Germany) mixed with autologous bone that was harvested locally, around the surgical site. In both groups, the wound was primarily closed with a resorbable collagen membrane and connective tissue graft harvested from the palate using resorbable 6.0 monofilament sutures (SMI, St. Vith, Belgium, Surgicryl Rapid 6.0.) (Figures 4 and 5).

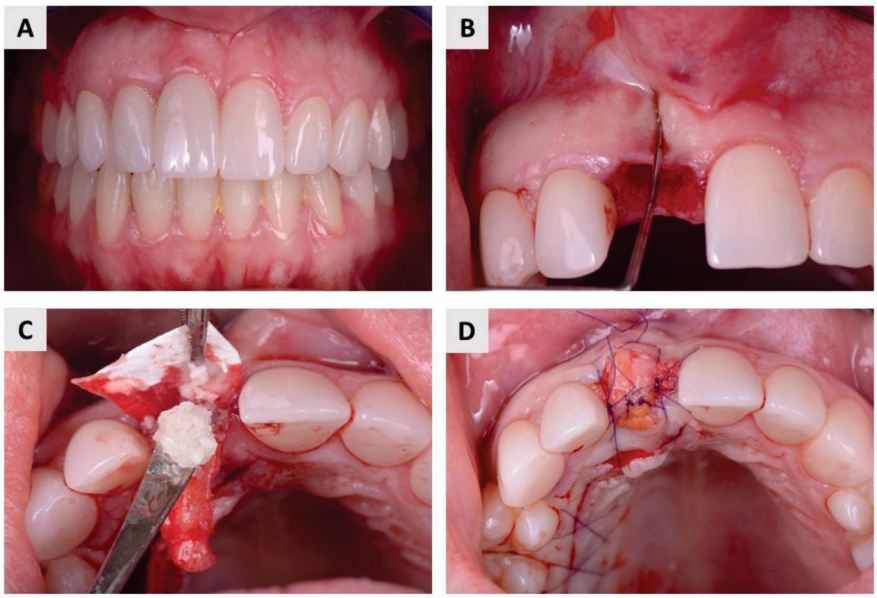


Figure 4. Surgical protocol in the test group. (**A**) The patient suffered from internal root resorption of the maxillary central incisor. (**B**) After atraumatic extraction, the integrity of the alveolar bone walls was checked with a dental probe. (**C**) An autologous dentin graft was placed in the extraction socket and covered with a resorbable membrane. (**D**) Finally, the wound was primary closed with connective tissue graft.

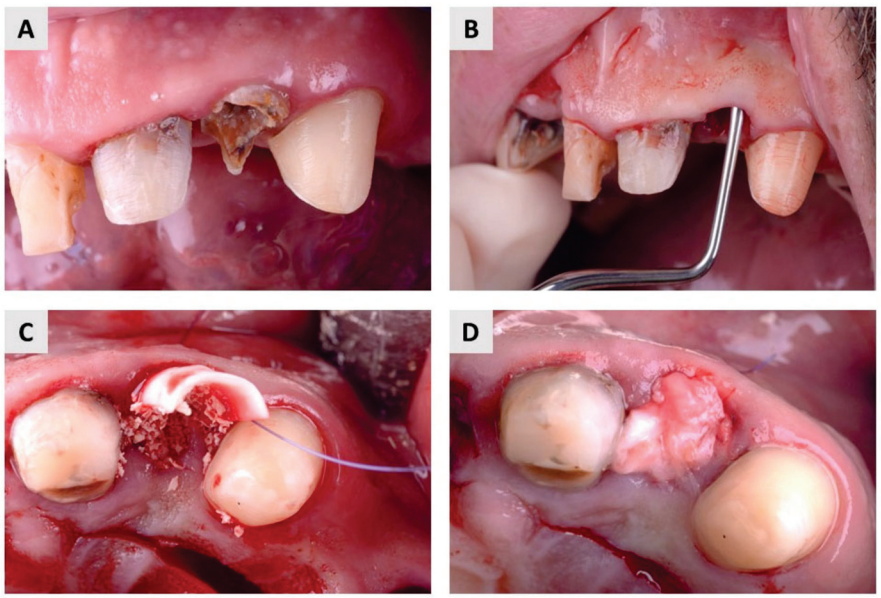


Figure 5. Surgical protocol in the control group. (**A**) A hopeless maxillary lateral incisor. (**B**) After extraction, a detailed curettage was carried out and the integrity of the alveolar bone walls was checked. (**C**) Bovine xenograft mixed with autologous bone and placed into extraction socket. A resorbable membrane was placed buccally. (**D**) Primary wound closure with connective tissue graft.

In the cases where autologous dentin graft was used, the material was prepared according to the manufacturer's recommendations [36]. The extracted teeth were thoroughly manually cleaned with a high-speed carbide bur. Before grinding, all filling materials, calculus, caries, periodontal ligament, discolored dentin and part of the enamel were removed. After drying with an air syringe, the clean teeth were ground in a sterile chamber of the Smart Dentin Grinder (SDG) (KometaBio Inc., Cresskill, NJ, USA). The SDG device was programmed to collect 300–1200 μm particles in the collection chamber. To remove all organic debris and bacteria, the particle teeth were immersed in an alcohol-based basic cleaner for 5 min in a sterile container. They were then dried with sterile gauze. The particles were then rinsed twice in sterile phosphate-buffered saline and were ready to be used as graft material.

All patients were instructed to take the prescribed antibiotics and analgesics as needed and to rinse the mouth with chlorhexidine-based fluids for one month after treatment. Follow-up examinations were performed 10, 30, and 60 days after the procedure. Four months later, patients were called again for restoration with a dental implant.

4.3. Bone Biopsy Collection

Bone biopsy was performed 4 months after bone augmentation simultaneously with implant bed preparation. Bone samples were harvested using a trephine burr with a diameter ranging from 2.3 to 2.8 mm (Helmut Zepf, Seitingen-Oberflacht, Germany) (Figure 6). The diameter of the trephine bur is smaller than that of the final burr in the implant set, which is important to avoid additional bone removal. The collected biopsies were preserved in 4% buffered paraformaldehyde and then forwarded to the laboratory for histological and immunohistochemical analysis. Finally, a dental implant (BEGO Semados RSX^{Pro}, Bego GmbH, Bremen, Germany) was placed.

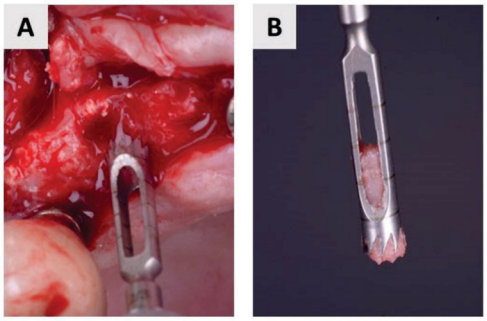


Figure 6. Biopsy collection. (**A**) Trephine bur in maxilla. (**B**) Closer view of the bone sample.

4.4. Histology and Immunohistochemistry

Fixed bone tissue samples were decalcified in Osteofast 2 solution (Biognost, Zagreb, Croatia), embedded in paraffin wax and cut into 5 μm thick tissue sections. Tissue sections were then stained with hematoxylin-eosin and examined under a light microscope with a video camera. For histomorphometric analysis, photomicrographs at 10× magnification were transferred to ImageJ v1.53 software (NIH, https://imagej.nih.gov/ij/). Histomorphometric analysis determined the percentage of newly formed bone, residual biomaterial, and soft tissue.

For immunohistochemical analysis, previously prepared 5 μm thick tissue sections were deparaffinized, dehydrated, and then treated with 0.3% H_2O_2 and incubated in citrate buffer for antigen retrieval. Sections were treated with rabbit polyclonal anti-TNF-α antibody (ab6671, Abcam, Cambridge, UK), and rabbit polyclonal anti- BMP-4 antibody (ab124715, Abcam, Cambridge, UK). After washing, incubation, and visualization with 3,3′-Diaminobenzidine (ab64238, Abcam, Cambridge, UK), the samples were embedded with entellan (Sigma-Aldrich, St. Louis, MO, USA) and examined under the light microscope in conjunction with a video camera.

Quantification of immunohistochemical staining was analyzed on previously recorded photomicrographs using the computer program cellSense v3.2. Photomicrographs taken at 200× magnification were subjected to intensity separation, its conversion to black and white, and background signal subtraction. The regions of interest were determined and placed on the obtained image display, and the final result was shown as the mean value of the color intensity—mean gray value. Histological and immunohistochemical examination were blindly performed by one investigator (O.C.P.).

4.5. Radiological Assessment

Cone beam computed tomography (CBCT) scans were performed with the three-dimensional (3D) Promax (Planmeca OY, Helsinki, Finland). The scan was performed with a resolution of 0.3 mm (scan time: 8.5 s, exposure time: 4 s, 120 kV, 5 mA). Radiographic assessment was performed at two time points. The first time point was before tooth extraction, and the second was at follow-up 4 months after extraction and augmentation. Identical configurations were used in both time periods. Radiological assessment was performed by measuring the width of the alveolar ridge (buccolingual dimension) at two time points. The width of the alveolar ridge was defined as the distance between the most prominent points buccally and orally (Figure 7). All measurements were performed by a single investigator (M.O.).

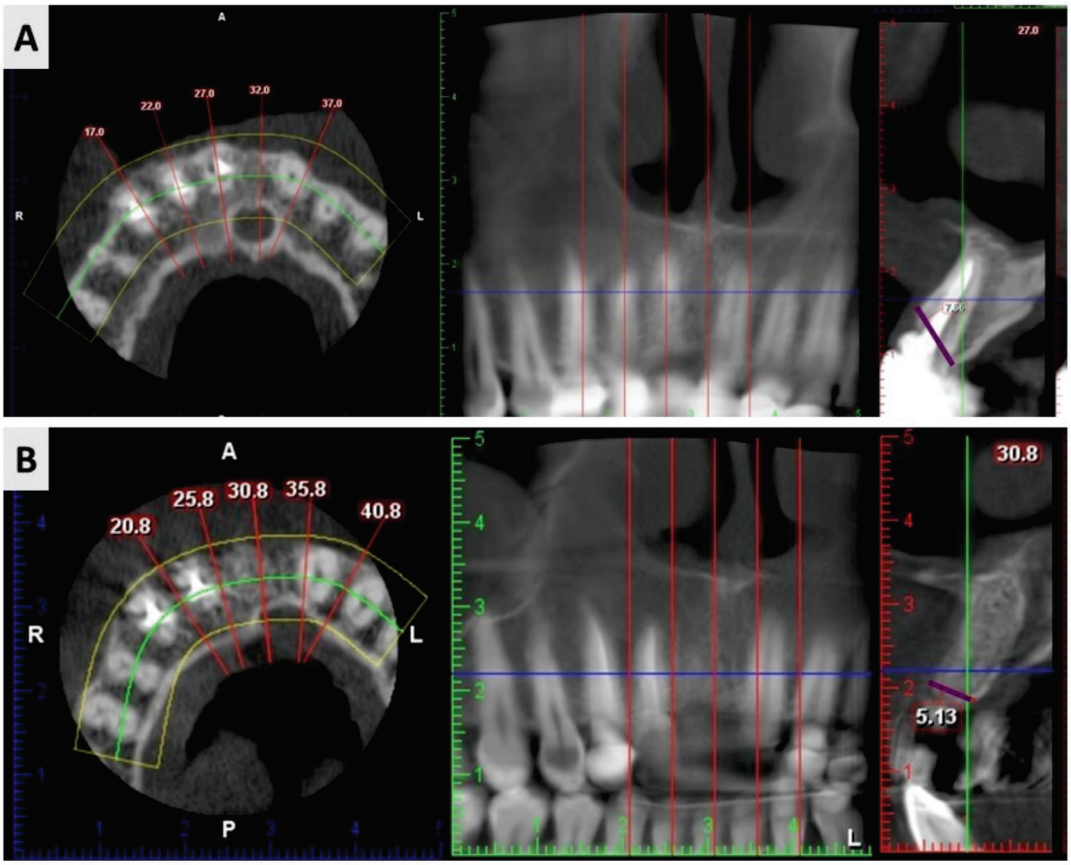


Figure 7. CBCT assessment protocol. The buccolingual dimension was measured between the most prominent points buccally and orally (purple marked line) at two time points—before extraction (**A**) and four months after (**B**).

4.6. Statistical Analysis

All data were transferred to a Microsoft Excel spreadsheet. Statistical analysis was performed using IBM SPSS Statistics (25.0, SPSS Inc., Chicago, IL, USA). Kolmogorov–Smirnov test was used to test the normality of the distribution. The data were normally

distributed. The mean and standard deviation were used to present quantitative data. To compare results between groups, the Student's *t*-test and two-tailed *t*-test were used. p values < 0.05 are considered significant.

Author Contributions: Conceptualization, M.O. and M.Č.; clinical work M.O. and D.K.; methodology M.Č., M.T., B.V. and S.Z.C.; histologic analysis O.C.P.; writing—original draft preparation, M.Č. and M.O.; writing—review and editing, O.C.P., M.B., S.Z.C. and A.T.J.R.; supervision, O.C.P.; project administration, M.O., B.V. and A.T.J.R. All authors have read and agreed to the published version of the manuscript.

Funding: This research was funded by the Croatian Science Foundation, grant number IP-2020-02-7875, and by the University of Rijeka, grant number UNIRI-biomed-18-280.

Institutional Review Board Statement: The study was conducted in accordance with the Declaration of Helsinki. The Ethics Committee of the Faculty of Medicine of the University of Rijeka (Class: 003-08/21-01/20, No. 2170-24-04-3-21-6) and the Clinical Hospital Centre Rijeka (Class: 003-05/20-1/151, No. 2170-29-02/1-20-2) approved the conduct of the study on human participants willing to sign inform consent.

Informed Consent Statement: Informed consent was obtained from all patients involved in the study. Written informed consent has been obtained from the patients to publish this paper.

Data Availability Statement: The data presented in this article are available on request from the corresponding author.

Conflicts of Interest: The authors declare no conflict of interest.

References

1. Horowitz, R.; Holtzclaw, D.; Rosen, P.S. A review on alveolar ridge preservation following tooth extraction. *J. Evid. Based Dent. Pract.* **2012**, *12*, 149–160. [CrossRef] [PubMed]
2. Tan, W.L.; Wong, T.L.T.; Wong, M.C.M.; Lang, N.P. A systematic review of post-extractional alveolar hard and soft tissue dimensional changes in humans. *Clin. Oral Implant. Res.* **2012**, *23* (Suppl. S5), 1–21. [CrossRef] [PubMed]
3. Chappuis, V.; Engel, O.; Reyes, M.; Shahim, K.; Nolte, L.P.; Buser, D. Ridge alterations post-extraction in the esthetic zone: A 3D analysis with CBCT. *J. Dent. Res.* **2013**, *92*, 195S–201S. [CrossRef] [PubMed]
4. Bassir, S.; Alhareky, M.; Wangsrimongkol, B.; Jia, Y.; Karimbux, N. Systematic Review and Meta-Analysis of Hard Tissue Outcomes of Alveolar Ridge Preservation. *Int. J. Oral Maxillofac. Implant.* **2018**, *33*, 979–994. [CrossRef] [PubMed]
5. Deguchi, T.; Takano-yamamoto, T.; Yabuuchi, T.; Ando, R.; Roberts, W.E. Histomorphometric evaluation of alveolar bone turnover between the maxilla and the mandible during experimental tooth movement in dogs. *Am. J. Orthod. Dentofac. Orthop.* **2008**, *133*, 889–897. [CrossRef]
6. Nkenke, E.; Hahn, M.; Weinzierl, K.; Radespiel-Tröger, M.; Neukam, F.W.; Engelke, K. Implant stability and histomorphometry: A correlation study in human cadavers using stepped cylinder implants. *Clin. Oral Implant. Res.* **2003**, *14*, 601–609. [CrossRef]
7. Cho, H.L.; Lee, J.K.; Um, H.S.; Chang, B.S. Esthetic evaluation of maxillary single-tooth implants in the esthetic zone. *J. Periodontal Implant. Sci.* **2010**, *40*, 188–193. [CrossRef]
8. Kalsi, A.S.; Kalsi, J.S.; Bassi, S. Alveolar ridge preservation: Why, when and how. *Br. Dent. J.* **2019**, *227*, 264–274. [CrossRef]
9. Darby, I.B.; Chen, S.T.; Buser, D. Ridge preservation for implant therapy. *Int. J. Oral Maxillofac. Implant.* **2009**, *24*, 260–271.
10. Dimitriou, R.; Tsiridis, E.; Giannoudis, P.V. Current concepts of molecular aspects of bone healing. *Injury* **2005**, *36*, 1392–1404. [CrossRef]
11. Haugen, H.J.; Lyngstadaas, S.P.; Rossi, F.; Perale, G. Bone grafts: Which is the ideal biomaterial? *J. Clin. Periodontol.* **2019**, *46*, 92–102. [CrossRef]
12. Yamada, M.; Egusa, H. Current bone substitutes for implant dentistry. *J. Prosthodont. Res.* **2018**, *62*, 152–161. [CrossRef]
13. Shamsoddin, E.; Houshmand, B.; Golabgiran, M. Biomaterial selection for bone augmentation in implant dentistry: A systematic review. *J. Adv. Pharm. Technol. Res.* **2019**, *10*, 46–50.
14. Misch, C.M. *Implant Dentistry*, 4th ed.; Mosby: St. Louis, MO, USA, 2010; p. 361.
15. Sakkas, A.; Wilde, F.; Heufelder, M.; Winter, K.; Schramm, A. Autogenous bone grafts in oral implantology—Is it still a "gold standard"? A consecutive review of 279 patients with 456 clinical procedures. *Int. J. Implant. Dent.* **2017**, *3*, 23. [CrossRef]
16. Gultekin, B.A.; Bedeloglu, E.; Kose, T.E.; Mijiritsky, E. Comparison of Bone Resorption Rates after Intraoral Block Bone and Guided Bone Regeneration Augmentation for the Reconstruction of Horizontally Deficient Maxillary Alveolar Ridges. *Biomed. Res. Int.* **2016**, *2016*, 4987437. [CrossRef]
17. Maiorana, C.; Beretta, M.; Salina, S.; Santoro, F. Reduction of autogenous bone graft resorption by means of bio-oss coverage: A prospective study-PubMed. *Int. J. Periodontics Restor. Dent.* **2005**, *25*, 19–25.

18. Kacarevic, Z.P.; Kavehei, F.; Houshmand, A.; Franke, J.; Smeets, R.; Rimashevskiy, D.; Wenisch, S.; Schnettler, R.; Jung, O.; Barbeck, M. Purification processes of xenogeneic bone substitutes and their impact on tissue reactions and regeneration. *Int. J. Artif. Organs* **2018**, *41*, 789–800. [CrossRef]
19. Schmitt, C.M.; Doering, H.; Schmidt, T.; Lutz, R.; Neukam, F.W.; Schlegel, K.A. Histological results after maxillary sinus augmentation with Straumann®BoneCeramic, Bio-Oss®, Puros®, and autologous bone: A randomized controlled clinical trial. *Clin. Oral Implant. Res.* **2013**, *24*, 576–585. [CrossRef]
20. Torres, J.; Tamimi, F.; Alkhraisat, M.H.; Manchón, Á.; Linares, R.; Prados-Frutos, J.C.; Hernández, G.; López Cabarcos, E. Platelet-rich plasma may prevent titanium-mesh exposure in alveolar ridge augmentation with anorganic bovine bone. *J. Clin. Periodontol.* **2010**, *37*, 943–951. [CrossRef]
21. Lindhe, J.; Cecchinato, D.; Donati, M.; Tomasi, C.; Liljenberg, B. Ridge preservation with the use of deproteinized bovine bone mineral. *Clin. Oral Implant. Res.* **2014**, *25*, 786–790. [CrossRef]
22. Berberi, A.; Samarani, A.; Nader, N.; Noujeim, Z.; Dagher, M.; Kanj, W.; Mearawi, R.; Salemeh, Z.; Badran, B. Physicochemical characteristics of bone substitutes used in oral surgery in comparison to autogenous bone. *Biomed. Res. Int.* **2014**, *2014*, 320790. [CrossRef] [PubMed]
23. Urist, M.R.; SIlverman, B.F.; Buring, K.; Dubuc, F.L.; Rosenberg, J.M. The bone induction principle. *Clin. Orthop. Relat. Res.* **1967**, *53*, 243–283. [CrossRef] [PubMed]
24. Bessho, K.; Tanaka, N.; Matsumoto, J.; Tagawa, T.; Murata, M. Human dentin-matrix-derived bone morphogenetic protein. *J. Dent. Res.* **1991**, *70*, 171–175. [CrossRef] [PubMed]
25. Xiao, Y.T.; Xiang, L.X.; Shao, J.Z. Bone morphogenetic protein. *Biochem. Biophys. Res. Commun.* **2007**, *362*, 550–553. [CrossRef]
26. Originalni, R.; Xhaferi, B.; Petreska, M.P.; Xheladini, A.; Papić, I. Use of mineralized dentin graft in augmentation of different indication areas in the jaw bones. *Serb. Dent. J.* **2021**, *68*, 113–121. [CrossRef]
27. Kim, J.-Y.; Kim, K.-W.; Um, I.-W.; Kim, Y.-K.; Lee, J.-K. Bone Healing Capacity of Demineralized Dentin Matrix Materials in a Mini-pig Cranium Defect. *J. Korean Dent. Sci.* **2012**, *5*, 21–28. [CrossRef]
28. Lee, D.H.; Yang, K.Y.; Lee, J.K. Porcine study on the efficacy of autogenous tooth bone in the maxillary sinus. *J. Korean Assoc. Oral Maxillofac. Surg.* **2013**, *39*, 120. [CrossRef]
29. Abrantes Pinheiro Carvalho, V.; De Olivera Tosello, D.; de Castillo Salgado, M.A.; Fernandes Gomes, M. Histomorphometric analysis of homogenous demineralized dentin matrix as osteopromotive material in rabbit mandibles. *Int. J. Oral Maxillofac. Implant.* **2004**, *19*, 679–686.
30. Pohl, S.; Binderman, I.; Tomac, J. Maintenance of Alveolar Ridge Dimensions Utilizing an Extracted Tooth Dentin Particulate Autograft and Platelet-Rich fibrin: A Retrospective Radiographic Cone-Beam Computed Tomography Study. *Materials* **2020**, *13*, 1083. [CrossRef]
31. Pang, K.M.; Um, I.W.; Kim, Y.K.; Woo, J.M.; Kim, S.M.; Lee, J.H. Autogenous demineralized dentin matrix from extracted tooth for the augmentation of alveolar bone defect: A prospective randomized clinical trial in comparison with anorganic bovine bone. *Clin. Oral Implant. Res.* **2017**, *28*, 809–815. [CrossRef]
32. Esposito, M.; Grusovin, M.; Worthington, H.; Coulthard, P. Interventions for replacing missing teeth: Bone augmentation techniques for dental implant treatment. In *Cochrane Database of Systematic Reviews*; Esposito, M., Ed.; John Wiley & Sons, Ltd.: Chichester, UK, 2006.
33. Avila-Ortiz, G.; Chambrone, L.; Vignoletti, F. Effect of alveolar ridge preservation interventions following tooth extraction: A systematic review and meta-analysis. *J. Clin. Periodontol.* **2019**, *46*, 195–223. [CrossRef]
34. Cenicante, J.; Botelho, J.; Machado, V.; Mendes, J.J.; Mascarenhas, P.; Alcoforado, G.; Santos, A. The Use of Autogenous Teeth for Alveolar Ridge Preservation: A Literature Review. *Appl. Sci.* **2021**, *11*, 1853. [CrossRef]
35. Sánchez-Labrador Martínez de Morentin, L.; Martínez-Pereda, M.; Martínez, L.-Q. Use of Autogenous Dentin as Graft Material in Oral Surgery Martín-Ares, María Martínez-González, José María. *Cient. Dent.* **2019**, *16*, 37–44.
36. Binderman, I.; Hallel, G.; Nardi, C.; Yaffe, A.; Sapoznikov, L. A novel procedure to process extracted teeth for immediate grafting of autogenous dentin. *J. Interdiscipl. Med. Dent. Sci.* **2014**, *2*, 2.
37. De Oliveira, G.S.; Miziara, M.N.; Silva, E.R.D.; Ferreira, E.L.; Biulchi, A.P.F.; Alves, J.B. Enhanced bone formation during healing process of tooth sockets filled with demineralized human dentine matrix. *Aust. Dent. J.* **2013**, *58*, 326–332. [CrossRef]
38. Reis-Filho, C.R.; Silva, E.R.; Martins, A.B.; Pessoa, F.F.; Gomes, P.V.N.; De Araújo, M.S.C.; Miziara, M.N.; Alves, J.B. Demineralised human dentine matrix stimulates the expression of VEGF and accelerates the bone repair in tooth sockets of rats. *Arch. Oral Biol.* **2012**, *57*, 469–476. [CrossRef]
39. Mazor, Z.; Horowitz, R.; Prasad, H.; Kotsakis, G. Healing Dynamics Following Alveolar Ridge Preservation with Autologous Tooth Structure. *Int. J. Periodontics Restor. Dent.* **2019**, *39*, 697–702. [CrossRef]
40. Derner, R.; Anderson, A.C. The bone morphogenic protein. *Clin. Podiatr. Med. Surg.* **2005**, *22*, 607–618. [CrossRef]
41. Boyce, B.F.; Xing, L. Functions of RANKL/RANK/OPG in bone modeling and remodeling. *Arch. Biochem. Biophys.* **2008**, *473*, 139. [CrossRef]
42. Algate, K.; Haynes, D.R.; Bartold, P.M.; Crotti, T.N.; Cantley, M.D. The effects of tumour necrosis factor-α on bone cells involved in periodontal alveolar bone loss; osteoclasts, osteoblasts and osteocytes. *J. Periodontal Res.* **2016**, *51*, 549–566. [CrossRef]

43. Rodriguez, A.E.; Nowzari, H. The long-term risks and complications of bovine-derived xenografts: A case series. *J. Indian Soc. Periodontol.* **2019**, *23*, 487. [CrossRef] [PubMed]
44. Li, P.; Zhu, H.C.; Huang, D.H. Autogenous DDM versus Bio-Oss granules in GBR for immediate implantation in periodontal postextraction sites: A prospective clinical study. *Clin. Implant. Dent. Relat. Res.* **2018**, *20*, 923–928. [CrossRef] [PubMed]

Disclaimer/Publisher's Note: The statements, opinions and data contained in all publications are solely those of the individual author(s) and contributor(s) and not of MDPI and/or the editor(s). MDPI and/or the editor(s) disclaim responsibility for any injury to people or property resulting from any ideas, methods, instructions or products referred to in the content.

International Journal of
Molecular Sciences

MDPI

Article

Histological and Histomorphometric Evaluation of Implanted Photodynamic Active Biomaterials for Periodontal Bone Regeneration in an Animal Study

Bernd Sigusch [1,†], Stefan Kranz [1,*,†], Andreas Clemm von Hohenberg [1], Sabine Wehle [1], André Guellmar [1], Dorika Steen [2], Albrecht Berg [3], Ute Rabe [1], Markus Heyder [1] and Markus Reise [1]

[1] Department of Conservative Dentistry and Periodontology, University Hospitals Jena, An der alten Post 4, 07743 Jena, Germany; vonhohenberg@gmx.at (A.C.v.H.)
[2] Biolitec Research GmbH, 07745 Jena, Germany
[3] Innovent Technologieentwicklung e.V., 07745 Jena, Germany
* Correspondence: stefan.kranz@med.uni-jena.de
† These authors contributed equally to this work.

Abstract: Recently, our group developed two different polymeric biomaterials with photodynamic antimicrobial surface activity for periodontal bone regeneration. The aim of the present study was to analyze the biocompatibility and osseointegration of these materials in vivo. Two biomaterials based on urethane dimethacrylate (BioM1) and tri-armed oligoester-urethane methacrylate (BioM2) that additionally contained ß-tricalcium phosphate and the photosensitizer mTHPC (meso-tetra(hydroxyphenyl)chlorin) were implanted in non-critical size bone defects in the femur (n = 16) and tibia (n = 8) of eight female domestic sheep. Bone specimens were harvested and histomorphometrically analyzed after 12 months. BioM1 degraded to a lower extent which resulted in a mean remnant square size of 17.4 mm^2, while 12.2 mm^2 was estimated for BioM2 ($p = 0.007$). For BioM1, a total percentage of new formed bone by 30.3% was found which was significant higher compared to BioM2 (8.4%, $p < 0.001$). Furthermore, BioM1 was afflicted by significant lower soft tissue formation (3.3%) as compared to BioM2 (29.5%). Additionally, a bone-to-biomaterial ratio of 81.9% was detected for BioM1, while 8.5% was recorded for BioM2. Implantation of BioM2 caused accumulation of inflammatory cells and led to fibrous encapsulation. BioM1 (photosensitizer-armed urethane dimethacrylate) showed favorable regenerative characteristics and can be recommended for further studies.

Keywords: alloplastic bone graft; alveolar bone; bone defects; bone label; bone substitute; meso-tetra(hydroxy phenyl)chlorin; ovine bone model; periodontitis; photodynamic therapy; polyfluorochromes

Citation: Sigusch, B.; Kranz, S.; von Hohenberg, A.C.; Wehle, S.; Guellmar, A.; Steen, D.; Berg, A.; Rabe, U.; Heyder, M.; Reise, M. Histological and Histomorphometric Evaluation of Implanted Photodynamic Active Biomaterials for Periodontal Bone Regeneration in an Animal Study. *Int. J. Mol. Sci.* **2023**, *24*, 6200. https://doi.org/10.3390/ijms24076200

Academic Editor: Daniel Arcos

Received: 28 February 2023
Revised: 17 March 2023
Accepted: 22 March 2023
Published: 24 March 2023

Copyright: © 2023 by the authors. Licensee MDPI, Basel, Switzerland. This article is an open access article distributed under the terms and conditions of the Creative Commons Attribution (CC BY) license (https://creativecommons.org/licenses/by/4.0/).

1. Introduction

Periodontitis is an infectious and inflammatory oral disease which is characterized by destruction of the tooth supporting tissue [1–3]. Clinically, periodontitis appears in signs of inflammation such as bleeding on probing, formation of periodontal pockets, and increased tooth mobility in the later stages.

A successful periodontitis treatment is characterized by a reduction in periodontal inflammation signs, a decrease in periodontal pocket depths and in long-term suppression of periodontopathogenic bacterial species.

After initial anti-infectious therapy, periodontal pockets might still persist which is often associated with the presence of deep intrabony defects [4].

In those cases, different surgical and non-surgical regenerative procedures are applied which also involve the use of resorbable or non-resorbable membranes, growth and differentiation factors, enamel matrix proteins and autologous, heterologous bone grafts and/or xenografts [5–11].

Because of the high practicability, alloplastic bone grafts such as bioceramics (e.g., absorbable/non-resorbable hydroxyapatite, beta-tricalcium phosphate), bioglasses, metals, calcium phosphate cements and polymers are also of special interest [12–15].

Unfortunately, none of these materials currently meet all necessary clinical requirements such as providing sufficient mechanical stability paired with efficient osteo-inductive and -conductive properties as well as mechanisms to fight local infections of the implant site.

In this regard, our group already published data showing that polymers of poly(vinyl butyral-co-vinyl alcohol-co-vinyl acetate), urethane methacrylate and functionalized oligolactones have promising characteristics [16]. Due to their highly adaptable nature, synthetic polymers meet the requirements of many biomedical approaches. This includes mechanisms for regulating mechanical properties, porosity, biodegradation, surface topography, and wettability [17,18]. Furthermore, synthetic polymers provide the necessary mechanical strength while being replaced by newly formed bone [19]. The opportunity to include antimicrobial agents into the polymeric matrix is a further advantage [20].

As there is also a high clinical need for new and innovative antibiotic-free materials, the incorporation of a so-called photosensitizer is one favorable approach [21–23]. As already proven by various authors, illumination of photosensitizer-armed materials by light of an appropriate wavelength results in sufficient suppression of local microbes [24–26]. Up to now, photodynamic active materials are mainly investigated in their efficiency to treat infected wounds or are tested for their practicability in tumor therapy [27–31].

To the best of our knowledge, there are currently no studies available that focus on photosensitizer-armed materials for bone regeneration. To fill this gap, our group recently introduced two different photosensitizer-doted biomaterials based on urethane dimethacrylate (BioM1) and tri-armed oligoester-urethane methacrylate (BioM2) [32]. In order to ensure a sufficient photodynamic antimicrobial effect, the photosensitizer meso-tetra(hydroxyphenyl)chlorin (mTHPC) was included into the matrix of both polymers. As already proven, mTHPC is of strong photodynamic activity and capable in suppressing oral pathogens to significantly high extents [32–34].

Up to now, osseointegration and biocompatibility of BioM1 and BioM2 were not yet observed in vivo. Therefore, the present animal study aimed to investigate the performance of both materials in non-critical bone defects after implantation for 12 months. Both materials were analyzed by histomorphometric and histological methods in order to determine their osseoinductive and bone integrative characteristics. Furthermore, newly formed tissue and the adjunctive bone were investigated for signs of adverse effects and inflammatory responses.

2. Results

In the present animal study, two different polymeric biomaterials armed with mTHPC were implanted in the femur and tibia of sheep. After 12 months of implantation bone samples were collected and analyzed by histological and histomorphometric methods.

After 12 months, BioM1 remnants showed a mean square area of 17.4 mm^2, while 12.2 mm^2 were estimated for BioM2. At baseline an initial area of the bone defect was calculated with 19.6 mm^2. Remnants of BioM2 were significant smaller in the tibia ($p < 0.001$) and in the femur ($p = 0.007$) as compared to BioM1 (Figure 1a).

Total bone was detected in the ROI by 30.3% in femur defects filled with BioM1, whereas only 8.4% was found in case of BioM2. Both values were also significantly different ($p < 0.001$). In the tibia defect sites a total bone value of 28.6% was estimated in the ROI for holes filled with BioM1 and 20.4% for those obturated with BioM2. The results are shown in Figure 1b.

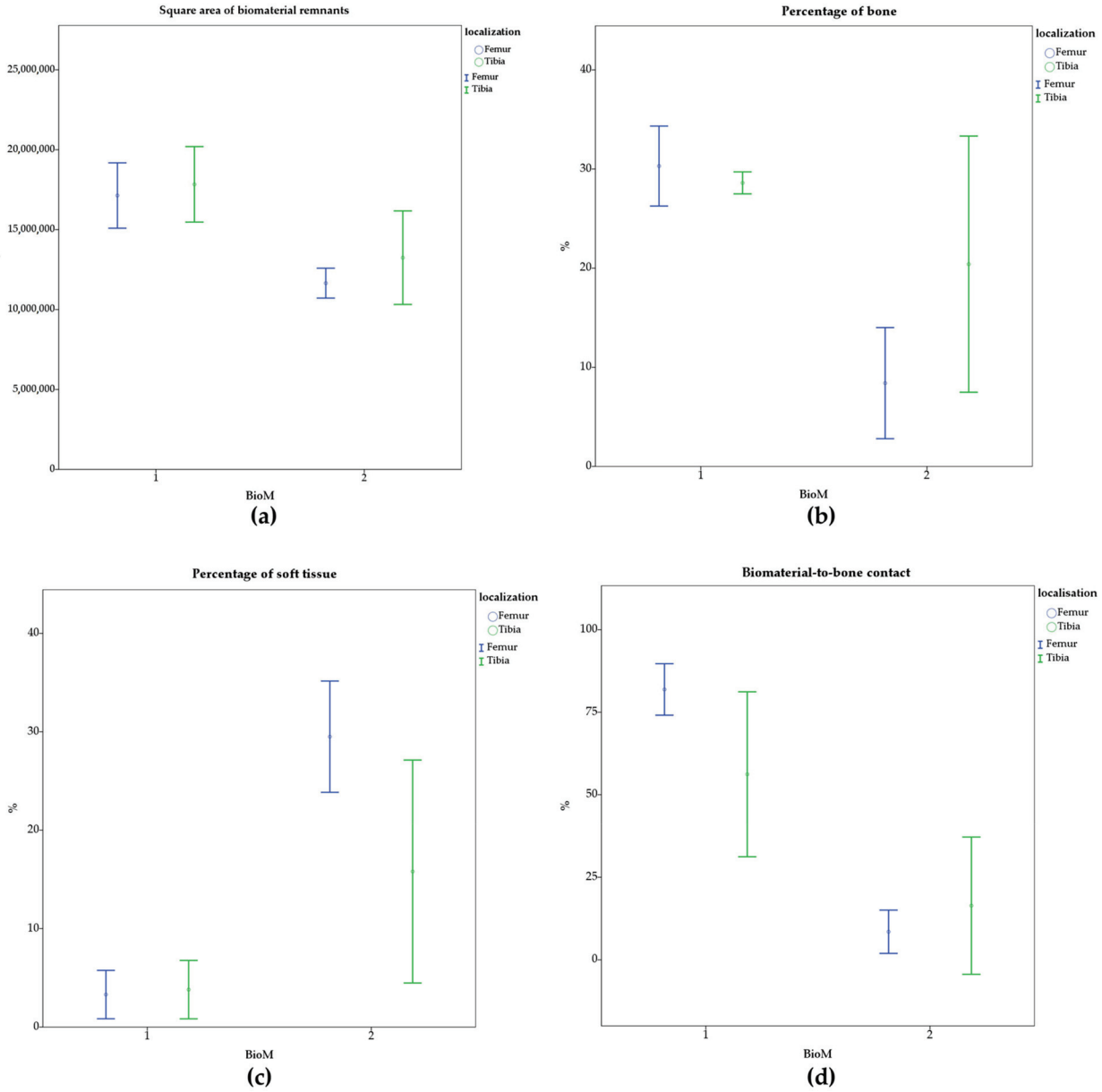


Figure 1. Histological evaluation after implantation of BioM1 and BioM2 in the femur and tibia of sheep for 12 months: (**a**) square area of the biomaterial remnants; (**b**) percentage of bone in the ROI; (**c**) percentage of soft tissue in the ROI; (**d**) bone-to-implant contact at the biomaterial to tissue interface.

In addition to the bone volume, the percentage of fibrous soft tissue in the ROI was also determined. BioM1 showed a soft tissue value of 3.3% in the femur samples, while in case of BioM2 a higher soft tissue value was detected (29.5 %, $p < 0.001$). In case of the tibia defects, soft tissue was estimated by 3.8% for BioM1 and 15.8% for BioM2 ($p = 0.014$), (Figure 1c).

In the present study, the bone-to-biomaterial contact was also evaluated at the bone interface. It was found that BioM1 showed a bone-to-biomaterial ratio of 81.9% in the femur and 56.2% in the tibia ($p = 0.005$). In contrary, BioM2 showed a bone-to-biomaterial contact of only 8.5% in the femur and 16.4% in the tibia. The results for both biomaterials are displayed in Figure 1d.

As observed in the decalcified histological bone sections, BioM2 was encapsulated by soft tissue to a much higher extent as compared to BioM1. Additionally, an infiltration with fat and giant cells was only observed in defects filled with BioM2.

In case of BioM1, a pronounced formation of trabecular bone was observed. Though, only minor bone formation occurred in defects filled with BioM2. Representative decalcified and stained histological sections of BioM1 and BioM2 are shown in Figure 2.

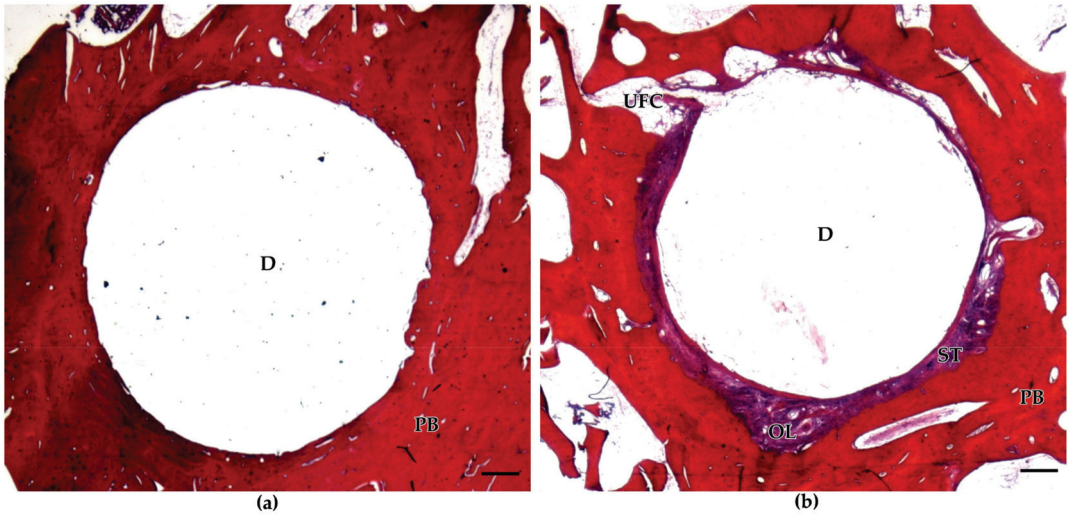


Figure 2. Representative decalcified and stained histological sections of BioM1 and BioM2: (**a**) defects (D) filled with BioM1 revealed a homogeneous bone-to-biomaterial interface with no signs of fibrous encapsulation; (**b**) defects filled with BioM2 are characterized by a pronounced enclosure with fibrous tissue (purple, ST). Further, osteolytic zones (OL) and univacular fat cells (UFC) are additionally present within the bone-to-biomaterial interface of implanted BioM2. Scale bar 500 µm. (PB: peripheral bone).

Defects filled with BioM1 showed no signs of inflammation or adverse effects. The interface of implanted BioM1 revealed homogeneous cancellous bone in close contact to the biomaterial surfaces.

On the other hand, remnants of BioM2 were enclosed by a sheath of fibrous tissue. Furthermore, osteolytic zones filled with fibrous tissue and fat cells were also discovered. Adjunctive tissue of BioM2 was affected by a strong infiltration with lymphocytes and giant cells (Figure 3).

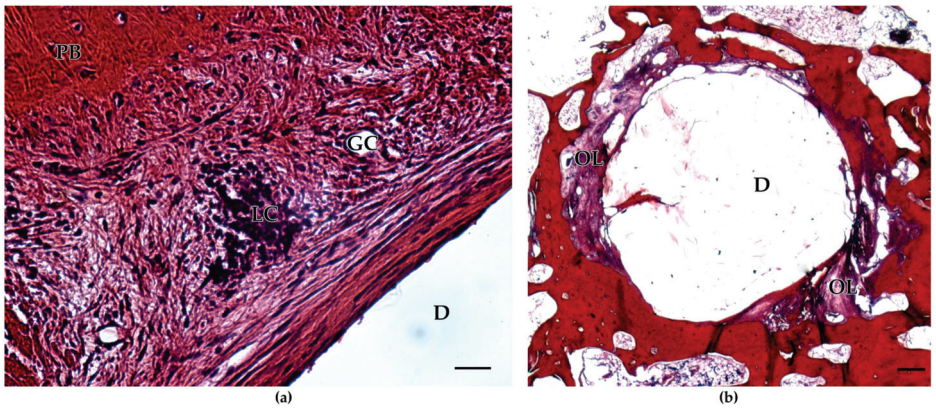


Figure 3. Histological sections of implanted BioM2: (**a**) surrounding tissue shows infiltration by lymphocytes (LC) and giant cells (GC) (left image). Peripheral bone (PB) is present in the left upper corner of the defect site (D). Scale bar 50 µm; (**b**) osteolytic zones (OL) filled with fibrous tissue and inflammatory signs are present in the interface regions. Scale bar 1000 µm.

The results of the assigned four-graded ROI evaluation score are presented in detail in Figure 4. It is clearly demonstrated that a score of grade 1 (new formed bone, totally mineralized) was detected most frequently in defects filled with BioM1 (p = 0.02). In contrast, in defects filled with BioM2 a score of grade 3 (fibrous soft tissue, uncalcified) was primarily assigned (p = 0.004).

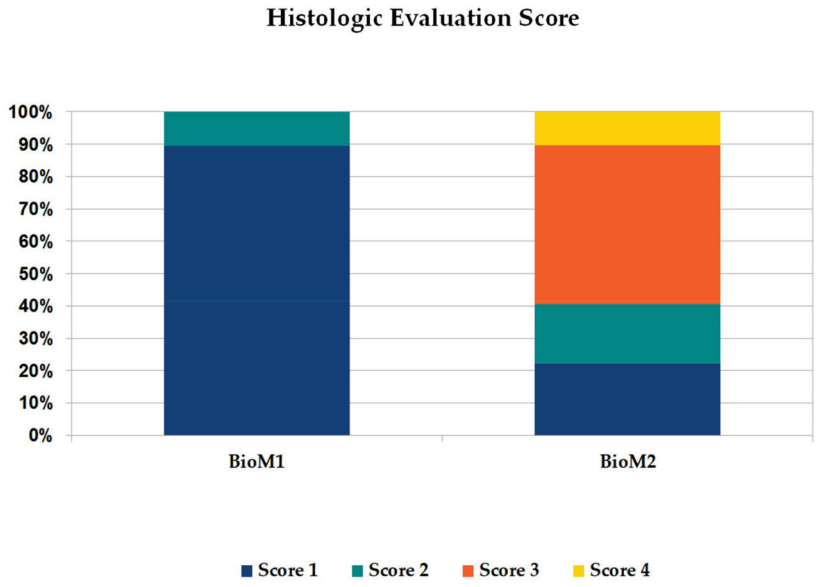


Figure 4. Summary of the four-graded histological evaluation score after implantation of BioM1 and BioM2 for 12 months.

In summary, bone defects filled with BioM1 showed high amounts of mineralized bone in the ROI (96.18%), while fibrinous tissue was detected for 3.82%, only. In the case of BioM2, bone was present by 18.3% only, while the amount of uncalcified fibrous tissue was clearly increased (grade 3).

3. Discussion

In the present study, osteointegration and biocompatibility of two polymeric biomaterials based on urethane dimethacrylate (BioM1) and a tri-armed oligoester-urethane methacrylate (BioM2) were investigated in an ovine bone model. Both biomaterials were implanted in non-critical size defects in the femur and tibia of sheep.

Osteointegration and biocompatibility was determined by histomorphometric analysis after an implantation period of 12 months. In detail, the remaining biomaterial size, the percentage of bone and soft tissue in the ROI as well as the bone-to-biomaterial contact were evaluated.

As shown by the results, BioM1 was sufficiently osseointegrated with the highest amount of mineralized tissue in the ROI. Results from the four-graded classification scale showed bone formation by 96.18%. In contrast, implantation of BioM2 (oligoester-urethane methacrylate based) caused chronic inflammation and fibrous encapsulation. In the case of BioM2, bone in the ROI was only detected by 18.3%.

Similar results are reported from scaffolds fabricated from polymethyl methacrylate (PMMA) which were also not osseointegrated after implantation for 12 months. The same as for BioM2, the implanted material was encapsulated by a sheath of fibrous tissue. In comparison, mineralized tissue was found for titanium scaffolds by 39.1%, followed by implants manufactured from poly(D,L-lactic acid) (31.5%) and porous ultra-high molecular weight polyethylene (6.4 to 10.1%) [35].

The performance of methacrylate-based grafting was also observed by other authors. Recently, it was reported that bioscaffolds composed of Sr-containing mesoporous bioactive glass nanoparticles embedded in a gelatin methacrylate matrix present enhanced

osteogenic, angiogenic, and immunomodulatory properties [36]. Furthermore, a novel graphene oxide modified expandable polymethyl methacrylate-based bone cement revealed improved physiochemical properties with sufficient cytocompatible, and osteogenic characteristics [37]. Methacrylated silk was also recently tested to verify its ability to support osteogenesis. It was shown that scaffolds from methacrylated silk are biocompatible and present reliable osteoconductive features [38]. Moreover, the performance of 3D printed gelatin methacrylate hydrogel has formerly been investigated after implantation in rat condyle defects. Whereas optimal tissue integration was observed via histology, no signs of fibrotic encapsulation or inhibited bone formation were attained [39].

Using sheep for biomaterial testing is common, especially in orthopedic research, because their parameters are similar to those of humans, such as the anatomic structure of bone and joints, body weight, mineral bone metabolism and responses to mechanical loads [40,41]. The applied model was first introduced in 2008 and revised in 2014 [42,43]. In the present investigation a modified version was introduced which allows serial sampling in the same animal with similar environmental conditions. If necessary, all stages in bone healing can easily be addressed. The applied surgical procedure was also well tolerated by the experimental animals. Although sheep cancellous bone models are now well established for the assessment of new bone substitutes, the limited availability of cancellous bone makes it difficult to find multiple comparable sites within the same animal [42]. Therefore, the described ovine model was chosen for testing biocompatibility and osseointegration of BioM1 and BioM2 in the present investigation.

In addition to large animal studies, in silico methods are of increasing interest. Computational simulation approaches for investigating mechano-biological principles behind scaffold-guided bone regeneration and the influence of the scaffold design on the regeneration process are already described [44,45]. Especially for the treatment of large bone defects with manufactured bone grafts and in joint replacement surgery, in silico analyzation methods show great predictive potential [46,47].

However, in the present investigation, both materials degraded to different extents. At the end of the study period a mean square area of 17.4 mm^2 was detected for remaining BioM1 and 12.2 mm^2 for BioM2, which was statistically significant in respect to the defect size estimated at baseline (19.6 mm^2).

These results are in line with findings observed by our group previously. As shown, BioM2 degrades to a much faster extent compared to BioM1. During immersion in distilled water for 28 d, BioM2 lost weight by 67%, while BioM1 degraded by only 4% [32].

The inert nature of BioM1 can thereby be referred to its hydrophobic chemical structure. Unlike BioM2, which is of higher hydrophilicity, BioM1 withstands hydrolytic cleavage to a much greater extent [48].

In the present study, the bone-to-biomaterial contact ratio was analyzed as well. As shown by the results, BioM1 presented a bone-to-biomaterial-contact of 81.9%. In contrast, a contact rate of only 8.5% was observed for BioM2.

Overall, the bone-to-biomaterial contact of BioM2 can be considered rather low. In a similar study, osseointegration of titanium and polyetheretherketone (PEEK) implants in the tibia and femur of sheep were observed. The results revealed a percentage of the bone-to-implant contact by 59.3% for titanium and 11.5% for PEEK [49].

In the present investigation, BioM2 was affected by fibrous tissue encapsulation, while BioM1 showed a close contact to the surrounding bone. Similar results as for BioM1 were reported for implants manufactured from hydroxyapatite. Here, a bone-to-implant contact of 74% was reported [50]. In this context, BioM1 showed a mean bone-to-biomaterial ratio of 81.9% in the femur and 56.2% in the tibia.

In addition, no inflammatory reactions or fibrous tissue formation was observed in the ROI of BioM1. In contrast, the implantation of BioM2 resulted in chronic inflammation. The inflammatory response associated to BioM2 can probably be referred to cytotoxic byproducts that origin from the degradation process. As it was shown, hydrolytic cleavage of polyester urethane acrylates causes the emerging of various acidic substances such as

poly-(methacrylic acid), ethylene glycol, diethylene glycol, lactic acid and glycolic acid which leads to a local drop in the tissue pH [51].

In this regard, it is known that the appearance of acidic degradation products causes tissue inflammation and an impaired healing [52]. In order to increase biocompatibility and to counteract the cytotoxic effects of the acidic degradation products, calcium phosphate particles are often additionally applied to the polymeric matrix [17,52,53].

In the present study, both polymers were also additionally substituted with ß-tricalcium phosphate nanoparticles for increasing the porosity of the biomaterial body and to improve osseointegration [32,54]. In this context it was observed that especially tortuosity has a significant effect upon the scaffolds' permeability and shear stress values [55]. Morphologic parameters such as porosity, specific surface area, thickness, and tortuosity are important and hence need to be discovered for BioM1 and BioM2.

In the case of BioM2, giant cells and osteolytic bone defect zones were discovered in the adjunct tissue. The formation of foreign body giant cells is in general a result of fused macrophages that faced a frustrated process of phagocytosis [56–58]. The presence of foreign body giant cells, osteolytic zones and signs of a fibrous encapsulation indicate that BioM2 is of rather low biocompatibility.

As a result of the inflammation process, BioM2 also showed a lower bone-to-biomaterial contact rate as compared to BioM1. In detail, BioM2 featured a bone contact of 8.5% in the femur and 16.4% in the tibia, while implantation of BioM1 resulted in a bone contact of 81.9% in the femur and 56.2% in the tibia. After 12 months of implantation, it was recognized that BioM2 was almost entirely enclosed by a sheath of fibrous tissue, while in case of BioM1 no signs of adverse effects were observed.

The formation of a fibrotic capsule can be referred to a variety of pro-fibrotic growth factors such as PDGF, VEGF, and TGF-β, which are secreted by macrophages and also by several other immune cells. These factors cause activation of fibroblasts and endothelial cells, which start to deposit collagen and other extracellular matrix proteins on the surface of the grafted material. The deposited matrix subsequently matures into a peripheral fibrous capsule, which causes mechanical impairment and insufficient interactions of the biomaterial with the adjunct tissue [59].

Both biomaterials, also contained the photosensitizer mTHPC that enables a strong antibacterial surface effect upon illumination with light at 652 nm. As shown by various authors, antimicrobial photodynamic therapy (aPDT) is efficient in suppressing different oral pathogenic bacterial species to significant high extents [33,34,60–63]. aPDT is also considered an alternative to the systemic treatment of biofilm-related infectious diseases with antibiotics [64–66]. Due to the incorporation of mTHPC into the biomaterial matrix, singlet oxygen and other reactive oxygen species (ROS) are produced upon light exposure causing destruction of adherent bacterial cells. Investigations of our group have already shown that illumination of the mTHPC-doted biomaterials with red laser light (652 nm) caused complete inhibition of *Porphyromonas gingivalis* and led to a significant decrease in *Enterococcus faecalis* [32]. The photodynamic antimicrobial activity of both implanted materials was not observed in the present investigation, which limits the overall merit. However, it still needs to be determined whether the photodynamic activity of both biomaterials is also efficient in vivo. A further limitation might be the fact that no additional controls are included. Therefore, the bone regenerative capacity is not comparable to already known grafting materials. Further, the number of tibial bone defects might be increased in order to obtain an even distribution of samples. Information upon the morphology of BioM1 and BioM2 is still limited. Parameters such as porosity, specific surface area, thickness, and tortuosity are important and need yet to be investigated in detail.

Up to now, various photodynamic active materials are already under investigation [67]. However, examinations upon the efficiency in vivo, especially in the case of periodontal lesions are hence needed.

4. Materials and Methods

4.1. Characterization of the Biomaterials

In the present animal study, two light curable biomaterials, BioM1 based on urethane dimethacrylate and BioM2 based on tri-armed oligoester-urethane methacrylate (BioM2) were applied. Both investigated biomaterials, BioM1 and BioM2, additionally contained β-tricalcium phosphate microparticles loaded with 20 wt% of the photosensitizer mTHPC. All chemicals were obtained from Sigma-Aldrich Chemie GmbH, Taufkirchen, Germany. The photosensitizer mTHPC was kindly provided by biolitec research GmbH, Jena, Germany. The biomechanical and antimicrobial photodynamic properties of both materials were evaluated by our group in a previous examination [32]. Structural formulas of the applied polymers (urethane dimethacrylate—BioM1, tri-armed oligoester-urethane methacrylate—BioM2) are presented below (Figures 5 and 6).

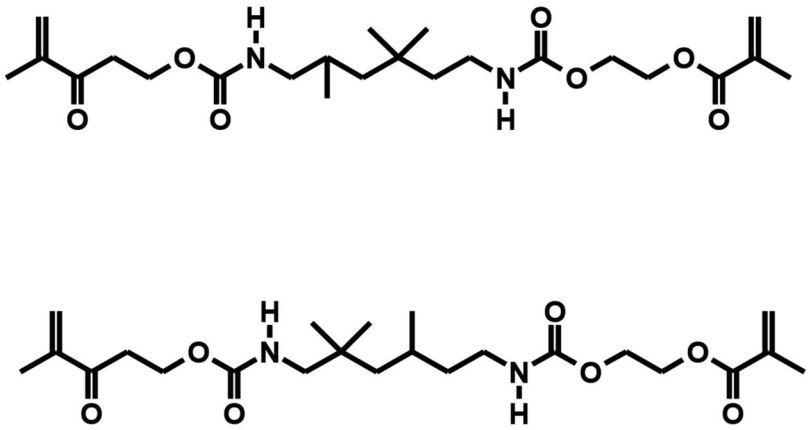


Figure 5. Structural formula of urethane dimethacrylate (the main component of BioM1).

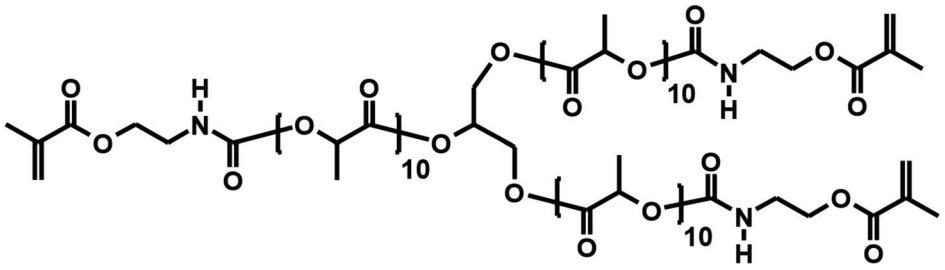


Figure 6. Structural formula of oligoester-urethane methacrylate (the main component of BioM2).

4.2. Surgical Procedure and Biomaterial Application

All experiments were conducted in accordance to the German law of animal protection and welfare. The investigation was authorized by the Thuringia Regional Office for Food Safety and Consumer Protection (protocol code: 02-036/10; date of approval: 14 October 2010).

Eight female domestic sheep (*Ovis gmelini aries*) obtained from a local breeder with a mean age of 12 months were used in this prospective study. Prior to surgery, all animals were acclimated for 2 weeks at the Central Animal Facility and Service Department, University Hospitals Jena, Germany. The sheep were assigned into two groups with four animals each. In the first group biomaterial 1 (BioM1) and in the second group biomaterial 2 (BioM2) was implanted.

For implantation, the femoral (distal) and tibial (proximal) epimethaphysial region of the right hind limb was chosen. Surgery was performed under general anesthesia. The animals were placed in right side recumbency and the skin of surgical side was disinfected with iodine (Braunoderm®, B.Braun AG, Melsungen, Germany). At first, an approximately

10 cm long incision was applied at the medial side of the distal femur epiphysis 1 cm proximal of the knee joint capsule longitudinally and parallel to the bone axis. The cortical bone was reached through incision of the local muscles and by dissection of the periosteum.

Two 5 × 6 mm cylindrical holes were drilled in the femoral epiphysis by using a water-cooled trephine. A minimal distance of 20 mm was kept in between the drilled holes to reduce the risk of fracture and to ensure proper healing and harvesting of the bone specimens at the end of the study.

The defects were filled with either BioM1 or BioM2. Prior to insertion of the biomaterials, the holes were dried using sterile cotton balls. When relative dryness was reached, the gel-like biomaterials were quickly injected in 2 mm thick layers and instantly photopolymerized for 40 s each using a calibrated dental light curing unit (Bluephase, 830 mW/cm^2, Ivoclar–Vivadent, Ellwangen, Germany). Polymerzation is shown in Figure 7a. After the bone defects were completely filled, the surface of each polymerized biomaterial was whipped once with a 70% ethanolic solution (Figure 7b). The position of the filled defects sites was marked by insertion of a 4 mm long titanium pin (Geistlich Biomaterials, Baden-Baden, Germany). The position of the pin in relation to the defect sites was transferred to a transparent plastic foil which was used for relocation after euthanasia. Subsequently, the periosteum was closed and the muscle fascia, subcutaneous tissue and skin were sutured with an absorbable thread.

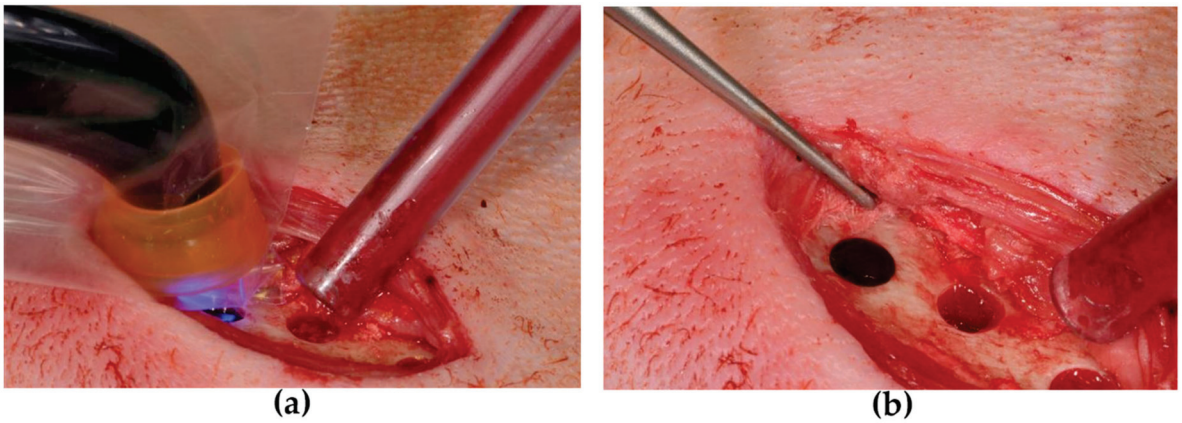


Figure 7. Biomaterial application: (**a**) light-polymerization; (**b**) solid biomaterial in the femur.

Afterwards, a second approximately 5 cm long incision was applied at the medial side of the proximal tibial epiphysis 1 cm distal of the knee joint capsule longitudinally and parallel to the bone axis. The cortical bone was exposed as described above and another defect of identical dimension was prepared and obturated by the identical biomaterial as already implanted into the femur.

After marking the location of the implant sites using a titanium pin and plastic foil, a suture was applied. Finally, both surgical sites were dressed with an aluminum based wound spray and medio-lateral as well as dorso-plantar X-ray images were taken as controls and for documentation of the healing progress. The location and total number of filled defect sites are summarized in Table 1. Antimicrobial prophylaxis and post-surgical pain control were applied. Animals were euthanized after 12 months of biomaterial implantation using a standardized protocol.

Table 1. Location and total number of bone defects filled with BioM1 or BioM2.

	Animal ID	Sample ID	Femur	Tibia
BioM1	S4	S4FP	2	-
		S4TP	-	1
	S5	S5FP	2	-
		S5TP	-	1
	S6	S6FP	2	-
		S6TP	-	1
	S7	S7FP	2	-
		S7TP	-	1
			8	4
BioM2	S12	S12FP	2	-
		S12TP	-	1
	S13	S13FP	2	-
		S13TP	-	1
	S14	S14FP	2	-
		S14TP	-	1
	S15	S15FP	2	-
		S15TP	-	1
			8	4

4.3. Sample Preparation and Histological Sectioning

After euthanasia, collected bone specimens were fixed in 5% formaldehyde solution for 5 d and subsequently cut under constant water cooling in two halves using the LEITZ 1600 microtome (Leica Microsystems GmbH, Bensheim, Germany). Each cortical halve of the bone sample was subjected to dehydration in solutions with increasing content of ethanol (50%, 70%, 80%, 2 × 96%, 3 × 100% ethanol) and afterwards embedded in Technovit 9100® (Kulzer GmbH Kulzer Technik, Wehrheim, Germany). The embedded specimens were then sectioned using the LEITZ 1600 microtome (Leica Microsystems GmbH, Bensheim, Germany). Subsequently, each sample was grounded to 10–20 µm of thickness using abrasive papers with different granulation from 300 to 4000 grit and subjected to Masson-Goldner staining.

The second halve of the divided bone sample was decalcified in 25% EDTA (pH 7.4) at 37 °C for 4 to 10 weeks. The decalcifying procedure was completed when the specimen could easily be penetrated by a fine needle.

After the decalcification process, samples were dehydrated in an alcoholic series and embedded into paraffin. Each paraffin block was then sectioned and the obtained 5 µm thick samples stained with hematoxylin eosin (HE). Histological allocation of the collected bone specimens can also be observed in Figure 8.

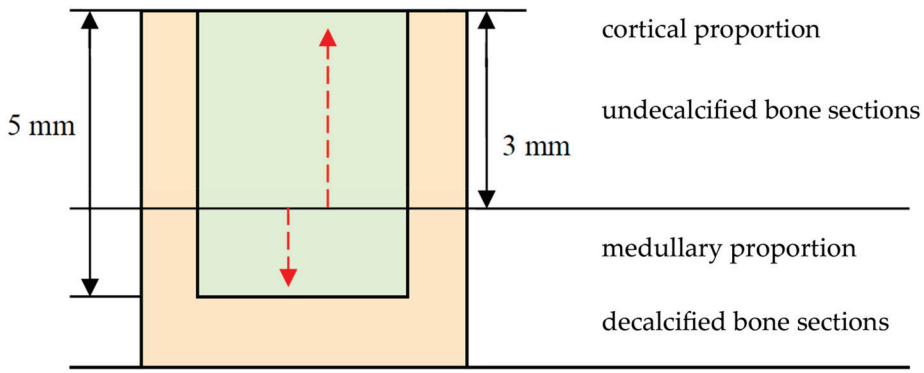


Figure 8. Assignment of the collected bone sample to the respective histologic evaluation method. The biomaterial remnant is expressed by light green. Bone is presented in light red color.

4.4. Histomorphometry

Undecalcified and stained histologic sections (n = 30) were observed using the microscope Jenaval (Carl Zeiss MicroImaging GmbH, Jena, Germany) at 10× to 125× magnification. Microscopic images were documented using the software AxioCam® and AxioVision® (release 4.6.3., Carl Zeiss MicroImaging GmbH, Jena, Germany). Data was analyzed using the freeware ImageJ® (1.50i, Wayne Rasband, National Institutes of Health, Bethesda, MD, USA). An ROI (region of interest) around the implanted biomaterial of 500 µm in width was defined and the percentage of bone and soft tissue determined (Figure 9).

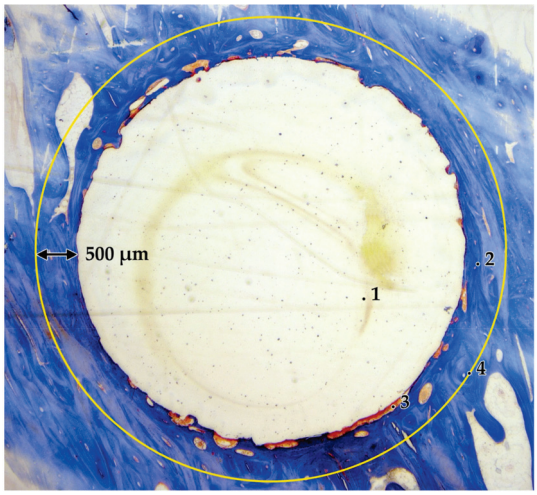


Figure 9. Masson-Goldner stained undecalcified section; (1: biomaterial, 2: bone, 3: soft tissue, 4: ROI 500 µm (yellow circle)).

In detail, each histological section was analyzed with regard to the square area of the biomaterial remnants, percentage of bone and soft tissue in the ROI and biomaterial-to-bone contact ratio.

Decalcified and HE stained sections were observed using the microscope Jenaval (Carl Zeiss MicroImaging GmbH, Jena, Germany) at 1× to 250× magnification. From each bone specimen, five different sections were chosen and evaluated by applying an ROI of 250 µm (Figure 10).

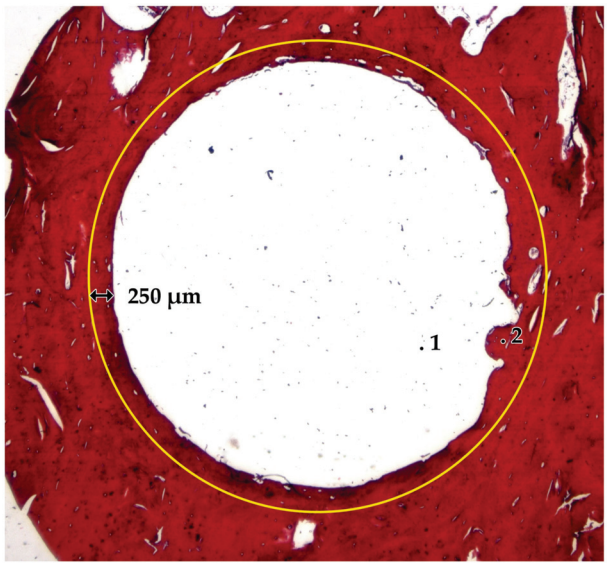


Figure 10. Decalcified and HE stained sections with a ROI of 250 µm (yellow circle). Biomaterial body (1) is in close contact to the surrounding bone (2).

The ROI was examined by applying a four-graded scoring system (Table 2). The score was adapted and modified [68] and comprises elements from the DIN EN ISO 10993-6:2017 guidelines [69]. Examples for each score (1–4) are presented in Figure 11. A workflow of the study is presented in Figure 12.

Table 2. Four-graded histological evaluation score adapted and modified from DIN EN ISO 10993-6 [69].

Score	Definition
1	Completely mineralized bone with the presence of osteoblasts and/or osteocytes
2	Deposited connective tissue within the bone matrix
3	Connective tissue without signs of bone in the ROI
4	Additional appearance of univacular fat cells

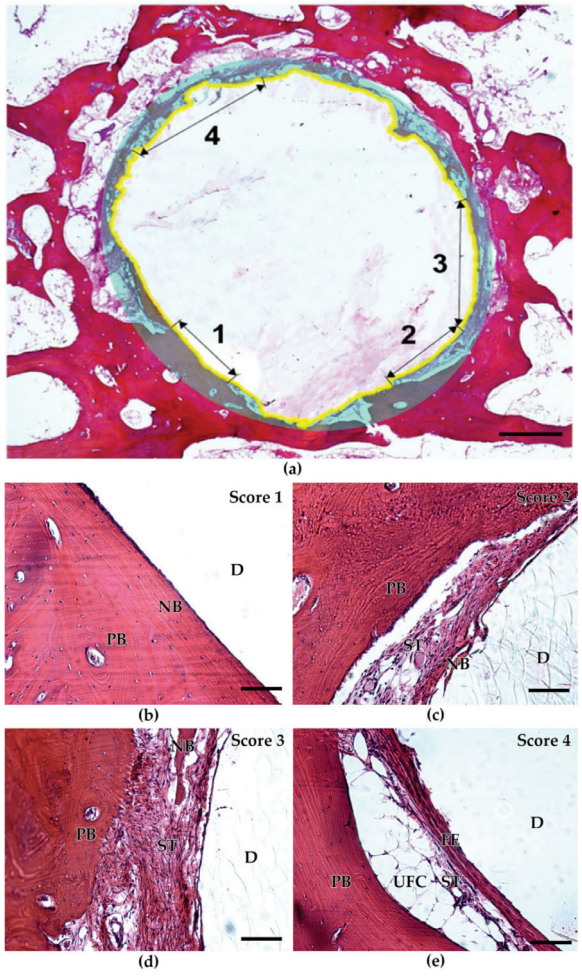


Figure 11. Four-graded histological evaluation score: (**a**) summary of all scores (1 to 4) blended in one single image. The ROI is marked by a greyish circular zone. Bone-to-biomaterial interface is indicated by a yellow line. Scale bar 500 µm; (**b**–**e**) respective examples for each evaluation score. Scale bar 100 µm. (D: defect zone with biomaterial remnants, NB: new-formed bone, ST: soft tissue, PB: peripheral bone, UFC: univacuolar fat cells, FE: fibrous encapsulation).

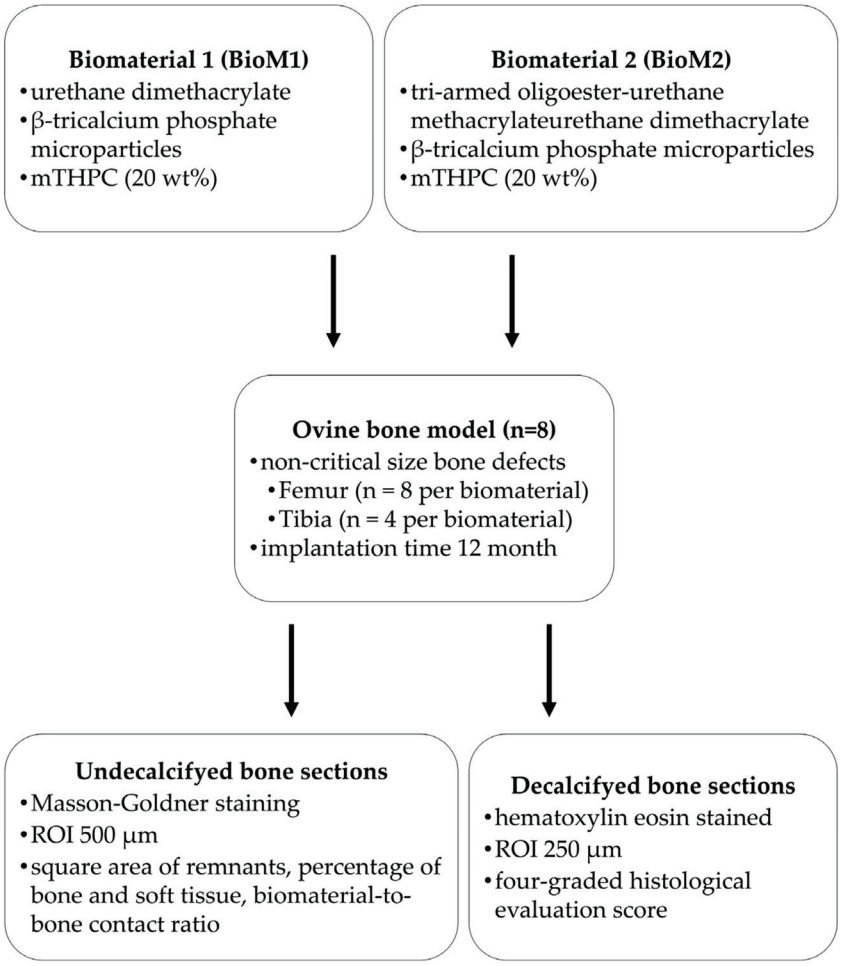


Figure 12. Workflow of the study.

5. Conclusions

The results of the present study revealed that BioM1 (photosensitizer-armed urethane dimethacrylate) was bone-integrated to a significantly higher extent compared to BioM2 (photosensitizer-armed oligoester-urethane methacrylate). In case of BioM1, high-quality bone was formed in the ROI without any signs of adverse effects. Due to the slow degradation of BioM1, structural stability is provided for a longer period of time. In contrast, implantation of BioM2 resulted in chronic inflammation and increased fibrous tissue formation at the bone-to-biomaterial interface.

It can be concluded that BioM1 has promising regenerative and biocompatible characteristics. The material can therefore be recommended for further studies that focus on bone regeneration in regions where an additional structural support as well as stabilization is needed. Hence, it needs to be investigated, if those materials are capable of treating intrabony periodontal lesions sufficiently. Moreover, detailed information upon the antibacterial efficiency of photosensitizer-armed grafting materials still has to be obtained in vivo.

Author Contributions: Conceptualization, S.K., B.S., A.B., D.S. and U.R.; methodology, S.K., U.R., A.C.v.H., S.W. and A.B.; software, S.K., A.C.v.H., S.W. and A.G.; validation, S.K., A.C.v.H., S.W., U.R., A.B. and A.G.; formal analysis, S.K., A.C.v.H., S.W. and A.G.; investigation, S.K., A.C.v.H., S.W., A.B., D.S. and A.G.; resources, M.H. and M.R.; data curation, S.K., A.C.v.H., S.W. and A.G.; writing—original draft preparation, S.K.; writing—review and editing, S.K., B.S., D.S. and A.B.; visualization, S.K., A.C.v.H., S.W. and A.G.; supervision, S.K., U.R., M.R. and B.S.; project administration, B.S.; funding acquisition, S.K., B.S., A.B. and D.S. All authors have read and agreed to the published version of the manuscript.

Funding: This research received no external funding.

Institutional Review Board Statement: The animal study protocol was approved by the Thuringia Regional Office for Food Safety and Consumer Protection (protocol code: 02-036/10; date of approval: 14 October 2010).

Informed Consent Statement: Not applicable.

Data Availability Statement: Available upon request from the corresponding author.

Acknowledgments: We acknowledge the entire staff of the Animal Research Institution of the University Hospital Jena. We further acknowledge support by the German Research Foundation Projekt-Nr. 512648189 and the Open Access Publication Fund of the Thueringer Universitaets-und Landesbibliothek Jena, Germany.

Conflicts of Interest: The authors declare no conflict of interest.

References

1. Kwon, T.; Lamster, I.B.; Levin, L. Current Concepts in the Management of Periodontitis. *Int. Dent. J.* **2021**, *71*, 462–476. [CrossRef] [PubMed]
2. Di Stefano, M.; Polizzi, A.; Santonocito, S.; Romano, A.; Lombardi, T.; Isola, G. Impact of Oral Microbiome in Periodontal Health and Periodontitis: A Critical Review on Prevention and Treatment. *Int. J. Mol. Sci.* **2022**, *23*, 5142. [CrossRef] [PubMed]
3. Plachokova, A.; Andreu-Sánchez, S.; Noz, M.; Fu, J.; Riksen, N. Oral Microbiome in Relation to Periodontitis Severity and Systemic Inflammation. *Int. J. Mol. Sci.* **2021**, *22*, 5876. [CrossRef] [PubMed]
4. Papapanou, P.N.; Tonetti, M.S. Diagnosis and epidemiology of periodontal osseous lesions. *Periodontology 2000* **2000**, *22*, 8–21. [CrossRef] [PubMed]
5. Stavropoulos, A.; Ivanovic, A.; Chapple, I.L.C.; Nikolidakis, D.; Nikou, G.; Sculean, A. Biomaterials for promoting periodontal regeneration in human intrabony defects: A systematic review. *Periodontology* **2000**, *68*, 182–216. [CrossRef]
6. Ren, Y.; Fan, L.; Alkildani, S.; Liu, L.; Emmert, S.; Najman, S.; Rimashevskiy, D.; Schnettler, R.; Jung, O.; Xiong, X.; et al. Barrier Membranes for Guided Bone Regeneration (GBR): A Focus on Recent Advances in Collagen Membranes. *Int. J. Mol. Sci.* **2022**, *23*, 14987. [CrossRef]
7. Paolantonio, M.; Di Tullio, M.; Giraudi, M.; Romano, L.; Secondi, L.; Paolantonio, G.; Graziani, F.; Pilloni, A.; De Ninis, P.; Femminella, B. Periodontal regeneration by leukocyte and platelet-rich fibrin with autogenous bone graft versus enamel matrix derivative with autogenous bone graft in the treatment of periodontal intrabony defects: A randomized non-inferiority trial. *J. Periodontol.* **2020**, *91*, 1595–1608. [CrossRef]
8. Sassano, P.; Gennaro, P.; Chisci, G.; Gabriele, G.; Aboh, I.V.; Mitro, V.; di Curzio, P. Calvarial onlay graft and submental incision in treatment of atrophic edentulous mandibles: An approach to reduce postoperative complications. *J. Craniofac. Surg.* **2014**, *25*, 693–697. [CrossRef]
9. Jepsen, S.; Gennai, S.; Hirschfeld, J.; Kalemaj, Z.; Buti, J.; Graziani, F. Regenerative surgical treatment of furcation defects: A systematic review and Bayesian network meta-analysis of randomized clinical trials. *J. Clin. Periodontol.* **2019**, *47*, 352–374. [CrossRef]
10. Chisci, G.; Fredianelli, L. Therapeutic Efficacy of Bromelain in Alveolar Ridge Preservation. *Antibiotics* **2022**, *11*, 1542. [CrossRef]
11. Vahdatinia, F.; Hooshyarfard, A.; Jamshidi, S.; Shojaei, S.; Patel, K.; Moeinifard, E.; Haddadi, R.; Farhadian, M.; Gholami, L.; Tayebi, L. 3D-Printed Soft Membrane for Periodontal Guided Tissue Regeneration. *Materials* **2023**, *16*, 1364. [CrossRef]
12. Ausenda, F.; Rasperini, G.; Acunzo, R.; Gorbunkova, A.; Pagni, G. New Perspectives in the Use of Biomaterials for Periodontal Regeneration. *Materials* **2019**, *12*, 2197. [CrossRef]
13. Deng, Y.; Liang, Y.; Liu, X. Biomaterials for Periodontal Regeneration. *Dent. Clin. N. Am.* **2022**, *66*, 659–672. [CrossRef]
14. Putra, R.U.; Basri, H.; Prakoso, A.T.; Chandra, H.; Ammarullah, M.I.; Akbar, I.; Syahrom, A.; Kamarul, T. Level of Activity Changes Increases the Fatigue Life of the Porous Magnesium Scaffold, as Observed in Dynamic Immersion Tests, over Time. *Sustainability* **2023**, *15*, 823. [CrossRef]
15. Tomas, M.; Čandrlić, M.; Juzbašić, M.; Ivanišević, Z.; Matijević, N.; Včev, A.; Peloza, O.C.; Matijević, M.; Kačarević, P. Synthetic Injectable Biomaterials for Alveolar Bone Regeneration in Animal and Human Studies. *Materials* **2021**, *14*, 2858. [CrossRef]
16. Ruediger, T.; Berg, A.; Guellmar, A.; Rode, C.; Schnabelrauch, M.; Urbanek, A.; Wagner, K.; Wyrwa, R.; Kinne, R.W.; Sigusch, B.W. Cytocompatibility of polymer-based periodontal bone substitutes in gingival fibroblast and MC3T3 osteoblast cell cultures. *Dent. Mater.* **2012**, *28*, e239–e249. [CrossRef]
17. Cheah, C.W.; Al-Namnam, N.M.; Lau, M.N.; Lim, G.S.; Raman, R.; Fairbairn, P.; Ngeow, W.C. Synthetic Material for Bone, Periodontal, and Dental Tissue Regeneration: Where Are We Now, and Where Are We Heading Next? *Materials* **2021**, *14*, 6123. [CrossRef]
18. Iaquinta, M.R.; Mazzoni, E.; Manfrini, M.; D'Agostino, A.; Trevisiol, L.; Nocini, R.; Trombelli, L.; Barbanti-Brodano, G.; Martini, F.; Tognon, M. Innovative Biomaterials for Bone Regrowth. *Int. J. Mol. Sci.* **2019**, *20*, 618. [CrossRef]
19. Dreifke, M.B.; Ebraheim, N.A.; Jayasuriya, A.C. Investigation of potential injectable polymeric biomaterials for bone regeneration. *J. Biomed. Mater. Res. Part A* **2013**, *101*, 2436–2447. [CrossRef]

20. Mariano, L.C.; Fernandes, M.H.R.; Gomes, P.S. Antimicrobial Biomaterials for the Healing of Infected Bone Tissue: A Systematic Review of Microtomographic Data on Experimental Animal Models. *J. Funct. Biomater.* **2022**, *13*, 193. [CrossRef]
21. Zhang, C.; Yang, D.; Wang, T.-B.; Nie, X.; Chen, G.; Wang, L.-H.; You, Y.-Z.; Wang, Q. Biodegradable hydrogels with photodynamic antibacterial activity promote wound healing and mitigate scar formation. *Biomater. Sci.* **2022**, *11*, 288–297. [CrossRef] [PubMed]
22. Chang, K.-C.; Chiu, K.-C.; Chen, W.-C.; Lan, W.-C.; Chen, C.-Y.; Hsia, S.-M.; Wang, T.-H.; Tu, H.-F.; Shih, Y.-H.; Shieh, T.-M. Effects of Temoporfin-Based Photodynamic Therapy on the In Vitro Antibacterial Activity and Biocompatibility of Gelatin-Hyaluronic Acid Cross-Linked Hydrogel Membranes. *Pharmaceutics* **2022**, *14*, 2314. [CrossRef] [PubMed]
23. Guan, M.; Chu, G.; Jin, J.; Liu, C.; Cheng, L.; Guo, Y.; Deng, Z.; Wang, Y. A Combined Cyanine/Carbomer Gel Enhanced Photodynamic Antimicrobial Activity and Wound Healing. *Nanomaterials* **2022**, *12*, 2173. [CrossRef] [PubMed]
24. Dong, J.; Ghiladi, R.A.; Wang, Q.; Cai, Y.; Wei, Q. Protoporphyrin-IX conjugated cellulose nanofibers that exhibit high antibacterial photodynamic inactivation efficacy. *Nanotechnology* **2018**, *29*, 265601. [CrossRef]
25. Nie, X.; Wu, S.; Hussain, T.; Wei, Q. PCN-224 Nanoparticle/Polyacrylonitrile Nanofiber Membrane for Light-Driven Bacterial Inactivation. *Nanomaterials* **2021**, *11*, 3162. [CrossRef]
26. Pereira, A.O.; Lopes, I.M.I.; Silva, T.R.; Corrêa, T.Q.; Paschoalin, R.T.; Inada, N.M.; Iermak, I.; Neto, F.V.R.; Araujo-Chaves, J.C.; Marletta, A.; et al. Bacterial Photoinactivation Using PLGA Electrospun Scaffolds. *ACS Appl. Mater. Interfaces* **2021**, *13*, 31406–31417. [CrossRef]
27. Jiang, S.; Ma, B.C.; Huang, W.; Kaltbeitzel, A.; Kizisavas, G.; Crespy, D.; Zhang, K.A.I.; Landfester, K. Visible light active nanofibrous membrane for antibacterial wound dressing. *Nanoscale Horiz.* **2018**, *3*, 439–446. [CrossRef]
28. Sun, D.; Zhang, Z.; Chen, M.; Zhang, Y.; Amagat, J.; Kang, S.; Zheng, Y.; Hu, B.; Chen, M. Co-immobilization of Ce6 Sono/photosensitizer and Protonated Graphitic-Carbon Nitride on PCL/gelation Fibrous Scaffolds for Combined Sono-photodynamic Cancer Therapy. *ACS Appl. Mater. Interfaces* **2020**, *12*, 40728–40739. [CrossRef]
29. Yang, Y.; Zhou, X.; Chan, Y.K.; Wang, Z.; Li, L.; Li, J.; Liang, K.; Deng, Y. Photo-Activated Nanofibrous Membrane with Self-Rechargeable Antibacterial Function for Stubborn Infected Cutaneous Regeneration. *Small* **2022**, *18*, 2105988. [CrossRef]
30. Prieto-Montero, R.; Prieto-Castañeda, A.; Katsumiti, A.; Cajaraville, M.; Agarrabeitia, A.; Ortiz, M.; Martínez-Martínez, V. Functionalization of Photosensitized Silica Nanoparticles for Advanced Photodynamic Therapy of Cancer. *Int. J. Mol. Sci.* **2021**, *22*, 6618. [CrossRef]
31. Lagos, K.J.; Buzzá, H.H.; Bagnato, V.S.; Romero, M.P. Carbon-Based Materials in Photodynamic and Photothermal Therapies Applied to Tumor Destruction. *Int. J. Mol. Sci.* **2021**, *23*, 22. [CrossRef]
32. Sigusch, B.; Dietsch, S.; Berg, A.; Voelpel, A.; Guellmar, A.; Rabe, U.; Schnabelrauch, M.; Steen, D.; Gitter, B.; Albrecht, V.; et al. Antimicrobial photodynamic active biomaterials for periodontal regeneration. *Dent. Mater.* **2018**, *34*, 1542–1554. [CrossRef]
33. Kranz, S.; Guellmar, A.; Völpel, A.; Gitter, B.; Albrecht, V.; Sigusch, B.W. Photodynamic suppression of *Enterococcus faecalis* using the photosensitizer mTHPC. *Lasers Surg. Med.* **2011**, *43*, 241–248. [CrossRef]
34. Ossmann, A.; Kranz, S.; Andre, G.; Völpel, A.; Albrecht, V.; Fahr, A.; Sigusch, B.W. Photodynamic killing of Enterococcus faecalis in dentinal tubules using mTHPC incorporated in liposomes and invasomes. *Clin. Oral Investig.* **2014**, *19*, 373–384. [CrossRef]
35. Voss, J.O.; Kasselmann, S.; Koerdt, S.; Rendenbach, C.; Fischer, H.; Jöhrens, K.; Czabanka, M.; Schmidt-Bleek, K.; Duda, G.N.; Heiland, M.; et al. Treatment options for critical size defects—Comparison of different materials in a calvaria split model in sheep. *Biomater. Adv.* **2022**, *136*, 212788. [CrossRef]
36. Xu, Z.; Qi, X.; Bao, M.; Zhou, T.; Shi, J.; Xu, Z.; Zhou, M.; Boccaccini, A.R.; Zheng, K.; Jiang, X. Biomineralization inspired 3D printed bioactive glass nanocomposite scaffolds orchestrate diabetic bone regeneration by remodeling micromilieu. *Bioact. Mater.* **2023**, *25*, 239–255. [CrossRef]
37. Tan, Q.-C.; Jiang, X.-S.; Chen, L.; Huang, J.-F.; Zhou, Q.-X.; Wang, J.; Zhao, Y.; Zhang, B.; Sun, Y.-N.; Wei, M.; et al. Bioactive graphene oxide-functionalized self-expandable hydrophilic and osteogenic nanocomposite for orthopaedic applications. *Mater. Today Bio* **2023**, *18*, 100500. [CrossRef]
38. Bucciarelli, A.; Petretta, M.; Grigolo, B.; Gambari, L.; Bossi, A.M.; Grassi, F.; Maniglio, D. Methacrylated Silk Fibroin Additive Manufacturing of Shape Memory Constructs with Possible Application in Bone Regeneration. *Gels* **2022**, *8*, 833. [CrossRef]
39. Celikkin, N.; Mastrogiacomo, S.; Dou, W.; Heerschap, A.; Oosterwijk, E.; Walboomers, X.F.; Święszkowski, W. In vitro and in vivo assessment of a 3D printable gelatin methacrylate hydrogel for bone regeneration applications. *J. Biomed. Mater. Res. Part B Appl. Biomater.* **2022**, *110*, 2133–2145. [CrossRef] [PubMed]
40. Nuss, K.; Auer, J.A.; Boos, A.; von Rechenberg, B. An animal model in sheep for biocompatibility testing of biomaterials in cancellous bones. *BMC Musculoskelet. Disord.* **2006**, *7*, 67. [CrossRef] [PubMed]
41. Pearce, A.I.; Richards, R.G.; Milz, S.; Schneider, E.; Pearce, S.G. Animal models for implant biomaterial research in bone: A review. *Eur. Cells Mater.* **2007**, *13*, 1–10. [CrossRef] [PubMed]
42. Atayde, L.M.; Cortez, P.; Pereira, T.; Armada-Da-Silva, P.; Afonso, A.; Lopes, M.A.; Santos, J.D.; Maurício, A.C. A new sheep model with automatized analysis of biomaterial-induced bone tissue regeneration. *J. Mater. Sci. Mater. Med.* **2014**, *25*, 1885–1901. [CrossRef]
43. Boure', L.; Zeiter, S.; Seidenglanz, U.; Leitner, M.; Van der Pol, B.; Matthys, R.; Pearce, S. A novel sheep model for evaluating biomaterials in cancellous bone. In Proceedings of the ECM IX Musculoskeletal Trauma—50 Years of AO Research, Davos, Switzerland, 15–18 June 2008; p. 16.

44. Perier-Metz, C.; Cipitria, A.; Hutmacher, D.W.; Duda, G.N.; Checa, S. An in silico model predicts the impact of scaffold design in large bone defect regeneration. *Acta Biomater.* **2022**, *145*, 329–341. [CrossRef]
45. Perier-Metz, C.; Duda, G.N.; Checa, S. Mechano-Biological Computer Model of Scaffold-Supported Bone Regeneration: Effect of Bone Graft and Scaffold Structure on Large Bone Defect Tissue Patterning. *Front. Bioeng. Biotechnol.* **2020**, *8*, 585799. [CrossRef]
46. Jamari, J.; Ammarullah, M.I.; Santoso, G.; Sugiharto, S.; Supriyono, T.; Permana, M.S.; Winarni, T.I.; van der Heide, E. Adopted walking condition for computational simulation approach on bearing of hip joint prosthesis: Review over the past 30 years. *Heliyon* **2022**, *8*, e12050. [CrossRef]
47. Perier-Metz, C.; Duda, G.N.; Checa, S. Initial mechanical conditions within an optimized bone scaffold do not ensure bone regeneration—An in silico analysis. *Biomech. Model. Mechanobiol.* **2021**, *20*, 1723–1731. [CrossRef]
48. Sideridou, I.D.; Karabela, M.M.; Bikiaris, D.N. Aging studies of light cured dimethacrylate-based dental resins and a resin composite in water or ethanol/water. *Dent. Mater.* **2007**, *23*, 1142–1149. [CrossRef]
49. Walsh, W.R.; Bertollo, N.; Christou, C.; Schaffner, D.; Mobbs, R.J. Plasma-sprayed titanium coating to polyetheretherketone improves the bone-implant interface. *Spine J.* **2015**, *15*, 1041–1049. [CrossRef]
50. Martini, L.; Staffa, G.; Giavaresi, G.; Salamanna, F.; Parrilli, A.; Serchi, E.; Pressato, D.; Arcangeli, E.; Fini, M. Long-Term Results following Cranial Hydroxyapatite Prosthesis Implantation in a Large Skull Defect Model. *Plast. Reconstr. Surg.* **2012**, *129*, 625e–635e. [CrossRef]
51. Ghaffar, A.; Verschuren, P.; Geenevasen, J.; Handels, T.; Berard, J.; Plum, B.; Dias, A.; Schoenmakers, P.; van der Wal, S. Fast in vitro hydrolytic degradation of polyester urethane acrylate biomaterials: Structure elucidation, separation and quantification of degradation products. *J. Chromatogr. A* **2010**, *1218*, 449–458. [CrossRef]
52. Alam Ansari, M.A.; Golebiowska, A.A.; Dash, M.; Kumar, P.; Jain, P.K.; Nukavarapu, S.P.; Ramakrishna, S.; Nanda, H.S. Engineering biomaterials to 3D-print scaffolds for bone regeneration: Practical and theoretical consideration. *Biomater. Sci.* **2022**, *10*, 2789–2816. [CrossRef] [PubMed]
53. Fukuba, S.; Okada, M.; Nohara, K.; Iwata, T. Alloplastic Bone Substitutes for Periodontal and Bone Regeneration in Dentistry: Current Status and Prospects. *Materials* **2021**, *14*, 1096. [CrossRef]
54. Hou, X.; Zhang, L.; Zhou, Z.; Luo, X.; Wang, T.; Zhao, X.; Lu, B.; Chen, F.; Zheng, L. Calcium Phosphate-Based Biomaterials for Bone Repair. *J. Funct. Biomater.* **2022**, *13*, 187. [CrossRef] [PubMed]
55. Prakoso, A.T.; Basri, H.; Adanta, D.; Yani, I.; Ammarullah, M.I.; Akbar, I.; Ghazali, F.A.; Syahrom, A.; Kamarul, T. The Effect of Tortuosity on Permeability of Porous Scaffold. *Biomedicines* **2023**, *11*, 427. [CrossRef]
56. Jones, K.S. Effects of biomaterial-induced inflammation on fibrosis and rejection. *Semin. Immunol.* **2008**, *20*, 130–136. [CrossRef]
57. Sheikh, Z.; Brooks, P.J.; Barzilay, O.; Fine, N.; Glogauer, M. Macrophages, Foreign Body Giant Cells and Their Response to Implantable Biomaterials. *Materials* **2015**, *8*, 5671–5701. [CrossRef]
58. Hu, Y.; Huang, J.; Chen, C.; Wang, Y.; Hao, Z.; Chen, T.; Wang, J.; Li, J. Strategies of Macrophages to Maintain Bone Homeostasis and Promote Bone Repair: A Narrative Review. *J. Funct. Biomater.* **2022**, *14*, 18. [CrossRef]
59. Klopfleisch, R.; Jung, F. The pathology of the foreign body reaction against biomaterials. *J. Biomed. Mater. Res. Part A* **2016**, *105*, 927–940. [CrossRef]
60. Kranz, S.; Huebsch, M.; Guellmar, A.; Voelpel, A.; Tonndorf-Martini, S.; Sigusch, B.W. Antibacterial photodynamic treatment of periodontopathogenic bacteria with indocyanine green and near-infrared laser light enhanced by Trolox^{TM}. *Lasers Surg. Med.* **2015**, *47*, 350–360. [CrossRef]
61. Sigusch, B.W.; Engelbrecht, M.; Völpel, A.; Holletschke, A.; Pfister, W.; Schütze, J. Full-Mouth Antimicrobial Photodynamic Therapy in *Fusobacterium nucleatum*–Infected Periodontitis Patients. *J. Periodontol.* **2010**, *81*, 975–981. [CrossRef]
62. Dias, L.M.; Ferrisse, T.M.; Medeiros, K.S.; Cilli, E.M.; Pavarina, A.C. Use of Photodynamic Therapy Associated with Antimicrobial Peptides for Bacterial Control: A Systematic Review and Meta-Analysis. *Int. J. Mol. Sci.* **2022**, *23*, 3226. [CrossRef] [PubMed]
63. Songca, S.P.; Adjei, Y. Applications of Antimicrobial Photodynamic Therapy against Bacterial Biofilms. *Int. J. Mol. Sci.* **2022**, *23*, 3209. [CrossRef]
64. Elashiry, M.; Morandini, A.; Timothius, C.C.; Ghaly, M.; Cutler, C. Selective Antimicrobial Therapies for Periodontitis: Win the "Battle and the War". *Int. J. Mol. Sci.* **2021**, *22*, 6459. [CrossRef]
65. Giannelli, M.; Lasagni, M.; Bani, D. Photonic Therapy in Periodontal Diseases an Overview with Appraisal of the Literature and Reasoned Treatment Recommendations. *Int. J. Mol. Sci.* **2019**, *20*, 4741. [CrossRef]
66. Maliszewska, I.; Zdubek, A. On the Photo-Eradication of Methicillin-Resistant *Staphylococcus aureus* Biofilm Using Methylene Blue. *Int. J. Mol. Sci.* **2023**, *24*, 791. [CrossRef]
67. Cao, H.; Qiao, S.; Qin, H.; Jandt, K.D. Antibacterial Designs for Implantable Medical Devices: Evolutions and Challenges. *J. Funct. Biomater.* **2022**, *13*, 86. [CrossRef]

68. Bielenstein, J.; Radenković, M.; Najman, S.; Liu, L.; Ren, Y.; Cai, B.; Beuer, F.; Rimashevskiy, D.; Schnettler, R.; Alkildani, S.; et al. In Vivo Analysis of the Regeneration Capacity and Immune Response to Xenogeneic and Synthetic Bone Substitute Materials. *Int. J. Mol. Sci.* **2022**, *23*, 10636. [CrossRef]
69. *ISO 10993-6:2017*; Biological Evaluation of Medical Devices—Part 6: Tests for Local Effects after Implantation. International Organization for Standardization: Geneva, Switzerland, 2017.

Disclaimer/Publisher's Note: The statements, opinions and data contained in all publications are solely those of the individual author(s) and contributor(s) and not of MDPI and/or the editor(s). MDPI and/or the editor(s) disclaim responsibility for any injury to people or property resulting from any ideas, methods, instructions or products referred to in the content.

International Journal of
Molecular Sciences

MDPI

Article

A Histologic, Histomorphometric, and Immunohistochemical Evaluation of Anorganic Bovine Bone and Injectable Biphasic Calcium Phosphate in Humans: A Randomized Clinical Trial

Matej Tomas [1,2], Matej Karl [1,3], Marija Čandrlić [1,3], Marko Matijević [2,4], Martina Juzbašić [1,2], Olga Cvijanović Peloza [5], Ana Terezija Jerbić Radetić [5], Davor Kuiš [1,6,7], Bruno Vidaković [1], Zrinka Ivanišević [1,*] and Željka Perić Kačarević [2,8,*]

1 Department of Dental Medicine, Faculty of Dental Medicine and Health Osijek, J. J. Strossmayer University of Osijek, 31 000 Osijek, Croatia
2 Interdisciplinary University Study of Molecular Biosciences, J. J. Strossmayer University of Osijek, 31 000 Osijek, Croatia
3 Faculty of Medicine Osijek, J. J. Strossmayer University of Osijek, 31 000 Osijek, Croatia
4 Community Healthcare Center of Osijek-Baranja County, 31 000 Osijek, Croatia
5 Department of Anatomy, Faculty of Medicine, University of Rijeka, 51 000 Rijeka, Croatia
6 Department of Periodontology, Faculty of Dental Medicine Rijeka, Univeristy of Rijeka, 51 000 Rijeka, Croatia
7 Clinical Hospital Center Rijeka, 51 000 Rijeka, Croatia
8 Department of Anatomy, Histology, Embriology, Pathology Anatomy and Pathology Histology, Faculty of Dental Medicine and Health Osijek, J. J. Strossmayer University of Osijek, 31 000 Osijek, Croatia
* Correspondence: zivanisevic@fdmz.hr (Z.I.); zpkacarevic@fdmz.hr (Ž.P.K.)

Abstract: Following trauma, chronic periapical process, or tooth extraction, a large loss of bone volume is noticed during the healing process. To facilitate the placement of dental implants, various surgical procedures are used for an optimal alveolar ridge profile, while maintaining adequate bone dimensions. The main aim of this study was to determine the healing ability (histologically and immunohistologically) of alveolar bone defects during augmentation with two different biomaterials: injectable biphasic calcium phosphate (BCP) and anorganic bovine bone (ABB). Thirty-eight subjects were randomly divided into two groups. The first group received the tested bone substitute biomaterial (BSB), i.e., BCP (maxresorb inject®), and the second group received an alternative to the gold standard, i.e., ABB (Bio-Oss®). The histopathological, histomorphometric, and immunohistochemical analyses gave comparable results for these bone substitute materials in terms of newly formed bone: (BCP: 39.91 ± 8.49%, ABB: 41.73 ± 13.99%), residual biomaterial (BCP: 28.61 ± 11.38%, ABB: 31.72 ± 15.52%), and soft tissue (BCP: 31.49 ± 11.09%, ABB: 26.54 ± 7.25%), with no significant difference found between the groups ($p < 0.05$, *t*-test), proving that BCP is equally suitable and successful for alveolar bone regeneration.

Keywords: alveolar bone regeneration; anorganic bovine bone; biphasic calcium phosphate; histology; immunohistochemistry

Citation: Tomas, M.; Karl, M.; Čandrlić, M.; Matijević, M.; Juzbašić, M.; Peloza, O.C.; Radetić, A.T.J.; Kuiš, D.; Vidaković, B.; Ivanišević, Z.; et al. A Histologic, Histomorphometric, and Immunohistochemical Evaluation of Anorganic Bovine Bone and Injectable Biphasic Calcium Phosphate in Humans: A Randomized Clinical Trial. *Int. J. Mol. Sci.* **2023**, *24*, 5539. https://doi.org/10.3390/ijms24065539

Academic Editor: Mary Anne Melo

Received: 27 February 2023
Revised: 8 March 2023
Accepted: 9 March 2023
Published: 14 March 2023

Copyright: © 2023 by the authors. Licensee MDPI, Basel, Switzerland. This article is an open access article distributed under the terms and conditions of the Creative Commons Attribution (CC BY) license (https://creativecommons.org/licenses/by/4.0/).

1. Introduction

Following trauma, chronic periapical process, or tooth extraction, a large loss of bone volume is noticed during the healing process [1,2]. Two-thirds of bone loss occurs on the vestibular side, and most alveolar changes in the extraction socket occur in the first year after tooth extraction [3,4]. In the first six months after tooth extraction, horizontal bone loss of 29–63% and vertical bone loss of 11–22% have been reported in previous human studies [5–7]. However, the ultimate goal of implant therapy is to restore missing teeth by positioning the implant in an anatomically correct, aesthetically pleasing, and functional location [8]. To facilitate the placement of dental implants, various surgical procedures are used for an optimal alveolar ridge profile, while maintaining adequate bone dimensions [9,10].

Alveolar ridge preservation is described as "any method before or after tooth extraction that aims to limit ridge resorption and promote bone growth within the alveolus"; as such, it has attracted the interest of many researchers. Alveolar bone regeneration provides many different biomaterials (BSB), such as autogenous bone from oral and extra oral sites, allografts, xenografts, and synthetic biomaterials [11–13]. The main function of the BSB is to provide mechanical support and stimulate bone regeneration, with the ultimate goal of creating new bone [14]. In addition, BSB must reduce the risk of biological side effects [15]. Furthermore, BSB must prevent the breakdown of the structural scaffold for bone formation and preferably be replaced by newly formed bone through bone resorption and remodeling by osteoclasts [16–19]. According to studies, all current BSBs reach only the osteoconductivity requirement and instead serve as a structural scaffold for regenerative processes [20–22]. None of the products available today have all the characteristics that make them ideal for BSBs, such as nontoxicity, ease of handling, low immunogenicity, affordability, ability to induce blood vessel growth, biocompatibility, and osteoinductive and osteoconductive properties [14,23]. Because it remains the only marrow for healing that possesses all four of the critical biological characteristics of bone, autogenous bone is considered the gold standard in the therapeutic use of bone augmentation [24,25]. However, autografts also have a number of disadvantages. During augmentation and remodeling, autogenous bone tends to lose up to 60% of its volume [26]. Due to additional disadvantages such as secondary surgical site, limited availability, bleeding risk, edema, postoperative pain, and increased surgical costs, BSBs have been developed as an alternative [27–34]. An allogeneic bone graft is derived from an individual belonging to the same species but with a different genotype. The avoidance of a secondary surgical site and a shortened procedure time are the advantages of such BSB. Several risks associated with such BSB can be mitigated by tissue processing, such as sterilization, ultrasonic cleaning, gamma irradiation, and demineralization [35]. In addition, increasing regulatory restrictions on the use of allografts in Europe have led to the production of new materials of other origins, such as animal or synthetic [36,37].

Xenografts are used as an alternative to the gold standard. Most scientific research mentions deproteinized bovine bone, porcine bone, and more recently, horse bone [38]. Deproteinized bovine bone is the most typical source of xenografts in dentistry. To produce a porous hydroxyapatite (HA) material containing only the anorganic components of bovine bone, the bone is either thermally deproteinized and/or chemically processed e.g., NaOH. The resulting porous structure can provide strong mechanical support and promote healing. The porous structure also has a large surface area and promotes angiogenesis, i.e., the formation of new blood vessels. Several studies have shown that HA is fully integrated into regenerated bone. Studies have shown that the risk of disease transmission is minimal, despite the suspected possibility of organic residues in bovine bone substitutes, but questions remain [39]. The absorption of bovine bone HA is active but seems to be very slow. Indeed, the material is degraded more slowly than it is resorbed [40–42]. A bone biopsy after alveolar ridge augmentation confirms that particles of bone graft substitute of bovine origin can be found up to 10 years after the procedure. Therefore, xenografts are considered as nonabsorbable biomaterials in daily practice [43].

The term alloplastic bone grafts refers to synthetic biomaterials. Synthetic materials currently exhibit only osteoconductive properties. Materials that belong in this category include metals, polymers, polyglycolides, calcium phosphate cements, HA, tricalcium phosphate (TCP), and bioglass [20,44]. The biocompatibility/histocompatibility and osteoconductivity of these alternatives are advantageous. In addition, no donor site is required and there is no risk of infectious disease transmission [45–47]. The efficacy of alloplastic biomaterials depends on maintaining the space for new bone formation and the rate of their resorption. Many of the alloplastic materials are resorbed slowly or not at all, which is one of the disadvantages. New bone requires the space originally occupied by the bone graft. However, if the bone material is not resorbed, the available space for bone formation is limited, reducing the overall volume of newly formed bone [48,49]. Synthetic calcium phos-

phates which are most commonly used in dentistry consist either of solid HA, β-tricalcium phosphate (β-TCP), or a mixture of the two called biphasic (two-phase) calcium phosphates (BCP), composed of 16.5% biphasic granules and 83.5% nano-HA gel, which was used in our study [28,50]. HA is very slowly resorbed, therefore serving as a support to maintain the integrity and completeness of the defect due to its osteoconductivity, whereas β-TCP is much more quickly resorbed and contributes to the formation of new bone by releasing calcium and phosphorus ions [50,51].

Also, after tooth extraction, the supply of metabolic products is interrupted. Immune cells produce various cytokines that are temporally and spatially controlled at the site of injury and cause acute inflammation, angiogenesis, and accumulation of mesenchymal cells. The recruited osteoprogenitor cells produce bone morphogenetic protein 2 (BMP-2), which, in coordination with other factors, promotes local accumulation and osteogenic differentiation of mesenchymal cells at the site of injury [52–56]. Mesenchymal cells differentiate into chondrocytes and osteoblasts and proliferate until they fully differentiate into a mature hypertrophic phenotype [57–59]. Several transcription factors control the differentiation of osteoblasts, which are responsible for synthesis and mineralization of the bone matrix. Osterix (Osx) has been identified as the most highly expressed transcription factor in the final stages of osteoblast differentiation in newly formed bone and induces the formation of collagen, osteocalcin (OCN), and osteopontin (OPN), promoting bone remodeling [60–62].

The main aim of this study was to determine the healing ability (histologically and immunohistologically) of alveolar bone defects during augmentation with two different biomaterials: injectable biphasic calcium phosphate (BCP) and anorganic bovine bone (ABB). The ability of BSB to restore damaged tissue was quantitatively and qualitatively evaluated, and pathohistological changes were described on bone biopsies six months after augmentation. In addition, the expression of Osx and BMP-2 in bone remodeling and mesenchymal cell differentiation was detected by immunohistochemistry.

2. Results

2.1. Demographic Data

The study included 38 participants, of whom 17 were males (45%) and 21 were females (55%). They were divided into two groups: the test group and the control group. The mean age of the respondents was 35.03 ± 9.16 years (female = 36.67 ± 6.39; male = 33.00 ± 11.61). A brief description of the characteristics of the sample itself can be found in Table 1.

Table 1. Comparison of test and control groups by average age of male and female.

	Male	Female
Control group [1]	33.54 ± 10.08	35.58 ± 7.48
Test group [2]	32.60 ± 13.10	38.11 ± 4.60
Total	33.00 ± 11.61	36.67 ± 6.39

[1] Anorganic bovine bone, [2] Injectable biphasic calcium phosphate.

2.2. Quantitative Analysis of the Histological Bone Biopsy Samples

In the quantitative analysis, the areas of newly formed bone, residual BSB, and soft tissue structures were determined with respect to the total area of the histological sample in the field of view. After processing all the results, the obtained areas were converted into volume percentages (%), as shown in Table 2.

Since the requirements for performing parametric tests were met, the *t*-test was used to compare the small samples. The *t*-test was used to compare each variable separately, i.e., newly formed bone (t (38) = 0.487; p = 0.629), residual biomaterial (t (38) = 0.705; p = 0.485), and soft tissue (t (38) = −1.626; p = 0.113), as shown in Table 3.

Table 2. Minimum and maximum values of newly formed bone, residual biomaterial, and soft tissue between the control and test groups, expressed in percentages.

	NB [1]		BM [2]		ST [3]	
	Min	Max	Min	Max	Min	Max
Control group	15.05%	68.61%	7.58%	65.62%	12.76%	38.86%
Test group	24.70%	51.77%	4.66%	50.04%	19.24%	55.00%

[1] Newly formed bone, [2] Residual biomaterial, [3] Soft tissue.

Table 3. Comparison of the tested and control groups according to variables, expressed as percentages.

	NB [1]	BM [2]	ST [3]
Control group [1]	41.73 ± 13.99%	31.72 ± 15.52%	26.54 ± 7.25%
Test group [2]	39.91 ± 8.49%	28.61 ± 11.38%	31.49 ± 11.09%
p-value *	$p = 0.629$	$p = 0.485$	$p = 0.113$

[1] Anorganic bovine bone, [2] Injectable biphasic calcium phosphate, [3] Soft tissue, * *t*-test.

As shown by the *t*-test values, there is no statistically significant difference between the test group and the control group in terms of newly formed bone, residual biomaterial, and soft tissue.

2.3. Qualitative Histological Analysis

In the qualitative analysis, the pathohistological response of the host tissue to the used BSB was evaluated, i.e., osteoblasts, osteocytes, fibroblasts, fibrocytes, blood vessels, and cells of the monocyte–macrophage system were described. In addition, the newly formed bone, the residual biomaterial, and the soft tissue were described.

HE histological Staining

Representative samples of the control group and histological staining with HE under magnification of 100, 200, and 400 times and labelling of newly formed bone, residual biomaterial, soft tissue, osteoblasts at the boundary between newly formed bone and residual biomaterial, osteocytes in newly formed bone and Howship lacunae in the bone bed with a blood vessel indicating the integration of biomaterials and newly formed bone (Figure 1).

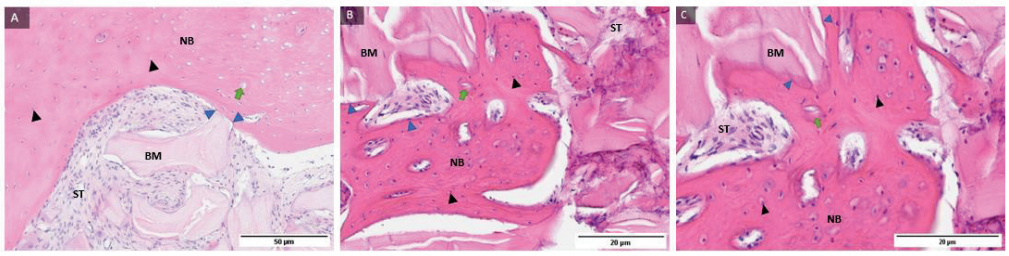


Figure 1. Examples of preparations of the control group (**A**–**C**) with labeled newly formed bone (NB), residual biomaterial (BM), soft tissue (ST), osteoblasts (blue filled triangle), osteocytes (black filled triangle), and Howship lacunae in the bone bed with a blood vessel (green arrow). Magnification: 100, 200, 400×.

Representative samples of the test group and histological staining with HE under magnification of 100, 200, and 400 times and labeling of newly formed bone, residual biomaterial, soft tissue, osteoblasts at the boundary between newly formed bone and residual biomaterial, osteocytes in newly formed bone and Howship lacune in the bone bed with a blood vessel indicating the integration of biomaterials and newly formed bone (Figure 2).

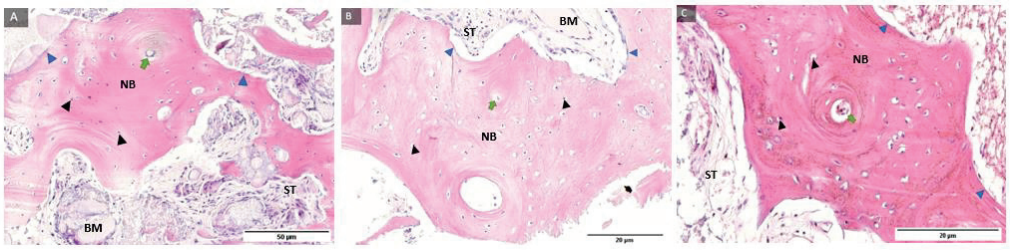


Figure 2. Examples of preparations of the test group (**A**–**C**) with labeled newly formed bone (NB), residual biomaterial (BM), soft tissue (ST), osteoblasts (blue filled triangle), osteocytes (black filled triangle), and Howship lacunae in the bone bed with a blood vessel (green arrow). Magnification: 100, 200, 400×.

Representative samples of the control group and histological staining with HE under magnification of 100, 200, and 400 times and labeled fibroblasts and fibrocytes in the soft tissue and cells of the monocyte–macrophage system around the residual biomaterial, indicating biomaterial degradation (Figure 3).

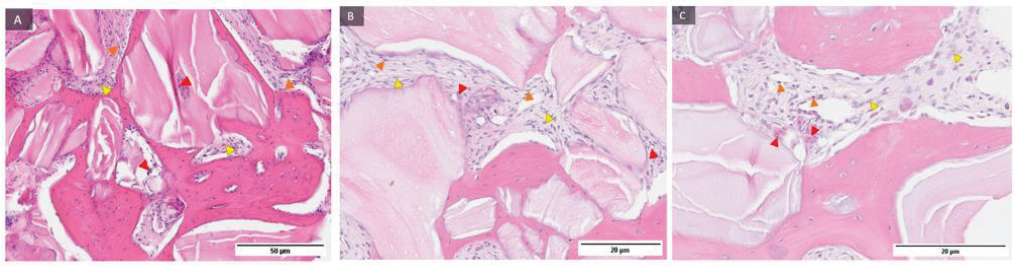


Figure 3. Examples of preparations of the control group (**A**–**C**) with labelled fibroblasts (yellow filled triangle), fibrocytes (orange filled triangle), and cells of the monocyte–macrophage system (red filled triangle). Magnification: 100, 200, 400×.

Representative samples of the test group and histological staining with HE under magnification of 100, 200, and 400 times and labelled fibroblasts and fibrocytes in the soft tissue and cells of the monocyte–macrophage system around the residual biomaterial, indicating the decomposition of the biomaterial (Figure 4).

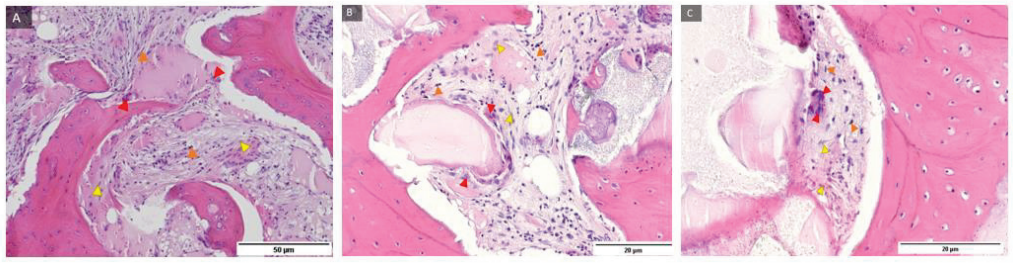


Figure 4. Examples of preparations of the test group (**A**–**C**) with labelled fibroblasts (yellow filled triangle), fibrocytes (orange filled triangle), and cells of the monocyte–macrophage system (red filled triangle). Magnification: 100, 200, 400×.

2.4. Immunohistochemical Analysis

Immunohistochemical analysis of bone biopsy samples was performed to detect Osx transcription factor and BMP-2 protein.

Representative samples of control group and Osx immunohistochemical staining at magnification of 100, 200, and 400 times (Figure 5) showed newly formed bone, residual biomaterial, and cells with 3 (+++) Osx expression in pre-osteoblasts anchored at the margin

of newly formed bone, indicating their transition into mature osteoblasts and osteocytes. Trabecularization of the new bone was also observed, indicating continuous remodeling.

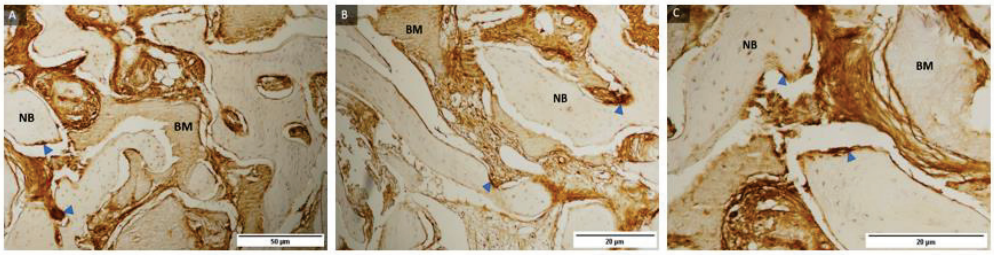


Figure 5. Examples of preparations of control group (**A**–**C**) and Osx immunohistochemical staining of bone sections after implantation of transcription factor Osx with labeled newly formed bone (NB), residual biomaterial (BM), and cells with 3 (+++) Osx expression (triangle marked in blue). 100, 200 and 400× magnification.

Representative samples of the test group and immunohistochemical Osx staining under magnification of 100, 200, and 400 times (Figure 6) and labeled newly formed bone, residual biomaterial, and cells with a strength of 3 (+++) expression of Osx in pre-osteoblasts anchored at the boundary of the newly formed bone, indicating their transition into mature osteoblasts and osteocytes. Trabecularization of the new bone was also observed, indicating continuous remodeling.

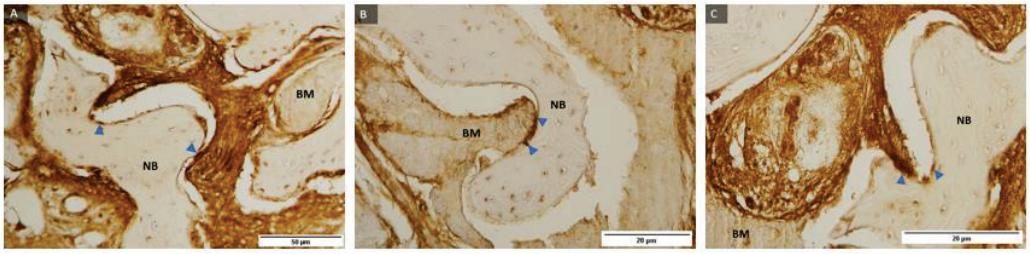


Figure 6. Examples of preparations of the test group (**A**–**C**) and immunohistochemical Osx staining of bone sections after implantation of transcription factor Osx with labelling of newly formed bone (NB), residual biomaterial (BM), and cells with a strength of 3 (+++) expression of Osx (blue marked triangle). 100, 200, and 400× magnification.

Representative samples of control group and BMP-2 immunohistochemical staining under magnification of 100, 200, and 400 times (Figure 7) and labelled newly formed bone, residual biomaterial, and cells with expression level 3 (+++) BMP-2 present mainly in zones where differentiation of mesenchymal cells into pre-osteoblasts continued, indicating regeneration of damaged tissue.

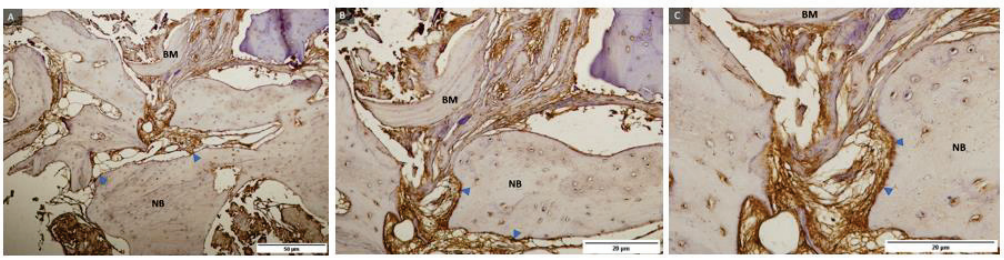


Figure 7. Examples of preparations of the control group (**A**–**C**) and BMP-2 immunohistochemical staining of bone sections after implantation of BMP-2 protein with labeled newly formed bone (NB), residual biomaterial (BM), and cells with expression level 3 (+++) BMP- 2 (blue marked triangle). 100, 200, and 400× magnification.

Representative samples of the test group and BMP-2 immunohistochemical staining under magnification of 100, 200, and 400 times (Figure 8) and labelled newly formed bone, residual biomaterial, and cells with expression level 3 (+++) BMP-2 present mainly in zones where differentiation of mesenchymal cells into pre-osteoblasts continued, indicating regeneration of damaged tissue.

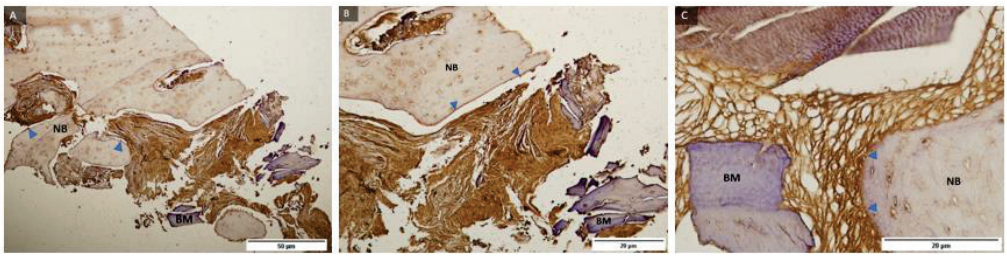


Figure 8. Examples of preparations of the test group (**A**–**C**) and BMP-2 immunohistochemical staining of bone sections after implantation of BMP-2 protein with labelling of newly formed bone (NB), residual biomaterial (BM), and cells with expression level 3 (+++) BMP-2 (triangle marked in blue). 100, 200, and 400× magnification.

3. Discussion

This study included 38 subjects, 17 (45%) male and 21 (55%) female. They were divided into two groups, the test group and the control group. The mean age of the respondents was 35.03 ± 9.16 years (females = 36.67 ± 6.39; males = 33.00 ± 11.61). Parallels can be drawn with human studies conducted by Čandrlić et al. [63], Jelušić et al. [64], and Cordaro et al. [65]. The study by Čandrlić et al. investigated the qualitative and quantitative effects of injectable BCP and other types of xenograft in the technique of alveolar preservation. That study included 40 participants, 15 (37.5%) male and 25 (62.5%) female. The study by Jelušić et al. investigated the qualitative and quantitative effects of pure single-phase ß-TCP and granulated BCP in the sinus floor lifting technique; it involved 43 subjects, 53.3% male and 46.7% female. The study by Cordaro et al. also investigated the effects of granulated BCP and other types of xenografts in the sinus floor lifting technique; it involved 37 subjects. These three studies, even though they used different xenografts and alloplastic BSBs, can confirm a study structure similar to those in which the lowest age of the subjects was 18 years and the main inclusion and exclusion criteria regarding indications and contraindications for implant therapy were confirmed in all studies. The bone biopsy was taken at the site of the future implant six months after the augmentation procedure, which is consistent with this and many other studies.

Quantitative and qualitative analysis of bone biopsy samples is used to evaluate regenerated augmentation areas, which is supported by many previous studies in addition to ours [66–68]. The results of the comparison of the observed structures in the control group, in which the xenograft (Bio-oss®) was used, were expressed as mean ± standard deviation of the mean and consisted of the following: newly formed bone (41.73 ± 13.99%), residual biomaterial (31.72 ± 15.52%), and soft tissue structures (26.54 ± 7.25%). On the other hand, the pathohistological response of the host tissue to the used BSB was evaluated by qualitative analysis.

In the literature, Bio-Oss® is one of the best-documented bovine xenografts and has been used as a control group in many studies [65,69,70]. Following the currently available literature on animal studies, such as the study by Jensen et al. in 1996, [71] for the first time a quantitative and qualitative analysis described the formation of newly formed bone and the ability of BSB to restore damaged tissue stimulated by the use of xenograft (Bio-Oss®); the effect of this was investigated in the control group in this study. This is the case with studies such as that of McAllister et al. [72,73]: In two studies of chimpanzees 7.5 months after augmentation, the percentage of newly formed bone was 47% and 62%, while the percentage of residual BSB was 19% in both studies. Mah et al. and Scarano et al. [74,75]

described percentages of newly formed bone of 47.4 ± 7.1% and 39 ± 3.3% in their studies of animal models of rat calvaria between 112 and 168 days. Similarly, in a more recent study of pigs performed by Aludden et al. in 2020 [76], the percentage of newly formed bone 20 weeks after the augmentation procedure was 60%, whereas the residual BSB was 25%. These results and the follow-up period roughly correlate with these results, regardless of the animal models and sample size mentioned.

According to the literature on human studies using this form of xenograft six months after augmentation, an older study by Zitzmann et al. in 2001 [77] confirmed 36.7 ± 26.6% newly formed bone, 30.5 ± 4.6% residual BSB, and 37.6 ± 20.5% soft tissue structures, which is similar to the results obtained in this study. A more recent study by Amoian et al. [78] can also be related to this control group in terms of newly formed bone, which was 38.66% in this study, although the sample consisted of only six patients. On the other hand, the study by Scarano et al. [79], although performed on a much larger number of subjects, confirmed the regenerative effect of Bio-Oss® in terms of newly formed bone with 39 ± 1.6%, 31 ± 1.4%, residual BSB, and 34 ± 1.6% soft tissue structures, which is the closest to the results obtained in this study six months after augmentation with the same BSB. It is interesting to mention the recent study by Wei et al. [80] investigating the effect of Bio-Oss® in socket preservation after molar extraction in patients with periodontitis. Although such patients were excluded in our study, the study by Wei. et al. showed promising results in terms of an increase in alveolar bone dimensions in the maxilla and mandible 6 months after augmentation. These conclusions confirm a good regenerative potential of Bio-Oss® in alveolar bone regeneration as shown in our study. Conversely, some human studies have shown that alveolar ridge defects grafted with Bio-Oss® resulted in different percentages of newly formed bone, residual BSB, and soft tissue structures from the above results, such as the studies by Froum et al. [81], Schmitt et al. [82], Lorenz et al. [83], Fienitz et al. [84], etc. Moreover, studies performed in recent years indicate different proportions of the variables already mentioned, as in the studies by Sivolella et al. [85], Pignaton et al. [86], and Santos et al. [87]. Such results can be explained by different initial morphology of the defect, type of wound closure, elevation of the flap, use of different membranes, location of the biopsy, and different follow-up periods.

In addition to histomorphometric analysis, the interest of previous studies, such as this one, focused on the interactions between BSB and host tissues, such as the biological response of the tissue related to the origin of BSB, which is crucial for qualitative analysis. Notwithstanding the slow resorption demonstrated in many studies, the qualitative light microscopic analyses in other studies as well as this study strongly demonstrate that the sites treated with Bio-Oss® show good integration between the biomaterial and the surrounding host tissue [82,88]. Furthermore, after a period of six months, osteoblasts at the boundary between newly formed bone and residual biomaterial, osteocytes in the newly formed bone, and Howship lacunae in the bone bed with a blood vessel indicate the integration of biomaterial. Moreover, newly formed bone can be observed in these samples. On representative samples of histological staining, cells of the monocyte–macrophage system are also observed around the residual biomaterial, indicating biomaterial degradation, which can be related to many other studies. For example, Piattelli et al., after a certain follow-up period on histological samples, demonstrated the presence of cells of the monocyte–macrophage system around the aforementioned BSB, indicating its slower resorption [43,89]. According to some authors, such behavior in vivo could be partially prevented by a specific high-temperature treatment of BSB in the course of the production process. This treatment alters the mineral structure of bone, so that the resulting BSB usually has a reduced resorption potential [38]. These findings correlate with the results obtained and indicate that more residual biomaterial remained in the control group (Bio-Oss®—31.72 ± 15.52%) than in the test group (maxresorb inject®—28.61 ± 11.38%) and that xenograft resorption was ultimately slower. Bio-Oss® has proven to be a valuable alternative to the gold standard from a clinical point of view, ensuring good quality of the newly formed bone and promising a long-term regeneration rate [90].

Injectable BCP (maxresorb® inject) with a composition of 16.5% biphasic granules and 83.5% nano-HA gel, representative of the group of alloplastic BSB, was used in the test group. The quantitative results of this study, i.e., the comparison of newly formed bone, residual BSB, and soft tissue structures in the test group in which injectable BCP (maxresorb® inject) was used, are also given as mean ± standard deviation of the mean and were as follows: newly formed bone (39.91 ± 8.49%), residual biomaterial (28.61 ± 11.38%), and soft tissue structures (31.49 ± 11.09%).

From the currently available literature, Gauthier et al. [91] were among the first to perform an animal study on the use of injectable synthetic BSB at a ratio of 60/40 HA/ß-TCP and their ability to induce new bone formation in dogs. After three months of augmentation, 48.96 ± 8.90% new bone was formed in the study. From the preliminary histomorphometric results of an animal study, it can be concluded that an alloplastic BSB with injectable capabilities in the ratio 60/40 HA /ß-TCP stimulates the formation of new bone tissue. The same authors showed in a 2004 study of dogs that three months after implantation of injectable BCP, the number of newly formed bone significantly exceeded the number of unfilled defects [92]. This was also confirmed by the study by Aral et al. [93] using BSB in injectable form. Moreover, in a slightly later study by Struillou et al. [94] using the injectable form of BCP, the percentage of newly formed bone was 35.5 ± 13.9%, which is very similar to the results obtained in this study. Three months after augmentation is a rather short period of time to detect biomaterial deterioration; accordingly, the authors mentioned above concluded at that time that long-term studies would be helpful to assess the biodegradation behavior of biomaterials. In order to obtain the most accurate and relevant results, histological samples were also taken from this group six months after augmentation.

The main evidence of regenerative potential and formation of the new bone is found in the current literature on human studies using the injectable form of BCP, but it is quite limited. Histologic and histomorphometric analyses of bone biopsy samples taken four and six months after augmentation, in the studies by Papanchev et al. [95] and Lorenzo et al. [96], indicated equal amounts of newly formed bone and soft tissue. Contrary to recommendations, bone biopsy samples were taken from 21 patients four months after augmentation in the study by Lorenzo et al. However, they showed a percentage of newly formed bone of 44.92 ± 5.16%, which also correlates with this study, in contrast to the residual biomaterial, which was 2.59 ± 2.05% in this study, and soft tissue structures of 52.49 ± 6.43%. In the previously mentioned study by Čandrlić et al. [63] using injectable BCP in combination with another xenograft, the percentage of newly formed bone was 26.47 ± 14.72%, residual biomaterial 13.1 ± 14.07%, and soft tissue structures 60.43 ± 12.73%. Regardless of the different results compared with this study, the regenerative potential of injectable BCP was demonstrated in both studies. It is also important to mention some recent studies using BCP with a composition of 60/40 HA /β-TCP in granular form, which showed similar results to this study with injectable BCP six months after augmentation. For example, in the study by Jelušić et al. [64] in 30 patients, the percentage of newly formed bone was 38.42 ± 61%; in the study by Nery et al. [97] in 10 patients, it was 43.4 ± 6.1%; and in the study by Flichy-Fernanadez et al. [98] in 16 patients, it was 34.09 ± 14.11%. These quantitative results confirm the osteoconductive potential of BCP.

Qualitative analysis was also used in this group to evaluate the pathohistological response of the host tissue to the BSB used. Alloplastic BSBs enhance growth and proliferation in vivo and stimulate osteoblasts to deposit mineralized extracellular matrix as a structural scaffold for osteogenic cell migration [99,100]. The geometry, ultrastructure, and mechanical properties of these BSBs, in addition to their chemical composition, are critical for effective bone defect repair, resorption, and concomitant replacement with newly formed bone [101]. Studies by Khaled et al. [102] and Georgiev et al. [103] combining injectable BSB with HA nanoparticles found that HA in the form of smaller granules promoted better cell contact, leading to faster biomaterial resorption and new bone formation. This was also confirmed in this study, in which BSB was used with the addition of HA. Histological

analysis showed that the BSB particles were integrated and gradually replaced by newly formed bone. On the other hand, the resorption of BSB can be explained by the fact that the aqueous part of the gel dissolves immediately after insertion, leaving behind nano-HA and HA /ß-TCP particles. As known from the instructions for use of this BSB and from some studies such as that by Gotz et al. [104], nano-HA particles show high biological activity due to their large surface area. The nanoporosity of biomaterials appears to facilitate the uptake of bone-specific molecules and growth factors such as alkaline phosphatase, BMP-2, collagen type I, osteocalcin, and osteopontin. This in turn facilitates the recruitment of osteoblast precursors and their differentiation into mature osteoblasts by means of the monocyte–macrophage cell adhesion system, ultimately leading to the gradual resorption of BSB and the formation of mature bone tissue. All the mentioned cells and structures are also described in the representative samples of this study. It is important to note that the samples in both groups showed no signs of an inflammatory response, while cells of the monocyte–macrophage system, indicating resorption, were detected only at the margin of BSBs.

Immunohistochemical analysis of the control and test groups was used to detect the transcription factor Osx and BMP-2 protein, which play a role in bone remodeling and the differentiation of mesenchymal cells. The immunohistochemical findings with expression level (Osx and BMP-2) were reviewed and evaluated semiquantitatively. Intensity level 3 (+++), i.e., strong staining indicating good osteoconductive properties of both BSBs, was detected in both groups. Representative samples from the control and test group and Osx immunohistochemical staining showed cells with Osx expression of intensity level 3 (+++) in pre-osteoblasts anchored to the margin of newly formed bone, indicating their transition into mature osteoblasts and osteocytes. In addition, trabecularization of the new bone was observed, indicating continuous remodeling. Osx has been shown to be involved in osteoblast differentiation, maturation, and activity; it regulates the expression of various markers, i.e., osteoblast proteins, the most important of which are osteopontin (OPN) and osteocalcin (OCN), etc., as indicated by the currently available literature. Previous studies have shown that Osx is an essential transcription factor in osteogenic differentiation [105,106].

On the other hand, representative samples from the control and test groups and BMP-2 immunohistochemical staining showed cells with BMP-2 expression levels of 3 (+++), present mainly in the zones where differentiation of mesenchymal cells into pre-osteoblasts continued, indicating recovery, i.e., regeneration of the damaged tissue. According to the literature, BMP-2 is a protein that acts as a potent osteogenic factor and promoter of osteoblast differentiation, which was expressed in similar studies with this type of BSB, confirming the results obtained [104,107].

4. Materials and Methods

4.1. Subjects

Thirty-eight subjects participated in this study. The main criteria for enrollment were that the patients had at least one tooth scheduled for extraction, all previous therapeutic options had been exhausted, and they had the possibility of dental implant placement at the extraction site after alveolar ridge augmentation. The criteria for inclusion were (1) age of subjects $\geq$18 and $\leq$60 years, (2) understanding of the protocol and informed consent signed by each subject, and (3) satisfactory physical and mental health of the subjects. Subjects who had some of the exclusion criteria were excluded from the study: (1) at least one absolute contraindication to implant therapy described by Wang and Hwang 2006. [108]; (2) subjects with systemic diseases such as osteoporosis, osteopenia, uncontrolled diabetes, vitamin D deficiency, bisphosphonate therapy, glucocorticoid therapy, hypothyroidism, uncontrolled cardiovascular diseases (hypertension, coronary artery disease, heart failure), and local factors: consumption of tobacco products (more than 10 cigarettes per day), poor oral hygiene; (3) patients with untreated periodontitis, patients with acute odontogenic infection, patients with periapical lesion, and patients who had previously received BSB

at the extraction site. In addition, pregnant and lactating women were not included. This study was approved by the Ethics Committee of the Osijek-Baranja County Health Center. In the treatment of all patients, the Declaration of Helsinki of the International Medical Association—1964 (most recent update—2013) was fully observed [109].

4.2. Surgical Phase

Before the start of the procedure, radiographs were taken at the planned tooth extraction sites. Patients who met the inclusion criteria were prescribed an antibiotic (amoxicillin 500 mg, Belupo, Koprivnica or clindamycin-MIP 600 mg, Chem.-pharm. Fabrik GmbH, Ingbert, Germany, in case of allergy to the penicillin group of antibiotics) one hour before the procedure; local anesthesia with 4% articaine and epinephrine 1:100,000 (Ubistesin forte®, 3M Deutschland GmbH, Neuss, Germany) was administered. Patients who agreed to participate in the study were randomized into two groups. The first group consisted of patients who received the test BSB (maxresorb® inject, botiss biomaterials, Zossen, Germany), and the second group consisted of patients who received an alternative to the gold standard, ABB (Bio-Oss®, Geistlich-Pharma, Wolhunsen, Switzerland). The socket was filled with injectable BCP in the test group and with ABB in the control group. Finally, after filling the defect, an absorbable collagen membrane (Jason® membrane, botiss biomaterials, Zossen, Germany) was fitted to the surgical wound in both groups and the mucoperiosteal flap was closed with nonabsorbable 5.0 monofilament suture (Sofsilk™, Covidien, Dublin, Ireland). The surgical procedure described is shown in Figures 9 and 10. The patient was prescribed an analgetic (ibuprofen 600 mg, Belupo, Koprivnica or paracetamol 500 mg, Lek Pharmaceu-ticals d.d., Ljubljana, Slovenia, if allergic to ibuprofen). The patients took the remaining dose of antibiotics for the next 7 days and 0.2% chlorhexidine solution (Curasept ADS® 220, Saronno, Italy) for postoperative care of the oral cavity. One week after augmentation, the patient was referred for a radiological examination of the augmented area by cone beam computed tomography (CBCT) to verify the stability of the BSB at the augmentation site. Before completion of the six months of healing, thepatient was invited to obtain a control CBCT scan, which measured the dimensions of the alveolar ridge at the site of implantation. Immediately thereafter, the second phase of the study was scheduled, i.e., biopsy of the alveolar bone with final placement of a dental implant.

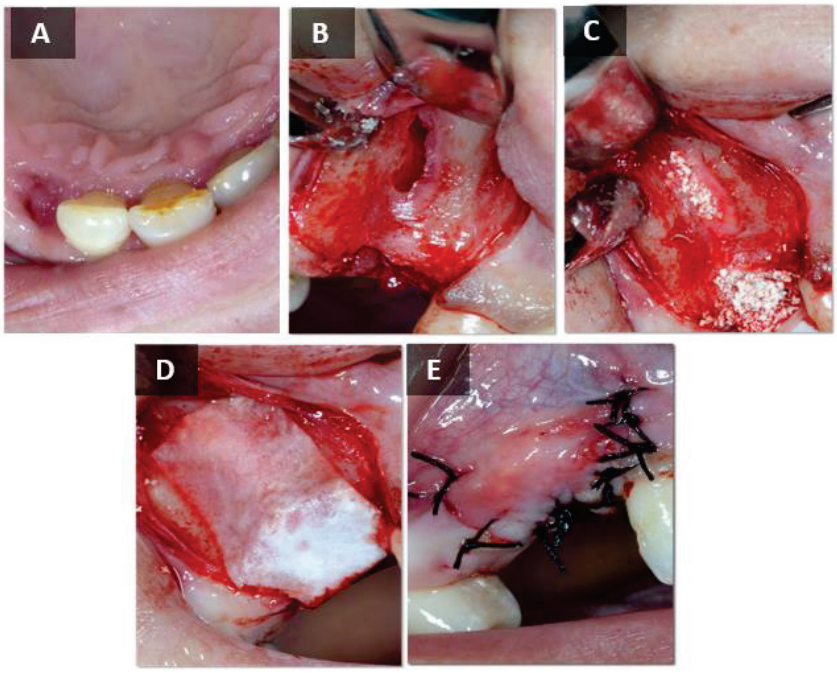


Figure 9. Surgical procedure—control group. (**A**) Hopeless tooth. (**B**) Alveolus and bone defect after tooth extraction. (**C**) Placement of the BSB. (**D**) Placement of the resorptive membrane. (**E**) Sutured wound.

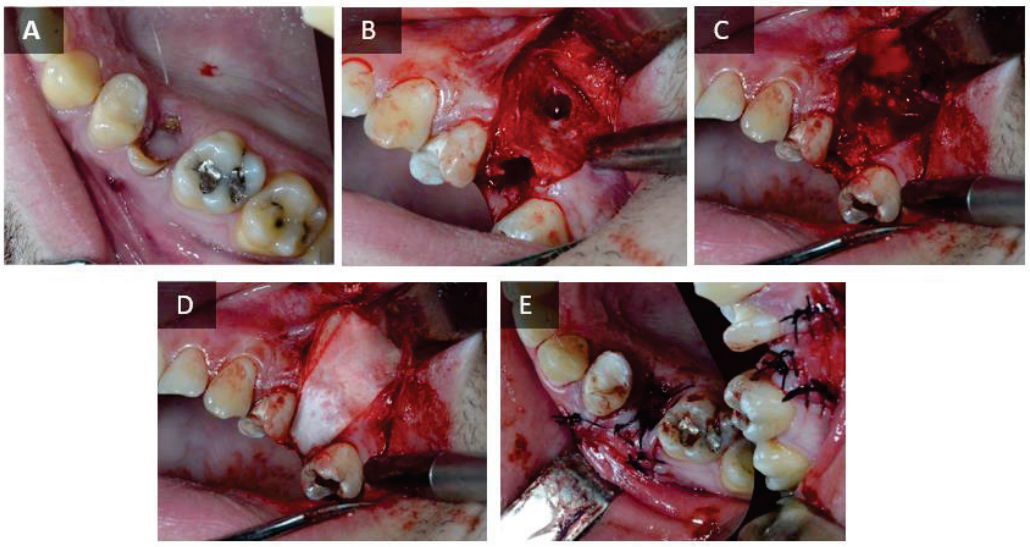


Figure 10. Surgical procedure—test group. (**A**) Hopeless tooth. (**B**) Alveolus and bone defect after tooth extraction. (**C**) Placement of the BSB. (**D**) Placement of the resorptive membrane. (**E**) Sutured wound.

The trepan drill (Komet Dental, Gebr. Brasseler GmbH & Co. KG, Lemgo, Germany) used to take the bone biopsy sample had a smaller inner diameter (2.5 mm) than the final drill from the standardized set for shaping and bed preparation of the dental implant (Ankylos, Denstply Sirona Implants, Mannheim, Germany). From an ethical point of view, this avoids excessive removal of healthy bone. The bone biopsy samples were then left in a 4% formaldehyde solution (BioGnost Ltd., Zagreb, Croatia) and sent to the laboratory for histological and immunohistochemical analysis.

4.3. Qualitative Analysis of the Histological Bone Biopsy Samples Was Performed

A standardized protocol for histological preparation of mineralized bone samples was applied to the samples, which included the following: fixation in a 4% formaldehyde solution (BioGnost Ltd., Zagreb, Croatia), dehydration in increasing alcohol concentrations (75%, 85%, 95%, and finally 100%), decalcification with ethyldiaminetetraacetic acid (EDTA, Osteomoll®, Sigma-Aldrich, St. Louis, MO, USA) for two weeks, embedding in paraffin blocks, and sectioning. Six contiguous sections with a thickness of 5 µm were prepared with a microtome (SLEE, Mainz, Germany) and placed on slides after drying. Before staining, the tissue had to be rehydrated by placing it twice in xylene (BioGnost Ltd., Zagreb, Croatia) for 15 min each, then in a descending series of alcohol (100%, 95%, 85%, and finally 75%), and finally in distilled water. The tissue was then stained with hemalaun-eosin (HE) using histological staining kits. Finally, dehydration was repeated in an increasing series of alcohols (75%, 85%, 95%, and finally 100%). Digital photomicrographs were taken using a light microscope (Leica DMRB, Leica Microsystems GmbH, Wetzlar, Germany) with an attached video camera (Axio Imager M2, Zeiss, Oberkochen, Germany) at magnification of 10, 20, and 40 times. In a qualitative analysis, the pathohistological response of the host tissue to the BSB used was evaluated, i.e., osteoblasts, osteocytes, fibroblasts, fibrocytes, blood vessels, and cells of the monocyte-macrophage system were described.

4.4. Quantitative Analysis of Histological Bone Biopsy Samples

Quantitative histological analysis of bone biopsies taken after six months of healing was performed on the same samples previously prepared for pathohistological analysis. The digital photomicrographs were stored in an uncompressed format used to store high-resolution images until analysis. The digital photomicrographs were loaded into the free ImageJ computer program (Wayne Rasband, National Institute of Health, Bethesda, MD, USA). All the photomicrographs were taken under the same conditions (magnification

of 100, 200, and 400 times, PNG format). Before starting the analysis, parameters such as setting the scale on the basis of the known distance and converting it to the unit of length (μm) were set. Also, the possibility of manual correction was set to exclude from the analysis any edge regions that were not completely clear or that represented an artifact. Each sample was analyzed individually such that the digital micrograph was adjusted using the threshold option, with manual manipulation allowing areas of interest (ROI) to be marked in different colors. Accordingly, the areas of newly formed bone, residual BSB, and soft tissue structures were determined in relation to the total area of the histological sample in the field of view, and after all the results were processed, the obtained areas were converted into volume percentages (%). All the preparations were additionally examined by two independent researchers.

4.5. Immunohistochemical Analysis of Bone Biopsy Samples

Immunohistochemical analysis was performed on four histological bone biopsy samples to detect Osx transcription factor and BMP-2 protein. Bone tissue samples with a thickness of 5 μm were deparaffinized in xylene (BioGnost Ltd., Zagreb, Croatia) and then rehydrated in alcohol of decreasing concentration (100%, 95%, 85%, and finally 75%). The next step was protein renaturation, which was achieved by incubating the slices in citrate buffer (10 mM sodium citrate, 0.05% Tween 20, pH 6.0) in a water bath at 90° for 10 min. After cooling, the samples were washed in a physiological solution buffered with phosphate-buffered saline (PBS) at pH 7.2. Blockade of endogenous peroxidase activity to avoid nonspecific binding was performed with 0.3% hydrogen peroxide H_2O_2 (Merck, Darmstadt, Germany), followed by a 10-min wash in PBS. According to the manufacturer's recommendations, the samples were incubated overnight at 4 °C with a rabbit polyclonal antibody to Sp7/Osx (ab229258, Abcam, Cambridge, UK) and a rabbit polyclonal antibody to BMP-2 (ab14933, Abcam, Cambridge, UK). Table 4 provides information on the antibodies and incubation procedures. At room temperature, the secondary antibody was incubated for 45 min. Then, 3,3'-diaminobenzidine (DAB, DakoCytomation, Glostrup, Denmark) and peroxidase-conjugated streptavidin (LSAB + kit, DakoCytomation, Glostrup, Denmark) were added for visualization. The samples were then purified with distilled water, filtered, and stained with hemalun-eosin. The slides were mounted on medium (Biomount, Biognost, Zagreb, Croatia) and analyzed using a light microscope (Olympus, Tokyo, Japan) and a digital camera (Sony, Tokyo, Japan). Immunohistochemical findings with the level of expression (Osx and BMP-2) were evaluated semiquantitatively by an experienced pathologist, who assigned a value of 0–3 "plus points" depending on the intensity of staining in the following manner: 0 = negative; 1 = weak staining (+); 2 = moderate staining (++); 3 = strong staining (+++). All the preparations were additionally examined by two independent researchers.

Table 4. Antibodies used for immunohistochemical analysis.

Antibody	Isotype	Manufacturer	Incubation
Anti-Sp7/Osx [1]	Rabbit polyclonal	Abcam, Cambridge, UK	1:200, overnight, 4°
Anti-BMP-2 [2]	Rabbit polyclonal	Abcam, Cambridge, UK	1:200, overnight, 4°

[1] Osterix, [2] Bone morphogenetic protein 2.

4.6. Statistical Methods

For statistical analysis, IBM SPSS (version 24, IBM Corporation, Armonk, NY, USA) was used. The results of the Shapiro–Wilk test were used to determine whether the distribution was normal. The mean and standard deviation of the mean were used for all results. A *t*-test was used to evaluate the significance of the difference between the two samples in the context of a normal distribution. Any p value less than 0.05 was considered significant.

5. Conclusions

Histopathologic, histomorphometric, and immunohistochemical analyzes of these two BSBs showed comparable results and proved that maxresorb® inject might be as suitable and successful as BSB for alveolar ridge augmenatation. It is necessary to highlight the strengths of this study. The study was conducted as a randomized controlled human clinical trial comparing quantitative, qualitative, and immunohistochemical analysis of two BSBs. The histomorphometric, histological, and immunohistochemical analysis and the use of a standardized free program with a detailed description of the samples allowed the methodology to be reproduced and the results obtained to be compared with future studies. All the subjects in the study underwent a standardized protocol in terms of surgical procedures and time from bone augmentation to biopsy. However, due to the small number of samples processed, especially for immunohistochemical analysis, further clinical studies with a larger sample and a longer follow-up period could be used to draw definitive conclusions in this regard. Notwithstanding some methodological limitations, the comparable results obtained with injectable BCP compared to the gold standard alternative, i.e., ABB, represent a promising outcome for the purpose of alveolar ridge augmentation after tooth extraction and dental implant placement.

Author Contributions: Conceptualization, M.T. and M.K.; clinical work, M.M.; methodology, M.T., M.Č. and Ž.P.K.; histologic analysis, M.T., Ž.P.K. and O.C.P.; writing—original draft preparation, M.T.; writing—review and editing, M.J., A.T.J.R., D.K. and B.V.; supervision, M.M. and Z.I.; project administration, M.T. All authors have read and agreed to the published version of the manuscript.

Funding: This research and APC were funded by the institutional project of the Faculty of Dental Medicine and Health Osijek, J. J. Strossmayer University of Osijek, Croatia, grant number IP-04 and by the Croatian Science Foundation, grant number IP-2020-02-7875.

Institutional Review Board Statement: The study was conducted in accordance with the Declaration of Helsinki and approved by the Ethics Committee of the Community Healthcare Center of Osijek-Baranja County, Croatia.

Informed Consent Statement: Informed consent was obtained from all patients involved in the study. Written informed consent has been obtained from the patients to publish this paper.

Data Availability Statement: The data presented in this article are available on request from the corresponding authors.

Acknowledgments: We hereby thank the technicians at Berlin Analytix, Berlin, Germany and the technicians at Laboratory of the Department of Anatomy, Faculty of Medicine Rijeka, Croatia for assistance with histologic preparation and analysis of the specimens.

Conflicts of Interest: Ž.P.K. is a part-time employee of botiss biomaterials GmbH.

References

1. Ono, T.; Nakashima, T. Oral Bone Biology. *J. Oral Biosci.* **2022**, *64*, 8–17. [CrossRef]
2. Devlin, H.; Hoyland, J.; Newall, J.F.; Ayad, S. Trabecular Bone Formation in the Healing of the Rodent Molar Tooth Extraction Socket. *J. Bone Miner. Res.* **1997**, *12*, 2061–2067. [CrossRef] [PubMed]
3. Schropp, L.; Wenzel, A.; Kostopoulos, L.; Karring, T. Bone Healing and Soft Tissue Contour Changes Following Single-Tooth Extraction: A Clinical and Radiographic 12-Month Prospective Study. *Int. J. Periodontics Restor. Dent.* **2003**, *23*, 313–323.
4. Irinakis, T.; Tabesh, M. Preserving the Socket Dimensions with Bone Grafting in Single Sites: An Esthetic Surgical Approach When Planning Delayed Implant Placement. *J. Oral Implant.* **2006**, *33*, 917–922. [CrossRef] [PubMed]
5. Araújo, M.G.; Lindhe, J. Dimensional Ridge Alterations Following Tooth Extraction. An Experimental Study in the Dog. *J. Clin. Periodontol.* **2005**, *32*, 212–218. [CrossRef]
6. Araújo, M.G.; Sukekava, F.; Wennström, J.L.; Lindhe, J. Ridge Alterations Following Implant Placement in Fresh Extraction Sockets: An Experimental Study in the Dog. *J. Clin. Periodontol.* **2005**, *32*, 645–652. [CrossRef]
7. Botticelli, D.; Berglundh, T.; Lindhe, J. Hard-Tissue Alterations Following Immediate Implant Placement in Extraction Sites. *J. Clin. Periodontol.* **2004**, *31*, 820–828. [CrossRef]
8. Shenoy, V.K. Single Tooth Implants: Pretreatment Considerations and Pretreatment Evaluation. *J. Interdiscip. Dent.* **2012**, *2*, 149. [CrossRef]

9. Darby, I.; Chen, S.; De Poi, R. Ridge Preservation: What Is It and When Should It Be Considered. *Aust. Dent. J.* **2008**, *53*, 11–21. [CrossRef]
10. Nevins, M.; Mellonig, J.T.; Clem, D.S.; Reiser, G.M.; Buser, D.A. Implants in Regenerated Bone: Long-Term Survival. *Int. J. Periodontics Restor. Dent.* **1998**, *18*, 34–45.
11. Sassano, P.; Gennaro, P.; Chisci, G.; Gabriele, G.; Aboh, I.V.; Mitro, V.; Di Curzio, P. Calvarial Onlay Graft and Submental Incision in Treatment of Atrophic Edentulous Mandibles: An Approach to Reduce Postoperative Complications. *J. Craniofac. Surg.* **2014**, *25*, 693–697. [CrossRef]
12. Crespi, R.; Toti, P.; Covani, U.; Crespi, G.; Menchini-Fabris, G.-B. Changes in Alveolar Bone Width Following Immediate Implant and Fresh Socket Preservation with Xenogeneic Gap-Filling Material Versus Guided Tissue Healing with Anatomical Tooth-Shaped Caps: A 3-Year Retrospective Case-Control Study. *Int. J. Periodontics Restor. Dent.* **2023**, *43*, 75–83. [CrossRef]
13. Chisci, G.; Fredianelli, L. Therapeutic Efficacy of Bromelain in Alveolar Ridge Preservation. *Antibiotics* **2022**, *11*, 1542. [CrossRef]
14. Bhatt, R.A.; Rozental, T.D. Bone Graft Substitutes. *Hand Clin.* **2012**, *28*, 457–468. [CrossRef]
15. Anderson, J.M.; Rodriguez, A.; Chang, D.T. Foreign Body Reaction to Biomaterials. *Semin. Immunol.* **2008**, *20*, 86–100. [CrossRef]
16. Buser, D.; Martin, W.; Belser, U.C. Optimizing Esthetics for Implant Restorations in the Anterior Maxilla: Anatomic and Surgical Considerations. *Int. J. Oral Maxillofac. Implant.* **2004**, *19*, 43–61.
17. Buser, D.; Chen, S.T.; Weber, H.; Belser, U. Early Implant Placement Following Single-Tooth Extraction in the Esthetic Zone: Biologic Rationale and Surgical Procedures. *Int. J. Periodontics Restor. Dent.* **2008**, *28*, 441–451.
18. Hämmerle, C.H.F.; Chiantella, G.C.; Karring, T.; Lang, N.P. The Effect of a Deproteinized Bovine Bone Mineral on Bone Regeneration around Titanium Dental Implants. *Clin. Oral Implant. Res.* **1998**, *9*, 151–162. [CrossRef] [PubMed]
19. Lee, J.; Byun, H.; Madhurakkat Perikamana, S.K.; Lee, S.; Shin, H. Current Advances in Immunomodulatory Biomaterials for Bone Regeneration. *Adv. Healthcare Mater.* **2019**, *8*, e1801106. [CrossRef] [PubMed]
20. Kolk, A.; Handschel, J.; Drescher, W.; Rothamel, D.; Kloss, F.; Blessmann, M.; Heiland, M.; Wolff, K.D.; Smeets, R. Current Trends and Future Perspectives of Bone Substitute Materials—From Space Holders to Innovative Biomaterials. *J. Craniomaxillofac. Surg.* **2012**, *40*, 706–718. [CrossRef]
21. Horch, H.H.; Sader, R.; Pautke, C.; Neff, A.; Deppe, H.; Kolk, A. Synthetic, Pure-Phase Beta-Tricalcium Phosphate Ceramic Granules (Cerasorb) for Bone Regeneration in the Reconstructive Surgery of the Jaws. *Int. J. Oral Maxillofac. Surg.* **2006**, *35*, 708–713. [CrossRef]
22. Buser, D.; Hoffmann, B.; Bernard, J.P.; Lussi, A.; Mettler, D.; Schenk, R.K. Evaluation of Filling Materials in Membrane–Protected Bone Defects. A Comparative Histomorphometric Study in the Mandible of Miniature Pigs. *Clin. Oral Implant. Res.* **1998**, *9*, 137–150. [CrossRef] [PubMed]
23. Haugen, H.J.; Lyngstadaas, S.P.; Rossi, F.; Perale, G. Bone Grafts: Which Is the Ideal Biomaterial? *J. Clin. Periodontol.* **2019**, *46*, 92–102. [CrossRef] [PubMed]
24. Pikos, M.A. Block Autografts for Localized Ridge Augmentation: Part II. The Posterior Mandible. *Implant. Dent.* **2000**, *9*, 67–75. [CrossRef] [PubMed]
25. Deshpande, S.; Deshmukh, J.; Deshpande, S.; Khatri, R.; Deshpande, S. Vertical and Horizontal Ridge Augmentation in Anterior Maxilla Using Autograft, Xenograft and Titanium Mesh with Simultaneous Placement of Endosseous Implants. *J. Indian Soc. Periodontol.* **2014**, *18*, 661–665. [CrossRef] [PubMed]
26. Johansson, B.; Grepe, A.; Wannfors, K.; Hirsch, J.M. A Clinical Study of Changes in the Volume of Bone Grafts in the Atrophic Maxilla. *Dentomaxillofacial Radiol.* **2001**, *30*, 157–161. [CrossRef] [PubMed]
27. Lindhe, J.; Cecchinato, D.; Donati, M.; Tomasi, C.; Liljenberg, B. Ridge Preservation with the Use of Deproteinized Bovine Bone Mineral. *Clin. Oral Implant. Res.* **2014**, *25*, 786–790. [CrossRef]
28. Helder, M.N.; van Esterik, F.A.S.; Kwehandjaja, M.D.; ten Bruggenkate, C.M.; Klein-Nulend, J.; Schulten, E.A.J.M. Evaluation of a New Biphasic Calcium Phosphate for Maxillary Sinus Floor Elevation: Micro-CT and Histomorphometrical Analyses. *Clin. Oral Implant. Res.* **2018**, *29*, 488–498. [CrossRef]
29. Ohayon, L. Maxillary Sinus Floor Augmentation Using Biphasic Calcium Phosphate: A Histologic and Histomorphometric Study. *Int. J. Oral Maxillofac. Implant.* **2014**, *29*, 1143–1148. [CrossRef]
30. Von Arx, T.; Buser, D. Horizontal Ridge Augmentation Using Autogenous Block Grafts and the Guided Bone Regeneration Technique with Collagen Membranes: A Clinical Study with 42 Patients. *Clin. Oral Implant. Res.* **2006**, *17*, 359–366. [CrossRef]
31. Martinez, A.; Balboa, O.; Gasamans, I.; Otero-Cepeda, X.L.; Guitian, F. Deproteinated Bovine Bone vs. Beta-Tricalcium Phosphate as Bone Graft Substitutes: Histomorphometric Longitudinal Study in the Rabbit Cranial Vault. *Clin. Oral Implant. Res.* **2015**, *26*, 623–632. [CrossRef]
32. Jensen, S.S.; Broggini, N.; Hjørting-Hansen, E.; Schenk, R.; Buser, D. Bone Healing and Graft Resorption of Autograft, Anorganic Bovine Bone and Beta-Tricalcium Phosphate. A Histologic and Histomorphometric Study in the Mandibles of Minipigs. *Clin. Oral Implant. Res.* **2006**, *17*, 237–243. [CrossRef]
33. Franco, M.; Viscioni, A.; Rigo, L.; Guidi, R.; Strohmenger, L.; Zollino, I.; Avantaggiato, A.; Carinci, F. Wide Diameter Implants Inserted in Jaws Grafted with Homologue Bone. *Acta Stomatol. Croat.* **2008**, *42*, 273–282.
34. Chiapasco, M.; Zaniboni, M.; Boisco, M. Augmentation Procedures for the Rehabilitation of Deficient Edentulous Ridges with Oral Implants. *Clin. Oral Implant. Res.* **2006**, *17*, 136–159. [CrossRef]
35. Kao, S.T.; Scott, D.D. A Review of Bone Substitutes. *Oral Maxillofac. Surg. Clin. N. Am.* **2007**, *19*, 513–521. [CrossRef]

36. Fernandez de Grado, G.; Keller, L.; Idoux-Gillet, Y.; Wagner, Q.; Musset, A.M.; Benkirane-Jessel, N.; Bornert, F.; Offner, D. Bone Substitutes: A Review of Their Characteristics, Clinical Use, and Perspectives for Large Bone Defects Management. *J. Tissue Eng.* **2018**, *9*, 2041731418776819. [CrossRef] [PubMed]
37. Al-Aql, Z.S.; Alagl, A.S.; Graves, D.T.; Gerstenfeld, L.C.; Einhorn, T.A. Molecular Mechanisms Controlling Bone Formation during Fracture Healing and Distraction Osteogenesis. *J. Dent. Res.* **2008**, *87*, 107–118. [CrossRef]
38. Kim, Y.; Nowzari, H.; Rich, S.K. Risk of Prion Disease Transmission through Bovine-Derived Bone Substitutes: A Systematic Review. *Clin. Implant. Dent. Relat. Res.* **2013**, *15*, 645–653. [CrossRef] [PubMed]
39. Wenz, B.; Oesch, B.; Horst, M. Analysis of the Risk of Transmitting Bovine Spongiform Encephalopathy through Bone Grafts Derived from Bovine Bone. *Biomaterials* **2001**, *22*, 1599–1606. [CrossRef]
40. Berglundh, T.; Lindhe, J. Healing around Implants Placed in Bone Defects Treated with Bio-Oss. An Experimental Study in the Dog. *Clin. Oral Implant. Res.* **1997**, *8*, 117–124. [CrossRef]
41. Urban, I.A.; Ravidà, A.; Saleh, M.H.A.; Galli, M.; Lozada, J.; Farkasdi, S.; Wang, H.L. Long-Term Crestal Bone Changes in Implants Placed in Augmented Sinuses with Minimal or Moderate Remaining Alveolar Bone: A 10-Year Retrospective Case-Series Study. *Clin. Oral Implant. Res.* **2021**, *32*, 60–74. [CrossRef] [PubMed]
42. Galindo-Moreno, P.; Abril-García, D.; Carrillo-Galvez, A.B.; Zurita, F.; Martín-Morales, N.; O'Valle, F.; Padial-Molina, M. Maxillary Sinus Floor Augmentation Comparing Bovine versus Porcine Bone Xenografts Mixed with Autogenous Bone Graft. A Split-Mouth Randomized Controlled Trial. *Clin. Oral Implant. Res.* **2022**, *33*, 524–536. [CrossRef] [PubMed]
43. Piattelli, M.; Favero, G.; Scarano, A.; Orsini, G.; Piattelli, A. Bone Reactions to Anorganic Bovine Bone (Bio-Oss) Used in Sinus Augmentation Procedures: A Histologic Long-Term Report of 20 Cases in Humans. *Int. J. Oral Maxillofac. Implant.* **1999**, *14*, 835–840.
44. Kumar, P.; Vinitha, B.; Fathima, G. Bone Grafts in Dentistry. *J. Pharm. Bioallied Sci.* **2013**, *5*, 125–127. [CrossRef] [PubMed]
45. Lorenz, J.; Barbeck, M.; Kirkpatrick, C.; Sader, R.; Lerner, H.; Ghanaati, S. Injectable Bone Substitute Material on the Basis of?—TCP and Hyaluronan Achieves Complete Bone Regeneration While Undergoing Nearly Complete Degradation. *Int. J. Oral Maxillofac. Implant.* **2018**, *33*, 636–644. [CrossRef]
46. Barbeck, M.; Jung, O.; Smeets, R.; Gosau, M.; Schnettler, R.; Rider, P.; Houshmand, A.; Korzinskas, T. Implantation of an Injectable Bone Substitute Material Enables Integration Following the Principles of Guided Bone Regeneration. *In Vivo* **2020**, *34*, 557–568. [CrossRef]
47. Ku, J.K.; Hong, I.; Lee, B.K.; Yun, P.Y.; Lee, J.K. Dental Alloplastic Bone Substitutes Currently Available in Korea. *J. Korean Assoc. Oral Maxillofac. Surg.* **2019**, *45*, 51–67. [CrossRef]
48. Al-Nawas, B.; Schiegnitz, E. Augmentation Procedures Using Bone Substitute Materials or Autogenous Bone—A Systematic Review and Meta-Analysis. *Eur. J. Oral Implantol.* **2014**, *7*, 219–234.
49. Onişor-Gligor, F.; Juncar, M.; Câmpian, R.S.; Băciuţ, G.; Bran, S.; Băciuţ, M.F. Subantral Bone Grafts, a Comparative Study of the Degree of Resorption of Alloplastic versus Autologous Grafts. *Rom. J. Morphol. Embryol.* **2015**, *56*, 1003–1009.
50. Kakar, A.; Rao, B.H.S.; Hegde, S.; Deshpande, N.; Lindner, A.; Nagursky, H.; Patney, A.; Mahajan, H. Ridge Preservation Using an in Situ Hardening Biphasic Calcium Phosphate (β-TCP/HA) Bone Graft Substitute—A Clinical, Radiological, and Histological Study. *Int. J. Implant. Dent.* **2017**, *3*, 25. [CrossRef]
51. Annibali, S.; Iezzi, G.; Sfasciotti, G.L.; Cristalli, M.P.; Vozza, I.; Mangano, C.; La Monaca, G.; Polimeni, A. Histological and Histomorphometric Human Results of HA-Beta-TCP 30/70 Compared to Three Different Biomaterials in Maxillary Sinus Augmentation at 6 Months: A Preliminary Report. *BioMed Res. Int.* **2015**, *2015*, 156850. [CrossRef] [PubMed]
52. Ono, T.; Takayanagi, H. Osteoimmunology in Bone Fracture Healing. *Curr. Osteoporos. Rep.* **2017**, *15*, 367–375. [CrossRef]
53. Schlundt, C.; Schell, H.; Goodman, S.B.; Vunjak-Novakovic, G.; Duda, G.N.; Schmidt-Bleek, K. Immune Modulation as a Therapeutic Strategy in Bone Regeneration. *J. Exp. Orthop.* **2015**, *2*, 1. [CrossRef]
54. Einhorn, T.A.; Gerstenfeld, L.C. Fracture Healing: Mechanisms and Interventions. *Nat. Rev. Rheumatol.* **2015**, *11*, 45–54. [CrossRef] [PubMed]
55. Mountziaris, P.M.; Mikos, A.G. Modulation of the Inflammatory Response for Enhanced Bone Tissue Regeneration. *Tissue Eng. Part. B Rev.* **2008**, *14*, 179–186. [CrossRef] [PubMed]
56. Jones, R.E.; Salhotra, A.; Robertson, K.S.; Ransom, R.C.; Foster, D.S.; Shah, H.N.; Quarto, N.; Wan, D.C.; Longaker, M.T. Skeletal Stem Cell-Schwann Cell Circuitry in Mandibular Repair. *Cell Rep.* **2019**, *28*, 2757–2766.e5. [CrossRef]
57. Gerstenfeld, L.C.; Cullinane, D.M.; Barnes, G.L.; Graves, D.T.; Einhorn, T.A. Fracture Healing as a Post-Natal Developmental Process: Molecular, Spatial, and Temporal Aspects of Its Regulation. *J. Cell. Biochem.* **2003**, *88*, 873–884. [CrossRef]
58. Cameron, J.A.; Milner, D.J.; Lee, J.S.; Cheng, J.; Fang, N.X.; Jasiuk, I.M. Employing the Biology of Successful Fracture Repair to Heal Critical Size Bone Defects. *Curr. Top. Microbiol. Immunol.* **2013**, *367*, 113–132. [CrossRef]
59. Dimitriou, R.; Tsiridis, E.; Giannoudis, P.V. Current Concepts of Molecular Aspects of Bone Healing. *Injury* **2005**, *36*, 1392–1404. [CrossRef]
60. Nakashima, K.; Zhou, X.; Kunkel, G.; Zhang, Z.; Deng, J.M.; Behringer, R.R.; de Crombrugghe, B. The Novel Zinc Finger-Containing Transcription Factor Osterix Is Required for Osteoblast Differentiation and Bone Formation. *Cell* **2002**, *108*, 17–29. [CrossRef]
61. Hojo, H.; Ohba, S.; He, X.; Lai, L.P.; McMahon, A.P. Sp7/Osterix Is Restricted to Bone-Forming Vertebrates Where It Acts as a Dlx Co-Factor in Osteoblast Specification. *Dev. Cell* **2016**, *37*, 238–253. [CrossRef] [PubMed]

62. Liu, Q.; Li, M.; Wang, S.; Xiao, Z.; Xiong, Y.; Wang, G. Recent Advances of Osterix Transcription Factor in Osteoblast Differentiation and Bone Formation. *Front. Cell Dev. Biol.* **2020**, *8*, 601224. [CrossRef] [PubMed]
63. Čandrlić, M.; Tomas, M.; Karl, M.; Malešić, L.; Včev, A.; Perić Kačarević, Ž.; Matijević, M. Comparison of Injectable Biphasic Calcium Phosphate and a Bovine Xenograft in Socket Preservation: Qualitative and Quantitative Histologic Study in Humans. *Int. J. Mol. Sci.* **2022**, *23*, 2539. [CrossRef] [PubMed]
64. Jelusic, D.; Zirk, M.L.; Fienitz, T.; Plancak, D.; Puhar, I.; Rothamel, D. Monophasic ß-TCP vs. Biphasic HA/ß-TCP in Two-Stage Sinus Floor Augmentation Procedures—A Prospective Randomized Clinical Trial. *Clin. Oral Implant. Res.* **2017**, *28*, e175–e183. [CrossRef] [PubMed]
65. Cordaro, L.; Bosshardt, D.D.; Palattella, P.; Rao, W.; Serino, G.; Chiapasco, M. Maxillary Sinus Grafting with Bio-Oss® or Straumann® Bone Ceramic: Histomorphometric Results from a Randomized Controlled Multicenter Clinical Trial. *Clin. Oral Implant. Res.* **2008**, *19*, 796–803. [CrossRef] [PubMed]
66. Menezes, J.D.; Pereira, R.D.S.; Bonardi, J.P.; Griza, G.L.; Okamoto, R.; Hochuli-Vieira, E. Bioactive Glass Added to Autogenous Bone Graft in Maxillary Sinus Augmentation: A Prospective Histomorphometric, Immunohistochemical, and Bone Graft Resorption Assessment. *J. Appl. Oral Sci.* **2018**, *26*, e20170296. [CrossRef]
67. Nizam, N.; Eren, G.; Akcalı, A.; Donos, N. Maxillary Sinus Augmentation with Leukocyte and Platelet-Rich Fibrin and Deproteinized Bovine Bone Mineral: A Split-Mouth Histological and Histomorphometric Study. *Clin. Oral Implant. Res.* **2018**, *29*, 67–75. [CrossRef]
68. Cömert Kılıç, S.; Güngörmüş, M.; Parlak, S.N. Histologic and Histomorphometric Assessment of Sinus-Floor Augmentation with Beta-Tricalcium Phosphate Alone or in Combination with Pure-Platelet-Rich Plasma or Platelet-Rich Fibrin: A Randomized Clinical Trial. *Clin. Implant. Dent. Relat. Res.* **2017**, *19*, 959–967. [CrossRef]
69. Artzi, Z.; Nemcovsky, C.E.; Tal, H.; Dayan, D. Histopathological Morphometric Evaluation of 2 Different Hydroxyapatite-Bone Derivatives in Sinus Augmentation Procedures: A Comparative Study in Humans. *J. Periodontol.* **2001**, *72*, 911–920. [CrossRef]
70. Dos Anjos, T.L.M.R.; De Molon, R.S.; Paim, P.R.F.; Marcantonio, E.; Marcantonio, E.; Faeda, R.S. Implant Stability after Sinus Floor Augmentation with Deproteinized Bovine Bone Mineral Particles of Different Sizes: A Prospective, Randomized and Controlled Split-Mouth Clinical Trial. *Int. J. Oral Maxillofac. Surg.* **2016**, *45*, 1556–1563. [CrossRef]
71. Jensen, S.; Aaboe, M.; Pinholt, E.; Hjørting-Hansen, E.; Melsen, F.; Ruyter, I.E. Tissue Reaction and Material Characteristics of Four Bone Substitutes. *Int. J. Oral Maxillofac. Implant.* **1996**, *11*, 55–66.
72. McAllister, B.; Margolin, M.; Cogan, A.; Taylor, M.; Wollins, J. Residual Lateral Wall Defects Following Sinus Grafting with Recombinant Human Osteogenic Protein-1 or Bio-Oss in the Chimpanzee. *Int. J. Periodontics Restor. Dent.* **1998**, *18*, 227–239.
73. McAllister, B.; Margolin, M.; Cogan, A.; Buck, D.; Hollinger, J.; Lynch, S. Eighteen-Month Radiographic and Histologic Evaluation of Sinus Grafting with Anorganic Bovine Bone in the Chimpanzee. *Int. J. Oral Maxillofac. Implant.* **1999**, *14*, 361–368.
74. Mah, J.; Hung, J.; Wang, J.; Salih, E. The Efficacy of Various Alloplastic Bone Grafts on the Healing of Rat Calvarial Defects. *Eur. J. Orthod.* **2004**, *26*, 475–482. [CrossRef] [PubMed]
75. Scarano, A.; Piattelli, A.; Pecora, G.; Petrizzi, L.; Valbonetti, L.; Varasano, V.; Iezzi, G. A Histomorphometric Comparison of Anorganic Bovine Bone (ABB) and Calcium Sulfate (CaS) Used in Sinus Augmentation Procedures: A Study in Sheep. *J. Osseointegration* **2009**, *2*, 75–81. [CrossRef]
76. Aludden, H.; Mordenfeld, A.; Dahlin, C.; Hallman, M.; Starch-Jensen, T. Histological and Histomorphometrical Outcome after Lateral Guided Bone Regeneration Augmentation of the Mandible with Different Ratios of Deproteinized Bovine Bone Mineral and Autogenous Bone. A Preclinical in Vivo Study. *Clin. Oral Implant. Res.* **2020**, *31*, 1025–1036. [CrossRef]
77. Zitzmann, N.U.; Schärer, P.; Marinello, C.P.; Schüpbach, P.; Berglundh, T. Alveolar Ridge Augmentation with Bio-Oss: A Histologic Study in Humans. *Int. J. Periodontics Restor. Dent.* **2001**, *21*, 288–295.
78. Amoian, B.; Moudi, E.; Majidi, M.S.; Ali Tabatabaei, S.M. A Histologic, Histomorphometric, and Radiographic Comparison between Two Complexes of CenoBoen/CenoMembrane and Bio-Oss/Bio-Gide in Lateral Ridge Augmentation: A Clinical Trial. *Dent. Res. J.* **2016**, *13*, 446–453. [CrossRef]
79. Scarano, A.; Degidi, M.; Iezzi, G.; Pecora, G.; Piattelli, M.; Orsini, G.; Caputi, S.; Perrotti, V.; Mangano, C.; Piattelli, A. Maxillary Sinus Augmentation with Different Biomaterials: A Comparative Histologic and Histomorphometric Study in Man. *Implant. Dent.* **2006**, *15*, 197–207. [CrossRef]
80. Wei, Y.; Xu, T.; Hu, W.; Zhao, L.; Wang, C.; Chung, K.-H. Socket Preservation Following Extraction of Molars with Severe Periodontitis. *Int. J. Periodontics Restor. Dent.* **2021**, *41*, 269–275. [CrossRef]
81. Froum, S.; Wallace, S.; Cho, S.-C.; Elian, N.; Tarnow, D. Histomorphometric Comparison of a Biphasic Bone Ceramic to Anorganic Bovine Bone for Sinus Augmentation: 6- to 8-Month Postsurgical Assessment of Vital Bone Formation. A Pilot Study. *Int. J. Periodontics Restor. Dent.* **2008**, *28*, 273–281.
82. Schmitt, C.M.; Doering, H.; Schmidt, T.; Lutz, R.; Neukam, F.W.; Schlegel, K.A. Histological Results after Maxillary Sinus Augmentation with Straumann® BoneCeramic, Bio-Oss®, Puros®, and Autologous Bone. A Randomized Controlled Clinical Trial. *Clin. Oral Implant. Res.* **2013**, *24*, 576–585. [CrossRef] [PubMed]
83. Lorenz, J.; Kubesch, A.; Korzinskas, T.; Barbeck, M.; Landes, C.; Sader, R.A.; Kirkpatrick, C.J.; Ghanaati, S. TRAP-Positive Multinucleated Giant Cells Are Foreign Body Giant Cells Rather Than Osteoclasts: Results From a Split-Mouth Study in Humans. *J. Oral Implantol.* **2015**, *41*, e257–e266. [CrossRef] [PubMed]

84. Fienitz, T.; Moses, O.; Klemm, C.; Happe, A.; Ferrari, D.; Kreppel, M.; Ormianer, Z.; Gal, M.; Rothamel, D. Histological and Radiological Evaluation of Sintered and Non-Sintered Deproteinized Bovine Bone Substitute Materials in Sinus Augmentation Procedures. A Prospective, Randomized-Controlled, Clinical Multicenter Study. *Clin. Oral Investig.* **2017**, *21*, 787–794. [CrossRef] [PubMed]
85. Sivolella, S.; Botticelli, D.; Prasad, S.; Ricci, S.; Bressan, E.; Prasad, H. Evaluation and Comparison of Histologic Changes and Implant Survival in Extraction Sites Immediately Grafted with Two Different Xenografts: A Randomized Clinical Pilot Study. *Clin. Oral Implant. Res.* **2020**, *31*, 825–835. [CrossRef]
86. Pignaton, T.B.; Spin-Neto, R.; de Ferreira, C.E.A.; Martinelli, C.B.; de Oliveira, G.J.P.L.; Marcantonio, E. Remodelling of Sinus Bone Grafts According to the Distance from the Native Bone: A Histomorphometric Analysis. *Clin. Oral Implant. Res.* **2020**, *31*, 959–967. [CrossRef]
87. Santos, A.; Botelho, J.; Machado, V.; Borrecho, G.; Proença, L.; Mendes, J.J.; Mascarenhas, P.; Alcoforado, G. Autogenous Mineralized Dentin versus Xenograft Granules in Ridge Preservation for Delayed Implantation in Post-Extraction Sites: A Randomized Controlled Clinical Trial with an 18 Months Follow-Up. *Clin. Oral Implant. Res.* **2021**, *32*, 905–915. [CrossRef]
88. Jensen, T.; Schou, S.; Stavropoulos, A.; Terheyden, H.; Holmstrup, P. Maxillary Sinus Floor Augmentation with Bio-Oss or Bio-Oss Mixed with Autogenous Bone as Graft in Animals: A Systematic Review. *Int. J. Oral Maxillofac. Surg.* **2012**, *41*, 114–120. [CrossRef]
89. Calasans-Maia, M.D.; de Mourão, C.F.A.B.; Alves, A.T.N.N.; Sartoretto, S.C.; de Uzeda, M.J.P.G.; Granjeiro, J.M. Maxillary Sinus Augmentation with a New Xenograft: A Randomized Controlled Clinical Trial. *Clin. Implant. Dent. Relat. Res.* **2015**, *17*, 586–593. [CrossRef]
90. Uzbek, U.H.; Rahman, S.A.B.; Alam, M.K.; Gillani, S.W. Bone Forming Potential of An-Organic Bovine Bone Graft: A Cone Beam CT Study. *J. Clin. Diagn. Res.* **2014**, *8*, 73–76. [CrossRef]
91. Gauthier, O.; Boix, D.; Grimandi, G.; Aguado, E.; Bouler, J.-M.; Weiss, P.; Daculsi, G. A New Injectable Calcium Phosphate Biomaterial for Immediate Bone Filling of Extraction Sockets: A Preliminary Study in Dogs. *J. Periodontol.* **1999**, *70*, 375–383. [CrossRef]
92. Boix, D.; Gauthier, O.; Guicheux, J.; Pilet, P.; Weiss, P.; Grimandi, G.; Daculsi, G. Alveolar Bone Regeneration for Immediate Implant Placement Using an Injectable Bone Substitute: An Experimental Study in Dogs. *J. Periodontol.* **2004**, *75*, 663–671. [CrossRef]
93. Aral, A.; Yalçn, S.; Karabuda, Z.C.; Anl, A.; Jansen, J.A.; Mutlu, Z. Injectable Calcium Phosphate Cement as a Graft Material for Maxillary Sinus Augmentation: An Experimental Pilot Study. *Clin. Oral Implant. Res.* **2008**, *19*, 612–617. [CrossRef]
94. Struillou, X.; Boutigny, H.; Badran, Z.; Fellah, B.H.; Gauthier, O.; Sourice, S.; Pilet, P.; Rouillon, T.; Layrolle, P.; Weiss, P.; et al. Treatment of Periodontal Defects in Dogs Using an Injectable Composite Hydrogel/Biphasic Calcium Phosphate. *J. Mater. Sci. Mater. Med.* **2011**, *22*, 1707–1717. [CrossRef]
95. Papanchev, G.; Georgiev, T.; Peev, S.; Arnautska, H.; Zgurova, N.; Borisova-Papancheva, T.; Dzhongova, E. Comparison of the Rates of Bone Regeneration in Sinus Lift Grafting with a Calcium-Phosphate Paste between the 6th and the 9th Month—A Clinical Case. *Scr. Sci. Med. Dent.* **2015**, *1*, 41. [CrossRef]
96. Ricci, L.; Perrotti, V.; Ravera, L.; Scarano, A.; Piattelli, A.; Iezzi, G. Rehabilitation of Deficient Alveolar Ridges Using Titanium Grids before and Simultaneously with Implant Placement: A Systematic Review. *J. Periodontol.* **2013**, *84*, 1234–1242. [CrossRef]
97. Nery, J.C.; Pereira, L.A.V.D.; Guimarães, G.F.; Scardueli, C.R.; França, F.M.G.; Spin-Neto, R.; Stavropoulos, A. β-TCP/HA with or without Enamel Matrix Proteins for Maxillary Sinus Floor Augmentation: A Histomorphometric Analysis of Human Biopsies. *Int. J. Implant. Dent.* **2017**, *3*, 18. [CrossRef] [PubMed]
98. Flichy-Fernández, A.J.; Blaya-Tárraga, J.A.; O'Valle, F.; Padial-Molina, M.; Peñarrocha-Diago, M.; Galindo-Moreno, P. Sinus Floor Elevation Using Particulate PLGA-Coated Biphasic Calcium Phosphate Bone Graft Substitutes: A Prospective Histological and Radiological Study. *Clin. Implant. Dent. Relat. Res.* **2019**, *21*, 895–902. [CrossRef] [PubMed]
99. Tetè, S.; Mastrangelo, F.; Carone, L.; Nargi, E.; Costanzo, G.; Vinci, R.; Burruano, F.; Tortorici, S.; Dadorante, V.; Caciagli, F.; et al. Morphostructural Analysis of Human Follicular Stem Cells on Highly Porous Bone Hydroxyapatite Scaffold. *Int. J. Immunopathol. Pharmacol.* **2007**, *20*, 819–826. [CrossRef] [PubMed]
100. Mastrangelo, F.; Nargi, E.; Carone, L.; Dolci, M.; Caciagli, F.; Ciccarelli, R.; de Lutiis, M.A.; Karapanou, V.; Shaik, B.Y.; Conti, P.; et al. Tridimensional Response of Human Dental Follicular Stem Cells onto a Synthetic Hydroxyapatite Scaffold. *J. Health Sci.* **2008**, *54*, 154–161. [CrossRef]
101. Stevens, B.; Yang, Y.; Mohandas, A.; Stucker, B.; Nguyen, K.T. A Review of Materials, Fabrication Methods, and Strategies Used to Enhance Bone Regeneration in Engineered Bone Tissues. *J. Biomed. Mater. Res. B Appl. Biomater.* **2008**, *85*, 573–582. [CrossRef] [PubMed]
102. Khaled, H.; Atef, M.; Hakam, M. Maxillary Sinus Floor Elevation Using Hydroxyapatite Nano Particles vs Tenting Technique with Simultaneous Implant Placement: A Randomized Clinical Trial. *Clin. Implant. Dent. Relat. Res.* **2019**, *21*, 1241–1252. [CrossRef]
103. Georgiev, T.; Peev, S.; Arnautska, H.; Gencheva, A.; Gerdzhikov, I. An Evaluation of Three-Dimensional Scans of the Time-Dependent Volume Changes in Bone Grafting Materials. *Int. J. Sci. Res. (IJSR)* **2017**, *6*, 562–571. [CrossRef]
104. Götz, W.; Gerber, T.; Michel, B.; Lossdörfer, S.; Henkel, K.O.; Heinemann, F. Immunohistochemical Characterization of Nanocrystalline Hydroxyapatite Silica Gel (NanoBone®) Osteogenesis: A Study on Biopsies from Human Jaws. *Clin. Oral Implant. Res.* **2008**, *19*, 1016–1026. [CrossRef] [PubMed]

105. Ortuño, M.J.; Susperregui, A.R.G.; Artigas, N.; Rosa, J.L.; Ventura, F. Osterix Induces Col1a1 Gene Expression through Binding to Sp1 Sites in the Bone Enhancer and Proximal Promoter Regions. *Bone* **2013**, *52*, 548–556. [CrossRef] [PubMed]
106. Yang, Y.; Huang, Y.; Zhang, L.; Zhang, C. Transcriptional Regulation of Bone Sialoprotein Gene Expression by Osx. *Biochem. Biophys. Res. Commun.* **2016**, *476*, 574–579. [CrossRef]
107. Friedmann, A.; Gissel, K.; Konermann, A.; Götz, W. Tissue Reactions after Simultaneous Alveolar Ridge Augmentation with Biphasic Calcium Phosphate and Implant Insertion—Histological and Immunohistochemical Evaluation in Humans. *Clin. Oral Investig.* **2015**, *19*, 1595–1603. [CrossRef] [PubMed]
108. Hwang, D.; Wang, H.L. Medical Contraindications to Implant Therapy: Part I: Absolute Contraindications. *Implant. Dent.* **2006**, *15*, 353–360. [CrossRef] [PubMed]
109. World Medical Association. Declaration of Helsinki: Ethical Principles for Medical Research Involving Human Subjects. *JAMA* **2013**, *310*, 2191–2194. [CrossRef]

Disclaimer/Publisher's Note: The statements, opinions and data contained in all publications are solely those of the individual author(s) and contributor(s) and not of MDPI and/or the editor(s). MDPI and/or the editor(s) disclaim responsibility for any injury to people or property resulting from any ideas, methods, instructions or products referred to in the content.

International Journal of
Molecular Sciences

MDPI

Article

A Non-Invasive Method for Monitoring Osteogenesis and Osseointegration Using Near-Infrared Fluorescent Imaging: A Model of Maxilla Implantation in Rats

Chien-Chou Lin [1], Li-Hsuan Chiu [2], Walter H. Chang [3], Cheng-An J. Lin [3], Ruei-Ming Chen [1], Yuan-Soon Ho [1], Chun S. Zuo [2], Austin Changou [4,5], Yue-Fa Cheng [6] and Wen-Fu T. Lai [2,7,8,*]

1 Graduate Institute of Medical Sciences, College of Medicine, Taipei Medical University, Taipei 110, Taiwan
2 McLean Imaging Center, McLean Hospital and Harvard Medical School, Belmont, MA 02478, USA
3 Department of Biomedical Engineering, Chung Yuan Christian University, Taoyuan 320, Taiwan
4 Ph.D. Program for Translational Medicine, College of Medicine and Technology, Taipei Medical University, Taipei 110, Taiwan
5 Core Facility Center, Office of Research and Development, Taipei Medical University, Taipei 110, Taiwan
6 College of Basic Medicine, North China University of Science and Technology, Tangshan 066008, China
7 Institute of Graduate Clinical Medicine, Taipei Medical University, Taipei 110, Taiwan
8 Department of Research and Department of Dentistry, Taipei Medical University-Shuang-Ho Hospital, New Taipei City 235, Taiwan
* Correspondence: laitw@tmu.edu.tw

Abstract: Currently, computed tomography and conventional X-ray radiography usually generate a micro-artifact around metal implants. This metal artifact frequently causes false positive or negative diagnoses of bone maturation or pathological peri-implantitis around implants. In an attempt to repair the artifacts, a highly specific nanoprobe, an osteogenic biomarker, and nano-Au-Pamidronate were designed to monitor the osteogenesis. In total, 12 Sprague Dawley rats were included in the study and could be categorized in 3 groups: 4 rats in the X-ray and CT group, 4 rats in the NIRF group, and 4 rats in the sham group. A titanium alloy screw was implanted in the anterior hard palate. The X-ray, CT, and NIRF images were taken 28 days after implantation. The X-ray showed that the tissue surrounded the implant tightly; however, a gap of metal artifacts was noted around the interface between dental implants and palatal bone. Compared to the CT image, a fluorescence image was noted around the implant site in the NIRF group. Furthermore, the histological implant-bone tissue also exhibited a significant NIRF signal. In conclusion, this novel NIRF molecular imaging system precisely identifies the image loss caused by metal artifacts and can be applied to monitoring bone maturation around orthopedic implants. In addition, by observing the new bone formation, a new principle and timetable for an implant osseointegrated with bone can be established and a new type of implant fixture or surface treatment can be evaluated using this system.

Keywords: artifact; near-infrared ray; gold nanoparticle; hydroxyapatite; osteoblast

Citation: Lin, C.-C.; Chiu, L.-H.; Chang, W.H.; Lin, C.-A.J.; Chen, R.-M.; Ho, Y.-S.; Zuo, C.S.; Changou, A.; Cheng, Y.-F.; Lai, W.-F.T. A Non-Invasive Method for Monitoring Osteogenesis and Osseointegration Using Near-Infrared Fluorescent Imaging: A Model of Maxilla Implantation in Rats. *Int. J. Mol. Sci.* **2023**, *24*, 5032. https://doi.org/10.3390/ijms24055032

Academic Editor: Mary Anne Melo

Received: 22 December 2022
Revised: 21 February 2023
Accepted: 22 February 2023
Published: 6 March 2023

Copyright: © 2023 by the authors. Licensee MDPI, Basel, Switzerland. This article is an open access article distributed under the terms and conditions of the Creative Commons Attribution (CC BY) license (https://creativecommons.org/licenses/by/4.0/).

1. Introduction

Radiography imaging of hard tissue is a prevalent diagnostic instrument in dentistry and orthopedics. Intraoral periapical radiography, conventional multi-slice computed tomography, and cone beam computed tomography are lower radiation dose systems commonly used to assess the marginal bone level and detect signs of failing osseointegration around dental implants [1,2]. However, they are susceptible to the appearance of artifacts generated by dental implants [3–7]. In recent years, near-infrared fluorescent (NIRF) imaging technologies have been developed for detecting and monitoring disease progression in joint and bone tissue [8–12]. The techniques also enable clinicians to evaluate the bone tissue healing process around implants at a molecular level. Bone is a metabolically active tissue that can execute remodeling. Remodeling balances osteoblast-induced mineralization and

osteoclast-induced demineralization [13]. During this process, hydroxyapatite (HA) is the prime mineral product of osteoblasts and binds to naturally occurring pyrophosphates and phosphonates with a high affinity [14–16]. Osteoblasts synthesize HA, which promotes cell adhesion and osteogenic differentiation in human mesenchymal stem cells [17]. Therefore, HA deposition is a marker of bone regeneration and also of the process of cancer formation and atherosclerosis [18–21].

Monitoring and evaluating osteogenesis and osteointegration around implant objects is proving to be valuable because a variety of dental and orthopedic implants have been utilized in the last 10 years. An ideal monitoring system or method in clinics to determine the optimal force loading time and to achieve the early diagnosis of pathological changes around implants is in high demand [6,7].

Currently, a non-isotopic method does not exist for directly detecting osteoblastic activity in vivo. The wavelength of 700–900 nm fluorescent light, the near-infrared (NIR) "window", possesses several inherent advantages for the detection of HA compared with ultraviolet and visible light ranges [22–25]. The NIR photon enables deep penetration into the tissue and subsequentlyexits the tissue easily. Tissue absorption and autofluorescence is minimized, yielding an inherently high contrast between the target and background, and the optical scatter within the tissue is lower [18]. A suitable fluorescence-based optical imaging agent, with emission in the NIR 700–900 nm window, should have in vitro and in vivo stability; resistance to photobleaching; high quantum yield and high absorbency; resistance to metabolic disintegration and nontoxicity; and adequate dispersibility in the biological environment [26]. Among numerous nanoparticles, Au nanoparticles (nano-Aus) not only correspond to the aforementioned criteria but their surface functionalization with molecular groups also exhibits calcium affinity that can enable the targeted delivery of nano-Aus to calcified tissue, including damaged bone tissue [27,28].

To evaluate osteogenesis and osseointegration, we designed a molecular imaging system, Taiwan 1 (TW1)-NIRF, including a new light detection; a charge-coupled device camera; and an HA binding reagent, pamidronate (Pam), which can rapidly conjugate to nano-Au particles to form a probe, nano-Au pamidronate (nano-Au-Pam). With the nano-Au-Pam probe, the camera enables the identification osteoblast-synthesized HA. The osteoblast-synthesized HA was also found to enhance cell adhesion and osteogenic differentiation in human mesenchymal stem cells [29,30]. TW1-NIRF is applied to monitor osteoblastic activity. This monitoring imaging system can trace/track cells differentiated within bone in vitro and in vivo in real time and can also quantify osseointegration. This novel method may provide a multimodality imaging where other imaging modalities can be employed simultaneously. Thus, this new imaging method can repair the artifacts caused by computed tomography.

2. Results

2.1. Animal Model Design and Imaging Evaluation of Implants

A titanium alloy screw was implanted in the anterior hard palate of a 6-month-old Sprague Dawley rat (Figure 1B). The sagittal images were taken from CT and X-ray of the titanium screw–implanted (Figure 2A) and sham-operation (Figure 2B) rats 28 days after surgery. The X-ray showed that the tissue surrounded the implant tightly. No gap was found between the bone tissue and the implant. However, a gap of metal artifacts was noted around the interface between the dental implants and rat palatal bone 28 days after the surgical implantation in micro-CT images (Figure 2C,D).

2.2. In Vivo Imaging

The TW1-NIRF image system specifically revealed the implantation site to present a significant NIRF signal. Metal artifacts appeared around the interface between the dental implants and rat palatal bone in micro-CT images (Figure 2E). The NIRF and merged TW1-NIRF images demonstrated that the probe specifically accumulated at the implantation site (Figure 2F). The areas of high HA synthesized around the implant are visible. The signal intensity exhibited

in the sham operation group compared to the titanium screw-implanted group (1.00 ± 0.028 to 3.02 ± 0.546, $p < 0.005$) is shown in Figure 2G. The 3-fold augmented fluorescence intensity indicates the probe's targeting of new bone formation sites around the implant.

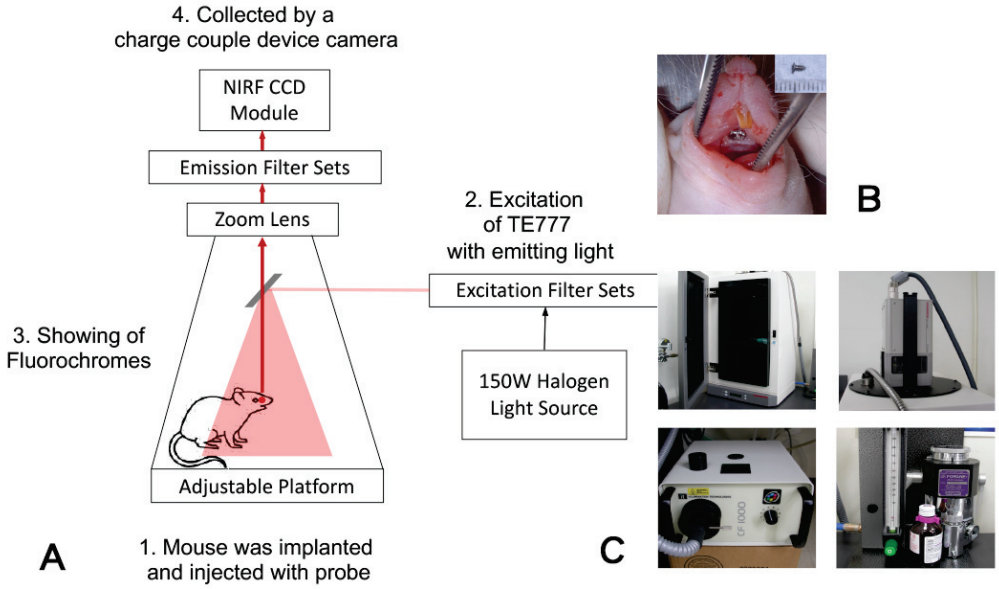


Figure 1. Illustration of monitoring osteogenesis and osseointegration using near-infrared fluorescent imaging. (**A**) The optical design of TW1-NIRF system. Briefly, the excitation wavelength of 800 nm was generated from a halogen light source. Study animals were gas-anesthetized with isoflurane and placed in the imaging chamber. The emission was 610–650 nm and was captured by a high-sensitivity CCD. (**B**) A titanium alloy screw was implanted in the anterior hard palate of 6-month-old Sprague Dawley rats. Titanium alloy screws (1.2 mm [diameter] × 2.4 mm [length], Ti-6AL-4V ELI, Self-Drilling Bone Screw System, ACE Surgical Supply Co., Inc., Brockton, MA, USA). (**C**) The TW1-NIRF imaging is composed of an imaging chamber, NIRF CCD module with lenses and a filter wheel, excitation light source, and gas anesthesia module.

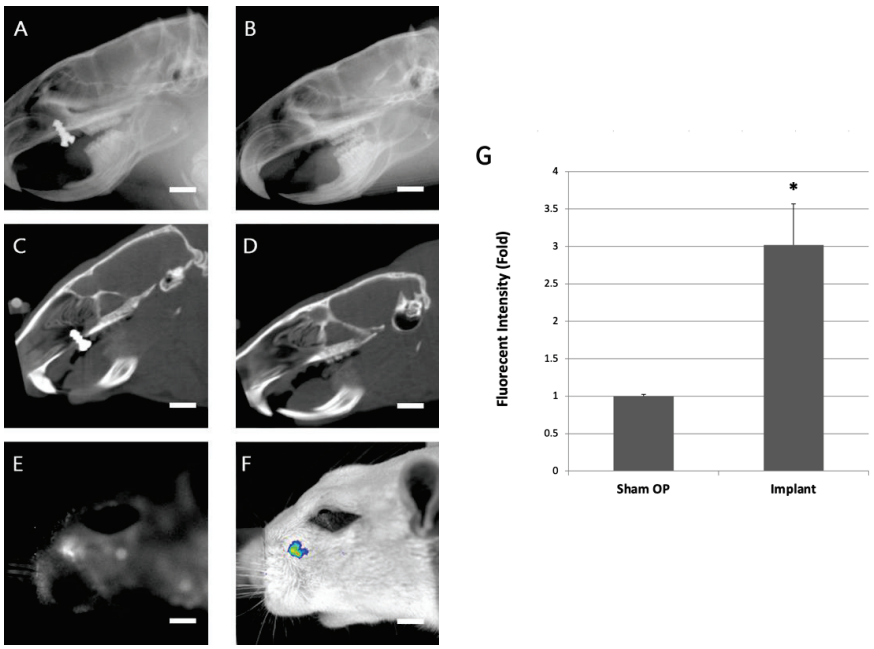


Figure 2. Animal model for computed tomography metal artifact adjustment. The sagittal X-ray of the (**A**) titanium screw–implanted and (**B**) sham-operation rats 28 days after surgical implantation.

The micro-CT images of the (**C**) titanium screw implanted and (**D**) the sham-operation rat 28 days after surgical implantation. In the sagittal X-ray image, the bone tissue surrounded the implant tightly and no gap was found between the bone tissue and the implant. However, in the micro-CT image, a gap of metal artifacts was noted around the interface between the dental implant and the rat palatal bone. (**E**) The fluorescence image was obtained using pamidronate-NIRF probes in the titanium screw-implanted group. (**F**) A merged in vivo image was used to improve the visual result in the titanium screw-implanted group. The scale bar represents 2.5 mm in (**A**–**F**). (**G**) The fluorescent intensity was quantified in the sham operation group versus the titanium screw-implanted group (right column chart). The error bars represent the standard deviation at each data point. The asterisk (*) indicates the statistical significance of differences at $p < 0.005$.

2.3. Histological and NIRF Analysis of Perio-Implant Tissue

To further confirm the ability of pamidronate-NIRF probes to detect new bone formation in vivo, rats were sacrificed for NIRF imaging and the histological analysis of the maxilla bone. The dissected maxilla bone was sectioned in different planes to evaluate the probe deposition at the new bone formation site around the implantation site (Figure 3A). The longitudinal (Figure 3B,C) and horizontal section (Figure 3D,E) images of the maxilla tissue also showed positive-probe-stained tissue around the implant, indicating that the pamidronate-NIRF probe was able to detect bone tissue formation around the implantation site.

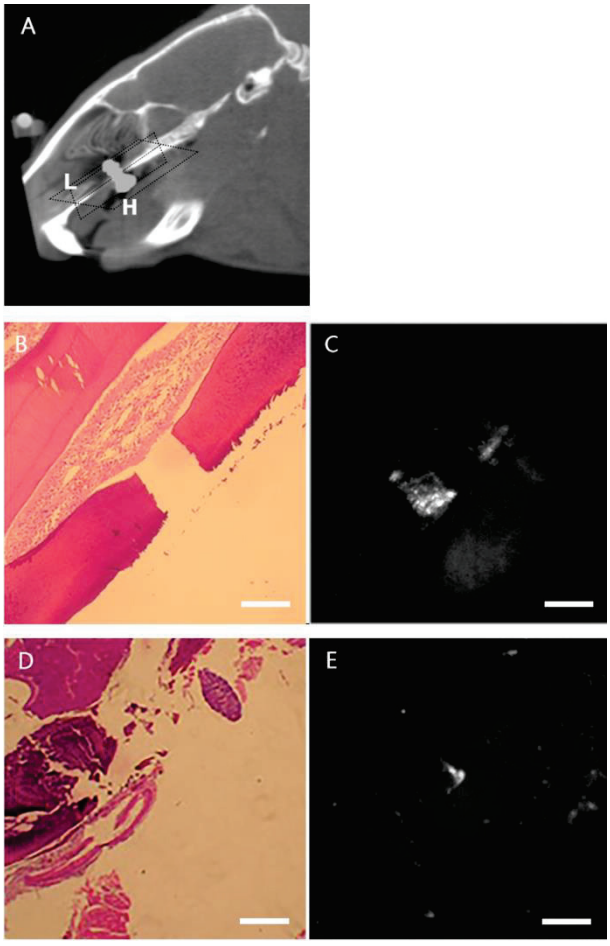


Figure 3. Evaluation of the correlation between histology and NIR fluorescence of peri-implant tissue. (**A**) Longitudinal and horizontal sections of pamidronate-NIRF probe injected 28 days after implantation. L = longitudinal section and H = horizontal section. (**B**) The peri-implant tissue was longitudinally excised en bloc. A gap of implantation is shown in the HE staining at ×4 magnification. (**C**) Fluorescence signal is noted at the peri-implant area (×4 magnification). (**D**) Horizontal section of

the en bloc of the peri-implant tissue. An implant defect is shown in the HE staining at ×2 magnification. (**E**) The fluorescence signal is seen at the peri-implant area (×2 magnification). The scale bar represents 1 mm in (**B**,**C**) and 2 mm in (**D**,**E**). The fluorescence indicates the areas of high HA synthesized around the implant.

3. Discussion

Colloid gold has been widely used in biomedical detection due to its strong surface plasmon absorption. In the last 10 years, gold particles have been used as a contrast agent to improve X-ray or MRI imaging [31,32]. Due to its biocompatibility and stable optical properties, colloid gold has become an alternative to quantum dots for in vivo application [33]. Gold nanoclusters have several advantages for molecular image application: a decent quantum yield, a highly colloidal stability, and an extremely small size (core diameter <1.5 nm); furthermore, they can also be conjugated with biological molecules. Moreover, the quantum yield of gold nanoclusters can be further improved through thermal treatment and biomolecule encapsulation. As a result, we hypothesized that pamidronate conjugated gold nanoclusters can be utilized to monitor the new bone formation. Therefore, the new bone, surrounding the implant, can be detected.

Our previous data showed that near-infrared (NIR) fluorescent probes can be used to monitor the in vitro differentiation of human mesenchymal stem cells into osteoblasts as well as the osteogenesis process at a cellular level [12]. In this study, we designed a new imaging system for the in vivo detection of NIR signals in rats, which are much larger than mice in size. Most studies examine NIR signal intensity using mice or nude mice, not only because of the easy manipulation of NIR signal penetrating into the subepithelial layer, but also because fluorescence signals exhibits are visible from the mouse body.

In this study, we used rats as the model, which have 10–12 times greater body weight compared to the mice. To successfully utilize this model, the newly designed system contains a back-illuminated Peltier 16-bit charge-coupled device (CCD, −90 °C cooled) (Hammamastu, Hammamastu City, Japan) with a pixel size of 24 μm × 24 μm, 230,000 electrons, and 8 × 8 binning. This imaging achieves >80% of the quantum efficiency at an emission of 800 nm. Thus, this allows the camera to identify the osseointegration of the implant within the bone tissue.

The lesion site in the rat reveals a significant fluorescence after the injection of the 20 nM nano-Au-Pam probe. Previous studies in other laboratories showed that an Au NP probe dose of 1 mg/Kg was administered in rats [34]. Our previous data also demonstrated a dosage of 2 nM for nude mice. The weight of the rat is 10–12 times than the nude mice. The Au NPs are considered to preserve a lower toxicity compared to the Cat B probe containing Cy5.5 [35]. Furthermore, an MTT experiment showed that the Au NPs exhibit a better viability compared to QD [36]. These indicate that a minimal dose can induce a significant signal intensity in this animal model [34–36]. Despite the fact that 20 nM is a minimal dose, the dosage should be reduced and the signal intensity should be increased before the NIR probes are applied in the clinic.

For the clinical translation, the NIR probe requires a decrease in the dose, an increase in the optical stability, selective targetability, reliable pharmacokinetic activity, complete clearance, and nontoxicity. Incomplete clearance will cause potential toxicity through biological interactions in the body. In order to overcome the clinical limitations, an NIR probe is necessary to consider the target specificity and biodistribution.

In this study, NIRF signals indicating new bone formation were observed around the implantation site in a maxilla implantation model, demonstrating a significant difference between the new bone formation site around the metal implant and normal tissue. This novel nano-Au imaging system can be applied to monitoring bone maturation around orthopedic implants or quantifying the osseointegration of bone and dental implants. Therefore, by observing the process and activity of osteoblasts, we can establish a new implant loading timetable. New types of implant fixtures or surface treatments can also be

evaluated through this system. In addition, according to this characteristic of observing the bone formation process, the system may be further applied in the early diagnosis of prostate cancer and other cancer metastases.

4. Materials and Methods

4.1. Probe Synthesis

A gold nanocluster-based pamidronate NIR fluorescent probe was synthesized according to the methods in our other studies [37–39]. Briefly, fluorescent gold nanoclusters were synthesized using nanoparticle-etching methods. Pamidronate was attached to the carboxylated surface of a nanocluster using an N-(3-dimethylaminopropyl)-N′-ethylcarbodiimide (EDC) (Sigma-Aldrich, St. Louis, MO, USA) crosslinker. Briefly, nano-Au-Pam (em 674 nm) was synthesized by immobilizing pamidronate (Sigma 2371) onto nano-Au particles using a zero-length crosslinking agent, 1-ethyl-3-[3-dimethylaminopropyl] carbodiimide hydrochloride (EDC). To link the pamidronate to nano-Au particles, equal volumes of Au nanoclusters (40 mM), pamidronate (3 mM), and EDC (80 mM) were mixed at room temperature for 2 h for the crosslinking reaction. To concentrate the conjugated nano-Au-Pam, the reaction solution was loaded in a 30-kDa molecular sieve (Amicon, Millipore, Bedford, MA, USA) and centrifuged to concentrate the conjugated nano-Au-Pam at 3000 rpm for 10 min. The solution was centrifuged twice and washed with phosphate-buffered saline (PBS) (Sigma-Aldrich, MO, USA) to remove any unbound reactants.

4.2. Animals

A bone defect model for the NIRF probe detection in rats was established. Briefly, 12 6-month-old Sprague Dawley rats were housed in a laboratory at 22.2 °C under a 12-h light and 12-h dark cycle and fed ad libitum. The animal study was approved by the Taipei Medical University Institutional Animal Care and Use Committee (LAC-2014-0391) and complied with the committee's regulations. All animal husbandry and handling procedures including animal monitoring, diet, primary enclosures, and environmental control followed standard operating procedures in accordance with the Animal (Scientific Procedures) Act of 1986.

4.3. Experimental Design and Surgical Techniques

The 12 Sprague Dawley rats included 3 groups: 4 rats in the X-ray and the (computed tomography) CT group, 4 rats in the NIRF group, and 4 rats in the sham group. Animals were anesthetized with Chanazine 2% dilute with 10× PBS 10 μL + Zoletil 50 dilute 2× PBS 10 μL with or without implantation by titanium alloy screws (1.2 mm [diameter] × 2.4 mm [length], Ti-6AL-4V ELI, Self-Drilling Bone Screw System, ACE Surgical Supply Co., Inc., Brockton, MA, USA) in the anterior hard palate. Rats were monitored using X-ray, microcomputed tomography, and NIRF imaging 28 days after the surgery (Figure 1A,B). After imaging evaluation, the rats were sacrificed and the maxilla was dissected and fixed in 10% buffered formalin for NIRF imaging and histological analysis.

4.4. In Vivo Imaging

Animals were examined using microcomputed tomography (micro computed tomography [CT]; Triumph XO CT System, Chatsworth, CA, USA) and optical imaging (TW1-NIRF; Taipei, Taiwan) 28 days after surgery. For micro-CT scans, rats were maintained under general anesthesia during the scanning procedure. Each rat was placed in a sample holder in the cranial–caudal direction and scanned using a high-resolution micro-CT system at a spatial resolution of 80 μm (voxel dimension) and in 1024 × 1024-pixel matrices. The animals were evaluated using both micro-CT and X-ray to confirm the success of the implantation. The bone tissue was segmented using a global thresholding procedure. The threshold was set to 1600 unit to investigate the peri-implant bone tissue.

The TW1-NIRF imaging system (Figure 1C), designed and assembled in our laboratory, contains a back-illuminated Peltier 16-bit charge-coupled device (CCD, −90 °C cooled)

(Hammamastu, Hammamastu City, Japan) with a pixel size 24 μm × 24 μm. This imaging gains >80% of quantum efficiency at emission 800 nm. The animals were injected with 20 nM of nano-Au-Pam probe systemically. Two hours after injection, the animals were anesthetized with isofluorane and subjected to NIRF imaging [40]. The TW1-NIRF system contained a 150 W halogen lamp, and an excitation, and an emission bandpass filter of 800 nm and 610–650 nm, respectively. Whole body NIRF images were obtained with acquisition times of 2 min, and the white light images were obtained in 0.075 s. HCImage Live software was used to compile the images (Hamamatsu, Sewickley, PA, USA).

In order to determine whether the osseointegration occurred in the metal artifacts, the NIRF image was compared to micro-CT in the same metal artifact areas. To visualize the fluorescent signal emitted from the probe in vivo, the animals were injected with 20 nM nano-Au-Pam probe and evaluated using the TW1-NIRF system for NIRF imaging, then followed by micro-CT. The ICG channel (excitation wavelength of 710–760 nm and emission wavelength of 810–875 nm) was used in the TW1-NIRF system for detection.

4.5. Histological and NIRF Analysis

After imaging evaluation, animals were sacrificed and the hard palate tissue was dissected for histological analysis. The hard palate tissue was fixed and embedded in paraffin. After the microtome section, HE staining and mounting were used. Longitudinal and horizontal section tissue samples were observed by NIRF (IR800 filter) to detect the visible areas of high HA synthesized around the implant.

4.6. Statistical Analysis

To quantitate the NIRF signal, a circular region-of-interest (ROI) was manually defined around the implant area, and the average signal within the ROI was obtained. Data are presented as mean ± SD. A two-tailed Student's *t*-test was conducted. $p < 0.05$ was considered significant.

5. Conclusions

Taken together, the results showed the potential application of this novel nanogold-based NIRF probe system for assessing changes in bone tissue formation after implantation. Using the probe design and image system as a prototype, this image platform could be further developed to repair the artifacts caused by computed tomography and upgrade the evaluation of dental implantation failure by detecting bone formation in situ.

Author Contributions: Conceptualization, C.-C.L., C.-A.J.L., C.S.Z. and W.-F.T.L.; Methodology, C.-C.L., C.-A.J.L., C.S.Z. and W.-F.T.L.; Software, C.-C.L., C.-A.J.L., C.S.Z., A.C. and W.-F.T.L.; Validation, C.-C.L., C.S.Z., A.C. and W.-F.T.L.; Formal analysis, W.H.C., A.C., Y.-F.C. and W.-F.T.L.; Investigation, L.-H.C., W.H.C., Y.-F.C. and W.-F.T.L.; Resources, L.-H.C., R.-M.C., Y.-S.H., Y.-F.C. and W.-F.T.L.; Data curation, L.-H.C., R.-M.C., Y.-S.H. and W.-F.T.L.; Writing—original draft, L.-H.C., R.-M.C., Y.-S.H. and W.-F.T.L.; Writing—review & editing, W.-F.T.L.; Visualization, W.-F.T.L.; Supervision, W.-F.T.L.; Project administration, W.-F.T.L. All authors have read and agreed to the published version of the manuscript.

Funding: This research received no external funding.

Acknowledgments: This study was supported by the Ministry of Science and Technology of Taiwan by grants MOST-104-2514-S-038-001, MOST-104-2622-B-038-006-CC1, MOST104-2622-B-038-007, MOST-105-2622-B-038-004-, and MOST 109-2622-M-038-004-.

Conflicts of Interest: The authors declare no conflict of interest.

References

1. Benic, G.I.; Sancho-Puchades, M.; Jung, R.E.; Deyhle, H.; Hammerle, C.H. In vitro assessment of artifacts induced by titanium dental implants in cone beam computed tomography. *Clin. Oral Implants Res.* **2013**, *24*, 378–383. [CrossRef] [PubMed]
2. Rustemeyer, P.; Streubuhr, U.; Suttmoeller, J. Low-dose dental computed tomography: Significant dose reduction without loss of image quality. *Acta Radiol.* **2004**, *45*, 847–853. [CrossRef]
3. Kalender, W.A.; Hebel, R.; Ebersberger, J. Reduction of CT artifacts caused by metallic implants. *Radiology* **1987**, *164*, 576–577. [CrossRef] [PubMed]
4. Zhao, S.; Robertson, D.D.; Wang, G.; Whiting, B.; Bae, K.T. X-ray CT metal artifact reduction using wavelets: An application for imaging total hip prostheses. *IEEE Trans. Med. Imaging* **2000**, *19*, 1238–1247. [CrossRef] [PubMed]
5. Draenert, F.G.; Coppenrath, E.; Herzog, P.; Muller, S.; Mueller-Lisse, U.G. Beam hardening artefacts occur in dental implant scans with the NewTom cone beam CT but not with the dental 4-row multidetector CT. *Dentomaxillofac. Radiol.* **2007**, *36*, 198–203. [CrossRef]
6. Razavi, T.; Palmer, R.M.; Davies, J.; Wilson, R.; Palmer, P.J. Accuracy of measuring the cortical bone thickness adjacent to dental implants using cone beam computed tomography. *Clin. Oral Implants Res.* **2010**, *21*, 718–725. [CrossRef]
7. Schulze, R.K.; Berndt, D.; d'Hoedt, B. On cone-beam computed tomography artifacts induced by titanium implants. *Clin. Oral Implants Res.* **2010**, *21*, 100–107. [CrossRef]
8. Jung, J.S.; Jo, D.; Jo, G.; Hyun, H. Near-Infrared Contrast Agents for Bone-Targeted Imaging. *Tissue Eng. Regen. Med.* **2019**, *16*, 443–450. [CrossRef]
9. Kim, S.H.; Park, J.H.; Kwon, J.S.; Cho, J.G.; Park, K.G.; Park, C.H.; Yoo, J.J.; Atala, A.; Choi, H.S.; Kim, M.S.; et al. NIR fluorescence for monitoring in vivo scaffold degradation along with stem cell tracking in bone tissue engineering. *Biomaterials* **2020**, *258*, 120267. [CrossRef]
10. Slooter, M.D.; Bierau, K.; Chan, A.B.; Lowik, C.W. Near infrared fluorescence imaging for early detection, monitoring and improved intervention of diseases involving the joint. *Connect. Tissue Res.* **2015**, *56*, 153–160. [CrossRef]
11. Zhou, H.; Yi, W.; Li, A.; Wang, B.; Ding, Q.; Xue, L.; Zeng, X.; Feng, Y.; Li, Q.; Wang, T.; et al. Specific Small-Molecule NIR-II Fluorescence Imaging of Osteosarcoma and Lung Metastasis. *Adv. Healthc. Mater.* **2020**, *9*, e1901224. [CrossRef] [PubMed]
12. Lin, C.C.; Chang, W.H.; Cheng, T.M.; Chiu, L.H.; Wang, Y.H.; Lin, C.J.; Ho, Y.S.; Zuo, C.S.; Wang, Y.M.; Lai, W.T. Two new, near-infrared, fluorescent probes as potential tools for imaging bone repair. *Sci. Rep.* **2020**, *10*, 2580. [CrossRef]
13. Robling, A.G.; Castillo, A.B.; Turner, C.H. Biomechanical and molecular regulation of bone remodeling. *Annu. Rev. Biomed. Eng.* **2006**, *8*, 455–498. [CrossRef]
14. Yewle, J.N.; Puleo, D.A.; Bachas, L.G. Enhanced affinity bifunctional bisphosphonates for targeted delivery of therapeutic agents to bone. *Bioconjug. Chem.* **2011**, *22*, 2496–2506. [CrossRef]
15. Bhushan, K.R.; Tanaka, E.; Frangioni, J.V. Synthesis of conjugatable bisphosphonates for molecular imaging of large animals. *Angew. Chem. Int. Ed.* **2007**, *46*, 7969–7971. [CrossRef]
16. Boanini, E.; Torricelli, P.; Gazzano, M.; Fini, M.; Bigi, A. The effect of alendronate doped calcium phosphates on bone cells activity. *Bone* **2012**, *51*, 944–952. [CrossRef]
17. Meesuk, L.; Suwanprateeb, J.; Thammarakcharoen, F.; Tantrawatpan, C.; Kheolamai, P.; Palang, I.; Tantikanlayaporn, D.; Manochantr, S. Osteogenic differentiation and proliferation potentials of human bone marrow and umbilical cord-derived mesenchymal stem cells on the 3D-printed hydroxyapatite scaffolds. *Sci. Rep.* **2022**, *12*, 19509. [CrossRef]
18. Zaheer, A.; Lenkinski, R.E.; Mahmood, A.; Jones, A.G.; Cantley, L.C.; Frangioni, J.V. In vivo near-infrared fluorescence imaging of osteoblastic activity. *Nat. Biotechnol.* **2001**, *19*, 1148–1154. [CrossRef]
19. Wang, D.; Wang, X.; Huang, L.; Pan, Z.; Liu, K.; Du, B.; Xue, Y.; Li, B.; Zhang, Y.; Wang, H.; et al. Unraveling an Innate Mechanism of Pathological Mineralization-Regulated Inflammation by a Nanobiomimetic System. *Adv. Healthc. Mater.* **2021**, *10*, e2101586. [CrossRef]
20. Chin, D.D.; Wang, J.; Mel de Fontenay, M.; Plotkin, A.; Magee, G.A.; Chung, E.J. Hydroxyapatite-binding micelles for the detection of vascular calcification in atherosclerosis. *J. Mater. Chem. B* **2019**, *7*, 6449–6457. [CrossRef]
21. Song, M.K.; Park, S.I.; Cho, S.W. Circulating biomarkers for diagnosis and therapeutic monitoring in bone metastasis. *J. Bone Miner. Metab.* **2023**, 1–8. [CrossRef] [PubMed]
22. Frangioni, J.V. In vivo near-infrared fluorescence imaging. *Curr. Opin. Chem. Biol.* **2003**, *7*, 626–634. [CrossRef] [PubMed]
23. Bachman, C.H.; Ellis, E.H. Fluorescence of bone. *Nature* **1965**, *206*, 1328–1331. [CrossRef] [PubMed]
24. Chance, B. Near-infrared images using continuous, phase-modulated, and pulsed light with quantitation of blood and blood oxygenation. *Ann. N. Y. Acad. Sci.* **1998**, *838*, 29–45. [CrossRef] [PubMed]
25. Prentice, A.I. Autofluorescence of bone tissues. *J. Clin. Pathol.* **1967**, *20*, 717–719. [CrossRef]
26. Sharma, P.; Brown, S.; Walter, G.; Santra, S.; Moudgil, B. Nanoparticles for bioimaging. *Adv. Colloid Interface Sci.* **2006**, *123*, 471–485. [CrossRef]
27. Ross, R.D.; Roeder, R.K. Binding affinity of surface functionalized gold nanoparticles to hydroxyapatite. *J. Biomed. Mater. Res. A* **2011**, *99*, 58–66. [CrossRef]
28. Zhang, Z.; Ross, R.D.; Roeder, R.K. Preparation of functionalized gold nanoparticles as a targeted X-ray contrast agent for damaged bone tissue. *Nanoscale* **2010**, *2*, 582–586. [CrossRef]

29. Ergun, C.; Liu, H.; Halloran, J.W.; Webster, T.J. Increased osteoblast adhesion on nanograined hydroxyapatite and tricalcium phosphate containing calcium titanate. *J. Biomed. Mater. Res. A* **2007**, *80*, 990–997. [CrossRef]
30. Ou, K.L.; Wu, J.; Lai, W.F.; Yang, C.B.; Lo, W.C.; Chiu, L.H.; Bowley, J. Effects of the nanostructure and nanoporosity on bioactive nanohydroxyapatite/reconstituted collagen by electrodeposition. *J. Biomed. Mater. Res. A* **2010**, *92*, 906–912. [CrossRef]
31. Narayanan, S.; Sathy, B.N.; Mony, U.; Koyakutty, M.; Nair, S.V.; Menon, D. Biocompatible magnetite/gold nanohybrid contrast agents via green chemistry for MRI and CT bioimaging. *ACS Appl. Mater. Interfaces* **2012**, *4*, 251–260. [CrossRef]
32. Orza, A.; Yang, Y.; Feng, T.; Wang, X.; Wu, H.; Li, Y.; Yang, L.; Tang, X.; Mao, H. A nanocomposite of Au-AgI core/shell dimer as a dual-modality contrast agent for X-ray computed tomography and photoacoustic imaging. *Med. Phys.* **2016**, *43*, 589. [CrossRef]
33. Lin, C.A.; Yang, T.Y.; Lee, C.H.; Huang, S.H.; Sperling, R.A.; Zanella, M.; Li, J.K.; Shen, J.L.; Wang, H.H.; Yeh, H.I.; et al. Synthesis, characterization, and bioconjugation of fluorescent gold nanoclusters toward biological labeling applications. *ACS Nano* **2009**, *3*, 395–401. [CrossRef]
34. Konduru, N.V.; Velasco-Alzate, K.; Adduri, S.; Zagorovsky, K.; Diaz-Diestra, D.; Fisol, F.; Sanches, M.; Ndetan, H.; Brain, J.D.; Molina, R.M. Pulmonary fate and consequences of transferrin-functionalized gold nanoparticles. *Nanotheranostics* **2021**, *5*, 309–320. [CrossRef]
35. Lai, W.F.; Chang, C.H.; Tang, Y.; Bronson, R.; Tung, C.H. Early diagnosis of osteoarthritis using cathepsin B sensitive near-infrared fluorescent probes. *Osteoarthr. Cartil.* **2004**, *12*, 239–244. [CrossRef]
36. Wang, H.H.; Lin, C.A.; Lee, C.H.; Lin, Y.C.; Tseng, Y.M.; Hsieh, C.L.; Chen, C.H.; Tsai, C.H.; Hsieh, C.T.; Shen, J.L.; et al. Fluorescent gold nanoclusters as a biocompatible marker for in vitro and in vivo tracking of endothelial cells. *ACS Nano* **2011**, *5*, 4337–4344. [CrossRef]
37. Lin, C.A.; Chuang, W.K.; Huang, Z.Y.; Kang, S.T.; Chang, C.Y.; Chen, C.T.; Li, J.L.; Li, J.K.; Wang, H.H.; Kung, F.C.; et al. Rapid transformation of protein-caged nanomaterials into microbubbles as bimodal imaging agents. *ACS Nano* **2012**, *6*, 5111–5121. [CrossRef]
38. Chiu, L.; Kung, F.; Yang, M.; Tsai, Y.; Chang, W.; Lai, W.-F. A Novel Near Infra-Red Fluorescent Probes to Repair Metal Artifact After Implantation. In Proceedings of the Technical Proceedings of the 2013 NSTI Nanotechnology Conference and Expo, NSTI-Nanotech 2013, Washington, DC, USA, 12–16 May 2013; pp. 13–15.
39. Yeh, S.; Chiu, L.; Lin, C.; Wan, R.; Chang, W.; Lai, W.-F. Early Detection of Prostate Cancers and Their Bone Metastasis using Near-Infrared Fluorescent Imaging. In Proceedings of the 3rd International NanoMedicine Conference, Sydney, Australia, 2–4 July 2012.
40. Wang, K.H.; Wang, Y.M.; Chiu, L.H.; Chen, T.C.; Tsai, Y.H.; Zuo, C.S.; Chen, K.C.; Changou, C.A.; Lai, W.T. Optical imaging of ovarian cancer using a matrix metalloproteinase-3-sensitive near-infrared fluorescent probe. *PLoS ONE* **2018**, *13*, e0192047. [CrossRef]

Disclaimer/Publisher's Note: The statements, opinions and data contained in all publications are solely those of the individual author(s) and contributor(s) and not of MDPI and/or the editor(s). MDPI and/or the editor(s) disclaim responsibility for any injury to people or property resulting from any ideas, methods, instructions or products referred to in the content.

International Journal of
Molecular Sciences

MDPI

Article

Can Modification with Urethane Derivatives or the Addition of an Anti-Hydrolysis Agent Influence the Hydrolytic Stability of Resin Dental Composite?

Agata Szczesio-Wlodarczyk [1,*], Izabela M. Barszczewska-Rybarek [2], Marta W. Chrószcz-Porębska [2], Karolina Kopacz [3,4], Jerzy Sokolowski [5] and Kinga Bociong [5,*]

1 University Laboratory of Materials Research, Medical University of Lodz, Pomorska 251 Str., 92-213 Lodz, Poland
2 Department of Physical Chemistry and Technology of Polymers, Silesian University of Technology, Strzody 9 Str., 44-100 Gliwice, Poland
3 "DynamoLab" Academic Laboratory of Movement and Human Physical Performance, Medical University of Lodz, Pomorska 251 Str., 92-216 Lodz, Poland
4 Department of Health Sciences, Medical University of Mazovia, Ludwika Rydygiera 8 Str., 01-793 Warszawa, Poland
5 Department of General Dentistry, Medical University of Lodz, Pomorska 251 Str., 92-213 Lodz, Poland
* Correspondence: agata.szczesio@umed.lodz.pl (A.S.-W.); kinga.bociong@umed.lodz.pl (K.B.)

Abstract: Due to the questionable durability of dental restorations, there is a need to increase the lifetime of composite restoration. The present study used diethylene glycol monomethacrylate/4,4′-methylenebis(cyclohexyl isocyanate) (DEGMMA/CHMDI), diethylene glycol monomethacrylate/isophorone diisocyanate (DEGMMA/IPDI) monomers, and bis(2,6-diisopropylphenyl)carbodiimide (CHINOX SA-1) as modifiers of a polymer matrix (40 wt% urethane dimethacrylate (UDMA), 40 wt% bisphenol A ethoxylateddimethacrylate (bis-EMA), and 20 wt% triethyleneglycol dimethacrylate (TEGDMA)). Flexural strength (FS), diametral tensile strength (DTS), hardness (HV), sorption, and solubility were determined. To assess hydrolytic stability, the materials were tested before and after two aging methods (I-7500 cycles, 5 °C and 55 °C, water and 7 days, 60 °C, 0.1 M NaOH; II-5 days, 55 °C, water and 7 days, 60 °C, 0.1 M NaOH). The aging protocol resulted in no noticeable change (median values were the same as or higher than the control value) or a decrease in the DTS value from 4 to 28%, and a decrease in the FS value by 2 to 14%. The hardness values after aging were more than 60% lower than those of the controls. The used additives did not improve the initial (control) properties of the composite material. The addition of CHINOX SA-1 improved the hydrolytic stability of composites based on UDMA/bis-EMA/TEGDMA monomers, which could potentially extend the service life of the modified material. Extended studies are needed to confirm the possible use of CHINOX SA-1 as an antihydrolysis agent in dental composites.

Keywords: dental composites; hydrolytic stability; aging; clinical performance; urethane-dimethacrylate derivatives; anti-hydrolysis agent; CHINOX SA-1

Citation: Szczesio-Wlodarczyk, A.; Barszczewska-Rybarek, I.M.; Chrószcz-Porębska, M.W.; Kopacz, K.; Sokolowski, J.; Bociong, K. Can Modification with Urethane Derivatives or the Addition of an Anti-Hydrolysis Agent Influence the Hydrolytic Stability of Resin Dental Composite? *Int. J. Mol. Sci.* **2023**, *24*, 4336. https://doi.org/10.3390/ijms24054336

Academic Editor: Mary Anne Melo

Received: 16 January 2023
Revised: 13 February 2023
Accepted: 17 February 2023
Published: 22 February 2023

Copyright: © 2023 by the authors. Licensee MDPI, Basel, Switzerland. This article is an open access article distributed under the terms and conditions of the Creative Commons Attribution (CC BY) license (https://creativecommons.org/licenses/by/4.0/).

1. Introduction

The literature is divided on the clinical longevity of composite dental restorations. Some sources report that premolars and molars require replacement after five or six years [1,2]. On the other hand, some researchers show that at least 60% of reconstructions made correctly with appropriate materials have a chance of surviving for more than ten years [3]. Due to the questionable durability of dental restorations, much research has focused on ways to increase the lifetime of composite restoration, particularly the polymer matrix, filler, and coupling agent.

The polymer matrix is one of the most important components of the composite. Due to its chemical structure, it is exposed to chemical reactions that can cause degradation. The

new monomers synthesized for the needs of dentistry can be classified as (I) methacrylate monomers, (II) vinyl monomers, (III) click chemistry monomers, and (IV) ring-opening polymerization monomers [4]. There is no extensive research into how new polymer matrices are resistant to long-term use in the oral cavity. New monomers are characterized by certain desirable features such as low water sorption values, high values of the degree of conversion or a homogeneous structure, which may increase resistance to hydrolytic degradation.

Compared to the matrix, the filler plays a greater role in the development of the strength of the composite material. One promising trend in filler research is nanotechnology. Nanofillers are characterized by various shapes and morphology, and using them as a co-filler may have a positive effect on improving the structure and degree of filling. A certain combination of micron size fillers (or nanoclusters) with a nano size filler has been shown to exhibit the best packing, yielding very good mechanical properties and increased abrasion resistance [5,6]. A high degree of filling and homogeneity of the system increase the stability of composite materials over time [7].

The last issue related to the longevity of dental composites in the oral environment is the coupling agent. The filler compatibility in a dental composite can be improved by chemical surface modification, typically with silanes [8–10]. Hydrolysis can be reduced at the matrix–filler interface by increasing the hydrophobicity of the silane molecule. This can be done using molecules with an alkoxy group instead of the C=C bond, e.g., in octyltrimethoxysilane [11]. Additionally, the so-called cross-linking silanes can be used, which contain two silicon atoms each with three alkoxy groups, e.g., bis-1,2-(triethoxysilyl) ethane, or bis-1,6-(trichloroxysilyl) ethane. These compounds are able to form extensive networks that hinder the diffusion of molecules into the bulk of the material, thus increasing the hydrolytic stability of the dental composite [12].

Composite materials introduced into the market must be evaluated as biomaterials, and they are often evaluated using the ISO 4049 standard. However, such evaluation is limited and it cannot be predicted how the material will behave during long-term use in the oral environment, which due to its variable temperature and pH, friction, and various biological factors, will limit the time of the restoration [13]. Research using complex and aggressive environmental factors is very popular in other industries to determine a product's lifetime. Hence, there is a need to evaluate the stability of dental materials in a complex operating environment when developing new materials [14–17].

The present study used diethylene glycol monomethacrylate/4,4′-methylenebis(cyclohexyl isocyanate) (DEGMMA/CHMDI) and diethylene glycol monomethacrylate/isophorone diisocyanate (DEGMMA/IPDI) monomers developed by Prof. I. Barszczewska-Rybarek [18]. These monomers are characterized by good strength properties and relatively low water sorption (Table 1). The structure of the DEGMMA/CHMDI and DEGMMA/IPDI monomers used in the study is presented in Figure 1A.

Table 1. The properties of the used monomers: molecular weight (MW), flexural strength (FS), flexural modulus (E), water sorption (WS), degree of conversion (DC).

Monomer	MW [g/mol]	FS [MPa]	E [GPa]	WS [μg/mm^3]	DC [%]
UDMA	470	134 [a]	1.8 [a]	42.3 [a]	72 [a]
Bis-EMA	540	87 [a]	1.1 [a]	21.3 [a]	76 [a]
TEGDMA	286	99 [a]	1.7 [a]	28.8 [a]	83 [a]
DEGMMA/CHMDI	611	139 [b]	3.4 [b]	18.5 [b]	41 [b]
DEGMMA/IPDI	571	141 [b]	2.8 [b]	29.9 [b]	66 [b]

a—taken from [19]; b—taken from [18]. UDMA—urethane dimethacrylate, bis-EMA—bisphenol A ethoxylated-dimethacrylate, TEGDMA—triethyleneglycol dimethacrylate, CHINOX SA-1—bis(2,6-diisopropylphenyl)carbodiimide, DEGMMA/CHMDI—diethylene glycol monomethacrylate/4,4′-methylenebis(cyclohexyl isocyanate), DEGMMA/IPDI—diethylene glycol monomethacrylate/isophorone diisocyanate.

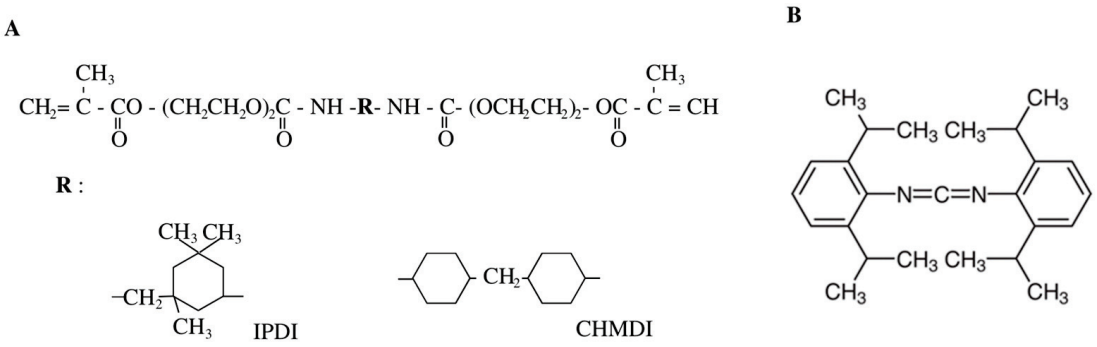


Figure 1. Structures of monomers (**A**) (DEGMMA/CHMDI—diethylene glycol monomethacrylate/4,4′-methylenebis(cyclohexyl isocyanate), DEGMMA/IPDI—diethylene glycol monomethacrylate/isophorone diisocyanate) and (**B**) CHINOX SA-1—bis(2,6-diisopropylphenyl)carbodiimide, used as modifiers.

In addition, being a pilot study, bis(2,6-diisopropylphenyl)carbodiimide (CHINOX SA-1) was added to the composite as an anti-hydrolysis agent in order to improve its hydrolytic stability (Figure 1B). The industry uses such additives that can increase the stability of polymeric materials [20]. Although its chemical structure may reduce its composite biocompatibility, it seems reasonable to conduct research with the use of minor additives not yet used in dental composites.

The authors did not find information in the literature indicating the use of both urethane derivatives and an antifhydrolysis agent as modifiers of composites based on UDMA, bis-EMA, and TEGDMA monomers. In addition, studies evaluating the durability of new experimental dental composites are not a common approach; however, taking into account the methods of evaluating materials in other industries, such an assessment should be a standard procedure. The null hypothesis was that the DEGMMA/CHMDI and DEGMMA/IPDI monomers or the agent CHINOX SA-1 would not affect the properties or the hydrolytic stability of the composite assessed based on two aging protocols.

2. Results

The data regarding the composite modified with DEGMMA/CHMDI and DEGMMA/IPDI are presented in Table 2.

The applied aging protocols had some impact on the selected materials compared to the control group. In all samples, a significant difference was noted for the hardness values after aging.

The percentage changes of the measured properties of composites modified with the DEGMMA/CHMDI and DEGMMA/IPDI monomers after the thermo_NaOH aging protocol and water_NaOH aging protocol are presented on Figures 2 and 3, respectively.

The thermo_NaOH aging protocol (7500 cycles, 5 °C and 55 °C, water and 7 days, 60 °C, 0.1 M NaOH) yielded greater changes than the water_NaOH aging protocol (5 days, 55 °C, water and 7 days, 60 °C, 0.1 M NaOH).

The obtained results of the composite modified with the CHINOX SA-1 anti-hydrolysis agent are presented in Table 3.

After application of the aging protocols, significant changes were observed in the hardness.

The percentage changes in the measured properties of the composites modified with CHINOX SA 1 after the thermo_NaOHaging protocol and water_NaOH aging protocol are presented on Figures 4 and 5, respectively.

The CHINOX SA-1-modified materials yielded smaller percentage changes compared to the non-modified control material.

Box-and-whisker plots of the collected results and exact *p*-values are provided in Appendix A (Figures A1–A6).

The sorption and solubility of the tested materials are presented in Table 4.

The applied modifications slightly increased the sorption value. The solubility of the tested materials increased.

Table 2. The results of the flexural strength (FS), diametral tensile strength (DTS), and hardness (HV) of the tested materials modified with DEGMMA/CHMDI and DEGMMA/IPDI after selected aging protocols. The results with the same assigned letter or uppercase and lowercase letters are significantly different ($p \leq 0.05$). Median values are presented with the interquartile range (IQR).

Number of Samples in the Study Group	DTS [MPa]	(IQR)	FS [MPa]	(IQR)	HV	(IQR)
	n = 9		*n* = 7		*n* = 9	
None, Control	39.14 ^{e}	2.29	93.8 ^{a,b,c,d,e}	11.6	32 $^{A(a–h)}$	1
None, thermo_NaOH	36.33	8.64	78.7	12.7	13	2
None, water_NaOH	40.13 ^{a,b,c,d}	1.20	82.6 ^{f}	15.1	13	1
IPDI(2.5)_CHMDI(2.5), control	36.90	5.60	86.7 ^{g,i}	21.6	29 $^{B(a–h)}$	1
IPDI(2.5)_CHMDI(2.5), thermo_NaOH	34.36	2.81	64.5 ^{b,i}	9.8	10 ^{Ab,Bb,Cb,Ea}	1
IPDI(2.5)_CHMDI(2.5), water_NaOH	32.94	7.29	62.3 ^{a,f,g,h}	7.0	10 ^{Aa,Ba,Ca}	1
CHMDI(5), control	37.42 ^{f}	2.66	72.9	8.4	30 $^{C(a–h)}$	1
CHMDI(5), thermo_NaOH	33.23 ^{a}	2.56	69.2 ^{c}	9.3	9 ^{Ac,Bc,Cc,Da,Eb,Fa}	1
CHMDI(5), water_NaOH	37.28 ^{g}	1.76	79.2 ^{h}	14.9	14 ^{G}	1
CHMDI(10), control	35.35	1.79	83.1	17.9	28 $^{D(a-d)}$	1
CHMDI(10), thermo_NaOH	34.18 ^{b}	3.01	64.5 ^{d}	23.7	9 ^{Ad,Bd,Cd,Db,Ec,Fb}	1
CHMDI(10), water_NaOH	30.38 ^{c,e,f,g,h}	4.77	73.0	13.8	8 ^{Ae,Be,Ce,Dc,Ed,Fc,G}	1
IPDI(5), control	34.17	2.68	80.6	8.1	29 $^{E(a–g)}$	1
IPDI(5), thermo_NaOH	33.34	4.52	65.1 ^{e}	10.9	9 ^{Af,Bf,Cf,Dd,Ee,Fd}	1
IPDI(5), water_NaOH	37.18 ^{h}	2.89	80.7	22.9	13	1
IPDI(10), control	35.99	1.80	73.7	14.9	27 $^{F(a–d)}$	2
IPDI(10), thermo_NaOH	33.90	6.80	71.0	12.0	10 ^{Ag,Bg,Cg,Ef}	1
IPDI(10), water_NaOH	32.10 ^{d}	5.91	70.7	5.8	10 ^{Ah,Bh,Ch,Eg}	1

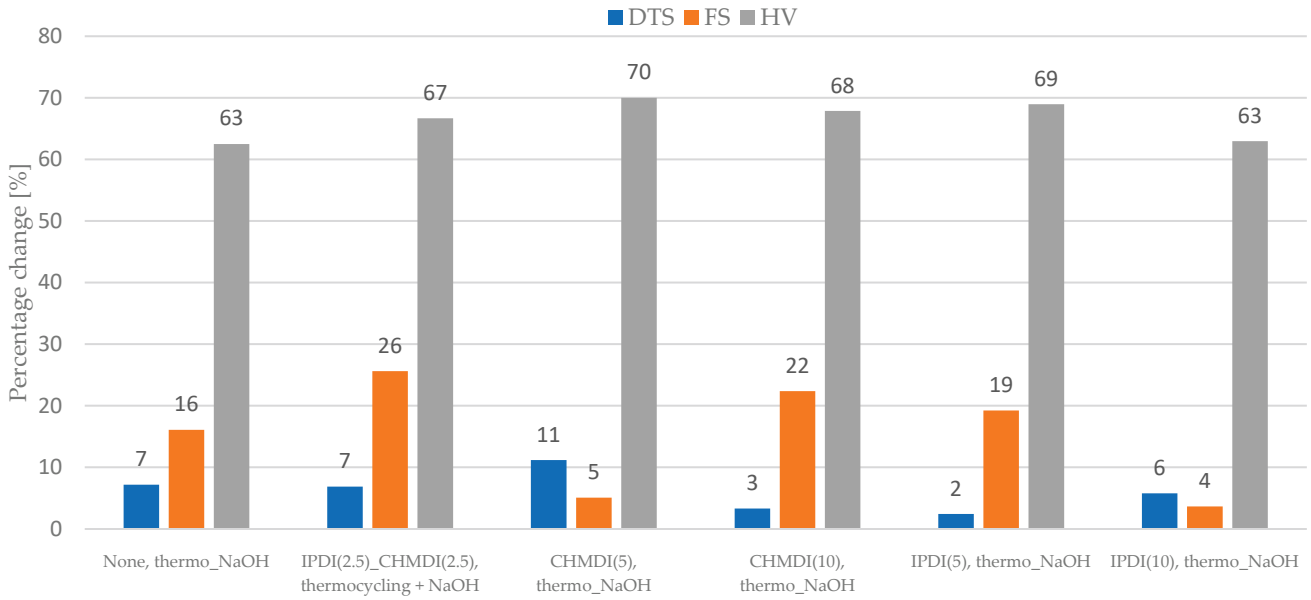


Figure 2. Percentage change in the flexural strength (FS), diametral tensile strength (DTS), and hardness (HV) after the thermo_NaOH aging protocol (7500 cycles, 5 °C and 55 °C, water and 7 days, 60 °C, 0.1 M NaOH) compared to control values.

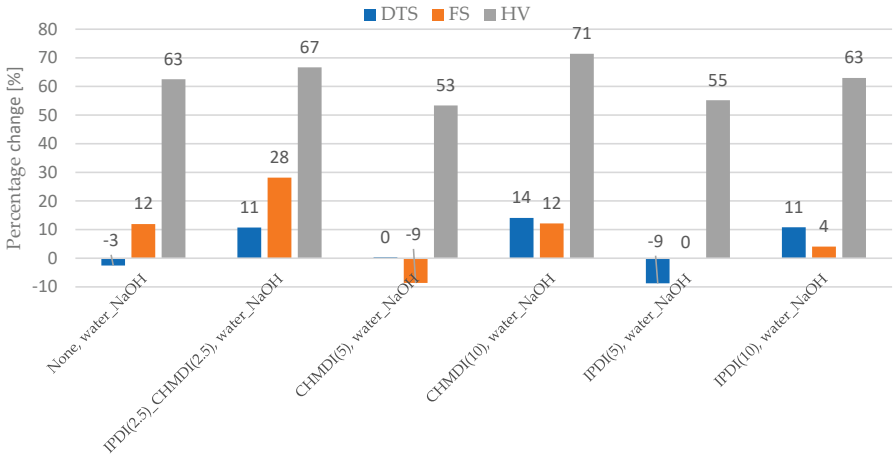


Figure 3. Percentage change in the flexural strength (FS), diametral tensile strength (DTS), and hardness (HV) after the water_NaOH aging protocol (5 days, 55 °C, water and 7 days, 60 °C, 0.1 M NaOH) compared to the control value. 0—no change; negative value—the selected property was higher than the control value after application of the protocol.

Table 3. The results of the flexural strength (FS), diametral tensile strength (DTS), and hardness (HV) for tested materials modified with CHINOX SA-1 after selected aging protocols. The results with the same assigned letter or uppercase and lowercase letters are significantly different. FS is presented as the mean with standard deviation (SD), while DTS and HV are presented as the median with the interquartile range (IQR).

Number of Samples in the Study Group	DTS [MPa]	IQR	FS [MPa]	SD	HV	IQR
	n = 9		*n* = 7		*n* = 9	
None, Control	39.14	2.29	95.0 $^{A(a–h)}$	7.6	32 ^{a,b,c,d,e}	1
None, thermo_NaOH	36.33	8.64	77.0 $^{Aa,C(a–c)}$	6.5	12 ^{a}	3
None, water_NaOH	40.13 ^{a,b,c}	1.20	82.5 $^{Ab,B(a–e)}$	8.1	12	2
CHINOX(0.5), control	34.13 ^{a}	2.33	73.0 ^{Ac,Ba,E}	7.2	29 ^{f,g,h,i}	1
CHINOX(0.5), thermo_NaOH	35.00	2.98	69.5 ^{Ad,Bb}	10.6	10 ^{b,f,j}	2
CHINOX(0.5), water_NaOH	31.28 ^{b}	7.13	77.7 $^{Ae,D(a–c)}$	5.4	11 ^{c,g,k}	2
CHINOX(1.5), control	33.89 ^{c}	1.64	65.0 ^{Af,Bc,Ca,Da}	11.5	28 ^{j,k,l,m}	2
CHINOX(1.5), thermo_NaOH	35.38	2.37	62.7 ^{Ag,Bd,Cb,Db,E}	9.0	11 ^{d,h,l}	1
CHINOX(1.5), water_NaOH	34.71	4.81	66.0 ^{Ah,Be,Cc,Dc}	8.5	10 ^{e,i,m}	2

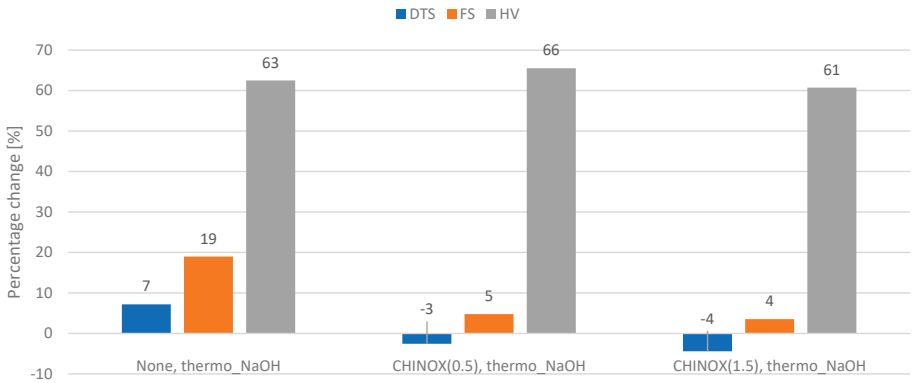


Figure 4. Percentage change in the flexural strength (FS), diametral tensile strength (DTS), and hardness (HV) after the thermo_NaOH aging protocol (7500 cycles, 5 °C and 55 °C, water and 7 days, 60 °C, 0.1 M NaOH) compared to controls. 0—no change; negative value—the value was higher than the control values after application of the protocol.

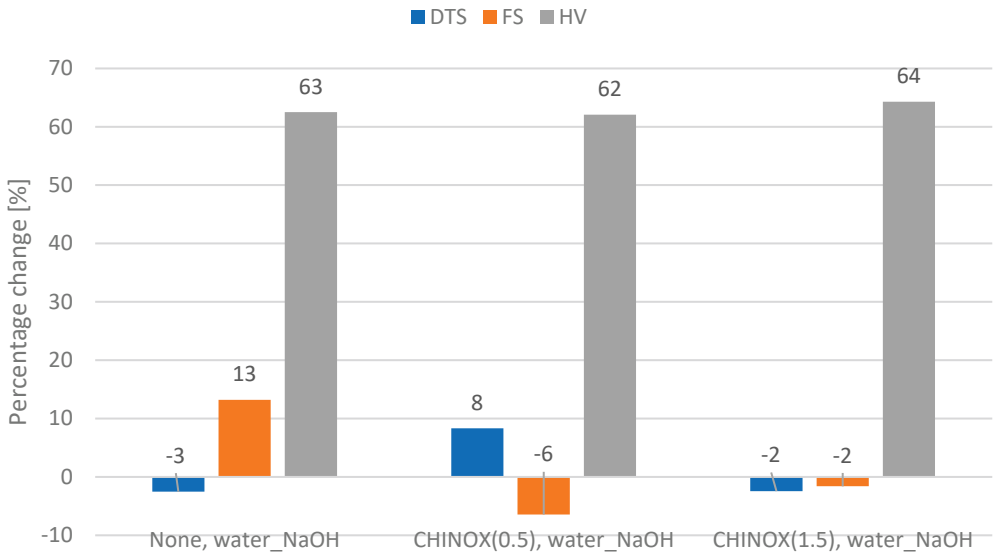


Figure 5. Percentage change in the flexural strength (FS), diametral tensile strength (DTS), and hardness (HV) after the water_NaOH aging protocol (5 days, 55 °C, water and 7 days, 60 °C, 0.1 M NaOH) compared to controls. 0—no change; negative value—the value was higher than the control values after application of the protocol.

Table 4. The results of sorption and solubility. The results are shown as the mean with standard deviation (SD).

		Control	CHMDI(2.5)_IPDI(2.5)	CHMDI(5)	CHMDI(10)	IPDI(5)	IPDI(10)	CHINOX(0.5)	CHINOX(1.5)
Sorption	n = 5	25.42 (0.53)	28.96 (0.40)	26.55 (1.07)	32.40 (1.56)	26.81 (0.60)	32.64 (2.41)	32.97 (1.53)	32.91 (0.73)
Solubility	n = 5	0.70 (0.20)	0.68 (0.15)	1.05 (0.28)	1.46 (0.42)	1.31 (0.08)	1.48 (0.48)	1.26 (0.71)	2.00 (0.29)

3. Discussion

There is a pressing need to identify a composite with increased resistance to hydrolytic degradation and hence a longer lifetime [21,22]. It should be borne in mind that the oral environment has a significant impact on composite durability. As such, it is crucial that materials are evaluated under accelerated aging conditions with increased environmental factors.

Our findings indicate that the selected modification did indeed influence the properties of the control (base) material, thus rejecting the null hypothesis. However, the use of the DEGMMA/CHMDI, DEGMMA/IPDI monomers and the addition of CHINOX SA-1 did not improve the initial (control) strength properties. The initial values of the tested properties were lower than those of the base material, but not all differences were statistically significant.

The properties of a composite material are influenced by its composition. Considering that the materials have the same filler, the observed differences in the properties will depend on the composition of the polymer matrix [23,24]. The tested materials, which consisted of a basic polymer matrix (40 wt% of UDMA, 40 wt% of Bis-EMA, 20 wt% of TEGDMA), was modified with two monomers (DEGMMA/CHMDI, DEGMMA/IPD) in different weight percentages. As the used monomers had two oxyethylene units (DEGMMA), the molecule showed limited flexibility. Additionally, the monomers contained cycloaliphatic diisocyanates: CHMDI or IPDI, which differed in their structure symmetry. The monomer with IPDI is more elastic than the one with CHMDI, which may result in higher DC and modulus [18]. In our research, a small addition (max 10 wt%) of the cycloaliphatic urethane-dimethacrylate derivatives did not improve the strength properties. However, the TEGDMA, Bis-EMA, or UDMA homopolymers demonstrated lower flexural strength and flexural modulus than the resins used as modification (Table 1). Even so, it should be taken into account that the properties of the composite result from complex relationships and

interactions between individual components that cannot be predicted under the current state of science. It is most likely that the addition of further substances could hinder the movement of macromolecules during polymerization due to their chemical structure (Figure 1A) [18]. Composite materials modified with CHMDI or IPDI monomers could achieve lower DC values resulting in lower FS and DTS values.

In addition, the modification with the anti-hydrolysis agent did not improve the control values. CHINOX SA-1 includes two phenyl groups connected to each other by a short carbodiimide group (Figure 1B). This stiff structure, similar to bis-GMA, may prevent the free movement of macromolecules during polymerization, resulting in a lower degree of conversion by the composite [25,26]. The lower DC can explain the decreased FS, DTS, and HV values and the increased sorption of modified composites with CHINOX SA-1.

Although dental materials placed on the market must meet certain requirements, such as biocompatibility, the relevant ISO and ADA standards include no tests for assessing the stability of materials in the oral cavity. Water sorption can be used to assess the behavior of materials in a water environment. The ISO 4049 standard specifies that the sorption of the composite material cannot be higher than 40 $\mu g/mm^{-3}$ at a solubility of 7.5 $\mu g/mm^{-3}$ [27]. For the tested modified monomers, the sorption was relatively low (Table 1). Regarding the DEGMMA/CHMDI monomer, the low sorption values are due to the presence of symmetrical cycloaliphatic moieties, which causes a reduction in the space between the polymer chains. In contrast, the asymmetric core in IPDI can create more free space in the polymer network for water to enter, resulting in higher sorption. In the study, composites modified with selected urethane derivatives showed similar sorption values as the control materials. Minor amounts of selected monomers were added (max. 10 wt%); therefore, the effect on sorption was small. The sorption values increased noticeably in comparison with the control when CHINOX SA-1 added, but these values were still at an acceptable level. There was also no difference between the addition of 0.5 and 1.5%. The solubility of the tested materials compared to the control material increased. The observed changes may also be related to the structure of the used modifiers, which could have resulted in a lower degree of the conversion values. Materials with lower DC showed higher sorption and solubility values [28].

Of the two tested aging protocols, the thermocycler approach (7500 cycles, 5 °C and 55 °C, water and 7 days, 60 °C, 0.1 M NaOH) reduced the value of the tested properties more effectively (Figures 2–5) than water (5 days, 55 ° C, water and 7 days, 60 °C, 0.1 M NaOH). It has been shown that thermocycles affect the degradation of the polymer matrix as well as the stability of the matrix–filler interface [29,30]. Boussès et al. reported slow degradation of at the filler–matrix interface for the first 5000 thermocycles, while significant changes were noted after 10,000 thermocycles [31]. From a chemical point of view, composite samples take up water during aging, resulting in hydrolysis of the polymer matrix and interface. Firstly, the matrix protects the interface from degradation until the polymer structure is saturated with water. Once water reaches the interphase, the siloxane bonds are exposed to hydrolysis. Unfortunately, this type of bond, which results from filler silanization, is not resistant to hydrolytic degradation [10,32]. Thermocycling causes successive contractions and expansions of the material due to temperature variations. In addition, due to different thermal expansion coefficients, local overstress is generated at the interface. This may cause the occurrence of micro-cracks and interface damage, leading to a greater decrease in strength [31]. In the present study, the effect of the thermocycler was enhanced by NaOH; this causes accelerated degradation of dental polymer materials due to a high amount of hydroxyl ions, which are responsible for the hydrolysis of the bonds present in the polymer matrix, the coupling agent or the interphase [33–35]. It is worth mentioning that the phenomenon of degradation of dental materials does not occur only under the influence of substances and physical conditions (aqueous environment, temperature, pH, chewing forces, friction) occurring in the oral cavity. Aging of materials also develops under the influence of biological factors—salivary enzymes and bacterial activity. It has been shown that these factors also cause the hydrolysis of chemical bonds found in composite

materials [36]. However, enzyme-based analyses are costly and more demanding than the proposed aging protocols.

Research has shown that the top layer is the most susceptible to aging and degradation. For most of the studied groups, the hardness values after aging were more than 60% lower than those of the controls. The aging medium reduces hardness by affecting the matrix and weakens the siloxane bonds in the silane coupling agent [37]. The alkalinity provides a large amount of hydroxyl ions, which are responsible for hydrolysis [38]. The microstructure of the dental composite changes after chemical or thermal aging. Plucking out, fractures of filler particles, and degradation–delamination of the matrix were observed [14,34,39,40]. The aging protocol resulted in no noticeable change (median values were the same as or higher than those of the control value) or a decrease in the DTS value from 4 to 28% and a decrease in the FS value by 2 to 14% (Figures 2–5). Considering the lower percentage changes in strength, it appears that the degradation effect is more superficial and does not propagate into the bulk of the material. However it should be underlined that in the oral environment, the top aged layer will be successively lost due to the continuous friction applied by chewing forces, allowing the restoration to be continually eroded [41].

No relationship was found between the percentage composition of the polymer matrix and the hydrolytic resistance, identified by changes in selected properties. Smaller changes in DTS and FS were observed in the CHMDI(5) and the IPDI(5) and (10) groups; these values were very close to those of the control. No significant improvement in stability against hydrolytic degradation was noted for most composites, which was probably more dependent on the network structure of the materials and the complex interaction between the used monomers. The UDMA monomer and its cycloaliphatic derivatives (DEGMMA/IPDI and DEGMMA/CHMDI) have urethane bonds, which are prone to form strong hydrogen bonds. These bonds acts as physical crosslinks in the resulting polymer network. The enrichment of the studied system with DEGMMA/IPDI and DEGMMA/CHMDI may cause increase in the physical crosslinked density. Hence, monomers of the UDMA/bis-EMA/TEGDMA matrix could form less homogeneous structures, which would influence the changes in the tested properties after aging. Some inhomogeneity in materials may create a spot where a stress accumulates, resulting in microcracks and treatment failure. It should be remembered that any imperfection in the material can influence its durability.

The addition of CHINOX SA-1 improved the hydrolytic stability of the tested materials. The percentage changes in the DTS and FS values following aging were limited, even at low CHINOX SA-1 concentrations (0.5%). Unfortunately, no data regarding this concentration in dental materials could be found in previous studies; however, research conducted, for example, with poly (lactic acid) has shown that carbodiimide compounds increase the resistance to hydrolytic degradation due to the water reacting with anti-hydrolysis compounds, producing urea derivatives [42,43]. It is most likely that the reaction of the CHINOX SA-1 anti-hydrolysis agent and water molecule proceeds according to the equation presented in Figure 6.

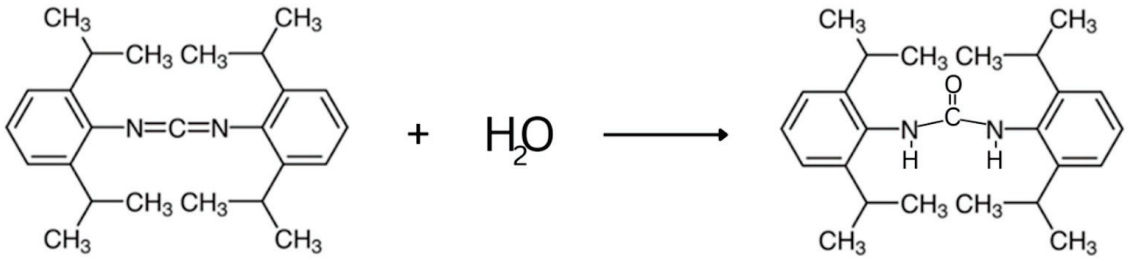


Figure 6. Reaction of bis(2,6-iisopropylphenyl)carbodiimide (CHINOX SA-1) with water.

As small additions have been found to be effective in increasing hydrolytic stability, it is likely that the cellular response will not be impaired. However, future studies are still needed to determine the biocompatibility of such composites.

4. Materials and Methods

The basic material used in this work was a polymer matrix consisting of 40 wt% UDMA, 40 wt%, bis-EMA, and 20 wt% TEGDMA. A resin matrix was prepared according to the weight percentage of the selected monomers. UDMA, TEGDMA, and bis-EMA were delivered by Esstech Inc. (Essington, PA, USA). Such a resin matrix was additionally modified with a specific amount of selected urethane monomers or anti-hydrolysis agent (Table 5). Each mixture contained camphorquinone (<1 wt%) and N, N-dimethylaminoethyl methacrylate. Monomers were synthesized, and their structure was confirmed as described previously [18,44]. CHINOX SA-1 was delivered by TCI Chemicals (Fukaya, Japan).

Table 5. Matrix composition of the tested composites, which contained 45 wt% of silanized silica.

Material Signature	Base Material	Modification
Control	UDMA 40 wt% bis-EMA 40 wt% TEGDMA 20 wt%	None
CHMDI(2.5)_IPDI(2.5)		DEGMMA/CHMDI 2.5 wt% and DEGMMA/IPDI 2.5 wt%
CHMDI(5)		DEGMMA/CHMDI 5 wt%
CHMDI(10)		DEGMMA/CHMDI 10 wt%
IPDI(5)		DEGMMA/IPDI 5 wt%
IPDI(10)		DEGMMA/IPDI 10 wt%
CHINOX(0.5)		CHINOX SA-1 0.5 wt%
CHINOX(1.5)		CHINOX SA-1 1.5 wt%

UDMA—urethane dimethacrylate, bis-EMA—bisphenol A ethoxylateddimethacrylate, TEGDMA—triethyleneglycol dimethacrylate, CHINOX SA-1—bis(2,6-diisopropylphenyl)carbodiimide, DEGMMA/CHMDI—diethylene glycol monomethacrylate/4,4′-methylenebis(cyclohexyl isocyanate), DEGMMA/IPDI—diethylene glycol monomethacrylate/isophorone diisocyanate.

After modification, 45 wt% filler was added to each of the prepared polymer matrices using a mortar. The filler was silica (Arsil, Zakłady Chemiczne "RUDNIKI" S.A., Rudniki, Poland) silanized with γ-Methacryloxypropyltrimethoxy silane (Unisil Sp. Z o. O., Tarnów, Poland).

Two different ageing protocols were used (Table 6) to evaluate the hydrolytic stability of the tested materials. The flexural strength, diametral tensile strength, and hardness were determined with and without the influence of the aging protocols. The protocols were selected on the basis of previous research [14]. Briefly, hydrolytic degradation was accelerated by NaOH solution. Thermocycles and increased temperature affect sorption and dissolution. The combination of thermal and chemical factors better mimic the prolonged influence of the oral environment on restoration. Accelerated aging with more aggressive or greater amounts of factors can be used to evaluate the lifetime performance of dental composite in vivo [14,45]. It can be assumed that the proposed aging protocols will simulate several years in the oral environment; however, such a prediction is very complex and difficult to make.

Table 6. Description of selected aging protocols used to evaluate the tested materials.

Ageing Protocol Signature	Description
control	24 h, 37 °C, distilled water
thermo_NaOH	7500 cycles, 5 °C and 55 °C, water and 7 days, 60 °C, 0.1 M NaOH
water_NaOH	5 days, 55 °C, water and 7 days, 60 °C, 0.1 M NaOH

The NaOH solution was prepared in a volumetric flask. The NaOH (Avantor Performance Materials, Gliwice, Poland) was measured on an analytical balance (Radwag XA 82/220/X, Puszczykowo, Poland). The samples were placed in plastic dishes in a DZ-2BCII Vacuum Drying Oven (ChemLand, Stargard Szczecinski, Poland) for a period (Table 6) or were subjected to 7500 thermocycles (water, 20 s dwell time, 5 and 55 °C) using a THE 1200 thermocycler (SD Mechatronic, Feldkirchen-Westerham, Germany).

Flexural strength (FS) was determined based on ISO 4049:2019. Seven measurements were made for each study group, using rectangular samples (25 mm long, 2 mm wide, 2 mm thick). Nine cylindrical samples (diameter 6 mm and thickness 3 mm) for each study group were used to establish the diametral tensile strength (DTS). The FS and DTS tests were performed using a Z020 universal testing machine (Zwick–Roell, Ulm, Germany). The traverse speed was 2 mm/min in the DTS test and 1 mm/min in FS. Nine measurements of Vickers hardness (1000 g applied load, 10 s penetration time) were carried out for each study group. The Zwick ZHV2–m hardness tester (Zwick–Roell, Ulm, Germany) was used in this study. In addition, water sorption and the solubility of the tested materials were evaluated, based on ISO standard (4049:2019 Dentistry—Polymer-based restorative materials). Five cylindrical samples (15 mm in diameter, 1 mm in width) were prepared for each composite.

Water sorption (W_{sp}) and solubility (W_{sl}) were calculated for each specimen using the following equations:

$$W_{sp} = \frac{m_2 - m_1}{V} \cdot 100\% \quad (1)$$

$$W_{sp} = \frac{m_1 - m_3}{V} \cdot 100\% \quad (2)$$

where m_1 is the conditioned mass of the specimen, m_2 is the mass of the specimen after immersion in water, m_3 is the reconditioned mass of the specimen, and V is the specimen volume.

The Shapiro–Wilk test was used to assess the normality of the distribution of the data. Based on the results, either the Kruskal–Wallis test with multiple comparisons of mean ranks or one-way ANOVA was applied, followed by Tukey's post hoc test. The accepted level of significance was $\alpha = 0.05$. Data with a normal distribution and homogeneity of variance are presented as mean values with standard deviation (SD), while those without are presented as median values with the interquartile range (IQR). All analyses were performed using Statistica version 13 software (StatSoft, Kraków, Poland).

5. Conclusions

These studies examined one composite, albeit as five variants with DEGMMA/CHMDI, DEGMMA/IPDI monomers, and two modifications with the CHINOX SA-1 anti-hydrolysis agent. Further research is needed with a wider group of materials and more testing methods. Nevertheless, our findings indicate the following:

- The additives (DEGMMA/CHMDI, DEGMMA/IPDI, CHINOX SA-1) did not improve the initial (control) properties of the composite material.
- No relationship was found between the percentage composition of the polymer matrix and hydrolytic stability, tested by changes in selected properties after aging.
- The addition of CHINOX SA-1 improved the hydrolytic stability of the composites based on the UDMA/bis-EMA/TEGDMA monomers.
- In all materials, the hardness dropped dramatically after the aging protocols. This may prove that the degradation of materials takes place mainly in the top layer.

The standardization of the aging protocol for dental materials is a separate project (funded by National Science Centre, Poland grant number: UMO-2020/37/N/ST5/00191, 2021).

Author Contributions: Conceptualization, A.S.-W. and J.S.; methodology, A.S.-W., K.B., and I.M.B.-R.; formal analysis, A.S.-W. and K.K.; investigation, A.S.-W. and M.W.C.-P.; data curation, A.S.-W. and K.K.; writing—original draft preparation, A.S.-W. and M.W.C.-P.; writing—review and editing, A.S.-W., I.M.B.-R., J.S., and K.B.; visualization, A.S.-W. and K.K.; supervision, J.S. and K.B.; project administration, A.S.-W. and K.B.; funding acquisition, J.S. All authors have read and agreed to the published version of the manuscript.

Funding: This study was conducted as part of the project: "InterChemMed–Interdisciplinary doctoral studies at Lodz public universities", implemented under the Operational Program Knowledge Education Development 2014–2020, co-financed by the European Social Fund (no. POWR.03.02.00-00-I029/16).

Institutional Review Board Statement: Not applicable.

Informed Consent Statement: Not applicable.

Data Availability Statement: Data are available in a publicly accessible repository: Zenodo at: 10.5281/zenodo.7656550.

Conflicts of Interest: The authors declare no conflict of interest. The funders had no role in the design of the study; in the collection, analyses, or interpretation of data; in the writing of the manuscript; or in the decision to publish the results.

Abbreviations

List of abbreviations:

bis-EMA	bisphenol A ethoxylateddimethacrylate,
CHINOX SA-1	bis(2,6-diisopropylphenyl)carbodiimide,
CHINOX(0.5)	addition of 0.5 wt% CHINOX SA-1,
CHINOX(1.5)	addition of 1.5 wt% CHINOX SA-1,
CHMDI(10)	addition of 10 wt% DEGMMA/CHMDI,
CHMDI(2.5)_IPDI(2.5)	addition of 2.5 wt% DEGMMA/CHMDI and 2.5 wt% DEGMMA/IPDI,
CHMDI(5)	addition of 5 wt% DEGMMA/CHMDI,
Control	24 h, 37 °C, distilled water,
DEGMMA/CHMDI	diethylene glycol monomethacrylate/4,4′-methylenebis (cyclohexyl isocyanate),
DEGMMA/IPDI	diethylene glycol monomethacrylate/isophorone diisocyanate
DTS	diametral tensile strength [MPa],
FS	flexural strength [MPa],
HV	hardness [-],
E	flexural modulus [GPa],
WS	water sorption [μg/mm^3],
DC	degree of conversion [%],
IPDI(10)	addition of 10 wt% DEGMMA/IPDI,
IPDI(5)	addition of 5 wt% DEGMMA/IPDI,
MW	molecular weight [g/mol],
TEGDMA	triethyleneglycol dimethacrylate,
thermo_NaOH	aging for 7500 cycles, 5 °C and 55 °C, water and 7 days, 60 °C, 0.1 M NaOH,
UDMA	urethane dimethacrylate,
water_NaOH	aging for 5 days, 55 °C, water and 7 days, 60 °C, 0.1 M NaOH.

Appendix A

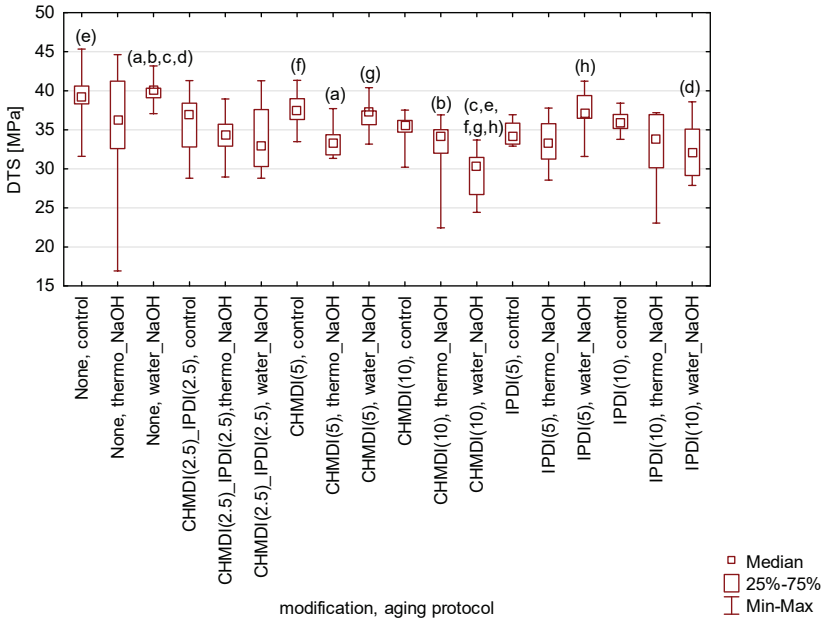


Figure A1. Box-and-whisker plot of the diametral tensile strength (DTS) of the tested materials. Statistically significant differences were detected between the following: (a,b,c,d) None, water_NaOH vs. (a) CHMDI(5), thermo_NaOH (p = 0.0261), (b) CHMDI(10), thermo_NaOH (p = 0.0272), (c) CHMDI(10), water_NaOH (p = 0.00002), (d) IPDI(10), water_NaOH (p = 0.0087); (e,f,g,h) CHMDI(10), water_NaOH vs. (e) None, control (p = 0.0005), (f) CHMDI(5), control (p = 0.0082), (g) CHMDI(5), water_NaOH (p = 0.0421), (h) IPDI(5), water_NaOH (p = 0.0095).

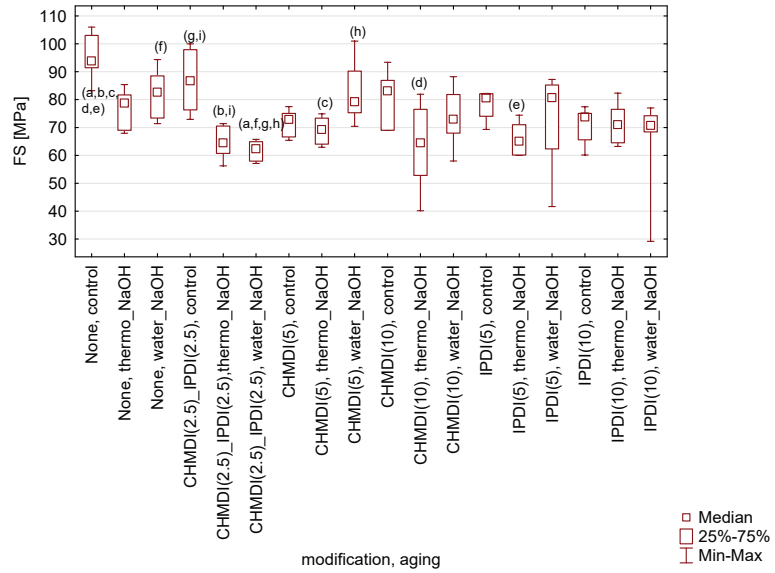


Figure A2. Box-and-whisker plot of the flexural strength (FS) of the tested materials. Statistically significant differences were detected between the following: (a,b,c,d,e) None, control vs. (a) CHMDI(2.5)_IPDI(2.5), water_NaOH (p = 0.00004), (b) CHMDI(2.5)_IPDI(2.5), thermo_NaOH (p = 0.0005), (c) CHMDI(5), thermo_NaOH (p = 0.0151), (d) CHMDI(10), thermo_NaOH (p = 0.0103), (e) IPDI(5), thermo_NaOH (p = 0.0034); (a,f,g,h) CHMDI(2.5)_IPDI(2.5), water_NaOH vs. (f) None, water_NaOH (p = 0.0165), (g) CHMDI(2.5)_IPDI(2.5), control (p = 0.0051), (h) CHMDI(5), water_NaOH (p = 0.0254); (i) CHMDI(2.5)_IPDI(2.5), control vs. (i) CHMDI(2.5)_IPDI(2.5), thermo_NaOH (p = 0.0459).

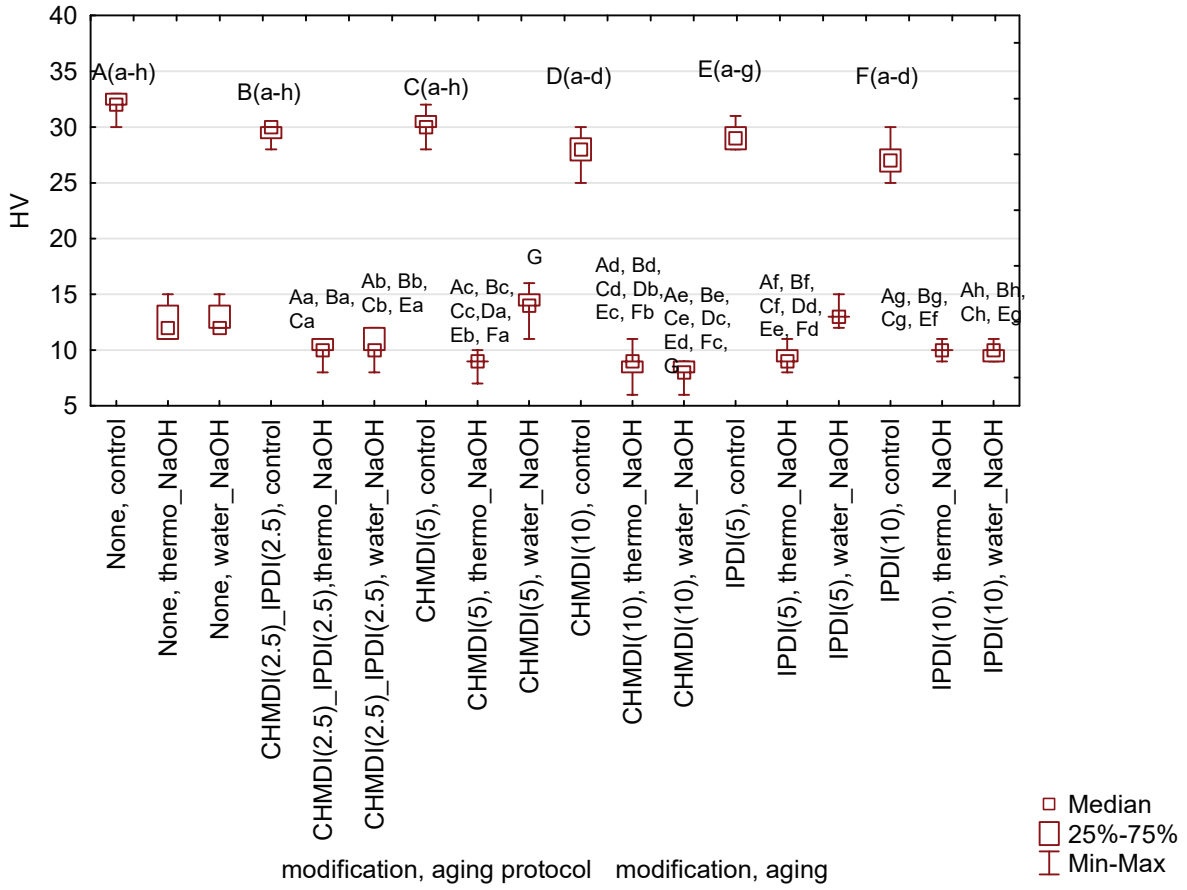


Figure A3. Box-and-whisker plot of the Vickers hardness (HV) of the tested materials. Statistically significant differences were detected between the following: (A(a–h)) None, control vs. (Aa) CHMDI(2.5)_IPDI(2.5), water_NaOH (p = 0.0005), (Ab) CHMDI(2.5)_IPDI(2.5), thermo_NaOH (p = 0.0004), (Ac) CHMDI(5), thermo_NaOH (p = 0.0000), (Ad) CHMDI(10), thermo_NaOH (p = 0.0000), (Ae) CHMDI(10), water_NaOH (p = 0.0000), (Af) IPDI(5), thermo_NaOH(0.0000), (Ag) IPDI(10), thermo_NaOH (p = 0.0001), (Ah) IPDI(10), water_NaOH (p = 0.0001); (B(a–h)) CHMDI(2.5)_IPDI(2.5), control vs. (Ba) CHMDI(2.5)_IPDI(2.5), water_NaOH (p = 0.0298), (Bb) CHMDI(2.5)_IPDI(2.5), thermo_NaOH (p = 0.0212), (Bc) CHMDI(5), thermo_NaOH (p = 0.0001), (Bd) CHMDI(10), thermo_NaOH (p = 0.0001), (Be) CHMDI(10), water_NaOH (p = 0.0000), (Bf) IPDI(5), thermo_NaOH(0.0007), (Bg) IPDI(10), thermo_NaOH (p = 0.005366), (Bh) IPDI(10), water_NaOH (p = 0.0049); (C(a-h)) CHMDI(5), control vs. (Ca) CHMDI(2.5)_IPDI(2.5), water_NaOH (p = 0.0080), (Cb) CHMDI(2.5)_IPDI(2.5), thermo_NaOH (p = 0.0055), (Cc) CHMDI(5), thermo_NaOH (p = 0.0000), (Cd) CHMDI(10), thermo_NaOH (p = 0.0000), (Ce) CHMDI(10), water_NaOH (p = 0.0000), (Cf) IPDI(5), thermo_NaOH(0.0002), (Cg) IPDI(10), thermo_NaOH (p = 0.0013), (Ch) IPDI(10), water_NaOH (p = 0.0011); (D(a–d)) CHMDI(10), control vs. (Da) CHMDI(5), thermo_NaOH (p = 0.0022); (Db) CHMDI(10), thermo_NaOH (p = 0.0016), (Dc) CHMDI(10), water_NaOH (p = 0.0001), (Dd) IPDI(5), thermo_NaOH (p = 0.0106); (E(a–g)) IPDI(5), control vs. (Ea) CHMDI(2.5)_IPDI(2.5), thermo_NaOH (p = 0.0401), (Eb) CHMDI(5), thermo_NaOH (p = 0.0003), (Ec) CHMDI(10), thermo_NaOH (p = 0.0002), (Ed) CHMDI(10), water_NaOH (p = 0.0000), (Ee) IPDI(5), thermo_NaOH(0.0016), (Ef) IPDI(10), thermo_NaOH (p = 0.0107), (Eg) IPDI(10), water_NaOH (p = 0.0097); (F(a–d)) IPDI(10), control vs. (Fa) CHMDI(5), thermo_NaOH (p = 0.0022); (Fb) CHMDI(10), thermo_NaOH (p = 0.0016), (Fc) CHMDI(10), water_NaOH (p = 0.0001), (Fd) IPDI(5), thermo_NaOH (p = 0.0106); (G) CHMDI(5), water_NaOH vs. (G) CHMDI(10), water_NaOH (p = 0.0289).

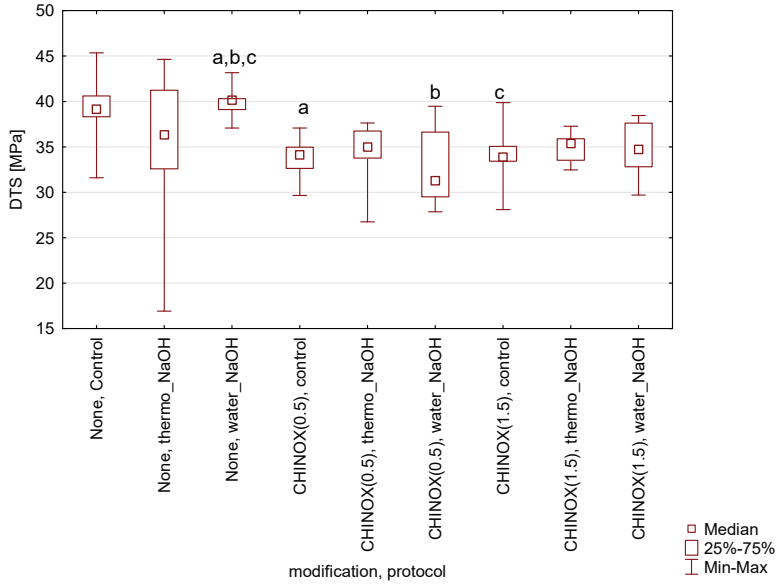


Figure A4. Box-and-whisker plot of the diametral tensile strength (DTS) of the tested materials. Statistically significant differences were detected between the following: (a,b,c) None, water_NaOH vs. (a) CHINOX(0.5), control (p = 0.0440); (b) CHINOX(0.5), water_NaOH (p = 0.0170), (c) CHINOX(1.5), control (p = 0.0340).

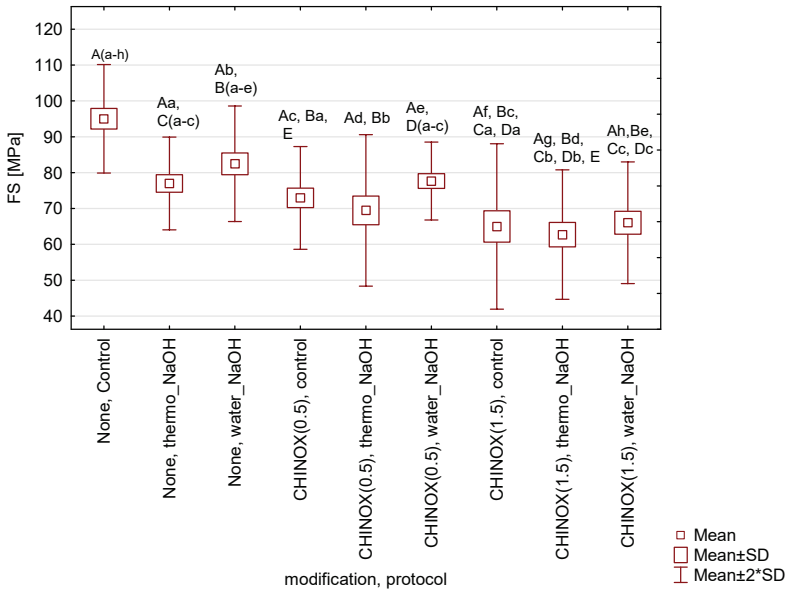


Figure A5. Box-and-whisker plot of the flexural strength (FS) of the tested materials. Statistically significant differences were detected between the following: A(a–h)) None, control vs. (Aa) None, thermo_NaOH (p = 0.0002), (Ab) None, water_NaOH (p = 0.0075),(Ac) CHINOX(0.5), control (p = 0.0000), (Ad) CHINOX(0.5), thermo_NaOH (p = 0.0000), (Ae) CHINOX(0.5), water_NaOH (p = 0.0003), (Af) CHINOX(1.5), control (p = 0.0000), (Ag) CHINOX(1.5), thermo_NaOH (p = 0.0000), (Ah) CHINOX(1.5), water_NaOH (p = 0.0000); B(a–e) None, water_NaOH vs. (Ba) CHINOX(0.5), control (p = 0.0389), (Bb) CHINOX(0.5), thermo_NaOH (p = 0.0057), (Bc) CHINOX(1.5), control (p = 0.0003), (Bd) CHINOX(1.5), thermo_NaOH (p = 0.0001), (Be) CHINOX(1.5), water_NaOH (p = 0.0006); C(a–c) None, thermo_NaOHvs. (Ca) CHINOX(1.5), control (p = 0.0104), (Cb) CHINOX(1.5), thermo_NaOH (p = 0.0026); (Cc) CHINOX(1.5), water_NaOH (p = 0.0187); D(a–c) CHINOX(0.5), water_NaOH vs. (Da) CHINOX(1.5), control (p = 0.0070), (Cb) CHINOX(1.5), thermo_NaOH (p = 0.0017); (Cc) CHINOX(1.5), water_NaOH (p = 0.0128); (E) CHINOX(0.5), control vs. (E) CHINOX(1.5), thermo_NaOH (p = 0.0272).

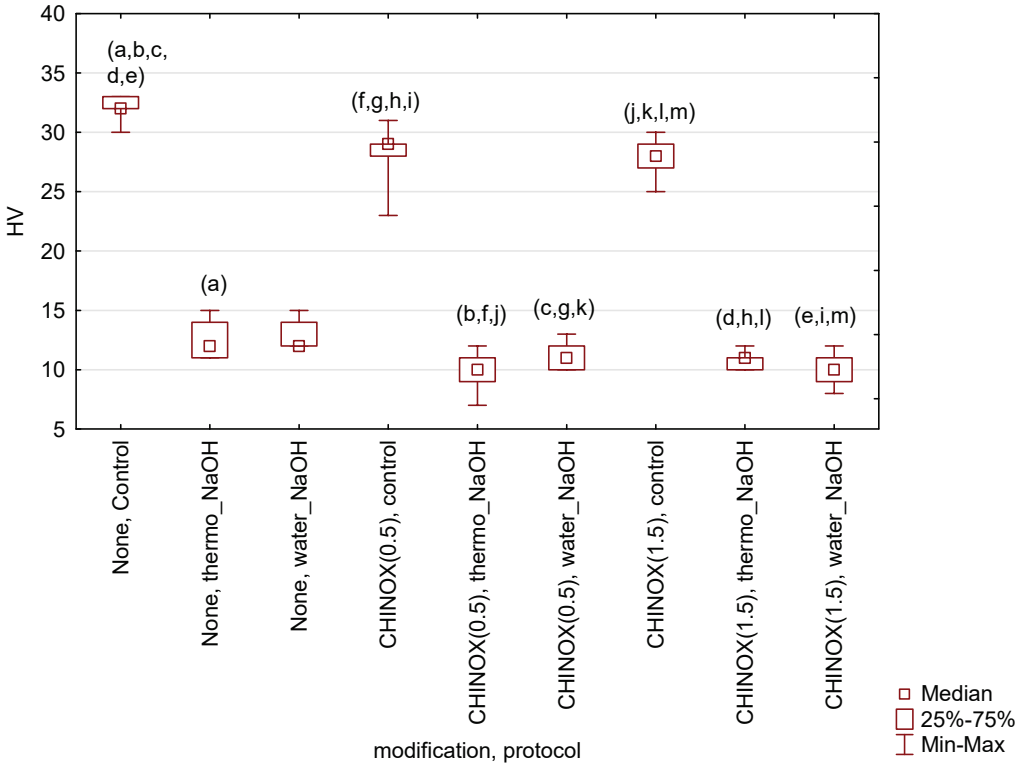


Figure A6. Box-and-whisker plot of the Vickers hardness (HV) of the tested materials. Statistically significant differences were detected between the following: (a,b,c,d,e) None, Control vs.(a) None, thermo_NaOH ($p = 0.0237$), (b) CHINOX(0.5), thermo_NaOH ($p = 0.0000$), (c) CHINOX(0.5), water_NaOH ($p = 0.0001$), (d) CHINOX(1.5), thermo_NaOH ($p = 0.0000$), (e) CHINOX(1.5), water_NaOH ($p = 0.0000$); (f,g,h,i) CHINOX(0.5), control vs. (f) CHINOX(0.5), thermo_NaOH($p = 0.0007$), (g) CHINOX(0.5), water_NaOH ($p = 0.0143$), (h) CHINOX(1.5), thermo_NaOH($p = 0.0059$), (i) CHINOX(1.5), water_NaOH ($p = 0.0006$); (j,k,l,m) CHINOX(1.5), control vs. (j) CHINOX(0.5), thermo_NaOH ($p = 0.0018$), (k) CHINOX(0.5), water_NaOH ($p = 0.0335$), (l) CHINOX(1.5), thermo_NaOH ($p = 0.0146$), (m) CHINOX(1.5), water_NaOH ($p = 0.0013$).

References

1. Forss, H.; Widström, E. Reasons for restorative therapy and the longevity of restorations in adults. *Acta Odontol. Scand.* **2004**, *62*, 82–86. [CrossRef] [PubMed]
2. Brunthaler, A.; König, F.; Lucas, T.; Sperr, W.; Schedle, A. Longevity of direct resin composite restorations in posterior teeth. *Clin. Oral Investig.* **2003**, *7*, 63–70. [CrossRef] [PubMed]
3. Kubo, S. Longevity of resin composite restorations. *Jpn. Dent. Sci. Rev.* **2011**, *47*, 43–55. [CrossRef]
4. Aminoroaya, A.; Neisiany, R.E.; Khorasani, S.N.; Panahi, P.; Das, O.; Madry, H.; Cucchiarini, M.; Ramakrishna, S. A review of dental composites: Challenges, chemistry aspects, filler influences, and future insights. *Compos. Part B Eng.* **2021**, *216*, 108852. [CrossRef]
5. Wang, R.; Zhang, M.; Liu, F.; Bao, S.; Wu, T.; Jiang, X.; Zhang, Q.; Zhu, M. Investigation on the physical-mechanical properties of dental resin composites reinforced with novel bimodal silica nanostructures. *Mater. Sci. Eng. C* **2015**, *50*, 266–273. [CrossRef]
6. Wang, R.; Bao, S.; Liu, F.; Jiang, X.; Zhang, Q.; Sun, B.; Zhu, M. Wear behavior of light-cured resin composites with bimodal silica nanostructures as fillers. *Mater. Sci. Eng. C* **2013**, *33*, 4759–4766. [CrossRef] [PubMed]
7. Finer, Y.; Santerre, J.P. Influence of silanated filler content on the biodegradation of bisGMA/TEGDMA dental composite resins. *J. Biomed. Mater. Res. Part A* **2006**, *79*, 963–973. [CrossRef]
8. Aydınoğlu, A.; Yoruç, A.B.H. Effects of silane-modified fillers on properties of dental composite resin. *Mater. Sci. Eng. C* **2017**, *79*, 382–389. [CrossRef]
9. Antonucci, J.M.; Dickens, S.H.; Fowler, B.O.; Xu, H.H.K.; McDonough, W.G. Chemistry of Silanes: Interfaces in Dental Polymers and Composites. *J. Res. Natl. Inst. Stand. Technol.* **2005**, *110*, 541–558. [CrossRef]
10. Karmaker, A.; Prasad, A.; Sarkar, N.K. Characterization of adsorbed silane on fillers used in dental composite restoratives and its effect on composite properties. *J. Mater. Sci. Mater. Med.* **2007**, *18*, 1157–1162. [CrossRef]
11. Karabela, M.M.; Sideridou, I.D. Effect of the structure of silane coupling agent on sorption characteristics of solvents by dental resin-nanocomposites. *Dent. Mater.* **2008**, *24*, 1631–1639. [CrossRef]

12. Karkanis, S.; Nikolaidis, A.K.; Koulaouzidou, E.A. Effect of Silica Nanoparticles Silanized by Functional/Functional or Functional/Non-Functional Silanes on the Physicochemical and Mechanical Properties of Dental Nanocomposite Resins. *Appl. Sci.* **2022**, *12*, 159. [CrossRef]
13. Gornig, D.C.; Maletz, R.; Ottl, P.; Warkentin, M. Influence of artificial aging: Mechanical and physicochemical properties of dental composites under static and dynamic compression. *Clin. Oral Investig.* **2022**, *26*, 1491–1504. [CrossRef]
14. Szczesio-Wlodarczyk, A.; Fronczek, M.; Ranoszek-Soliwoda, K.; Grobelny, J.; Sokolowski, J.; Bociong, K. The First Step in Standardizing an Artificial Aging Protocol for Dental Composites—Evaluation of Basic Protocols. *Molecules* **2022**, *27*, 3511. [CrossRef]
15. Jamali, R.; Bordbar-Khiabani, A.; Yarmand, B.; Mozafari, M.; Kolahi, A. Effects of co-incorporated ternary elements on biocorrosion stability, antibacterial efficacy, and cytotoxicity of plasma electrolytic oxidized titanium for implant dentistry. *Mater. Chem. Phys.* **2022**, *276*, 125436. [CrossRef]
16. Lee, J.; Son, C.; Kim, S.; Mohammed, N.B.; Daily, Z.A.; Alsharbaty, M.H.; Abullais, S.S. Effect of PMMA sealing treatment on the corrosion behavior of plasma electrolytic oxidized titanium dental implants in fluoride-containing saliva solution Effect of PMMA sealing treatment on the corrosion behavior of plasma electrolytic oxidized titanium. *Mater. Res. Express* **2022**, *9*, 125401.
17. Oja, J.; Lassila, L.; Vallittu, P.K.; Garoushi, S. Effect of Accelerated Aging on Some Mechanical Properties and Wear of Different Commercial Dental Resin Composites. *Materials* **2021**, *14*, 2769. [CrossRef]
18. Barszczewska-Rybarek, I.M. Characterization of urethane-dimethacrylate derivatives as alternative monomers for the restorative composite matrix. *Dent. Mater.* **2014**, *30*, 1336–1344. [CrossRef]
19. Gajewski, V.E.S.; Pfeifer, C.S.; Fróes-Salgado, N.R.G.; Boaro, L.C.C.; Braga, R.R. Monomers used in resin composites: Degree of conversion, mechanical properties and water sorption/solubility. *Braz. Dent. J.* **2012**, *23*, 508–514. [CrossRef]
20. Holcapkova, P.; Stloukal, P.; Kucharczyk, P.; Omastova, M.; Kovalcik, A. Anti-hydrolysis effect of aromatic carbodiimide in poly(lactic acid)/wood flour composites. *Compos. Part A* **2017**, *103*, 283–291. [CrossRef]
21. Gonyalez-Bonet, A.; Kaufman, G.; Yang, Y.; Wong, C.; Jackson, A.; Huyang, G.; Bowen, R.; Sun, J. Preparation of Dental Resins Resistant to Enzymatic and Hydrolytic Degradation in Oral Environments. *Biomacromolecules* **2016**, *118*, 3381–3388. [CrossRef]
22. Fugolin, A.P.P.; Pfeifer, C.S. New Resins for Dental Composites. *J. Dent. Res.* **2017**, *96*, 1085–1091. [CrossRef]
23. Randolph, L.D.; Palin, W.M.; Leloup, G.; Leprince, J.G. Filler characteristics of modern dental resin composites and their influence on physico-mechanical properties. *Dent. Mater.* **2016**, *32*, 1586–1599. [CrossRef]
24. Yadav, R.; Kumar, M. Dental restorative composite materials: A review. *J. Oral Biosci.* **2019**, *61*, 78–83. [CrossRef]
25. Sideridou, I.; Tserki, V.; Papanastasiou, G. Effect of chemical structure on degree of conversion in light-cured dimethacrylate-based dental resins. *Biomaterials* **2002**, *23*, 1819–1829. [CrossRef] [PubMed]
26. Barszczewska-Rybarek, I.; Jurczyk, S. Comparative Study of Structure-Property Relationships in Polymer Networks Based on Bis-GMA, TEGDMA and Various Urethane-Dimethacrylates. *Materials* **2015**, *8*, 1230–1248. [CrossRef] [PubMed]
27. Müller, J.A.; Rohr, N.; Fischer, J. Evaluation of ISO 4049: Water sorption and water solubility of resin cements. *Eur. J. Oral Sci.* **2017**, *125*, 141–150. [CrossRef]
28. AL-Rawas, M.; Johari, Y.; Mohamad, D.; Khamis, M.F.; Ahmad, W.M.A.W.; Ariffin, Z.; Husein, A. Water sorption, solubility, degree of conversion, and surface hardness and topography of flowable composite utilizing nano silica from rice husk. *J. Mater. Res. Technol.* **2021**, *15*, 4173–4184. [CrossRef]
29. Pieniak, D.; Przystupa, K.; Walczak, A.; Niewczas, A.M.; Krzyzak, A.; Bartnik, G.; Gil, L.; Lonkwic, P. Hydro-thermal fatigue of polymer matrix composite biomaterials. *Materials* **2019**, *12*, 3650. [CrossRef]
30. Pala, K.; Tekçe, N.; Tuncer, S.; Demirci, M.; Öznurhan, F.; Serim, M. Flexural strength and microhardness of anterior composites after accelerated aging. *J. Clin. Exp. Dent.* **2017**, *9*, e424–e430. [CrossRef]
31. Boussès, Y.; Brulat-bouchard, N.; Bouchard, P. A numerical, theoretical and experimental study of the effect of thermocycling on the matrix-filler. *Dent. Mater.* **2021**, *37*, 772–782. [CrossRef]
32. Ferracane, J.L.; Berge, H.X.; Condon, J.R. In vitro aging of dental composites in water–effect of degree of conversion, filler volume, and filler/matrix coupling. *J. Biomed. Mater. Res.* **1998**, *42*, 465–472. [CrossRef]
33. Krüger, J.; Maletz, R.; Ottl, P.; Warkentin, M. In vitro aging behavior of dental composites considering the influence of filler content, storage media and incubation time. *PLoS ONE* **2018**, *13*, e0195160. [CrossRef] [PubMed]
34. Sarkar, N.K. Internal corrosion in dental composite wear: Its Significance and Simulation. *J. Biomed. Mater. Res.* **2000**, *53*, 371–380. [CrossRef]
35. Szczesio-Wlodarczyk, A.; Sokolowski, J.; Kleczewska, J.; Bociong, K. Ageing of dental composites based on methacrylate resins—A critical review of the causes and method of assessment. *Polymers* **2020**, *12*, 882. [CrossRef]
36. Delaviz, Y.; Finer, Y.; Santerre, J.P. Biodegradation of resin composites and adhesives by oral bacteria and saliva: A rationale for new material designs that consider the clinical environment and treatment challenges. *Dent. Mater.* **2014**, *30*, 16–32. [CrossRef]
37. Al Sunbul, H.; Silikas, N.; Watts, D.C. Surface and bulk properties of dental resin- composites after solvent storage. *Dent. Mater.* **2016**, *32*, 987–997. [CrossRef]
38. Moon, J.-D.; Seon, E.-M.; Son, S.-A.; Jung, K.-H.; Kwon, Y.-H.; Park, J.-K. Effect of immersion into solutions at various pH on the color stability of composite resins with different shades. *Restor. Dent. Endod.* **2015**, *40*, 270. [CrossRef]
39. Palin, W.M.; Fleming, G.J.P.; Burke, F.J.T.; Marquis, P.M.; Randall, R.C. The influence of short and medium-term water immersion on the hydrolytic stability of novel low-shrink dental composites. *Dent. Mater.* **2005**, *21*, 852–863. [CrossRef]

40. Ghavami-Lahiji, M.; Firouzmanesh, M.; Bagheri, H.; Jafarzadeh Kashi, T.S.; Razazpour, F.; Behroozibakhsh, M. The effect of thermocycling on the degree of conversion and mechanical properties of a microhybrid dental resin composite. *Restor. Dent. Endod.* **2018**, *43*, e26. [CrossRef]
41. Chadwick, R.G.; McCabe, J.F.; Walls, A.W.G.; Storer, R. The effect of storage media upon the surface microhardness and abrasion resistance of three composites. *Dent. Mater.* **1990**, *6*, 123–128. [CrossRef]
42. Porfyris, A.; Vasilakos, S.; Zotiadis, C.; Papaspyrides, C.; Moser, K.; Van Der Schueren, L.; Buyle, G.; Pavlidou, S.; Vouyiouka, S. Accelerated ageing and hydrolytic stabilization of poly(lactic acid) (PLA) under humidity and temperature conditioning. *Polym. Test.* **2018**, *68*, 315–332. [CrossRef]
43. Stloukal, P.; Jandikova, G.; Koutny, M.; Sedla, V. Carbodiimide additive to control hydrolytic stability and biodegradability of PLA. *Polym. Test.* **2016**, *54*, 19–28. [CrossRef]
44. Barszczewska-rybarek, I.; Gibas, M.; Kurcok, M. Evaluation of the network parameter in aliphatic poly(urethane dimethacrylate)s by dynamic thermal analysis. *Polymer* **2000**, *41*, 3129–3135. [CrossRef]
45. Szczesio-Wlodarczyk, A.; Kopacz, K.; Szynkowska-Jozwik, M.I.; Sokolowski, J.; Bociong, K. An Evaluation of the Hydrolytic Stability of Selected Experimental Dental Matrices and Composites. *Materials* **2022**, *15*, 5055. [CrossRef]

Disclaimer/Publisher's Note: The statements, opinions and data contained in all publications are solely those of the individual author(s) and contributor(s) and not of MDPI and/or the editor(s). MDPI and/or the editor(s) disclaim responsibility for any injury to people or property resulting from any ideas, methods, instructions or products referred to in the content.

International Journal of
Molecular Sciences

MDPI

Article

Assessment of Inhibition of Biofilm Formation on Non-Thermal Plasma-Treated TiO_2 Nanotubes

Min-Kyung Ji [1,†], Seon-Ki Lee [2,†], Hee-Seon Kim [3], Gye-Jeong Oh [4], Hoonsung Cho [5,*] and Hyun-Pil Lim [3,*]

1 Dental 4D Research Center, Chonnam National University, 33 Yongbong-ro, Buk-gu, Gwangju 61186, Republic of Korea
2 Department of Prosthodontics, Daejeon Dental Hospital, Wonkwang University, 77 Dunsan-ro, Seo-gu, Daejeon 35233, Republic of Korea
3 Department of Prosthodontics, School of Dentistry, Chonnam National University, 33 Yongbong-ro, Buk-gu, Gwangju 61186, Republic of Korea
4 Biomedical Evaluation & Research Center, Chonnam National University, 33 Yongbong-ro, Buk-gu, Gwangju 61186, Republic of Korea
5 School of Materials Science & Engineering, Chonnam National University, 77 Yongbong-ro, Buk-gu, Gwangju 61186, Republic of Korea
* Correspondence: cho.hoonsung@jnu.ac.kr (H.C.); mcnihil@jnu.ac.kr (H.-P.L.); Tel.:+82-62-530-1717 (H.C.); +82-62-530-5577 (H.-P.L.)
† These authors contributed equally to this work.

Abstract: Peri-implantitis is an inflammatory disease similar to periodontitis, caused by biofilms formed on the surface of dental implants. This inflammation can spread to bone tissues and result in bone loss. Therefore, it is essential to inhibit the formation of biofilms on the surface of dental implants. Thus, this study examined the inhibition of biofilm formation by treating TiO_2 nanotubes with heat and plasma. Commercially pure titanium specimens were anodized to form TiO_2 nanotubes. Heat treatment was performed at 400 and 600 °C, and atmospheric pressure plasma was applied using a plasma generator (PGS-200, Expantech, Suwon, Republic of Korea). Contact angles, surface roughness, surface structure, crystal structure, and chemical compositions were measured to analyze the surface properties of the specimens. The inhibition of biofilm formation was assessed using two methods. The results of this study showed that the heat treatment of TiO_2 nanotubes at 400 °C inhibited the adhesion of *Streptococcus mutans* (*S. mutans*), associated with initial biofilm formation, and that heat treatment of TiO_2 nanotubes at 600 °C inhibited the adhesion of *Porphyromonas gingivalis* (*P. gingivalis*), which causes peri-implantitis. Applying plasma to the TiO_2 nanotubes heat-treated at 600 °C inhibited the adhesion of *S. mutans* and *P. gingivalis*.

Keywords: TiO_2 nanotube; heat treatment; non-thermal plasma treatment; peri-implantitis; biofilms

Citation: Ji, M.-K.; Lee, S.-K.; Kim, H.-S.; Oh, G.-J.; Cho, H.; Lim, H.-P. Assessment of Inhibition of Biofilm Formation on Non-Thermal Plasma-Treated TiO_2 Nanotubes. *Int. J. Mol. Sci.* **2023**, *24*, 3335. https://doi.org/10.3390/ijms24043335

Academic Editor: Mary Anne Melo

Received: 6 January 2023
Revised: 1 February 2023
Accepted: 2 February 2023
Published: 7 February 2023

Copyright: © 2023 by the authors. Licensee MDPI, Basel, Switzerland. This article is an open access article distributed under the terms and conditions of the Creative Commons Attribution (CC BY) license (https://creativecommons.org/licenses/by/4.0/).

1. Introduction

Bacterial colonies that cause periodontitis are formed on the surface of dental implants within two weeks after being placed and exposed to an oral environment. Subgingival bacterial flora is established within four weeks, resulting in tissue inflammation and, thus, dental implant failure [1]. Since dental implants, unlike natural teeth, do not have any blood vessels or nervous tissues, patients do not feel any particular pain associated with peri-implantitis, and the inflammation is highly likely to spread to bone tissues and result in bone loss [2]. Therefore, it is essential to increase the bioactivity of the surface of the implants and suppress the formation of biofilms in order to maintain dental implants.

Various attempts have been made to modify the surface of dental implants to suppress bacterial growth and improve the adhesion of osteocytes [3]. Anodization is one method of modifying the titanium surface [4]. A thin, rough, porous amorphous TiO_2 oxide film is electrochemically created on the titanium surface to modify its physical properties. Once amorphous TiO_2 nanotubes are formed on the surface of the titanium implants

via anodization, their surface area is expanded, and cell adhesion, proliferation, and differentiation are improved, which was reported to increase bone–implant integration, accelerate bone formation and reduce treatment times [5–7]. Peng et al. [8] reported that the initial adhesion and colonization of *Staphylococcus epidermidis* on TiO_2 nanotubes were significantly reduced when compared with polished or acid-etched titanium. In addition, heat treatment of the titanium surface changes the crystal structure of the TiO_2 films and suppresses the adhesion of bacteria without inhibiting the activity of cells [9,10]. Del Curto et al. [11] reported that the adhesion of bacteria was inhibited on the titanium surface by modifying its amorphous oxide film into an anatase crystal structure through heat treatment without inhibiting the activity of cells. However, in another study, osseointegration was further improved on a rutile crystal structure surface [12]. Furthermore, opinions are divided on whether anatase or rutile is a better TiO_2 oxide film for titanium implants. The adhesion of bacteria and the activity of cells are affected not only by the physical properties of dental implants, such as surface structure and roughness, but also by chemical properties, such as surface-free energy and hydrophilicity [5,6,13].

The chemical properties of dental implants, such as surface-free energy and hydrophilicity, play a critical role in the interaction between osteocytes and proteins and thus improve the treatment of cuts in the early stage of treatment [14,15]. Sawase et al. [16] found that the surface of dental implants with improved hydrophilicity showed better osseointegration than that of general implants. These results indicated that the chemical properties of the surface of dental implants are more important factors for the activity of cells than their surface structure.

Plasma is a gas with an energy that is loosely and partially ionized [17] and is used to sterilize the surfaces of dental equipment and biomaterials and to modify the surfaces of implants [18,19]. By applying plasma, the oxide layer on the surface of implants is modified due to the chemical properties of the applied gas without any change in the surface structure, which results in chemical changes, such as hydrophilicity [20]. Yoo et al. [21] reported that the shape of bacterial colonies cultured on the surface of titanium treated with plasma was changed and that over 80% of bacteria were killed. In addition, Duske et al. [13] found that plasma decreased contact angles and thus increased hydrophilicity, improving the early adhesion of osteoblasts and osseointegration.

Even though the chemical properties of the surface of dental implants are as important as their surface structure in inhibiting the adhesion of bacteria and the activity of cells, studies have been conducted only to evaluate changes in the surface structure and roughness of dental implants. Authors have been mostly focused on changes in the activity of cells and osseointegration after applying atmospheric pressure plasma to the surface of implants. However, there has been no study published on the inhibition of peri-implantitis. Moreover, previous studies on biofilm inhibition of TiO_2 nanostructures use antimicrobial agents (e.g., Ag, Au) on TiO_2 nanostructures [22,23]. This study created TiO_2 nanotubes on the titanium surface to change the physical properties of the surface of dental implants. In addition, heat treatment and atmospheric pressure plasma were applied to change the chemical properties of the surface of dental implants.

This study examined the effects of heat and plasma treatment on the surface of TiO_2 nanotubes on biofilm formation.

2. Results

2.1. Surface Characteristics

2.1.1. Contact Angles

The contact angle of the non-heat-treated (H0), 400 °C heat-treated (H400), and 600 °C heat-treated (H600) samples was 19.5 ± 2°, 14.2 ± 2°, and 18.0 ± 2°, respectively. After the plasma treatment, the contact angle of all groups was reduced. The contact angle of the non-heat-treated plasma-treated samples (H0P) was 3.3 ± 6°, and the contact angle of the 400 °C heat-treated plasma-treated samples (H400P) and the 600 °C heat-treated

plasma-treated samples (H600P) was reduced to the point that could not be measured (Figure 1).

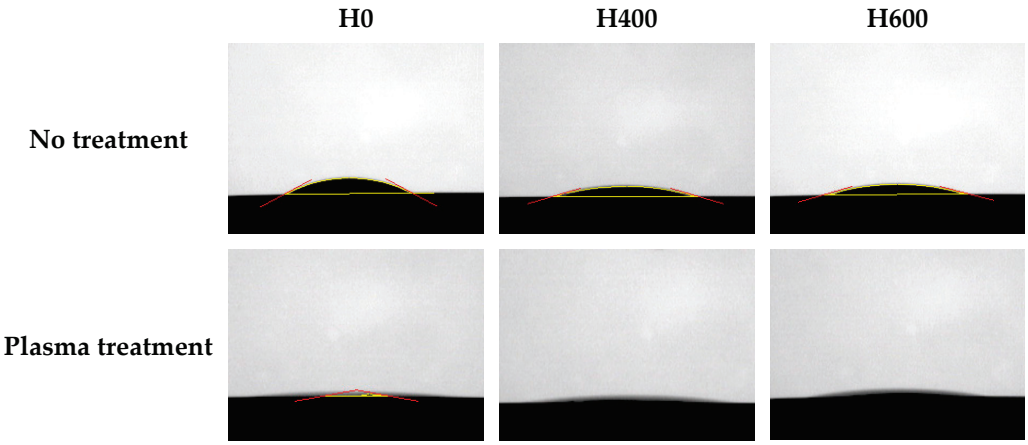


Figure 1. The water contact angle of the samples. The yellow line indicates the solid-liquid interface and the liquid-fluid interface. The red line indicates the contact angle.

2.1.2. Surface Structures

There were no changes in the height and surface structures of the TiO_2 nanotubes after the heat treatment at 400 °C. However, when the samples were heat-treated at 600 °C, the diameter was decreased to 91.2 ± 1 nm, and their height was reduced to 498.0 ± 7 nm (Figure 2, Table 1). There was no change in the surface structure of the samples before or after the plasma treatment.

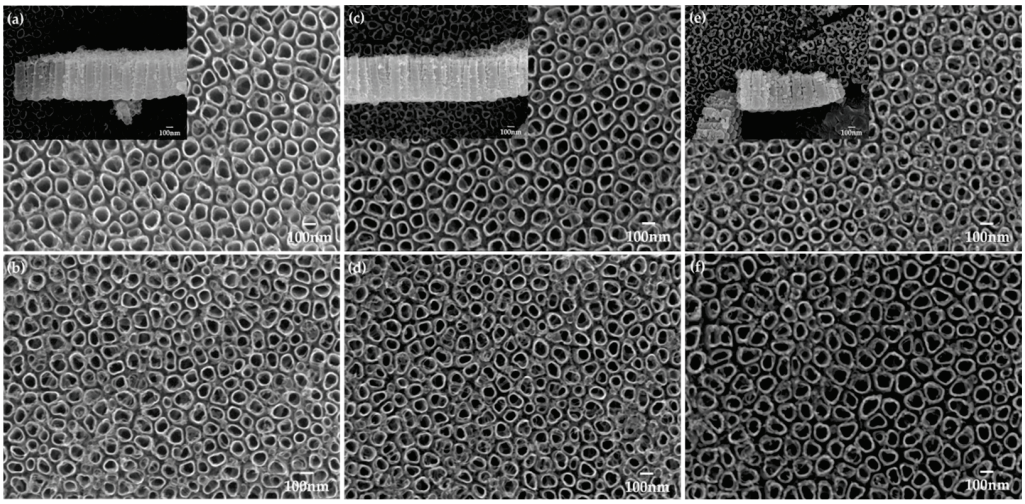


Figure 2. Field emission-scanning electron microscopy images on (**a**) H0, (**b**) H0P, (**c**) H400, (**d**) H400P, (**e**) H600, and (**f**) H600P samples (magnification = 50,000). The mini-subfigures of the left-top corner indicate the height of TiO_2 nanotubes.

Table 1. The mean value and standard deviation of TiO_2 nanotubes.

Group	Diameter (nm)	Thickness (nm)
H0	111.3 ± 2	522.6 ± 4
H400	106.7 ± 1	500.8 ± 4
H600	91.2 ± 1	498.0 ± 7

2.1.3. X-ray Diffraction (XRD) Analysis

Figure 3 shows the X-ray diffraction patterns of samples. The H400 samples showed titanium reflections at (010), (002), (011), (012), (110), (013) and (112), and TiO_2 anatase reflections at (011), (020), (015), and (121). The H600 samples showed a different peak pattern; however, the same reflections were observed as the H400 samples plus new TiO_2 rutile reflections at (110), (011), (111), (120), and (121). The analysis results of H600 samples showed that the titanium, TiO_2 anatase and rutile crystal structures were mixed.

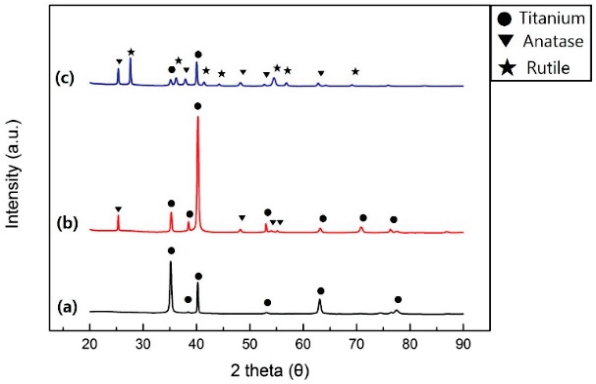


Figure 3. X-ray diffraction patterns of specimens. (**a**) H0, (**b**) H400, and (**c**) H600 samples.

2.1.4. X-ray Photoelectron Spectroscopy (XPS) Analysis

Figure 4 shows the XPS high-resolution spectra of C1s, O1s and Ti2p on samples. Out of the three C1s peaks (285.0 eV, 286.7 eV, and 288.7 eV) detected in the H0 samples, the 285.0 eV peak represents C-C or C-H bonded carbon, the 286.7 eV peak represents C-O bonded carbon, and the 288.7 eV peak represents C=O bonded carbon. Out of the three O1s peaks (529.9 eV, 531.3 eV, and 532.6 eV), the 529.9 eV and 531.3 eV peaks are associated with Ti-O and O-H bonds, while the 532.6 eV peak is associated with C-O or C=O bonds. In the case of Ti2p, two distinct peaks were observed at 464.1 eV and 458.3 eV, representing TiO_2.

After heat treatment, the O1s peaks (530.0 eV, 531.5 eV, and 532.6 eV) and the Ti2p peaks (464.5 eV and 458.7 eV) of the H400 samples, as well as the O1s peaks (530.1 eV, 531.6 eV, and 532.7 eV) and the Ti2p peaks (464.7 eV and 458.9 eV) of the H600 samples were slightly shifted to a higher bonding energy.

After plasma treatment, the C1s peaks were reduced, and the low peaks between 292.1 eV and 281.2 eV were slightly shifted to a higher bonding energy. Another C1s peak was observed in 283.6 eV and 281.9 eV, which are associated with C=C and C-Ti. Two additional O1s peaks (528.6 eV and 527.2 eV) were observed, which represent O^{2-}. The Ti2p1/2 and Ti2p3/2 peaks were observed at 461.7 eV and 456.1 eV, respectively, which are associated with TiO_2 and Ti_2O_3. Another C1s peak in the H400P samples was observed at 289.7 eV, which is associated with O-C=O. Moreover, another Ti2p peak in the H600P samples was observed at 460.9 eV, which is associated with TiOx, a titanium compound.

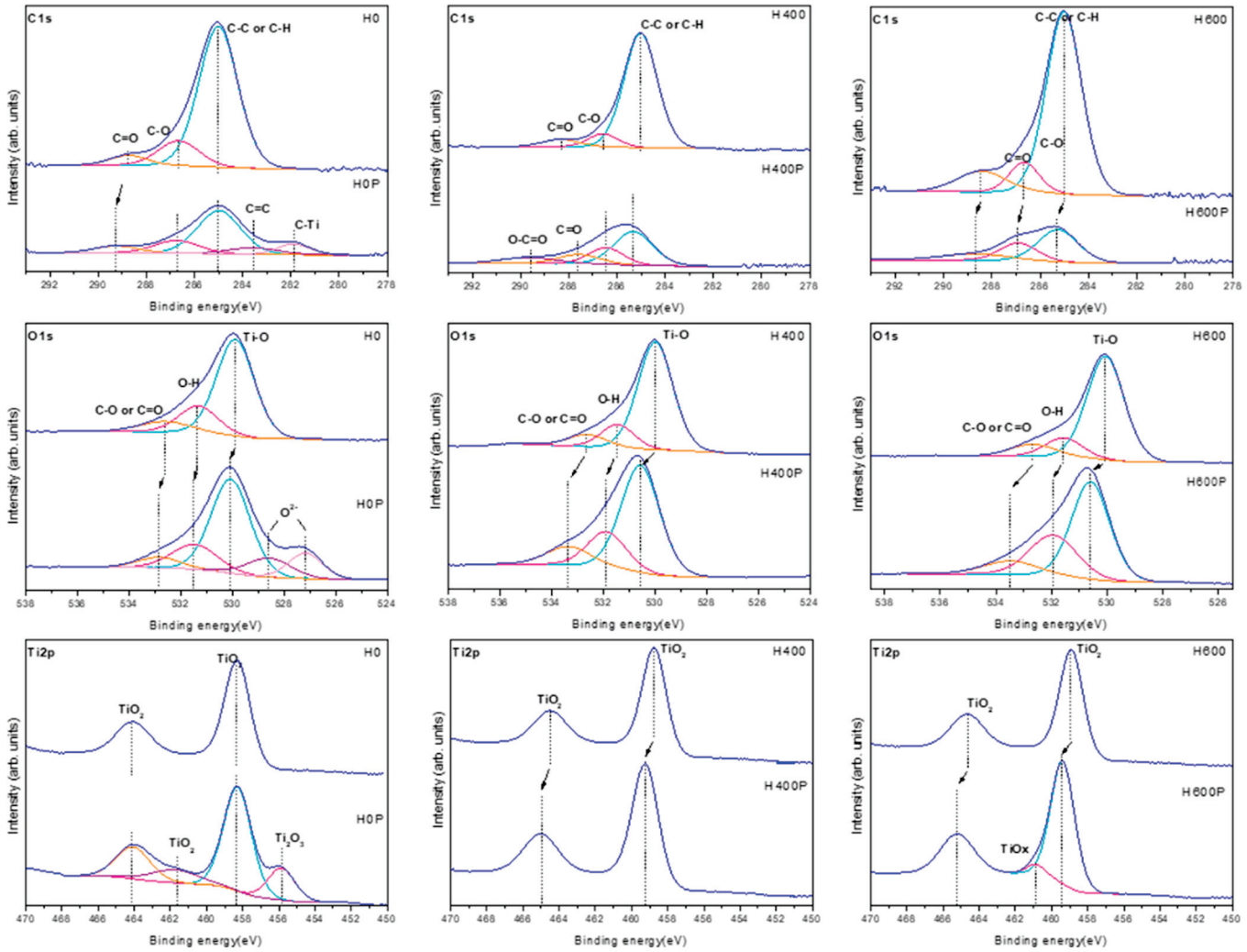


Figure 4. XPS high-resolution spectra of C1s, O1s and Ti2p on samples.

2.2. Assessment of Capacity to Inhibit Biofilm Formation

2.2.1. *Streptococcus mutans*

The changes in the thickness of *S. mutans* biofilms after the heat and plasma treatments to the TiO_2 nanotubes are shown in Table 2 and Figure 5.

Compared with the H400 samples, the H0 and H600 samples showed a significantly smaller thickness of *S. mutans* biofilms ($p < 0.017$). There were statistically significant decreases in the thickness of *S. mutans* biofilms in all the groups after plasma treatment ($p < 0.05$).

Table 2. The biofilm thickness of *Streptococcus mutans* ($n = 3$).

Group	Biofilm Thickness (μm)		Percentage Thickness Reduction after Plasma Treatment at the Same Heat Treatment (%)
	No Treatment	Plasma Treatment	
H0 [a,b]	38.1 ± 5	11.1 ± 1 *	70.9
H400 [c]	22.1 ± 2	17.4 ± 1 *	21.3
H600 [a,b]	40.9 ± 1	32.9 ± 2 *	19.6

[a, b, c]: Significant at $p < 0.017$ in the column. *: Significant at $p < 0.05$ in the row.

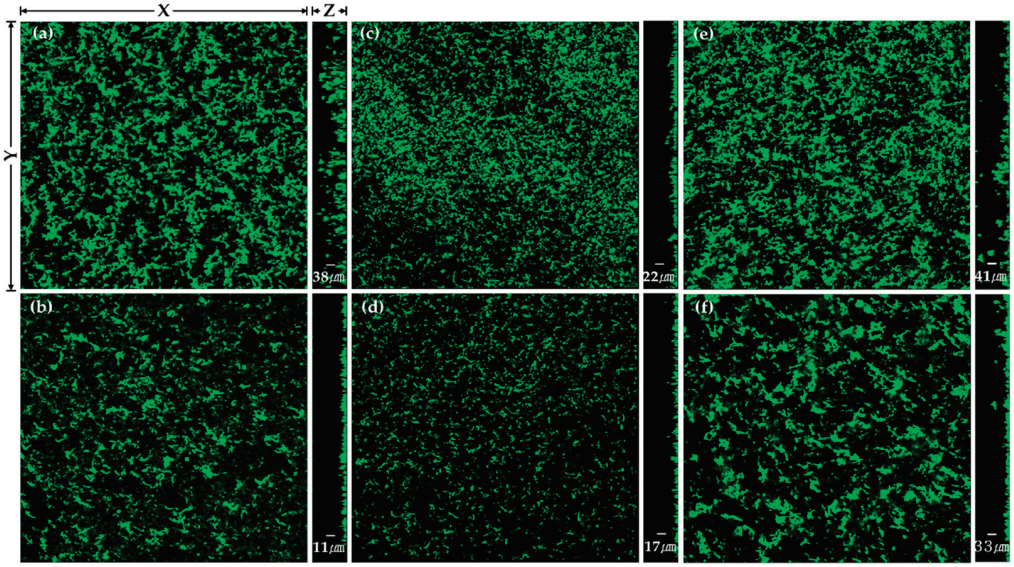


Figure 5. CLSM image of *Streptococcus mutans* biofilm on (**a**) H0, (**b**) H0P, (**c**) H400, (**d**) H400P, (**e**) H600, and (**f**) H600P samples. Green fluorescence indicates viable cells.

2.2.2. *Porphyromonas gingivalis*

The changes in the thickness of *P. gingivalis* biofilms after the heat and plasma treatments to the TiO_2 nanotubes are shown in Table 3 and Figure 6.

Table 3. The biofilm thickness of *Porphyromonas gingivalis* (n = 3).

Group	Biofilm Thickness (μm)		Percentage Thickness Reduction after Plasma Treatment at the Same Heat Treatment (%)
	No Treatment	Plasma Treatment	
H0	25.5 ± 1	30.4 ± 4	−19.2
H400	28.4 ± 4	30.9 ± 2	−8.8
H600	26.4 ± 4	24.5 ± 4	7.2

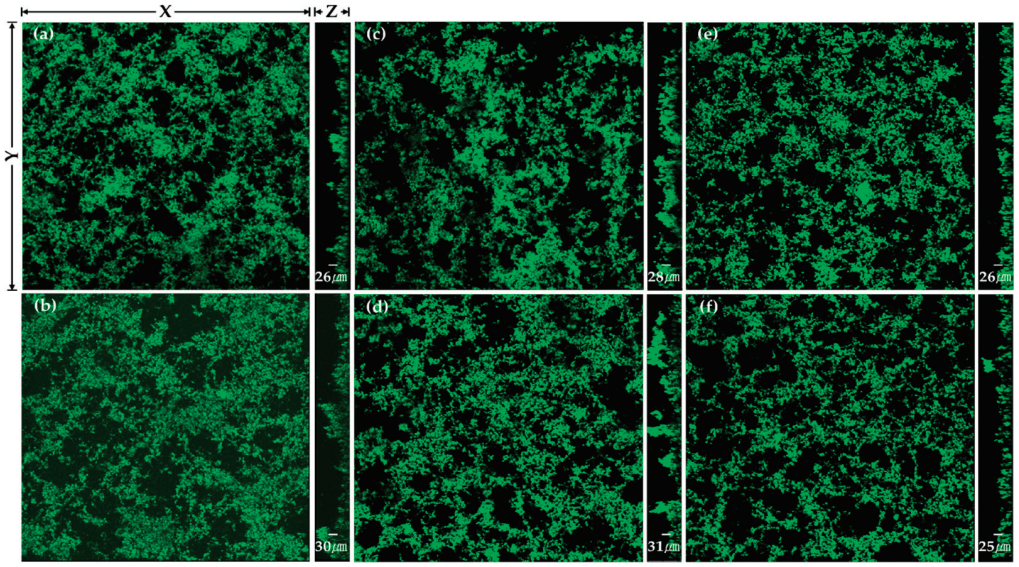


Figure 6. CLSM image of *Porphyromonas gingivalis* biofilm on (**a**) H0, (**b**) H0P, (**c**) H400, (**d**) H400P, (**e**) H600, and (**f**) H600P samples. Green fluorescence indicates viable cells.

There were no statistically significant differences in the thickness of *P. gingivalis* biofilms after the heat treatment ($p > 0.017$). There were also no statistically significant differences in the thickness of *P. gingivalis* biofilms after the plasma treatment ($p > 0.05$).

3. Discussion

It is essential to inhibit the adhesion of bacteria to the surface of dental implants to improve the adhesion between the surface and surrounding tissues. In this study, TiO_2 nanotubes were formed on the titanium surface to increase its surface area. The TiO_2 nanotubes were heat-treated under different conditions to modify the structure of the TiO_2 oxide films. In addition, atmospheric pressure plasma was applied to the TiO_2 nanotubes to change their surface energy and hydrophilicity and, thus, inhibit the formation of biofilms. Figure 7 shows a schematic of a summary of possible events on the plasma-treated TiO_2 nanotube surface. Recently it has been reported that the adhesion and proliferation of osteoblasts were increased on the surface of materials that had nanotube structures, and studies have been conducted to create nano-level structures on the surface of materials [24–26]. Electrochemical anodization can be used to create nano-level tubes on the surface of titanium, and the structure of nanotubes can be changed by controlling certain variables, such as the composition of electrolytes, temperature, and current density [27–29]. In this study, TiO_2 nanotubes were created using the anodic oxidation method suggested by Kim et al. [30] to form a nano-level amorphous TiO_2 oxide film on the surface of the titanium.

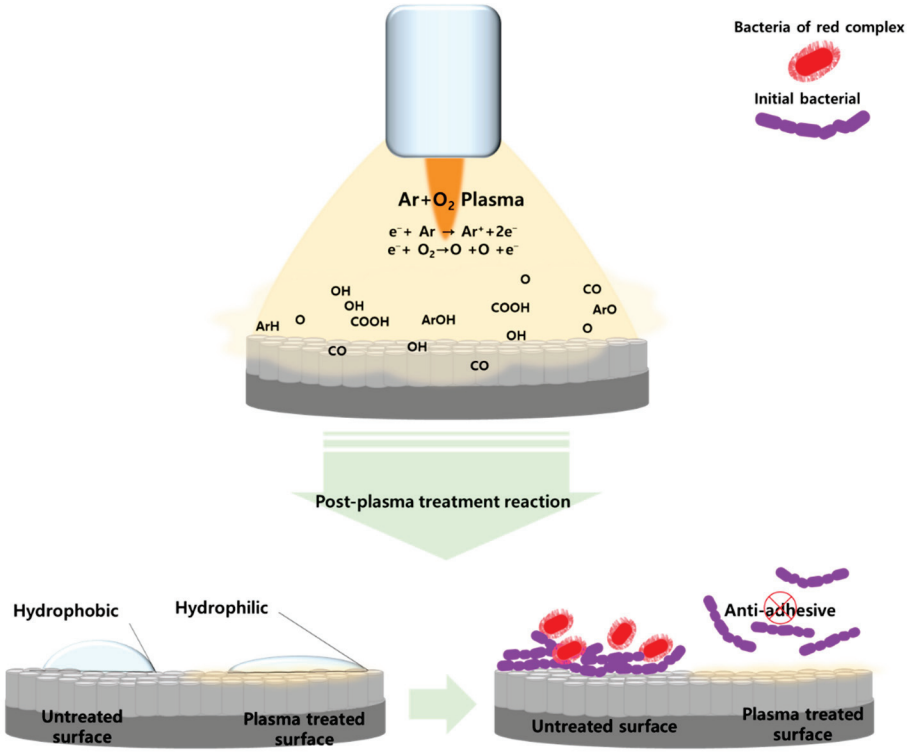


Figure 7. Schematic of a summary of possible events on the plasma-treated TiO_2 nanotube surface.

Heat treatment of titanium can modify the crystal structure of the TiO_2 oxide film. Park et al. [31] reported that heat treatment of 400 °C changed the phase of the amorphous TiO_2 into anatase TiO_2 and that temperatures over 600 °C changed the phase to an intermixed population of anatase and rutile phases with the TiO_2 rutile phase forming a major X-ray peak. Therefore, in this study, the temperature of the heat treatment was set at 400 °C and 600 °C to assess the adhesion of bacteria to amorphous TiO_2, anatase TiO_2, and anatase/rutile mixed-phase TiO_2.

When TiO_2, which has photocatalytic properties, is combined with light, it reacts with H_2O and O_2 and generates photo-generated holes (h+) that have a high oxidizing

power, such as hydroxyl radicals (OH) and superoxide free radicals (O^{2-}) [32]. These photogenerated holes (h+) interact with proteins, nucleic acids, and bacterial cell membranes and can damage the structures of bacteria [33,34]. However, the adhesion of bacteria after heat treatment showed different results with the two species of bacteria. The lowest adhesion of *S. mutans* was seen in the anatase TiO_2 (H400), and the lowest adhesion of *P. gingivalis* was seen in the anatase/rutile mixed TiO_2 (H600). The relative photocatalytic activity differed depending on the crystal structure. Zhang et al. [35] reported that anatase TiO_2 usually exhibited higher photocatalytic activity than rutile TiO_2. In addition to the crystal structure, the metabolism of bacteria is associated with complex factors that control the biointerface and bacterial behaviors. In this study, the adhesion of *S. mutans* onto anatase TiO_2 seemed to be inhibited as the photocatalytic activities that affected the metabolism of *S. mutans* were more strongly dependent on the crystal structure.

Fluoride ions seemed to be detected on every surface due to the anodic oxidation of electrolytes since fluorine in the anodized electrolytes remained on the surface of the TiO_2 nanotubes. The heat treatment reduced the amount of residual fluorine, and the two species of bacteria observed in this study showed different results depending on the fluorine content *P. gingivalis* showed the lowest adhesion in the H0 samples where the fluorine content was the highest and statistically more adhesion in the H400 samples, where the fluorine content was the lowest. In comparison, *S. mutans* showed statistically less adhesion in the H400 samples, where the fluorine content was the lowest. Yoshinari et al. [36] reported that fluorine has two mechanisms that affect bacteria. One is that fluoride ions act as an enzyme inhibitor, affecting the metabolism of bacteria, and the other is that metal–fluoride complexes suppress proton-translocating F-ATPases. In *P. gingivalis*, the enzyme inhibitor mechanism of fluoride ions seemed to work more strongly.

Chemical changes were observed on the surface of samples treated with plasma due to the composition of process gases [37]. The results of this study did not show any change in the surface structure of TiO_2 nanotubes after the plasma treatment. Although there was no change in the surface structure, specimens treated with plasma showed a lower contact angle than those that were not treated. XPS analysis was performed to identify the functional groups that determine surface hydrophilicity and electric charge. The results showed that C-H and C-C peaks after plasma treatment were reduced and that O-H, O1s, and TiO_2 peaks were increased. Previous studies have found that plasma treatment formed various oxygen functional groups on the surface of materials through chemical oxidation, which breaks C-C and C-H bonds on the surface and removes carbohydrates connected to C-H bonds [38,39]. It was also reported that oxygen, mixed for plasma treatments, attaches a hydroxy group (O-H) on the surface of titanium, and generates reactive oxygen species (ROS), which improves hydrophilicity [40].

In this study, a fluorescent nucleic acid staining method was used to assess the adhesion of bacteria after the plasma treatment, and the two species of bacteria showed different results. In *S. mutans*, the biofilm thickness on all surfaces was significantly reduced after plasma treatment regardless of heat treatment, while *P. gingivalis* did not show any statistically significant differences. It has been reported that bacteria adhere better to hydrophobic or nonpolar surfaces than to hydrophilic surfaces [41]. Hydrophobic surfaces increase the adhesion of hydrophobic bacteria [42], and hydrophilic surfaces increase the adhesion of hydrophilic bacteria [43]. *S. mutans,* used to test the changes in biofilm formation in this study, is a hydrophobic bacterial species [44], while *P. gingivalis* is hydrophobic and hydrophilic [45]. Therefore, the increase in the hydrophilicity of the TiO_2 nanotubes after applying atmospheric pressure plasma can be attributed to the decrease in the adhesion of *S. mutans*, a hydrophobic species.

This study assessed the adhesion of bacteria based on the thickness of their biofilms. If bacteria that adhere to the surfaces can be quantified, the adhesion of bacteria can be more accurately assessed. Only the reactions of two species of bacteria were observed in this study. Since various bacteria cause peri-implantitis, it is necessary to conduct further research on peri-implantitis using various species of bacteria or mixed bacterial colonies. In addition,

this study was carried out using a single gas plasma and one treatment time; thus, it is also necessary to apply different gas processes and treatment times in future studies. The results of this study showed that heat and plasma treatments inhibited the adhesion of bacteria. However, it will be necessary to perform additional in vitro and in vivo experiments to verify the biostability of TiO_2 nanotubes on the surfaces of dental implants.

4. Materials and Methods

4.1. Samples

Disk-shaped (diameter: 15 mm, thickness: 3 mm) commercially pure titanium specimens (ASTM Grade IV, Kobe Steel, Kobe, Japan) were wet ground (Labopol-5, Struers, Ballerup, Denmark) using #600 silicon carbide (SiC) paper. All specimens treated with heat and plasma were sterilized using ethylene oxide (E.O) gas.

4.2. Surface Treatment

4.2.1. Anodic Oxidation

Anodic oxidation was performed using a DC power supplier (Fine Power F-3005, SG EMD, Anyang, Republic of Korea). An electrolyte mixture was prepared by adding 1 M phosphoric acid and 1.5 wt% hydrofluoric (HF) acid to distilled water. The titanium specimen was connected to the anode, and a platinum plate (3 mm × 4 mm × 0.1 mm) was connected to the cathode. The specimen and platinum plate were placed approximately 10 mm apart and dipped in the electrolyte mixture for one minute. After that, 20 V were applied to the specimen and platinum plate for anodic oxidation for 10 min.

4.2.2. Heat Treatment

The heat treatment was performed using a sintering furnace (DUOTRON PRO ex-6100, ADDIN Co., LTD, Suwon, Republic of Korea). Under an air atmosphere, the temperature was increased to 400 °C and 600 °C at a rate of 1 °C/min. The furnace was cooled after maintaining the temperature for one hour.

4.2.3. Non-Thermal Plasma Treatment

The non-thermal plasma treatment was performed using an atmospheric pressure plasma generator (PGS-200, Expantech Co., Suwon, Republic of Korea) (Table 4). Ar and O_2 gases were mixed in a ratio of 99% to 1%, and applied to the specimen at 300 W at a rate of 10 L/min. The distance between the plasma flame and the specimen was maintained at 5 mm. The specimen was rotated at 180 rpm, and the plasma flame was moved to the right and left ten times (12 s for one time) to evenly apply the atmospheric pressure plasma to the specimen. Thus, the plasma flame was applied for a total of 120 s (Figure 2).

Table 4. Parameters of plasma generator.

Parameter	Value
Average working power (W)	300
Voltage (V)	27
Frequency (MHz) *	900
Atmospheric pressure (Torr)	760
Electrode type	Electrodeless
Cooling type	Air cooled
Plasma density	$10^{15}/cm^3$

*: Variable frequency.

4.3. Assessment of Surface Properties

4.3.1. Contact Angles

Four microliters of distilled water were dropped onto the surfaces of the specimens to compare the changes in the hydrophilicity. The angle between the surface and the solution was measured after ten seconds using a video contact angle measuring device (Phoenix 300,

SEO Co., Suwon, Republic of Korea). For each group, the angle of three specimens was measured and averaged.

4.3.2. Surface Structures

The changes in the surface structure of the specimens were observed using a scanning electron microscope (FE-SEM S-4700, Hitachi Horiba, Tokyo, Japan).

4.3.3. XRD Analysis

The changes in the crystal structure on the surface of the specimens were analyzed using an X-ray diffractometer (XRD) (X'Pert PRO Multi-Purpose X-ray Diffractometer, PANalytical, Almelo, The Netherlands). Diffraction was analyzed using X-rays of CuKα at a speed of 1.5°/min at an angle of 2θ ranging from 20° to 90°.

4.3.4. XPS Analysis

The chemical compositions and bonds of specimens were analyzed using X-ray photoelectron spectroscopy (XPS, VG Mulrilab 2000, Thermo Scientific, Oxford, UK). The peak area values of each element detected were normalized and expressed as a quantitative ratio.

4.4. Assessment of Inhibition of Biofilm Formation

4.4.1. Bacterial Culture

In this study, *Streptococcus mutans* (KCOM 1504), a Gram-positive aerobic bacterium associated with initial biofilm formation, and *Porphyromonas gingivalis* (KCOM 2804), a Gram-negative anaerobic bacterium that causes peri-implantitis, were used. The two species of bacteria were obtained from the Korean Collection for Oral Microbiology (KCOM, Gwangju, Republic of Korea). *S. mutans* was cultured in a Brain Heart Infusion broth (BHI, Becton, Dickinson and Company, Sparks, MD, USA), and *P. gingivalis* was cultured in a Tryptic Soy Broth (TSB, Becton, Dickinson and Company, Sparks, MD, USA). Single colonies cultured on a solid medium were cultured in a liquid medium and grown to a concentration of 1.5×10^7 CFU/mL.

4.4.2. Artificial Saliva Coating

Specimens were coated with artificial saliva to create an oral environment. The artificial saliva used in this study was prepared by adding 1% mucin (Mucin from porcine stomach, M1778; Sigma-Aldrich, St. Louis, MO, USA) to an adhesion buffer [46]. Three specimens per group were put in a 24-well plate, and the prepared artificial saliva was applied. The specimens were slowly stirred in the culture medium at 37 °C for two hours to coat the specimens with the artificial saliva. *S. mutans* was cultured in BHI at 37 °C (LIB-150M, DAIHAN Labtech Co., Namyangju, Republic of Korea), and *P. gingivalis* was cultured in anaerobic TSB at 37 °C (Forma Anaerobic System 1029; Thermo Fisher Scientific, Waltham, MA, USA).

4.4.3. Bacterial Inoculation

After two hours, the artificial saliva was removed, and the specimens were dried for 15 min. Bacteria were inoculated on the surface of the specimens at a concentration of 1.5×10^7 CFU/mL. *S. mutans* was cultured for 24 h, and *P. gingivalis* was cultured for 48 h.

4.4.4. Fluorescent Nucleic Acid Staining Assessment

The biofilm formation was assessed using a green-fluorescent nucleic acid stain (SYTO 9®, Molecular Probes Europe BV, Leiden, The Netherlands). After culturing bacteria, the culture medium was removed. The specimens were carefully cleaned two times using phosphate-buffered saline (PBS) to remove bacteria that did not adhere. Afterwards, 200 μL of fluorescent dye (SYTO 9®:dH_2O = 1.5 μL:1 mL) was injected onto the specimens. The plate was sealed with aluminum foil to block out light and was placed at room temperature for 15 min. After the reaction, the residual staining solution was carefully cleaned using

PBS, and the surfaces of the specimens were observed using a laser confocal scanning microscope (Leica TCS SP5 AOBS/tandem, Leica, Bensheim, Germany). The thickness of the biofilms formed on the specimens was measured using an analysis program (Leica LAS AF software, Leica Microsystems, Bensheim, Germany).

4.5. Statistical Analysis

4.5.1. Results of Heat Treatment

When the assumption of normality was met, the significance of the heat treatment results was tested using a parametric one-way analysis of variance (ANOVA) and Tukey's post-hoc test. The significance level was set at a *p*-value less than 0.05. When the assumption of normality was not met, the results were statistically analyzed using a non-parametric Kruskal–Wallis test. The two groups were paired and tested using a Mann–Whitney U-test. Type I errors were corrected using Bonferroni's method. The significance level was set at a *p*-value less than 0.017.

4.5.2. Results of Plasma Treatment

When the assumption of normality was met, the significance of the plasma treatment results was statistically analyzed using a parametric independent *t*-test. When the assumption of normality was not met, the two groups were compared using a non-parametric Mann–Whitney U-test. The significance level was set at a *p*-value less than 0.05.

5. Conclusions

In this study, TiO_2 nanotubes were formed on the titanium surface of dental implants to increase the surface area. TiO_2 nanotubes were heat-treated under different conditions to modify the structure of the TiO_2 oxide films. In addition, atmospheric pressure plasma was applied to the TiO_2 nanotubes to change their surface energy and hydrophilicity. This study found that the TiO_2 nanotubes heat-treated at 400 °C inhibited the adhesion of *S. mutans*, associated with early biofilm formation, and the TiO_2 nanotubes heat-treated at 600 °C inhibited the adhesion of *P. gingivalis,* which causes peri-implantitis. Applying plasma to TiO_2 nanotubes heat-treated at 600 °C can also inhibit the adhesion of *S. mutans* and *P. gingivalis*.

Author Contributions: Conceptualization, M.-K.J., S.-K.L. and H.-P.L.; methodology, H.C. and H.-P.L.; software and validation, S.-K.L.; formal analysis, M.-K.J.; investigation and data curation M.-K.J. and H.-S.K.; writing—original draft preparation, M.-K.J. and S.-K.L.; writing—review and editing, G.-J.O.; visualization and supervision, H.C. and H.-P.L.; project administration, H.C. and H.-P.L.; funding acquisition, M.-K.J. All authors have read and agreed to the published version of the manuscript.

Funding: This work was supported by the National Research Foundation of Korea (NRF) grant funded by the Korean government (MSIT) (No. NRF-2020R1C1C1005683).

Institutional Review Board Statement: Not applicable.

Informed Consent Statement: Not applicable.

Data Availability Statement: Not applicable.

Acknowledgments: This work was supported by the National Research Foundation of Korea (NRF) grant funded by the Korean government (MSIT) (No. NRF-2020R1C1C1005683, M.-K.J.; No. NRF-2020R1I1A1A01073015, G.-J.O.).

Conflicts of Interest: The authors declare no conflict of interest.

References

1. Becker, W.; Becker, B.E.; Newman, M.G.; Nyman, S. Clinical and microbiologic findings that may contribute to dental implant failure. *Int. J. Oral Implants* **1990**, *5*, 31–38.
2. Leonhardt, Å.; Renvert, S.; Dahlén, G. Microbial findings at failing implants. *Clin. Oral Implant. Res.* **1999**, *10*, 339–345. [CrossRef] [PubMed]
3. Wennerberg, A.; Albrektsson, T. On implant surfaces: A review of current knowledge and opinions. *Int. J. Oral Maxillofac. Implant.* **2010**, *25*, 63–74.

4. Zhao, J.; Wang, X.; Chen, R.; Li, L. Fabrication of titanium oxide nanotube arrays by anodic oxidation. *Solid State Commun.* **2005**, *134*, 705–710. [CrossRef]
5. Brammer, K.S.; Oh, S.; Frandsen, C.J.; Jin, S. Biomaterials and biotechnology schemes utilizing TiO_2 nanotube arrays. In *Biomaterials Science Engineering*; IntechOpen: Rijela, Croatia, 2011; pp. 193–210.
6. Lavenus, S.; Louarn, G.; Layrolle, P. Nanotechnology and dental implants. *Int. J. Biomater.* **2010**, *2010*, 915327. [CrossRef]
7. Ellingsen, J.E.; Johansson, C.B.; Wennerberg, A.; Holmén, A. Improved retention and bone-to-implant contact with fluoride-modified titanium implants. *Int. J. Oral Maxillofac. Implant.* **2004**, *19*, 659–666.
8. Peng, Z.; Ni, J.; Zheng, K.; Shen, Y.; Wang, X.; He, G.; Jin, S.; Tang, T. Dual effects and mechanism of TiO_2 nanotube arrays in reducing bacterial colonization and enhancing C3H10T1/2 cell adhesion. *Int. J. Nanomed.* **2013**, *8*, 3093–3105.
9. Roguska, A.; Belcarz, A.; Pisarek, M.; Ginalska, G.; Lewandowska, M. TiO_2 nanotube composite layers as delivery system for ZnO and Ag nanoparticles—An unexpected overdose effect decreasing their antibacterial efficacy. *Mater. Sci. Eng. C* **2015**, *51*, 158–166. [CrossRef]
10. Yang, B.; Uchida, M.; Kim, H.-M.; Zhang, X.; Kokubo, T. Preparation of bioactive titanium metal via anodic oxidation treatment. *Biomaterials* **2004**, *25*, 1003–1010. [CrossRef]
11. Del Curto, B.; Brunella, M.F.; Giordano, C.; Pedeferri, M.; Valtulina, V.; Visai, L.; Cigada, A. Decreased bacterial adhesion to surface-treated titanium. *Int. J. Artif. Organs* **2005**, *28*, 718–730. [CrossRef]
12. Salou, L.; Hoornaert, A.; Louarn, G.; Layrolle, P. Enhanced osseointegration of titanium implants with nanostructured surfaces: An experimental study in rabbits. *Acta Biomater.* **2015**, *11*, 494–502. [CrossRef] [PubMed]
13. Duske, K.; Koban, I.; Kindel, E.; Schröder, K.; Nebe, B.; Holtfreter, B.; Jablonowski, L.; Weltmann, K.D.; Kocher, T. Atmospheric plasma enhances wettability and cell spreading on dental implant metals. *J. Clin. Periodontol.* **2012**, *39*, 400–407. [CrossRef] [PubMed]
14. Kieswetter, K.; Schwartz, Z.; Dean, D.; Boyan, B. The role of implant surface characteristics in the healing of bone. *Crit. Rev. Oral Biol. Med.* **1996**, *7*, 329–345. [CrossRef] [PubMed]
15. MacDonald, D.; Deo, N.; Markovic, B.; Stranick, M.; Somasundaran, P. Adsorption and dissolution behavior of human plasma fibronectin on thermally and chemically modified titanium dioxide particles. *Biomaterials* **2002**, *23*, 1269–1279. [CrossRef]
16. Sawase, T.; Jimbo, R.; Baba, K.; Shibata, Y.; Ikeda, T.; Atsuta, M. Photo-induced hydrophilicity enhances initial cell behavior and early bone apposition. *Clin. Oral Implant. Res.* **2008**, *19*, 491–496. [CrossRef]
17. Arora, V.; Nikhil, V.; Suri, N.; Arora, P. Cold atmospheric plasma (CAP) in dentistry. *Dentistry* **2014**, *4*, 1. [CrossRef]
18. Chen, M.; Zhang, Y.; Driver, M.S.; Caruso, A.N.; Yu, Q.; Wang, Y. Surface modification of several dental substrates by non-thermal, atmospheric plasma brush. *Dent. Mater.* **2013**, *29*, 871–880. [CrossRef]
19. Fricke, K.; Koban, I.; Tresp, H.; Jablonowski, L.; Schröder, K.; Kramer, A.; Weltmann, K.-D.; von Woedtke, T.; Kocher, T. Atmospheric pressure plasma: A high-performance tool for the efficient removal of biofilms. *PLoS ONE* **2012**, *7*, e42539. [CrossRef]
20. Dautov, G.Y. Generators of nonequilibrium low-temperature plasma. *J. Eng. Phys.* **1988**, *53*, 966–975. [CrossRef]
21. Yoo, E.-M.; Uhm, S.-H.; Kwon, J.-S.; Choi, H.-S.; Choi, E.H.; Kim, K.-M.; Kim, K.-N. The study on inhibition of planktonic bacterial growth by non-thermal atmospheric pressure plasma jet treated surfaces for dental application. *J. Biomed. Nanotechnol.* **2015**, *11*, 334–341. [CrossRef]
22. Sun, L.; Chen, X.; Chen, R.; Ji, Z.; Mu, H.; Liu, C.; Yu, J.; Wang, J.; Xia, R.; Zhang, S. Balancing Antibacterial and Osteogenic Effects of Double-layer TiO2 Nanotubes Loaded with Silver Nanoparticles for Osseointegration of Implants. *Nanoscale* **2023**, *15*, 2911–2923. [CrossRef] [PubMed]
23. Arkusz, K.; Paradowska, E.; Nycz, M.; Mazurek-Popczyk, J.; Baldy-Chudzik, K. Evaluation of the antibacterial activity of Ag-and Au-nanoparticles loaded TiO_2 nanotubes. *J. Biomed. Nanotechnol.* **2020**, *16*, 1416–1425. [CrossRef] [PubMed]
24. Giavaresi, G.; Ambrosio, L.; Battiston, G.A.; Casellato, U.; Gerbasi, R.; Finia, M.; Aldini, N.N.; Martini, L.; Rimondini, L.; Giardino, R. Histomorphometric, ultrastructural and microhardness evaluation of the osseointegration of a nanostructured titanium oxide coating by metal-organic chemical vapour deposition: An in vivo study. *Biomaterials* **2004**, *25*, 5583–5591. [CrossRef] [PubMed]
25. Webster, T.J.; Ejiofor, J.U. Increased osteoblast adhesion on nanophase metals: Ti, Ti_6Al_4V, and CoCrMo. *Biomaterials* **2004**, *25*, 4731–4739. [CrossRef]
26. De Oliveira, P.T.; Nanci, A. Nanotexturing of titanium-based surfaces upregulates expression of bone sialoprotein and osteopontin by cultured osteogenic cells. *Biomaterials* **2004**, *25*, 403–413. [CrossRef]
27. Macák, J.M.; Tsuchiya, H.; Schmuki, P. High-aspect-ratio TiO_2 nanotubes by anodization of titanium. *Angew. Chem. Int. Ed.* **2005**, *44*, 2100–2102. [CrossRef]
28. Beranek, R.; Hildebrand, H.; Schmuki, P. Self-organized porous titanium oxide prepared in H_2SO_4/HF electrolytes. *Electrochem. Solid State Lett.* **2003**, *6*, B12. [CrossRef]
29. Tsuchiya, H.; Macak, J.M.; Taveira, L.; Balaur, E.; Ghicov, A.; Sirotna, K.; Schmuki, P. Self-organized TiO_2 nanotubes prepared in ammonium fluoride containing acetic acid electrolytes. *Electrochem. Commun.* **2005**, *7*, 576–580. [CrossRef]
30. Kim, H.S.; Yang, Y.; Koh, J.T.; Lee, K.K.; Lee, D.J.; Lee, K.M.; Park, S.W. Fabrication and characterization of functionally graded nano-micro porous titanium surface by anodizing. *J. Biomed. Mater. Res. Part B Appl. Biomater.* **2009**, *88*, 427–435. [CrossRef]
31. Park, S.; Min, D.; Lim, H.; Yoon, D.; Lee, K. Effect of heat treatment on phase transition of nanotubular titanium oxide arrays. *J. Nanosci. Nanotechnol.* **2011**, *11*, 1476–1479. [CrossRef]

32. Storz, G.; Imlayt, J.A. Oxidative stress. *Curr. Opin. Microbiol.* **1999**, *2*, 188–194. [CrossRef] [PubMed]
33. Kohen, R.; Nyska, A. Invited review: Oxidation of biological systems: Oxidative stress phenomena, antioxidants, redox reactions, and methods for their quantification. *Toxicol. Pathol.* **2002**, *30*, 620–650. [CrossRef] [PubMed]
34. Gallardo-Moreno, A.M.; Pacha-Olivenza, M.A.; Fernández-Calderón, M.-C.; Pérez-Giraldo, C.; Bruque, J.M.; González-Martín, M.-L. Bactericidal behaviour of Ti6Al4V surfaces after exposure to UV-C light. *Biomaterials* **2010**, *31*, 5159–5168. [CrossRef] [PubMed]
35. Zhang, J.; Zhou, P.; Liu, J.; Yu, J. New understanding of the difference of photocatalytic activity among anatase, rutile and brookite TiO2. *Phys. Chem. Chem. Phys.* **2014**, *16*, 20382–20386. [CrossRef]
36. Yoshinari, M.; Oda, Y.; Kato, T.; Okuda, K. Influence of surface modifications to titanium on antibacterial activity in vitro. *Biomaterials* **2001**, *22*, 2043–2048. [CrossRef]
37. Bazaka, K.; Jacob, M.V.; Crawford, R.J.; Ivanova, E.P. Plasma-assisted surface modification of organic biopolymers to prevent bacterial attachment. *Acta Biomater.* **2011**, *7*, 2015–2028. [CrossRef]
38. Seo, H.Y.; Kwon, J.-S.; Choi, Y.-R.; Kim, K.-M.; Choi, E.H.; Kim, K.-N. Cellular attachment and differentiation on titania nanotubes exposed to air-or nitrogen-based non-thermal atmospheric pressure plasma. *PLoS ONE* **2014**, *9*, e113477. [CrossRef]
39. Choi, Y.-R.; Kwon, J.-S.; Song, D.-H.; Choi, E.H.; Lee, Y.-K.; Kim, K.-N.; Kim, K.-M. Surface modification of biphasic calcium phosphate scaffolds by non-thermal atmospheric pressure nitrogen and air plasma treatment for improving osteoblast attachment and proliferation. *Thin Solid Film.* **2013**, *547*, 235–240. [CrossRef]
40. Kolb, J.F.; Price, R.O.; Chiavarini, R.; Schoenbach, K.H. Cold atmospheric pressure air plasma microjet for medical applications. In Proceedings of the 2007 IEEE 34th International Conference on Plasma Science (ICOPS), Albuquerque, NM, USA, 17–22 June 2007; p. 831.
41. Flemming, H.-C.; Wingender, J. Relevance of microbial extracellular polymeric substances (EPSs)—Part I: Structural and ecological aspects. *Water Sci. Technol.* **2001**, *43*, 1–8. [CrossRef]
42. Pavithra, D.; Doble, M. Biofilm formation, bacterial adhesion and host response on polymeric implants—Issues and prevention. *Biomed. Mater.* **2008**, *3*, 034003. [CrossRef]
43. Gottenbos, B.; Grijpma, D.W.; van der Mei, H.C.; Feijen, J.; Busscher, H.J. Antimicrobial effects of positively charged surfaces on adhering Gram-positive and Gram-negative bacteria. *J. Antimicrob. Chemother.* **2001**, *48*, 7–13. [CrossRef] [PubMed]
44. McBride, B.; Song, M.; Krasse, B.; Olsson, J. Biochemical and immunological differences between hydrophobic and hydrophilic strains of *Streptococcus mutans*. *Infect. Immun.* **1984**, *44*, 68–75. [CrossRef] [PubMed]
45. Kerosuo, E.; Haapasalo, M.; Alli, K.; Lounatmaa, K. Ingestion of Bacteroides buccae, Bacteroides oris, *Porphyromonas gingivalis*, and *Fusobacterium nucleatum* by human polymorphonuclear leukocytes in vitro. *Oral Microbiol. Immunol.* **1990**, *5*, 202–207. [CrossRef] [PubMed]
46. Li, Y.-H.; Tang, N.; Aspiras, M.B.; Lau, P.C.; Lee, J.H.; Ellen, R.P.; Cvitkovitch, D.G. A quorum-sensing signaling system essential for genetic competence in *Streptococcus mutans* is involved in biofilm formation. *J. Bacteriol.* **2002**, *184*, 2699–2708. [CrossRef]

Disclaimer/Publisher's Note: The statements, opinions and data contained in all publications are solely those of the individual author(s) and contributor(s) and not of MDPI and/or the editor(s). MDPI and/or the editor(s) disclaim responsibility for any injury to people or property resulting from any ideas, methods, instructions or products referred to in the content.

International Journal of
Molecular Sciences

MDPI

Article

Effect of Hydroxyapatite/β-Tricalcium Phosphate on Osseointegration after Implantation into Mouse Maxilla

Sanako Makishi †, Taisuke Watanabe †, Kotaro Saito and Hayato Ohshima *

Division of Anatomy and Cell Biology of the Hard Tissue, Department of Tissue Regeneration and Reconstruction, Niigata University Graduate School of Medical and Dental Sciences, Niigata 951-8514, Japan
* Correspondence: histoman@dent.niigata-u.ac.jp; Tel.: +81-25-227-2812
† These authors contributed equally to this work.

Abstract: In our previous study we established an animal model for immediately placed implants using mice and clarified that there were no significant differences in the chronological healing process at the bone-implant interface between immediately and delayed placed implants blasted with hydroxyapatite (HA)/β-tricalcium phosphate (β-TCP) (ratio 1:4). This study aimed to analyze the effects of HA/β-TCP on osseointegration at the bone-implant interface after immediately placed implants in the maxillae of 4-week-old mice. Right maxillary first molars were extracted and cavities were prepared with a drill and titanium implants, blasted with or without HA/β-TCP, were placed. The fixation was followed-up at 1, 5, 7, 14, and 28 days after implantation, and the decalcified samples were embedded in paraffin and prepared sections were processed for immunohistochemistry using anti-osteopontin (OPN) and Ki67 antibodies, and tartrate-resistant acid phosphatase histochemistry. The undecalcified sample elements were quantitatively analyzed by an electron probe microanalyzer. Bone formation occurred on the preexisting bone surface (indirect osteogenesis) and on the implant surface (direct osteogenesis), indicating that osseointegration was achieved until 4 weeks post-operation in both of the groups. In the non-blasted group, the OPN immunoreactivity at the bone-implant interface was significantly decreased compared with the blasted group at week 2 and 4, as well as the rate of direct osteogenesis at week 4. These results suggest that the lack of HA/β-TCP on the implant surface affects the OPN immunoreactivity on the bone-implant interface, resulting in decreased direct osteogenesis following immediately placed titanium implants.

Keywords: dental implants; hydroxyapatite; maxilla; osseointegration; osteopontin; titanium; tooth extraction

Citation: Makishi, S.; Watanabe, T.; Saito, K.; Ohshima, H. Effect of Hydroxyapatite/β-Tricalcium Phosphate on Osseointegration after Implantation into Mouse Maxilla. *Int. J. Mol. Sci.* **2023**, *24*, 3124. https://doi.org/10.3390/ijms24043124

Academic Editor: Mary Anne Melo

Received: 10 January 2023
Revised: 31 January 2023
Accepted: 2 February 2023
Published: 4 February 2023

Copyright: © 2023 by the authors. Licensee MDPI, Basel, Switzerland. This article is an open access article distributed under the terms and conditions of the Creative Commons Attribution (CC BY) license (https://creativecommons.org/licenses/by/4.0/).

1. Introduction

Clinicians and researchers who are involved with dental implants require a comprehensive understanding of the biology of wound healing after endosseous implant placement. Osseointegration, as defined by Brånemark, refers to the direct contact between living bone and the implant surface at the level of a light microscope [1] and is considered to be a determinant of successful implant therapy. Mesenchymal stem cells differentiate into pre-, immature-, and mature-osteoblasts, and runt-related transcription factor 2 (Runx2), SP7, and Wnt signaling act as promoting factors of this differentiation process [2]. Osteoclast progenitor cells differentiate into osteoclasts via the macrophage colony-stimulating factor (M-CSF) receptor, receptor activator of nuclear factor-κ B (RANK) through the secretion of M-CSF and RANK ligand expression by osteoblasts that are activated by $1,25(OH)_2D_3$ and parathyroid hormone (PTH), and these activated osteoclasts resorb bone [3]. The healing of peri-implant tissues can be divided into the bioreactive (bleeding, hemostasis, blood clots, and blood clot degradation), osteoconductive (migration and adhesion of mesenchymal cells and osteoblast differentiation), bone-forming (collagen formation by osteoblasts, calcification, and bone formation), and bone-remodeling (bone resorption and

apposition) phases [4]. In the mouse experimental model [5], the bioreactive (0–3 days), osteoconductive (3–5 days), neoplastic (5–7 days), and bone remodeling (2–4 weeks) phases occur earlier than the bone-forming (1–2 weeks) and bone remodeling (6 weeks) phases in humans. Osseointegration can be divided into two modalities [4]: distance osteogenesis, in which bone is gradually added from the surrounding preexisting bone to the implant, and contact osteogenesis, in which mesenchymal stem cells migrate onto the implant surface and differentiate into osteoblasts to form bone. We have previously proposed that the former is called indirect osteogenesis and the latter is called direct osteogenesis [6]. Our previous study established an experimental animal model for the immediate implant placement using a titanium implant that was blasted with hydroxyapatite (HA)/β-tricalcium phosphate (TCP) in the mouse maxilla [5]. In this model, indirect and direct osteogeneses occur simultaneously. In indirect osteogenesis, osteoclast precursor cells are recruited onto the damaged bone surface and differentiate into bone-resorbing osteoclasts. When the osteoclasts leave the bone surface after bone resorption, osteoblast progenitors are recruited onto the bone surface where they differentiate and become osteocytes after bone formation. Although bone deposition continuously occurs from the preexisting bone to the implant surface, eventually establishing osseointegration, the intervening cells remain and are embedded in the matrix at the bone-implant interface. In direct osteogenesis, osteoclast precursor cells are recruited onto the implant surface where they differentiate and become polarized. When the osteoclast-like cells leave the implant surface, osteoblast precursor cells are recruited onto the implant surface where they differentiate into osteoblasts and deposit cell-free bone matrix at the bone-implant interface. Bone deposition continues from the implant surface to the preexisting bone. Thus, promoting direct osteogenesis contributes to achieving the osseointegration faster.

Although osteopontin (OPN) is produced by osteoblasts, osteocytes, and osteoclasts as well as inflammatory cells in the bone, OPN functions as a bridge between HA and the extracellular matrix [7]. OPN receptors contain integrins and CD44 variants and are involved in the adhesion, migration, and survival of various cell types. During direct osteogenesis, inflammatory cells and osteoclast lineage cells produce OPN, which is deposited onto the implant surface [6]. As a result, there is a correlation between the rate of direct osteogenesis and OPN deposition on the implant surface. Furthermore, the addition of recombinant OPN protein onto the implant surface results in the early establishment of direct osteogenesis [8]. However, there is no data available regarding the factors that promote the deposition of OPN onto the implant surface.

The initial stage where osteoblasts are recruited onto the surface of the implant is defined as "osteoconduction" and the ability to form bone in the areas other than bone tissue is called "osteoinduction" [9]. Similarities of HA to the bone minerals together with the HA bioactivity and biocompatibility have made it a promising scaffold for bone tissue engineering [10]. Although HA has been widely used in bone regeneration and dental implants, the effect of HA on cellular events are not fully understood. The key questions that this study aims to answer are: (i) does HA on the implant surface promote direct osteogenesis, and if it does, (ii) how does HA affect the cellular events during the osseointegration process after implant placement. Regarding the effect of HA/β-TCP, its presence has been reported to increase the attachment level and bone regeneration in the treatment of periodontal osseous defects [11]. Direct and indirect osteogenesis occurs simultaneously, and osseointegration is completed when the two meet. If direct osteogenesis does not occur, the time to osseointegration completion is extended. Clinically, it is desirable for direct and indirect osteogenesis to occur simultaneously and for osseointegration to be established at an early stage because initial fixation of the implant is important. This study aimed to clarify the effect of HA on osseointegration at the bone-implant interface after implantation in the maxillae of mice.

2. Results

2.1. Day 1

In both the blasted (HA) and non-blasted (smooth: Sm) groups on postoperative day 1, the bone-implant interface consisted of a fibrin network and inflammatory cellular infiltrate, while the preexisting bone surface was positive for tartrate-resistant acid phosphatase (TRAP) and OPN (Figure 1).

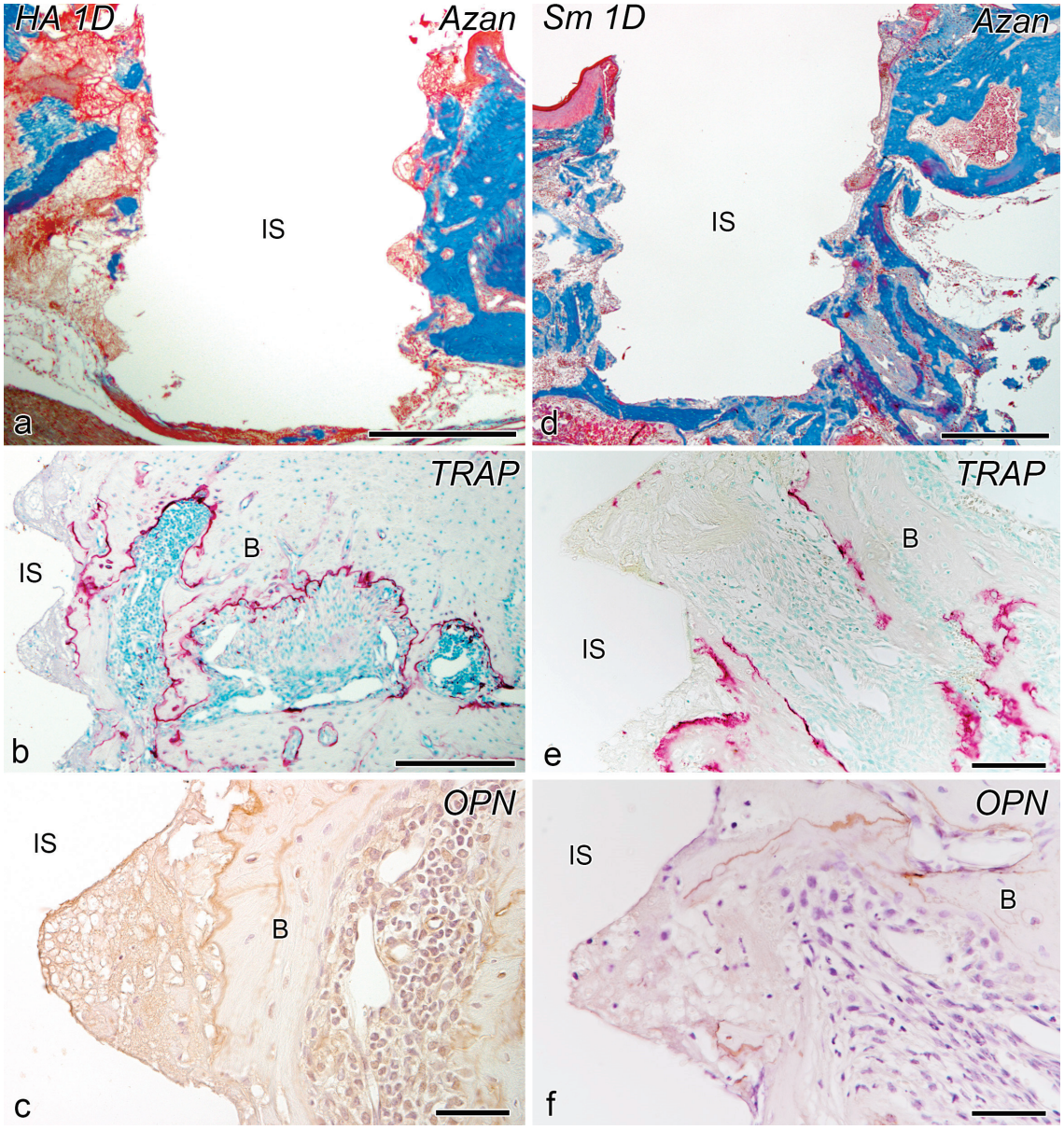


Figure 1. Azan staining (**a**,**d**), tartrate-resistant acid phosphatase (TRAP) reaction (**b**,**e**), and osteopontin (OPN)-immunoreactivity (**c**,**f**) in the tissues surrounding the implants in the blasted (HA) (**a**–**c**) and non-blasted (Sm) groups (**d**–**f**) at day 1 after implantation. (**a**–**f**) The bone-implant interface consists of a fibrin network and inflammatory cellular infiltrate, while the preexisting bone surface is positive for TRAP and OPN. B, bone; IS, implant space. Scale bars = (**a**,**d**) 500 μm, (**b**) 250 μm, (**e**) 100 μm, and (**c**,**f**) 50 μm.

2.2. Day 5

On postoperative day 5, granulation progressed at the peri-implant interface and bone formation began on the implant surface in the HA group (Figure 2a–f). In addition, TRAP-positive osteoclast lineage cells appeared around the implants, and OPN-positive reactions

were observed at the bone-implant interface. In contrast, neither bone formation nor OPN-positive reaction was observed around the implant in the Sm group (Figure 2g–i).

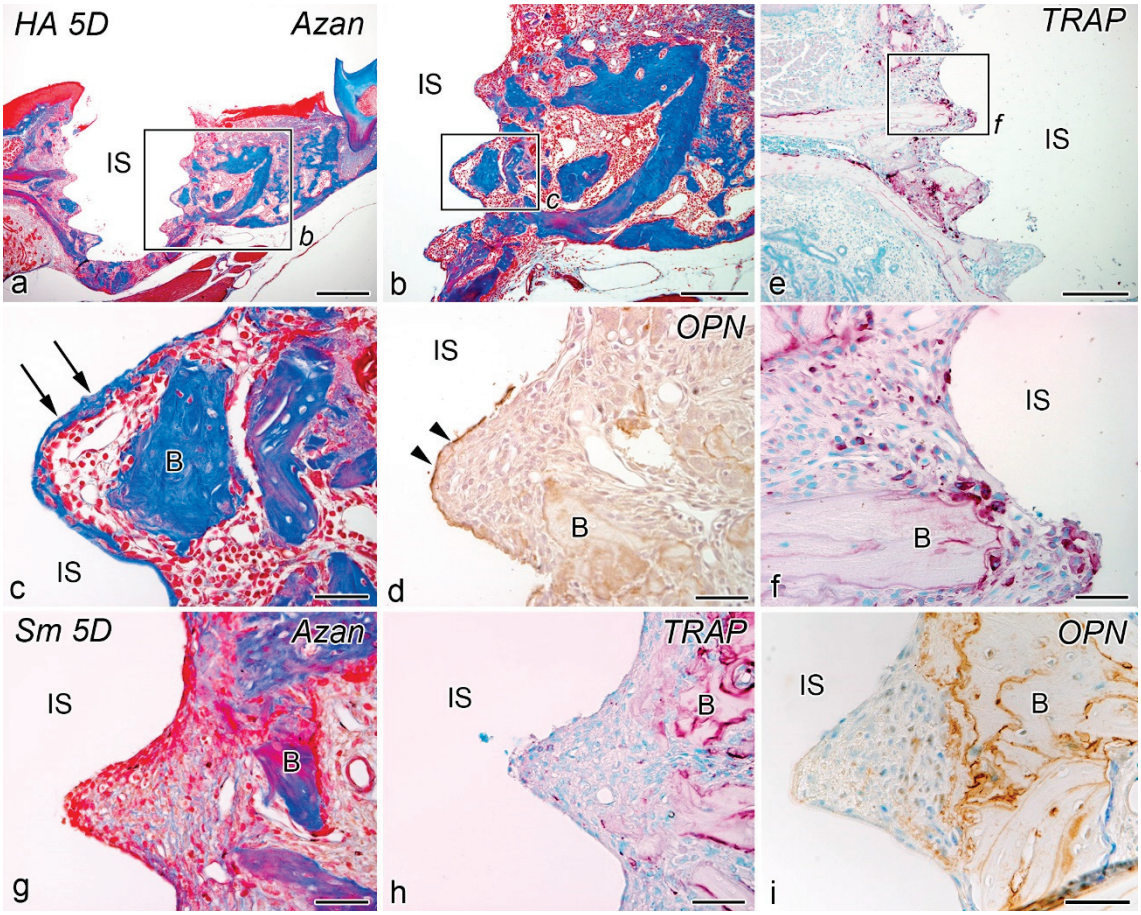


Figure 2. Azan staining (**a**–**c**,**g**), TRAP reaction (**e**,**f**,**h**), and OPN-immunoreactivity (**d**,**i**) in tissues surrounding the implants in the HA (**a**–**f**) and Sm groups (**g**–**i**) at day 5 after implantation. (**b**,**c**,**f**) are the higher magnifications of the boxed areas in (**a**,**b**,**e**), respectively. (**a**–**f**) Granulation progresses at the bone-implant interface and bone formation has begun on the implant surface. TRAP-positive osteoclast lineage cells appear around the implants, and an OPN-positive reaction (arrowheads) is observed at the bone-implant interface. (**g**–**i**) No bone formation is observed around the implant. Arrows, direct osteogenesis; B, bone; IS, implant space. Scale bars = (**a**) 500 μm, (**b**,**e**) 250 μm, and (**c**–**i**) 50 μm.

2.3. Weeks 2–4

At postoperative week 2, both the HA and Sm groups showed progressive bone formation over the entire implant. In both groups, OPN-positive reactions were observed at the bone-implant interface at the site of bone formation, and TRAP-positive reactions were observed in the new bone (Figure 3a–f).

Although the histological features of postoperative week 4 were similar to those of week 2 in both the HA and Sm groups, bone formation progressed all around the implants (Figure 3g–l). In both groups, OPN-positive reactions were observed in the bone-implant interface at the site of bone formation, and TRAP-positive reactions were observed in the new bone.

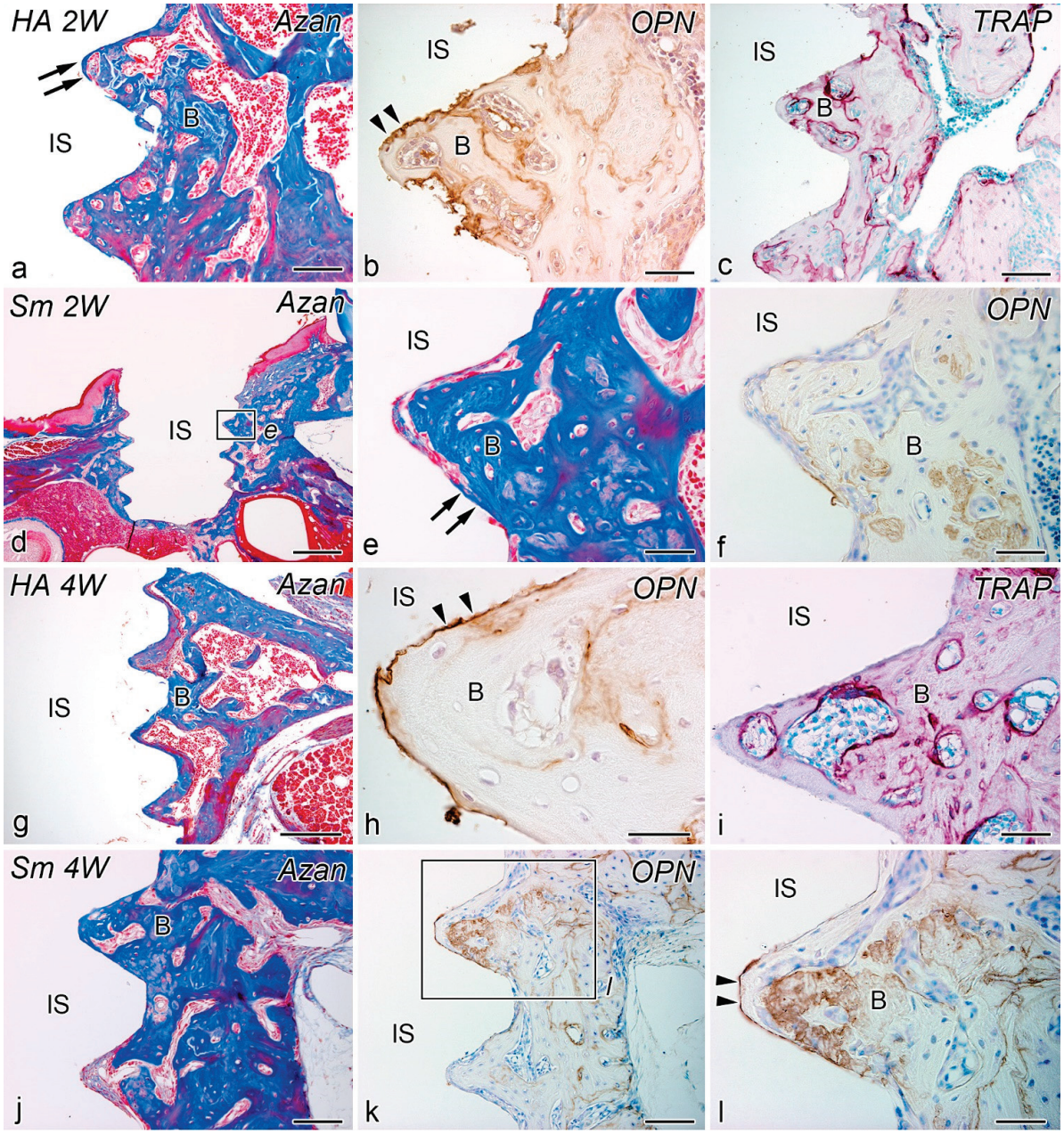


Figure 3. Azan staining (**a**,**d**,**e**,**g**,**j**), TRAP reaction (**c**,**i**), and OPN-immunoreactivity (**b**,**f**,**h**,**l**) in tissues surrounding the implants in the HA (**a**–**c**,**g**–**i**) and Sm groups (**d**–**f**,**j**–**l**) at week 2 (**a**–**f**) and 4 (**g**–**l**) after implantation. (**e**) and (**l**) are higher magnifications of the boxed areas in (**d**) and (**k**), respectively. (**a**–**l**) Progressive bone formation occur over the entire implant. OPN-positive reactions (arrowheads) are observed in the bone-implant interface at the site of bone formation, and TRAP-positive reactions are observed in the new bone. (**l**) is the higher magnification of the boxed area in (**k**). Arrows, direct osteogenesis; B, bone; IS, implant space. Scale bars = (**d**) 500 μm, (**g**) 250 μm, (**a**,**c**,**j**,**k**) 100 μm, and (**b**,**e**,**f**,**h**,**i**,**l**) 50 μm.

The success rates of immediately placed implants in the HA and Sm groups were 93.3% (36/37) and 74.4% (29/39), respectively.

2.4. Osseointegration and OPN-Positive Rates and Cell Proliferation

Although the osseointegration rate of postoperative week 2–4 was not significantly different between the HA and Sm groups, there was a significant difference in direct osteogenesis between HA and Sm groups at week 4 (Figure 4a). OPN-positive rates in the

HA group were significantly higher than those of the Sm group at week 2 and 4 (Figure 4b). Cell proliferative activity peaked on postoperative day 5 in both the HA and Sm groups and was significantly higher in the Sm group than in the HA group on day 5 (Figure 4c).

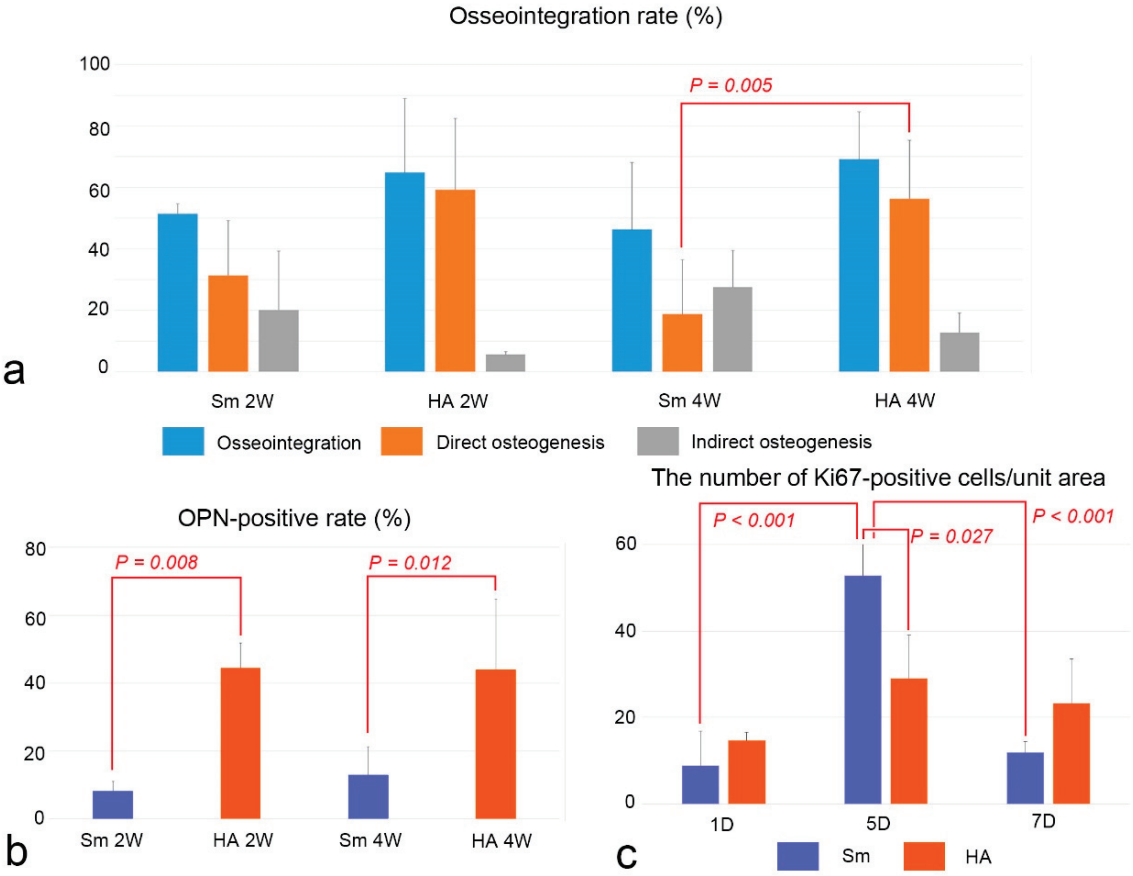


Figure 4. Osseointegration rate (**a**), OPN-positive rate (**b**), and the number of cell proliferation (**c**) in the HA and Sm groups. (**a**) The osseointegration rates between two groups are compared using the two-tailed Student's *t*-test. There is a significant difference in direct osteogenesis between the HA and Sm groups at week 4. (**b**) The number of OPN-positive rates between the two groups are compared using the two-tailed Student's *t*-test. The OPN-positive rate in the HA group is significantly higher than the Sm group at weeks 2 and 4. (**c**) The number of Ki67-positive cells among different stages after implantation is compared using one-way analysis of variance (ANOVA) followed by the Bonferroni test for multiple comparisons and the number of Ki67-positive cells between two groups are compared using the two-tailed Student's *t*-test. Cell proliferative activity peaks at postoperative day 5 in both the HA and Sm groups and is significantly higher in the Sm group than the HA group at day 5. The numbers are the mean + standard deviation (SD).

2.5. EPMA Analysis

Electron probe microanalyzer (EPMA) images of the HA and Sm groups at postoperative week 4 showed direct contact completion between the implant surface and surrounding bone, although certain areas were not covered with bone (Figure 5). Quantitative analysis showed that the phosphorus levels were significantly higher in the HA group for mineral concentrations at postoperative week 4 (Figure 6). More precise measurements of the mineral concentrations showed no significant differences between the HA and Sm groups (Figure 7). In addition, calcium deposition on the surface of the implant surface was observed in both groups.

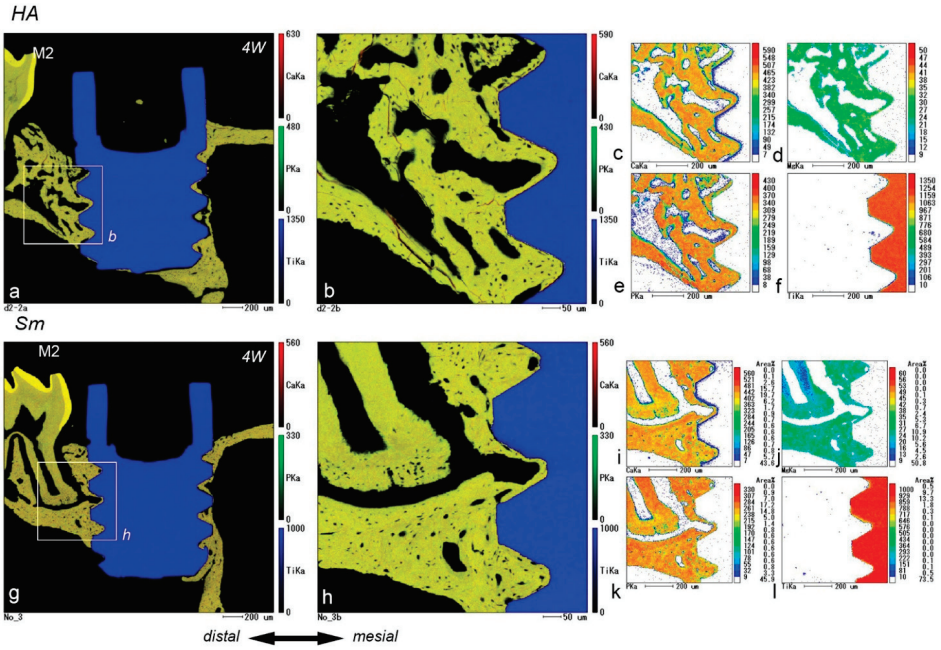


Figure 5. Sagittal views of the tissues surrounding the implants in the HA (**a**–**f**) and Sm groups (**g**–**l**) at week 4 after implantation obtained by EPMA procedures. (**b**) and (**h**) are higher magnifications of the boxed areas in (**a**) and (**g**), respectively. (**a**,**b**,**g**,**h**) Direct contact between the implant surface and surrounding bone is completed, although certain areas are not covered with bone. (**c**–**f**,**i**–**l**) The calcium (**c**,**l**), phosphorus (**e**,**k**), and magnesium concentrations (**d**,**j**) in the surrounding bone do not appear to be different from those of the preexisting bone. Low calcium levels are observed on the surface of the implant (**f**,**l**). IS, implant space. Scale bars = (**a**,**c**–**g**,**i**–**l**) 200 μm, and (**b**,**h**) 50 μm.

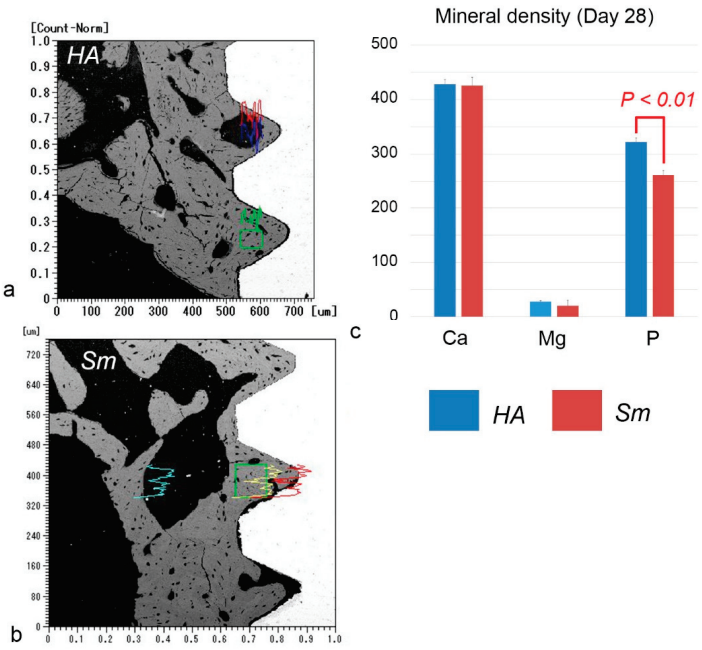


Figure 6. Quantitative analyses of the element densities of calcium, magnesium, and phosphorus in the surrounding bone demonstrate a significant difference in the phosphorous levels between the HA and Sm groups. The boxes in (**a**,**b**) indicate the areas analyzed for the element density. (**a**,**b**) Back scattered electron images. The line graphs colored with red, green, and blue or yellow indicate the mineral density of calcium, magnesium, and phosphorus, respectively. (**c**) The phosphorus level is significantly higher in the HA group for mineral density at postoperative week 4.

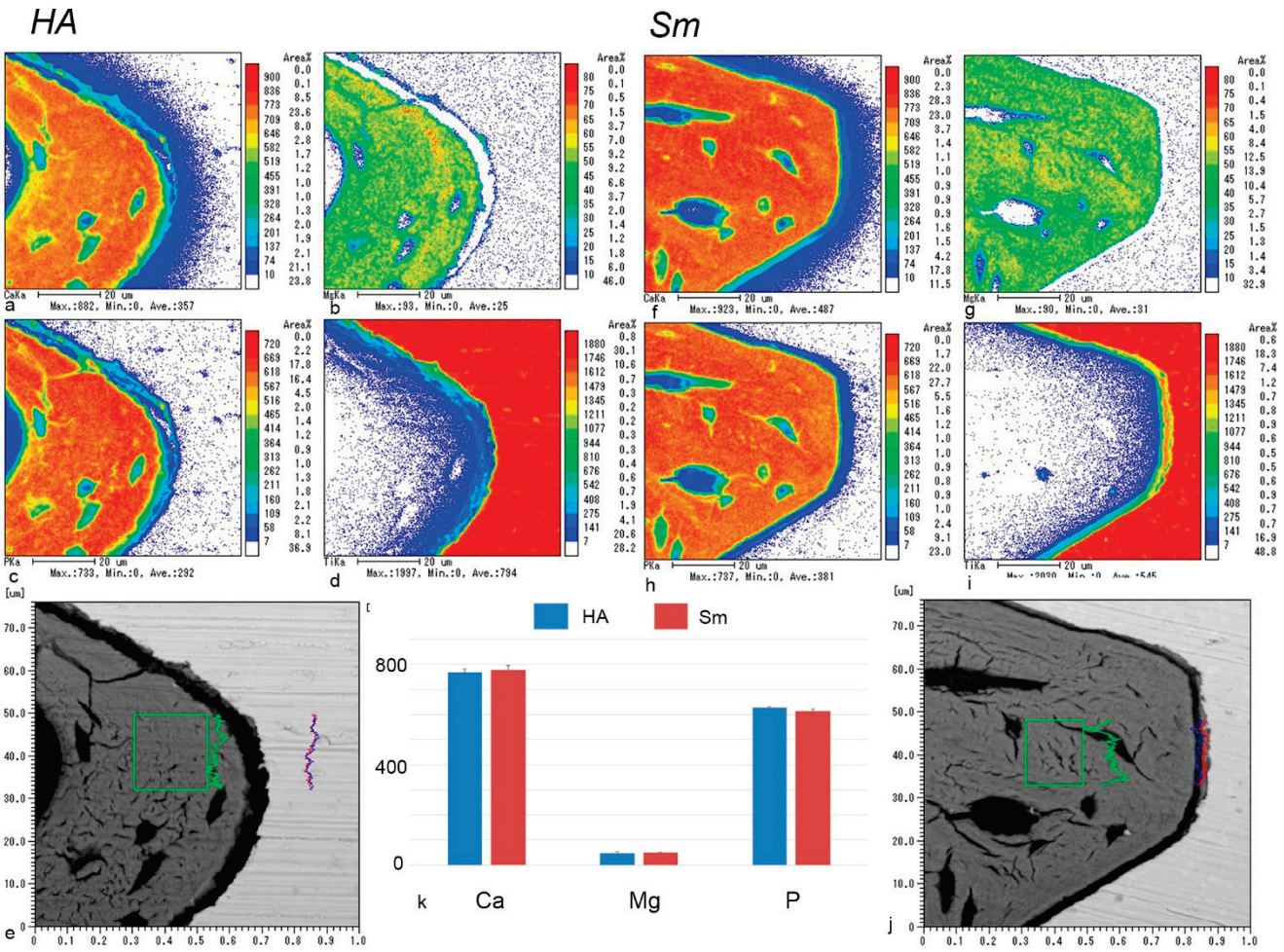


Figure 7. Sagittal views of the tissues surrounding implants in the HA (**a**–**e**) and Sm groups (**f**–**j**) and the element densities (**k**) at week 4 after implantation obtained by EPMA procedures. (**a**–**d**,**f**–**i**) The calcium (**a**,**f**), magnesium (**b**,**g**), and phosphorus (**c**,**h**) in the surrounding bone are similar to those of the preexisting bone. Low calcium levels are observed on the surface of the titanium (**d**,**i**) implant. (**k**) Quantitative analyses of the element densities of calcium, magnesium, and phosphorus in the surrounding bone demonstrate no significant difference in the element densities between the HA and Sm groups. The boxes in (**e**,**j**) indicate the areas analyzed for the element density. (**e**,**j**) Back scattered electron images. The line graphs colored with red, green, and blue indicate the mineral density of calcium, magnesium, and phosphorus, respectively. Scale bars = (**a**–**d**,**f**–**i**) 20 μm.

3. Discussion

Bone formation occurred on the preexisting bone surface (indirect osteogenesis) and/or on the implant surface (direct osteogenesis), and osseointegration was established at postoperative week 4 in both the HA and Sm groups. A comparison of the osseointegration rates, including direct and indirect osteogenesis, between the two groups revealed that direct osteogenesis was significantly lower in the Sm group at postoperative week 4. In addition, OPN immunoreactivity at the bone-implant interface was significantly decreased in the Sm group at postoperative weeks 2 and 4. These results indicate that the lack of HA on the implant surface affected the OPN immunoreactivity at the bone-implant interface, resulting in decreased direct osteogenesis after immediate placement of titanium implants. In the experiment in which a titanium implant is placed in a rat maxilla, the healing pattern is different depending on the gap between the bone and implant [12]. Bone formation begins in an island-like fashion if there is a large gap at the bone-implant interface, whereas if there is a narrow gap preexisting bone is first resorbed by osteoclasts followed by bone

formation, resulting in indirect osteogenesis. In addition, the area where the bone and implant are in close proximity may remain dead bone for a long period after implantation and eventually undergo remodeling. When HA-coated titanium implants are placed in the rat maxilla, osteoclast-like cells appear on the implant surface, followed by osteoblast alignment on the implant surface and then direct osteogenesis from the implant surface [13]. Thus, the presence of HA on the implant surface indicates that direct osteogenesis is stimulated. Furthermore, it contributed to the high success rate of immediately placed implants in the HA group (93.3%), compared with that of Sm group (74.4%). Regarding the healing of long bone diaphyseal fractures, many therapeutic strategies, such as scaffolds, growth factors, cell therapies, and systemic pharmacological treatments, have been proposed in combination with surgical treatment to enhance the healing process. Clinical evidence of scaffolds effect on bone repair of acute long bone shaft fractures revealed that the level of clinical evidence of HA or β-TCP was weak, compared with autologous or allogenic bone graft [14]. The combination of growth factors including bone morphogenetic proteins or platelet rich plasma (PRP), an autologous blood concentrate suspension of platelets, may be recommended to accelerate the healing process during HA-blasted titanium implantation. A systematic review suggests that PRP has a positive effect on secondary implant stability after implant placement in patients [15].

A problematic complication after dental implant treatment is peri-implantitis, with an incidence rate of 56% [16]. Peri-implantitis is defined as mucosal lesions with suppuration and deepened pockets and a loss of supporting marginal bone. Biofilm formation plays an important role in the initiation and progression of peri-implant diseases and is associated with gram-negative anaerobes similar to those found around natural teeth in patients with severe chronic periodontitis [17]. Machined-surface implants have been replaced with implants that utilize two technologies to improve the osteoconductivity of titanium implants. One is a technique where the metal implant is coated with bioactive compounds that promote bone formation, and the other is a technique in which a rough surface is formed directly on the metal implant surface [18]. Machined-surface implants have the highest rate of decontamination, whereas HA-coated implants have the lowest rate [19]. Thus, there is a trade-off between osteoconductivity and the risk of peri-implantitis.

This study demonstrated that the rate of OPN positivity at the bone-implant interface correlated with the rate of osseointegration. OPN plays an important role in bone remodeling, where the resting osteoblasts are activated by $1,25(OH)_2D_3$ and PTH to secrete proteinase and OPN [7]. OPN is deposited at the calcification front of the bone matrix, and subsequently osteoclasts are recruited at the calcified bone tissue. When the osteoclasts resorb the bone matrix and secret OPN, OPN is deposited at the bone matrix in the resorbed fossa and osteoblasts are recruited to begin bone formation. During direct osteogenesis, the deposition of OPN on the implant surface also occurs prior to bone formation. Thus, the deposition of OPN on the implant surface triggers direct osteogenesis. The importance of OPN in direct osteogenesis is supported by reports that have demonstrated that direct osteogenesis is significantly reduced in *Opn*-deficient mice [6] and that the addition of recombinant OPN on the surface of implants in wild-type mice causes early direct osteogenesis [20].

In this study, EPMA analysis showed that calcium deposition on the implant surface was observed in both the HA and Sm groups. In addition, a gap existed at the bone-implant interface as seen in the back scattered electron images. When the HA and Sm implants were compared, the gap was wider in the HA implants. The gap probably included artifacts due to the width of the HA blasting and the expansion and contraction of the resin. Elemental analysis by EPMA may not accurately reflect the elemental concentrations in vivo because of edge effects at the boundaries between samples made of different materials, such as the bone-implant interface. However, a comparison of the elemental concentrations of calcium and phosphorus indicates that calcium incorporation onto the titanium implant is higher than phosphorus, suggesting that calcium deposition on the implant surface occurs in vivo as well.

4. Materials and Methods

4.1. Animals and Experimental Procedure

Male Crlj:CD1 (ICR) mice were purchased from Charles River Laboratories (Yokohama, Japan). All surgeries were conducted under anesthesia using an intraperitoneal injection of a combined solution (0.05–0.1 mL/10 g) of 1.875 mL Domitor® (Nippon Zenyaku Kogyo Co., Ltd., Koriyama, Japan), 2 mL midazolam (Sandoz KK, Tokyo, Japan), 2.5 mL Vetorphale® (Meiji Seika Pharma Co., Ltd., Tokyo, Japan), and 18.625 mL physiological saline.

4.2. Immediate Implant Placement

The right maxillary first molars (M1) from 4-week-old mice were extracted with a pair of modified dental forceps under anesthesia and replaced with titanium implants blasted with HA and β-TCP (1:4) (HA group) or non-blasted machined-surface titanium implants (Sm group). The implant design was a cylindrical, threaded screw type [5]. The detailed procedure has been reported in a previous study [5]. The surface morphology of the non-blasted implant (secondary and backscattered images) on the implant surface was analyzed using an EPMA (EPMA-1610; Shimadzu, Kyoto, Japan) (Figure 8a–c). The percentage weights of each element were as follows: titanium 84.9%, vanadium 8.6%, aluminum 5.9%, and iron 0.7% (Figure 8d). The information of the blasted implant has been detailed in a previous study [5].

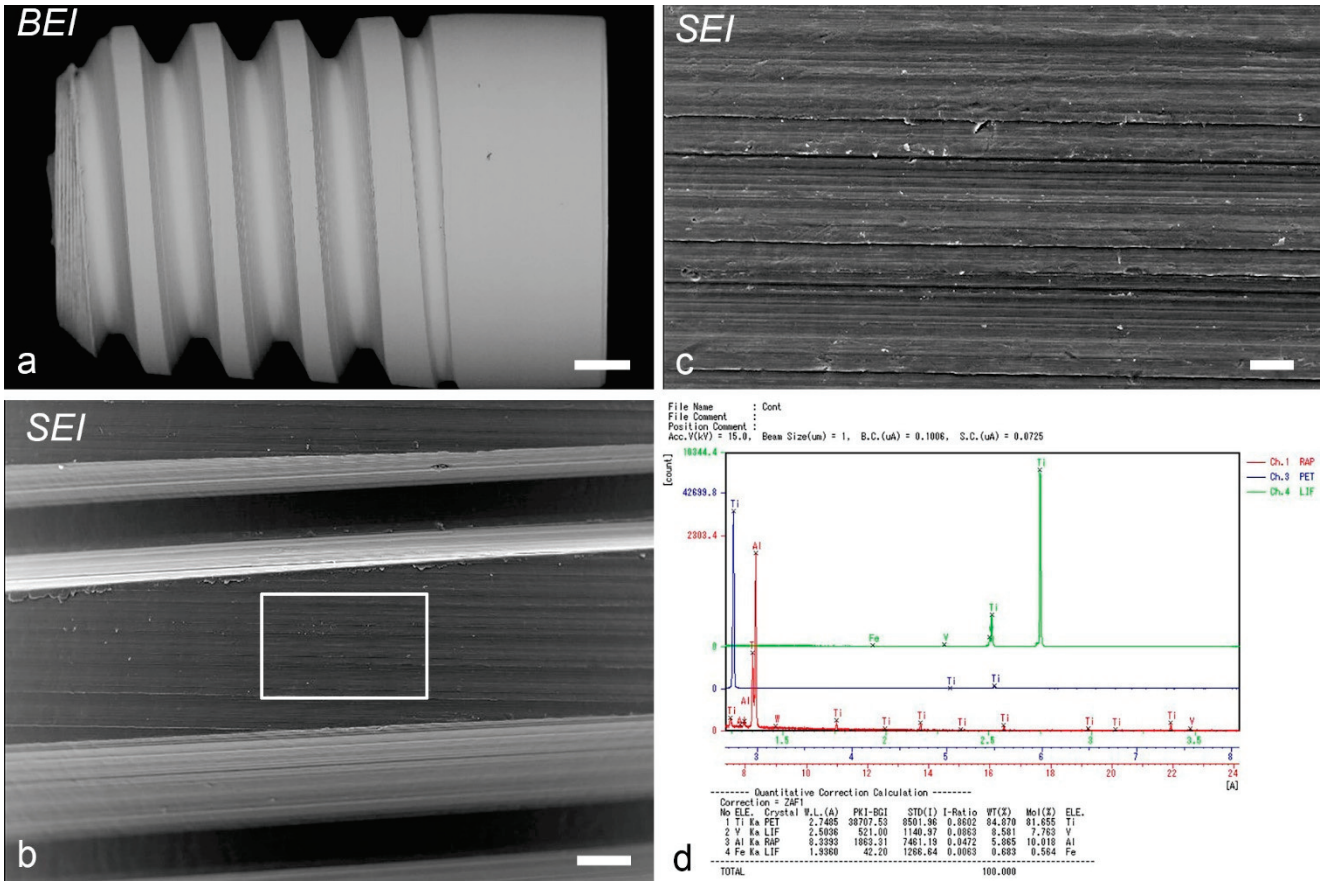


Figure 8. The surface morphology of a non-blasted implant (**a**–**c**) and the percentage weights of each element on the implant surface (**d**) as determined by EPMA. (**a**) A backscattered electron image of the implant. (**b**,**c**) A secondary electron image of the implant. (**c**) Higher magnification of the *boxed area* in (**b**). (**d**) Quantitative data of minerals on the implant surface. Scale bars = (**a**) 200 μm, (**b**) 50 μm, and (**c**) 10 μm.

4.3. Histological Procedure and Immunohistochemical and Histochemical Analysis

Following the fixation of mice at 1, 5, 7, 14, and 28 days after implantation (Table 1), the samples were processed for the following procedures: decalcified samples were processed for Hematoxylin & Eosin (H&E) and Azan staining, immunohistochemistry for OPN and Ki67, and TRAP histochemistry. Detailed information regarding these procedures is presented in a previous study [5].

Table 1. Number of animals for histological and immunohistochemical analyses for Ki67 and OPN and TRAP histochemistry.

Group	Method	Day 1	Day 5	Week 1	Week 2	Week 4	Total
HA	Histological section	3 [1]	4 [1]	4 [1]	3 [1]	6 (4 [1])	20 (18 [1])
	Ki67	(3 [1])	(4 [1])	(4 [1])		-	(11 [1])
	OPN	(3 [1])	(4 [1])	(4 [1])	(3 [1])	(6 (4 [1]))	(20 [1])
	TRAP	(3 [1])	(4 [1])	(4 [1])	(3 [1])	(4 [1])	(18 [1])
	EPMA					3 [1]	3 [1]
Sm	Histological section	3	3	4	4	6	20
	Ki67	(3)	(3)	(4)		-	(10)
	OPN	(3)	(3)	(4)	(4)	(6)	(20)
	TRAP	(3)	(3)	(4)	(4)	(6)	(20)
	EPMA					3	3
Total		6	7	8	7	18	46

[1] These samples were used in a previous study [5].

4.4. EPMA Analysis

Undecalcified samples embedded in Epon 812 (Taab, Berkshire, UK) were ground down to be exposed at a position approximately equal to the central plane of the implants and were used for element analysis using an EPMA (EPMA-1610, Shimadzu Co., Kyoto, Japan). The EPMA settings were as follows: spot size 1 μm; pixel matrix 380 × 380 to 446 × 446; voltage 15.0 kv; electrical current 19.95–30.10 μA. The density of calcium, magnesium, phosphorus, and titanium in the surrounding bone between the screw pitches was analyzed.

4.5. Statistical Analysis

The number of Ki67-positive cells at the bone-implant interface of each specimen (283 × 355 μm^2 grid was selected) was counted by the counter tool in Photoshop 2021 (Adobe Inc., San Jose, CA, USA). Data were obtained from 21 maxillae from the HA and Sm groups (Table 1) for the cell proliferation assay using the immunoreactivity of Ki67. The rate of OPN-positive perimeter around the implant or the direct and indirect osteogenesis was statistically analyzed in the OPN immunostained or H&E-stained sections using the two-tailed Student's *t*-test in the same manner as our previous study [6]. The percentage of osseointegration and OPN-positive perimeters in the total perimeter of the bone-implant interface was calculated using software (Image J 1.45s; National Institutes of Health, Bethesda, MD, USA). The direct and indirect osteogeneses were determined in the histological sections: the direct osteogenesis showed the direct bone deposition on the implant surface, whereas the soft tissue intervened at the bone-implant surface in the indirect osteogenesis. Furthermore, the number of Ki67-positive cells among the different stages after implantation was compared using one-way ANOVA followed by the Bonferroni test for multiple comparisons and the rate of osseointegration, OPN-positive perimeter, and the number of Ki67-positive cells between the different groups were compared using the two-tailed Student's *t*-test with statistical software after the confirmation of data normality and homogeneity of variance (SPSS 16.0J for Windows; SPSS Japan, Tokyo, Japan). The threshold for significance was defined as $\alpha = 0.05$. The samples that did not demonstrate a normal distribution were compared with the Kruskal–Wallis test followed by the Bonferroni

test for multiple comparisons for more than three groups or the Mann–Whitney U test for two groups. Data were reported as mean + SD, *P* denoted the *p*-value.

5. Conclusions

In the Sm group, the OPN immunoreactivity rate at the bone-implant interface significantly decreased compared with the HA group at weeks 2 and 4, as well as the rate of direct osteogenesis at week 4. These results suggest that the presence of HA/β-TCP on the implant surface affects the OPN immunoreactivity at the bone-implant interface, resulting in the increase of direct osteogenesis following the immediately placed titanium implant and contributes to the high success rate in the HA group. A complication after dental implant treatment is peri-implantitis. Machined-surface implants have the highest rate and HA-coated implants have the lowest rate of decontamination. Thus, there is a trade-off between osteoconductivity and peri-implantitis risk.

Author Contributions: Conceptualization, T.W. and H.O.; methodology, H.O.; validation, T.W., S.M., K.S. and H.O.; formal analysis, T.W., S.M., K.S. and H.O.; investigation, T.W., S.M., K.S. and H.O.; data curation, T.W., S.M., K.S. and H.O.; writing—original draft preparation, S.M. and H.O.; writing—review and editing, T.W. and K.S.; visualization, S.M. and H.O.; supervision, H.O.; funding acquisition, S.M. All authors have read and agreed to the published version of the manuscript.

Funding: This research was funded by a Grant-in-Aid for the Japan Society for the Promotion of Science Fellows (no. 19J11806 to S.M.).

Institutional Review Board Statement: All animal experiments were reviewed by the Institutional Animal Care and Use Committee and approved by the President of Niigata University (Permit Number: 143-2).

Informed Consent Statement: Not applicable.

Data Availability Statement: All data generated or analyzed during this study are included in this published article.

Acknowledgments: The authors cordially thank Messrs. M. Kobayashi (Center for Coordination of Research Facilities, Institute for Research Promotion, Niigata University) and S. Kenmotsu for their technical assistance.

Conflicts of Interest: The authors declare no conflict of interest.

References

1. Adell, R.; Lekholm, U.; Rockler, B.; Branemark, P.I. A 15-year study of osseointegrated implants in the treatment of the edentulous jaw. *Int. J. Oral Surg.* **1981**, *10*, 387–416. [CrossRef] [PubMed]
2. Komori, T. Whole Aspect of Runx2 Functions in Skeletal Development. *Int. J. Mol. Sci.* **2022**, *23*, 5776. [CrossRef] [PubMed]
3. Nakamichi, Y.; Udagawa, N.; Suda, T.; Takahashi, N. Mechanisms involved in bone resorption regulated by vitamin D. *J. Steroid Biochem. Mol. Biol.* **2018**, *177*, 70–76. [CrossRef] [PubMed]
4. Davies, J.E. Understanding peri-implant endosseous healing. *J. Dent. Educ.* **2003**, *67*, 932–949. [CrossRef] [PubMed]
5. Watanabe, T.; Nakagawa, E.; Saito, K.; Ohshima, H. Differences in Healing Patterns of the Bone-Implant Interface between Immediately and Delayed-Placed Titanium Implants in Mouse Maxillae. *Clin. Implant. Dent. Relat. Res.* **2016**, *18*, 146–160. [CrossRef] [PubMed]
6. Makishi, S.; Saito, K.; Ohshima, H. Osteopontin-deficiency disturbs direct osteogenesis in the process of achieving osseointegration following immediate placement of endosseous implants. *Clin. Implant. Dent. Relat. Res.* **2017**, *19*, 496–504. [CrossRef] [PubMed]
7. Sodek, J.; Ganss, B.; McKee, M.D. Osteopontin. *Crit. Rev. Oral Biol. Med.* **2000**, *11*, 279–303. [CrossRef] [PubMed]
8. Makishi, S.; Yamazaki, T.; Ohshima, H. Osteopontin on the Dental Implant Surface Promotes Direct Osteogenesis in Osseointegration. *Int. J. Mol. Sci.* **2022**, *23*, 1039. [CrossRef]
9. Garcia-Gareta, E.; Coathup, M.J.; Blunn, G.W. Osteoinduction of bone grafting materials for bone repair and regeneration. *Bone* **2015**, *81*, 112–121. [CrossRef]
10. Tour, G.; Wendel, M.; Tcacencu, I. Cell-derived matrix enhances osteogenic properties of hydroxyapatite. *Tissue Eng. Part A* **2011**, *17*, 127–137. [CrossRef] [PubMed]
11. Nery, E.B.; LeGeros, R.Z.; Lynch, K.L.; Lee, K. Tissue response to biphasic calcium phosphate ceramic with different ratios of HA/beta TCP in periodontal osseous defects. *J. Periodontol.* **1992**, *63*, 729–735. [CrossRef]

12. Futami, T.; Fujii, N.; Ohnishi, H.; Taguchi, N.; Kusakari, H.; Ohshima, H.; Maeda, T. Tissue response to titanium implants in the rat maxilla: Ultrastructural and histochemical observations of the bone-titanium interface. *J. Periodontol.* **2000**, *71*, 287–298. [CrossRef]
13. Shirakura, M.; Fujii, N.; Ohnishi, H.; Taguchi, Y.; Ohshima, H.; Nomura, S.; Maeda, T. Tissue response to titanium implantation in the rat maxilla, with special reference to the effects of surface conditions on bone formation. *Clin. Oral Implant. Res.* **2003**, *14*, 687–696. [CrossRef] [PubMed]
14. Marongiu, G.; Contini, A.; Lepri, A.C.; Donadu, M.; Verona, M.; Capone, A. The treatment of acute diaphyseal long-bones fractures with orthobiologics and pharmacological interventions for bone healing enhancement: A systematic review of clinical evidence. *Bioengineering* **2020**, *7*, 22. [CrossRef]
15. Lyris, V.; Millen, C.; Besi, E.; Pace-Balzan, A. Effect of leukocyte and platelet rich fibrin (L-PRF) on stability of dental implants. A systematic review and meta-analysis. *Br. J. Oral Maxillofac. Surg.* **2021**, *59*, 1130–1139. [CrossRef] [PubMed]
16. Lindhe, J.; Meyle, J.; Periodontology, E.W. Peri-implant diseases: Consensus Report of the Sixth European Workshop on Periodontology. *J. Clin. Periodontol.* **2008**, *35*, 282–285. [CrossRef] [PubMed]
17. Poli, P.P.; Cicciu, M.; Beretta, M.; Maiorana, C. Peri-Implant Mucositis and Peri-Implantitis: A Current Understanding of Their Diagnosis, Clinical Implications, and a Report of Treatment Using a Combined Therapy Approach. *J. Oral Implant.* **2017**, *43*, 45–50. [CrossRef] [PubMed]
18. Kuroda, K.; Okido, M. Hydroxyapatite Coating of Titanium Implants Using Hydroprocessing and Evaluation of Their Osteoconductivity. *Bioinorg. Chem. Appl.* **2012**, *2012*, 730693. [CrossRef] [PubMed]
19. Kubasiewicz-Ross, P.; Fleischer, M.; Pitulaj, A.; Hadzik, J.; Nawrot-Hadzik, I.; Bortkiewicz, O.; Dominiak, M.; Jurczyszyn, K. Evaluation of the three methods of bacterial decontamination on implants with three different surfaces. *Adv. Clin. Exp. Med.* **2020**, *29*, 177–182. [CrossRef] [PubMed]
20. Suzuki-Barrera, K.; Makishi, S.; Nakatomi, M.; Saito, K.; Ida-Yonemochi, H.; Ohshima, H. Role of osteopontin in the process of pulpal healing following tooth replantation in mice. *Regen. Ther.* **2022**, *21*, 460–468. [CrossRef] [PubMed]

Disclaimer/Publisher's Note: The statements, opinions and data contained in all publications are solely those of the individual author(s) and contributor(s) and not of MDPI and/or the editor(s). MDPI and/or the editor(s) disclaim responsibility for any injury to people or property resulting from any ideas, methods, instructions or products referred to in the content.

International Journal of
Molecular Sciences

MDPI

Article

Zirconia Nanoparticles as Reinforcing Agents for Contemporary Dental Luting Cements: Physicochemical Properties and Shear Bond Strength to Monolithic Zirconia

Anastasia Beketova [1,†], Emmanouil-Georgios C. Tzanakakis [1,†], Evangelia Vouvoudi [2], Konstantinos Anastasiadis [3], Athanasios E. Rigos [1,4], Panagiotis Pandoleon [1], Dimitrios Bikiaris [2], Ioannis G. Tzoutzas [5] and Eleana Kontonasaki [1,*]

[1] Department of Prosthodontics, School of Dentistry, Faculty of Health Sciences, Aristotle University of Thessaloniki, 54124 Thessaloniki, Greece
[2] Laboratory of Polymers Chemistry and Technology, Department of Chemistry, Faculty of Sciences, Aristotle University of Thessaloniki, 54124 Thessaloniki, Greece
[3] Department of Biomaterials, School of Dentistry, National Kapodistrian University of Athens, 2 Thivon Str., Goudi, 11527 Athens, Greece
[4] Department of Comprehensive Dentistry, College of Dentistry, Texas A&M University, 3000 Gaston Avenue, Dallas, TX 75226, USA
[5] Department of Operative Dentistry, School of Dentistry, National Kapodistrian University of Athens, 2 Thivon Str., Goudi, 11527 Athens, Greece
* Correspondence: kont@dent.auth.gr
† These authors contributed equally to this work.

Abstract: Nanofillers in resin materials can improve their mechanical and physicochemical properties. The present work investigated the effects of zirconia nanoparticles (NPs) as fillers in commercial dental luting cements. Two dual-cured self-adhesive composites and one resin modified glass ionomer (RMGI) luting cement were employed. Film thickness (FT), flexural strength (FS), water sorption (W_{sp}), and shear bond strength (SBS) to monolithic zirconia were evaluated according to ISO 16506:2017 and ISO 9917-2:2017, whereas polymerization progress was evaluated with FTIR. Photopolymerization resulted in double the values of *DC*%. The addition of 1% wt NPs does not significantly influence polymerization, however, greater amounts do not promote crosslinking. The sorption behavior and the mechanical performance of the composites were not affected, while the film thickness increased in all luting agents, within the acceptable limits. Thermocycling (TC) resulted in a deteriorating effect on all composites. The addition of NPs significantly improved the mechanical properties of the RMGI cement only, without negatively affecting the other cements. Adhesive primer increased the initial SBS significantly, however after TC, its application was only beneficial for RMGI. The MDP containing luting cement showed higher SBS compared to the RMGI and 4-META luting agents. Future commercial adhesives containing zirconia nanoparticles could provide cements with improved mechanical properties.

Keywords: zirconia nanoparticles; luting cements; bond strength; film thickness; flexural strength; thermocycling; water sorption; dual-curing; FTIR

Citation: Beketova, A.; Tzanakakis, E.-G.C.; Vouvoudi, E.; Anastasiadis, K.; Rigos, A.E.; Pandoleon, P.; Bikiaris, D.; Tzoutzas, I.G.; Kontonasaki, E. Zirconia Nanoparticles as Reinforcing Agents for Contemporary Dental Luting Cements: Physicochemical Properties and Shear Bond Strength to Monolithic Zirconia. *Int. J. Mol. Sci.* **2023**, *24*, 2067. https://doi.org/10.3390/ijms24032067

Academic Editor: Mary Anne Melo

Received: 27 December 2022
Revised: 6 January 2023
Accepted: 18 January 2023
Published: 20 January 2023

Copyright: © 2023 by the authors. Licensee MDPI, Basel, Switzerland. This article is an open access article distributed under the terms and conditions of the Creative Commons Attribution (CC BY) license (https://creativecommons.org/licenses/by/4.0/).

1. Introduction

Since the introduction of zirconia in restorative dentistry as an alternative to metal frameworks, the optimization of bond strength to this new material still remains a popular area of research that has expanded to all generations of zirconia materials including monolithic prosthetic restorations [1,2]. The zirconia in vitro bond strength testing methods vary and may influence the results [3]. Although many in vitro and in vivo experiments have been conducted and researchers have already introduced several different combinations of

surface conditioning methods and luting materials, the results have not led to a method that has been universally accepted [4–6].

Translucent cubic zirconia materials and hybrid multilayered zirconia materials have recently been introduced to further zirconia indications and meet all posterior and anterior restoration demands. The adhesive potential of these new materials can be different due to their different chemical composition [7].

High strength ceramics, especially zirconia, have been characterized as inert materials. The increased fracture toughness, hardness, and absence of a glass phase result in a surface that requires high energy levels to be modified [8,9]. Increased surface roughness is very important to obtain micromechanical retention with any adhesive, however, the contribution of the chemical factor based on the composition of the primer, or the luting agent, is crucial [10–12]. The rheological properties, mechanical properties, and the chemical composition of the luting agent influence the adhesion potential to challenging zirconia surfaces [13,14].

Older generations of luting cements have been characterized as materials with poor mechanical properties and high sensitivity to water sorption [15,16]. Glass ionomer cements have demonstrated a significant increase in adhesion and minimal film thickness [17]. The development of resin-modified glass ionomers improved the mechanical properties of glass ionomers, but the first generation presented a high tendency to water sorption [18], which is now reduced in contemporary materials [15,19]. Moreover, contemporary resin cements, although more viscous than older generations, present extremely low film thickness in most commercial products due to the smaller filler size [20]. The optimum thickness for the clinical use of resin cements, depending on the adhesive substrate, is less than 100 μm [21].

The role of the luting agent is to embrace a dental prosthesis to a dental abutment, to prevent microleakage, and withstand chemical dissolution in the hostile oral environment [17]. Doubtful chemical affinity of the available luting cements and adhesive primers have urged the investigation to seek modifications in the chemical composition of many well-established commercial products to achieve a higher compatibility to zirconia substrates. Most manufacturers have followed this trend and modified their chemical composition where two basic trends have been adopted: either the incorporation of reactive adhesive monomers in the bulk of luting materials or accompanying these materials with specialized liquid primers that contain reactive monomers [6].

Notwithstanding, a new trend in research is the reinforcement of dental restorative materials with different inorganic fillers, apart from traditional amorphous glasses. The target is to increase the mechanical properties of these materials. Recently, nanoparticles have been integrated in glass ionomer resin cements to enhance their mechanical properties with promising results [22]. Moreover, zirconia nanoparticles have been used to strengthen adhesives [23], in resin restorative materials, and core build-up materials [24–26]. Moreover, favorable data have recently been published following the integration of nanoparticles in high impact heat-cured acrylic resin (PMMA) [27,28].

Until now, zirconia (ZrO_2) particles stabilized with tetragonal yttria (Y_2O_3) have not been utilized for the reinforcement of a luting cement. However, zirconia-based nanoparticles are applied in restorative dentistry to improve the mechanical and antibacterial properties of different resin-based materials [29]. The most frequently reported methods for ceramic nanoparticles fabrication include sol–gel synthesis, co-precipitation, hydrothermal, spray-drying, spray pyrolysis, and freeze-drying. By sol–gel synthesis, uniform, nano-sized powders with high purity can be produced [30].

Particularly for the reinforcement of resin luting cements, ZrO_2-based nanofillers could be beneficial for the establishment of durable bonds to zirconia-fixed restorations. Adhesive monomers containing phosphates, especially 10-MDP, create chemical bonds with metal and zirconia substrates [31,32]. There is strong evidence that 10-MDP creates both ionic and hydrogen bonds with zirconia. Moreover, the concentration and purity of 10-MDP is important since at least 1% wt. seems to be efficient in SBS tests [32]. On the other hand, as early as in 1978, Takeyama et al. added a carboxylic adhesive monomer (4-META) to

increase the bond strength between enamel and acrylic resin [33]. Later, this monomer was incorporated in commercially available resin cements, and it is surprising that 4-META products have had the same ingredients since their inception [34]. It is well-established that carboxylic acids can bond to oxidizable metals such as aluminum oxide [35]. In a theoretical model, the insertion of zirconia nanoparticles could enhance the cohesive strength and alter the physicochemical properties of resin cements containing adhesive monomers. Increased mechanical properties in luting materials may promise bond strength durability after aging. The influence of inorganic fillers in any changes of the degree of conversion during the polymerization of dental composites is usually small. Nano-powders, specifically, do not hinder irradiation diffusion in the restoration and thus favorable curing and bond opening is achieved [36,37].

The aim of this research was the characterization of the physico-mechanical properties of zirconia nanoparticles reinforcing contemporary luting cements and the evaluation of the shear bond strength to translucent zirconia. The first null hypothesis of this study is that reinforcement with zirconia nanoparticles does not influence either the physicochemical properties or the polymerization progress of the luting agents tested. The second null hypothesis is that the shear bond strength of three different commercial luting cements to zirconia is not influenced by the integration of zirconia nanoparticles. The third null hypothesis is that the SBS of cements reinforced with zirconia nanoparticles is not influenced by thermal cycling.

2. Results

2.1. Fourier Transform Infrared Spectroscopy (FTIR) Characterization

Many spectra were collected in order to clarify the influence of each parameter in the progress of polymerization for the materials studied. Figure 1 shows the full spectra recorded for the composite materials right after dual polymerization. The effect of the addition of ZrO_2 NPs could not be detected in the full spectra, since tetragonal zirconia presents broad bands at about 430–440 cm^{-1} and a weak broad band at around 600–650 cm^{-1} [1,2]. The spectra were not identical in shape or in the intensity of peaks, but it is apparent that all three commercial materials contained similar ingredients in their nature. Parts from the full spectra were isolated to accurately identify each peak. Figure 2 (top) demonstrates the influence of photopolymerization in the MER, PAN, and SOL luting cements. The chart includes the absorptions in the range of 1660–1560 cm^{-1}, taken right after mixing (control sample), 1 h and 1 d after self-curing, plus a day after additional photocuring. Figure 2 (bottom), on the other hand, presents the partial spectra of the MER, PAN, and SOL adhesive, dual-cured, when ZrO_2 particles were added in 1, 2.5, or 5% wt. The values of *DC*% are given by the equation:

$$DC\% = 100 \cdot \left[1 - \frac{\left(A_{1637/A_{1608}} \right)_t}{\left(A_{1637/A_{1608}} \right)_0} \right]$$

where *A* is the peak area value for the particular peak and time interval, while absorption at 1637 cm^{-1} corresponds to C=C and at 1608 cm^{-1} to C⋯C bonds.

The integration of the peaks for quantitative results via FTIR is a demanding task, taking into consideration the bonds found, the shape, intensity, and limits of the peaks. In the present study, the great absorption at 1637 cm^{-1} illustrates the presence of vinyl bonds C=C in dimethacrylates, which react and produce polydimethacrylate networks. The reaction occurs with self-curing and/or with photocuring, given the correct initiators: BPO for self-polymerization and camphorquinone for photopolymerization (Table 1). Apart from the area beneath the 1637 cm^{-1} peak, the simultaneous integration of another neighboring peak, indicating a group that does not participate in the polymerization reaction, is crucial for comparison reasons (internal standard). Thus, the absolute area numbers do not lead to conclusions, unless they are taken as ratios with the areas of another peak of the spectra (elimination of experimental inconsistencies). For PAN and SOL materials, this other peak is the neighboring 1608 cm^{-1}, corresponding to aromatic bonds C⋯C (due to the

Bis-GMA monomer, Table 1) and for MER, this is the neighboring 1540 cm^{-1} absorption, corresponding to the N–H bond (due to the UDMA monomer). Table 1 lists the results obtained from the calculations.

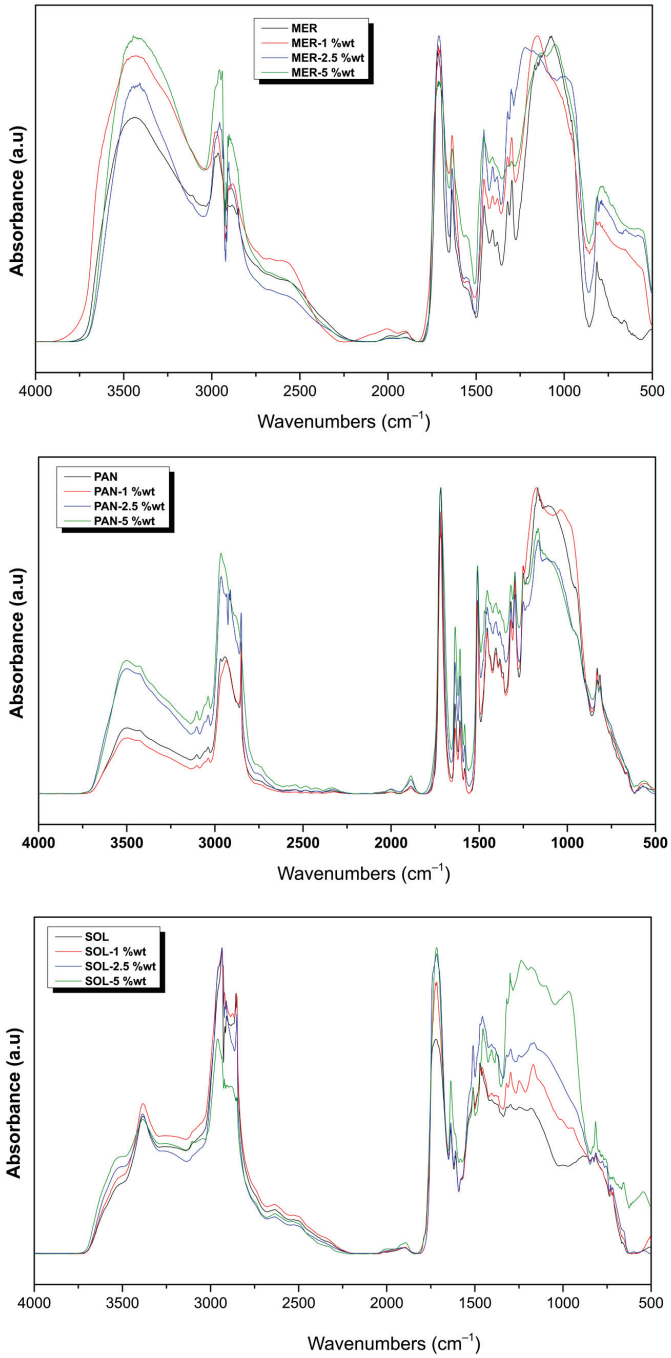


Figure 1. Comparison of the spectra of the three luting cements following the addition of zirconia nanoparticles (ZrO_2 NPs) at all ratios, right after dual polymerization. MER = Meron plus QM, MER-1wt% = Meron plus QM with 1% wt zirconia NPs, MER−2.5wt% = Meron plus QM with 2.5% wt zirconia NPs, MER−5wt% = Meron plus QM with 5% wt zirconia NPs, PAN = Panavia SA Universal, PAN−1wt% = Panavia SA Universal with 1% wt zirconia NPs, PAN−2.5wt% = Panavia SA Universal with 2.5% wt zirconia NPs, PAN−5wt% = Panavia SA Universal with 5% wt zirconia NPs, SOL = Solocem, SOL−1wt% = Solocem with 1% wt zirconia NPs, SOL−2.5wt% = Solocem with 2.5% wt zirconia NPs, SOL−5wt% = Solocem with 5% wt zirconia NPs.

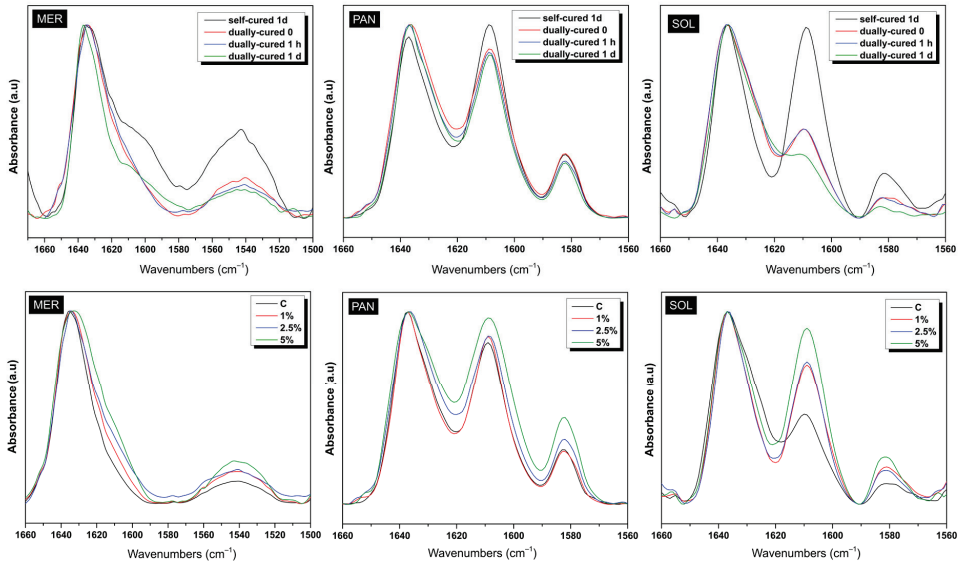


Figure 2. Comparisons of the limited-area spectra for all cements. (**Top**) Effect of curing and (**Bottom**) influence of the nanoparticle (NP) content on the polymerization progress. MER = Meron plus QM, SOL = Solocem, PAN = Panavia SA Universal, C = control without NPs, 1% = 1% wt. NPs, 2% = 2% wt. NPs, 5% = 5% wt. NPs.

Table 1. The *DC*% results derived from the FTIR calculations for all materials when ZrO_2 powder was added in the mixture (mean ± s.d., n = 2). MER = Meron plus QM, PAN = Panavia SA Universal, SOL = Solocem.

Time	Sample	*DC*%	Sample	*DC*%	Sample	*DC*%
t = 0	MER-C	0.0	PAN-C	0.0	SOL-C	0.0
t = 1 h		30.6 ± 1.2 ^{a}		24.6 ± 3.2 ^{a}		31.2 ± 0.8 ^{a}
t = 1 d		39.9 ± 2.4 ^{b}		32.0 ± 2.4 ^{b}		41.1 ± 1.1 ^{b}
t = 0	MER_{dual}	60.6 ± 1.5 ^{c}	PAN_{dual}	64.4 ± 1.1 ^{c}	SOL_{dual}	77.8 ± 2.6 ^{c}
t = 1 h		63.9 ± 0.8 ^{c}		63.5 ± 0.8 ^{c}		78.8 ± 2.4 ^{c}
t = 1 d		62.6 ± 1.2 ^{c}		71.8 ± 1.5 ^{d}		78.5 ± 2.4 ^{c}
t = 0	MER-1_{dual}	58.3 ± 2.0 ^{c,d}	PAN-1_{dual}	57.4 ± 2.3 ^{e}	SOL-1_{dual}	75.5 ± 1.2 ^{c}
t = 1 h		58.6 ± 1.0 ^{d}		60.2 ± 2.1 ^{c,e}		76.2 ± 1.6 ^{c}
t = 1 d		59.4 ± 1.6 ^{c,d}		61.3 ± 1.8 ^{c}		77.0 ± 0.9 ^{c}
t = 0	MER-2.5_{dual}	56.8 ± 2.5 ^{d}	PAN-2.5_{dual}	53.3 ± 3.1 ^{e}	SOL-2.5_{dual}	66.3 ± 2.1 ^{e}
t = 1 h		59.3 ± 0.6 ^{c,d}		55.1 ± 2.9 ^{e}		68.4 ± 0.8 ^{e}
t = 1 d		60.6 ± 0.7 ^{c,d}		56.3 ± 2.4 ^{e}		73.8 ± 1.9 ^{c,e}
t = 0	MER-5_{dual}	50.8 ± 2.4 ^{e}	PAN-5_{dual}	55.1 ± 2.5 ^{e}	SOL-5_{dual}	61.7 ± 3.8 ^{e}
t = 1 h		54.4 ± 1.9 ^{e}		57.3 ± 1.0 ^{e}		66.6 ± 2.1 ^{e}
t = 1 d		59.4 ± 1.9 ^{c,d}		58.1 ± 0.9 ^{e}		71.3 ± 2.6 ^{e}

Common lowercase letter as superscript in the same column indicates no significant difference at the $p < 0.05$ level. MER_{dual} = Meron plus QM after dual curing, MER-1_{dual} = Meron plus QM with 1% zirconia NPs after dual curing, MER-2.5_{dual} = Meron plus QM with 2.5% zirconia NPs after dual curing, MER-5_{dual} = Meron plus QM with 5% zirconia NPs after dual curing, SOL_{dual} = Solocem after dual curing, SOL-1_{dual} = Solocem with 1% zirconia NPs after dual curing, SOL-2.5_{dual} = Solocem with 2.5% zirconia NPs after dual curing, SOL-5_{dual} = Solocem with 5% zirconia NPs after dual curing, PAN_{dual} = Panavia SA Universal after dual curing, PAN-1_{dual} = Panavia SA Universal with 1% zirconia NPs after dual curing, PAN-2.5_{dual} = Panavia SA Universal with 2.5% zirconia NPs after dual curing, PAN-5_{dual} = Panavia SA Universal with 5% zirconia NPs after dual curing.

2.2. Water Sorption and Solubility

As seen in Figure 3, the addition of NPs did not statistically significantly influence the initial W_{sp} values of all three luting cements. The best performance with the lowest water sorption was measured in the PAN group, followed by the SOL group. The highest values

were measured in the MER group (0.22 mg/mm^3), all within the clinically acceptable levels.

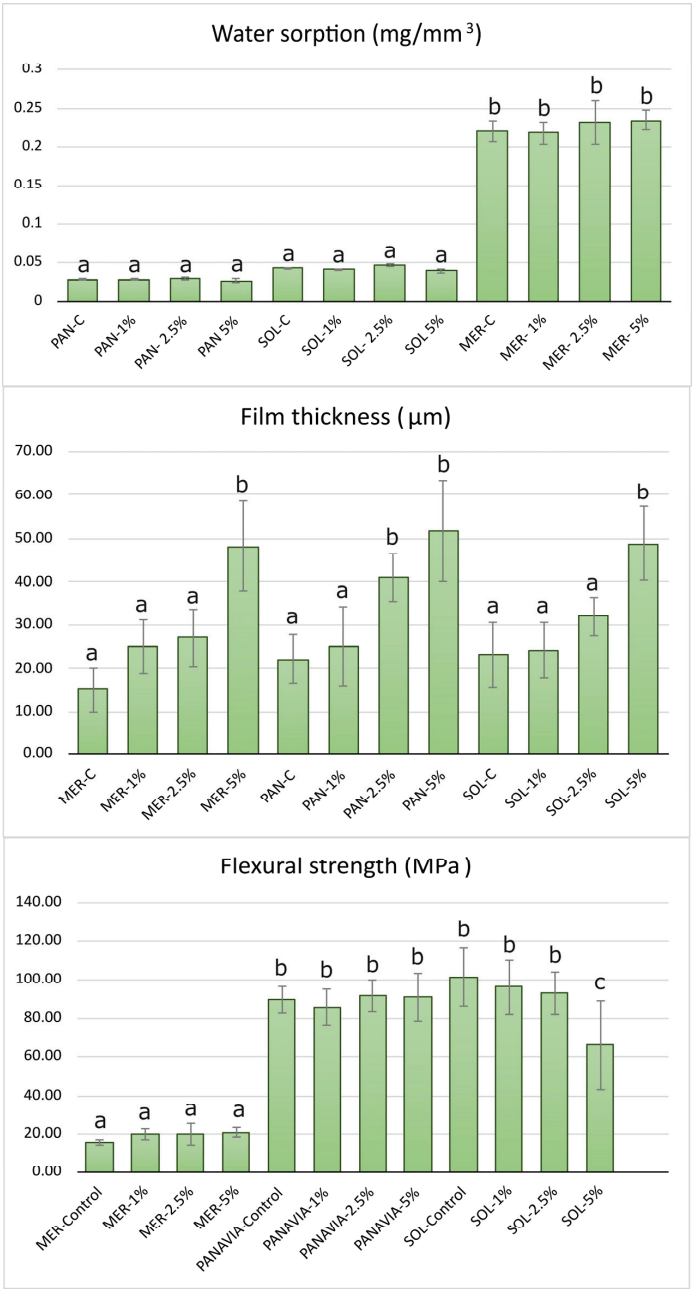


Figure 3. Mean values and SD (error bars) for water sorption, film thickness, and flexural strength of the composite specimens. Different letters suggest significant differences in the mean values. MER = Meron plus QM, MER−1% = Meron plus QM with 1% wt zirconia NPs, MER−2.5% = Meron plus QM with 2.5% wt zirconia NPs, MER−5% = Meron plus QM with 5% wt zirconia NPs, PAN = Panavia SA Universal, PAN−1% = Panavia SA Universal with 1% wt zirconia NPs, PAN−2.5% = Panavia SA Universal with 2.5% wt zirconia NPs, PAN−5% = Panavia SA Universal with 5% wt zirconia NPs, SOL = Solocem, SOL−1% = Solocem with 1% wt zirconia NPs, SOL−2.5% = Solocem with 2.5% wt zirconia NPs, SOL−5% = Solocem with 5% wt zirconia NPs.

2.3. Film Thickness

As seen in Figure 3 the film thickness in all control groups was less than 50 µm and in all cases less than 10 µm above the manufacturer's measurements. The ranking was MER−C (15 ± 5 µm) < PAN−C (22 ± 5 µm) < SOL−C (24 ± 5 µm) at 0.05. After the addition of

nanoparticles at 1% wt, no significant differences were found. The ranking after the addition of 2.5% wt ZrO_2 NPs was MER−2.5 (25 ± 8 μm) < SOL−2.5 (32 ± 4 μm) < PAN−2.5 (41 ± 5 μm). Finally, the visual observation that the viscosity decreased after the addition of 5% nanoparticles predicted the significantly increased film thickness in all groups (Figure 3).

2.4. Estimation of Flexural Strength

The flexural strength results showed a significant difference between MER and the two other resin cements, PAN and SOL. The addition of 2.5% of nanoparticles resulted in higher values for the MER group (20 ± 5 MPa). The PAN and SOL groups resulted in similar values in almost all groups except for SOL−5%. In all cases, the different % amounts of nanoparticles did not significantly affect the flexural strength except for the SOL group, where a 5% wt addition significantly reduced the strength, while for the MER group, all concentrations led to an increase in the flexural strength but not on a significant level.

2.5. Shear Bond Strength Results

A total of 24 groups were subjected to the SBS test. The initial values before thermocycling and the final values for each group are both summarized in Table 2. Groups MER−C, MER−2.5, and SOL resulted in the lowest values of all groups studied. On the other hand, groups SOL-G, SOL−G−2.5, PAN−G, and PAN−G−2.5 exhibited higher values and group PAN−G−2.5 had the highest (22 ± 5 MPa). All other groups ranged between 5 and 10 MPa.

Table 2. Results of the shear bond strength tests for all composite cements studied.

	Before TC	After TC		
Sample	**SBS (MPa)**	**SBS (MPa)**	**Change %**	***p* Value**
MER−C	3.73 ± 0.40 [a]	0 ± 0	-	-
MER−2.5	4.01 ± 0.30 [a]	0 ± 0	-	-
MER−GL−C	13.02 ± 2.98 [b]	15.12 ± 4.81 [c]	16.12	0.401
MER−GL−2.5	13.22 ± 3.42 [b]	6.69 ± 1.74 [b]	−49.36	0.051
SOL−C	4.69 ± 1.91 [d]	1.46 ± 0.24 [f]	−68.91	0.304
SOL−2.5	7.83 ± 4.32 [d]	0 ± 0	−100	-
SOL−GL−C	20.38 ± 5.63 [e]	6.45 ± 2.39 [f]	−68.35	<0.01
SOL−GL−2.5	23.15 ± 1.97 [e]	4.87 ± 1.38 [f]	−78.95	<0.01
PAN−C	13.62 ± 5.08 [g]	12.87 ± 4.41 [i]	−5.50	<0.01
PAN−2.5	12.78 ± 0.83 [g]	9.00 ± 5.09 [i]	−29.59	<0.01
PAN−GL−C	24.31 ± 5.65 [h]	3.35 ± 1.09 [j]	−86.20	<0.01
PAN−GL−2.5	29.96 ± 7.74 [h]	6.03 ± 3.22 [i]	−79.89	<0.01

Different letters within each column show statistically significant differences among groups of the same cement brand with or without NPs and Gluma (GL) adhesive, while *p* value shows difference before and after TC. MER−C = Meron plus QM, MER−2.5 = Meron plus QM with 2.5% wt zirconia NPs, MER−GL−C = Meron plus QM after Gluma application, MER−GL−2.5 = Meron plus QM with 2.5% wt zirconia NPs after Gluma application, SOL = Solocem, SOL−2.5 = Solocem with 2.5% wt zirconia NPs, SOL−GL−C = Solocem after Gluma application, SOL−GL−2.5 = Solocem with 2.5% wt zirconia NPs after Gluma application, PAN = Panavia SA Universal, PAN−2.5 = Panavia SA Universal with 2.5% wt zirconia NPs, PAN−GL−C = Panavia SA Universal after Gluma application, PAN−GL−2.5 = Panavia SA Universal with 2.5% wt zirconia NPs after Gluma application.

For MER three-way ANOVA showed that the presence of Gluma had a significant effect on the shear bond strength ($p = 0.006$), while this was not the case for the addition of NPs. However, the interaction of the addition of NPs and TC presented a significant effect ($p = 0.045$), and pairwise comparisons demonstrated a significant difference between MER-C and MER−2.5% after thermocycling. Regarding the PAN, TC, and Gluma adhesives, they all presented a significant main effect ($p < 0.001$ and $p = 0.03$, respectively) as well as their interaction ($p < 0.01$). Similarly to MER, the presence of NPs did not affect the SBS.

The main effects of Gluma and TC were also significant for SOL ($p < 0.001$) as well as their interaction ($p = 0.05$). The presence of NPs did not affect the shear bond strength mean values in a statistically significant manner.

After thermocycling, there was a significant decrease in SBS in all groups. The lowest values were observed in MER−C−TC, MER−2.5−TC, SOL−C−TC, and SOL−2.5−TC. The highest values were observed in PAN−C−TC, PAN−2.5−TC, and MER−G−C−TC. All the other groups values ranged from 0 to 6.7 MPa. It was observed that TC was detrimental to groups with high initial values except for the case of MER−G−C. Only the PAN−C, PAN−2.5, and MER−G−C groups showed resistance in thermal degradation after 5000 cycles. Three groups with 2.5% nanoparticle addition (MER−G 2.5, SOL−2.5, PAN−G−2.5) showed a significant reduction in SBS, but showed a higher ranking than their control groups after TC.

2.6. Failure Mode Results

Using image analysis, the adhesive failure mode (ADFM%) was calculated from every specimen in each group and is presented in Figure 4. Only PAN groups presented significantly lower ADFM% than the other groups (64–86%). Groups PAN-GL and PAN 2.5%−GL showed the best failure mode results of 67% and 71% respectively. MER groups without adhesive presented the least favorable results (88–94%). In the MER groups, the high ADFM% was decreased after GL treatment (82–83%), except for group MER−GL−TC (88%). In the SOL and PAN groups, GL treatment resulted in a decrease in ADFM. Figure 5 illustrates indicative snapshots of the failed samples through stereomicroscopic imaging.

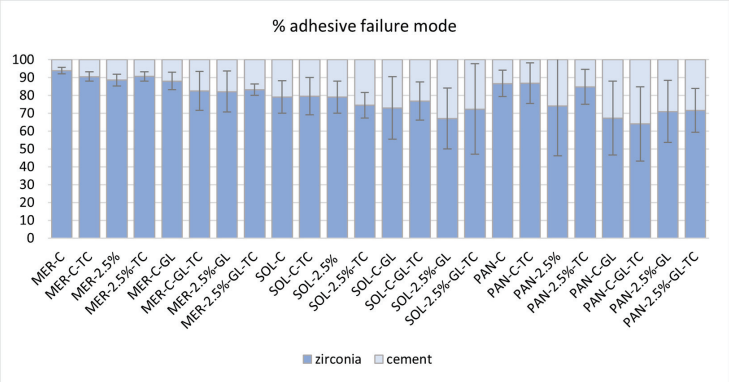


Figure 4. Adhesive failure mode (ADFM %) as calculated from stereoscope images using image analysis software. MER−C = Meron plus QM Control, MER−C−TC = Meron plus QM Control after thermal cycling, MER 2.5% = Meron plus QM with 2.5% zirconia NPs, MER 2.5%−TC = Meron plus QM with 2.5% zirconia NPs after thermal cycling, MER−C−GL = Meron plus QM Control after Gluma application, MER−C−GL−TC = Meron plus QM Control after Gluma application and thermal cycling, MER 2.5%−GL = Meron plus QM with 2.5% zirconia NPs after Gluma application, MER 2.5%−GL−TC = Meron plus QM with 2.5% zirconia NPs after Gluma application and thermal cycling, SOL−C = Solocem Control, SOL−C−TC = Solocem Control after thermal cycling, SOL 2.5% = Solocem with 2.5% zirconia NPs, SOL 2.5%−TC= Solocem with 2.5% zirconia NPs after thermal cycling, SOL−C−GL = Solocem Control after Gluma application, SOL−C−GL−TC = Solocem Control after Gluma application and thermal cycling, SOL 2.5%−GL = Solocem with 2.5% zirconia NPs after Gluma application, SOL 2.5%−GL−TC = Solocem with 2.5% zirconia NPs after Gluma application and thermal cycling, PAN−C = Panavia SA Universal Control, PAN−C−TC = Panavia SA Universal Control after thermal cycling, PAN 2.5% = Panavia SA Universal with 2.5% zirconia NPs, PAN 2.5%−TC = Panavia SA Universal with 2.5% zirconia NPs after thermal cycling, PAN−C−GL = Panavia SA Universal Control after Gluma application, PAN−C−GL−TC = Panavia SA Universal Control after Gluma application and thermal cycling, PAN 2.5%−GL = Panavia SA Universal with 2.5% zirconia NPs after Gluma application, PAN 2.5%−GL−TC = Panavia SA Universal with 2.5% zirconia NPs after Gluma application and thermal cycling.

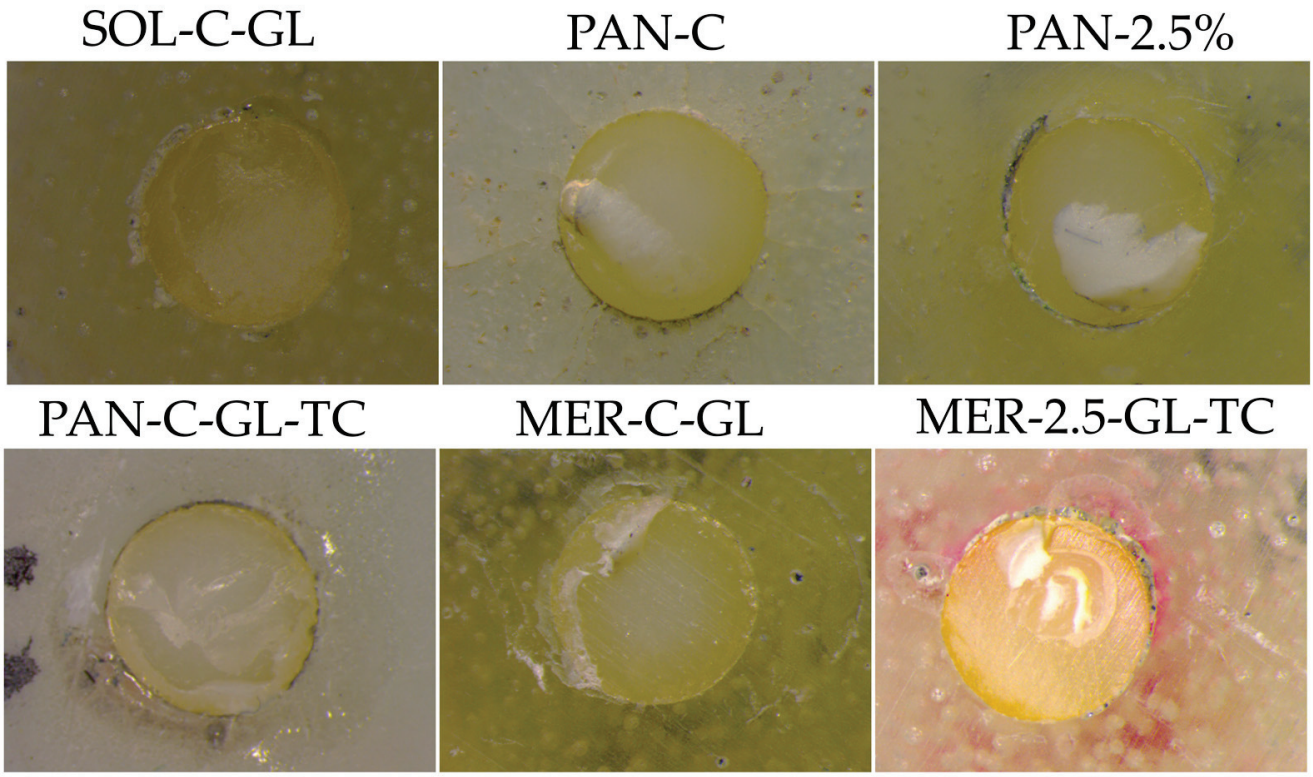


Figure 5. Indicative images from the stereomicroscope of different types of adhesive failure modes. SOL−C−GL = Solocem Control after Gluma application, PAN−C = Panavia SA Universal Control, PAN−2.5% = Panavia SA Universal with 2.5% wt zirconia NPs, PAN−C−GL−TC = Panavia SA Universal Control after Gluma application and thermal cycling, MER−C−GL = Meron plus QM Control after Gluma application, MER−2.5−GL−TC = Meron plus QM WITH 2.5% zirconia NPs after Gluma application and thermal cycling.

3. Discussion

According to the results of the present study, the first null hypothesis was partially rejected because several physicochemical properties (film thickness, flexural strength) of the tested luting cements were affected by the addition of NPs. On the other hand, water sorption was not influenced by the addition of 2.5% tetragonal zirconia nanoparticles. Film thickness was influenced in the PAN and MER groups, while SOL showed a non-significant increase. In the flexural strength tests, a significant increase was measured only in the MER groups. The second null hypothesis partially failed to be rejected, since the shear bond strength was not affected by the addition of NPs before TC, but was affected in two of the three cements after TC. Finally, the third null hypothesis was rejected, since almost all groups presented reduced SBS values after TC.

In the present study, the selection of adhesive materials was based on their different compositions and represented a wide range of clinically accepted luting cements used for zirconia substrates.

Zirconia NPs were fabricated following a sol–gel technique as previously published [38]. In general, YSZ (tetragonal) nanoparticles present chemical inertness, low thermal conductivity, and offer higher mechanical properties than monoclinic zirconia particles [39]. The NPs used in the present study presented low agglomeration and sizes ranging from 20 to 50 nm [38].

After observing Figure 1, one can note the main groups included in all cases: at 3425 cm^{-1}, the –OH groups were shown; at the 2960–2870 cm^{-1} region, all the $–CH_3$, $–CH_2–$, and C–H bonds absorbed; the sharp and intensive peak at 1716 cm^{-1} corresponded to the C=O group; the medium peak of 1637 cm^{-1} indicated the C=C absorption; and

the one at 1608 cm^{-1} the aromatic double bonds. At lower wavenumbers, the peak at 1540 cm^{-1} was attributed to N–H present in the urethane dimethacrylate monomer, while the great peak at 1152 cm^{-1} corresponded to the C–O bonds [3,4]. However, the fingerprint region beneath 1200 cm^{-1} was hard to evaluate in detail and the overlapping of various peaks was evident.

Regarding the presence of the inorganic fillers in the composite materials, the peak at 1298 for the Si–CH_3 bond was apparent and the Si–O–Si group absorbed in the region 1130–1000 cm^{-1} was difficult to identify alone, while the shoulder at 953 cm^{-1} was attributed to the stretching vibration of this group. The Si–OH group was included in the 3452 cm^{-1} vast peak, while the small peak at 815 cm^{-1} was also characteristic of amorphous silica.

Particularly for the PAN adhesive, the absorptions located in the area beneath 1200 cm^{-1} also included the P–O vibrations from the $–PO_3^{2-}$ group. The 10-MDP monomer bears a methacrylate structure on one side and a $–PO_3^{2-}$ group on the other side. The –OH absorptions are located in the 3400 cm^{-1} area of the PAN spectra. The main P–O absorption was found at 1086 cm^{-1}, while at 1249 cm^{-1} and 945 cm^{-1}, two slight shoulders could be attributed to the same bond vibration [40]. There were also two apparent small peaks, seen only for the PAN adhesive, at 830–813 cm^{-1}, but the literature provides no evidence for P–O absorptions in this area.

Regarding the presence of ZrO_2 in the composite materials, the Zr–O bond was found in the regions where the Si–O bond also absorbs. Thus, for the three composite materials already containing silicates, it was hard to isolate the Zr–O bond. The small difference the authors noticed concerned the appearance of a small peak at the right-end of the spectra. In fact, the addition of ZrO_2 provided a shoulder for the MER adhesive at 553 cm^{-1}, for the PAN adhesive at 561 cm^{-1}, and for SOL at 541 cm^{-1}. The change was obvious mainly in the 5% wt sample of each case. The literature is lacking evidence regarding the IR absorptions of ZrO_2 in the fingerprint region due to the numerous and noisy recordings, an issue the authors also faced.

Figure 2 (top) points out the influence of photocuring on the already self-cured composites. The additional energy provided to the films had a great effect, since the area of the peak of C=C shown was minimized relative to the area of the unreactive bonds. For the SOL material, the *DC* of 77% was achieved once the photocuring was fulfilled, while for the PAN and MER cements, it was 64 and 60%, respectively, almost double the *DC*% values achieved after their self-polymerization. Thus, it can be concluded that the intervention of photopolymerization after self-polymerization is beneficial for the hardening of the material (Table 2) [36]. The influence of the 10-MDP monomer for the PAN adhesive cannot be evaluated by the *DC*% results, since the exact organic content of the composites is unknown to the authors (the dimethacrylate percentages compared to 10-MDP). Likewise, the influence of the 4-META monomer on the SOL adhesive cannot be estimated in the *DC*% results, since the exact synthesis of the matrix is unknown [41]. All in all, the influence of light curing is effective for composite materials given the fact that the analogous photo-initiators are present in their composition.

It is worthy to note that as MER does not include a photo-initiator (usually camphorquinone), photocuring does not result in new radicals for the monomer reactions. Thus, MER may not be considered as a "dual adhesive", and it may not be appropriate to call it a "dual adhesive". However, the authors believe that after the application of light onto films, a second curing occurs, since the beam also provides thermal energy, apart from the quanta specific for light-activation. The energy provided activates the "frozen" macro-chains to be mobilized, so new monomers react, and further curing is promoted.

Figure 2 (bottom) demonstrates the influence of the addition of ZrO_2 NPs in the cements when mixed at various ratios. The calculation of the *DC*% values proves that the addition of 1% wt ZrO_2 NPs does not influence the degree of polymerization, either after self-curing only or dual-curing. However, the addition of 2.5 or 5% wt of zirconia powder does affects the polymerization progress by obstructing the conversion of C=C to

C–C, especially for the PAN composites. The values obtained for all materials when 2.5 or 5% wt zirconia was added were diminished to a lower conversion by 10–15% (Table 1). Thus, regarding the polymerization efficiency, the lowest addition tested is recommended, taking into consideration that the mixing occurred manually, and that mechanical mixing might be more effective. The reasons why a filler addition might prevent the evolution of the radical reactions are two: (a) a possible blocking of irradiation into the mass of the material reinforced with extra NPs, preventing light from finding the initiators to react, and, (b) the oligomers that have been produced do not move easily into the stiffer mass of the composite in order to attack the monomers and attach them to the macro-chains. Consequently, the ZrO_2-reinforced composites present lower *DC*% values compared to the untreated materials.

The integration of pure nanoparticles to commercial products that have already been reinforced by a high load of silica fillers seems promising. The concept of this research was based on the possible direct bond of zirconia to phosphoric or carboxylic adhesive monomers [32,41]. In addition, zirconia nanoparticles enhance radiopacity [42,43] and transform luting agents to more viscous materials, and probably increase the micro-hardness [44]. Although silanization has been proposed for inorganic fillers to increase the mechanical properties of composite resins [45], because silica particles are hydrophobic, zirconia NPs are hydrophilic and can be used without further silanization [46]. However, the silanization of zirconia nanoparticles has recently been proposed in the reinforcement of PMMA and adhesives with promising results [23,28]. Moreover, in our study, if those particles were silanized, the advantage of direct contact with the MDP or 4-META adhesive monomer could be lost. In addition, the influence of zirconia nanoparticles on the color stability of cements should be carefully considered, as contemporary zirconia materials show high translucency that could affect the final shade of the cemented restoration [47].

The initial values of film thickness in all luting agents were far lower than the ISO requirements (<50 μm). The lowest value was measured in the MER−C group (15 μm). The addition of nanoparticles increased the film thickness, but it was found to be statistically significant only at the 5% concentration for all cements and 2.5% for PAN. The results of this study are comparable to other recent or earlier studies since the film thickness of RMGIs range from 15 to 50 μm [20,48–51]. The particle size of inorganic fillers determines the limits of the minimum film thickness. Although the SOL group contained a smaller filler size than PAN (5 μm vs. 20 μm), our measurements revealed a similar film thickness in these groups.

The increase in the film thickness could be partially explained by the extended mixing time of the luting agents to homogenize the nanoparticles in the mass of all groups. The visible increase in viscosity during mixing could also explain the increased values in film thickness after NP insertion, which could be attributed to NP agglomerations possibly introduced during hand-mixing. However, with a 1 and 2.5% addition in all groups, this resulted in a clinically acceptable film thickness. In the PAN group, a significant increase was measured in the PAN−2.5 and PAN−5 groups. The initial film thickness agreed with all of the manufacturers' internal studies. In the SOL group, only 5% of nanoparticles showed a significant increase in the film thickness. Group SOL−2.5 presented a lower thickness than PAN−2.5, which can partially be explained by the smaller medium size in inorganic filler content.

The analysis of the water sorption results revealed that resin-based luting agents were far less sensitive to water uptake than the RMGI product. The sensitivity of RMGI to high water uptake has been observed in older generations of both RMGI lining and cementing products [16]. The RMGI luting agent tested in this study exhibited statistically significant higher water sorption in relation to the composite cements, which agrees with most similar studies [52,53]. The addition of 1, 2.5, and 5% NPs resulted in a non-significant increased water sorption for the case of MER. The self-adhesive resin luting agent (PAN) presented the lowest water sorption among all groups, in agreement with the manufacturer. Solocem measurements also confirmed the manufacturers' claim. Measurements were

higher than the PAN group, but not statistically significant. One possible explanation could be attributed to the different monomer composition, since materials that have more HEMA in their composition may have a higher water sorption [54]. The addition of NPs in both the PAN and SOL groups did not cause any statistically significant changes in W_{sp}.

The initial values of the flexural strength test confirmed the theory that resin based products present higher values than other conventional luting agents or even resin-modified glass ionomers [55]. The group SOL presented the highest FS values and confirmed the internal studies of the manufacturer (110 MPa). However, the addition of 5% nanoparticles significantly reduced FS, while all other concentrations had almost no effect in the σ values. In all groups reinforced with NPs, it should be noted that hand mixing is a technically sensitive method influencing some mechanical properties compared to automix protocols [48]. In the PAN group, the manufacturer's claim was also confirmed (90 MPa) and NP addition did not affect the values. Our measurements agree with a recent study that demonstrated values of 87.8 MPa in the self-cure mode and 100.7 MPa in the dual-cure mode of preparation [56]. The MER group showed low values in the control samples, below the ISO 9917-2:2017 acceptance values (20 MPa), but all groups showed higher levels of FS after NP addition (20 MPa), although this was not statistically significant. A recent study demonstrated that MER presents higher FS (37.5 MPa) and this value was further optimized after TC to 43.8 MPa [57]. The significant difference compared to our results could be attributed to differences in the experimental setup. It is also known that in RMGIs, acid–base and polymerization reactions are antagonistic [57].

As mentioned in the Materials and Methods (Section 4), zirconia specimens designed for the SBS test were not polished to simulate clinically relevant conditions. The internal surface of a zirconia crown cannot be efficiently polished clinically. However, most research papers have preferred to polish the zirconia surface to standardize the initial roughness of the specimens [11,58,59].

The use of primer (GLUMA adhesive) in all groups resulted in higher SBS. In the clinical application of self-adhesive luting agents, most manufacturers do not recommend additional adhesive primers. However, recently, manufacturers have suggested a 10-MDP containing primer to promote adhesion to substrates such as zirconia [60,61].

The lowest values were recorded in the MER group, and many spontaneous detachments before the SBS test were observed. However, this measurement (~4 MPa) was higher than that of the adhesive-free resin cement shown in previous studies [62], and implies a weak chemical affinity to zirconia substrates. RMGI cements incorporate poly-carboxylate groups that might adhere to zirconia surfaces [35]. Fracture analysis showed an almost exclusively adhesive failure mode (ADFM 82–90%). However, in some samples, the remnants of RMGI were visible under 60X magnification (Figure 5). The universal adhesive significantly increased SBS, which was performed against the recommendations of the manufacturers. The unexpected resistance to TC denotes that the 10-MDP and 4-META adhesives were both active to the zirconia surface and glass ionomers. The increased values of MER-GL after TC imply a post-polymerization effect of the cement or a resistance to water absorption due to the high initial water sorption of MER. The addition of NPs did not influence the initial values of SBS in any of the MER groups. Moreover, the reinforced group (2.5% NP) was more sensitive to TC, minimizing the beneficial effect of Gluma. A possible delay in the light curing due to NP insertion and extended mixing time can partially explain these results. Additionally, the setting of RMGIs is more complex since acid–base and polymerization reactions are antagonistic [63]. Since the RMGI luting agents are free of adhesive monomers, weak bonds between carboxylate groups and NPs can occur. However, a possible reaction of NPs can be expected in the interface since the primer contains MDP and 4-META monomers. Moreover, the observation that the RMGI was more viscous after the NP load could also partially explain the reduced SBS.

The initial measured SBS values of SOL were similar to MER. The addition of NPs increased the SBS values but after TC, the SBS dropped detrimentally in both groups. A significant increase in SBS after the application of the primer was observed (+20 MPa).

It seems that the manufacturers' recommendation for an additional primer for adhesive cementation (one coat 7.0/Coltene-MDP and nanofillers) was confirmed by our results. On the other hand, after TC, a significant negative influence in SBS was also noticed. A possible incompatibility or susceptibility of this material combination to water intake could explain this effect. The reinforced with NP sample groups after TC presented similar SBS values to the non-adhesive group.

The PAN group presented the highest values of all groups. Without any additional treatment, the initial values were maintained after TC, showing an exceptional resistance to thermal stress and hydrolysis. It was demonstrated from the W_{sp} results that the material is extremely stable with a minimum water sorption. Moreover, this product is the only self-adhesive luting agent that incorporates two adhesives, one containing 10-MDP and one novel adhesive with a long carbon chain silane (LCSi) [61]. The addition of a primer was beneficial, resulting in higher initial SBS values. However, after TC, a totally different behavior was revealed. The high values dropped by 77% in the PAN−G group after TC indicated a vulnerable combination or an unexpected incompatibility of these two products. The manufacturer recommends another additional primer for zirconia bonding that increases the SBS to zirconia. Moreover, the zirconia surface contains no silica, neutralizing the possible benefits from LCSi, if the surface is treated with a silicatization sandblasting technique, as proven in an earlier study [62]. The addition of NPs presented a beneficial initial effect in this group, but after TC, a detrimental effect in SBS was observed. In this group, the presence of MDP in both the primer and luting agent can partially explain the high initial values in SBS. This observation may be attributed to the increased complexity or possible incompatibility with 4-META and LCSi monomers in the primer and luting agent, respectively. The interaction of NPs with 10-MDP in both the luting agent and primer could partially explain this finding. Further studies in a chewing simulator to evaluate resistance to cyclic fatigue should be performed to confirm these findings [64].

Only three out of 12 groups showed resistance to TC. The water sorption and thermal stresses caused a detrimental decrease in the SBS values. In the MER group, the primer treatment presented a significant resistance in TC. In the SOL group, a minor effect was observed, while the combination of the primer did not withstand the effect of TC. PAN was resistant to TC, and the product after the addition of NPs showed a significant decrease after TC. The combination of PAN with Gluma presented a susceptibility to water and TC. It seems that incompatibility or extreme hydrophilic behavior could explain this finding and that the addition of NPs intensifies the influence of water in this group.

4. Materials and Methods

4.1. Preparation and Characterization of Nanoparticles

Yttria-stabilized zirconia nanoparticles (ZrO_2-7% wt Y_2O_3) were synthesized by the sol–gel method using zirconium oxychloride octahydrate ($ZrOCl_2 \cdot 8H_2O$) and yttrium nitrate hexahydrate ($Y(NO_3)_3 \cdot 6H_2O$) as reagents. Raw materials were dissolved in distilled water, and then ethylene glycol (brand) and an aqueous citric acid concentrate (brand) were added under heating and stirring. The molar ratios of citric acid:metal (Zr) was 3.65 and citric acid:ethylene glycol was 1, respectively. The material was gradually heated to a temperature of 300 °C to eliminate organic materials [65] and then sintered at 1000 °C for 2 h. To avoid agglomeration, the obtained NPs underwent ultrasonic treatment in ethanol (brand) for 20 min before application. The characterization of the NPs is presented elsewhere [38].

4.2. Zirconia Specimen Preparation

Zirconia specimens were fabricated using CAD/CAM technology from translucent zirconia blocks (priti®multidisc ZrO_2, monochrome, pritidenta® GmbH, Leinfelden-Echterdingen, Germany, 5Y-TZP) following the manufacturer's instructions for sintering. The final dimensions of the zirconia specimens were 4 mm in diameter and 6 mm in height. The zirconia specimens designed for the shear bond strength (SBS) test were not polished (to simulate

clinically relevant conditions) or sandblasted and were embedded in a transparent acrylic resin (Jet Liquid, Lang) using Plexiglas molds of 16 mm. The specimens were ultrasonicated in isopropyl alcohol (brand) for 15 min and finally dried with oil-free air 0.25 MPa for 10 s.

4.3. Incorporation of Zirconia NPs into Luting Cements

One resin-modified glass ionomer and two different types of composite luting cements were used: (a) RMGI cement (Meron plus QM, VOCO, Cuxhaven, Germany), (b) self-adhesive composite luting cement containing 4-META adhesive monomers (Solocem, Coltene, Altstätten, Switzerland), and (c) self-adhesive composite luting cement containing the adhesive monomer 10-MDP (Panavia SA Universal, Kuraray, Japan) (Table 3). An additional Universal primer Gluma (Kulzer, Germany) was applied for the shear bond strength test.

Table 3. Composition of the used commercial materials.

Product's Name	Type of Material	Composition	Filler
Solocem (Coltene, Altstätten, Switzerland)	Self-adhesive, dual-curing composite-based luting cement	Zinc oxide dental glass, urethane-dimethacrylate (UDMA), triethyleneglycol dimethacrylate (TEGDMA), 4-methacryloxyethyl trimellitate anhydride (4-META), 2-hydroxyethylmethacrylate (HEMA), dibenzoylperoxide, benzoylperoxide	Average particle size diameter 2 μm Filler particle size distribution 0.1–5 μm Filling ratio by weight wt% = 69% Inorganic fillers (barium glass, ytterbium trifluoride, spheroid mixed oxide, titanium oxide.)
Meron Plus QM (VOCO, Cuxhaven, Germany)	Self-curing fluoride releasing resin modified glass ionomer cement	Polyacrylic acid peroxide, BHT, methacrylates (hydroxypropyl methacrylate 10–25%, dimethacrylate 5–10%, UDMA 2.5–5%), glycerine	Fluoroaluminosilicate glass 50–100%
Panavia SA Cement Universal (Kuraray, Japan)	Dual-curing fluoride releasing, self-adhesive resin cement	Paste A—10-Methacryloyloxydecyl dihydrogen phosphate (MDP)—Bisphenol A diglycidylmethacrylate (Bis-GMA)—TEGDMA—Hydrophobic aromatic dimethacrylate—2-Hydroxymethacrylate (HEMA)—Silanated barium glass filler—Silanated colloidal silica—dl-Camphorquinone—Peroxide—Catalysts—Pigments Paste B—Hydrophobic aromatic dimethacrylate—Silane coupling agent—Silanated barium glass filler—Aluminum oxide filler—Surface treated sodium fluoride (Less than 1%)—dl-Camphorquinone—Accelerators—Pigments	Inorganic filler (silanated barium glass, aluminum oxide, colloidal silica) is approx. 43 vol%. The particle size 0.02–20 μm
Gluma bond universal (Kulzer, Germany)	Light-curing, self-conditioning all-in-one adhesive	4-META and MDP monomers Methacrylates, Acetone Water	Contains fillers

Zirconia NPs were added in percentages of 1, 2.5, and 5% wt. The incorporation of the powder zirconia NPs in several ratios was performed after appropriate weighing (Mettler Toledo A250 balance, ±0.0001 g) and mixed manually with the two pastes simultaneously. After initial self-curing, the materials were then additionally photopolymerized. A curing photopolymerizing device with a light intensity of 1200 mW/cm^2 at the spectral range of 380–515 nm was used (Curing Pen-E, Eighteenth, Changzhou Sifary Medical Technology Co. Ltd., Changzhou, China) [38]. Different specimens were prepared depending on the test as described in the following paragraphs and shown schematically in Figure 6.

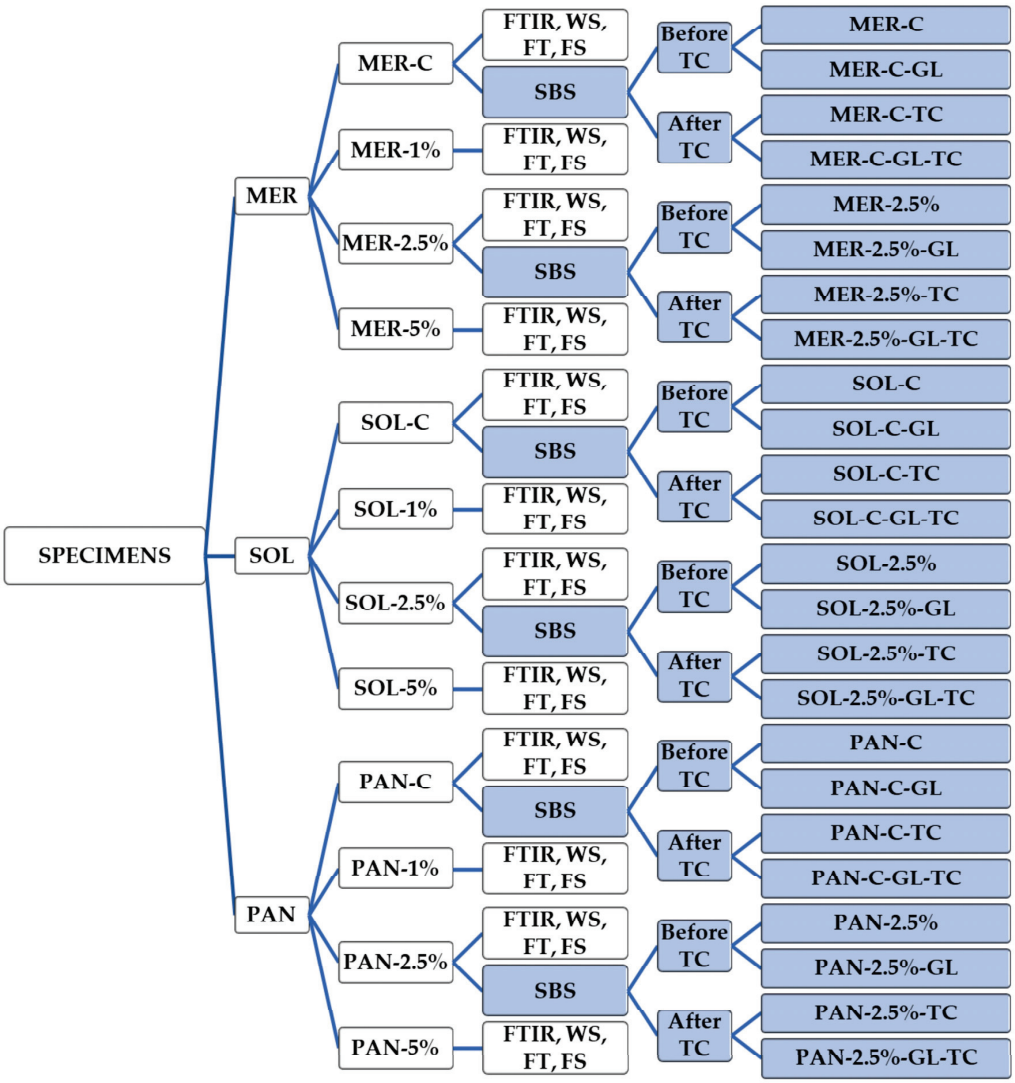


Figure 6. Schematic representation of the study groups and performed analysis. MER = Meron QM, SOL = Solocem, PAN = Panavia SA Universal, GL = Gluma, C = Control, FTIR = Fourier Transform Infrared Spectroscopy, WS = water sorption, FT = film thickness, FS = flexural strength, SBS = shear bond strength test, TC = thermocycling.

4.4. Investigation of Physical and Mechanical Properties of Modified Luting Cements

4.4.1. FTIR Analysis

To evaluate the effects of the addition of NPs on the photopolymerization of the materials, FTIR analysis was performed on a Spectrum One (Perkin Elmer, Waltham, MA, USA) instrument. First, the spectrum of the pastes of each composite cement was recorded. Then, the mixing of the two pastes of each composite occurred, as indicated by the manufacturers, and the polymerized material produced was analyzed (self-cured materials). Self-cured materials were analyzed immediately (time = 0), after 1 h (time = 1 h), and after 24 h (time = 24 h). In a second step, the materials were evaluated after dual polymerization (5 × 10 s photopolymerization). For all cases, right after mixing, the pastes were pressed between two glass plates (5 mm thick) covered with commercial polyethylene sheets and a thin film was shaped to be analyzed. The cured film was placed between two round NaCl IR crystals (Sigma-Aldrich, Lot #: z123595-1EA, Batch #: 3110, 25 mm × 4 mm) for the transmittance recordings. The spectral range was 4000–600 cm^{-1}, the resolution at 4 cm^{-1}, after 32 scans. No external natural light was available during the experiments and the samples were placed in a dry and shady place until 24 h after polymerization.

4.4.2. Evaluation of Water Sorption and Solubility

Five disk specimens (15 mm ×1 mm) of each group were fabricated and photopolymerized by overlapping irradiation at eight points according to manufacturer's instructions. The specimens were placed in a desiccator for 24 h and their initial weight and volume was recorded. Then, the specimens were immersed in distilled water for 7 d at 37 °C and weighed with an accuracy of 0.001 mg. The values of water sorption (W_{sp}, mg/mm^3) were calculated using the following equations (ISO/TS 16506:2017):

$$W_{sp} = \frac{m_i - m_f}{V}$$

where m_i is the specimen mass before immersion (mg); m_f is the specimen mass after immersion (mg); and V is the specimen volume before immersion (mm^3).

4.4.3. Estimation of Film Thickness

To calculate the film thickness, an appropriate amount of each cement (0.05 mL), with or without the addition of NPs, was placed between two optically flat square glass plates, each having a contact surface area of 225 mm^2 and a uniform thickness of 5 mm. A customized loading device with 150 N force was manufactured to fulfill the ISO/TS 16506:2017 and ISO 9917-2:2017 requirements. Specimens were photopolymerized at the center of the upper glass plate for twice the exposure time, as recommended by the manufacturer. The combined thickness of the two glass plates with (T1) and without the cement (T2) film was measured using a micrometer with accuracy of 0.5 μm, while the film thickness was estimated as the difference between these two values.

4.4.4. Determination of Flexural Strength

Ten bar-shaped specimens of 25 mm length, 2 mm thickness, and 2 mm width (Figure 7a) of each group of materials were fabricated using a Teflon mold covered with glass plates before polymerization (Figure 7a). These underwent a 3-point bending test with a constant crosshead speed 0.5 mm/min and rate of loading of 50 N/min on a Instron 3344 dynamometer. Flexural strength (MPa) was calculated according to the equation (ISO/TS 16506: 2017):

$$\sigma = \frac{3FL}{2bh^2}$$

where F is the load until failure in N; L is bar length; b is width; and h the height in m. Failed specimens were observed by SEM.

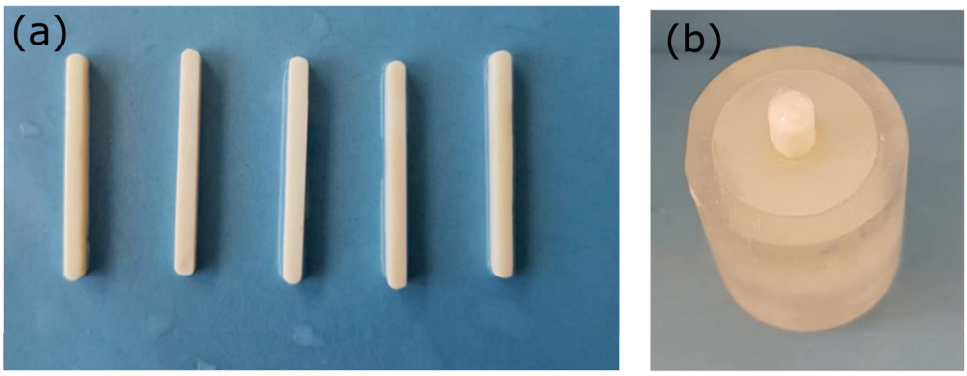


Figure 7. (**a**) Specimens prepared for flexural strength, (**b**) embedded zirconia specimens after cementation for shear bond strength test.

4.4.5. Preparation of Specimens for Adhesive Bonding

All zirconia surfaces were cleaned using ethanol and thoroughly dried, and a thin layer of the universal primer (Gluma, Kulzer) containing both the 10-MDP and 4-META adhesive monomers was applied in half of the specimens and photopolymerized. Then, each cement

was mixed according to the manufacturer's instructions, while all NP reinforced cements were hand mixed. An optimal NP content of 2.5 wt% was chosen, based on the results derived from the previous experiments. The cement was placed in a split mold to standardize a 3 mm diameter adhesive area (Figure 7b). Each cement was photo-polymerized according to the manufacturer's instructions as described in Section 4.3. The mold was carefully removed, and each specimen was held in a humid environment (100% distilled water) at 37 °C to maintain the standard temperature. Half of these specimens underwent additional thermal aging, following 5000 cycles between 5 and 55 °C with a dwelling time of 20 s and a rest time of 10 s.

4.4.6. Shear Bond Strength to Translucent Zirconia Substrate

All bonded specimens were subjected to the shear bond strength test using a Universal testing machine (Instron 3344; Instron, Burlington, ONT, Canada) with a cross-head speed of 1 mm/min until failure. Specimens were assembled in a custom-made device according to ISO 29022 and the Ultra-tester (Ultradent Products, Inc., South Jordan, UT, USA). The maximum shear force was measured for each specimen and the stress was calculated following the equation $\sigma = F/A$, where F is the force applied and A is the cross-sectional area of the specimen.

4.4.7. Failure Mode Analysis

All specimens were observed under a stereomicroscope (M80, Leica, Weltzar, Germany) at 25× magnification to evaluate the failure mode. Failure mode was quantified as the percentage % of the cement-free intact zirconia surface relative to the total zirconia bonded area corresponding to the adhesive failure mode (ADFM%) by image analysis utilizing Photoshop CC software (Adobe Systems, San Jose, CA, USA).

4.5. Statistical Analysis

The values reported in the tables and figures represent the mean values ± standard deviation of the replicates. To determine the effect of NP addition on water sorption, film thickness, and flexural strength, one-way analysis of variance (ANOVA) was applied, followed by the Bonferroni test for multiple comparisons (significance level set at a = 0.05). Normal distribution was verified with the Shapiro–Wilks test and the equality of variances with Levene's test. To test the effect of the addition of NPs, adhesive (Gluma), and thermocycling on the bond strength to zirconia, three-way ANOVA was used with pairwise comparisons (significance level set at a = 0.05).

5. Conclusions

Within the limitations of this in vitro study, the following conclusions were drawn:

1. The addition of NPs did not significantly change the physicochemical and mechanical properties of the investigated luting cements, except for the case of the RMGI cement, where a significant increase in flexural strength was recorded.
2. The addition of NPs at the concentration of 2.5% wt increased the film thickness in all luting agents, however, the values were kept below 30 μm for the RMGI, 40 μm for 10-MDP, and 35 μm for the 4-META cement.
3. The application of 1% wt NPs did not significantly affect the *DC*% values for all of the composite cements, but greater amounts resulted in a dose dependent reduction in the *DC*% values up to 7.2% for the 4-META and 15.5% for 10-MDP cement.
4. The application of an adhesive primer increased the initial SBS values significantly for all commercial products, however, it was beneficial only in RMGI after thermocycling (~16.12% increase).
5. Thermocycling presented a detrimental effect on most of the groups after the addition of NPs.
6. The 10-MDP-containing luting cements demonstrated higher SBS values compared to the RMGI cements and luting cements with 4-META.

Author Contributions: Conceptualization, A.E.R. and E.K.; Methodology, A.B., E.-G.C.T. and A.E.R.; Validation, E.-G.C.T.; Formal analysis P.P., K.A., E.V. and E.K.; Investigation, A.B., E.-G.C.T. and E.V.; Data curation, E.K.; Writing—original draft preparation, E.-G.C.T., A.B. and E.V.; Writing—review and editing, E.K., D.B. and A.E.R.; Visualization, K.A.; Supervision, E.K. and I.G.T.; Project administration, E.K. and I.G.T.; Funding acquisition, E.K. All authors have read and agreed to the published version of the manuscript.

Funding: This research was co-financed by Greece and the European Union (EUROPEAN SOCIALFUND-ESF) through the Operational Program "Human Resources Development, Education, and Lifelong Learning 2014–2020" in the context of the project "Development of zirconia adhesion cements with stabilized zirconia nanoparticles: physicochemical properties and bond strength under aging conditions", grant number MIS5047876.

Institutional Review Board Statement: Not applicable.

Informed Consent Statement: Not applicable.

Data Availability Statement: Data are contained within the article.

Acknowledgments: The authors would like to acknowledge Tsaprazis S.A., the representative of Kuraray in Greece for providing the Panavia SA luting cements for the experiments; Tolidis K., Department of Operative Dentistry, AUTh for providing the thermocycling device; Eliades G., Department of Biomaterials, UoA for providing the stereomicroscope; and Ztoukopoulos L. from the Department of Operative dentistry of AUTh for the technical support.

Conflicts of Interest: The authors declare no conflict of interest.

References

1. Kontonasaki, E.; Rigos, A.E.; Ilia, C.; Istantsos, T. Monolithic zirconia: An update to current knowledge. Optical properties, wear, and clinical performance. *Dent. J.* **2019**, *7*, 90. [CrossRef] [PubMed]
2. Comba, A.; Baldi, A.; Tempesta, R.M.; Carossa, M.; Perrone, L.; Saratti, C.M.; Rocca, G.T.; Femiano, R.; Femiano, F.; Scotti, N. Do chemical-based bonding techniques affect the bond strength stability to cubic zirconia? *Materials* **2021**, *14*, 3920. [CrossRef] [PubMed]
3. Lopes, G.R.S.; Ramos, N.C.; Grangeiro, M.T.V.; Matos, J.D.M.; Bottino, M.A.; Özcan, M.; Valandro, L.F.; Melo, R.M. Adhesion between zirconia and resin cement: A critical evaluation of testing methodologies. *J. Mech. Behav. Biomed Mater.* **2021**, *120*, 104547. [CrossRef] [PubMed]
4. Quigley, N.P.; Loo, D.S.S.; Choy, C.; Ha, W.N. Clinical efficacy of methods for bonding to zirconia: A systematic review. *J. Prosthet. Dent.* **2021**, *125*, 231–240. [CrossRef]
5. Russo, D.S.; Cinelli, F.; Sarti, C.; Giachetti, L. Adhesion to zirconia: A systematic review of current conditioning methods and bonding materials. *Dent. J.* **2019**, *7*, 74. [CrossRef]
6. Comino-Garayoa, R.; Peláez, J.; Tobar, C.; Rodríguez, V.; Suárez, M.J. Adhesion to zirconia: A systematic review of surface pretreatments and resin cements. *Materials* **2021**, *14*, 2751. [CrossRef]
7. Ban, S. Classification and properties of dental zirconia as implant fixtures and superstructures. *Materials* **2021**, *14*, 4879. [CrossRef]
8. Schünemann, F.H.; Galárraga-Vinueza, M.E.; Magini, R.; Fredel, M.; Silva, F.; Souza, J.C.M.; Zhang, Y.; Henriques, B. Zirconia surface modifications for implant dentistry. *Mater. Sci. Eng. C* **2019**, *98*, 1294–1305. [CrossRef]
9. Tzanakakis, E.G.C.; Skoulas, E.; Pepelassi, E.; Koidis, P.; Tzoutzas, I.G. The use of lasers in dental materials: A review. *Materials* **2021**, *14*, 3370. [CrossRef]
10. De Souza, G.; Hennig, D.; Aggarwal, A.; Tam, L.E. The use of MDP-based materials for bonding to zirconia. *J. Prosthet. Dent.* **2014**, *112*, 895–902. [CrossRef]
11. Tzanakakis, E.-G.C.; Beketova, A.; Papadopoulou, L.; Kontonasaki, E.; Tzoutzas, I.G. Novel Femto Laser Patterning of High Translucent Zirconia as an Alternative to Conventional Particle Abrasion. *Dent. J.* **2021**, *9*, 20. [CrossRef] [PubMed]
12. Tzanakakis, E.; Kontonasaki, E.; Voyiatzis, G.; Andrikopoulos, K.; Tzoutzas, I. Surface characterization of monolithic zirconia submitted to different surface treatments applying optical interferometry and raman spectrometry. *Dent. Mater. J.* **2020**, *39*, 111–117. [CrossRef] [PubMed]
13. Papadogiannis, D.; Dimitriadi, M.; Zafiropoulou, M.; Gaintantzopoulou, M.D.; Eliades, G. Reactivity and bond strength of universal dental adhesives with Co-Cr alloy and zirconia. *Dent. J.* **2019**, *7*, 78. [CrossRef] [PubMed]
14. Müller, N.; Husain, N.A.H.; Chen, L.; Özcan, M. Adhesion of Different Resin Cements to Zirconia: Effect of Incremental versus Bulk Build Up, Use of Mould and Ageing†. *Materials* **2022**, *15*, 2186. [CrossRef] [PubMed]
15. Roberts, H.; Berzins, D.; Nicholson, J. Long-Term Water Balance Evaluation in Glass Ionomer Restorative Materials. *Materials* **2022**, *15*, 807. [CrossRef] [PubMed]
16. Kanchanavasita, W.; Anstice, H.M.; Pearson, G.J. Water sorption characteristics of resin-modified glass-ionomer cements. *Biomaterials* **1997**, *18*, 343–349. [CrossRef]

17. Nicholson, J.W.; Sidhu, S.K.; Czarnecka, B. Enhancing the mechanical properties of glass-ionomer dental cements: A review. *Materials* **2020**, *13*, 2510. [CrossRef]
18. Mitsuhashi, A.; Hanaoka, K.; Teranaka, T. Fracture toughness of resin-modified glass ionomer restorative materials: Effect of powder/liquid ratio and powder particle size reduction on fracture toughness. *Dent. Mater.* **2003**, *19*, 747–757. [CrossRef]
19. Spajić, J.; Prskalo, K.; Šariri, K.; Par, M.; Pandurić, V.; Demoli, N. Dimensional changes of glass ionomers and a giomer during the setting time. *Acta Stomatol. Croat.* **2018**, *52*, 293–306. [CrossRef]
20. Bagheri, R. Film thickness and flow properties of resin-based cements at different temperatures. *J. Dent. (Shiraz Iran)* **2013**, *14*, 57–63.
21. D'Arcangelo, C.; Cinelli, M.; De Angelis, F.; D'Amario, M. The effect of resin cement film thickness on the pullout strength of a fiber-reinforced post system. *J. Prosthet. Dent.* **2007**, *98*, 193–198. [CrossRef] [PubMed]
22. Gjorgievska, E.; Nicholson, J.W.; Gabrić, D.; Guclu, Z.A.; Miletić, I.; Coleman, N.J. Assessment of the impact of the addition of nanoparticles on the properties of glass-ionomer cements. *Materials* **2020**, *13*, 276. [CrossRef] [PubMed]
23. Almutairi, B.; Binhasan, M.; Shabib, S.; Al-Qahtani, A.S.; Tulbah, H.I.; Al-Aali, K.A.; Vohra, F.; Abduljabbar, T. Adhesive bond integrity of silanized zirconia nanoparticles in polymeric resin dentin bonding agent. An FTIR, SEM, and micro-tensile experiment. *Int. J. Adhes. Adhes.* **2022**, *114*, 103069. [CrossRef]
24. Keul, C.; Köhler, P.; Hampe, R.; Roosd, M.; Stawarczyke, B. Glass fiber post/composite core systems bonded to human dentin: Analysis of tensile load vs calculated tensile strength of various systems using pull-out tests. *J. Adhes. Dent.* **2016**, *18*, 247–256. [CrossRef] [PubMed]
25. Walcher, J.G.; Leitune, V.C.B.; Collares, F.M.; de Souza Balbinot, G.; Samuel, S.M.W. Physical and mechanical properties of dual functional cements—An in vitro study. *Clin. Oral Investig.* **2019**, *23*, 1715–1721. [CrossRef] [PubMed]
26. Säilynoja, E.; Garoushi, S.; Vallittu, P.K.; Lassila, L. Characterization of experimental short-fiber-reinforced dual-cure core build-up resin composites. *Polymers* **2021**, *13*, 2281. [CrossRef]
27. Alhotan, A.; Yates, J.; Zidan, S.; Haider, J.; Silikas, N. Assessing fracture toughness and impact strength of PMMA reinforced with nano-particles and fibre as advanced denture base materials. *Materials* **2021**, *14*, 4127. [CrossRef]
28. Zidan, S.; Silikas, N.; Al-Nasrawi, S.; Haider, J.; Alshabib, A.; Alshame, A.; Yates, J. Chemical characterisation of silanised zirconia nanoparticles and their effects on the properties of pmma-zirconia nanocomposites. *Materials* **2021**, *14*, 3212. [CrossRef]
29. Habib, E.; Wang, R.; Wang, Y.; Zhu, M.; Zhu, X.X. Inorganic Fillers for Dental Resin Composites: Present and Future. *ACS Biomater. Sci. Eng.* **2016**, *2*, 1–11. [CrossRef]
30. Heshmatpour, F.; Khodaiy, Z.; Aghakhanpour, R.B. Synthesis and characterization of pure tetragonal nanocrystalline sulfated 8YSZ powder by sol-gel route. *Powder Technol.* **2012**, *224*, 12–18. [CrossRef]
31. Pilo, R.; Kaitsas, V.; Zinelis, S.; Eliades, G. Interaction of zirconia primers with yttria-stabilized zirconia surfaces. *Dent. Mater.* **2016**, *32*, 353–362. [CrossRef] [PubMed]
32. Nagaoka, N.; Yoshihara, K.; Feitosa, V.P.; Tamada, Y.; Irie, M.; Yoshida, Y.; Van Meerbeek, B.; Hayakawa, S. Chemical interaction mechanism of 10-MDP with zirconia. *Sci. Rep.* **2017**, *7*, 45563. [CrossRef] [PubMed]
33. Atsuta, M.; Abell, A.K.; Turner, D.T.; Nakabayashi, N.; Takeyama, M. A new coupling agent for composite materials: 4-Methacryloxyethyl trimellitic anhydride. *J. Biomed. Mater. Res.* **1982**, *16*, 619–628. [CrossRef] [PubMed]
34. Chang, J.C.; Hurst, T.L.; Hart, D.A.; Estey, A.W. 4-META use in dentistry: A literature review. *J. Prosthet. Dent.* **2002**, *87*, 216–224. [CrossRef] [PubMed]
35. Jadhav, S.A. Self-assembled monolayers (SAMs) of carboxylic acids: An overview. *Cent. Eur. J. Chem.* **2011**, *9*, 369–378. [CrossRef]
36. Vouvoudi, E.C.; Baxevani, T.I.; Sideridou, I.D. Dental dimethacrylate-based nanohybrid composite Kalore GC: Kinetic study of its light-curing. *J. Taibah Univ. Med. Sci.* **2016**, *11*, 63–71. [CrossRef]
37. Fernandez Lopez, E.; Sanchez Escribano, V.; Panizza, M.; Carnasciali, M.M.; Busca, G. Vibrational and electronic spectroscopic properties of zirconia powders. *J. Mater. Chem.* **2001**, *11*, 1891–1897. [CrossRef]
38. Beketova, A.; Theocharidou, A.; Tsamesidis, I.; Rigos, A.E.; Pouroutzidou, G.K.; Tzanakakis, E.G.C.; Kourtidou, D.; Liverani, L.; Ospina, M.A.; Anastasiou, A.; et al. Sol–gel synthesis and characterization of ysz nanofillers for dental cements at different temperatures. *Dent. J.* **2021**, *9*, 128. [CrossRef]
39. Kumari, L.; Li, W.Z.; Xu, J.M.; Leblanc, R.M.; Wang, D.Z.; Li, Y.; Guo, H.; Zhang, J. Controlled hydrothermal synthesis of zirconium oxide nanostructures and their optical properties. *Cryst. Growth Des.* **2009**, *9*, 3874–3880. [CrossRef]
40. Chen, Y.; Lu, Z.; Qian, M.; Zhang, H.; Xie, H.; Chen, C. Effect of 10-methacryloxydecyl dihydrogen phosphate concentration on chemical coupling of methacrylate resin to yttria-stabilized zirconia. *J. Adhes. Dent.* **2017**, *19*, 349–355. [CrossRef]
41. Shimizu, H.; Takagaki, T.; Minakuchi, S. Bonding Efficacy of 4-META/MMA-TBB Resin to Surface-treated Highly Translucent Dental Zirconia. *J. Adhes. Dent.* **2018**, *20*, 453–460. [CrossRef] [PubMed]
42. Guerreiro Tanomaru, J.M.; Storto, I.; da Silva, G.F.; Bosso, R.; Costa, B.C.; Bernardi, M.I.B.; Tanomaru-Filho, M. Radiopacity, pH and antimicrobial activity of Portland cement associated with micro- and nanoparticles of zirconium oxide and niobium oxide. *Dent. Mater. J.* **2014**, *33*, 466–470. [CrossRef] [PubMed]
43. Tzanakakis, E.; Tzoutzas, I.; Kontonasaki, E. Zirconia: Contemporary views of a much talked material: Structure, applications and clinical considerations. *Zirconia Hel. Stom. Rev.* **2013**, *57*, 101–137.
44. El-Tamimi, K.M.; Bayoumi, D.A.; Ahmed, M.M.Z.; Albaijan, I.; El-Sayed, M.E. The Effect of Salinized Nano ZrO_2 Particles on the Microstructure, Hardness, and Wear Behavior of Acrylic Denture Tooth Nanocomposite. *Polymers* **2022**, *14*, 302. [CrossRef]

45. Aydınoğlu, A.; Yoruç, A.B.H. Effects of silane-modified fillers on properties of dental composite resin. *Mater. Sci. Eng. C* **2017**, *79*, 382–389. [CrossRef]
46. Dai, S.; Chen, Y.; Yang, J.; He, F.; Chen, C.; Xie, H. Surface treatment of nanozirconia fillers to strengthen dental bisphenol a–glycidyl methacrylate–based resin composites. *Int. J. Nanomed.* **2019**, *14*, 9185–9197. [CrossRef]
47. Comba, A.; Paolone, G.; Baldi, A.; Vichi, A.; Goracci, C.; Bertozzi, G.; Scotti, N. Effects of Substrate and Cement Shade on the Translucency and Color of CAD/CAM Lithium-Disilicate and Zirconia Ceramic Materials. *Polymers* **2022**, *14*, 1778. [CrossRef]
48. Sulaiman, T.A.; Abdulmajeed, A.A.; Altitinchi, A.; Ahmed, S.N.; Donovan, T.E. Physical Properties, Film Thickness, and Bond Strengths of Resin-Modified Glass Ionomer Cements According to Their Delivery Method. *J. Prosthodont.* **2019**, *28*, 85–90. [CrossRef]
49. Garner, J.R.; Wajdowicz, M.N.; DuVall, N.B.; Roberts, H.W. Selected physical properties of new resin-modified glass ionomer luting cements. *J. Prosthet. Dent.* **2017**, *117*, 277–282. [CrossRef]
50. Kious, A.R.; Roberts, H.W.; Brackett, W.W. Film thicknesses of recently introduced luting cements. *J. Prosthet. Dent.* **2009**, *101*, 189–192. [CrossRef]
51. Tsukada, G.; Tanaka, T.; Kajihara, T.; Torii, M.; Inoue, K. Film thickness and fluidity of various luting cements determined using a trial indentation meter. *Dent. Mater.* **2006**, *22*, 183–188. [CrossRef] [PubMed]
52. Laiteerapong, A.; Reichl, F.X.; Hickel, R.; Högg, C. Effect of eluates from zirconia-modified glass ionomer cements on DNA double-stranded breaks in human gingival fibroblast cells. *Dent. Mater.* **2019**, *35*, 444–449. [CrossRef] [PubMed]
53. Gavranović-Glamoč, A.; Ajanović, M.; Korać, S.; Zukić, S.; Strujić-Porović, S.; Kamber-Ćesir, A.; Kazazić, L.; Berhamović, E. Evaluation of the water sorption of luting cements in different solutions. *Acta Med. Acad.* **2017**, *46*, 124–132. [CrossRef] [PubMed]
54. Takahashi, M.; Nakajima, M.; Hosaka, K.; Ikeda, M.; Foxton, R.M.; Tagami, J. Long-term evaluation of water sorption and ultimate tensile strength of HEMA-containing/-free one-step self-etch adhesives. *J. Dent.* **2011**, *39*, 506–512. [CrossRef] [PubMed]
55. Li, Z.C.; White, S.N. Mechanical properties of dental luting cements. *J. Prosthet. Dent.* **1999**, *81*, 597–609. [CrossRef]
56. Kawashima, M.; Yamaguchi, S.; Mine, A.; Li, H.; Imazato, S. Novel testing method to evaluate the mechanical strength of self-adhesive resin cements with reflection of cement thickness. *Dent. Mater. J.* **2021**, *40*, 1235–1242. [CrossRef]
57. Ilie, N. Comparative analysis of static and viscoelastic mechanical behavior of different luting material categories after aging. *Materials* **2021**, *14*, 1452. [CrossRef]
58. Kang, L.L.; Chuang, S.F.; Li, C.L.; Lin, J.C.; Lai, T.W.; Wang, C.C. Enhancing Resin Cement Adhesion to Zirconia by Oxygen Plasma-Aided Silicatization. *Materials* **2022**, *15*, 5568. [CrossRef]
59. Kim, M.; Kim, R.H.; Lee, S.C.; Lee, T.K.; Hayashi, M.; Yu, B.; Jo, D.W. Evaluation of Tensile Bond Strength between Self-Adhesive Resin Cement and Surface-Pretreated Zirconia. *Materials* **2022**, *15*, 3089. [CrossRef]
60. Rohr, N.; Brunner, S.; Märtin, S.; Fischer, J. Influence of cement type and ceramic primer on retention of polymer-infiltrated ceramic crowns to a one-piece zirconia implant. *J. Prosthet. Dent.* **2018**, *119*, 138–145. [CrossRef]
61. Yoshihara, K.; Nagaoka, N.; Maruo, Y.; Nishigawa, G.; Yoshida, Y.; Van Meerbeek, B. Silane-coupling effect of a silane-containing self-adhesive composite cement. *Dent. Mater.* **2020**, *36*, 914–926. [CrossRef] [PubMed]
62. Tzanakakis, E.G.; Dimitriadi, M.; Tzoutzas, I.; Koidis, P.; Zinelis, S.; Eliades, G. Effect of Water Storage on Hardness and Interfacial Strength of Resin Composite Luting Agents Bonded to Surface-Treated Monolithic Zirconia. *Dent. J.* **2021**, *9*, 78. [CrossRef] [PubMed]
63. Berzins, D.W.; Abey, S.; Costache, M.C.; Wilkie, C.A.; Roberts, H.W. Resin-modified glass-ionomer setting reaction competition. *J. Dent. Res.* **2010**, *89*, 82–86. [CrossRef] [PubMed]
64. Baldi, A.; Comba, A.; Ferrero, G.; Italia, E.; Michelotto Tempesta, R.; Paolone, G.; Mazzoni, A.; Breschi, L.; Scotti, N. External gap progression after cyclic fatigue of adhesive overlays and crowns made with high translucency zirconia or lithium silicate. *J. Esthet. Restor. Dent.* **2022**, *34*, 557–564. [CrossRef] [PubMed]
65. Hajizadeh-Oghaz, M.; Razavi, R.S.; Estarki, M.L. Large-scale synthesis of YSZ nanopowder by Pechini method. *Bull. Mater. Sci.* **2014**, *37*, 969–973. [CrossRef]

Disclaimer/Publisher's Note: The statements, opinions and data contained in all publications are solely those of the individual author(s) and contributor(s) and not of MDPI and/or the editor(s). MDPI and/or the editor(s) disclaim responsibility for any injury to people or property resulting from any ideas, methods, instructions or products referred to in the content.

International Journal of
Molecular Sciences

MDPI

Article

A Novel High-Energy Vacuum Ultraviolet Light Photofunctionalization Approach for Decomposing Organic Molecules around Titanium

Toshikatsu Suzumura, Takanori Matsuura, Keiji Komatsu and Takahiro Ogawa *

Division of Regenerative and Reconstructive Sciences and Weintraub, Center for Reconstructive Biotechnology, UCLA School of Dentistry, Los Angeles, CA 90095-1668, USA
* Correspondence: togawa@dentistry.ucla.edu; Tel.: +1-310-794-7653; Fax: +1-310-825-6345

Abstract: Titanium undergoes biological aging, represented by increased hydrophobicity and surface accumulation of organic molecules over time, which compromises the osseointegration of dental and orthopedic implants. Here, we evaluated the efficacy of a novel UV light source, 172 nm wavelength vacuum UV (VUV), in decomposing organic molecules around titanium. Methylene blue solution used as a model organic molecule placed in a quartz ampoule with and without titanium specimens was treated with four different UV light sources: (i) ultraviolet C (UVC), (ii) high-energy UVC (HUVC), (iii) proprietary UV (PUV), and (iv) VUV. After one minute of treatment, VUV decomposed over 90% of methylene blue, while there was 3-, 3-, and 8-fold more methylene blue after the HUVC, PUV, and UVC treatments, respectively. In dose-dependency experiments, maximal methylene blue decomposition occurred after one minute of VUV treatment and after 20–30 min of UVC treatment. Rapid and effective VUV-mediated organic decomposition was not influenced by the surface topography of titanium or its alloy and even occurred in the absence of titanium, indicating only a minimal photocatalytic contribution of titanium dioxide to organic decomposition. VUV-mediated but not other light source-mediated methylene blue decomposition was proportional to its concentration. Plastic tubes significantly reduced methylene blue decomposition for all light sources. These results suggest that VUV, in synergy with quartz ampoules, mediates rapid and effective organic decomposition compared with other UV sources. This proof-of-concept study paves the way for rapid and effective VUV-powered photofunctionalization of titanium to overcome biological aging.

Keywords: photofunctionalization; osseointegration; dental and orthopedic implants; hydrocarbon; biological aging of titanium

Citation: Suzumura, T.; Matsuura, T.; Komatsu, K.; Ogawa, T. A Novel High-Energy Vacuum Ultraviolet Light Photofunctionalization Approach for Decomposing Organic Molecules around Titanium. *Int. J. Mol. Sci.* **2023**, *24*, 1978. https://doi.org/10.3390/ijms24031978

Academic Editor: Mary Anne Melo

Received: 22 November 2022
Revised: 1 January 2023
Accepted: 11 January 2023
Published: 19 January 2023

Copyright: © 2023 by the authors. Licensee MDPI, Basel, Switzerland. This article is an open access article distributed under the terms and conditions of the Creative Commons Attribution (CC BY) license (https://creativecommons.org/licenses/by/4.0/).

1. Introduction

Dental implants, orthopedic implants, and many other prosthetic components are made of titanium-based materials, especially commercially pure titanium or titanium alloys. Titanium and titanium alloys show excellent biocompatibility and osseointegration compared with other materials [1–19]. However, it has recently been shown that titanium undergoes biological aging, characterized by the loss of hydrophilicity of titanium surfaces over time [20–27], which correlates with their decreasing ability to osseointegrate. Aging is also associated with the accumulation of hydrocarbons on titanium surfaces, which further contributes to a loss of osseointegration [20–23,28–30]. Biological aging is an inevitable and undesirable process for all types of titanium and titanium alloys [28,29,31–36]. One effective way to increase the osseointegration of titanium is to remove carbon molecules from its surface before placing it into bone [37–47].

UV photofunctionalization or UV activation was developed to overcome the biological aging of titanium [20,23,34,35,45–75]. The treatment of titanium with UV light decomposes and removes carbon-containing molecules, reducing the atomic percentage of carbon from

40–75% to 15–20% [20,48–50,76]. Treated titanium surfaces consequently regain hydrophilicity. UV-treated, decarbonized titanium surfaces then recruit osteogenic cells, facilitate cell attachment and adhesion, promote osteoblastic proliferation and differentiation, and accelerate and increase bone formation around titanium [21,23,24,48,49,57,62,77,78]. However, there remain three major challenges to the practical and effective use of UV photofunctionalization in clinical practice [50,51,53,79,80]. First, UV treatment has not been optimized; there is still uncertainty about the optimal UV dose or if there even is an optimal dose. Second, the treatment time remains long; despite significant advances in photo-technology, the proposed UV treatment time is still 48 h [48,49,81], 20 min [38,44,51–53,63,80,82–84], or 12 min [33,37,42] depending on the light source; these intervals which may be acceptable for research but are all too long for routine clinical use. Third, current UV treatment can only be achieved when titanium specimens have been removed from their sterile containers due to only very limited penetration of UV light into these containers [53,60,63,85,86]. Implantable medical devices, including dental and orthopedic implants, pins, plates, and screws, are packed in sterilized plastic or metal containers and are expected to be immediately delivered to patients directly from these containers. Exposing the devices to the atmosphere or surroundings during UV treatment carries a risk of contamination. Unfortunately, the higher the UV photon energy is, the lower the penetration through current container materials is.

UV photofunctionalization was originally described using a bactericidal UV lamp for 48 h [49]. The lamp emitted UV-C (200–280 nm wavelength), with a peak around 254 nm. The UV-mediated decomposition of carbon-containing molecules is thought to occur via two mechanisms: direct decomposition or through photocatalytic decomposition via titanium dioxide [49,50,87–90]. In the direct UV decomposition mechanism, UV light breaks atomic bonds according to the strength of photon energy; for instance, a relatively weak, single oxygen–carbon (C-O) bond can be broken by low-energy UV-A (374 nm wavelength), while double oxygen bonds (O=O) can be dissociated by high-energy UV-B (243 nm wavelength). Another mechanism of direct UV-mediated organic decomposition is the generation of oxygen radicals. For example, UV-C produces radicals through ozone, which attacks organic molecules, with dissociated molecules such as CO_2, H_2O, and O_2 being released into the atmosphere. In the second mechanism, photocatalytic organic decomposition is induced by two reactive oxygen species produced on titanium dioxide [89–92]. UV energy releases free electrons (e^-) and forms a positive hole (h^+) on titanium dioxide as a result. Free electrons (e^-) react with atmospheric oxygen (O_2) to produce superoxide anions ($O_2^{\cdot -}$), which in turn dissolve organic molecules through oxidation. Positive holes (h^+) react with atmospheric water (H_2O) to generate hydroxy radicals ($^{\cdot}OH$), which act in a manner similar to that of superoxide anions.

Recent technical advances have resulted in a high-energy, low-pressure mercury vapor lamp that reduced UV treatment to 20 min to generate a similar effect to 48 h bactericidal UV treatment, and the latest UV device uses a proprietary wavelength for 12 min treatment. Here, we tested the potential of a novel, xenon excimer lamp emitting 172 nm wavelength vacuum UV (VUV; defined as UV < 200 nm) to decompose organic molecules around titanium. Specifically, we determined whether the combined use of 172 nm VUV and a quartz ampoule [93,94] as a specimen container overcame the above-mentioned three challenges. Methylene blue ($C_{16}H_{18}ClN_3S$), a benzene ring, hydrocarbon-containing molecule, was used as a model organic molecule. We tested the device on microroughened commercially pure titanium surfaces (most commonly used in dental and orthopedic implants), machined titanium surfaces, and machined titanium alloy surfaces. The efficacy of organic decomposition was assessed according to (i) direct decomposition induced by UV light and (ii) photocatalytic decomposition induced by UV-excited titanium dioxide. Finally, we attempted to optimize the UV dose by identifying a plateau in efficacy.

2. Results

2.1. Surface Characteristics of Titanium Materials

The surface morphology and hydrophilic/hydrophobic state of three titanium test materials were examined. The surface of acid-etched commercially pure grade 4 titanium was significantly rougher than that of machined grade 4 titanium and machined grade 5 titanium alloy according to low-magnification SEM (Figure 1). The high-magnification images showed that the acid-etched commercially pure titanium was evenly roughened, with a combination of scattered supra-micron concavities (arrowheads in lower-left panel) and micro-pits over the surface. The machined surfaces, regardless of titanium type, had no defined topography except for linear traces from machine milling.

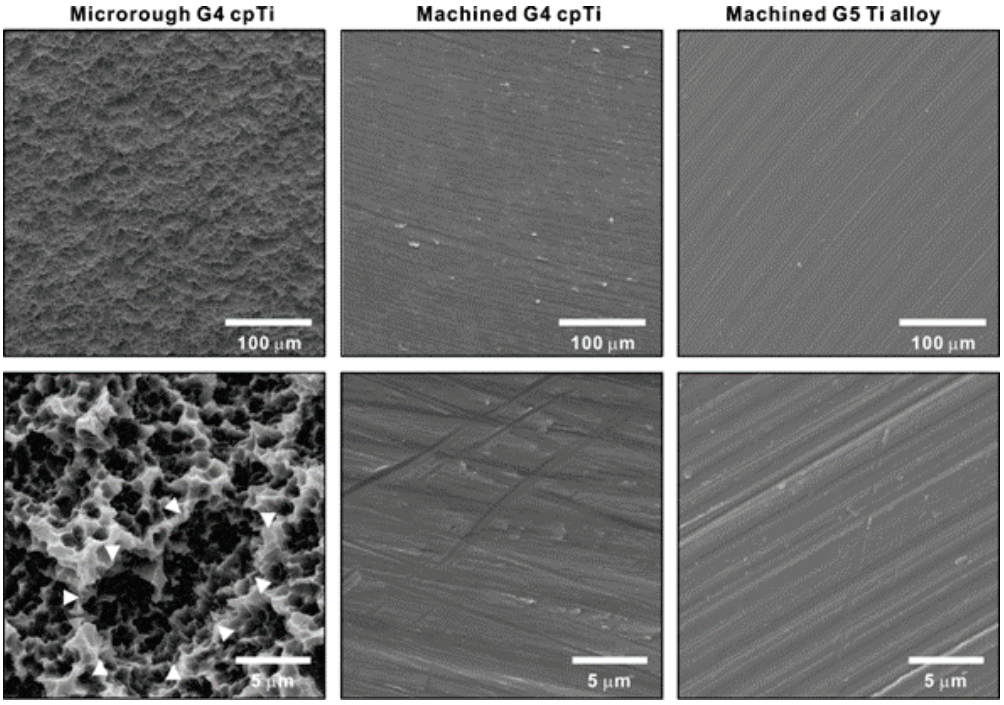


Figure 1. Surface morphology of titanium specimens used in this study. Low (**upper** panels)- and high (**lower** panels)-magnification SEM images of three different specimens.

The hydrophilicity of acid-etched microroughened commercially pure titanium was examined before and after UV treatment for 1 min using four different light sources: (i) ultraviolet C (UVC), (ii) high-energy UVC (HUVC), (iii) proprietary UV (PUV), and (iv) VUV (Figure 2). Original titanium surfaces were hydrophobic, with a contact angle > 90°. All UV treatments converted the surfaces to hydrophilic (defined as a contact angle < 30°), the degree varied according to the UV source, with the HUVC, PUV, and VUV treatments all resulting in a contact angle of 0° and UVC in a contact angle of ~30%.

2.2. Organic Molecule Decomposition Induced by Different UV Light Sources

We next compared the ability of different UV sources to decompose organic molecules. Microroughened commercially pure titanium was used as a representative test material and methylene blue as a model organic molecule. Methylene blue placed in a quartz ampoule was treated with UV light for 1 min with or without a titanium specimen. All UV treatments significantly decomposed methylene blue regardless of the light source; however, the amount of remaining methylene blue varied considerably ($p < 0.001$, two-way ANOVA), with UVC being the highest and VUV the lowest (Figure 3A) ($p < 0.001$, Bonferroni-corrected). With a titanium specimen, one minute of VUV treatment decomposed over 90% of methylene blue, versus ~25% for UVC and ~75% for HUVC and PUV. UV treatment with a titanium specimen decomposed more methylene blue than without a titanium specimen

for all light sources ($p < 0.05$, Bonferroni-corrected). The difference in methylene blue decomposition with and without a titanium specimen was represented as photocatalytic contribution (%), which was significantly lower for HUVC, PUV, and VUV (<5%) than for UVC (~45%) ($p < 0.001$; Figure 3B).

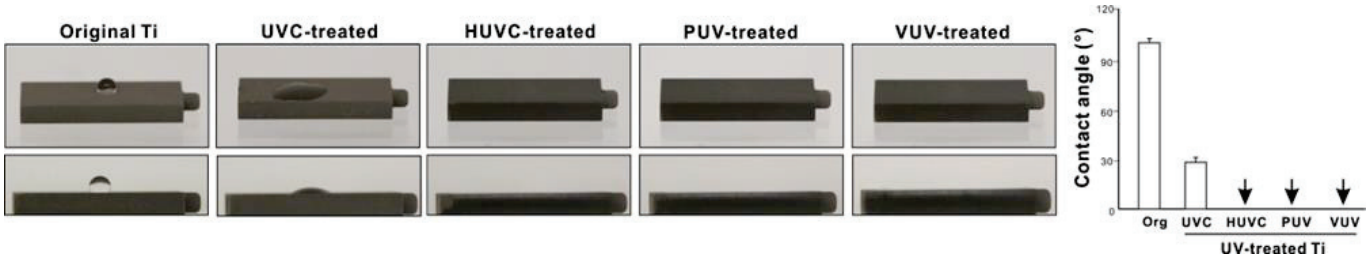


Figure 2. Hydrophilic/hydrophobic state of acid-etched microroughened titanium surfaces before and after UV treatment exposed to four different UV light sources for one minute: UVC from a low-pressure mercury lamp (UVC); high-energy UVC (HUVC); a UV device with a proprietary protocol (PUV); and 172 nm vacuum UV (VUV). Birds-eye and side-view photographs of a 3 μL drop of ddH_2O placed on microroughened titanium specimens, and a histogram showing contact angle measurements. Arrows indicate 0°.

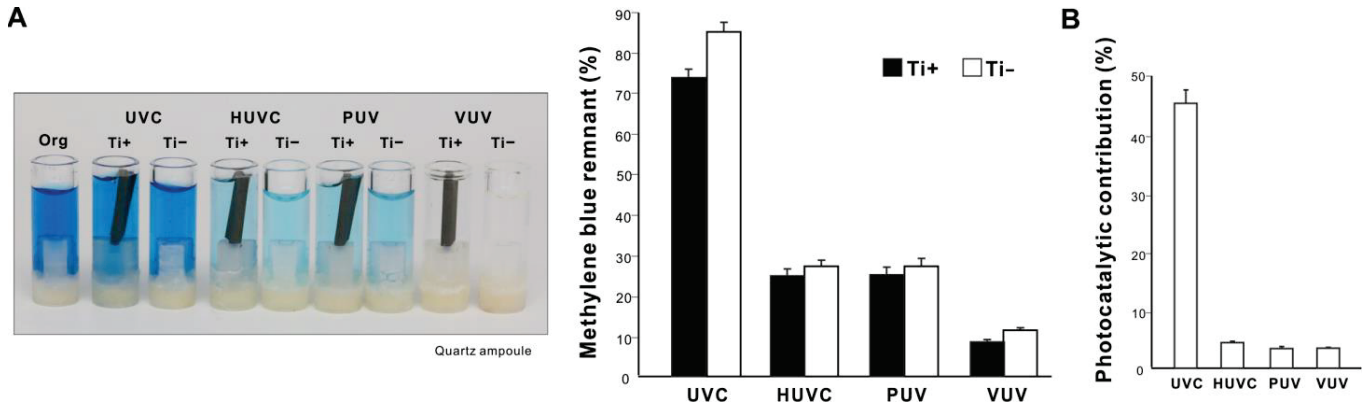


Figure 3. UV-mediated decomposition of methylene blue induced by various UV sources. (**A**) Photographs of the original methylene blue solution in a quartz ampoule together with solutions after UV treatment presented side-by-side for comparison. Four different UV light sources were used for one minute: (1) UVC from a low-pressure mercury lamp (UVC); (2) high-energy UVC (HUVC); (3) a UV device with a proprietary protocol (PUV); and (4) 172 nm vacuum UV (VUV). Methylene blue was UV-treated with or without a microroughened titanium specimen. A histogram showing remnant methylene blue after UV treatment (%). (**B**) Photocatalytic contribution (%) calculated as the difference in the amount of decomposed methylene blue with and without a titanium specimen.

2.3. Dose Dependency of Organic Decomposition Induced by VUV and UVC

After establishing that VUV had the greatest methylene blue decomposition efficacy, we tested for dose dependency by varying the treatment time. With a titanium specimen in a quartz ampoule, the amount of remnant methylene blue significantly decreased with the increase in treatment time up to 60 s to then plateau at about 10%, fitting a negative exponential curve with a remarkably high coefficient of determination (Figure 4A). VUV treatment without a titanium specimen showed a similar dose dependency, but with a lower efficacy of decomposition. The photocatalytic contribution decreased with longer treatment time (Figure 4B). Thus, the maximum efficacy of organic decomposition induced by VUV was achieved with an optimized treatment time of 1 min.

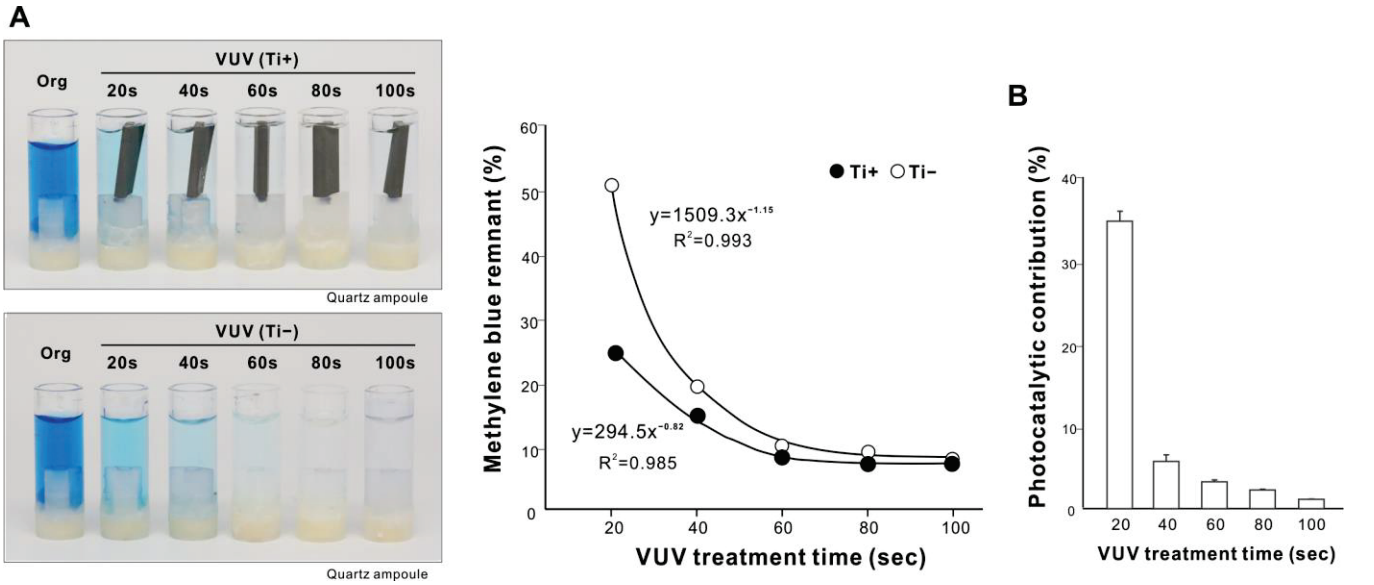


Figure 4. Dose dependency and optimization of VUV-mediated organic decomposition. (**A**) Photographs of the original methylene blue solution in a quartz ampoule together with solutions after VUV treatment for various treatment times from 20 to 100 s. The remaining methylene blue was quantified and plotted against UV treatment time; it showed a highly fitted, negative exponential curve. (**B**) Photocatalytic contribution (%) calculated as the difference in the amount of decomposed methylene blue with and without a microroughened titanium specimen.

We further tested for the presence of UV dose dependency using UVC. Again, the length of UVC treatment was proportional to the degree of methylene blue decomposition (Figure 5A), plateauing at 20–30 min along a negative exponential curve. With both UV sources, UV treatment was unable to completely decompose methylene blue within the treatment time tested, suggesting a general limit to UV-mediated organic decomposition. Photocatalysis induced by a titanium specimen contributed less as treatment time increased (Figure 5B).

2.4. Effect of Quartz Ampoules on UV-Mediated Organic Decomposition

We next compared the impact of quartz ampoules and laboratory-grade plastic tubes on organic decomposition efficacy by assessing methylene blue decomposition using one minute of UV treatment with or without a titanium specimen. Methylene blue decomposition was greater in quartz ampoules than plastic tubes for all UV treatments (Figures 3A and 6A); for instance, there was >90% residual methylene blue in plastic tubes after UVC treatment compared with 75% in quartz ampoules. VUV showed the highest efficacy of decomposition among the UV sources, with approximately 55% remnant methylene blue, although significantly more than the 9% seen in the quartz ampoule (Figures 3A and 6A). The photocatalytic contribution was significantly higher in plastic tubes than in quartz ampoules (Figures 3B and 6B), with the majority of methylene blue decomposition in plastic tubes being due to titanium photocatalysis during UVC decomposition.

2.5. Effects of Different Titanium Materials and Surfaces

We next determined if the organic decomposition efficacy differed between titanium specimens using UV treatment under four representative conditions (1 min UVC in quartz ampoules, 1 min UVC in plastic tubes, 1 min VUV in quartz ampoules, and 1 min VUV in plastic tubes). There was no significant difference in efficacy between microroughened commercially pure titanium, machine-surfaced commercially pure titanium, and machine-

surfaced titanium alloy (Figure 7), indicating that the photocatalytic activity was not significantly affected by different titanium materials or surfaces.

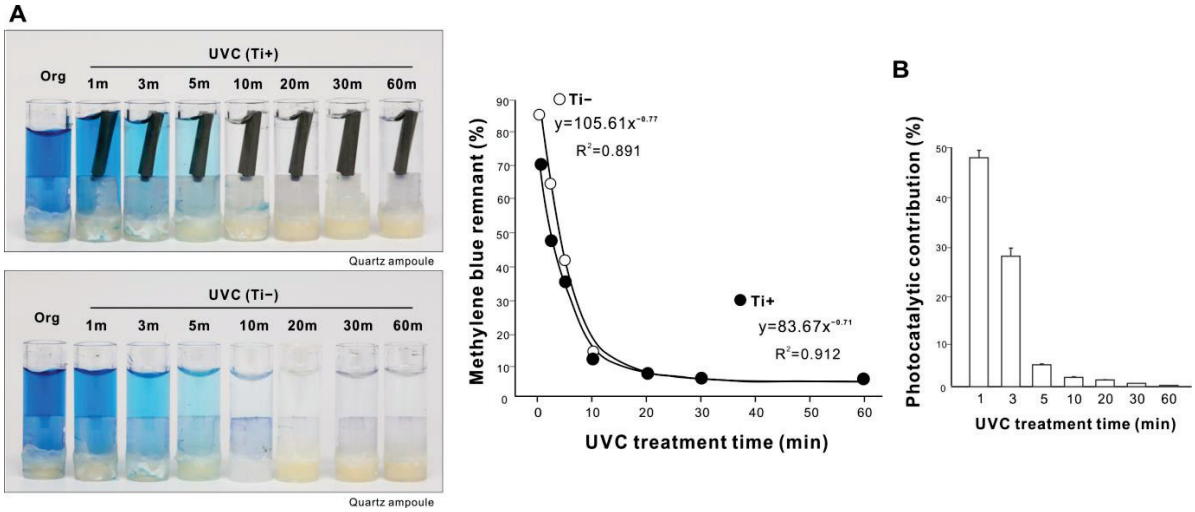


Figure 5. Dose dependency of UVC organic decomposition. (**A**) Photographs of the original methylene blue solution in a quartz ampoule together with solutions after UVC treatment for various treatment times from 1 to 60 min. The remaining methylene blue was quantified and plotted against UV treatment time; it showed a highly fitted, negative exponential curve. (**B**) Photocatalytic contribution (%) calculated as the difference in the amount of decomposed methylene blue with and without a microroughened titanium specimen.

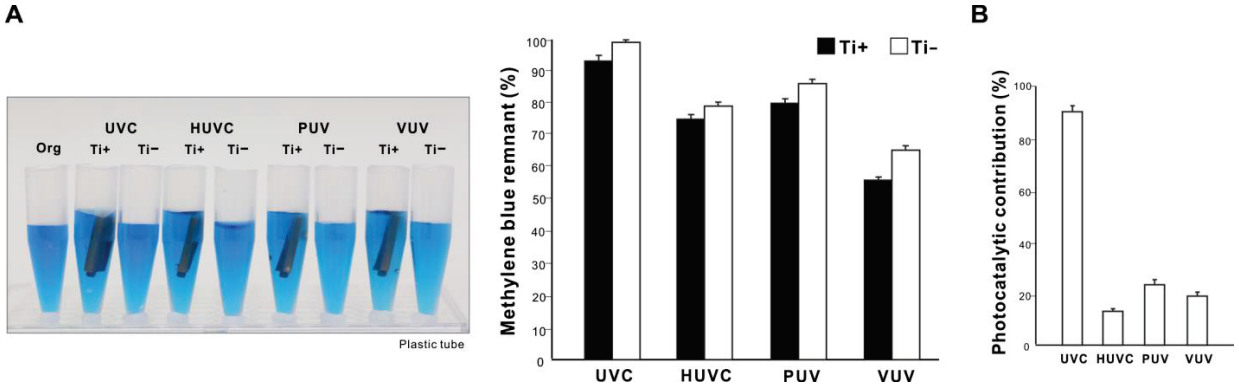


Figure 6. UV-mediated decomposition of methylene blue in plastic tubes. (**A**) Photographs of the original methylene blue solution in a laboratory-grade plastic tube together with solutions after UV treatment presented side-by-side for comparison. Four different UV light sources were used for one minute, as in Figure 3. UV treatment was conducted with or without a microroughened titanium specimen. A histogram showing remnant methylene blue after UV treatment (%). (**B**) Photocatalytic contribution (%) calculated as the difference in the amount of decomposed methylene blue with and without a titanium specimen.

2.6. Load Testing of UV-Mediated Organic Decomposition

We next load-tested the four different UV sources to determine their tolerance to or capacity of organic decomposition. Using a one-minute treatment protocol, various concentrations of methylene blue were decomposed in a quartz ampoule. The UVC treatment did not increase the amount of decomposed methylene blue, rather declining it to near zero as the methylene blue concentration increased (Figure 8). The HUVC and PUV treatments showed a load-dependent increase up to x4 load, followed by a plateau or decline. The regression analysis fitted a polynomial equation for UVC, HUVC, and

PUV treatments, with very high coefficients of correlation. In contrast, methylene blue decomposition linearly increased with the increase in VUV treatment load, with greater concentrations of methylene blue resulting in greater removal. These results indicate unlimited tolerance of VUV-mediated organic decomposition compared with a maximal capacity for other UV sources within the range of loading tested in this study.

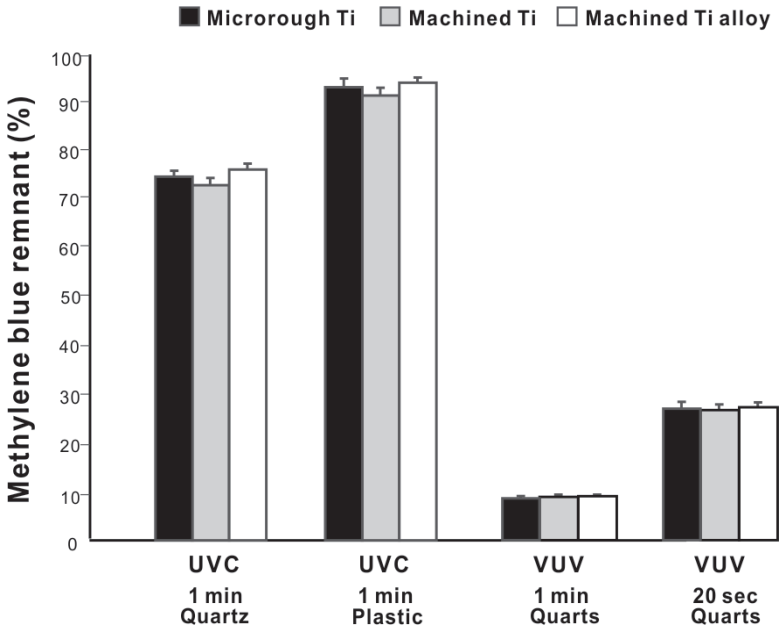


Figure 7. Effects of different titanium materials and surfaces on UV-mediated organic decomposition. UV treatment was conducted under the selected conditions with either microroughened commercially pure titanium, machined commercially pure titanium, or machined grade 5 titanium alloy. A histogram showing remnant methylene blue after UV treatment (%).

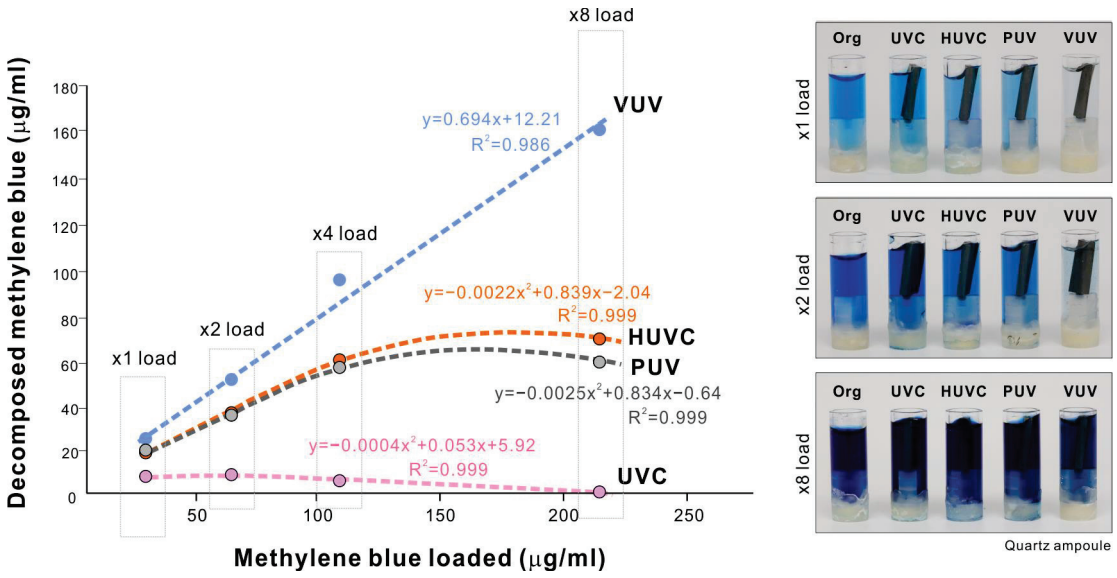


Figure 8. Load testing of organic decomposition induced by four different UV light sources. Methylene blue at four different concentrations (1× to 8×) in a quartz ampoule was treated with four different UV light sources for 1 min. Remnant methylene blue is plotted against the methylene blue concentration along with results of the regression analysis. Note that a linear positive correlation was only found for VUV, while the other UV sources fitted a polynomial equation. Representative photographs of the methylene blue solutions are presented.

3. Discussion

In pursuit of advancing UV photofunctionalization for routine application to dental and orthopedic implants, here, we conducted a series of experiments to optimize the speed and efficacy of organic molecule decomposition induced by UV light sources, especially a novel, xenon excimer lamp emitting 172 nm wavelength VUV. VUV showed particularly high efficacy, which here we tested for the first time on titanium implants [95–99]. Only 9% of methylene blue remained after one minute of VUV treatment, while 25% remained after HUVC and PUV treatments, a 2.8-fold difference in efficacy. UVC was the least effective light source tested, with 74% of methylene blue remaining after treatment. HUVC and PUV have been commercialized for photofunctionalizing dental implants using 20 and 12 min treatment protocols, respectively [33,52,100,101]. The substantial improvement offered by VUV demonstrated here strongly suggests that this approach requires further clinical validation. Furthermore, our dose-dependency experiments revealed that VUV achieved maximum organic decomposition in one minute, considerably faster than existing protocols. This optimization (1) provides empirical evidence on which to further refine the UV photofunctionalization protocol for bone integration and (2) drastically expedites the processing time for clinical application.

Robust VUV-mediated organic decomposition was only possible with the synergy afforded by the use of quartz ampoules. VUV decays proportionally with the increase in the distance from the source due to progressive absorption by the atmosphere or any intervening materials [102–106]. Unfortunately, higher-energy UV light with shorter wavelength decays even more when passing through materials. Furthermore, UV light decays by 60 to 100% through plastic, depending on its thickness and molecular structure, and even glass nearly completely absorbs UV light <300 nm due to impurities such as iron oxide. Indeed, we found that methylene blue decomposition was significantly compromised by plastic, but despite this, VUV retained high performance. As mentioned in the Introduction section, implantable medical devices, including dental and orthopedic implants, are packed in sterilized plastic or metal containers. The present result, revealing excellent UV permeability of quartz ampoules, provides a novel strategy and solution for packaging medical implants, compatible with photofunctionalization. Synthetic quartz can be shaped freely as shown in the present study and is widely used in the industrial field. Now that the clinically viable one-minute protocol has been introduced for effective and rapid photofunctionalization, re-designing implant packages is justified. Thus, exploiting a synergy of VUV and quartz ampoules could open the door to a new standard of implant therapy.

Three mechanisms of UV-mediated organic decomposition are outlined in Figure 9, in which contribution to titanium-mediated photocatalysis was remarkably smaller than that of direct decomposition induced by UV light (photochemical and photophysical decomposition in Figure 9) for all light sources tested. Titanium is a semiconductor, so its photocatalytic activity is induced by UVA at wavelengths of ~375 nm, whose energy corresponds to the band gap of 3.2 eV on TiO_2 surfaces to release e^- to the conduction band. The longer wavelength of UVA affords it higher permeability than UVB and UVC. Therefore, the photocatalytic contribution of UVC might be due to the relatively low intensity of UVC used in this study absorbed by the atmosphere and water, while the majority of UVA reached the titanium surfaces. As a result, UVA-triggered photocatalysis was pronounced. By contrast, the other UV sources of HUVC, PUV, and VUV, emitting high-intensity, short-wavelength UV rays, allowed the partial permeation of shorter UV rays through the atmosphere and water and less UVA-driven photocatalysis to be obtained. More importantly, our results suggest that photocatalytic decomposition is generally slow and has low efficiency and that direct decomposition induced by UV light is the most important parameter to consider when meeting requirements for clinical use (Figure 9). Previous studies have shown that 48 h of treatment is required to functionalize titanium using low-power bactericidal UV light [31,48,49].

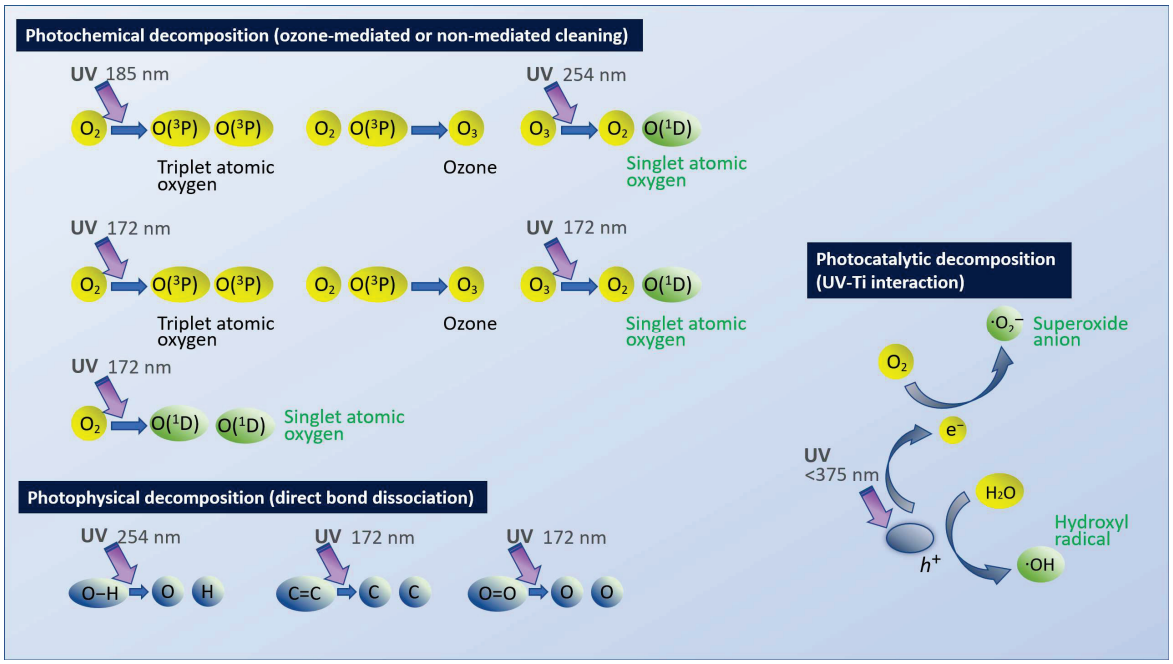


Figure 9. Schematic of three different mechanisms of UV-mediated organic decomposition. During photochemical and photocatalytic decomposition, the generated reactive oxygens (highlighted in green) attack organic molecules. Note that 172 nm VUV light has both photochemical and photophysical advantages, enabling faster and more efficient decomposition.

We postulate that our finding that different materials and surfaces contributed little to the overall decomposition is due to the small contribution of photocatalysis to organic molecule decomposition. We conducted the experiment under the selected conditions using UVC and VUV light sources because information on light intensity was only available for these two sources. We selected the conditions in order to examine the effect of treatment time and type of container. There were no significant effects of different materials or surfaces under all conditions. In theory, the enlarged surface area of acid-etched microroughened titanium may increase photocatalysis. However, this must also be considered in the context of the different crystal properties of titanium surfaces processed in different ways. Heat-manufactured titanium dioxide particles form two crystal types, anatase and rutile; in general, anatase is stable at relatively low temperatures and more reactive to photocatalytic stimuli due to the favorable structure of the conduction band, while rutile is formed at high temperatures and is less photocatalytic [107–113]. Regular bulk titanium such as the machined surface used in this study is unlikely to have a crystal structure, but acid-etched titanium may have an altered crystal structure due to high-temperature acid etching. Future studies should further explore these material structures, including the effect of grade 5 titanium alloy; nevertheless, the photocatalytic contribution appears to be a relatively small component of the rapid organic decomposition required for clinical applications.

High-energy 172 nm VUV should be able to break strong carbon bonds. As shown in the photophysical decomposition illustrated in Figure 9, for instance, oxygen double bonds (O=O) and carbon double bonds (C=C) can be dissociated by 243 nm and 204 nm UV. However, UVC, with a peak wavelength of 254 nm, cannot break them. Thus, shorter wavelengths should decompose more molecules. Methylene blue is a synthetic, organic chloride salt ($C_{16}H_{18}ClN_3S$) containing many carbon double bonds in their benzene rings, making degradation very difficult [97,114]. In light of this, the remarkable capability of VUV to decompose methylene blue and its linear load-testing capacity are of particular note. In photochemical decomposition (Figure 9), reactive oxygen species (ROS) generated by UV play an essential role. Although a low-pressure mercury lamp can generate ROS-excited atomic oxygen, $O(^1D)$, through the production of ozone O_3, VUV excimer lamps

can also generate O(^{1}D) directly from O_2 with a higher efficiency in addition to ozone-mediated generation, providing another explanation for the rapid and efficient VUV-mediated decomposition seen here.

One of the objectives of this study was to find a peak of decarbonization for VUV treatment. In light of this, as mentioned earlier, the one-minute treatment optimized in the dose-dependency experiment was more satisfactory than we anticipated, while the UVC light source took 20–30 min to accomplish the same. We conducted a dose-dependency test for HUVC and PUV sources but had to discontinue because the methylene blue solution started to evaporate after 1.5–3 min. Future studies using a dry technique instead of the wet technique used in this study need to be planned. More importantly, VUV is known to generate less heat than UVC, which has been demonstrated in this study and can be another advantage of VUV in clinical applications over other UV sources.

In this study, hydrophilicity/hydrophobicity and organic decomposition outcomes were not closely related. The efficacy of methylene blue removal varied considerably between the different UV light sources tested, while hydrophilic conversion was not significantly different. In fact, all light sources except for UVC converted titanium surfaces from hydrophobic to very hydrophilic or superhydrophilic (defined as a contact angle of 0°). This confirmed the importance of surface carbon rather than hydrophilicity as a marker for osseointegration, as reported previously [20,23,47,49]. Indeed, residual methylene blue varied between 75% and 9% on hydrophilic surfaces. We propose that surface hydrophilicity is an early marker of titanium photofunctionalization, i.e., hydrophilicity is a necessary but not sufficient factor for improved titanium bioactivity. More significantly, VUV treatment resulted in maximal hydrophilicity and organic decomposition within a minute.

4. Materials and Methods

4.1. Titanium Specimens and Surface Characterization

Titanium test specimens in rectangular plate form (14 mm × 6 mm, 2 mm in thickness) were machined from commercially pure grade 4 titanium and grade 5 Ti-6Al-4V alloy (Figure 10A). To modify the surface from machine-smooth to microroughened, grade 4 commercially pure titanium plates were sandblasted and acid-etched. All test specimens were prepared and provided by DIO (Busan, Korea). Surface morphology was examined using scanning electron microscopy (SEM; Nova 230 Nano SEM; FEI, Hillsboro, Oregon). The hydrophilicity/hydrophobicity of titanium surfaces with and without UV treatment was evaluated by measuring the contact angle of 3 mL of ddH_2O.

4.2. Methylene Blue as a Model Organic Molecule and Containers

Methylene blue was used as a model organic molecule to decompose using UV light. A 0.002% stock solution was prepared. Quartz ampoules in hollow cylinder form (10 mm in diameter, 25 mm in height, 1 mm thick) made from synthetic quartz glass (Figure 10B) and laboratory-grade 1.5 mL plastic tubes (Fisher Scientific, Pittsburgh, PA, USA) (Figure 10C) were prepared as containers for methylene blue solution during UV treatment. Quartz ampoules or plastic tubes were filled with 750 mL of methylene blue stock solution for UV treatment. UV treatment was administered with and without a titanium specimen in each container.

4.3. UV-Mediated Decomposition of Methylene Blue

Methylene blue in quartz and plastic containers was treated with four different UV light sources (Figure 11): (i) UVC from a commercially available low-pressure mercury lamp (1.2 mW/cm^2; Iwasaki Electric, Tokyo, Japan); (ii) high-energy UVC (HUVC) from a commercially available UV device for dental implants (TheraBeam Affiny, Ushio, Tokyo, Japan); (iii) a commercially available UV device for dental implants with a proprietary protocol (PUV) (SuperOsseo, Ushio, Tokyo, Japan); and (iv) 172 nm vacuum UV (VUV; ~60 mW/cm^2) (DIO, Busan, Korea). UVC and VUV were irradiated at 6 mm and HUVC and PUV following the manufacturers' instructions. The treatment time was 1 min for

most experiments and was varied for dose-dependency experiments. The methylene blue concentrations in the original solution and after UV treatment were measured using a microplate reader at 650 nm (Synergy H1; BioTek Instruments, Winooski, VT, USA), and remnant methylene blue was calculated as a percentage relative to the original solution.

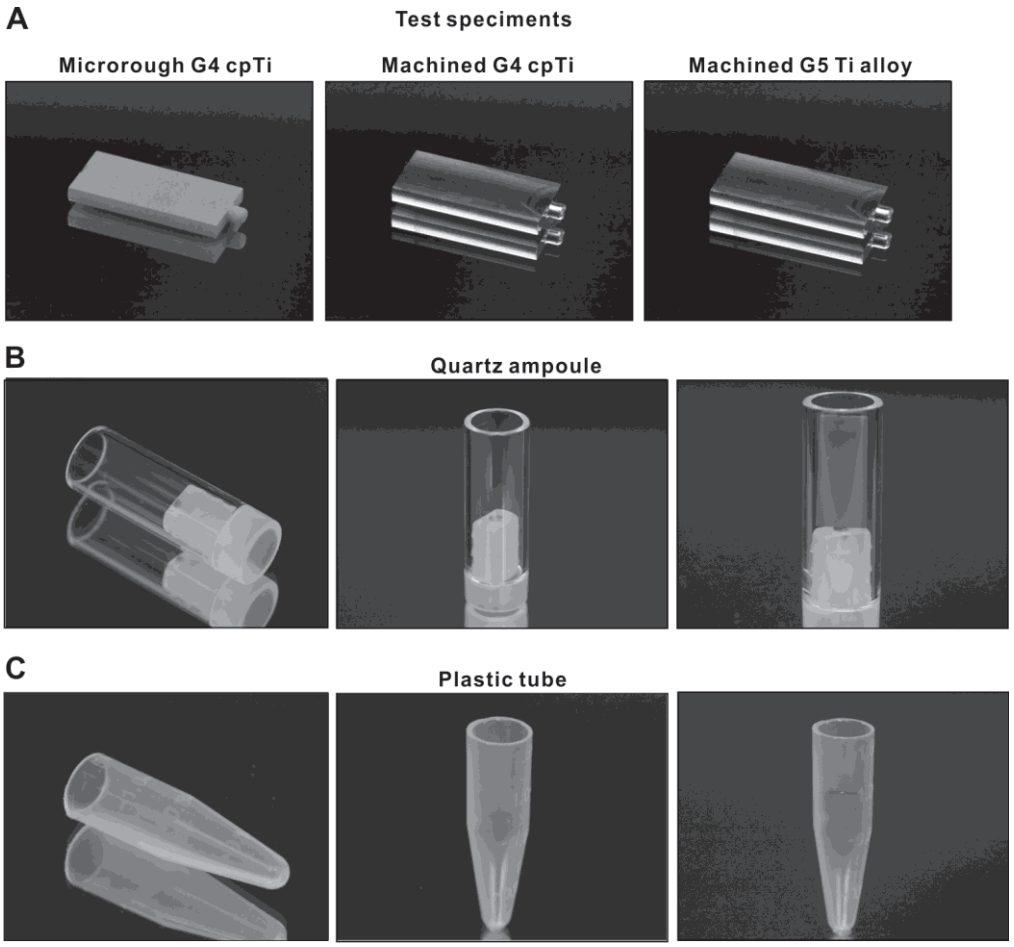


Figure 10. The titanium specimens and containers used in this study. (**A**) Test specimens made of different materials and surface topographies. (**B**) An ampoule made of synthetic quartz. A titanium specimen is placed in the quartz ampoule (**right** panel). (**C**) A laboratory-grade clear plastic tube. A titanium specimen is placed in the plastic tube (**right** panel).

4.4. Statistical Analyses

Three test specimens were used for all methylene blue decomposition experiments (n = 3). One- or two-way ANOVA was performed to examine the effect of different UV light sources, the presence or absence of a titanium specimen, and treatment time. The Bonferroni test was used as a post hoc multiple comparison test where appropriate. p-values < 0.05 were considered to be statistically significant. Regression analysis was applied to determine the associations between methylene blue decomposition parameters and UV treatment factors.

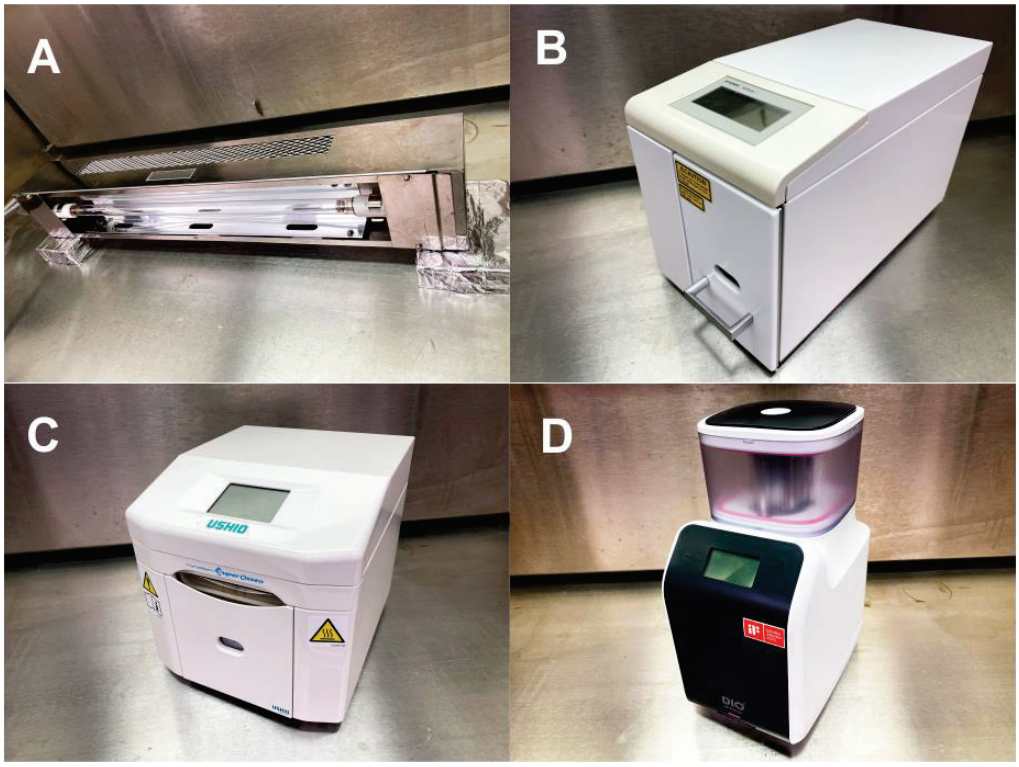


Figure 11. Photographs of UV devices used in this study. (**A**) UVC device (UVC). (**B**) High-energy UVC (HUVC). (**C**) UV device with a proprietary protocol (PUV). (**D**) 172 nm vacuum UV (VUV).

5. Conclusions

Here, we determined the capability of a novel xenon excimer-generated VUV light source to decompose organic molecules around titanium, with a view to optimizing the photofunctionalization or activation of titanium implants for clinical use. VUV decomposed methylene blue molecules in a quartz ampoule significantly faster and with greater efficacy than other UV light sources, including low-pressure mercury-generated UVC and commercially available UV devices for dental implants. We achieved >90% VUV-mediated organic decomposition in one minute. Load testing revealed that VUV light decomposed more methylene blue as it was more concentrated, whereas there was a limit to the decomposing capacity of other UV light sources. All UV light sources tested here generated hydrophilic titanium surfaces after one minute of treatment. Thus, the ability and capacity of different UV light sources to induce organic decomposition varied considerably, with the fastest and most effective decomposition being achieved with VUV, paving the way for VUV-mediated photofunctionalization protocols and devices in clinical practice.

Author Contributions: T.S. performed experiments and data analysis and drafted the manuscript; T.M. contributed to the interpretation of data and reviewed the manuscript; K.K. was involved in experimental design and performed experiments and data analysis; T.O. was involved in experimental design, data analysis, interpretation, and the drafting of the manuscript; all authors discussed the results and commented on the manuscript. All authors have approved the final version of the manuscript.

Funding: This work was partially supported by a research gift from DIO IMPLAMT Co., Ltd.

Institutional Review Board Statement: Not applicable.

Informed Consent Statement: Not applicable.

Data Availability Statement: The data presented in this study are available upon request from the corresponding author.

Conflicts of Interest: The authors declare no conflict of interest.

References

1. Tsukimura, N.; Ueno, T.; Iwasa, F.; Minamikawa, H.; Sugita, Y.; Ishizaki, K.; Ikeda, T.; Nakagawa, K.; Yamada, M.; Ogawa, T. Bone integration capability of alkali- and heat-treated nanobimorphic Ti-15Mo-5Zr-3Al. *Acta Biomater.* **2011**, *7*, 4267–4277. [CrossRef] [PubMed]
2. Hasegawa, M.; Saruta, J.; Hirota, M.; Taniyama, T.; Sugita, Y.; Kubo, K.; Ishijima, M.; Ikeda, T.; Maeda, H.; Ogawa, T. A Newly Created Meso-, Micro-, and Nano-Scale Rough Titanium Surface Promotes Bone-Implant Integration. *Int. J. Mol. Sci.* **2020**, *21*, 783. [CrossRef] [PubMed]
3. Ueno, T.; Tsukimura, N.; Yamada, M.; Ogawa, T. Enhanced bone-integration capability of alkali- and heat-treated nanopolymorphic titanium in micro-to-nanoscale hierarchy. *Biomaterials* **2011**, *32*, 7297–7308. [CrossRef] [PubMed]
4. Saruta, J.; Sato, N.; Ishijima, M.; Okubo, T.; Hirota, M.; Ogawa, T. Disproportionate Effect of Sub-Micron Topography on Osteoconductive Capability of Titanium. *Int. J. Mol. Sci.* **2019**, *20*, 4027. [CrossRef] [PubMed]
5. Saruta, J.; Ozawa, R.; Okubo, T.; Taleghani, S.R.; Ishijima, M.; Kitajima, H.; Hirota, M.; Ogawa, T. Biomimetic Zirconia with Cactus-Inspired Meso-Scale Spikes and Nano-Trabeculae for Enhanced Bone Integration. *Int. J. Mol. Sci.* **2021**, *22*, 7969. [CrossRef]
6. Takeuchi, K.; Saruwatari, L.; Nakamura, H.K.; Yang, J.M.; Ogawa, T. Enhanced intrinsic biomechanical properties of osteoblastic mineralized tissue on roughened titanium surface. *J. Biomed. Mater. Res. A* **2005**, *72A*, 296–305. [CrossRef] [PubMed]
7. Tsukimura, N.; Kojima, N.; Kubo, K.; Att, W.; Takeuchi, K.; Kameyama, Y.; Maeda, H.; Ogawa, T. The effect of superficial chemistry of titanium on osteoblastic function. *J. Biomed. Mater. Res. A* **2008**, *84*, 108–116. [CrossRef]
8. Nakamura, H.; Saruwatari, L.; Aita, H.; Takeuchi, K.; Ogawa, T. Molecular and biomechanical characterization of mineralized tissue by dental pulp cells on titanium. *J. Dent. Res.* **2005**, *84*, 515–520. [CrossRef]
9. Nakamura, H.; Shim, J.; Butz, F.; Aita, H.; Gupta, V.; Ogawa, T. Glycosaminoglycan degradation reduces mineralized tissue-titanium interfacial strength. *J. Biomed. Mater. Res. A* **2006**, *77*, 478–486. [CrossRef]
10. Nakamura, H.K.; Butz, F.; Saruwatari, L.; Ogawa, T. A role for proteoglycans in mineralized tissue-titanium adhesion. *J. Dent. Res.* **2007**, *86*, 147–152. [CrossRef]
11. Saruwatari, L.; Aita, H.; Butz, F.; Nakamura, H.K.; Ouyang, J.; Yang, Y.; Chiou, W.A.; Ogawa, T. Osteoblasts generate harder, stiffer, and more delamination-resistant mineralized tissue on titanium than on polystyrene, associated with distinct tissue micro- and ultrastructure. *J. Bone Min. Res.* **2005**, *20*, 2002–2016. [CrossRef] [PubMed]
12. Kubo, K.; Tsukimura, N.; Iwasa, F.; Ueno, T.; Saruwatari, L.; Aita, H.; Chiou, W.A.; Ogawa, T. Cellular behavior on TiO_2 nanonodular structures in a micro-to-nanoscale hierarchy model. *Biomaterials* **2009**, *30*, 5319–5329. [CrossRef] [PubMed]
13. Att, W.; Kubo, K.; Yamada, M.; Maeda, H.; Ogawa, T. Biomechanical properties of jaw periosteum-derived mineralized culture on different titanium topography. *Int. J. Oral Maxillofac. Implant.* **2009**, *24*, 831–841.
14. Att, W.; Tsukimura, N.; Suzuki, T.; Ogawa, T. Effect of supramicron roughness characteristics produced by 1- and 2-step acid etching on the osseointegration capability of titanium. *Int. J. Oral Maxillofac. Implant.* **2007**, *22*, 719–728.
15. Ishizaki, K.; Sugita, Y.; Iwasa, F.; Minamikawa, H.; Ueno, T.; Yamada, M.; Suzuki, T.; Ogawa, T. Nanometer-thin TiO(2) enhances skeletal muscle cell phenotype and behavior. *Int. J. Nanomed.* **2011**, *6*, 2191–2203.
16. Kojima, N.; Ozawa, S.; Miyata, Y.; Hasegawa, H.; Tanaka, Y.; Ogawa, T. High-throughput gene expression analysis in bone healing around titanium implants by DNA microarray. *Clin. Oral Implant. Res.* **2008**, *19*, 173–181. [CrossRef] [PubMed]
17. Rowlands, D.S.; Shultz, S.P.; Ogawa, T.; Aoi, W.; Korte, M. The effects of uniquely-processed titanium on biological systems: Implications for human health and performance. *J. Funct. Biomater.* **2014**, *5*, 1–14. [CrossRef]
18. Sugita, Y.; Ishizaki, K.; Iwasa, F.; Ueno, T.; Minamikawa, H.; Yamada, M.; Suzuki, T.; Ogawa, T. Effects of pico-to-nanometer-thin TiO_2 coating on the biological properties of microroughened titanium. *Biomaterials* **2011**, *32*, 8374–8384. [CrossRef]
19. Hori, N.; Iwasa, F.; Ueno, T.; Takeuchi, K.; Tsukimura, N.; Yamada, M.; Hattori, M.; Yamamoto, A.; Ogawa, T. Selective cell affinity of biomimetic micro-nano-hybrid structured TiO_2 overcomes the biological dilemma of osteoblasts. *Dent. Mater. Off. Publ. Acad. Dent. Mater.* **2010**, *26*, 275–287. [CrossRef]
20. Att, W.; Hori, N.; Takeuchi, M.; Ouyang, J.; Yang, Y.; Anpo, M.; Ogawa, T. Time-dependent degradation of titanium osteoconductivity: An implication of biological aging of implant materials. *Biomaterials* **2009**, *30*, 5352–5363. [CrossRef]
21. Att, W.; Ogawa, T. Biological aging of implant surfaces and their restoration with ultraviolet light treatment: A novel understanding of osseointegration. *Int. J. Oral Maxillofac. Implant.* **2012**, *27*, 753–761.
22. Hori, N.; Att, W.; Ueno, T.; Sato, N.; Yamada, M.; Saruwatari, L.; Suzuki, T.; Ogawa, T. Age-dependent degradation of the protein adsorption capacity of titanium. *J. Dent. Res.* **2009**, *88*, 663–667. [CrossRef] [PubMed]
23. Hori, N.; Ueno, T.; Suzuki, T.; Yamada, M.; Att, W.; Okada, S.; Ohno, A.; Aita, H.; Kimoto, K.; Ogawa, T. Ultraviolet light treatment for the restoration of age-related degradation of titanium bioactivity. *Int. J. Oral Maxillofac. Implant.* **2010**, *25*, 49–62.
24. Suzuki, T.; Hori, N.; Att, W.; Kubo, K.; Iwasa, F.; Ueno, T.; Maeda, H.; Ogawa, T. Ultraviolet treatment overcomes time-related degrading bioactivity of titanium. *Tissue Eng. Part A* **2009**, *15*, 3679–3688. [CrossRef] [PubMed]

25. Suzuki, T.; Kubo, K.; Hori, N.; Yamada, M.; Kojima, N.; Sugita, Y.; Maeda, H.; Ogawa, T. Nonvolatile buffer coating of titanium to prevent its biological aging and for drug delivery. *Biomaterials* **2010**, *31*, 4818–4828. [CrossRef] [PubMed]
26. Ueno, T.; Takeuchi, M.; Hori, N.; Iwasa, F.; Minamikawa, H.; Igarashi, Y.; Anpo, M.; Ogawa, T. Gamma ray treatment enhances bioactivity and osseointegration capability of titanium. *J. Biomed. Mater. Research. Part B Appl. Biomater.* **2012**, *100*, 2279–2287. [CrossRef]
27. Hirota, M.; Hori, N.; Sugita, Y.; Ikeda, T.; Park, W.; Saruta, J.; Ogawa, T. A Novel Cell Delivery System Exploiting Synergy between Fresh Titanium and Fibronectin. *Cells* **2022**, *11*, 2158. [CrossRef]
28. Iwasa, F.; Tsukimura, N.; Sugita, Y.; Kanuru, R.K.; Kubo, K.; Hasnain, H.; Att, W.; Ogawa, T. TiO_2 micro-nano-hybrid surface to alleviate biological aging of UV-photofunctionalized titanium. *Int. J. Nanomed.* **2011**, *6*, 1327–1341.
29. Nakhaei, K.; Ishijima, M.; Ikeda, T.; Ghassemi, A.; Saruta, J.; Ogawa, T. Ultraviolet Light Treatment of Titanium Enhances Attachment, Adhesion, and Retention of Human Oral Epithelial Cells via Decarbonization. *Materials* **2020**, *14*, 151. [CrossRef]
30. Hayashi, R.; Ueno, T.; Migita, S.; Tsutsumi, Y.; Doi, H.; Ogawa, T.; Hanawa, T.; Wakabayashi, N. Hydrocarbon Deposition Attenuates Osteoblast Activity on Titanium. *J. Dent. Res.* **2014**, *93*, 698–703. [CrossRef]
31. Att, W.; Hori, N.; Iwasa, F.; Yamada, M.; Ueno, T.; Ogawa, T. The effect of UV-photofunctionalization on the time-related bioactivity of titanium and chromium-cobalt alloys. *Biomaterials* **2009**, *30*, 4268–4276. [CrossRef] [PubMed]
32. Ikeda, T.; Hagiwara, Y.; Hirota, M.; Tabuchi, M.; Yamada, M.; Sugita, Y.; Ogawa, T. Effect of photofunctionalization on fluoride-treated nanofeatured titanium. *J. Biomater. Appl.* **2014**, *28*, 1200–1212. [CrossRef] [PubMed]
33. Ikeda, T.; Okubo, T.; Saruta, J.; Hirota, M.; Kitajima, H.; Yanagisawa, N.; Ogawa, T. Osteoblast Attachment Compromised by High and Low Temperature of Titanium and Its Restoration by UV Photofunctionalization. *Materials* **2021**, *14*, 5493. [CrossRef] [PubMed]
34. Ikeda, T.; Ueno, T.; Saruta, J.; Hirota, M.; Park, W.; Ogawa, T. Ultraviolet Treatment of Titanium to Enhance Adhesion and Retention of Oral Mucosa Connective Tissue and Fibroblasts. *Int. J. Mol. Sci.* **2021**, *22*, 12396. [CrossRef]
35. Iwasaki, C.; Hirota, M.; Tanaka, M.; Kitajima, H.; Tabuchi, M.; Ishijima, M.; Park, W.; Sugita, Y.; Miyazawa, K.; Goto, S.; et al. Tuning of Titanium Microfiber Scaffold with UV-Photofunctionalization for Enhanced Osteoblast Affinity and Function. *Int. J. Mol. Sci.* **2020**, *21*, 738. [CrossRef]
36. Minamikawa, H.; Att, W.; Ikeda, T.; Hirota, M.; Ogawa, T. Long-Term Progressive Degradation of the Biological Capability of Titanium. *Materials* **2016**, *9*, 102. [CrossRef]
37. Okubo, T.; Ikeda, T.; Saruta, J.; Tsukimura, N.; Hirota, M.; Ogawa, T. Compromised Epithelial Cell Attachment after Polishing Titanium Surface and Its Restoration by UV Treatment. *Materials* **2020**, *13*, 3946. [CrossRef]
38. Saita, M.; Ikeda, T.; Yamada, M.; Kimoto, K.; Lee, M.C.; Ogawa, T. UV photofunctionalization promotes nano-biomimetic apatite deposition on titanium. *Int. J. Nanomed.* **2016**, *11*, 223–234.
39. Sugita, Y.; Saruta, J.; Taniyama, T.; Kitajima, H.; Hirota, M.; Ikeda, T.; Ogawa, T. UV-Pre-Treated and Protein-Adsorbed Titanium Implants Exhibit Enhanced Osteoconductivity. *Int. J. Mol. Sci.* **2020**, *21*, 4194. [CrossRef]
40. Tabuchi, M.; Ikeda, T.; Hirota, M.; Nakagawa, K.; Park, W.; Miyazawa, K.; Goto, S.; Ogawa, T. Effect of UV Photofunctionalization on Biologic and Anchoring Capability of Orthodontic Miniscrews. *Int. J. Oral Maxillofac. Implant.* **2015**, *30*, 868–879. [CrossRef]
41. Tabuchi, M.; Ikeda, T.; Nakagawa, K.; Hirota, M.; Park, W.; Miyazawa, K.; Goto, S.; Ogawa, T. Ultraviolet photofunctionalization increases removal torque values and horizontal stability of orthodontic miniscrews. *Am J. Orthod. Dentofac. Orthop.* **2015**, *148*, 274–282. [CrossRef] [PubMed]
42. Taniyama, T.; Saruta, J.; Mohammadzadeh Rezaei, N.; Nakhaei, K.; Ghassemi, A.; Hirota, M.; Okubo, T.; Ikeda, T.; Sugita, Y.; Hasegawa, M.; et al. UV-Photofunctionalization of Titanium Promotes Mechanical Anchorage in A Rat Osteoporosis Model. *Int. J. Mol. Sci.* **2020**, *21*, 1235. [CrossRef] [PubMed]
43. Ueno, T.; Ikeda, T.; Tsukimura, N.; Ishijima, M.; Minamikawa, H.; Sugita, Y.; Yamada, M.; Wakabayashi, N.; Ogawa, T. Novel antioxidant capability of titanium induced by UV light treatment. *Biomaterials* **2016**, *108*, 177–186. [CrossRef] [PubMed]
44. Hirota, M.; Ikeda, T.; Sugita, Y.; Ishijima, M.; Hirota, S.; Ogawa, T. Impaired osteoblastic behavior and function on saliva-contaminated titanium and its restoration by UV treatment. *Mater. Sci. Eng. C Mater. Biol. Appl.* **2019**, *100*, 165–177. [CrossRef] [PubMed]
45. Hirota, M.; Ikeda, T.; Tabuchi, M.; Iwai, T.; Tohnai, I.; Ogawa, T. Effect of ultraviolet-mediated photofunctionalization for bone formation around medical titanium mesh. *J. Oral Maxillofac. Surg.* **2014**, *72*, 1691–1702. [CrossRef] [PubMed]
46. Hirota, M.; Ikeda, T.; Tabuchi, M.; Nakagawa, K.; Park, W.; Ishijima, M.; Tsukimura, N.; Hagiwara, Y.; Ogawa, T. Bone Generation Profiling Around Photofunctionalized Titanium Mesh. *Int. J. Oral Maxillofac. Implant.* **2016**, *31*, 73–86. [CrossRef]
47. Hirota, M.; Sugita, Y.; Ishijima, M.; Ikeda, T.; Saruta, J.; Maeda, H.; Ogawa, T. UV photocatalytic activity of titanium dioxide (TiO_2) surface contaminated with bacterial biofilm: Implications for photo- restoration of osteoconductivity. *Mater. Today Adv.* **2021**, *12*, 1235. [CrossRef]
48. Aita, H.; Att, W.; Ueno, T.; Yamada, M.; Hori, N.; Iwasa, F.; Tsukimura, N.; Ogawa, T. Ultraviolet light-mediated photofunctionalization of titanium to promote human mesenchymal stem cell migration, attachment, proliferation and differentiation. *Acta Biomater.* **2009**, *5*, 3247–3257. [CrossRef]
49. Aita, H.; Hori, N.; Takeuchi, M.; Suzuki, T.; Yamada, M.; Anpo, M.; Ogawa, T. The effect of ultraviolet functionalization of titanium on integration with bone. *Biomaterials* **2009**, *30*, 1015–1025. [CrossRef]
50. Ogawa, T. Ultraviolet photofunctionalization of titanium implants. *Int. J. Oral Maxillofac. Implant.* **2014**, *29*, e95–e102. [CrossRef]

51. Funato, A.; Ogawa, T. Photofunctionalized dental implants: A case series in compromised bone. *Int. J. Oral Maxillofac. Implant.* **2013**, *28*, 1589–1601. [CrossRef] [PubMed]
52. Funato, A.; Yamada, M.; Ogawa, T. Success rate, healing time, and implant stability of photofunctionalized dental implants. *Int. J. Oral Maxillofac. Implant.* **2013**, *28*, 1261–1271. [CrossRef] [PubMed]
53. Hirota, M.; Ozawa, T.; Iwai, T.; Ogawa, T.; Tohnai, I. Effect of Photofunctionalization on Early Implant Failure. *Int. J. Oral Maxillofac. Implant.* **2018**, *33*, 1098–1102. [CrossRef] [PubMed]
54. Hirota, M.; Tanaka, M.; Ishijima, M.; Iwasaki, C.; Park, W.; Ogawa, T. Effect of Photofunctionalization on Ti6Al4V Screw Stability Placed in Segmental Bone Defects in Rat Femurs. *J. Oral Maxillofac. Surg.* **2016**, *74*, 861.e1–861.e16. [CrossRef]
55. Hori, N.; Iwasa, F.; Tsukimura, N.; Sugita, Y.; Ueno, T.; Kojima, N.; Ogawa, T. Effects of UV photofunctionalization on the nanotopography enhanced initial bioactivity of titanium. *Acta Biomater.* **2011**, *7*, 3679–3691. [CrossRef]
56. Hori, N.; Ueno, T.; Minamikawa, H.; Iwasa, F.; Yoshino, F.; Kimoto, K.; Lee, M.C.; Ogawa, T. Electrostatic control of protein adsorption on UV-photofunctionalized titanium. *Acta Biomater.* **2010**, *6*, 4175–4180. [CrossRef]
57. Iwasa, F.; Baba, K.; Ogawa, T. Enhanced intracellular signaling pathway in osteoblasts on ultraviolet lighttreated hydrophilic titanium. *Biomed. Res.* **2016**, *37*, 1–11. [CrossRef]
58. Iwasa, F.; Hori, N.; Ueno, T.; Minamikawa, H.; Yamada, M.; Ogawa, T. Enhancement of osteoblast adhesion to UV-photofunctionalized titanium via an electrostatic mechanism. *Biomaterials* **2010**, *31*, 2717–2727. [CrossRef]
59. Jokstad, A.; Sanz, M.; Ogawa, T.; Bassi, F.; Levin, L.; Wennerberg, A.; Romanos, G.E. A Systematic Review of the Role of Implant Design in the Rehabilitation of the Edentulous Maxilla. *Int. J. Oral Maxillofac. Implant.* **2016**, *31*, s43–s99. [CrossRef]
60. Kitajima, H.; Ogawa, T. The Use of Photofunctionalized Implants for Low or Extremely Low Primary Stability Cases. *Int. J. Oral Maxillofac. Implant.* **2016**, *31*, 439–447. [CrossRef]
61. Lee, J.H.; Ogawa, T. The biological aging of titanium implants. *Implant Dent.* **2012**, *21*, 415–421. [CrossRef] [PubMed]
62. Minamikawa, H.; Ikeda, T.; Att, W.; Hagiwara, Y.; Hirota, M.; Tabuchi, M.; Aita, H.; Park, W.; Ogawa, T. Photofunctionalization increases the bioactivity and osteoconductivity of the titanium alloy Ti6Al4V. *J. Biomed. Mater. Res. A* **2014**, *102*, 3618–3630. [CrossRef] [PubMed]
63. Suzuki, S.; Kobayashi, H.; Ogawa, T. Implant stability change and osseointegration speed of immediately loaded photofunctionalized implants. *Implant Dent.* **2013**, *22*, 481–490. [CrossRef] [PubMed]
64. Al Qahtani, M.S.; Wu, Y.; Spintzyk, S.; Krieg, P.; Killinger, A.; Schweizer, E.; Stephan, I.; Scheideler, L.; Geis-Gerstorfer, J.; Rupp, F. UV-A and UV-C light induced hydrophilization of dental implants. *Dent. Mater.* **2015**, *31*, e157–e167. [CrossRef] [PubMed]
65. Altmann, B.; Kohal, R.J.; Steinberg, T.; Tomakidi, P.; Bachle-Haas, M.; Wennerberg, A.; Att, W. Distinct cell functions of osteoblasts on UV-functionalized titanium- and zirconia-based implant materials are modulated by surface topography. *Tissue Eng. Part C Methods* **2013**, *19*, 850–863. [CrossRef]
66. Choi, B.; Lee, Y.C.; Oh, K.C.; Lee, J.H. Effects of photofunctionalization on early osseointegration of titanium dental implants in the maxillary posterior region: A randomized double-blinded clinical trial. *Int. J. Implant Dent.* **2021**, *7*, 37. [CrossRef]
67. de Avila, E.D.; Lima, B.P.; Sekiya, T.; Torii, Y.; Ogawa, T.; Shi, W.; Lux, R. Effect of UV-photofunctionalization on oral bacterial attachment and biofilm formation to titanium implant material. *Biomaterials* **2015**, *67*, 84–92. [CrossRef]
68. Flanagan, D. Photofunctionalization of Dental Implants. *J. Oral Implant.* **2016**, *42*, 445–450. [CrossRef]
69. Gao, Y.; Liu, Y.; Zhou, L.; Guo, Z.; Rong, M.; Liu, X.; Lai, C.; Ding, X. The effects of different wavelength UV photofunctionalization on micro-arc oxidized titanium. *PLoS ONE* **2013**, *8*, e68086. [CrossRef]
70. Ghassemi, A.; Ishijima, M.; Hasegawa, M.; Mohammadzadeh Rezaei, N.; Nakhaei, K.; Sekiya, T.; Torii, Y.; Hirota, M.; Park, W.; Miley, D.D.; et al. Biological and Physicochemical Characteristics of 2 Different Hydrophilic Surfaces Created by Saline-Storage and Ultraviolet Treatment. *Implant Dent.* **2018**, *27*, 405–414. [CrossRef]
71. Park, K.H.; Koak, J.Y.; Kim, S.K.; Heo, S.J. Wettability and cellular response of UV light irradiated anodized titanium surface. *J. Adv. Prosthodont.* **2011**, *3*, 63–68. [CrossRef]
72. Pyo, S.W.; Park, Y.B.; Moon, H.S.; Lee, J.H.; Ogawa, T. Photofunctionalization enhances bone-implant contact, dynamics of interfacial osteogenesis, marginal bone seal, and removal torque value of implants: A dog jawbone study. *Implant Dent.* **2013**, *22*, 666–675. [CrossRef] [PubMed]
73. Ueno, T.; Yamada, M.; Suzuki, T.; Minamikawa, H.; Sato, N.; Hori, N.; Takeuchi, K.; Hattori, M.; Ogawa, T. Enhancement of bone-titanium integration profile with UV-photofunctionalized titanium in a gap healing model. *Biomaterials* **2010**, *31*, 1546–1557. [CrossRef] [PubMed]
74. Att, W.; Takeuchi, M.; Suzuki, T.; Kubo, K.; Anpo, M.; Ogawa, T. Enhanced osteoblast function on ultraviolet light-treated zirconia. *Biomaterials* **2009**, *30*, 1273–1280. [CrossRef]
75. Sugita, Y.; Honda, Y.; Kato, I.; Kubo, K.; Maeda, H.; Ogawa, T. Role of photofunctionalization in mitigating impaired osseointegration associated with type 2 diabetes in rats. *Int. J. Oral Maxillofac. Implant.* **2014**, *29*, 1293–1300. [CrossRef] [PubMed]
76. Ogawa, T. Photofunctionalization of TiO_2 for optimal integration of titanium with bone. In *Benign Photocatalysts. Applications of Titanium Oxide-Based Materials*; Kamat, P., Anpo, M., Eds.; Springer USA Inc.: Greer, SC, USA, 2010; pp. 699–713.
77. Miyauchi, T.; Yamada, M.; Yamamoto, A.; Iwasa, F.; Suzawa, T.; Kamijo, R.; Baba, K.; Ogawa, T. The enhanced characteristics of osteoblast adhesion to photofunctionalized nanoscale TiO_2 layers on biomaterials surfaces. *Biomaterials* **2010**, *31*, 3827–3839. [CrossRef]

78. Yamada, M.; Miyauchi, T.; Yamamoto, A.; Iwasa, F.; Takeuchi, M.; Anpo, M.; Sakurai, K.; Baba, K.; Ogawa, T. Enhancement of adhesion strength and cellular stiffness of osteoblasts on mirror-polished titanium surface by UV-photofunctionalization. *Acta Biomater.* **2010**, *6*, 4578–4588. [CrossRef]
79. Hirota, M.; Ikeda, T.; Tabuchi, M.; Ozawa, T.; Tohnai, I.; Ogawa, T. Effects of Ultraviolet Photofunctionalization on Bone Augmentation and Integration Capabilities of Titanium Mesh and Implants. *Int. J. Oral Maxillofac. Implant.* **2017**, *32*, 52–62. [CrossRef] [PubMed]
80. Hirota, M.; Ozawa, T.; Iwai, T.; Mitsudo, K.; Ogawa, T. UV-Mediated Photofunctionalization of Dental Implant: A Seven-Year Results of a Prospective Study. *J. Clin. Med.* **2020**, *9*, 2733. [CrossRef]
81. Aita, H.; Oh, W.; Kubo, K.; Tsukimura, N.; Maeda, H.; Ogawa, T. Light-induced bone cement-philic titanium surface. *J. Mater. Sci.* **2008**, *43*, 1552–1558. [CrossRef]
82. Kitajima, H.; Hirota, M.; Iwai, T.; Hamajima, K.; Ozawa, R.; Hayashi, Y.; Yajima, Y.; Iida, M.; Koizumi, T.; Kioi, M.; et al. Computational Fluid Simulation of Fibrinogen around Dental Implant Surfaces. *Int. J. Mol. Sci.* **2020**, *21*, 660. [CrossRef] [PubMed]
83. Funato, A.; Tonotsuka, R.; Murabe, H.; Hirota, M.; Ogawa, T. A novel strategy for bone integration and regeneration-Photofunctionalization of dental implants and Ti mesh. *J. Cosmet. Dent.* **2014**, *29*, 74–86.
84. Ishikawa, T.; Salama, M.; Funato, A.; Kitajima, H.; Moroi, H.; Salama, H.; Garber, D. Three-dimensional bone and soft tissue requirements for optimizing esthetic results in compromised cases with multiple implants. *Int. J. Periodontics Restor. Dent.* **2010**, *30*, 503–511.
85. Hirota, M.; Ozawa, T.; Iwai, T.; Ogawa, T.; Tohnai, I. Implant Stability Development of Photofunctionalized Implants Placed in Regular and Complex Cases: A Case-Control Study. *Int. J. Oral Maxillofac. Implant.* **2016**, *31*, 676–686. [CrossRef]
86. Ishikawa, T.; Vela, X.; Kida, K.; Moroi, H.; Kitajima, H.; Ogawa, T. Restoration of optimum esthetics in complex clinical situations using an interdisciplinary strategy in combination with advanced techniques and technologies in regenerative medicine. *J. Cosmet. Dent.* **2014**, *29*, 60–72.
87. Takeuchi, M.; Martra, G.; Coluccia, S.; Anpo, M. Investigations of the structure of H_2O clusters adsorbed on TiO_2 surfaces by near-infrared absorption spectroscopy. *J. Phys. Chem. B* **2005**, *109*, 7387–7391. [CrossRef]
88. Takeuchi, M.; Sakamoto, K.; Martra, G.; Coluccia, S.; Anpo, M. Mechanism of photoinduced superhydrophilicity on the TiO_2 photocatalyst surface. *J. Phys. Chem. B* **2005**, *109*, 15422–15428. [CrossRef]
89. Chen, H.; Nanayakkara, C.E.; Grassian, V.H. Titanium dioxide photocatalysis in atmospheric chemistry. *Chem. Rev.* **2012**, *112*, 5919–5948. [CrossRef]
90. Gopinath, K.P.; Madhav, N.V.; Krishnan, A.; Malolan, R.; Rangarajan, G. Present applications of titanium dioxide for the photocatalytic removal of pollutants from water: A review. *J. Environ. Manag.* **2020**, *270*, 110906. [CrossRef]
91. Wang, R.; Hashimoto, K.; Fujishima, A. Light-induced amphiphilic surfaces. *Nature* **1997**, *388*, 431–432. [CrossRef]
92. Gyorgyey, A.; Janovak, L.; Adam, A.; Kopniczky, J.; Toth, K.L.; Deak, A.; Panayotov, I.; Cuisinier, F.; Dekany, I.; Turzo, K. Investigation of the in vitro photocatalytic antibacterial activity of nanocrystalline TiO_2 and coupled TiO_2/Ag containing copolymer on the surface of medical grade titanium. *J. Biomater. Appl.* **2016**, *31*, 55–67. [CrossRef] [PubMed]
93. Ballman, A.A.; Dodd, D.M.; Kuebler, N.A.; Laudise, R.A.; Wood, D.L.; Rudd, D.W. Synthetic quartz with high ultraviolet transmission. *Appl. Opt.* **1968**, *7*, 1387–1390. [CrossRef] [PubMed]
94. Donat, C.P. Ultraviolet radiation from quartz lamps. *Rev. Radiol. Fisioter* **1945**, *12*, 182–184. [PubMed]
95. Lei, D.; Xie, X.; Xiang, Y.; Huang, X.; Xiao, F.; Cao, J.; Li, G.; Leung, D.Y.C.; Huang, H. An efficient process for aromatic VOCs degradation: Combination of VUV photolysis and photocatalytic oxidation in a wet scrubber. *Chemosphere* **2022**, *309 Pt 2*, 136656. [CrossRef]
96. Zaplotnik, R.; Vesel, A. Effect of VUV Radiation on Surface Modification of Polystyrene Exposed to Atmospheric Pressure Plasma Jet. *Polymers* **2020**, *12*, 1136. [CrossRef]
97. Wen, D.; Li, W.; Lv, J.; Qiang, Z.; Li, M. Methylene blue degradation by the VUV/UV/persulfate process: Effect of pH on the roles of photolysis and oxidation. *J. Hazard. Mater.* **2020**, *391*, 121855. [CrossRef] [PubMed]
98. Fu, P.; Ma, Y.; Lei, B.; Li, G.; Lin, X. Decomposition of refractory aniline aerofloat collector in aqueous solution by an ozone/vacuum-UV (O3/VUV) process. *Environ. Technol.* **2021**, *42*, 659–670. [CrossRef] [PubMed]
99. Long, L.; Bu, Y.; Chen, B.; Sadiq, R. Removal of urea from swimming pool water by UV/VUV: The roles of additives, mechanisms, influencing factors, and reaction products. *Water Res.* **2019**, *161*, 89–97. [CrossRef] [PubMed]
100. Park, W.; Ishijima, M.; Hirota, M.; Soltanzadeh, P.; Ogawa, T. Engineering bone-implant integration with photofunctionalized titanium microfibers. *J. Biomater. Appl.* **2016**, *30*, 1242–1250. [CrossRef]
101. Tateshima, S.; Kaneko, N.; Yamada, M.; Duckwiler, G.; Vinuela, F.; Ogawa, T. Increased affinity of endothelial cells to NiTi using ultraviolet irradiation: An in vitro study. *J. Biomed. Mater. Res. A* **2018**, *106*, 1034–1038. [CrossRef]
102. Bono, N.; Ponti, F.; Punta, C.; Candiani, G. Effect of UV Irradiation and TiO_2-Photocatalysis on Airborne Bacteria and Viruses: An Overview. *Materials* **2021**, *14*, 1075. [CrossRef] [PubMed]
103. Bertagna Silva, D.; Buttiglieri, G.; Babic, S. State-of-the-art and current challenges for TiO_2/UV-LED photocatalytic degradation of emerging organic micropollutants. *Environ. Sci. Pollut. Res. Int.* **2021**, *28*, 103–120. [CrossRef]
104. Iervolino, G.; Zammit, I.; Vaiano, V.; Rizzo, L. Limitations and Prospects for Wastewater Treatment by UV and Visible-Light-Active Heterogeneous Photocatalysis: A Critical Review. *Top. Curr. Chem.* **2019**, *378*, 7. [CrossRef] [PubMed]

105. Matafonova, G.; Batoev, V. Recent advances in application of UV light-emitting diodes for degrading organic pollutants in water through advanced oxidation processes: A review. *Water Res.* **2018**, *132*, 177–189. [CrossRef] [PubMed]
106. Egerton, T.A. UV-absorption–the primary process in photocatalysis and some practical consequences. *Molecules* **2014**, *19*, 18192–18214. [CrossRef]
107. Jing, J.; Feng, J.; Li, W.; Yu, W.W. Low-temperature synthesis of water-dispersible anatase titanium dioxide nanoparticles for photocatalysis. *J. Colloid Interface Sci.* **2013**, *396*, 90–94. [CrossRef]
108. Li, W.; Bai, Y.; Liu, C.; Yang, Z.; Feng, X.; Lu, X.; van der Laak, N.K.; Chan, K.Y. Highly thermal stable and highly crystalline anatase TiO_2 for photocatalysis. *Environ. Sci. Technol.* **2009**, *43*, 5423–5428. [CrossRef]
109. Lee, K.; Kim, D.; Roy, P.; Paramasivam, I.; Birajdar, B.I.; Spiecker, E.; Schmuki, P. Anodic formation of thick anatase TiO_2 mesosponge layers for high-efficiency photocatalysis. *J. Am Chem.. Soc.* **2010**, *132*, 1478–1479. [CrossRef]
110. Liu, M.; Piao, L.; Zhao, L.; Ju, S.; Yan, Z.; He, T.; Zhou, C.; Wang, W. Anatase TiO(2) single crystals with exposed {001} and {110} facets: Facile synthesis and enhanced photocatalysis. *Chem. Commun.* **2010**, *46*, 1664–1666. [CrossRef]
111. Setvin, M.; Shi, X.; Hulva, J.; Simschitz, T.; Parkinson, G.S.; Schmid, M.; Di Valentin, C.; Selloni, A.; Diebold, U. Methanol on Anatase TiO_2 (101): Mechanistic Insights into Photocatalysis. *ACS Catal* **2017**, *7*, 7081–7091. [CrossRef]
112. Sun, B.; Smirniotis, P.G.; Boolchand, P. Visible light photocatalysis with platinized rutile TiO_2 for aqueous organic oxidation. *Langmuir* **2005**, *21*, 11397–11403. [CrossRef] [PubMed]
113. Walenta, C.A.; Kollmannsberger, S.L.; Kiermaier, J.; Winbauer, A.; Tschurl, M.; Heiz, U. Ethanol photocatalysis on rutile TiO_2(110): The role of defects and water. *Phys. Chem. Chem. Phys.* **2015**, *17*, 22809–22814. [CrossRef] [PubMed]
114. Liu, C.; Yang, B.; Chen, J.; Jia, F.; Song, S. Synergetic degradation of Methylene Blue through photocatalysis and Fenton reaction on two-dimensional molybdenite-Fe. *J. Environ. Sci.* **2022**, *111*, 11–23. [CrossRef] [PubMed]

Disclaimer/Publisher's Note: The statements, opinions and data contained in all publications are solely those of the individual author(s) and contributor(s) and not of MDPI and/or the editor(s). MDPI and/or the editor(s) disclaim responsibility for any injury to people or property resulting from any ideas, methods, instructions or products referred to in the content.

International Journal of
Molecular Sciences

MDPI

Article

In Vivo Biofilm Formation on Novel PEEK, Titanium, and Zirconia Implant Abutment Materials

Andreas Wiessner [1,†], Torsten Wassmann [1,*,†], Johanna Maria Wiessner [2], Andrea Schubert [1], Bernhard Wiechens [2], Tristan Hampe [1] and Ralf Bürgers [1]

[1] Department of Prosthodontics, University Medical Center Göttingen, 37075 Göttingen, Germany
[2] Department of Orthodontics, University Medical Center Göttingen, 37075 Göttingen, Germany
* Correspondence: torsten.wassmann@med.uni-goettingen.de
† These authors contributed equally to this work.

Abstract: The formation of biofilms on the surface of dental implants and abutment materials may lead to peri-implantitis and subsequent implant failure. Recently, innovative materials such as polyether-ether-ketone (PEEK) and its modifications have been used as abutment materials. However, there is limited knowledge on microbial adhesion to PEEK materials. The aim of this in vivo study was to investigate biofilm formation on the surface of conventional (titanium and zirconia) and PEEK implant abutment materials. Split specimens of titanium, zirconia, PEEK, and modified PEEK (PEEK-BioHPP) were manufactured, mounted in individual removable acrylic upper jaw splints, and worn by 20 healthy volunteers for 24 h. The surface roughness was determined using widefield confocal microscopy. Biofilm accumulation was investigated by fluorescence microscopy and quantified by imaging software. The surface roughness of the investigated materials was <0.2 µm and showed no significant differences between the materials. Zirconia showed the lowest biofilm formation, followed by titanium, PEEK, and PEEK-BioHPP. Differences were significant ($p < 0.001$) between the investigated materials, except for the polyether-ether-ketones. Generally, biofilm formation was significantly higher ($p < 0.05$) in the posterior region of the oral cavity than in the anterior region. The results of the present study show a material-dependent susceptibility to biofilm formation. The risk of developing peri-implantitis may be reduced by a specific choice of abutment material.

Keywords: implant abutment; dental biomaterial; biofilm; in vivo study; zirconia; PEEK; titanium; peri-implantitis; biofilm management

Citation: Wiessner, A.; Wassmann, T.; Wiessner, J.M.; Schubert, A.; Wiechens, B.; Hampe, T.; Bürgers, R. In Vivo Biofilm Formation on Novel PEEK, Titanium, and Zirconia Implant Abutment Materials. *Int. J. Mol. Sci.* **2023**, *24*, 1779. https://doi.org/10.3390/ijms24021779

Academic Editors: Yury A. Skorik and Dario Puppi

Received: 9 December 2022
Revised: 16 December 2022
Accepted: 11 January 2023
Published: 16 January 2023

Copyright: © 2023 by the authors. Licensee MDPI, Basel, Switzerland. This article is an open access article distributed under the terms and conditions of the Creative Commons Attribution (CC BY) license (https://creativecommons.org/licenses/by/4.0/).

1. Introduction

The human oral cavity harbors a diverse and unique variety of more than 700 different microorganisms that normally organize themselves in complex structured biofilms [1,2]. These oral biofilms form immediately on any natural or artificial surface exposed to saliva and other oral fluids, which in turn serve as reservoirs for bacterial, viral, and fungal cells [3]. The eubiosis within biofilms may shift towards a predominance of disease-causing strains [4]. As a consequence, pathological biofilms attached to dental implants and implant-prosthetic abutments may, in the long term, lead to destructive inflammation of the peri-implant soft and hard tissues (i.e., peri-implant mucositis and peri-implantitis [5]), and in the worst case can result in the loss of the implant and the corresponding prosthetic superstructure [6–8]. Peri-implantitis, by definition associated with irreversible loss of surrounding bone, occurs frequently (overall implant based prevalence > 20%) [9,10] and is the main reason for serious complications in implant-retained prosthetic restorations [11–15].

Prosthetic materials used for implant abutments and removable or fixed reconstructions are of particular importance in the pathogenesis of peri-implant inflammation, because they are directly located at the biological weak point of the implant at the transition from peri-implant hard to soft tissue above the implant shoulder [16,17]. These parts of the

implant superstructure are not enclosed by the alveolar bone like the implant itself, but directly exposed to the biological emergence profile, which additionally is the predilection site for the adhesion and accumulation of peri-implant biofilms [16,18–22]. Prosthetic abutments have a much more complex geometry than conventional tooth-supported prosthesis and are, therefore, even more difficult to access for oral hygiene by the patient, which in turn increases the potential of biofilm-associated infections [23–25]. Therefore, the development of novel anti-microbial and anti-adhesive implant abutment surfaces seems not only desirable, but essential [15,26–29].

In recent years, two biomechanically stable and biocompatible materials, in particular, have proven their worth as gold standard materials in implant-prosthodontics, namely titanium and zirconium oxide [30–35]. Both show reduced biofilm accumulation compared to other dental materials, mainly due to their bioinert properties and excellent polishability [17,31,36,37]. The urge of innovation by implant manufacturers and dedicated scientists to simultaneously improve osseointegration and reduce biofilm accumulation has led to an above-average number of promising novel implant-(prosthetic) materials and surfaces [38–40]. Polyether-ether-ketone (PEEK), a thermoplastic biocompatible polymer, has prevailed over other new developments in respect of mechanical/chemical resistance, biocompatibility, and low plaque affinity [41–43]. Therefore, PEEK has already been used commercially for some years in a wide variety of dental indications, and as an alternative to titanium and zirconia in clinical implantology [41,44–46]. Regarding biofilm accumulation, and apart from a small number of in vitro studies, surprisingly, no conclusive in vivo or clinical studies on microbial adhesion to PEEK are available [28,46–48].

Therefore, in the present study, we investigated the in vivo biofilm accumulation on four different implant abutment materials. In particular, the initial accumulation of microorganisms in the human oral cavity on two novel PEEK surfaces should be compared with that on titanium and zirconia, two well-proven implant-prosthetic materials (gold standards).

2. Results

2.1. Characterization of Test Surfaces

No statistically significant differences in surface roughness values Ra ($p = 0.197$) and Sa ($p = 0.116$) were found between any of the tested materials after high polishing (Table 1).

Table 1. The arithmetic mean roughness (R_a) and the area-related mean arithmetic height (S_a) of the test materials (medians and 25/75 percentiles); no significant differences were found.

	Surface Roughness [µm]	
Material	**R_a**	**S_a**
PEEK-BioHPP	0.099 (0.086/0.114)	0.133 (0.114/0.152)
PEEK-VestaKeep DC4430R	0.100 (0.085/0.121)	0.130 (0.108/0.168)
Titanium	0.114 (0.087/0.128)	0.130 (0.111/0.150)
Zirconia	0.100 (0.090/0.112)	0.117 (0.103/0.130)

Widefield confocal micrographs also did not reveal any significant morphological differences between the four test substrata in the two- and three-dimensional display of both PEEK, the zirconia, or the titanium surfaces (Figure 1a,b).

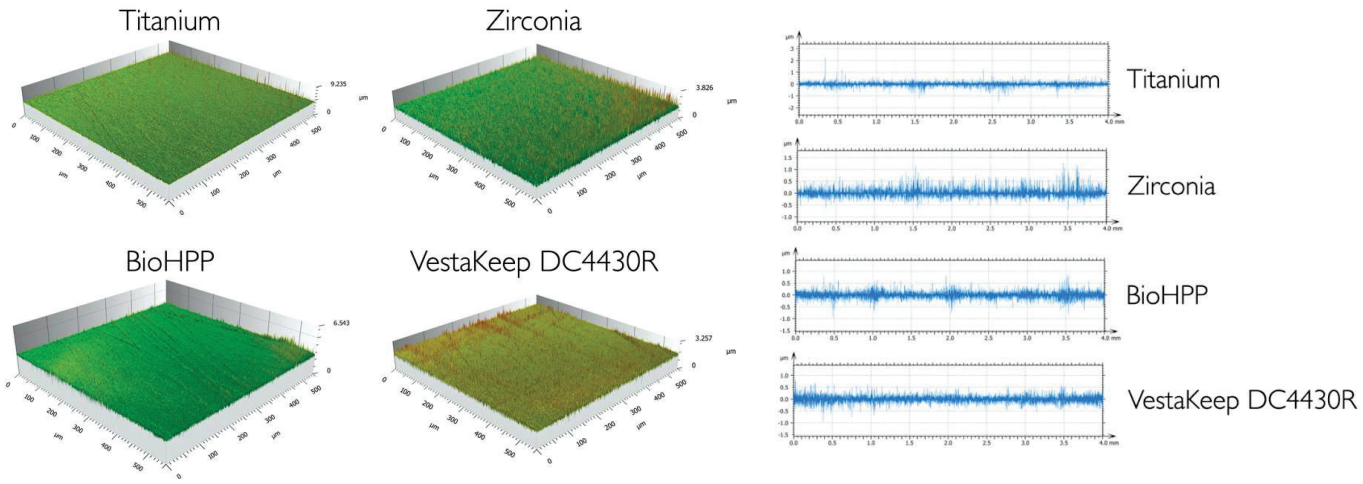


Figure 1. (**a**). Widefield confocal micrographs of the test materials, 3D-profile (500 × 500 µm^2). (**b**). Widefield confocal micrographs of the test materials, 2D-profile (40 mm).

2.2. In Vivo Biofilm Formation

The highest quantity of dental biofilms on the tested implant abutment surfaces was found for PEEK-BioHPP, where 19.7% (9.4%/25.3%; median and 25/75 percentiles) of the material surface was covered by oral biofilms, followed by PEEK-VestaKeep DC4430R with 17.81% (12.1%/24.1%), titanium with 11.1% (5.9%/15.7%), and zirconia with 6.5% (2.9%/9.6%) (Figure 2). Statistical analysis (linear mixed effect model) revealed significant differences in biofilm accumulation between titanium and the other three materials ($p < 0.001$). Subsequent post hoc analyses indicated statistically significant differences in microbial colonization between all tested materials ($p < 0.001$, respectively), except for the comparison between both PEEK materials (PEEK-BioHPP and PEEK-VestaKeep DC4430R, $p = 0.953$). Figure 3 shows representative fluorescent micrographs of the in vivo biofilm accumulations on the tested materials.

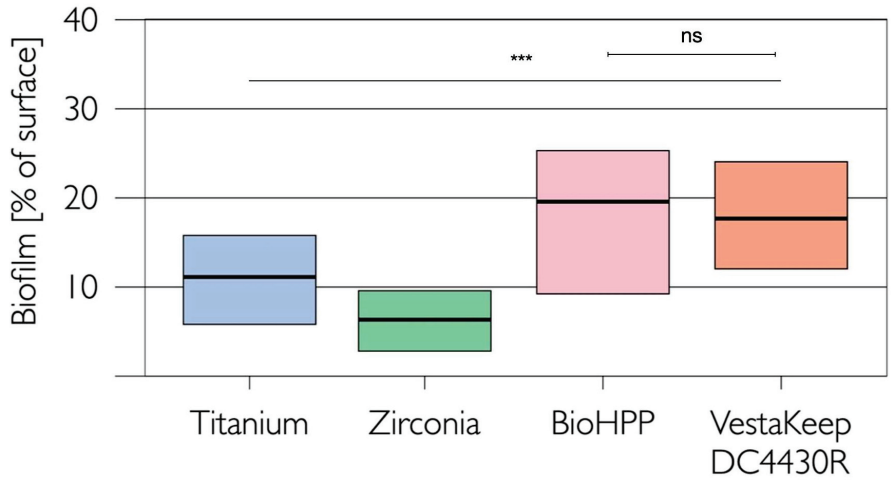


Figure 2. Coverage [% of the of specific standard microscopic fields (500 µm × 750 µm] with in vivo biofilm after 24 h on four test implant abutment materials (medians and 25/75 percentiles), ns = not significant, *** = $p < 0.001$.

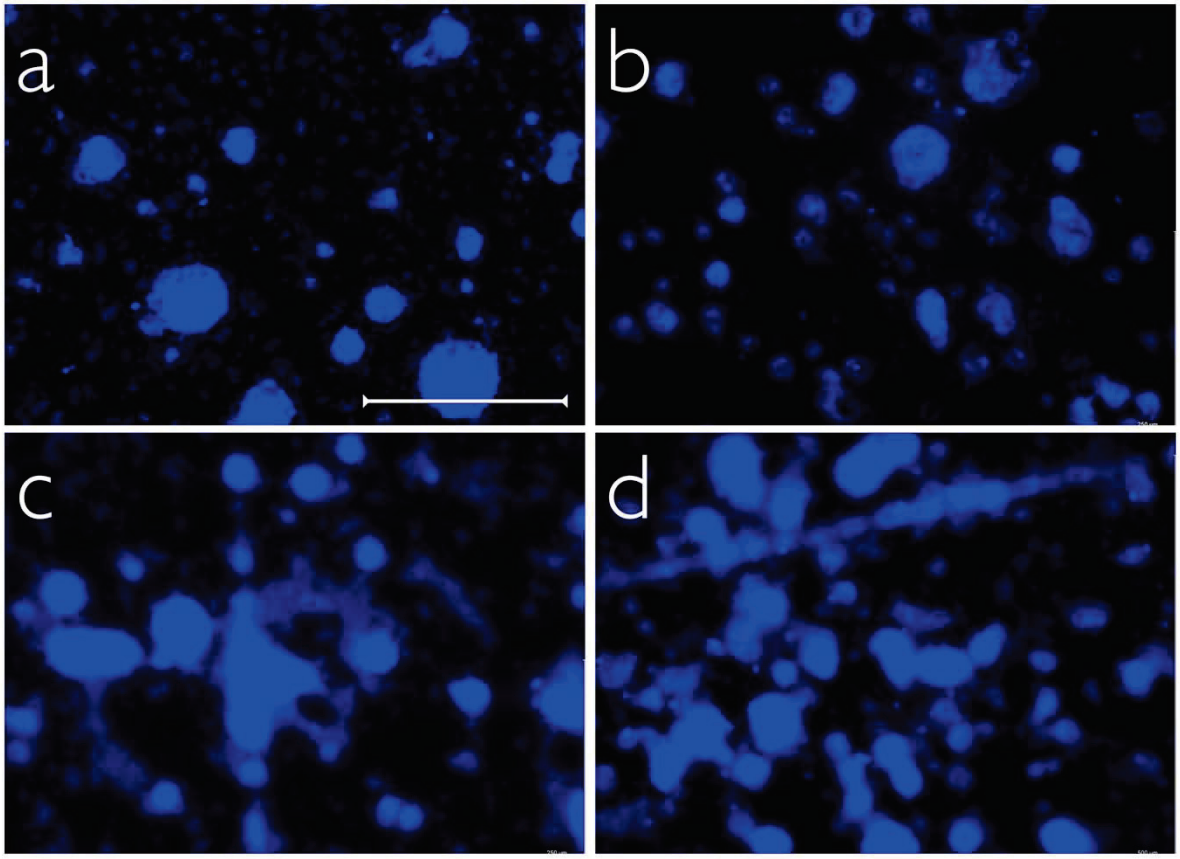


Figure 3. Exemplary fluorescence micrographs of titanium (**a**), zirconia (**b**), PEEK-BioHPP (**c**), and PEEK-VestaKeep DC4430R (**d**) after 24 h of in vivo biofilm formation and fluorescence staining (Hoechst 33342), scale bar equals 250 µm.

The multiple linear mixed effects model revealed significant differences in biofilm accumulation between the different intraoral localizations (canine vs. first molar) of the test specimens ($p = 0.0123$). Specimens located in the posterior region of the splints showed significantly higher overall biofilm adhesion (18.8%, median) than those positioned in the anterior region (8.9%). These differences were observed for all tested materials. Trend differences in overall biofilm accumulation were found between men and women, but they were not statistically significant ($p = 0.079$, Table 2).

Table 2. Biofilm formation [% of the area] on four different test materials (medians and 25/75 percentiles) in correlation with the localization of the test specimens and the gender of the subjects. Significant differences ($p < 0.05$) are indicated by equal letters.

	Intraoral Position		Gender	
	Canine	First Molar	Female	Male
Titanium	5.3 (1.5/12.8) [a]	11.6 (6.3/24.3) [a]	15.1 (10.6/20.6)	7.7 (5.4/13.2)
Zirconia	1.9 (1.1/5.6) [b]	5.4 (3.5/18.0) [b]	8.6 (3.2/15.1)	3.6 (3.0/8.4)
PEEK-BioHPP	14.2 (3.8/19.4) [c]	19.6 (9.0/44.9) [c]	21.5 (14.9/34.9)	17.7 (9.3/23.4)
PEEK-VestaKeep DC4430R	8.7 (4.2/19.3) [d]	22.5 (10.7/38.8) [d]	21.2 (17.0/25.3)	15.5 (11.4/21.5)

3. Discussion

Microbial adhesion on implant-prosthetic substrata may cause peri-implant inflammation and therefore compromise long-term implant survival. This clinical trial investigated the in vivo plaque accumulation on four different implant abutment materials, with two established standard materials (titanium, zirconia) and two novel PEEK materials. To our

knowledge, the present study is the first prospective clinical trial that compares initial in vivo biofilm accumulation between these implant abutment materials [30–35]. Previously conducted studies on biofilm accumulation on PEEK materials were performed in vitro throughout, and therefore significant clinical data are still missing. Although in vitro biofilm models may be used to generate initial indications of varying degrees of biofilm accumulation on different surfaces in a reproducible and manageable setting, it is not possible to simulate realistic conditions of a complex microflora or an interacting immune system of the host [49–51]. Therefore, in vitro results should always be verified by subsequent in vivo testing in the best case [52]. Due to the heterogeneous study setups and varying specimen preparation, existing in vitro studies on biofilm accumulation on PEEK, zirconia, and titanium led to deviating results [47,48]. Hahnel et al. showed significantly lower in vitro biofilm accumulation on PEEK than on titanium and zirconia abutments, whereas Barkarmo et al. did not find any significant differences in bacterial accumulation between PEEK and titanium [47,48].

Only for titanium, a surface roughness value of 0.2 µm (R_a) has been established as a threshold below which no further influence of R_a on microbial accumulation is observed [53,54] In the present study, the surface roughness values (R_a and S_a) of all tested material were below this threshold, with no statistically significant differences in all comparisons; therefore, the influence of roughness on biofilm formation in our clinical trial setup was eliminated. In biofilm testing, significant differences between the four implant-prosthetic materials were found, with the lowest biofilm accumulation on zirconia specimens (median covered surface: 6.5%), followed by titanium (median covered surface: 11.1%), and both PEEK materials (median covered surface PEEK-VestaKeep DC4430R: 17.51%; median covered surface PEEK-BioHPP: 19.7%). The differences between PEEK-VestaKeep DC4430R and PEEK-BioHPP were not significant. PEEK materials chemically belong to the polyaryletherketones (PAEK) and present favorable clinical properties such as high mechanical stability, biocompatibility, and chemical inertness [55,56]. Therefore, the application range of PEEK in restorative dentistry is growing rapidly and more and more clinical applications are being developed. In the present study, one conventional PEEK material (PEEK-VestaKeep DC4430R) and one PEEK material reinforced with 20% ceramic fillers (PEEK PEEK-BioHPP) were investigated, which represent the two most significant material specifications of PEEK. The addition of ceramic fillers is supposed to improve mechanical and aesthetic properties [57]. However, regarding biofilm accumulation, no significant difference between both materials was found. There are countless modifications of PAEK; therefore, the results of the present study cannot be applied to all materials, especially in comparison to titanium and zirconia, without any limitations. For example, in a recent in vivo study by Zeller et al., similar biofilm accumulation on a titanium-modified PAEK and zirconia were found [58]. In contrast, there are already some clinical investigations that compare microbial adhesion on titanium and zirconia. In most of these studies, no difference is found between titanium and zirconia, and if there is, zirconia seems to have a slightly lower potential for the accumulation of oral biofilms [31,59–62].

Additionally to the comparison between different implant-prosthetic substrata, we investigated the influence of the intra-oral localization of the specimens on biofilm formation. A significantly elevated biofilm accumulation in the posterior region was observed when compared to the canine position. These results agree with data from the recent literature [63,64]. The higher quantity of biofilm adhesion in the posterior regions of the oral cavity is associated with the localization of the excretory ducts of the large salivary glands, and a reduced manual cleaning by the soft tissue of the oral cavity [65,66].

Within the limitations of this study, we conclude that biofilm accumulation on implant-abutment substrata is material-dependent. The area covered by biofilm decreased in the following order: PEEK-BioHPP > PEEK-VestaKeep DC4430R > titanium > zirconia. All differences, except those found between both PEEK materials, were significant. In contrast to previous studies, this study is a prospective clinical trial using specimens with a standardized surface roughness below the threshold of 0.2 µm, and therefore the measured

differences in biofilm formation are most likely influenced by the material and not by general surface characteristics. The risk of developing peri-implantitis may be reduced by a specific choice of abutment material. Future research could focus on biomaterials as such, or the direct alteration of the oral microbiome. The former might be achieved by the development of abutment materials with active antimicrobial effects that can inhibit bacterial growth, the latter by the domiciliary use of pro- or postbiotics and ozonized water to alter or to eradicate biofilms [67–69].

4. Materials and Methods

4.1. Preparation and Characterization of the Test Specimens

In order to achieve a high level of comparability between the four implant abutment materials in biofilm testing, special split specimens were developed. Firstly, square rods (height/length/width = 30.0/2.0/2.0 mm^3) were produced from the test materials (titanium, zirconia, PEEK-BioHPP, and PEEK-VestaKeep DC4430R, see Table 3) strictly according to the manufacturer's instructions. These rods were bonded together on their long sides with a dental luting composite (Panavia 21, Kuraray Noritake Dental Inc., Okayama, Japan) and sawed into specimens of equal height (height/length/width = 1.0/4.0/4.0 mm^3, see Figure 4) with a diamond saw (Exakt 300, Exakt GmbH, Norderstedt, Germany).

Table 3. Test implant abutment materials used in this study.

Class of Material	No.	Test Material	Manufacturer
Titanium (grade 2)	1	Zenotec Ti pur	Wieland Dental + Technik GmbH & Co. KG, Pforzheim, Germany
Zirconia (zirconium dioxide)	2	Cercon base	Dentsply Sirona, Charlotte, NC, USA
PEEK (polyetheretherketone)	3	BioHPP	Bredent GmbH & Co. KG, Senden, Germany
	4	VestaKeep DC4430R	Evonik Industries AG, Essen, Germany

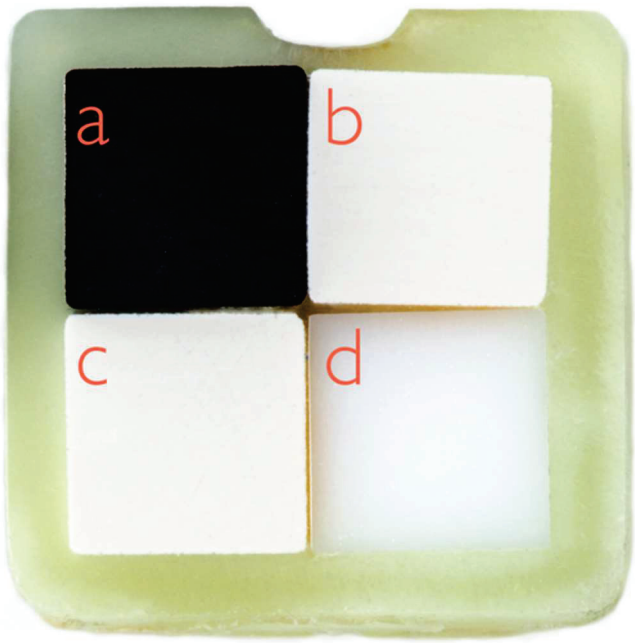


Figure 4. Split specimens consisting of four implant abutment test substrata (each 4 mm × 4 mm): titanium (**a**), zirconia (**b**), PEEK-BioHPP (**c**), and PEEK-VestaKeep DC4430R (**d**).

Specimens (n = 80) were polished to a high gloss in order to reduce the influence of surface morphologies on biofilm formation by using a standardized polishing process with silicon carbide grinding paper with descending abrasiveness (500, 800, 1200, and

4000) and an automated polishing machine (Exakt 400 CS, Exakt GmbH, Norderstedt, Germany). The arithmetic mean roughness (R_a) and the area-related mean arithmetic height (S_a) were calculated via widefield confocal microscopy (Zeiss Smartproof 5, Carl Zeiss, Jena, Germany) and automated software analysis (ConfoMap ST 7.4.8076, Carl Zeiss, Jena, Germany).

Specimens were disinfected by ultrasonication in 3% sodium hypochlorite for 20 min and then washed in distilled water before further processing. For each study object, four split specimens were fixed to an individual removable acrylic upper jaw splint (Figure 5) used to position the specimens in the buccal region of the canines and first molars (teeth 13, 16, 23, and 26, respectively).



Figure 5. Individual splint in situ with two split specimens on the canine and first molar of the left side of the upper jaw.

4.2. In Vivo Biofilm Formation

The present study was conducted as a prospective clinical trial. The subject collective included ten women and ten men (age 22 to 34 years, mean 25.7 years, all healthy and non-smokers). The cohort size was chosen according to a prior in vivo study of our research group [70]. None of the volunteers had used antibacterial mouth rinses or systemic antibiotics in the two months prior to the start of the study. All participants had excellent oral hygiene and no periodontal diseases (plaque indices < 15%, sulcus bleeding indices < 10%) and no caries lesions. The oral examination was carried out by an experienced dentist. Informed written consent had been given by all subjects, and the study had been approved by the Ethics Committee of the Faculty of Medicine, University Medical Center Göttingen (application number 17-7-15).

The subjects were instructed to insert and remove their splint only for oral hygiene measures and food or beverage intake. The splints were worn for 24 h. Then, the plaque-covered specimens were carefully detached under sterile conditions and immediately processed for fluorescence staining.

4.3. Visualization and Quantification of Adhering Biofilms

Specimens were transferred to 24-well-plates, fixed in the wells by duplicating silicone (Z-Dupe Shore A-20, Henry Schein Inc., Melville, NY, USA) and washed threefold in PBS to remove non-adhered cells. The fluorescence dye Hoechst 33342 (Sigma-Aldrich, St. Louis, MO, USA) was used to quantify adhering biofilms (fluorescence emission maximum for approximately 461 nm; excitation maximum of 355 nm). The fluorescence staining solution

was prepared by diluting 5 µL of the fluorescence stain (1 mg/mL) in one milliliter of sterile 0.85% sodium chloride (Merck KGaA, Darmstadt, Germany) for each well. The specimens were incubated in the staining solution for 13 min. After washing with 1 mL of sterile 0.85% sodium chloride, the stained biofilms were fixed with 2% paraformaldehyde (PFA) (Sigma Aldrich, St. Louis, MO, USA). Each specimen was carefully positioned on a coverslip and stored in the dark at 4 °C until further processing.

Fluorescence emission was determined with a fluorescence microscope (Keyence BZ-X710, Keyence Corporation, Osaka, Japan) in combination with an image processing software (BZ-X Analyzer, Keyence Corporation, Osaka, Japan). In each specimen, the fluorescent microscopic images of three randomly selected sites on each of the four test substrata were captured (20× magnification). Thus, 12 images were obtained for each specimen and with a number of 20 subjects, a total of 960 images were obtained. The areas covered by cells were calculated as the percentage of specific standard microscopic fields (500 µm × 750 µm = 0.375 mm^2) with the image analysis software Image J 1.51k Fiji (National Institute of Health, MD, USA).

4.4. Statistical Analysis

Calculations were performed with statistical software R (version 3.4.0, The R Foundation of Statistical Computing, Vienna, Austria). The significance level was set to $\alpha = 0.05\%$. A Box–Cox transformation was applied to the dependent variable 'area in percent'. Titanium was set to be the reference material. A linear mixed effect model was used to assess the influence of material, intraoral position, as well as participants' gender and age on the quantitative plaque accumulation. To determine topographical differences in the specimens' surfaces, data from the roughness measurements were analyzed using a two-way ANOVA. Subsequently significant differences were calculated using post hoc analyses by Tukey.

Author Contributions: Conceptualization, R.B.; methodology, T.W. and A.S.; validation, A.S. and T.H.; formal analysis, T.H. and A.S.; investigation, A.W. and J.M.W.; resources, R.B. and T.W.; writing—original draft preparation, A.W. and T.W.; writing—review and editing, A.S., R.B. and B.W.; visualization, J.M.W. and B.W.; supervision, R.B.; project administration, T.W. All authors have read and agreed to the published version of the manuscript.

Funding: We acknowledge support from the Open Access Publication Funds of the Göttingen University.

Institutional Review Board Statement: The study was conducted in accordance with the Declaration of Helsinki, and approved by the Institutional Ethics Committee of University Medical Centre Göttingen, application number 17-7-15.

Informed Consent Statement: Informed consent was obtained from all subjects involved in the study.

Data Availability Statement: Not applicable.

Acknowledgments: We acknowledge technical support from Susanne Kiecke.

Conflicts of Interest: The authors declare no conflict of interest.

References

1. The Human Microbiome Project Consortium. Structure, Function and Diversity of the Healthy Human Microbiome. *Nature* **2012**, *486*, 207–214. [CrossRef] [PubMed]
2. Dewhirst, F.E.; Chen, T.; Izard, J.; Paster, B.J.; Tanner, A.C.R.; Yu, W.-H.; Lakshmanan, A.; Wade, W.G. The Human Oral Microbiome. *J. Bacteriol.* **2010**, *192*, 5002–5017. [CrossRef] [PubMed]
3. Samaranayake, L.; Bandara, N.; Pesee, S. Oral Biofilms: What Are They? In *Oral Biofilms and Modern Dental Materials*; Ionescu, A.C., Hahnel, S., Eds.; Springer International Publishing: Cham, Switzerland, 2021; pp. 1–7. ISBN 978-3-030-67387-1.
4. Butera, A.; Pascadopoli, M.; Pellegrini, M.; Gallo, S.; Zampetti, P.; Scribante, A. Oral Microbiota in Patients with Peri-Implant Disease: A Narrative Review. *Appl. Sci.* **2022**, *12*, 3250. [CrossRef]
5. Berglundh, T.; Armitage, G.; Araujo, M.G.; Avila-Ortiz, G.; Blanco, J.; Camargo, P.M.; Chen, S.; Cochran, D.; Derks, J.; Figuero, E.; et al. Peri-Implant Diseases and Conditions: Consensus Report of Workgroup 4 of the 2017 World Workshop on the Classification of Periodontal and Peri-Implant Diseases and Conditions. *J. Periodontol.* **2018**, *89* (Suppl. S1), S313–S318. [CrossRef] [PubMed]

6. Mombelli, A.; Décaillet, F. The Characteristics of Biofilms in Peri-Implant Disease. *J. Clin. Periodontol.* **2011**, *38*, 203–213. [CrossRef] [PubMed]
7. Lee, A.; Wang, H.-L. Biofilm Related to Dental Implants. *Implant Dent.* **2010**, *19*, 387–393. [CrossRef] [PubMed]
8. Dabdoub, S.M.; Tsigarida, A.A.; Kumar, P.S. Patient-Specific Analysis of Periodontal and Peri-Implant Microbiomes. *J. Dent. Res.* **2013**, *92*, 168S–175S. [CrossRef] [PubMed]
9. Derks, J.; Tomasi, C. Peri-Implant Health and Disease. A Systematic Review of Current Epidemiology. *J. Clin. Periodontol.* **2015**, *42* (Suppl. S16), S158–S171. [CrossRef]
10. Lee, C.-T.; Huang, Y.-W.; Zhu, L.; Weltman, R. Prevalences of Peri-Implantitis and Peri-Implant Mucositis: Systematic Review and Meta-Analysis. *J. Dent.* **2017**, *62*, 1–12. [CrossRef]
11. Mombelli, A.; Oosten, M.A.C.; Schürch, E.; Lang, N.P. The Microbiota Associated with Successful or Failing Osseointegrated Titanium Implants. *Oral Microbiol. Immunol.* **1987**, *2*, 145–151. [CrossRef]
12. Roos-Jansåker, A.-M.; Lindahl, C.; Renvert, H.; Renvert, S. Nine- to Fourteen-Year Follow-up of Implant Treatment. Part II: Presence of Peri-Implant Lesions. *J. Clin. Periodontol.* **2006**, *33*, 290–295. [CrossRef]
13. Koldsland, O.C.; Scheie, A.A.; Aass, A.M. Prevalence of Peri-Implantitis Related to Severity of the Disease with Different Degrees of Bone Loss. *J. Periodontol.* **2010**, *81*, 231–238. [CrossRef] [PubMed]
14. Derks, J.; Schaller, D.; Håkansson, J.; Wennström, J.L.; Tomasi, C.; Berglundh, T. Peri-Implantitis—Onset and Pattern of Progression. *J. Clin. Periodontol.* **2016**, *43*, 383–388. [CrossRef]
15. Hickok, N.J.; Shapiro, I.M.; Chen, A.F. The Impact of Incorporating Antimicrobials into Implant Surfaces. *J. Dent. Res.* **2018**, *97*, 14–22. [CrossRef]
16. Schwarz, F.; Derks, J.; Monje, A.; Wang, H.-L. Peri-Implantitis. *J. Clin. Periodontol.* **2018**, *45* (Suppl. S20), S246–S266. [CrossRef] [PubMed]
17. Subramani, K.; Jung, R.E.; Molenberg, A.; Hammerle, C.H.F. Biofilm on Dental Implants: A Review of the Literature. *Int. J. Oral Maxillofac. Implant.* **2009**, *24*, 616–626.
18. Belibasakis, G.N.; Charalampakis, G.; Bostanci, N.; Stadlinger, B. Peri-Implant Infections of Oral Biofilm Etiology. *Adv. Exp. Med. Biol.* **2015**, *830*, 69–84. [CrossRef]
19. Shah, S.R.; Tatara, A.M.; D'Souza, R.N.; Mikos, A.G.; Kasper, F.K. Evolving Strategies for Preventing Biofilm on Implantable Materials. *Mater. Today* **2013**, *16*, 177–182. [CrossRef]
20. Rimondini, L.; Cochis, A.; Varoni, E.; Azzimonti, B.; Carrassi, A. Biofilm Formation on Implants and Prosthetic Dental Materials. In *Handbook of Bioceramics and Biocomposites*; Antoniac, I.V., Ed.; Springer International Publishing: Cham, Switzerland, 2015; pp. 1–37. ISBN 978-3-319-09230-0.
21. Heitz-Mayfield, L.J.A. Peri-Implant Diseases: Diagnosis and Risk Indicators. *J. Clin. Periodontol.* **2008**, *35*, 292–304. [CrossRef]
22. Papavasileiou, D.; Behr, M.; Gosau, M.; Gerlach, T.; Buergers, R. Peri-Implant Biofilm Formation on Luting Agents Used for Cementing Implant-Supported Fixed Restorations: A Preliminary in Vivo Study. *Int. J. Prosthodont.* **2015**, *28*, 371–373. [CrossRef]
23. Jepsen, S.; Berglundh, T.; Genco, R.; Aass, A.M.; Demirel, K.; Derks, J.; Figuero, E.; Giovannoli, J.L.; Goldstein, M.; Lambert, F.; et al. Primary Prevention of Peri-Implantitis: Managing Peri-Implant Mucositis. *J. Clin. Periodontol.* **2015**, *42* (Suppl. S16), S152–S157. [CrossRef] [PubMed]
24. Matthews, D.C. Prevention and Treatment of Periodontal Diseases in Primary Care. *Evid. Based Dent.* **2014**, *15*, 68–69. [CrossRef]
25. Tonetti, M.S.; Eickholz, P.; Loos, B.G.; Papapanou, P.; van der Velden, U.; Armitage, G.; Bouchard, P.; Deinzer, R.; Dietrich, T.; Hughes, F.; et al. Principles in Prevention of Periodontal Diseases: Consensus Report of Group 1 of the 11th European Workshop on Periodontology on Effective Prevention of Periodontal and Peri-Implant Diseases. *J. Clin. Periodontol.* **2015**, *42*, S5–S11. [CrossRef]
26. Ramburrun, P.; Pringle, N.A.; Dube, A.; Adam, R.Z.; D'Souza, S.; Aucamp, M. Recent Advances in the Development of Antimicrobial and Antifouling Biocompatible Materials for Dental Applications. *Materials* **2021**, *14*, 3167. [CrossRef]
27. Tobias, R.S. Antibacterial Properties of Dental Restorative Materials: A Review. *Int. Endod. J.* **1988**, *21*, 155–160. [CrossRef]
28. Brum, R.S.; Labes, L.G.; Volpato, C.Â.M.; Benfatti, C.A.M.; Pimenta, A.d.L. Strategies to Reduce Biofilm Formation in PEEK Materials Applied to Implant Dentistry-A Comprehensive Review. *Antibiotics* **2020**, *9*, 609. [CrossRef] [PubMed]
29. Berglundh, T.; Jepsen, S.; Stadlinger, B.; Terheyden, H. Peri-Implantitis and Its Prevention. *Clin. Oral Implant. Res.* **2019**, *30*, 150–155. [CrossRef] [PubMed]
30. Hisbergues, M.; Vendeville, S.; Vendeville, P. Zirconia: Established Facts and Perspectives for a Biomaterial in Dental Implantology. *J. Biomed. Mater. Res. Part B Appl. Biomater.* **2009**, *88*, 519–529. [CrossRef]
31. Scarano, A.; Piattelli, M.; Caputi, S.; Favero, G.A.; Piattelli, A. Bacterial Adhesion on Commercially Pure Titanium and Zirconium Oxide Disks: An in Vivo Human Study. *J. Periodontol.* **2004**, *75*, 292–296. [CrossRef]
32. Yin, L.; Nakanishi, Y.; Alao, A.-R.; Song, X.-F.; Abduo, J.; Zhang, Y. A Review of Engineered Zirconia Surfaces in Biomedical Applications. *Procedia CIRP* **2017**, *65*, 284–290. [CrossRef]
33. Della Bona, A.; Pecho, O.E.; Alessandretti, R. Zirconia as a Dental Biomaterial. *Materials* **2015**, *8*, 4978–4991. [CrossRef]
34. Depprich, R.; Zipprich, H.; Ommerborn, M.; Mahn, E.; Lammers, L.; Handschel, J.; Naujoks, C.; Wiesmann, H.-P.; Kübler, N.R.; Meyer, U. Osseointegration of Zirconia Implants: An SEM Observation of the Bone-Implant Interface. *Head Face Med.* **2008**, *4*, 25–31. [CrossRef] [PubMed]

35. Buser, D.; Sennerby, L.; de Bruyn, H. Modern Implant Dentistry Based on Osseointegration: 50 Years of Progress, Current Trends and Open Questions. *Periodontol. 2000* **2017**, *73*, 7–21. [CrossRef] [PubMed]
36. Roehling, S.; Astasov-Frauenhoffer, M.; Hauser-Gerspach, I.; Braissant, O.; Woelfler, H.; Waltimo, T.; Kniha, H.; Gahlert, M. In Vitro Biofilm Formation on Titanium and Zirconia Implant Surfaces. *J. Periodontol.* **2017**, *88*, 298–307. [CrossRef]
37. De Avila, E.D.; Avila-Campos, M.J.; Vergani, C.E.; Spolidório, D.M.P.; Mollo, F.d.A. Structural and Quantitative Analysis of a Mature Anaerobic Biofilm on Different Implant Abutment Surfaces. *J. Prosthet. Dent.* **2016**, *115*, 428–436. [CrossRef]
38. Pellegrini, G.; Francetti, L.; Barbaro, B.; Del Fabbro, M. Novel Surfaces and Osseointegration in Implant Dentistry. *J. Investig. Clin. Dent.* **2018**, *9*, e12349. [CrossRef] [PubMed]
39. Schünemann, F.H.; Galárraga-Vinueza, M.E.; Magini, R.; Fredel, M.; Silva, F.; Souza, J.C.M.; Zhang, Y.; Henriques, B. Zirconia Surface Modifications for Implant Dentistry. *Mater. Sci. Eng. C Mater. Biol. Appl.* **2019**, *98*, 1294–1305. [CrossRef]
40. Grischke, J.; Eberhard, J.; Stiesch, M. Antimicrobial Dental Implant Functionalization Strategies—A Systematic Review. *Dent. Mater. J.* **2016**, *35*, 545–558. [CrossRef]
41. Panayotov, I.V.; Orti, V.; Cuisinier, F.; Yachouh, J. Polyetheretherketone (PEEK) for Medical Applications. *J. Mater. Sci. Mater. Med.* **2016**, *27*, 118. [CrossRef]
42. Bathala, L.; Majeti, V.; Rachuri, N.; Singh, N.; Gedela, S. The Role of Polyether Ether Ketone (Peek) in Dentistry—A Review. *J. Med. Life* **2019**, *12*, 5–9. [CrossRef]
43. Alexakou, E.; Damanaki, M.; Zoidis, P.; Bakiri, E.; Mouzis, N.; Smidt, G.; Kourtis, S. PEEK High Performance Polymers: A Review of Properties and Clinical Applications in Prosthodontics and Restorative Dentistry. *Eur. J. Prosthodont. Restor. Dent.* **2019**, *27*, 113–121. [CrossRef] [PubMed]
44. Najeeb, S.; Zafar, M.S.; Khurshid, Z.; Siddiqui, F. Applications of Polyetheretherketone (PEEK) in Oral Implantology and Prosthodontics. *J. Prosthodont. Res.* **2016**, *60*, 12–19. [CrossRef] [PubMed]
45. Zoidis, P.; Papathanasiou, I.; Polyzois, G. The Use of a Modified Poly-Ether-Ether-Ketone (PEEK) as an Alternative Framework Material for Removable Dental Prostheses. A Clinical Report. *J. Prosthodont.* **2016**, *25*, 580–584. [CrossRef] [PubMed]
46. Mishra, S.; Chowdhary, R. PEEK Materials as an Alternative to Titanium in Dental Implants: A Systematic Review. *Clin. Implant Dent. Relat. Res.* **2019**, *21*, 208–222. [CrossRef] [PubMed]
47. Hahnel, S.; Wieser, A.; Lang, R.; Rosentritt, M. Biofilm Formation on the Surface of Modern Implant Abutment Materials. *Clin. Oral Implant. Res.* **2015**, *26*, 1297–1301. [CrossRef]
48. Barkarmo, S.; Longhorn, D.; Leer, K.; Johansson, C.B.; Stenport, V.; Franco-Tabares, S.; Kuehne, S.A.; Sammons, R. Biofilm Formation on Polyetheretherketone and Titanium Surfaces. *Clin. Exp. Dent. Res.* **2019**, *5*, 427–437. [CrossRef] [PubMed]
49. Sissons, C.H. Artificial Dental Plaque Biofilm Model Systems. *Adv. Dent. Res.* **1997**, *11*, 110–126. [CrossRef]
50. Schmalz, G. Determination of Biocompatibility. In *Biocompatibility of Dental Materials*; Schmalz, G., Arenholt-Bindslev, D., Eds.; Springer International Publishing: Berlin/Heidelberg, Germany, 2009; pp. 13–43. ISBN 978-3-540-77782-3.
51. Olson, H.; Betton, G.; Robinson, D.; Thomas, K.; Monro, A.; Kolaja, G.; Lilly, P.; Sanders, J.; Sipes, G.; Bracken, W.; et al. Concordance of the Toxicity of Pharmaceuticals in Humans and in Animals. *Regul. Toxicol. Pharmacol.* **2000**, *32*, 56–67. [CrossRef]
52. Anderson, J.M. Future Challenges in the in Vitro and in Vivo Evaluation of Biomaterial Biocompatibility. *Regen. Biomater.* **2016**, *3*, 73–77. [CrossRef]
53. Quirynen, M.; Marechal, M.; Busscher, H.J.; Weerkamp, A.H.; Darius, P.L.; van Steenberghe, D. The Influence of Surface Free Energy and Surface Roughness on Early Plaque Formation: An in Vivo Study in Man. *J. Clin. Periodontol.* **1990**, *17*, 138–144. [CrossRef]
54. Bollen, C.M.; Papaioanno, W.; van Eldere, J.; Schepers, E.; Quirynen, M.; van Steenberghe, D. The Influence of Abutment Surface Roughness on Plaque Accumulation and Peri-Implant Mucositis. *Clin. Oral Implant. Res.* **1996**, *7*, 201–211. [CrossRef] [PubMed]
55. Kern, M.; Lehmann, F. Influence of Surface Conditioning on Bonding to Polyetheretherketon (PEEK). *Dent. Mater.* **2012**, *28*, 1280–1283. [CrossRef]
56. Fuhrmann, G.; Steiner, M.; Freitag-Wolf, S.; Kern, M. Resin Bonding to Three Types of Polyaryletherketones (PAEKs)-Durability and Influence of Surface Conditioning. *Dent. Mater.* **2014**, *30*, 357–363. [CrossRef]
57. Porojan, L.; Toma, F.R.; Vasiliu, R.D.; Topală, F.-I.; Porojan, S.D.; Matichescu, A. Optical Properties and Color Stability of Dental PEEK Related to Artificial Ageing and Staining. *Polymers* **2021**, *13*, 4102. [CrossRef] [PubMed]
58. Zeller, B.; Stöckli, S.; Zaugg, L.K.; Astasov-Frauenhoffer, M.; Hauser-Gerspach, I.; Waltimo, T.; Zitzmann, N.U. Biofilm Formation on Metal Alloys, Zirconia and Polyetherketoneketone as Implant Materials in Vivo. *Clin. Oral Implant. Res.* **2020**, *31*, 1078–1086. [CrossRef] [PubMed]
59. Rimondini, L.; Cerroni, L.; Carrassi, A.; Torricelli, P. Bacterial Colonization of Zirconia Ceramic Surfaces: An in Vitro and in Vivo Study. *Int. J. Oral Maxillofac. Implant.* **2002**, *17*, 793–798.
60. Al-Ahmad, A.; Wiedmann-Al-Ahmad, M.; Faust, J.; Bächle, M.; Follo, M.; Wolkewitz, M.; Hannig, C.; Hellwig, E.; Carvalho, C.; Kohal, R. Biofilm Formation and Composition on Different Implant Materials in Vivo. *J. Biomed. Mater. Res. Part B Appl. Biomater.* **2010**, *95*, 101–109. [CrossRef]
61. Al-Ahmad, A.; Karygianni, L.; Schulze Wartenhorst, M.; Bächle, M.; Hellwig, E.; Follo, M.; Vach, K.; Han, J.-S. Bacterial Adhesion and Biofilm Formation on Yttria-Stabilized, Tetragonal Zirconia and Titanium Oral Implant Materials with Low Surface Roughness—An in Situ Study. *J. Med. Microbiol.* **2016**, *65*, 596–604. [CrossRef]

62. Desch, A.; Freifrau von Maltzahn, N.; Stumpp, N.; Dalton, M.; Yang, I.; Stiesch, M. Biofilm Formation on Zirconia and Titanium over Time—An in Vivo Model Study. *Clin. Oral Implant. Res.* **2020**, *31*, 865–880. [CrossRef]
63. Sreenivasan, P.K.; DeVizio, W.; Prasad, K.V.V.; Patil, S.; Chhabra, K.G.; Rajesh, G.; Javali, S.B.; Kulkarni, R.D. Regional Differences within the Dentition for Plaque, Gingivitis, and Anaerobic Bacteria. *J. Clin. Dent.* **2010**, *21*, 13–19.
64. Sreenivasan, P.K.; Prasad, K.V.V. Distribution of Dental Plaque and Gingivitis within the Dental Arches. *J. Int. Med. Res.* **2017**, *45*, 1585–1596. [CrossRef] [PubMed]
65. Haffajee, A.D.; Teles, R.P.; Patel, M.R.; Song, X.; Yaskell, T.; Socransky, S.S. Factors Affecting Human Supragingival Biofilm Composition. II. Tooth Position. *J. Periodontal Res.* **2009**, *44*, 520–528. [CrossRef] [PubMed]
66. Palk, L.; Sneyd, J.; Shuttleworth, T.J.; Yule, D.I.; Crampin, E.J. A Dynamic Model of Saliva Secretion. *J. Theor. Biol.* **2010**, *266*, 625–640. [CrossRef] [PubMed]
67. Butera, A.; Gallo, S.; Pascadopoli, M.; Luraghi, G.; Scribante, A. Ozonized Water Administration in Peri-Implant Mucositis Sites: A Randomized Clinical Trial. *Appl. Sci.* **2021**, *11*, 7812. [CrossRef]
68. Butera, A.; Pascadopoli, M.; Pellegrini, M.; Gallo, S.; Zampetti, P.; Cuggia, G.; Scribante, A. Domiciliary Use of Chlorhexidine vs. Postbiotic Gels in Patients with Peri-Implant Mucositis: A Split-Mouth Randomized Clinical. *Trial. Appl. Sci.* **2022**, *12*, 2800. [CrossRef]
69. Jennes, M.-E.; Naumann, M.; Peroz, S.; Beuer, F.; Schmidt, F. Antibacterial Effects of Modified Implant Abutment Surfaces for the Prevention of Peri-Implantitis—A Systematic Review. *Antibiotics* **2021**, *10*, 1350. [CrossRef]
70. Wassmann, T.; Schubert, A.; Malinski, F.; Rosentritt, M.; Krohn, S.; Techmer, K.; Bürgers, R. The Antimicrobial and Cytotoxic Effects of a Copper-Loaded Zinc Oxide Phosphate Cement. *Clin. Oral Investig.* **2020**, *24*, 3899–3909. [CrossRef]

Disclaimer/Publisher's Note: The statements, opinions and data contained in all publications are solely those of the individual author(s) and contributor(s) and not of MDPI and/or the editor(s). MDPI and/or the editor(s) disclaim responsibility for any injury to people or property resulting from any ideas, methods, instructions or products referred to in the content.

International Journal of
Molecular Sciences

MDPI

Article

Physicochemical Properties of Novel Copolymers of Quaternary Ammonium UDMA Analogues, Bis-GMA, and TEGDMA

Marta W. Chrószcz-Porębska [1], Izabela M. Barszczewska-Rybarek [1,*] and Grzegorz Chladek [2]

[1] Department of Physical Chemistry and Technology of Polymers, Faculty of Chemistry, Silesian University of Technology, Strzody 9 Str., 44-100 Gliwice, Poland; marta.chroszcz@polsl.pl
[2] Department of Engineering Materials and Biomaterials, Faculty of Mechanical Engineering, Silesian University of Technology, Konarskiego 18A Str., 44-100 Gliwice, Poland; grzegorz.chladek@polsl.pl
* Correspondence: izabela.barszczewska-rybarek@polsl.pl

Abstract: This study aimed to elucidate the physicochemical properties of copolymers comprising 40 wt.% bisphenol A glycerolate dimethacrylate (Bis-GMA), 40 wt.% quaternary ammonium urethane-dimethacrylate analogues (QAUDMA-m, where *m* corresponds to the number of carbon atoms in the *N*-alkyl substituent), and 20 wt.% triethylene glycol dimethacrylate (TEGDMA) copolymers (BG:QAm:TEGs). The BG:QAm:TEG liquid monomer compositions and reference compositions (40 wt.% Bis-GMA, 40 wt.% urethane-dimethacrylate (UDMA), 20 wt.% TEGDMA (BG:UD:TEG) and 60 wt.% Bis-GMA, 40 wt.% TEGDMA (BG:TEG)) were characterized in terms of their refractive index (*RI*) and monomer glass transition temperature (Tg_m) and then photocured. The resulting copolymers were characterized in terms of the polymer glass transition temperature (Tg_p), experimental polymerization shrinkage (S_e), water contact angle (*WCA*), water sorption (*WS*), and water solubility (*SL*). The prepared BG:QAm:TEG liquid monomer compositions had *RI* in the range 1.4997–1.5129, and Tg_m in the range −52.22 to −42.12 °C. The BG:QAm:TEG copolymers had Tg_p ranging from 42.21 to 50.81 °C, S_e ranging from 5.08 to 6.40%, *WCA* ranging from 81.41 to 99.53°, *WS* ranging from 25.94 to 68.27 μg/mm^3, and *SL* ranging from 5.15 to 5.58 μg/mm^3. Almost all of the developed BG:QAm:TEGs fulfilled the requirements for dental materials (except BG:QA8:TEG and BG:QA10:TEG, whose *WS* values exceeded the 40 μg/mm^3 limit).

Keywords: quaternary ammonium methacrylate; urethane-dimethacrylate analogue; dimethacrylate-based dental material; photocured copolymer; physicochemical property

Citation: Chrószcz-Porębska, M.W.; Barszczewska-Rybarek, I.M.; Chladek, G. Physicochemical Properties of Novel Copolymers of Quaternary Ammonium UDMA Analogues, Bis-GMA, and TEGDMA. *Int. J. Mol. Sci.* **2023**, *24*, 1400. https://doi.org/10.3390/ijms24021400

Academic Editors: Jordi Puiggalí and Mary Anne Melo

Received: 2 December 2022
Revised: 3 January 2023
Accepted: 9 January 2023
Published: 11 January 2023

Copyright: © 2023 by the authors. Licensee MDPI, Basel, Switzerland. This article is an open access article distributed under the terms and conditions of the Creative Commons Attribution (CC BY) license (https://creativecommons.org/licenses/by/4.0/).

1. Introduction

Over the past three decades, quaternary ammonium methacrylates (QAMs) have attracted the attention of scientists in the field of antibacterial dimethacrylate-based dental composites [1,2]. This is due to the fact that QAMs show high antibacterial activity caused by the presence of quaternary ammonium (QA) moieties in their structures. As the QA moiety contains a positively charged quaternary nitrogen atom, it can adsorb on the negatively charged bacteria cell surface. As a result, the long alkyl chain attached to the quaternary nitrogen can interact with the lipid chains in a cell wall and disturb the cell's electric balance. This causes an increase in the bacteria cell osmotic pressure which leads to its death [3]. What is more, QAMs can be permanently embedded into composite matrices via copolymerization of their double bonds with double bonds of other dimethacrylates constituting the composite matrix [4]. Thus, QAMs may offer long-term antibacterial activity [5,6]. Various QAMs have been described in the literature, including 2-(dimethylamino)ethyl methacrylate derivatives with chloride [7–9], bromide [10–15], and iodide [16,17] counter ions, quaternary ammonium derivative of bisphenol A glycerolate dimethacrylate [18], and fully aliphatic [19] and cycloaliphatic [20,21] urethane-dimethacrylates. Such QAMs represent potential antibacterial components of dental composites because they offer high antibacterial activity against various strains, including

Streptococcus mutans [4,5,10,13–15,18,20,21], *Staphylococcus aureus* [5,18], and *Escherichia coli* [18]. However, the well-known QAMs induce a loss of mechanical properties and an increase in the amount of water absorbed by the material and in residual fraction release [4,5,10,13–15,18,19,21,22]. Nevertheless, the field of antibacterial dimethacrylates has continued to evolve, and there are still many possibilities to design new compounds with chemical structures that are suitable for obtaining dental composites with appropriate physicochemical, mechanical, and antibacterial characteristics.

This study provides insights relevant for preparing bioactive dimethacrylate matrices for dental composite restorative materials. Our proposal is based on the utilization of quaternary ammonium urethane-dimethacrylate analogues (QAUDMA-m, where *m* is number of carbon atoms in the *N*-alkyl substituent) (Figure 1) [23]. These compounds comprise a 2,2,4-trimethylhexamethylene diisocyanate (TMDI) core and two methacrylate-terminated wings. The quaternary ammonium groups, each substituted with an *N*-alkyl chain of 8, 10, 12, 14, 16, or 18 carbon atoms, are located in the middle of each wing. Because the QAUDMA-m monomers were viscous resins with suitable physicochemical parameters (refractive index (*RI*) from 1.50 to 1.52, monomer glass transition temperature (Tg_m) from −31 to −15 °C, degree of conversion (*DC*) from 0.53 to 0.78, experimental polymerization shrinkage (S_e) from 1.24 to 2.99%) [23], we evaluated them in the context of their copolymers with common dental dimethacrylates: bisphenol A glycerolate dimethacrylate (Bis-GMA), urethane-dimethacrylate monomer (UDMA), and triethylene glycol dimethacrylate (TEGDMA) (Figure 1).

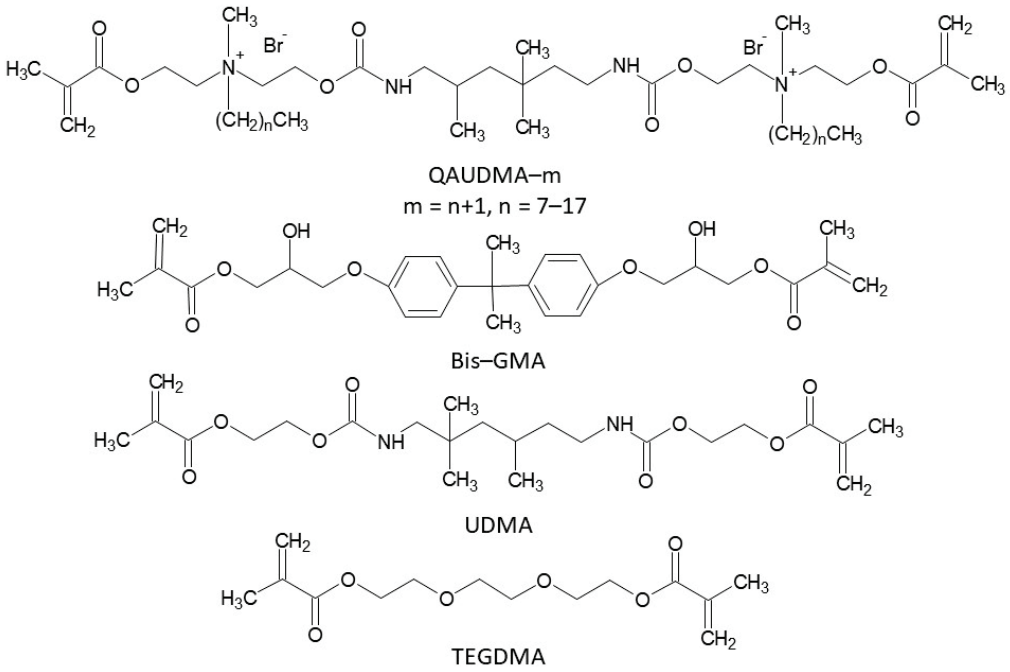


Figure 1. Chemical structures of dimethacrylate monomers used in this study.

First, the physicochemical, mechanical, and antibacterial properties of QAUDMA-m copolymers with 40 wt.% TEGDMA (QAm:TEGs) were characterized [24,25]. The uncured QAm:TEGs had appropriate transparency (*RI* from 1.4895 to 1.5001) and molecular mobility (Tg_m from −33.82 to −25.84 °C). The QA:TEG copolymers were characterized by low volumetric contraction (S_e from 6.4 to 6.9%), high polymerization efficiency (*DC* from 84.0 to 88.7%), high stiffness (polymer glass transition temperature (Tg_p) from 60.33 to 66.32 °C), suitable surface properties (water contact angle (*WCA*) from 82.1 to 98.7°), and high antibacterial activity against *S. aureus* (number of adhered bacteria from 0 (no adhered bacteria) to 4.84 log(CFU/mL), inhibition zone from 6 to 19 mm), and *E. coli* (number of adhered bacteria from 0 (no adhered bacteria) to 3.34 log(CFU/mL), inhibition zone from 6 to 10 mm) [24]. However, they showed excessively high water sorption (*WS* from 116.08 to

148.31 μg/mm^3) and solubility (*SL* from 12.67 to 52.39 μg/mm^3) [25]. These properties excluded them from potential use as matrices for dental composites.

Therefore, the present study aimed to achieve and characterize the novel copolymers comprising 40 wt.% Bis-GMA, 40 wt.% QAUDMA-m, and 20 wt.% TEGDMA (BG:QAm:TEGs).

Proper functioning and longevity of dental restorations equally depends on the physicochemical properties and mechanical performance. The most important physicochemical properties of dental materials' matrices include (i) *DC*—which should exceed 0.55 to provide clinical efficacy [26]; (ii) S_e—which should be as low as possible, because the lower the S_e, the narrower the marginal gaps between the reconstruction and adjacent tooth tissue, and therefore, the smaller the area privileged for bacteria growth [27]; (iii) Tg_p—which should be higher than 40 °C, ensuring that the material is in a glassy state in a temperature range occurring in the oral cavity [28]; (iv) *WS*—which should not exceed 40 μg/mm^3 [29], because the excess of water absorbed by the material can cause its swelling and decrease its mechanical properties [30]; and (v) *SL*—which should not be higher than 7.5 μg/mm^3 [29], because usually, the higher the *SL*, the lower the mechanical stability of the restoration [31].

Despite the crucial role of the dental composites' physicochemical properties in governing their stability, longevity, and functionality, these aspects are rarely examined. In most cases, studies on dental composite matrices modified with QAMs are only limited to the examination of their antibacterial activity, *DC*, and mechanical properties.

The aim of this study was the preliminary assessment of the applicability of BG:QAm:TEGs as matrices for dental dimethacrylate-based composites from the perspective of their physicochemical properties. These evaluations were based on measurements of the *RI* and Tg_m of liquid monomer compositions and the Tg_p, S_e, theoretical polymerization shrinkage (S_t), *WCA*, *WS*, and *SL* of corresponding copolymers. The *DC* [32] was also discussed.

2. Results

In this study, eight compositions of dimethacrylate monomers were prepared. Six of them consisted of 40 wt.% Bis-GMA, 40 wt.% QAUDMA-m, and 20 wt.% TEGDMA (BG:QAm:TEGs). For comparison, the 40 wt.% Bis-GMA, 40 wt.% UDMA, 20 wt.% TEGDMA (BG:UD:TEG), 60 wt.% Bis-GMA, and 40 wt.% TEGDMA (BG:TEG) compositions were also prepared. Liquid monomers were characterized in terms of density (d_m), *RI*, and Tg_m, and the corresponding polymers were characterized in terms of density (d_p), S_t, S_e, Tg_p, *WCA*, *WS*, and *SL*.

In the BG:QAm:TEG notation, the *m* still corresponds to the number of carbon atoms in the *N*-alkyl substituent. Later, *Cm* is used to denote the length of the *N*-alkyl substituent in QAUDMA-m and BG:QAm:TEG.

2.1. Properties of Liquid Monomer Compositions

Table 1 summarizes the *RI* and d_m values of the studied liquid monomer compositions.

The *RI* of BG:QAm:TEGs ranged from 1.4982 to 1.5129. The BG:QAm:TEGs with *Cm* of C8 and C10 had lower *RI* than BG:TEG (*RI* = 1.5048) ($p \leq 0.05$), while BG:QAm:TEGs with *Cm* from C12 to C18 had higher *RI* ($p \leq 0.05$). The BG:QAm:TEGs with *Cm* of C12 and C14 had *RI* values similar to that of BG:UD:TEG (*RI* = 1.5127; $p > 0.05$), whereas the *RI* values of the remaining BG:QAm:TEGs were lower than those of BG:UD:TEG ($p \leq 0.05$).

The d_m of BG:QAm:TEGs ranged from 1.099 to 1.154 g/cm^3 and decreased as *Cm* increased. Specifically, BG:QAm:TEGs with *Cm* from C8 to C12 had higher d_m values than the reference copolymers ($d_{mBG:UD:TEG}$ = 1.115 g/cm^3, $d_{mBG:TEG}$ = 1.102 g/cm^3) ($p \leq 0.05$), whereas the remaining BG:QAm:TEGs had d_m values similar to the reference copolymers ($p > 0.05$).

Table 1. The properties of studied monomer compositions: the length of the *N*-alkyl substituent in QAUDMA-m (*Cm*), molecular weight (*MW*), double-bond concentration (x_{DB}), refractive index (*RI*), and density (d_m). Lowercase letters indicate statistically insignificant differences with a column ($p > 0.05$, non-parametric Wilcoxon test).

Sample Name	*Cm*	*MW* (g/mol)	x_{DB} (kg/mol)	*RI* [1]	d_m (g/cm^3) Average	*SD*
BG:QA8:TEG	C8	528.74	3.78	1.4997	1.154	0.005
BG:QA10:TEG	C10	535.11	3.74	1.4982	1.142	0.006
BG:QA12:TEG	C12	540.95	3.70	1.5128 [a,b]	1.127	0.005
BG:QA14:TEG	C14	546.33	3.66	1.5129 [a,c]	1.116 [a–d]	0.007
BG:QA16:TEG	C16	551.29	3.63	1.5099	1.113 [a,e–g]	0.010
BG:QA18:TEG	C18	555.89	3.60	1.5097	1.099 [b,e,h,i]	0.013
BG:UD:TEG	-	389.27	5.14	1.5127 [b,c]	1.115 [c,f,h]	0.007
BG:TEG	-	429.39	4.66	1.5048	1.102 [d,g,i]	0.005

[1] The standard deviation of *RI* was 0.0001 in each case.

The Tg_m of BG:QAm:TEGs ranged from −52.22 to −42.12 °C and decreased as *Cm* increased. Almost all of the investigated BG:QAm:TEGs had lower Tg_m than BG:UD:TEG (Tg_m = −44.89 °C) ($p \leq 0.05$), except BG:QA10:TEG and BG:QA8:TEG. BG:QA10:TEG had a similar Tg_m ($p > 0.05$), whereas BG:QA8:TEG had a higher Tg_m ($p \leq 0.05$) compared with that of BG:UD:TEG. All BG:QAm:TEGs had higher Tg_m than BG:TEG (Tg_m = −56.45 °C) ($p \leq 0.05$). Representative differential scanning calorimetry (DSC) thermograms of liquid monomer compositions are shown in Figure 2.

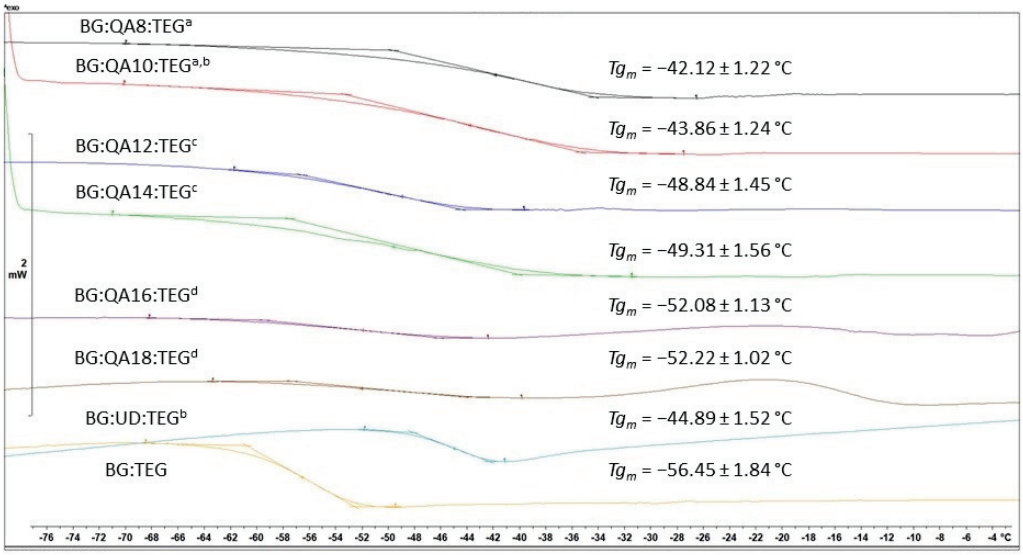


Figure 2. Results of DSC experiments involving the investigated liquid monomer compositions, revealing their glass transition temperatures. Lowercase letters indicate statistically insignificant differences ($p > 0.05$, non-parametric Wilcoxon test).

2.2. Properties of Copolymers

Table 2 summarizes the d_p, S_t, and S_e of the studied copolymers.

The d_p of BG:QAm:TEGs ranged from 1.174 to 1.216 g/cm^3 and decreased as the *Cm* increased. BG:QA8:TEG had a higher d_p than BG:TEG (d_p = 1.206 g/cm^3) ($p \leq 0.05$), while BG:QA10:TEG and BG:QA12:TEG had d_p values similar to that of BG:TEG ($p > 0.05$). The remaining BG:QAm:TEGs had d_p values lower than those of BG:TEG ($p \leq 0.05$). The BG:QAm:TEGs generally had lower d_p than BG:UD:TEG (d_p = 1.215 g/cm^3) ($p \leq 0.05$), except for BG:QA8:TEG, which had a similar d_p ($p > 0.05$).

Table 2. The properties of studied copolymers: density (d_p), experimental (S_e), and theoretical (S_t) polymerization shrinkages, and degree of conversion (*DC*). Lowercase letters indicate statistically insignificant differences with a column ($p > 0.05$, non-parametric Wilcoxon test).

Sample Name	d_p (g/cm^3)		S_e (%)		S_t (%)	*DC* [32]
	Average	SD	Average	SD		
BG:QA8:TEG	1.216 ^{a}	0.007	5.08	0.40	9.81	0.59
BG:QA10:TEG	1.208 ^{b}	0.004	5.48 ^{a}	0.37	9.60	0.60
BG:QA12:TEG	1.200 ^{c}	0.002	6.07 $^{a–d}$	0.49	9.38	0.61
BG:QA14:TEG	1.189 ^{d}	0.002	6.14 ^{b,e,f}	0.41	9.18	0.63
BG:QA16:TEG	1.186 ^{d}	0.005	6.24 ^{c,e,g}	0.54	9.04	0.66
BG:QA18:TEG	1.174	0.004	6.40 ^{d,f,g}	0.48	8.90	0.68
BG:UD:TEG	1.215 ^{a}	0.002	8.35 ^{h}	0.23	12.90	0.64
BG:TEG	1.206 ^{b,c}	0.003	8.07 ^{h}	0.80	11.61	0.68

The S_t of BG:QAm:TEGs ranged from 8.90% to 9.81% and decreased as the *Cm* increased. All of the studied BG:QAm:TEGs had lower S_t values compared with the reference samples ($S_{tBG:UD:TEG}$ = 12.90%, $S_{tBG:TEG}$ = 11.61%) ($p \leq 0.05$). The opposite relationship was observed for S_e. Specifically, the S_e of BG:QAm:TEGs ranged from 5.08% to 6.40% and increased as the *Cm* increased. Compared with the reference samples ($S_{eBG:UD:TEG}$ = 8.35%, $S_{eBG:TEG}$ = 8.07%), all of the studied BG:QAm:TEGs had lower S_e ($p \leq 0.05$).

The Tg_p of BG:QAm:TEGs ranged from 42.21 to 50.81 °C and increased as the *Cm* increased. All of the studied BG:QAm:TEGs had lower Tg_p values compared with the reference copolymers ($Tg_{pBG:UD:TEG}$ = 55.90 °C, $Tg_{pBG:TEG}$ = 61.46 °C) ($p \leq 0.05$). Representative DSC thermograms of the copolymers are shown in Figure 3.

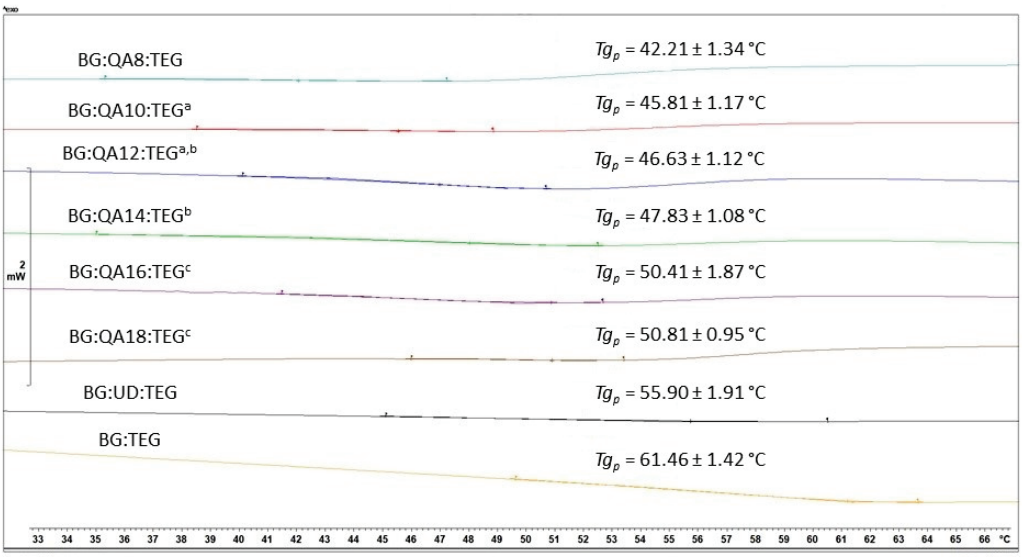


Figure 3. Results of DSC experiments involving the studied copolymers revealing their glass transition temperatures. Lowercase letters indicate statistically insignificant differences ($p > 0.05$, non-parametric Wilcoxon test).

The *WCA* results are presented in Figure 4. The *WCA* of BG:QAm:TEGs ranged from 81.41° to 99.53° and increased as the *Cm* increased. Compared with BG:UD:TEG (*WCA* = 80.76°), all studied BG:QAm:TEGs had higher *WCA* values. Almost all of these differences were statistically significant ($p \leq 0.05$), except that for BG:QA8:TEG, which was statistically insignificant ($p > 0.05$). Notably, BG:QA8:TEG had a lower *WCA* than BG:TEG (*WCA* = 86.57°), whereas the BG:QAm:TEGs with *Cm* of C10, C12, and C14 had similar *WCA* ($p > 0.05$). The remaining BG:QAm:TEGs had higher *WCA* ($p \leq 0.05$) than BG:TEG.

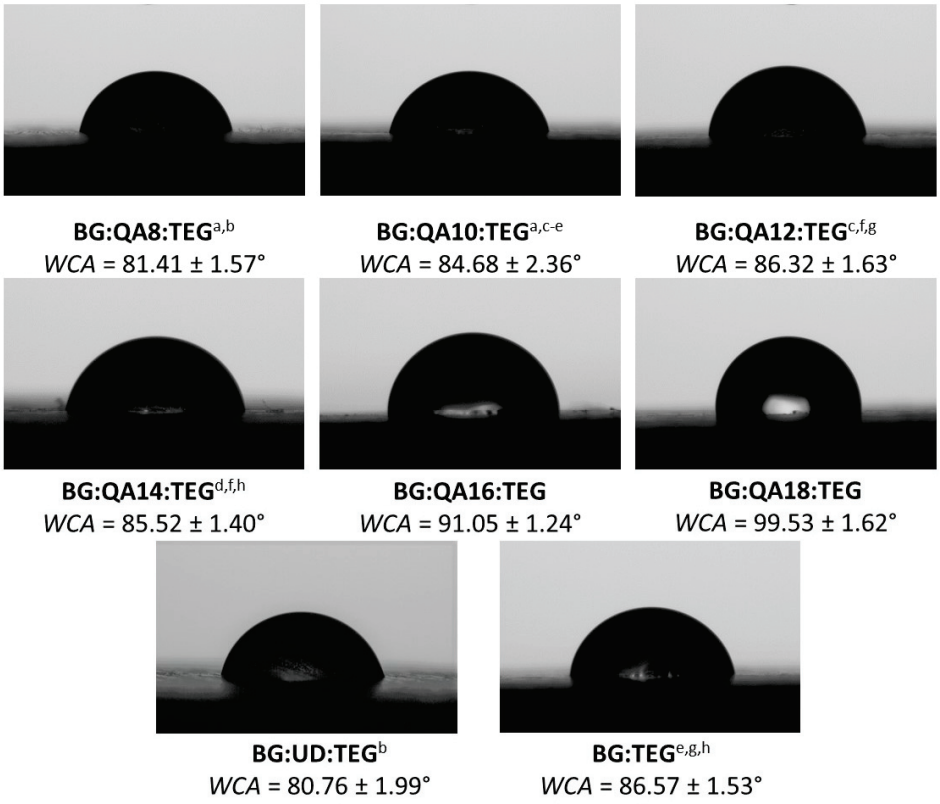


Figure 4. Images captured with the goniometer camera showing droplets of deionized water on the surfaces of the studied copolymers. Lowercase letters indicate statistically insignificant differences ($p > 0.05$, non-parametric Wilcoxon test).

The *WS* and *SL* results are presented in Figure 5a,b, respectively.

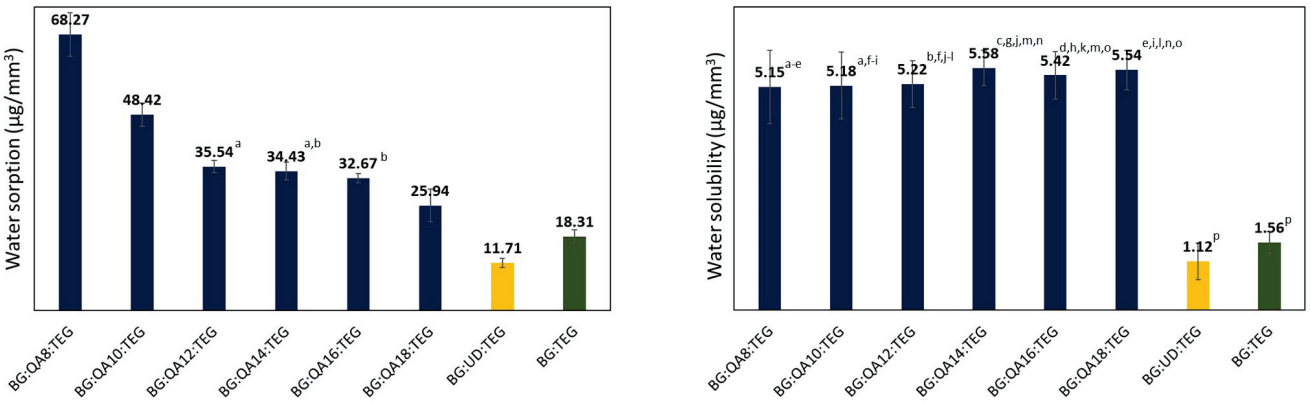


Figure 5. (**a**) Water sorption and (**b**) water solubility of the studied copolymers. Lowercase letters indicate statistically insignificant differences ($p > 0.05$, non-parametric Wilcoxon test).

The *WS* of BG:QAm:TEGs ranged from 25.94 to 68.27 µg/mm^3 and decreased as the *Cm* increased. All BG:QAm:TEGs had higher *WS* ($p \leq 0.05$) than the reference copolymers ($WS_{BG:UD:TEG}$ = 11.71 µg/mm^3, $WS_{BG:TEG}$ = 18.31 µg/mm^3). The *SL* values of BG:QAm:TEGs were similar ($p > 0.05$) and ranged from 5.15 to 5.58 µg/mm^3. Compared with the reference copolymers ($SL_{BG:UD:TEG}$ = 1.12 µg/mm^3, $SL_{BG:TEG}$ = 1.56 µg/mm^3), all of the studied BG:QAm:TEGs had higher *SL* ($p \leq 0.05$).

3. Discussion

In this study, novel dimethacrylate liquid monomer compositions and their corresponding copolymers consisting of 40 wt.% Bis-GMA, 40 wt.% QAUDMA-m, and 20 wt.% TEGDMA (BG:QAm:TEGs) were prepared, and their physicochemical properties were discussed. It is essential to understand these fundamental properties in order to assess the potential applicability of such copolymers in newly designed dental composite matrices; however, they are rarely studied.

The organic matrix in a dental composite is responsible for the proper functioning and longevity of dental restoration materials. This matrix sticks the filler particles together, transfers stress to those particles, and gives shape to the restoration. Therefore, the matrix should have adequate physicochemical properties and should be stable over the entire desired service time and intraoral temperature range.

3.1. Properties of Liquid Monomer Compositions

The *RI* defines the optical properties of a composite matrix, which should provide similar transparency to enamel [33]. All of the prepared BG:QAm:TEGs met the requirements for dental materials, according to which the *RI* should be within the range from 1.46 to 1.55 [34]. These results suggest that all tested BG:QAm:TEGs have suitable aesthetic properties.

The Tg_m of BG:QAm:TEGs ranging from −52.22 to −42.12 °C indicates that all the monomeric systems exist in a liquid state at working temperatures. The Tg_m values were analyzed to assess the molecular mobility of liquid monomers; the higher the Tg_m, the lower the molecular mobility [35]. The lowest Tg_m was recorded for BG:QA18:TEG, which had the highest *Cm*; its Tg_m value was 4.23 °C higher than that of BG:TEG and 7.33 °C lower than that of BG:UD:TEG. In contrast, BG:QA8:TEG, which had the shortest *Cm*, was characterized by the highest Tg_m; its Tg_m value was 14.33 °C and 2.77 °C higher than those of BG:TEG and BG:UD:TEG, respectively. In general, all of the studied BG:QAm:TEGs were characterized by higher Tg_m values than BG:TEG (Figure 2). Relative to the BG:UD:TEG reference, BG:QA8:TEG had a higher Tg_m, BG:QA10:TEG had a similar Tg_m, and the remaining BG:QAm:TEGs had lower Tg_m. These results suggest that the prepared BG:QAm:TEG monomeric systems had lower molecular mobility than BG:TEG. Accordingly, relative to the BG:UD:TEG reference, BG:QA8:TEG showed lower molecular mobility, BG:QA10:TEG showed similar molecular mobility, and the remaining BG:QAm:TEGs showed higher molecular mobility. These distinctions can be explained by differences in the character and the resulting strength of intermolecular interactions between the monomer molecules. Among the two references, BG:UD:TEG had a lower molecular mobility than BG:TEG (i.e., $Tg_{m\ BG:UD:TEG} > Tg_{m\ BG:TEG}$) because of the presence of urethane groups in the UDMA monomer. These moieties are willing to form strong hydrogen bonds with the hydroxyl groups of Bis-GMA, which are also stronger than any other hydrogen bonds occurring in systems comprising Bis-GMA, UDMA, and TEGDMA [36]. Owing to the fact that QAUDMA-m molecules can form strong hydrogen bonds with the hydroxyl groups of Bis-GMA as well as UDMA, all of the BG:QAm:TEG liquid monomer compositions were characterized by lower molecular mobility than BG:TEG. Analysis of the Tg_m values further revealed that the *Cm* affects the Tg_m. Specifically, Tg_m decreased (i.e., molecular mobility increased) as *Cm* increased. This relationship can be attributed to the increasing distance between monomer molecules caused by the increasing *Cm*, which weakens the intermolecular interactions.

3.2. Properties of Copolymers

The polymerization shrinkage (*S*) was determined to be a factor influencing the restoration shrinking [37]. This phenomenon results from double-bond polymerization, whereby the van der Waals forces between the monomer molecules are replaced by much stronger covalent bonds. As a result, the entire system shrinks, and marginal gaps are formed between the tooth filling and adjacent tissue [38]. The higher the *S* value, the greater

the marginal gap; therefore, the *S* should be as low as possible to enable optimal restoration implantation. In addition, the narrow space between the restoration and the tooth tissue creates an environment that is extremely conducive to bacteria colonization, which can lead to secondary caries or gum inflammation [27].

The S_t can be calculated considering that (i) shrinkage results from the polymerization of the methacrylate group and (ii) the reduced molar volume of methacrylate groups is equal to 22.5 cm^3/mol [39]. The S_t values of all studied BG:QAm:TEGs were lower than those of the reference copolymers and decreased as *Cm* increased (Table 2). The highest S_t was recorded for BG:QA8:TEG, which was 15.50% and 23.95% lower than those of BG:TEG and BG:UD:TEG, respectively. In contrast, BG:QA18:TEG had the lowest S_t, which was 23.34% and 31.01% lower than those of BG:TEG and BG:UD:TEG, respectively. Thus, all tested BG:QAm:TEG liquid monomer compositions theoretically shrink less than the reference compositions. In addition, increasing the *Cm* reduced the degree of shrinking because increasing the *MW* of the QAUDMA-m decreased the x_{DB} (Table 1).

In practice, S_t is always higher than S_e because polymerization is never complete. The S_e was calculated according to the d_m (Table 1) and d_p (Table 2). Similar to S_t, the S_e values of BG:QAm:TEGs were lower than those of the reference copolymers owing to the higher *MW* of BG:QAm:TEG monomer systems. In contrast to S_t, the S_e values of BG:QAm:TEGs increased as C_m increased (Table 2). The highest S_e was recorded for BG:QA18:TEG, which was 20.69% and 23.35% lower than those of BG:TEG and BG:UD:TEG, respectively. The BG:QA8:TEG had the lowest S_e, which was 37.05% and 39.16% lower than those of BG:TEG and BG:UD:TEG, respectively. These relationships can be explained based on the *DC*. Table 2 indicates that the *DC* values of BG:QAm:TEGs increased as *Cm* increased; therefore, S_e also increased.

The Tg_p is related to the stiffness of dimethacrylate polymer networks that create the dental composite matrix; the higher the Tg_p, the stiffer the polymer network [40]. The Tg_p values of BG:QAm:TEGs were lower than those of the reference copolymers and increased as *Cm* increased (Figure 3). The reduction in BG:QAm:TEG stiffness in comparison to the reference copolymers can be attributed to the presence of long *N*-alkyl chains that act as pendant groups and loosen the polymer network structure. The lowest Tg_p was recorded for BG:QA8:TEG, which was 19.25 °C and 13.69 °C lower than that of BG:TEG and BG:UD:TEG, respectively. In contrast, BG:QA18:TEG had the highest Tg_p, which was only 10.65 °C and 5.09 °C lower than that of BG:TEG and BG:UD:TEG, respectively. Considering the target applications of these materials (dental restorations), the Tg_p should be higher than the maximum intraoral temperature to ensure that the material will be in a glassy state, with stable mechanical properties over the entire range of working temperatures [28]. For this reason, the Tg_p should not be lower than 40 °C because the temperature of the oral cavity during a fever usually does not exceed 39 °C [41]. Therefore, it can be concluded that the *Cm* did not negatively affect the Tg_p to a significant extent because the Tg_p values of all studied BG:QAm:TEGs were higher than 40 °C.

The *WCA* was measured to assess the hydrophilicity of the copolymer surfaces. Common dental composite fillers [42,43] and dental tissues [44] are both highly hydrophilic. Therefore, the higher the matrix hydrophilicity, the greater its ability to physically bond with the filler and tissue adjacent to the restoration. The hydrophilicity can be expressed according to the *WCA*, i.e., if $WCA < 90°$, the surface is hydrophilic, and if $WCA > 90°$, the surface is hydrophobic [45]. The *WCA* values of the studied BG:QAm:TEGs increased as *Cm* increased. As shown in Figure 4, increasing the *Cm* from C8 to C14 caused only a slight increase in *WCA*, which remained lower than 90°. Therefore, the surfaces of these polymers could be classified as hydrophilic. Further lengthening the *Cm* to C16 and C18 significantly increased the *WCA*, thereby changing the nature of the surface from hydrophilic to hydrophobic. These results suggested that the main factor influencing the *WCA* was the length of the *N*-alkyl substituents. The trend observed for *WCA* is consistent with published reports, which indicate that the hydrophobic character of the alkyl chains increases with their length [46]. The slower increase in *WCA* among BG:QAm:TEGs with

C8 to C14 relative to those with C16 and C18 was attributed to the dominant influence of the hydrophilic quaternary ammonium group [47] in the BG:QAm:TEGs with shorter *Cm*. In the remaining BG:QAm:TEGs, the hydrophobic nature of the *N*-alkyl chains played a key role. The lowest *WCA* was recorded for BG:QA8:TEG, which was 5.96% lower than that of BG:TEG and 0.80% higher than that of BG:UD:TEG. The BG:QA18:TEG was characterized by the highest *WCA*, which was 14.97% and 23.24% higher than that of BG:TEG and BG:UD:TEG, respectively. These results confirm that the surfaces of all studied BG:QAm:TEGs were less hydrophilic than that of BG:UD:TEG. Compared with BG:TEG, only the surfaces of BG:QA16:TEG and BG:QA18:TEG were more hydrophobic, whereas the remaining BG:QAm:TEGs were more hydrophilic.

Dental materials are constantly exposed to moisture, which results in their swelling due to water absorption [30]. This can compensate for the decrease in material volume caused by polymerization [48]. However, excessive *WS* leads to excess swelling, which may deteriorate the restoration's mechanical properties, and in extreme cases, cause mechanical damage [49]. Therefore, according to the standard, ISO 4049, the *WS* of dental materials should not exceed 40 $\mu g/mm^3$ [29]. The *WS* values of the studied BG:QAm:TEGs were higher than those of the reference copolymers and decreased as *Cm* increased. The lowest *WS* was recorded for BG:QA18:TEG, which was 41.67% and 121.52% higher than that of BG:TEG and BG:UD:TEG, respectively. The BG:QA8:TEG was characterized by the highest *WS*, which was 272.86% and 483.01% higher than that of BG:TEG and BG:UD:TEG, respectively. The BG:QAm:TEG copolymers with *Cm* from C12 to C18 met the requirements for dental materials because their *WS* values were lower than 40 $\mu g/mm^3$. The high *WS* of studied BG:QAm:TEGs can be explained based on several factors. The most influential factor is likely the presence of two quaternary ammonium groups in the QAUDMA-m, which are primed to absorb water [20]. Additionally, as the *MW* of QAUDMA-m increased (i.e., with increasing *Cm*), the molar ratio of QAUDMA-m in the BG:QAm:TEG decreased; therefore, the proportion of hydrophilic quaternary ammonium groups in the BG:QAm:TEGs decreased, thereby reducing the *WS*. The reduction in *WS* as the *Cm* increased can be explained by the increasing hydrophobicity of the longer *N*-alkyl chains [46]. It is also possible that the longer *N*-alkyl chains can shield the positively charged quaternary nitrogen ion, thus limiting its ability to absorb water [50].

Leachability of the residual monomers to water (*SL*) is another parameter that should be controlled when considering materials for dental applications. The *SL* should be as low as possible because excessive leaking decreases the restoration's lifetime and promotes the deterioration of its mechanical properties [31]. Therefore, according to the standard, ISO 4049, the *SL* of dental materials should not exceed 7.5 $\mu g/mm^3$ [29]. The *SL* values of the studied BG:QAm:TEGs were higher than those of the reference copolymers and were unaffected by the *Cm*. The lowest *SL* was recorded for BG:QA8:TEG, which was 230.13% and 359.82% higher than that of BG:TEG and BG:UD:TEG, respectively. In contrast, BG:QA14:TEG had the highest *SL*, which was 257.69% and 398.21% higher than that of BG:TEG and BG:UD:TEG, respectively. However, all of the studied BG:QAm:TEGs met the requirements for dental materials because their *SL* values were lower than 7.5 $\mu g/mm^3$. The significantly higher *SL* of BG:QAm:TEGs can be explained by the presence of quaternary ammonium groups in QAUDMA-m. As previously stated, these groups have a high affinity to water; therefore, they can easily migrate through the polymer network with water.

4. Materials and Methods

4.1. Chemicals and Reagents

The QAUDMA-m analogues were synthesized from 2-(methacryloyloxy)ethyl-2-hydroxyethylmethylalkylammonium bromides (QAHAMAs) TMDI (Tokyo Chemical Industry, Tokyo, Japan). The QAHAMAs were synthesized from *N*,*N*-(2-hydroxyethyl)methylaminoethyl methacrylate (HAMA) and alkyl bromides with chain lengths of 8, 10, 12, 14, 16, or 18 carbon atoms (all purchased from Acros Organics, Geel, Belgium). The HAMA was synthesized from methyl methacrylate (MMA; Acros Organics, Geel, Belgium) and

N-methyldiethanolamine (MDEA; Acros Organics, Geel, Belgium). All syntheses were performed following the procedures described in a previous report [23]. Camphorquinone (CQ), 2-dimethylaminoethyl methacrylate (DMAEMA), Bis-GMA, TEGDMA, and UDMA were purchased from Sigma-Aldrich, St. Louis, MO, USA and used as received.

4.2. Sample Preparation

In total, eight compositions of dimethacrylate monomers were prepared, six of which comprised 40 wt.% Bis-GMA, 40 wt.% QAUDMA-m, and 20 wt.% TEGDMA (i.e., BG:QAm:TEGs). For comparison, compositions of 40 wt.% Bis-GMA, 40 wt.% UDMA, 20 wt.% TEGDMA (i.e., BG:UD:TEG), and 60 wt.% Bis-GMA, 40 wt.% TEGDMA (i.e., BG:TEG) were also prepared.

The homogenous mixtures of monomers were enriched with a photoinitiating system comprising 0.4 wt.% CQ (initiator) and 1 wt.% DMAEMA (accelerator). The mixtures were poured into Teflon disc-like molds (diameter × thickness = 15 mm × 1.5 mm), covered with a PET film, and subjected to irradiation with a UV-Vis lamp (Ultra Vitalux 300, Osram, Munich, Germany, 280–780 nm wavelength range, radiation exitance = 2400 mW/cm^2) for 1 h at room temperature.

4.3. Refractive Index

The *RI* of the liquid monomer compositions was determined according to the standard, ISO 489:1999 [51], using a DR 6100T (Krüss Optronic, Germany) refractometer. Briefly, 2 mL of each liquid monomer composition was placed on the refractometer plate, and the measurement was performed at 20 °C.

4.4. Density and Polymerization Shrinkage

The d_m was determined according to the standard, ISO 1675 [52], using a 1 mL pyknometer. The d_p was determined using an analytical balance (XP Balance, Mettler Toledo, Greifensee, Switzerland) equipped with a density determination kit, which operated on the basis of Archimedes' principle.

The S_e was calculated using Equation (1),

$$S_e(\%) = \left(1 - \frac{d_m}{d_p}\right) \times 100 \quad (1)$$

where d_m is the liquid monomer composition density, and d_p is the copolymer density.

The S_t was calculated using Equation (2),

$$S_t(\%) = \left(\frac{f \times \Delta V \times d_m}{MW}\right) \times 100 \quad (2)$$

where f is the methacrylate functionality (f = 2), ΔV is the decrease in molar volume attributable to the polymerization of one mole of methacrylate (ΔV = 22.5 cm^3/mol [39]), d_m is the liquid monomer composition density, and MW is the liquid monomer composition molecular weight.

4.5. Glass Transition Temperature

The Tg_m and Tg_p were determined using a differential scanning calorimeter (DSC 3, Mettler Toledo, Greifensee, Switzerland) according to the standard, ISO 11357-2:2020 [53]. Briefly, 2 mg of sample were placed in a standard aluminum crucible and heated in air within the temperature range from −90 to 200 °C, with a heating rate of 10 K/min.

The Tg was taken as the midpoint of the transition region.

4.6. Water Contact Angle

The *WCA* was determined using an OCA15EC goniometer (Data Physics, Filderstadt, Germany) via the sessile drop method. Briefly, 4 μL of deionized water were dropped on the surface of disc-shaped copolymer samples (diameter × thickness = 15 mm × 1.5 mm).

4.7. Water Sorption and Solubility

The *WS* and *SL* were determined according to the standard, ISO 4049 [29], using disc-shaped copolymer samples (diameter × thickness = 15 mm × 5 mm).

Initially, the samples were dried at 100 °C in a conditioning oven until they reached a constant weight (m_0), which was usually achieved after 72 h. Then, samples were placed in glass vials containing distilled water and stored for seven days at room temperature. Next, samples were removed from the water, blotted dry, and weighted (m_1). Finally, the samples were once again dried to a constant mass (m_2) at 100 °C in a conditioning oven. Sample weights were measured using an analytical balance (XP Balance, Mettler Toledo, Greifensee, Switzerland) with 0.01 mg accuracy.

The *WS* and *SL* were calculated using Equations (3) and (4), respectively,

$$WS\ (\mu g/mm^3) = \frac{m_1 - m_0}{V} \quad (3)$$

$$SL\ (\mu g/mm^3) = \frac{m_0 - m_2}{V} \quad (4)$$

where m_0 is the initial mass of the dried sample, m_1 is the mass of the swollen sample, m_2 is the mass of the dried sample after storage in water, and V is the initial volume of the dried sample.

4.8. Statistical Analysis

The experimental results reported herein were expressed as an average of five measurements and presented with the associated standard deviations (*SD*). The data were analyzed and compared using the non-parametric Wilcoxon test with a significance level (p) of 0.05 using Statistica 13.1 software (TIBCO Software Inc., Palo Alto, CA, USA).

5. Conclusions

The physicochemical properties of six dimethacrylate-based compositions comprising 40 wt.% Bis-GMA, 40 wt.% QAUDMA-m, 20 wt.% TEGDMA, and their corresponding copolymers mainly depended on the length of the *N*-alkyl substituent. It was observed that: (i) Tg_m decreased with increasing *Cm*, whereas the opposite trend was observed for Tg_p, (ii) S_e increased with increasing *Cm*, (iii) hydrophobicity (determined from *WCA*) increased with increasing *Cm*, and (iv) *WS* decreased with increasing *Cm*. Only *RI* and *SL* were unaffected by the *Cm*.

In relation to the properties of the reference copolymers, the following conclusions were drawn. All liquid BG:QAm:TEG monomer compositions had suitable *RI* and Tg_m. Moreover, all studied BG:QAm:TEG copolymers were characterized by low *S* values and Tg_p values higher than 40 °C, suggesting that they would have stable mechanical properties over the working temperature range of dental restorations. The surfaces of two of the BG:QAm:TEGs adopted a hydrophobic character (BG:QA16:TEG and BG:QA18:TEG), whereas the remaining BG:QAm:TEGs had hydrophilic surfaces. All of the studied BG:QAm:TEGs had higher *SL* than the reference copolymers; however, the obtained *SL* values did not exclude their use as matrices of dimethacrylate-based dental composites. Only BG:QA8:TEG and BG:QA10:TEG did not fulfill the *WS* requirements because their *WS* values were higher than 40 $\mu g/mm^3$; this feature would prevent their use as matrices for dental composites.

Author Contributions: Conceptualization, I.M.B.-R. and M.W.C.-P.; methodology, I.M.B.-R. and M.W.C.-P.; Investigation, M.W.C.-P.; Statistical analysis, G.C.; Resources, I.M.B.-R. and M.W.C.-P.; Data curation, M.W.C.-P.; Writing—original draft preparation, I.M.B.-R. and M.W.C.-P.; Writing—review and editing, I.M.B.-R.; Visualization, M.W.C.-P.; Supervision, I.M.B.-R.; Project administration, I.M.B.-R. and M.W.C.-P.; Funding acquisition, I.M.B.-R., M.W.C.-P. and G.C. All authors have read and agreed to the published version of the manuscript.

Funding: This research was funded by the Rector's grant for scientific research and development activities at the Silesian University of Technology, grant number: 32/014/RGJ22/2004.

Institutional Review Board Statement: Not applicable.

Informed Consent Statement: Not applicable.

Data Availability Statement: Data supporting the reported results are available from the authors upon reasonable request.

Conflicts of Interest: The authors declare no conflict of interest. The funders had no role in the design of the study; in the collection, analyses, or interpretation of data; in the writing of the manuscript; or in the decision to publish the results.

References

1. Makvandi, P.; Jamaledin, R.; Jabbari, M.; Nikfarjam, N.; Borzacchiello, A. Antibacterial Quaternary Ammonium Compounds in Dental Materials: A Systematic Review. *Dent. Mater.* **2018**, *34*, 851–867. [CrossRef] [PubMed]
2. Ge, Y.; Wang, S.; Zhou, X.; Wang, H.; Xu, H.H.K.; Cheng, L. The Use of Quaternary Ammonium to Combat Dental Caries. *Materials* **2015**, *8*, 3532–3549. [CrossRef] [PubMed]
3. Kwaśniewska, D.; Chen, Y.L.; Wieczorek, D. Biological Activity of Quaternary Ammonium Salts and Their Derivatives. *Pathogens* **2020**, *9*, 459. [CrossRef] [PubMed]
4. Huang, L.; Yu, F.; Sun, X.; Dong, Y.; Lin, P.T.; Yu, H.H.; Xiao, Y.H.; Chai, Z.G.; Xing, X.D.; Chen, J.H. Antibacterial Activity of a Modified Unfilled Resin Containing a Novel Polymerizable Quaternary Ammonium Salt MAE-HB. *Sci. Rep.* **2016**, *6*, 33858. [CrossRef] [PubMed]
5. Huang, L.; Xiao, Y.H.; Xing, X.D.; Li, F.; Ma, S.; Qi, L.L.; Chen, J.H. Antibacterial Activity and Cytotoxicity of Two Novel Cross-Linking Antibacterial Monomers on Oral Pathogens. *Arch. Oral Biol.* **2011**, *56*, 367–373. [CrossRef] [PubMed]
6. Imazato, S.; Kinomoto, Y.; Tarumi, H.; Ebisu, S.; Tay, F.R. Antibacterial Activity and Bonding Characteristics of an Adhesive Resin Containing Antibacterial Monomer MDPB. *Dent. Mater.* **2003**, *19*, 313–319. [CrossRef]
7. Li, F.; Li, F.; Wu, D.; Ma, S.; Gao, J.; Li, Y.; Xiao, Y.; Chen, J. The Effect of an Antibacterial Monomer on the Antibacterial Activity and Mechanical Properties of a Pit-and-Fissure Sealant. *J. Am. Dent. Assoc.* **2011**, *142*, 184–193. [CrossRef]
8. Xiao, Y.H.; Chen, J.H.; Fang, M.; Xing, X.D.; Wang, H.; Wang, Y.J.; Li, F. Antibacterial Effects of Three Experimental Quaternary Ammonium Salt (QAS) Monomers on Bacteria Associated with Oral Infections. *J. Oral Sci.* **2008**, *50*, 323–327. [CrossRef]
9. Chai, Z.; Li, F.; Fang, M.; Wang, Y.; Ma, S.; Xiao, Y.; Huang, L.; Chen, J. The Bonding Property and Cytotoxicity of a Dental Adhesive Incorporating a New Antibacterial Monomer. *J. Oral Rehabil.* **2011**, *38*, 849–856. [CrossRef]
10. Antonucci, J.M.; Zeiger, D.N.; Tang, K.; Lin-Gibson, S.; Fowler, B.O.; Lin, N.J. Synthesis and Characterization of Dimethacrylates Containing Quaternary Ammonium Functionalities for Dental Applications. *Dent. Mater.* **2012**, *28*, 219–228. [CrossRef]
11. Li, F.; Weir, M.D.; Xu, H.H.K. Effects of Quaternary Ammonium Chain Length on Antibacterial Bonding Agents. *J. Dent. Res.* **2013**, *92*, 932–938. [CrossRef] [PubMed]
12. Lu, G.; Wu, D.; Fu, R. Studies on the Synthesis and Antibacterial Activities of Polymeric Quaternary Ammonium Salts from Dimethylaminoethyl Methacrylate. *React. Funct. Polym.* **2007**, *67*, 355–366. [CrossRef]
13. Manouchehri, F.; Sadeghi, B.; Najafi, F.; Mosslemin, M.H.; Niakan, M. Synthesis and Characterization of Novel Polymerizable Bis-Quaternary Ammonium Dimethacrylate Monomers with Antibacterial Activity as an Efficient Adhesive System for Dental Restoration. *Polym. Bull.* **2019**, *76*, 1295–1315. [CrossRef]
14. Yanwei, Y.; Li, H.; Yan, D.; Hongchen, Z.; Wei, Z.; Jinghao, B.; Jingjing, W.; Yan, L.; Jing, G.; Jihua, C. In Vitro Antibacterial Activity of a Novel Resin-Based Pulp Capping Material Containing the Quaternary Ammonium Salt Mae-Db and Portland Cement. *PLoS ONE* **2014**, *9*, e0112549. [CrossRef]
15. Li, F.; Weir, M.D.; Chen, J.; Xu, H.H.K. Comparison of Quaternary Ammonium-Containing with Nano-Silver-Containing Adhesive in Antibacterial Properties and Cytotoxicity. *Dent. Mater.* **2013**, *29*, 450–461. [CrossRef]
16. Cherchali, F.Z.; Mouzali, M.; Tommasino, J.B.; Decoret, D.; Attik, N.; Aboulleil, H.; Seux, D.; Grosgogeat, B. Effectiveness of the DHMAI Monomer in the Development of an Antibacterial Dental Composite. *Dent. Mater.* **2017**, *33*, 1381–1391. [CrossRef]
17. He, J.; Söderling, E.; Österblad, M.; Vallittu, P.K.; Lassila, L.V.J. Synthesis of Methacrylate Monomers with Antibacterial Effects against S. Mutans. *Molecules* **2011**, *16*, 9755–9763. [CrossRef]
18. Makvandi, P.; Ghaemy, M.; Mohseni, M. Synthesis and Characterization of Photo-Curable Bis-Quaternary Ammonium Dimethacrylate with Antimicrobial Activity for Dental Restoration Materials. *Eur. Polym. J.* **2016**, *74*, 81–90. [CrossRef]

19. Liang, X.; Söderling, E.; Liu, F.; He, J.; Lassila, L.V.J.; Vallittu, P.K. Optimizing the Concentration of Quaternary Ammonium Dimethacrylate Monomer in Bis-GMA/TEGDMA Dental Resin System for Antibacterial Activity and Mechanical Properties. *J. Mater. Sci. Mater. Med.* **2014**, *25*, 1387–1393. [CrossRef]
20. Liang, X.; Huang, Q.; Liu, F.; He, J.; Lin, Z. Synthesis of Novel Antibacterial Monomers (UDMQA) and Their Potential Application in Dental Resin. *J. Appl. Polym. Sci.* **2013**, *129*, 3373–3381. [CrossRef]
21. Huang, Q.; Lin, Z.; Liang, X.; Liu, F.; He, J. Preparation and Characterization of Antibacterial Dental Resin with UDMQA-12. *Adv. Polym. Technol.* **2014**, *33*, 21395. [CrossRef]
22. Huang, Q.T.; He, J.W.; Lin, Z.M.; Liu, F.; Lassila, L.V.J.; Vallittu, P.K. Physical and Chemical Properties of an Antimicrobial Bis-GMA Free Dental Resin with Quaternary Ammonium Dimethacrylate Monomer. *J. Mech. Behav. Biomed. Mater.* **2016**, *56*, 68–76. [CrossRef]
23. Chrószcz, M.W.; Barszczewska-Rybarek, I.M. Synthesis and Characterization of Novel Quaternary Ammonium Urethane-Dimethacrylate Monomers—A Pilot Study. *Int. J. Mol. Sci.* **2021**, *22*, 8842. [CrossRef] [PubMed]
24. Chrószcz, M.W.; Barszczewska-Rybarek, I.M.; Kazek-K, A. Novel Antibacterial Copolymers Based on Quaternary Ammonium Urethane-Dimethacrylate Analogues and Triethylene Glycol Dimethacrylate. *Int. J. Mol. Sci.* **2022**, *23*, 4954. [CrossRef] [PubMed]
25. Chrószcz-Porębska, M.W.; Barszczewska-Rybarek, I.M.; Chladek, G. Characterization of the Mechanical Properties, Water Sorption, and Solubility of Antibacterial Copolymers of Quaternary Ammonium Urethane-Dimethacrylates and Triethylene Glycol Dimethacrylate. *Materials* **2022**, *15*, 5530. [CrossRef] [PubMed]
26. Alshali, R.Z.; Silikas, N.; Satterthwaite, J.D. Degree of conversion of bulk-fill compared to conventional resin-composites at two time intervals. *Dent. Mater.* **2013**, *29*, e213–e217. [CrossRef]
27. Ensaff, H.; O'Doherty, D.M.; Jacobsen, P.H. Polymerization Shrinkage of Dental Composite Resins. *Proc. Inst. Mech. Eng. Part H J. Eng. Med.* **2001**, *215*, 367–375. [CrossRef]
28. Moraes, J.C.S.; Sostena, M.M.D.S.; Grandini, C.R. The Glass Transition Temperature in Dental Composites. In *Metal, Ceramic and Polymeric Composites for Various Uses*; Cuppoletti, J., Ed.; IntechOpen: London, UK, 2011. [CrossRef]
29. *ISO 4049:2019*; Dentistry—Polymer Based Restorative Materials. International Standard Organisation: London, UK, 2019.
30. Bociong, K.; Szczesio, A.; Sokolowski, K.; Domarecka, M.; Sokolowski, J.; Krasowski, M.; Lukomska-Szymanska, M. The Influence of Water Sorption of Dental Light-Cured Composites on Shrinkage Stress. *Materials* **2017**, *10*, 1142. [CrossRef]
31. Kumar, N.; Sangi, L. Water Sorption, Solubility, and Resultant Change in Strength among Three Resin-Based Dental Composites. *J. Investig. Clin. Dent.* **2014**, *5*, 144–150. [CrossRef]
32. Chrószcz-Porębska, M.W.; Barszczewska-Rybarek, I.M.; Kazek-Kęsik, A.; Chladek, G. Novel mechanically strong and antibacterial dimethacrylate copolymers based on quaternary ammonium urethane-dimethacrylate analogues. *Dent. Mater.* 2022, *submitted*.
33. Meng, Z.; Yao, X.S.; Yao, H.; Liang, Y.; Liu, T.; Li, Y.; Wang, G.; Lan, S. Measurement of the Refractive Index of Human Teeth by Optical Coherence Tomography. *J. Biomed. Opt.* **2009**, *14*, 034010. [CrossRef]
34. Manappallil, J.J. *Basic Dental Materials*, 4th ed.; Jaypee Brothers Medical Publishers: New Delhi, India, 2015.
35. Véchambre, C.; Buléon, A.; Chaunier, L.; Gauthier, C.; Lourdin, D. Understanding the Mechanisms Involved in Shape Memory Starch: Macromolecular Orientation, Stress Recovery and Molecular Mobility. *Macromolecules* **2011**, *44*, 9384–9389. [CrossRef]
36. Barszczewska-Rybarek, I.M. Structure–Property Relationships in Dimethacrylate Networks Based on Bis-GMA, UDMA and TEGDMA. *Dent. Mater.* **2009**, *25*, 1082–1089. [CrossRef] [PubMed]
37. Schricker, S.R. Composite Resin Polymerization and Relevant Parameters. In *Orthodontic Applications of Biomaterials*; Woodhead Publishing: Sawston, UK, 2017; pp. 153–170. [CrossRef]
38. Soares, C.J.; Faria-E-Silva, A.L.; de Paula Rodrigues, M.; Fernandes Vilela, A.B.; Pfeifer, C.S.; Tantbirojn, D.; Versluis, A. Polymerization Shrinkage Stress of Composite Resins and Resin Cements—What Do We Need to Know? *Braz. Oral Res.* **2017**, *31*, 49–63. [CrossRef] [PubMed]
39. Watts, D.C. Adhesives and Sealants. In *Biomaterials Science: An Introduction to Materials*, 3rd ed.; Ratner, B., Hoffman, A., Schoen, F., Lemons, J., Eds.; Elsevier Inc.: Amsterdam, The Netherlands, 2013; pp. 889–904.
40. Wang, R.-M.; Zheng, S.-R.; Zheng, Y.-P. Matrix Materials. In *Polymer Matrix Composites and Technology*; Woodhead Publishing: Sawston, UK, 2011; pp. 101–548. [CrossRef]
41. Walker, H.K.; Hall, W.D.; Hurst, J.W. *Clinical Methods: The History, Hysical, and Laboratory Examinations*, 3rd ed.; Butterworths: Boston, MA, USA, 1990.
42. Pratap, B.; Gupta, R.K.; Bhardwaj, B.; Nag, M. Resin Based Restorative Dental Materials: Characteristics and Future Perspectives. *Jpn. Dent. Sci. Rev.* **2019**, *55*, 126–138. [CrossRef]
43. Farooq, I.; Ali, S.; Al-Saleh, S.; Alhamdan, E.M.; Alrefeai, M.H.; Abduljabbar, T.; Vohra, F. Synergistic Effect of Bioactive Inorganic Fillers in Enhancing Properties of Dentin Adhesives—A Review. *Polymers* **2021**, *13*, 2169. [CrossRef] [PubMed]
44. Ayar, M.K. A Review of Ethanol Wet-Bonding: Principles and Techniques. *Eur. J. Dent.* **2016**, *10*, 155–159. [CrossRef]
45. Purkait, M.K.; Sinha, M.K.; Mondal, P.; Singh, R. Photoresponsive Membranes. *Interface Sci. Technol.* **2018**, *25*, 115–144. [CrossRef]
46. Gao, Y.; Duan, L.; Guan, S.; Gao, G.; Cheng, Y.; Ren, X.; Wang, Y. The Effect of Hydrophobic Alkyl Chain Length on the Mechanical Properties of Latex Particle Hydrogels. *RSC Adv.* **2017**, *7*, 44673–44679. [CrossRef]
47. Kowalczyk, I.; Pakiet, M.; Szulc, A.; Koziróg, A. Antimicrobial Activity of Gemini Surfactants with Azapolymethylene Spacer. *Molecules* **2020**, *25*, 4054. [CrossRef]

48. Feilzer, A.J.; Kakaboura, A.I.; de Gee, A.J.; Davidson, C.L. The Influence of Water Sorption on the Development of Setting Shrinkage Stress in Traditional and Resin-Modified Glass Ionomer Cements. *Dent. Mater.* **1995**, *11*, 186–190. [CrossRef]
49. Al-Bader, R.M.; Ziadan, K.M.; Al-Ajely, M.S. Water Adsorption Characteristics of New Dental Composites. *Int. J. Med. Res. Health Sci.* **2015**, *4*, 281. [CrossRef]
50. Yudovin-Farber, I.; Beyth, N.; Weiss, E.I.; Domb, A.J. Antibacterial Effect of Composite Resins Containing Quaternary Ammonium Polyethyleneimine Nanoparticles. *J. Nanoparticle Res.* **2010**, *12*, 591–603. [CrossRef]
51. *ISO 489:1999*; Plastics—Determination of Refractive Index. International Standard Organisation: London, UK, 1999.
52. *ISO 1675:2002*; Plastics—Liquid Resins—Determination of Density by the Pyknometer Method. International Standard Organisation: London, UK, 2002.
53. *ISO 11357-2:2020*; Plastics—Differential Scanning Calorimetry (DSC)—Part 2: Determination of Glass Transition Temperature and Step Height. International Standard Organisation: London, UK, 2020.

Disclaimer/Publisher's Note: The statements, opinions and data contained in all publications are solely those of the individual author(s) and contributor(s) and not of MDPI and/or the editor(s). MDPI and/or the editor(s) disclaim responsibility for any injury to people or property resulting from any ideas, methods, instructions or products referred to in the content.

International Journal of
Molecular Sciences

MDPI

Article

Biomimetic Nanopillar Silicon Surfaces Rupture Fungal Spores

Denver P. Linklater [1,2,†], Phuc H. Le [1,2,†], Arturo Aburto-Medina [1,2], Russell J. Crawford [1], Shane Maclaughlin [2,3], Saulius Juodkazis [4] and Elena P. Ivanova [1,2,*]

[1] School of Science, STEM College, RMIT University, Melbourne, VIC 3000, Australia
[2] ARC Research Hub for Australian Steel Manufacturing, Wollongong, NSW 2505, Australia
[3] BlueScope Steel Ltd., Port Kembla, Wollongong, NSW 2505, Australia
[4] Optical Science Centre, Swinburne University of Technology, Hawthorn, Melbourne, VIC 3122, Australia
* Correspondence: elena.ivanova@rmit.edu.au
† These authors contributed equally to this work.

Abstract: The mechano-bactericidal action of nanostructured surfaces is well-documented; however, synthetic nanostructured surfaces have not yet been explored for their antifungal properties toward filamentous fungal species. In this study, we developed a biomimetic nanostructured surface inspired by dragonfly wings. A high-aspect-ratio nanopillar topography was created on silicon (nano-Si) surfaces using inductively coupled plasma reactive ion etching (ICP RIE). To mimic the superhydrophobic nature of insect wings, the nano-Si was further functionalised with trichloro(1H,1H,2H,2H-perfluorooctyl)silane (PFTS). The viability of *Aspergillus brasiliensis* spores, in contact with either hydrophobic or hydrophilic nano-Si surfaces, was determined using a combination of standard microbiological assays, confocal laser scanning microscopy (CLSM), and focused ion beam scanning electron microscopy (FIB-SEM). Results indicated the breakdown of the fungal spore membrane upon contact with the hydrophilic nano-Si surfaces. By contrast, hydrophobised nano-Si surfaces prevented the initial attachment of the fungal conidia. Hydrophilic nano-Si surfaces exhibited both antifungal and fungicidal properties toward attached *A. brasiliensis* spores via a 4-fold reduction of attached spores and approximately 9-fold reduction of viable conidia from initial solution after 24 h compared to their planar Si counterparts. Thus, we reveal, for the first time, the physical rupturing of attaching fungal spores by biomimetic hydrophilic nanostructured surfaces.

Keywords: antifungal surface; *Aspergillus brasiliensis*; nanopillar surface; biomimetic surface

Citation: Linklater, D.P.; Le, P.H.; Aburto-Medina, A.; Crawford, R.J.; Maclaughlin, S.; Juodkazis, S.; Ivanova, E.P. Biomimetic Nanopillar Silicon Surfaces Rupture Fungal Spores. *Int. J. Mol. Sci.* **2023**, *24*, 1298. https://doi.org/10.3390/ijms24021298

Academic Editor: Lia Rimondini

Received: 5 December 2022
Revised: 17 December 2022
Accepted: 28 December 2022
Published: 9 January 2023

Copyright: © 2023 by the authors. Licensee MDPI, Basel, Switzerland. This article is an open access article distributed under the terms and conditions of the Creative Commons Attribution (CC BY) license (https://creativecommons.org/licenses/by/4.0/).

1. Introduction

Synthetic nanomaterials with high-aspect-ratio nanoprotrusions that resemble the epicuticle of insect wings like dragonfly and damselfly exhibit broad spectrum antibacterial properties [1–4] The bactericidal activity of nanopillar surfaces is characterised by mechanical lysis of the bacterial cell membrane as the cell contacts the surface [1–4]. This activity also extends to bacterial endospores [4]. Nevertheless, the interactions between biomimetic nanopillar surfaces and filamentous fungal conidia have not yet been characterised. While bacteria demonstrate significant variation in their size, shape, and composition of the cell wall, filamentous fungal spores exhibit even greater diversity. The size of filamentous fungal spores can range from a few micron to tens-of-micron in diameter [5]. Furthermore, spores are characterised by a resilient protective layer on their cell wall that makes them impervious to multiple environmental stressors such as salts, UV, temperature, antifungal molecules, and even physical disruption [6,7]. Therefore, filamentous fungal spores would require a greater deformational stress to be susceptible to mechanical lysis or rupture.

Fungi are a diverse group of eukaryotic organisms that are widespread within nature. Filamentous fungal species such as *Aspergillus* spp. including *A. fumigatus*, *A. terreus*, *A niger*, *A. brasisiensis* and *A. flavus* have been identified as opportunistic pathogens that pose a significant health risk to immunocompromised individuals [8]. These fungi can cause

various diseases, and some have been detected in the water of dental equipment. This environment offers suitable conditions for the emergence of fungal biofilms [9]. Antimicrobial resistance (azole resistance) in *A. fumigatus* has been reported to cause invasive infections with high mortality rates [10,11]. This is particularly concerning as the incidences of an invasive human fungal infection often result in a mortality rate greater than 50% [12]. *Aspergillus* spp. have been implicated in aspergillosis of the oral cavity after tooth extraction or endodontic treatment [13–15]. Water flow through the tubes of dental units is known to contain multiple microorganisms [16]. This water is a potential source of microbial contamination and a potential threat to the patients' and professionals' health. The American Dental Association has established that the bacterial load in the water of dental units must not exceed 200 CFU/mL, but the limit of fungal load has not been recorded [17]. During endodontic treatment, direct contact with contaminated water may cause various respiratory infections, allergies, and infect wounds on the mucosal membranes [18]. Oral aspergillosis is rare, and mandibular aspergillus osteomyelitis is even rarer; however, the outcomes are severe and often involve invasive, multiple surgical debridement procedures and resolution with dental implants [19]. Furthermore, *Aspergillus* spp. are known to grow and proliferate on various bone substitutes [20], implicating the susceptibility of dental biomaterials to contamination by environmental filamentous fungi that are also opportunistic pathogens. In addition, the presence of zinc oxide endodontic sealers into the maxillary sinus are known to increase the risk of filamentous fungal infection in immunocompromised individuals [21]. Thus, fungal contamination needs to be controlled on the surface of dental biomaterials for the prevention of invasive fungal infections in both immunocompromised and immunocompetent individuals.

Early research toward the development of antifungal coatings that could resist filamentous fungi colonisation of surfaces involved the creation of nano-composite coatings consisting of embedded nanosized metal oxide particles such as zinc oxide and copper oxide [22–24]. Some other approaches include the surface immobilisation of biocides or functionalised nanoparticles [25–29], the addition of photocatalytic materials, and the physical-chemical modification of the surface [30,31] which we recently reviewed [32].

Surface nanotexturing may present a unique opportunity to develop surfaces that exhibit robust and long-lasting antifungal activity. We recently showed that black damselfly *Calopteryx haemorrhoidalis* wings can prevent the attachment of *A. brasiliensis* spores [33]. Like other Odonates (i.e., damselflies and dragonflies), *C. haemorrhoidalis* wings possess a dense layer of crystalline wax over the surface that creates a characteristic dense nanopillar topography. The combination of wax and surface nanoprotrusions facilitate the entrapment of a layer of air that effectively repels attaching conidia [34–36].

In this work, we studied the cell-surface interactions between filamentous fungi *A. brasiliensis* spores and nanotextured silicon surfaces. Herein, the mechanisms of filamentous fungi spore adhesion to nanostructured surfaces were studied by investigating the role of surface wettability on the resulting degree of attachment using a combination of electron and fluorescent microscopy techniques. The cell-surface interface was characterised using FIB milling to allow visualisation of the nanopillar-fungal spore bio-interface.

2. Results

2.1. Surface Characterisation of Nano-Si Surfaces

The nanopattern present on damselfly wings was replicated on silicon surfaces using reactive ion etching method to create a substrate that contained dense high aspect ratio nanoprotrusions, herein referred to as nano-Si (Figure 1A) [4]. Nano-Si surfaces were further modified via silanisation to produce hydrophobic surfaces (nSi-H). Hydrophilic planar silicon (Si) and silanised planer silicon (Si-H) surfaces were used as controls.

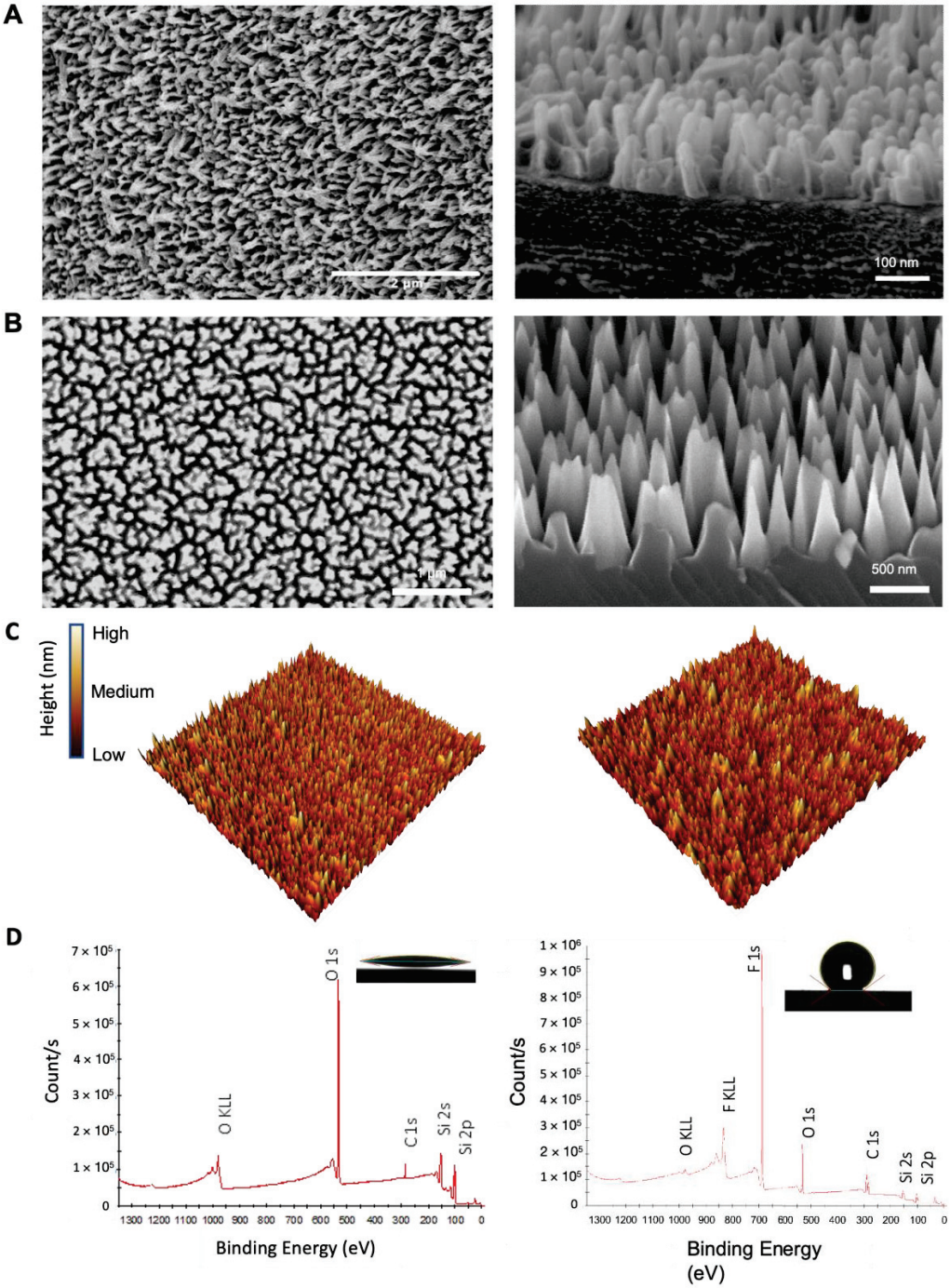


Figure 1. Surface topographic analysis of nSi-H and nSi surfaces, which were synthesised to mimic the nanotopography of damselfly wings. (**A**) The representative image of a damselfly wing and representative SEM micrographs of nanopillars on damselfly wings, included for comparison. Dragonfly wing nanopillars are approximately 250 nm in height with interpillar spacing of 200 nm. (**B**) Representative SEM micrograph of nano-Si surfaces, including top-view and titled micrographs. Pillars were recorded to have a height of 796 ± 96 nm, and a tip-tip separation of 182 nm. (**C**) Corresponding 3D visualisation of AFM micrographs of the surface topography of nSi and nSi-H. (**D**) XPS survey scan results for surface chemical composition and wettability of nSi (left) and nSi-H (right).

The nanotopography of damselfly and dragonfly wings has been widely recognised to possess broad-spectrum antimicrobial activity in that the nanopillars can not only rupture and kill attaching bacteria, but also have the ability to repel fungal conidia, preventing their attachment [2,4,33,37,38]. The efficacy of the mechano-bactericidal action of the wing nanotopography is governed by a few factors; the nanopillar pattern, i.e., height, spacing (density) and flexural rigidity of the nanopillars, and the cell surface characteristics of the attaching microbe [2,3,39]. The nanopillar height must be such that the adsorbing cell wall cannot reach the base of the nanoprotrusion before the elastic limit of the cell membrane is reached [2]. Thus, for microbes in the order of 5 μm diameter, such as filamentous fungi conidia, taller pillars were hypothesised to have the capacity to induce cell lysis. The height of the nanopillars was controlled according to the period of the etching time, with a greater etching time resulting in the development of taller pillars [37,40]. SEM imaging was used to characterise the surface nanoarchitecture, including height, pillar-to-pillar spacing, and pillar density. Plasma etching of silicon surfaces for 45 min resulted in fabrication of nanostructured surfaces that possessed high aspect ratio nanopillars of approximately 800 nm in height with interpillar spacing of approximately 200 nm, and a pillar density of approximately 5.5 μm^{-2}, as determined from SEM imaging (Figure 1B). The typical random distribution and pyramidal shape of nano-Si nanopillars is shown in the SEM and AFM micrographs presented in Figure 1. The as-fabricated nano-Si surfaces were highly wettable, exhibiting a water contact angle (WCA) of ~10° (Figure 1D). All surfaces had a uniform black appearance due to the tapered Si pillars that render a gradual refractive index change [41], hence, achieving anti-reflectivity. To simulate the superhydrophobic properties of insect wings, the nano-Si surfaces were coated with an organofunctional fluorosilane [37,42]. A hydrophobic self-assembled monolayer of silane was achieved, as observed by a water contact angle (WCA) of ~160° and confirmed by XPS (Figure 1D). No change in surface topography was identified, as confirmed through AFM characterisation (Figures 1C and S1). Further AFM analysis and surface roughness parameters of newly fabricated surfaces are included in Table 1. AFM surface roughness values report lower S_{max} values that what is estimated from SEM images due to the highly dense nature of the pattern which restricts the ability to scan the entirety of the high aspect ratio pillar.

Table 1. Surface roughness parameters as determined by AFM analysis.

Surface Roughness Parameters	S_a	S_q	S_{max}
nSi-H	29.16 ± 0.42	36.97 ± 0.59	323.02 ± 10.71
Si-H	7.60 ± 2.50	9.64 ± 3.10	86.94 ± 32.75
nSi	35.03 ± 0.59	44.12 ± 0.56	380.18 ± 32.75
Si	14.25 ± 4.54	17.58 ± 4.31	130.52 ± 34.80

2.2. Interfacial Interactions of A. brasiliensis Spores with Hydrophilic and Hydrophobic Nano-Si Surfaces

The spore-substratum interface between *A. brasiliensis* spores and the nanopillar substratum were investigated via FIB milling and SEM (Figure 2A). Analysis of tilted SEM micrographs of spores on nSi-H (hydrophobic) surfaces revealed that the spores retained their rounded morphology, and in most cases, the spore body was observed to be 'hovering' above the surface. Cross-sections of the spore-nanopillar interface revealed that, indeed, the spore was not in contact with the surface. Further examination revealed that the spore coat and inner membrane were well-preserved. By contrast, the spore morphology after attachment to the nSi (hydrophilic) surfaces appears compromised (Figure 2A), as seen in the tilted SEM images. The FIB cross-sections show the nSi nanopillars were in direct contact with the spore (indicated by the yellow arrows). Sequential milling of the spore-nanopillar interface showed there was obvious damage sustained by the spore coat, together with a loss of membrane integrity evidenced by the lack of defined continuous inner and outer membranes and the incidence of airspace, or holes, between the cell wall and the inner membrane that might point to a loss of turgor pressure and the leakage

of the cytosolic content (Figure 3). Multiple points of nanopillar contact, and insertion, are obvious in the SEM micrographs. Thus, we assume that the spore has been lysed by increased contact between the nanopillar surface and spore coat. The super-wetting state of the nano-Si surface would facilitate enhanced contact between the spore coat and nanopillar surface [43]. Micrographs of consecutive milling through the spore-substratum interface have been included in Supplementary Figures S2 and S3.

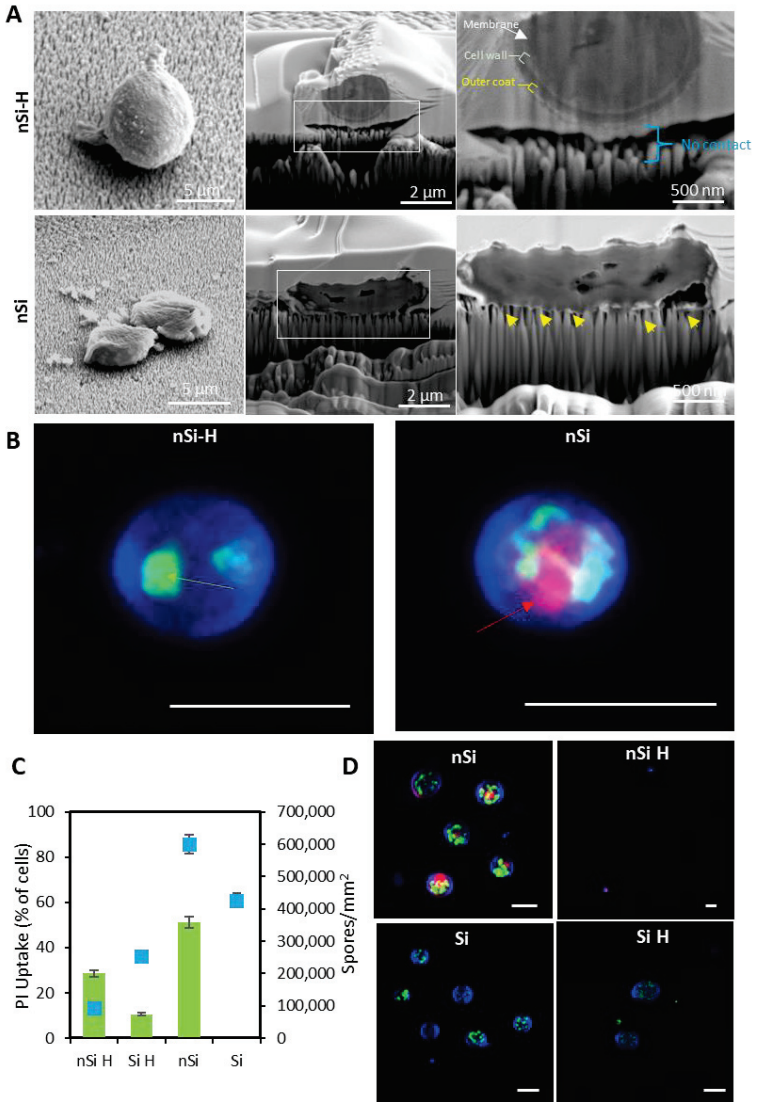


Figure 2. The interaction of *A. brasiliensis* spores with the nSi-H and nSi surfaces. (**A**) Representative FIB-SEM micrographs of *A. brasiliensis* spores present on the nSi-H and nSi substrates. The nanopillars of the hydrophilic nSi surface pierced the cell wall of the spores (yellow arrow), whereas the spores do not appear in direct contact with superhydrophobic surfaces (cyan bracket). Spore-surface interface is highlighted in white frames. (**B**) Representative high-resolution CLSM micrographs showing the cell membrane status of *A. brasiliensis* spores when attached onto nSi and Si surfaces, as determined by PI uptake. The conidia were stained with Calcofluor white (blue colour), which binds to cellulose and chitin in fungal cell walls; Syto9 (green colour), which is a membrane-permeable nucleic acid stain (green arrow); and propidium iodide (red colour), which also stains nucleic acids but is only membrane-permeable to damaged cells (red arrow). Scale bars are 5 µm. (**C**) Graph showing the percentage of spores that display internalised PI at day 1 incubation on studied surfaces (green colour) versus the number of spores observed per mm^2 (blue colour). Error bars are 1 standard deviation. (**D**) CLSM micrographs of PI uptake in *A. brasiliensis* spores. Scale bars are 5 µm.

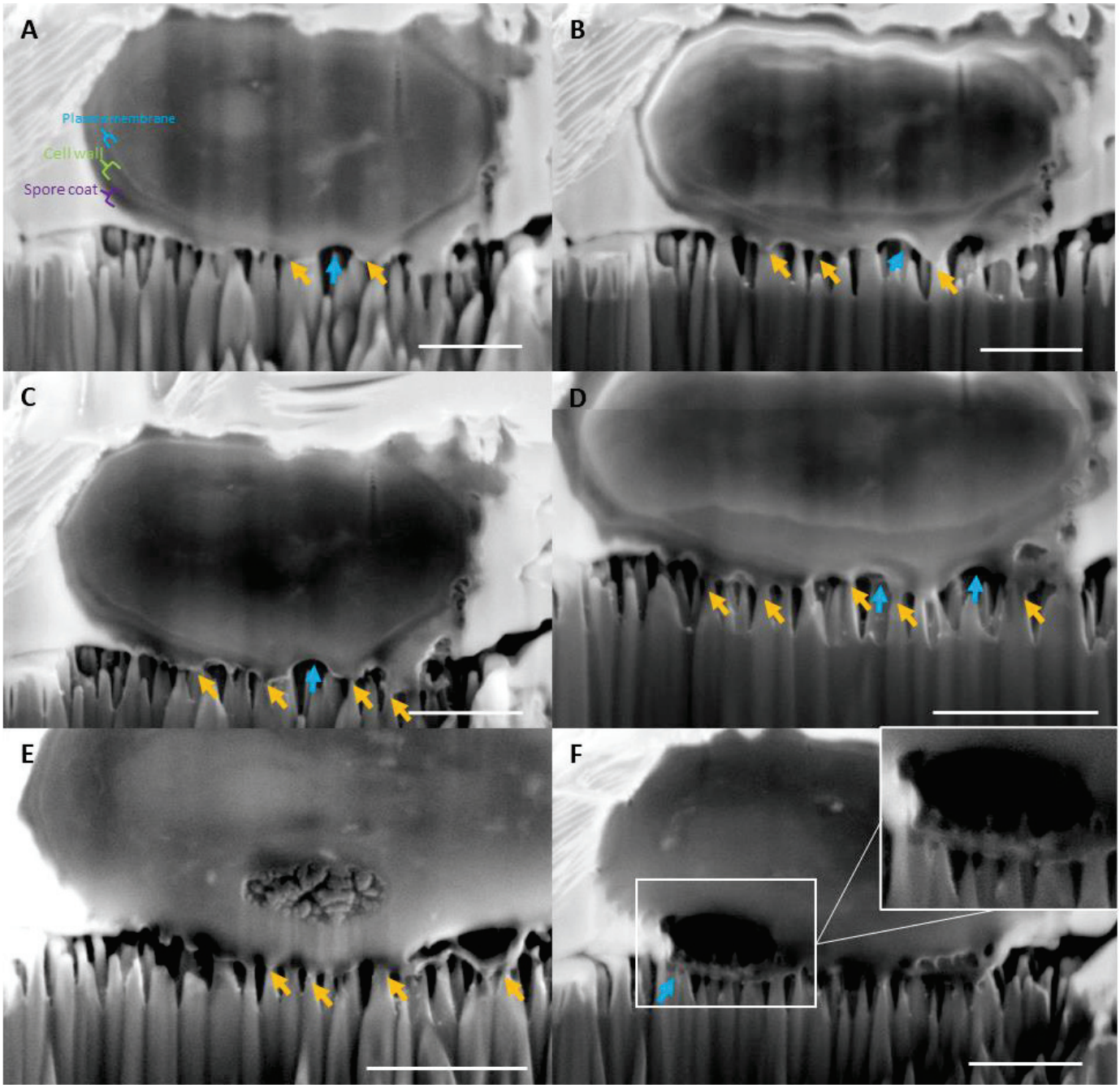


Figure 3. Sequential FIB milling of the spore-nanopillar interface on hydrophilic nSi surfaces. SEM micrographs show the adhesion of the spore coat to the nanopillars (orange arrows indicate direct comtact). (**A**) Breakage of the cell wall and inner plasma membrane is evident at the points between spore coat adsorption to the substratum surface (blue arrows indicate the lack of contact). (**B**–**E**) Consecutive micrographs show an increase in the number of nanopillars in contact with the cell and consequently greater deterioration of the cell wall and plasma membrane. (**F**) Cell lysis is confirmed by the occurrence of large holes in the body of the cell. Nanopillars are observed inside the cell. Scale bars are 1 µm.

To confirm whether the interaction between the *A. brasiliensis* spores and hydrophilic nSi surface led to membrane rupture, monitoring of propidium iodide (PI) uptake by fluorescence microscopy was used to confirm cell membrane permeabilisation (Figure 2B,D). PI can only be taken into cells that have become permeable through physical damage, or otherwise [44]. Spores were also counterstained with calcofluor white (spore coat) and Syto 9® (nucleic acids). PI uptake was observed in approximately 55% of those non-germinated (non-germinated spore size confirmed to be 5 μm, Figure S7) spores in contact with the hydrophilic nanostructured surfaces (Figure 2C). By contrast, those spores attached onto the planar Si control surfaces did not exhibit PI uptake (Figures 2C,D and S6). As PI is a non-membrane permeable nucleic acid stain [45], evidence of PI uptake via red fluoresence observed under confocal microscopy indicated that the nano-Si nanopillars were capable of rupturing both the spore coating and the inner plasma membrane of the spores, as observed in the FIB-SEM micrographs.

2.3. Assessment of the Structural Integrity, Morphology and Viability of the Fungal Spores during Interactions with Nano-Si Surfaces

To study changes to the structural integrity of spores when they encounter the nano-Si surfaces, an in-depth analysis of spore morphology was carried out using a combination of electron and fluorescence microscopy (Figure 4). Analysis of the resulting SEM images revealed that, over a 24 h incubation period under immersed conditions, the *A. brasiliensis* spores maintained their typical spherical morphology on nSi-H, Si-H and Si surfaces similar to that of spores as collected from the *A. brasiliensis* conidiophores after growth on potato dextrose agar (PDA) plates (Figures 4D and S7). However, on hydrophilic nSi surfaces, an altered spore morphology was clearly evident in the SEM micrographs (Figure 4D, false coloured red). The spores appear lysed, having lost their structural integrity. Similarly, CLSM imaging highlighted that the uniformity of the coat for spores attached to nSi surfaces was also disrupted (Figure 4D, red arrow). Analysis of the morphology of *A. brasiliensis* spores on nano-Si and control surfaces after a 3-day incubation period also highlights that those spores attached on nSi surfaces appear to have deteriorated structural integrity (yellow arrows).

Fluorescence microscopy was used to directly analyse the attachment of *A. brasiliensis* spores to the nano-Si substratum (Figure S4). The number of spores attached to the nano-Si surface was found to be approximately 140.2 ± 73.1 mm^{-2}. These values were approximately 5× lower than the number of spores attached to the planar control Si surface (713.3 ± 267.0 mm^{-2}) after the same 24 h incubation period (** $p < 0.01$) (Figure 4A). The same trend in attachment patterns were observed after 3 days of incubation, indicating that the fungal spores had a reduced ability to settle and germinate on the nano-Si surfaces (Figure S5).

The metabolic activity of attached spores was also determined using an Alamarblue™ cell viability assay, which measures the reduction of resazurin to resofurin by the cell (Figure 4B). Any decrease in the reduction of resazurin may indicate a disturbance in the cellular metabolism [46]. Specifically, the data demonstrated that the spore metabolic activity of conidia attached to the nSi surface was markedly reduced after a 3-day incubation period. These results are consistent with our investigation of the spore-nanopillar interface using FIB-SEM that *A. brasiliensis* spores may be ruptured on nSi but not on nSi-H surfaces. Thus, the nSi surfaces may prevent the spore germination and proliferation through physical rupturing of attached spores, whereas on the planar control Si surfaces, the *A. brasiliensis* spores remained metabolically active and showed a marked increase in their respiratory activity.

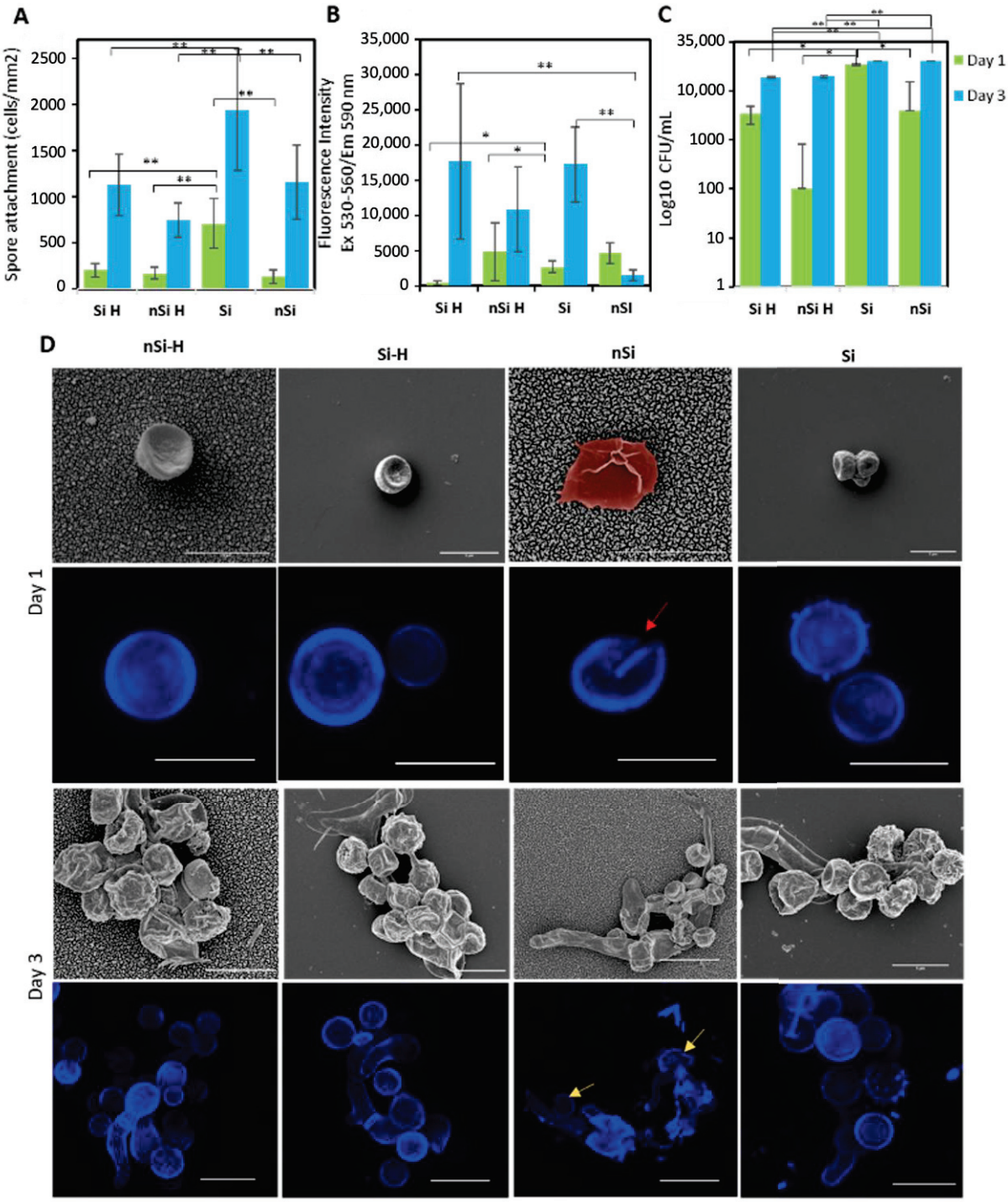


Figure 4. The density and morphology of *A. brasiliensis* spores when attached onto nano-Si and Si surfaces after a 24 and 72 h incubation period. (**A**) Attachment density of *A. brasiliensis* on substrata studied over a 1-day and 3-day incubation period. The number of attached spores was calculated using CLSM images (n = 12). (**B**) Quantification of metabolic assay measured by Alamarblue^{TM} assay of attached *A. brasilensis* spores on Si, Si-H, nSi and nSi-H surfaces after a 1- and 3-day incubation period. (**C**) The colony-forming units derived from attached spores on studies surfaces (n = 3). Statistically significant differences were determined using a one-way ANOVA and Tukey's multiple comparisons post hoc test (* $p < 0.05$; ** $p < 0.01$). (**D**) Representative SEM and CLSM micrographs showing the morphology of *A. brasiliensis* spores attached to nSi and Si surfaces. The cell wall of the fungal spores was stained with Calcofluor white (blue colour). The red and yellow arrows indicate the disruption of fungal spore coat. Scale bars on SEM and CLSM micrographs are 5 μm.

A direct plate counting technique was used to assess the number of *viable* spores [47] retrieved from the nano-Si surfaces, and this was compared to that obtained from spores retrieved from the planar Si surface (Figure 4C). The hydrophilic nSi surface exhibited a reduction in the number of viable conidia (4.0×10^3 CFU mL^{-1}), in comparison to Si surfaces (3.5×10^4 CFU mL^{-1}), corresponding to a ~9-fold reduction of viable conidia after 24 h interaction with the nanopillar surfaces. By contrast, there were only 1.0×10^2 CFU mL^{-1} spores retrieved from the nSi-H surfaces, which is ~35× less than retrieved from Si-H surfaces. By day 3, the number of viable spores retrieved from both nanostructured surfaces were similar to their planar counterparts. These data corroborate the (initial) lesser attachment of *A. brasiliensis* spores to hydrophobised surfaces, as directly confirmed by fluorescence microscopy.

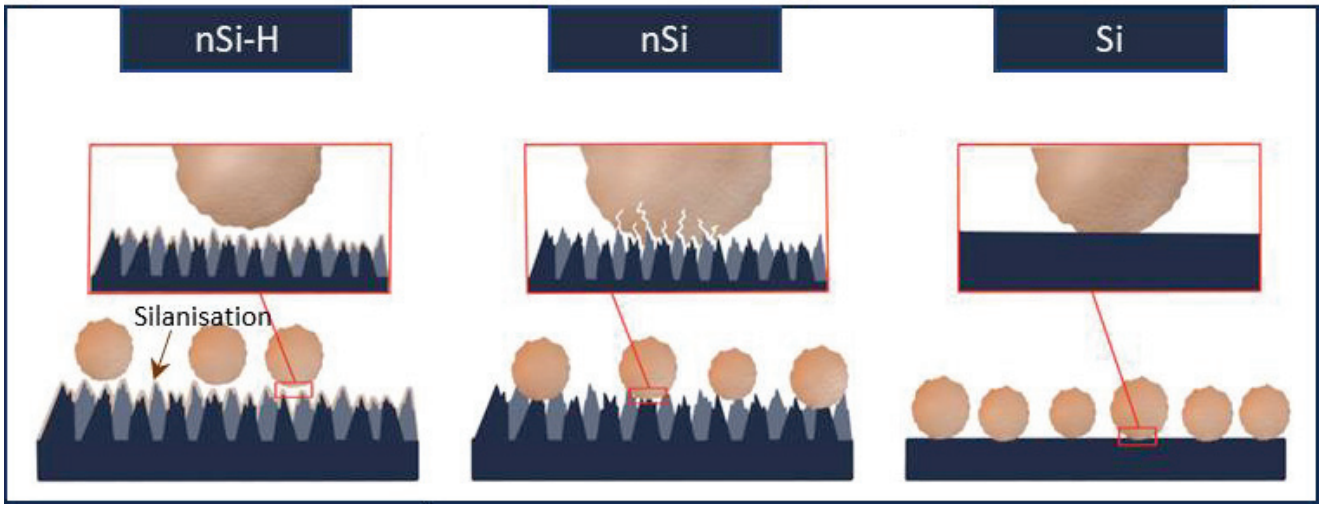
3. Discussion

We recently demonstrated that the antifungal properties of *Calopteryx haemorrhoidalis* damselfly wings was driven by the remarkable antiwetting properties exhibited by the nanopillar array present on the wing epicuticle [33]. Sustainable air entrapment on the nano-, micro-, and macro-scales facilitated spore-repellent behaviour that enabled the wings to remain contamination free when immersed in a suspension of *A. brasiliensis* fungal spores. To develop a synthetic substratum nanotopography that would show fungicidal propensity toward large micro-organisms, such as filamentous fungi spores that possess a rigid, multilayered spore coat, we used etched silicon substrates possessing nanopillars ~800 nm in height. The anti-wetting properties of insect wing surfaces were then mimicked by surface functionalisation with a self-assembled monolayer of fluoro-silane molecules [37]. Analysis of non-germinated *A. brasiliensis* spore interactions with both superhydrophobic and superhydrophilic nanostructured surfaces was achieved using a combination of fluorescence and electron microscopy, and classical microbiological techniques.

In order to form a biofilm, a microorganisms must first undergo attachment to a substrate [48]. In case of filamentous fungi, initiation of the biofilm starts with the germination of spores attached to a substrate surface. Recently the antifungal capabilities of nanostructured surfaces toward *Candida albicans* and other yeasts were shown to result from a purported physical mechanism, sometimes in addition to the toxic activity of generated strong reactive oxygen species (ROS) [49–53]. For example, Xie et al. reported that *C. albicans* cells were mechanically ruptured when interacting with ZnO nanostructured substrates (a polygonal column structure with a height of 3–5 μm and a width of 100–200 nm) [54]. Upon interaction with ZnO-TiO_2-nanostructured surfaces, it was discovered that the *A. flavus* conidia lost their typical round morphology [55]. In addition to the intrinsic mechanism of the ROS-mediated antimicrobial effects, the physical orientation (an extended tubular shape) of MoS_2 has also been shown to play a substantial role in imparting the fungicidal effects of these surfaces toward *Alternaria alternata* cells [56]. In another example, the spores of the filamentous fungi *A. fumigatus* attached onto the nanopillar topography of poly(methyl methacrylate) (PMMA) substrates were observed to have lost their structural integrity, appearing either half or fully deflated [57]. Nevertheless, to the best of our knowledge, the *fungicidal action* of nanostructured hydrophilic surfaces toward filamentous fungi spores has never been previously demonstrated.

In this work, exposing *A. brasiliensis* fungal spores to hydrophilic nano-Si surfaces achieved substantial reductions in spore viability as determined by assessment of cell metabolic activity and plate counting technique (Figure 4B,C). Importantly, *A. brasiliensis* conidia that were attached to nSi surfaces were found to be metabolically inactive. We hypothesise that the hydrophilicity of the nano-Si surfaces led to an increased contact between the spores and the nanopillar surface, resulting in the rupture of the spore coat and inner membrane, leading to cell lysis and death (Scheme 1). The biointerface between fungal conidia and surface nanopillars was evaluated using FIB-SEM in order to obtain an insight into the fungicidal properties of the hydrophilic nanostructured surfaces. We verified that a direct interaction took place between the spores and the nanopillars present

on the nano-Si surface. The spore coat was adhered to the tips of the nanopillars and the spore coat and membrane was ruptured at the points between nanopillar adhesion. Top-view SEM morphological analysis of the spores adhering to the nano-Si revealed that the spores appeared disturbed, with some displaying a flattened and stretched morphology (Figure 2A, second panel and Figure 4D, false coloured red). The spore coat is composed of glucans, glycoproteins, and chitin, with the rigidity of the cell wall resulting from the unique composition of the β-1,3-glucan and chitin [58,59]. Both the outer spore coat, and the inner membrane appeared to be compromised when in contact with the nano-Si substrate. The loss of membrane integrity was corroborated by the uptake of PI by *A. brasiliensis* spores attached to nSi surfaces (Figure 2B–D). Therefore, we hypothesise that the physical contact between the Si nanopillars contributed to the lysis and death of *A. brasiliensis* conidia attached to these surfaces (Figures 2 and 4D). These findings demonstrate that surfaces containing high aspect ratio nanopillars can play a significant role in inhibiting the degree of fungal attachment and also be fungicidal to the attaching cells through a physical rupture mechanism, similar to what has been observed for bacteria attached on high aspect ratio nanostructured surfaces [4].



Scheme 1. The antifungal modes of action of hydrophobic and hydrophilic nanostructured surfaces toward *A. brasiliensis* spores. nSi-H surfaces were able to prevent *A. brasiliensis* spore attachment by reducing attachment affinity through both surface chemistry and reduced attachment points, effectively repelling the spores from the surface. By contrast, the nanostructured hydrophilic surfaces were shown to rupture attaching fungal conidia upon contact.

Contrastingly, the *antibiofouling* characteristics of superhydrophobic nSi-H surfaces were demonstrated by a reduction in the attachment of fungal spores; notably, the spore density was found to be 5× lower than observed on planar Si surfaces (Figure 4A). The spores displayed a reduced degree of interaction with the nanopillar surface, as evidenced by the presence of an air layer underneath the cell body (Figure 2A).

The loose association of spores to the nSi-H surface may facilitate a self-cleaning effect as *A. brasiliensis* spores may be easily displaced by an external force which is consistent with the interfacial behaviour of *A. brasiliensis* spores observed by Ivanova et al. on damselfly wings [33]. By contrast, the attachment propensity of spores on hydrophilic nSi surfaces was found to be increased in comparison to the hydrophobised nanostructured Si but was still lower than that observed for their respective planar Si counterparts. Our data agrees with recent research that found that biomimetic chitosan hydrogel nanopillars, with an average aspect ratio of 2.1, inhibited the attachment of the filamentous fungi *Fusarium oxysporum* by 99% compared to that observed on a non-structured surface after a 24 h incubation period [48]. Cell-surface interactions represent part of a very complex attachment process, which is governed both by surface physicochemical characteristics and by the cell surface

characteristics, i.e., hydrophobicity and surface charge. For example, more hydrophobic cell walls may be more greatly attracted to hydrophobic surfaces [60]. However, as per our previous experiments [33], *A. brasiliensis* spores have a zeta potential of -10.7 ± 1.5 mV and a hydrophobicity index (HI) of 0.71 ± 0.07. WCA measurements of fungal conidia were found to be $107.2 \pm 5.4^{\circ}$. These data suggest that the spore coat of *A. brasiliensis* conidia is only moderately hydrophobic and, indeed, may not display an enhanced affinity for hydrophobic surfaces.

4. Materials and Methods

4.1. Fabrication of Nano-Si Surfaces

P-type boron doped silicon wafers were rinsed in isopropanol and dried with nitrogen gas before being subjected to mask-less plasma etching using a Samco RIE inductively coupled plasma etching system (Model: RIE-101iPH, Samco Inc., Fushimi-ku, Kyoto, Japan). Gases SF_6 and O_2 were set at flow rates of 35 and 45 sccm, respectively. ICP RIE power was 150 W and bias power was 15 W. Etch time was 45 min. Following etching, the surfaces were cleaned with 10% H_2SO_4 sonication for 10 min.

Nano-Si surfaces were hydrophobised by first exposing to 1 min of O_2 plasma to generate hydroxyl (Si−OH) surface groups. Then, the substrata were placed in a glass Petri dish inside a desiccator at room temperature, and 100 µL of trichloro(1H,1H,2H,2H-perfluorooctyl)silane was placed beside the samples. The desiccator was placed under vacuum for 1 h. After venting, the samples were rinsed twice with chloroform, twice with ethanol and then dried with gentle nitrogen gas flow.

4.2. Atomic Force Microscopy (AFM)

The surface topography of the substrata was characterised using a NanoWizard®4 tip scanning AFM (JPK BioAFM Business, Bruker NanoGmbH, Berlin, Germany). The AFM head was placed on an upright optical microscope (IX81, Olympus, Japan), and the tests were conducted in an acoustic hood and on an active vibration isolation table (Accurion, Goettingen, Germany). The scans were conducted in an air-conditioned environment at a temperature of around 22 °C using an n-type antimony doped silicon probe (SICON, AppNano, Mountain View, CA, USA) in the Quantitative Imaging™ (Qi) mode of JPK. The cantilever's spring constant ranged between 0.1 and 0.6 N m^{-1}. Triplicate scans of each surface were taken across scan regions of 10×10 µm^2, and a set of roughness parameters, including average roughness (S_a), root mean square roughness (S_q), and maximum height, were then calculated (S_{max}). Gwyddion (ver. 2.53) was used to analyse the AFM images, and Amira Avizo software (Thermo Fisher Scientific, Waltham, MA, USA) was utilised to create the three-dimensional scans.

4.3. Surface Wettability

The static water contact angle was determined for each substrate using the sessile drop technique. Contact angles were determined using a Phoenix-MT(T) instrument (SEO Co., Yongin, Gyeonggi, Republic of Korea) coupled with SurfaceWare 9 software. Static water contact angles were measured within two seconds of the 10 µL droplet. The results are an average of five independent measurements taken on each substratum.

4.4. X-ray Photoelectron Spectrometry

The elemental analysis of the sample surfaces was conducted using a Thermo Scientific K-alpha X-ray photoelectron spectrometer (XPS) (Thermo Fischer Scientific, USA). The K-alpha EPS instrument was equipped with a monochromatic X-ray source (Al Kα, hν = 1486.6 eV) operating at 150 W. Photoelectrons emitted at 90° to the surface from an area of 400×400 µm^2 were analysed at 200 eV for survey spectra and then at 50 eV for region spectra. Survey spectra were recorded at 1.0 eV per step, while the region spectra were recorded at 0.1 eV per step. The relative atomic concentrations of elements obtained by XPS were measured using the peak area in the specified high-resolution region and the

instrument-specific sensitivity parameters. High-resolution scans were performed across each of the titanium 2p, carbon 1s and oxygen 1s peaks.

4.5. Microorganism, Growth Conditions and Experimental Set-Up

Aspergillus brasiliensis ATTC 9642™ was acquired from the American Type Culture Collection (ATCC, Manassas, Virginia, U.S.A.). The fungal stocks were prepared in 20% glycerol nutritional broth (Oxoid - Thermo Fisher Scientific, Waltham, MA, USA) and kept at −80 °C. Fungi from the glycerol stock were growth on potato dextrose agar (PDA) plates (Neogen® Culture Media, Bundamba, QLD, Australia). These plates were incubated at 27 °C for a week until the fungal spores were fully growth on top of the agar plates. Sterilised MilliQ water (resistivity: 18.2 MΩ cm, 25 °C) was pour onto the fungal agar plates and then the plates were shaken for removing spores from the top layer of the agar plate. To obtain conidial suspension, this suspension was filtered using Whatman® Grade 1 filter paper (Sigma-Aldrich Pty Ltd., Melbourne, VIC, Australia). The final density of the working conidial suspension was adjusted to 1×10^5 mL^{-1} using the TC20 Automated Cell Counter (Bio-Rad, South Granville, NSW, Australia).

Hydrophobic nano-Si (nSi-H), hydrophobic Si (Si-H), hydrophilic nano-Si (nSi) and hydrophilic Si (Si) were cut into 0.5 cm^2 pieces using a diamond pen (ProSciTech Pty Ltd., Kirwan, QLD, Australia). Surfaces were sterilised by sequential sonication in 100% and 70% ethanol (EtOH) (Chem-supply, Gillman, South Australia, Australia) for 15 min each. The studied surfaces were gently dried with nitrogen gas flow and placed in a desiccator to prevent moisture adsorption until required.

The surfaces were immersed in a suspension of 1×10^5 of *A. brasiliensis* conidia and incubated at 25° for 24 h. Afterward, samples were collected and analysed as outlined below.

4.6. Confocal Laser Scanning Microscopy

A Zeiss LSM 880 Airyscan upright CLSM (Carl Zeiss Microscopy, Oberkochen, Germany) operated with a 63× water-immersion objective (ZEISS 60x/1.0 VIS-IR) was used for visualisation of *A. brasiliensis* attachment on surfaces after 1-Day and 3-Day incubation period. The examined surfaces were carefully washed 3× with MilliQ water (2 mL each time) to remove non-attached cells and then put in a 3.5 mm glass-bottomed Petri dish filled with 3 mL MilliQ water. In terms of fungal attachment study, Calcofluor white (Biotium, Fremont, CA, USA) (blue colour) was used to stain the fungal spores, which binds to cellulose and chitin in fungal cell wall, and NucSpot (Biotium, Fremont, CA, USA) (green colour) was used to stain the fungal nuclei containing DNA. The adhesion of *A. brasiliensis* conidia to surfaces was quantified using 15 distinct fields of view of 135×135 μm^2 for each sample. The ImageJ 1.52a Cell Counter plugin was used to recognise and count cells on CLSM micrographs. Results were derived from the average of at least 3 independent experiments, containing two replicates for each experiment.

For assessment of cell viability, LiveDead staining was carried out using a combination of Syto9 (Thermo Fischer Scientific, USA), a membrane permeable nucleic acid stain (green colour) and Propidium iodide (PI) (Thermo Fischer Scientific, USA), a non-membrane permeable nucleic acid stain (red colour). Cell membrane damage was determined by the uptake of PI.

Regarding CLSM settings, ZEN Black software (Carl Zeiss Microscopy, Germany) was used for CLSM imaging and operation. The information of the dyes used in this investigation were selected from the Smart Setup database integrated in the software. In addition, the Z-stack feature was enabled to capture the whole attached fungus spores and adjustments were made to the laser's intensity until neither blur nor noise were visible. Scanning speed was maintained at 7 with the pixel dwell at 1.58 µs and the scan time at 7.75 s.

4.7. Scanning Electron Microscopy (SEM)

The samples with attached *A. brasiliensis* spores were fixed with 2.5% glutaraldehyde for 45 min and then washed 3× with 0.1 M cacodylate buffer containing 2 mM calcium chloride. The surfaces were plunge-frozen in liquid nitrogen and then freeze-dried for SEM imaging. Prior to imaging, 5 nm of iridium (Ir) was sputtered on the surface. Imaging was performed using an FEI Nova NanoSEM at 5kV.

4.8. Focused Ion Beam SEM

FIB milling of *A. brasiliensis* spores incubated on the nano-Si surfaces was performed using an FEI Scios dual-beam FIB system. The samples were fixed with 2.5% glutaraldehyde for 45 min and then washed 3× with 0.1 M cacodylate buffer containing 2 mM calcium chloride. The samples were post-fixed with 2% osmium tetroxide and 1.5% potassium ferrocyanide for 1 h at room temperature and then washed extensively. Following this, samples were incubated for 20 min with thiocarbohydrazide, used as a mordant. A second staining was completed using 2% osmium tetroxide for 30 min. Afterwards, the samples underwent ethanol dehydration over ice and drying using a critical point drying system, the sample surfaces were finally coated with a Pt protection layer using an e-beam Pt deposition process prior to milling.

4.9. Statistical Analysis

The data were examined to validate their normal distribution and homogeneity of variance using the Shapiro–Wilk and Levene's tests, respectively, using SPSS Statistics 26 software (IBM, New York, NY, USA). Values was given as the mean value ± one standard deviation. Statistical data were evaluated using one-way ANOVA. Differences between the mean values were evaluated using Tukey's range test. Values were deemed statistically significant differences if p-values were less than 0.05 (* $p < 0.05$, ** $p < 0.01$, and *** $p < 0.001$).

5. Conclusions

In this study, the influence of hydrophilicity on the antifungal properties of nanostructured surfaces was revealed for the first time. Both superhydrophobic and superhydrophilic nanostructured Si surfaces displayed antifungal behaviour; however, the behaviour observed was distinct depending on the wettability of the substrate. The combination of superhydrophobicity and high-aspect ratio nanopillar pattern on the surface of hydrophobised nanostructured Si was shown to play an essential role in determining its antifouling capabilities, as it significantly reduced the extent of fungal adhesion in an aqueous environment, leading to a marked reduction in spore association and/or attachment over a several-day incubation period in comparison with control planar surfaces. By contrast, the results obtained in this study revealed that the viability of *A. brasiliensis* spores were directly affected by direct interaction with the hydrophilic nanopillar surface, whereby the nanopillars were able to rupture the cell wall of conidia, leading to the uptake of propidium iodide into the cells and reduced metabolic activity. This work demonstrates that nanopillar surface hydrophilicity greatly contributes to the fungicidal activity of nano-Si surfaces. By a combination of the superhydrophobicity and nanopillar surface topography, we have duplicated the antibiofouling effect of damselfly wings toward *A. brasiliensis* conidia. Conversely, we have also determined that hydrophilic nanopillar-surfaces may achieve the physical rupture and cell death of *A. brasiliensis* conidia attaching to these surfaces. This study enhances the present understanding of the effects of surface nanotopography and surface wettability on fungal spore attachment and proposes a potential surface that has the potential to be applied to the development of antifungal biomaterials, including dental biomaterials. Future work is necessary to apply the surface defined in the current study to relevant biomaterials.

Supplementary Materials: The following supporting information can be downloaded at: https://www.mdpi.com/article/10.3390/ijms24021298/s1.

Author Contributions: E.P.I. designed the research; P.H.L., D.P.L. and A.A.-M. performed the research; P.H.L., D.P.L. and A.A.-M. analysed the data; D.P.L. and P.H.L. wrote the paper; E.P.I., R.J.C., S.M. and S.J. reviewed and edited the manuscript. All authors have read and agreed to the published version of the manuscript.

Funding: This study was supported by the Australian Research Council through the ARC Research Hub for Australian Steel Manufacturing under the Industrial Transformation Research Hubs scheme (Project ID: IH130100017).

Institutional Review Board Statement: Not applicable.

Informed Consent Statement: Not applicable.

Data Availability Statement: Data could be provided upon request.

Acknowledgments: The authors would like to thank the ARC Research Hub for Australian Steel Manufacturing for funding this research and the ARC Training Centre for Surface Engineering for Advanced Materials (SEAM) support. We would like to thank the Microscopy and Microanalysis Facility (RMMF) at RMIT University for the use of their facilities.

Conflicts of Interest: The authors declare that they have no known competing financial interests or personal relationships that could have appeared to influence the work reported in this paper.

References

1. Linklater, D.P.; Ivanova, E.P. Nanostructured antibacterial surfaces—What can be achieved? *Nano Today* **2022**, *43*, 101404. [CrossRef]
2. Linklater, D.P.; Baulin, V.A.; Juodkazis, S.; Crawford, R.J.; Stoodley, P.; Ivanova, E.P. Mechano-bactericidal actions of nanostructured surfaces. *Nat. Rev. Microbiol.* **2020**, *19*, 8–22. [CrossRef] [PubMed]
3. Ivanova, E.P.; Linklater, D.P.; Werner, M.; Baulin, V.A.; Xu, X.; Vrancken, N.; Rubanov, S.; Hanssen, E.; Wandiyanto, J.; Truong, V.K.; et al. The multi-faceted mechano-bactericidal mechanism of nanostructured surfaces. *Proc. Natl. Acad. Sci. USA* **2020**, *117*, 12598–12605. [CrossRef] [PubMed]
4. Ivanova, E.P.; Hasan, J.; Webb, H.K.; Gervinskas, G.; Juodkazis, S.; Truong, V.K.; Wu, A.H.F.; Lamb, R.N.; Baulin, V.A.; Watson, G.S.; et al. Bactericidal activity of black silicon. *Nat. Commun.* **2013**, *4*, 2838. [CrossRef] [PubMed]
5. Golan, J.J.; Pringle, A. Long-Distance Dispersal of Fungi. *Microbiol. Spectr.* **2017**, *5*. [CrossRef] [PubMed]
6. Valsecchi, I.; Dupres, V.; Stephen-Victor, E.; Guijarro, J.; Gibbons, J.; Beau, R.; Bayry, J.; Coppee, J.-Y.; Lafont, F.; Latgé, J.-P.; et al. Role of Hydrophobins in Aspergillus fumigatus. *J. Fungi* **2017**, *4*, 2. [CrossRef] [PubMed]
7. Beauvais, A.; Latgé, J.-P. Special Issue: Fungal Cell Wall. *J. Fungi* **2018**, *4*, 91. [CrossRef]
8. Binder, U.; Lass-Florl, C. Epidemiology of invasive fungal infections in the mediterranean area. *Mediterr. J. Hematol. Infect. Dis.* **2011**, *3*, e20110016. [CrossRef]
9. Damasceno, J.L.; Santos, R.A.d.; Barbosa, A.H.; Casemiro, L.A.; Pires, R.H.; Martins, C.H.G. Risk of Fungal Infection to Dental Patients. *Sci. World J.* **2017**, *2017*, 2982478. [CrossRef]
10. Van Dijck, P.; Sjollema, J.; Camue, B.P.A.; Lagrou, K.; Berman, J.; d'Enfert, C.; Andes, D.R.; Arendrup, M.C.; Brakhage, A.A.; Calderone, R.; et al. Methodologies for in vitro and in vivo evaluation of efficacy of antifungal and antibiofilm agents and surface coatings against fungal biofilms. *Microb. Cell* **2018**, *5*, 300–326. [CrossRef]
11. Verweij, P.E.; Chowdhary, A.; Melchers, W.J.G.; Meis, J.F. Azole Resistance inAspergillus fumigatus: Can We Retain the Clinical Use of Mold-Active Antifungal Azoles? *Clin. Infect. Dis.* **2015**, *62*, 362–368. [CrossRef] [PubMed]
12. Brown, G.D.; Denning, D.W.; Levitz, S.M. Tackling human fungal infections. *Science* **2012**, *336*, 647. [CrossRef] [PubMed]
13. Beyki, A.; Zardast, M.; Nasrollahi, Z. Maxillary sinus aspergillosis: A case report of the timely failure to treatment. *Iran. J Microbiol.* **2019**, *11*, 345. [CrossRef] [PubMed]
14. Urs, A.B.; Singh, H.; Nunia, K.; Mohanty, S.; Gupta, S. Post endodontic Aspergillosis in an immunocompetent individual. *J. Clin. Exp. Dent.* **2015**, *7*, e535. [CrossRef] [PubMed]
15. Legent, F.; Billet, J.; Beauvillain, C.; Bonnet, J.; Miegeville, M. The role of dental canal fillings in the development of *Aspergillus sinusitis*. *Arch. Oto-Rhino-Laryngol.* **1989**, *246*, 318–320. [CrossRef]
16. Mazari, W.; Boucherit-Otmani, Z.; Boucherit, K. In vitro susceptibility of amphotericin-B, voriconazole and caspofungin against *Candida guilliermondii* biofilms, isolated from dentals units water pipes, under different growth phases. *J. Mycol. Méd.* **2015**, *25*, 57–62. [CrossRef]
17. ADA. Statement on dental unit waterlines. *J. Am. Dent. Assoc.* **1996**, *127*, 185–186. [CrossRef]
18. Kadaifciler, D.G.; Ökten, S.; Sen, B. Mycological contamination in dental unit waterlines in Istanbul, Turkey. *Braz. J. Microbiol.* **2013**, *44*, 977–981. [CrossRef]

19. Faustino, I.S.P.; Ramos, J.C.; Mariz, B.A.L.A.; Papadopoulou, E.; Georgaki, M.; Nikitakis, N.G.; Vargas, P.A.; Santos-Silva, A.R.; Lopes, M.A. A Rare Case of Mandibular *Aspergillus* Osteomyelitis in an Immunocompetent Patient. *Dent. J.* **2022**, *10*, 213. [CrossRef]
20. Stacchi, C.; Del Lupo, V.; Berton, F.; Lombardi, T.; Bressan, R.; Di Lenarda, R.; Lagatolla, C. *Aspergillus fumigatus* biofilm formation on different bone substitutes used in maxillary sinus augmentation: An in vitro analysis. *Int. J. Implant. Dent.* **2019**, *5*, 22. [CrossRef]
21. Pagella, F.; Matti, E.; Bernardi, F.D.; Semino, L.; Cavanna, C.; Marone, P.; Farina, C.; Castelnuovo, P. Paranasal sinus fungus ball: Diagnosis and management. *Mycoses* **2007**, *50*, 451–456. [CrossRef] [PubMed]
22. Hill, B.R.; Watson Sr, T.F.; Triplett, B.L. Antimicrobial Microporous Coating. U.S. Patent No. 5,024,875, 18 June 1991.
23. Khan, A.; Horner, C. Nanosized Metal and Metal Oxide Particles as a Biocides In roofing Coatings. U.S. Patent Application No. 11/454,335, 24 May 2007.
24. Ivanov-Omskii, V.I.; Panina, L.K.; Yastrebov, S.G. Amorphous hydrogenated carbon doped with copper as antifungal protective coating. *Carbon* **2000**, *38*, 495–499. [CrossRef]
25. Coad, B.R.; Griesser, H.J.; Peleg, A.Y.; Traven, A.J.P.p. Anti-infective surface coatings: Design and therapeutic promise against device-associated infections. *PLoS Pathog.* **2016**, *12*, e1005598. [CrossRef] [PubMed]
26. Eversdijk, J.; Erich, S.; Hermanns, S.; Adan, O.; De Bolle, M.; De Meyer, K.; Bylemans, D.; Bekker, M.; Ten Cate, A.J.P.i.O.C. Development and evaluation of a biocide release system for prolonged antifungal activity in finishing materials. *Prog. Org. Coat.* **2012**, *74*, 640–644. [CrossRef]
27. Griesser, S.S.; Jasieniak, M.; Coad, B.R.; Griesser, H.J. Antifungal coatings by caspofungin immobilization onto biomaterials surfaces via a plasma polymer interlayer. *Biointerphases* **2015**, *10*, 04A307. [CrossRef]
28. Arreche, R.A.; Igal, K.; Bellotti, N.; Deyá, C.; Vázquez, P.G. Functionalized zirconia compounds as antifungal additives for hygienic waterborne coatings. *Prog. Org. Coat.* **2019**, *128*, 1–10. [CrossRef]
29. Knowles, B.R.; Yang, D.; Wagner, P.; Maclaughlin, S.; Higgins, M.J.; Molino, P.J. Zwitterion Functionalized Silica Nanoparticle Coatings: The Effect of Particle Size on Protein, Bacteria, and Fungal Spore Adhesion. *Langmuir* **2019**, *35*, 1335–1345. [CrossRef]
30. Lee, J.-W.; Hwang, W. Fabrication of a superhydrophobic surface with fungus-cleaning properties on brazed aluminum for industrial application in heat exchangers. *Appl. Surf. Sci.* **2018**, *442*, 461–466. [CrossRef]
31. Li, G.; Zhao, H.; Hong, J.; Quan, K.; Yuan, Q.; Wang, X. Antifungal graphene oxide-borneol composite. *Colloids Surf. B* **2017**, *160*, 220–227. [CrossRef]
32. Aburto-Medina, A.; Le, P.H.; MacLaughlin, S.; Ivanova, E. Diversity of experimental designs for the fabrication of antifungal surfaces for the built environment. *Appl. Microbiol. Biotechnol.* **2021**, *105*, 2663–2674. [CrossRef]
33. Ivanova, E.P.; Linklater, D.P.; Medina, A.A.; Le, P.; Baulin, V.A.; Khuong Duy Nguyen, H.; Curtain, R.; Hanssen, E.; Gervinskas, G.; Hock Ng, S.; et al. Antifungal versus antibacterial defence of insect wings. *J. Colloid Interface Sci.* **2021**, *603*, 886–897. [CrossRef] [PubMed]
34. Elbourne, A.; Dupont, M.F.; Collett, S.; Truong, V.K.; Xu, X.; Vrancken, N.; Baulin, V.; Ivanova, E.P.; Crawford, R.J. Imaging the air-water interface: Characterising biomimetic and natural hydrophobic surfaces using in situ atomic force microscopy. *J. Colloid Interface Sci.* **2019**, *536*, 363–371. [CrossRef] [PubMed]
35. Byun, D.; Hong, J.; Saputra; Ko, J.H.; Lee, Y.J.; Park, H.C.; Byun, B.-K.; Lukes, J.R. Wetting Characteristics of Insect Wing Surfaces. *J. Bionic Eng.* **2009**, *6*, 63–70. [CrossRef]
36. Truong, V.K.; Geeganagamage, N.M.; Baulin, V.A.; Vongsvivut, J.; Tobin, M.J.; Luque, P.; Crawford, R.J.; Ivanova, E.P. The susceptibility of *Staphylococcus aureus* CIP 65.8 and *Pseudomonas aeruginosa* ATCC 9721 cells to the bactericidal action of nanostructured *Calopteryx haemorrhoidalis* damselfly wing surfaces. *Appl. Microbiol. Biotechnol.* **2017**, *101*, 4683–4690. [CrossRef]
37. Linklater, D.P.; Juodkazis, S.; Rubanov, S.; Ivanova, E.P. Comment on "Bactericidal Effects of Natural Nanotopography of Dragonfly Wing on Escherichia coli". *ACS Appl. Mater. Interfaces* **2017**, *9*, 29387–29393. [CrossRef]
38. Vellwock, A.E.; Yao, H. Biomimetic and bioinspired surface topographies as a green strategy for combating biofouling: A review. *Bioinspir. Biomim.* **2021**, *16*, 041003. [CrossRef]
39. Vellwock, A.E.; Su, P.; Zhang, Z.; Feng, D.; Yao, H. Reconciling the Conflict between Optical Transparency and Fouling Resistance with a Nanowrinkled Surface Inspired by Zebrafish's Cornea. *ACS Appl. Mater. Interfaces* **2022**, *14*, 7617–7625. [CrossRef]
40. Linklater, D.P.; Nguyen, H.K.D.; Bhadra, C.M.; Juodkazis, S.; Ivanova, E.P. Influence of nanoscale topology on bactericidal efficiency of black silicon surfaces. *Nanotechnology* **2017**, *28*, 245301. [CrossRef]
41. Žukauskas, A.; Malinauskas, M.; Kadys, A.; Gervinskas, G.; Seniutinas, G.; Kandasamy, S.; Juodkazis, S. Black silicon: Substrate for laser 3D micro/nano-polymerization. *Opt. Express* **2013**, *21*, 6901–6909. [CrossRef]
42. Gervinskas, G.; Seniutinas, G.; Hartley, J.S.; Kandasamy, S.; Stoddart, P.R.; Fahim, N.F.; Juodkazis, S. Surface-enhanced Raman scattering sensing on black silicon. *Ann. Phys.* **2013**, *525*, 907–914. [CrossRef]
43. Fan, H.; Guo, Z. Bioinspired surfaces with wettability: Biomolecule adhesion behaviors. *Biomater. Sci.* **2020**, *8*, 1502–1535. [CrossRef] [PubMed]
44. Mosquera, S.; Stergiopoulos, I.; Leveau, J.H.J. Interruption of *Aspergillus niger* spore germination by the bacterially produced secondary metabolite collimomycin. *Environ. Microbiol. Rep.* **2020**, *12*, 306–313. [CrossRef] [PubMed]
45. Firstencel, H.; Butt, T.M.; Carruthers, R.I. A fluorescence microscopy method for determining the viability of entomophthoralean fungal spores. *J. Invertebr. Pathol.* **1990**, *55*, 258–264. [CrossRef]

46. Rampersad, S.N. Multiple applications of Alamar Blue as an indicator of metabolic function and cellular health in cell viability bioassays. *Sensors* **2012**, *12*, 12347–12360. [CrossRef]
47. Fung, D.Y.C. Biochemical and modern identification techniques—Introduction. In *Encyclopedia of Food Microbiology*, 2nd ed.; Batt, C.A., Tortorello, M.L., Eds.; Academic Press: Oxford, UK, 2014; pp. 223–231.
48. Heedy, S.; Marshall, M.E.; Pineda, J.J.; Pearlman, E.; Yee, A.F. Synergistic Antimicrobial Activity of a Nanopillar Surface on a Chitosan Hydrogel. *ACS Appl. Bio Mater.* **2020**, *3*, 8040–8048. [CrossRef]
49. Riduan, S.N.; Zhang, Y. Recent Advances of Zinc-based Antimicrobial Materials. *Chem. Asian J.* **2021**, *16*, 2588–2595. [CrossRef]
50. Hayles, A.; Bright, R.; Wood, J.; Palms, D.; Zilm, P.; Brown, T.; Barker, D.; Vasilev, K. Spiked Nanostructures Disrupt Fungal Biofilm and Impart Increased Sensitivity to Antifungal Treatment. *Adv. Mater. Interfaces* **2022**, *9*, 2102353. [CrossRef]
51. Valdez-Salas, B.; Beltran-Partida, E.; Nedev, N.; Ibarra-Wiley, R.; Salinas, R.; Curiel-Alvarez, M.; Valenzuela-Ontiveros, Y.; Perez, G. Controlled antifungal behavior on Ti6Al4V nanostructured by chemical nanopatterning. *Mater. Sci. Eng. C Mater. Biol. Appl.* **2019**, *96*, 677–683. [CrossRef]
52. Beltrán-Partida, E.; Valdez-Salas, B.; Curiel-Álvarez, M.; Castillo-Uribe, S.; Escamilla, A.; Nedev, N. Enhanced antifungal activity by disinfected titanium dioxide nanotubes via reduced nano-adhesion bonds. *Mater. Sci. Eng. C* **2017**, *76*, 59–65. [CrossRef]
53. Le, P.H.; Nguyen, D.H.K.; Medina, A.A.; Linklater, D.P.; Loebbe, C.; Crawford, R.J.; MacLaughlin, S.; Ivanova, E.P. Surface Architecture Influences the Rigidity of *Candida albicans* Cells. *Nanomaterials* **2022**, *12*, 567. [CrossRef]
54. Xie, Y.; Pan, Y.; Cai, P. Cellulose-based antimicrobial films incroporated with ZnO nanopillars on surface as biodegradable and antimicrobial packaging. *Food Chem.* **2022**, *368*, 130784. [CrossRef] [PubMed]
55. Najibi Ilkhechi, N.; Mozammel, M.; Yari Khosroushahi, A. Antifungal effects of ZnO, TiO2 and ZnO-TiO2 nanostructures on *Aspergillus flavus*. *Pestic. Biochem. Physiol.* **2021**, *176*, 104869. [CrossRef] [PubMed]
56. Basu, P.; Chakraborty, J.; Ganguli, N.; Mukherjee, K.; Acharya, K.; Satpati, B.; Khamrui, S.; Mandal, S.; Banerjee, D.; Goswami, D.; et al. Defect-Engineered MoS_2 Nanostructures for Reactive Oxygen Species Generation in the Dark: Antipollutant and Antifungal Performances. *ACS Appl. Mater. Interfaces* **2019**, *11*, 48179–48191. [CrossRef] [PubMed]
57. Rosenzweig, R.; Marshall, M.; Parivar, A.; Ly, V.K.; Pearlman, E.; Yee, A.F. Biomimetic Nanopillared Surfaces Inhibit Drug Resistant Filamentous Fungal Growth. *ACS Appl. Bio Mater.* **2019**, *2*, 3159–3163. [CrossRef] [PubMed]
58. Garcia-Rubio, R.; de Oliveira, H.C.; Rivera, J.; Trevijano-Contador, N. The Fungal Cell Wall: *Candida*, *Cryptococcus*, and *Aspergillus* Species. *Front. Microbiol.* **2019**, *10*, 2993. [CrossRef] [PubMed]
59. Kang, X.; Kirui, A.; Muszynski, A.; Widanage, M.C.D.; Chen, A.; Azadi, P.; Wang, P.; Mentink-Vigier, F.; Wang, T. Molecular architecture of fungal cell walls revealed by solid-state NMR. *Nat. Commun.* **2018**, *9*, 2747. [CrossRef]
60. Krasowska, A.; Sigler, K. How microorganisms use hydrophobicity and what does this mean for human needs? *Front. Cell. Infect. Microbiol.* **2014**, *4*, 112. [CrossRef]

Disclaimer/Publisher's Note: The statements, opinions and data contained in all publications are solely those of the individual author(s) and contributor(s) and not of MDPI and/or the editor(s). MDPI and/or the editor(s) disclaim responsibility for any injury to people or property resulting from any ideas, methods, instructions or products referred to in the content.

International Journal of
Molecular Sciences

MDPI

Article

Effects of Different Surface Treatments of Woven Glass Fibers on Mechanical Properties of an Acrylic Denture Base Material

Zdravko Schauperl [1], Luka Ivanković [1], Leonard Bauer [2], Sanja Šolić [3] and Marica Ivanković [2,*]

[1] Faculty of Mechanical Engineering and Naval Architecture, University of Zagreb, Ivana Lučića 5, 10000 Zagreb, Croatia
[2] Faculty of Chemical Engineering and Technology, University of Zagreb, Trg Marka Marulića 19, 10001 Zagreb, Croatia
[3] Department of Mechanical Engineering, University North, J. Križanića 31b, 42000 Varaždin, Croatia
* Correspondence: mivank@fkit.hr

Abstract: Silanized glass fibers are popular reinforcements of acrylic denture base materials. To increase the number of surface hydroxyl groups and to improve interfacial adhesion between the matrix and reinforcements, acid or base treatments of glass fibers are commonly performed before the silanization. However, limited data are available on the effect of these treatments on the mechanical properties of acrylic matrix composite materials used for denture base applications. In this work, before the silanization of a woven glass fiber fabric (GF) with 3-(trimethoxysilyl) propyl methacrylate, activation pretreatments using HCl and NH_4OH aqueous solutions have been performed. To characterize the glass surface, FTIR spectroscopy was used. Specimens of cured acrylic denture base resin and composites were divided into five groups: (1) cured acrylic denture base resin-control group; (2) composite with non-silanized GF; (3) composite with silanized GF; (4) composite with NH_4OH activated and silanized GF; (5) composite with HCl activated and silanized GF. The flexural and impact properties of specimens were evaluated by means of three-point-bending tests and Charpy impact testing, respectively. The residual reactivity of the samples was analyzed using differential scanning calorimetry. The results of mechanical testing showed that acid and base pretreatments of the glass fabric had a positive effect on the flexural modulus of prepared composites but a negative effect on their impact strength. Possible interfacial adhesion mechanisms and the diffusion control of isothermal cure reactions due to vitrification have been discussed.

Keywords: dentures; DSC; FTIR; glass fibers; mechanical properties; polymer composite; polymethylmethacrylate (PMMA); treatments; acid; base; silane

Citation: Schauperl, Z.; Ivanković, L.; Bauer, L.; Šolić, S.; Ivanković, M. Effects of Different Surface Treatments of Woven Glass Fibers on Mechanical Properties of an Acrylic Denture Base Material. *Int. J. Mol. Sci.* **2023**, *24*, 909. https://doi.org/10.3390/ijms24020909

Academic Editor: Mary Anne Melo

Received: 30 November 2022
Revised: 20 December 2022
Accepted: 24 December 2022
Published: 4 January 2023

Copyright: © 2023 by the authors. Licensee MDPI, Basel, Switzerland. This article is an open access article distributed under the terms and conditions of the Creative Commons Attribution (CC BY) license (https://creativecommons.org/licenses/by/4.0/).

1. Introduction

Despite advances in preventive dentistry, edentulism is still a big public health problem worldwide [1]. Although there is a growing interest in dental implants, there is still a need for mobile dentures, partial or complete. Materials for dentures must meet a number of requirements since the denture in the oral cavity is exposed to chewing forces, changes in temperature, and changes in pH, and saliva is rich in enzymes and bacteria. During use, the material must remain inert, not dissolve in the oral cavity, have a neutral taste and smell, and be dimensionally stable.

The most commonly used materials in prosthetic dentistry are those based on poly (methyl methacrylate) (PMMA) owing to a reasonable cost, ease of processing and good esthetic properties [2]. However, PMMA denture base is relatively brittle and easily breaks if the patient applies high masticatory forces or if an accident happened (e.g., a denture has been dropped on a hard surface when cleaning, coughing or sneezing, in traffic accidents, sports, etc.) [2–4]. Frequent fractures of the denture base represent not only an inconvenience but also an additional cost to patients.

In the past decades, extensive research efforts have been made to develop novel composite materials. Polymer-matrix composites (PMC) have been reported as an excellent alternative to metals and ceramics in automotive, aerospace, building or medical applications. The range of PMC applications continues to grow and increase in diversity with every new development, as shown in recent review papers [5,6]. Fiber reinforcements are used primarily to improve strength, stiffness, fracture resistance, impact and fatigue resistance of PMC. The fiber surface conditions significantly influence the fiber-matrix interfacial bond, which in turn, determines the mechanical properties of composites. The strength properties achieved from fiber reinforcement depend also on fiber orientation [7]. To obtain optimal composite structures, more efficient manufacturing processes, higher quality products, advanced computational tools and artificial-intelligence modeling have been applied [5,8,9].

The scientists have focused their attention on fiber-reinforced PMMA composite materials to improve the denture base's mechanical properties [10–15]. Among the available fibers (glass, aramid, carbon, nylon, ultrahigh-modulus polyethylene), glass fibers are the most popular due to their transparency and beneficial surface chemistry, which allows their adhesion to the denture base resin [15]. The adhesion of fibers is primarily based on the presence of hydroxyl groups on the surface of glass fibers and the reaction of the groups with resin monomers via silane coupling agents [16,17]. Acid or base treatments of glass substrates are commonly performed before the silanization to increase the number of surface hydroxyl groups. Increased impact [18–20] and fatigue strengths [21] have been reported with the use of woven glass fibers for the reinforcement of PMMA denture base materials, compared to the unidirectional fibers.

Limited data on the acid or base surface treated glass fibers effects on the mechanical properties of PMMA matrix composite materials used for denture base applications are available. This work studied the activation pretreatments of a woven glass-fiber fabric, using HCl and NH_4OH aqueous solutions and their effects on mechanical properties of PMMA/woven glass fibers composite materials. Possible interfacial adhesion mechanisms and the diffusion control of isothermal cure reactions due to vitrification have been discussed.

2. Results

2.1. FTIR Analysis

FTIR spectra of the pristine, NH_4OH-treated, and HCl-treated woven glass-fiber fabric are compared in Figure 1.

The FTIR spectrum of NH_4OH-treated glass-fiber fabric is very similar to the FTIR spectrum of untreated glass-fiber fabric, i.e., no changes in chemical bonds due to the base treatment are observed. Compared to the FTIR spectrum of the pristine glass-fiber fabric, the FTIR spectrum of HCl-treated glass-fiber fabric showed increased intensities of the absorption band at 1633 cm^{-1} and the broad band, with a peak at 3335 cm^{-1}, related to the vibrations of OH bonds. This suggests that the glass surface is becoming increasingly hydrated and hydroxylated due to the acid treatment [22]. The increased band intensity at 1080 cm^{-1}, related to the Si–O–Si siloxane bonds, and the decreased band intensity at 1437 cm^{-1} associated with other oxides (such as aluminum oxide, boron oxide, and so on, present in E glass fibers), indicate the leaching of soluble oxides from the glass fibers [23]. Such leaching may be responsible for the generation of reactive hydroxyl ions at the fiber surface, facilitating the formation of siloxane bonds.

The FTIR spectra of silanized NH_4OH- or HCl-pretreated glass-fiber fabric were very similar to the spectra of non-silanized NH_4OH- or HCl-treated glass-fiber fabric. This may indicate that the amount of the silane coupling agent on the glass surface is below the detection limit of the equipment.

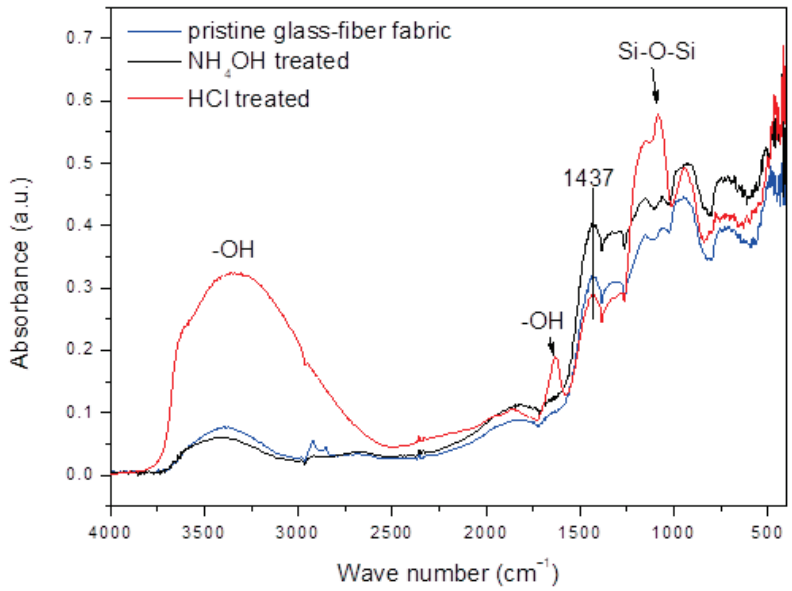


Figure 1. FTIR spectra of the pristine, the NH_4OH-treated, and the HCl-treated glass-fiber fabric.

2.2. Mechanical Testing

Specimens of cured acrylic denture base resin and composites were divided into five groups: (1) cured acrylic denture base resin-control group (PMMA); (2) composite with non-silanized glass fibers (PMMA/GF); (3) composite with silanized glass fibers (PMMA/GF_S); (4) composite with NH_4OH activated and silanized glass fibers (PMMA/GF_ NH_4OH _S); (5) composite with HCl activated and silanized glass fibers (PMMA/GF_ HCl _S).

Flexural and impact properties of specimens were evaluated by means of three-point-bending tests and Charpy impact testing, respectively.

The appearance of the specimens after the three-point bending test is shown in Figure 2.

As shown in Figure 2, all the PMMA specimens had fractured into two pieces showing a rectilinear and smooth fracture surface. Visual inspection of PMMA/GF specimens indicated that only one layer of the matrix was broken, while the second matrix layer and the glass fiber layer were preserved. In the vicinity of the rupture, the broken matrix layer was partially separated from the fiber layer. Three of the five PMMA/GF_S composite specimens had fractured into two pieces, and in the other two (marked as 2 and 4), two parts of specimens are held together by some unbroken glass fibers. In two of the five specimens of the PMMA/GF__NH_4OH_S group, there was a complete fracture of the composite, and in the other three there was a fracture of only one layer of the matrix, as seen in the PMMA/GF group. All composite specimens of PMMA_/GF_HCl had fractured into two pieces.

Photographs of the two groups of specimens after the impact testing are shown in Figure 3.

During the impact testing, the PMMA specimens had fractured into two or three pieces. The PMMA/GF_HCl_S photo illustrates the composite specimens' typical appearance after impact testing. In all composite specimens, only one matrix layer had fractured, at one or more places, while the second matrix layer and the glass fiber layer were preserved. In the vicinity of the ruptures, the broken matrix layer was partially separated from the fiber layer.

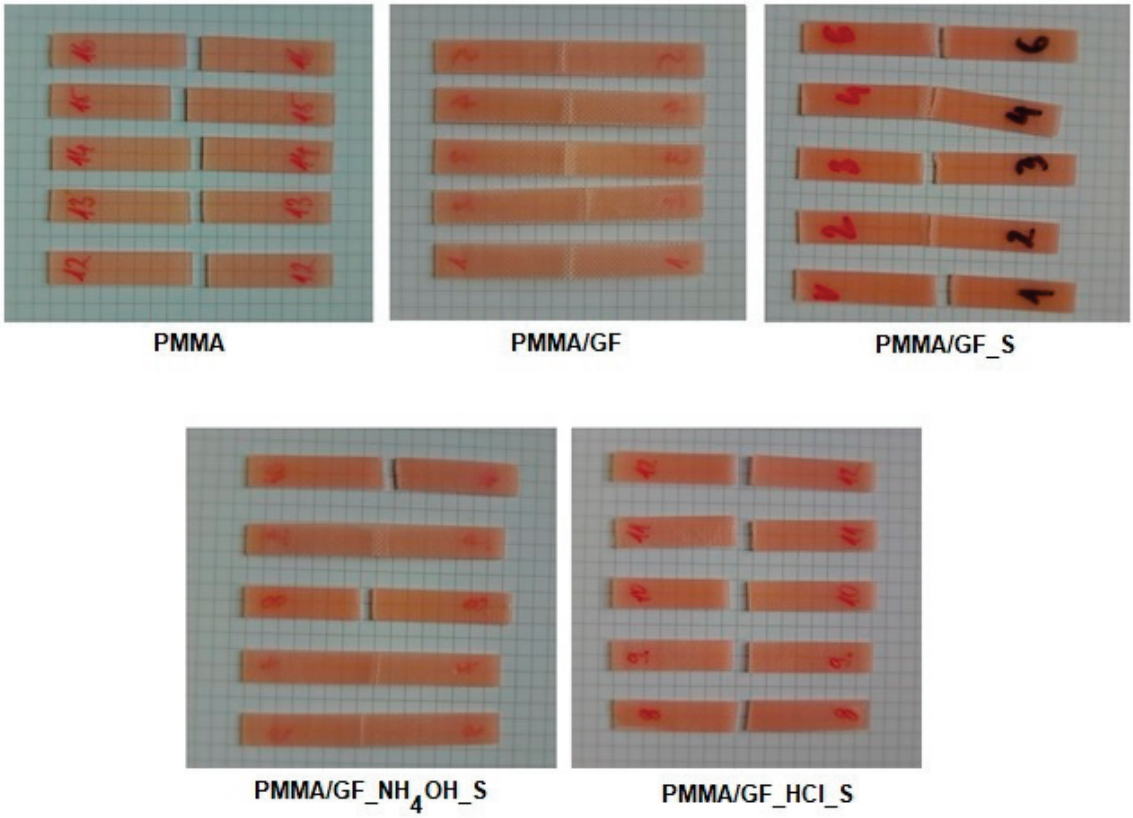


Figure 2. The appearance of the specimens after the three-point bending test. PMMA-cured acrylic denture base resin-control group; PMMA/GF -composite with non-silanized glass fibers; PMMA/GF_S -composite with silanized glass fibers; PMMA/GF_ NH_4OH _S -composite with NH_4OH activated and silanized glass fibers; PMMA/GF_ HCl _S composite with HCl activated and silanized glass fibers.

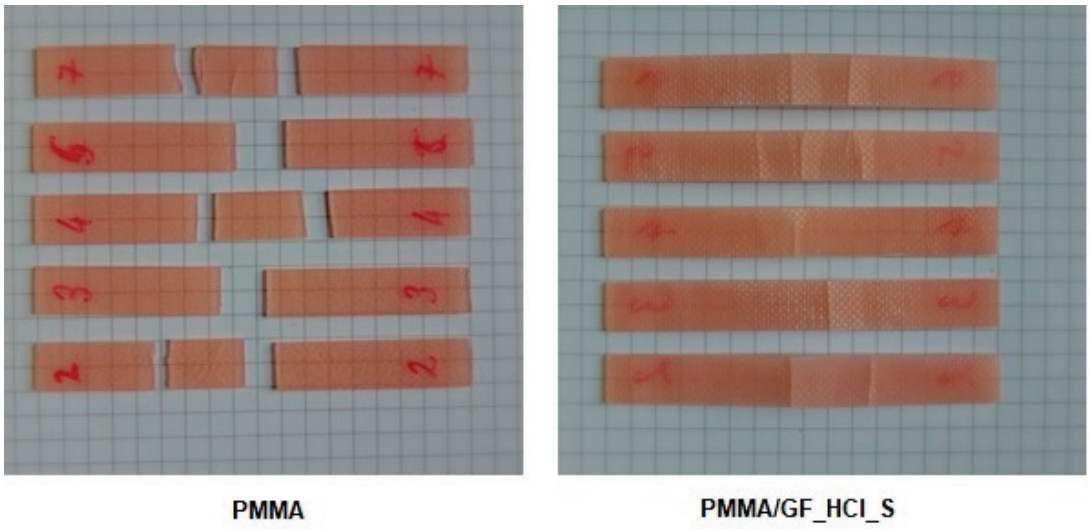


Figure 3. The appearance of the specimens after impact testing. PMMA-cured acrylic denture base resin-control group (specimens had fractured into two or three pieces); PMMA/GF_ HCl _S composite with HCl activated and silanized glass fibers (only one matrix layer had fractured, at one or more places, and the second matrix layer and the glass fiber layer were preserved). In the vicinity of the ruptures, the broken matrix layer was partially separated from the fiber layer.

The flexural strength, flexural modulus, and impact strength for tested groups are compared in Figure 4a–c, respectively. The mean values and standard deviations of flexural strength, flexural modulus, and impact strength of investigated groups of specimens are presented in Table 1.

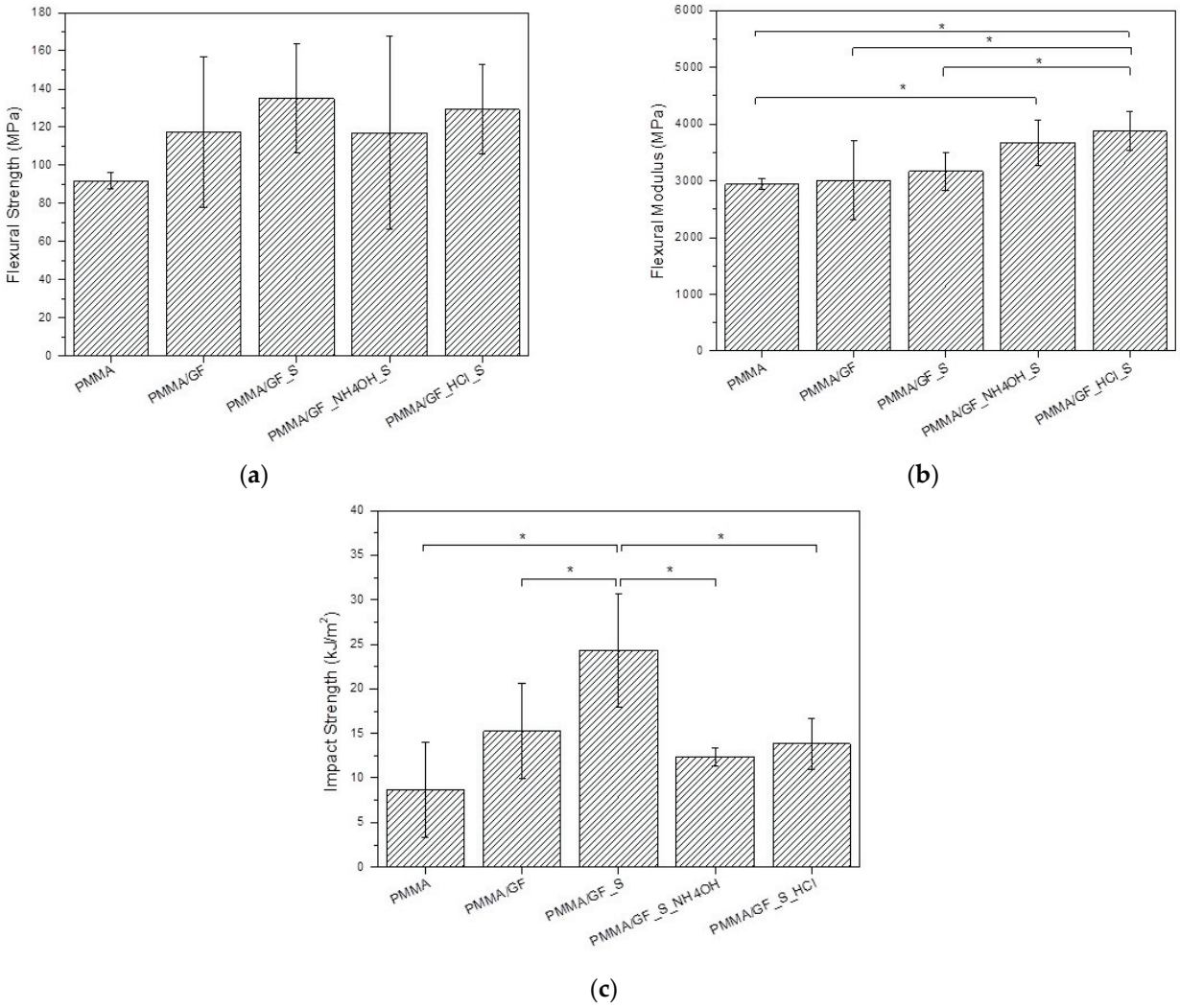


Figure 4. Mechanical properties of the test specimens: (**a**) Flexural strength; (**b**) Flexural modulus; (**c**) Impact strength. The significant difference between two groups is denoted by asterisk (*) with $p < 0.05$.

Table 1. The mean values and standard deviations of flexural strength, flexural modulus, and impact strength of investigated groups of specimens. The values followed by the same letter are not significantly different from each other.

Title 1	Flexural Strength (MPa) Mean ± SD	Flexural Modulus (GPa) Mean ± SD	Impact Strength (kJ/m^2) Mean ± SD
PMMA	91.9 ± 4.3 a	2.94 ± 0.10 a	8.68 ± 5.36 a
PMMA/GF	117.4 ± 39.5 a	3.01 ± 0.69 a	15.26 ± 5.36 a
PMMA/GF_S	135.1 ± 28.57 a	3.17 ± 0.33 a	24.31 ± 6.34 b
PMMA/GF_ NH_4OH _S	117.0 ± 50.5 a	3.67 ± 0.40 b	12.37 ± 1.04 a
PMMA/GF_ HCl _S	129.3 ± 23.5 a	3.87 ± 0.34 b	13.85 ± 2.87 a

The mean flexural strength values of all groups of the reinforced specimens were higher, but not significantly, when compared to the unreinforced PMMA matrix. The highest value of flexural strength is shown in the PMMA/GF_S group, followed by the PMMA/GF_ HCl _S group.

The mean flexural modulus values of reinforced specimens PMMA/GF and PMMA/GF_S were higher, but not significantly, when compared to the unreinforced PMMA matrix. The highest values of flexural modulus are shown in the PMMA/GF_ HCl _S group (3.87 ± 0.34 GPa), which are significantly higher when compared to the unreinforced PMMA matrix, and composite specimens PMMA/GF and PMMA/GF_S, but not significantly different compared to the PMMA/GF_ NH_4OH _S group (3.67 ± 0.40 GPa). Further, there were statistically significant differences in the flexural modulus of the control PMMA specimens and PMMA/GF_ NH_4OH _S specimens.

The lowest mean impact strength value belonged to the control PMMA matrix, which is not significantly different compared to PMMA/GF, PMMA/GF_ NH_4OH _S and PMMA/GF_ HCl _S. The highest mean impact strength (24.31 ± 6.34 kJ/m^2) is shown in the PMMA/GF_S group, which is significantly higher compared to the control PMMA matrix and reinforced specimens PMMA/GF, PMMA/GF_ NH_4OH _S and PMMA/GF_ HCl _S. A comparison between the PMMA/GF_S and PMMA/GF_ HCl _S groups shows similar values of flexural strength but superior values of flexural modulus for the PMMA/GF_ HCl _S composite. On the contrary, the acid pretreatment of glass fabric has been associated to a significant decrease in the impact strength of the PMMA/GF_ HCl _S composites, compared to PMMA/GF_S.

2.3. DSC Analysis

Figure 5 shows dynamic DSC curves obtained for unreinforced acrylic systems (PMMAs), that were previously cured at room temperature (Figure 5a) or 55 °C (Figure 5b) for 2 h. The samples were heated to around 250 °C, then cooled down to room temperature and immediately reheated to 150 or 200 °C.

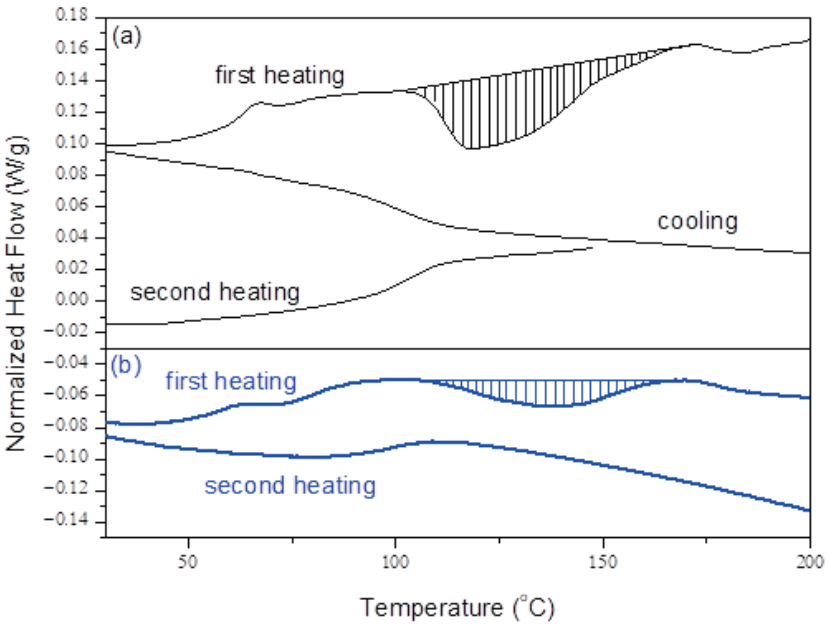


Figure 5. Dynamic DSC curves obtained for unreinforced acrylic systems (PMMA), previously cured at room temperature (**a**) or 55 °C (**b**) for 2 h. Heating/cooling rate: 5 °C/min.

DSC curves obtained during the first heating show glass transition as an endothermic shift over a temperature interval between cca. 50 °C and 70 °C and an exothermic peak between 110 °C and 170 °C, indicating residual reactivity of the system. As expected, the area of the exothermic peak, corresponding to the residual heat of the reaction, is larger

for the sample cured at room temperature compared to the sample cured at 55 °C. The DSC curves obtained by cooling and reheating show only the glass transition of completely cured material.

3. Discussion

The adhesion of glass fibers to the denture base resin is primarily based on the presence of hydroxyl groups on the surface of glass fibers, and the reaction of the groups with resin monomers via silane coupling agents. To increase the number of surface hydroxyl groups, acid or base treatments of glass substrates are commonly performed before the silanization.

Possible trialkoxysilane surface modification reactions are illustrated in Figure 6. During the treatment of glass fibers with the 3-(trimethoxysilyl) propyl methacrylate (3-TMSPMA), the methoxy groups can hydrolyze in an aqueous environment, producing silanol groups and liberating methanol. Silanol groups may self-condense, forming polymeric siloxane structures, and/or condense with hydroxyl groups present on the surface of glass fibers to form a covalent bond to the substrate. On the other side, the methacryloyl group of the silane coupling agent radically polymerizes with double bonds in the matrix resin and chemically binds fibers with the matrix resin.

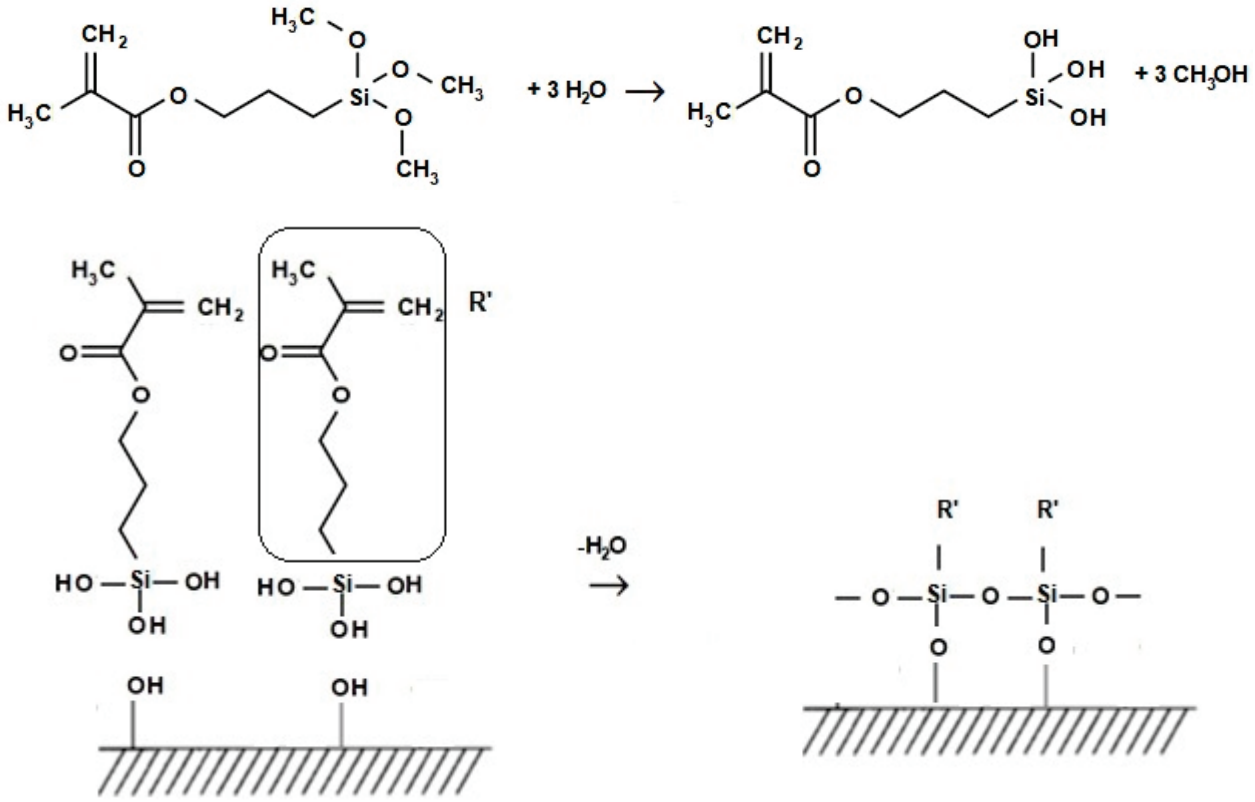


Figure 6. Hydrolysis of a trialkoxysilane and its reaction with a substrate with surface OH groups: vertical condensation forming covalent bonds to the substrate, and horizontal condensation forming polymeric siloxane structures.

The results of mechanical testing showed that acid and base pretreatments of the glass fiber fabric had a positive effect on the flexural modulus of prepared composites but a negative effect on their impact strength. The highest values of flexural modulus are shown in the PMMA/GF_ HCl _S group (3.87 ± 0.34 GPa), which is significantly higher when compared to unreinforced PMMA matrix (2.94 ± 0.10 GPa), and composite specimens PMMA/GF (3.01 ± 0.69 GPa) and PMMA/GF_S (3.17 ± 0.33 GPa), but not significantly different compared to the PMMA/GF_ NH_4OH _S group (3.67 ± 0.40 GPa). Additionally, there were statistically significant differences in the flexural modulus of the

control PMMA specimens and PMMA/GF_ NH_4OH _S specimens. The highest mean impact strength (24.31 ± 6.34 kJ/m^2) is shown in the PMMA/GF_S group, which is significantly higher compared to control PMMA matrix (8.68 ± 5.36 kJ/m^2) and reinforced specimens PMMA/GF (15.26 ± 5.36 kJ/m^2), PMMA/GF_ NH_4OH _S (12.37 ± 1.04 kJ/m^2) and PMMA/GF_ HCl _S (13.85 ± 2.87 kJ/m^2). The impact strength of PMMA/GF_S is an order of magnitude larger than the values reported by Kanie et al. [24], and approximately twice the value reported by Dikbas et al. [25]. The flexural strength (135.1 ± 28.57 MPa) and flexural modulus (3.17 ± 0.33 GPa) of the PMMA/GF_S composite are comparable to the values reported by Kanie et al. [24].

Many factors have an impact on the mechanical properties of composites and cannot be considered in an isolated way. As seen from the FTIR results, the pretreatment of glass fibers with HCl resulted in an increase of hydroxyl groups that may facilitate chemical bonding, via silane coupling agents, and adhesion between the glass fibers and polymer matrix. Furthermore, it can be assumed that HCl etching increases the surface roughness of the fibers providing mechanical interlocking. However, the HCl pretreatment can also weaken the structure of glass fibers due to the leaching ions from the fiber surface as well as from the fiber bulk [22,23]. Our results suggest that the flexural modulus of composites depends much more on the adhesion between the glass fabric and matrix, while the microstructure of the fibers has a pronounced influence on the impact strength of composites.

Dynamic DSC characterization indicated a residual reactivity of the polymer matrix. The incomplete curing obtained in isothermal conditions can be explained in terms of diffusion control effects in the vicinity of isothermal vitrification. The structural changes produced by the polymerization reactions are associated with an increase of the glass transition temperature, Tg, of the reactive system. When the increasing Tg approaches the isothermal cure temperature, the molecular mobility is strongly reduced, and the reaction becomes diffusion controlled and eventually stops. Subsequent exposure to temperatures greater than the previous isothermal cure temperature results in the increase of the molecular mobility and further reaction.

The presence of unreacted residual monomers in denture base acrylic resins is undesirable since they are leached out from the denture base into the saliva and transferred to the oral structures, causing adverse allergic reactions [26]. Therefore, a post curing of the denture base materials at a temperature slightly higher than the Tg of the completely cured system (cca. 110 °C) can be recommended.

Our future research will be focused on optimizing the glass fiber pretreatments, using different concentrations of HCl solutions with different time periods. The effect of post curing on the mechanical properties of the acrylic matrix composite materials will be evaluated, as well.

4. Materials and Methods

In this study, commercially available self-curing acrylic resin as a denture base material (Meliodent® Rapid Repair, powder and liquid, Kulzer GmbH, Hanau, Germany) was used. The composition of the material, as provided by the manufacturer, is presented in Table 2.

Table 2. Composition of denture base material (manufacturer information).

Material	Composition
Meliodent® Rapid Repair Powder	methacrylate copolymers
Meliodent® Rapid Repair Liquid	methyl methacrylate, >90%, Tetramethylene dimethacrylate ≥ 1–≤5% 2-(2H-Benzotriazol-2-yl)-4-methylphenol, ≥0.25–<1% *N*,*N*-Dimethyl-*p*-toluidine, <1%

Woven glass fibers (Satin Weave E Glass, density 163 g/m^2, Kelteks, Karlovac, Croatia) were used to reinforce the denture base material. 3-(trimethoxysilyl) propyl methacrylate

silane (98%, Acros Organics, Geel, Belgium), hydrochloric acid (35%, LACH-NER) were of reagent-grade quality and were used without further purification.

4.1. Surface Functionalization of Glass Fibers

A mat of woven glass fibers was cleaned by immersion in ethanol for 24 h. After drying in air, the activation pretreatment of glass fiber mat was performed using hydrochloric acid (HCl) and ammonium hydroxide (NH_4OH) aqueous solutions, both of concentration 1 mol dm^{-3}, for 24 h. Woven glass fibers were rinsed with deionized water (five consecutive immersions for 15 min each) followed by drying at room temperature for 24 h. Dried fabric was treated with a 2% (v/v) solution of 3-(trimethoxysilyl) propyl methacrylate silane (TMSPMA) in ethanol for 24 h at room temperature.

4.2. FTIR Analysis

Diffuse reflectance Fourier-transform infrared (DRIFT) spectroscopy was performed by Bruker Vertex 70 spectroscope. E-glass fibers were manually chopped, mixed with KBr (Sigma-Aldrich, St. Louis, MO, USA) in the mass ratio 25/75, and placed in a sample cup. Spectra were collected over the 4000 to 400 cm^{-1} range with 4 cm^{-1} resolution and 32 scans.

4.3. Preparation of Composite Materials

The preparation of composite materials turned out to be quite demanding because curing reactions already took place at room temperature. Due to this, the mixing of denture base materials and impregnating the fibers had to be fast, while the resin had a relatively low viscosity. Meliodent resin denture base material was hand mixed, using a powder-to liquid ratio of 10 g to 10 mL. Precut, single-layer woven glass fiber mat was placed in a glass mold between two poured layers of resin. A brush was used to incorporate the resin into the fibers and to remove air from the composite. The mold was covered with a clean glass plate and kept at room temperature for 20 min under 9.8 N load, and then at 55 °C for 2 h. Specimens of cured acrylic denture base resin, without fiber reinforcement, were also prepared as a control. Prepared materials were classified into five groups: (1) control group-cured acrylic denture base resin, without fiber reinforcement (PMMA); (2) composite with non-silanized glass fibers (PMMA/GF); (3) composite with silanized glass fibers (PMMA/GF_S); (4) composite with NH_4OH activated and silanized glass fibers (PMMA/GF_ NH_4OH _S); (5) composite with HCl activated and silanized glass fibers (PMMA/GF_ HCl _S). A minimum of five rectangular specimens (1.2 × 10 × 80 mm) were produced for each type of material.

4.4. Mechanical Testing

4.4.1. Flexural Strength Test

All groups of specimens were tested for flexural strength with a three-point bending test with a universal testing machine (Inspekt Table Blue 20 kN, Hegewald and Peschke Meß- und Prüftechnik GmbH, Germany) at a crosshead speed of 5 mm/min and a span length of 20 mm. The flexural strength, $R_{mf,}$ and the flexural modulus, E, were calculated with the Equations (1) and (2), respectively:

$$R_{mf} = \frac{3 \cdot F_{\max} \cdot L}{2 \cdot b \cdot h^2} \quad (1)$$

$$E = \frac{F_1 \cdot L^3}{4 \cdot b \cdot h^3 \cdot d} \quad (2)$$

where R_{mf} is flexural strength (MPa), $F_{\max}$ is the fracture load applied (N), L is the span length (mm), b is the specimen width (mm), and h is the specimen thickness (mm). F_1 is the load at a point in the straight-line portion of the load/displacement curve [N], and d is the deflection at load F_1 [mm].

4.4.2. Charpy Impact Test

The impact strength was evaluated using the Charpy method. The impact test was performed with unnotched rectangular specimens at room temperature in an impact testing machine (Karl Frank GmbH, Weinheim-Birkenau, Germany), with a pendulum energy of 10 kpcm (approximately 1 J) at room temperature. The specimens were horizontally positioned with a distance of 62 mm between the two fixed supports. The Charpy impact strength of each test specimen was calculated using the Equation (3).

$$a_{cU} = \frac{10^3 E_c}{b \cdot h} \quad (3)$$

where a_{cU} is Charpy impact strength of the unnotched specimen (kJ/m^2), E_c is corrected energy absorbed by breaking, or in some cases damaging the test specimen (J), h is thickness of specimen (mm) and b is width of specimen (mm).

4.5. DSC Analysis

The dynamic DSC analysis of cured specimens was performed on DSC 3500 Sirius® Differential Scanning Calorimeter (NETZSCH-Gerätebau GmbH, Selb, Germany) at a heating/cooling rate of 5 °C/min in a nitrogen atmosphere.

4.6. Statistical Analysis

The data were statistically analyzed using a one-way analysis of variance (ANOVA) followed by Tukey's post-hoc method ($p < 0.05$).

Author Contributions: Conceptualization, Z.S.; methodology, Z.S. and M.I.; data analysis, L.I., L.B. and S.Š.; investigation, L.I. and L.B.; resources Z.S.; writing—original draft preparation, L.I. and L.B.; writing—review and editing, Z.S., S.Š. and M.I.; supervision, Z.S. and M.I.; funding acquisition, Z.S. All authors have read and agreed to the published version of the manuscript.

Funding: This research was funded by the European Regional Development Fund (grant KK.01.1.1.07.0013-Innovative Ti-Mg dental implants for the world market, and grant KK.01.2.1.02.0121-Integrated protection of logistics vehicles).

Institutional Review Board Statement: Not applicable.

Informed Consent Statement: Not applicable.

Data Availability Statement: The data presented in this study are available on request from the corresponding author.

Conflicts of Interest: The authors declare no conflict of interest.

References

1. Emami, E.; de Souza, R.F.; Kabawat, M.; Feine, J.S. The impact of edentulism on oral and general health. *Int. J. Dent.* **2013**, *2013*, 498305. [CrossRef] [PubMed]
2. Zafar, M.S. Prosthodontic Applications of Polymethyl Methacrylate (PMMA): An Update. *Polymers* **2020**, *12*, 2299. [CrossRef] [PubMed]
3. Hersek, N.; Uzun, G. Comparison of the fracture resistance of six denture base acrylic resins. *J. Biomater. Appl.* **2002**, *17*, 19–29.
4. Darbar, U.R.; Huggett, R.; Harrison, A. Denture fracture-a survey. *Br. Dent. J.* **1994**, *176*, 342–345. [CrossRef]
5. Elsheikh, A. Bistable Morphing Composites for Energy-Harvesting Applications. *Polymers* **2022**, *14*, 1893. [CrossRef]
6. Elsheikh, A.; Panchal, H.; Sengottain, S.; Muthuramalingam, T.; El-Kassas, A.; Ramesh, B. Recent progresses in wood-plastic composites: Pre-processing treatments, manufacturing techniques, recyclability and eco-friendly assessment. *Clean. Eng. Technol.* **2022**, *8*, 100450. [CrossRef]
7. Rangasamy, G.; Mani, S.; Kolandavelu, S.K.S.; Alsoufi, M.S.; Ibrahim, A.M.M.; Muthusamy, S.; Panchal, H.; Sadasivuni, K.K.; Elsheikh, A.H. An extensive analysis of mechanical, thermal and physical properties of jute fiber composites with different fiber orientations. *Case Stud. Therm. Eng.* **2021**, *28*, 101612. [CrossRef]
8. Elsheikh, A.H.; Abd Elaziz, M.; Ramesh, B.; Egiza, M.; Al-qaness, M.A.A. Modeling of drilling process of GFRP composite using a hybrid random vector functional link network/parasitism-predation algorithm. *J. Mater. Res. Technol.* **2021**, *14*, 298–311. [CrossRef]

9. Raj, M.K.A.; Muthusamy, S.; Panchal, H.; Ibrahim, A.M.M.; Alsoufi, M.S.; Elsheikh, A.H. Investigation of mechanical properties of dual-fiber reinforcement in polymer composite. *J. Mater. Res. Technol.* **2022**, *18*, 3908–3915. [CrossRef]
10. Ekstrand, K.; Ruyter, I.E.; Wellendorf, H. Carbon/graphite fiber reinforced poly(methyl methacrylate): Properties under dry and wet conditions. *J. Biomed. Mater. Res.* **1987**, *21*, 1065–1080. [CrossRef]
11. Gutteridge, D.L. The effect of including ultra-high-modulus polyethylene fibre on the impact strength of acrylic resin. *Br. Dent. J.* **1988**, *164*, 177–180. [CrossRef] [PubMed]
12. Vallittu, P.K.; Vojtkova, H.; Lassila, V.P. Impact strength of denture polymethyl methacrylate reinforced with continuous glass fibers or metal wire. *Acta Odontol. Scand.* **1995**, *53*, 392–396. [CrossRef] [PubMed]
13. Vallittu, P.K. Glass fiber reinforcement in repaired acrylic resin removable dentures: Preliminary results of a clinical study. *Quintessence Int.* **1997**, *28*, 39–44.
14. Foo, S.H.; Lindquist, T.J.; Aquilino, S.A.; Schneider, R.L.; Williamson, D.L.; Boyer, D.B. Effect of polyaramid fiber reinforcement on the strength of 3 denture base polymethyl methacrylate resins. *J. Prosthodont.* **2001**, *10*, 148–153. [CrossRef] [PubMed]
15. Hamouda, I.M.; Beyari, M.M. Addition of glass fibers and titanium dioxide nanoparticles to the acrylic resin denture base material: Comparative study with the conventional and high impact types. *Oral Health Dent. Manag.* **2014**, *13*, 107–112.
16. Solnit, G.S. The effect of methyl methacrylate reinforcement with silane-treated and untreated glass fibers. *J. Prosthet. Dent.* **1991**, *66*, 310–314. [CrossRef]
17. Matinlinna, J.P.; Lassila, L.V.J.; Ozcan, M.; Yli-Urpo, A.; Vallittu, P.K. An Introduction to Silanes and Their Clinical Applications in Dentistry. *Int. J. Prosthodont.* **2004**, *17*, 155–164. [PubMed]
18. Uzun, G.; Hersek, N.; Tinçer, T. Effect of five woven fiber reinforcements on the impact and transverse strength of a denture base resin. *J. Prosthet. Dent.* **1999**, *81*, 616–620. [CrossRef]
19. Kim, S.H.; Watts, D.C. The effect of reinforcement with woven E-glass fibers on the impact strength of complete dentures fabricated with high-impact acrylic resin. *J. Prosthet. Dent.* **2004**, *91*, 274–280. [CrossRef]
20. Unalan, F.D.I.; Gurbuz, O. Transverse strength of polymethyl methacrylate reinforced with different forms and concentrations of e-glass fibres. *Oral Health Dent. Manag.* **2010**, *9*, 144–147.
21. Rantala, L.I.; Lastumäki, T.M.; Peltomäki, T.; Vallittu, P.K. Fatigue resistance of removable orthodontic appliance reinforced with glass fibre weave. *J. Oral Rehabil.* **2003**, *30*, 501–506. [CrossRef] [PubMed]
22. Sheth, N.; Hahn, S.H.; Ngo, D.; Howzen, A.; Bermejo, R.; van Duin, A.C.T.; Mauro, J.C.; Pantano, C.G.; Kim, S.H. Influence of acid leaching surface treatment on indentation cracking of soda lime silicate glass. *J. Non-Cryst. Solids* **2020**, *543*, 120144. [CrossRef]
23. Larena, A.; Martínez Urreaga, J.; de la Orden, M.U. Effects of previous leaching with hydrochloric acid of E-glass short fibre on the fibre reaction with chlorosilanes. *Mater. Lett.* **1992**, *12*, 415–418. [CrossRef]
24. Kanie, T.; Fujii, K.; Arikawa, H.; Inoue, K. Flexural properties and impact strength of denture base polymer reinforced with woven glass fibers. *Dent. Mater.* **2000**, *16*, 150–158. [CrossRef] [PubMed]
25. Dikbas, I.; Gurbuz, O.; Unalan, F.; Koksal, T. Impact strength of denture polymethyl methacrylate reinforced with different forms of E-glass fibers. *Acta Odontol. Scand.* **2013**, *71*, 727–732. [CrossRef] [PubMed]
26. Rashid, H.; Sheikh, Z.; Vohra, F. Allergic effects of the residual monomer used in denture base acrylic resins. *Eur. J. Dent.* **2015**, *9*, 614–619. [CrossRef]

Disclaimer/Publisher's Note: The statements, opinions and data contained in all publications are solely those of the individual author(s) and contributor(s) and not of MDPI and/or the editor(s). MDPI and/or the editor(s) disclaim responsibility for any injury to people or property resulting from any ideas, methods, instructions or products referred to in the content.

International Journal of
Molecular Sciences

MDPI

Article

Effect of Pre-Heating on the Monomer Elution and Porosity of Conventional and Bulk-Fill Resin-Based Dental Composites

Erika Dunavári [1], Gergely Berta [2,3], Tamás Kiss [3], József Szalma [4], Márk Fráter [5], Katalin Böddi [6,†] and Edina Lempel [1,*,†]

[1] Department of Restorative Dentistry and Periodontology, University of Pécs Medical School, Tüzér Street 1, 7624 Pécs, Hungary
[2] Department of Medical Biology and Central Electron Microscope Laboratory, University of Pécs Medical School, Szigeti Street 12, 7624 Pécs, Hungary
[3] Szentágothai Research Centre, University of Pécs, Ifjúság Street 20, 7624 Pécs, Hungary
[4] Department of Oral and Maxillofacial Surgery, University of Pécs Medical School, Tüzér Street 1, 7624 Pécs, Hungary
[5] Department of Operative and Esthetic Dentistry, Faculty of Dentistry, University of Szeged, Tisza Lajos Street 64, 6720 Szeged, Hungary
[6] Department of Biochemistry and Medical Chemistry, University of Pécs Medical School, Szigeti Street 12, 7624 Pécs, Hungary
* Correspondence: lempel.edina@pte.hu; Tel.: +36-7253-9402
† These authors contributed equally to this work.

Abstract: The pre-heating of dental resin-based composites (RBCs) improves adaptability to cavity walls, reducing microleakages. However, the rapid cooling of the pre-heated RBC may change the polymerization kinetics, and thus the final network configuration of the RBC. It is well known that unreacted monomers remaining in the set RBC can leach into the oral cavity. However, it is still not clear how the pre-heating and cooling of RBCs alter monomer elution (ME). Thus, the purpose was to determine the ME from room-temperature and pre-heated RBCs, in addition to determining the closed porosity (CP) volume. Bulk-filled RBCs and layered conventional RBC samples were prepared. The pre-polymerization temperature was set at 24 °C and 55/65 °C. The ME from RBC samples was assessed with high-performance liquid chromatography using standard monomers. CP was measured with micro-computed tomography. ME decreased significantly from bulk fills and increased from layered samples as a result of pre-heating. Pre-heating was unfavorable in terms of CP in most RBCs. Based on the effect size analysis, ME and CP were greatly influenced by both material composition, pre-polymerization temperature, and their interaction. While the pre-heating of high-viscosity bulk-fill RBCs is advantageous from a clinical aspect regarding biocompatibility, it increases CP, which is undesirable from a mechanical point of view.

Keywords: resin composite; bulk fill; pre-heating; monomer elution; porosity

Citation: Dunavári, E.; Berta, G.; Kiss, T.; Szalma, J.; Fráter, M.; Böddi, K.; Lempel, E. Effect of Pre-Heating on the Monomer Elution and Porosity of Conventional and Bulk-Fill Resin-Based Dental Composites. *Int. J. Mol. Sci.* **2022**, *23*, 16188. https://doi.org/10.3390/ijms232416188

Academic Editor: Jyh-Ping Chen

Received: 17 November 2022
Accepted: 16 December 2022
Published: 19 December 2022

Publisher's Note: MDPI stays neutral with regard to jurisdictional claims in published maps and institutional affiliations.

Copyright: © 2022 by the authors. Licensee MDPI, Basel, Switzerland. This article is an open access article distributed under the terms and conditions of the Creative Commons Attribution (CC BY) license (https://creativecommons.org/licenses/by/4.0/).

1. Introduction

As one of the most common dental restorative materials, resin-based composites (RBCs) have been widely and effectively used in clinical practice [1]. Their gradual improvement in formulation, properties, and esthetics has made them popular among dentists [2]. In order to achieve durable and successful direct restoration, the most important factors include the mechanical properties, degree of conversion (DC), polymerization stress, handling characteristics, and marginal adaptation [3]. High viscosity and stickiness impair the handling of the RBC, resulting in deficient adaptation to the cavity walls and margins and potentially increasing void incorporation [4,5]. Flowable RBCs present significantly lower viscosity, which can improve the adaptation through the increased wettability of the walls [4]. Viscosity, among other things, is strongly dependent on the composition of the resin matrix, filler size, distribution, and fraction [6]. A lower filler load is reflected in

inferior functional wear and physical properties, and therefore are drawbacks of flowable RBCs [7]. However, a significant reduction in viscosity can be achieved by the pre-heating of condensable RBCs without compromising the mechanical properties [8]. At elevated temperatures, thermal vibration allows the monomers to slide by each other more easily, leading to decreased internal friction [9]. The increased flow of pre-heated condensable RBCs improves the adaptation of the uncured material to the cavity walls, potentially reducing microleakages [10]. In addition to good adaptation, other advantages of pre-heated RBCs, such as a higher DC, increased surface hardness, and compressive and diametral tensile strength, have made them popular among clinicians [10,11]. In addition, flexural strength is unaffected, while polymerization shrinkage is adversely influenced by pre-heating [12].

Since an inverse correlation was detected between the DC and unreacted monomer elution from RBCs by several investigations, the question arises as to how pre-heating affects the biocompatibility of RBCs [13,14]. The DC expresses the extent of polymerization. A higher DC corresponds to increased microhardness, flexural strength and modulus, fracture resistance, tensile strength, dimensional and color stability, and decreased solubility and monomer elution [15–18]. RBC polymers with similar DCs may exhibit distinct cross-link densities due to the differences in polymerization kinetics [10,19]. The process of monomer-to-polymer conversion and the properties of the set polymer network are influenced by the polymerization temperature [10]. Pre-heating transfers heat energy to the system, which changes the kinetics due to the reduction in viscosity and the promotion of reactive radical mobility and collision frequency, which results in higher monomer-to-polymer conversion and delayed autodeceleration [20]. This may alter the network configuration and may influence the arrangement of polymerized, pendant, and free monomer molecules [21,22]. Several studies concluded that rapid cooling during removal from the heating device may compromise the monomer-to-polymer conversion depending on the type of RBC [23–25]. In a recent study, pre-heating was not shown to influence the DC of a newly introduced thermoviscous bulk fill; however, a decreased DC at the bottom surface of a contemporary bulk-fill RBC was shown [26]. As a consequence of incomplete polymerization, the unreacted and also pendant monomers can reduce the physical properties of the RBCs, and their detection plays an important role in the evaluation of RBC biocompatibility [27].

The amounts of leachable monomers could be higher in the presence of oxygen-containing pores and voids since the oxygen-inhibited layer is similar to the unpolymerized RBC and may potentially release unreacted monomers [28]. Upon investigating the impact of different insertion techniques on internal pore and void formation, Demirel et al. found that the application of a thermoviscous bulk-fill RBC with the utilization of the pre-heating technique showed the lowest void percentage [29].

As the result of the above-referred studies, pre-heating and the consequential rapid cooling may differently alter the polymerization kinetics of resin composites depending on their composition and manipulation method. Thus, the final network configuration and the arrangement of the connected and unconnected monomer units could be different. In addition to the setting kinetics, the application technique may also influence pore formation, leading to a change in the amount of leachable unreacted monomers. Although the release of unreacted monomers from room-temperature conventional or bulk-fill RBCs has been extensively investigated, there is no available literature about how pre-heating may change monomer release and porosity, which are important factors with regard to biocompatibility.

Therefore, the purpose of the present study was to investigate the unreacted monomer release from different types of restorative RBCs as a result of pre-heating, using reversed-phase high-performance liquid chromatography (RP-HPLC). A further aim was to evaluate the effect of pre-heating on the closed porosity of RBCs with the help of micro-computed tomography (micro-CT) measurements. The null hypotheses were: (1) pre-heating has no effect on the porosity of RBCs, and (2) pre-cure temperature does not affect the amount of released unreacted monomers.

2. Results

The maximum radiant exitance of the LED LCU measured by the radiometer was 1250 ± 15 mW/cm^2. The delivered radiant exposure was 25 ± 3 J/cm^2.

2.1. Micro-Computed Tomography Measurements

According to the 3D evaluation, the volume of internal voids relative to the total volume of the RBC sample was higher in pre-heated samples compared to the room-temperature samples for each material (Figure 1). The differences found to be significant according to the independent *t*-test were FOB: t(4) = −6.26; $p < 0.001$; VCB: t(4) = −2.99; $p < 0.02$; FZ: t(4) = −4.46; $p = 0.002$; GP: t(4) = −16.37; $p < 0.001$; EP: t(4) = −6.3; $p < 0.001$, except ESQ t(4) = −2.09; $p = 0.07$.

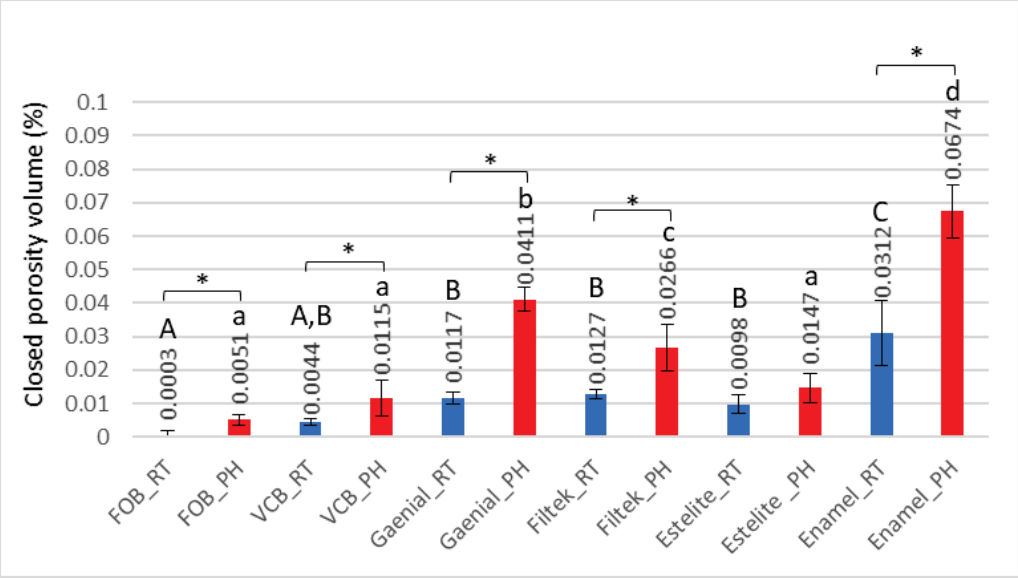


Figure 1. Closed-porosity volume (%) of the room temperature and pre-heated samples analyzed with micro-computed tomography. Different letters denote statistically significant differences among the materials analyzed by one-way analysis of variance (ANOVA) and Tukey's post hoc test. The * mark indicates statistically significant differences between the room-temperature (RT) and pre-heated (PH) groups according to the independent two-tailed *t*-test.

Among the investigated materials, the lowest porosity was detected in the bulk-fill samples (FOB and VCB), while the highest values were found in EP, especially in its pre-heated form. The order of measured porosities among RBCs was: FOB < VCB < ESQ < FZ < GP < EP.

The general linear model revealed that both the *Material* ($p = 0.001$) and *Temperature* ($p = 0.001$) factors have a significant effect on closed porosity and the effect size was considered to be large (*Material* $\eta p^2 = 0.38$; *Temperature* $\eta p^2 = 0.18$).

2.2. Reversed-Phase High-Performance Liquid Chromatography Measurements

Bisphenol A-glycidyl methacrylate (BisGMA), urethane-dimethacrylate (UDMA), trietylene-glycol-dimethacrylate (TEGDMA), 1,12-dodecanediol-dimethacrylate (DDMA), and tricyclodecane-dimethanol-dimethacrylate (TCDDD) standard monomers were selected to detect the elution of these monomers from the investigated bulk-fill and layered contemporary RBCs. In addition to the monomers specified by the manufacturers, other methacrylates were also detected from FOB (BisGMA), VCB (TEGDMA), and EP (DDMA) RBCs. Although TCDDD is a component of GP, the free monomer was not released in a detectable amount.

Depending on the brand, and thus the composition of the RBC, the detected monomer elution varied extensively. The highest amount of monomer was released from GP (UDMA), followed by VCB (BisGMA), then EP (DDMA, UDMA), and ESQ (BisGMA, TEGDMA). Less than 1 nmol/1 mg RBC monomer elution was detected from both the conventional (FZ) and bulk-fill (FOB) Filtek RBCs. Figures 2–7 show the chromatograms and the amount of identified eluted monomers from the investigated room temperature and pre-heated RBCs. Several chromatograms show peaks of eluted, but not identified substances besides the monomers identified as standard dimethacrylates.

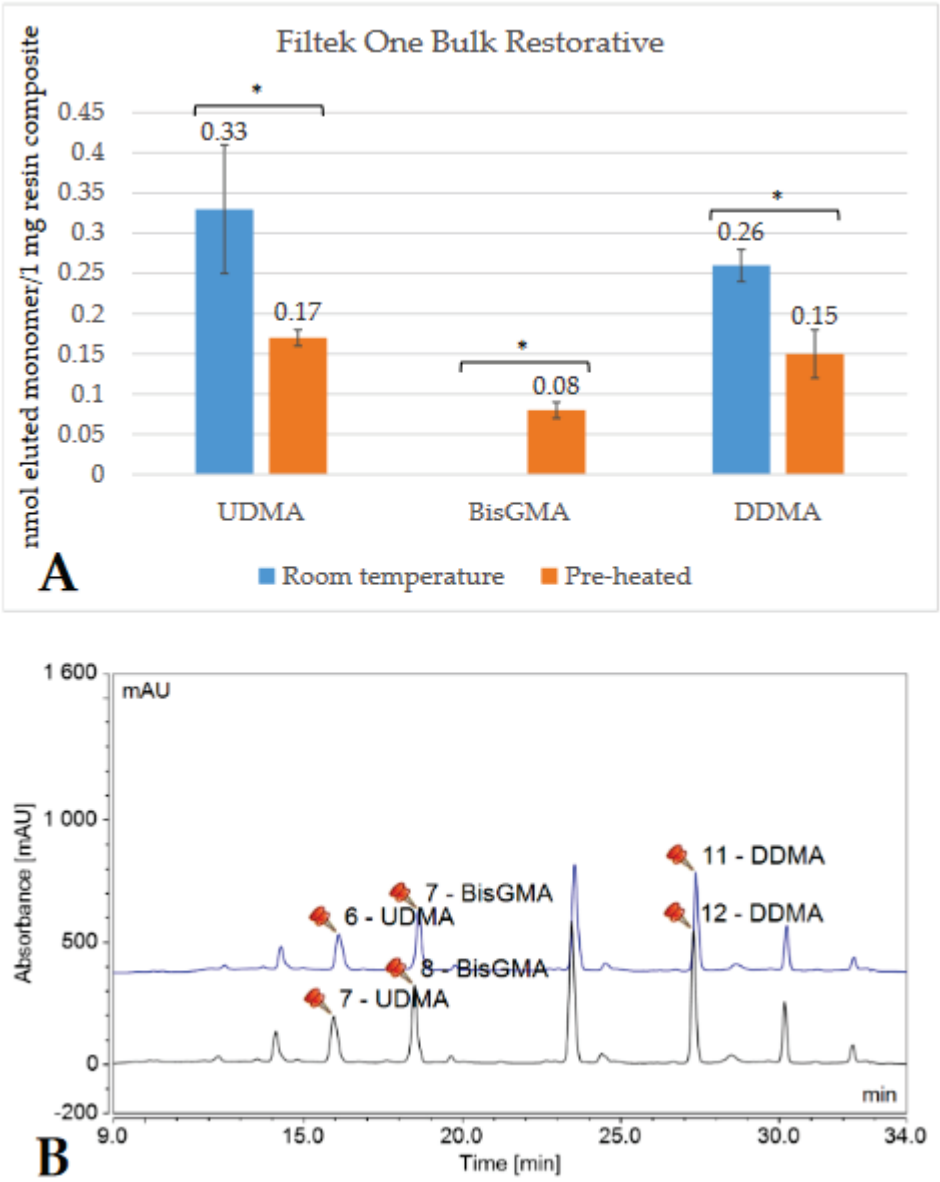


Figure 2. Comparison (**A**) of the amount of eluted monomers from room-temperature (blue bars) and pre-heated (orange bars) Filtek One Bulk Restorative samples. The * mark indicates statistically significant differences between the groups according to the independent two-tailed *t*-test. The chromatogram (**B**) shows the detected monomers eluting from room-temperature (black chromatogram) and pre-heated (blue chromatogram) Filtek One Bulk Restorative (FOB) and their retention times based on the standard monomers, evaluated at a 205 nm wavelength. (Abbreviations: UDMA, urethane-dimethacrylate; BisGMA, bisphenol A-glycidyl methacrylate; DDMA, 1,12-dodecanediol-dimethacrylate; mAU, milli-Absorbance Units).

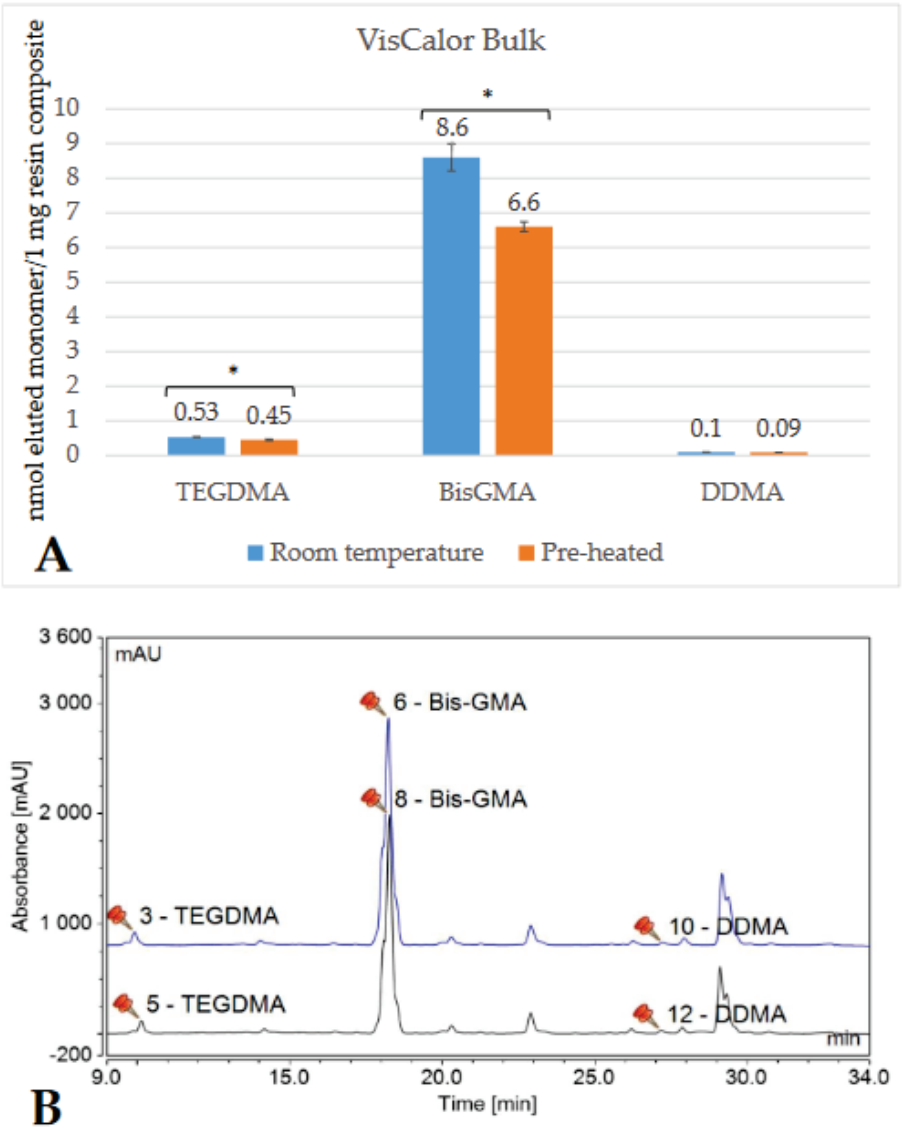


Figure 3. Comparison (**A**) of the amount of eluted monomers from room-temperature (blue bars) and pre-heated (orange bars) VisCalor Bulk samples. The * mark indicates statistically significant differences between the groups according to the independent two-tailed *t*-tests. The chromatogram (**B**) shows the detected monomers eluting from room-temperature (black chromatogram) and pre-heated (blue chromatogram) VisCalor Bulk and their retention time based on the standard monomers, evaluated at a 205 nm wavelength. (Abbreviations: BisGMA, bisphenol A-glycidyl methacrylate; TEGDMA, trietylene-glycol-dimethacrylate; DDMA, 1,12-dodecanediol-dimethacrylate; mAU, milli-Absorbance Units).

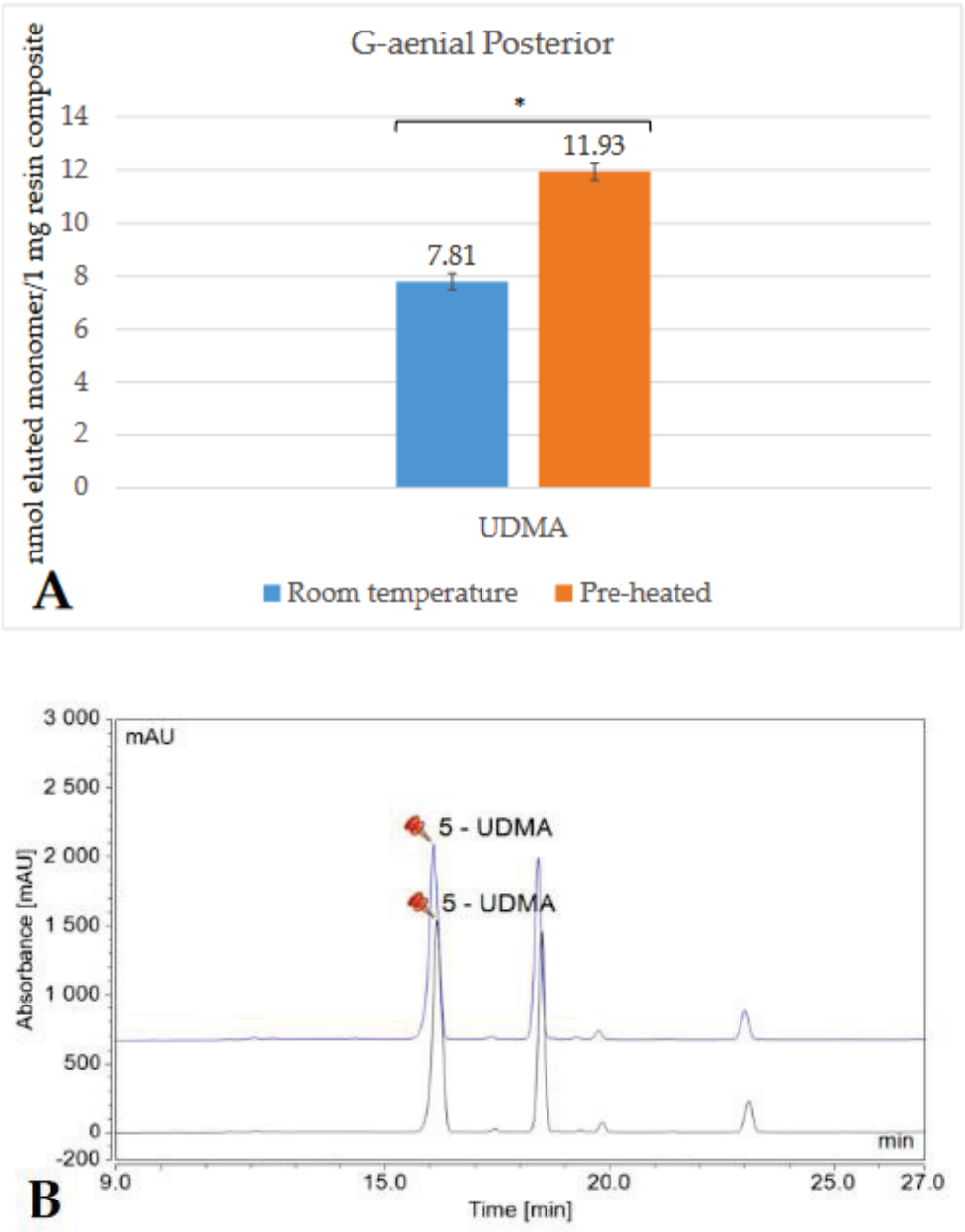


Figure 4. Comparison (**A**) of the amount of eluted monomers from room-temperature (blue bar) and pre-heated (orange bar) G-aenial Posterior samples. The * mark indicates statistically significant differences between the groups according to the independent two-tailed *t*-test. The chromatogram (**B**) shows the detected monomers eluting from room-temperature (black chromatogram) and pre-heated (blue chromatogram) G-aenial Posterior and their retention times based on the standard monomers, evaluated at a 205 nm wavelength. (Abbreviations: UDMA, urethane-dimethacrylate; mAU, milli-Absorbance Units).

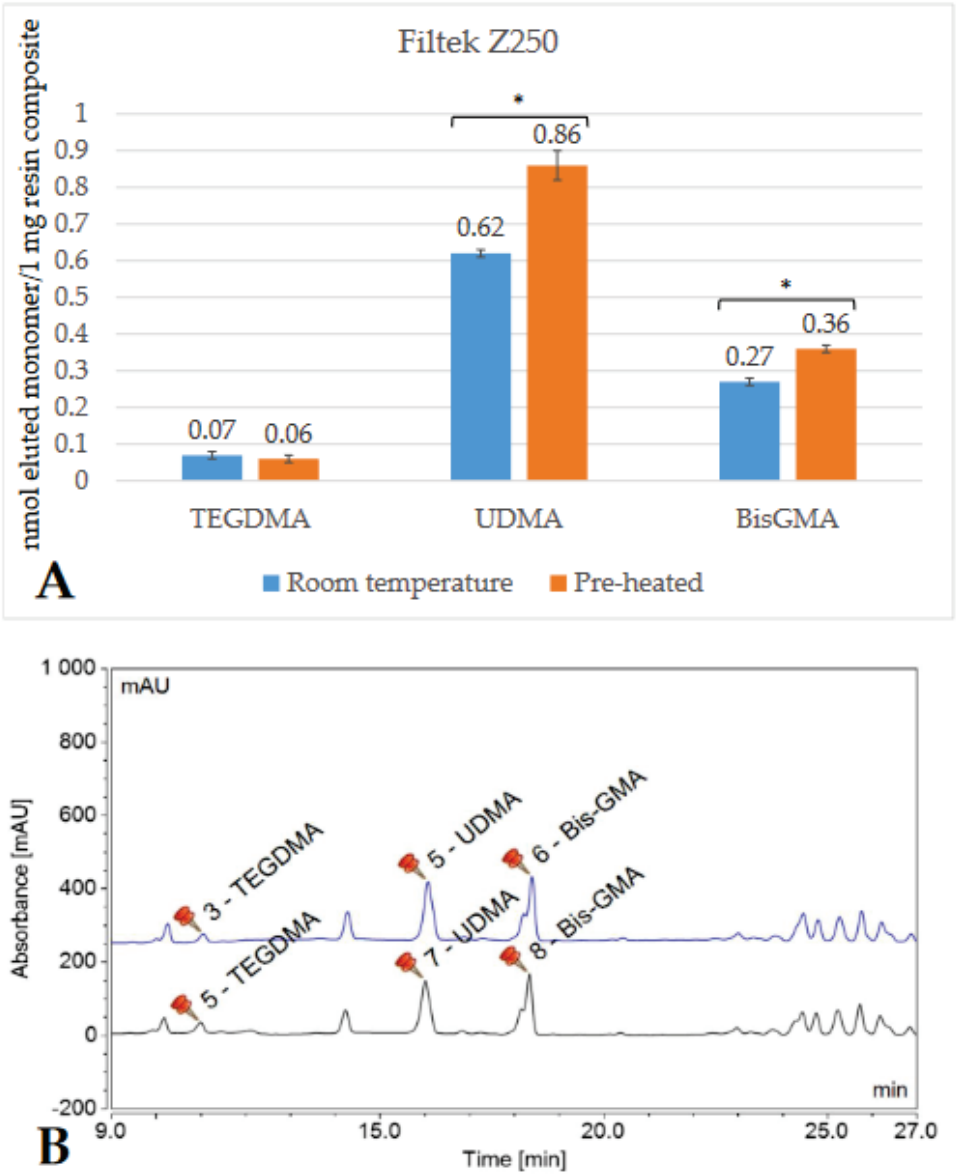


Figure 5. Comparison (**A**) of the amount of eluted monomers from room-temperature (blue bars) and pre-heated (orange bars) Filtek Z250 samples. The * mark indicates statistically significant differences between the groups according to the independent two-tailed *t*-test. The chromatogram (**B**) shows the detected monomers eluting from room-temperature (black chromatogram) and pre-heated (black chromatogram) Filtek Z250 and their retention times based on the standard monomers, evaluated at a 205 nm wavelength. (Abbreviations: TEGDMA, trietylene-glycol-dimethacrylate; UDMA, urethane-dimethacrylate; BisGMA, bisphenol A-glycidyl methacrylate; mAU, milli-Absorbance Units).

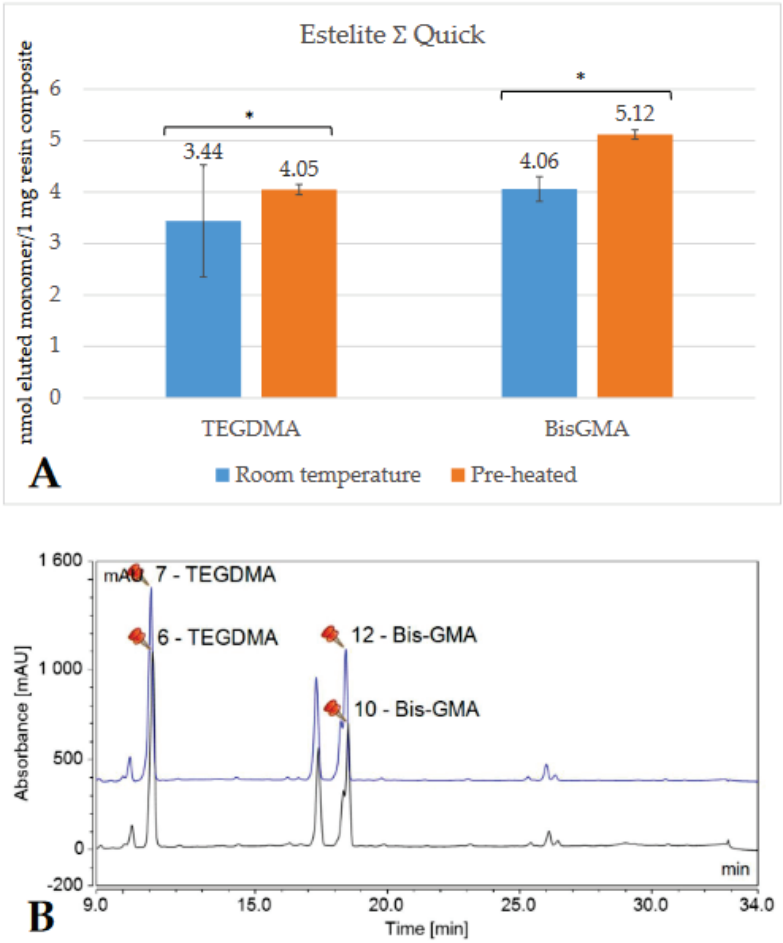


Figure 6. Comparison (**A**) of the amount of eluted monomers from room-temperature (blue bars) and pre-heated (orange bars) Estelite ΣQuick samples. The * mark indicates statistically significant differences between the groups according to the independent two-tailed *t*-test. The chromatogram (**B**) shows the detected monomers eluting from room-temperature (black chromatogram) and pre-heated (blue chromatogram) Estelite ΣQuick and their retention times based on the standard monomers, evaluated at a 205 nm wavelength. (Abbreviations: TEGDMA, trietylene-glycol-dimethacrylate; BisGMA, bisphenol A-glycidyl methacrylate; mAU, milli-Absorbance Units).

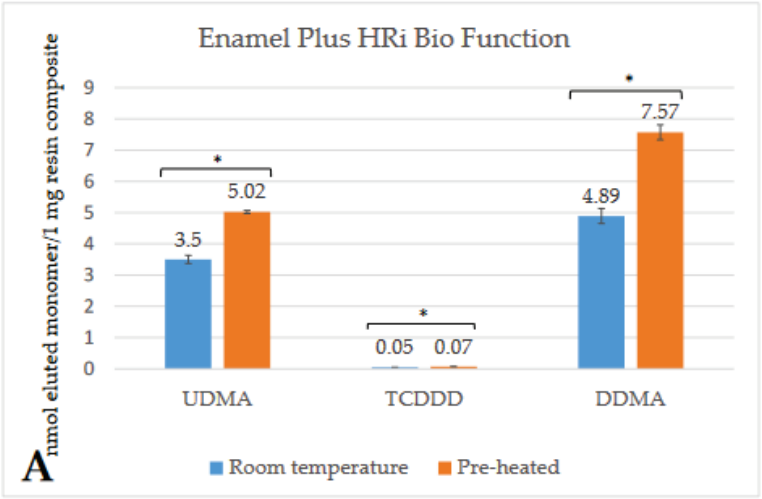


Figure 7. *Cont.*

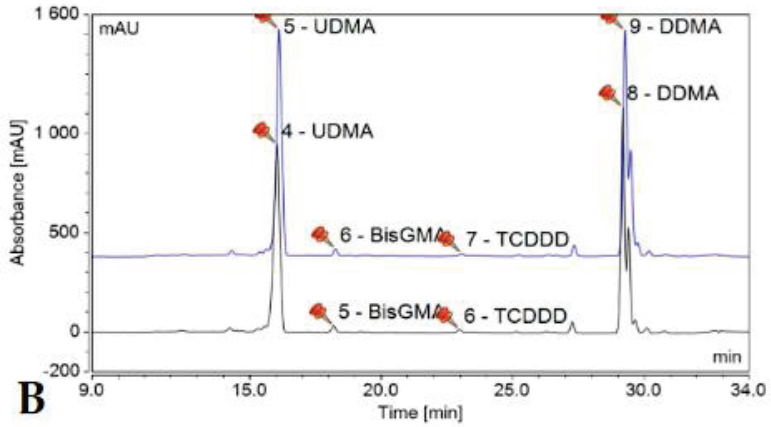


Figure 7. Comparison (**A**) of the amount of eluted monomers from room-temperature (blue bars) and pre-heated (orange bars) Enamel Plus HRi Bio Function samples. The * mark indicates statistically significant differences between the groups according to the independent two-tailed *t*-test. The chromatogram (**B**) shows the detected monomers eluting from room-temperature (black chromatogram) and pre-heated (blue chromatogram) Enamel Plus HRi Bio Function and their retention times based on the standard monomers, evaluated at a 205 nm wavelength. (Abbreviations: UDMA, urethane-dimethacrylate; DDMA, 1,12-dodecanediol-dimethacrylate; TCDDD, tricyclodecane-dimethanol-dimethacrylate; mAU, milli-Absorbance Units).

The evaluated monomers from both the bulk-fill FOB and VCB showed a significantly greater degree of elution when applied at room temperature compared to the pre-heated samples. The monomer elution from the FOB_55 decreased by ~50%, while the elution from VCB_65 was reduced by 15–20%. However, the opposite tendency was observed in the case of the layered contemporary RBCs. Their monomer release was significantly higher in the pre-heated groups (in GP_55, increased by 35%; in FZ_55 by 25–30%; in ESQ _55 by 15–20%; and in EP_55 by 30–35%) (Table 1).

Table 1. Differences in mean values of eluted monomers (nmol/1 mg RBC) between room-temperature (RT) and pre-heated (PH) resin-based composites. Data are provided using a two-tailed independent *t*-test.

RBC	Monomer	Temp	Mean (S.D.)	t-Value	*p*-Value	95% CI	
						Lower Value	Upper Value
Enamel Plus HRi	UDMA	RT	3.5 (0.13)	26.5	<0.001	1.37	1.66
		PH	5.02 (0.05)				
	DDMA	RT	4.89 (0.24)	10.1	<0.001	0.005	0.03
		PH	7.57 (0.24)				
	TCDDD	RT	0.05 (0.01)	19.1	<0.001	2.36	3
		PH	0.07 (0.01)				
Estelite Σ Quick	TEGDMA	RT	3.44 (1.13)	11.2	<0.001	−0.6	1.78
		PH	4.05 (0.1)				
	BisGMA	RT	4.06 (0.24)	7.9	<0.001	0.79	1.32
		PH	5.12 (0.09)				
Filtek Z250	TEGDMA	RT	0.07 (0.01)	3.7	0.006	−0.003	0.02
		PH	0.06 (0.01)				
	UDMA	RT	0.62 (0.01)	9.6	<0.001	0.19	0.28
		PH	0.86 (0.04)				
	BisGMA	RT	0.27 (0.01)	15.2	<0.001	0.08	0.1
		PH	0.36 (0.01)				

Table 1. *Cont.*

RBC	Monomer	Temp	Mean (S.D.)	t-Value	*p*-Value	95% CI	
						Lower Value	Upper Value
Gaenial Posterior	UDMA	RT PH	7.81 (0.3) 11.93 (0.3)	27.7	<0.001	3.66	4.57
Viscalor Bulk	TEGDMA	RT PH	0.53 (0.01) 0.45 (0.02)	6.7	<0.001	0.05	0.09
	BisGMA	RT PH	8.6 (0.39) 6.6 (0.14)	10.5	<0.001	1.54	2.39
	DDMA	RT PH	0.1 (0) 0.1 (0)	1.5	0.17	−0.003	0.02
Filtek One Bulk	UDMA	RT PH	0.49 (0.02) 0.46 (0.01)	2.7	0.28	0.004	0.05
	BisGMA	RT PH	0.59 (0.02) 0.55 (0.03)	2.5	0.04	0.003	0.07
	DDMA	RT PH	1.21 (0.04) 1.13 (0.03)	3.9	0.004	0.03	0.13

Abbreviations: RBC: resin-based composite; Temp: temperature; S.D.: standard deviation; CI: confidence interval; BisGMA: bisphenol-A diglycidil ether dimethacrylate; DDMA: 1,12-dodecane dimethacrylate; TCDDD: tricyclodecane dimethanol dimethacrylate; TEGDMA: trietylene glycol di-methacrylate; UDMA: urethane dimethacrylate.

The general linear model showed a statistically significant effect for both the *Material* and *Temperature* factors and also for their interaction on BisGMA, UDMA, TEGDMA, and DDMA elution. The partial eta-squared value was considered to be large for both factors and their interaction, as well (Table 2).

Table 2. Relative effect size of *Material* (*M*) and *Temperature* (*T*) factors and their interaction ($M \times T$) on the amounts of released monomers. The general linear model and partial eta-squared statistics (η^2) show a large and significant effect of both the type of resin composite (*M*) and pre-polymerization temperature (*T*) and their interaction on the release of those monomers that can be found in more resin composites.

Factor	Monomer release							
	BisGMA		UDMA		TEGDMA		DDDMA	
	p-Value	η^2	*p*-Value	η^2	*p*-Value	η^2	*p*-Value	η^2
Material	<0.001	0.99	<0.001	0.99	<0.001	0.99	<0.001	0.99
Temperature	<0.001	0.98	<0.001	0.98	<0.001	0.79	<0.001	0.93
$M \times T$	<0.001	0.98	<0.001	0.98	<0.001	0.92	<0.001	0.97

Abbreviations: BisGMA: bisphenol-A diglycidil ether dimethacrylate; DDDMA: 1,12-dodecane dimethacrylate; TEGDMA: trietylene glycol di-methacrylate; UDMA: urethane dimethacrylate.

The TCDDD monomer was not included in the effect size analysis, since its release was only detected from EP.

3. Discussion

In this in vitro study, the volume of the internal pores and the elution of the unreacted monomers of room-temperature and pre-heated conventional layered and bulk-fill dental resin composites were assessed using micro-computed tomography and high-performance liquid chromatography.

It was assumed that (1) pre-heating has no effect on the porosity of RBCs and that (2) the pre-cure temperature does not affect the amounts of unreacted monomers released. However, both hypotheses should be rejected, since the pre-heating of the investigated RBCs had a significant impact on internal pore formation as well as on monomer elution.

The accuracy of three-dimensional, high-resolution micro-CT allowed the detection of small voids and air incorporation within the RBCs [30]. Although submicron pores are already present in the material delivered by the manufacturer [31], further air bubbles are incorporated

into the restoration during the clinical manipulation [32]. Porosity is an undesirable property of the RBC, which can significantly decrease the strength, increase water solubility and microleakages, and thus compromise the success of the restoration [33,34].

Porosity correlates with layer thickness, placement technique, and operator skill [35,36]. Our findings showed that the two bulk placements (FOB and VCB) resulted in less pore formation compared to the ones that were layered (GP, FZ, ESQ, and EP); however, the values do not differ in a statistically significant manner in every case.

Our findings are consistent with other studies that evaluated different techniques of posterior RBC placement [35,37]. They found a high rate of air incorporation in the examined samples, but a higher incidence of pores was found in the samples that were layered in thicker increments [31].

A more pronounced effect was found on pore formation when the RBCs were pre-heated. Compared to the room temperature samples, significantly higher closed porosity values were measured as a result of pre-heating in all tested RBCs, except ESQ. Pre-heating reduces the viscosity of RBC, which helps material handling as it flows into the cavity. Although several studies showed that the use of high-viscosity RBCs increased the risk of air incorporation, it was also detected that the use of flowable RBCs cannot eliminate the risk of void formation [35,38]. However, Balthazard et al., through their investigation into the porosity of RBCs, concluded, that the less viscous the material was, the greater its porosity, regardless of the handling conditions [39]. Highly viscous RBCs need a higher condensing force to adapt the material to the walls, which may squeeze out the air bubbles from the material [39].

Furthermore, the vaporization of monomers also resulted in increased porosity. The elevation of the pre-cure temperature increases the vaporization of the organic resin components, especially the low-molecular-weight monomers [34].

Although porosity strongly depends on the consistency and handling conditions, it is a multifactorial phenomenon and is also influenced by the polymerization of the material. The curing protocol and the resin matrix composition have an impact on the polymer network architecture, and its heterogeneity may lead to increased porosity [40]. In contrast to studies reporting the improved monomer conversion of pre-heated RBCs under isothermal conditions, in a clinical setting, the RBC shows rapid cooling after removal from the warming device [41,42]. In a recent study, it was detected that the temperature of the pre-heated RBC decreased by ~26 °C immediately after removal from the heating device regardless of the pre-heating temperature. Further decreases by 1–2.6 °C were measured during RBC application into the mold [26]. The equilibration of the pre-heated RBCs and the ambient temperature resulted in faster cooling of the warmer RBCs, which may compromise the polymerization kinetics [23]. The rapid temperature decrease results in excess heat loss, which may deprive energy from the system, hinder the exothermic reaction, and prevent a sufficient increase in polymerization reactivity. Since the exothermic reaction during RBC polymerization reflects the extent of monomer-to-polymer conversion [10,43], the hindered propagation with reduced exothermic reaction can lead to a decreased DC, as was measured by Kincses et al. [26]. Moreover, the rapid cooling of the pre-heated RBC before polymerization may contribute to the structural heterogeneity of the polymer network [44]. A rapid decrease in temperature may lead to early vitrification, which restricts molecular mobility and hinders the diffusion of air bubbles which will become trapped in the material [40], resulting in higher porosity detected by micro-CT.

Among the above-mentioned phenomena, oxygen diffusion, as a side effect of elevated RBC temperatures, may play a significant role in the increased porosity of pre-heated RBCs [45]. As the temperature increases, the decrease in viscosity promotes oxygen penetration into the RBC. Oxygen also reduces the extent of conversion by scavenging on free radicals, resulting in less-reactive peroxy radicals and/or the quenching of the excited state of the initiator [45].

Insufficient polymerization decreases the degree of conversion and, as a consequence, might increase the released unreacted components from the RBC [15,17]. Unreacted

monomers are not only the result of insufficient conversion. They are also present on the inner surface of air inclusions—related to porosity formation—due to oxygen inhibition [34,46]. The above issues may compromise the biocompatibility of RBCs and create favorable conditions for the proliferation of microorganisms [47]. The solubility of RBCs, furthermore, can accelerate degradation, which adversely affects the physical properties of the material [14].

RP-HPLC was used in this study to detect the released monomers, as it allows the accurate quantitative detection of monomers of interest. The analysis of selected unreacted dimethacrylates (BisGMA, UDMA, TEGDMA, DDMA, TCDDD) cannot provide an absolute measure of the quality of released components, as the chromatograms demonstrated other unidentified eluted ingredients. This can be considered a limitation of this study. Furthermore, the literature regarding monomer release from pre-heated RBCs is limited; hence, the discussion of this issue and subsequent comparisons to other results are also restricted. The amounts of eluted monomers were given in the nanomolar range, which was then converted to elution from 1 mg RBC to exclude the differences that arise from distinct weights of RBC samples. In clinical situations, the local concentrations of leached monomers can be in the millimolar range, which is considered to be high enough to induce a variety of adverse biological effects [22].

A 75 vol% ethanol/water medium was applied to extract the unreacted monomers as it is considered to be a good food simulator, and therefore clinically relevant according to the US Food and Drug Administration (FDA) [48].

Regarding the monomer elution in this study, distinctive results were found in high-viscosity conventional and bulk-fill RBCs. The former released 15–35% more monomer from its pre-heated form, meanwhile the monomer elution from bulk fills was reduced by 15–20% (VCB_65) and 50% (FOB_55) when the RBC was warmed.

Bulk-fill materials have higher volume, which can keep the increased temperature inside the material for a relatively prolonged period [49]. This can store enough energy in the polymerizing system for a higher DC even if the system temperature decreases rapidly. Additionally, high filler content can also contribute to the thermal storing capacity and may delay autodeceleration, thereby prolonging the vitrification of the polymer mass [23]. The absolute filler content and thus the filler/matrix interface is also higher in thicker restoratives. A possible role for the silane interface was suggested by Pluddemann, according to which the coupling agent can create dynamic thermal equilibrium between the organic matrix and inorganic filler, which results in a greater exothermic reaction during polymerization [50]. The results of recent studies, however, only partially confirm the above speculation regarding the DC of highly filled, pre-heated bulk-fill RBCs [23,26,42]. These findings support the strong effect of RBC composition on the results, as was also detected in our study [25]. Although the DC and monomer elution are inversely related [51], Kincses et al. detected contradictory results, as such—that pre-heating not only decreased the DC of FOB but also the monomer elution [26]. Chaharom et al. investigated the monomer release of pre-heated bulk-fill RBCs and detected slightly lower, although not significantly, elution from the pre-heated samples compared to the room-temperature specimens [52]. According to our results, pre-heating significantly reduced the unreacted monomer release from both bulk-fill RBCs. On the contrary, the monomer release was increased when the conventional layered RBCs were pre-heated. A possible explanation may be that the above-mentioned rapid cooling and, additionally, the cold-condensing instruments deplete more energy from the thinner (2 mm) layers. This may accelerate the vitrification and, with that, the termination of polymerization, leading to a decreased DC, a more heterogeneous network formation, and, thus, a higher amount of unreacted monomers. In contrast, Deb et al. found that increasing the pre-cure temperature to 60 °C in conventional RBCs caused a significant increase in the DC [53]. However, as was mentioned above, monomer release from RBC does not solely depend on the DC and the nature of the monomers but also may be related to the chemical structure of the polymer network. In polymerized structures,

monomers stuck in micro-porosities are more susceptible to elution during water sorption, and heterogeneous materials have a higher volume of micro-pores [54].

In general, regardless of pre-cure temperature, a high amount of monomer was released from GP, followed by VCB, then EP, and ESQ; meanwhile, the monomer elution from FOB and FZ was fairly small. Despite the reduced monomer elution seen with the application of pre-heating, the absolute amount of BisGMA was still the highest from VCB (6.6 nmol/1 mg RBC) compared to all the investigated BisGMA-based RBCs. VCB is a BisGMA/aliphatic dimethacrylate-based thermoviscous RBC, according to the technical product profile. Following HPLC measurements, small amounts of TEGDMA and DDMA were detected as eluted aliphatic dimethacrylates. Strong intermolecular hydrogen bonds make BisGMA the most viscous molecule among resin matrix monomers. The strong bonding can decrease the reactivity and mobility of BisGMA during polymerization, which may lead to a higher amount of unconverted monomers [55]. On the other hand, the 75% ethanol/water used as an extraction medium showed easy penetration, especially in BisGMA-based RBCs. The resulting resin-softening expands the spaces within the polymer, creating soluble units [56]. In support of the above hypotheses, other studies also demonstrated elevated BisGMA, TEGDMA, and UDMA levels in the alcohol-based medium [13,57]. Like VCB, ESQ is a BisGMA/TEGDMA-based system, and the detected elution was high not only for BisGMA but also for TEGDMA. It can be assumed that the higher TEGDMA ratio resulted in higher elution compared to VCB. Additionally, TEGDMA is a low-molecular-weight monomer with higher mobility, which allows for a higher and faster rate of elution [58]. The UDMA-based GP and EP released high amounts of UDMA and diluting monomers, such as TEGDMA, DDMA, or TCDDD as well.

Although FOB is also a UDMA-based RBC and FZ is a BisGMA/UDMA/BisEMA-based restorative material, the elution of different monomers from both RBCs was 10 to 70-fold lower compared to the other RBCs tested, regardless of pre-curing temperature. One would assume that the similarly very low monomer dissolution is caused by the identical composition of the two RBCs. However, neither the organic matrix nor the filler content is the same. Moreover, FOB is a bulk fill, while FZ is a conventional RBC from the same company. In addition to UDMA, AUDMA, and DDMA, FOB also released BisGMA, although this monomer is not an officially listed constituent of this RBC. FOB contains a so-called addition fragmentation monomer (AFM) which contains a complementary internal double bond with a β-quaternary carbon center functional group. This provides living polymerization where the active center effectively diffuses throughout the network, simultaneously creating free radicals that initiate a new propagating radical and enable bond rearrangement [59,60]. The benefits of AFM include a more homogenous polymer network, increased DC, decreased shrinkage, stress, and increased toughness [59]. It is assumed that the inclusion of AFM is responsible for the increased DC, leaving fewer monomers unreacted. Furthermore, aside from aliphatic UDMA, aromatic UDMA is also a component of FOB. The proximity of reactive groups facilitates the reaction diffusion, which may lead to an increased DC, and the planar geometry of benzene rings allows for the building of tighter structures [22]. The amount of free residual monomer, however, does not necessarily correlate with the DC, since the carbon–carbon double bonds may remain as pendant groups bonded to the polymer structure and are not free to be released [22]. It is worth mentioning, as a limitation of this study, that the DC was not measured.

FZ composition differs from FOB; nevertheless, the monomer release was similarly low. The copolymerization of BisGMA and TEGDMA with UDMA and BisEMA may result in synergistic effects on double bond conversion and rotational freedom, thus increasing polymer network homogeneity [22].

Supporting the above findings, the results of the general linear model and the partial eta-squared statistics proved, that both *Material* and *Temperature* as influencing factors, as well as their interaction, have a strong effect on monomer elution.

4. Materials and Methods

4.1. Sample Preparation

During this in vitro study, six brands of high-viscosity RBC were analyzed. The brands, the manufacturers, the acronym codes, and the chemical compositions are presented in Table 3.

Table 3. Composition, manufacturers, codes, and pre-polymerization temperature of the investigated resin-based composites.

Material	Manufacturer	PPT	Acronym Code	Matrix	Filler	Filler Load
VisCalor Bulk	Voco, Cuxhaven, Germany	24 °C 65 °C	VCB_24 VCB_65	BisGMA, aliphatic DMA	Nano-hybrid (not detailed by the company)	83 wt%
Filtek One Bulk Fill Restorative	3M ESPE, St. Paul, MN, USA	24 °C 55 °C	FOB_24 FOB_55	AFM, UDMA, AUDMA, DDMA	20 nm silica, 4–11 nm Zr, Zr-silica, 0.1 μm ytterbium-trifluoride	58.5 vol% 76.5 wt%
Filtek Z250	3M ESPE, St. Paul, MN, USA	24 °C 55 °C	FZ_24 FZ_55	BisGMA, BisEMA, TEGDMA, UDMA	0.01–3.5 μm (mean 0.6 μm) silanated Zr-silica	60 vol% 82 wt%
G-ænial Posterior	GC, Leuven, Belgium	24 °C 55 °C	GP_24 GP_55	UDMA, TCDDD DMA	F-Al-silicate, Sr-glass, lanthanide-F	65 vol% 77 wt%
Enamel Plus Hri Bio Function	Micerium S.p.A., Avegno, Italy	24 °C 55 °C	EP_24 EP_55	UDMA, TCDDD	0.005–0.05 μm dispersed SiO_2, 0.2–3 μm glass particle	60 vol% 74 wt%
Estelite Sigma Quick	Tokuyama, Tokio, Japan	24 °C 55 °C	ESQ_24 ESQ_55	TEGDMA, BisGMA	0.2 μm spherical Si-Zr, TiO_2	71 vol% 82 wt%

Abbreviations: PPT: pre-polymerization temperature; BisGMA: bisphenol-A diglycidil ether dimethacrylate; DMA: dimethacrylate; AFM: addition fragmentation monomer; UDMA: urethane dimethacrylate; AUDMA: aromatic urethane dimethacrylate; 1,12-DDMA: 1,12-dodecane dimethacrylate; BisEMA: bisphenol A ethoxylate dimethacrylate; DUDMA: diurethane dimethacrylate; TEGDMA: trietylene glycol dimethacrylate; TCDDD: tricyclodecane dimethanol dimethacrylate; BDDMA: 1,4-butanediol dimethacrylate; vol%: volume%; wt%: weight%.

According to the pre-polymerization temperature of the RBC, specimens were divided into two experimental groups. The pre-polymerization temperature of the RBC in the first group was 24 ± 1 °C (room temperature—RT), while RBCs in the second group were pre-heated (PH) before the sample preparation. The thermoviscous VCB was pre-heated by VisCalor Dispenser (VOCO, Cuxhaven, Germany) using the T1 setting (30 s pre-warming to 65 °C). This pre-heating dispenser uses near-infrared technology for rapid warming and provides immediate application with the same device. The pre-warming of the other RBCs was undertaken by the Ena Heat Composite Heating Conditioner (Micerium, Avegno, Italy) using the T2 setting (55 min pre-warming of the device to 55 °C and 15 min pre-warming of the RBC). Five specimens were prepared in each group from each material. The specimens were prepared in a cylindrical polytetrafluoroethylene (PTFE) mold with an internal diameter of 6 mm, an external diameter of 12 mm, and a height of 4 mm. The mold was placed on a thermostatically controlled (30 ± 1 °C) glass slide to represent the isolated tooth. The bulk-fill materials (VCB and FOB) were used in a 4 mm-thick bulk layer; meanwhile, the contemporary RBCs were stratified in 2 × 2 mm layers. A room-temperature hand instrument was used to perform the condensation of the RBCs. Before light-curing, the sample was covered with a polyester strip to avoid contact with oxygen. The 4 mm specimens and both layers of the 2 × 2 mm samples were irradiated with a Light Emitting Diode (LED) curing unit (LED.D, Woodpecker, Guilin, China; average light output given by the manufacturer 850–1000 mW/cm^2; Λ = 420–480 nm; 8 mm exit diameter fiberglass light guide) in full mode for 20 s, powered by a line cord. The tip of the fiberglass light guide was centrally positioned and parallel to the mold and in direct contact with the polyester strip, which covered the RBC. The irradiance of the LED unit was monitored before and after polymerization with a radiometer (CheckMARC, Bluelight Analytics, Halifax, Canada).

4.2. Micro-Computed Tomography Measurements

To analyze the closed-pore volume, micro-computed tomography (micro-CT) scans were performed (Skyscan 1176, Bruker, Kontich, Belgium) on the samples after 24 h following polymerization. Each specimen was scanned for 36 min. The parameters (operating energy: 80 kV, 350 μA; resolution: 8.74 μm/slice; rotation step: 0.7°, exposure time: 1500 ms; and the filter: Al 1 mm) for the micro-CT device were kept constant for all measurements. The SkyScan reconstruction program (NRecon, v.1.7.4.2, Bruker, Kontich, Belgium) was used to reconstruct the raw images and prepare for analysis. Images were converted to 1404 × 1404 pixel resolution in *.bmp format. The 3D microarchitecture analyses of the images were performed according to the following workflow (Skyscan software CTAn, v.1.20.8.0, Bruker, Kontich, Belgium): raw image acquisition, identification of the region of interest, binary selection, morphometry, and custom processing. The region of interest (ROI) included the entire RBC specimen. The pores were calculated using the grayscale images processed with a Gaussian low-pass filter for noise reduction. A global threshold was used to process the gray level ranges to obtain an imposed image of only black and white pixels. The volume of internal voids relative to the total volume of the RBC samples was calculated (%) by measuring the internal voids and specimen volumes of each RBC specimen.

4.3. Reversed-Phase High-Performance Liquid Chromatography Measurements

The specimens were kept in separate glass vials, fully immersed in 1.0 mL of 75% ethanol/water storage medium, and stored in a 37 °C incubator for 72 h. The qualitative and quantitative analysis of the eluted unreacted monomers was performed from the collected medium. Reversed-phase high-performance liquid chromatography (RP-HPLC) measurement was used for the analysis. The RP-HPLC system (Dionex Ultimate 3000, Thermo Fisher Scientific Inc., Sunnyvale, CA, USA) consists of the following units: Dionex LPG 3400 SD gradient pump, Rheodyne injector (Rheodyne, CA, USA), and a Dionex DAD 3000 RS UV-VIS detector (Dionex GmbH, Germering, Germany). Chromeleon software (version: 7.2.10) was used to collect the data. The separations were performed on a Brisa "LC^2" (Teknokroma, Sant Cugat del Vallés, Spain) C18 reversed-phase column (250 mm × 4.60 mm; particle size: 5 μm) and a general reversed/apolar stationary phase C18 with gradient elution. The more polar mobile phase, such as 100% bidistilled water, was used as eluent "A", whereas mobile phase "B" was 100% *v*/*v* acetonitrile (ACN) (VWR International, Radnor, PA, USA). ACN as the mobile phase is advantageous because of its high elution force and relatively low viscosity. Furthermore, it has lower self-absorption at the detection wavelength used to detect the eluted monomers. During the 30 min chromatographic separation procedure, the "B" eluent content was increased from 40% to 95%. The flow rate was 1.2 mL × min^{-1}. The content of mobile phase B was decreased from 95% to 40% in 1 min as the regeneration of the stationary phase (31–46 min), and afterward, the system was washed with 40% "A". Since the polarity of the monomers varies, but not in such a wide range to reach the complete separation of the components, the polarity of the mobile phase is continuously changed by varying its composition during the chromatographic measurement.

Wavelengths of 205, 215, 227, and 254 nm were tested to detect the eluted monomers.

The evaluation relied on the data collected at a 205 nm wavelength, which was found to be optimal for monomer detection. The amounts of the eluted monomers BisGMA, UDMA, TEGDMA, DDMA, and TCDDD (*Merck KGaA*, Darmstadt, Germany) were calculated using the calibration curve with the areas under the curve of peaks produced by the monomers, respectively. The amounts of released monomers were calculated for every 1 mg of RBC. TEGDMA, UDMA, BisGMA, TCDDD, and DDMA standard monomers had retention times of 11.07, 16.10, 18.42, 23.39, and 29.20 min, respectively. The peaks were well separated from each other.

4.4. Statistical Analysis

Previous study results [26] and sample size formula were used to estimate sample size [61]. Sample size formula:

$$n = \frac{\left(z_{1-\frac{\alpha}{2}} + z_{1-\beta}\right)^2 (s_1 + s_2)^2}{(M_1 - M_2)^2}$$

where z = standard score; α = probability of Type I error at 95% confidence level = 0.05; $z_{1-\alpha/2}$ = 1.96 for 95% confidence; β = probability of Type II error = 0.20; $1 - \beta$ = the power of the test = 0.80; $z_{1-\beta}$ = value of standard normal variate corresponding to 0.80 value of power = 0.84; s_1 = standard deviation of the outcome variable of group 1 = 0.01; s_2 = standard deviation of the outcome variable of group 2 = 0.08; M_1 = mean of the outcome variable of group 1 = 0.22; and M_2 = mean of the outcome variable of group 2 = 0.08. The predicted sample size (n) was found to be a total of 3.24 samples per group. According to the calculation, n = 5 per group sample size was selected.

The statistical analyses were performed with SPSS (Version 26.0; IBM, Armonk, NY, USA). The Kolmogorov–Smirnov test was applied to test the normal distribution of the data, followed by a parametric statistical test.

The closed-porosity volume of the investigated RBCs was compared with a one-way analysis of variance (ANOVA). Tukey's post hoc adjustment was used for multiple comparisons.

A two-tailed independent *t*-test was applied to compare the difference in porosity and monomer elution between the room temperature and pre-heated groups of the investigated RBCs.

The general linear model and partial eta-squared statistics were used to test the influence and describe the relative effect size for *Material* and pre-cure *Temperature* as independent factors. *p*-values below 0.05 were considered statistically significant.

5. Conclusions

The elevated pre-polymerization temperature of the investigated bulk-fill and conventional high-viscosity dental RBCs significantly increased the closed-porosity volume relative to the total volume of the RBC samples. The evaluated monomers from the investigated bulk-fill RBCs showed a significantly greater degree of elution when applied at room temperature compared to the pre-heated samples. In contrast, the elution of monomers increased from layered conventional RBCs, when their pre-polymerization temperature was elevated. The absolute amount of released monomers was strongly dependent on the material's composition and not related to the bulk or layered application method.

As a future direction, a long-term clinical trial is necessary to clarify the effect of pre-heating on the success and survival of RBCs.

Author Contributions: Conceptualization, E.D. and E.L.; methodology, E.D., E.L. and K.B.; software, E.D., E.L. and J.S.; validation, K.B. and E.L.; formal analysis, E.L., M.F. and J.S.; investigation, E.D., T.K. and K.B.; resources, E.L. and K.B.; data curation, K.B. and E.L.; writing—original draft preparation, E.D. and E.L.; writing—review and editing, E.L. and K.B.; visualization, K.B., E.L. and J.S.; supervision, G.B., M.F. and J.S.; project administration, E.L.; funding acquisition, E.L. and K.B. All authors have read and agreed to the published version of the manuscript.

Funding: This research was funded by the Bolyai János Research Scholarship of Hungarian Academy of Sciences (BO/713/20/5 and BO/701/20/5); the ÚNKP-22-5 New National Excellence Program of the Ministry for Innovation and Technology from the Source of the National Research, Development and Innovation Fund (ÚNKP-22-5-PTE-1733); Research Fund of University of Pécs Medical School (PTE-ÁOK-KA-2020/24 and PTE-ÁOK-KA-2020/29).

Institutional Review Board Statement: Not applicable.

Data Availability Statement: Data are available from the corresponding author.

Acknowledgments: Special thanks to Bálint Viktor Lovász for the English correction.

Conflicts of Interest: The authors declare no conflict of interest.

References

1. Lempel, E.; Lovász, B.V.; Bihari, E.; Krajczár, K.; Jeges, S.; Tóth, Á.; Szalma, J. Long-term clinical evaluation of direct resin composite restorations in vital vs. endodontically treated posterior teeth—Retrospective study up to 13 years. *Dent. Mater.* **2019**, *35*, 1308–1318. [CrossRef] [PubMed]
2. Samuel, S.P.; Li, S.; Mukherjee, I.; Guo, Y.; Patel, A.C.; Baran, G.; Wei, Y. Mechanical properties of experimental dental composites containing a combination of mesoporous and nonporous spherical silica as fillers. *Dent. Mater.* **2009**, *25*, 296–301. [CrossRef] [PubMed]
3. Lohbauer, U.; Zinelis, S.; Rahiotis, C.; Petschelt, A.; Eliades, G. The effect of resin composite pre-heating on monomer conversion and polymerization shrinkage. *Dent. Mater.* **2009**, *25*, 514–519. [CrossRef] [PubMed]
4. Loumprinis, N.; Maier, E.; Belli, R.; Petschelt, A.; Eliades, G.; Lohbauer, U. Viscosity and stickiness of dental resin composites at elevated temperatures. *Dent. Mater.* **2021**, *37*, 413–422. [CrossRef] [PubMed]
5. Opdam, N.J.; Roeters, J.J.; Peters, T.C.; Burgersdijk, R.C.; Kuijs, R.H. Consistency of resin composites for posterior use. *Dent. Mater.* **1996**, *12*, 350–354. [CrossRef]
6. Elbishari, H.; Satterthwaite, J.; Silikas, N. Effect of filler size and temperature on packing stress and viscosity of resin-composites. *Int. J. Mol. Sci.* **2011**, *12*, 5330–5338. [CrossRef]
7. Baroudi, K.; Rodrigues, J.C. Flowable resin composites: A systematic review and clinical considerations. *J. Clin. Diagn. Res.* **2015**, *9*, ZE18–ZE24. [CrossRef]
8. Al-Ahdal, K.; Silikas, N.; Watts, D.C. Rheological properties of resin composites according to variations in composition and temperature. *Dent. Mater.* **2014**, *30*, 517–524. [CrossRef]
9. Wagner, W.C.; Aksu, M.N.; Neme, A.M.; Linger, J.B.; Pink, F.E.; Walker, S. Effect of pre-heating resin composite on restoration microleakage. *Oper. Dent.* **2008**, *33*, 72–78. [CrossRef]
10. Daronch, M.; Rueggeberg, F.A.; De Goes, M.F. Monomer conversion of pre-heated composite. *J. Dent. Res.* **2005**, *84*, 663–667. [CrossRef]
11. Nada, K.; El-Mowafy, O. Effect of precuring warming on mechanical properties of restorative composites. *Int. J. Dent.* **2011**, *2011*, 536212. [CrossRef]
12. Kampanas, N.S. Resin composite pre-heating—A literature review of the laboratory results. *Int. J. Oral Dent. Health* **2018**, *4*, 074.
13. Lempel, E.; Czibulya, Z.; Kovács, B.; Szalma, J.; Tóth, Á.; Kunsági-Máté, S.; Varga, Z.; Böddi, K. Degree of conversion and BisGMA, TEGDMA, UDMA elution from flowable bulk fill composites. *Int. J. Mol. Sci.* **2016**, *7*, 732. [CrossRef]
14. Silva, G.S.; Almeida, G.; Poskus, L.T.; Guimarães, J.G. Relationship between the degree of conversion; solubility and salivary sorption of a hybrid and nanofilled resin composite: Influence of the light activation mode. *Appl. Oral Sci.* **2008**, *16*, 161–166. [CrossRef]
15. Moldovan, M.; Balazsi, R.; Soanca, A.; Roman, A.; Sarosi, C.; Prodan, D.; Vlassa, M.; Cojocaru, I.; Saceleanu, V.; Cristescu, I. Evaluation of the degree of conversion, residual monomers and mechanical properties of some light-cured dental resin composites. *Materials* **2019**, *12*, 2109. [CrossRef]
16. Colombo, M.; Gallo, S.; Poggio, C.; Ricaldone, V.; Arciola, C.R.; Scribante, A. New resin-based bulk-fill composites: In vitro evaluation of micro-hardness and depth of cure as infection risk indexes. *Materials* **2020**, *13*, 1308. [CrossRef]
17. Lempel, E.; Czibulya, Z.; Kunsági-Máté, S.; Szalma, J.; Sümegi, B.; Böddi, K. Quantification of conversion degree and monomer elution from dental composite using HPLC and micro-Raman spectroscopy. *Chromatographia* **2014**, *77*, 1137–1144. [CrossRef]
18. Durner, J.; Obermaier, J.; Draenert, M.; Ilie, N. Correlation of the degree of conversion with the amount of elutable substances in nano-hybrid dental composites. *Dent. Mater.* **2012**, *28*, 1146–1153. [CrossRef]
19. El-Korashy, D.I. Post-gel shrinkage strain and degree of conversion of preheated resin composite cured using different regimens. *Oper. Dent.* **2010**, *35*, 172–179. [CrossRef]
20. Daronch, M.; Rueggeberg, F.A.; De Goes, M.F.; Giudici, R. Polymerization kinetics of pre-heated composite. *J. Dent. Res.* **2006**, *85*, 38–43. [CrossRef]
21. Ferracane, J. Elution of leachable components from composites. *J. Oral Rehabil.* **1994**, *21*, 441–452. [CrossRef] [PubMed]
22. Barszczewska-Rybarek, I.M. A guide through the dental dimethacrylate polymer network structural characterization and interpretation of physico-mechanical properties. *Materials* **2019**, *12*, 4047. [CrossRef] [PubMed]
23. Lempel, E.; Őri, Z.; Szalma, J.; Lovász, B.V.; Kiss, A.; Tóth, Á.; Kunsági-Máté, S. Effect of exposure time and pre-heating on the conversion degree of conventional, bulk-fill, fibre-reinforced and polyacid-modified resin composites. *Dent. Mater.* **2019**, *35*, 217–228. [CrossRef] [PubMed]
24. Daronch, M.; Rueggeberg, F.A.; Moss, L.; de Goes, M.F. Clinically relevant issues related to preheating composites. *J. Esthet. Restor. Dent.* **2006**, *18*, 340–350. [CrossRef] [PubMed]
25. Fróes-Salgado, N.R.; Silva, L.M.; Kawano, Y.; Francci, C.; Reis, A.; Loguercio, A.D. Composite pre-heating: Effects on marginal adaptation, degree of conversion and mechanical properties. *Dent. Mater.* **2010**, *26*, 908–914. [CrossRef]

26. Kincses, D.; Böddi, K.; Őri, Z.; Lovász, B.V.; Jeges, S.; Szalma, J.; Kunsági-Máté, S.; Lempel, E. Pre-heating effect on monomer elution and degree of conversion of contemporary and thermoviscous bulk-fill resin-based composites. *Polymers* **2021**, *13*, 3599. [CrossRef]
27. Franz, A.; Konig, F.; Lucas, T.; Watts, D.C.; Schedle, A. Cytotoxic effects of dental bonding substances as a function of degree of conversion. *Dent. Mater.* **2009**, *25*, 232–239. [CrossRef]
28. Murray, P.E.; Garcia–Godoy, C.; Garcia–Godoy, F. How is the biocompatibility of dental biomaterials evaluated? *Med. Oral Pathol. Oral Chir. Buccal* **2007**, *12*, E258–E266.
29. Demirel, G.; Orhan, A.I.; Irmak, Ö.; Aydin, F.; Buyuksungur, A.; Bilecenoğlu, B.; Orhan, K. Micro-computed tomographic evaluation of the effects of pre-heating and sonic delivery on the internal void formation of bulk-fill composites. *Dent. Mater. J.* **2021**, *40*, 525–531. [CrossRef]
30. Sun, J.; Lin-Gibson, S. X-ray microcomputed tomography for measuring polymerization shrinkage of polymeric dental composites. *Dent. Mater.* **2008**, *24*, 228–234. [CrossRef]
31. Samet, N.; Kwon, K.R.; Good, P.; Weber, H.-P. Voids and interlayer gaps in Class 1 posterior composite restorations: A comparison between a microlayer and a 2-layer technique. *Quintessence Int.* **2006**, *37*, 803–809.
32. Ironside, J.G.; Makinson, O.F. Resin restorations: Causes of porosities. *Quintessence Int.* **1993**, *24*, 867–873.
33. Malkoç, M.A.; Sevimay, M.; Tatar, İ.; Çelik, H.H. Micro-CT detection and characterization of porosity in luting cements. *J. Prosthodont.* **2015**, *24*, 553–561. [CrossRef]
34. Hiramatsu, D.A.; Moretti-Neto, R.T.; Ferraz, B.F.R.; Porto, V.C.; Rubo, J.H. Roughness and porosity of provisional crowns. *Pós-Grad. Rev.* **2011**, *18*, 108–112.
35. Opdam, N.J.; Roeters, J.J.; Joosten, M.; Veeke, O. Porosities and voids in Class I restorations placed by six operators using a packable or syringable composite. *Dent. Mater.* **2002**, *18*, 58–63. [CrossRef]
36. Zhao, X.Y.; Zhang, W.; Lee, S.; Roggenkamp, C.L. The porosities or voids included in composite resin restorations. *Adv. Mater. Res.* **2013**, *833*, 349–354.
37. Chuang, S.F.; Jin, Y.T.; Lin, T.S.; Chang, C.H.; Garcia-Godoy, F. Effects of lining materials on microleakage and internal voids of Class II resin-based composite restorations. *Am. J. Dent.* **2003**, *16*, 84–90.
38. Mullejans, R.; Lang, H.; Schuler, N.; Baldawi, M.O.; Raab, W.H. Increment technique for extended Class V restorations: An experimental study. *Oper. Dent.* **2003**, *28*, 352–356.
39. Balthazard, R.; Jager, S.; Dahoun, A.; Gerdolle, D.; Engels-Deutsch, M.; Mortie, E. High-resolution tomography study of the porosity of three restorative resin composites. *Clin. Oral. Investig.* **2014**, *18*, 1613–1618. [CrossRef]
40. Buelvas, D.D.A.; Besegato, J.F.; Vicentin, B.L.S.; Jussiani, E.I.; Hoeppner, M.G.; Andrello, A.C.; Di Mauro, E. Impact of light-cure protocols on the porosity and shrinkage of commercial bulk fill resin composites with different flowability. *J. Polym. Res.* **2020**, *27*, 292. [CrossRef]
41. Yang, J.; Silikas, N.; Watts, D.C. Pre-heating effects on extrusion force, stickiness and packability of resin-based composite. *Dent. Mater.* **2019**, *35*, 1594–1602. [CrossRef] [PubMed]
42. Tauböck, T.T.; Tarle, Z.; Marovic, D.; Attin, T. Pre-heating of high-viscosity bulk-fill resin composites: Effects on shrinkage force and monomer conversion. *J. Dent.* **2015**, *43*, 1358–1364. [CrossRef] [PubMed]
43. Atai, M.; Ahmadi, M.; Babanzadeh, S.; Watts, D.C. Synthesis, characterization, shrinkage and curing kinetics of a new low-shrinkage urethane dimethacrylate monomer for dental application. *Dent. Mater.* **2007**, *23*, 1030–1041.
44. Marcondes, R.L.; Lima, V.P.; Barbon, F.J.; Isolan, C.P.; Carvalho, M.A.; Salvador, M.V.; Lima, A.F.; Moraes, R.R. Viscosity and thermal kinetics of 10 preheated restorative resin composites and effect of ultrasound energy on film thickness. *Dent. Mater.* **2020**, *36*, 1356–1364. [CrossRef] [PubMed]
45. Anseth, K.S.; Newman, S.M.; Bowman, C.M. Polymeric dental composites: Properties and reaction behavior of multimethacrylate dental restorations. *Adv. Polym. Sci.* **1995**, *122*, 177–217.
46. Gauthier, M.A.; Stangel, I.; Ellis, T.H.; Zhy, X.X. Oxygen inhibition in dental resins. *J. Dent. Res.* **2005**, *84*, 725–729. [CrossRef]
47. Guo, X.; Yu, Y.; Gao, S.; Zhang, Z.; Zhao, H. Biodegradation of dental resin-based compositeZEA potential factor affecting the bonding effect: A narrative review. *Biomedicines* **2022**, *10*, 2313. [CrossRef]
48. Sideridou, I.D.; Achilias, D.S.; Karabela, M.M. Sorption kinetics of ethanol/water solution by dimethacrylate-based dental resins and resin composites. *J. Biomed. Mater. Res. B Appl. Biomater.* **2007**, *81*, 207–218. [CrossRef]
49. Lempel, E.; Őri, Z.; Kincses, D.; Lovász, B.V.; Kunsági-Máté, S.; Szalma, J. Degree of conversion and in vitro temperature rise of pulp chamber during polymerization of flowable and sculptable conventional, bulk-fill and short-fibre reinforced resin composite. *Dent. Mater.* **2021**, *37*, 983–997. [CrossRef]
50. Pluddemann, E.P. Silane coupling agents. In *Plenum*; Springer: New York, NY, USA, 1982; p. 111.
51. Pongprueksa, P.; De Munck, J.; Duca, R.C.; Poels, K.; Covaci, A.; Hoet, P. Monomer elution in relation to degree of conversion for different types of composite. *J. Dent.* **2015**, *43*, 1448–1455. [CrossRef]
52. Chaharom, M.E.E.; Safyari, L.; Safarvand, H.; Jafari-Navimipour, E.; Alizadeh-Oskoee, P.; Ajami, A.A.; Abed-Kahnamouei, M.; Bahari, M. The effect of pre-heating on monomer elution from bulk-fill resin composites. *J. Clin. Exp. Dent.* **2020**, *12*, e813–e820. [CrossRef]
53. Deb, S.; Di Silvio, L.; Mackler, H.E.; Millar, B.J. Pre-warming of dental composites. *Dent. Mater.* **2011**, *27*, e51–e59. [CrossRef]

54. Łagocka, R.; Mazurek-Mochol, M.; Jakubowska, K.; Bendyk-Szeffer, M.; Chlubek, D.; Buczkowska-Radlinska, J. Analysis of base monomer elution from 3 flowable bulk-fill composite resins using high performance liquid chromatography (HPLC). *Med. Sci. Monit.* **2018**, *24*, 4679–4690. [CrossRef]
55. Sideridou, I.D.; Karabela, M.M. Effect of the amount of 3-methacryloxypropyltrimethoxysilane coupling agent on physical properties of dental resin nanocomposites. *Dent. Mater.* **2009**, *25*, 1315–1324. [CrossRef]
56. Szczesio-Wlodarczyk, A.; Sokolowski, J.; Kleczewska, J.; Bociong, K. Ageing of dental composites based on methacrylate resins-A critical review of the causes and method of assessment. *Polymers* **2020**, *12*, 882. [CrossRef]
57. Polydorou, O.; Huberty, C.; Wolkewitz, M.; Bolek, R.; Hellwig, E.; Kümmerer, K. The effect of storage medium on the elution of monomers from composite materials. *J. Biomed. Mater. Res. B Appl. Biomater.* **2012**, *100*, 68–74. [CrossRef]
58. Tanaka, K.; Taira, M.; Shintani, H.; Wakasa, K.; Yamaki, M. Residual monomers (TEGDMA and Bis-GMA) of a set visible-light-cured dental composite resin when immersed in water. *J. Oral Rehabil.* **1991**, *18*, 353–362. [CrossRef]
59. Moad, C.L.; Moad, G. Fundamentals of reversible addition–fragmentation chain transfer (RAFT). *Chem. Teach. Int. Best Pract. Chem. Educ.* **2021**, *3*, 3–17. [CrossRef]
60. Gorsche, C.; Koch, T.; Moszner, N.; Liska, R. Exploring the benefits of β-allyl sulfones for more homogeneous dimethacrylate photopolymer networks. *Polym. Chem.* **2015**, *6*, 2038–2047. [CrossRef]
61. Padam, S. Sample size for experimental studies. *J. Clin. Prev. Card.* **2012**, *1*, 88–93.

International Journal of
Molecular Sciences

MDPI

Article

N-Acetyl Cysteine-Mediated Improvements in Dental Restorative Material Biocompatibility

Takanori Matsuura, Keiji Komatsu and Takahiro Ogawa *

Weintraub Center for Reconstructive Biotechnology, Division of Regenerative and Reconstructive Sciences, UCLA School of Dentistry, Los Angeles, CA 90095, USA
* Correspondence: togawa@dentistry.ucla.edu; Tel.: +1-310-794-7653; Fax: +1-310-825-6345

Abstract: The fibroblast-rich gingival tissue is usually in contact with or adjacent to cytotoxic polymer-based dental restoration materials. The objective of this study was to determine whether the antioxidant amino acid, N-acetyl cysteine (NAC), reduces the toxicity of dental restorative materials. Human oral fibroblasts were cultured with bis-acrylic, flowable composite, bulk-fill composite, self-curing acrylic, and titanium alloy test specimens. Cellular behavior and function were analyzed on and around the materials. Impregnation of the bulk-fill composite and self-curing acrylic with NAC reduced their toxicity, improving the attachment, growth, and function of human oral fibroblasts on and around the materials. These mitigating effects were NAC dose dependent. However, NAC impregnation of the bis-acrylic and flowable composite was ineffective, with no cells attaching to nor around the materials. Although supplementing the culture medium with NAC also effectively improved fibroblast behaviors, direct impregnation of materials with NAC was more effective than supplementing the cultures. NAC-mediated improvements in fibroblast behavior were associated with reduced production of reactive oxygen species and oxidized glutathione together with increased glutathione reserves, indicating that NAC effectively directly scavenged ROS from materials and reinforced the cellular antioxidant defense system. These results establish a proof of concept of NAC-mediated improvements in biocompatibility in the selected dental restorative materials.

Keywords: fibroblast; composite; PMMA; reactive oxygen spices (ROS); glutathione

Citation: Matsuura, T.; Komatsu, K.; Ogawa, T. N-Acetyl Cysteine-Mediated Improvements in Dental Restorative Material Biocompatibility. *Int. J. Mol. Sci.* **2022**, *23*, 15869. https://doi.org/10.3390/ijms232415869

Academic Editor: Ihtesham Ur Rehman

Received: 23 November 2022
Accepted: 12 December 2022
Published: 14 December 2022

Publisher's Note: MDPI stays neutral with regard to jurisdictional claims in published maps and institutional affiliations.

Copyright: © 2022 by the authors. Licensee MDPI, Basel, Switzerland. This article is an open access article distributed under the terms and conditions of the Creative Commons Attribution (CC BY) license (https://creativecommons.org/licenses/by/4.0/).

1. Introduction

Polymer- or resin-based materials are routinely used in various dental procedures, including but not limited to filling cavities, making dentures, and fabricating provisional crowns and implant provisional restorations [1–10]. All these procedures either pave the way for final restorations or represent a transitional phase of treatment important for successful restoration and clinical outcomes. These materials must therefore be fully biocompatible [9–12]. There are many different polymer-based restorative materials, including self-curing poly(methyl methacrylate) (PMMA) acrylics, bis-acrylics, and composite resins. These materials have fundamentally different compositions, i.e., self-curing acrylics are based on PMMA, whereas bis-acrylics contain acrylates and methacrylates with silicate glass filler particles. Composite materials consist of bisphenol A-glycidyl methacrylate (Bis-GMA) and urethane dimethacrylate (UDMA). Furthermore, different materials use different polymerization initiators. Unfortunately, although specific toxicities remain unquantified, there are general concerns that current polymer-based materials are all toxic to some degree, compromising biocompatibility [3,8–10,12–21].

However, there is a critical knowledge gap regarding material biocompatibility, clinical relevancy and impact, and the choice of material [21–29]. For instance, in dental implant practice, where peri-implant gingival inflammation is a clinical problem, materials are empirically chosen for implant provisional restorations with little consideration of their biological properties. In cavity fillings, provisional crowns, and implant provisional restorations, polymer-based materials are often in direct contact and/or close to the gingival

tissue. For instance, provisional crowns and cavity fillings can be either sub-gingival or supra-gingival, depending on the prosthetic strategy and extent of decay, while implant provisional restorations are mostly placed sub-gingivally. Given these diverse clinical situations, the biological impact of even a single material might be quite variable.

N-acetyl cysteine (NAC), the acetylated form of the amino acid L-cysteine, is a biochemically safe molecule used in the management of various diseases such as pneumonia and bronchitis [30–35]. Its thiol (sulfhydryl) group imparts a direct antioxidant effect and neutralizes free radicals. NAC is also a precursor of glutathione, the strongest antioxidant scavenger in the body. It has been shown that adding NAC into orthopedic acrylic bone cement significantly mitigates its toxicity by effectively scavenging polymerization radicals [36–39]. Functionally, osteoblasts can survive on NAC-impregnated bone cement but not on control bone cement [38,40]. Orthopedic bone cement and dental materials based on polymers differ with respect to their other ingredients and polymerization initiators [37,41], and of the many polymer-based materials available, most have not been tested in the context of dental restorations [42–48]. In particular, dental restorative materials with photoinitiators are empirically considered less toxic due to their presumed complete polymerization, but this still requires biological proof.

Here, we quantified the biocompatibility of different dental restorative materials (self-curing PMMA, bis-acrylic, and two types of composite resin, with titanium alloy used as a biocompatible control) by examining their impact on the behavior and function of human oral fibroblasts. Fibroblast functions were examined both in direct contact with and in close proximity to the materials. Materials with low biocompatibility were impregnated with NAC in an effort to decrease their toxicity. Subsequently, we explored the mechanisms underlying NAC-mediated detoxification by examining intracellular reactive oxygen species (ROS) production and glutathione redox system stimulation.

2. Results

2.1. Initial Cell Attachment

Initial cell attachment was evaluated after two days of culture in both contact (i.e., growing on the material) and proximity (i.e., growing around the material) assays. In contact experiments, fibroblasts attached to the titanium alloy and minimally to the self-curing acrylic, but not to bis-acrylic, flowable composite, or bulk-fill composite materials (Figure 1A). In proximity experiments, fibroblasts survived and attached to the culture dish around the titanium alloy and self-curing acrylic (to a greater extent than in contact experiments; Figure 1B). There was also some fibroblast attachment to the culture dish around the bulk-fill composite.

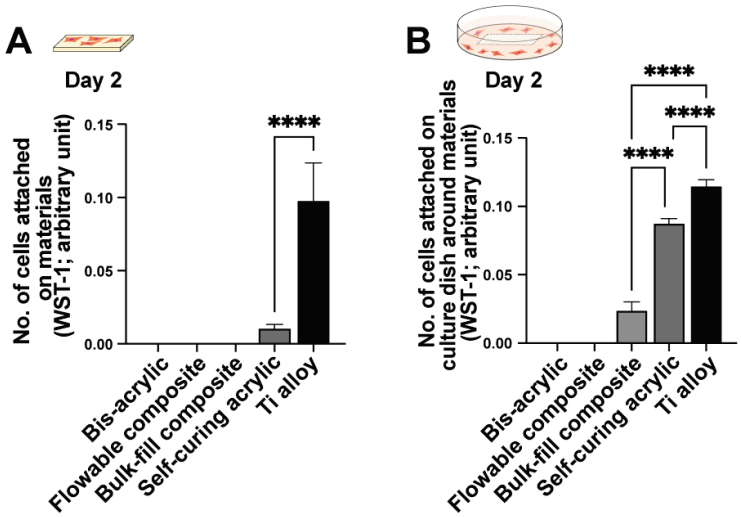


Figure 1. Initial attachment of fibroblasts to and around various dental restorative materials. Titanium alloy was used as a control. Contact (**A**) and proximity (**B**) experiments were performed. The WST-1

assay was performed on culture day two to quantify the number of cells attached to each material (**A**) and in the culture well around each material (**B**): **** $p < 0.0001$.

2.2. Cell Proliferation

The number of fibroblasts cultured with different materials was measured after four and six days of culture in contact and proximity assays. Cells were only detected on the self-curing acrylic and titanium alloy in contact experiments (Figure 2A), increasing from day four to six on the titanium alloy but not the self-curing acrylic. In proximity experiments, more cells grew around the self-curing acrylic than in the contact experiment (Figure 2B), increasing from day four to day six. A few fibroblasts grew around the bulk-fill composite in the proximity experiment, but there was no cell growth on or around the bis-acrylic and flowable composite.

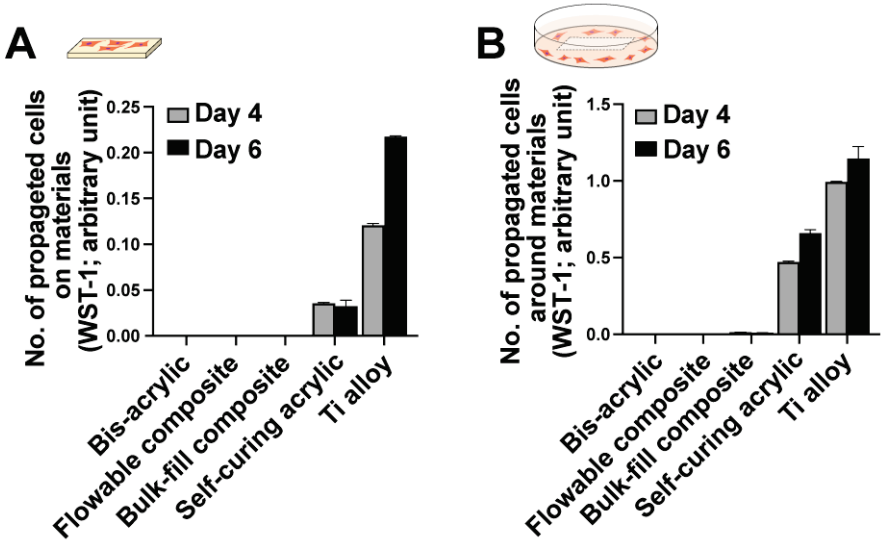


Figure 2. Propagation of fibroblasts on and around various dental restorative materials. Contact (**A**) and proximity (**B**) experiments were performed. The WST-1 assay was performed on culture days four and six to quantify the number of cells propagated on each material (**A**) and in the culture well around each material (**B**).

2.3. NAC-Dependent Improvements in Initial Cell Attachment

To determine whether NAC detoxifies or mitigates the toxicity of the materials, we impregnated NAC into all the materials at two different concentrations, 3% and 6%. On day two, no cells were observed on or around the bis-acrylic and flowable composite even when impregnated with NAC at either concentration. However, there was significantly more growth in and around the NAC-impregnated bulk-fill composite and self-curing acrylic than native forms (Figure 3). Some cells survived and attached on the NAC-impregnated bulk-fill composite (Figure 3A), with more cells attaching at the higher NAC concentration. In the proximity experiment, there was a dose-dependent increase in the number of cells around the NAC-impregnated bulk-fill composite (Figure 3B), while there was also a clear dose-dependent increase in the number of cells around the NAC-impregnated self-curing acrylic in both the contact and proximity experiments (Figure 3C,D). Of note, with 6% NAC, the cell count was equivalent to that observed with the titanium alloy.

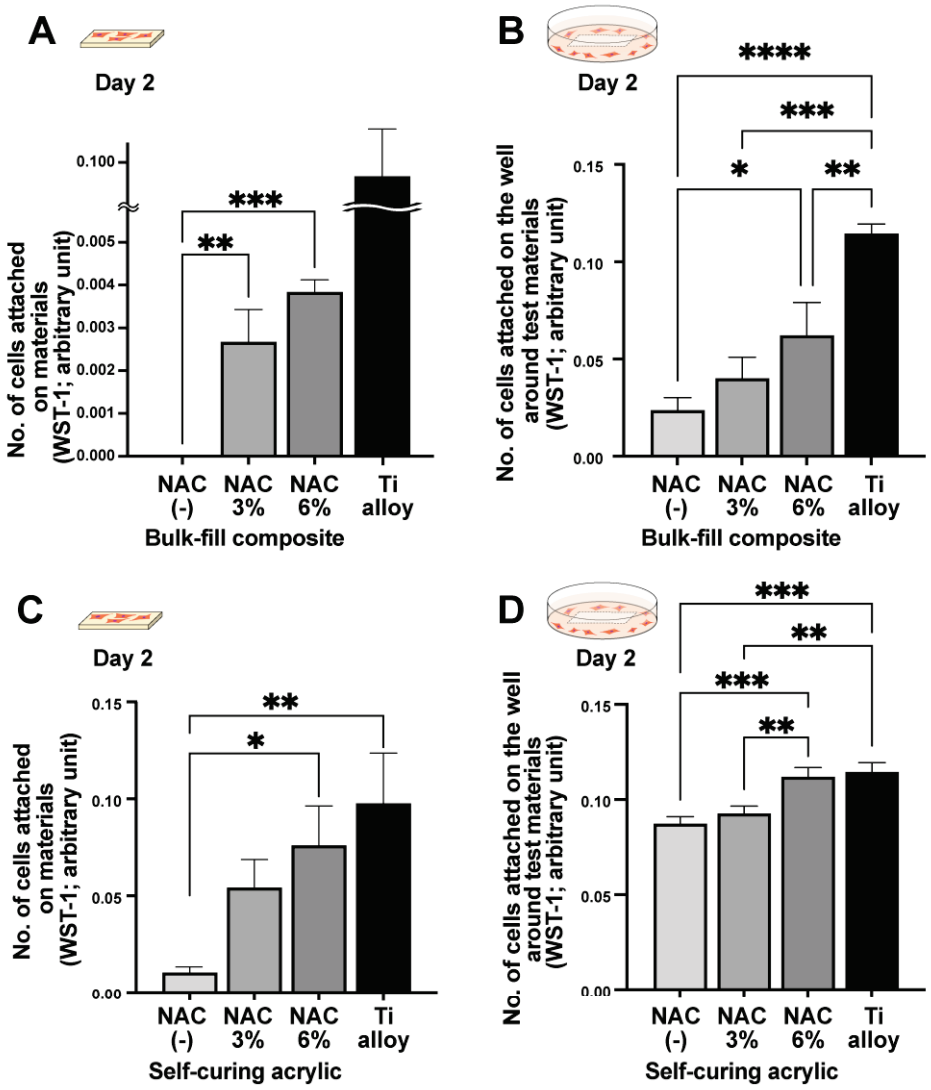


Figure 3. NAC-mediated improvements in material biocompatibility. NAC was impregnated into the materials at two different concentrations. Results of WST-1 assays performed on day two to quantify the number of cells attaching to bulk-fill composite (**A**) and to the well around bulk-fill composite (**B**). The number of cells attaching to self-curing acrylic (**C**) and to the well around self-curing acrylic (**D**): * $p < 0.05$, ** $p < 0.01$, *** $p < 0.001$, and **** $p < 0.0001$.

2.4. NAC-Dependent Improvements in Cellular Propagation

Similar to day two cell attachment results, significantly more fibroblasts survived and propagated after NAC impregnation at four and six days of culture. No cells were quantifiable on or around the bis-acrylic and flowable composite after four and six days of culture regardless of the NAC concentration. Therefore, only the bulk-fill composite and self-curing acrylic results are presented (Figure 4A–D). In general, the number of cells increased in an NAC dose-dependent manner. NAC more effectively reduced the toxicity of the self-curing acrylic than the bulk-fill composite, with cellular proliferation on and around the self-curing acrylic similar to the titanium alloy. However, NAC had a greater relative effect on the bulk-fill composite than the self-curing acrylic, increasing proliferation from a baseline of zero. Fluorescence microscopy with image-based cell counting confirmed an NAC dose-dependent effect on the bulk-fill composite and self-curing acrylic (Figure 5).

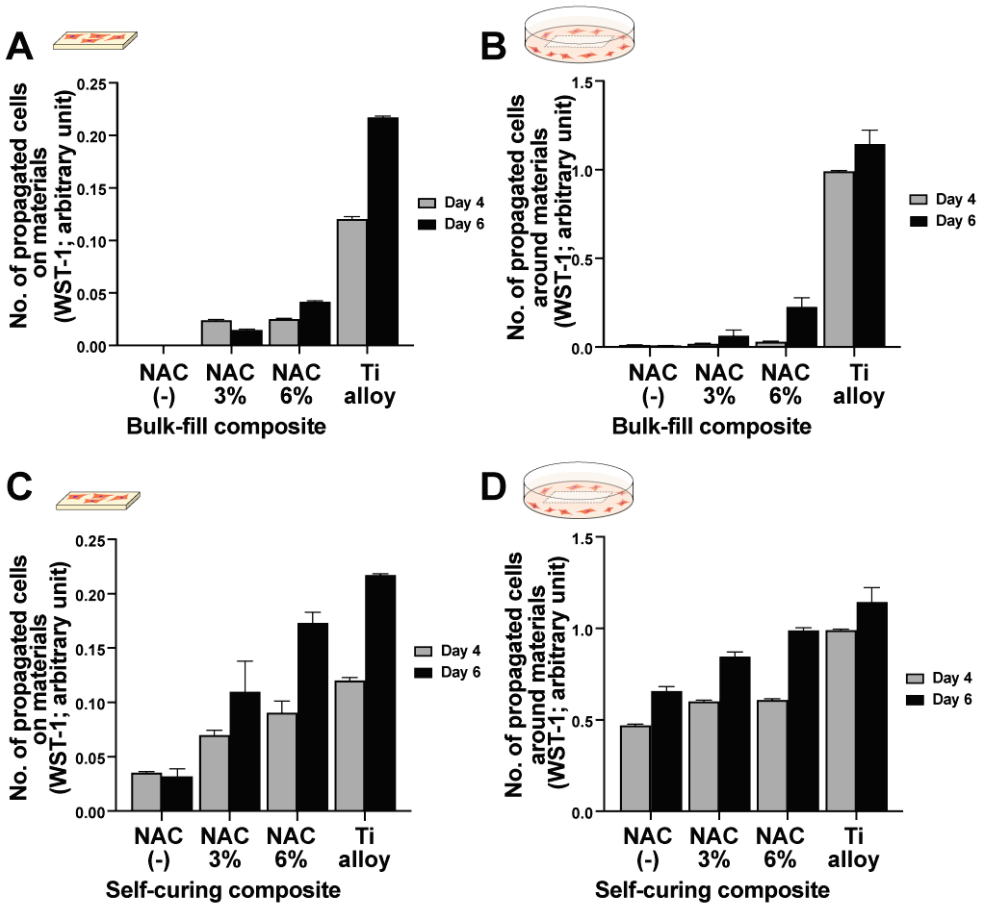


Figure 4. NAC-mediated improvements in material biocompatibility. WST-1 assays were performed on days four and six to quantify the number of cells proliferating on bulk-fill composite (**A**) and around bulk-fill composite (**B**). The number of cells proliferating on self-curing acrylic (**C**) and around self-curing acrylic (**D**).

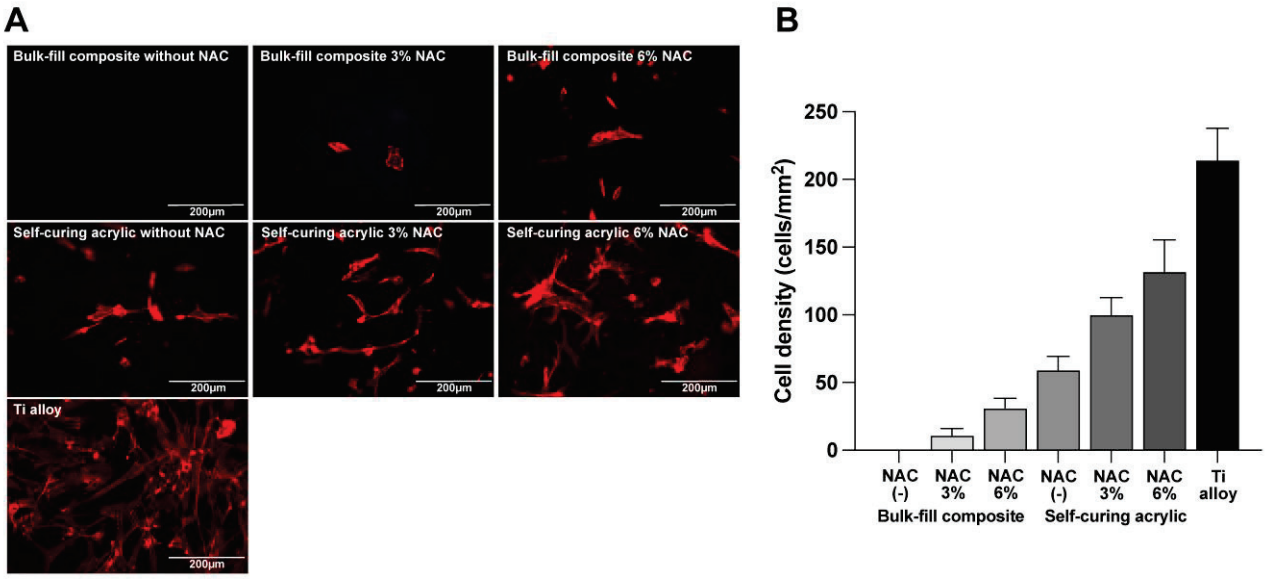


Figure 5. Fibroblasts visualized on materials with or without NAC impregnation. (**A**) Fluorescence microscopy images of fibroblasts on culture day four stained for cytoskeletal actin filaments (red). (**B**) Cell density was quantified based on the images.

2.5. NAC-Dependent Changes in Fibroblast Gene Expression

We next examined the expression of fibroblast-related genes in fibroblasts grown on and around the materials with or without NAC. Given that no cells were detected on or around the bis-acrylic and flowable composite regardless of NAC impregnation, only results for the bulk-fill composite and self-curing acrylic are presented (Figure 6). In contact experiments, fibroblasts growing on the self-curing acrylic expressed significantly more type 1 collagen alpha in an NAC dose-dependent manner (Figure 6A). Collagen type 3 alpha expression also increased in cells grown on the self-curing acrylic impregnated with NAC, but to a much lesser degree than on the titanium alloy (Figure 6B). No collagen type 1 or 3 expression was detected in cultures with the bulk-fill composite with or without NAC in contact experiments (Figure 6A,B). In proximity experiments, there were significant increases in both collagen type 1 and 3 expression in the self-curing acrylic cultures with NAC, but not in a dose-dependent manner (Figure 6A,B). In cultures with the bulk-fill composite, the gene expression was exclusively detected in the presence of NAC impregnation.

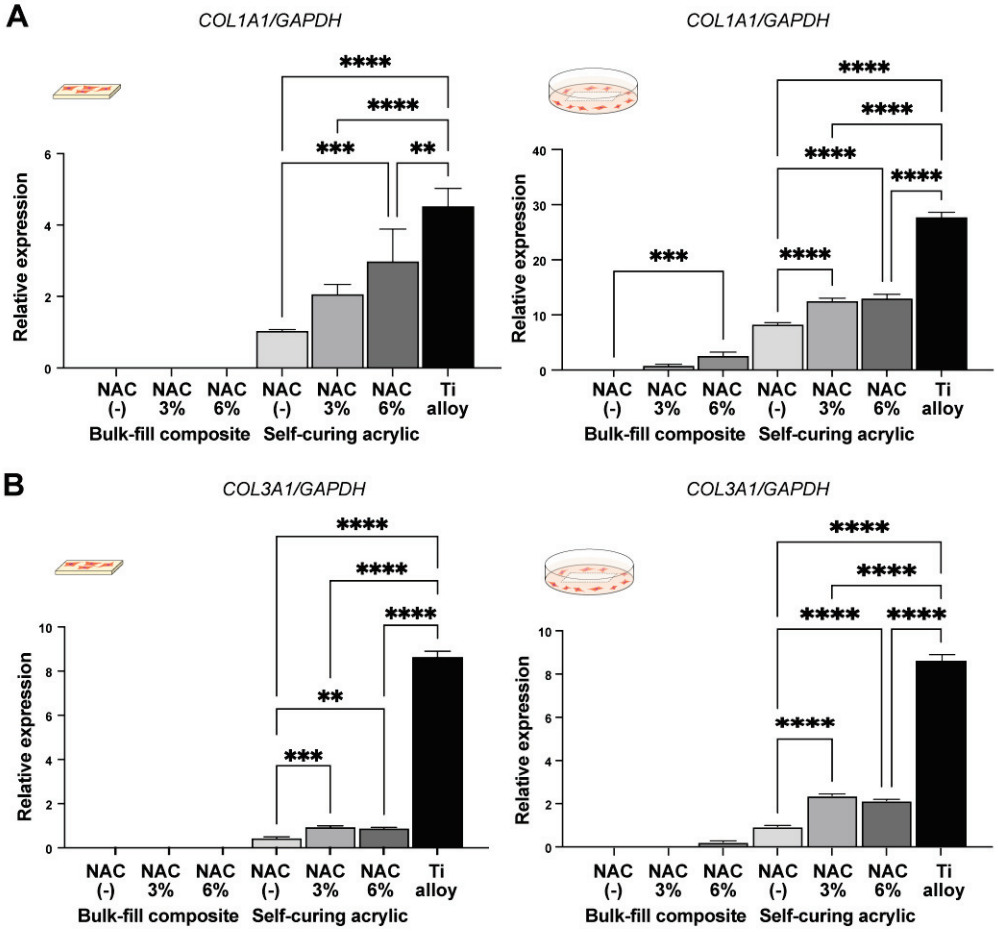


Figure 6. NAC-mediated improvements in material biocompatibility. Real-time PCR for collagen type 1 (**A**) and 3 (**B**) genes conducted on day four are shown. RNA was extracted from contact and proximity experiments: ** $p < 0.01$, *** $p < 0.001$, **** $p < 0.0001$.

2.6. Effect of NAC Administration Type on Biocompatibility

We next examined the effect of NAC impregnation or culture supplementation on cell counts on and around the self-curing acrylic on day two. In contact experiments, NAC impregnation more effectively promoted cell attachment than supplementation (Figure 7A); indeed, adding NAC to the medium failed to significantly increase the cell count compared with control. Conversely, in proximity experiments, supplementing the medium with NAC

was more effective than impregnation (Figure 7B), with an equivalent number of cells counted around the self-curing acrylic as around the titanium alloy.

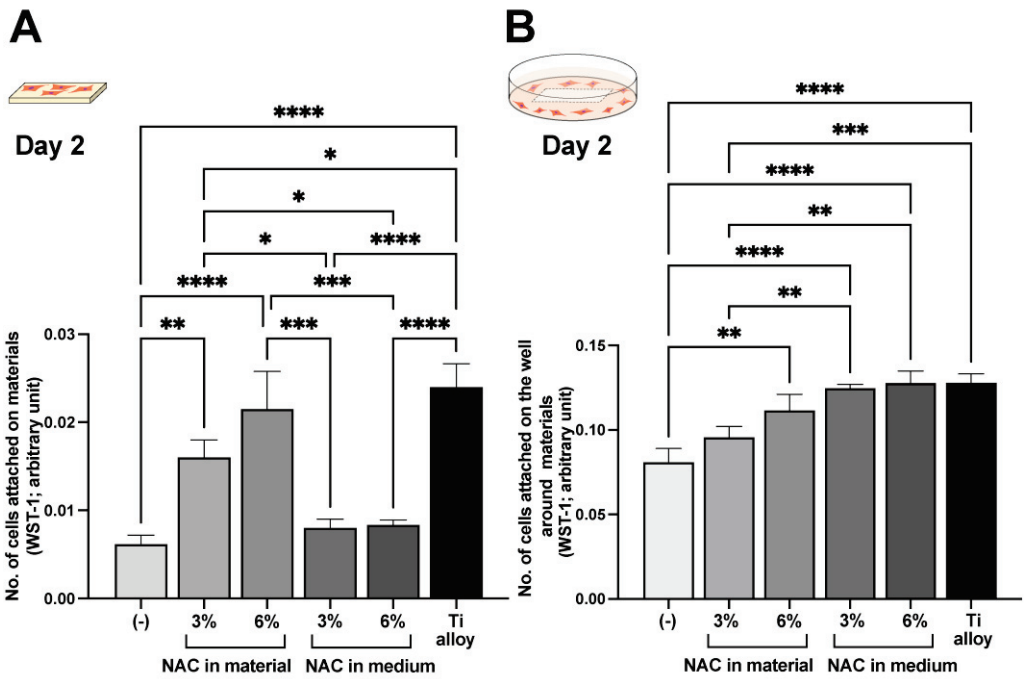


Figure 7. Effects of NAC administration methods. NAC was administered by material impregnation or by supplementing in the culture medium. The WST-1 assay was conducted on culture day two to quantify the number of cells attached to each material (**A**) and to the culture well around each material (**B**). Note that the same amount of NAC was added between the impregnation and supplementation methods. See the Materials and Methods sections for details: * $p < 0.05$, ** $p < 0.01$, *** $p < 0.001$, and **** $p < 0.0001$.

2.7. NAC-Dependent Activation of the Antioxidant Redox System

To understand the mechanism underlying the NAC-mediated effects on fibroblast viability and gene expression, we first assessed NAC-dependent changes in reactive oxygen species (ROS) production by fibroblasts in proximity experiments around the bulk-fill composite and self-curing acrylic. There was a clear trend in decreasing ROS production with increasing NAC concentration for both materials (Figure 8A), especially for the bulk-fill composite due to the higher baseline. ROS levels around the 6% NAC-impregnated self-curing acrylic were nearly equal to those around the titanium alloy.

Finally, we examined reduced and oxidized glutathione (GSH/GSSG) levels in fibroblasts in the proximity assay (Figure 8B–D). GSSG decreased around the bulk-fill composite impregnated with NAC in a dose-dependent manner (Figure 8B), whereas GSSG levels around the self-curing acrylic remained low and were not significantly affected by NAC. Although GSH levels were low around the bulk-fill composite, NAC impregnation significantly increased the levels (Figure 8C). NAC significantly increased GSH levels around the self-curing acrylic in a dose-dependent manner, while the GSSG/GSH ratio decreased with increasing NAC around both materials (Figure 8D).

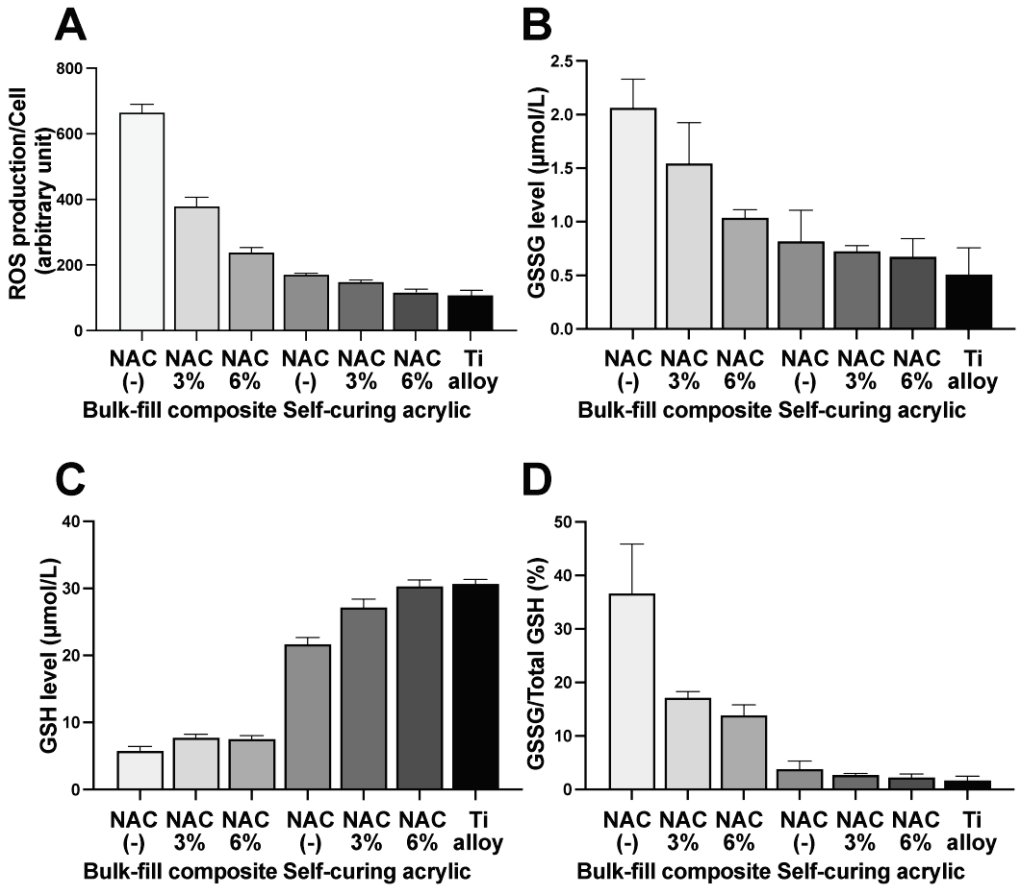


Figure 8. NAC-mediated improvements in antioxidant defenses. (**A**) ROS levels in fibroblasts collected from the proximity experiment. (**B**) GSSG (glutathione disulfide, an oxidized form of glutathione) levels in fibroblasts collected from proximity experiment. (**C**) GSH (a reduced form of glutathione) levels in fibroblasts collected from proximity experiments. (**D**) GSSH/GSH in fibroblasts collected from the proximity experiment.

3. Discussion

Here we show that NAC can mitigate against the adverse cytotoxic effects of polymer-based dental restoration materials. There were, however, limits to the observed effect at the NAC concentrations tested here; for instance, NAC did not significantly improve the biocompatibility of the flowable composite to exert a biological impact. Self-curing acrylic was most improved by NAC, with impregnation with 6% NAC producing similar biocompatibility to the titanium alloy, i.e., improving the biocompatibility from biotolerant to bioinert [49–55]. NAC impregnation of the bulk-fill composite resulted in some cell attachment from a baseline of zero without impregnation, i.e., improving the material biocompatibility from lethal to biotolerant. Of note, the biological impact differed depending on whether the fibroblasts were in contact with or in close proximity to the materials, with a general trend of lower material toxicity in proximity experiments with fibroblast attachment and gene expression even for the bulk-fill composite. In particular, initial cell attachment in proximity to the NAC-impregnated self-curing acrylic was similar to that around the titanium alloy, albeit with subsequently impaired proliferation and gene expression at later time points.

Discriminating between the effects of NAC impregnation and supplementation provided important mechanistic insights. NAC impregnation of the material, but not the medium, significantly improved cellular attachment to self-curing resin. However, adjacent cells benefitted much more from NAC supplementation of the medium. These results indicate that (1) the material was very toxic and treatment of the cells was not sufficient to

maintain cellular viability; (2) to rescue cells growing on materials, detoxification of the material rather than the environment with NAC was necessary; (3) cells adjacent to the material are subjected to less toxicity, so NAC treatment in the medium was more effective; (4) nonetheless, impregnation of the material with NAC was effective both for contacting and adjacent cells.

There are three possible pathways by which NAC might improve cellular function on and around the materials. The first is NAC-mediated scavenging of free radicals, monomer remnants, and other ROS within materials; NAC acts as a direct ROS scavenger due to its redox potential as a thiol donor [38,39,43,44,56,57]. A significant reduction in polymerization radicals and other oxidative stresses by NAC was demonstrated in bone cement [38,58]. This pathway could explain the considerable improvement in cellular function seen in both contact and proximity experiments. Indeed, levels of GSSH (glutathione disulfide), the oxidized form of glutathione, decreased with increasing NAC, indicating that glutathione (GSH), a major redox system within cells, was not depleted. The second pathway is the release of NAC from a material into the local environment, where it might permeate into or be taken up by cells. In addition to direct scavenging, NAC is a precursor of glutathione, a major antioxidant defense system, and it increases glutathione reserves. The third pathway would be NAC scavenging ROS released from a material. The latter two pathways could in part explain the biological improvements seen in proximity experiments. These two pathways were demonstrated in osteoblasts on NAC-impregnated bone cement [38]. Indeed, this study demonstrated that the ROS in fibroblasts were inversely correlated with the impregnated NAC dose. Furthermore, cellular GSH increased with NAC concentration in the material, indicating that NAC was released from the materials and exploited to increase cellular glutathione reserves. The plausibility of the second and third pathways playing a role is also supported by the positive results from the experiment in which the medium was supplemented with NAC.

For clinical correlation, it was necessary to examine both the effects of materials in direct contact with and in close proximity to cells to simulate the clinical context. The marked differences in the contact and proximity results suggest a need for separate assessments depending on the biological and clinical contexts and validate the model used in this study. Our model was also able to differentiate between different cellular responses caused by different materials. The test specimens occupied a quarter of a 12-well culture dish well. A very small specimen would be insufficient to count adherent or attaching cells and may not have a sufficient biological impact. Conversely, a large specimen might prevent any cellular growth. Other techniques exist to examine the biological effects of materials, such as the use of extracts from materials; however, the concentration and quantity of extract to use in culture are critical and difficult to optimize, and, more importantly, the contact effect cannot be evaluated. Our optimized model has the advantages of using the actual test specimens and the ability to test both contact and non-contact effects. Regarding the time points of assays, cell attachment is usually assessed within one day of culture. However, this study dealt with toxic materials, and the number of cells attached to the materials was anticipated to be very low. The result of the WST-1 assay could be none, even though there were a few cells that survived and attached, due to the value being lower than the detection limit of the assay. Further, as mentioned above, the surface area of the test specimens was only a quarter of a single well of the 12-well culture dish, which made the detection more difficult. Therefore, considering the sensitivity and validity, we evaluated the cell attachment on day 2 in this particular culture model.

The negative impact of the materials tested was more than anticipated, with no cells surviving and attaching to the bis-acrylic, flowable composite, or bulk-fill composite [24,56,59,60]. The self-curing acrylic was the most biocompatible material tested. The composite materials used a photoinitiator, and polymerization is supposed to be complete by the end of light irradiation. Of note, the composite materials were more cytotoxic than the self-curing acrylic, which is considered to take longer to polymerize [3–5,61]. Our results not only highlight some of the limitations of currently used dental restorative mate-

rials but also provide a potential solution in exploiting the biocompatibility effects of NAC to develop or improve future materials. In particular, the NAC-impregnated self-curing acrylic reached (for some parameters) equivalent biocompatibility to the titanium alloy, a bioinert material. Although we examined four different representative materials, other commercial and experimental materials are available that would be worth studying, and NAC concentrations could be further optimized. To date, there have been no comparative studies of the effect of NAC in several materials, but here we report material-specific NAC efficacy due to highly variable baseline biocompatibility and the behavior of polymerization, suggesting the need for material-specific NAC optimization.

4. Materials and Methods

4.1. Material Preparation and Characterization

Five different test materials in rectangular plate form (6 mm × 14 mm, 2 mm thickness) were prepared (Table 1, Figure 9A). Bis-acrylic, flowable composite, bulk-fill composite, and self-curing acrylic were prepared using standardized silicone molds and according to the manufacturers' instructions. All acrylic plates were washed with a steam cleaner and disinfected with 75% ethanol. Test plates impregnated with NAC were also evaluated. NAC was prepared as a 2 M stock solution in HEPES buffer, pH 7.2–7.5. For self-curing acrylic, the NAC solution was put into the monomer first and then mixed with the polymer powders for polymerization. For composite materials, the NAC solution was spatulated into the composite and light-cured according to the manufacturer's instructions. The final NAC concentrations impregnated in the materials were adjusted to 3% and 6% w/w. To supplement NAC in the culture media, the amount of NAC corresponding to the above-mentioned 3% and 6% w/w was added into the culture medium.

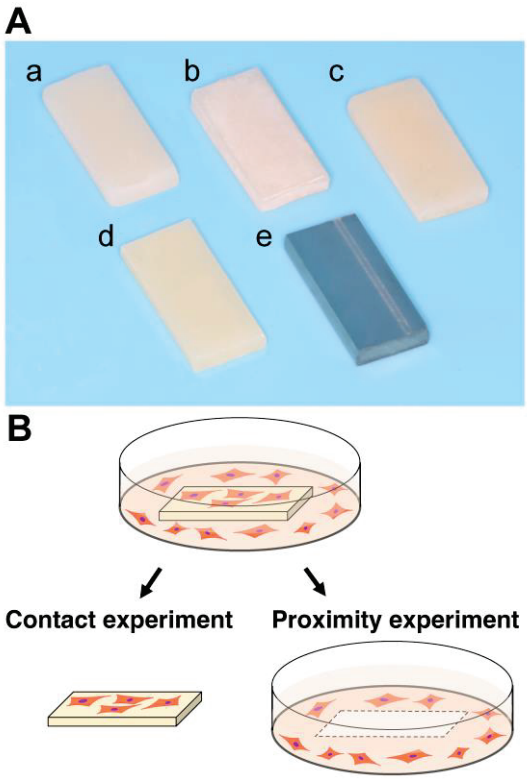


Figure 9. (**A**) Test specimens made of bis-acrylic (**a**), flowable composite (**b**), bulk-fill composite (**c**), self-curing acrylic (**d**), and grade 5 titanium alloy (**e**). (**B**) Culture experiment design. The contact and proximity experiments were conducted separately to differentiate the reaction of cells in direct contact with and close to each material.

Table 1. Materials used in this study.

Material	Principal Ingredient
Bis-acrylic (Integrity® Multi-Cure Temporary Crown and Bridge Material, Dentsply Sirona Inc., Charlotte, NC, USA)	Acrylates and methacrylates (bis- and multifunctional) Barium boro alumino silicate glass
Flowable composite (Aelite™ Flo, BISCO Inc., Schaumburg, IL, USA)	Bis-GMA
Bulk-fill composite (Aelite™ Aesthetic Enamel, BISCO Inc.)	Bis-GMA, UDMA
Self-curing acrylic (UNIFAST™ Trad, GC corporation, Tokyo, Japan)	Liquid: MMA Powder: PMMA
Ti alloy	Ti-6Al-4V

Abbreviations: Bis-GMA, bisphenol A glycidyl methacrylate; UDMA, urethane dimethacrylate; MMA, methyl methacrylate; PMMA, poly(methyl methacrylate).

4.2. Cell Culture

Human gingival fibroblasts were purchased from ScienCell Research Laboratories (Carlsbad, CA, USA) and grown in a fibroblast medium supplemented with 5% FBS, 1% fibroblast growth supplement-2, and 1% penicillin/streptomycin solution. At 80% confluence, cells were detached using 0.05% trypsin-EDTA and seeded onto subsequent culture plates. Passage 5–8 cells were seeded onto each test material placed in a well (20 mm diameter) of 12-well culture plates at a density of 4×10^4 cells/well. The culture medium was renewed every three days. This study was approved by the UCLA Institutional Biosafety Committee (BUA-2-22-036-001).

4.3. Quantification of Attached and Propagated Cells

The number of attached fibroblasts was counted in (i) contact and (ii) proximity experiments, the former being the quantification of fibroblasts attached to test materials and the latter quantification of fibroblasts attached to the wells around the materials (Figure 9B). The water-soluble tetrazolium salt (WST-1)-based colorimetric assay was used to quantify the cell number. Attached fibroblasts were measured two days after seeding, while propagated fibroblasts were measured four and six days after seeding. The amount of formazan product was measured at 450 nm using a microplate reader (Synergy H1 microplate reader, BioTek Instruments, Winooski, VT, USA).

4.4. Cell Visualization

Cells were visualized and observed using fluorescence microscopy (DMI6000B, Leica Microsystems, Wetzlar, Germany) four days after seeding. Fibroblasts were stained with rhodamine-phalloidin for actin filaments. The density of fibroblasts on each test material was obtained by counting cells in the images.

4.5. Gene Expression Analysis

Total RNA was extracted from cells on day four attached to materials and the wells around the materials using TRIzol reagent (Life Technologies, Carlsbad, CA, USA) and purified using the Direct-zol™ RNA MiniPrep kit (Zymo Research, Irvine, CA, USA) according to the manufacturers' protocols. RNA was quantified with a NanoDrop™ One (Thermo Fisher Scientific, Waltham, MA, USA). Reverse transcription of total RNA was performed with a SuperScript® VILO ™ cDNA Synthesis Kit (Invitrogen, Carlsbad, CA, USA). Real-time quantitative polymerase chain reaction (PCR) was performed with the QuantStudio™ 3 Real-Time PCR System (Applied Biosystems, Waltham, MA, USA) to quantify expression of collagen type I alpha 1 (*Col1a1*; assay ID: Hs00164004_m1, Applied Biosystems) and collagen type III alpha 1 (*Col3a1*; assay ID: Hs00943809_m1, Applied Biosystems) mRNA.

Gene expression levels were normalized to glyceraldehyde-3-phosphate dehydrogenase (*Gapdh*; Assay ID: Hs02786624_g1, Applied Biosystems) expression.

4.6. Intracellular ROS Detection

Intracellular ROS were detected using the OxiSelect™ Intracellular ROS Assay Kit (Cell Biolabs, Inc., San Diego, CA, USA). Cells cultured for two days were incubated and loaded with 1 mM 2′, 7′-dichlorodihydrofluorescin diacetate (DCFH-DA) for 60 min at 37 °C. Each test material was then placed in each well. Afterwards, excessive DCFH-DA and test materials were removed and washed with PBS. Oxidized DCF was measured using a microplate reader at excitation and emission wavelengths of 480 and 530 nm, respectively.

4.7. Intracellular Glutathione Detection

To quantify total intracellular glutathione, a 5,50-dithiobis(2-nitrobenzoic acid) (DTNB)-based total glutathione quantification kit (Dojindo Molecular Technologies, Inc., Gaithersburg, MD, USA) was used. Oxidized glutathione (GSSG) was detected by masking reduced glutathione (GSH) with a masking reagent. Three days after seeding on test materials, the cells around materials were collected and lysed, and the supernatant was incubated with DTNB and glutathione reductase for 10 min at 37 °C. Total glutathione and GSSG concentrations were determined by measuring the absorbance at 405 nm.

4.8. Statistical Analysis

The results are expressed as means ± standard deviations (SD). Comparisons between multiple groups, such as between 0% NAC, 3% NAC, and 6% NAC, were performed with one-way analysis of variance (ANOVA) followed by the Tukey–Kramer post-hoc test. Comparisons of two groups were performed using the unpaired Student's *t*-test; p-values < 0.05 were statistically significant.

5. Conclusions

NAC impregnation of bulk-fill composite and self-curing acrylic reduced their toxicity and improved the behavior and function of human oral fibroblasts on and around the materials. The mitigating effects were NAC dose dependent. However, NAC impregnation was not effective for the bis-acrylic and flowable composite. Although supplementing the culture medium with NAC also improved fibroblast behavior, direct NAC impregnation into the materials was more effective. The NAC-mediated improvements in fibroblastic behavior and function were corroborated by an observed reduction in cellular ROS and an increase in cellular glutathione, indicating that NAC effectively scavenged ROS within materials and reinforced the cellular antioxidant defense system. These results establish a proof of concept of NAC-mediated improvements in biocompatibility of dental restorative materials.

Author Contributions: T.M. performed experiments and data analysis and drafted the manuscript. K.K. contributed to interpretation of data and reviewed the manuscript. T.O. was involved in experimental design, data analysis, interpretation, and drafting the manuscript. All authors have read and agreed to the published version of the manuscript.

Funding: This work was partially supported by the divisional research fund.

Institutional Review Board Statement: Not applicable.

Informed Consent Statement: Not applicable.

Data Availability Statement: The data presented in this study are available on request from the corresponding author.

Conflicts of Interest: The authors declare no conflict of interest.

References

1. Ogawa, T.; Aizawa, S.; Tanaka, M.; Matsuya, S.; Hasegawa, A.; Koyano, K. Effect of water temperature on the fit of provisional crown margins during polymerization. *J. Prosthet. Dent.* **1999**, *82*, 658–661. [CrossRef] [PubMed]
2. Ogawa, T.; Hasegawa, A. Effect of curing environment on mechanical properties and polymerizing behaviour of methylmethacrylate autopolymerizing resin. *J. Oral Rehabil.* **2005**, *32*, 221–226. [CrossRef] [PubMed]
3. Nakagawa, K.; Ikeda, T.; Saita, M.; Hirota, M.; Tabuchi, M.; Park, W.; Lee, M.; Ogawa, T. Biological and biochemical characterization of 4-META/MMA-TBB resin. *J. Dent. Oral Disord. Ther.* **2015**, *3*, 1–7.
4. Nakagawa, K.; Saita, M.; Ikeda, T.; Hirota, M.; Park, W.; Lee, M.C.; Ogawa, T. Biocompatibility of 4-META/MMA-TBB resin used as a dental luting agent. *J. Prosthet. Dent.* **2015**, *114*, 114–121. [CrossRef]
5. Ogawa, T.; Tanaka, M.; Matsuya, S.; Aizawa, S.; Koyano, K. Setting characteristics of five autopolymerizing resins measured by an oscillating rheometer. *J. Prosthet. Dent.* **2001**, *85*, 170–176. [CrossRef]
6. Funato, A.; Moroi, H.; Ogawa, T. Guided bone regeneration assisted by tooth roots with periodontal ligament: Case reports of immediate and staged approaches to implant therapy. *Int. J. Esthet. Dent.* **2022**, *17*, 276–291.
7. Funato, A.; Tonotsuka, R.; Murabe, H.; Hirota, M.; Ogawa, T. A novel strategy for bone integration and regeneration-Photofunctionalization of dental implants and Ti mesh. *J. Cosmet. Dent.* **2014**, *29*, 74–86.
8. Chang, J.C.; Hurst, T.L.; Hart, D.A.; Estey, A.W. 4-META use in dentistry: A literature review. *J. Prosthet. Dent.* **2002**, *87*, 216–224. [CrossRef]
9. Geurtsen, W. Biocompatibility of resin-modified filling materials. *Crit. Rev. Oral Biol. Med.* **2000**, *11*, 333–355. [CrossRef]
10. Hume, W.R.; Gerzia, T.M. Bioavailability of components of resin-based materials which are applied to teeth. *Crit. Rev. Oral Biol. Med.* **1996**, *7*, 172–179. [CrossRef]
11. Imazato, S. Bio-active restorative materials with antibacterial effects: New dimension of innovation in restorative dentistry. *Dent. Mater. J.* **2009**, *28*, 11–19. [CrossRef] [PubMed]
12. Nicholson, J.W.; Czarnecka, B. The biocompatibility of resin-modified glass-ionomer cements for dentistry. *Dent. Mater.* **2008**, *24*, 1702–1708. [CrossRef] [PubMed]
13. Nakabayashi, N. Adhesive bonding with 4-META. *Oper. Dent.* **1992**, *5*, 125–130.
14. Schweikl, H.; Spagnuolo, G.; Schmalz, G. Genetic and cellular toxicology of dental resin monomers. *J. Dent. Res.* **2006**, *85*, 870–877. [CrossRef] [PubMed]
15. Lan, W.H.; Lan, W.C.; Wang, T.M.; Lee, Y.L.; Tseng, W.Y.; Lin, C.P.; Jeng, J.H.; Chang, M.C. Cytotoxicity of conventional and modified glass ionomer cements. *Oper. Dent.* **2003**, *28*, 251–259.
16. Paranjpe, A.; Bordador, L.C.; Wang, M.Y.; Hume, W.R.; Jewett, A. Resin monomer 2-hydroxyethyl methacrylate (HEMA) is a potent inducer of apoptotic cell death in human and mouse cells. *J. Dent. Res.* **2005**, *84*, 172–177. [CrossRef]
17. Souza, P.P.; Aranha, A.M.; Hebling, J.; Giro, E.M.; Costa, C.A. In vitro cytotoxicity and in vivo biocompatibility of contemporary resin-modified glass-ionomer cements. *Dent. Mater.* **2006**, *22*, 838–844. [CrossRef]
18. Spagnuolo, G.; Galler, K.; Schmalz, G.; Cosentino, C.; Rengo, S.; Schweikl, H. Inhibition of phosphatidylinositol 3-kinase amplifies TEGDMA-induced apoptosis in primary human pulp cells. *J. Dent. Res.* **2004**, *83*, 703–707. [CrossRef]
19. Stanislawski, L.; Soheili-Majd, E.; Perianin, A.; Goldberg, M. Dental restorative biomaterials induce glutathione depletion in cultured human gingival fibroblast: Protective effect of N-acetyl cysteine. *J. Biomed. Mater. Res.* **2000**, *51*, 469–474. [CrossRef]
20. Krifka, S.; Spagnuolo, G.; Schmalz, G.; Schweikl, H. A review of adaptive mechanisms in cell responses towards oxidative stress caused by dental resin monomers. *Biomaterials* **2013**, *34*, 4555–4563. [CrossRef]
21. Goldberg, M. In vitro and in vivo studies on the toxicity of dental resin components: A review. *Clin. Oral Investig.* **2008**, *12*, 1–8. [CrossRef] [PubMed]
22. Lopes-Rocha, L.; Ribeiro-Goncalves, L.; Henriques, B.; Ozcan, M.; Tiritan, M.E.; Souza, J.C.M. An integrative review on the toxicity of Bisphenol A (BPA) released from resin composites used in dentistry. *J. Biomed. Mater. Res. B Appl. Biomater.* **2021**, *109*, 1942–1952. [CrossRef] [PubMed]
23. Goiato, M.C.; Freitas, E.; dos Santos, D.; de Medeiros, R.; Sonego, M. Acrylic Resin Cytotoxicity for Denture Base–Literature Review. *Adv. Clin. Exp. Med.* **2015**, *24*, 679–686. [CrossRef] [PubMed]
24. Schmalz, G.; Widbiller, M. Biocompatibility of Amalgam vs Composite—A Review. *Oral Health Prev. Dent.* **2022**, *20*, 149–156. [CrossRef] [PubMed]
25. Chaves, C.A.; Machado, A.L.; Vergani, C.E.; de Souza, R.F.; Giampaolo, E.T. Cytotoxicity of denture base and hard chairside reline materials: A systematic review. *J. Prosthet. Dent.* **2012**, *107*, 114–127. [CrossRef] [PubMed]
26. Bettencourt, A.F.; Neves, C.B.; de Almeida, M.S.; Pinheiro, L.M.; Oliveira, S.A.; Lopes, L.P.; Castro, M.F. Biodegradation of acrylic based resins: A review. *Dent. Mater.* **2010**, *26*, e171–e180. [CrossRef]
27. Leggat, P.A.; Smith, D.R.; Kedjarune, U. Surgical applications of methyl methacrylate: A review of toxicity. *Arch. Environ. Occup. Health* **2009**, *64*, 207–212. [CrossRef]
28. Azarpazhooh, A.; Main, P.A. Is there a risk of harm or toxicity in the placement of pit and fissure sealant materials? A systematic review. *J. Can. Dent. Assoc.* **2008**, *74*, 179–183.
29. Jorge, J.H.; Giampaolo, E.T.; Machado, A.L.; Vergani, C.E. Cytotoxicity of denture base acrylic resins: A literature review. *J. Prosthet. Dent.* **2003**, *90*, 190–193. [CrossRef]

30. Gillissen, A.; Nowak, D. Characterization of N-acetylcysteine and ambroxol in anti-oxidant therapy. *Respir. Med.* **1998**, *92*, 609–623. [CrossRef]
31. Zafarullah, M.; Li, W.Q.; Sylvester, J.; Ahmad, M. Molecular mechanisms of N-acetylcysteine actions. *Cell. Mol. Life Sci.* **2003**, *60*, 6–20. [CrossRef] [PubMed]
32. Abdulrab, S.; Mostafa, N.; Al-Maweri, S.A.; Abada, H.; Halboub, E.; Alhadainy, H.A. Antibacterial and anti-inflammatory efficacy of N-acetyl cysteine in endodontic treatment: A scoping review. *BMC Oral Health* **2022**, *22*, 398. [CrossRef] [PubMed]
33. Comino-Sanz, I.M.; Lopez-Franco, M.D.; Castro, B.; Pancorbo-Hidalgo, P.L. The Role of Antioxidants on Wound Healing: A Review of the Current Evidence. *J. Clin. Med.* **2021**, *10*, 3558. [CrossRef] [PubMed]
34. Schloss, J.; Leach, M.; Brown, D.; Hannan, N.; Kendall-Reed, P.; Steel, A. The effects of N-acetyl cysteine on acute viral respiratory infections in humans: A rapid review. *Adv. Integr. Med.* **2020**, *7*, 232–239. [CrossRef]
35. Stey, C.; Steurer, J.; Bachmann, S.; Medici, T.C.; Tramer, M.R. The effect of oral N-acetylcysteine in chronic bronchitis: A quantitative systematic review. *Eur. Respir. J.* **2000**, *16*, 253–262. [CrossRef]
36. Aita, H.; Tsukimura, N.; Yamada, M.; Hori, N.; Kubo, K.; Sato, N.; Maeda, H.; Kimoto, K.; Ogawa, T. N-acetyl cysteine prevents polymethyl methacrylate bone cement extract-induced cell death and functional suppression of rat primary osteoblasts. *J. Biomed. Mater. Res. A* **2010**, *92*, 285–296. [CrossRef]
37. Sugita, Y.; Okubo, T.; Saita, M.; Ishijima, M.; Torii, Y.; Tanaka, M.; Iwasaki, C.; Sekiya, T.; Tabuchi, M.; Rezaei, N.M.; et al. Novel Osteogenic Behaviors around Hydrophilic and Radical-Free 4-META/MMA-TBB: Implications of an Osseointegrating Bone Cement. *Int. J. Mol. Sci.* **2020**, *21*, 2405. [CrossRef]
38. Tsukimura, N.; Yamada, M.; Aita, H.; Hori, N.; Yoshino, F.; Chang-Il Lee, M.; Kimoto, K.; Jewett, A.; Ogawa, T. N-acetyl cysteine (NAC)-mediated detoxification and functionalization of poly(methyl methacrylate) bone cement. *Biomaterials* **2009**, *30*, 3378–3389. [CrossRef]
39. Yamada, M.; Ogawa, T. Chemodynamics underlying N-acetyl cysteine-mediated bone cement monomer detoxification. *Acta Biomater.* **2009**, *5*, 2963–2973. [CrossRef]
40. Hamajima, K.; Ozawa, R.; Saruta, J.; Saita, M.; Kitajima, H.; Taleghani, S.R.; Usami, D.; Goharian, D.; Uno, M.; Miyazawa, K.; et al. The Effect of TBB, as an Initiator, on the Biological Compatibility of PMMA/MMA Bone Cement. *Int. J. Mol. Sci.* **2020**, *21*, 4016. [CrossRef]
41. Saruta, J.; Ozawa, R.; Hamajima, K.; Saita, M.; Sato, N.; Ishijima, M.; Kitajima, H.; Ogawa, T. Prolonged Post-Polymerization Biocompatibility of Polymethylmethacrylate-Tri-n-Butylborane (PMMA-TBB) Bone Cement. *Materials* **2021**, *14*, 1289. [CrossRef] [PubMed]
42. Sato, N.; Ueno, T.; Kubo, K.; Suzuki, T.; Tsukimura, N.; Att, W.; Yamada, M.; Hori, N.; Maeda, H.; Ogawa, T. N-Acetyl cysteine (NAC) inhibits proliferation, collagen gene transcription, and redox stress in rat palatal mucosal cells. *Dent. Mater.* **2009**, *25*, 1532–1540. [CrossRef] [PubMed]
43. Minamikawa, H.; Yamada, M.; Deyama, Y.; Suzuki, K.; Kaga, M.; Yawaka, Y.; Ogawa, T. Effect of N-acetylcysteine on Rat Dental Pulp Cells Cultured on Mineral Trioxide Aggregate. *J. Endod.* **2011**, *37*, 637–641. [CrossRef] [PubMed]
44. Yamada, M.; Ueno, T.; Minamikawa, H.; Sato, N.; Iwasa, F.; Hori, N.; Ogawa, T. N-acetyl cysteine alleviates cytotoxicity of bone substitute. *J. Dent. Res.* **2010**, *89*, 411–416. [CrossRef]
45. Yamada, M.; Watanabe, J.; Ueno, T.; Ogawa, T.; Egusa, H. Cytoprotective Preconditioning of Osteoblast-Like Cells with N-Acetyl-L-Cysteine for Bone Regeneration in Cell Therapy. *Int. J. Mol. Sci.* **2019**, *20*, 5199. [CrossRef]
46. Yamada, M.; Tsukimura, N.; Ikeda, T.; Sugita, Y.; Att, W.; Kojima, N.; Kubo, K.; Ueno, T.; Sakurai, K.; Ogawa, T. N-acetyl cysteine as an osteogenesis-enhancing molecule for bone regeneration. *Biomaterials* **2013**, *34*, 6147–6156. [CrossRef]
47. Suzuki, T.; Kubo, K.; Hori, N.; Yamada, M.; Kojima, N.; Sugita, Y.; Maeda, H.; Ogawa, T. Nonvolatile buffer coating of titanium to prevent its biological aging and for drug delivery. *Biomaterials* **2010**, *31*, 4818–4828. [CrossRef]
48. Yamada, M.; Kojima, N.; Att, W.; Minamikawa, H.; Sakurai, K.; Ogawa, T. Improvement in the osteoblastic cellular response to a commercial collagen membrane and demineralized freeze-dried bone by an amino acid derivative: An in vitro study. *Clin. Oral Implant. Res.* **2011**, *22*, 165–172. [CrossRef]
49. Tsukimura, N.; Kojima, N.; Kubo, K.; Att, W.; Takeuchi, K.; Kameyama, Y.; Maeda, H.; Ogawa, T. The effect of superficial chemistry of titanium on osteoblastic function. *J. Biomed. Mater. Res. A* **2008**, *84*, 108–116. [CrossRef]
50. Nakamura, H.; Saruwatari, L.; Aita, H.; Takeuchi, K.; Ogawa, T. Molecular and biomechanical characterization of mineralized tissue by dental pulp cells on titanium. *J. Dent. Res.* **2005**, *84*, 515–520. [CrossRef]
51. Saruwatari, L.; Aita, H.; Butz, F.; Nakamura, H.K.; Ouyang, J.; Yang, Y.; Chiou, W.A.; Ogawa, T. Osteoblasts generate harder, stiffer, and more delamination-resistant mineralized tissue on titanium than on polystyrene, associated with distinct tissue micro- and ultrastructure. *J. Bone Miner Res.* **2005**, *20*, 2002–2016. [CrossRef] [PubMed]
52. Takeuchi, K.; Saruwatari, L.; Nakamura, H.K.; Yang, J.M.; Ogawa, T. Enhanced intrinsic biomechanical properties of osteoblastic mineralized tissue on roughened titanium surface. *J. Biomed. Mater. Res. A* **2005**, *72A*, 296–305. [CrossRef]
53. Tateshima, S.; Kaneko, N.; Yamada, M.; Duckwiler, G.; Vinuela, F.; Ogawa, T. Increased affinity of endothelial cells to NiTi using ultraviolet irradiation: An in vitro study. *J. Biomed. Mater. Res. A* **2018**, *106*, 1034–1038. [CrossRef] [PubMed]
54. Tsukimura, N.; Ueno, T.; Iwasa, F.; Minamikawa, H.; Sugita, Y.; Ishizaki, K.; Ikeda, T.; Nakagawa, K.; Yamada, M.; Ogawa, T. Bone integration capability of alkali- and heat-treated nanobimorphic Ti-15Mo-5Zr-3Al. *Acta Biomater.* **2011**, *7*, 4267–4277. [CrossRef] [PubMed]

55. Minamikawa, H.; Ikeda, T.; Att, W.; Hagiwara, Y.; Hirota, M.; Tabuchi, M.; Aita, H.; Park, W.; Ogawa, T. Photofunctionalization increases the bioactivity and osteoconductivity of the titanium alloy Ti6Al4V. *J. Biomed. Mater. Res. A* **2014**, *102*, 3618–3630. [CrossRef] [PubMed]
56. Minamikawa, H.; Yamada, M.; Iwasa, F.; Ueno, T.; Deyama, Y.; Suzuki, K.; Yawaka, Y.; Ogawa, T. Amino acid derivative-mediated detoxification and functionalization of dual cure dental restorative material for dental pulp cell mineralization. *Biomaterials* **2010**, *31*, 7213–7225. [CrossRef]
57. Yamada, M.; Minamikawa, H.; Ueno, T.; Sakurai, K.; Ogawa, T. N-acetyl cysteine improves affinity of beta-tricalcium phosphate granules for cultured osteoblast-like cells. *J. Biomater. Appl.* **2012**, *27*, 27–36. [CrossRef]
58. Ueno, T.; Yamada, M.; Igarashi, Y.; Ogawa, T. N-acetyl cysteine protects osteoblastic function from oxidative stress. *J. Biomed. Mater. Res. A* **2011**, *99*, 523–531. [CrossRef]
59. Kielbassa, A.M.; Glockner, G.; Wolgin, M.; Glockner, K. Systematic review on highly viscous glass-ionomer cement/resin coating restorations (Part II): Do they merge Minamata Convention and minimum intervention dentistry? *Quintessence Int.* **2017**, *48*, 9–18. [CrossRef]
60. Caldas, I.P.; Alves, G.G.; Barbosa, I.B.; Scelza, P.; de Noronha, F.; Scelza, M.Z. In vitro cytotoxicity of dental adhesives: A systematic review. *Dent. Mater.* **2019**, *35*, 195–205. [CrossRef]
61. Ogawa, T.; Tanaka, M.; Koyano, K. Effect of water temperature during polymerization on strength of autopolymerizing resin. *J. Prosthet. Dent.* **2000**, *84*, 222–224. [CrossRef] [PubMed]

International Journal of
Molecular Sciences

MDPI

Article

The Treatment Efficiency and Microbiota Analysis of *Sapindus mukorossi* Seed Oil on the Ligature-Induced Periodontitis Rat Model

Shih-Kai Lin [1], Yi-Fan Wu [1], Wei-Jen Chang [1,2], Sheng-Wei Feng [1,*] and Haw-Ming Huang [1,*]

[1] School of Dentistry, College of Oral Medicine, Taipei Medical University, Taipei 11031, Taiwan; middlesky00@gmail.com (S.-K.L.); yfwu@tmu.edu.tw (Y.-F.W.); cweijen1@tmu.edu.tw (W.-J.C.)
[2] Department of Dentistry, Shuang Ho Hospital, Taipei Medical University, New Taipei City 235041, Taiwan
* Correspondence: shengwei@tmu.edu.tw (S.-W.F.); hhm@tmu.edu.tw (H.-M.H.); Tel.: +886-2-2736-1661 (ext. 5401) (S.-W.F.); +886-2-2736-1661 (ext. 5128) (H.-M.H.)

Abstract: Periodontitis is a common oral disease mainly caused by bacterial infection and inflammation of the gingiva. In the prevention or treatment of periodontitis, anti-bacterial agents are used to inhibit pathogen growth, despite increasing levels of bacterial resistance. *Sapindus mukorossi Gaertn* (SM) seed oil has proven anti-bacterial and anti-inflammation properties. However, the possibility of using this plant to prevent or treat periodontitis has not been reported previously. The aim of this study was to evaluate the effects of SM oil on experimental periodontitis in rats by using micro-CT and microbiota analysis. The distance between cementoenamel junction (CEJ) and alveolar bone crest (ABC) on the sagittal micro-CT slide showed that total bone loss (TBL) was significantly lower in CEJ-ABC distances between SM oil and SM oil-free groups on Day 14. Histology data also showed less alveolar bone resorption, a result consistent result with micro-CT imaging. The microbiota analyzed at phylum and class levels were compared between the SM oil and SM oil-free groups on Day 7 and Day 14. At the phylum level, *Proteobacteria*, *Firmicutes*, *Bacteroidetes*, and *Actinobacteria* were the dominant bacterium. *Firmicutes* in box plot analysis was significantly less in the SM oil group than in the SM oil-free group on Day 7. At the class level, *Bacteroidia*, *Gammaproteobacteria*, *Bacilli*, *Clostridia*, and *Erysipelotrichia* were the dominant bacteria. The bacteria composition proportion of *Bacilli*, *Clostridiay*, and *Erysipelotrichia* could be seen in the SM oil group significantly less than in t SM oil-free group on Day 7. Overall, the present results show that topical application of SM oil can reduce bone resorption and change bacteria composition in the ligature-induced periodontitis model. According to these results, it is reasonable to suggest SM oil as a potential material for preventing oral disease.

Keywords: *Sapindus mukorossi*; ligature-induced periodontitis rat model; micro CT; microbiota

Citation: Lin, S.-K.; Wu, Y.-F.; Chang, W.-J.; Feng, S.-W.; Huang, H.-M. The Treatment Efficiency and Microbiota Analysis of *Sapindus mukorossi* Seed Oil on the Ligature-Induced Periodontitis Rat Model. *Int. J. Mol. Sci.* **2022**, *23*, 8560. https://doi.org/10.3390/ijms23158560

Academic Editor: Mary Anne Melo

Received: 9 July 2022
Accepted: 30 July 2022
Published: 2 August 2022

Publisher's Note: MDPI stays neutral with regard to jurisdictional claims in published maps and institutional affiliations.

Copyright: © 2022 by the authors. Licensee MDPI, Basel, Switzerland. This article is an open access article distributed under the terms and conditions of the Creative Commons Attribution (CC BY) license (https://creativecommons.org/licenses/by/4.0/).

1. Introduction

Periodontitis is a common chronic oral inflammatory disease that leads to the destruction of tooth-supporting tissues, which may be caused by genetic variations [1], imbalanced oral microbiome [2], or elevated levels of systemic pro-inflammatory mediators in the blood [3,4]. The occurrence of periodontal pathogens with persistent inflammation from dental plaque destroys periodontal structures such as periodontal ligament, alveolar bone, cementum, and soft tissue. Notably, over 10% of adults suffer from severe periodontitis, making the condition a severe public health threat, with evidence from the 2019 Global Burden of Disease (GBD) study indicating that global population growth accounted for 67.9% of the increase in severe periodontitis [5–7]. Commonly used and effective treatment for periodontal disease are achieved through non-surgical approaches (i.e., scaling and root planning (SRP), sonic/ultrasonic treatment, locally delivered antibiotic drugs [8],

diode laser treatment, photodynamic therapy) and surgical interventions such as guided tissue/bone regeneration (GTR/GBR), pocket reduction surgery, and osseous surgery (OS).

Natural plant-based products and traditional medicines have been considered promising candidates for the prevention and treatment of oral diseases. [9,10]. Sapindaceae (also called "wu-huan-zi" in Chinese), a natural plant-based product used in traditional Chinese medicine, has attracted increasing attention. *Sapindus mukorossi* (SM) Gaertn is one of the more commonly used major species. SM can be easily found in tropical and sub-tropical regions of the Pacific Rim [11]. Many studies have shown that the pericarp of the SM fruit also has medicinal value and positive biological effects, including insecticidal, antitrichomonal, anti-cancer, hepatoprotective, anxiolytic, molluscicidal, fungicidal, free radical scavenging, anti-inflammatory and anti-platelet aggregation activity [12,13]. More recent studies have also indicated that SM extract exhibits significant anti-microbial activities and could potentially be used as a source of agents to cure dental caries [14] and for skin care [15]. These studies have clearly shown that SM's major anti-bacterial effect is from saponins extracted from the fruit's pericarp [12,14,16].

Besides the pericarp, which makes up 56% of the SM fruit, SM contains a seed covered by a hard, black shell with kernel pulp inside [17,18]. The kernel of the SM seed contains an abundant amount of oil (23%), mainly composed of fatty acids and triglycerides [19]. While the inedible SM seeds have been regarded as a useless waste product in the past [20,21], possible dental applications of SM seed kernel have been recorded in the Compendium of Materia Medica (Mandarin: Bencao Gangmou), a Chinese pharmaceutical volume written almost 500 years ago. According to this work, the kernel of the SM seed can be used to treat gingival swelling and reduce oral malodor. Since it is well known that bacteria predispose the development of bad breath, the SM seed kernel is likely to provide anti-inflammatory and anti-bacterial effects, thus reducing periodontal disease and oral caries. An interesting modern in vivo experiment by Chen and colleagues concluded that SM oil could potentially promote the healing of skin wounds through anti-inflammatory and anti-microbial activities [13].

A report demonstrated that SM fruit pericarp extract could inhibit the growth of bacteria associated with oral diseases, including *P. gingivalis*, *A. odontolyticus*, *F. nucleatum* and *C. albicans* [22]. However, whether SM seed oil can be used to treat periodontal disease remains unknown. Since the bacterial communities that cause periodontitis are complex [23–26], clarifying the changes in the composition of microbiota associated with infected periodontal tissue will be the first step toward understanding the treatment effect of SM oil on periodontitis and to establish therapeutic strategies.

Accordingly, this study used a ligatured animal model of periodontal disease to determine correlations between microbiota and periodontitis, as well as to assess SM oil application through micro-CT and histological analysis during the progress of periodontal disease in rats. In addition, 16s rRNA sequencing techniques were used to gain deeper insights into inflammatory and microbiota changes in periodontitis after SM oil treatment.

2. Results

2.1. Micro-CT Analysis of Bone Resorption

The typical reconstructed micro-CT images and analysis of the bone resorption, such as CEJ-ABC distance and subsequent bony changes around CEJ, are shown in Figure 1. Compared to the blank control (Figure 1a), distances between CEJ and ABC in w/o oil groups on Day 7 (Figure 1b) and Day 14 (Figure 1c) were visibly increased. These results indicate that induction of periodontitis in the experimental animal model was effective. However, when the silk ligatures tied on the rat's maxillary molar were pre-immersed with SM oil, the CEJ-ABC distance decreased on Day 7 (Figure 1d) and Day 14 (Figure 1e).

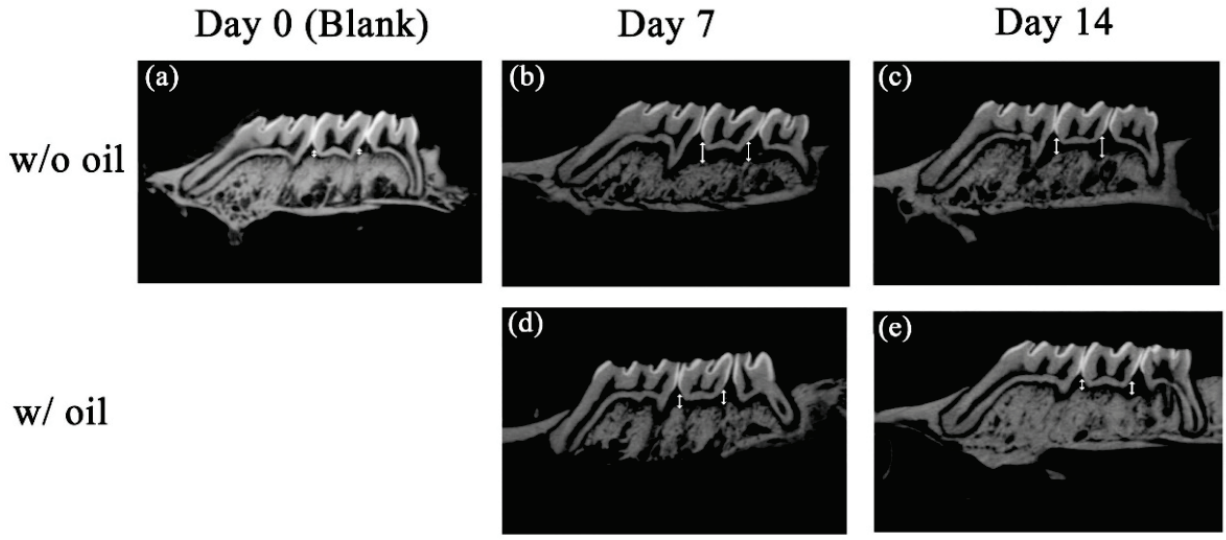


Figure 1. Micro CT images showing bone loss measurements for each group at Day 0 (**a**), Day 7 (**b**,**d**) and Day 14 (**c**,**e**). On the sagittal side, radiographic bone loss was detected from CEJ to ABC (white arrow). The bone loss for SM oil samples (**b**,**c**) were lower than the oil-free groups (**d**,**e**).

Figure 2 shows total bone loss (TBL) and furcation bone loss (FBL). These figures show that the change in furcation bone loss level showed no significant difference during the entire experimental period (p = 0.891 and 0.284 for Day 7 and Day 14, respectively) (Figure 2a). Nevertheless, a significant difference for TBL was seen in CEJ-ABC distances between sample teeth ligated with and without SM oil on Day 14 ($p < 0.05$) (Figure 2b).

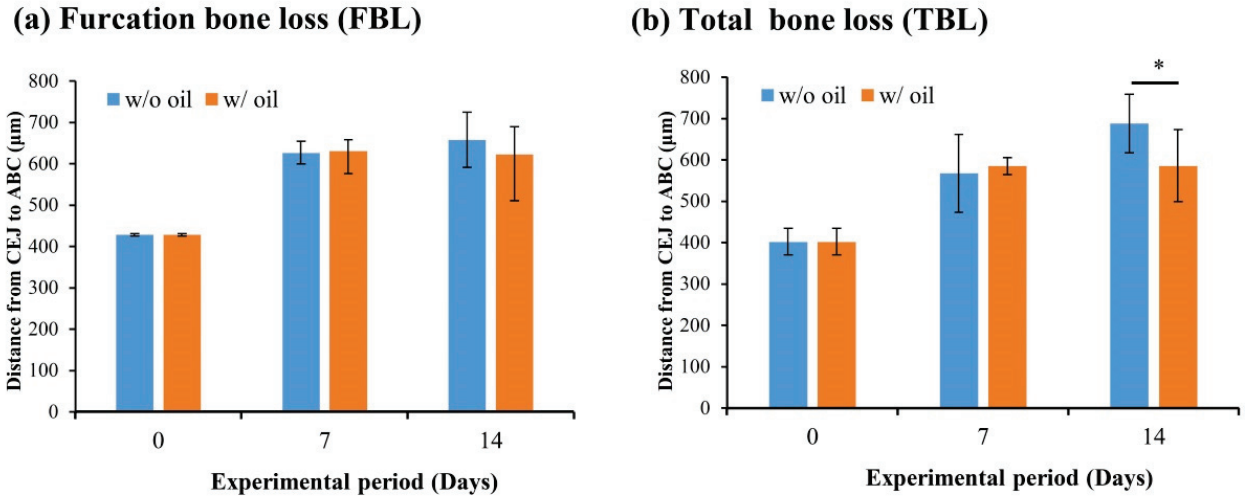


Figure 2. Influence of SM oil on alveolar bone loss at (**a**) furcation area and (**b**) total surrounding bone area. Quantitative analyses of bone loss were obtained by measuring CEJ-ABC distance w/ oil and w/o oil represented tooth samples ligated with or without SM oil pre-immersion, respectively. Significant differences between w/ and w/o oil groups were observed on Day14. * denotes $p < 0.05$.

2.2. Histologic Analysis of Periodontitis Progression

Figure 3 shows typical histopathologic images of the periodontitis progress of the experimental samples. Periodontal tissue in sample teeth tied with ligatures had obvious pouch-like periodontal pockets on Day 7 (Figure 3b) and Day 14 (Figure 3d). In addition, compared with the blank control group (Figure 3a), apical migration of the epithelium along the tooth surface was apparent on the exposed cementum when SM oil-free ligatures were used. When ligatures were pre-immersed with the SM oil, no visible change

in inflammatory infiltration was found during the 14-day period (Figure 3c,e). However, we found that samples ligatured with SM oil-immersed silk had less alveolar bone resorption (Figure 3c,e) as compared with teeth ligatured with SM seed oil-free silk at both Day 7 (Figure 3b) and Day 14 (Figure 3d). In addition, unlike samples treated with SM oil-immersed ligature that showed thick and continuous epithelium, samples in the SM oil-free group exhibited thin and discontinuous epithelium (Figure 3f), and looser lamina propria and submucosa on Day 14 (Figure 3g).

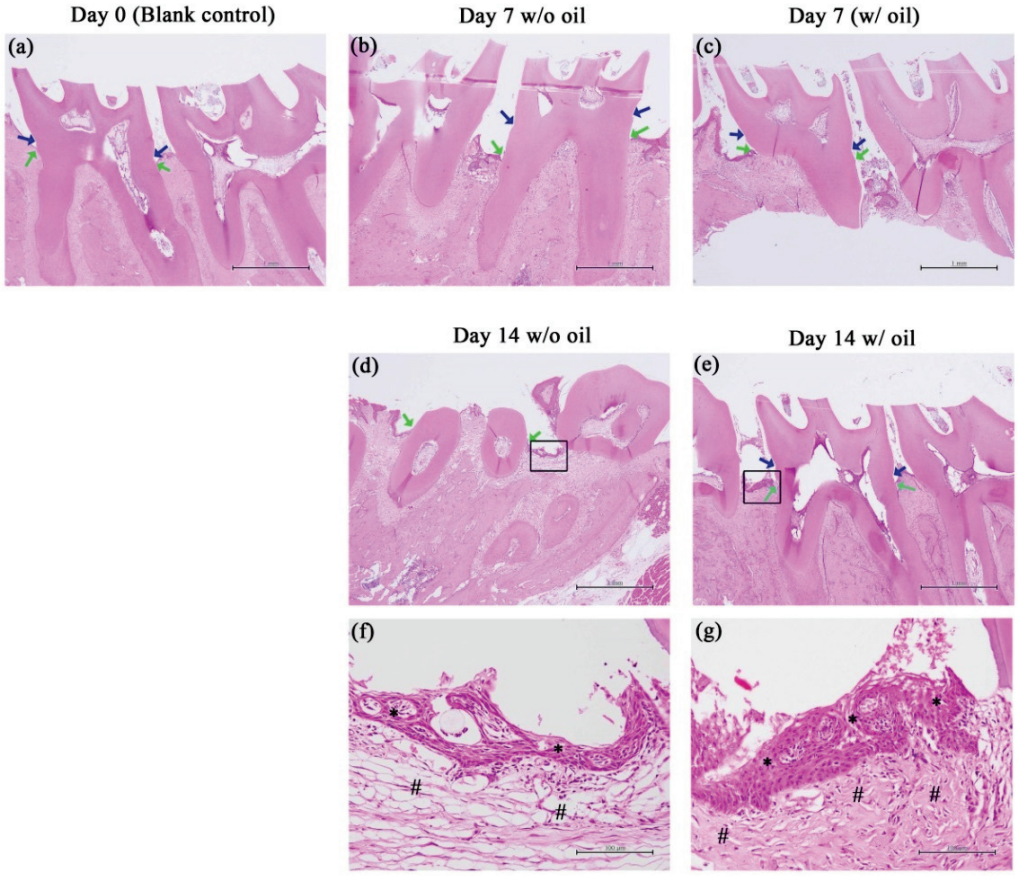


Figure 3. Histological results of tested molars at Day 0 (**a**), Day 7 (**b**,**c**) and Day 14 (**d**,**e**) with a magnification of 40×. Images of bone-surrounding tissue interface (black box) of oil-treated (**d**) and oil-free (**e**) samples on Day14 were enhanced by higher magnification micrographs of 400× (**f**,**g**, respectively). Blue arrows indicate cemento-enamel junction (CEJ). Green arrows indicate the most coronal level of the alveolar bone crest (ABC). * and # signs identify the epithelium and lamina propria, respectively. Scale bar is 1 mm for (**a**–**c**), and 100 μm for (**f**,**g**).

2.3. Microbiota Investigation of Periodontitis Progression

In Figure 4, the overall heatmap distribution shows that microbial species become more diverse in the SM oil-free group at all time points. Compared to the oil-free group, sample teeth tied with SM oil-immersed ligatures had lower diversity at the family (Figure 4a) and genus (Figure 4b) levels.

Bacterial communities were compared between samples ligated with SM oil pre-immersed and SM oil-free silk ligature at phylum (Figure 5a) and class (Figure 5b) levels. As shown in Figure 5a, we found that *Proteobacteria*, *Firmicutes*, *Bacteroidetes*, and *Actinobacteria* were dominant both in SM oil (w/ oil) and SM oil-free groups (w/o oil). *Proteobacteria* was the most dominant bacterium in all samples. On Day 7, the relative abundance of *Proteobacteria* in the SM oil group was 50.41%, approximately 1.34 fold higher than the oil-free group (37.58%). After a 14-day experimental period, the proportions of the two groups became similar (Figure 6b). *Firmicutes* had significantly less relative abundance in

the SM oil group (32.16%) compared to the oil-free group (45.68%) on Day 7 (Figure 6a). As with *Proteobacteria*, the proportion of *Firmicutes* detected in the two groups became similar on Day 14 (Figure 6a). The relative abundance of *Bacteroides* in samples ligated with SM oil pre-immersed ligature was 1.79%, slightly lower than in the SM oil-free ligature samples (2.26%) on Day 7. However, this result reversed on Day 14 (Figure 6a). The relative abundance of *Bacteroides* in SM oil and SM oil-free groups were 4.73% and 2.82%, respectively. The relative abundance of *Actinomycetes* detected in sample teeth tied with SM oil and oil-free samples were 15.41% and 14.42% on Day 7, respectively. These values increased to 32.95% (SM oil group) and 31.50% (SM oil-free group) on Day 14 (Figure 6d).

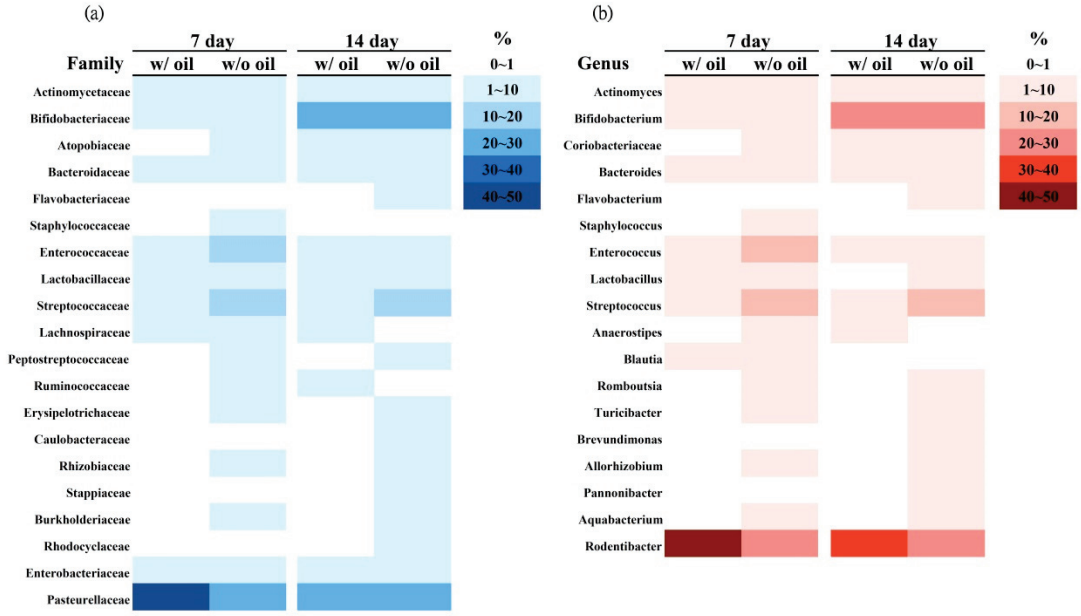


Figure 4. Heatmaps from microbiota analysis of samples treated with or without SM oil at (**a**) family and (**b**) genus levels during the experimental period. Values are presented in percentages.

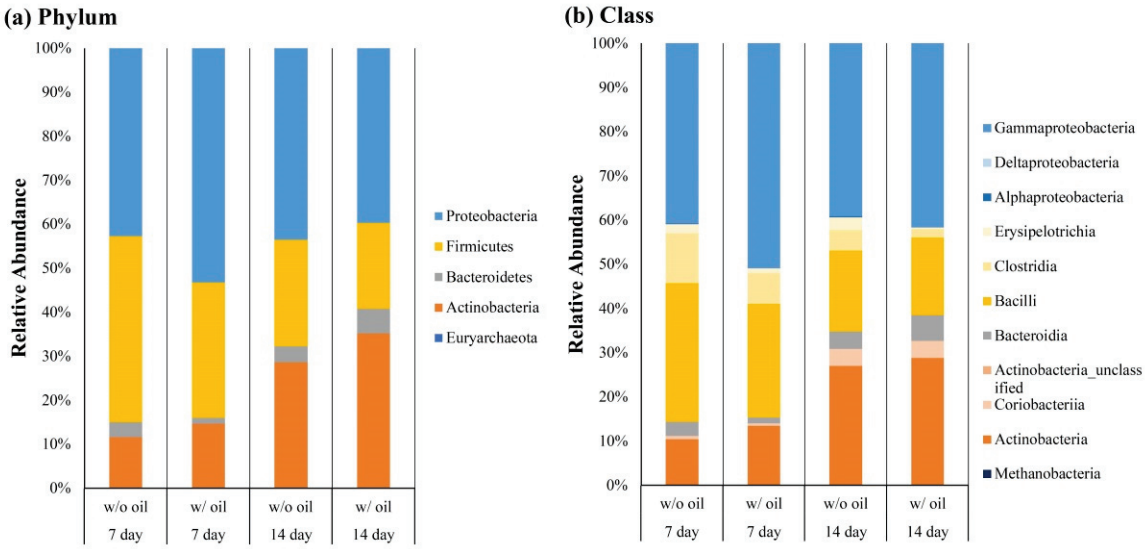


Figure 5. Relative abundance of bacteria in (**a**) phylum and (**b**) class levels on Day 7 and Day 14, when the tested teeth were treated with and without SM oil.

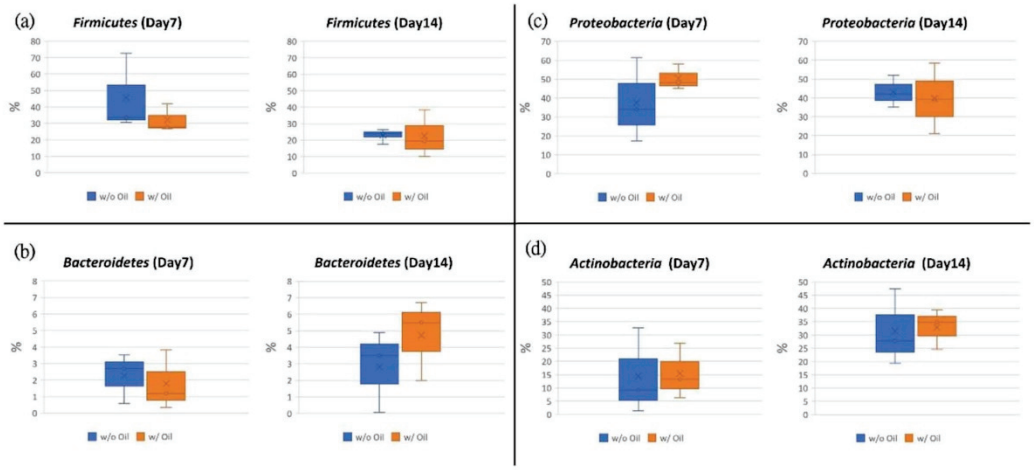


Figure 6. Tested teeth were subjected to ligature-induced periodontitis. Data from samples treated with and without SM oil were compared. Sub-figures show box plot analysis in the phylum of (**a**) *Firmicutes*, (**b**) *Bacteroidetes*, (**c**) *Proteobacteria* and (**d**) *Actinobacteria*.

At the class level, *Bacteroidia*, *Gammaproteobacteria*, *Bacilli*, *Clostridia*, and *Erysipelotrichia* were the dominant classes found in the samples. *Gammaproteobacteria* was the dominant bacterium in both groups (Figure 5b). The proportion of *Bacilli* bacteria on Day 7 in the SM oil group (w/ group) was 25.72%, lower than samples treated with SM oil-free ligatures (w/o group) (33.93%). These values became similar by the end of the 14-day experimental period (Figure 7a). A similar tendency was found for *Clostridiay* (Figure 7b). During the entire experimental period, the relative abundance of *Erysipelotrichia* for the SM oil-free group was higher than in samples tied with SM oil ligature (Figure 7c). Interestingly, on Day 14, the value for SM oil-free group (1.87%) was almost 4.2 fold higher than in samples tied with SM oil pre-immersed silk ligatures (0.45%) (Figure 7c). On Day 7 the proportion of *Bacterodia* in the SM oil group was 1.78%, lower than in the SM oil-free samples (2.26%). This tendency had reversed by Day 14 (Figure 7d). For *Gammaproteobacteria*, the composition proportion for the SM oil group was higher than the SM oil-free group on Day 7 and Day 14 (Figure 7e).

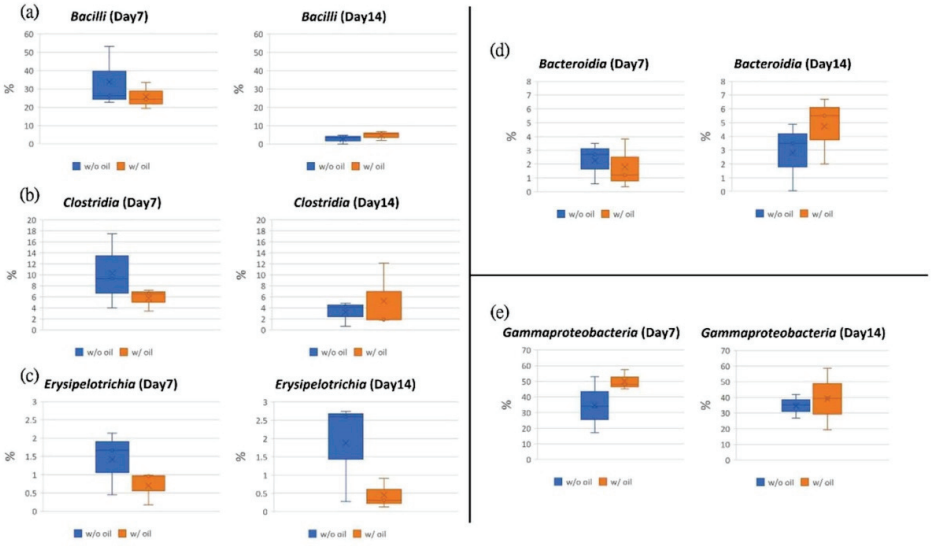


Figure 7. Tested teeth were subjected to ligature-induced periodontitis. Data from samples treated with and without SM oil were compared. Sub-figures showed the box plot analysis in the class of (**a**) *Bacilli*, (**b**) *Clostridia*, (**c**) *Erysipelotrichia*, (**d**) *Bacteroidia* and (**e**) *Gammaproteobacteria*.

2.4. Firmicutes/Bacteroidetes (F/B) Ratio

F/B ratio was considered to assess alternating inflammatory phases when SM oil pre-immersed ligatures were used to produce periodontitis. Figure 8 shows that on Day 7 the acute inflammatory phase for sample teeth treated with SM seed oil-free ligatures was obviously lower than in samples ligated with SM oil-free silk ligatures. However, the difference in the F/B ratio had fallen sharply by the end of the experimental period (Figure 8).

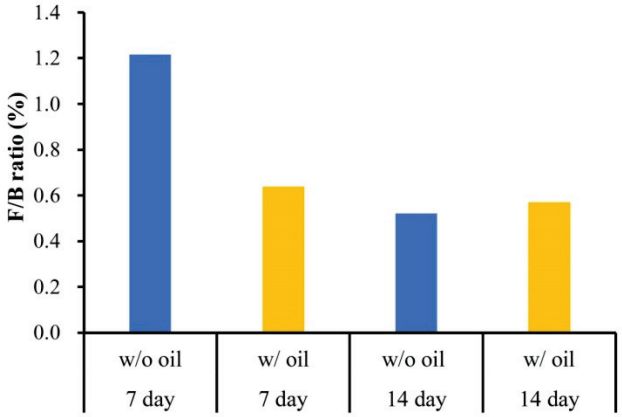


Figure 8. *Firmicutes*/*Bacteroidetes* (F/B) ratio from the median on Day 7 and Day 14 between samples treated with and without SM oil.

3. Discussion

Ligature-induced periodontitis was used in the present study to evaluate the treatment efficiency of SM oil in an animal model. This model is one of the most widely used methods to assess the relationship between periodontal disease and potential treatment materials [27,28]. Our micro-CT results (Figures 1 and 2) showed that total bone loss (TBL) was significantly lower in the seed oil group than the oil-free group on Day 14 (Figure 2b). SM oil can reduce bone resorption in a ligatured animal model and maintain a healthy periodontal environment, suggesting that SM oil is a potential material for inhibiting the progression of periodontitis. Although a previous study by Goncalves-Zillo et al. found that Bdkrb1-/- mice with ligatured-induced periodontitis had increased bone loss in the furcation area [28], there is no significant difference in bone resorption found between SM oil-treated and oil-free samples in the root furcation area (Figure 2a) in this study. This phenomenon is due to the SM oil applied at the CEJ surface not reaching the furcation area.

Typically, burst-destruction bone loss occurs within two weeks [29,30], which was confirmed by our histological experiments in which pouch-like surrounding bone was observed on Day 7 and Day 14 (Figure 3). However, the inflammatory response in ligated teeth was not apparent during the experimental period, possibly due to the sulcular epithelium of tested rats being keratinized (Figure 3f,g) [31]. From Figure 3g, thicker keratinized epithelium and dense lamina propria of the SM-oil treated sample were found when compared to the oil-free group (Figure 3f). Since a thickened keratinized epithelium acts as a barrier that provides more efficient resistance to bacterial invasion, it is reasonable that there is no obvious inflammatory response found in our experimental model [32,33]. This provides histological evidence to support SM oil's action against periodontitis by maintaining the healthy status of surrounding soft tissue.

The positive effect of SM oil on bone growth was first reported by Shiu et al. (2020) [34], which showed that SM oil exhibits a significant effect on dental pulp stem cells via alkaline phosphatase gene expression and extracellular matrix vesicle secretion, identifying the possible active component of SM oil for maintaining bone quality as β-sitosterol found in seed kernel pulp. In 2019, Yildirim et al. reported that β-sitosterol contained in morus nigra (known as the black mulberry) inhibited regional alveolar bone resorption in a rat

periodontitis model via a reduction in MMP-8 expression [35]. MMP-8 has been reported as a collagenase that can destroy the extracellular matrix [36] in the soft tissue around teeth, which results in periodontitis [37,38]. In 2019, Mahmoudi et al. reported that a plant seed oil (*Alyssum homolocarpum*) promoted stem cell proliferation and differentiation through β-sitosterol inside the oil [39]. It was reported that SM oil also contains abundant β-sitosterol in the seed kernel pulp [13]. Since β-sitosterol exhibits various pharmacological and biological activities during bone regeneration [40], it is reasonable to speculate that β-sitosterol in SM oil plays an important role in preventing bone loss during the progression of periodontitis.

With bacteria known to be the major factor inducing bone loss in periodontitis [28,30] and the ability to accumulating commensal microbial biomass to trigger a switch from homeostasis to inflammation [41], SM oil's anti-bacterial properties suggest the material as a potential periodontitis inhibitor. Increased microbial diversity is characteristic of disease development in the root apex, and the increased specific bacterial communities are closely associated with disease progression [42]. The heatmap in Figure 4 shows that samples tied with SM oil-immersed ligatures exhibited lower diversity at both family and genus levels (Figure 4). These results provide another piece of evidence to strengthen the hypothesis that SM oil exhibits anti-periodontitis qualities.

According to a study by Abe et al. [30], bacteria constitution is the major factor in the induction of bone loss in ligature-induced periodontitis. As shown in Figure 5, *Proteobacteria*, *Firmicutes*, *Bacteroidetes*, and *Actinobacteria* were dominant phyla in both ligated molars tied with oil-immersed and oil-free ligatures. This population is similar to microbiota found in the analysis of saliva, pulp chamber, and root apex [42] and is often identified in healthy subjects [43]. However, our results demonstrated that the microbial community of ligated molars changed after SM oil treatment. This result is consistent with previous findings that also showed a similar change in microbiota results among healthy and diseased periodontal tissues [44–47]. Previous reports have also indicated that *Proteobacteria* and *Actinobacteria* decreased in abundance while *Bacteroidetes* and *Firmicutes* increased during oral disease [48,49]. Although SM oil seemed not to influence *Actinobacteria* in our animal study (Figure 6d), we found that *Firmicutes* and *Bacteroidetes* had decreased in the SM oil group on Day 7 (Figure 6a,b). Our results also show that the average abundance of *Proteobacteria*, the most prevalent species in the blood [50,51] and gut [52], was higher in the SM oil-treated sample than in oil-free teeth on Day 7 (Figure 6c). Since *Proteobacteria* have been reported to be more abundant in healthy human sub-gingiva [24], this can be considered evidence that SM oil exhibits a positive effect on maintaining healthy bacteria populations at phylum level.

At the class level, *Bacilli*, *Clostridia*, and *Erysipelotrichia* were inhibited by SM oil on Day 7 (Figure 7a–c), and *Erysipelotrichia* remained lower in the SM group on Day 14. These reduced bacterial populations would inhibit alveolar bone resorption [53] and periodontitis [54–56]. At the same time, SM oil's positive effect on *Gammaproteobacteria* (Figure 7e) was more pronounced, confirming that SM oil tends to maintain the health of silk-ligated molars [49]. These results suggest that SM oil exhibits a positive effect on tooth health by maintaining a normal microbial community at the class level.

F/B ratio identified in the inflammatory phase is a good indicator of microbiota dysbiosis in the oral cavity [57,58]. In our study, the F/B ratio was lower in the SM oil group compared to the oil-free group (Figure 8) due to SM oil's inhibition of *Firmicutes* overgrowth, also indicating that SM oil reduces the burst process of the inflammatory condition [59]. Our present results thus prove the beneficial effect of SM oil in preventing ligature-induced periodontitis and improving periodontal tissue health at an early stage.

The advantages of using SM oil over conventional agents as a treatment for periodontitis are that the product is a safe, natural, and sustainable. However, this study has several limitations. First, SM oil was applied only once at the initial stage. Because not providing a continuous application of the oil prevents observations of long-term effects, future studies could evaluate the effect of SM oil on chronic periodontitis across a longer timeframe. In

addition, the main etiological agents of periodontal disease are different between humans and animals. For example, *Porphyromonas gingivalis*, *Aggregatibacter actinomycetemcomitans*, *Prevotella intermedia* and *Tannerella forsythia* play an important role in periodontal disease in humans. However, according to previous reports, these bacteria were only rarely detected in animals with periodontitis [60]. Because the periodontal microflora of the rat is still unclear, and because over 50% of common oral bacterial species have not been formally named [61], microbiota analysis at the species level was difficult in this experiment. Since the major impetus of this study was to evaluate the effect of SM oil on periodontitis, and because Qian et al.'s results indicate that microbiota analysis at the phylum level represent the health status and treatment efficiency in apical periodontitis [24], though species-level bacterial populations in periodontitis are well known in humans, microbiota analysis was not performed at this level in the current animal study.

4. Materials and Methods

4.1. Preparation of SM Oil

SM used in the experiment was obtained from a company (He-He Com. Ltd., Taipei, Taiwan). After removing fruit pulp and pericarp, seeds were washed under running water and then sterilized in distilled water before oil extraction. After drying in a cabinet drier (40 °C for 72 h), the seeds were milled to separate kernels. The cold-press extraction method was used to extract seed oil following the procedure outlined by Chhetri et al. [11]. Finally, the extracted oil was filtrated and stored in a freezer at −20 °C.

4.2. Animal Preparation and Experimental Design

The animal study procedure in this experiment was reviewed and approved by the Institution Animal Care and Use Committee or Panel (IACUC Approval No. MI202001-01). All efforts were made to minimize the number of animals used and reduce any suffering while producing reliable scientific data. A total of 15 pathogen-free eight-week-old SD rats were randomly and evenly assigned to two experimental groups and one blank control (five rats for each group). Rats in the two experimental groups were sacrificed on Day 7 and Day 14, respectively. The blank control was sacrificed on Day 0. In order to ensure a randomized experimental design, different operators grouped the SD rats and conducted the ligature experiment. During the experimental period, all animals were fed a standard diet and kept independently in clean cages with adequate ventilation. The experimental design is shown in Figure 9a.

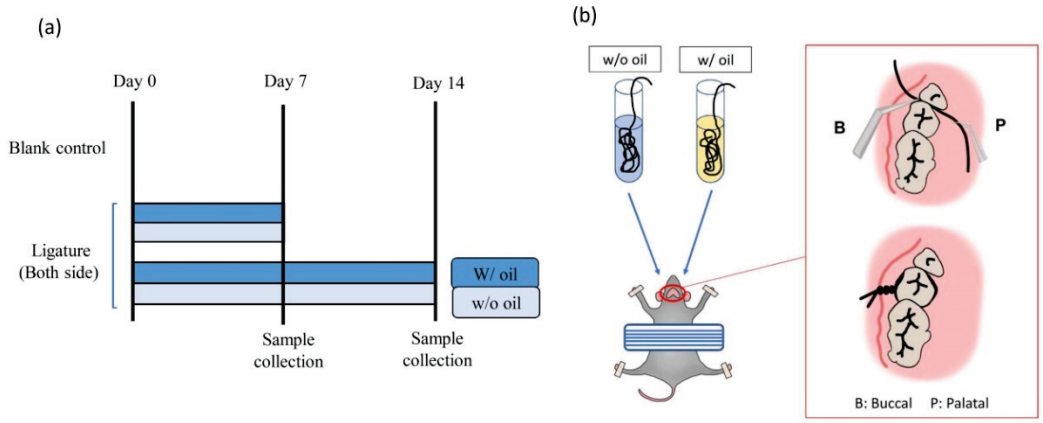


Figure 9. (**a**) Ligature-induced periodontitis experimental design with sacrifice time points. Blank control was the ligature-free samples at Day 0. In the ligature group, the second left molar was ligated with silk pre-immersed with SM oil (w/ oil). The corresponding tooth on the right side was tied with silk-free of SM oil (w/o oil) on Day 0. Rats were euthanized after 7 and 14 days. (**b**) Detailed procedures and preparation of the periodontitis animals were ligated with 3-0 silk around the cervical of the second molar of maxillary bone.

4.3. Ligature-Induced Periodontitis Model

According to previous studies, the ligature method was used to prepare a periodontitis model [19–22]. Under pentobarbital anesthesia, 3-0 silk ligatures were tied on the rats' bilateral maxillary second molar areas. In the experimental group, ten rats had ligatures pretreated with an immersion of SM oil (w/ oil) tied on their right side, while ligatures free of SM oil (w/o oil) were tied on the left side to serve as a comparison group (w/o oil) (Figure 9b). Five rats without ligatures served as the blank control group and were sacrificed on Day 0 [62]. To ensure the experiment was performed under blind conditions, different operators prepared ligature samples and ligatured the teeth of SD rats. Control group samples (w/o oil) were only immersed in normal saline.

Silk ligatures are predicted to induce periodontal inflammation with pathological biofilms forming both on ligatures and tooth surfaces [30,62]. According to a previous protocol, maxillary samples were collected at three time-points: Day 0, Day 7, and Day 14 [63]. Animals were sacrificed under anesthesia, and their jawbones were collected at the time or observation. After removing excessive soft tissue, preserved maxillary bones from the experimental groups, including samples ligated both with oil pre-immersed and oil-free silk, were split in half and collected in separate 1.5 mL test tubes, followed by fixation and storage in 10% formalin. The periodontal status condition of these maxillary bone samples was evaluated by micro-CT and histological images. Collected ligatures were preserved in a freezer at −20 °C prior to 16s rRNA sequencing.

4.4. Micro-CT Analysis

Maxillary samples were collected on Day 0, Day 7, and Day 14 after surgery and scanned with a SkyScan 1076 scanner (SkyScan, Bruker, Kontich, Belgium) with a resolution of 35μm at 90 kV. 3D images of the buccal and palatal sides were reconstructed using NRecon (version 1.7.4.2, Bruker). For bone loss evaluation, distances between the cemento-enamel junction (CEJ) and alveolar bone crest (ABC) were analyzed using CTAn (version 1.19.4.0, Bruker). Six sites, including BM (buccal-mesial), BF (buccal-furcation), BD (buccal-distal), PM (palatal-mesial), PF (palatal-furcation), and PD (palatal-distal) from each maxillary molar were chosen for measurement, and average distances were calculated. In this study, total bone loss (TBL) was defined as the sum of measured data from six sites (BM + BF + BD + PM + PF + PD). Furcation bone loss (FBL) was defined as the sum of measured values at BF and PF.

4.5. Histological Analysis

In order to assess the samples' periodontal conditions, maxillae were dissected at 0, 7, and 14 days and subsequently fixed with 10% formaldehyde. Demineralization was performed according to Ayukawa et al. (1998) [64]. Briefly, both sides of each maxilla were decalcified with 10% ethylene-diamine-tetra-acetic acid solution (pH 7.0) (Ajax Finechem, Thermo Fisher Scientific; Taren Point, Australia) [65] for 4 weeks at 4 °C. Then tissue blocks were embedded in paraffin and cut into serial mesial-distal sections (5 μm thick) using an ultramicrotome (Bright 5040, Bright Instrument, Cambs, UK). After staining with hematoxylin and eosin (H&E) (HD Scientific Supplies; Wetherill Park, Australia) [65], histological images were acquired using a microscope slide scanner (OPTIKA, Ponteranica, Italia) [63].

4.6. 16s rRNA Extraction, Sequencing, and Bioinformatics Analysis

For sequencing and bioinformatics analysis, ligature samples (n = 3) from Day 7 and Day 14 were selected. Biofilm was extracted from ligatures and plaque on the tooth surfaces at the CEJ and furcation areas, and 16s genes on the ligatures were amplified by specific primers 341F-805R [5′-CCTACGGGNGGCWGCAG-3′ and 5′-GACTACHVGGGTATCTAATCC-3′]. All polymerase chain reactions (PCR) were performed in 25 μL reagents with 0.5 μL KAPA® High-Fidelity PCR Master Mix (KAPA BIOSYSTEMS, Cape Town, South Africa). The final regent amount was 0.5 μM of forward and reverse primers and 1 ng DNA template.

Amplification was performed with 30 cycles of denaturation at 95 °C for 30 s, annealing at 57 °C for 30 s, and elongation at 72 °C for 30 s, followed by 5 min extension at 72 °C. The amplified gene samples were purified using a commercial extraction kit (QIAquick Gel Extraction Kit, QIAGEN, Germantown, MD, USA). Purified gene sequences were processed using V3-V4 genomics analysis (Illumina MiSeq platform, Genomics BioSci & Tech Co., New Taipei City, Taiwan). The standard taxonomic identification procedure is length > 150 bp, with a default error rate = 0.1% with minimal overlapping > 10 bp. Genes with a similarity value of more than 97% were classified as the same operation taxonomic unit (OTU) identity using an open-source software platform (Mothur) with SILVA database (Microbial Genomics and Bioinformatics Research Group, Bremen, Germany) [66–70]. The gathered data was analyzed using open-source microbial community analysis software (QIIME, Quantitative Insights Into Microbial Ecology, ver. 1.9.0, Knight and Caporaso labs, http://qiime.org/1.4.0/; assessed on 15 November 2020) to provide microbiome information from raw DNA sequencing data [71]. Sequencing reads without ambiguous reads (n = 3) and chimeric sequences were processed for the bioinformatics analysis as previously described. Differences in bacterial community patterns among samples ligated with and without SM oil for Day 7 and Day 14 were evaluated using median and percentage.

4.7. Statistical Analyses

Differences in bone loss between groups were evaluated using t-test analysis. Differences at $p < 0.05$ were considered significant. Statistical analyses were performed using commercial software (SPSS Inc., Chicago, IL, USA). The groups' differences in bacteria composition were evaluated using box plot analysis with commercial software (Microsoft Excel, Roselle, IL, USA).

5. Conclusions

This study demonstrates that SM oil can significantly decrease total bone loss (TBL) and bone resorption in a ligatured animal model. Our results also show that SM oil inhibits pathogenic bacteria associated with oral disease and suppress the F/B ratio. Therefore, SM oil can potentially protect periodontal tissue by altering the microbiota composition in the initial phase of periodontitis. The data shown in this study can be an important reference for future studies that examine larger sample sizes and in clinical studies in humans.

Author Contributions: S.-K.L., contributed to data curation, investigation, and writing—original draft; Y.-F.W., contributed to conceptualization, validation, and writing—review & editing; W.-J.C., contributed to funding acquisition, formal analysis, and methodology. S.-W.F. and H.-M.H., contributed to conceptualization, project administration, supervision, writing—review & editing. All authors have read and agreed to the published version of the manuscript.

Funding: This research was supported by grants (grant number: MOST 109-2314-B-038-025 and MOST 107-2314-B-038-037) from Ministry of Science and Technology, Taiwan.

Institutional Review Board Statement: Animal use and experimental protocols were designed according to the National Research Council's Guide for the Care and Use of Laboratory Animals guidelines. The entire protocol was approved by the Institution Animal Care and Use Committee (IACUC Approval No. MI202001-01, 23 January 2018).

Informed Consent Statement: Not applicable.

Data Availability Statement: Not applicable.

Conflicts of Interest: All authors declare no conflict of interest related to this study.

References

1. Brodzikowska, A.; Górski, B. Polymorphisms in genes involved in inflammation and periodontitis: A narrative review. *Biomolecules* **2022**, *12*, 552. [CrossRef] [PubMed]
2. Guerra, F.; Mazur, M.; Ndokaj, A.; Corridore, D.; La Torre, G.; Polimeni, A.; Ottolenghi, L. Periodontitis and the microbiome: A systematic review and meta-analysis. *Minerva Stomatol.* **2018**, *67*, 250–258. [CrossRef] [PubMed]

3. Irwandi, R.A.; Kuswandani, S.O.; Harden, S.; Marletta, D.; D'Aiuto, F. Circulating inflammatory cell profiling and periodontitis: A systematic review and meta-analysis. *J. Leukoc. Biol.* **2022**, *111*, 1069–1096. [CrossRef] [PubMed]
4. Irwandi, R.; Chiesa, S.; Hajishengallis, G.; Papayannopoulos, V.; Deanfield, J.; D'Aiuto, F. The roles of neutrophils linking periodontitis and atherosclerotic cardiovascular diseases. *Front. Immunol.* **2022**, *13*, 915081. [CrossRef]
5. Wei, Y.; Shi, M.; Zhen, M.; Wang, C.; Hu, W.; Nie, Y.; Wu, X. Comparison of subgingival and buccal mucosa microbiome in chronic and aggressive periodontitis: A pilot study. *Front. Cell. Infect. Microbiol.* **2019**, *9*, 53. [CrossRef] [PubMed]
6. Van Dyke, T.E.; Bartold, P.M.; Reynolds, E.C. The nexus between periodontal inflammation and dysbiosis. *Front. Immunol.* **2020**, *11*, 511. [CrossRef]
7. Chen, M.X.; Zhong, Y.J.; Dong, Q.Q.; Wong, H.M.; Wen, Y.F. Global, regional, and national burden of severe periodontitis, 1990–2019: An analysis of the Global Burden of Disease Study 2019. *J. Clin. Periodontol.* **2021**, *48*, 1165–1188. [CrossRef]
8. Hajishengallis, G.; Chavakis, T. Local and systemic mechanisms linking periodontal disease and inflammatory comorbidities. *Nat. Rev. Immunol.* **2021**, *21*, 426–440. [CrossRef]
9. Prabu, G.R.; Gnanamani, A.; Sadulla, S. Guaijaverin-a plant flavonoid as potential antiplaque agent against *Streptococcus mutans*. *J. Appl. Microbiol.* **2006**, *101*, 487–495. [CrossRef]
10. Palombo, E.A. Traditional medicinal plant extracts and natural products with activity against oral bacteria: Potential application in the prevention and treatment of oral diseases. *Evid. Based Complement. Alternat. Med.* **2011**, *2011*, 680354. [CrossRef]
11. Chhetri, A.B.; Tango, M.S.; Budge, S.M.; Watts, K.C.; Islam, M.R. Non-edible plant oils as new sources for biodiesel production. *Int. J. Mol. Sci.* **2008**, *9*, 169–180. [CrossRef]
12. Upadhyay, A.; Singh, D.K. Pharmacological effects of *Sapindus mukorossi*. *Rev. Inst. Med. Trop. Sao Paulo* **2012**, *54*, 273–280. [CrossRef] [PubMed]
13. Chen, C.C.; Nien, C.J.; Chen, L.G.; Huang, K.Y.; Chang, W.J.; Huang, H.M. Effects of *Sapindus mukorossi* seed oil on skin wound healing: In vivo and in vitro testing. *Int. J. Mol. Sci.* **2019**, *20*, 2579. [CrossRef]
14. Aneja, K.R.; Joshi, R.; Sharma, S. In vitro antimicrobial activity of *Sapindus mukorossi* and *Emblica officinalis* against dental caries pathogens. *Ethnobot. Leafl.* **2010**, *3*, 402–412.
15. Wei, M.P.; Qiu, J.D.; Li, L.; Xie, Y.F.; Guo, Y.H.; Yu, H.; Cheng, Y.L.; Qian, H.; Yao, W.R. The chemical profile and biological activity of different extracts of *Sapindus mukorossi* Gaertn. against *Cutibacterium acnes*. *Nat. Prod. Res.* **2021**, *35*, 4740–4745. [CrossRef]
16. Dhar, J.; Bajpai, V.; Setty, B.; Kamboj, V. Morphological changes in human spermatozoa as examined under scanning electron microscope after in vitro exposure to saponins isolated from *Sapindus mukorossi*. *Contraception* **1989**, *39*, 563–568. [CrossRef]
17. Yin, S.W.; Chen, J.C.; Sun, S.D.; Tang, C.H.; Yang, X.Q.; Wen, Q.B.; Qi, J.R. Physicochemical and structural characterisation of protein isolate, globulin and albumin from soapnut seeds (*Sapindus mukorossi* Gaertn.). *Food Chem.* **2011**, *128*, 420–426. [CrossRef]
18. Shah, M.A.H.; Dutta, K.; Deka, D.C. Fatty acid composition of *Sapindus mukorossi* seed oil. *Adv. Appl. Sci. Res.* **2014**, *5*, 43–50.
19. Sonawane, S.M.; Sonawane, H. A review of recent and current research studies on the biological and pharmalogical activities of *Sapindus mukorossi*. *Int. J. Interdiscip. Res. Innov.* **2015**, *3*, 85–95.
20. Kumar, P.; Vijeth, P.F.; Raju, K. Study on performance and emission characteristics of cotton seed methyl ester, *Sapindous mukorossi* seed oil, and diesel blends on CI engine. *Energy Power* **2015**, *5*, 10–14.
21. Mahar, K.S.; Rana, T.S.; Ranade, S.A. Molecular analyses of genetic variability in soap nut (*Sapindus mukorossi* Gaertn.). *Ind. Crops. Prod.* **2011**, *34*, 1111–1118. [CrossRef]
22. Touyz, L. Oral malodor—A review. *J. Can. Dent. Assoc.* **1993**, *59*, 607–610. [PubMed]
23. Saglik, İ.; Güçlüer, Ö.; Özhak, B. Investigation of the antimicrobial effects of *Sapindus mukorossi* on endodontic pathogens. *J. Exp. Clin. Med.* **2020**, *37*, 111–118.
24. Qian, W.; Ma, T.; Ye, M.; Li, Z.; Liu, Y.; Hao, P. Microbiota in the apical root canal system of tooth with apical periodontitis. *BMC Genom.* **2019**, *20*, 189. [CrossRef] [PubMed]
25. Chen, W.P.; Chang, S.H.; Tang, C.Y.; Liou, M.L.; Tsai, S.J.J.; Lin, Y.L. Composition analysis and feature selection of the oral microbiota associated with periodontal disease. *BioMed. Res. Int.* **2018**, *2018*, 3130607. [CrossRef]
26. Colombo, A.P.V.; Boches, S.K.; Cotton, S.L.; Goodson, J.M.; Kent, R.; Haffajee, A.D.; Socransky, S.S.; Hasturk, H.; Van Dyke, T.E.; Dewhirst, F. Comparisons of subgingival microbial profiles of refractory periodontitis, severe periodontitis, and periodontal health using the human oral microbe identification microarray. *J. Periodontol.* **2009**, *80*, 1421–1432. [CrossRef]
27. Jünemann, S.; Prior, K.; Szczepanowski, R.; Harks, I.; Ehmke, B.; Goesmann, A.; Stoye, J.; Harmsen, D. Bacterial community shift in treated periodontitis patients revealed by ion torrent 16S rRNA gene amplicon sequencing. *PLoS ONE* **2012**, *7*, e41606. [CrossRef]
28. Rovin, S.; Costich, E.R.; Gordon, H.A. The influence of bacteria and irritation in the initiation of periodontal disease in germfree and conventional rats. *J. Periodontal Res.* **1966**, *1*, 193–203. [CrossRef]
29. Maekawa, S.; Onizuka, S.; Katagiri, S.; Hatasa, M.; Ohsugi, Y.; Sasaki, N.; Watanabe, K.; Ohtsu, A.; Komazaki, R.; Ogura, K.; et al. RNA sequencing for ligature induced periodontitis in mice revealed important role of S100A8 and S100A9 for periodontal destruction. *Sci. Rep.* **2019**, *9*, 14663. [CrossRef]
30. Abe, T.; Hajishengallis, G. Optimization of the ligature-induced periodontitis model in mice. *J. Immunol. Methods* **2013**, *394*, 49–54. [CrossRef]
31. Listgarten, M.A. Similarity of epithelial relationships in the gingiva of rat and man. *J. Periodontol.* **1975**, *46*, 677–680. [CrossRef] [PubMed]

32. Shang, L.; Deng, D.; Buskermolen, J.K.; Janus, M.M.; Krom, B.P.; Roffel, S.; Waaijman, T.; van Loveren, C.; Crielaard, W.; Gibbs, S. Multi-species oral biofilm promotes reconstructed human gingiva epithelial barrier function. *Sci. Rep.* **2018**, *8*, 16061. [CrossRef] [PubMed]
33. Groeger, S.E.; Meyle, J. Epithelial barrier and oral bacterial infection. *Periodontol. 2000* **2015**, *69*, 46–67. [CrossRef] [PubMed]
34. Shiu, S.T.; Lew, W.Z.; Lee, S.Y.; Feng, S.W.; Huang, H.M. Effects of *Sapindus mukorossi* seed oil on proliferation, osteogenetic/odontogenetic differentiation and matrix vesicle secretion of human dental pulp mesenchymal stem cells. *Materials* **2020**, *13*, 4063. [CrossRef]
35. Yildirim, T.T.; Ozan, G.; Dundar, S.; Bozoglan, A.; Karaman, T.; Dildes, N.; Kaya, C.A.; Kaya, N.; Erdem, E. The effects of morus nigra on the alveolar bone loss in experimentally-induced periodontitis. *Eur. Oral Res.* **2019**, *53*, 99–105. [CrossRef]
36. Bastos, M.; Tucci, M.; De Siqueira, A.; De Faveri, M.; Figueiredo, L.; Vallim, P.; Duarte, P. Diabetes may affect the expression of matrix metalloproteinases and their inhibitors more than smoking in chronic periodontitis. *J. Periodontal Res.* **2017**, *52*, 292–299. [CrossRef]
37. Balli, U.; Cetinkaya, B.O.; Keles, G.C.; Keles, Z.P.; Guler, S.; Sogut, M.U.; Erisgin, Z. Assessment of MMP-1, MMP-8 and TIMP-2 in experimental periodontitis treated with kaempferol. *J. Periodontal Implant Sci.* **2016**, *46*, 84–95. [CrossRef] [PubMed]
38. Johnson, N.; Ebersole, J.; Kryscio, R.; Danaher, R.; Dawson, D., III; Al-Sabbagh, M.; Miller, C. Rapid assessment of salivary MMP-8 and periodontal disease using lateral flow immunoassay. *Oral Dis.* **2016**, *22*, 681–687. [CrossRef]
39. Dweck, A.C. Isoflavones, phytohormones and phytosterols. *J. Appl. Cosmetol.* **2006**, *24*, 17–33.
40. Mahmoudi, R.; Ghareghani, M.; Zibara, K.; Ardakani, M.T.; Jand, Y.; Azari, H.; Nikbakht, J.; Ghanbari, A. *Alyssum homolocarpum* seed oil (AHSO), containing natural alpha linolenic acid, stearic acid, myristic acid and β-sitosterol, increases proliferation and differentiation of neural stem cells in vitro. *BMC Complement. Altern. Med.* **2019**, *19*, 113. [CrossRef]
41. Belkaid, Y.; Harrison, O.J. Homeostatic immunity and the microbiota. *Immunity* **2017**, *46*, 562–576. [CrossRef] [PubMed]
42. Park, O.J.; Jeong, M.H.; Lee, E.H.; Cho, M.R.; Hwang, J.; Cho, S.; Yun, C.H.; Han, S.H.; Kim, S.Y. A pilot study of chronological microbiota changes in a rat apical periodontitis model. *Microorganisms* **2020**, *8*, 1174. [CrossRef] [PubMed]
43. Chen, T.; Shi, Y.; Wang, X.; Wang, X.; Meng, F.; Yang, S.; Yang, J.; Xin, H. Highthroughput sequencing analyses of oral microbial diversity in healthy people and patients with dental caries and periodontal disease. *Mol. Med. Rep.* **2017**, *16*, 127–132. [CrossRef] [PubMed]
44. Griffen, A.L.; Beall, C.J.; Campbell, J.H.; Firestone, N.D.; Kumar, P.S.; Yang, Z.K.; Podar, M.; Leys, E.J. Distinct and complex bacterial profiles in human periodontitis and health revealed by 16S pyrosequencing. *ISME J.* **2012**, *6*, 1176–1185. [CrossRef]
45. Wang, J.; Qi, J.; Zhao, H.; He, S.; Zhang, Y.; Wei, S.; Zhao, F. Metagenomic sequencing reveals microbiota and its functional potential associated with periodontal disease. *Sci. Rep.* **2013**, *3*, 1843. [CrossRef]
46. Sedghi, L.M.; Bacino, M.; Kapila, Y.L. Periodontal disease: The good, the bad, and the unknown. *Front. Cell Infect. Microbiol.* **2021**, *11*, 766944. [CrossRef]
47. Cai, Z.; Lin, S.; Hu, S.; Zhao, L. Structure and function of oral microbial community in periodontitis based on untegrated data. *Front. Cell. Infect. Microbiol.* **2021**, *11*, 663756. [CrossRef]
48. Perez-Chaparro, P.J.; Goncalves, C.; Figueiredo, L.C.; Faveri, M.; Lobao, E.; Tamashiro, N.; Duarte, P.; Feres, M. Newly identified pathogens associated with periodontitis: A systematic review. *J. Dent. Res.* **2014**, *93*, 846–858. [CrossRef] [PubMed]
49. López-Martínez, J.; Chueca, N.; Padial-Molina, M.; Fernandez-Caballero, J.A.; García, F.; O'Valle, F.; Galindo-Moreno, P. Bacteria associated with periodontal disease are also increased in health. *Med. Oral Patol. Oral Cir. Bucal* **2020**, *25*, e745. [CrossRef]
50. Païssé, S.; Valle, C.; Servant, F.; Courtney, M.; Burcelin, R.; Amar, J.; Lelouvier, B. Comprehensive description of blood microbiome from healthy donors assessed by 16S targeted metagenomic sequencing. *Transfusion* **2016**, *56*, 1138–1147. [CrossRef]
51. Emery, D.C.; Cerajewska, T.L.; Seong, J.; Davies, M.; Paterson, A.; Allen-Birt, S.J.; West, N.X. Comparison of blood bacterial communities in periodontal health and periodontal disease. *Front. Cell. Infect. Microbiol.* **2021**, *10*, 577485. [CrossRef] [PubMed]
52. Lee, S.H.; Yun, Y.; Kim, S.J.; Lee, E.J.; Chang, Y.; Ryu, S.; Shin, H.; Kim, H.L.; Kim, H.N.; Lee, J.H. Association between cigarette smoking status and composition of gut microbiota: Population-based cross-sectional study. *J. Clin. Med.* **2018**, *7*, 282. [CrossRef]
53. Jiao, Y.; Hasegawa, M.; Inohara, N. The role of oral pathobionts in dysbiosis during periodontitis development. *J. Dent. Res.* **2014**, *93*, 539–546. [CrossRef] [PubMed]
54. Saeb, A.T.M.; Al-Rubeaan, K.A.; Aldosary, K.; Raja, G.K.U.; Mani, B.; Abouelhoda, M.; Tayeb, H.T. Relative reduction of biological and phylogenetic diversity of the oral microbiota of diabetes and pre-diabetes patients. *Microb. Pathog.* **2019**, *128*, 215–229. [CrossRef] [PubMed]
55. Galimanas, V.; Hall, M.W.; Singh, N.; Lynch, M.D.J.; Goldberg, M.; Tenenbaum, H.; Cvitkovitch, D.G.; Neufeld, J.D.; Senadheera, D.B. Bacterial community composition of chronic periodontitis and novel oral sampling sites for detecting disease indicators. *Microbiome* **2014**, *2*, 32. [CrossRef] [PubMed]
56. Kumar, P.S.; Griffen, A.L.; Moeschberger, M.L.; Leys, E.J. Identification of candidate periodontal pathogens and beneficial species by quantitative 16S clonal analysis. *J. Clin. Microbiol.* **2005**, *43*, 3944–3955. [CrossRef] [PubMed]
57. Wu, Y.F.; Lee, W.F.; Salamanca, E.; Yao, W.L.; Su, J.N.; Wang, S.Y.; Hu, C.J.; Chang, W.J. Oral microbiota changes in elderly patients, an indicator of Alzheimer's disease. *Int. J. Environ. Res. Public Health* **2021**, *18*, 4211. [CrossRef]
58. Ling, Z.; Liu, X.; Cheng, Y.; Jiang, X.; Jiang, H.; Wang, Y.; Li, L. Decreased diversity of the oral microbiota of patients with hepatitis B virus-induced chronic liver disease: A pilot project. *Sci. Rep.* **2015**, *5*, 17098. [CrossRef]

59. Wu, Y.F.; Salamanca, E.; Chen, I.W.; Su, J.N.; Chen, Y.C.; Wang, S.Y.; Sun, Y.S.; Teng, N.C.; Chang, W.J. Xylitol-containing chewing gum reduces cariogenic and periodontopathic bacteria in dental plaque-microbiome investigation. *Front. Nutr.* **2022**, *9*, 882636. [CrossRef] [PubMed]
60. Kato, Y.; Shirai, M.; Murakami, M.; Mizusawa, T.; Hagimoto, A.; Wada, K.; Nomura, R.; Nakano, K.; Ooshima, T.; Asai, F. Molecular detection of human periodontal pathogens in oral swab specimens from dogs in Japan. *J. Vet. Dent.* **2011**, *28*, 84–89. [CrossRef]
61. Dewhirst, F.E.; Chen, T.; Izard, J.; Paster, B.J.; Tanner, A.C.R.; Yu, W.H.; Lakshmanan, A.; Wade, W.G. The human oral microbiome. *J. Bacteriol.* **2010**, *192*, 5002–5017. [CrossRef] [PubMed]
62. Wu, Y.-H.; Taya, Y.; Kuraji, R.; Ito, H.; Soeno, Y.; Numabe, Y. Dynamic microstructural changes in alveolar bone in ligature-induced experimental periodontitis. *Odontology* **2020**, *108*, 339–349. [CrossRef] [PubMed]
63. de Molon, R.S.; Park, C.H.; Jin, Q.; Sugai, J.; Cirelli, J.A. Characterization of ligature-induced experimental periodontitis. Microsc. *Res. Tech.* **2018**, *81*, 1412–1421. [CrossRef] [PubMed]
64. Ayukawa, Y.; Takeshita, F.; Inoue, T.; Yoshinari, M.; Shimono, M.; Suetsugu, T.; Tanaka, T. An immunoelectron microscopic localization of noncollagenous bone proteins (osteocalcin and osteopontin) at the bone–titanium interface of rat tibiae. *J. Biomed. Mater. Res.* **1998**, *41*, 111–119. [CrossRef]
65. Savi, F.M.; Brierly, G.I.; Baldwin, J.; Theodoropoulos, C.; Woodruff, M.A. Comparison of different decalcification methods using rat mandibles as a model. *J. Histochem. Cytochem.* **2017**, *65*, 705–722. [CrossRef]
66. Quast, C.; Pruesse, E.; Yilmaz, P.; Gerken, J.; Schweer, T.; Yarza, P.; Peplies, J.; Glöckner, F.O. The SILVA ribosomal RNA gene database project: Improved data processing and web-based tools. *Nucleic Acids Res.* **2012**, *41*, D590–D596. [CrossRef]
67. Glöckner, F.O.; Yilmaz, P.; Quast, C.; Gerken, J.; Beccati, A.; Ciuprina, A.; Bruns, G.; Yarza, P.; Peplies, J.; Westram, R. 25 years of serving the community with ribosomal RNA gene reference databases and tools. *J. Biotechnol.* **2017**, *261*, 169–176. [CrossRef] [PubMed]
68. Yilmaz, P.; Parfrey, L.W.; Yarza, P.; Gerken, J.; Pruesse, E.; Quast, C.; Schweer, T.; Peplies, J.; Ludwig, W.; Glöckner, F.O. The SILVA and "all-species living tree project (LTP)" taxonomic frameworks. *Nucleic Acids Res.* **2014**, *42*, D643–D648. [CrossRef] [PubMed]
69. Ludwig, W.; Strunk, O.; Westram, R.; Richter, L.; Meier, H.; Yadhukumar; Buchner, A.; Lai, T.; Steppi, S.; Jobb, G. ARB: A software environment for sequence data. *Nucleic Acids Res.* **2004**, *32*, 1363–1371. [CrossRef] [PubMed]
70. Schloss, P.D.; Westcott, S.L.; Ryabin, T.; Hall, J.R.; Hartmann, M.; Hollister, E.B.; Lesniewski, R.A.; Oakley, B.B.; Parks, D.H.; Robinson, C.J. Introducing mothur: Open-source, platform-independent, community-supported software for describing and comparing microbial communities. *Appl. Environ. Microbiol.* **2009**, *75*, 7537–7541. [CrossRef] [PubMed]
71. Caporaso, J.G.; Kuczynski, J.; Stombaugh, J.; Bittinger, K.; Bushman, F.D.; Costello, E.K.; Fierer, N.; Peña, A.G.; Goodrich, J.K.; Gordon, J.I. QIIME allows analysis of high-throughput community sequencing data. *Nat. Methods* **2010**, *7*, 335–336. [CrossRef] [PubMed]

International Journal of
Molecular Sciences

MDPI

Article

Parameter Screening and Optimization for a Polycaprolactone-Based GTR/GBR Membrane Using Taguchi Design

Lohitha Kalluri and Yuanyuan Duan *

Department of Biomedical Materials Science, University of Mississippi Medical Center, Jackson, MS 39216, USA; lkalluri@umc.edu
* Correspondence: yduan@umc.edu

Abstract: Our objective was to determine and optimize the significant parameters affecting mechanical properties and mean fiber diameter (MFD) of a novel GTR/GBR membrane composed of polycaprolactone (PCL) and chicken eggshell membrane (ESM). For this, we prepared electrospun membrane specimens (n = 16) with varying concentrations of PCL, ESM, nano-hydroxyapatite (HAp), and altered electrospinning parameters as generated by DOE++ software. After the determination of MFD and mechanical properties for all specimens, Taguchi orthogonal array L8 design was used to screen significant factors affecting the MFD and mechanical properties. PCL wt%, ESM wt%, HAp wt%, applied voltage (AV), flow rate (FR), and spinneret-collector distance (SCD) were the independent variables investigated. The response variables analyzed were MFD, tensile strength (TS), and elastic modulus. ANOVA outlined ESM wt%, HAp wt%, AV, FR, SCD, and an interactive effect between PCL wt% and AV to be the significant factors affecting modulus values of an electrospun PCL/ESM membrane ($p < 0.05$). Furthermore, concentrations of PCL and ESM were the significant factors affecting MFD ($p < 0.05$) and there were no significant factors affecting the TS values. Optimization using DOE++ software predicted that the maximal TS of 3.125 MPa, modulus of 278.168 MPa, and MFD of 882.75 nm could be achieved.

Keywords: eggshell membrane; electrospinning; guided tissue regeneration/guided bone regeneration; nanofibers; polycaprolactone; Taguchi orthogonal arrays

Citation: Kalluri, L.; Duan, Y. Parameter Screening and Optimization for a Polycaprolactone-Based GTR/GBR Membrane Using Taguchi Design. *Int. J. Mol. Sci.* **2022**, *23*, 8149. https://doi.org/10.3390/ijms23158149

Academic Editor: Mary Anne Melo

Received: 21 June 2022
Accepted: 19 July 2022
Published: 24 July 2022

Publisher's Note: MDPI stays neutral with regard to jurisdictional claims in published maps and institutional affiliations.

Copyright: © 2022 by the authors. Licensee MDPI, Basel, Switzerland. This article is an open access article distributed under the terms and conditions of the Creative Commons Attribution (CC BY) license (https://creativecommons.org/licenses/by/4.0/).

1. Introduction

Guided tissue regeneration/guided bone regeneration (GTR/GBR) is a surgical regenerative approach that is widely employed in clinical practice for the treatment of periodontitis. Briefly, it involves the mucogingival flap elevation around affected teeth, followed by the scaling and root planing procedures, and temporary positioning of a barrier membrane beneath the gingiva [1,2]. The biological basis of this approach is to prevent the apical migration of gingival epithelium to the space over the denuded root surface by using a barrier membrane; thus, facilitating the formation of PDL tissues and alveolar bone by PDL cells and osteoblasts, respectively [2–4]. The majority of commercially available resorbable GTR/GBR membranes, which is a key component of the GTR/GBR technique, are either polyester-based products (synthetic) or tissue-derived collagen-based products (natural). The polyester-based synthetic membranes are biodegradable, allow tissue integration, and are easier to handle surgically compared with non-resorbable membranes. However, their poor cell response is a major limitation [4,5]. In contrast, collagen-based membranes have shown favorable regenerative results due to their excellent cell affinity and biocompatibility. Nevertheless, they demonstrated relatively poor mechanical properties and dimensional stability due to their rapid degradation and early collapse. Additionally, the high cost, availability, poor surgical handling abilities, and potential risk of disease transmission from animal-based products limit their widespread clinical usage [3–7]. Thus, there is a need to develop a novel economical GTR/GBR membrane that could assimilate the advantages of

natural and synthetic biomaterials and promote effective bone regeneration even in cases of moderate and severe periodontitis.

Natural chicken eggshell membrane (ESM) is a bilayered microporous structure that lies in between eggshell and egg white. It is composed of highly cross-linked interwoven protein fibers made up of collagen (Types I, V, and X), osteopontin, and sialoprotein, and is functionally equivalent to the extracellular matrix in avian egg development. It acts as a natural scaffold for biomineralization during the formation of an eggshell [8,9]. Additionally, eggshell biomineralization occurs within 24 h and is the most rapid biomineralization process ever known [9]. ESM has a unique fibrous structure on the outer and inner surfaces, which facilitates the mineralization of eggshells on the outer side while preventing the mineralization of egg yolk on the inner side. Owing to this unique barrier membrane property coupled with the rapid biomineralization process, it has gained attention as a potential natural biomaterial in GTR/GBR membrane applications [10].

Inspired by the unique natural bio-membrane-like structure and rapid biomineralization process assisted by the ESM, coupled with the enormous clinical demand for GTR/GBR membrane, we are developing this novel cost-efficient ESM-based fibrous GTR/GBR membrane using a blend electrospinning process. It is a promising, environment-friendly, and cost-effective alternative for commercial collagen-based GTR/GBR membrane products because ESM comes from abundant industrial waste, unlike collagen. However, pure ESM is a low molecular weight biodegradable polymer with poor mechanical properties, which is the main limitation for GTR/GBR membrane application. Thus, usually, it is used with another polymer either as a blend or by crosslinking or physical entrapment, etc., for potential biomedical applications [10–21]. In this study, we blend electrospun ESM with Poly (ε-caprolactone) (PCL), a synthetic biopolymer, and a bioceramic nano-hydroxyapatite (HAp) to prepare a novel composite GTR/GBR membrane.

An ideal GTR/GBR membrane should fulfill all the desirable characteristics such as mechanical properties including tensile strength (TS) and modulus, porosity, biocompatibility, and controlled biodegradation [2]. Thus, the membrane composition should be optimized to achieve a compromise between the minimal requirements, target levels, and relative importance of desired mechanical properties and mean fiber diameter (MFD). Apart from the membrane composition (ESM wt%, PCL wt%, HAp wt%), other factors such as electrospinning parameters (flow rate of solution (FR), spinneret-collector distance (SCD), and applied voltage (AV)) also might have a significant effect on the physical, mechanical, and biological properties of this novel electrospun membrane. Thus, the Design of Experiments (DOE++) approach using Taguchi orthogonal array design is an effective tool to outline the significant factors and to further optimize the membrane composition to achieve the desired outcomes.

Thus, the objectives of this study were to determine and optimize the significant factors affecting the mechanical properties as well as the MFD of a novel biomimetic electrospun composite GTR/GBR membrane, using Taguchi orthogonal arrays in DOE++ software. The null hypothesis was that there was no significant difference in TS, modulus, and MFD of PCL/ESM composite membrane with electrospinning parameters or the polymer solution composition.

2. Results

The SEM images obtained for all 16 specimens are depicted in Figure 1a–p, respectively.

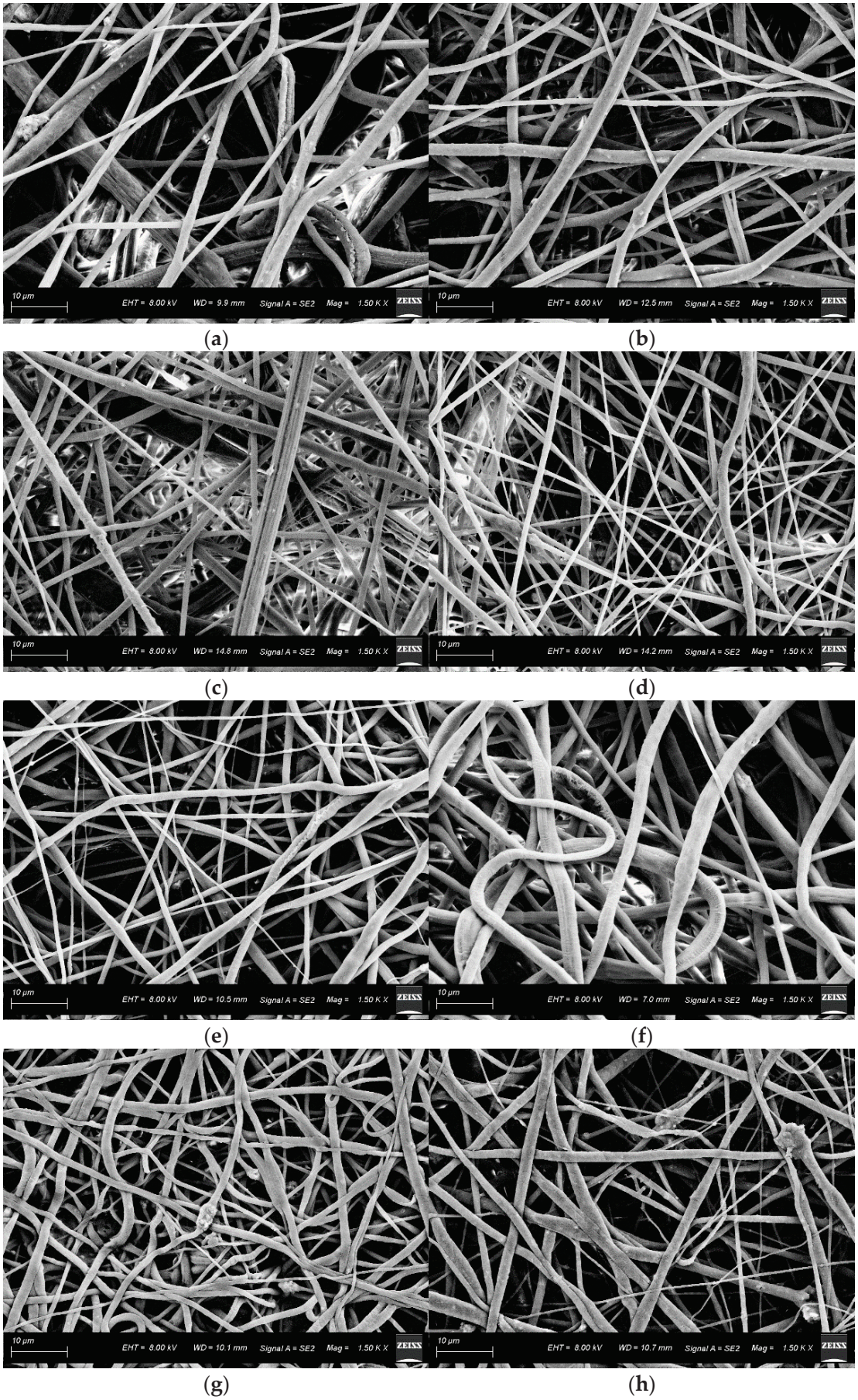


Figure 1. *Cont.*

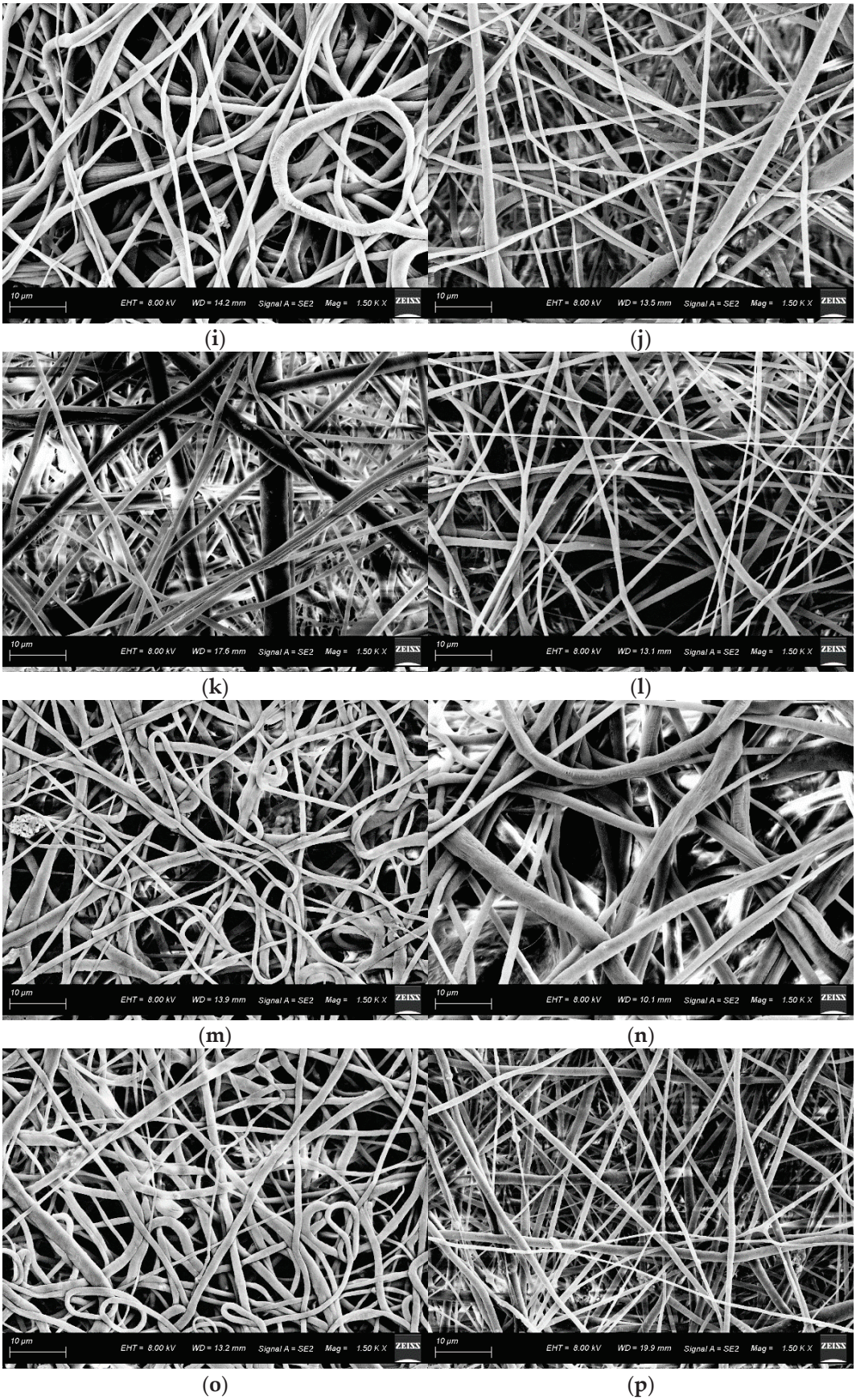


Figure 1. SEM micrographs of 16 specimens (**a**–**p**) prepared for Taguchi orthogonal array analysis. All the SEM micrographs were collected at 1500× magnification and at an accelerating voltage of 8 kV.

The modulus, TS, and MFD values calculated for all 16 specimens were tabulated in Table 1. The MFD, modulus, and TS values of tested specimens varied from 932 to 1925 nm, 16.62 to 207.3 MPa, and 1.2 to 3.5 MPa, respectively. ANOVA outlined ESM wt%, HAp wt%, AV, FR, SCD, and an interactive effect between PCL wt% and AV to be the significant factors affecting the modulus values of an electrospun PCL/ESM membrane ($p < 0.05$). Furthermore, concentrations of PCL and ESM were the significant factors affecting MFD values ($p < 0.05$). However, there were no significant factors observed to be affecting the TS values.

Table 1. TS, modulus, and MFD values for all 16 specimens.

n #	Tensile Strength (MPa)	Elastic Modulus (MPa)	Mean Fiber Diameter (nm)
1	3.5	128.678	1649
2	2.3	194.813	1459
3	1.7	31.578	1201
4	2.6	29.981	932
5	2.9	68.888	993
6	3.1	104.391	1925
7	3	32.196	1067
8	1.9	23.488	1261
9	1.3	89.305	1532
10	1.2	207.338	1311
11	0.8	20.061	1592
12	1.6	16.622	956
13	2.7	41.67	1258
14	3	115.557	1672
15	3.1	24.867	1259
16	1.7	16.749	1141

ANOVA outlined ESM wt%, HAp wt%, AV, FR, SCD, and an interactive effect between PCL wt% and AV to be the significant factors affecting the elastic modulus values of this GTR/GBR membrane ($p < 0.05$) as observed in the Pareto chart depicted in Figure 2. However, there were no significant factors observed to be affecting the TS values as depicted in the Pareto chart in Figure 3. Additionally, from the Pareto chart, as depicted in Figure 4, PCL and ESM concentrations were observed to be the significant factors affecting MFD values ($p < 0.05$).

The analytical quadratic model obtained by multiple regression analysis for variations within response variables of this GTR/GBR membrane is shown in Equation (1). The coefficients of the quadratic Equation (1) after fitting the data to analyzed response variables are tabulated in Table 2.

$$\mathbf{Y = X + X_1A + X_2B + X_3C + X_4D + X_5E + X_6F + X_7(A \cdot D)} \quad (1)$$

Y is the response variable analyzed. A, B, C, D, E, and F are the coded values for PCL wt%, ESM wt%, HAp wt%, AV, FR, and SCD, respectively. X, X_1, X_2, X_3, X_4, X_5, X_6, and X_7 are the respective coefficients.

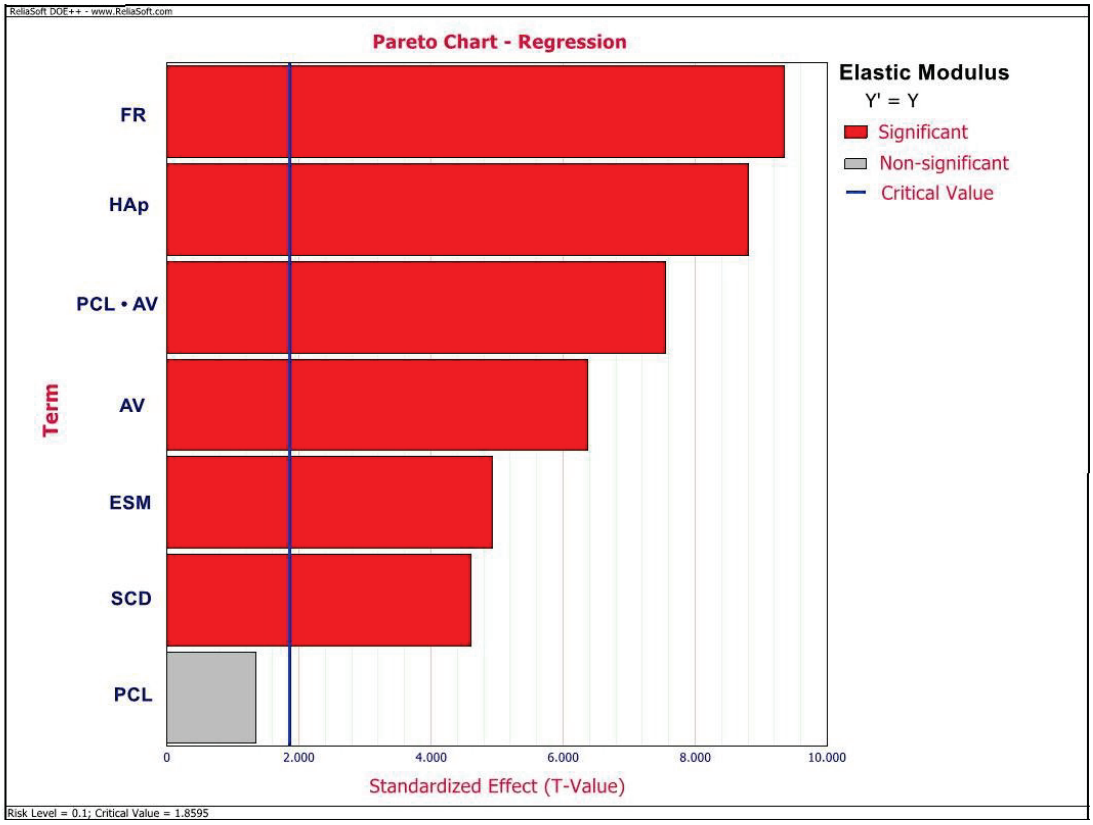


Figure 2. Pareto chart depicting the significant factors affecting elastic modulus values of an electrospun composite membrane.

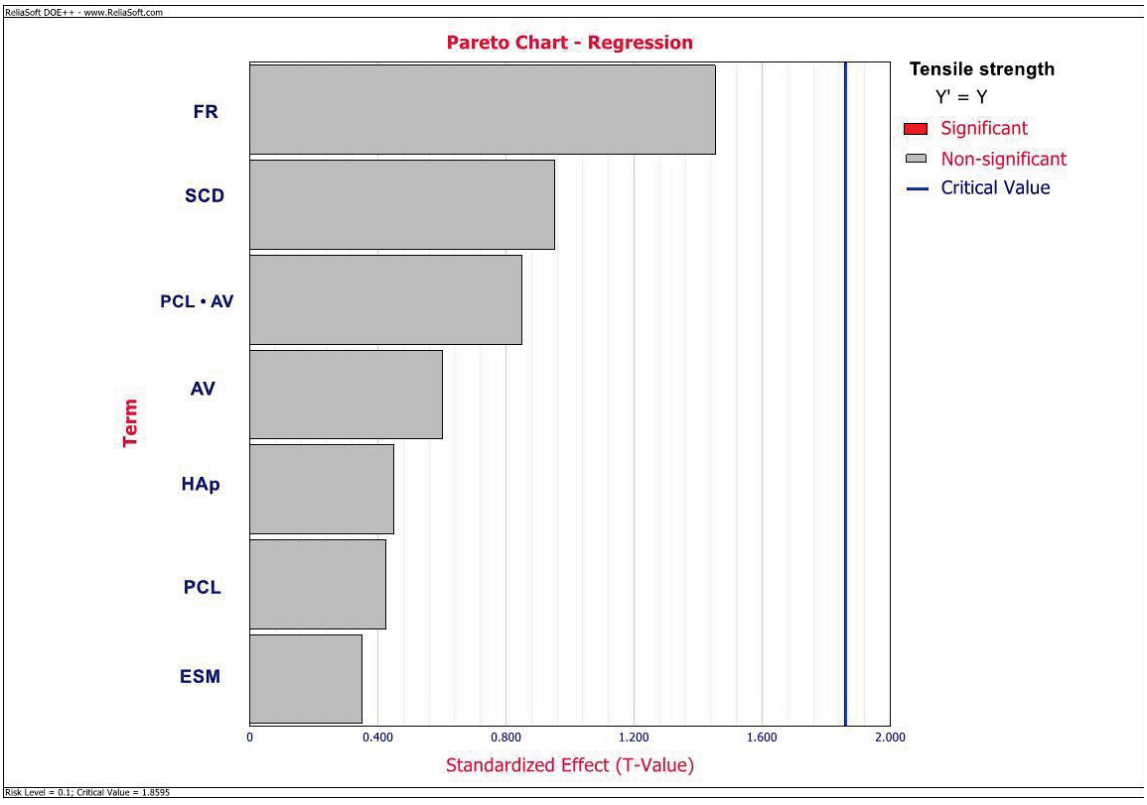


Figure 3. Pareto chart depicting the significant factors affecting TS values of an electrospun composite membrane.

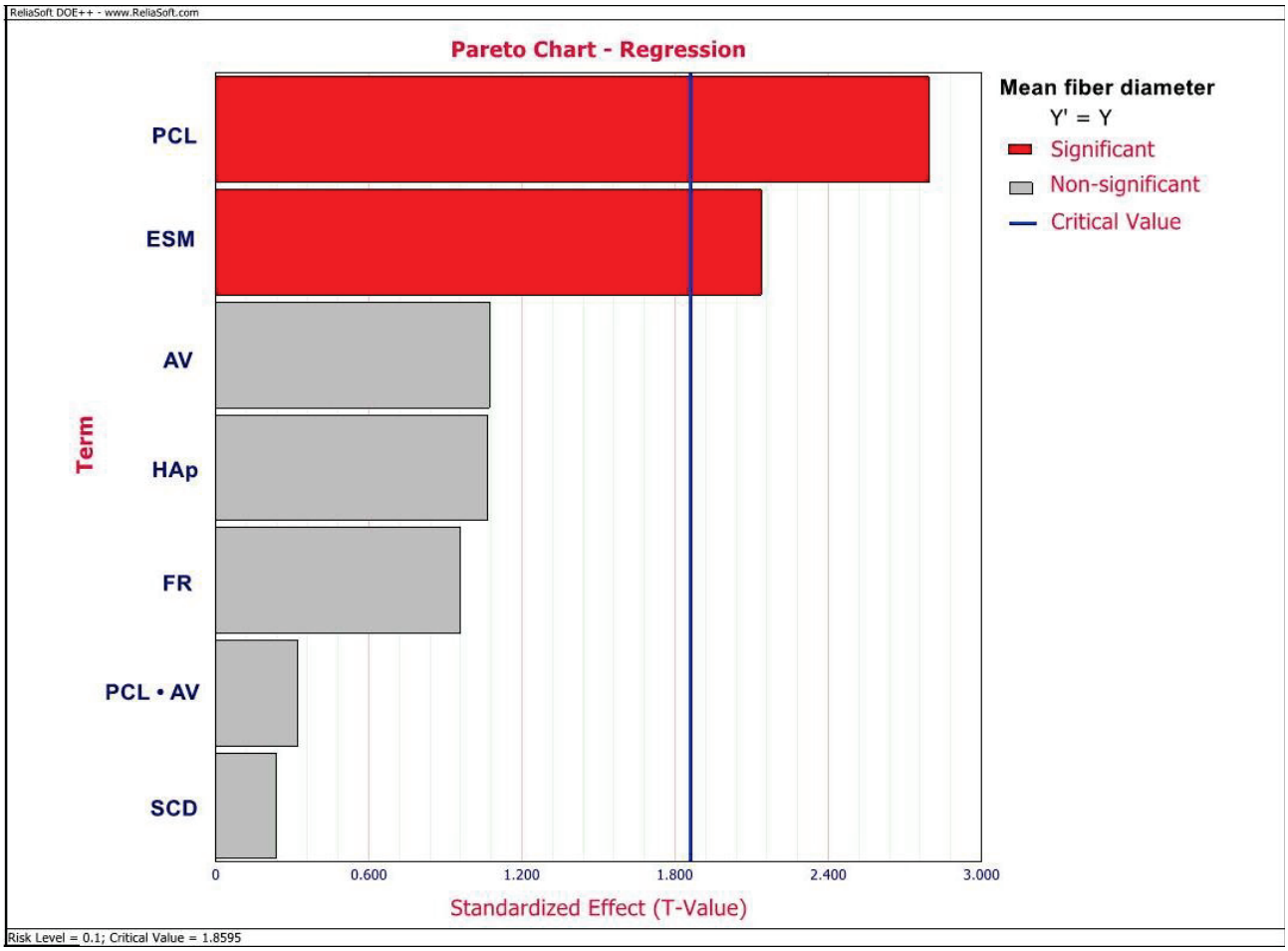


Figure 4. Pareto chart depicting the significant factors affecting mean MFD values of an electrospun composite membrane.

Table 2. Regression information for analyzed response variables.

Y	X/SE *	X_1/SE *	X_2/SE *	X_3/SE *	X_4/SE *	X_5/SE *	X_6/SE *	X_7/SE *
Elastic Modulus	97.4075/4.8274	−9.2295/6.8269	23.8167/4.8274	42.5065/4.8274	−30.7697/4.8274	45.1215/4.8274	22.2252/4.8274	51.5422/6.8269
Tensile Strength	2.425/0.2494	−0.15/0.3527	−0.0875/0.2494	−0.1125/0.2494	0.15/0.2494	0.3625/0.2494	−0.2375/0.2494	0.3/0.3527
Mean Fiber Diameter	1313.25/54.094	213.75/76.5004	−115.625/54.094	−57.625/54.094	58 /54.094	51.875/54.094	12.875/54.094	−24.5/76.5004

* SE = standard error.

Additionally, optimization using DOE++ software predicted that the maximal TS of 3.125 MPa, modulus of 278.168 MPa, and MFD of 882.75 nm could be achieved using 12 wt% PCL, 6 wt% SEP, 2 wt% HAp, 13 kV AV, 1.4 mL/h FR, and 8 cm SCD with a global desirability of 0.1025 as depicted in Figure 5.

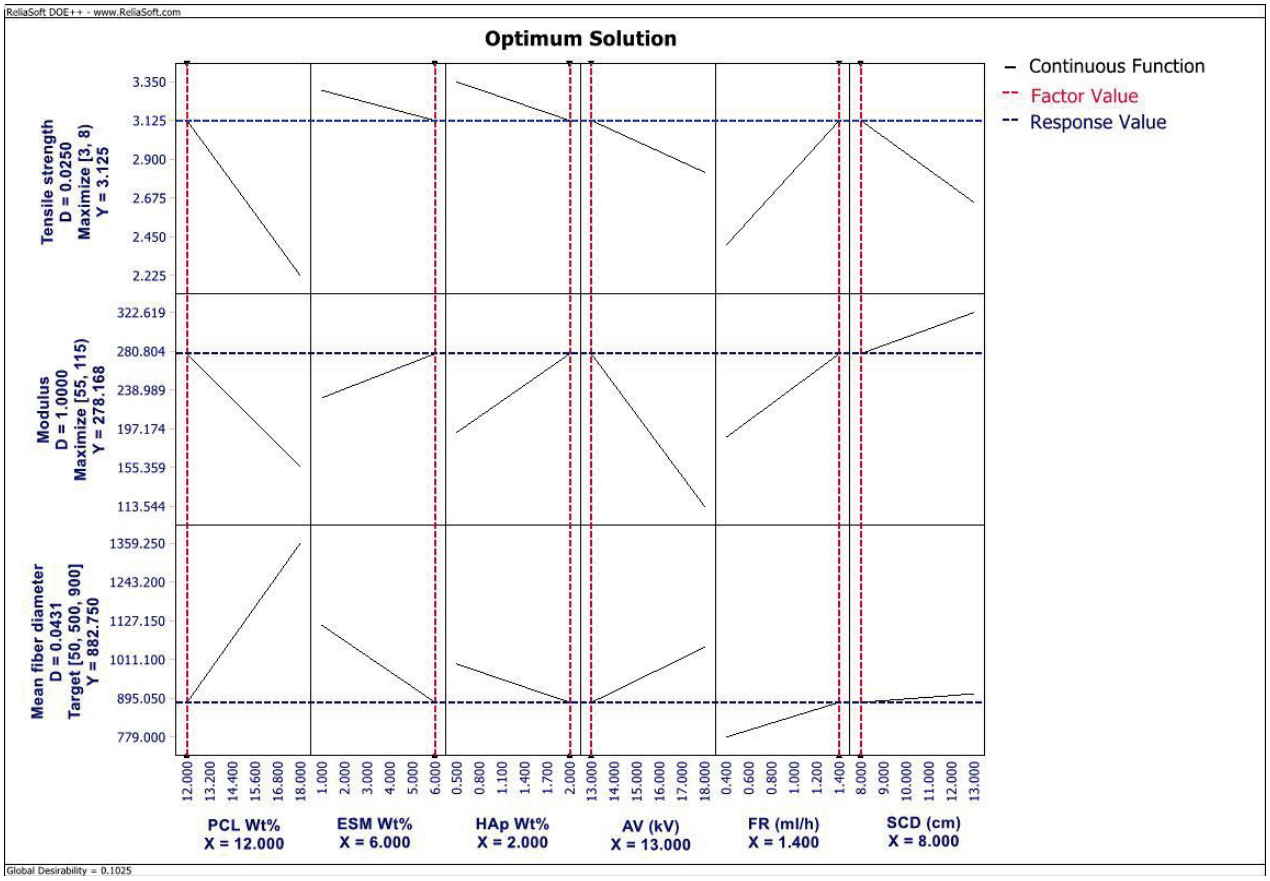


Figure 5. The optimal solution for maximizing the mechanical properties and MFD values of an electrospun composite membrane.

3. Discussion

For GTR/GBR membrane applications, adequate mechanical properties are a primary requisite to prevent collapse into the underlying alveolar bone defect region and to protect the bone defect region for alveolar bone and periodontal ligament regeneration. Thus, optimization of mechanical properties, by controlling various electrospinning parameters and mean fiber diameter is necessary to obtain a durable GTR/GBR membrane with maximum mechanical properties. In this study, there were six independent parameters (PCL wt%, ESM wt%, HAp wt%, AV, FR, SCD) that could alter the desired responses and each parameter had two levels (low and high). Hence, there could be 64 different combinations of parameters per response variable for the preparation of this membrane, using a full-factorial method. To avoid the cumbersome process of preparing 64 groups of specimens and to save time and resources, the method of Taguchi orthogonal arrays was used to generate a reduced set of combinations of independent factors to derive an optimum combination of the parameters necessary for the preparation of this membrane. Taguchi orthogonal array is a fractional factorial method that ensures equal consideration of all the levels of all factors and evaluates the effects of individual parameters and the lower-order two-way interactions [22]. Our experimental design strategy was based on the Pareto principle, which advocates that 20% of the main factors and their lower-order interactions account for 80% of the outcomes [23]. This also implies that the higher-order interactions typically do not have a significant effect on the response, and hence was rational to use a Taguchi orthogonal array design for this study. DOE++ generated 16 combinations of parameters and thus 16 n specimens were used for analysis.

Bead-on-string fibers were usually considered a "by-product" of the electrospun fibers and confer detrimental properties to the electrospun membrane by reducing the surface area of the membrane [24,25]. Thus, the production of smooth bead-free uniform fibers

is desirable. From the SEM micrographs (Figure 1a–p), we can observe that the bead-free uniform fibers are formed for all the tested specimens. Furthermore, from the SEM images (Figure 1a–p), we can observe the presence of HAp agglomerates. The presence of agglomerates within nanofibrous scaffolds on the addition of bioceramics as HAp and β-tricalcium phosphate was also previously reported by Castro VO et al. [26] and Santos VI et al. [27].

From the results (Figures 2 and 5 and Table 2), we can observe that except for AV, the rest of all significant factors, including ESM wt%, HAp wt%, SCD, FR, and interaction between PCL wt% and AV have a positive correlation with an elastic modulus of this membrane. Regarding TS of th membrane, the Pareto chart (Figure 3) showed that there are no significant parameters affecting TS. However, from the regression information (Table 2), we can observe that TS has a negative correlation with all tested parameters except for FR, AV, and the interaction between PCL wt% and AV. The results observed in this study were in contrast with the results reported by Xiong X et al. [13], Jia J et al. [14], and Qi Q et al. [28], wherein they observed increased mechanical properties of ESM-based membranes on incorporating increased amounts of the additive synthetic polymers and chitosan. This might be due to the interaction with bioceramic, HAp in this composite and could also be attributed to the difference in the processed commercially available ESM powder used in this study.

Furthermore, PCL wt% and ESM wt% are the significant factors affecting the MFD of the PCL/ESM membrane (Figure 3). Additionally, the optimal solution (Figure 5) and regression information for MFD (Table 2) demonstrated that except for ESM wt%, HAp wt%, and interaction between PCL wt% and AV, all other tested factors have a positive correlation with the MFD of final nanofibers. The negative correlation of MFD with HAp wt% observed in this study agrees with results reported by Doustgani A et al. [29], wherein they attributed it to the increase in conductivity of the polymer solution and the surface charge density of the solution jet with the addition of HAp. Furthermore, the negative correlation of MFD with ESM wt% could also be attributed to the increased surface charge density of polymer solution jet with increased ESM concentration.

Additionally, the optimization of the formulation to prepare an electrospun PCL/ESM GTR/GBR membrane with global maximal mechanical properties such as TS, and elastic modulus as well as to achieve the MFD close to the collagen fibers in the native extracellular matrix, is completed with an optimization tool in DOE++ software. Since we have three responses (TS, modulus, and MFD), the optimal setting of independent variables for one of the responses may not be good for the other two. Therefore, a compromise should be made and a balanced setting of independent variables that can optimize the overall desired responses should be found. DOE++ software used in this study employed a statistical and mathematical approach to efficiently optimize the mechanical properties including modulus and TS, along with targeted MFD values for this electrospun composite membrane by a compromise between the minimal requirements, target level, and relative importance of each desired outcome. From Figure 5, we can observe that the PCL/ESM electrospun membrane prepared using polymer solution concentrations of 12 wt% of PCL, 6 wt% of ESM, 2 wt% of HAp, and electrospinning parameters of 13 kV AV, 1.4 mL/h FR, and 8 cm SCD will have the predicted TS of 3.125 MPa with a desirability value of 0.025; predicted modulus of about 278.168 MPa with a desirability value of 1; and a predicted MFD of 882.75 nm with a desirability value of 0.0431. The achieved overall desirability value is 0.1025.

Apart from the parameters tested in this study, the effect of additional environmental parameters such as temperature, relative humidity, and additional polymer solution parameters such as viscosity and solution conductivity could be investigated further. Future studies correlating the effect of mechanical properties and MFD with degradation properties are necessary to determine the applicability of these nanofibers in various biomedical applications. Additionally, characterization of the optimized GTR/GBR membrane to determine the porosity, chemical structure, physical properties, and biocompatibility testing

using cell culture studies are necessary to validate the applicability of these nanofibrous GTR/GBR membranes in periodontal regeneration applications.

4. Materials and Methods

Poly (ε-caprolactone) (PCL, Mn:80,000), Chloroform (CF, ≥99.5%), and N, N-Dimethylformamide (DMF, 99.8%) were procured from Sigma-Aldrich (Millipore Sigma, St. Louis, MO, USA). Nano-Hydroxyapatite (HAp, particle size:100 nm) was purchased from Berkeley advanced biomaterials (Berkeley, CA, USA). Natural eggshell membrane powder was bought from Healthy Origins (Pittsburg, PA, USA). All reagents were used as received without further purification.

4.1. Taguchi Orthogonal Array Study Design

In this study, the independent variables such as PCL wt%, ESM wt%, HAp wt%, AV, FR, and SCD used for the preparation of electrospun membrane were considered as input factors while, TS, elastic modulus, and MFD were measured as the three objectives or response variables. A Taguchi orthogonal array L8 design (DOE folio, Weibull++ software, Reliasoft, AZ, USA) using two levels of factors (low and high) was used to screen out significant factors affecting the MFD and mechanical properties of this electrospun membrane as well as to obtain an optimum formulation of independent variables that could maximize the modulus, TS, and MFD values. The range and levels of the independent factors which were used in optimization are tabulated in Table 3. The minimum and maximum levels of the independent factors were chosen by considering the preliminary studies, trial experiments, practical limitations, and represent the attainable limits for nanofiber formation and/or equipment operation. For instance, the polymer solution becomes highly viscous and could not be electrospun at PCL concentrations greater than 18 wt%, particularly when used together with ESM concentrations greater than 6 wt%. Furthermore, HAp concentrations greater than 2 wt% resulted in agglomerate formation and precipitation of HAp powder particles at the bottom of the test tube during polymer solution preparation. At PCL concentrations lesser than 12 wt%, there are beads and spindle-shaped fiber formation observed within the electrospun fiber mats, even with higher ESM concentrations.

Table 3. The range and levels of the independent variables used for Taguchi orthogonal array design.

Independent Variables	Level 1 (Low)	Level 2 (High)
PCL wt%	12	18
ESM wt%	1	6
HAp wt%	0.5	2
Applied Voltage (AV) (kV)	13	18
Flow Rate of Solution (FR) (mL/h)	0.4	1.4
Spinneret to Collector Distance (SCD) (cm)	8	13

Based on the range of input variables, no. of replicates, and desired response variables, Taguchi orthogonal array design folio in DOE++ software generated 16 electrospun membrane specimen combinations (two replicates of eight combinations of various independent parameters (2n × 8 combinations)) with varying concentrations of PCL, ESM, HAp, and altered electrospinning parameters needed to run the analysis.

4.2. Preparation of Electrospun Membrane Specimens

The 16 specimen combinations generated by DOE++ software as tabulated in Table 4 were prepared using the blend electrospinning technique. Polymer solution for the blend electrospinning process was prepared by initially dissolving the premeasured quantity of HAp powder (Table 4) in a mixture of CF and DMF (3:1) solvents for 30 min using a

sonicator. Then, premeasured quantities of PCL and ESM as tabulated in Table 4 were blended and dissolved in the HAp/CF/DMF mixture overnight using a bench rocker. The resulting PCL/ESM solution was loaded into a syringe and an 18-gauge needle is attached to it to carry out the electrospinning process using a custom electrospinning setup [30]. The same process was repeated with various polymer solution concentrations and altered electrospinning parameters for the preparation of 16 specimens as tabulated in Table 4. All 16 specimens were collected after 10 h of electrospinning to obtain the desired thickness range at the laboratory conditions of 23 ± 2 °C temperature and 50% ± 1% relative humidity and left to dry overnight before analysis to allow for the residual solvent evaporation.

Table 4. The 16 specimen combinations of various input independent variables generated by DOE++.

n #	PCL (wt%)	SEP (wt%)	HAp (wt%)	Applied Voltage (kV)	Flow Rate (ml/h)	S-C Distance (cm)
1	18	1	2	13	1.4	8
2	18	6	2	13	1.4	13
3	18	6	0.5	13	0.4	13
4	12	6	2	18	0.4	8
5	12	1	0.5	13	0.4	8
6	18	1	0.5	18	1.4	13
7	12	6	0.5	18	1.4	8
8	12	1	2	18	0.4	13
9	18	1	2	13	1.4	8
10	18	6	2	13	1.4	13
11	18	6	0.5	13	0.4	13
12	12	6	2	18	0.4	8
13	12	1	0.5	13	0.4	8
14	18	1	0.5	18	1.4	13
15	12	6	0.5	18	1.4	8
16	12	1	2	18	0.4	13

4.3. Mechanical Testing and MFD Assessment of PCL/ESM Membrane Specimens

The morphology of all the fibrous mats was characterized using Field-Emission Scanning Electron Microscopy (SEM, Supra 40, Carl Zeiss, Germany). Specimens were sputter-coated with Ag-Pd alloy using a sputter coater (Q150T, Carl Zeiss, Germany) to improve the electrical conductivity, then observed using SEM at a voltage of 8 kV and 1500 X magnification. ImageJ software (ImageJ, Version 1.53b, National Institute of Health, Bethesda, MD, USA) was used to assess the MFD based on the obtained SEM images. Mean fiber diameter was calculated as an average of fiber diameters measured at 30 different positions on each SEM image of the specimen.

For the mechanical testing, all specimens were prepared to have a width of 13 mm and further taped at both ends to prevent gripping failures. The VHX Digital Microscope (Keyence Corp, Osaka, Japan) was used to precisely record the thickness ($n \geq 5$) of the electrospun membrane without any compression by mechanical instrumentation. Uniaxial tensile testing was carried out according to ASTM D882 Standard test method using a Sintech 2/G Materials Testing System (MTS, Eden Prairie, MN, USA) at an extension rate

of 0.5 in/min as depicted in Figure 6a,b. Mechanical properties such as elastic modulus and TS were calculated using MTS Testworks 4.0 software (MTS, Eden Prairie, MN, USA).



(**a**) (**b**)

Figure 6. Electrospun membrane specimen (**a**) loaded onto the Sintech 2/G materials testing system for uniaxial tensile testing, and (**b**) tested till failure.

4.4. Screening and Optimization of Significant Factors

After the determination of MFD, TS, and modulus values for all 16 specimens, the obtained values were input into DOE++ software and Taguchi orthogonal array analysis was run. From the Taguchi analysis, ANOVA was used to screen the independent parameters that had significant effects on the MFD, TS, and elastic modulus of the final membrane ($\alpha = 0.05$). Furthermore, after finding the significant factors and interactions, optimization was completed using the optimize feature in the DOE++ software to find the optimum values of independent factors needed to maximize modulus and TS as well as to achieve a maximum MFD of around 500 nm to resemble the MFD values of collagen fibers in the natural extracellular matrix as reported in the literature [31,32].

5. Conclusions

To conclude, the results showed that the elastic modulus of this novel PCL-based GTR/GBR membrane varies with the ESM wt%, HAp wt%, AV, FR, SCD, and an interactive effect between PCL wt% and AV. However, there is no significant variation observed with TS values with any of the parameters tested. Additionally, there is a significant variation in MFD values observed with ESM and PCL polymer concentrations within the electrospinning polymer solution. Thus, the null hypothesis stating that there was no significant variation in mechanical properties and MFD of final membranes with altered electrospinning parameters and polymer solution concentration was partially accepted.

Furthermore, the results show that the Taguchi orthogonal arrays and optimization by Design of Experiments employed in this study are effective modeling tools for screening and optimizing various parameters during the preparation of this novel GTR/GBR membrane.

Author Contributions: Conceptualization, Y.D.; methodology, L.K. and Y.D.; validation, Y.D.; formal analysis, L.K.; investigation, L.K.; resources, Y.D.; data curation, L.K.; writing—original draft preparation, L.K.; writing—review and editing, Y.D.; visualization, L.K.; supervision, Y.D.; funding acquisition, Y.D. All authors have read and agreed to the published version of the manuscript.

Funding: This research was funded by Osteo Science Foundation.

Institutional Review Board Statement: Not applicable.

Informed Consent Statement: Not applicable.

Data Availability Statement: Not applicable.

Conflicts of Interest: The authors declare no conflict of interest.

References

1. Wu, Y.C.; Lin, L.K.; Song, C.J.; Su, Y.X.; Tu, Y.K. Comparisons of periodontal regenerative therapies: A meta-analysis on the long-term efficacy. *J. Clin. Periodontol.* **2017**, *44*, 511–519. [CrossRef] [PubMed]
2. Newman, M.G.; Takei, H.H.; Klokkevold, P.R.; Carranza, F.A. *Newman and Carranza's Clinical Periodontology*, 13th ed.; Elsevier: Philadelphia, PA, USA, 2019.
3. Sculean, A.; Nikolidakis, D.; Schwarz, F. Regeneration of periodontal tissues: Combinations of barrier membranes and grafting materials—Biological foundation and preclinical evidence: A systematic review. *J. Clin. Periodontol.* **2008**, *35*, 106–116. [CrossRef] [PubMed]
4. Bottino, M.C.; Thomas, V.; Schmidt, G.; Vohra, Y.K.; Chu, T.M.; Kowolik, M.J.; Janowski, G.M. Recent advances in the development of GTR/GBR membranes for periodontal regeneration—A materials perspective. *Dent. Mater.* **2012**, *28*, 703–721. [CrossRef]
5. Liang, Y.; Luan, X.; Liu, X. Recent advances in periodontal regeneration: A biomaterial perspective. *Bioact. Mater.* **2020**, *5*, 297–308. [CrossRef]
6. Bosshardt, D.D.; Sculean, A. Does periodontal tissue regeneration really work? *Periodontol. 2000* **2009**, *51*, 208–219. [CrossRef]
7. Villar, C.C.; Cochran, D.L. Regeneration of periodontal tissues: Guided tissue regeneration. *Dent. Clin. N. Am.* **2010**, *54*, 73–92. [CrossRef] [PubMed]
8. Rose, M.L.H.; Hincke, M.T. Protein constituents of the eggshell: Eggshell-specific matrix proteins. *Cell. Mol. Life Sci.* **2009**, *66*, 2707–2719. [CrossRef]
9. Nys, Y.; Gautron, J.; Garcia-Ruiz, J.M.; Hincke, M.T. Avian eggshell mineralization: Biochemical and functional characterization of matrix proteins. *Comptes Rendus Palevol* **2004**, *3*, 549–562. [CrossRef]
10. Sah, M.K.; Rath, S.N. Soluble eggshell membrane: A natural protein to improve the properties of biomaterials used for tissue engineering applications. *Mater. Sci. Eng. C* **2016**, *67*, 807–821. [CrossRef]
11. Kang, J.; Kotaki, M.; Okubayashi, S.; Sukigara, S. Fabrication of electrospun eggshell membrane nanofibers by treatment with catechin. *J. Appl. Polym. Sci.* **2010**, *117*, 2042–2049. [CrossRef]
12. Kang, J.; Chen, L.; Sukigara, S. Preparation and characterization of electrospun polycaprolactone nanofiber webs containing water-soluble eggshell membrane and catechin. *J. Fiber Bioeng. Inform.* **2012**, *5*, 217–226. [CrossRef]
13. Xiong, X.; Li, Q.; Lu, J.W.; Guo, Z.X.; Sun, Z.H.; Yu, J. Fibrous scaffolds made by co-electrospinning soluble eggshell membrane protein with biodegradable synthetic polymers. *J. Biomater. Sci. Polym. Ed.* **2012**, *23*, 1217–1230. [CrossRef] [PubMed]
14. Jia, J.; Liu, G.; Guo, Z.-X.; Yu, J.; Duan, Y. Preparation and Characterization of Soluble Eggshell Membrane Protein/PLGA Electrospun Nanofibers for Guided Tissue Regeneration Membrane. *J. Nanomater.* **2012**, *2012*, 282736. [CrossRef]
15. Jia, J.; Duan, Y.Y.; Yu, J.; Lu, J.W. Preparation and immobilization of soluble eggshell membrane protein on the electrospun nanofibers to enhance cell adhesion and growth. *J. Biomed. Mater. Res. A* **2008**, *86*, 364–373. [CrossRef] [PubMed]
16. Chen, L.; Kang, J.; Sukigara, S. Preparation and characterization of polyurethane/soluble eggshell membrane nanofibers. *Biomed. Mater. Eng.* **2014**, *24*, 1979–1989. [CrossRef]
17. Lu, J.-W.; Li, Q.; Qi, Q.-L.; Guo, Z.-X.; Yu, J. Surface engineering of poly(D,L-lactic acid) by entrapment of soluble eggshell membrane protein. *J. Biomed. Mater. Res. Part A* **2009**, *91A*, 701–707. [CrossRef]
18. Takahashi, K.; Shirai, K.; Kitamura, M.; Hattori, M. Soluble egg shell membrane protein as a regulating material for collagen matrix reconstruction. *Biosci. Biotechnol. Biochem.* **1996**, *60*, 1299–1302. [CrossRef]
19. Yi, F.; Lu, J.-W.; Guo, Z.-X.; Yu, J. Mechanical properties and biocompatibility of soluble eggshell membrane protein/poly(vinyl alcohol) blend films. *J. Biomater. Sci. Polym. Ed.* **2006**, *17*, 1015–1024. [CrossRef]
20. Durmuş, E.; Celik, I.; Ozturk, A.; Ozkan, Y.; Aydin, M.F. Evaluation of the potential beneficial effects of ostrich eggshell combined with eggshell membranes in healing of cranial defects in rabbits. *J. Int. Med. Res.* **2003**, *31*, 223–230. [CrossRef]
21. Dupoirieux, L.; Pourquier, D.; Picot, M.C.; Neves, M. Comparative study of three different membranes for guided bone regeneration of rat cranial defects. *Int. J. Oral Maxillofac. Surg.* **2001**, *30*, 58–62. [CrossRef]
22. Yang, K.; El-Haik, B.S. Taguchi's Orthogonal Array Experiment. In *Design for Six Sigma: A Roadmap for Product Development*, 2nd ed.; McGraw-Hill Education: New York, NY, USA, 2009.
23. Erridge, P. The Pareto principle. *Br. Dent. J.* **2006**, *201*, 419. [CrossRef]
24. Subbiah, T.; Bhat, G.S.; Tock, R.W.; Parameswaran, S.; Ramkumar, S.S. Electrospinning of nanofibers. *J. Appl. Polym. Sci.* **2005**, *96*, 557–569. [CrossRef]
25. Zhao, H.; Chi, H. *Electrospun Bead-on-String Fibers: Useless or Something of Value?* IntechOpen: London, UK, 2018.
26. Castro, V.O.; Fredel, M.C.; Aragones, Á.; de Oliveira Barra, G.M.; Cesca, K.; Merlini, C. Electrospun fibrous membranes of poly (lactic-co-glycolic acid) with β-tricalcium phosphate for guided bone regeneration application. *Polym. Test.* **2020**, *86*, 106489. [CrossRef]
27. dos Santos, V.I.; Merlini, C.; Aragones, Á.; Cesca, K.; Fredel, M.C. Influence of calcium phosphates incorporation into poly(lactic-co-glycolic acid) electrospun membranes for guided bone regeneration. *Polym. Degrad. Stab.* **2020**, *179*, 109253. [CrossRef]
28. Qi, Q.-l.; Li, Q.; Lu, J.-w.; Guo, Z.-x.; Yu, J. Preparation and characterization of soluble eggshell membrane protein/chitosan blend films. *Chin. J. Polym. Sci.* **2009**, *27*, 387–392. [CrossRef]
29. Doustgani, A.; Ahmadi, E. Evaluation of Electrospinning Process Parameters of Poly Lactic-Co-Glycolic Acid and Hydroxyapatite Nanocomposite Nanofibrous Scaffolds. *J. Eng. Fibers Fabr.* **2016**, *11*, 155892501601100. [CrossRef]

30. Lohitha Kalluri, M.S.; Duan, Y. Effect of Electrospinning Parameters on the Fiber Diameter and Morphology of PLGA Nanofibers. *J. Dent. Oral Biol. Craniofac. Res.* **2021**, *4*, 3–7. [CrossRef]
31. Shoulders, M.D.; Raines, R.T. Collagen structure and stability. *Annu. Rev. Biochem.* **2009**, *78*, 929–958. [CrossRef]
32. Feltz, K.; Growney, E.; Chen, C.; Martin, R.; Sell, S. A review of electrospinning manipulation techniques to direct fiber deposition and maximize pore size. *Electrospinning* **2017**, *2*, 46–61. [CrossRef]

International Journal of
Molecular Sciences

MDPI

Article

Antibacterial and Cytocompatible: Combining Silver Nitrate with Strontium Acetate Increases the Therapeutic Window

Marjan Kheirmand Parizi [1,2,*], Katharina Doll [1,2], Muhammad Imran Rahim [1,2], Carina Mikolai [1,2], Andreas Winkel [1,2] and Meike Stiesch [1,2,*]

[1] Department of Prosthetic Dentistry and Biomedical Materials Science, Hannover Medical School, Carl-Neuberg-Strasse 1, 30625 Hannover, Germany; doll.katharina@mh-hannover.de (K.D.); rahim.muhammad@mh-hannover.de (M.I.R.); mikolai.carina@mh-hannover.de (C.M.); winkel.andreas@mh-hannover.de (A.W.)
[2] Lower Saxony Center for Biomedical Engineering, Implant Research and Development (NIFE), Stadtfelddamm 34, 30625 Hannover, Germany
* Correspondence: kheirmand-parizi.marjan@mh-hannover.de (M.K.P.); stiesch.meike@mh-hannover.de (M.S.)

Abstract: Microbial infection and insufficient tissue formation are considered to be the two main causes of dental implant failure. Novel studies have focused on designing dual-functional strategies to promote antibacterial properties and improve tissue cell response simultaneously. In this study, we investigated the antibacterial properties and cytocompatibility of silver nitrate ($AgNO_3$) and strontium acetate (SrAc) in a mono-culture setup for dental application. Additionally, we defined the therapeutic window between the minimum inhibitory concentration against pathogenic bacteria and maximum cytocompatible dose in the case of combined applications in a co-culture setup. Antibacterial properties were screened using *Aggregatibacter actinomycetemcomitans* and cell response experiments were performed with osteoblastic cells (MC3T3) and fibroblastic cells (NIH3T3). The osteoinductive behavior was investigated separately on MC3T3 cells using alizarin red staining. A therapeutic window for $AgNO_3$ as well as SrAc applications could be defined in the case of MC3T3 cells while the cytocompatibility of NIH3T3 cells was compromised for all concentrations with an antibacterial effect. However, the combined application of $AgNO_3$/SrAc caused an enhanced antibacterial effect and opened a therapeutic window for both cell lines. Enhanced mineralization rates could be observed in cultures containing SrAc. In conclusion, we were able to demonstrate that adding SrAc to $AgNO_3$ not only intensifies antibacterial properties but also exhibits bone inductive characteristics, thereby offering a promising strategy to combat peri-implantitis and at the same time improve osseointegration in implant therapy.

Keywords: therapeutic window; silver; strontium; peri-implantitis; osseointegration; antibacterial; cytocompatible

Citation: Parizi, M.K.; Doll, K.; Rahim, M.I.; Mikolai, C.; Winkel, A.; Stiesch, M. Antibacterial and Cytocompatible: Combining Silver Nitrate with Strontium Acetate Increases the Therapeutic Window. *Int. J. Mol. Sci.* **2022**, *23*, 8058. https://doi.org/10.3390/ijms23158058

Academic Editor: Mary Anne Melo

Received: 29 June 2022
Accepted: 19 July 2022
Published: 22 July 2022

Publisher's Note: MDPI stays neutral with regard to jurisdictional claims in published maps and institutional affiliations.

Copyright: © 2022 by the authors. Licensee MDPI, Basel, Switzerland. This article is an open access article distributed under the terms and conditions of the Creative Commons Attribution (CC BY) license (https://creativecommons.org/licenses/by/4.0/).

1. Introduction

Nowadays, dental implants represent a common treatment to replace missing teeth. However, certain complications and challenges are associated with this treatment option. The median prevalence of peri-implantitis, as the most frequent complication reported in implant dentistry, ranged from 7% among healthy populations to 38.4% in subjects with 10 year functional implants [1]. More severe risk factors such as smoking, systemic diseases, and poor oral hygiene can negatively impact the peri-implantitis prevalence rate [1]. Inflammatory processes caused by bacterial colonization damage both hard and soft tissues at the implant's site and have been described as a major contributor to low success rates [2]. In addition, the success rate of dental implants further relies on sufficient initial osseointegration that determines prolonged stability [3]. As a consequence, optimized tissue integration as well as limited bacterial colonization are considered key factors for a sustainable functional implant [4,5]. In an effort to reduce dental implant

failure, mutual implant functionalization strategies should be considered which address anti-bacterial properties as well as tissue regeneration at the same time.

Silver, as one of the most effective antimicrobial metals, has been extensively employed in implant research due to its broad-spectrum activity and long-term stable antibacterial ability [6]. Accordingly, until the year 2016, 37.8% of studies used different forms of silver in antimicrobial dental implant functionalization strategies [7]. On the other hand, several investigations have reported the dose-dependent toxic effect of silver not only on bacteria but also on tissue cells [8,9]. The minimal inhibitory concentration (MIC) of silver towards procaryotic cells usually overlaps with the acceptable biocompatible concentration for eucaryotic cells, which limits any potential therapeutic window to a narrow range [10]. Currently, two different approaches are used in order to increase the therapeutic window for silver administration: (i) changing the physicochemical properties of the applied silver (e.g., shape, size, electrochemistry, and concentration) or (ii) incorporating a secondary element or bioactive chemical to reduce cell toxicity of silver while enhancing tissue formation but maintaining antibacterial properties [11]. Organic bioactive chemicals (e.g., hydroxyapatite (HA), chitosan (CS)), inorganic elements (e.g., zinc (Zn), copper (Cu), gold (Au), and strontium (Sr)), or various combinations of them have been incorporated with different chemical forms of silver in order to reach the optimal balance between antibacterial behavior, chemical biocompatibility, and osteogenic response [12–20]. Among these elements, strontium as an alkaline metal with a strong inductive effect on bone tissue appears to be a particularly promising agent. It not only concurrently impedes bone resorption by suppressing osteoclast activity but can also enhance bone formation by increasing osteoblast function [21]. Several studies have already demonstrated the bone formative properties of strontium-leaching biomaterials in clinical settings [22]. Additionally, some in vitro investigations also reported an antibacterial impact of strontium; amongst them, one recent investigation was carried out on bacteria associated with dental implant infections [23–26].

The combination of silver and strontium was previously assessed in some studies for antibacterial activity and cytocompatibility when applied as surface coating [16,20,24,27–29]. Although the majority of these investigations reported good antibacterial effects and biocompatibility, their application of coated surfaces did not include the definition of the optimum concentrations of both metals in order to determine the range of a desired therapeutic window. The biological effects or interactions of these two chemicals (regardless of coating effects in case of chemical composition or surface topography) separately and in combination were not assessed in a comprehensive manner. Furthermore, the antibacterial activity of combined silver/strontium against oral pathogens related to dental peri-implantitis and, thus, the specific therapeutic window for this application in dentistry has not been investigated so far.

Therefore, the present study aimed to systematically analyze both the antibacterial effect and the cytocompatibility of silver, strontium, as well as combinations of both within one study to define the therapeutic window in mono-culture and co-culture setups for dental application. The antibacterial activity was evaluated against *Aggregatibacter actinomycetemcomitans*, one of the major bacterial pathogens in dental peri-implantitis [30]. At the same time, the cellular cytotoxicity of the different metal combinations was determined for fibroblasts and osteoblasts, which are the most relevant cells for dental implant studies [31]. Finally, the most promising concentrations were analyzed in a co-culture assay containing both bacterial and tissue cells, and osteogenic differentiation was also addressed.

2. Results

2.1. Antibacterial Activity and Cytocompatibility of Silver Nitrate

In this study, the effects of different combinations of additives were tested regarding antibacterial properties and cytotoxicity in mono-culture and co-culture settings to define putative therapeutic windows. In order to ensure the best possible comparability of the results, all experiments were performed in the same mixed culture medium (DMEM + αMEM, 1:1), which was selected in preliminary experiments. The antibacterial effect of $AgNO_3$ at

concentrations of 0.5, 1.5, 3, 6, 9, 12, 15, and 20 µg/mL against the periodontal pathogen *A. actinomycetemcomitans* was evaluated after a 24 h incubation period by counting the number of bacterial colonies (CFU) grown on FAA plates (Figure 1A). A dose-dependent antimicrobial effect on *A. actinomycetemcomitans* was determined. Treatment with $AgNO_3$ concentrations of 0.5 µg/mL resulted in a reduction of 87% in bacterial colony numbers, but did not reach statistical significance ($p = 0.051$). With an increasing concentration of $AgNO_3$ ($\geq$1.5 µg/mL), a statistically significant reduction was observed. No viable bacteria could be detected at $AgNO_3$ concentrations of $\geq$3 µg/mL, indicated by 100% growth inhibition. Therefore, the minimum inhibitory concentration (MIC), which we defined as the lowest concentration with statistically significant CFU reduction, of $AgNO_3$ in this mono-culture assay was set as 1.5 µg/mL.

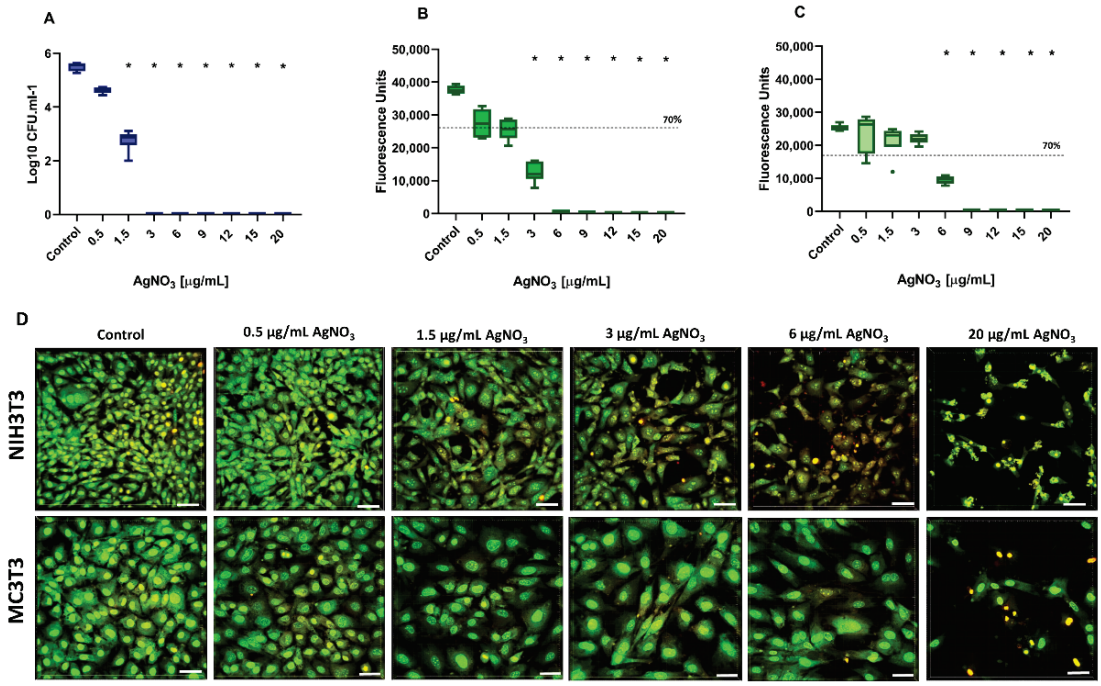


Figure 1. Antibacterial Activity and Cytocompatibility of Silver Nitrate. Tukey Box Plots of (**A**) bacterial colony numbers (expressed as log CFU/mL) of *A. actinomycetemcomitans* and cell metabolic activity determined by CellTiter-Blue assay of (**B**) NIH3T3 and (**C**) MC3T3 after 24 h incubation with $AgNO_3$ at different concentrations. The dashed lines represent 70% of cell viability. Black stars indicate statistically significant decreases compared to the control with $p \leq 0.05$. (**D**) BacLight staining of NIH3T3 and MC3T3 cells treated with corresponding $AgNO_3$ concentrations. The samples were examined under the CLSM. Scale bars: 50 µm.

Parallel to the antibacterial effect, the cellular viability of fibroblasts (NIH3T3) and osteoblasts (MC3T3) following exposure to $AgNO_3$ was investigated at the same concentration range using the CTB viability assay (Figure 1B,C). Statistically significant viability reduction was detected for $AgNO_3$ concentrations of $\geq$3 µg/mL in the case of NIH3T3 cells and for concentrations of $\geq$6 µg/mL in case of MC3T3 cells. However, a reduction of more than 30% of cell viability was already considered as a cytotoxic effect according to DIN ISO 10993-5 [32]. In this regard, an $AgNO_3$ concentration of $\geq$1.5 µg/mL (for NIH3T3) and $\geq$6 µg/mL (for MC3T3) must be considered cytotoxic. To support these observations, cell fluorescence staining and CLSM microscopy were used to document morphological alterations following exposure to test substances (Figure 1D). The microscopy results confirmed cell compatibility at low concentrations of $AgNO_3$ (0.5 µg/mL) in both cell lines with normal elongated morphologies and green fluorescence, but different sensitivities when using higher concentrations. In the case of NIH3T3, $AgNO_3$ concentrations $\geq$1.5 µg/mL led to reduced cell numbers, rounded cell structures, and a slightly reddish color, which became

even more intense as the dose increased (Figure 1D). Such visible morphological changes could not be observed for MC3T3 up to a concentration of 6 µg/mL. According to the combined results of antibacterial and cytotoxicity testing, a desired therapeutic window, defined as the concentration interval between MIC and the maximum cytocompatible dose of $AgNO_3$, could be determined as from ≥1.5 µg/mL to <6 µg/mL for MC3T3 cells. No therapeutic window could be identified for NIH3T3 cells in this mono-culture setup.

2.2. Antibacterial Activity and Cytocompatibility of Strontium Acetate

Similar to the analyses for $AgNO_3$, the effects of SrAc on bacteria and tissue cells were initially tested in mono-culture approaches. For *A. actinomycetemcomitans*, a dose-dependent decrease in CFU/mL could be observed within the range of 0.1 to 20 mg/mL. This reduction became statistically significant at SrAc concentrations ≥5 mg/mL (Figure 2A). Thus, SrAc showed an MIC of 5 mg/mL in the mono-culture experiment.

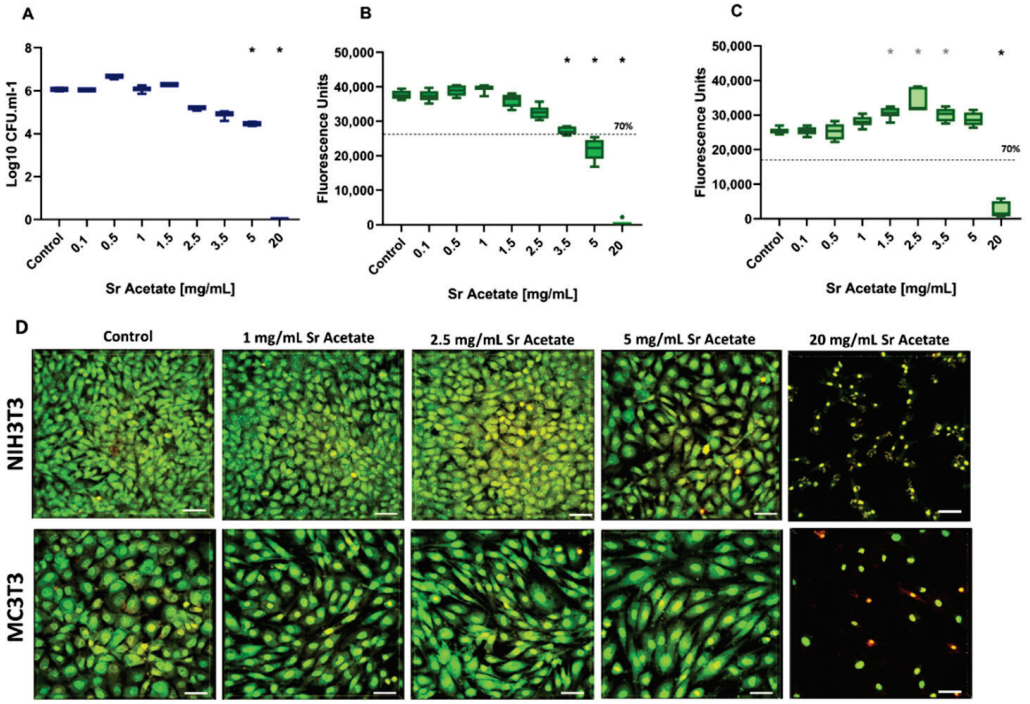


Figure 2. Antibacterial Activity and Cytocompatibility of Strontium Acetate. Tukey Box Plots of (**A**) *A. actinomycetemcomitans* growth given as log CFU/mL measured after 24 h inoculation. Metabolic activity of (**B**) NIH3T3 and (**C**) MC3T3 cell lines cultivated in the presence of Sr Acetate with different concentrations. The dashed lines represent 70% of cell viability. Black and grey stars indicate statistically significant decreases and increases, respectively, compared to the control with $p \leq 0.05$. (**D**) BacLight staining of NIH3T3 and MC3T3 treated with corresponding Sr Acetate concentrations. The samples were examined under the CLSM. Scale bars: 50 µm.

Cellular metabolic activity was again quantified using CTB assay. Regarding cytocompatibility, it could be observed that the viability of NIH3T3 cells did not diminish in comparison to non-treated cells up to SrAc concentrations ≤3.5 mg/mL. A reduction of more than 30% in metabolic activity was detected following treatments with concentrations ≥5 mg/mL (Figure 2B). The metabolic activity of MC3T3 cells initially significantly increased with increasing concentrations of SrAc (1.5, 2.5, and 3.5 mg/mL) compared to the control group ($p = 0.003$, $p = 0.0002$, and $p = 0.008$, respectively). Additionally, in contrast to fibroblasts, a significant reduction in viability was only detected at 20 mg/mL which exceeded 30%. The qualitative analysis using CLSM images of stained cells confirmed the results of the quantitative CTB assay (Figure 2D). At up to 2.5 mg/mL, no dominant alterations in morphology or visible cell amounts could be observed neither for NIH3T3 nor

MC3T3. Beginning with 5 mg/mL, the fibroblasts appeared slightly rounded and fewer in number, whereas only isolated reddish dots remained in 20 mg/mL. In the case of MC3T3, a collapse of the cell culture was not indicated at lower concentrations and was observed exclusively for 20 mg/mL. However, it should be mentioned that the osteoblasts appeared slightly more elongated with aligned orientation when adding SrAc in a concentration range from 1 to 5 mg/mL (Figure 2D). Taken together, SrAc concentrations of $\leq$3.5 mg/mL (for NIH3T3) and $\leq$5 mg/mL (for MC3T3), respectively, were shown to be cytocompatible, indicating a possible therapeutic window of around 5 mg/mL in the case of MC3T3 cells. No therapeutic window could be defined following SrAc administration on NIH3T3.

2.3. Cell Viability in Combined Treatment with Silver Nitrate and Strontium Acetate

The cytotoxic effects of a combined challenge with $AgNO_3$ and SrAc were screened using NIH3T3 or MC3T3 cells before suitable concentrations were also tested for antibacterial effects in a co-culture approach, since cellular viability could not be addressed in a co-culture setup due to artefacts caused by bacterial viability. For this purpose, the cytocompatible concentration of SrAc for both cell lines (2.5 mg/mL) was combined with increasing concentrations of $AgNO_3$ (0.5, 1.5, 3, 6, 9, 12, and 20 µg/mL), which was applied to the cells and analysed using CTB assay as well as CLSM microscopy as described before. Against the background stimulation of 2.5 mg/mL SrAc, the addition of $AgNO_3 \geq 3$ µg/mL resulted in a significant reduction in metabolic activity, while 0.5 µg/mL $AgNO_3$ remained non-cytotoxic for NIH3T3 cells (Figure 3A). In the case of MC3T3 cells, $AgNO_3$ concentrations $\geq$6 µg/mL appeared cytotoxic when combined with 2.5 mg/mL SrAc as indicated by the cell viability reduction of 30% (Figure 3B). Additionally, the previously observed significant increase in the metabolic activity of MC3T3 in the presence of 2.5 mg/mL SrAc could be confirmed and was not compromised by $AgNO_3$ concentrations $\leq$3 µg/mL. When comparing the fluorescence units in Figures 1 and 3 (effects of $AgNO_3$ in different concentrations with and without adding SrAc 2.5 mg/mL) for NIH3T3, a significant increase in cell metabolism could be observed with 0.5 µg/mL $AgNO_3$ in the presence of SrAc. The same effect could be detected for MC3T3 after treatment with $AgNO_3$ at concentrations of 0.5 µg/mL, 1.5 µg/mL, and 3 µg/mL. In contrast, for cell cultures with higher concentrations of $AgNO_3$ (NIH3T3: 3µg/mL $AgNO_3$; MC3T3: 6 µg/mL $AgNO_3$), metabolic activity was reduced when additionally stimulated with 2.5 mg/mL SrAc (Figures 1 and 3).

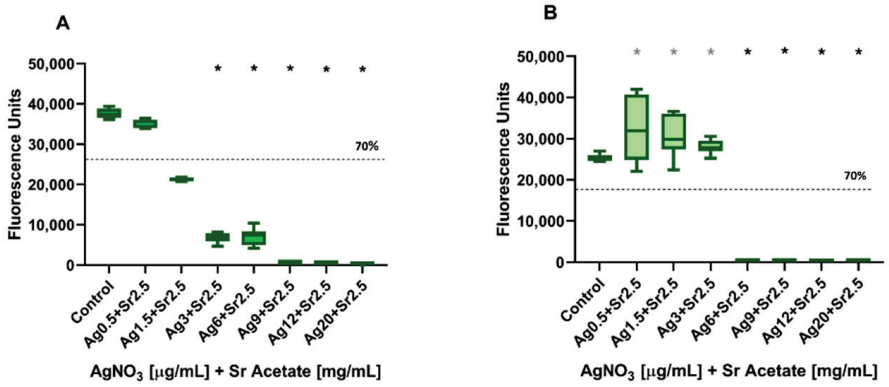


Figure 3. Cell viability of Silver Nitrate and Strontium Acetate in combination. CellTiter-Blue assay of (**A**) NIH3T3 and (**B**) MC3T3 treated with increasing concentrations of $AgNO_3$ and 2.5 mg/mL Sr Acetate after 24 h. The dashed lines represent 70% cell viability. Black and grey stars indicate statistically significant decreases and increases, respectively, compared to the control with $p \leq 0.05$.

2.4. Antibacterial Effect and Cytocompatibility of Combined Treatment with Silver Nitrate and Strontium Acetate in a Co-Culture System

Based on all results of the mono-culture experiments, for both cell lines, a co-culture setup with *A. actinomycetemcomitans* in the presence of 2.5 mg/mL SrAc was considered appropriate to investigate the effect of $AgNO_3$ concentrations in the range of 0.5 to 6 µg/mL and to identify a possible therapeutic window for future applications. Similar to mono-culture experiments, the MIC regarding *A. actinomycetemcomitans* was measured by analyzing significant reductions in log CFU/mL (Figure 4A,B), and fluorescence staining followed by CLSM microscopy were used to determine cell morphology of both cell lines (Figure 4C,D). A statistically significant reduction in bacterial growth was observed in co-cultures with both cell lines after treatment with $AgNO_3$ alone for concentrations $\geq$3 mg/mL (Figure 1). In contrast, bacterial growth was already statistically significantly reduced with a combined stimulus of 0.5 µg/mL $AgNO_3$ together with 2.5 mg/mL SrAc. Therefore, this concentration could be defined as the MIC value for combination treatment. Such a decrease in bacterial growth in the presence of 2.5 mg/mL SrAc could be detected for any investigated $AgNO_3$ treatment (Figure 4A,B). Regarding the cytocompatibility analysis, only CLSM imaging was performed (see above) and color change as well as morphological alterations were evaluated (Figure 4C,D). When NIH3T3 cells in the co-culture setup were treated with $AgNO_3$ alone, only a concentration of 0.5 µg/mL caused no changes in cell shape and microscopically visible cell amounts. In the presence of SrAc, an $AgNO_3$ concentration of 1.5 µg/mL still had no visible effect. However, if treated with $AgNO_3 \geq$ 1.5 µg/mL (or $\geq$3 µg/mL in combination with 2.5 mg/mL SrAc), cells appeared more rounded and reddish in color. This decrease in viability was more pronounced when SrAc was added and confirmed its ambivalent effect regarding attenuation (with low $AgNO_3$ concentrations) or enforcement (with high concentrations of $AgNO_3$) of cytotoxicity observed in the context of silver treatment for both cell lines (Figure 4C,D). For MC3T3 cells in the co-culture setup, treatment with $AgNO_3$ up to 3 µg/mL showed no changes in visible cell numbers independent of additional SrAc stimulation. As in the mono-culture, only the morphology of cells was affected by the addition of SrAc as cells appeared more elongated and aligned (Figure 4D). A visibly decreased amount of MC3T3 and more reddish stained cells were detected only when treated with 6 µg/mL $AgNO_3$, an effect enhanced again in the presence of SrAc (similar to the findings in the mono-culture and confirming the results of the CTB assay). According to these data, cytocompatible doses of $AgNO_3$ in combination with 2.5 mg/mL SrAc could be defined as <3 µg/mL for NIH3T3 and <6 µg/mL for MC3T3. For MC3T3, this concentration was in line with the CTB analysis of combined treatment in the mono-culture (Figure 3), whereas NIH3T3 appeared to be less affected in the co-culture setup. Regarding an inferable therapeutic window in the presence of 2.5 mg/mL SrAc, it was shifted for MC3T3 cells towards lower concentrations of $AgNO_3$ (0.5–3 µg/mL) and for NIH3T3 cells it opened in a range of 0.5–1.5 µg/mL $AgNO_3$. Thus, 0.5–1.5 µg/mL $AgNO_3$/SrAc (2.5 mg/mL) could be identified as a common therapeutic window for both cell lines.

2.5. Osteogenic Differentiation of MC3T3 Cells

Since MC3T3 cells exhibited morphological changes upon treatment with SrAc alone as well as in combination with $AgNO_3$, potential osteogenic differentiation was analyzed both in mono- and co-culture using Alizarin Red staining (ARS). MC3T3 were cultured in an osteogenic medium for up to 14 days and treated with the lowest identified therapeutic combination of $AgNO_3$ (0.5 µg/mL)/SrAc (2.5 mg/mL) as well as $AgNO_3$ (0.5 µg/mL) and SrAc (2.5 mg/mL) alone. Isolated calcium deposits stained with ARS, which visualized mineralized nodules, appeared in the control and 0.5 µg/mL $AgNO_3$-treated cultures only on day 14, whereas days 3 and 7 revealed no mineralization (Figure 5A). There were also no further differences in cell appearance between these two groups, which confirmed once more the cytocompatibility of 0.5 µg/mL $AgNO_3$ (Figure 5C). When treated with 2.5 mg/mL SrAc (alone or in combination with 0.5 µg/mL $AgNO_3$), at day

3 extracellular matrix mineralization was statistically significantly elevated already in comparison to the control or cultures only challenged with $AgNO_3$. However, SrAc alone induced mineralization faster than combined treatment with $AgNO_3$ and SrAc, which was apparent through more intense staining on day 3 (Figure 5B). From day 3 onwards, mineralization increased statistically significantly in both groups and reached its maximum after 14 days (approximately 11-fold increase in comparison to cultures without SrAc) (Figure 5C).

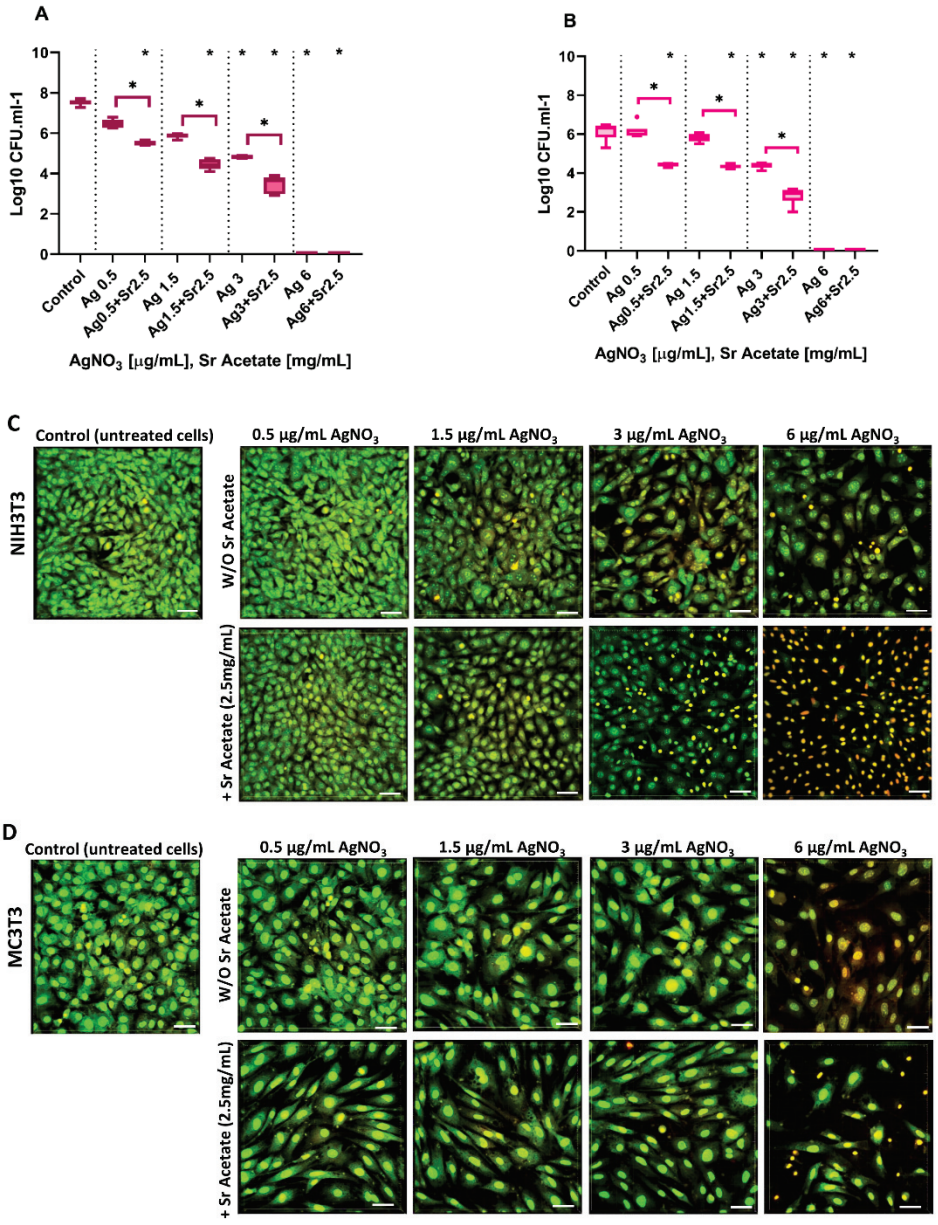
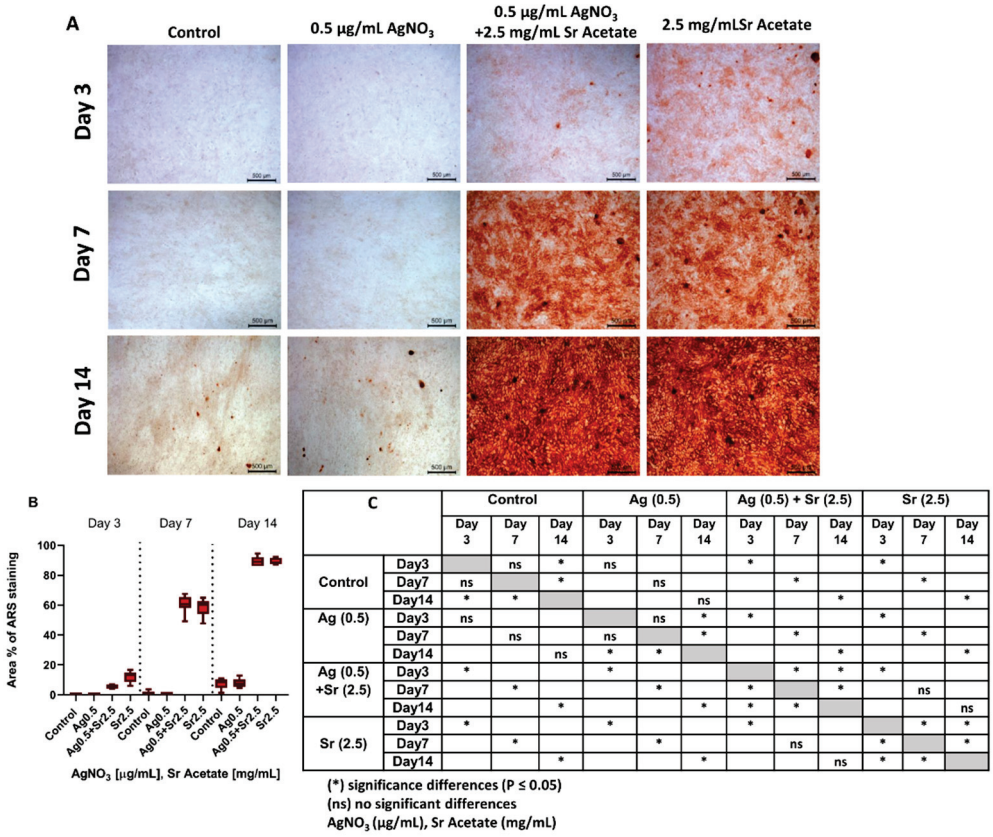


Figure 4. Antibacterial Effect and Cytocompatibility in Co-culture system. Bacterial growth in co-culture setup measured as log10 CFU/mL (**A**): NIH3T3, (**B**): MC3T3. Black stars show statistically significant decreases compared to the control with $p \leq 0.05$. Brackets show statistically significant differences within groups with the same $AgNO_3$ concentration but with or without Sr Acetate addition with $p \leq 0.05$. NIH3T3 (**C**) or MC3T3 (**D**) were simultaneously co-cultured with *A. actinomycetemcomitans* and $AgNO_3$ in two different groups (with or without adding 2.5 mg/mL Sr Acetate). Morphological alteration of co-cultured cells in different groups was imaged after 1 day by BacLight staining and CLSM. Scale bars: 50 µm.



C		Control			Ag (0.5)			Ag (0.5) + Sr (2.5)			Sr (2.5)		
		Day 3	Day 7	Day 14	Day 3	Day 7	Day 14	Day 3	Day 7	Day 14	Day 3	Day 7	Day 14
Control	Day3		ns	*	ns			*			*		
	Day7	ns		*		ns			*			*	
	Day14	*	*				ns			*			*
Ag (0.5)	Day3	ns				ns	*	*			*		
	Day7		ns		ns		*		*			*	
	Day14			ns	*	*				*			*
Ag (0.5) +Sr (2.5)	Day3	*			*				*	*	*		
	Day7		*			*		*		*		ns	
	Day14			*			*	*	*				ns
Sr (2.5)	Day3	*			*			*				*	*
	Day7		*			*			ns		*		*
	Day14			*			*			ns	*	*	

Figure 5. Differentiation of MC3T3 cells. (**A**) Alizarin Red staining results observed by microscopy on day 3, 7 and 14 to show the osteogenesis of MC3T3 treated with $AgNO_3$ (0.5 µg/mL), Sr Acetate (2.5 mg/mL) or combination of both. (**B**) Area percentage of MC3T3 cells stained with ARS processed using Image J software. (**C**) Significant differences between groups. Scale bar: 500 µm.

3. Discussion

Long-term dental implant function depends on both sufficient tissue integration and avoidance of bacterial colonization. Consequently, a great interest has risen in substances with dual functionality, biofilm control as well as cell compatibility. In a recent study, the antimicrobial potential of strontium hydroxide against pathogenic oral bacteria was demonstrated [23], and related reviews reported the antimicrobial effects of functionalized surfaces with silver, strontium, or combinations of both [13,33]. Therefore, the aim of the present study was to systematically describe a therapeutic window for the application of silver and strontium salts on tissue cells and pathogenic bacteria of the oral cavity for the first time.

For this purpose, the antibacterial properties of $AgNO_3$ on *A. actinomycetemcomitans* as well as the cytotoxic effects for osteoblasts (MC3T3) and fibroblasts (NIH3T3) were investigated first. Cytotoxicity was quantitatively and qualitatively assessed by measuring metabolic activity and observing cell morphologies using cell staining with CLSM. The combination of both methods provides more information regarding the cytocompatibility of tested chemical substances than analyzing only one parameter. Since bacteria and cell culture media in general are differently composed and the influence of media composition on the toxicity of silver ions was documented in several studies [34,35], this should be taken into account if a putative therapeutic window is to be derived from in vitro data. In the present study, the same culture medium (DMEM + αMEM, 1:1 ratio) was found appropriate for the cultivation of bacteria, as well as different tissue cells, and facilitated the direct comparison of mono-cultures, co-cultures and the effect of different additives. Since the therapeutic ranges of silver in solution were shown to be much smaller than silver derived from coatings [36], it illustrates the importance of using dissolved silver ions for

the analysis of mutual functionality. In line with previous studies, results of separate mono-culture experiments showed a linear reduction in the viability of both bacteria and tissue cells reflecting the concentration-dependent toxic activity of silver [37]. The underlying mechanisms include the production of reactive oxygen species (ROS) resulting in cellular disruption and subsequent cell death [6]. From the results presented here for the effect of silver ions in monocultures, only a therapeutic range for MC3T3 could be derived based on the lowest inhibitory concentration for bacteria (MIC) and the highest dose that is still tolerated by cells (Table 1). In contrast, no therapeutic range could be defined when considering NIH3T3 cells. In the context of an intended therapeutic application, it is therefore of great importance to consider all affected tissues as early as possible in the investigations, since various cell types present different sensitivities to silver. In particular, the minimum $AgNO_3$ concentration showing cytotoxicity towards MC3T3 cells were found to be 4 times higher than the cytotoxic ones in NIH3T3 cells. Similar observations regarding NIH3T3 sensitivity were reported previously by Sambale et al. [38]. The finding that treatment with $AgNO_3$ reveals a therapeutic window in the case of osteoblasts, on the other hand, is much more controversially discussed in scientific journals [37,39–43]. For instance, Kirmanidou et al. showed antibacterial activity against *Porphyromonas gingivalis* and *Prevotella intermedia*, and cytocompatibility for SaOS-2 osteoblast-like cell lines using silver nanoparticle doped titanium surfaces [43]. In contrast, some studies indicated that silver concentrations of higher than cytocompatible doses are needed to observe their bactericidal effects [10,42]. In most cases, this contradiction is probably due to the different study designs, with different bacterial strains, cell lines, media and types of silver administration, which makes cross-study comparability considerably more difficult [38,44,45]. Thus, a therapeutic window always needs to be identified for specific application purposes.

Table 1. Therapeutic windows of Silver Nitrate, Strontium Acetate and their combination.

Cell Line \ Chemical	$AgNO_3$ (μg/mL)	SrAc (mg/mL)	$AgNO_3$/SrAc * (μg/mL)
NIH3T3	---	---	0.5–1.5
MC3T3	1.5–3	5	0.5–3

* Combined treatment with $AgNO_3$ in presence of SrAc 2.5 mg/mL.

In the same mono-culture setups, the cytocompatibility and antibacterial potential of strontium acetate were also tested. Despite the beneficial osteogenic effects of strontium, which have been extensively investigated, only a few studies evaluated the bactericidal effect of strontium against pathogenic oral bacteria [23,33]. In the present study, a minimum inhibitory concentration of SrAc (5 mg/mL) against *A. actinomycetemcomitans* after 24 h of incubation was defined. These results are in line with findings of Alshammari et al., who reported similar antibacterial results after using strontium hydroxide against six periodontal pathogens [23]. Concentrations in a range of 1.21 mg/mL to 12.1 mg/mL showed complete growth inhibition in planktonic cultures and biofilm assays, respectively [23]. The differences between the bactericidal concentrations in the above mentioned study and the research presented here can be attributed to different experimental designs and chemical forms of strontium. Although the exact process regarding the antibacterial behavior of strontium is not yet fully understood, two possible mechanisms have been proposed. The first mechanism occurs directly through the induction of oxidative stress (ROS) or interruption in adenosine triphosphate (ATP) synthesis, causing DNA damage and ultimately the death of bacteria; the second mechanism works indirectly by changing the physicochemical conditions of the pericellular microenvironment, such as higher osmotic forces and pH change, which are unfavorable for some bacterial strains [23,46]. The specific mechanism responsible for the antibacterial effect observed in this study should be addressed in follow-up studies.

According to the CTB and cell morphology analyses, low doses of SrAc (up to 3.5 mg/mL) can be considered cytocompatible for both investigated cell lines. However,

similar to $AgNO_3$, the minimum concentration of SrAc which causes more than a 30% reduction in metabolic activity differs between fibroblasts and osteoblasts, revealing the higher sensitivity of NIH3T3. In contrast to silver, the administration of SrAc directly below the cytotoxic concentration (1.5 to 3.5 mg/mL) even leads to a significant increase in the metabolic activity of MC3T3. This observation can probably be attributed to the specific effect of strontium on osteoblasts expressing Ca-sensing receptors (CaSR). Strontium is known to bind CaSR, thereby activating various signaling pathways which are essential in cell proliferation, differentiation, and osteogenic gene expression impacting metabolic activity change [21]. In the present study, a therapeutic concentration (5 mg/mL) of SrAc could be defined, which exhibited antibacterial activity without compromising the cytocompatibility of MC3T3, if not stimulating cell activity. Unfortunately, no therapeutic window could be determined in the case of NIH3T3. Promoted osteogenic responses in MC3T3 cells and bactericidal effects toward *A. actinomycetemcomitans* and *P. gingivalis* have also been reported in a study using Sr-substituted bioactive glasses, even though a synergistic effect of the bioactive glasses could not be excluded [47]. However, at high concentrations the toxic effects of SrAc were observed for both cell lines as well. Accordingly, some studies demonstrated the inhibitive effect of high doses of strontium on cell proliferation and differentiation in an in vitro setup, and interference of high doses of strontium (>510 mg/kg/ day) with Ca metabolism causing hypocalcemia and bone mineralization defects in vivo [21]. In this study, only low doses of strontium in a cytocompatible range were considered, which are also suitable for future investigations regarding clinically safe local application.

After defining therapeutic windows of $AgNO_3$ and SrAc in the mono-culture experiments (Table 1), dilutions of $AgNO_3$ were combined with an SrAc concentration that can be considered cytocompatible for MC3T3 as well as NIH3T3 (2.5 mg/mL) in order to achieve intensified antibacterial and optimal cytocompatibility results. The concentration of $AgNO_3$ in combination with 2.5 mg/mL SrAc, which could inhibit > 99% of bacterial growth in a co-culture setup for both cell lines, was determined to be 0.5 µg/mL. This concentration is six times lower than required to exert the same effect without adding SrAc. As 0.5 µg/mL $AgNO_3$ or 2.5 mg/mL SrAc alone were not considered bactericidal in mono-culture experiments, a synergistic antibacterial effect was inferred for combined treatment. Similar synergistic responses were achieved in other studies after the addition of different bactericidal agents to silver, such as antibiotics, bactericidal metals, hydrogen peroxide, etc. [29,48–50]. To our knowledge, the exact mechanism behind the synergistic bactericidal effect of silver/strontium combinations still needs to be addressed. This might be due to different antibacterial modes of action. The co-culture system also influenced the antibacterial effect of $AgNO_3$ without SrAc. However, a lower effectiveness in the co-culture setup was observed than in the mono-culture experiments. As the effect of different media can be excluded, this finding was probably related to the influence of cells or the co-culture design. It is known that osteoblast lineage can internalize some bacteria and protect them from antibacterial substances [51]. However, no studies have investigated this effect on *A. actinomycetemcomitans*. Additionally, higher total cell numbers (prokaryotes plus eukaryotes) were exposed to the same concentration of chemical substances in the co-culture setup. This might have reduced the available amount of silver for every separate biological unit. On the other hand, the combination of a low concentration of $AgNO_3$ with 2.5 mg/mL SrAc also exhibited less cytotoxicity in NIH3T3 and MC3T3 cells compared to $AgNO_3$ treatment without SrAc. This phenomenon was also described previously [19,29] and was attributed to the ability of strontium to occupy specific binding sites prior to silver which can directly influence cellular functions or indirectly activate cell proliferation signaling pathways [52]. In contrast, high concentrated $AgNO_3$ in combined treatment with SrAc led to a significant decrease in cytocompatibility, which might represent a turning point in the mitigating effect of additive SrAc, which was observed for both cell lines albeit in different concentration ranges due to varying sensitivity levels. The ambivalent effect of SrAc on cells and the synergistic antibacterial effect of combined treatment ($AgNO_3$/SrAc)

might raise concerns regarding the clinical application where not only several factors can change the concentration of these two chemicals, subsequently missing the therapeutic range, but also adverse effects such as allergic reactions might occur due to their combination. So far, no other study has been reported that compared various cell responses and their susceptibility following the use of $AgNO_3$/SrAc with different concentrations. However, some investigations were carried out reporting varied silver sensitivities in mammalian cell lines and improved cytocompatibility in fibroblasts and osteoblasts after using low doses of Sr [21,38,53]. This could be due to different amounts of ROS formation, but a detailed analysis would be required for further investigation.

As in all experimental setups, morphology alterations in MC3T3 after SrAc treatment and increased metabolic activity in combined treatment with low concentrations could be detected. Their potential effect on osteogenic differentiation was analyzed by matrix mineralization staining. Indeed, clearly increased mineralization rates could be observed in cultures containing SrAc at all time points. This is in agreement with previous studies, which already reported on the osteogenic potential of strontium [21]. The slightly delayed mineralization for combined treatment might be related to the time-dependent impact of $AgNO_3$. Other studies showed lower cell viability and proliferation during the initial days of treatment due to the differential uptake of silver into the cells [54,55]. In contrast, no significant differences in osteogenic differentiation could be detected between the untreated control and $AgNO_3$ stimulus alone which is in line with the literature for low concentrations [56].

The subsequent therapeutic windows of an $AgNO_3$ treatment in combination with SrAc (2.5 mg/mL) shifted in the case of MC3T3 to 0.5–3 µg/mL, while for NIH3T3 it was described for the first time (0.5–1.5 µg/mL). Considering hard and soft tissue in an oral application, 0.5–1.5 µg/mL of $AgNO_3$ together with 2.5 mg/mL SrAc can be considered as an expedient treatment. Notably, no therapeutic range (for both $AgNO_3$ and SrAc) was detected in NIH3T3 in separate treatments, nor were any of these concentrations initially defined as therapeutic for both cell lines in mono-culture experiments (Table 1). Taken together, beside a synergistic antibacterial effect and increased therapeutic window, combining $AgNO_3$ with SrAc also seemed to stimulate the differentiation of osteogenic cells. When comparing the results of this study—the synergistic dual function of $AgNO_3$/SrAc with additional osteogenic effect—with the literature, it is apparent that different studies already used silver/strontium combinations to benefit from the antibacterial characteristics of silver and bone formative properties of strontium [20,24,27]. However, there are some differences between the current study and previously reported strategies. First of all, most strategies involved surface coatings instead of an analysis of soluble substances which does not allow for an accurate conclusion on the effect of these chemicals due to the background effect of the coating. Secondly, none of these studies reported antibacterial effects following the use of strontium alone. Moreover, controversial results of the synergistic antibacterial activities and enhanced therapeutic windows of silver/strontium combinations were reported [20,28,29]. In this regard, Van Hengel et al. observed an osteogenic response and synergistic antibacterial action against methicillin-resistant *Staphylococcus aureus* (MRSA) on a porous implant surface biofunctionalized with SrAc and silver nanoparticles while no significant difference in osteogenic activity of porous implant surfaces with and without strontium was observed [29]. However, in a different study, the substitution of silver and strontium in hydroxyapatite (HA) coatings showed no synergistic antimicrobial properties [28]. This emphasizes the impact of the coating strategy itself on the expected antibacterial and osteoinductive effectiveness. Therefore, this needs to be taken into account if desirable combinations of $AgNO_3$ and SrAc as defined in the present study are going to be applied in an innovative implant surface strategy. The established systematic analysis of synergistic combinations of active ingredients will guide this process. It also sets the basis for a variety of studies that will address the exact molecular mechanisms behind the cytotoxicity and antibacterial effects of silver and strontium, which remain unknown to this date. The aspect of more complex bacterial compositions, such as biofilms

instead of planktonic bacteria, and different interactions between cellular and extracellular environments in tissue in comparison to monolayer cell cultures is considered as another area requiring investigation on the way to successful clinical application.

4. Materials and Methods

4.1. Preparation of Silver Nitrate and Strontium Acetate Solutions

Silver Nitrate ($AgNO_3$, BioXtra, >99%) and Strontium Acetate (SrAc, $Sr(CH_3CO_2)_2$) were obtained from Sigma-Aldrich® (Merck KGaA, Darmstadt, Germany). Solutions were freshly prepared by dissolving them in sterile Milli-Q water and further diluted to the final concentrations (Table 2) in experimental volume (vol/vol not exceeding 2.5%).

Table 2. Chemicals concentrations in all experimental setups.

Chemical \ Setups	Mono-Culture	Co-Culture
$AgNO_3$ (µg/mL)	0.5, 1.5, 3, 6, 9, 12, 15, 20	0.5, 1.5, 3, 6
SrAc (mg/mL)	0.1, 0.5, 1, 1.5, 2.5, 3.5, 5, 20	2.5

4.2. Determination of Cell Viability and Morphology in Mono-Culture

Immortalized murine fibroblasts (NIH3T3) and immortalized murine pre-osteoblasts (MC3T3-E1) obtained from American Type Culture Collection (ATCC, Manassas, VA, USA) were used in this study. Both cell lines were cultivated in a mixture of Dulbecco's modified Eagle's medium (DMEM, Cat. No P04-04500, PAN-Biotech, Aidenbach, Germany) and Alpha Minimum Essential Medium (αMEM, Cat. N° BE02-002F, Lonza, Cologne, Germany) (in a 1:1 ratio) supplemented with 10% fetal bovine serum (FBS, PAN-Biotech GmbH,) (*v/v*) and 1% penicillin/streptomycin (P/S, Sigma-Aldrich, Steinheim, Germany) under a humidified environment at 37 °C with 5% CO_2. The cells at passage numbers 7–13 were allowed to grow to up to 80% confluence, trypsinized and adjusted to 1×10^5 cells/mL before being seeded in experiments. All cell experiments were performed in three independent biological replicates. Cells cultured without any test substances served as controls.

4.2.1. Cell Titer-Blue (CTB) Cell Viability Assay

The viability of tissue cells was assessed using a CTB assay kit (Promega, Madison, WI, USA). Cells were seeded in 96-well microtiter plates (CELLSTAR-Greiner Bio-One, Kremsmünster, Austria) with a density of 1×10^5 cells/mL (100 µL/well). They were incubated for 24 h at 37 °C in 5% CO_2. The medium was changed the next day and cells were treated with different concentrations of $AgNO_3$, SrAc, or combinations of both which had been previously dissolved in medium. They were incubated for another 24 h under the same conditions. A CTB-assay was performed based on the manufacturer's protocol. Briefly, 20 µL of CTB reagent was added to seeded cells and the plates were incubated at 37 °C for 4 h. The metabolic reduction of resazurin to fluorescent resorufin was recorded at 560/590 nm using a plate reader (Tecan, Infinite M200Pro, Männedof, Switzerland).

4.2.2. Cell Morphology Analyses by Confocal Laser Scanning Microscopy

Live/dead staining of both cell lines was performed to confirm cell compatibility and evaluate cell appearance/morphological change following exposure to test substances. Cells were seeded in 6-well plates (CELLSTAR-Greiner Bio-One, Kremsmünster, Austria) with a density of 1×10^5 cells/mL (3 mL/well) and incubated at 37 °C in 5% CO_2. The medium was changed the next day and cells were treated with different concentrations of $AgNO_3$, SrAc, or combinations of both for 24 h. Finally, cells were fluorescently stained using SYTO9 and Propidium Iodide (PI) (BacLight Bacterial Viability Kit, Thermo Fisher Scientific GmbH, Dreideich, Germany). The working staining solution was prepared in 1:1000 dilution by adding SYTO 9 and PI into phosphate-buffered saline (PBS, Sigma-Aldrich®). Stained cells were fixed using 2.5% glutaraldehyde (Roth, Germany; 1:10

dilution with PBS) for 30 min at 4 °C. Images were taken by performing confocal laser scanning microscopy (CLSM; Leica TCS SP8, Leica Microsystems, Mannheim, Germany).

4.3. Determination of Antibacterial Activity in Mono-Culture

Aggregatibacter actinomycetemcomitans (ATCC 33384) was obtained from the American Type Culture Collection (Manassas, USA) and routinely stored as glycerol stocks. Bacteria were cultured for 48 h on fastidious anaerobe agar (FAA, Oxoid Limited, Wesel, Germany) plates with 5% sheep blood (Thermo Fisher Scientific, Germany) under anaerobic conditions. Colonies from FAA plates were inoculated into brain heart infusion medium (BHI; Oxoid Limited) supplemented with 10 µg/mL vitamin K (Carl Roth GmbH & Co. KG, Karlsruhe, Germany) within an anaerobic chamber (80% N_2, 10% H_2, 10% CO_2 and 37 °C). The overnight pre-culture was centrifuged and resuspended in phosphate-buffered saline (PBS, Sigma-Aldrich®) to a final optical density (OD) of 0.1 at 600 nm. A total of 15 µL of bacterial suspension was mixed with 3 mL mixed cell culture medium (DMEM + αMEM, 1:1) containing 10% FBS (*v/v*) without antibiotics (P/S) and seeded in 96-well microtiter plates. $AgNO_3$ and SrAc were added in different concentrations and combinations (Table 2) to evaluate the minimum concentration able to inhibit bacteria growth. After 24 h of incubation at 37 °C and 5% CO_2, serial 10-fold dilutions in PBS were made from each well. Aliquots of 100 µL of each dilution were plated on FAA plates (+ 5% blood) and incubated at 37 °C and 5% CO_2 for 48 h. The colony-forming units (CFU/mL) were counted from the plates. As a form of growth control, the bacteria were cultivated without Ag and Sr additives. Three independent experiments each with an intra-experiment duplicate were carried out.

4.4. Co-Culture of NIH3T3/MC3T3 with A. actinomycetemcomitans

NIH3T3 and MC3T3 were cultured separately in 6-well plates with a concentration of 1×10^5 cell/mL (3 mL/well) as described previously. *A. actinomycetemcomitans* was inoculated in BHI broth supplemented with 10 µg/mL vitamin K under anaerobic conditions (80% N_2, 10% H_2, 10% CO_2 and 37 °C) on the same day. After 24 h, the bacterial suspension was centrifuged, resuspended in PBS and adjusted to the desired optical density of 0.1 measured at 600 nm. A total of 15 µL of this suspension was used to challenge both cell lines representing a multiplicity of infection (MOI) of 5:1 (bacteria:cells). Different concentrations of $AgNO_3$, SrAc, or a combination of both were added to the wells, while the control groups received a medium without test substances. The co-cultured cells were incubated for 24 h at 37 °C and 5% CO_2. Subsequently, CFU counting and cell staining were performed as described above for mono-culture experiments. The experiments were carried out in three independent repetitions.

4.5. Characterization of Cell Differentiation

Osteogenesis was characterized by the extracellular calcium deposition of MC3T3-E1 cells (Alizarin red S staining, ARS). MC3T3-E1 cells were seeded in 24-well plates (CELLSTAR-Greiner Bio-One) with a density of 1×10^5 cells/mL (1 mL/well) and grown to >100 % confluence. Subsequently, the medium was replaced with an osteogenic differentiation medium consisting of the basic culture medium supplemented with 10% FCS, 1% P/S, 0.1 mM Ascorbate (Sigma-Aldrich®, Merck KGaA), 5 mM β-Glycerophosphat (Sigma-Aldrich®, Merck KGaA), 1.8 mM KH_2PO_4 (Carl Roth GmbH & Co. KG), 10 nM Dexamethason (Sigma-Aldrich®, Merck KGaA) and the respective $AgNO_3$ and SrAc concentrations as specified in the results section every 3 days. After 3, 7, and 14 days, cells were washed three times with PBS and fixed with a 4% paraformaldehyde solution (Carl Roth GmbH & Co., KG) for 20 min at room temperature. After washing thrice with diH_2O, the cells were stained with 2% Alizarin Red S (pH 4.2) (Sigma-Aldrich®, Merck KgaA) for 30 min at room temperature. The cells were washed an additional four times with diH_2O and finally covered with 200 µL PBS. The qualitative examination was performed by imaging stained cells under an optical microscope (Leica DMi1) using 10-fold mag-

nification objective and LAS V4.8 software. Images were quantitatively analyzed using Image J software (National Institutes of Health, Bethesda, MD, USA). The blue channel, which corresponds to ARS staining, was used to threshold images and the stained area percentage was processed subsequently. Three individual experiments each in quadruplicate were performed.

4.6. Statistical Analysis

GraphPad Prism Software 8.4 (GraphPad Software Inc., La Jolla, USA) was used to perform statistical analysis and graphic processing on the data. All data were checked for normal distribution using the Kolmogorov–Smirnov test. For all mono-culture and co-culture experiments, the significant differences with the control groups were determined by conducting a Kruskal–Wallis test. The Mann–Whitney U test was used to define the significance between $AgNO_3$ and $AgNO_3$/SrAc treated groups in a co-culture setup. A two-way analysis of variance (ANOVA) was used to compare groups over all time points in the ARS experiment. The significance level was set to $\alpha = 0.05$ for all comparisons.

5. Conclusions

The results presented here on the antibacterial and cytocompatible properties of $AgNO_3$ and SrAc clearly defined (i) an optimum $AgNO_3$ concentration that can impede the growth of bacteria associated with peri-implantitis while exhibiting cell compatibility, (ii) an optimum SrAc concentration exerting osseoinductive and antibacterial effects, and (iii) an enhanced therapeutic window of $AgNO_3$/SrAc combination. Herein, using $AgNO_3$ and SrAc with low concentrations resulted in cytocompatible properties with potential antimicrobial activity. Interestingly, by combining non-therapeutic concentrations of these two chemicals ($AgNO_3$, SrAc), we observed a synergistically intensified antibacterial effect, cell compatibility, and osteogenic differentiation in a co-culture model. The results also suggest that silver/strontium coating of implants may be a promising therapeutic strategy for the prevention of peri-implantitis and poor osseointegration and therefore requires further research.

Author Contributions: Conceptualization, M.K.P., K.D., M.I.R. and M.S.; methodology, M.K.P., K.D., C.M. and M.I.R.; formal analysis, M.K.P. and K.D.; investigation, M.K.P.; resources, M.S.; writing—original draft, M.K.P.; writing—review and editing, K.D., M.I.R., C.M., A.W. and M.S.; visualization, M.K.P.; supervision, A.W. and M.S.; project administration, M.S.; funding acquisition, M.I.R. and M.S. All authors have read and agreed to the published version of the manuscript.

Funding: This research was Funded by the Deutsche Forschungsgemeinschaft (DFG, German Research Foundation)–SFB/TRR-298-SIIRI–Project-ID 426335750.

Institutional Review Board Statement: Not applicable.

Informed Consent Statement: Not applicable.

Data Availability Statement: Data are available upon reasonable request from the corresponding authors.

Acknowledgments: The authors acknowledge the support of Henning Hartwig for excellent technical assistance. This project was supported by the Hannover Biomedical Research School (HBRS) and the PhD program "Regenerative Sciences".

Conflicts of Interest: The authors declare no conflict of interest.

References

1. Dreyer, H.; Grischke, J.; Tiede, C.; Eberhard, J.; Schweitzer, A.; Toikkanen, S.E.; Glöckner, S.; Krause, G.; Stiesch, M. Epidemiology and risk factors of peri-implantitis: A systematic review. *J. Periodontal Res.* **2018**, *53*, 657–681. [CrossRef]
2. Thomas, M.V.; Puleo, D.A. Infection, inflammation, and bone regeneration: A paradoxical relationship. *J. Dent. Res.* **2011**, *90*, 1052–1061. [CrossRef] [PubMed]
3. Sakka, S.; Baroudi, K.; Nassani, M.Z. Factors associated with early and late failure of dental implants. *J. Investig. Clin. Dent.* **2012**, *3*, 258–261. [CrossRef] [PubMed]

4. Siaili, M.; Chatzopoulou, D.; Gillam, D.G. An overview of periodontal regenerative procedures for the general dental practitioner. *Saudi Dent. J.* **2018**, *30*, 26–37. [CrossRef] [PubMed]
5. Mediratta, S. Guidelines for periodontal therapy—A review. *Ann. Dent. Spec.* **2014**, *2*, 91–94.
6. Zhang, E.; Zhao, X.; Hu, J.; Wang, R.; Fu, S.; Qin, G. Antibacterial metals and alloys for potential biomedical implants. *Bioact. Mater.* **2021**, *6*, 2569–2612. [CrossRef]
7. Grischke, J.; Eberhard, J.; Stiesch, M. Antimicrobial dental implant functionalization strategies—A systematic review. *Dent. Mater. J.* **2016**, *35*, 545–558. [CrossRef]
8. Greulich, C.; Braun, D.; Peetsch, A.; Diendorf, J.; Siebers, B.; Epple, M.; Köller, M. The toxic effect of silver ions and silver nanoparticles towards bacteria and human cells occurs in the same concentration range. *RSC Adv.* **2012**, *2*, 6981–6987. [CrossRef]
9. Liao, C.; Li, Y.; Tjong, S.C. Bactericidal and cytotoxic properties of silver nanoparticles. *Int. J. Mol. Sci.* **2019**, *20*, 449. [CrossRef]
10. Chernousova, S.; Epple, M. Silver as antibacterial agent: Ion, nanoparticle, and metal. *Angew. Chem. Int. Ed.* **2013**, *52*, 1636–1653. [CrossRef]
11. Akter, M.; Sikder, M.T.; Rahman, M.M.; Ullah, A.K.M.A.; Hossain, K.F.B.; Banik, S.; Hosokawa, T.; Saito, T.; Kurasaki, M. A systematic review on silver nanoparticles-induced cytotoxicity: Physicochemical properties and perspectives. *J. Adv. Res.* **2018**, *9*, 1–16. [CrossRef] [PubMed]
12. Hsueh, Y.-H.; Cheng, C.-Y.; Chien, H.-W.; Huang, X.-H.; Huang, C.-W.; Wu, C.-H.; Chen, S.-T.; Ou, S.-F. Synergistic effects of collagen and silver on the deposition characteristics, antibacterial ability, and cytocompatibility of a collagen/silver coating on titanium. *J. Alloy. Compd.* **2020**, *830*, 154490. [CrossRef]
13. van Hengel, I.A.J.; Tierolf, M.W.A.M.; Fratila-Apachitei, L.E.; Apachitei, I.; Zadpoor, A.A. Antibacterial Titanium Implants Biofunctionalized by Plasma Electrolytic Oxidation with Silver, Zinc, and Copper: A Systematic Review. *Int. J. Mol. Sci.* **2021**, *22*, 3800. [CrossRef] [PubMed]
14. Li, W.; Yang, Y.; Zhang, H.; Xu, Z.; Zhao, L.; Wang, J.; Qiu, Y.; Liu, B. Improvements on biological and antimicrobial properties of titanium modified by AgNPs-loaded chitosan-heparin polyelectrolyte multilayers. *J. Mater. Sci. Mater. Med.* **2019**, *30*, 1–12. [CrossRef] [PubMed]
15. Divakar, D.D.; Jastaniyah, N.T.; Altamimi, H.G.; Alnakhli, Y.O.; Alkheraif, A.A.; Haleem, S. Enhanced antimicrobial activity of naturally derived bioactive molecule chitosan conjugated silver nanoparticle against dental implant pathogens. *Int. J. Biol. Macromol.* **2018**, *108*, 790–797. [CrossRef]
16. Saleem, O.; Wahaj, M.; Akhtar, M.A.; Ur Rehman, M.A. Fabrication and Characterization of Ag–Sr-Substituted Hydroxyapatite/Chitosan Coatings Deposited via Electrophoretic Deposition: A Design of Experiment Study. *ACS Omega* **2020**, *5*, 22984–22992. [CrossRef]
17. Mao, Z.; Li, Y.; Yang, Y.; Fang, Z.; Chen, X.; Wang, Y.; Kang, J.; Qu, X.; Yuan, W.; Dai, K. Osteoinductivity and antibacterial properties of strontium ranelate-loaded poly (lactic-co-glycolic acid) microspheres with assembled silver and hydroxyapatite nanoparticles. *Front. Pharmacol.* **2018**, *9*, 368. [CrossRef]
18. Grade, S.; Eberhard, J.; Jakobi, J.; Winkel, A.; Stiesch, M.; Barcikowski, S. Alloying colloidal silver nanoparticles with gold disproportionally controls antibacterial and toxic effects. *Gold Bull.* **2014**, *47*, 83–93. [CrossRef]
19. Li, Y.; Wang, W.; Han, J.; Li, Z.; Wang, Q.; Lin, X.; Ge, K.; Zhou, G. Synthesis of Silver-and Strontium-Substituted Hydroxyapatite with Combined Osteogenic and Antibacterial Activities. *Biol. Trace Elem. Res.* **2022**, *200*, 931–942. [CrossRef]
20. Fielding, G.A.; Roy, M.; Bandyopadhyay, A.; Bose, S. Antibacterial and biological characteristics of plasma sprayed silver and strontium doped hydroxyapatite coatings. *Acta Biomater.* **2012**, *8*, 3144. [CrossRef]
21. Marx, D.; Yazdi, A.R.; Papini, M.; Towler, M. A review of the latest insights into the mechanism of action of strontium in bone. *Bone Rep.* **2020**, *12*, 1872–2352. [CrossRef] [PubMed]
22. Neves, N.; Linhares, D.; Costa, G.; Ribeiro, C.C.; Barbosa, M.A. In vivo and clinical application of strontium-enriched biomaterials for bone regeneration: A systematic review. *Bone Jt. Res.* **2017**, *6*, 366–375. [CrossRef] [PubMed]
23. Alshammari, H.; Neilands, J.; Svensäter, G.; Stavropoulos, A. Antimicrobial Potential of Strontium Hydroxide on Bacteria Associated with Peri-Implantitis. *Antibiotics* **2021**, *10*, 150. [CrossRef] [PubMed]
24. Masamoto, K.; Fujibayashi, S.; Yamaguchi, S.; Otsuki, B.; Okuzu, Y.; Kawata, T.; Goto, K.; Shimizu, T.; Shimizu, Y.; Kawai, T. Bioactivity and antibacterial activity of strontium and silver ion releasing titanium. *J. Biomed. Mater. Res. Part B Appl. Biomater.* **2021**, *109*, 238–245. [CrossRef] [PubMed]
25. Zhou, J.; Wang, X.; Zhao, L. Antibacterial, angiogenic, and osteogenic activities of Ca, P, Co, F, and Sr compound doped titania coatings with different Sr content. *Sci. Rep.* **2019**, *9*, 1–11. [CrossRef]
26. Querido, W.; Rossi, A.L.; Farina, M. The effects of strontium on bone mineral: A review on current knowledge and microanalytical approaches. *Micron* **2016**, *80*, 122–134. [CrossRef]
27. Cochis, A.; Barberi, J.; Ferraris, S.; Miola, M.; Rimondini, L.; Vernè, E.; Yamaguchi, S.; Spriano, S. Competitive surface colonization of antibacterial and bioactive materials doped with strontium and/or silver ions. *Nanomaterials* **2020**, *10*, 120. [CrossRef]
28. O'Sullivan, C.; O'Neill, L.; O'Leary, N.D.; O'Gara, J.P.; Crean, A.M.; Ryan, K.B. Osteointegration, antimicrobial and antibiofilm activity of orthopaedic titanium surfaces coated with silver and strontium-doped hydroxyapatite using a novel blasting process. *Drug Deliv. Transl. Res.* **2021**, *11*, 702–716. [CrossRef]

29. Van Hengel, I.A.J.; Gelderman, F.S.A.; Athanasiadis, S.; Minneboo, M.; Weinans, H.; Fluit, A.C.; Van der Eerden, B.C.J.; Fratila-Apachitei, L.E.; Apachitei, I.; Zadpoor, A.A. Functionality-packed additively manufactured porous titanium implants. *Mater. Today Bio* **2020**, *7*, 100060. [CrossRef]
30. Lafaurie, G.I.; Sabogal, M.A.; Castillo, D.M.; Rincón, M.V.; Gómez, L.A.; Lesmes, Y.A.; Chambrone, L. Microbiome and microbial biofilm profiles of peri-implantitis: A systematic review. *J. Periodontol.* **2017**, *88*, 1066–1089. [CrossRef]
31. Pivodova, V.; Frankova, J.; Ulrichova, J. Osteoblast and gingival fibroblast markers in dental implant studies. *Biomed. Pap. Med. Fac. Palacky Univ. Olomouc* **2011**, *155*, 109–116. [CrossRef] [PubMed]
32. ISO. *Biological Evaluation of Medical Devices–Part 5: Tests for In Vitro Cytotoxicity*; ISO: Geneva, Switzerland, 2009.
33. Alshammari, H.; Bakitian, F.; Neilands, J.; Andersen, O.Z.; Stavropoulos, A. Antimicrobial Properties of Strontium Functionalized Titanium Surfaces for Oral Applications, A Systematic Review. *Coatings* **2021**, *11*, 810. [CrossRef]
34. Kaiser, J.-P.; Roesslein, M.; Diener, L.; Wichser, A.; Nowack, B.; Wick, P. Cytotoxic effects of nanosilver are highly dependent on the chloride concentration and the presence of organic compounds in the cell culture media. *J. Nanobiotechnol.* **2017**, *15*, 1–11. [CrossRef] [PubMed]
35. Souter, P.; Cunningham, J.C.; Horner, A.; Genever, P.G. The variable toxicity of silver ions in cell culture media. *Toxicol. In Vitro* **2019**, *60*, 154–159. [CrossRef]
36. Hrkac, T.; Röhl, C.; Podschun, R.; Zaporojtchenko, V.; Strunskus, T.; Papavlassopoulos, H.; Garbe-Schönberg, D.; Faupel, F. Huge increase of therapeutic window at a bioactive silver/titania nanocomposite coating surface compared to solution. *Mater. Sci. Eng. C* **2013**, *33*, 2367–2375. [CrossRef]
37. Abram, S.L.; Fromm, K.M. Handling (nano) silver as antimicrobial agent: Therapeutic window, dissolution dynamics, detection methods and molecular interactions. *Chem.—A Eur. J.* **2020**, *26*, 10948–10971. [CrossRef]
38. Sambale, F.; Wagner, S.; Stahl, F.; Khaydarov, R.R.; Scheper, T.; Bahnemann, D. Investigations of the toxic effect of silver nanoparticles on mammalian cell lines. *J. Nanomater.* **2015**, *2015*, 136765. [CrossRef]
39. Tîlmaciu, C.-M.; Mathieu, M.; Lavigne, J.-P.; Toupet, K.; Guerrero, G.; Ponche, A.; Amalric, J.; Noël, D.; Mutin, P.H. In vitro and in vivo characterization of antibacterial activity and biocompatibility: A study on silver-containing phosphonate monolayers on titanium. *Acta Biomater.* **2015**, *15*, 266–277. [CrossRef]
40. Xing, Z.-C.; Chae, W.-P.; Baek, J.-Y.; Choi, M.-J.; Jung, Y.; Kang, I.-K. In vitro assessment of antibacterial activity and cyto-compatibility of silver-containing PHBV nanofibrous scaffolds for tissue engineering. *Biomacromolecules* **2010**, *11*, 1248–1253. [CrossRef]
41. Grade, S.; Eberhard, J.; Wagener, P.; Winkel, A.; Sajti, C.L.; Barcikowski, S.; Stiesch, M. Therapeutic Window of Ligand-Free Silver Nanoparticles in Agar-Embedded and Colloidal State: In Vitro Bactericidal Effects and Cytotoxicity. *Adv. Eng. Mater.* **2012**, *14*, B231–B239. [CrossRef]
42. Albers, C.E.; Hofstetter, W.; Siebenrock, K.A.; Landmann, R.; Klenke, F.M. In vitro cytotoxicity of silver nanoparticles on osteoblasts and osteoclasts at antibacterial concentrations. *Nanotoxicology* **2013**, *7*, 30–36. [CrossRef]
43. Kirmanidou, Y.; Sidira, M.; Bakopoulou, A.; Tsouknidas, A.; Prymak, O.; Papi, R.; Choli-Papadopoulou, T.; Epple, M.; Michailidis, N.; Koidis, P. Assessment of cytotoxicity and antibacterial effects of silver nanoparticle-doped titanium alloy surfaces. *Dent. Mater.* **2019**, *35*, e220–e233. [CrossRef] [PubMed]
44. Kędziora, A.; Wieczorek, R.; Speruda, M.; Matolínová, I.; Goszczyński, T.M.; Litwin, I.; Matolín, V.; Bugla-Płoskońska, G. Comparison of antibacterial mode of action of silver ions and silver nanoformulations with different physico-chemical properties: Experimental and computational studies. *Front. Microbiol.* **2021**, *12*, 659614. [CrossRef] [PubMed]
45. Tang, S.; Zheng, J. Antibacterial activity of silver nanoparticles: Structural effects. *Adv. Healthc. Mater.* **2018**, *7*, 1701503. [CrossRef] [PubMed]
46. Tan, J.; Wang, D.; Cao, H.; Qiao, Y.; Zhu, H.; Liu, X. Effect of local alkaline microenvironment on the behaviors of bacteria and osteogenic cells. *ACS Appl. Mater. Interfaces* **2018**, *10*, 42018–42029. [CrossRef] [PubMed]
47. Liu, J.; Rawlinson, S.C.F.; Hill, R.G.; Fortune, F. Strontium-substituted bioactive glasses in vitro osteogenic and antibacterial effects. *Dent. Mater.* **2016**, *32*, 412–422. [CrossRef]
48. Alkawareek, M.Y.; Bahlool, A.; Abulateefeh, S.R.; Alkilany, A.M. Synergistic antibacterial activity of silver nanoparticles and hydrogen peroxide. *PLoS ONE* **2019**, *14*, e0220575. [CrossRef]
49. Deng, H.; McShan, D.; Zhang, Y.; Sinha, S.S.; Arslan, Z.; Ray, P.C.; Yu, H. Mechanistic study of the synergistic antibacterial activity of combined silver nanoparticles and common antibiotics. *Environ. Sci. Technol.* **2016**, *50*, 8840–8848. [CrossRef]
50. Jin, G.; Qin, H.; Cao, H.; Qian, S.; Zhao, Y.; Peng, X.; Zhang, X.; Liu, X.; Chu, P.K. Synergistic effects of dual Zn/Ag ion implantation in osteogenic activity and antibacterial ability of titanium. *Biomaterials* **2014**, *35*, 7699–7713. [CrossRef]
51. Tran, H.A.; Tran, P.A. In Situ Coatings of Silver Nanoparticles for Biofilm Treatment in Implant-Retention Surgeries: Antimicrobial Activities in Monoculture and Coculture. *ACS Appl. Mater. Interfaces* **2021**, *13*, 41435–41444. [CrossRef]
52. Geng, Z.; Wang, R.; Zhuo, X.; Li, Z.; Huang, Y.; Ma, L.; Cui, Z.; Zhu, S.; Liang, Y.; Liu, Y. Incorporation of silver and strontium in hydroxyapatite coating on titanium surface for enhanced antibacterial and biological properties. *Mater. Sci. Eng. C* **2017**, *71*, 852–861. [CrossRef] [PubMed]
53. Amudha, S.; Ramya, J.R.; Arul, K.T.; Deepika, A.; Sathiamurthi, P.; Mohana, B.; Asokan, K.; Dong, C.-L.; Kalkura, S.N. Enhanced mechanical and biocompatible properties of strontium ions doped mesoporous bioactive glass. *Compos. Part B Eng.* **2020**, *196*, 108099. [CrossRef]

54. Pauksch, L.; Hartmann, S.; Rohnke, M.; Szalay, G.; Alt, V.; Schnettler, R.; Lips, K.S. Biocompatibility of silver nanoparticles and silver ions in primary human mesenchymal stem cells and osteoblasts. *Acta Biomater.* **2014**, *10*, 439–449. [CrossRef] [PubMed]
55. Holmila, R.J.; Vance, S.A.; King, S.B.; Tsang, A.W.; Singh, R.; Furdui, C.M. Silver nanoparticles induce mitochondrial protein oxidation in lung cells impacting cell cycle and proliferation. *Antioxidants* **2019**, *8*, 552. [CrossRef]
56. Qin, H.; Zhu, C.; An, Z.; Jiang, Y.; Zhao, Y.; Wang, J.; Liu, X.; Hui, B.; Zhang, X.; Wang, Y. Silver nanoparticles promote osteogenic differentiation of human urine-derived stem cells at noncytotoxic concentrations. *Int. J. Nanomed.* **2014**, *9*, 2469. [CrossRef]

International Journal of
Molecular Sciences

MDPI

Review

Applications of Plasma-Activated Water in Dentistry: A Review

Noala Vicensoto Moreira Milhan [1,*], William Chiappim [2], Aline da Graça Sampaio [1], Mariana Raquel da Cruz Vegian [1], Rodrigo Sávio Pessoa [2] and Cristiane Yumi Koga-Ito [1,3]

[1] Oral Biopathology Graduate Program, São José dos Campos Institute of Science & Technology, São Paulo State University, UNESP, São Paulo 12245-000, Brazil; aline.sampaio@unesp.br (A.d.G.S.); mary.rcv@hotmail.com (M.R.d.C.V.); cristiane.koga-ito@unesp.br (C.Y.K.-I.)
[2] Plasma and Processes Laboratory, Department of Physics, Aeronautics Institute of Technology, Praça Marechal Eduardo Gomes 50, São José dos Campos 12228-900, Brazil; chiappimjr@yahoo.com.br (W.C.); rspessoa@ita.br (R.S.P.)
[3] Department of Environment Engineering, São José dos Campos Institute of Science & Technology, São Paulo State University, UNESP, São Paulo 12247-016, Brazil
* Correspondence: milhan.noala@gmail.com; Tel.: +55-12-991851206

Abstract: The activation of water by non-thermal plasma creates a liquid with active constituents referred to as plasma-activated water (PAW). Due to its active constituents, PAW may play an important role in different fields, such as agriculture, the food industry and healthcare. Plasma liquid technology has received attention in recent years due to its versatility and good potential, mainly focused on different health care purposes. This interest has extended to dentistry, since the use of a plasma–liquid technology could bring clinical advantages, compared to direct application of non-thermal atmospheric pressure plasmas (NTAPPs). The aim of this paper is to discuss the applicability of PAW in different areas of dentistry, according to the published literature about NTAPPs and plasma–liquid technology. The direct and indirect application of NTAPPs are presented in the introduction. Posteriorly, the main reactors for generating PAW and its active constituents with a role in biomedical applications are specified, followed by a section that discusses, in detail, the use of PAW as a tool for different oral diseases.

Keywords: plasma-activated water; plasma-treated water; atmospheric plasma; gliding arc discharge; DBD; dentistry; decontamination; oral cancer; tooth bleaching

Citation: Milhan, N.V.M.; Chiappim, W.; Sampaio, A.d.G.; Vegian, M.R.d.C.; Pessoa, R.S.; Koga-Ito, C.Y. Applications of Plasma-Activated Water in Dentistry: A Review. *Int. J. Mol. Sci.* **2022**, *23*, 4131. https://doi.org/10.3390/ijms23084131

Academic Editor: Mary Anne Melo

Received: 5 March 2022
Accepted: 6 April 2022
Published: 8 April 2022

Publisher's Note: MDPI stays neutral with regard to jurisdictional claims in published maps and institutional affiliations.

Copyright: © 2022 by the authors. Licensee MDPI, Basel, Switzerland. This article is an open access article distributed under the terms and conditions of the Creative Commons Attribution (CC BY) license (https://creativecommons.org/licenses/by/4.0/).

1. Introduction

Plasma medicine is a multidisciplinary research field that investigates the uses of plasma in the healthcare field. Currently, non-thermal plasma technology is mainly focused on applications at atmospheric pressure, which is commonly referred to as non-thermal atmospheric pressure plasmas (NTAPPs). Direct applications of NTAPP have been used for decontamination of food [1,2] and food contact surfaces [1,3] in the food industry, in air purification [4] and as an antimicrobial agent in the medical and dentistry fields [5–9]. In 2021, NTAPP focused on plasma medicine reached a quarter of a century since the first published study [10]. Over time, in addition to the antimicrobial effects, other applications of NTAPP have been discovered in biomedical fields, such as the benefits for wound healing and cancer treatment [11,12].

NTAPPs can also be applied indirectly through the activation of water or liquids and through the treatment of contaminated or polluted water [13,14]. Their antimicrobial effect [15,16] and applicability in the treatment of cancer [17,18] and wound healing [19] have also been observed in the indirect modality of treatment. In recent years, plasma medicine has expanded the frontiers towards plasma dentistry. NTAPP has shown efficacy against oral microorganisms, in addition to anti-inflammatory properties, with possible application in cariology, endodontic, periodontics and oral oncology [20]. Besides, plasma-activated water (PAW) has also demonstrated potential application in dentistry fields [21,22].

It is important to emphasize the differences between both modalities of treatment: direct and indirect. The first implies that plasma is applied directly on a given substrate, such as wounds, skin, food etc., [23,24]. Conversely, in the indirect modality of NTAPPs, a given liquid is activated prior to the application to the substrate. To exemplify, Table 1 shows the main review articles published in the last three years on the applications of direct and indirect NTAPPs, in areas ranging from medicine, biomedicine, dentistry, agriculture and the food industry. It is worth mentioning that although the present work is focused on dentistry, the direct and indirect NTAPPs are of great importance for agriculture and the food industry. This wide range of applications of direct and indirect NTAPPs is schematically presented in Figure 1. Figure 1a highlights the applicability of direct NTAPPs that cover different human and food healthcare areas. Figure 1b illustrates the applications of NTAPPs through the modality of generating plasma-activated liquid (PAL) or PAW, which are later applied to substrates. As described, PAW and PAL studies are focused on different purposes, which shows the effort of many scientists to improve and make plasma technology more accessible.

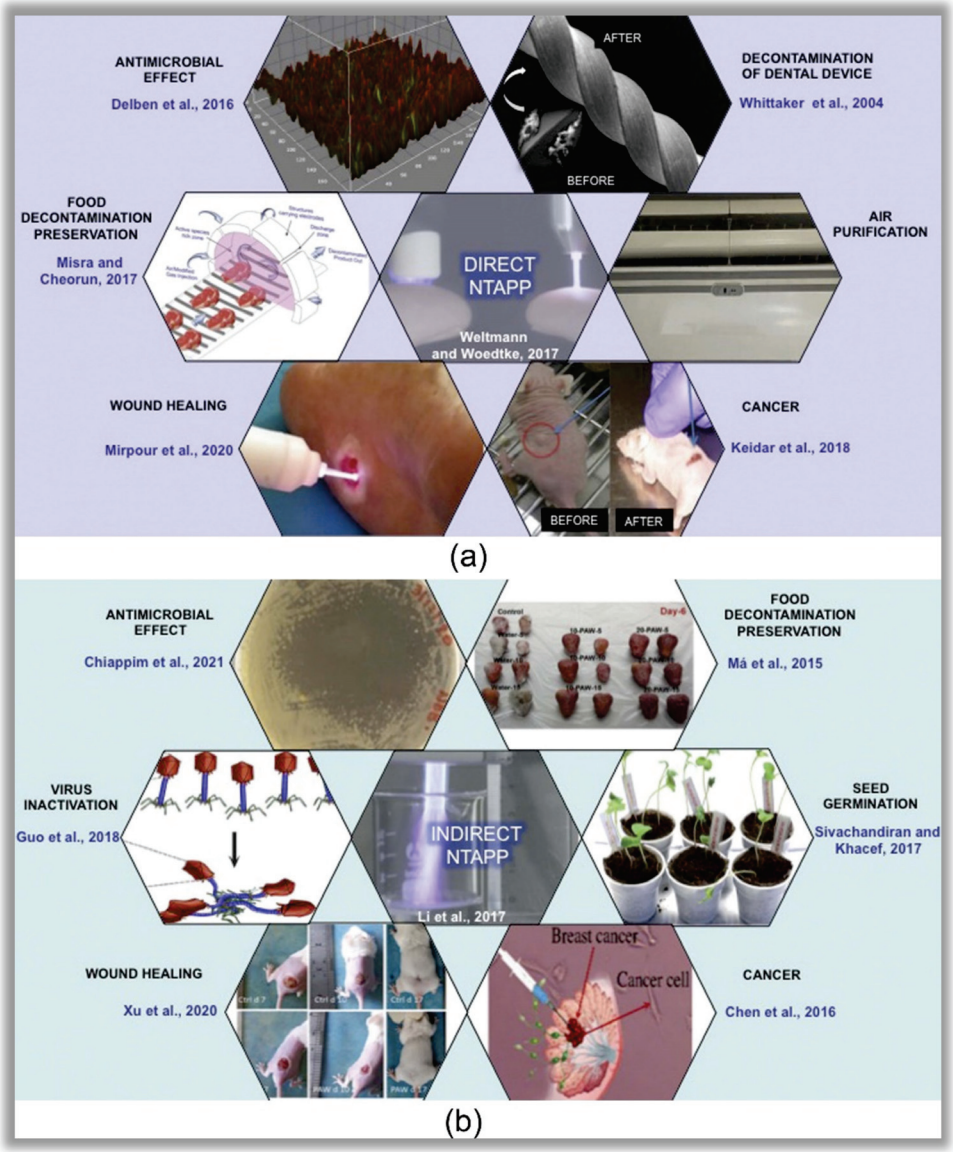


Figure 1. Schematic illustration of direct (**a**) and indirect (**b**) applications of non-thermal atmospheric pressure plasmas (NTAPPs). Note that due its antimicrobial effect, direct NTAPPs have been used for

different purposes such as decontamination/preservation of food, air purification and decontamination of medical and dental devices. Additionally, an improvement in wound healing and anti-cancer properties has also been observed after direct exposure to NTAPPs. Similarly, the indirect modality has demonstrated antimicrobial effect against some types of microorganisms, with applicability in different fields. The reactive oxygen and nitrogen species generated in the liquids after plasma exposure may favor the seed germination. In addition, good responses have also been observed in wound healing and cancer treatment, which brings good perspectives for healthcare due to the clinical advantages of plasma-activated water (PAW) compared to direct NTAPPs. Some figures were reprinted with permission from Delben et al. [25], CC BY 4.0 license (2016); Whittaker et al. [26], copyright Elsevier (2004); Weltmann and Woedtke, [7], copyright IOP (2017); Misra and Cheorun, [27], copyright elsevier (2017); Keidar et al. [28], CC BY 4.0 license (2011); Sivachandiran and Khacef, [29], CC BY 3.0 license (2017); Guo et al. [15], CC BY 4.0 license (2018); Chen et al. [18], copyright Wiley (2016); Xu et al. [19], CC BY 4.0 license (2020); Li et al. [22], copyright Wiley (2017); Ma et al. [30], copyright Elsevier (2015); Chiappim et al. [31], copyright Wiley (2021).

To understand the mechanisms of action related to NTAPPs, it is essential to know that the plasma is a partially ionized gas consisting of particles as electrons, ions, metastable species, radiation as ultraviolet (UV), visible (VIS), the electromagnetic field and reactive species. It is worth highlighting that the term reactive species is commonly used for free radicals and reactive oxygen species (ROS) and reactive nitrogen species (RNS). It is highly reactive due to the presence of unpaired valence electrons or non-static bonds on its structure. Despite the various components produced in plasma, reactive oxygen and nitrogen species (RONS) play a fundamental role in plasma medicine [32,33]. RONS generated in NTAPP are divided into short-lived and long-lived species. Hydroxyl radical (OH^-), delta oxygen singlet ($^1O_2$) and superoxide anion ($O_2{}^-$) are examples of short-lived species, which last from a few seconds to minutes [34]. In contrast, hydrogen peroxide (H_2O_2), nitrite (NO_2), nitrate ($NO_3{}^-$), nitrous acid (HNO_2) and ozone (O_3) belong to the groups of long-lived species [35,36]. When NTAPP is used in an indirect mode, i.e., in liquid or water activation, most RONS found in the liquid phase are long-lived ones, generated from the gas phase of the plasma and the plasma–liquid interface interaction. The generation of RONS also occurs through the primary transformation of reactive species generated in the liquid [37]. Therefore, water or liquid exposure to NTAPP induces active constituents, called RONS, which are useful for biomedical applications [21].

Due to the growing interest of the scientific community in plasma technology applied to dentistry, a review article is presented here to serve as a quick guide for dentists, physicians, physicists, engineers and health professionals in general. This review aims to discuss the applicability of PAW in dentistry, which, as can be seen in Table 1, is a topic review with little or no exploration. Thus, based on the published literature, the findings of PAW applied to dentistry are presented, as well as the future perspectives for the area considering the main results related to direct and indirect NTAPP for biomedical applications.

Table 1. Summary of the main review articles published in the last three years on applications of direct and indirect NTAPPs.

Approach	NTAPP Modalities	Publication Year/Reference
Molecular Mechanisms of the Efficacy of NTAPP in Cancer Treatment	Direct	2020 [38]
A Powerful Tool for Modern Medicine	Direct	2020 [11]
The New Frontier in Low Temperature Plasma Applications	Direct	2020 [39]
Atmospheric Cold Plasma Treatment in Fruit Juices	Direct	2020 [40]
Chemical, Physical and Physiological Quality Attributes of Fruit and Vegetables Induced by Cold Plasma Treatment	Direct	2020 [41]

Table 1. *Cont.*

Approach	NTAPP Modalities	Publication Year/Reference
Cold Plasma as a New Hope in the Field of Virus Inactivation	Direct	2020 [42]
The Effects of Plasma on Plant Growth, Development and Sustainability	Direct	2020 [43]
Cold Plasma for the Control of Biofilms in Food Industry	Direct	2020 [44]
Potential of Cold Plasma Technology in Ensuring the Safety of Foods and Agricultural Produce	Direct	2020 [45]
Plasma Agriculture from Laboratory to Farm	Direct	2020 [46]
Aurora Borealis in Dentistry	Direct	2021 [47]
Applications of Cold Atmospheric Pressure Plasma in Dentistry	Direct	2021 [20]
Cold Atmospheric Pressure Plasma Technology in Medicine, Agriculture and Food Industry	Direct	2021 [48]
The Antimicrobial Effect of Cold Atmospheric Plasma against Dental Pathogens	Direct	2021 [49]
Influence of Atmospheric Cold Plasma on Spore Inactivation	Direct	2021 [50]
Plasma-Assisted Agriculture: History, Presence and Prospects	Direct	2021 [51]
Improving Seed Germination by Cold Atmospheric Plasma	Direct	2022 [52]
Reactive Nitrogen Species in Plasma-Activated Water	Indirect	2020 [53]
Recent Advances in Plasma-Activated Water for Food Safety	Indirect	2022 [54]
Influence of Plasma-Activated Water on Physical and Physical–Chemical Soil Properties	Indirect	2020 [55]
PAW Triggers Plant Defense Responses	Indirect	2020 [56]
PAW Generation, Origin of Reactive Species and Biological Applications	Indirect	2020 [36]
Interactions of Plasma-Activated Water with Biofilms	Indirect	2020 [57]
A Comprehensive Review of PAW for Enhanced Food Safety and Quality	Indirect	2021 [58]
Applications of PAW in the Food Industry	Indirect	2020 [59]
PAW for Cancer Treatment: Positives, Potentials and Problems of Clinical Translation	Indirect	2020 [60]
Review on Discharge Plasma for Water Treatment	Indirect	2020 [61]
PAW on Microbial Growth and Storage Quality of Fresh-cut Apple	Indirect	2020 [62]
PAW Production and its Application in Agriculture	Indirect	2021 [63]
Diagnostic Analysis of Reactive Species in PAW: Current Advances and Outlooks	Indirect	2021 [64]
PAW from DBD as a source of Nitrogen for Agriculture	Indirect	2021 [65]
PAW, Hydrogen Peroxide and Nitrates on Lettuce Growth	Indirect	2021 [66]

Therefore, this review is divided as follows; Section 2 shows the main reactors used for PAW/PAL and plasma-treated water (PTW). Another essential point demonstrated in this section is the formation of RONS, the fundamental species for plasma medicine. Section 3 explores the main text of this review, focusing on PAW applied to different areas of dentistry. In this context, the following topics are explored: decontamination of dental devices, treatment of oral infectious diseases, anti-inflammatory properties and wound healing, anti-cancer therapy and tooth bleaching. Finally, Section 4 presents the conclusion of the work.

2. Plasma-Activated and Plasma-Treated Water

In the literature, the terms treatment and activation are often misused. To avoid doubt, treatment is defined as a practical means or refinements used to combat/mitigate a problem. In the specific case of water treated by plasma, the term treated refers to the process of elimination or complete mineralization in wastewater of synthetic dyes, pharmaceuticals products and pathogenic bacteria, among other pollutants. Therefore, plasma water treatment is commonly used to purify or decontaminate small or large amounts of water. In contrast, activation is understood as increased activity, becoming active, boosting, accelerating, or intensifying some specific property. In this case, the non-pollutant water exposed to the plasma becomes activated, i.e., it obtains new properties. Unlike treatment, activation is carried out in small amounts of water (between 1 mL to 1000 mL) [36,53,66], but the reactors used are the same, with a slight modification in both cases. It is important to note that deionized water, distilled water, filtered water and potable tap water, i.e., pure water without pollutants, are usually used for activation.

2.1. Main Reactors of Producing

Two main types of plasma reactors are used in PAW generation: dielectric barrier discharges (DBDs) and plasma jets (PJs). Both are non-thermal plasmas, i.e., they are NTAPP and have a wide range of types [65,67]. DBDs for PAW generation are considered indirect sources of plasma, as the plasma is mainly produced between the reactor electrodes without any contact with the water, taking advantage of the interactions of the gas with the liquid. Some reactive plasma species can reach the water surface through ionizing wave mechanisms using electric field propagation, convection through airflow and diffusion [65]. In contrast, the PJs used for PAW generation are considered direct sources of plasma, i.e., there is direct contact between the plasma and the water and the water can act as a counter electrode so that the discharge current can flow through the liquid. The PJs are the most widely used reactors, as some of them generate a stable volume of plasma that is controllable without the confinement between the electrodes, as in the case of the DBDs [67]. In both reactors, the formation of RONS occurs at the interface between the gaseous and liquid phases and/or within the liquid, which drastically changes the concentration of the RONS constituents [36]. In contrast, in the treatment of water by plasma, the reactors can be immersed in the treated liquid [68,69]. Therefore, in this case, both DBD reactors and PJ reactors can be used.

It is important to note that NTAPPs operate at a high voltage. As reported in the literature, these voltages range from 1 to 50 kV, with operating frequencies that can start in the tens to thousands of Hz (kHz) and powers that generally do not exceed values greater than 10 W. Commonly used working gases are helium (He), argon (Ar), oxygen (O_2), nitrogen (N_2), air or a mixture of these gases. Working gases are used with flow rates ranging from 1 to 30 L/min [36,53–58]. Indeed, there is a range of reactors used for water and liquid activation and, every day, a new article is published with new reactors that have minor changes. Therefore, a dedicated review article would be needed to demonstrate the NTAPP generation reactors and their characteristics, but the focus of the present work is not that. Thus, below we show some reactors used to generate PAW.

As seen in Figure 2, discharges are used directly into the water and on the surface of the water, which considerably affects the chemical composition of PAW. This difference in chemical composition is basically due to the differences between the rupture forces in the gas phase (discharge on the surface) and the water (discharge inside) [70,71]. However, as reported in the literature, the most applied systems are those that operate with plasma discharge in contact with the water, i.e., PJ and DBD as a plasma source [72,73]. As demonstrated in the next section, these plasmas deliver the RONS from the plasma gas to the liquid phase more efficiently.

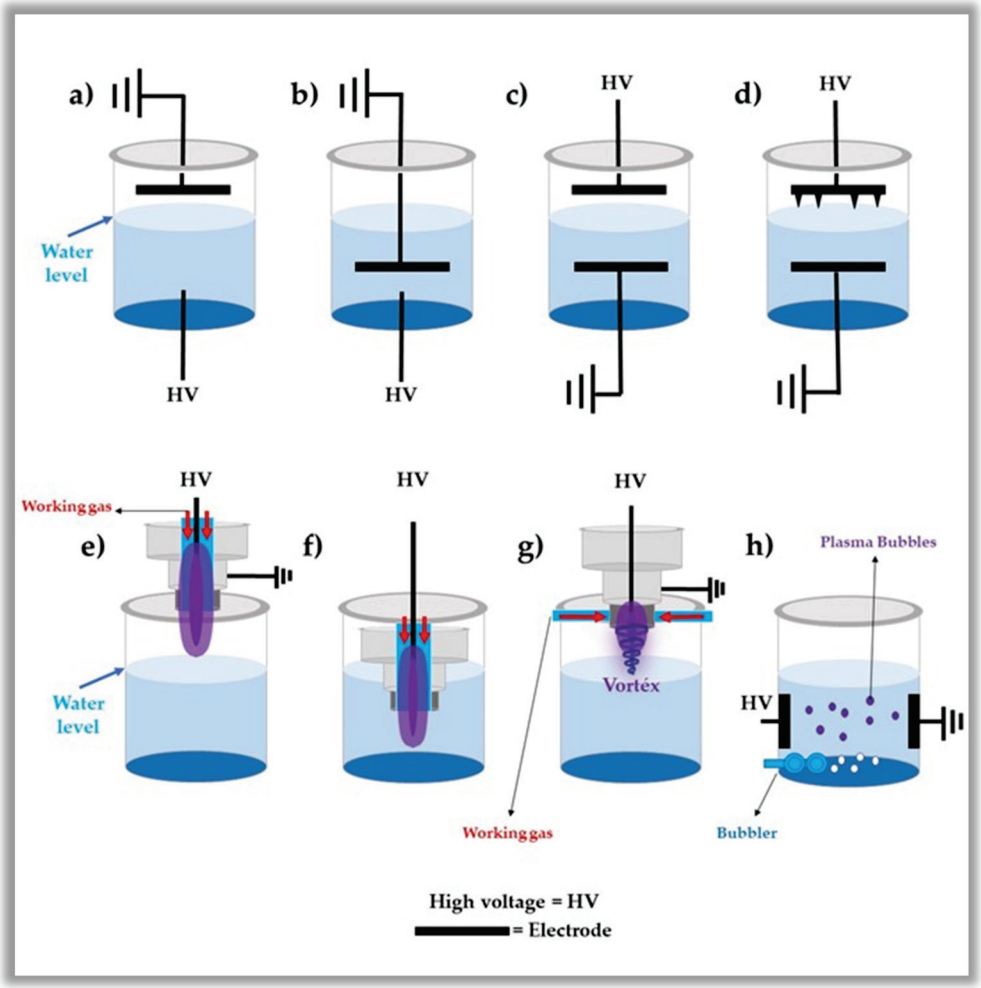


Figure 2. Schematic drawing of different discharges used for the preparation of plasma-activated water [47,74] (**a**–**c**) direct discharge into the water and (**d**) direct discharge into the water with multi-electrodes; (**e**) discharge in the gaseous phase onto the water surface; (**f**) discharge in the gaseous phase into the water; (**g**) discharge in the gas phase onto the water surface with plasma generated on forward vortex flow reactor (FVFR); (**h**) discharges in bubbles into the water.

An important question is whether there is commercial equipment that can be applied in clinical practice. Recently, Andrasch et al. [72], Pemen et al. [73] and Schnabel et al. [75] developed pilot units with potential for practical applications. Andrasch et al. [72] and Schnabel et al. [75] obtained a PAW production rate of 1 L/min. Pemen et al. [73] obtained 0.5 L/min. However, these devices cannot meet the application requirements in dentistry and medicine, which are low pH and high concentrations of RONS. On the other hand, in agriculture and in the food industry, the production of millions of liters of PAW at a low cost is required. Therefore, it can be said that PAW-generating equipment is still in the pilot phase and has great commercialization potential in the coming years.

2.2. Origin of Reactive Oxygen and Nitrogen Species

The RONS induced in PAW are dependent on many different parameters such as (i) the composition of the solution, (ii) the distance between the plasma and the liquid surface, (iii) the types of power supply used in the plasma generation, (iv) electrode configuration, (v) applied voltage, (vi) voltage polarity, (vii) water volume, (viii) gas type and flow, among other parameters [31,76–78]. It is also important to highlight that both the chemistry and the reaction processes of PAW produced with the reactor in a few centimeters of water are different from those made in the generation of PAW with the reactors submerged in water.

The gas–liquid system generated for electrical discharges placed in a few centimeters of water is more interesting, as they can cause post-electrical discharge reactions capable of forming other long-lived reactive species [59,70]. For example, when using compressed air as the plasma-generating gas for water activation, the gas–liquid interface produces numerous short-lived species, ranging from hydroxyl radicals, superoxide and nitrous oxide to the generation of atomic oxygen and nitrogen [36]. Short-lived species later generate long-lived species, such as nitrites, nitrates and hydrogen peroxide (see Figure 3).

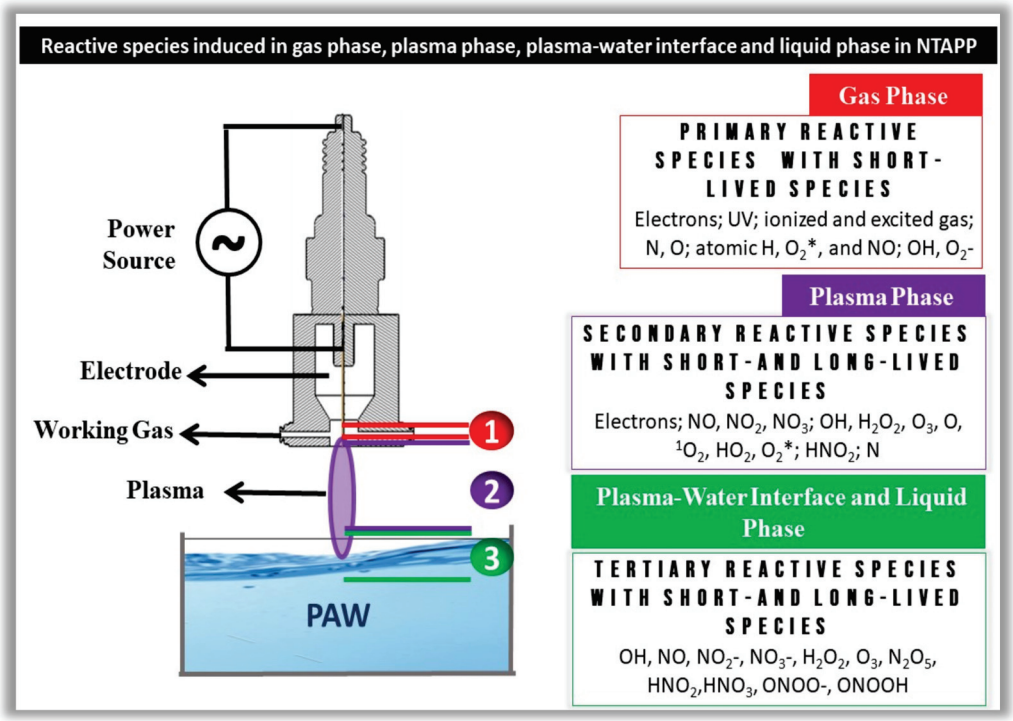


Figure 3. Schematic diagram that shows the regions of reactive species generation induced by NTAPP used to activate water. Note the three regions of RONS formation in an NTAPP device in contact with water. The primary reactive species, short-lived species, electrons and electromagnetic radiation in the ultraviolet range are found in region 1 and are in the gas phase. In region 2, we can observe the secondary reactive species made up of short-lived and long-lived species, and this region is contained in the plasma phase. Tertiary reactive species are short-lived and long-lived species, and their region is limited to the plasma–water interface and liquid phase.

With the significant increase in PAW applications, it is necessary to understand which RONS can be formed and how they are formed, in addition to the quantification of their concentrations. In Appendix A, the generation and recombination mechanisms of the main plasma-induced long-lived reactive species are described in water activation processes that play a crucial role in healthcare applications.

3. PAW Applied in Dentistry

3.1. Decontamination of Dental Devices

The surfaces of medical and dental devices are constantly exposed to different microorganisms during procedures, working as a reservoir of pathogens and a potential source of contamination for the patients [79]. To avoid the risk of contamination, different methods and chemical products may be used to control pathogenic or nonpathogenic microorganisms. However, limitations such as ineffective sterilization, low penetration, incompatibility with materials that are sensitive to heat and corrosion, residue release, toxicity to the environment and individuals [80,81] and an inability to penetrate biofilm cell structures [82] support a constant search for new methods. In addition to being useful

in the inactivation of microorganisms when applied over, inside, or touching the water surface [83], NTAPPs are also efficient against prion proteins [84], which are resistant to traditional cleaning methods [85].

The direct application of NTAPPs for the disinfection of heat-sensitive materials has been explored in the literature [86,87]. The disinfection of endodontic devices [26], silicone, diamond dental drills [88], metals [89], titanium alloy surfaces [90] and titanium disc surfaces [91] were analyzed with satisfactory results. The effectiveness of biological decontamination by NTAPPs depends on some parameters such as equipment configuration (frequency, power), gas (type and flow), the geometry of the analyzed material, distance, exposure time and also the position and design of the device [80,86,92]. Depending on the geometry of the material, multiple exposures may be required to eliminate the microorganisms.

As an alternative method, solutions activated with plasma, such as PAW, have also been evaluated for disinfection [93]. In fact, this in an interesting field of investigation as the possibility of disinfecting a device with a simple washing seems easier, compared to multiple exposures that may be needed to decontaminate a device/biomaterial with a complex geometry. It was previously observed that microbicide action may be related to the main reactive species and also the low pH acquired during aqueous plasma activation [94]. The use of PAW for the sterilization of medical devices was previously suggested, considering its antimicrobial properties [95]. One of the main advantages of this technology is that plasma-activated liquids may keep the antimicrobial effect over one month after PAW generation, when stored at a minimum of −80 °C [96,97]. However, the antimicrobial activity may be reduced, depending on the storage temperature, by decreasing the number of reactive species. Inactivation of *S. aureus* was observed after 20 min of treatment with PAW stored at −80 °C. However, this potential decreased significantly when plasma-activated distilled water was stored at −20 °C for 1, 7, 15 and 30 days [96]. Similarly, another study observed that 60 min of exposure to PAW stored at –80 or –150 °C may promote microbial inactivation of *S. aureus* and *E. coli*, even after six months of storage. On the other hand, temperatures equal to or higher than −16 °C showed reduced antimicrobial properties in short or long periods of storage [97]. In addition to the possibility of disinfecting dental materials in the easiest way, the conservation properties of PAW indicate another advantage of using this technology compared to direct NTAPP, since it would considerably reduce the demand for using the plasma device.

The decontamination of dental unit waterline system tubes (DUWLs) is a challenge for dentistry due to the risk of cross-contamination [98] and also the limitation of some traditional disinfectants, which may be toxic [79,99]. The reduction in the viability of mature *Enterococcus faecalis* biofilms formed in DUWLs for 5 days after PAW treatment was detected. For this, distilled water was activated for 3 min by a continuous plasma jet of compressed air gas. A significant reduction in viable cells was observed after 1–3 min of treatment. Treatment for up to 5 min led to a 100% reduction. Moreover, 3 min of contact showed similar effects to 1% H_2O_2 and 10 mg/L NaOCl; antimicrobial agents that are routinely used. The low pH (2.21) and the presence of NO, OH, NO_3 and H+ species probably contributed together to the bactericidal effect [99]. Further investigations on PAW with this type of device and other microorganisms would be interesting.

The disinfection of stainless steel and polyethylene substrates by PAW has also been explored [100]. It is important to highlight that these materials present a wide application in the dental fields [101,102]. For these tests, 20 mL of sterile distilled water was activated for 5 min by non-thermal GlidArc plasma formed by moist air gas. After 30 min of exposure to PAW, microbial reduction both in planktonic and biofilm forms, were observed on Gram-positive and Gram-negative bacteria, as well as in yeasts. More than a 5 log reduction in viable cells was observed for bacterial biofilms, while there was a decrease of approximately 3 log in yeasts. Advantageously, the disinfection of the solid materials with PAW did not show damage to the materials, especially to stainless steel, which was free of corrosive signs [100].

Resin based materials have an important applicability in dentistry [103]. Sterilization by PAW of a duodenoscope coated with a polymer resin was also previously analyzed. Distilled water (300 mL) was activated for 10 min, with a discharge of GlidArc plasma operated with air gas. The treatment produced an acidified water of pH 2.78 that reduced the viable cells of *Escherichia coli* and *Acinetobacter baumannii* after 20 min of exposure, without any damage to the surface and composition of the equipment. The decontamination effect was also observed for *Klebsiella pneumoniae* and *Pseudomonas aeruginosa* after 30 min of PAW exposure [104].

Taken together, the studies with PAW have shown good decontamination properties of materials that are widely used in dentistry, such as stainless steel, polyethylene and polymer resin. These results bring insights for a new sterilization method in the dental field. Despite that, new studies with other materials and mostly with polymicrobial biofilms, which are closer to the clinical environment [105], would be interesting to explore this application.

3.2. Treatment of Oral Infectious Diseases

The use of PAW in the treatment of oral infectious diseases is a promising field of investigation. Several groups of microorganisms are involved in the etiopathogenesis and progression of the main infectious diseases that affect the oral cavity, such as caries, periodontitis and candidiasis. Considering the antimicrobial properties of NTAPPs, the control of these microorganisms by PAW or other plasma-activated solutions has also been investigated as an alternative treatment to traditional therapies that have their limitations.

Biological, behavioral, psychosocial and environmental factors are related to the development of caries [106]. The imbalance between demineralization and remineralization, caused by fluctuations in pH, promotes tooth decay [107]. The metabolic activity of dental biofilm, formed by microorganisms embedded in a matrix of extracellular polymeric substances adhered to the teeth surface, is responsible for these pH fluctuations, especially with the intake of a sugar-rich diet. The biofilm continues to grow progressively if undisturbed. In its composition, there are many groups of microorganisms and some of them are especially involved in the carious process [108].

Streptococcus mutans and *Lactobacillus* spp. are considered the main cariogenic bacteria responsible for producing acid and, consequently, the demineralization of the tooth structure [109,110]. Interestingly, PAL has shown to be effective against cariogenic microorganisms [22,111]. A previous study observed that PBS or a saline solution activated with a non-thermal plasma of argon (Ar) and oxygen (O_2) for 5 min are able to reduce the number of *S. mutans* viable cells. This reduction was verified in both planktonic and biofilm forms of *S. mutans* after 1 h of treatment. The authors further reported that the activated liquids were not cytotoxic to fibroblasts [111].

Modifications in the composition of the oral biofilm may be observed due to dietary habits, type of dentition (primary or secondary) and even with the disease progression. Although *S. mutans* and *Lactobacillus spp.* are considered the most important microogasnisms related to dental caries, previous findings demonstrated that *Actinomyces spp.* may be associated with the disease progression in root caries [108]. A previous study evaluated the role of distilled water activated by a plasma jet of Ar and O2 (98% and 2%, *v*/*v*, respectively) for 20 min, in the reduction in *S. mutans*, *Porphyromonas gingivalis* and *Actinomyces viscosus*. The treatment that was performed from 0 to 120 s reduced the viability of all microbial species. A significant reduction in *A. viscosus* was observed within 40 s while *S. mutans* achieved a similar reduction after 60 s of treatment [22].

Candida albicans is another microorganism that may be found in the carious dentin of active root carious lesions and some authors have suggested that this fungus might play a role in the progression of the disease [112]. This species was detected on the biofilm in cases of childhood caries [113] and it was associated with an increase in plaque glucosyltransferase (Gtf) enzyme activity, a virulence factor associated with caries, in children with early carious lesions [114]. In addition to its possible role in dental caries, *C. albicans* is the main species related to oral candidiasis, the most common oral fungal disease. Local

and systemic factors such as impaired salivary gland function, inhaled steroids, dentures, oral cancer/leukoplakia, broad-spectrum antibiotics, immunosuppressive drugs and conditions, nutritional deficiencies, diabetes, smoking and Cushing's syndrome may contribute to oral candidiasis [115]. Previous studies demonstrated that the direct application of NTAPPs is effective against *C. albicans* [116,117], both in planktonic and biofilm forms. Investigations into the effects of PAW on *C. albicans* have also been conducted with different methodologies and findings. A reduction in *C. albicans* viability after 5 min of treatment with distilled water, activated by a dielectric barrier discharge (DBD) with atmospheric air, for 5 and 10 min, was reported. The authors attributed the antimicrobial action to the higher concentration of NO^-_3 and lower concentrations of NO^-_2 and H_2O_2 in PAW [118]. Antimicrobial effects against *C. albicans* was also reported in hydrogels constituted by plasma-activated deionized water, after 24, 48 and 72 h of contact time. An increase in the inhibition zones of the microorganism was observed in longer exposure times, with the best result after 30 min. Hydroxyl radical and NO^-_3 were suggested to be the main components with antifungal activity [119]. On the contrary, one study reported no effect of plasma-activated tap water for 10 and 30 min on *C. albicans* planktonic cells. The water was activated with an atmospheric air plasma, generated by a forward vortex flow reactor (FVFR), for 30 min [16].

In the context of cariology, it is also important to emphasize the positive property of NTAPPs in adhesive restorations. Plasma exposure generates the deposition of free radicals and ions on the tooth substrate, changing the surface proteins of dentin, which has led to an increased bond strength in adhesive restorations. The enhance in bone bond strength avoids microleakage and consequently prevents secondary caries [47]. It is not known whether PAW can also increase the bond strength, improving the restoration performance. This process could also probably occur with plasma–liquid technology due to the action of the reactive species on the surface of dentin.

In the evolution of the carious process, traumatic injuries and cracks allow that pathogens and their products to pass through the dentin and reach the pulp. The pulpal infection frequently progresses to necrosis of the tissue and the infection may spread to the apex of the tooth, promoting periapical disease [120]. *Enterococcus faecalis* is commonly found in primary and secondary endodontic infections [120–122]. This microorganism expresses virulence factors and resistance mechanisms that favor its presence in the root canal and consequently can lead to endodontic therapy failure [120,123]. Some studies have investigated the action of PAW on *E. faecalis* [99,124], which is interesting for dentistry as it could be used as an antimicrobial irrigator in endodontic treatments. Considering the particularities of root canals, such as the presence of accessory canals, the antimicrobial irrigation with PAW would be more useful than the direct application of NTAPPs. As mentioned, a reduction in *E. faecalis* viable cells in 5-day DUWLs biofilms was observed after 1–3 min of treatment with previously activated water. The treatment of the *E. faecalis* suspensions, in deionized water, was also performed with satisfactory results. The bacterial suspension was exposed to microjet plasma formed by atmospheric air for 10 to 90 s. The antimicrobial effect occurred progressively after 45, 60 and 90 min of treatment, while inhibitory effects on the biofilm formation was detected even in shorter exposure times (10, 20 and 30 s) [124]. Another microorganism that may be isolated from root canals, though not often, is *Escherichia coli* [120]. It was demonstrated that the planktonic treatment with PAW significantly reduced the number of *E. coli* colonies after 10 min of exposure [16]. In this same study, 10 and 30 min of PAW contact was effective against *Staphylococcus aureus*, a bacteria commonly found in chronic osteomyelitis of the jaw, in association with anaerobic pathogens [125].

The development and progression of periodontal disease is related to specific groups of Gram-negative bacteria, the so-called periodontopathogens. The transition from healthy periodontium to periodontitis is related to three important factors: the polymicrobial synergy, the dysbiotic microbiota and a susceptible host [126]. The multifactorial etiology of periodontal disease contributes to the difficulty in the treatment and alternative thera-

pies have been investigated [127]. *Porphyromonas gingivalis*, *Treponema denticola*, *Tannerella forsythia* and *Aggregatibacter actinomycetemcomitans* have been considered important periodontopathogens [128]. A progressive inhibition of *P. gingivalis* in planktonic and biofilm forms was previously observed after 1, 3, 5 or 7 min of NTAPP exposure. Moreover, improved periodontal tissue recovery was obtained after 5 min of exposure, proportionally to the number of applications [129]. Interestling, a previous study demonstrated that PAW may also be effective against *P. gingivalis*. A reduction of 5-log in planktonic bacteria was observed after 20 s of exposure [22]. Considering the particularities of subgingival biofilm and its relationship with the progression of the disease, the treatment with PAW would be even more interesting since it would be able to reach areas of restricted access, such as the subgingival sites.

The mechanisms of action suggested in all of these studies, evaluating the antimicrobial properties of PAW, mainly involved the reactive oxygen and nitrogen species (RONS) produced in the solutions by plasma activation. Different biological effects could be observed in each study, which is probably related to differences in methodology and groups of microorganisms. Further in vitro and in vivo investigations are needed to standardize the best parameters for each solution and microorganism. Considering the potential antimicrobial effects observed in these studies, they could probably contribute to the treatment of oral infectious diseases.

3.3. Anti-Inflammatory Properties and Wound Healing

An important feature of non-thermal plasma is the possibility of tissue antisepsis without causing damage, which makes NTAPPs a good alternative treatment for infectious diseases. This selectivity probably occurs due to biochemical, metabolic and cell cycle differences between eukaryotes and prokaryotes and also the surface/volume ratio of mammalian cells, that is higher compared to bacterial and fungal ones [130]. It was demonstrated that no important side effect occurs after oral application of NTAPP on the mucosa of mice, in short-term experiments [131]. A previous study investigated the effect of PAW intake in mice after 90 days of administration, as its use in dentistry may lead to accidental ingestion. The mineral composition and surface micro-morphology of vital mouse teeth after long-term exposure, as well as local and systemic toxicity, were evaluated. The authors observed that there were not significant changes in the mineral composition and surface micro-morphology of the teeth. Moreover, the long-term exposure was not toxic to the tongue, oral mucosa, sublingual glands or other body organs, which presented normal structure and physiology [132]. In addition to not being harmful to mammalian cells, NTAPPs have been demonstrated to decrease inflammation and contribute to tissue repair [133].

Studies on skin inflammatory diseases such as allergic contact dermatitis and atopic dermatitis have shown anti-inflammatory effects of non-thermal plasma [134–136]. These effects have also been observed in oral studies. The treatment of oral candidiasis in mice showed a low occurrence of inflammatory alterations. After plasma exposure, the cell inflammatory infiltrate was predominantly mononuclear and macrophage-rich, with scarce polymorphonuclear cells [116]. Additionally, a study evaluating the role of NTAPP as an adjuvant therapy for the treatment of periodontitis induced in rats, observed that the expression of inflammatory-related cytokines such as TNF-α and IL-1β decreased significantly in the group where NTAPP was used as an adjuvant approach, while the level of the anti-inflammatory cytokine IL-10 showed a significant increase [137].

The behavior mast cells and keratinocyte cell line (HaCat) after the contact with non-thermal plasma-activated medium has been analyzed. Interestingly, the plasma-activated liquid prevented an enhancement of the pro-inflammatory genes and cytokines TNF-α, IL-6 and IL-13 in activated mast cells, by inhibiting the NF-κB signaling pathway. The activation of NF-κB by TNF-α/IFN-γ was also inhibited in HaCat cells suggesting that this treatment could be effective against, not only acute, but also chronic inflammation [136]. Similarly, in another study the pro-inflammatory responses of HaCat, activated by TNF-α/IFN-γ

or LPS, was also suppressed by PAL. Moreover, STAT3, which is an important pathway for Th17 cell activation, was inhibited by PAL in IL-6-stimulated HaCaT [135]. In this way, plasma-activated liquids have shown to act in different inflammatory signaling pathways of keratinocytes. These findings are important for dentistry as NF-κB e STAT3 pathways are involved in the etiopathogenesis of periodontitis [138]. Moreover, these pathways also play a role in oral candidiasis as mucosal candidiasis promotes NF-κB activation [139] and STAT3 signaling is related to IL-17-mediated immunity in oral mucosal candidiasis [140].

The possibility of treating autoimmune skin diseases by direct application of plasma or plasma-activated liquids may also be interesting for dentists, who also have to deal with some autoimmune conditions, such as oral lichen planus [141], pemphigus and mucous membrane pemphigoid [142]. The effects of NTAPP on oral lichen planus (OLP) were previously investigated [143]. For this, biopsies from healthy and OLP areas were performed, followed by the application of NTAPP in the ex-vivo tissues for 3 min. From these lesions, 24 were reticular, 3 erosive and 1 atrophic. The treatment decreased the infiltration of T-cells in OLP, compared with healthy samples. Additionally, the levels of IL1β, IL2, IL10 and GM-CSF decreased significantly after the treatment and a tendency to decrease other inflammatory markers was observed, suggesting an immunomodulatory role of NTAPPs in OLP. The authors also presented a clinical report from a 73-year-old man suffering from erosive OLP. The treatment consisted of 5 min of application, two to three times per week (12 sessions). It promoted relief of the burning sensation after four sessions. During the treatment, the oral inflammation decreased and the ulcerated area of the lesion healed almost totally [143]. Considering that the erosive presentation is usually symptomatic, requiring treatment with topic steroids and sometimes systemic ones [141], clinical studies evaluating a large number of these cases are welcome. The efficiency of PAW should also be evaluated, since washing with a plasma-activated liquid could reach the entire area of OLP without the need for direct application at several areas of the lesion.

The exposure of diabetic animals to NTAPPs has also shown anti-inflammatory properties [144,145] and improvement in wound healing [146], which brings perspectives for dentistry, especially considering the proven relationship between diabetes and periodontal disease. Severe periodontal destruction is usually observed in diabetic patients, while poor glycemic control is more common in diabetic people who also have periodontal disease [147]. Interestingly, diabetic mice treated with NTAPP showed a decrease in oxidative stress biomarkers, advanced glycation end products (AGEs) and inflammatory cytokines, such as IL-1, IL-6 and TNF-α [145]. It has been suggested that increased accumulation of AGEs and their interaction with specific receptors (RAGE) in diabetic gingival tissue could promote the hyperproduction of proinflammatory cytokines, as well as vascular alterations and a loss of tissue integrity, contributing to the worsening of periodontitis [148]. Thus, the adjunct treatment for diabetes mellitus with plasma modalities could possibly act indirectly and positively in periodontitis and in other inflammatory oral diseases. The direct action of NTAPPs or PAW in periodontal disease should also be considered, since it is a multifactorial condition in which the microbial biofilm activates the immune system with the production of proinflammatory cytokines and, consequently, tissue loss [149]. The selective role of plasma could be useful in both, in the elimination of periodontopathogenic microorganisms and also in the gingival tissue, decreasing the inflammatory process. Considering the generalized subtype of chronic periodontitis, treatment with PAW could be clinically easier, reaching different affected areas in a single use.

The anti-inflammatory and microbicide functions of NTAPPs have been demonstrated to favor tissue repair [133]. Clinical trials evaluating NTAPPs have already been performed, in which this technique was considered safe, painless and effective against bacterial load [150,151]. Solutions activated with plasma, such as medium, saline and water have also shown good results in vitro and in vivo concerning the wound healing [19,133,152]. Cell proliferation and migration were observed in human keratinocytes exposed to 15 s of medium activated with Helium-and-Argon (He/Ar)-generated NTAPP [133], which could favor the re-epithelialization of wounds on the skin and also on the oral mucosa that has

keratinocytes in the epithelial composition. There is no study evaluating the effect of PAW or PAL on mouth wound healing, although two studies carried out in rats and mice have observed a tendency to improve periodontal tissue loss after the experimental treatment of periodontitis with NTAPPs [129,137]. Moreover, wound healing of some infected ulcerated areas of advanced oral squamous cell carcinoma was observed after NTAPP exposure [153]. Considering that wound repair is important for different modalities of dentistry such as oral surgery, periodontics, oral pathology and implantology, PAW could be an option to accelerate the healing after oral diseases or oral surgeries.

NTAPPs were previously suggested as a good possibility for oral surgery because NTAPP was tested with osteoblast-like cells (MG-63), leading to cell proliferation and in vitro wound closure [154]. Oral implant modification with NTAPPs has also been suggested since this treatment may enhance the roughness and wettability of the implant surface, thus improving the cell adhesion and consequently the osseointegration [47]. These results with the direct application of NTAPPs, open perspectives for the use of PAW in oral surgery and implantology. PAW could be used even more easily in these procedures, such as surgeries, for the removal of oral lesions and tooth extractions, especially in impacted third molars. Thus, the use of PAW in dentistry should be considered, given the antimicrobial, anti-inflammatory and wound healing properties of NTAPPs, in addition to their ability to alter the surface of dental implants. The simplicity of the technique, considering the use of PAW as a mouthwash or an irrigation agent and possibly the lower price of PAW compared to the direct application of NTAPPs, which would necessarily demand a device in the dental office, make PAW a potential adjuvant oral tool for conditions requiring tissue repair.

3.4. Anti-Cancer Therapy

Sensitivity of cancer cells to NTAPPs has been demonstrated in many studies. Reactive oxygen and nitrogen species may penetrate cancer cells more easily, compared to healthy ones, make them more vulnerable to their harmful effects. This fact may be explained by the higher amount of water channels (aquaporins) in cancer cells, that facilitates the transport of reactive species into cytosol. Additionally, the lipid peroxidation caused by free radicals generates pores in the membrane, which also allow the entry of reactive species into the cell. This process is attenuated by the condensation of membrane lipids in normal cells that are rich in cholesterol. However, cancer cells usually present fewer amount of lipids, which impairs this defense mechanism. The large influx of reactive species into cancer cells triggers signaling cascade pathways that may culminate in different types of cell death, such as apoptosis, necrosis or senescence, depending on the dose of exposure. Another important anti-cancer molecular mechanism of NTAPPs is their capacity to reduce the expression of some integrins. These molecules are essential for the adhesion, migration and invasion of cancer, which indicates that NTAPPs can be useful against metastases [38].

Besides the direct action of NTAPPs in cancer cells, they may be useful in this approach by their interaction with the tumor microenvironment. Reactive oxygen and nitrogen species are able to damage important extracellular matrix components, such as collagen, fibronectin and hyaluronic acid. The induction of an antitumor immunity has also been proposed as an action mechanism [38]. Anti-cancer properties of NTAPPs have been observed against many types of cancer cells [155–159]. Interestingly, clinical reports have already been conducted showing the role of NTAPPs in advanced squamous cell carcinoma (SCC) [153,160,161], most of them in intraoral sites [153,160]. SCC is the most prevalent oral cancer. More than 90% of the cases occur in men over 45 years of age, exposed to tobacco and/or alcohol. The lip is the most prevalent site, followed by the tongue [162]. An improvement in the quality of life of patients with advanced SCC located at intra-oral sites or the jaw was described, after NTAPPs treatment, by the reduction in odor and pain. Partial remission of the lesion occurred in some cases [153,160]. Additionally, a reduction in microbial load, wound healing of some infected ulcerated areas [153] and enhancement of apoptotic cells were described [161]. Partial or total remission of pre-malignant skin lesions, resulting from chronic ultraviolet exposure, referred to as actinic keratoses, were

also observed after NTAPP treatment [163], which opens perspectives for actinic cheilitis, the pre-malignant lip counterpart, that precedes the emergence of lip SCC [164]. The adjunct treatment of initial SCC with NTAPPs has not been evaluated yet and it would be interesting, considering some in vitro responses of oral SCC to NTAPPs. A synergistic effect of cisplatin and NTAPP against oral SCC cells in vitro was described, associated with low cytotoxicity to normal oral cells [165]. Moreover, a combination of NTAPP with cetuximab inhibited invasion/migration of cetuximab-resistant oral SCC cells in vitro [166].

The possibility of using this technology of plasma-activated liquid is promising considering that PAL/PAW may be injected into large or deep tumors, facilitating the action in the entire lesion. Moreover, this kind of treatment would probably be faster and easier for the clinician compared to NTAPPs and more comfortable for the patient who is usually weakened by radiotherapy and/or chemotherapy. Treatment using liquids activated directly on the substrate or indirectly (activated first and then in contact with the substrate later) has been performed satisfactorily in many types of cancer cells with the use of different liquids, such as deionized water, cell culture media, Ringer's solution and saline [17,18,167–171]. Apoptotic cells were observed in cancer cells exposed to activated deionized water [18,171]. Different studies have shown that PAL is also efficient against cancer, due to the toxic effects of oxygen and nitrogen species that are accumulated in these solutions and also by the immuno-stimulatory properties [172]. Different cancer cells may respond to PAL with decreased proliferation and migration and increased cell death by apoptosis, necrosis, autophagy and senescence [173]. A reduction in tumor burden and a metastasis-inhibitory effect were also observed with the use of PAL [169]. It was suggested that RNS could play a more relevant role in cancer cell death than ROS [171].

A previous study evaluating the effect of PAL on an oral squamous cell line (SCC15), observed an anti-cancer capacity of the plasma-activated medium. A reduction in cell viability was observed with an increasing incubation time. Moreover, they have demonstrated that many signaling pathways, such as p-53 pathway, could play a critical role in this process [174]. The effectiveness of PAW, as well as its possible mechanisms of action in oral cancer, has not been evaluated yet. Considering that the treatment of SCC is the entire removal of the lesion, this kind of treatment could be useful in two situations: (1) Prior to surgery, by washing the lesion or through the injection of plasma-activated water in deep neoplasms and (2) After the surgery, by reducing the microbial load and favoring wound healing. The anti-cancer properties could also be positive to avoid recurrences. The role of plasma-activated water in oral premalignant lesions, such as oral leukoplakia, erythroplasia and actinic cheilitis, should also be evaluated. Different kinds of treatments have been used in patients with actinic cheilitis, such as combinatory treatment with PDT and laser ablation. However, carbon dioxide laser ablation and vermilionectomy, that are invasive for the patients, have been considered the most effective treatments [164]. In this way, plasma-activated water could represent a non-invasive approach to be used in oral premalignant lesions with other therapies or even alone, depending on the results and risk factors of each patient.

3.5. Tooth Bleaching

Some studies showed that NTAPPs may be efficient for tooth bleaching, with a synergistic effect with other whitening agents [175,176]. In addition to lower concentrations of hydrogen peroxide solution (HP), its applicability might replace conventional light sources that present some limitations, such as questionable efficacy and high temperatures [176]. The association of HP and plasma exposure for 10 min generated a three-times higher bleaching than only HP, which probably occurred due to the presence of •OH, that was mostly present in the plasma-treated groups [175]. In addition to its efficiency for tooth bleaching, it was demonstrated that NTAPPs do not promote thermal damage or inflammatory responses in the pulp and oral soft tissues [177].

The role of NTAPPs applied to liquids for tooth bleaching has already been analyzed with interesting results. A helium-based NTAPP applied to the tooth surface with saline

was evaluated. According to the authors, the wettability would enable the reactivity of ROS in the solution, attenuating the tooth dye, and it also would reduce the amounts of toxic gas produced using the air plasma method. The bleaching efficacy after 20 min of treatment was improved. It was 2.4 times higher than the effect produced by the whitening agent (35% of HP). The authors observed that H_2O_2 and •OH were generated in the saline solution, probably being a key factor for the observed effectiveness. Moreover, a scanning electron microscope (SEM) indicated smoother surfaces in the group treated with NTAPP + saline, which was probably less harmful to the enamel [178].

Satisfactory results of NTAPPs for tooth bleaching have also been observed in the presence of water. A previous study demonstrated that deionized water activated by NTAPP for 5 or 10 min, on the surface of the teeth, showed similar whitening presented by HP, with similar color stability [179]. Another piece of work that evaluated the whitening properties of bleaching agents and deionized water activated by NTAPP, in the pulp chamber of non-vital teeth, also obtained interesting findings. A total of 50 µL of water or bleaching agents were put in the pulp chamber, followed by plasma discharge, for 5 min. Interestingly, in addition to the improved bleaching of the whitening agents promoted by NTAPP, the generation of PAW was also effective. These findings indicate that PAW generated in the pulp chamber could be used as a substitute for conventional tooth bleaching in cases of non-vital teeth [180]. Considering the available results, PAW or saline generated on the surface of the teeth seems to be effective for tooth whitening, by the formation of H_2O_2 and •OH. Further studies are still required to investigate the effectiveness and to rule out possible toxicity effects of the reactive species to vital teeth. Moreover, studies evaluating the tooth bleaching potential of prior activated water (indirect method) or other plasma-activated liquids are also needed, since its application would be easier and possibly performed at home.

4. Conclusions

Plasma-activated water demonstrates antimicrobial activity, with promising applicability in both the decontamination of dental devices and the treatment of oral infectious diseases. The anti-inflammatory properties and wound healing benefits of PAW suggest that, in addition to its antimicrobial effect, PAW could favor the repair of previously infected lesions. In vivo studies are still needed to prove this effectiveness in oral diseases and rule out damage to the host. While RONS generated in PAW seems to present a fundamental role in decontamination and wound healing, the specific constituents H_2O_2 and •OH generated in plasma-activated liquids on the tooth surface may favor tooth bleaching. The findings related to plasma-activated water and liquids indicate that they could play an important role in the adjuvant treatment of some cancers by their antitumor response. Studies of PAW involving oral cancer would be interesting to investigate its application in oral neoplasms and the exact mechanisms of action inherent to this effect.

Author Contributions: N.V.M.M.—writing of abstract, introduction, Section 3 and conclusion, review and editing; W.C.—writing of introduction, Section 2, Appendix A, review and editing; A.d.G.S.—writing of Section 3.1 and review; M.R.d.C.V.—writing of Section 3.2 and review; R.S.P.—supervision and review; and C.Y.K.-I.—supervision and review. All authors have read and agreed to the published version of the manuscript.

Funding: This research was funded by The São Paulo Research Foundation (FAPESP), grant nº. 19/05856-7. C.Y.K.-I. and R.S.P. thank the research fellowship from National Council for Scientific and Technological Development 308127/2018-8 and 405653/2016-6, respectively. N.V.M.M., W.C. and A.d.G.S. thank the individual grants financed by FAPESP, nº. 21/00046-7; 20/10450-7 and 19/25652-7, respectively.

Institutional Review Board Statement: Not applicable.

Informed Consent Statement: Not applicable.

Conflicts of Interest: The authors declare no conflict of interest.

Appendix A

In this section we will show the main mechanisms for generating long-term RONS that are found in PAW after the plasma–liquid phase interaction. Hydrogen peroxide (H_2O_2), nitrite (NO_2), nitrate (NO_3^-), nitrous acid (HNO_2) and ozone (O_3) are the main reactive species that will be presented below.

Appendix A.1. Nitrite: Nitrate and Nitrous Acid

Nitrite and nitrate ions, together with nitrous acid, are long-lived reactive species formed as by-products from primary, secondary and tertiary species, generated in regions 1, 2 and 3 (as can be seen in Figure 3). These reactive species have a high microbial capacity in acidic environments, mainly against bacteria [30,181].

In the gas phase, Equations (A1)–(A3) occur, accompanied by NO generation [33,182].

$$e^- + N_2 \rightarrow \bullet N + \bullet N + e^- \quad \text{(A1)}$$

$$e^- + O_2 \rightarrow \bullet O + \bullet O + e^- \quad \text{(A2)}$$

$$\bullet N + \bullet O \rightarrow NO \quad \text{(A3)}$$

In the plasma phase, Equations (A4)–(A7) occur with NO_x dissociation [183].

$$NO + O \rightarrow NO_2 \quad \text{(A4)}$$

$$NO + O_3 \rightarrow NO_2 + O_2 \quad \text{(A5)}$$

$$NO_2 + O_3 \leftrightarrow NO_3 + O_2 \quad \text{(A6)}$$

$$NO + NO_3 \leftrightarrow NO_2 + NO_2 \quad \text{(A7)}$$

In the plasma–water interface region (region 3), nitrites are generated in PAW through the NO_x conversion generated from Equation (A7) and shown in Equations (A8) and (A9). In the Equations (A10) and (A11), we see the generation of NO_3^- which is generated from the coexistence of NO_2^- with the hydrogen peroxide and ozone present in PAW [70,184].

$$NO_2 + NO_2 + H_2O \rightarrow NO_2^- + NO_3^- + 2H^+ \quad \text{(A8)}$$

$$NO + NO_2 + H_2O \rightarrow 2NO_2^- + 2H^+ \quad \text{(A9)}$$

$$NO_2^- + O_3 \rightarrow NO_3^- + O_2 \quad \text{(A10)}$$

$$NO + O_2^- \rightarrow NO_3^- \quad \text{(A11)}$$

It is essential to highlight that together with the generation of nitrite and nitrate, the pH of the water also decreases, which can be seen by Equations (A8) and (A9). As demonstrated in the literature, the increase in NO_2^- and NO_3^- production is directly related to two factors: the increase in the discharge voltage and the rise in the time of water exposure to plasma [71,96,185].

In contrast, nitrous acid (HNO_2) is generated in the destruction reaction of nitrous oxide (NO) which is formed in the gas phase, as seen in Equations (A12)–(A15) [186]. The formation of NO at the plasma–water interface and at PAW itself is also observed, as showed in the Equations (A16)–(A25).

$$* e^- + \frac{N_2}{O_2} \rightarrow \bullet N + \bullet O + e^- \quad \text{(A12)}$$

$$\bullet N + \bullet O \rightarrow \bullet NO \quad \text{(A13)}$$

$$\bullet N + NO_3 \rightarrow NO_2 + \bullet NO \quad \text{(A14)}$$

$$O_2 + \bullet N \rightarrow \bullet NO + \bullet O \quad \text{(A15)}$$

$$\bullet N + \bullet OH \rightarrow \bullet NO + \bullet H \quad \text{(A16)}$$

$$\bullet H + NO_2^- \rightarrow \bullet NO + OH^- \quad \text{(A17)}$$

$$N_2O_3 \leftrightarrow \bullet NO + \bullet NO_2 \quad \text{(A18)}$$

$$HNO_2 + \bullet H \rightarrow \bullet NO + H_2O \quad \text{(A19)}$$

$$HNO_2 + HNO_2 \rightarrow \bullet NO + \bullet NO_2 + H_2O \quad \text{(A20)}$$

$$NO_2^- + H_2O_2 \rightarrow ONOO^- \leftrightarrow \bullet NO + \bullet O_2 \quad \text{(A21)}$$

$$\bullet OH + ONOOH \rightarrow \bullet NO + O_2 + H_2O \quad \text{(A22)}$$

$$\bullet NO_2 + \bullet O \rightarrow \bullet NO + O_2 \quad \text{(A23)}$$

$$\bullet NO_2 + \bullet N \rightarrow 2 \bullet NO \quad \text{(A24)}$$

$$NO_2 + \bullet H \rightarrow \bullet NO + OH^- \quad \text{(A25)}$$

Finally, the HNO_2 formation reactions occur in the gas phase, at the plasma–water interface and at PAW [36,186], as seen in Equations (A26) and (A27).

$$\bullet NO + \bullet OH \rightarrow HNO_2 \quad \text{(A26)}$$

$$\bullet NO + \bullet NO_2 + H_2O \rightarrow 2HNO_2 \quad \text{(A27)}$$

Depending on the pH level of the PAW, an equilibrium dissociation reaction between nitrous acid and nitrite can occur, as shown below [187].

$$HNO_2 \leftrightarrow H^+ + NO_2^- \quad \text{(A28)}$$

Appendix A.2. Hydrogen Peroxide

Due to the multiple functions of hydrogen peroxide in cellular redox pathways, this reactive species is widely used in medicine and dentistry. The hydrogen peroxide generated in PAW has been considered a potential method for inhibiting microorganisms, cancer treatment, wound healing benefits, among other applications [188–190].

However, there is an excellent debate about the H_2O_2 generation mechanism in PAW. In the present work, we will approach the following mechanisms: (i) recombination of •OH dissolved in solution (Equations (A29)–(A32)) and, (ii) dissociation of water molecules via collisions with electrons.

In the first set of reactions, it is possible to see that OH^- in the gas phase generates OH^- in the liquid phase with subsequent formation of H_2O_2 in the liquid phase [77,191–193].

$$OH_{gas\ phase} \rightarrow OH_{liquid\ phase} + OH_{liquid\ phase} \rightarrow H_2O_{2\ liquid\ phase} \quad \text{(A29)}$$

$$H_2O \overset{UV}{\rightarrow} H_{liquid\ phase} + OH_{liquid\ phase} \quad \text{(A30)}$$

$$OH_{gas\ phase} + OH_{gas\ phase} \rightarrow H_2O_{2\ gas\ phase} \rightarrow H_2O_{2\ liquid\ phase} \quad \text{(A31)}$$

$$H_2O \overset{e^-\ radiation}{\rightarrow} H_{liquid\ phase} + OH_{liquid\ phase} \quad \text{(A32)}$$

In the second set of reactions, there is dissociation of water molecules via collisions with electrons, as shown in Equations (A33) and (A34) [194,195]. Equations (A35) and (A36) lead to the penning ionization reactions that occur at the plasma–water interface [194–196]. In PAW, UV photolysis can be activated, as demonstrated by Equations (A37) and (A38) [194,195]. Finally, the OH radicals generated in Equations (A33), (A34), (A36) and (A38) form hydrogen peroxide through Equation (A39) [194,195,197].

$$e^- + H_2O \rightarrow H + OH + e^- \quad \text{(A33)}$$

$$e^- + H_2O \rightarrow H + OH \quad \text{(A34)}$$

$$e^- + O_2 \rightarrow O(^1D) + O(^3P) \quad \text{(A35)}$$

$$O(^1D) + H_2O \rightarrow 2OH \quad \text{(A36)}$$

$$UV + H_2O \rightarrow H_2O* \quad \text{(A37)}$$

$$UV + H_2O* \rightarrow H + OH \quad \text{(A38)}$$

$$OH + OH \rightarrow H_2O_2 \quad \text{(A39)}$$

Appendix A.3. Ozone

Ozone is the reactive species with the highest redox potential among all oxidants [70]. According to Pavlovich et al., O_3 has higher bactericidal effect compared to H_2O_2 and $NO_2{}^-$ [198]. It is worth highlighting that O_3 is transported through the plasma–water interface after its production. Another way is to generate ozone directly in water, for example, using plasma in O_2 bubbles [199]. The ozone generation reaction can be observed below:

$$O + \bullet O_2 \rightarrow O_3 \rightarrow O_{3\ liquid\ phase} \quad \text{(A40)}$$

References

1. Mandal, R.; Singh, A.; Pratap Singh, A. Recent developments in cold plasma decontamination technology in the food industry. *Trends Food Sci. Technol.* **2018**, *80*, 93–103. [CrossRef]
2. Rathod, N.B.; Ranveer, R.C.; Bhagwat, P.K.; Ozogul, F.; Benjakul, S.; Pillai, S.; Annapure, U.S. Cold plasma for the preservation of aquatic food products: An overview. *Compr. Rev. Food Sci. Food Saf.* **2021**, *20*, 4407–4425. [CrossRef] [PubMed]
3. Katsigiannis, A.S.; Bayliss, D.L.; Walsh, J.L. Cold plasma decontamination of stainless steel food processing surfaces assessed using an industrial disinfection protocol. *Food Control* **2021**, *121*, 107543. [CrossRef]
4. Giardina, A.; Schiorlin, M.; Marotta, E.; Paradisi, C. Atmospheric Pressure Non-thermal Plasma for Air Purification: Ions and Ionic Reactions Induced by dc+ Corona Discharges in Air Contaminated with Acetone and Methanol. *Plasma Chem. Plasma Process.* **2020**, *40*, 1091–1107. [CrossRef]
5. Kolb, J.F.; Mohamed, A.A.H.; Price, R.O.; Swanson, R.J.; Bowman, A.; Chiavarini, R.L.; Stacey, M.; Schoenbach, K.H. Cold atmospheric pressure air plasma jet for medical applications. *Appl. Phys. Lett.* **2008**, *92*, 24–27. [CrossRef]
6. Kang, W.-S.; Hong, Y.-C.; Hong, Y.-B.; Kim, J.-H.; Uhm, H.S. Atmospheric-pressure cold plasma jet for medical applications. *Surf. Coatings Technol.* **2010**, *205*, S418–S421. [CrossRef]
7. Weltmann, K.-D.; von Woedtke, T. Plasma medicine—current state of research and medical application. *Plasma Phys. Control. Fusion* **2016**, *59*, 14031. [CrossRef]
8. Cha, S.; Park, Y.-S. Plasma in dentistry Seunghee. *Clin. Plasma Med.* **2014**, *176*, 139–148. [CrossRef]
9. Gherardi, M.; Tonini, R.; Colombo, V. Plasma in Dentistry: Brief History and Current Status. *Trends Biotechnol.* **2018**, *36*, 583–585. [CrossRef]
10. Laroussi, M. Sterilization of contaminated matter with an atmospheric pressure plasma. *IEEE Trans. Plasma Sci.* **1996**, *24*, 1188–1191. [CrossRef]
11. Braný, D.; Dvorská, D.; Halašová, E.; Škovierová, H. Cold atmospheric plasma: A powerful tool for modern medicine. *Int. J. Mol. Sci.* **2020**, *21*, 2932. [CrossRef] [PubMed]
12. Laroussi, M. Plasma Medicine: A Brief Introduction. *Plasma* **2018**, *1*, 47–60. [CrossRef]
13. Konchekov, E.M.; Glinushkin, A.P.; Kalinitchenko, V.P.; Artem'ev, K.V.; Burmistrov, D.E.; Kozlov, V.A.; Kolik, L.V. Properties and Use of Water Activated by Plasma of Piezoelectric Direct Discharge. *Front. Phys.* **2021**, *8*. [CrossRef]
14. Takeuchi, N.; Yasuoka, K. Review of plasma-based water treatment technologies for the decomposition of persistent organic compounds. *Jpn. J. Appl. Phys.* **2020**, *60*, SA0801. [CrossRef]
15. Guo, L.; Xu, R.; Gou, L.; Liu, Z.; Zhao, Y.; Liu, D.; Zhang, L.; Chen, H.; Kong, M.G. Mechanism of Virus Inactivation by Cold Atmospheric-Pressure Plasma and Plasma-Activated Water. *Appl. Environ. Microbiol.* **2018**, *84*. [CrossRef]
16. Chiappim, W.; Sampaio, A.d.G.; Miranda, F.; Fraga, M.; Petraconi, G.; da Silva Sobrinho, A.; Kostov, K.; Koga-Ito, C.; Pessoa, R. Antimicrobial effect of plasma-activated tap water on staphylococcus aureus, escherichia coli, and Candida albicans. *Water* **2021**, *13*, 1480. [CrossRef]

17. Chen, Z.; Cheng, X.; Lin, L.; Keidar, M. Cold atmospheric plasma discharged in water and its potential use in cancer therapy. *J. Phys. D Appl. Phys.* **2017**, *50*, 015208. [CrossRef]
18. Chen, Z.; Lin, L.; Cheng, X.; Gjika, E.; Keidar, M. Effects of cold atmospheric plasma generated in deionized water in cell cancer therapy. *Plasma Process. Polym.* **2016**, *13*, 1151–1156. [CrossRef]
19. Xu, D.; Wang, S.; Li, B.; Qi, M.; Feng, R.; Li, Q.; Zhang, H.; Chen, H.; Kong, M.G. Effects of plasma-activated water on skin wound healing in mice. *Microorganisms* **2020**, *8*, 1091. [CrossRef]
20. Borges, A.C.; Kostov, K.G.; Pessoa, R.S.; de Abreu, G.M.A.; Lima, G.d.M.G.; Figueira, L.W.; Koga-Ito, C.Y. Applications of Cold Atmospheric Pressure Plasma in Dentistry. *Appl. Sci.* **2021**, *11*, 1975. [CrossRef]
21. Kaushik, N.K.; Ghimire, B.; Li, Y.; Adhikari, M.; Veerana, M.; Kaushik, N.; Jha, N.; Adhikari, B.; Lee, S.-J.; Masur, K.; et al. Biological and medical applications of plasma-activated media, water and solutions. *Biol. Chem.* **2018**, *400*, 39–62. [CrossRef] [PubMed]
22. Li, Y.; Pan, J.; Ye, G.; Zhang, Q.; Wang, J.; Zhang, J.; Fang, J. In vitro studies of the antimicrobial effect of non-thermal plasma-activated water as a novel mouthwash. *Eur. J. Oral Sci.* **2017**, *125*, 463–470. [CrossRef] [PubMed]
23. Mirpour, S.; Fathollah, S.; Mansouri, P.; Larijani, B.; Ghoranneviss, M.; Mohajeri Tehrani, M.; Amini, M.R. Cold atmospheric plasma as an effective method to treat diabetic foot ulcers: A randomized clinical trial. *Sci. Rep.* **2020**, *10*, 10440. [CrossRef]
24. Muhammad, A.I.; Xiang, Q.; Liao, X.; Liu, D.; Ding, T. Understanding the Impact of Nonthermal Plasma on Food Constituents and Microstructure—A Review. *Food Bioprocess Technol.* **2018**, *11*, 463–486. [CrossRef]
25. Aparecida Delben, J.; Evelin Zago, C.; Tyhovych, N.; Duarte, S.; Eduardo Vergani, C. Effect of atmospheric-pressure cold plasma on pathogenic oral biofilms and in vitro reconstituted oral epithelium. *PLoS ONE* **2016**, *11*, e0155427. [CrossRef]
26. Whittaker, A.G.; Graham, E.M.; Baxter, R.L.; Jones, A.C.; Richardson, P.R.; Meek, G.; Campbell, G.A.; Aitken, A.; Baxter, H.C. Plasma cleaning of dental instruments. *J. Hosp. Infect.* **2004**, *56*, 37–41. [CrossRef]
27. Misra, N.N.; Jo, C. Applications of cold plasma technology for microbiological safety in meat industry. *Trends Food Sci. Technol.* **2017**, *64*, 74–86. [CrossRef]
28. Keidar, M.; Walk, R.; Shashurin, A.; Srinivasan, P.; Sandler, A.; Dasgupta, S.; Ravi, R.; Guerrero-Preston, R.; Trink, B. Cold plasma selectivity and the possibility of a paradigm shift in cancer therapy. *Br. J. Cancer* **2011**, *105*, 1295–1301. [CrossRef]
29. Sivachandiran, L.; Khacef, A. Enhanced seed germination and plant growth by atmospheric pressure cold air plasma: Combined effect of seed and water treatment. *RSC Adv.* **2017**, *7*, 1822–1832. [CrossRef]
30. Ma, R.; Wang, G.; Tian, Y.; Wang, K.; Zhang, J.; Fang, J. Non-thermal plasma-activated water inactivation of food-borne pathogen on fresh produce. *J. Hazard. Mater.* **2015**, *300*, 643–651. [CrossRef]
31. Chiappim, W.; Sampaio, A.; Miranda, F.; Petraconi, G.; da Silva Sobrinho, A.; Cardoso, P.; Kostov, K.; Koga-Ito, C.; Pessoa, R. Nebulized plasma-activated water has an effective antimicrobial effect on medically relevant microbial species and maintains its physicochemical properties in tube lengths from 0.1 up to 1.0 m. *Plasma Process. Polym.* **2021**, *18*, e2100010. [CrossRef]
32. Kim, S.J.; Chung, T.H. Cold atmospheric plasma jet-generated RONS and their selective effects on normal and carcinoma cells. *Sci. Rep.* **2016**, *6*, 20332. [CrossRef] [PubMed]
33. Khlyustova, A.; Labay, C.; Machala, Z.; Ginebra, M.P.; Canal, C. Important parameters in plasma jets for the production of RONS in liquids for plasma medicine: A brief review. *Front. Chem. Sci. Eng.* **2019**, *13*, 238–252. [CrossRef]
34. Edge, R.; Truscott, T.G. The Reactive Oxygen Species Singlet Oxygen, Hydroxy Radicals, and the Superoxide Radical Anion—Examples of Their Roles in Biology and Medicine. *Oxygen* **2021**, *1*, 77–95. [CrossRef]
35. Judée, F.; Simon, S.; Bailly, C.; Dufour, T. Plasma-activation of tap water using DBD for agronomy applications: Identification and quantification of long lifetime chemical species and production/consumption mechanisms. *Water Res.* **2018**, *133*, 47–59. [CrossRef]
36. Zhou, R.; Zhou, R.; Wang, P.; Xian, Y.; Mai-Prochnow, A.; Lu, X.; Cullen, P.J.; Ostrikov, K.; Bazaka, K. Plasma-activated water: Generation, origin of reactive species and biological applications. *J. Phys. D Appl. Phys.* **2020**, *53*, 303001. [CrossRef]
37. Morabit, Y.; Hasan, M.I.; Whalley, R.D.; Robert, E.; Modic, M.; Walsh, J.L. A review of the gas and liquid phase interactions in low-temperature plasma jets used for biomedical applications. *Eur. Phys. J. D* **2021**, *75*, 32. [CrossRef]
38. Semmler, M.L.; Bekeschus, S.; Schäfer, M.; Bernhardt, T.; Fischer, T.; Witzke, K.; Seebauer, C.; Rebl, H.; Grambow, E.; Vollmar, B.; et al. Molecular mechanisms of the efficacy of cold atmospheric pressure plasma (CAP) in cancer treatment. *Cancers* **2020**, *12*, 269. [CrossRef]
39. Laroussi, M. Cold Plasma in Medicine and Healthcare: The New Frontier in Low Temperature Plasma Applications. *Front. Phys.* **2020**, *8*, 1–7. [CrossRef]
40. Ozen, E.; Singh, R.K. Atmospheric cold plasma treatment of fruit juices: A review. *Trends Food Sci. Technol.* **2020**, *103*, 144–151. [CrossRef]
41. Chen, Y.-Q.; Cheng, J.-H.; Sun, D.-W. Chemical, physical and physiological quality attributes of fruit and vegetables induced by cold plasma treatment: Mechanisms and application advances. *Crit. Rev. Food Sci. Nutr.* **2020**, *60*, 2676–2690. [CrossRef] [PubMed]
42. Filipić, A.; Gutierrez-Aguirre, I.; Primc, G.; Mozetič, M.; Dobnik, D. Cold Plasma, a New Hope in the Field of Virus Inactivation. *Trends Biotechnol.* **2020**, *38*, 1278–1291. [CrossRef] [PubMed]

43. Adhikari, B.; Adhikari, M.; Park, G. The Effects of Plasma on Plant Growth, Development, and Sustainability. *Appl. Sci.* **2020**, *10*, 6045. [CrossRef]
44. Zhu, Y.; Li, C.; Cui, H.; Lin, L. Feasibility of cold plasma for the control of biofilms in food industry. *Trends Food Sci. Technol.* **2020**, *99*, 142–151. [CrossRef]
45. Varilla, C.; Marcone, M.; Annor, G.A. Potential of Cold Plasma Technology in Ensuring the Safety of Foods and Agricultural Produce: A Review. *Foods* **2020**, *9*, 1435. [CrossRef]
46. Attri, P.; Ishikawa, K.; Okumura, T.; Koga, K.; Shiratani, M. Plasma Agriculture from Laboratory to Farm: A Review. *Processes* **2020**, *8*, 1002. [CrossRef]
47. Lata, S.; Chakravorty, S.; Mitra, T.; Pradhan, P.K.; Mohanty, S.; Patel, P.; Jha, E.; Panda, P.K.; Verma, S.K.; Suar, M. Aurora Borealis in dentistry: The applications of cold plasma in biomedicine. *Mater. Today Bio* **2022**, *13*, 100200. [CrossRef]
48. Domonkos, M.; Tichá, P.; Trejbal, J.; Demo, P. Applications of Cold Atmospheric Pressure Plasma Technology in Medicine, Agriculture and Food Industry. *Appl. Sci.* **2021**, *11*, 4809. [CrossRef]
49. Jungbauer, G.; Moser, D.; Müller, S.; Pfister, W.; Sculean, A.; Eick, S. The Antimicrobial Effect of Cold Atmospheric Plasma against Dental Pathogens—A Systematic Review of In-Vitro Studies. *Antibiotics* **2021**, *10*, 211. [CrossRef]
50. Umair, M.; Jabbar, S.; Ayub, Z.; Aadil, R.M.; Abid, M.; Zhang, J.; Liqing, Z. Recent Advances in Plasma Technology: Influence of Atmospheric Cold Plasma on Spore Inactivation. *Food Rev. Int.* **2021**, 1–23. [CrossRef]
51. Šimek, M.; Homola, T. Plasma-assisted agriculture: History, presence, and prospects—a review. *Eur. Phys. J. D* **2021**, *75*, 210. [CrossRef]
52. Yan, D.; Lin, L.; Zvansky, M.; Kohanzadeh, L.; Taban, S.; Chriqui, S.; Keidar, M. Improving Seed Germination by Cold Atmospheric Plasma. *Plasma* **2022**, *5*, 98–110. [CrossRef]
53. Bradu, C.; Kutasi, K.; Magureanu, M.; Puač, N.; Živković, S. Reactive nitrogen species in plasma-activated water: Generation, chemistry and application in agriculture. *J. Phys. D Appl. Phys.* **2020**, *53*, 223001. [CrossRef]
54. Xiang, Q.; Fan, L.; Li, Y.; Dong, S.; Li, K.; Bai, Y. A review on recent advances in plasma-activated water for food safety: Current applications and future trends. *Crit. Rev. Food Sci. Nutr.* **2022**, *62*, 2250–2268. [CrossRef]
55. Šimečková, J.; Krčma, F.; Klofáč, D.; Dostál, L.; Kozáková, Z. Influence of Plasma-Activated Water on Physical and Physical–Chemical Soil Properties. *Water* **2020**, *12*, 2357. [CrossRef]
56. Zambon, Y.; Contaldo, N.; Laurita, R.; Várallyay, E.; Canel, A.; Gherardi, M.; Colombo, V.; Bertaccini, A. Plasma activated water triggers plant defence responses. *Sci. Rep.* **2020**, *10*, 19211. [CrossRef]
57. Mai-Prochnow, A.; Zhou, R.; Zhang, T.; Ostrikov, K.; Mugunthan, S.; Rice, S.A.; Cullen, P.J. Interactions of plasma-activated water with biofilms: Inactivation, dispersal effects and mechanisms of action. *npj Biofilms Microbiomes* **2021**, *7*, 11. [CrossRef]
58. Herianto, S.; Hou, C.Y.; Lin, C.M.; Chen, H.L. Nonthermal plasma-activated water: A comprehensive review of this new tool for enhanced food safety and quality. *Compr. Rev. Food Sci. Food Saf.* **2021**, *20*, 583–626. [CrossRef]
59. Zhao, Y.M.; Patange, A.; Sun, D.W.; Tiwari, B. Plasma-activated water: Physicochemical properties, microbial inactivation mechanisms, factors influencing antimicrobial effectiveness, and applications in the food industry. *Compr. Rev. Food Sci. Food Saf.* **2020**, *19*, 3951–3979. [CrossRef]
60. Harley, J.C.; Suchowerska, N.; McKenzie, D.R. Cancer treatment with gas plasma and with gas plasma–activated liquid: Positives, potentials and problems of clinical translation. *Biophys. Rev.* **2020**, *12*, 989–1006. [CrossRef]
61. Zeghioud, H.; Nguyen-Tri, P.; Khezami, L.; Amrane, A.; Assadi, A.A. Review on discharge Plasma for water treatment: Mechanism, reactor geometries, active species and combined processes. *J. Water Process Eng.* **2020**, *38*, 101664. [CrossRef]
62. Liu, C.; Chen, C.; Jiang, A.; Sun, X.; Guan, Q.; Hu, W. Effects of plasma-activated water on microbial growth and storage quality of fresh-cut apple. *Innov. Food Sci. Emerg. Technol.* **2020**, *59*, 102256. [CrossRef]
63. Guo, D.; Liu, H.; Zhou, L.; Xie, J.; He, C. Plasma-activated water production and its application in agriculture. *J. Sci. Food Agric.* **2021**, *101*, 4891–4899. [CrossRef] [PubMed]
64. Hu, X.; Zhang, Y.; Wu, R.A.; Liao, X.; Liu, D.; Cullen, P.J.; Zhou, R.-W.; Ding, T. Diagnostic analysis of reactive species in plasma-activated water ({PAW}): Current advances and outlooks. *J. Phys. D Appl. Phys.* **2021**, *55*, 23002. [CrossRef]
65. Ganesh, G.S.; Ananthanarasimhan, J.; Leelesh, P.; Rao, H.; Shivapuji, A.M.; Girard-Lauriault, P.L.; Rao, L. Plasma-activated water from DBD as a source of nitrogen for agriculture: Specific energy and stability studies. *J. Appl. Phys.* **2021**, *129*. [CrossRef]
66. Kučerová, K.; Henselová, M.; Slováková, Ľ.; Bačovčinová, M.; Hensel, K. Effect of Plasma Activated Water, Hydrogen Peroxide, and Nitrates on Lettuce Growth and Its Physiological Parameters. *Appl. Sci.* **2021**, *11*, 1985. [CrossRef]
67. Laroussi, M.; Akan, T. Arc-free atmospheric pressure cold plasma jets: A review. *Plasma Process. Polym.* **2007**, *4*, 777–788. [CrossRef]
68. Quyen, N.T.; Traikool, T.; Nitisoravut, R.; Onjun, T. Improvement of water quality using dielectric barrier discharge plasma. *J. Phys. Conf. Ser.* **2017**, *860*, 12031. [CrossRef]
69. Hamdan, A.; Profili, J.; Cha, M.S. Microwave Plasma Jet in Water: Effect of Water Electrical Conductivity on Plasma Characteristics. *Plasma Chem. Plasma Process.* **2020**, *40*, 169–185. [CrossRef]
70. Zhou, R.; Zhou, R.; Prasad, K.; Fang, Z.; Speight, R.; Bazaka, K.; Ostrikov, K. Cold atmospheric plasma activated water as a prospective disinfectant: The crucial role of peroxynitrite. *Green Chem.* **2018**, *20*, 5276–5284. [CrossRef]

71. Park, J.Y.; Park, S.; Choe, W.; Yong, H.I.; Jo, C.; Kim, K. Plasma-Functionalized Solution: A Potent Antimicrobial Agent for Biomedical Applications from Antibacterial Therapeutics to Biomaterial Surface Engineering. *ACS Appl. Mater. Interfaces* **2017**, *9*, 43470–43477. [CrossRef] [PubMed]
72. Andrasch, M.; Stachowiak, J.; Schlüter, O.; Schnabel, U.; Ehlbeck, J. Scale-up to pilot plant dimensions of plasma processed water generation for fresh-cut lettuce treatment. *Food Packag. Shelf Life* **2017**, *14*, 40–45. [CrossRef]
73. Pemen, A.J.M.; van Ooij, P.P.; Beckers, F.J.C.M.; Hoeben, W.F.L.M.; Koonen-Reemst, A.M.C.B.; Huiskamp, T.; Leenders, P.H.M. Power Modulator for High-Yield Production of Plasma-Activated Water. *IEEE Trans. Plasma Sci.* **2017**, *45*, 2725–2733. [CrossRef]
74. Locke, B.R.; Sato, M.; Sunka, P.; Hoffmann, M.R.; Chang, J.-S. Electrohydraulic Discharge and Nonthermal Plasma for Water Treatment. *Ind. Eng. Chem. Res.* **2006**, *45*, 882–905. [CrossRef]
75. Schnabel, U.; Handorf, O.; Stachowiak, J.; Boehm, D.; Weit, C.; Weihe, T.; Schäfer, J.; Below, H.; Bourke, P.; Ehlbeck, J. Plasma-Functionalized Water: From Bench to Prototype for Fresh-Cut Lettuce. *Food Eng. Rev.* **2021**, *13*, 115–135. [CrossRef]
76. Bruggeman, P.; Ribežl, E.; Maslani, A.; Degroote, J.; Malesevic, A.; Rego, R.; Vierendeels, J.; Leys, C. Characteristics of atmospheric pressure air discharges with a liquid cathode and a metal anode. *Plasma Sources Sci. Technol.* **2008**, *17*, 25012. [CrossRef]
77. Bruggeman, P.; Leys, C. Non-thermal plasmas in and in contact with liquids. *J. Phys. D Appl. Phys.* **2009**, *42*, 53001. [CrossRef]
78. Bruggeman, P.J.; Kushner, M.J.; Locke, B.R.; Gardeniers, J.G.E.; Graham, W.G.; Graves, D.B.; Hofman-Caris, R.C.H.M.; Maric, D.; Reid, J.P.; Ceriani, E.; et al. Plasma–liquid interactions: A review and roadmap. *Plasma Sources Sci. Technol.* **2016**, *25*, 53002. [CrossRef]
79. Kohn, W.G.; Collins, A.S.; Cleveland, J.L.; Harte, J.A.; Eklund, K.J.; Malvitz, D.M. Guidelines for infection control in dental health-care settings—2003. *MMWR Recomm. Rep.* **2003**, *52*, 1–61.
80. Halfmann, H.; Bibinov, N.; Wunderlich, J.; Awakowicz, P. A double inductively coupled plasma for sterilization of medical devices. *J. Phys. D Appl. Phys.* **2007**, *40*, 4145–4154. [CrossRef]
81. Rutala, W.A.; Weber, D.J. Disinfection and Sterilization in Health Care Facilities: An Overview and Current Issues. *Infect. Dis. Clin. North Am.* **2016**, *30*, 609–637. [CrossRef] [PubMed]
82. Papaioannou, E.; Giaouris, E.D.; Berillis, P.; Boziaris, I.S. Dynamics of biofilm formation by Listeria monocytogenes on stainless steel under mono-species and mixed-culture simulated fish processing conditions and chemical disinfection challenges. *Int. J. Food Microbiol.* **2018**, *267*, 9–19. [CrossRef] [PubMed]
83. Thirumdas, R.; Kothakota, A.; Annapure, U.; Siliveru, K.; Blundell, R.; Gatt, R.; Valdramidis, V.P. Plasma activated water (PAW): Chemistry, physico-chemical properties, applications in food and agriculture. *Trends Food Sci. Technol.* **2018**, *77*, 21–31. [CrossRef]
84. Elmoualij, B.; Thellin, O.; Gofflot, S.; Heinen, E.; Levif, P.; Séguin, J.; Moisan, M.; Leduc, A.; Barbeau, J.; Zorzi, W. Decontamination of prions by the flowing afterglow of a reduced-pressure N_2-O_2 cold-plasma. *Plasma Process. Polym.* **2012**, *9*, 612–618. [CrossRef]
85. Fichet, G.; Comoy, E.; Duval, C.; Antloga, K.; Dehen, C.; Charbonnier, A.; McDonnell, G.; Brown, P.; Lasmézas, C.I.; Deslys, J.-P. Novel methods for disinfection of prion-contaminated medical devices. *Lancet* **2004**, *364*, 521–526. [CrossRef]
86. Brandenburg, R.; Ehlbeck, J.; Stieber, M.; Woedtke, T.V.; Zeymer, J.; Schlüter, O.; Weltmann, K.D. Antimicrobial treatment of heat sensitive materials by means of atmospheric pressure Rf-driven plasma jet. *Contrib. Plasma Phys.* **2007**, *47*, 72–79. [CrossRef]
87. Weltmann, K.D.; Brandenburg, R.; von Woedtke, T.; Ehlbeck, J.; Foest, R.; Stieber, M.; Kindel, E. Antimicrobial treatment of heat sensitive products by miniaturized atmospheric pressure plasma jets (APPJs). *J. Phys. D Appl. Phys.* **2008**, *41*. [CrossRef]
88. Sung, S.-J.; Huh, J.-B.; Yun, M.-J.; Chang, B.M.W.; Jeong, C.-M.; Jeon, Y.-C. Sterilization effect of atmospheric pressure non-thermal air plasma on dental instruments. *J. Adv. Prosthodont.* **2013**, *5*, 2–8. [CrossRef]
89. Stapelmann, K.; Fiebrandt, M.; Raguse, M.; Awakowicz, P.; Reitz, G.; Moeller, R. Utilization of low-pressure plasma to inactivate bacterial spores on stainless steel screws. *Astrobiology* **2013**, *13*, 597–606. [CrossRef]
90. Monetta, T.; Scala, A.; Malmo, C.; Bellucci, F. Antibacterial activity of cold plasma-treated titanium alloy. *Plasma Med.* **2011**, *1*, 205–214. [CrossRef]
91. Koban, I.; Holtfreter, B.; Hübner, N.-O.; Matthes, R.; Sietmann, R.; Kindel, E.; Weltmann, K.-D.; Welk, A.; Kramer, A.; Kocher, T. Antimicrobial efficacy of non-thermal plasma in comparison to chlorhexidine against dental biofilms on titanium discs in vitro—Proof of principle experiment. *J. Clin. Periodontol.* **2011**, *38*, 956–965. [CrossRef] [PubMed]
92. Herrmann, H.W.; Henins, I.; Park, J.; Selwyn, G.S. Decontamination of chemical and biological warfare (CBW) agents using an atmospheric pressure plasma jet (APPJ). *Phys. Plasmas* **1999**, *6*, 2284–2289. [CrossRef]
93. Uchida, G.; Nakajima, A.; Ito, T.; Takenaka, K.; Kawasaki, T.; Koga, K.; Shiratani, M.; Setsuhara, Y. Effects of nonthermal plasma jet irradiation on the selective production of H_2O_2 and NO_{2-} in liquid water. *J. Appl. Phys.* **2016**, *120*, 203302. [CrossRef]
94. Naïtali, M.; Kamgang-Youbi, G.; Herry, J.-M.; Bellon-Fontaine, M.-N.; Brisset, J.-L. Combined effects of long-living chemical species during microbial inactivation using atmospheric plasma-treated water. *Appl. Environ. Microbiol.* **2010**, *76*, 7662–7664. [CrossRef] [PubMed]
95. Abuzairi, T.; Ramadhanty, S.; Puspohadiningrum, D.F.; Ratnasari, A.; Poespawati, N.R.; Purnamaningsih, R.W. Investigation on physicochemical properties of plasma-activated water for the application of medical device sterilization. *AIP Conf. Proc.* **2018**, *1933*, 040017. [CrossRef]
96. Shen, J.; Tian, Y.; Li, Y.; Ma, R.; Zhang, Q.; Zhang, J.; Fang, J. Bactericidal Effects against S. aureus and Physicochemical Properties of Plasma Activated Water stored at different temperatures. *Sci. Rep.* **2016**, *6*, 28505. [CrossRef] [PubMed]

97. Tsoukou, E.; Bourke, P.; Boehm, D. Temperature stability and effectiveness of plasma-activated liquids over an 18 months period. *Water* **2020**, *12*, 3021. [CrossRef]
98. Uzel, A.; Cogulu, D.; Oncag, O. Microbiological evaluation and antibiotic susceptibility of dental unit water systems in general dental practice. *Int. J. Dent. Hyg.* **2008**, *6*, 43–47. [CrossRef]
99. Pan, J.; Li, Y.L.; Liu, C.M.; Tian, Y.; Yu, S.; Wang, K.L.; Zhang, J.; Fang, J. Investigation of Cold Atmospheric Plasma-Activated Water for the Dental Unit Waterline System Contamination and Safety Evaluation in Vitro. *Plasma Chem. Plasma Process.* **2017**, *37*, 1091–1103. [CrossRef]
100. Kamgang-Youbi, G.; Herry, J.-M.; Meylheuc, T.; Brisset, J.-L.; Bellon-Fontaine, M.-N.; Doubla, A.; Naïtali, M. Microbial inactivation using plasma-activated water obtained by gliding electric discharges. *Lett. Appl. Microbiol.* **2009**, *48*, 13–18. [CrossRef]
101. Seale, N.S.; Randall, R. The use of stainless steel crowns: A systematic literature review. *Pediatr. Dent.* **2015**, *37*, 145–160. [PubMed]
102. Rokaya, D.; Srimaneepong, V.; Sapkota, J.; Qin, J.; Siraleartmukul, K.; Siriwongrungson, V. Polymeric materials and films in dentistry: An overview. *J. Adv. Res.* **2018**, *14*, 25–34. [CrossRef] [PubMed]
103. Pratap, B.; Gupta, R.K.; Bhardwaj, B.; Nag, M. Resin based restorative dental materials: Characteristics and future perspectives. *Jpn. Dent. Sci. Rev.* **2019**, *55*, 126–138. [CrossRef] [PubMed]
104. Bălan, G.G.; Roşca, I.; Ursu, E.L.; Doroftei, F.; Bostănaru, A.C.; Hnatiuc, E.; Năstasă, V.; Şandru, V.; Ştefănescu, G.; Trifan, A.; et al. Plasma-activated water: A new and effective alternative for duodenoscope reprocessing. *Infect. Drug Resist.* **2018**, *11*, 727–733. [CrossRef]
105. Gabrilska, R.A.; Rumbaugh, K.P. Biofilm models of polymicrobial infection. *Future Microbiol.* **2015**, *10*, 1997–2015. [CrossRef]
106. MacHiulskiene, V.; Campus, G.; Carvalho, J.C.; Dige, I.; Ekstrand, K.R.; Jablonski-Momeni, A.; Maltz, M.; Manton, D.J.; Martignon, S.; Martinez-Mier, E.A.; et al. Terminology of Dental Caries and Dental Caries Management: Consensus Report of a Workshop Organized by ORCA and Cariology Research Group of IADR. *Caries Res.* **2020**, *54*, 7–14. [CrossRef]
107. Tan, H.; Richards, L.; Walsh, T.; Worthington, H.V.; Clarkson, J.E.; Wang, L.; Mattar de Amoedo Campos Velo, M. Interventions for managing root caries. *Cochrane Database Syst. Rev.* **2017**, *2017*, CD012750. [CrossRef]
108. Awadh Al-Shahrani, M. Microbiology of Dental Caries: A Literature Review. *Ann. Med. Health Sci. Res.* **2019**, *9*, 655–659.
109. Aas, J.A.; Griffen, A.L.; Dardis, S.R.; Lee, A.M.; Olsen, I.; Dewhirst, F.E.; Leys, E.J.; Paster, B.J. Bacteria of dental caries in primary and permanent teeth in children and young adults. *J. Clin. Microbiol.* **2008**, *46*, 1407–1417. [CrossRef]
110. Anderson, A.C.; Rothballer, M.; Altenburger, M.J.; Woelber, J.P.; Karygianni, L.; Vach, K.; Hellwig, E.; Al-Ahmad, A. Long-Term Fluctuation of Oral Biofilm Microbiota following Different Dietary Phases. *Appl. Environ. Microbiol.* **2020**, *86*. [CrossRef]
111. Hong, Q.; Dong, X.; Yu, H.; Sun, H.; Chen, M.; Wang, Y.; Yu, Q. The Antimicrobial Property of Plasma Activated Liquids (PALs) against Oral Bacteria Streptococcus mutans. *Dental* **2021**, *3*, 1–7. [CrossRef]
112. Ev, L.D.; Damé-Teixeira, N.; Do, T.; Maltz, M.; Parolo, C.C.F. The role of Candida albicans in root caries biofilms: An RNA-seq analysis. *J. Appl. Oral Sci.* **2020**, *28*, e20190578. [CrossRef] [PubMed]
113. Hajishengallis, E.; Parsaei, Y.; Klein, M.I.; Koo, H. Advances in the microbial etiology and pathogenesis of early childhood caries. *Mol. Oral Microbiol.* **2017**, *32*, 24–34. [CrossRef] [PubMed]
114. Xiao, J.; Grier, A.; Faustoferri, R.C.; Alzoubi, S.; Gill, A.L.; Feng, C.; Liu, Y.; Quivey, R.G.; Kopycka-Kedzierawski, D.T.; Koo, H.; et al. Association between Oral Candida and Bacteriome in Children with Severe ECC. *J. Dent. Res.* **2018**, *97*, 1468–1476. [CrossRef] [PubMed]
115. Singh, A.; Verma, R.; Murari, A.; Agrawal, A. Oral candidiasis: An overview. *J. Oral Maxillofac. Pathol.* **2014**, *18*, S81-5. [CrossRef] [PubMed]
116. Borges, A.C.; de Morais Gouvêa Lima, G.; Mayumi Castaldelli Nishime, T.; Vidal Lacerda Gontijo, A.; Kostov, K.G.; Koga-Ito, C.Y. Amplitude-modulated cold atmospheric pressure plasma jet for treatment of oral candidiasis: In vivo study. *PLoS ONE* **2018**, *13*, e0199832. [CrossRef] [PubMed]
117. Chiodi Borges, A.; Castaldelli Nishime, T.M.; Kostov, K.G.; de Morais Gouvêa Lima, G.; Vidal Lacerda Gontijo, A.; Nóbrega Martins Marchesotti de Carvalho, J.; Yzumi Honda, R.; Koga-Ito, C.Y. Cold atmospheric pressure plasma jet modulates Candida albicans virulence traits. *Clin. Plasma Med.* **2017**, *7–8*, 9–15. [CrossRef]
118. Laurita, R.; Barbieri, D.; Gherardi, M.; Colombo, V.; Lukes, P. Chemical analysis of reactive species and antimicrobial activity of water treated by nanosecond pulsed DBD air plasma. *Clin. Plasma Med.* **2015**, *3*, 53–61. [CrossRef]
119. Liu, Z.; Zheng, Y.; Dang, J.; Zhang, J.; Dong, F.; Wang, K.; Zhang, J. A Novel Antifungal Plasma-Activated Hydrogel. *ACS Appl. Mater. Interfaces* **2019**, *11*, 22941–22949. [CrossRef]
120. Gomes, B.P.F.d.A.; Herrera, D.R. Etiologic role of root canal infection in apical periodontitis and its relationship with clinical symptomatology. *Braz. Oral Res.* **2018**, *32*, 82–110. [CrossRef]
121. Jacinto, R.C.; Gomes, B.P.F.A.; Desai, M.; Rajendram, D.; Shah, H.N. Bacterial examination of endodontic infections by clonal analysis in concert with denaturing high-performance liquid chromatography. *Oral Microbiol. Immunol.* **2007**, *22*, 403–410. [CrossRef]
122. Gomes, B.P.F.A.; Pinheiro, E.T.; Sousa, E.L.R.; Jacinto, R.C.; Zaia, A.A.; Ferraz, C.C.R.; de Souza-Filho, F.J. Enterococcus faecalis in dental root canals detected by culture and by polymerase chain reaction analysis. *Oral Surg. Oral Med. Oral Pathol. Oral Radiol. Endod.* **2006**, *102*, 247–253. [CrossRef] [PubMed]

123. Subramanian, K.; Mickel, A.K. Molecular analysis of persistent periradicular lesions and root ends reveals a diverse microbial profile. *J. Endod.* **2009**, *35*, 950–957. [CrossRef] [PubMed]
124. Li, Y.; Pan, J.; Wu, D.; Tian, Y.; Zhang, J.; Fang, J. Regulation of Enterococcus faecalis Biofilm Formation and Quorum Sensing Related Virulence Factors with Ultra-low Dose Reactive Species Produced by Plasma Activated Water. *Plasma Chem. Plasma Process.* **2019**, *39*, 35–49. [CrossRef]
125. Gaetti-Jardim Júnior, E.; Fardin, A.C.; Gaetti-Jardim, E.C.; de Castro, A.L.; Schweitzer, C.M.; Avila-Campos, M.J. Microbiota associated with chronic osteomyelitis of the jaws. *Brazilian J. Microbiol.* **2010**, *41*, 1056–1064. [CrossRef]
126. Hajishengallis, G.; Lamont, R.J. Beyond the red complex and into more complexity: The polymicrobial synergy and dysbiosis (PSD) model of periodontal disease etiology. *Mol. Oral Microbiol.* **2012**, *27*, 409–419. [CrossRef]
127. Kinane, D.F.; Stathopoulou, P.G.; Papapanou, P.N. Periodontal diseases. *Nat. Rev. Dis. Prim.* **2017**, *3*, 17038. [CrossRef] [PubMed]
128. Sanz, M.; Beighton, D.; Curtis, M.A.; Cury, J.A.; Dige, I.; Dommisch, H.; Ellwood, R.; Giacaman, R.A.; Herrera, D.; Herzberg, M.C.; et al. Role of microbial biofilms in the maintenance of oral health and in the development of dental caries and periodontal diseases. Consensus report of group 1 of the Joint EFP/ORCA workshop on the boundaries between caries and periodontal disease. *J. Clin. Periodontol.* **2017**, *44* (Suppl. 1), S5–S11. [CrossRef]
129. Lima, G.d.M.G.; Borges, A.C.; Nishime, T.M.C.; Santana-Melo, G.d.F.; Kostov, K.G.; Mayer, M.P.A.; Koga-Ito, C.Y. Cold Atmospheric Plasma Jet as a Possible Adjuvant Therapy for Periodontal Disease. *Molecules* **2021**, *26*, 5590. [CrossRef]
130. Dobrynin, D.; Fridman, G.; Friedman, G.; Fridman, A. Physical and biological mechanisms of direct plasma interaction with living tissue. *New J. Phys.* **2009**, *11*. [CrossRef]
131. Jablonowski, L.; Kocher, T.; Schindler, A.; Müller, K.; Dombrowski, F.; von Woedtke, T.; Arnold, T.; Lehmann, A.; Rupf, S.; Evert, M.; et al. Side effects by oral application of atmospheric pressure plasma on the mucosa in mice. *PLoS ONE* **2019**, *14*, e0215099. [CrossRef] [PubMed]
132. Nastasa, V.; Pasca, A.-S.; Malancus, R.-N.; Bostanaru, A.-C.; Ailincai, L.-I.; Ursu, E.-L.; Vasiliu, A.-L.; Minea, B.; Hnatiuc, E.; Mares, M. Toxicity Assessment of Long-Term Exposure to Non-Thermal Plasma Activated Water in Mice. *Int. J. Mol. Sci.* **2021**, *22*, 11534. [CrossRef] [PubMed]
133. Lou, B.S.; Hsieh, J.H.; Chen, C.M.; Hou, C.W.; Wu, H.Y.; Chou, P.Y.; Lai, C.H.; Lee, J.W. Helium/Argon-Generated Cold Atmospheric Plasma Facilitates Cutaneous Wound Healing. *Front. Bioeng. Biotechnol.* **2020**, *8*, 1–11. [CrossRef] [PubMed]
134. Xiong, Q.; Wang, X.; Yin, R.; Xiong, L.; Chen, Q.; Zheng, M.; Xu, L.; Huang, Q.; Hamblin, M.R.; Hospital, S.; et al. Surface Treatment with Non-thermal Humid Argon Plasma as a Treatment for Allergic Contact Dermatitis in a Mouse Model. *Clin. Plasma Med.* **2019**, *12*, 10–16. [CrossRef]
135. Lee, Y.S.; Lee, M.H.; Kim, H.J.; Won, H.R.; Kim, C.H. Non-thermal atmospheric plasma ameliorates imiquimod-induced psoriasis-like skin inflammation in mice through inhibition of immune responses and up-regulation of PD-L1 expression. *Sci. Rep.* **2017**, *7*, 1–12. [CrossRef]
136. Lee, M.H.; Lee, Y.S.; Kim, H.J.; Han, C.H.; Kang, S.U.; Kim, C.H. Non-thermal plasma inhibits mast cell activation and ameliorates allergic skin inflammatory diseases in NC/Nga mice. *Sci. Rep.* **2019**, *9*, 1–10. [CrossRef]
137. Zhang, Y.; Xiong, Y.; Xie, P.; Ao, X.; Zheng, Z.; Dong, X.; Li, H.; Yu, Q.; Zhu, Z.; Chen, M.; et al. Non-thermal plasma reduces periodontitis-induced alveolar bone loss in rats. *Biochem. Biophys. Res. Commun.* **2018**, *503*, 2040–2046. [CrossRef]
138. Ambili, R.; Janam, P.; Saneesh Babu, P.S.; Prasad, M.; Vinod, D.; Anil Kumar, P.R.; Kumary, T.V.; Asha Nair, S. Differential expression of transcription factors NF-κB and STAT3 in periodontal ligament fibroblasts and gingiva of healthy and diseased individuals. *Arch. Oral Biol.* **2017**, *82*, 19–26. [CrossRef]
139. Gratacap, R.L.; Rawls, J.F.; Wheeler, R.T. Mucosal candidiasis elicits NF-κB activation, proinflammatory gene expression and localized neutrophilia in zebrafish. *Dis. Model. Mech.* **2013**, *6*, 1260–1270. [CrossRef]
140. Aggor, F.E.Y.; Break, T.J.; Trevejo-Nuñez, G.; Whibley, N.; Coleman, B.M.; Bailey, R.D.; Kaplan, D.H.; Naglik, J.R.; Shan, W.; Shetty, A.C.; et al. Oral epithelial IL-22/STAT3 signaling licenses IL-17-mediated immunity to oral mucosal candidiasis. *Sci. Immunol.* **2020**, *5*. [CrossRef]
141. Lavanya, N.; Jayanthi, P.; Rao, U.; Ranganathan, K. Oral lichen planus: An update on pathogenesis and treatment. *J. Oral Maxillofac. Pathol.* **2011**, *15*, 127–132. [CrossRef] [PubMed]
142. Saccucci, M.; di Carlo, G.; Bossù, M.; Giovarruscio, F.; Salucci, A.; Polimeni, A. Autoimmune diseases and their manifestations on oral cavity: Diagnosis and clinical management. *J. Immunol. Res.* **2018**, *2018*, 6061825. [CrossRef] [PubMed]
143. Seebauer, C.; Freund, E.; Hasse, S.; Miller, V.; Segebarth, M.; Lucas, C.; Kindler, S.; Dieke, T.; Metelmann, H.R.; Daeschlein, G.; et al. Effects of cold physical plasma on oral lichen planus: An in vitro study (Effects of CAP on OLP). *Oral Dis.* **2020**, *27*, 1728–1737. [CrossRef] [PubMed]
144. Cheng, K.Y.; Lin, Z.H.; Cheng, Y.P.; Chiu, H.Y.; Yeh, N.L.; Wu, T.K.; Wu, J.S. Wound Healing in Streptozotocin-Induced Diabetic Rats Using Atmospheric-Pressure Argon Plasma Jet. *Sci. Rep.* **2018**, *8*, 1–15. [CrossRef]
145. Rezaeinezhad, A.; Eslami, P.; Mirmiranpour, H.; Ghomi, H. The effect of cold atmospheric plasma on diabetes-induced enzyme glycation, oxidative stress, and inflammation; in vitro and in vivo. *Sci. Rep.* **2019**, *9*, 1–11. [CrossRef]
146. He, R.; Li, Q.; Shen, W.; Wang, T.; Lu, H.; Lu, J.; Lu, F.; Luo, M.; Zhang, J.; Gao, H.; et al. The efficacy and safety of cold atmospheric plasma as a novel therapy for diabetic wound in vitro and in vivo. *Int. Wound J.* **2020**, *17*, 851–863. [CrossRef]
147. Llambés, F. Relationship between diabetes and periodontal infection. *World J. Diabetes* **2015**, *6*, 927. [CrossRef]

148. Lalla, E.; Lamster, I.B.; Drury, S.; Fu, C.; Schmidt, A.M. Hyperglycemia, glycoxidation and receptor for advanced glycation endproducts: Potential mechanisms underlying diabetic complications, including diabetes-associated periodontitis. *Periodontol. 2000* **2000**, *23*, 50–62. [CrossRef]
149. Ramadan, D.E.; Hariyani, N.; Indrawati, R.; Ridwan, R.D.; Diyatri, I. Cytokines and Chemokines in Periodontitis. *Eur. J. Dent.* **2020**, *14*, 483–495. [CrossRef]
150. Isbary, G.; Heinlin, J.; Shimizu, T.; Zimmermann, J.L.; Morfill, G.; Schmidt, H.U.; Monetti, R.; Steffes, B.; Bunk, W.; Li, Y.; et al. Successful and safe use of 2 min cold atmospheric argon plasma in chronic wounds: Results of a randomized controlled trial. *Br. J. Dermatol.* **2012**, *167*, 404–410. [CrossRef]
151. Brehmer, F.; Haenssle, H.A.; Daeschlein, G.; Ahmed, R.; Pfeiffer, S.; Görlitz, A.; Simon, D.; Schön, M.P.; Wandke, D.; Emmert, S. Alleviation of chronic venous leg ulcers with a hand-held dielectric barrier discharge plasma generator (PlasmaDerm®VU-2010): Results of a monocentric, two-armed, open, prospective, randomized and controlled trial (NCT01415622). *J. Eur. Acad. Dermatol. Venereol.* **2015**, *29*, 148–155. [CrossRef] [PubMed]
152. Won, H.R.; Kang, S.U.; Kim, H.J.; Jang, J.Y.; Shin, Y.S.; Kim, C.H. Non-thermal plasma treated solution with potential as a novel therapeutic agent for nasal mucosa regeneration. *Sci. Rep.* **2018**, *8*, 1–11. [CrossRef] [PubMed]
153. Metelmann, H.R.; Nedrelow, D.S.; Seebauer, C.; Schuster, M.; von Woedtke, T.; Weltmann, K.D.; Kindler, S.; Metelmann, P.H.; Finkelstein, S.E.; von Hoff, D.D.; et al. Head and neck cancer treatment and physical plasma. *Clin. Plasma Med.* **2015**, *3*, 17–23. [CrossRef]
154. Eggers, B.; Marciniak, J.; Memmert, S.; Kramer, F.J.; Deschner, J.; Nokhbehsaim, M. The beneficial effect of cold atmospheric plasma on parameters of molecules and cell function involved in wound healing in human osteoblast-like cells in vitro. *Odontology* **2020**, *108*, 607–616. [CrossRef]
155. Mahdikia, H.; Saadati, F.; Freund, E.; Gaipl, U.S.; Majidzadeh-a, K.; Shokri, B.; Bekeschus, S. Gas plasma irradiation of breast cancers promotes immunogenicity, tumor reduction, and an abscopal effect in vivo. *Oncoimmunology* **2021**, *10*, 1859731. [CrossRef]
156. Hirst, A.M.; Frame, F.M.; Maitland, N.J.; O'Connell, D. Low temperature plasma: A novel focal therapy for localized prostate cancer? *Biomed Res. Int.* **2014**, *2014*, 1–5. [CrossRef] [PubMed]
157. Zubor, P.; Wang, Y.; Liskova, A.; Samec, M.; Koklesova, L.; Dankova, Z.; Dørum, A.; Kajo, K.; Dvorska, D.; Lucansky, V.; et al. Cold atmospheric pressure plasma (CAP) as a new tool for the management of vulva cancer and vulvar premalignant lesions in gynaecological oncology. *Int. J. Mol. Sci.* **2020**, *21*, 7988. [CrossRef] [PubMed]
158. Verloy, R.; Privat-Maldonado, A.; Smits, E.; Bogaerts, A. Cold atmospheric plasma treatment for pancreatic cancer–the importance of pancreatic stellate cells. *Cancers* **2020**, *12*, 2782. [CrossRef]
159. Mateu-Sanz, M.; Tornín, J.; Ginebra, M.-P.; Canal, C. Cold Atmospheric Plasma: A New Strategy Based Primarily on Oxidative Stress for Osteosarcoma Therapy. *J. Clin. Med.* **2021**, *10*, 893. [CrossRef]
160. Metelmann, H.R.; Seebauer, C.; Miller, V.; Fridman, A.; Bauer, G.; Graves, D.B.; Pouvesle, J.M.; Rutkowski, R.; Schuster, M.; Bekeschus, S.; et al. Clinical experience with cold plasma in the treatment of locally advanced head and neck cancer. *Clin. Plasma Med.* **2018**, *9*, 6–13. [CrossRef]
161. Schuster, M.; Seebauer, C.; Rutkowski, R.; Hauschild, A.; Podmelle, F.; Metelmann, C.; Metelmann, B.; von Woedtke, T.; Hasse, S.; Weltmann, K.D.; et al. Visible tumor surface response to physical plasma and apoptotic cell kill in head and neck cancer. *J. Cranio-Maxillofacial Surg.* **2016**, *44*, 1445–1452. [CrossRef] [PubMed]
162. Scully, C.; Bagan, J.V. Oral squamous cell carcinoma: Overview of current understanding of aetiopathogenesis and clinical implications. *Oral Dis.* **2009**, *15*, 388–399. [CrossRef] [PubMed]
163. Wirtz, M.; Stoffels, I.; Dissemond, J.; Schadendorf, D.; Roesch, A. Actinic keratoses treated with cold atmospheric plasma. *J. Eur. Acad. Dermatol. Venereol.* **2018**, *32*, e37–e39. [CrossRef]
164. Trager, M.H.; Farmer, K.; Ulrich, C.; Basset-Seguin, N.; Herms, F.; Geskin, L.J.; Bouaziz, J.D.; Lebbé, C.; de Masson, A.; Bagot, M.; et al. Actinic cheilitis: A systematic review of treatment options. *J. Eur. Acad. Dermatol. Venereol.* **2021**, *35*, 815–823. [CrossRef] [PubMed]
165. Lee, C.M.; Jeong, Y.I.; Kook, M.S.; Kim, B.H. Combinatorial effect of cold atmosphere plasma (Cap) and the anticancer drug cisplatin on oral squamous cell cancer therapy. *Int. J. Mol. Sci.* **2020**, *21*, 7646. [CrossRef] [PubMed]
166. Chang, J.W.; Kang, S.U.; Shin, Y.S.; Seo, S.J.; Kim, Y.S.; Yang, S.S.; Lee, J.S.; Moon, E.; Lee, K.; Kim, C.H. Combination of NTP with cetuximab inhibited invasion/migration of cetuximab-resistant OSCC cells: Involvement of NF-κB signaling. *Sci. Rep.* **2015**, *5*, 1–12. [CrossRef] [PubMed]
167. Rezaei, F.; Vanraes, P.; Nikiforov, A.; Morent, R.; Geyter, N. De Applications of Plasma-Liquid Systems: A Review. *Materials* **2019**, *12*, 2751. [CrossRef]
168. Freund, E.; Liedtke, K.R.; van der Linde, J.; Metelmann, H.R.; Heidecke, C.D.; Partecke, L.I.; Bekeschus, S. Physical plasma-treated saline promotes an immunogenic phenotype in CT26 colon cancer cells in vitro and in vivo. *Sci. Rep.* **2019**, *9*, 1–18. [CrossRef]
169. Nakamura, K.; Peng, Y.; Utsumi, F.; Tanaka, H.; Mizuno, M.; Toyokuni, S.; Hori, M.; Kikkawa, F.; Kajiyama, H. Novel Intraperitoneal Treatment With Non-Thermal Plasma-Activated Medium Inhibits Metastatic Potential of Ovarian Cancer Cells. *Sci. Rep.* **2017**, *7*, 1–14. [CrossRef]
170. Nakamura, K.; Yoshikawa, N.; Mizuno, Y.; Ito, M.; Tanaka, H.; Mizuno, M.; Toyokuni, S.; Hori, M.; Kikkawa, F.; Kajiyama, H. Preclinical verification of the efficacy and safety of aqueous plasma for ovarian cancer therapy. *Cancers* **2021**, *13*, 1141. [CrossRef]

171. Chen, Z.; Lin, L.; Cheng, X.; Gjika, E.; Keidar, M. Treatment of gastric cancer cells with nonthermal atmospheric plasma generated in water. *Biointerphases* **2016**, *11*, 031010. [CrossRef] [PubMed]
172. Tanaka, H.; Bekeschus, S.; Yan, D.; Hori, M.; Keidar, M.; Laroussi, M.; Rns, R.O.S.; Rns, R.O.S.; Rns, R.O.S. Plasma-Treated Solutions (PTS) in Cancer Therapy. *Cancers* **2021**, *13*, 1737. [CrossRef] [PubMed]
173. Motaln, H.; Recek, N.; Rogelj, B. Intracellular responses triggered by cold atmospheric plasma and plasma-activated media in cancer cells. *Molecules* **2021**, *26*, 1336. [CrossRef] [PubMed]
174. Shi, L.; Yu, L.; Zou, F.; Hu, H.; Liu, K.; Lin, Z. Gene expression profiling and functional analysis reveals that p53 pathway-related gene expression is highly activated in cancer cells treated by cold atmospheric plasma-activated medium. *PeerJ* **2017**, *5*, e3751. [CrossRef]
175. Lee, H.W.; Kim, G.J.; Kim, J.M.; Park, J.K.; Lee, J.K.; Kim, G.C. Tooth Bleaching with Nonthermal Atmospheric Pressure Plasma. *J. Endod.* **2009**, *35*, 587–591. [CrossRef]
176. Nam, S.H.; Lee, H.W.; Cho, S.H.; Lee, J.K.; Jeon, Y.C.; Kim, G.C. High-efficiency tooth bleaching using nonthermal atmospheric pressure plasma with low concentration of hydrogen peroxide. *J. Appl. Oral Sci.* **2013**, *21*, 265–270. [CrossRef] [PubMed]
177. Nam, S.H.; Choi, B.B.R.; Kim, G.C. The whitening effect and histological safety of nonthermal atmospheric plasma inducing tooth bleaching. *Int. J. Environ. Res. Public Health* **2021**, *18*, 4714. [CrossRef]
178. Cheng, Y.C.; Wu, C.H.; Liu, C.T.; Lin, C.Y.; Chiang, H.P.; Chen, T.W.; Chen, C.Y.; Wu, J.S. Tooth bleaching by using a helium-based low-temperature atmospheric pressure plasma jet with saline solution. *Plasma Process. Polym.* **2017**, *14*, 1600235. [CrossRef]
179. Yilmaz, F.; Celik, E.U.; Ercan, U.K.; Ibis, F. Efficacy of Plasma Activation on Bleaching. *ARC J. Dent. Sci.* **2018**, *3*. [CrossRef]
180. Çelik, B.; Çapar, İ.D.; İbiş, F.; Erdilek, N.; Ercan, U.K. Deionized water can substitute common bleaching agents for nonvital tooth bleaching when treated with non-thermal atmospheric plasma. *J. Oral Sci.* **2019**, *61*, 103–110. [CrossRef]
181. Girard, P.M.; Arbabian, A.; Fleury, M.; Bauville, G.; Puech, V.; Dutreix, M.; Sousa, J.S. Synergistic Effect of H_2O_2 and NO_2 in Cell Death Induced by Cold Atmospheric He Plasma. *Sci. Rep.* **2016**, *6*, 1–17. [CrossRef] [PubMed]
182. Buxton, G.V.; Greenstock, C.L.; Helman, W.P.; Ross, A.B. Critical Review of rate constants for reactions of hydrated electrons, hydrogen atoms and hydroxyl radicals ($\cdot OH/\cdot O^-$ in Aqueous Solution. *J. Phys. Chem. Ref. Data* **1988**, *17*, 513–886. [CrossRef]
183. Zhou, R.; Zhang, X.; Bi, Z.; Zong, Z.; Niu, J.; Song, Y.; Liu, D.; Yang, S. Inactivation of Escherichia coli cells in aqueous solution by atmospheric-pressure N_2, He, air, and O_2 microplasmas. *Appl. Environ. Microbiol.* **2015**, *81*, 5257–5265. [CrossRef] [PubMed]
184. Zhou, R.; Zhou, R.; Zhuang, J.; Zong, Z.; Zhang, X.; Liu, D.; Bazaka, K.; Ostrikov, K. Interaction of atmospheric-pressure air microplasmas with amino acids as fundamental processes in aqueous solution. *PLoS ONE* **2016**, *11*, e0155584. [CrossRef]
185. Tian, Y.; Ma, R.; Zhang, Q.; Feng, H.; Liang, Y.; Zhang, J.; Fang, J. Assessment of the physicochemical properties and biological effects of water activated by non-thermal plasma above and beneath the water surface. *Plasma Process. Polym.* **2015**, *12*, 439–449. [CrossRef]
186. Jablonowski, H.; Schmidt-Bleker, A.; Weltmann, K.D.; von Woedtke, T.; Wende, K. Non-touching plasma-liquid interaction-where is aqueous nitric oxide generated? *Phys. Chem. Chem. Phys.* **2018**, *20*, 25387–25398. [CrossRef]
187. Tachibana, K.; Nakamura, T. Examination of UV-absorption spectroscopy for analysis of O_3, NO_2^-, and HNO_2 compositions and kinetics in plasma-activated water. *Jpn. J. Appl. Phys.* **2020**, *59*, 56004. [CrossRef]
188. Niethammer, P.; Grabher, C.; Look, A.T.; Mitchison, T.J. A tissue-scale gradient of hydrogen peroxide mediates rapid wound detection in zebrafish. *Nature* **2009**, *459*, 996–999. [CrossRef]
189. Vilema-Enríquez, G.; Arroyo, A.; Grijalva, M.; Amador-Zafra, R.I.; Camacho, J. Molecular and Cellular Effects of Hydrogen Peroxide on Human Lung Cancer Cells: Potential Therapeutic Implications. *Oxid. Med. Cell. Longev.* **2016**, *2016*, 1908164. [CrossRef]
190. Subramanian, P.S.G.; Jain, A.; Shivapuji, A.M.; Sundaresan, N.R.; Dasappa, S.; Rao, L. Plasma-activated water from a dielectric barrier discharge plasma source for the selective treatment of cancer cells. *Plasma Process. Polym.* **2020**, *17*, 1–13. [CrossRef]
191. Samukawa, S.; Hori, M.; Rauf, S.; Tachibana, K.; Bruggeman, P.; Kroesen, G.; Whitehead, J.C.; Murphy, A.B.; Gutsol, A.F.; Starikovskaia, S.; et al. The 2012 Plasma Roadmap. *J. Phys. D Appl. Phys.* **2012**, *45*, 253001. [CrossRef]
192. Kovačević, V.V.; Dojčinović, B.P.; Jović, M.; Roglić, G.M.; Obradović, B.M.; Kuraica, M.M. Measurement of reactive species generated by dielectric barrier discharge in direct contact with water in different atmospheres. *J. Phys. D Appl. Phys.* **2017**, *50*, 155205. [CrossRef]
193. He, X.; Lin, J.; He, B.; Xu, L.; Li, J.; Chen, Q.; Yue, G.; Xiong, Q.; Liu, Q.H. The formation pathways of aqueous hydrogen peroxide in a plasma-liquid system with liquid as the cathode. *Plasma Sources Sci. Technol.* **2018**, *27*, 85010. [CrossRef]
194. Attri, P.; Kim, Y.H.; Park, D.H.; Park, J.H.; Hong, Y.J.; Uhm, H.S.; Kim, K.N.; Fridman, A.; Choi, E.H. Generation mechanism of hydroxyl radical species and its lifetime prediction during the plasma-initiated ultraviolet (UV) photolysis. *Sci. Rep.* **2015**, *5*, 1–8. [CrossRef]
195. Ghimire, B.; Sornsakdanuphap, J.; Hong, Y.J.; Uhm, H.S.; Weltmann, K.D.; Choi, E.H. The effect of the gap distance between an atmospheric-pressure plasma jet nozzle and liquid surface on OH and N_2 species concentrations. *Phys. Plasmas* **2017**, *24*, 073502. [CrossRef]
196. Szili, E.J.; Ghimire, B.; Patenall, B.L.; Rohaim, M.; Mistry, D.; Fellows, A.; Munir, M.; Jenkins, A.T.A.; Short, R.D. On-demand cold plasma activation of acetyl donors for bacteria and virus decontamination. *Appl. Phys. Lett.* **2021**, *119*. [CrossRef]

197. Guragain, R.P.; Baniya, H.B.; Pradhan, S.P.; Pandey, B.P.; Subedi, D.P. Influence of plasma-activated water (PAW) on the germination of radish, fenugreek, and pea seeds. *AIP Adv.* **2021**, *11*, 125304. [CrossRef]
198. Pavlovich, M.J.; Chang, H.-W.; Sakiyama, Y.; Clark, D.S.; Graves, D.B. Ozone correlates with antibacterial effects from indirect air dielectric barrier discharge treatment of water. *J. Phys. D Appl. Phys.* **2013**, *46*, 145202. [CrossRef]
199. Lukes, P.; Locke, B.R.; Brisset, J.L. Aqueous-Phase Chemistry of Electrical Discharge Plasma in Water and in Gas-Liquid Environments. In *Plasma Chemistry and Catalysis in Gases and Liquids*, 1st ed.; Parvulescu, V.I., Magureanu, M., Lukes, P., Eds.; Wiley: Hoboken, NJ, USA, 2012; pp. 243–308. [CrossRef]

International Journal of
Molecular Sciences

MDPI

Article

Preclinical Evaluation of BMP-9-Treated Human Bone-like Substitutes for Alveolar Ridge Preservation following Tooth Extraction

Fabien Kawecki [1,2], Jessica Jann [3], Michel Fortin [1,4,5], François A. Auger [1,2], Nathalie Faucheux [3] and Julie Fradette [1,2,*]

[1] Centre de Recherche en Organogénèse Expérimentale de l'Université Laval, LOEX, Division of Regenerative Medicine, CHU de Québec Research Center-Université Laval, Quebec City, QC G1V 0A6, Canada; fabien.kawecki.1@ulaval.ca (F.K.); michel.fortin@fmd.ulaval.ca (M.F.); francois.auger@fmed.ulaval.ca (F.A.A.)
[2] Department of Surgery, Faculty of Medicine, Université Laval, Quebec City, QC G1V 0A6, Canada
[3] Clinical Research Center of CHU de Sherbrooke, Department of Chemical and Biotechnological Engineering, Pharmacology Institute of Sherbrooke, Université de Sherbrooke, Sherbrooke, QC J1H 5N4, Canada; jessica.jann@usherbrooke.ca (J.J.); nathalie.faucheux@usherbrooke.ca (N.F.)
[4] Faculty of Dentistry, Université Laval, Quebec City, QC G1V 0A6, Canada
[5] Service of Oral and Maxillofacial Surgery, CHU de Québec-Université Laval, Quebec City, QC G1V 0A6, Canada
* Correspondence: julie.fradette@chg.ulaval.ca

Abstract: The success of dental implant treatment after tooth extraction is generally maximized by preserving the alveolar ridge using cell-free biomaterials. However, these treatments can be associated with inflammatory reactions, leading to additional bone volume loss hampering dental implant positioning. Our group developed a self-assembled bone-like substitute constituted of osteogenically induced human adipose-derived stromal/stem cells (hASCs). We hypothesized that a bone morphogenetic protein (BMP) supplementation could improve the in vitro osteogenic potential of the bone-like substitute, which would subsequently translate into enhanced alveolar bone healing after tooth extraction. ASCs displayed a better osteogenic response to BMP-9 than to BMP-2 in monolayer cell culture, as shown by higher transcript levels of the osteogenic markers *RUNX2*, *osterix* (*OSX*/*SP7*), and *alkaline phosphatase* after three and six days of treatment. Interestingly, BMP-9 treatment significantly increased *OSX* transcripts and alkaline phosphatase activity, as well as pro-angiogenic *angiopoietin-1* gene expression, in engineered bone-like substitutes after 21 days of culture. Alveolar bone healing was investigated after molar extraction in nude rats. Microcomputed tomography and histological evaluations revealed similar, or even superior, global alveolar bone preservation when defects were filled with BMP-9-treated bone-like substitutes for ten weeks compared to a clinical-grade biomaterial, with adequate gingival re-epithelialization in the absence of resorption.

Keywords: bone; mesenchymal stem cells; bone morphogenetic protein-9; tissue engineering; dental biomaterial

Citation: Kawecki, F.; Jann, J.; Fortin, M.; Auger, F.A.; Faucheux, N.; Fradette, J. Preclinical Evaluation of BMP-9-Treated Human Bone-like Substitutes for Alveolar Ridge Preservation following Tooth Extraction. *Int. J. Mol. Sci.* **2022**, *23*, 3302. https://doi.org/10.3390/ijms23063302

Academic Editor: Mary Anne Melo

Received: 8 February 2022
Accepted: 16 March 2022
Published: 18 March 2022

Publisher's Note: MDPI stays neutral with regard to jurisdictional claims in published maps and institutional affiliations.

Copyright: © 2022 by the authors. Licensee MDPI, Basel, Switzerland. This article is an open access article distributed under the terms and conditions of the Creative Commons Attribution (CC BY) license (https://creativecommons.org/licenses/by/4.0/).

1. Introduction

Tooth extraction may be necessary for several reasons such as periodontal diseases, tooth decay, and dento-alveolar trauma, among others [1]. Clinical studies have demonstrated that alveolar ridge bone resorption is initiated immediately after tooth removal in the vertical and horizontal planes [2–4]. This process leads to an average of 40 to 60% bone loss during the first two years after tooth extraction [5]. Furthermore, the resorption rate is significantly elevated in the maxillary bone during the first six months post-extraction period [6]. Since the alveolar ridge is damaged after a dental extraction, bone tissue

preservation is required to optimize dental implant positioning. Various materials are used in dentistry for alveolar ridge preservation, including autografts, demineralized freeze-dried human (allografts) or bovine (xenografts) bone (DFDBA), mineralized freeze-dried bone allografts, inorganic synthetic or bovine hydroxyapatite (HA), or synthetic biomaterials [4,7–10]. Even if these graft materials can preserve alveolar ridge dimensions to some extent, the quality and the quantity of new bone tissue that may form in the alveolar socket vary between patients [11,12]. In addition, these biomaterials may cause inflammatory reactions, foreign body responses, and/or fibrous encapsulation once grafted [13].

Promising options involving bone tissue engineering have been recently developed in the field of dental and oral reconstruction [14]. In general, tissue-engineered substitutes combine human cells with biomaterial scaffolds and growth factors to produce native-like substitutes [15,16]. Growth factors play an important role in the maturation and differentiation processes of the cells composing the bone substitutes. In particular, the use of several bone morphogenetic proteins (BMPs) from the transforming growth factor-ß (TGF-ß) superfamily was granted permission for the treatment of spinal fusion, long-bone fractures, long-bone non-unions, and dental implant placement in humans [17–19]. In the context of oral surgery, recombinant human BMP-2 (rhBMP-2) loaded with either deproteinized bovine bone mineral blocks (Geistlich Bio-Oss®) or autogenous bone blocks has been shown to favor primary ridge augmentation in patients four months after implantation [20]. In addition, it was revealed that BMP-9 is widely expressed in odontoblasts, ameloblasts, dental pulp cells, and osteoblasts in alveolar bones [21]. It has been shown that rhBMP-9 combined with biomaterials, such as Geistlich Bio-Oss® blocks or Geistlich Bio-Gide® collagen barrier membranes, positively induced bone formation in a guided bone regeneration rabbit model eight weeks after implantation [22]. Therefore, BMPs represent an interesting option for ridge augmentation.

Over the years, our research team has developed all-natural bone-like substitutes based on cell-assembled extracellular matrix components surrounding live osteogenically induced human adipose-derived stromal/stem cells (hASCs) [23–25]. The capacity to differentiate towards the osteogenic lineage had already been established for this mesenchymal cell population [26]. We hypothesized that rhBMP-2 or rhBMP-9 treatments during the bioproduction could improve in vitro osteogenesis of hASCs within the engineered substitutes and ultimately favor in vivo alveolar bone preservation after tooth extraction in a nude rat model.

2. Results

2.1. Better Osteogenic Differentiation Is Achieved When Monolayer Cultures of Osteogenically Induced hASCs Are Treated with rhBMP-9 Compared with rhBMP-2

Osteogenic differentiation of hASCs treated for three and six days with 1 nM rhBMP-2 or 1 nM rhBMP-9 was assessed by determining *runt-related transcription factor 2* (*RUNX2*), *osterix* (*OSX*), and *alkaline phosphatase* (*ALP*) gene expression in 2D cell cultures using RT-qPCR. Gene expressions for each group were referred to the untreated non-induced stromal group (Figure 1). Results showed that in 2D cell culture, the *RUNX2* transcript of hASCs remained unchanged despite osteogenic induction (gene expressions relative to non-induced hASCs approximate the value of one; Figure 1A). However, hASCs treated for three days with rhBMP-9 in the absence of osteogenic medium displayed more elevated *RUNX2* gene expression compared with either an osteogenic induction alone (1.6-fold; * $p < 0.05$) or a rhBMP-2 treatment (1.9-fold; ** $p < 0.01$) (Figure 1A). In addition, significantly higher *RUNX2* gene expression was measured at the early stage of culture (after three days of treatment) when osteogenically induced hASCs were treated with rhBMP-9 compared with rhBMP-2 (4.1-fold; #### $p < 0.0001$) or compared with cells induced with osteogenic medium alone (3.4-fold; #### $p < 0.0001$) (Figure 1A). *RUNX2* transcripts of osteogenically induced hASCs treated for six days with rhBMP-9 drastically decreased, suggesting that the cells are at a later stage of osteogenesis.

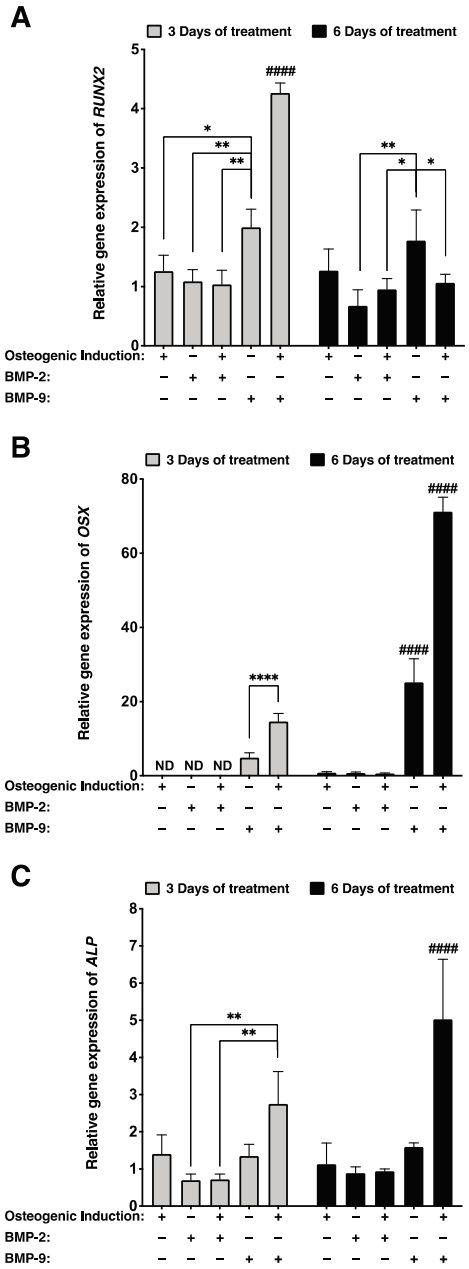


Figure 1. Robust osteogenic gene expression profiles from osteogenically induced hASCs when treated with rhBMP-9 in 2D cell culture. (**A**–**C**) Relative gene expression of (**A**) *runt-related transcription factor 2* (*RUNX2*), (**B**) *osterix* (*OSX*), and (**C**) *alkaline phosphatase* (*ALP*) measured by RT-qPCR on osteogenically induced and non-induced hASCs treated with 1 nM of rhBMP-2 or rhBMP-9 for three or six days. (Two-way ANOVA with a Bonferroni's multiple comparison post-hoc test; significant differences between two conditions per time point: * $p < 0.05$, ** $p < 0.01$, **** $p < 0.0001$ and significant difference between one condition and all other conditions: #### $p < 0.0001$).

At the early stage of culture, *OSX* gene expression was only detectable when hASCs were treated with rhBMP-9 for three days, and the association of this treatment with osteogenic induction significantly increased transcript levels (3-fold; **** $p < 0.0001$) (Figure 1B). A similar trend was observed after six days of treatment since low levels of *OSX* gene expression were detected in the absence of rhBMP-9 treatment and osteogenic induction associated with rhBMP-9 significantly upregulated gene expression (2.8-fold; #### $p < 0.0001$) (Figure 1B).

After three days of treatment, *ALP* gene expression was significantly more elevated in osteogenically induced hASCs treated with rhBMP-9 than with rhBMP-2 (3.8-fold; ** $p < 0.01$) (Figure 1C). In addition, *ALP* gene expression was considerably increased after six days of culture and became significantly higher than for other conditions ($^{\#\#\#\#}$ $p < 0.0001$) (Figure 1C). These results showed that an osteogenic induction protocol including a 1 nM rhBMP-9 supplementation improves the osteogenesis of hASCs in 2D cell culture. In addition, these results suggest that rhBMP-9 is a better candidate than rhBMP-2 for the production of bone-like substitutes composed of osteogenically induced hASCs.

2.2. Increased Osteogenic Differentiation When Bone-like Substitutes Are Produced with Concomitant rhBMP-9 Supplementation

The pro-osteogenic gene expression profiles of 3D substitutes cultured for 21 days were also assessed using RT-qPCR. A sustained rhBMP-9 treatment associated with osteogenic induction during the engineering of self-assembled bone-like substitutes significantly increased *OSX* gene transcript (33.6-fold; * $p < 0.05$) (Figure 2A). While bone-like substitutes supplemented or not with rhBMP-9 showed similar *ALP* gene expression, expression levels were significantly more elevated than for stromal substitutes treated with rhBMP-9 (3.3-fold; ** $p < 0.01$ and 2.8-fold; * $p < 0.05$, respectively) (Figure 2B). Herein, *ALP* activity was measured in the media conditioned for 48 h by engineered substitutes, prior to in vivo implantation (21 days of culture). Results show that an rhBMP-9 treatment associated with an osteogenic induction for the engineering of bone-like substitutes significantly enhanced *ALP* activity compared to other culture conditions (**** $p < 0.0001$) (Figure 2C). These results support that an osteogenic induction protocol including supplementation with 1 nM BMP-9 favors the osteogenesis of the hASC-derived substitutes during engineering.

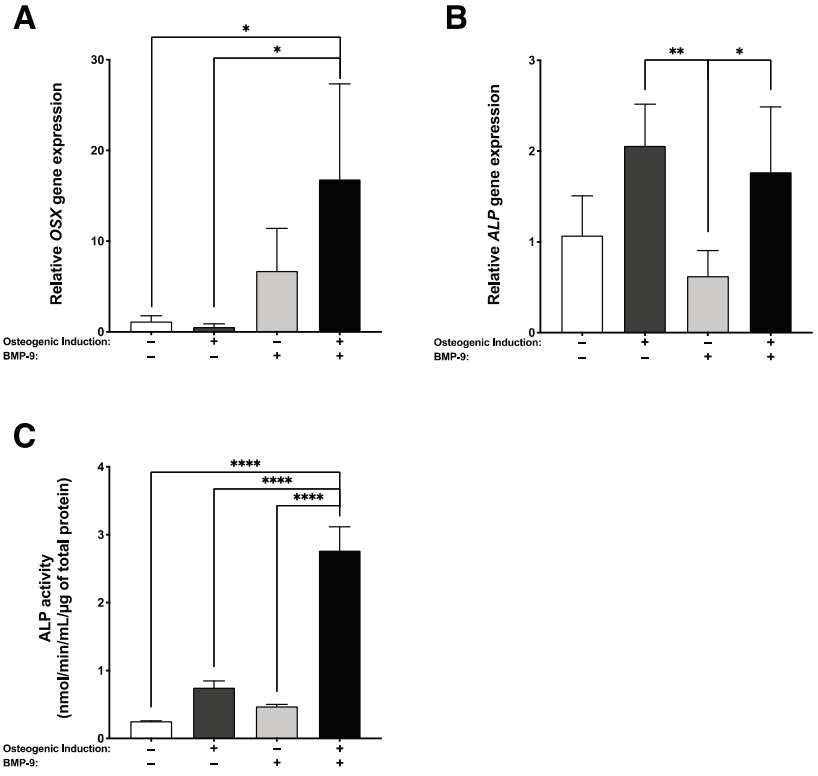


Figure 2. Superior osteogenic profile of the BMP-9 treated bone-like substitutes. Gene expression of (**A**) *osterix* (*OSX*) and (**B**) *alkaline phosphatase* (*ALP*) were measured by RT-qPCR on substitutes cultured for 21 days. (**C**) For osteogenically induced substitutes treated with 1 nM of rhBMP-9, *ALP* activity was higher compared to other conditions. (One-way ANOVA with a Bonferroni's multiple comparison post-hoc test, * $p < 0.05$, ** $p < 0.01$, **** $p < 0.0001$).

2.3. Increase in Angiopoietin-1 Gene Expression When Bone-like Substitutes Are Treated with rhBMP-9

After 21 days of tissue culture, the pro-angiogenic *ANG-1* gene transcript levels were evaluated by RT-qPCR. Results show that an rhBMP-9 treatment associated with an osteogenic induction for the engineering of bone-like substitutes significantly increases *ANG-1* gene expression compared to other culture conditions (**** $p < 0.0001$) (Figure 3). These data suggest that exposure to an osteogenic induction media supplemented with 1 nM rhBMP-9 changed every two/three days for 18 days (21 days of culture) could favor a pro-angiogenic profile of the hASC-derived substitutes.

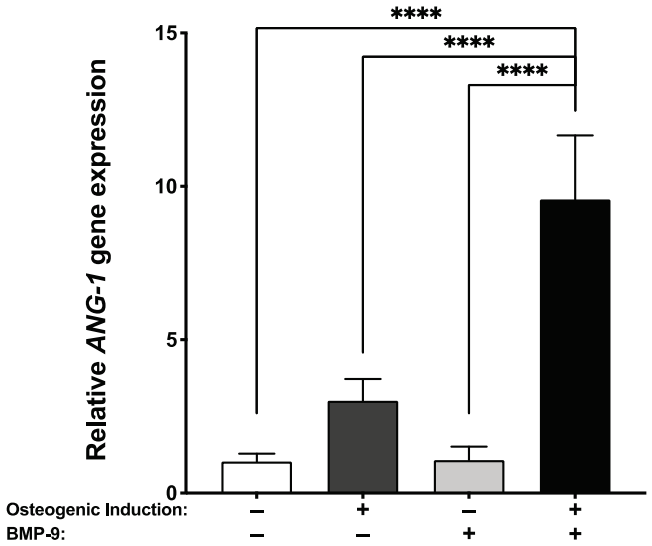


Figure 3. Superior expression of *angiopoietin-1* transcript for the BMP-9 treated bone-like substitutes. Gene expression of *angiopoietin-1* (*ANG-1*) was measured by RT-qPCR after 21 days of tissue culture. (One-way ANOVA with a Bonferroni's multiple comparison post-hoc test, **** $p < 0.0001$).

2.4. Microcomputed Tomography Imaging and Analysis of the Alveolar Bone Tissue Preservation

To evaluate the alveolar bone healing capacity of the various engineered substitutes, microcomputed tomography scans were performed on the same anesthetized animals at four, six, and ten weeks after implantation. Coronal plane images of the animal's heads (Figure 4A–F) showed elevated new bone formation (within dotted areas) when alveolar bone defects were filled for ten weeks with either rhBMP-9-treated bone-like substitutes (Figure 4D) or a clinical-grade biomaterial (Figure 4F). These observations were confirmed with bone volume fraction (BVF) measurements of the areas where the implantation of the substitutes was performed (Figure 4G). Globally, all engineered substitutes and untreated defects showed BVF augmentation over time at the extraction sites. This was clearly observed for the BMP-9-treated bone-like substitute group, which exhibited a linear BVF increase over time (Figure S1A; linear regression; $R^2 = 0.84$) and reached the mean level of the group grafted with the clinical-grade biomaterial after ten weeks. Indeed, relatively similar levels were observed between the BMP-9-treated bone-like substitute (BVF = 0.4743) and the clinical-grade biomaterial (BVF = 0.4789) after ten weeks (Figures 4G and S1B). After ten weeks of alveolar bone healing, BMP-9-treated bone-like substitutes showed more elevated BVT compared to untreated (4.5-fold; *** $p < 0.001$) or BMP-9-treated (2.1-fold; * $p < 0.05$) stromal substitutes, and defects left empty (3.7-fold; ** $p < 0.01$) (Figure 4G). BVF results were similar for untreated and BMP-9-treated bone-like substitutes using two-way ANOVA with a Bonferroni's multiple comparison post-hoc test on the complete set of data including all groups. However, statistical analysis focusing on the untreated and BMP-9-treated bone-like substitute groups' data sets revealed a significant increase when the animals were grafted for ten weeks with substitutes that were osteogenically induced and treated with rhBMP-9 (1.6-fold; ** $p < 0.01$) (Figure S1A). The biomaterial

group displayed important variability in terms of bone healing, and this was demonstrated by elevated coefficients of variation at Week 4 (63.9%), Week 6 (60.3%), and Week 10 (55.2%). Furthermore, several animals grafted with this biomaterial showed resorption of the graft over time (Figure S2). These results suggest that BMP-9-treated bone-like substitutes represent a promising bone filler for alveolar ridge preservation following tooth extraction.

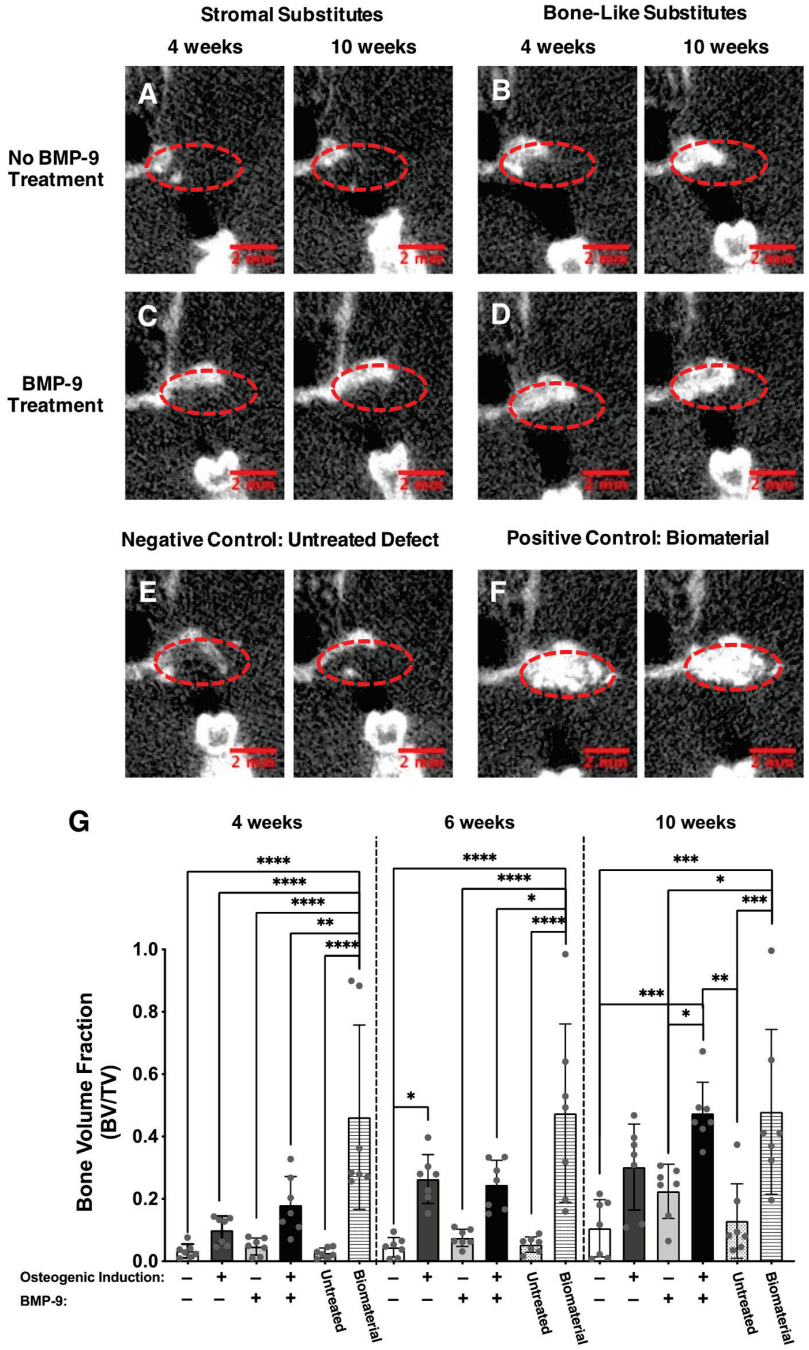


Figure 4. Microcomputed tomography imaging and analysis of the implantation sites. (**A**–**F**) Representative coronal plane images of the implantation sites (red dotted circles) showing alveolar bone preservation (white) following tooth extraction either four and ten weeks after grafting. Scale bars: 2 mm. (**G**) The ratio of bone volume (BV) reported on the tissue volume (TV), also named bone volume fraction (BVF), was calculated at the implantation site four, six, and ten weeks after implantation. Each gray dot represents an implantation site. (Two-way ANOVA with a Bonferroni's multiple comparison post-hoc test, * $p < 0.05$, ** $p < 0.01$, *** $p < 0.001$, **** $p < 0.0001$).

2.5. Gingival Healing

Qualitative assessment of gingival healing was performed ten weeks after tooth extraction before proceeding with the terminal tissue analyses. While no systematic macroscopic imaging follow-ups were realized over time (four, six, and ten weeks), no severe inflammatory and adverse reactions were observed post-operatively on the anesthetized animals during the microcomputed tomography imaging. After ten weeks of implantation, untreated defects, as well as BMP-9-treated stromal substitutes, showed a low rate of re-epithelialization (42.9% and 28.6%, respectively) with the presence of dehiscence or graft exposure (Figure S3A). Elevated re-epithelialization rates were observed when the implantation sites were grafted with bone-like substitutes treated or not with BMP-9 (both 85.7%) (Table 1 and Figure S3B). Gingival healing was considered sufficient when the percentage of re-epithelialization was superior to 85%. These results indicate that, independently of BMP-9 treatment, the bone-like substitutes are interesting candidates to favor gingival healing after tooth extraction.

Table 1. Qualitative evaluation of gingival healing at the implantation sites ten weeks after grafting.

Conditions	Number of Implantation Site Featuring Complete Re-Epithelialization/Total Number of Implantation Sites (% of Re-Epithelialization)
Stromal substitutes	5/7 (71.4%)
Bone-like substitutes	6/7 (85.7%)
BMP-9-treated stromal substitutes	2/7 (28.6%)
BMP-9-treated bone-like substitutes	6/7 (85.7%)
Untreated defects	3/7 (42.9%)
Straumann® BoneCeramic™ biomaterials	5/7 (71.4%)

2.6. Improved Alveolar Bone Healing Observed following Histological Analyses

Alveolar bone healing was evaluated ten weeks after surgery on cross-sections on tissues from the implantation sites stained with hematoxylin and eosin dyes. Stromal substitutes without rhBMP-9 treatment (Figure 5A) and untreated groups (Figure 5E) showed low levels of new bone formation (observable by the presence of purple-colored dense and regular connective tissue) with incomplete regeneration of the bone defects after ten weeks. The BMP-9-treated stromal substitute group revealed a moderate formation of new bone (purple-colored dense and regular connective tissues in Figure 5C). An elevated alveolar bone healing was observed in both the bone-like substitutes supplemented or not with rhBMP-9 treatment (purple-colored dense and regular connective tissues in Figure 5B,D). Observations of the edges of the initial defect showed great integration of the substitutes. On the other hand, histological observations of the biomaterial group showed moderate new bone formation associated with the presence of void spaces (Figure 5F). These empty spaces in histological sections likely correspond to the disappearance of biomaterial granules dissolved during the demineralization step before embedding and staining. Altogether, these results validate the results obtained by microcomputed tomography.

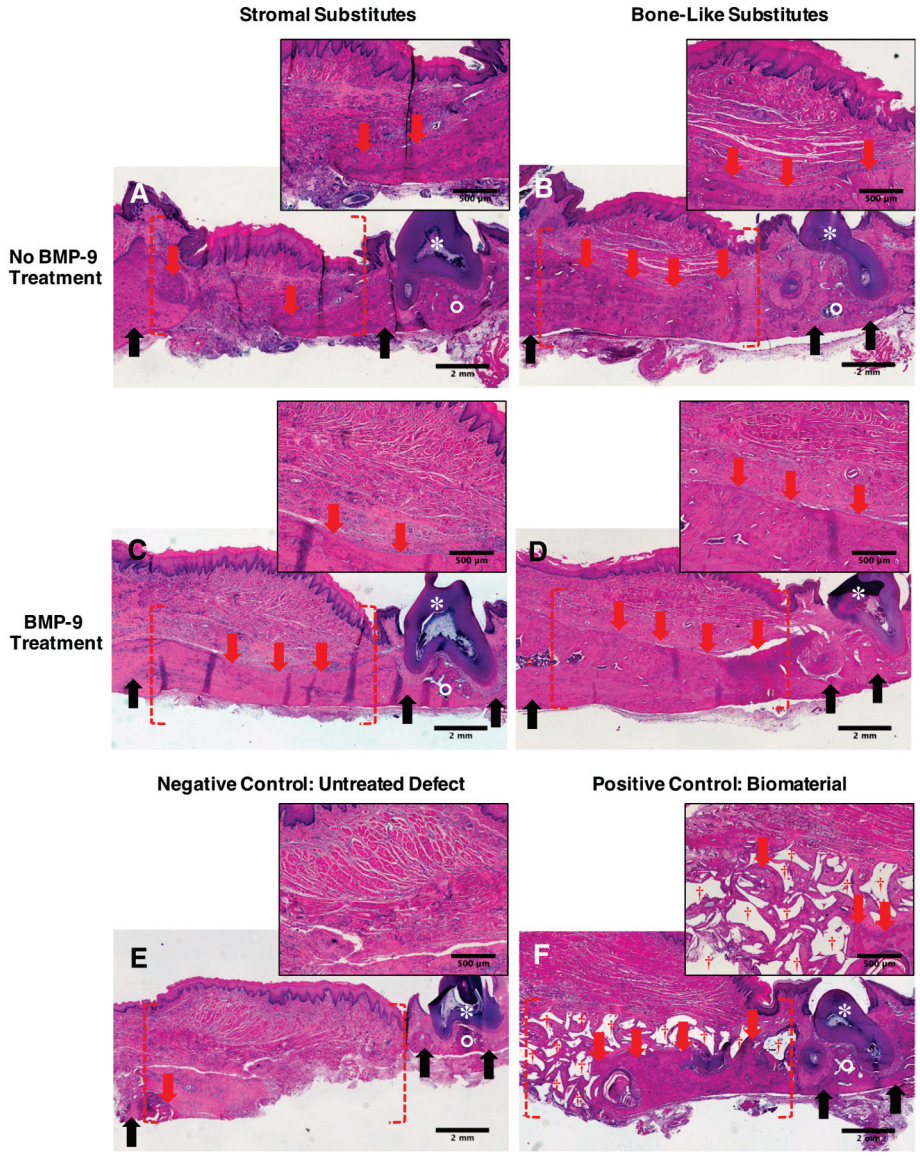


Figure 5. Representative histological observations of the grafting sites. (**A**–**F**) Maxillaries were harvested, fixed, demineralized, paraffin-embedded, and stained using hematoxylin and eosin dyes ten weeks after grafting of the substitutes. Implantation sites (red dashed parentheses) can be identified next to the third superior molar (white asterisks; color: dark purple). The area containing the remaining tooth is delimited by native bone (black arrows; color: purple) surrounding bone marrow (white circle color: dark purple). The new bone that is formed (red arrows; color: purple) is surrounded by dense irregular connective tissue (color: pink) and observed at the grafting sites. (**F**) The presence of empty spaces (red crosses) surrounded by newly formed bone corresponds to the presence of the demineralized biomaterial granules and was observed in the positive control group. Scale bars: 2 mm (large panels) and 500 µm (insets).

3. Discussion

BMPs are widely known for their role in bone regeneration [27–30]. This study evaluated the osteogenic effect of a BMP supplementation during the engineering of self-assembled bone-like substitutes using osteogenically induced hASCs in vitro and the associated potential for alveolar bone healing in vivo. BMP-2 and -9 growth factors are members of the TGF-β superfamily [31,32]. Similar to other BMPs, they activate the Smad-signaling pathway after binding BMP receptors [33] and initiate osteogenic gene expression by the promotion of pro-osteogenic transcription factors such as *RUNX2*, *OSX*, or

functional genes such as *ALP* in various stem cells (rabbit ASCs, C3H10T1/2 mesenchymal cells, C2C12 murine multilineage cells, or mouse embryonic fibroblasts) [34–37]. Runx2 transcription factor plays an essential role in the engagement of stem cells/osteoprogenitors towards the osteochondral differentiation pathway, whereas the osterix transcription factor mainly acts on the terminal phases of osteoblastic differentiation [38,39]. The *ALP* gene is highly expressed by osteoblast cells and is considered an early osteoblastic marker [40].

The osteogenic effect of BMP-9 has been historically established using immortalized murine ASCs [41]. In this study, we show that human postnatal ASCs have a better osteogenic response when exposed to 1 nM of rhBMP-9 than 1 nM of rhBMP-2 in 2D cell culture. This osteogenic induction was reflected by a significant expression of the pro-osteogenic genes *RUNX2*, *OSX*, and *ALP*. Our findings are consistent with a study by Rivera et al. showing that hASCs have higher *ALP* activity under BMP-9 than BMP-2 treatment [42].

Using recombinant adenoviruses expressing fourteen human BMPs, the research group of Dr. He found that BMP-9 is one of the most potent osteoinductive factors [27,43]. The fact that BMP-9 was not affected by Noggin, an extracellular inhibitor of BMPs such as BMP-2, might explain such osteoinductive potential [44]. Our previous studies also showed that both murine and human muscle resident stromal cells (CD31(−) CD34(−) CD90(−) CD73(+) CD105(+) CD140(−) or murine preosteoblasts strongly respond to rhBMP-9 compared with rhBMP-2 in the presence of fetal bovine serum (FBS) [45–47]. For example, based on *ALP* activity measurement, the half-maximum effective concentration (EC50) for rhBMP-9 treatment on human muscle resident mesenchymal stromal cells (hmrSCs) in FBS presence is approximately 40-fold lower compared to rhBMP-2 and 12 times more rhBMP-2 is required to reach the plateau compared with rhBMP-9 (plateau at 1 nM) [45]. Interestingly, human hematoma from fractures and serum from healthy human donors can also potentiate the hmrSC response to rhBMP-9 drastically in terms of osteogenic differentiation [45].

Based on their sequence homology, BMP-2 and BMP-9 are not classified in the same BMP subfamily, and they also do not use the same Ser/Thr kinase type I receptors [31]. BMP-9 interacts with activin receptor-like kinase (ALK) 1 (high affinity) and ALK2, while BMP-2 forms with ALK3 a thermodynamically more stable complex than BMP-9/ALK3 in aqueous solution [31,48,49]. BMP-9 and BMP-2 can induce different mitogen-activated protein kinases cascades activation. For example, the extracellular-signal-regulated kinase 1/2 pathway inhibition and increased p38 phosphorylation in MC3T3-E1 preosteoblasts were suggested to explain the effect of serum on preosteoblast response to rhBMP-9 compared with rhBMP-2 [47]. In addition, the costs being similar between rhBMP-9 and -2, combined with the better osteogenic response of hASCs to BMP-9 compared to BMP-2, suggest a high clinical potential of the treatment proposed in this study. Further studies are required to understand better how BMP-2 and BMP-9 transduce their signal in hASCs.

We thus selected rhBMP-9 to promote osteogenesis within hASC-derived 3D bone-like substitutes, with the aim to achieve more efficient in vivo alveolar bone preservation after tooth extraction. In vitro, the long-term rhBMP-9 supplementation (18 days) of hASC-based bone-like substitutes during their bioproduction (21 days) resulted in a significant increase in osteogenic markers. The cell-secreted *ALP* enzyme is a standard marker used to determine osteogenesis induction level in several mesenchymal cells since it allows the release of phosphate ions from matrix vesicles that are subsequently associated with calcium ions to form hydroxyapatite crystals [50,51]. Indeed, the combined detection of elevated *OSX* and *ALP* gene transcripts and *ALP* enzyme activity suggests that hASCs have reached an advanced stage of osteogenic differentiation in vitro.

To evaluate the alveolar bone preservation potential of the substitutes, engineered tissues were grafted into defects generated after tooth extraction. The positive control group was composed of animals grafted with the clinical-grade BoneCeramic^{TM} biomaterial. This biomaterial already showed effectiveness for calvarial bone defect reconstruction [52] and alveolar bone defect preservation during tooth movement in rats [53]. A clinical trial including thirty patients suffering from posterior edentulous maxillary defects and vertical

bone reductions established that a treatment involving this biomaterial provided similar histological and radiological outcomes compared to autologous bone graft [54]. Therefore, we used this group as a reference although our experimental design did not include the use of an overlying membrane placement as usually performed in a clinical setting.

Our results support that, compared to clinical-grade biomaterial, hASC-derived bone-like substitutes treated in vitro with 1 nM of rhBMP-9 display similar, or even superior, alveolar bone preservation potential following tooth extraction with low variability of bone volume fraction, no sign of resorption, and a stable alveolar bone healing over time (Figure S1A). In addition, the rhBMP-9-treated bone-like substitute showed interesting outcomes of gingival healing, thus suggesting that these new alveolar bone fillers may be as efficient as the clinical-grade biomaterial, which was more exposed to resorption in our study (Figure S2).

Other research groups developed different BMP-9-based strategies for the treatment of bone defects. For example, Nie et al. reported the use of a scaffold composed of coralline hydroxyapatite associated with rat dental follicle stem cells (DFCs) transfected with a recombinant adenoviral vector to overexpress BMP-9 [55]. Briefly, they subcutaneously implanted the scaffolds including DFCs that were transduced with an adenovirus expressing BMP-9, or not, in the *dorsa* of immunodeficient mice. Higher bone volume fractions were measured by micro-CT when the scaffolds were cellularized with untransduced and transduced DFCs compared to the scaffold alone. Additionally, elevated ectopic bone formation was observed when scaffolds were seeded with BMP-9-transduced DFCs compared to control DFCs. More recently, Freitas et al. proposed a cell therapy using genetically edited immortalized bone-marrow MSCs to overexpress BMP-9 using CRISPR-Cas9 technology to favor in vivo bone formation in rat calvarial bone defects [56]. Their micro-CT results clearly showed that genetically modified cells injected within the defects enhanced new bone formation. However, these types of approaches are complex and require careful considerations since the transduction or gene editing processes may remain difficult to control in vivo for long-term bone formation. In this study, we propose a self-assembly approach of tissue engineering that uses a more basic construct composed of a completely biological material composed of human cell-assembled extracellular matrix components. In addition, this bioinspired material includes living human ASCs that were osteogenically induced, but not genetically modified, and treated with a precise concentration of 1 nM rhBMP-9 in vitro until implantation. While rhBMP-9 can be trapped within the biomaterial during its bioproduction, the quantity of molecules released should be low and short-term once implanted. This type of molecular action makes the biomaterial safer than one containing genetically modified cells that continuously secrete BMP-9 molecules.

We previously showed that a traditional osteogenic induction cocktail can enhance the transcription and protein secretion of *angiopoietin-1* by hASCs [24]. The current results indicated that rhBMP-9 supplementation to the same osteogenic media further increased the expression of *angiopoietin-1* gene transcript. The *angiopoietin-1* (*ANG-1*) protein promotes in vitro angiogenesis by stimulating endothelial cell migration, tubule-like structure formation, and in vivo neovascularization [57–59]. These pro-angiogenic properties are expected to enhance therapeutic outcomes when substitutes are implanted in vivo, in particular by promoting graft neovascularization that would favor bone healing [57–59]. Since we previously showed in a rodent calvarial bone defect model that prevascularized bone-like substitutes improved the graft survival after 12 weeks of implantation [25], we hypothesize that adding a rhBMP-9 treatment to our protocols would allow the production of a prevascularized bone-like substitute with superior in vivo bone healing level and graft survival.

4. Materials and Methods

4.1. Human Adipose-Derived Stromal/Stem Cell Isolation, and Expansion

Human ASCs were isolated from a donor (informed written consent was obtained from a healthy female donor, age: 35, body mass index: 21.0 (weight in kilograms divided by the

square of the height in meters)) according to our previously described protocols [60], following subcutaneous adipose tissue lipoaspiration procedures. For the monolayer cultures with BMPs, as well as before the production of the tissue-engineered substitutes, cryopreserved hASCs (Passages 5 and 6, respectively) were first expanded in Dulbecco's modified Eagle's medium (DMEM) supplemented with 10% fetal bovine serum (FBS) (Wisent Bioproducts, St-Bruno, QC, Canada) and antibiotics (100 U/mL penicillin (Sigma-Aldrich, Oakville, ON, Canada) and 25 g/mL gentamicin (Schering-Plough Canada Inc./Merck, Scarborough, ON, Canada)) and cultured in a humidified 37 °C incubator with 8% CO_2.

4.2. Monolayer Cell Culture and BMP Response Assays

To determine which BMP favored hASC osteogenesis in vitro, cells were seeded at a density of 4000 cells/cm^2 (Passage 5) in 6-well plates and grown in DMEM supplemented with 10% FBS (Wisent Bioproducts), antibiotics (100 U/mL penicillin and 25 μg/mL gentamicin), and 1.8 mM calcium chloride ($CaCl_2$; Sigma-Aldrich) (referred to as stromal control medium). Cells were grown until approximately 80% confluency (three days of culture). After three days of culture, osteogenic induction was initiated for half of the cultures by supplementing the medium with an osteogenic cocktail composed of 10 nM dexamethasone, 10 nM 1α,25-dihydroxyvitamin D_3, 50 μM ascorbate-2-phosphate, and 3.5 mM β-glycerophosphate (induction medium). All described supplements were purchased from Sigma-Aldrich. At the same time, for the BMP-treated groups, half of the osteogenically induced hASCs and half of the non-induced controls were treated with 1 nM rhBMP-2 or 1 nM rhBMP-9 (carrier-free CHO, R&D Systems, Minneapolis, MN, USA) for three or six days. The dose was selected based upon previous BMP dose responses performed on human muscle-resident mesenchymal stromal cells [45] and was confirmed with hASCs (Figure S4). The medium was changed three times per week with a freshly prepared BMP supplementation.

4.3. Production of the Tissue-Engineered Substitutes

For in vitro and in vivo studies, substitutes were assigned to four experimental groups: stromal substitutes, bone-like substitutes, BMP-9-treated stromal substitutes, and BMP-9-treated bone-like substitutes (Table 2). Tissues were obtained by seeding hASCs at a density of 4000 cells/cm^2 (Passage 7) in 6-well plates containing a peripheric anchorage device (Whatman paper, Fisher Scientific, Quebec City, QC, Canada), as previously described [23–25,61]. Cells were first grown in DMEM supplemented with 10% FBS, antibiotics, and 1.8 mM calcium chloride ($CaCl_2$) (basal stromal control medium). Stromal substitutes composed of undifferentiated hASCs were obtained using the basal stromal control medium supplemented with fresh sodium L-ascorbate solution (50 μg/mL; Sigma-Aldrich) at each media change for 21 days of culture. For the bone-like group, hASCs were osteogenically induced by supplementing complete DMEM with an osteogenic cocktail composed of 10 nM dexamethasone, 10 nM 1α,25-dihydroxyvitamin D_3, and 50 μM ascorbate-2-phosphate (induction medium) after three days of culture including fresh sodium L-ascorbate solution (50 μg/mL) at each media change until the end of the culture. The induction medium was supplemented with 3.5 mM β-glycerophosphate at Day 10 of culture to initiate biomineralization. BMP-treated groups were produced by adding rhBMP-9 to freshly prepared induction or basal stromal control media (1 nM final) after three days and until the end of the culture. Of note, hASC cultures were exposed to a wave-like dynamic movement using an orbital platform (Model 260301F, Ocelot, Fisher Scientific) set at 35 rpm, beginning one day after initial seeding until the end of the culture period. Substitutes were analyzed or implanted after 21 days of culture (18 days of osteogenic induction for the bone-like groups) since this time point allows the best balance between culture time and handling ability [24].

Table 2. List of the experimental groups for in vitro assays and in vivo implantation studies.

Groups	In Vitro Osteogenic Induction	In Vitro BMP Treatment
Stromal substitutes	-	-
Bone-like substitutes	+	-
BMP-9-treated stromal substitutes	-	+
BMP-9-treated bone-like substitutes	+	+
Untreated defects	N/A	N/A
Straumann® BoneCeramic™ biomaterial	N/A	N/A

N/A: Not applicable.

4.4. Real-Time Quantitative Polymerase Chain Reactions

Quantitative reverse-transcription polymerase chain reaction (RT-qPCRs) was performed on 2D cell cultures (n = 6 samples/condition) and tissue-engineered substitutes (n = 4 substitutes/condition, Day 21 of culture). Total ribonucleic acid (RNA) was extracted using the TRIzol reagent (Invitrogen, Carlsbad, ON, Canada) following the manufacturer's instructions. RNA was then precipitated with isopropanol (Fisher, Mississauga, ON, Canada), centrifuged (12,000× g), washed twice with ethyl alcohol (75% v/v; Fisher), and partially dried in a vacuum centrifuge IA120 SpeedVac concentrator; Thermo Electron Corporation, Madison, WI, USA). The total RNA concentration was quantified by spectrophotometry at 260/280 nm using GeneQuant Pro (Biochrom, Cambridge, UK). Aliquots of RNA (1 µg) were treated with DNase I (1 U/µL), and the first-strand cDNA was synthesized using dNTP (10 mM), Oligo(dT)$_{12–18}$ primer (500 µg/µL), and Superscript™ II reverse transcriptase (200 U/µL) (Invitrogen, Carlsbad, Canada). Quantitative reverse-transcription PCR (RT-qPCR) was carried out using the primers (Qiagen, Montréal, QC, Canada), listed in Table 3, and iQ™ SYBR® Green Supermix (Taq polymerase with SYBR green; BioRad Laboratories, Mississauga, ON, Canada), in triplicate, on an iQ™ Real-Time PCR detection system (BioRad Laboratories, Mississauga, Canada). All assays were normalized to the *Glyceraldehyde-3-phosphate dehydrogenase* (*GADPH*) reference gene, and relative expression levels of the target genes were calculated using the $2^{-\Delta\Delta CT}$ model [62].

Table 3. List of the primer sequences of target genes used for RT-qPCR.

Human Gene	Description	QuantiTect Primer Assay
ALP	*Alkaline phosphatase*	Hs_ALPL_1_SG
RUNX2	*Runt-related transcription factor 2*	Hs_Runx2_1_SG
OSX/SP7	*Osterix transcription factor Sp7*	Hs_Sp7_1_SG
ANG-1	*Angiopoietin-1*	Hs_ANGPT1_1_SG
GAPDH	*Glyceraldehyde-3-phosphate dehydrogenase*	Hs_GAPDH_1_SG

4.5. Alkaline Phosphatase Activity Measurement

ALP activity was measured after 21 days of culture within media conditioned for 48 h by the substitutes before their in vivo implantation. The activity was evaluated by measuring the hydrolysis rate of p-nitrophenyl phosphate disodium hexahydrate (pNPP) (Santa Cruz Biotechnology, Dallas, TX, USA) as a 5 mM solution in 0.5 M 2-amino-2-methyl-1,3-propanediol/2 mM $MgCl_2$ buffer (pH = 10.0). For each condition, fifty microliters of conditioned supernatant were combined with an equal volume of 5 mM pNPP and run in duplicate in a 96-well plate. The *ALP* activity converted substrate pNPP into a p-nitrophenol (pNP) product that was measured at 405 nm using a spectrophotometer after a 30-min incubation period. Results were normalized by total protein content determined by micro-BCA assay quantification (ThermoFisher Scientific, Burlington, ON, Canada) (n = 3 substitutes/conditions).

4.6. In Vivo Surgical Procedures

To evaluate the bone tissue preservation's potential of the engineered substitutes, alveolar bone defects were generated using a model of immunocompromised NIH-Foxn1^{rnu} rats (21 males, 6–7 weeks old at time of surgery; Charles River, Saint-Constant, QC, Canada) (Figure 6). These animals have a compromised adaptive immune system that tolerates the grafting of human tissues [63]. The surgeries were performed under general anesthesia using ketamine/xylazine intraperitoneal (IP) injection (80/10 mg/kg). Analgesia was provided by IP injection of buprenorphine (0.05 mg/kg) and local injection of lidocaine/bupivacaine (3.5 mg/kg). To generate the defects, two molars on both sides of the superior maxilla were extracted (Figure 6A). A 2 mm diameter drill was then used to simulate alveolar bone loss following tooth extraction and to generate bone defects of approximately 4 mm^3 (Figure 6B). Before implantation, each type of engineered substitute was washed using sterile PBS and gently detached from the culture plates to generate a compact tissue mass (Figure 6C). The sockets were then filled to the crest with these compacted substitutes (one engineered tissue by socket) or granules of Straumann® BoneCeramic™ biomaterials according to the groups described in Table 2 (for each animal, two different types of substitutes were randomly implanted bilaterally, $n = 7$ for each group) (Figure 6D). Finally, the buccal and palatal gingivae surrounding the implantation site were sutured using a non-traumatic needle and sterile 5-0 nylon suture thread (Mononylon®, Ethicon, Bridgewater Township, NJ, USA) (Figure 6E). The sockets of the untreated animals remained empty, and the gingivae were sutured as described for the other groups.

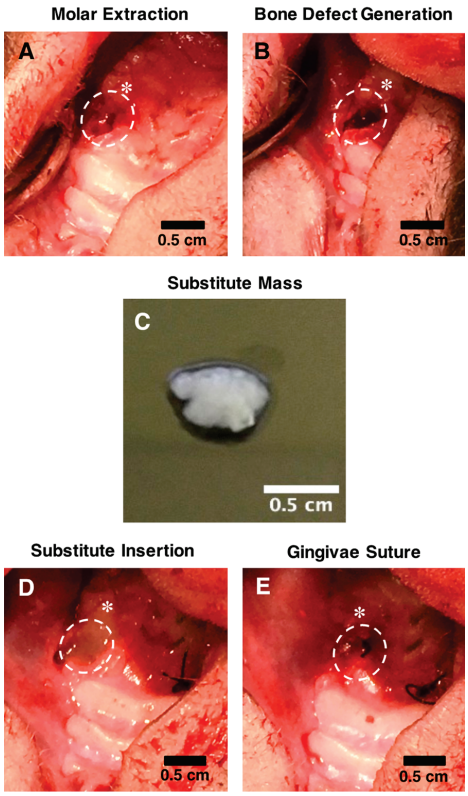


Figure 6. Surgical procedure to assess alveolar bone preservation within a nude RNU rat model. (**A**) Two front molars were extracted bilaterally from the superior maxilla of the rats, and (**B**) 4 mm^3 holes were subsequently generated using a drill to simulate bone loss following tooth extraction. (**C**) Before grafting, the engineered substitutes were detached from the peripheral anchoring device used during culture and compacted into a tissue mass. (**D**) Bone defects were filled with the substitutes (random allocation) when applicable, and (**E**) gingivae were sutured to maintain the substitutes in the socket. Dotted white circles show the implantation site. The white stars indicate the remaining molar. Scale bars: 0.5 cm.

4.7. Microcomputed Tomography Imaging and Analysis

A longitudinal study was performed with non-invasive assessments using a micro-computed tomography system with the GE eXplore Locus 80 scanner (GE Healthcare Technologies, Milwaukee, WI, USA). The animal heads were imaged using standard scanning conditions (tube voltage: 80 kV, tube current: 100 µA, exposure time: 90 mS, detectors bin mode: 2 × 2) after four, six, and ten weeks of implantation. Animals were anesthetized by isoflurane inhalation during imaging. The calibration of the standard curve was based on the density of air: −1000 Hounsfield Units (HU), water: 0 HU, and bone (hydroxyapatite): +3000 to +4000 HU. Imaging and bone volume analysis of the 2 mm × 1 mm × 2 mm ellipsoidal regions of interest (ROIs) were performed using the MicroView software (Parallax Innovations, Ilderton, ON, Canada). All analyses were performed using the same threshold level set at 700 (n = 7 grafts/condition).

4.8. Gingival Healing Evaluation at the Implantation Sites

Macroscopic imaging of the implantation sites was realized post-mortem ten weeks after grafting using a Nikon camera. The quality of gingival healing was evaluated by observing the degree of re-epithelialization at the implantation sites (n = 7 implantation sites/condition). Data are expressed as the percentage of implantation sites that featured complete re-epithelialization.

4.9. Histological Analysis of Explanted Alveolar Implantation Sites

Histological analysis was performed along the implantation sites ten weeks after grafting. These areas were isolated post-mortem from dissected rat skulls. Briefly, the fresh skulls were fixed in 3.7% formaldehyde overnight and demineralized in 0.6 N hydrochloric acid (HCl) for approximately three weeks at room temperature. Then, these areas were isolated from the maxilla of the skull using a scalpel and processed for paraffin embedding and sectioning. Five micrometer thick cross-sections of the samples were stained following a hematoxylin and eosin protocol. Mosaics were obtained by stitching multiple pictures of the samples captured under brightfield using a Zeiss Observer Z1 inverted microscope (Zeiss) equipped with an AxioCam ICc1 camera.

4.10. Statistical Analyses

The mean differences between groups were evaluated by performing one-way or two-way (for data where the time factor is involved) ANOVA with Bonferroni's multiple comparison post-hoc tests using the GraphPad Prism software (version 8). All data are expressed as the mean ± standard deviation (SD), and differences with a $p < 0.05$ are considered significant.

5. Conclusions

In this study, we have shown that hASCs display a better osteogenic response to rhBMP-9 than rhBMP-2 in monolayer cell culture. This was confirmed through the engineering of a 3D bone-like substitute composed of hASCs and cell-assembled extracellular matrix components since rhBMP-9 treatment significantly increased *OSX* pro-osteogenic gene expression and alkaline phosphatase activity after 21 days of culture in vitro. Surprisingly, the long-term rhBMP-9 treatment also significantly increased the gene expression of the pro-angiogenic *angiopoietin-1*. Then, upon grafting, BMP-9-treated bone-like substitutes procured favorable alveolar bone and gingival healing following tooth extraction after ten weeks using a nude rat model. Globally, these substitutes offer promising potential as new biological bone fillers to improve oral bone healing for patients, with the goal of reducing postoperative complications and optimizing dental implant positioning.

Supplementary Materials: The following supporting information can be downloaded at: https://www.mdpi.com/article/10.3390/ijms23063302/s1.

Author Contributions: F.K.: conceptualization, methodology, validation, formal analysis, investigation, data curation, writing—original draft, and visualization. J.J.: methodology and formal analysis. M.F.: methodology, validation, writing—review and editing, resources, and funding acquisition. F.A.A.: conceptualization, validation, resources, and funding acquisition. N.F.: conceptualization, validation, writing—review and editing, resources, and funding acquisition. J.F.: conceptualization, validation, writing—review and editing, resources, project administration, and funding acquisition. All authors have read and agreed to the published version of the manuscript.

Funding: This work was funded by the Quebec Network for cell, tissue, and gene therapy—*ThéCell*, a thematic network supported by "*Fonds de recherche du Québec–Santé*" (*FRQS*). The confocal imaging system was obtained through the "*Fonds des leaders*" program from the Canada Foundation for Innovation (CFI) (to J.F.).

Institutional Review Board Statement: Protocols using human cells were approved by the institutional review board of the Centre de Recherche du CHU de Québec-Université Laval (DR-002-1117). For studies involving animals, protocols were approved by the "*Comité de Protection des Animaux de l'Université Laval*" (*CPAUL*) (Protocol Approval Number: 17-075-1).

Informed Consent Statement: Informed written consent was obtained from the donors according to approbations granted by the institutional review board of the "*Centre de Recherche du CHU de Québec-Université Laval*".

Data Availability Statement: The data presented in this study are available on request from the corresponding author.

Acknowledgments: The authors acknowledge the support of the "*CHU de Québec-Université Laval*" Research Center of the *FRQS*, as well as their animal facilities ("*Hôpital Enfant-Jésus*" for the surgery and "*Centre Hospitalier de l'Université Laval*" for housing). F. Kawecki received studentships by the "*CHU de Québec*" Foundation—Regenerative Medicine Division and the "*Laboratoire d'Organogenèse EXperimentale*" (*LOEX*). The authors thank Jean Lagueux and Marc-André Fortin from the small animal imaging center of the "*CRCHU de Québec-Université Laval*" for micro-CT scanning. The authors also thank the histology team of the *LOEX*, as well as Todd Galbraith, William P. Clafshenkel, and Mathieu Blais.

Conflicts of Interest: The authors declare no conflict of interest.

References

1. Passarelli, P.C.; Pagnoni, S.; Piccirillo, G.B.; Desantis, V.; Benegiamo, M.; Liguori, A.; Papa, R.; Papi, P.; Pompa, G.; D'Addona, A. Reasons for tooth extractions and related risk factors in adult patients: A cohort study. *Int. J. Environ. Res. Public Health* **2020**, *17*, 2575. [CrossRef]
2. Avila-Ortiz, G.; Elangovan, S.; Kramer, K.W.O.; Blanchette, D.; Dawson, D.V. Effect of alveolar ridge preservation after tooth extraction: A systematic review and meta-analysis. *J. Dent. Res.* **2014**, *93*, 950–958. [CrossRef] [PubMed]
3. Guglielmotti, M.B.B.; Cabrini, R.L.L. Alveolar wound healing and ridge remodeling after tooth extraction in the rat: A histologic, radiographic, and histometric study. *J. Oral Maxillofac. Surg.* **1985**, *43*, 359–364. [CrossRef]
4. Horowitz, R.; Holtzclaw, D.; Rosen, P.S. A review on alveolar ridge preservation following tooth extraction. *J. Evid. Based. Dent. Pract.* **2012**, *12*, 149–160. [CrossRef]
5. Johnson, K. A study of the dimensional changes occurring in the maxilla following tooth extraction. *Aust. Dent. J.* **1969**, *14*, 241–244. [CrossRef]
6. Cardaropoli, G.; Araújo, M.; Lindhe, J. Dynamics of bone tissue formation in tooth extraction sites: An experimental study in dogs. *J. Clin. Periodontol.* **2003**, *30*, 809–818. [CrossRef]
7. Becker, W.; Becker, B.E.; Caffesse, R. A Comparison of Demineralized Freeze-Dried Bone and Autologous Bone to Induce Bone Formation in Human Extraction Sockets. *J. Periodontol.* **1994**, *65*, 1128–1133. [CrossRef]
8. Cantín, M.; Olate, S.; Fuentes, R.; Vásquez, B. Alveolar Ridge Conservation by Early Bone Formation After Tooth Extraction in Rabbits: A Histomorphological Study. *Int. J. Morphol.* **2015**, *33*, 369–374. [CrossRef]
9. Wang, S.; Zhang, Z.; Zhao, J.; Zhang, X.; Sun, X.; Xia, L.; Chang, Q.; Ye, D.; Jiang, X. Vertical alveolar ridge augmentation with beta-tricalcium phosphate and autologous osteoblasts in canine mandible. *Biomaterials* **2009**, *30*, 2489–2498. [CrossRef]
10. Araujo-Pires, A.C.; Mendes, V.C.; Ferreira-Junior, O.; Carvalho, P.S.P.; Guan, L.; Davies, J.E. Investigation of a Novel PLGA/CaP Scaffold in the Healing of Tooth Extraction Sockets to Alveolar Bone Preservation in Humans. *Clin. Implant Dent. Relat. Res.* **2016**, *18*, 559–570. [CrossRef]

11. Mardas, N.; Chadha, V.; Donos, N. Alveolar ridge preservation with guided bone regeneration and a synthetic bone substitute or a bovine-derived xenograft: A randomized, controlled clinical trial. *Clin. Oral Implants Res.* **2010**, *21*, 688–698. [CrossRef] [PubMed]
12. Heberer, S.; Al-Chawaf, B.; Hildebrand, D.; Nelson, J.J.; Nelson, K. Histomorphometric analysis of extraction sockets augmented with Bio-Oss Collagen after a 6-week healing period: A prospective study. *Clin. Oral Implants Res.* **2008**, *19*, 1219–1225. [CrossRef] [PubMed]
13. Sheikh, Z.; Brooks, P.J.; Barzilay, O.; Fine, N.; Glogauer, M. Macrophages, foreign body giant cells and their response to implantable biomaterials. *Materials* **2015**, *8*, 5671–5701. [CrossRef] [PubMed]
14. Berbéri, A.; Fayyad-kazan, M.; Ayoub, S.; Bou Assaf, R.; Sabbagh, J.; Ghassibe-Sabbagh, M.; Badran, B. Osteogenic potential of dental and oral derived stem cells in bone tissue engineering among animal models: An update. *Tissue Cell* **2021**, *71*, 101515. [CrossRef]
15. Kalyani, P.; Santhosh Kumar, M.P. Tissue engineering in oral and maxillofacial surgery—A literature review. *Int. J. Pharm. Res.* **2020**, *12*, 1948–1954.
16. Patel, N.; Kim, B.; Zaid, W.; Spagnoli, D. Tissue Engineering for Vertical Ridge Reconstruction. *Oral Maxillofac. Surg. Clin.* **2017**, *29*, 27–49. [CrossRef]
17. Barcak, E.A.; Beebe, M.J. Bone Morphogenetic Protein: Is There Still a Role in Orthopedic Trauma in 2017? *Orthop. Clin.* **2017**, *48*, 301–309. [CrossRef]
18. Dietz, N.; Sharma, M.; Kelly, M.; Ugiliweneza, B.; Wang, D.; Osorio, J.; Karikari, I.; Drazin, D.; Boakye, M. Recombinant Human Bone Morphogenetic Protein–2 Use in Adult Spinal Deformity Surgery: Comparative Analysis and Healthcare Utilization at 24 Months' Follow-up. *Glob. Spine J.* **2020**, *26*, 2192568220947377. [CrossRef]
19. Jung, R.E.; Windisch, S.I.; Eggenschwiler, A.M.; Thoma, D.S.; Weber, F.E.; Hämmerle, C.H.F. A randomized-controlled clinical trial evaluating clinical and radiological outcomes after 3 and 5 years of dental implants placed in bone regenerated by means of GBR techniques with or without the addition of BMP-2. *Clin. Oral Implants Res.* **2009**, *20*, 660–666. [CrossRef]
20. Thoma, D.S.; Bienz, S.P.; Payer, M.; Hüsler, J.; Schmidlin, P.R.; Hämmerle, C.H.F.; Jakse, N.; Jung, R.E. Randomized clinical study using xenograft blocks loaded with bone morphogenetic protein-2 or autogenous bone blocks for ridge augmentation—A three-dimensional analysis. *Clin. Oral Implants Res.* **2019**, *30*, 872–881. [CrossRef]
21. Huang, X.; Wang, F.; Zhao, C.; Yang, S.; Cheng, Q.; Tang, Y.; Zhang, F.; Zhang, Y.; Luo, W.; Wang, C.; et al. Dentinogenesis and Tooth-Alveolar Bone Complex Defects in BMP9/GDF2 Knockout Mice. *Stem Cells Dev.* **2019**, *28*, 683–694. [CrossRef] [PubMed]
22. Saulacic, N.; Fujioka-Kobayashi, M.; Kobayashi, E.; Schaller, B.; Miron, R.J. Guided bone regeneration with recombinant human bone morphogenetic protein 9 loaded on either deproteinized bovine bone mineral or a collagen barrier membrane. *Clin. Implant Dent. Relat. Res.* **2017**, *19*, 600–607. [CrossRef] [PubMed]
23. Galbraith, T.; Clafshenkel, W.P.; Kawecki, F.; Blanckaert, C.; Labbé, B.; Fortin, M.; Auger, F.A.; Fradette, J. A Cell-Based Self-Assembly Approach for the Production of Human Osseous Tissues from Adipose-Derived Stromal/Stem Cells. *Adv. Healthc. Mater.* **2017**, *6*, 1600889. [CrossRef] [PubMed]
24. Kawecki, F.; Clafshenkel, W.P.; Auger, F.A.; Bourget, J.M.; Fradette, J.; Devillard, R. Self-assembled human osseous cell sheets as living biopapers for the laser-assisted bioprinting of human endothelial cells. *Biofabrication* **2018**, *10*, 035006. [CrossRef]
25. Kawecki, F.; Galbraith, T.; Clafshenkel, W.P.; Fortin, M.; Auger, F.A.; Fradette, J. In vitro prevascularization of self-assembled human bone-like tissues and preclinical assessment using a rat calvarial bone defect model. *Materials* **2021**, *14*, 2023. [CrossRef]
26. Zuk, P.A.; Ph, D.; Zhu, M.I.N.; Mizuno, H.; Benhaim, P.; Lorenz, H.P. Multilineage Cells from Human Adipose Tissue: Implications for Cell-Based Therapies. *Tissue Eng.* **2001**, *7*, 211–228. [CrossRef]
27. Kang, Q.; Sun, M.H.; Cheng, H.; Peng, Y.; Montag, A.G.; Deyrup, A.T.; Jiang, W.; Luu, H.H.; Luo, J.; Szatkowski, J.P.; et al. Characterization of the distinct orthotopic bone-forming activity of 14 BMPs using recombinant adenovirus-mediated gene delivery. *Gene Ther.* **2004**, *11*, 1312–1320. [CrossRef] [PubMed]
28. Lee, J.-S.; Jung, J.-S.; Im, G.-I.; Kim, B.-S.; Cho, K.-S.; Kim, C.-S. Ridge regeneration of damaged extraction sockets using rhBMP-2: An experimental study in canine. *J. Clin. Periodontol.* **2015**, *42*, 678–687. [CrossRef]
29. Schmidmaier, G.; Schwabe, P.; Wildemann, B.; Haas, N.P. Use of bone morphogenetic proteins for treatment of non-unions and future perspectives. *Injury* **2007**, *38*, S35–S41. [CrossRef]
30. Wikesjö, U.; Qahash, M.; Huang, Y.-H.; Xiropaidis, A.; Polimeni, G.; Susin, C. Bone morphogenetic proteins for periodontal and alveolar indications; biological observations—clinical implications. *Orthod. Craniofac. Res.* **2009**, *12*, 263–270. [CrossRef]
31. Brown, M.A.; Zhao, Q.; Baker, K.A.; Naik, C.; Chen, C.; Pukac, L.; Singh, M.; Tsareva, T.; Parice, Y.; Mahoney, A.; et al. Crystal structure of BMP-9 and functional interactions with pro-region and receptors. *J. Biol. Chem.* **2005**, *280*, 25111–25118. [CrossRef] [PubMed]
32. Urist, M.R. Bone Morphogenetic Protein: The Molecularization of Skeletal System Development. *J. Bone Miner. Res.* **1997**, *12*, 343–346. [CrossRef]
33. Blanco Calvo, M.; Bolós Fernández, V.; Medina Villaamil, V.; Aparicio Gallego, G.; Díaz Prado, S.; Grande Pulido, E. Biology of BMP signalling and cancer. *Clin. Transl. Oncol.* **2009**, *11*, 126–137. [CrossRef] [PubMed]
34. Rahman, M.S.; Akhtar, N.; Jamil, H.M.; Banik, R.S.; Asaduzzaman, S.M. TGF-β/BMP signaling and other molecular events: Regulation of osteoblastogenesis and bone formation. *Bone Res.* **2015**, *3*, 15005. [CrossRef] [PubMed]

35. Chai, Y.; Liu, F.; Li, Q.; Shen, Y.; Ding, W.Y. BMP-9 induces rabbit adipose-derived stem cells to differentiation into osteoblasts via BMP signaling pathway. *Anal. Quant. Cytol. Histol.* **2013**, *35*, 171–177.
36. Cao, J.; Wei, Y.; Lian, J.; Yang, L.; Zhang, X.; Xie, J.; Liu, Q.; Luo, J.; He, B.; Tang, M. Notch signaling pathway promotes osteogenic differentiation of mesenchymal stem cells by enhancing BMP9/Smad signaling. *Int. J. Mol. Med.* **2017**, *40*, 378–388. [CrossRef]
37. Ji, C.; Liu, X.; Xu, L.; Yu, T.; Dong, C.; Luo, J. RUNX1 Plays an Important Role in Mediating BMP9-Induced Osteogenic Differentiation of Mesenchymal Stem Cells Line C3H10T1/2, Murine Multi-Lineage Cells Lines C2C12 and MEFs. *Int. J. Mol. Sci.* **2017**, *18*, 1348. [CrossRef]
38. Nakashima, K.; Zhou, X.; Kunkel, G.; Zhang, Z.; Deng, J.M.; Behringer, R.R.; De Crombrugghe, B. The novel zinc finger-containing transcription factor Osterix is required for osteoblast differentiation and bone formation. *Cell* **2002**, *108*, 17–29. [CrossRef]
39. Wu, L.; Wu, Y.; Lin, Y.; Jing, W.; Nie, X.; Qiao, J.; Liu, L.; Tang, W.; Tian, W. Osteogenic differentiation of adipose derived stem cells promoted by overexpression of osterix. *Mol. Cell. Biochem.* **2007**, *301*, 83–92. [CrossRef]
40. Buchet, R.; Millán, J.L.; Magne, D. Multisystemic functions of alkaline phosphatases. In *Phosphatase Modulators. Methods in Molecular Biology (Clifton, N.J.)*; Millán, J., Ed.; Humana Press: Totowa, NJ, USA, 2013; Volume 1053, pp. 27–51.
41. Lu, S.; Wang, J.; Ye, J.; Zou, Y.; Zhu, Y.; Wei, Q.; Wang, X.; Tang, S.; Liu, H.; Fan, J.; et al. Bone morphogenetic protein 9 (BMP9) induces effective bone formation from reversibly immortalized multipotent adipose-derived (iMAD) mesenchymal stem cells. *Am. J. Transl. Res.* **2016**, *8*, 3710–3730.
42. Rivera, J.C.; Strohbach, C.A.; Wenke, J.C.; Rathbone, C.R. Beyond osteogenesis: An in vitro comparison of the potentials of six bone morphogenetic proteins. *Front. Pharmacol.* **2013**, *4*, 125. [CrossRef]
43. Cheng, H.; Jiang, W.; Phillips, F.M.; Haydon, R.C.; Peng, Y.; Zhou, L.; Luu, H.H.; An, N.; Breyer, B.; Vanichakarn, P.; et al. Osteogenic activity of the fourteen types of human bone morphogenetic proteins (BMPs). *J. Bone Jt. Surg. Ser. A* **2003**, *85*, 1544–1552. [CrossRef] [PubMed]
44. Wang, Y.; Hong, S.; Li, M.; Zhang, J.; Bi, Y.; He, Y.; Liu, X.; Nan, G.; Su, Y.; Zhu, G.; et al. Noggin resistance contributes to the potent osteogenic capability of BMP9 in mesenchymal stem cells. *J. Orthop. Res.* **2013**, *31*, 1796–1803. [CrossRef] [PubMed]
45. Alinejad, Y.; Lauzon, M.A.; Grenier, G.; Balg, F.; Faucheux, N. Both human hematoma punctured from pelvic fractures and serum increase muscle resident stem cells response to BMP9: A multivariate statistical approach. *J. Clin. Med.* **2020**, *9*, 1175. [CrossRef] [PubMed]
46. Drouin, G.; Couture, V.; Lauzon, M.A.; Balg, F.; Faucheux, N.; Grenier, G. Muscle injury-induced hypoxia alters the proliferation and differentiation potentials of muscle resident stromal cells. *Skelet. Muscle* **2019**, *9*, 1–14. [CrossRef] [PubMed]
47. Lauzon, M.-A.; Daviau, A.; Drevelle, O.; Marcos, B.; Faucheux, N. Identification of a Growth Factor Mimicking the Synergistic Effect of Fetal Bovine Serum on BMP-9 Cell Response. *Tissue Eng. Part A* **2014**, *20*, 2524–2535. [CrossRef]
48. Coskuner, O.; Uversky, V.N. BMP-2 and BMP-9 binding specificities with ALK-3 in aqueous solution with dynamics. *J. Mol. Graph. Model.* **2017**, *77*, 181–188. [CrossRef]
49. Scharpfenecker, M.; van Dinther, M.; Liu, Z.; van Bezooijen, R.L.; Zhao, Q.; Pukac, L.; Löwik, C.W.G.M.; ten Dijke, P. BMP-9 signals via ALK1 and inhibits bFGF-induced endothelial cell proliferation and VEGF-stimulated angiogenesis. *J. Cell Sci.* **2007**, *120*, 964–972. [CrossRef]
50. Golub, E.E.; Boesze-Battaglia, K. The role of alkaline phosphatase in mineralization. *Curr. Opin. Orthop.* **2007**, *18*, 444–448. [CrossRef]
51. Glimcher, M.J. The nature of the mineral component of bone and the mechanism of calcification. *Instr. Course Lect.* **1987**, *36*, 49–69.
52. Fabris, A.L.d.S.; Faverani, L.P.; Gomes-Ferreira, P.H.S.; Polo, T.O.B.; Santiago-Júnior, J.F.; Okamoto, R. Bone repair access of BoneCeramic™ in 5-mm defects: Study on rat calvaria. *J. Appl. Oral Sci.* **2018**, *26*, e20160531. [CrossRef] [PubMed]
53. Ru, N.; Liu, S.S.-Y.; Bai, Y.; Li, S.; Liu, Y.; Zhou, G. Microarchitecture and Biomechanical Evaluation of BoneCeramic Grafted Alveolar Defects during Tooth Movement in Rat. *Cleft Palate. Craniofac. J.* **2018**, *55*, 798–806. [CrossRef] [PubMed]
54. Schmitt, C.M.; Doering, H.; Schmidt, T.; Lutz, R.; Neukam, F.W.; Schlegel, K.A. Histological results after maxillary sinus augmentation with Straumann® BoneCeramic, Bio-Oss®, Puros®, and autologous bone. A randomized controlled clinical trial. *Clin. Oral Implants Res.* **2013**, *24*, 576–585. [CrossRef] [PubMed]
55. Nie, L.; Yang, X.; Duan, L.; Huang, E.; Pengfei, Z.; Luo, W.; Zhang, Y.; Zeng, X.; Qiu, Y.; Cai, T.; et al. The healing of alveolar bone defects with novel bio-implants composed of Ad-BMP9-transfected rDFCs and CHA scaffolds. *Sci. Rep.* **2017**, *7*, 6373. [CrossRef]
56. Freitas, G.P.; Lopes, H.B.; Souza, A.T.P.; Gomes, M.P.O.; Quiles, G.K.; Gordon, J.; Tye, C.; Stein, J.L.; Stein, G.S.; Lian, J.B.; et al. Mesenchymal stem cells overexpressing BMP-9 by CRISPR-Cas9 present high in vitro osteogenic potential and enhance in vivo bone formation. *Gene Ther.* **2021**, *8*, 748–759. [CrossRef]
57. Cascone, I.; Audero, E.; Giraudo, E.; Napione, L.; Maniero, F.; Philips, M.R.; Collard, J.G.; Serini, G.; Bussolino, F. Tie-2-dependent activation of RhoA and Rac1 participates in endothelial cell motility triggered by angiopoietin-1. *Blood* **2003**, *102*, 2482–2490. [CrossRef]
58. Suri, C.; McClain, J.; Thurston, G.; McDonald, D.M.; Zhou, H.; Oldmixon, E.H.; Sato, T.N.; Yancopoulos, G.D. Increased vascularization in mice overexpressing angiopoietin-1. *Science* **1998**, *282*, 468–471. [CrossRef]
59. Cho, C.H.; Sung, H.K.; Kim, K.T.; Cheon, H.G.; Oh, G.T.; Hong, H.J.; Yoo, O.J.; Koh, G.Y. COMP-angiopoietin-1 promotes wound healing through enhanced angiogenesis, lymphangiogenesis, and blood flow in a diabetic mouse model. *Proc. Natl. Acad. Sci. USA.* **2006**, *103*, 4946–4951. [CrossRef]

60. Vermette, M.; Trottier, V.; Ménard, V.; Saint-Pierre, L.; Roy, A.; Fradette, J. Production of a new tissue-engineered adipose substitute from human adipose-derived stromal cells. *Biomaterials* **2007**, *28*, 2850–2860. [CrossRef]
61. Kawecki, F.; Clafshenkel, W.P.; Fortin, M.; Auger, F.A.; Fradette, J. Biomimetic Tissue-Engineered Bone Substitutes for Maxillofacial and Craniofacial Repair: The Potential of Cell Sheet Technologies. *Adv. Healthc. Mater.* **2018**, *7*, 1700919. [CrossRef]
62. Livak, K.J.; Schmittgen, T.D. Analysis of Relative Gene Expression Data Using Real-Time Quantitative PCR and the $2-\Delta\Delta CT$ Method. *Methods* **2001**, *25*, 402–408. [CrossRef] [PubMed]
63. Rolstad, B. The athymic nude rat: An animal experimental model to reveal novel aspects of innate immune responses? *Immunol. Rev.* **2001**, *184*, 136–144. [CrossRef] [PubMed]

International Journal of
Molecular Sciences

MDPI

Article

Microstructure and Selected Properties of Advanced Biomedical n-HA/ZnS/Sulfonated PEEK Coatings Fabricated on Zirconium Alloy by Duplex Treatment

Filip Kuśmierczyk [1,*], Aleksandra Fiołek [1], Alicja Łukaszczyk [2], Agnieszka Kopia [1], Maciej Sitarz [3], Sławomir Zimowski [4], Łukasz Cieniek [1] and Tomasz Moskalewicz [1,*]

[1] Faculty of Metals Engineering and Industrial Computer Science, AGH University of Science and Technology, al. Mickiewicza 30, 30-059 Kraków, Poland; kruka@agh.edu.pl (A.F.); kopia@agh.edu.pl (A.K.); lukasz.cieniek@agh.edu.pl (Ł.C.)
[2] Faculty of Foundry Engineering, AGH University of Science and Technology, al. Mickiewicza 30, 30-059 Kraków, Poland; alicjal@agh.edu.pl
[3] Faculty of Materials Science and Ceramics, AGH University of Science and Technology, al. Mickiewicza 30, 30-059 Kraków, Poland; msitarz@agh.edu.pl
[4] Faculty of Mechanical Engineering and Robotics, AGH University of Science and Technology, al. Mickiewicza 30, 30-059 Kraków, Poland; zimowski@agh.edu.pl
* Correspondence: kusmierczyk@agh.edu.pl (F.K.); tmoskale@agh.edu.pl (T.M.); Tel.: +48-12-617-4527 (T.M.)

Abstract: In this work, sulfonated polyetheretherketone (S-PEEK)-based coatings, nanocrystalline ZnS and hydroxyapatite (n-HA) particles were developed on Zr-2.5Nb zirconium alloy substrates by electrophoretic deposition (EPD) combined with subsequent heat treatment. The properties of suspensions and deposition kinetics were studied. Cationic chitosan polyelectrolyte ensured the stabilization of the suspension and allowed for the co-deposition of all coating components on the cathode. The heating of the coated samples at a temperature of 450 °C and slow cooling resulted in sulfonation of the PEEK and the formation of dense coatings. The coatings were characterized by high roughness, hardness, modulus of elasticity and adhesion strength. The coatings revealed mild hydrophilicity, improved the electrochemical corrosion resistance of the alloy and induced the formation of hydroxyapatite with a cauliflower-like morphology on its surface during the Kokubo test. This work explored the great development potential of advanced sulfonated PEEK-based coatings, incorporating antibacterial and bioactive components by EPD combined with heat treatment to stimulate the surface properties of zirconium alloy for prospective dental and orthopedic applications. The antibacterial and osteoconductive properties of the obtained coatings should be further investigated.

Keywords: zirconium alloy; bioactive coating; sulfonated PEEK; electrophoretic deposition; adhesion strength; corrosion resistance

Citation: Kuśmierczyk, F.; Fiołek, A.; Łukaszczyk, A.; Kopia, A.; Sitarz, M.; Zimowski, S.; Cieniek, Ł.; Moskalewicz, T. Microstructure and Selected Properties of Advanced Biomedical n-HA/ZnS/Sulfonated PEEK Coatings Fabricated on Zirconium Alloy by Duplex Treatment. *Int. J. Mol. Sci.* **2022**, *23*, 3244. https://doi.org/10.3390/ijms23063244

Academic Editor: Mary Anne Melo

Received: 9 February 2022
Accepted: 14 March 2022
Published: 17 March 2022

Publisher's Note: MDPI stays neutral with regard to jurisdictional claims in published maps and institutional affiliations.

Copyright: © 2022 by the authors. Licensee MDPI, Basel, Switzerland. This article is an open access article distributed under the terms and conditions of the Creative Commons Attribution (CC BY) license (https://creativecommons.org/licenses/by/4.0/).

1. Introduction

Zirconium alloys are among the most suitable metallic biomaterials generally exploited as bone implants, i.e., dental and orthopedic replacements [1–3]. Their importance in biomedical applications results from their outstanding properties, such as high electrochemical corrosion resistance, biocompatibility, elasticity modulus of around 90 GPa and density of 6.5 g/cm^3 in the range between titanium alloys and stainless steels [4,5]. The Zr-2.5Nb alloy is one of the best known among biomedical zirconium alloys. It exhibits higher strength, hardness, wear resistance and electrochemical corrosion resistance than that of pure Zr, as well as good in vitro cytocompatibility and emphatically lower magnetic susceptibility than the widely-used cobalt-based alloys and Ti-6Al-4V alloy [6]. Although Zr-2.5Nb biocompatibility is excellent, it has poor osteointegration with bone cells [5,7]. One of the most promising ways of improving its biological properties is the development of bioactive coatings.

The use of polymers as coating materials is beneficial in comparison to metals, because of the reduction in weight and higher electrochemical corrosion resistance. In recent years, polyetheretherketone (PEEK) has been widely studied as a suitable coating material [8–11]. PEEK is a semi-crystalline, high-performance polymer. It is characterized by its outstanding chemical and thermal stability, elastic modulus (3–4 MPa) that is similar to human cancellous bone, good tribological properties, low density (1.32 g/cm^3) and stiffness [10,12,13]. Therefore, it is often used as a replacement for metals in high-end applications, including medical equipment and implants. It is insolvable in water and resistant to a wide range of bases, hydrocarbons, organic solvents and acids [14–18]. PEEK is recognized as having one of the highest levels of chemical stability, mechanical strength and biocompatibility among other biocompatible synthetic polymers. It was found [9,18–21] that the coatings with a PEEK matrix exhibited superior adhesion to metallic substrates, which is crucial for every application. Although it has outstanding properties, PEEK is bioinert [12,18,22,23]. For this reason, various approaches have been used to strengthen these properties, e.g., by introducing bioactive and antibacterial agents into PEEK and sulfonation by chemical treatment with the use of sulfuric acid. In the present work, we propose the use of those two approaches simultaneously by (i) introducing hydroxyapatite (HA) and ZnS nanoparticles into PEEK and (ii) subsequent novel thermal sulfonation combined with the heat treatment of coated zirconium alloy.

HA is one of the most effective and versatile bioactive materials. It is calcium phosphate with the molecular formula $Ca_{10}(PO_4)_6(OH)_2$. This form of calcium phosphate is the least soluble and the most stable of all [24]. Moreover, this bioceramic is an accepted object of research due to its similarity to an inorganic fraction of bone. The presence of hydroxyapatite induces bone formation, which is necessary for implant osteointegration providing excessive fixation to the human bone [18]. Despite its beneficial properties, HA is brittle and has limited resistance to bacterial infections, which are among the most important implant failure factors. The most effective way to overcome this drawback is via the application of an antibacterial agent in coatings. The most important antiseptic agents competing with harmful antibiotics involve metals, their ions and compounds [25–28]. A prospective coating component with an antibacterial function is zinc sulfide, which is newly studied in this regard [29,30]. The ZnS nanoparticle is a potential inorganic antibacterial agent due to its high stability, antimicrobial activity and non-toxicity [29]. Monodisperse zinc sulfide nanospheres exhibited high antibacterial activity against, for example, the strain of *E. coli* bacteria [30,31]. In addition, sulfur is a biogenic element that can increase bioactivity and antimicrobial properties. The sulfur content of this compound may also be a potential source of this element that is required for the thermal sulfonation process of PEEK. Recent studies [32,33] confirmed that sulfonated polyetheretherketone (S-PEEK) exhibits antibacterial properties. Moreover, PEEK sulfonated to an appropriate degree can exceed proliferation and osteogenesis [32]. The most widely used method of PEEK sulfonation is its immersion in concentrated sulfuric acid [32–34]. Despite its versatility, this technique has been reported to have a negative effect on living cells and their DNA, due to sulfur dioxide (SO_2) originating from the use of acid and the production of oxygen free radicals caused by sulfur compounds of low valence [35,36]. In addition, such treatment is not acceptable for coatings due to their easy detachment from metallic substrates. In our study, we propose novel thermal sulfonation combined with heat treatment of the coating, which allows PEEK to be efficiently sulfonated without sulfuric acid. As far as we are aware, no studies have been reported on the development of S-PEEK coatings containing dual antibacterial and bioactive components, which can conceivably improve the osteointegration effect. The application of this coating type is potentially beneficial as it is superior to coated metallic bone implants.

One of the most advantageous surface-engineering methods of developing polymer-based coatings with ceramic particles is electrophoretic deposition (EPD) [9,11,14,18,20–22,37–40]. The process consists of the migration of charged particles immersed in the suspension in the presence of an electric field toward an oppositely

charged electrode. Then, particles deposit on the electrode and form the coating. As for the PEEK coatings, subsequent heat treatment is necessary for their densification. The literature regarding PEEK-based coatings developed by the EPD procedure concerns coatings with osteogenic factors, such as sol-gel glass [17], HA [11,18] as well as bioglass [9,14,21,22,38] and coatings with antibacterial agents involving silver [21] and MoS_2 [20,41]. Bastan et al. [18] concluded that the addition of HA stimulates in vitro bioactivity in HA/PEEK coatings. Advanced PEEK-based composite coatings have been developed using EPD with both osteointegration and antiseptic ingredients. Ur Rehman et al. [15] fabricated PEEK coatings with the addition of lawsone, chitosan and bioglass, while Virk et al. [16] introduced curcumin, bioactive glass and hexagonal boron nitride into the PEEK matrix. In both studies, the coatings showed antibacterial activity, and the formation of an apatite-like layer during the bioactivity test was achieved. However, these coatings were fabricated as multilayers, which usually requires multiple operations during EPD. According to our knowledge, there is a limited number of studies on obtaining multicomponent PEEK-based complexes with bioactive and antibacterial factors simultaneously in one operation [11,20,21]. Seuss et al. [21] reported that electrophoretically deposited PEEK coatings with the addition of Ag particles and bioglass particles provided antibacterial activity. Abdulakareem et al. [11] proved the antiseptic capability of chitosan in HA and chitosan coatings with the addition of PEEK. However, in both of the above-mentioned references, bioactivity studies were not provided.

The aim of this study was to develop a duplex route based on electrophoretic co-deposition and subsequent heat treatment for obtaining multicomponent n-HA/ZnS/S-PEEK coatings on the Zr-2.5Nb alloy, which was used as a substrate material for EPD for the first time. The EPD kinetics were systematically studied and deposition conditions were optimized. The coating surface topography, microstructure and selected properties, including electrochemical corrosion resistance, micromechanical properties, adhesion strength and scratch resistance of the coatings, were investigated.

2. Materials and Methods

2.1. Materials

A Zr-2.5Nb zirconium alloy was used as a substrate for coating deposition. It was supplied by Luoyang Dingding Tungsten and Molybdenum Materials Co., Ltd. (Luoyang, China). A rod with a diameter of 20 mm was cut into discs with a thickness of 3 mm. The discs were ground with sandpaper with a final grade of 600. PEEK (VICOTE 704) powder with a particle size of up to 10 μm was provided by Victrex Europa GmbH, Hofheim am Taunus, Germany. ZnS nanoparticles with a size up to 100 nm were supplied by Nanoshel UK Ltd. (Congleton, U.K.). The n-HA nanoparticles (mean size up to 10 nm, according to the supplier) were produced by the Institute of High Pressure Physics of the Polish Academy of Sciences (Warsaw).

2.2. Coating Deposition and Duplex Treatment Process

Suspensions containing 30 g/L of PEEK 704, 0.4 g/L of ZnS and 1 g/L of n-HA, were used for coating deposition. A mixture of ethanol (with 99.8% purity) and chitosan polyelectrolyte (CHp), with a content of 95 and 5 vol %, respectively, was used as the liquid phase in suspensions. CHp was prepared by dissolving 0.5 g/L of chitosan powder and 1% acetic acid in distilled water by mixing at 600 rpm for 3 days at 23 °C with the use of a magnetic stirrer (IKA RO 5, Burladingen, Germany). The chemical structures of the PEEK and chitosan are presented in Figure 1. After the addition of ZnS and PEEK into the ethanol-CHp solution, it was magnetically stirred for 10 min and ultrasonically dispersed for 20 min to separate the agglomerates of particles. After the addition of n-HA powder, the suspension was further mixed and dispersed for 10 min. Zeta potential (ZDP) of the suspensions with respect of their pH values in the range of 3–12 was determined using a Zetasizer Nano ZS 90 that was equipped with an MPT-2 multi-purpose titrator of Malvern Instruments Ltd. (Malvern, U.K.). The electrophoretic light scattering technique based on

the Doppler effect was used for investigations. The changes in the pH of mixtures were made by adding hydrochloric acid (HCl) or sodium hydroxide (NaOH).

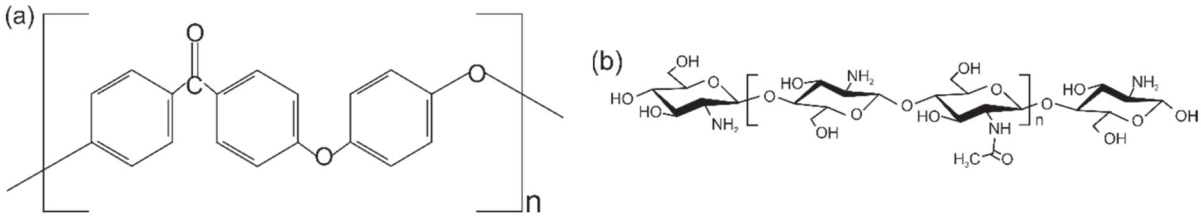


Figure 1. Chemical structures of PEEK (**a**) based on [42] and chitosan (**b**) based on [43].

The EPD process was executed in a two-electrode system, using an EX752M Multimode PSU power supply (AIM TTI, Huntingdon, UK) used as a direct current (DC) source. Zirconium alloy was the working electrode, and the counter electrode was an austenitic stainless steel plate. The constant current voltage range from 10 V to 150 V (with a change of 20 V) and a stable deposition time of 30 s were employed. A Tektronix DMM 4040 multimeter (TEKTRONIX, Bracknell, UK) was utilized to measure the current density during the process. The deposition yield and rate of particles were studied during deposition at a constant voltage of 90 V and different times of 10 s, 20 s and 30 s. The samples were weighed using an Ohaus Europe GmbH analytical scale (Nänikon, Switzerland).

Heat treatment of the samples was carried out in a Czylok MRT-20 (Czylok, Jastrzębie-Zdrój, Poland) laboratory furnace. It consisted of heating at 450 °C for 30 min (heating rate of 15 °C/min) and cooling (rate of 2 °C/min).

2.3. Characterization: Microstructure and Surface Topography

Microstructural investigations of the substrate, coating components and coatings were carried out using a light microscope (LM) from OPTA-TECH SK (Warsaw, Poland), FEI Nova NanoSEM 450 (FEI, Eindhoven, The Netherlands) scanning electron microscope (SEM) and JEOL JEM-2010 ARP (JEOL, Tokyo, Japan) transmission electron microscope (TEM). The lamella from the cross-section of the coating for TEM investigations was prepared using a focused ion beam (FIB) using an FEI QUANTA 3D 200i device (FEI, Eindhoven, The Netherlands). A phase analysis was performed by X-ray diffractometry (XRD) in the Bragg-Brentano arrangement using a Panalytical Empyrean DY1061 diffractometer (Malvern Panalytical, Almelo, The Netherlands) and by the selected area electron diffraction (SAED) in TEM. The patterns were interpreted with the use of a JEMS diffraction simulation software, Switzerland. The chemical composition of the coatings was analyzed using energy-dispersive X-ray spectroscopy (EDS). Structural studies in the middle infra-red region were carried out using a Bruker Vertex 70v vacuum spectrometer (Bruker, Billerica, MA, USA). The Harrick Scientific Seagull adapter was used to conduct measurements by means of external reflection spectroscopy. A total of 128 scans with a resolution of 4 cm^{-1} were collected.

The surface roughness of the coatings was examined using a Filmetrics Profilm3D non-contact optical profilometer (Filmertics, San Diego, CA, USA). Several images of the surface topography of the areas of 400 μm × 500 μm were obtained at various locations from the sample and analyzed with Filmetrics Profilm (Filmetrics, San Diego, CA, USA) software.

2.4. Characterization: Selected Properties

The wetting angle (WA) and interfacial free energy (IFE) of materials were examined with a Krüss DSA25E goniometer (Krüss, Hamburg, Germany), by applying distilled water (as the polar liquid) and diiodomethane (as the nonpolar liquid). Measurements were made 10 times using 10 drops of each liquid. The IFE was calculated using the Owens–Wendt–Rabel–Kaelble (OWRK) method.

Cross-cut adhesion tests were performed utilizing a cutting knife from Elcometer (Manchester, UK) in agreement with ASTM D3359B. A mesh was cut in the coating, then the tape was glued and torn off after 90 s. The surface of the samples after the tests was observed with the naked eye as well as using LM and SEM. After that, the coating area removed from the alloy surface was measured and the adhesion class was determined.

Micro-scratch tests were conducted using the Micro Combi Tester (MCT) from CSM Instruments (Peseux, Switzerland). A Rockwell C diamond stylus with an apex angle of 120° and a tip radius of 200 μm was used. The test parameters were as follows: load 0.01 N to 30 N (linear increasing), scratch length 5 mm and sample speed 5 mm/min. Microhardness and elastic modulus of the coatings were examined using the instrumental indentation technique according to the procedure described by Oliver and Pharr [44]. The Vickers indenter was pressed into the surface of the coatings with a load of 100 mN, with a constant loading and unloading rate of 200 mN/min. The dwell time under the maximum load was 15 s. The measurements were made at least ten times, each time in a different area of the coating.

A three-electrode cell assembly consisted of the working electrode (sample), a counter electrode (Pt) and a reference electrode (saturated calomel electrode) immersed in electrolyte of 8.6 g/L of NaCl, 0.3 g/L of KCl, and 0.25 g/L of $CaCl_2$ dissolved in 1 L of water. The electrolyte with a pH value of 7.4 was deaerated and had a constant temperature of 37 °C. Open-circuit potential (OCP), Linear Sweep Voltammetry (LSV) and Electrochemical Impedance Spectroscopy (EIS) were carried out using an AUTOLAB PGSTAT128n potentiostat/galvanostat (Metrohm Autolab, Utrecht, The Netherlands). LSV was acquired using a scan rate of 1 mV/s, starting at −1.3 V to 2.2 V. For the EIS measurements, an amplitude of the perturbation signal ΔV = 10 mV was employed and the frequency ranged from 10^5 Hz to 10^{-3} Hz. The EIS data were fitted using AUTOLAB NOVA software by Metrohm Autolab, The Netherlands. Error minimization for fitting an equivalent circuit was performed by means of chi-squared criteria.

To evaluate the apatite formation ability, the heat-treated n-HA/ZnS/S-PEEK-coated alloy was immersed in 1.5 simulated body fluid (SBF) for three weeks in accordance with the modified Kokubo method described by Tanahashi et al. [45]. SBF was changed weekly. After the soaking period, samples were investigated with SEM (EDS) and Raman spectroscopy. Raman measurement was performed with the use of a WITec Alpha 300M+ spectrometer (WITec Ulm, Germany). A 100× objective along with a 488 nm diode laser and 600 grating were used. The laser power was selected in such a way as to avoid the degradation of the sample.

3. Results and Discussion

Based on the XRD phase analysis, it was detected that the Zr-2.5Nb alloy consisted principally of α phase with a hexagonal close packed (hcp) structure and sporadically of β phase with a body centered cubic (bcc) structure (Figure 2a). Based on LM observations, grains of the primary β phase had equivalent diameters in the range of 50–500 μm (Figure 2b). The SEM observation revealed that the α phase occurred in the form of numerous, elongated plates with an average width of 1.5 μm and length in the range of 0.5–30 μm (Figure 2c). The almost parallel plates formed colonies of differently oriented systems. According to the literature [46], β is an Nb-rich phase that occurs as a result of the prolonged aging of alloys quenched below the monotectoid temperature. The microstructure of the Zr-2.5Nb alloy was similar to that obtained in the same alloy by Srivastava et al. [47] after hot extrusion.

Interestingly, PEEK 704 powder has been investigated previously and described elsewhere [17,48]. They involve amorphous particles with an irregular shape and equivalent diameter ranging from 2 to 15 μm. The ZnS powder used for coating deposition consisted of rhombohedral primitive (rp) and hexagonal primitive (hp) phases (Figure 3a). The XRD pattern displayed both intensive diffraction peaks of the rp phase of (1 1 20) and (1 1 60) and hp phase of (100) and (110) as well as minor diffraction peaks of both phases.

A representative TEM micrograph of the particles is presented in Figure 3b. The particles had an equivalent diameter in the range of 40–430 nm. The following two particle shapes were observed: oblong with an average equivalent diameter of about 200 nm and globular with an equivalent diameter in the whole above-mentioned range (Figure 3b). The analysis of SAED patterns confirmed the presence of particles with both hp and rp crystallographic structures.

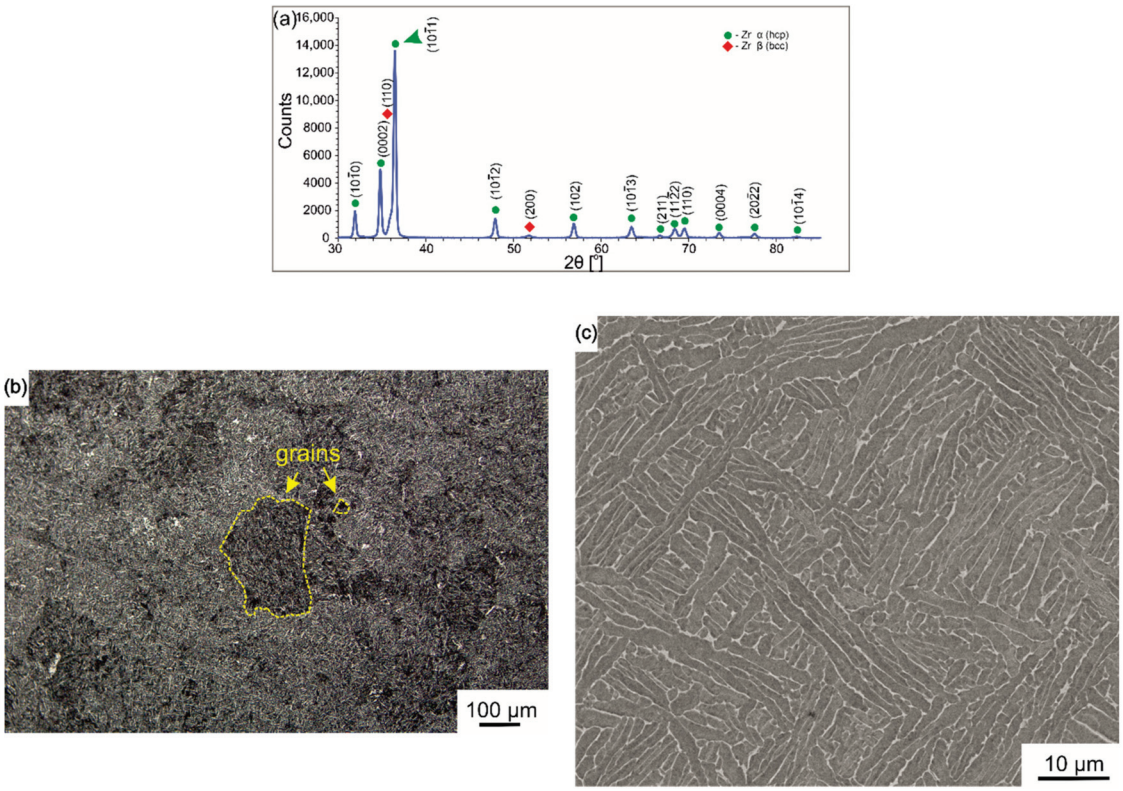


Figure 2. XRD pattern of Zr-2.5Nb alloy (**a**) and microstructure of the cross-section of the bar observed using LM (**b**) and SEM (**c**).

The n-HA powder contained fine longitudinal nanoparticles that exhibiting a needle-like shape with length in the range of 20–120 nm and width of about 5 nm (Figure 4). Electron diffraction analysis revealed the hp structure of particles. The Ca:P atomic ratio obtained from SEM-EDS microanalysis (analyzed area of 540 µm × 430 µm) was roughly 1.83.

It was found that the ZDP of particles in EtOH depended on their type. According to that, the ZDP of PEEK particles in EtOH exhibited positive values for mixtures with a pH from 3.0 to 5.5 and negative values for suspensions with a pH above that value. ZnS and HA particles displayed similar, negative ZDP values for suspensions with pH above 8.5. Both particle types had positive values in mixtures with a pH that varied from 3.0 to 8.5 (Figure 5a). After the addition of CHp into the suspension, all coating components established positive ZDP values in the investigated pH range of 3.0–12.0, as shown in Figure 5b. Interestingly, CHp addition lowered the ZDP of ZnS particles in the mixtures with the pH range of 6.0–8.5 and changed its highest value of about 30 mV from pH = 7.0 in the pure EtOH to about 20 mV in the suspension of pH = 5.5. As for n-HA particles, the ZDP was lowered for suspensions in the pH range of 3.0–8.5, but it was increased in the range of 9.0–12.0. It reached the highest value of about 9 mV in the suspension of pH equal to 11.0. The ZDP increased significantly for PEEK particles in the suspension with CHp over the entire pH range, reaching the highest value of about 11 mV for the pH of 4. The addition of CHp contributed to the stabilization of the suspension used for coating deposition (pH = 5.36). In addition, it enabled effective cathodic co-deposition of all coating

components. A similar phenomenon was observed by Pang and Zhitomirsky [49] for HA–Ag–chitosan nanocomposite coatings and in our previous study [20] for the co-deposition of PEEK, HA and MoS_2 particles on titanium alloy substrates.

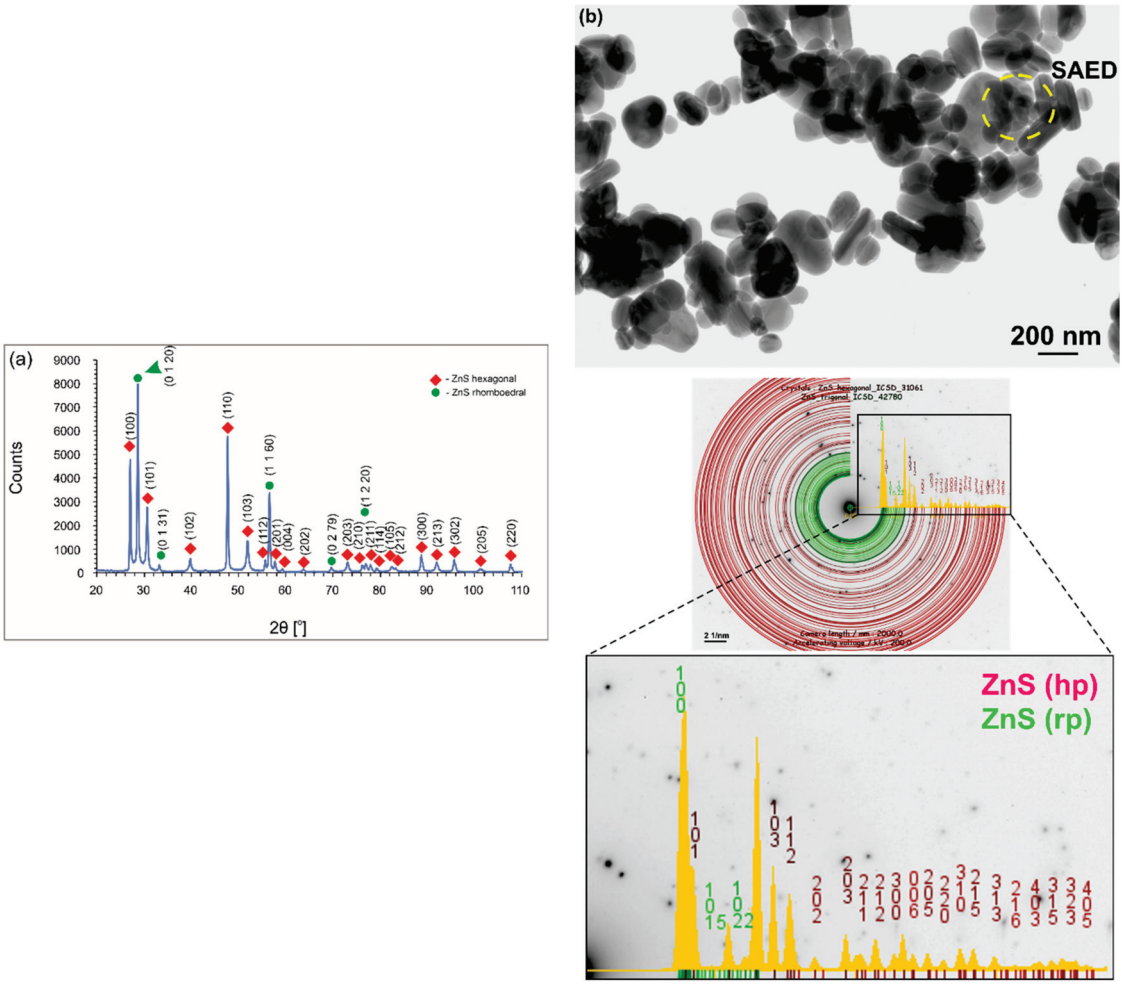


Figure 3. XRD pattern (**a**) and TEM micrograph (**b**) of ZnS particles. (**b**) also shows the SAED pattern obtained from the area marked by a circle and its interpretation with JEMS software.

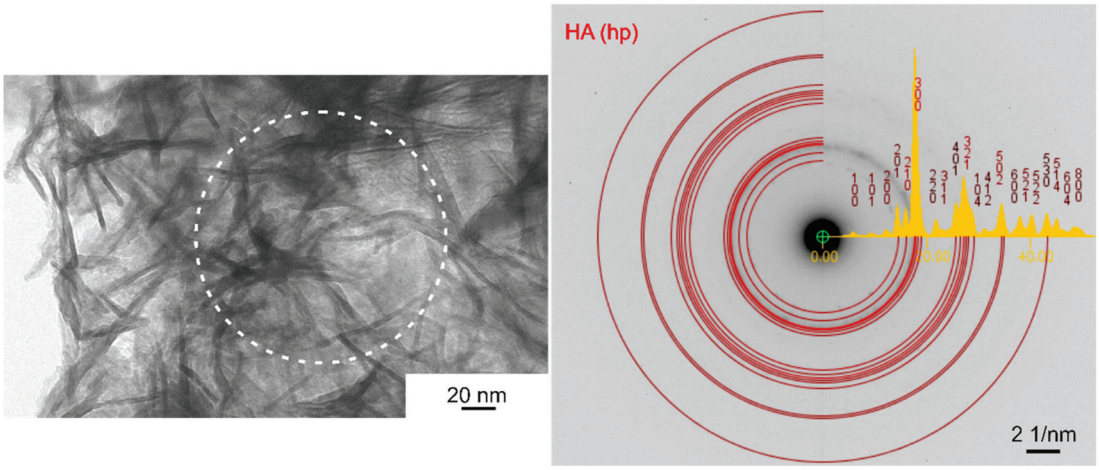


Figure 4. HA nano-particles and electron diffraction pattern from the area marked by the circle, TEM.

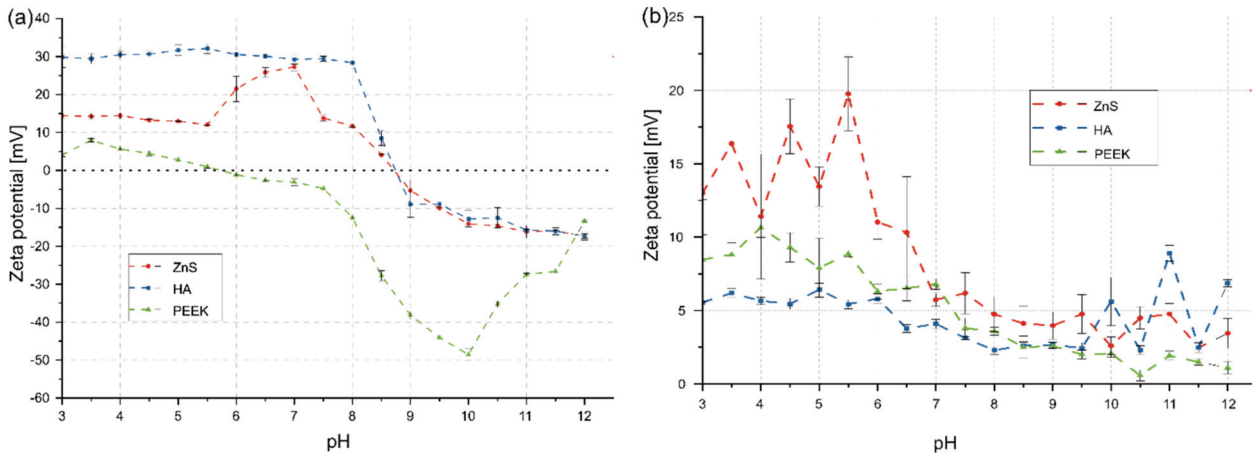


Figure 5. ZDP of n-HA, ZnS and PEEK particles in pure EtOH (**a**) and EtOH with the addition of 5 vol % CHp (**b**) in accordance with the suspension pH.

Fiołek et al. [50] also showed that the addition of chitosan polyelectrolyte allowed for the co-deposition of different polymer particles, such as PEEK and PTFE, by changing their charge from negative to positive and via the steric stabilization of the suspension. The mechanism of interaction, as a result of which PEEK acquires a positive charge in the presence of chitosan, has been studied and described by Luo and Zhitomirsky [51]. According to them, electrochemical decomposition of water takes place at the cathode, which results in a local increase in the pH value of the suspension. Neutralization of the chitosan amino group charge and adsorption of protonated chitosan to PEEK particles induces cathodic deposition. Shi et al. [52] showed that positively charged chitosan particles attracted HA nanoparticles in the suspension, resulting in electrostatic stabilization. However, Molaei et al. [53] found that the interaction between chitosan and the halloysite nanotube (HNT) causes the surface modification of HNT particles and the repulsive forces between chitosan chains induce a mechanism of steric stabilization in the suspension. Avcu et al. [37] also proved that the presence of various particle types (e.g., hydroxyapatite, bioglass, carbon nanotubes, and graphene oxide) in the suspension and their interaction with chitosan can generate steric or electrostatic stabilization. Therefore, it can be concluded that the coating deposition mechanism in this work is similar to that described above based on steric and electrostatic stabilization.

The effect of the voltage used for the deposition of coatings on their homogeneity was easily noticeable. It was observed that the deposition of particles on the substrate below the voltage level of 30 V was negligible. After deposition at a voltage of 50 V, 60 V and 70 V, coatings were inhomogeneous and thin. The coatings had numerous closed inequalities on their surface. The number of defects increased drastically for voltages above 110 V.

The deposition yield and deposition rate of coatings was investigated (Figure 6). As EPD continued, the deposition yield grew rapidly from about 0.12 mm/mg^2 for 20 s to 0.20 mm/mg^2 for 30 s. The deposition rate reached its peak after 10 s and began growing dynamically, then it stabilized at 0.06 mm/mg^2·s until the 20th second, to finally grow slowly for the last 10 s until the end of the process, reaching a level of 0.07 mm/mg^2·s.

Current density change and macroscopic images of coated substrates deposited at corresponding voltages of 30 V, 90 V and 150 V are shown in Figure 7.

Significant current density instability was noted for 90 V and 150 V for the measurement point of 10 s. After that, it was stable until the process was completed. Except for initial (5 s) fluctuations, the current density was constant at a level of 20 mA/mm^2 for the voltage of 90 V. The highest current density vacillations were observed at the voltage of 150 V.

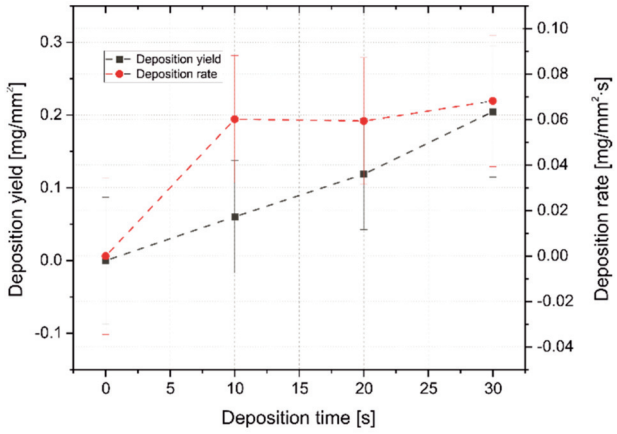


Figure 6. The changes in the deposition yield and the deposition rate with respect to deposition time at a constant voltage of 90 V.

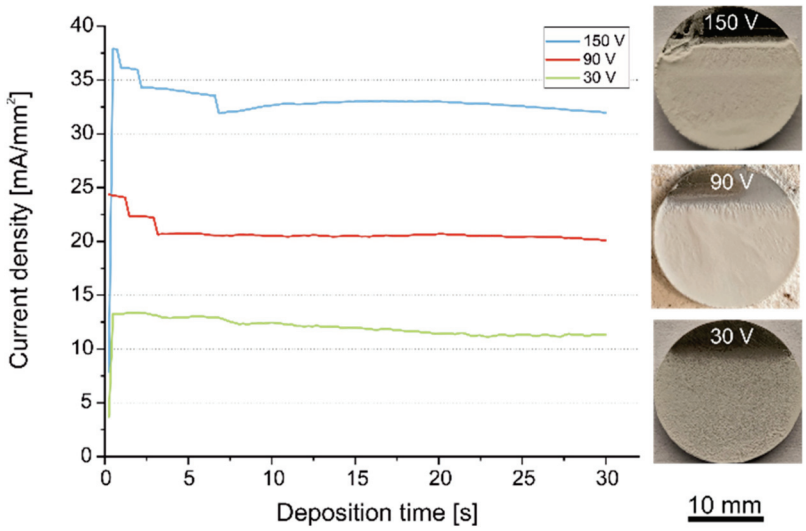


Figure 7. Current density variation for the EPD of n-HA/ZnS/PEEK coatings with macroscopic images of as-deposited coatings for the corresponding voltages.

This phenomenon was manifested in coating heterogeneity. At the voltages at which greater current fluctuations occurred, larger macroscopic inhomogeneities of the obtained coatings were observed. The coatings obtained at 30 V voltage were generally homogeneous, but relatively thin. The coatings achieved at 150 V voltage were characterized by a considerable thickness and irregular surface morphology with the presence of inconsistencies and pores. Utilization of the deposition voltage of 90 V resulted in the development of coatings with a moderate amount of inconsistencies in the form of valleculae and rare pores. Comparable with our previous study on PEEK-based coatings with MoS_2 incorporation [20], an increased concentration of HA powder in the suspension above 1 g/L multiplied the occurrence of pores and inconsistencies.

Although coatings deposited at 150 V voltage were satisfactorily uniform and thick, after heat treatment they were converged, exposing a significant part of the substrate surface due to the uneven thickness and the disclosure of hidden defects under its surface. Therefore, coatings obtained at 90 V for 30 s were chosen for heat treatment and a further investigation of microstructure and properties. The determination of heating temperature was executed by an experimental approach as well as an XRD and FTIR structural analysis of the coatings. In our previous study on MoS_2/PEEK coatings, a lower temperature of 390 °C was sufficient for PEEK sulfonation [41]. However, a different type of polymer (PEEK 708) was used and the MoS_2 were in the form of nanosheets. It was also found

that a temperature of 390 °C was not sufficient to induce amorphization and sulfonation of PEEK 704 in multicomponent HA/MoS_2/PEEK coatings [20]. Based on these previous experiences [20,41], the heating temperature of 450 °C was selected for heating the coated substrates to ensure the occurrence of PEEK sulfonation. This was conducted for 40 min and cooled with a furnace. The coatings after the treatment were macroscopically homogeneous and dense, but single and open pores on their surface were observed. The XRD pattern of the coated alloy is presented in Figure 8. The pattern confirmed the presence of all components in the coating and exhibited an amorphous PEEK structure, indicating that the sulfonation process took place.

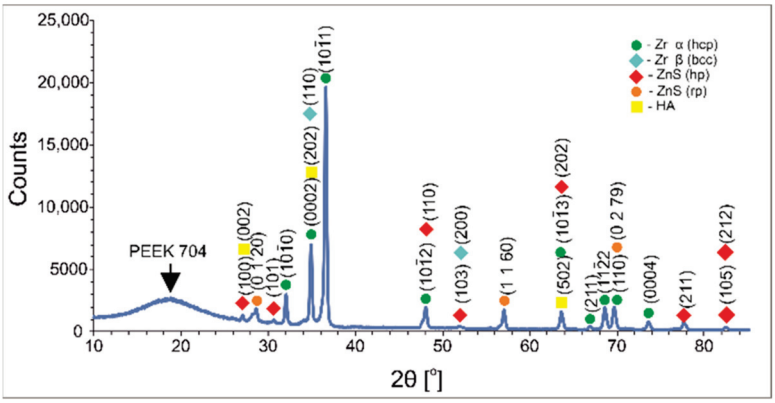


Figure 8. XRD patterns of n-HA/ZnS/S-PEEK coated alloy heated at 450 °C showing an amorphous PEEK structure.

An FTIR analysis was performed to confirm the occurrence of the sulfonation process. Figure 9 shows the MIR spectra of PEEK powder (a) and the n-HA/ZnS/S-PEEK coating heated at 450 °C (b).

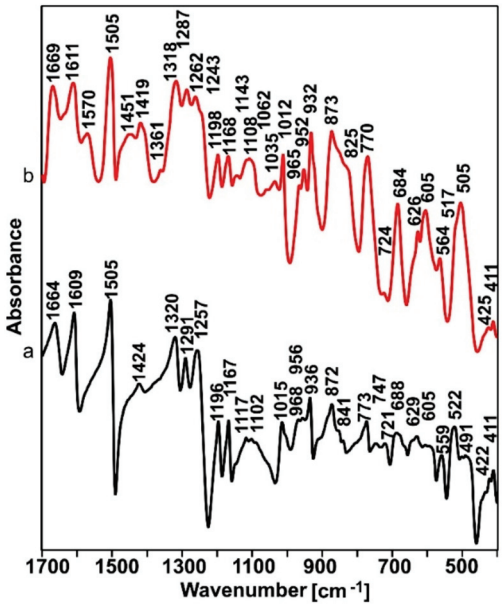


Figure 9. MIR spectra of PEEK powder (**a**) and the n-HA/ZnS/S-PEEK coating heated at 450 °C (**b**).

The first noticeable difference was the much larger half-width of most of the bands on the spectra of the PEEK coating with ZnS and HA heated at 450 °C (b). This clearly indicates a higher degree of disorder (amorphization) of the coating compared to the initial PEEK (a). Literature data indicate that the process of PEEK sulfonation leads to the amorphization of its structure [54], therefore it can be assumed that the sulfonation

process took place in the coatings. In order to unequivocally confirm the occurrence of the sulfonation process, the MIR spectra were analyzed for the presence of bands characteristic for S-O and S=O bonds. This analysis is difficult due to the small quantity of sulfur ions in the investigated layers and the overlapping of the characteristic bands of S-O and S=O bonding with the characteristic bands of PEEK. Nevertheless, an in-depth analysis revealed the characteristic bands of vibrations of sulfur-oxygen bonding at approx. 1240 cm^{-1} (asymmetric O=S=O stretching) and 1035 cm^{-1} (symmetric O=S=O stretching) in spectrum (b), which did not appear in spectrum (a) [55,56]. The increase in the intensity of the bands at 684, 1035, 1112 and 1243 cm^{-1} associated with vibrations of the S-O bonds is also an observed characteristic [57].

It was validated by microstructure observation that no spherulites were observed on the surface of coatings with S-PEEK. The PEEK changed during heat treatment from globular particles to a homogeneous, stiff and dense coating matrix (Figure 10a). The SEM-EDS microanalysis confirmed the presence of elements belonging to all coating components (Figure 10b). The coating thickness measured by contact profilometry was in the range of 55–60 µm.

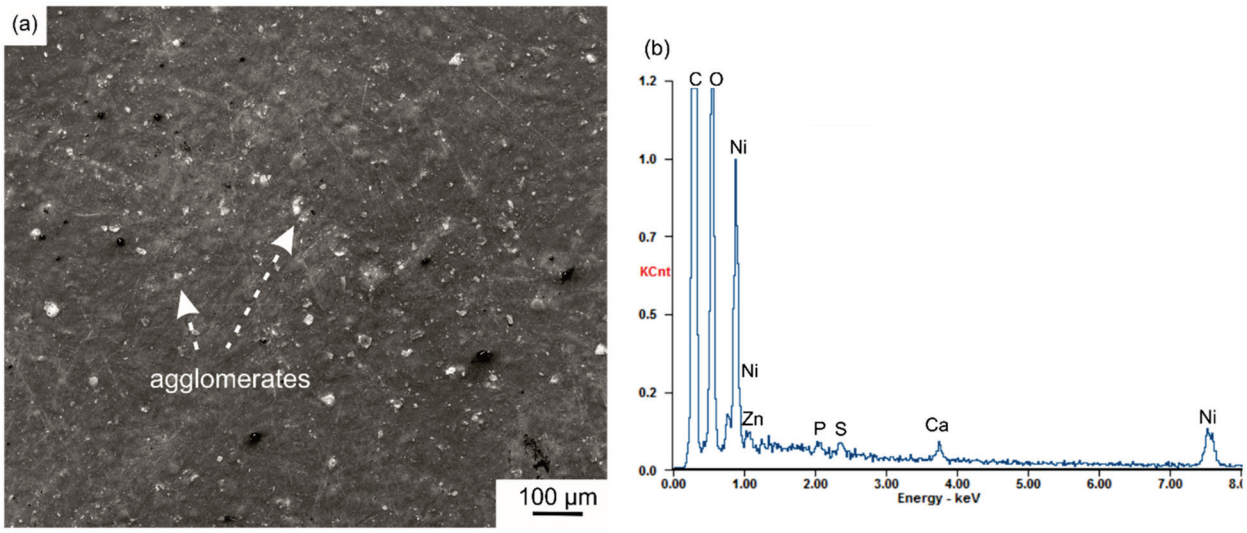


Figure 10. Surface morphology (**a**) and SEM-EDS spectrum (**b**) of the n-HA/ZnS/S-PEEK coating, SEM. Ni in the spectrum was generated from the sputtered conductive layer.

The microstructure on the traverse section of the coating's outer region was characterized using TEM. Large agglomerates of HA nanocrystals with a diameter of about 6 µm and smaller agglomerates of ZnS particles with a diameter of about 0.5 µm were found in the amorphous polymeric matrix (Figure 11). The coating was compact in the investigated area, no closed porosity was observed and the ceramic particles were well embedded in the polymer. The n-HA/ZnS/S-PEEK coatings were characterized by a relatively high surface roughness. The arithmetic mean height Sa and root mean square height Sq parameters obtained from three averaged measurements from various locations of the coating in accordance with ISO 25178 equaled 1.27 ± 0.12 µm and 1.73 ± 0.21 µm, respectively. A characteristic image of the coating surface is shown in Figure 12.

The surface properties of the wettability angle (WA) and interfacial free energy (IFE) were examined for coatings in relation to the uncoated Zr-2.5Nb alloy and PEEK coatings without any additives. The WA and IFE for water and diiodomethane are presented in Table 1. All investigated surfaces had a WA of below 90°, while the lowest WA with water was measured for the base alloy (53 ± 8°). The coatings had a WA of slightly above 70°, which indicates mild hydrophilicity of their surfaces. These WA values were close to those obtained for pure PEEK coatings with a semicrystalline structure, which demonstrates that thermal sulfonation has no significant effect on PEEK wettability. In addition, the

presence of the ZnS or n-HA particles in the coating did not change the wettability of the PEEK as they were completely embedded in the polymer. The n-HA/ZnS/S-PEEK coating revealed a considerable IFE at above 40 mN/m. However, the base alloy and pure PEEK coating exhibited higher IFE values. It is known that bare PEEK is often qualified as a material with WA values between hydrophobic and hydrophilic levels, usually in the range of 70–90° [58,59]. A WA close to the most preferable hydrophilic range of 40–70° and substantial IFE are important in the case of the osteointegration of the biomaterials with surrounding bone tissues [60,61]. Although the wettability of coatings obtained in this work was lower than for the HA/PEEK coatings developed by Bastan et al. [18], the WA of coatings was not significantly reduced compared to the PEEK coating. However, the presence of bioactive HA particles and sulfur in PEEK allows the bioactive properties of the coating to develop.

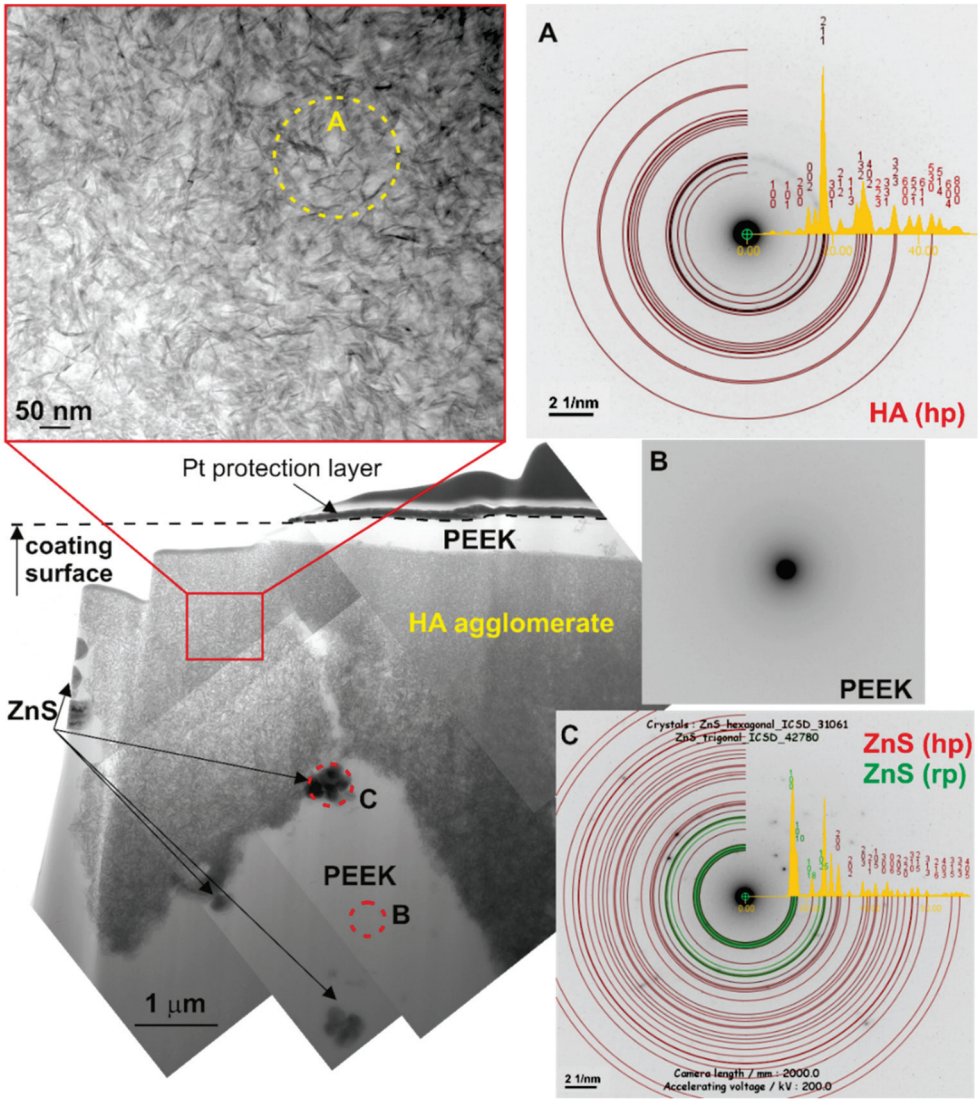


Figure 11. Microstructure of the n-HA/ZnS/S-PEEK coating on the cross-section and diffraction patterns (**A**–**C**) from the traverse sections of the area indicated in the figure and their interpretation, TEM.

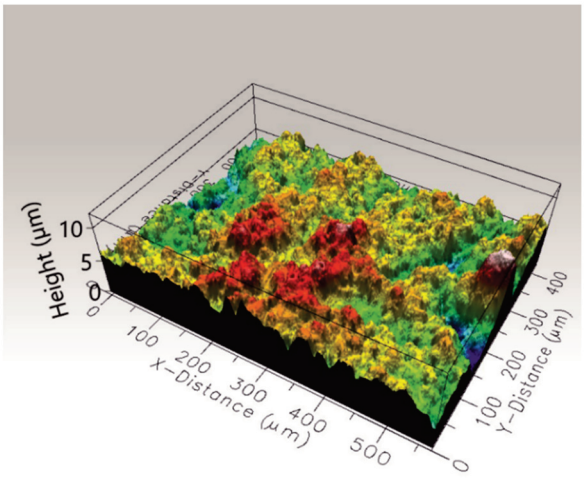


Figure 12. 3D image of the n-HA/ZnS/PEEK coating surface after heat treatment at 450 °C, optical profilometry.

Table 1. Water and diiodomethane wettability angle and interfacial free energy of the Zr-2.5Nb alloy, PEEK and n-HA/ZnS/S-PEEK coatings.

Material	WA [°]		IFE [mN/m]	
	H_2O	CH_2I_2	Polar	Disperse
Zr-2.5Nb alloy	53.0 ± 8.0	48.3 ± 2.0	53.6 ± 6.0	
			18.4 ± 4.9	35.2 ± 1.1
PEEK coating	71.1 ± 9.0	25.8 ± 1.4	51.3 ± 4.1	
			5.4 ± 3.6	45.9 ± 0.5
n-HA/ZnS/S-PEEK coating	73.1 ± 3.5	36.9 ± 3.4	46.8 ± 3.1	
			5.7 ± 1.5	41.2 ± 1.6

The modulus of elasticity (E_{IT}) and hardness (H_{IT}), examined by the method of instrumented indentation, were carried out for different loads (P_{max}) of 100, 200, 400 and 1000 mN. However, only measurements obtained for 100 mN were considered because other loads exceeded the recommended penetration depth of 0.1 for the coating thickness, which increased the hardness and modulus of elasticity caused by the interaction with the alloy substrate. Relatively high hardness was obtained for the coating of 0.32 ± 0.08 GPa and elastic modulus of 4.3 ± 0.8 GPa. The hardness value for coatings was close to the hardness of 0.33 GPa obtained by Wang et al. [62] for HA/PEEK composites with 15 vol % HA produced by injection molding. Similar to our previous study on HA/MoS_2/PEEK coatings with a semi-crystalline PEEK structure [20], the HA filler increased hardness (about 0.32 ± 0.02 GPa) compared to the unfilled PEEK 704 coating, for which H_{IT} was equal to 0.26 ± 0.03 GPa. The modulus of elasticity E_{IT} of both coatings was comparable.

The adhesion strength and resistance against mechanical scratching of the coatings was assessed based on tape tests and scratch resistance tests, respectively. The n-HA/ZnS/S-PEEK coating exhibited excellent adhesion to the zirconium alloy substrate, of the highest class 5B according to ASTM D3359-17, as shown by the tape test. The coating surface after the test is shown in Figure 13. Detailed observations of the coating surface by SEM revealed minor exfoliation on a few cutting edges only.

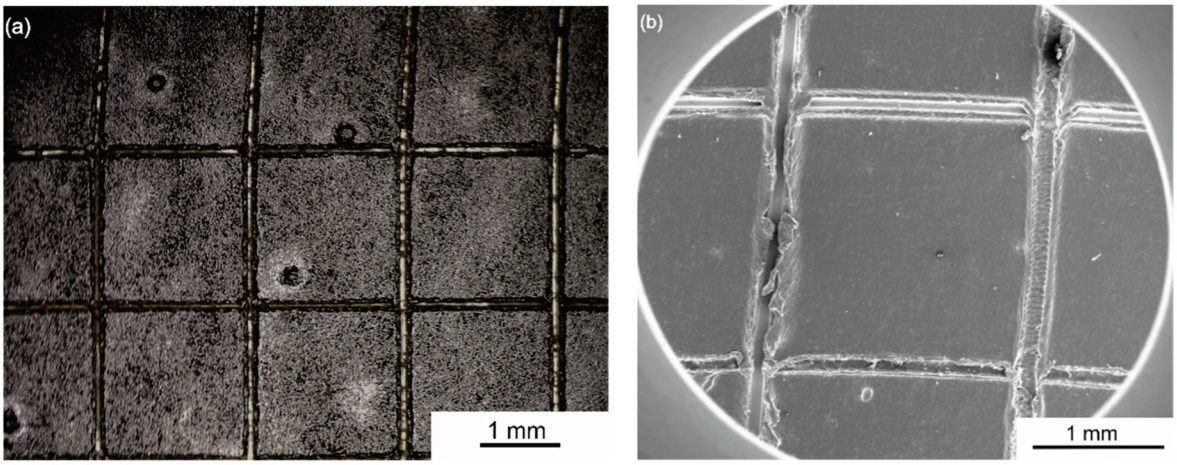


Figure 13. The surface of the n-HA/ZnS/S-PEEK coating (**a**) on the Zr-2.5Nb alloy after tape tests observed with a stereoscopic microscope. The enlarged detail (SEM image) of the cuts is presented in (**b**).

A micro-scratch test was conducted for an accurate analysis of the scratch damage mechanism and analysis of the coating adhesion. The scratch test allows the data concerning adhesion of the coatings to the substrate to be completed quantitatively. For this purpose, the critical load at which the characteristic form of the coating failure occurred was determined. The critical load L_{c1} is defined as the load at which the first cohesive crack appears in the scratch track, L_{c2} is the load followed by the adhesive failure of the coating and a slight exposure of the substrate, and L_{c3} is the load at which the coating is completely removed from the substrate on a large area due to delamination. The relative motion of the stylus with the ascending load is the cause of the increase in the interfacial shear stress occurring between the moving and deformed surface of the coating. Furthermore, it causes the tensile stresses following it, and the pile-ups of the coating material on the edges of the scratch.

During the tests, the acoustic emission signal was recorded, which proved their fragile nature of destruction during scratching. Cohesive cracks were observed under the load of L_{c1} = 16 N (Figure 14). The coatings deteriorated with an increase in the load and, under an L_{c2} equal to 27 N, an exposition of the substrate occurred.

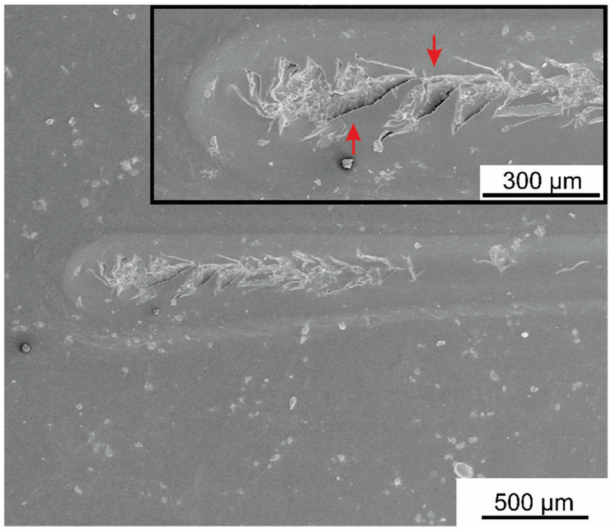


Figure 14. Scratch tracks in the n-HA/ZnS/S-PEEK coating in the places where the characteristic forms of failure occurred; cohesive cracks were marked with arrows.

The electrochemical behavior of the base and coated alloy was investigated in Ringer's solution at a temperature of 37 °C. For each of the samples, open circuit potentials (E_{ocp}) were registered as a function of time. It was observed that the free corrosion potential (Figure 15a) slightly increased from −0.5 V for the Zr-2.5Nb alloy and reached a stable value after about 10 h of immersion in Ringer's solution at a value of around −0.15 V. The E_{ocp} for the coated alloy shows a stable and significantly higher value of about 0.33 V. E_{ocp} values for the coated alloy indicate more noble behavior, confirming the positive effect of the n-HA/ZnS/S-PEEK coating on the substrate corrosion resistance.

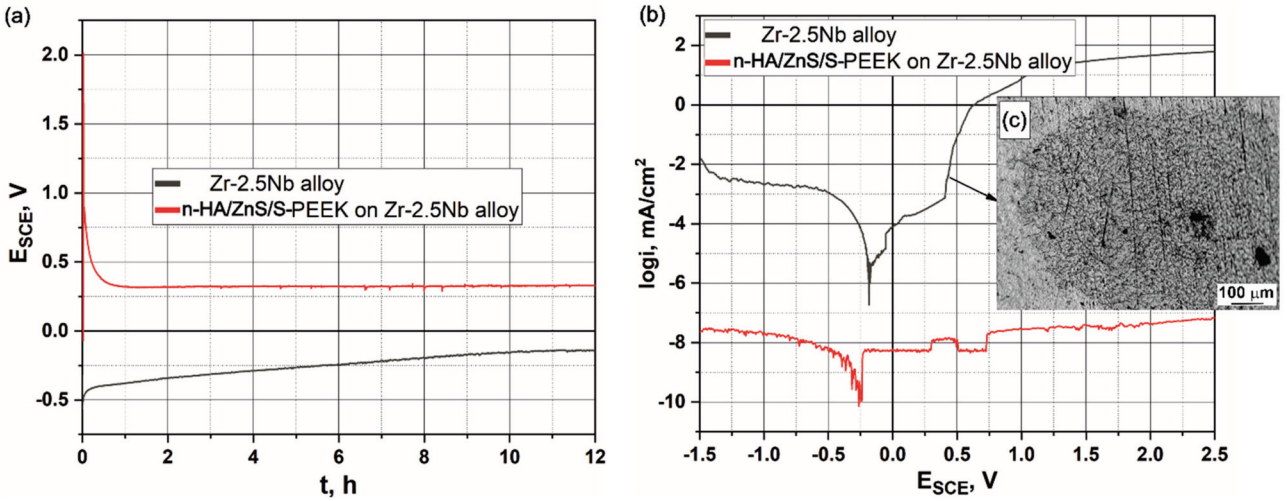


Figure 15. Electrochemical results for the Zr-2.5Nb alloy and the alloy coated with the n-HA/ZnS/S-PEEK coating in Ringer's solution at 37 °C, (**a**) OCP vs. time, (**b**) Anodic polarization curves at scan rate 1 mV/s and (**c**) light microscope image of the alloy surface after the LSV experiment.

The anodic polarization curves registered for the alloy and coated alloy substrate in deaerated Ringer's solution are shown in Figure 15b. A large, weakly potential-dependent current region, which is an indication of the passive state of the coated surfaces, was observed. By contrast, the base alloy showed a continuous increase in current with potential. This is not a consequence of an active corrosion process but evidence of the continuous growth of the oxide during anodic polarization [5,63]. From about 0.4 V, a breakdown of the passive layer was observed and active dissolution of the alloy started (transpassive region). The surface morphology of the pure alloy after polarization measurements is shown in Figure 15c. In general, randomly distributed pitting spots were present on the sample surface, which confirmed the pits' occurrence. In addition, the growth and stability of the oxide films on zirconium alloy were greatly affected by the electrolytic medium. Their corrosion properties were deteriorated by the presence of chloride ions [64,65]. The passive films were easily attacked due to the Cl^- migration towards and into the oxide films, which caused pitting. Thus, the decrease in the current density during the passive state (by about 4 orders of magnitude) at the anodic branch of the polarization curve indicates an improvement in their corrosion behavior. All OCP and potentiodynamic polarization data are given in Table 2.

Table 2. Corrosion parameters for Zr-2.5Nb and coated alloy obtained from the analysis of OCP and polarization results.

Samples	OCP [V]	$E_{K\text{-}A}$ [V]	Icorr [μA/cm^2]
Zr-2.5Nb	−0.15	−0.18	93
n-HA/ZnS/S-PEEK coated Zr-2.5Nb	0.33	−0.26	0.00002

In the present paper, an equivalent circuit given by the scheme [R1(Q1[R2Q2])] (shown in Figure 16) was employed to fit the EIS data for the case of a single passive film formed on the metal surface. The R1 and R2 parameters represented electrolyte resistance and the charge transfer resistance for the passive film/solution interface, respectively. Furthermore, Q1 was a constant phase element (CPE), which took into account the non-ideal capacitive behavior of the film. Circuit element Q2 described the CPE for the passive film/substrate interface. The values of the fitted parameters (R1, Q1, n1, R2, Q2, n2) are listed in Table 3. A good agreement between the experimental data and fitted curve was obtained with the $\chi 2$ of about 8×10^{-3}. Parameters of equivalent circuit elements found by fitting for the uncoated Zr-2.5Nb substrate indicate that, due to a rather high value of exponent $n1 \approx 0.975$ for the constant phase element CPE1, its nature is capacitive, whereas in the case of the constant phase element CPE2, a more resistive behavior dominates, $n2 \approx 0.174$. On the other hand, it was impossible to register impedance spectra for the coated samples due to extremely low current values (please refer to those obtained in the LSV experiment for the coated alloy), resulting in very high impedance—all registered spectra resembled clouds of randomly scattered points and are therefore not presented in this paper.

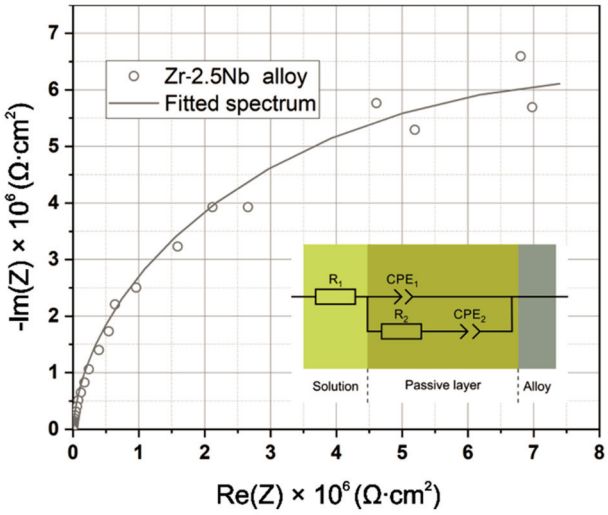


Figure 16. Nyquist impedance plot and equivalent circuit for the Zr-2.5Nb alloy.

Table 3. Equivalent circuit parameters calculated by means of fitting for the Zr-2.5Nb alloy.

Element of Equivalent Circuit	Quantity	Value
R1	Rs (solution resistance) (Ω)	36.72
CPE1	Y0 (S)	4.918×10^{-6}
	n1	0.978
R2	Rp (polarization resistance) (Ω)	2248.7
CPE2	Y0 (S)	1.850×10^{-7}
	n2	0.170
	χ^2	8×10^{-3}

The initial response of the n-HA/ZnS/S-PEEK coated alloy after its incubation in SBF was studied using the modified Kokubo test [45]. After soaking in SBF for 1 and 3 days, no mass gain of samples was detected and no HA formation was recognized on the coating surface. This behaviour may be due to the specific microstructure of the coatings. The n-HA separate nanoparticles and their agglomerates were completely embedded in the polymer matrix (Figure 11), which significantly delayed the release of Ca and P ions. Thus the formation of carbonated hydroxyapatite on the surface of the coating was difficult. A longer incubation time (7 and 10 days) resulted in slight changes (about 1 mg for 7 days and 2 mg after 10 days) in the weight of the sample, thereby indicating that apatite had started

to nucleate and grow, which is visible in Figure 17a,b. After incubation for 21 days, the mass gain of the apatite layer was 8 mg, and its thickness, determined from the differences in the sample mass before and after the test, taking into account the HA density of 3.16 g/cm^3, was about 10 µm. The SBF was changed weekly during the test. The pH of the initial SBF and that measured at RT after 1, 2 and 3 weeks of the test was the same at a level of 7.95 ± 0.02. The pH values depended on the SBF temperature and decreased to about 7.40 at 36.5 °C. The pH of SBF measured at the test temperature (36.5 °C) increased after 1 day to about 7.59 and after 7 days of immersion to 7.61. After 10, 14 and 21 days of the immersion pH equalled 7.66. No further increase in the pH of the SBF was observed. This may be due to the weekly change of the solution. Similarly, Khazeni et al. [66] showed that the pH of SBF increased over time to a level above 7.60. However, their study was conducted for 120 h of immersion of HA-CNTs composite coatings on magnesium alloy at a temperature of 37 ± 1 °C, without changing SBF.

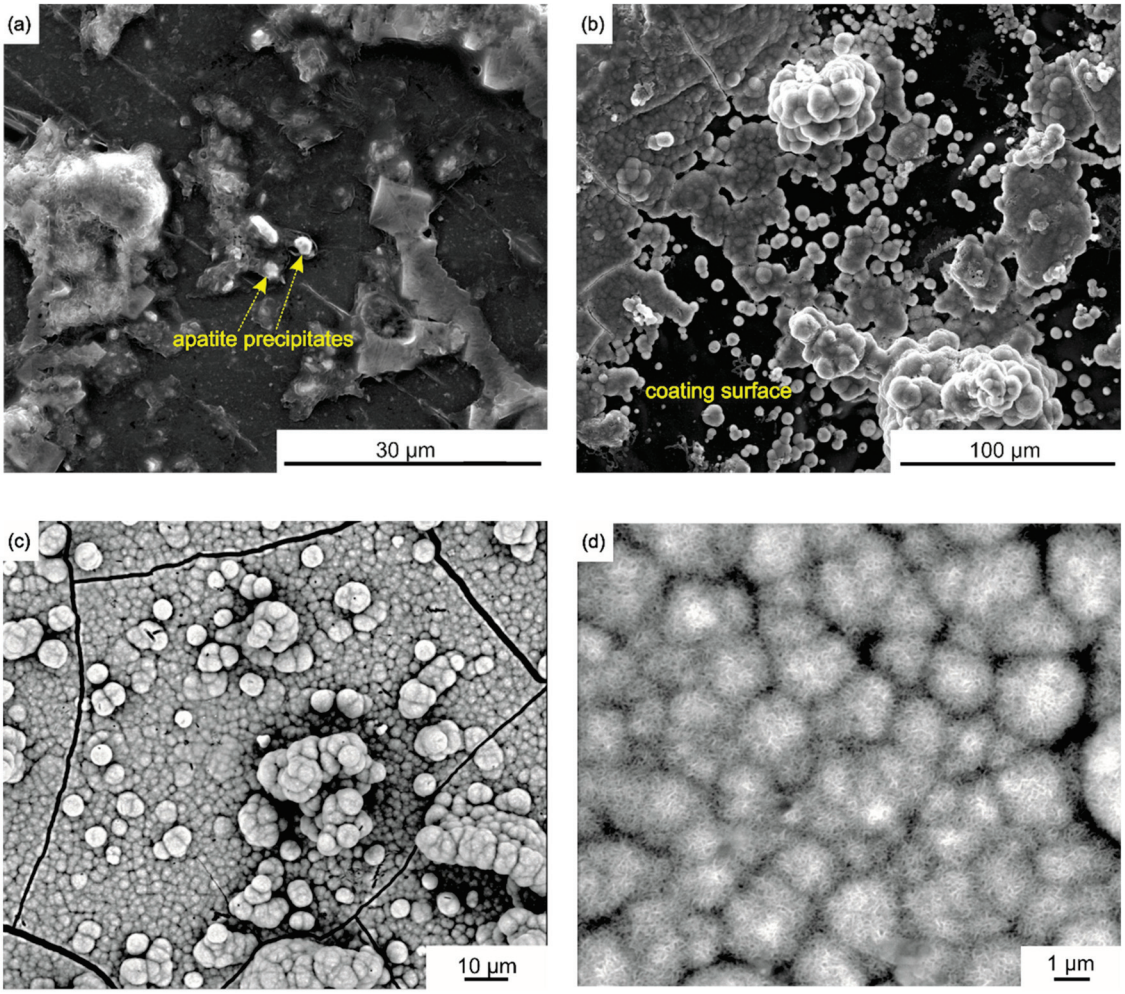


Figure 17. SEM images of the coated zirconium alloy after incubation in the SBF for 7 days (**a**), 10 days (**b**) and 21 days (**c**,**d**). (**c**) shows cauliflower-like morphology, while (**d**) shows flake-like morphology of the apatite layer.

It was found that the first small precipitates of apatite appeared after 7 days (Figure 17a). Precipitates grew rapidly, which became visible on the coating surface after 10 days of the test (Figure 17b). A characteristic cauliflower-like apatite morphology was observed on the whole coating surface after a three-week-long test (Figure 17c). These changes on the sample surfaces correspond well with the changes in pH and weight of the samples described above. A similar layer with cauliflower-like morphology was obtained on the

HA/PEEK coating after a bioactivity test in SBF by Bastan et al. [18]. Further SEM observation revealed that the whole coating surface was covered by apatite precipitates with flake morphology arranged in spherical aggregates with a size of 1–3 μm (Figure 17d). The presence of apatite on the n-HA/ZnS/S-PEEK coating indicates the high potential bioactivity of the coatings. The SEM-EDS microanalysis performed for a large coating area of 1100 μm × 930 μm revealed that the Ca:P atomic fraction was roughly 1.6. Such a value corresponds to non-stoichiometric carbonate hydroxyapatite.

In order to identify the phases that formed on the surface of the tested sample after the incubation process in SBF, Raman microscopy studies were carried out, focusing the beam on the characteristic layer visible in the SEM images (Figure 17c,d). As is clearly noticeable, the obtained Raman spectrum (Figure 18) shows an intense band at 960 cm^{-1} and two low-intensity bands at 595 and 431 cm^{-1}. Such an arrangement of bands [56,67] and the results of the EDS microanalysis allow us to assume that hydroxyapatite is present on the surface of the tested sample after incubation.

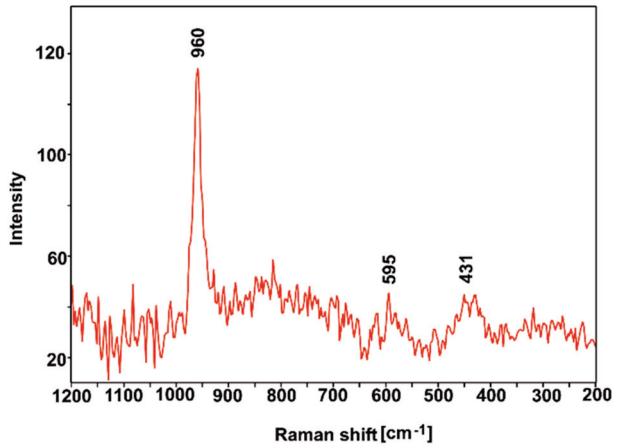


Figure 18. Raman spectrum of the layer formed after incubation in SBF.

Carbonate hydroxyapatite is the most common apatite occurring in human bone [68]. It is the preferable form of stoichiometric HA with low crystallinity and improved solubility, which leads to full resorbility and more accessible bone formation [69]. Hence, its presence may indicate the potential of bioactivity and osteoconductivity of the obtained coating.

4. Conclusions

In this study, the possibility of the co-deposition of PEEK 704 with ZnS and HA nanoparticles for obtaining n-HA/ZnS/S-PEEK coatings was discussed. The main conclusions are:

1. Duplex treatment based on EPD and heat treatment allowed for the development of homogeneous multicomponent coatings on Zr-2.5Nb alloy substrates. Coatings were obtained at a constant voltage of 90 V during 30 s. The n-HA/ZnS/PEEK coating deposition rate and yield was the highest at 30 s of the process.
2. Heat treatment caused PEEK transformation from particles into a continuous phase, in which ceramic particles were embedded. As a result of heat treatment at a temperature of 450 °C, a sulfonation process occurred in the coating, leading to the formation of an amorphous PEEK matrix. The surface of n-HA/ZnS/S-PEEK coatings showed high roughness.
3. The HA/ZnS/S-PEEK coatings demonstrated excellent adhesion to the alloy substrate and moderate scratch resistance.
4. Coatings with the addition of HA displayed higher hardness and modulus of elasticity compared to the PEEK coating without additives.

5. LSV and EIS experiment results indicate a significant improvement in corrosion resistance of the coated Zr-2.5Nb alloy compared to the bare substrate. However, due to the very low current densities registered for this coating, it was not possible to obtain any meaningful EIS data—the observed impedance values were above the limits of the potentiostat/galvanostat used, which in turn suggests a very high stability of the n-HA/ZnS/S-PEEK coating in aggressive Ringer's solution.
6. After immersion in simulated body fluid, an apatite-like layer was formed on the n-HA/ZnS/S-PEEK coating surface.

Author Contributions: Conceptualization, T.M.; formal analysis, F.K., A.F., M.S., A.Ł., Ł.C., S.Z., A.K. and T.M.; investigation, F.K., A.F., M.S., A.Ł., Ł.C., S.Z., A.K. and T.M.; supervision, T.M.; validation, F.K., A.F., M.S., A.Ł., Ł.C., S.Z., A.K. and T.M.; visualization, F.K., M.S., A.Ł. and T.M.; writing—original draft, F.K. and A.F.; writing—review and editing, T.M. All authors have read and agreed to the published version of the manuscript.

Funding: The study was supported by AGH-UST (project no. 16.16.110.663).

Institutional Review Board Statement: Not applicable.

Informed Consent Statement: Not applicable.

Data Availability Statement: The data presented in this study are available on request from the corresponding author.

Conflicts of Interest: The authors declare no conflict of interest. The funders had no role in the design of the study; in the collection, analyses, or interpretation of data; in the writing of the manuscript, or in the decision to publish the results.

References

1. Vitti, R.P.; Catelan, A.; Amaral, M.; Pacheco, R.R. *Zirconium in Dentistry*; Elsevier: Amsterdam, The Netherlands, 2019; pp. 317–345.
2. Chopra, D.; Gulati, K.; Ivanovski, S. Micro + Nano: Conserving the Gold Standard Microroughness to Nanoengineer Zirconium Dental Implants. *ACS Biomater. Sci. Eng.* **2021**, *7*, 3069–3074. [CrossRef] [PubMed]
3. Matuła, I.; Dercz, G.; Barczyk, J. Titanium/Zirconium functionally graded materials with porosity gradients for potential biomedical applications. *Mater. Sci. Technol.* **2020**, *36*, 972–977. [CrossRef]
4. Branzoi, I.V.; Iordoc, M.; Codescu, M. Electrochemical studies on the stability and corrosion resistance of new zirconium-based alloys for biomedical applications. *Surf. Interface Anal.* **2008**, *40*, 167–173. [CrossRef]
5. Zhou, F.; Wang, B.; Qiu, K.; Lin, W.; Li, L.; Wang, Y.; Nie, F.; Zheng, Y. Microstructure, corrosion behavior and cytotoxicity of Zr–Nb alloys for biomedical application. *Mater. Sci. Eng. C* **2012**, *32*, 851–857. [CrossRef]
6. Zhou, F.; Qiu, K.; Bian, D.; Zheng, Y.; Lin, J. A Comparative in vitro Study on Biomedical Zr–2.5X (X = Nb, Sn) Alloys. *J. Mater. Sci. Technol.* **2014**, *30*, 299–306. [CrossRef]
7. Mehjabeen, A.; Song, T.; Xu, W.; Tang, H.P.; Qian, M. Zirconium Alloys for Orthopaedic and Dental Applications. *Adv. Eng. Mater.* **2018**, *20*, 1–21. [CrossRef]
8. Corni, I.; Neumann, N.; Eifler, D.; Boccaccini, A.R. Polyetheretherketone (PEEK) Coatings on Stainless Steel by Electrophoretic Deposition. *Adv. Eng. Mater.* **2008**, *10*, 559–564. [CrossRef]
9. Boccaccini, A.R.; Peters, C.T.; Roether, J.A.; Eifler, D.; Misra, S.K.; Minay, E.J. Electrophoretic deposition of polyetheretherketone (PEEK) and PEEK/Bioglass® coatings on NiTi shape memory alloy wires. *J. Mater. Sci.* **2006**, *41*, 8152–8159. [CrossRef]
10. Panayotov, I.V.; Orti, V.; Cuisinier, F.; Yachouh, J. Polyetheretherketone (PEEK) for medical applications. *J. Mater. Sci. Mater. Med.* **2016**, *27*, 118. [CrossRef]
11. Abdulkareem, M.H.; Abdalsalam, A.H.; Bohan, A.J. Influence of chitosan on the antibacterial activity of composite coating (PEEK /HAp) fabricated by electrophoretic deposition. *Prog. Org. Coatings* **2019**, *130*, 251–259. [CrossRef]
12. Kurtz, S.M. *An Overview of PEEK Biomaterials*, 2nd ed.; William Andrew Publishing: Oxford, UK, 2019; ISBN 9780128125243.
13. Heary, R.F.; Parvathreddy, N.; Sampath, S.; Agarwal, N. Elastic modulus in the selection of interbody implants. *J. Spine Surg.* **2017**, *3*, 163–167. [CrossRef] [PubMed]
14. Rehman, M.A.U.; Bastan, F.E.; Haider, B.; Boccaccini, A.R. Electrophoretic deposition of PEEK/bioactive glass composite coatings for orthopedic implants: A design of experiments (DoE) study. *Mater. Des.* **2017**, *130*, 223–230. [CrossRef]
15. Rehman, M.A.U.; Bastan, F.E.; Nawaz, Q.; Goldmann, W.H.; Maqbool, M.; Virtanen, S.; Boccaccini, A.R. Electrophoretic deposition of lawsone loaded bioactive glass (BG)/chitosan composite on polyetheretherketone (PEEK)/BG layers as antibacterial and bioactive coating. *J. Biomed. Mater. Res. Part A* **2018**, *106*, 3111–3122. [CrossRef]

16. Virk, R.S.; Rehman, M.A.U.; Munawar, M.A.; Schubert, D.W.; Goldmann, W.H.; Dusza, J.; Boccaccini, A.R. Curcumin-Containing Orthopedic Implant Coatings Deposited on Poly-Ether-Ether-Ketone/Bioactive Glass/Hexagonal Boron Nitride Layers by Electrophoretic Deposition. *Coatings* **2019**, *9*, 572. [CrossRef]
17. Moskalewicz, T.; Zych, A.; Łukaszczyk, A.; Cholewa-Kowalska, K.; Kruk, A.; Dubiel, B.; Radziszewska, A.; Berent, K.; Gajewska, M. Electrophoretic Deposition, Microstructure, and Corrosion Resistance of Porous Sol–Gel Glass/Polyetheretherketone Coatings on the Ti-13Nb-13Zr Alloy. *Met. Mater. Trans. A* **2017**, *48*, 2660–2673. [CrossRef]
18. Baştan, F.E.; Rehman, M.A.U.; Avcu, Y.Y.; Avcu, E.; Üstel, F.; Boccaccini, A.R. Electrophoretic co-deposition of PEEK-hydroxyapatite composite coatings for biomedical applications. *Colloids Surf. B Biointerfaces* **2018**, *169*, 176–182. [CrossRef]
19. Fiołek, A.; Zimowski, S.; Kopia, A.; Moskalewicz, T. The Influence of Electrophoretic Deposition Parameters and Heat Treatment on the Microstructure and Tribological Properties of Nanocomposite Si3N4/PEEK 708 Coatings on Titanium Alloy. *Coatings* **2019**, *9*, 530. [CrossRef]
20. Kuśmierczyk, F.; Zimowski, S.; Łukaszczyk, A.; Kopia, A.; Cieniek, L.; Moskalewicz, T. Development of Microstructure and Properties of Multicomponent MoS2/HA/PEEK Coatings on a Titanium Alloy Via Electrophoretic Deposition and Heat Treatment. *Met. Mater. Trans. A* **2021**, *52*, 3880–3895. [CrossRef]
21. Seuss, S.; Heinloth, M.; Boccaccini, A.R. Development of bioactive composite coatings based on combination of PEEK, bioactive glass and Ag nanoparticles with antibacterial properties. *Surf. Coatings Technol.* **2016**, *301*, 100–105. [CrossRef]
22. Rehman, M.A.U.; Bastan, F.E.; Nawaz, A.; Nawaz, Q.; Wadood, A. Electrophoretic deposition of PEEK/bioactive glass composite coatings on stainless steel for orthopedic applications: An optimization for in vitro bioactivity and adhesion strength. *Int. J. Adv. Manuf. Technol.* **2020**, *108*, 1849–1862. [CrossRef]
23. Ma, R.; Tang, T. Current Strategies to Improve the Bioactivity of PEEK. *Int. J. Mol. Sci.* **2014**, *15*, 5426–5445. [CrossRef]
24. Bordea, I.R.; Candrea, S.; Alexescu, G.T.; Bran, S.; Băciuț, M.; Băciuț, G.; Lucaciu, O.; Dinu, C.M.; Todea, D.A. Nano-hydroxyapatite use in dentistry: A systematic review. *Drug Metab. Rev.* **2020**, *52*, 319–332. [CrossRef] [PubMed]
25. Sanpo, N.; Tan, M.L.; Cheang, P.; Khor, K. Antibacterial Property of Cold-Sprayed HA-Ag/PEEK Coating. *J. Therm. Spray Technol.* **2008**, *18*, 10–15. [CrossRef]
26. Wang, J.; Gong, X.; Hai, J.; Li, T. Synthesis of silver–hydroxyapatite composite with improved antibacterial properties. *Vacuum* **2018**, *152*, 132–137. [CrossRef]
27. Akhtar, M.A.; Ilyas, K.; Dlouhý, I.; Siska, F.; Boccaccini, A.R. Electrophoretic Deposition of Copper(II)–Chitosan Complexes for Antibacterial Coatings. *Int. J. Mol. Sci.* **2020**, *21*, 2637. [CrossRef] [PubMed]
28. Bi, Q.; Song, X.; Chen, Y.; Zheng, Y.; Yin, P.; Lei, T. Zn-HA/Bi-HA biphasic coatings on Titanium: Fabrication, characterization, antibacterial and biological activity. *Colloids Surf. B Biointerfaces* **2020**, *189*, 110813. [CrossRef] [PubMed]
29. Kumar, R.; Sakthivel, P.; Mani, P. Structural, optical, electrochemical, and antibacterial features of ZnS nanoparticles: Incorporation of Sn. *Appl. Phys. A* **2019**, *125*, 543. [CrossRef]
30. Hojamberdiev, M.; Piccirillo, C.; Cai, Y.; Kadirova, Z.; Yubuta, K.; Ruzimuradov, O. ZnS-containing industrial waste: Antibacterial activity and effects of thermal treatment temperature and atmosphere on photocatalytic activity. *J. Alloy. Compd.* **2019**, *791*, 971–982. [CrossRef]
31. Aqeel, M.; Ikram, M.; Asghar, A.; Haider, A.; Ul-Hamid, A.; Naz, M.; Imran, M.; Ali, S. Synthesis of capped Cr-doped ZnS nanoparticles with improved bactericidal and catalytic properties to treat polluted water. *Appl. Nanosci.* **2020**, *10*, 2045–2055. [CrossRef]
32. Ouyang, L.; Zhao, Y.; Jin, G.; Lu, T.; Li, J.; Qiao, Y.; Ning, C.; Zhang, X.; Chu, P.; Liu, X. Influence of sulfur content on bone formation and antibacterial ability of sulfonated PEEK. *Biomaterials* **2016**, *83*, 115–126. [CrossRef]
33. Montero, J.F.; Tajiri, H.A.; Barra, G.M.D.O.; Fredel, M.C.; Benfatti, C.A.; Magini, R.S.; Pimenta, A.L.; Souza, J.C. Biofilm behavior on sulfonated poly(ether-ether-ketone) (sPEEK). *Mater. Sci. Eng. C* **2017**, *70*, 456–460. [CrossRef] [PubMed]
34. Ma, R.; Wang, J.; Li, C.; Ma, K.; Wei, J.; Yang, P.; Guo, D.; Wang, K.; Wang, W. Effects of different sulfonation times and post-treatment methods on the characterization and cytocompatibility of sulfonated PEEK. *J. Biomater. Appl.* **2020**, *35*, 342–352. [CrossRef] [PubMed]
35. Meng, Z.; Qin, G.; Zhang, B.; Bai, J. DNA damaging effects of sulfur dioxide derivatives in cells from various organs of mice. *Mutagenesis* **2004**, *19*, 465–468. [CrossRef] [PubMed]
36. Meng, Z.; Liu, Y.; Wu, D. Effect of Sulfur Dioxide Inhalation on Cytokine Levels in Lungs and Serum of Mice. *Inhal. Toxicol.* **2005**, *17*, 303–307. [CrossRef] [PubMed]
37. Avcu, E.; Bastan, F.E.; Abdullah, H.Z.; Rehman, M.A.U.; Avcu, Y.Y.; Boccaccini, A.R. Electrophoretic deposition of chitosan-based composite coatings for biomedical applications: A review. *Prog. Mater. Sci.* **2019**, *103*, 69–108. [CrossRef]
38. Moskalewicz, T.; Seuss, S.; Boccaccini, A.R. Microstructure and properties of composite polyetheretherketone/Bioglass® coatings deposited on Ti–6Al–7Nb alloy for medical applications. *Appl. Surf. Sci.* **2013**, *273*, 62–67. [CrossRef]
39. Boccaccini, A.R.; Gerhardt, L.-C.; Rebeling, S.; Blaker, J.J. Fabrication, characterisation and assessment of bioactivity of poly (d,l lactid acid) (PDLLA)/TiO_2 nanocomposite films. *Compos. Part A Appl. Sci. Manuf.* **2005**, *36*, 721–727. [CrossRef]
40. Zhitomirsky, D.; Roether, J.; Boccaccini, A. Electrophoretic deposition of bioactive glass/polymer composite coatings with and without HA nanoparticle inclusions for biomedical applications. *J. Mater. Process. Technol.* **2009**, *209*, 1853–1860. [CrossRef]

41. Moskalewicz, T.; Kruk, A.; Sitarz, M.; Kopia, A. Effect of the Processing and Heat Treatment Route on the Microstructure of MoS2/Polyetheretherketone Coatings Obtained by Electrophoretic Deposition. *J. Electrochem. Soc.* **2019**, *166*, D151–D161. [CrossRef]
42. Najeeb, S.; Khurshid, Z.; Matinlinna, J.P.; Siddiqui, F.; Nassani, M.Z.; Baroudi, K. Nanomodified Peek Dental Implants: Bioactive Composites and Surface Modification—A Review. *Int. J. Dent.* **2015**, *2015*, 381759. [CrossRef]
43. Brasselet, C.; Pierre, G.; Dubessay, P.; Dols-Lafargue, M.; Coulon, J.; Maupeu, J.; Vallet-Courbin, A.; De Baynast, H.; Doco, T.; Michaud, P.; et al. Modification of Chitosan for the Generation of Functional Derivatives. *Appl. Sci.* **2019**, *9*, 1321. [CrossRef]
44. Oliver, W.C.; Pharr, G.M. An improved technique for determining hardness and elastic modulus using load and displacement sensing indentation experiments. *J. Mater. Res.* **1992**, *7*, 1564–1583. [CrossRef]
45. Tanahashi, M.; Yao, T.; Kokubo, T.; Minoda, M.; Miyamoto, T.; Nakamura, T.; Yamamuro, T. Apatite Coating on Organic Polymers by a Biomimetic Process. *J. Am. Ceram. Soc.* **1994**, *77*, 2805–2808. [CrossRef]
46. Perović, V.; Weatherly, G.C. The β to α transformation in a Zr-2.5 wt% Nb alloy. *Acta Met.* **1989**, *37*, 813–821. [CrossRef]
47. Srivastava, D.; Dey, G.K.; Banerjee, S. Evolution of microstructure during fabrication of Zr-2.5 Wt pct Nb alloy pressure tubes. *Met. Mater. Trans. A* **1995**, *26*, 2707–2718. [CrossRef]
48. Moskalewicz, T.; Zimowski, S.; Zych, A.; Łukaszczyk, A.; Reczyńska, K.; Pamuła, E. Electrophoretic Deposition, Microstructure and Selected Properties of Composite Alumina/Polyetheretherketone Coatings on the Ti-13Nb-13Zr Alloy. *J. Electrochem. Soc.* **2018**, *165*, D116–D128. [CrossRef]
49. Pang, X.; Zhitomirsky, I. Electrodeposition of hydroxyapatite–silver–chitosan nanocomposite coatings. *Surf. Coatings Technol.* **2008**, *202*, 3815–3821. [CrossRef]
50. Fiołek, A.; Zimowski, S.; Kopia, A.; Sitarz, M.; Moskalewicz, T. Effect of Low-Friction Composite Polymer Coatings Fabricated by Electrophoretic Deposition and Heat Treatment on the Ti-$_6$Al-$_4$V Titanium Alloy's Tribological Properties. *Met. Mater. Trans. A* **2020**, *51*, 4786–4798. [CrossRef]
51. Luo, D.; Zhitomirsky, I. Electrophoretic Deposition of Polyetheretherketone Composites, Containing Huntite and Alumina Platelets. *J. Electrochem. Soc.* **2015**, *162*, D3057–D3062. [CrossRef]
52. Shi, Y.Y.; Li, M.; Liu, Q.; Jia, Z.J.; Xu, X.C.; Cheng, Y.; Zheng, Y.F. Electrophoretic deposition of graphene oxide reinforced chitosan–hydroxyapatite nanocomposite coatings on Ti substrate. *J. Mater. Sci. Mater. Med.* **2016**, *27*, 48. [CrossRef]
53. Molaei, A.; Amadeh, A.; Yari, M.; Afshar, M. Structure, apatite inducing ability, and corrosion behavior of chitosan/halloysite nanotube coatings prepared by electrophoretic deposition on titanium substrate. *Mater. Sci. Eng. C* **2016**, *59*, 740–747. [CrossRef]
54. Zaidi, S.M.J. Polymer Sulfonation A Versatile Route to Prepare Proton-Conducting Membrane Material for Advanced Technologies. *Arab. J. Sci. Eng.* **2003**, *28*, 183–194.
55. Jin, X.; Bishop, M.T.; Ellis, T.S.; Karasz, F.E. A sulphonated poly(aryl ether ketone). *Br. Polym. J.* **1985**, *17*, 4–10. [CrossRef]
56. Jastrzębski, W.; Sitarz, M.; Rokita, M.; Bułat, K. Infrared spectroscopy of different phosphates structures. *Spectrochim. Acta Part A Mol. Biomol. Spectrosc.* **2011**, *79*, 722–727. [CrossRef] [PubMed]
57. Li, Y.; Liu, X.; Li, Z.; Ren, Y.; Wang, Y.; Zhang, W. Preparation, characterization and application of red mud, fly ash and desulfurized gypsum based eco-friendly road base materials. *J. Clean. Prod.* **2021**, *284*, 124777. [CrossRef]
58. Rupp, F.; Gittens, R.A.; Scheideler, L.; Marmur, A.; Boyan, B.D.; Schwartz, Z.; Geis-Gerstorfer, J. A review on the wettability of dental implant surfaces I: Theoretical and experimental aspects. *Acta Biomater.* **2014**, *10*, 2894–2906. [CrossRef] [PubMed]
59. Novotna, Z.; Reznickova, A.; Rimpelova, S.; Vesely, M.; Kolska, Z.; Svorcik, V. Tailoring of PEEK bioactivity for improved cell interaction: Plasma treatment in action. *RSC Adv.* **2015**, *5*, 41428–41436. [CrossRef]
60. Elawadly, T.A.; Radi, I.A.W.; El Khadem, A.; Osman, R.B. Can PEEK Be an Implant Material? Evaluation of Surface Topography and Wettability of Filled Versus Unfilled PEEK with Different Surface Roughness. *J. Oral Implant.* **2017**, *43*, 456–461. [CrossRef]
61. Liber-Kneć, A.; Łagan, S. Surface Testing of Dental Biomaterials—Determination of Contact Angle and Surface Free Energy. *Materials* **2021**, *14*, 2716. [CrossRef]
62. Wang, L.; Weng, L.; Song, S.; Zhang, Z.; Tian, S.; Ma, R. Characterization of polyetheretherketone–hydroxyapatite nanocomposite materials. *Mater. Sci. Eng. A* **2011**, *528*, 3689–3696. [CrossRef]
63. Farina, S.B.; Sanchez, A.G.; Ceré, S. Effect of Surface Modification on the Corrosion Resistance of Zr-2.5Nb as Material for Permanent Implants. *Procedia Mater. Sci.* **2015**, *8*, 1166–1173. [CrossRef]
64. Satpati, A.K.; Phadnis, S.V.; Sundaresan, R.I. Electrochemical and XPS studies and the potential scan rate dependent pitting corrosion behavior of Zircaloy-2 in 5% NaCl solution. *Corros. Sci.* **2005**, *47*, 1445–1458. [CrossRef]
65. Palit, G.C.; Gadiyar, H.S. Pitting Corrosion of Zirconium in Chloride Solution. *Corrosion* **1987**, *43*, 140–148. [CrossRef]
66. Khazeni, D.; Saremi, M.; Soltani, R. Development of HA-CNTs composite coating on AZ31 Magnesium alloy by cathodic electrodeposition. Part 2: Electrochemical and in-vitro behavior. *Ceram. Int.* **2019**, *45*, 11186–11194. [CrossRef]
67. Stammeier, J.A.; Purgstaller, B.; Hippler, D.; Mavromatis, V.; Dietzel, M. In-situ Raman spectroscopy of amorphous calcium phosphate to crystalline hydroxyapatite transformation. *MethodsX* **2018**, *5*, 1241–1250. [CrossRef]
68. Januariyasa, I.K.; Ana, I.D.; Yusuf, Y. Nanofibrous poly(vinyl alcohol)/chitosan contained carbonated hydroxyapatite nanoparticles scaffold for bone tissue engineering. *Mater. Sci. Eng. C* **2020**, *107*, 110347. [CrossRef]
69. Ezekiel, I.; Kasim, S.R.; Ismail, Y.M.B.; Noor, A.-F.M. Nanoemulsion synthesis of carbonated hydroxyapatite nanopowders: Effect of variant CO32−/PO43− molar ratios on phase, morphology, and bioactivity. *Ceram. Int.* **2018**, *44*, 13082–13089. [CrossRef]

International Journal of
Molecular Sciences

MDPI

Article

Effect of the Plasma Gas Type on the Surface Characteristics of 3Y-TZP Ceramic

Sung-Un Kang [1], Chul-Ho Kim [1,2,*], Hee-Kyung Kim [3,*], Ye-Won Yoon [4], Yu-Kwon Kim [4] and Seung-Joo Kim [4]

1 Department of Otolaryngology, Ajou University School of Medicine, Suwon 16499, Korea; cows79@ajou.ac.kr
2 Department of Molecular Science and Technology, Ajou University School of Medicine, Suwon 16499, Korea
3 Department of Prosthodontics, Institute of Oral Health Science, Ajou University School of Medicine, Suwon 16499, Korea
4 Department of Chemistry and Department of Energy Systems Research, Ajou University, Suwon 16499, Korea; yyw0902@ajou.ac.kr (Y.-W.Y.); yukwonkim@ajou.ac.kr (Y.-K.K.); sjookim@ajou.ac.kr (S.-J.K.)
* Correspondence: ostium@ajou.ac.kr (C.-H.K.); denthk@ajou.ac.kr (H.-K.K.)

Abstract: Plasma surface treatment can be an attractive strategy for modifying the chemically inert nature of zirconia to improve its clinical performance. This study aimed to clarify the effect of plasma gas compositions on the physicochemical surface modifications of 3 mol% yttria-stabilized zirconia (3Y-TZP). The cold, atmospheric plasma discharges were carried out by using four different plasma gases, which are He/O_2, N_2/Ar, N_2, and Ar from an application distance of 10 mm for 60 s. Static contact angles were measured to define the surface free energy. Changes in elemental composition, surface crystallinity, and surface topography were assessed with X-ray photoelectron spectroscopy (XPS), X-ray diffraction (XRD), confocal laser scanning microscopy (CLSM), and scanning electron microscopy (SEM), respectively. A significant decrease in water contact angle was observed in all plasma groups with the lowest value of 69° in the N_2/Ar group. CLSM and SEM investigations exhibited no morphological changes in all plasma groups. XPS revealed that a reduction in the surface C content along with an increase in O content was pronounced in the case of N_2/Ar compared to others, which was responsible for high hydrophilicity of the surface. XRD showed that the changes in crystallite size and microstrain due to oxygen atom displacements were observed in the N_2/Ar group. The N_2/Ar plasma treatment may contribute to enhancing the bioactivity as well as the bonding performance of 3Y-TZP by controlling the plasma-generated nitrogen functionalities.

Keywords: plasma gases; zirconium oxide; surface properties; nitrogen; wettability

Citation: Kang, S.-U.; Kim, C.-H.; Kim, H.-K.; Yoon, Y.-W.; Kim, Y.-K.; Kim, S.-J. Effect of the Plasma Gas Type on the Surface Characteristics of 3Y-TZP Ceramic. *Int. J. Mol. Sci.* **2022**, *23*, 3007. https://doi.org/10.3390/ijms23063007

Academic Editor: Mary Anne Melo

Received: 18 February 2022
Accepted: 9 March 2022
Published: 10 March 2022

Publisher's Note: MDPI stays neutral with regard to jurisdictional claims in published maps and institutional affiliations.

Copyright: © 2022 by the authors. Licensee MDPI, Basel, Switzerland. This article is an open access article distributed under the terms and conditions of the Creative Commons Attribution (CC BY) license (https://creativecommons.org/licenses/by/4.0/).

1. Introduction

The surface modification strategies for biomaterials help to tailor the outcome of biological-material interactions by controlling the surface energy, biocompatibility, and adhesion strength of the substrates [1]. Plasma modification is one way to alter the surface properties of biomaterials with high-energy ion bombardment through physical collisions or chemical reactions of the excited gas molecules [2]. Atmospheric-pressure glow discharge (APGD) plasma, especially cold atmospheric plasma (CAP), has recently attracted a great deal of interest for a variety of industrial and medical applications, such as surface processing [3], film deposition [3], ozone production for water purification [4], biomedical decontamination [4], wound healing [5,6], muscle regeneration [7], and cancer treatment [8,9], etc. CAP, also named non-thermal plasma (NTP), consists of a partially ionized gas that is not in the thermodynamic equilibrium. CAP generates a large amount of chemically reactive oxygen and nitrogen species (RONS) in biological systems [3,10]. One of the typical CAP sources is dielectric-barrier discharge (DBD), which is responsible for a self-pulsing plasma operation with an insulating (dielectric) material in the discharge gap. A DBD system requires a high voltage AC source (1–100 kV_{rms}) in the kHz range [11].

Zirconia ceramics stabilized with 3 mol% of yttria (3Y-TZP) have been widely used in dental applications for fabricating crown and bridge restorations, dental implants, orthodontic brackets, and endodontic posts due to their excellent biocompatibility, sufficient mechanical strength, and high esthetic potential [12]. However, zirconia is characterized by a chemically inert surface with low reactivity which limits a reliable bonding with resin cement, cell adhesion, or osseointegration [13,14]. Although mechanical surface treatments tended to increase the bond strength of zirconia with resin cement through micromechanical retention, the induced cracks and surface damages could cause a deterioration of fracture resistance of zirconia [15]. Therefore, the plasma surface treatment has been considered as an alternative to the mechanical surface treatment aiming to raise the surface energy of materials by the generation of polar groups at the surface [16]. Although the plasma surface treatments have been found to increase the surface hydrophilicity of 3Y-TZP without altering the surface topography [17], several studies demonstrated that the plasma treatment did not significantly enhance relevant shear bond strength (SBS) between zirconia and composite resin [18,19]. Conversely, oxygen radicals created in plasmas could mainly remove organic contaminants at the surface with a potential prospect for antibacterial efficacy around the zirconia abutments [10].

Nevertheless, the plasma performance of all those applications significantly depends on the experimental parameters. One of the most important characteristics is the gas species [20,21]. A noble gas, such as helium (He) or argon (Ar), as a carrier gas is usually employed to trigger CAP discharge because of its low breakdown voltage. However, a previous study reported that no chemical reaction was found on the micro-organisms with argon gas plasma due to the inert nature of argon despite intensive ion bombardments [22]. By contrast, some reactive gases, such as oxygen, nitrogen, or air can be mixed in small quantities into the background of noble gas for the production of chemically active species, such as O_3, OH, H_2O_2, NO, and OH radicals at low temperatures with a reduction in the breakdown voltage [23,24]. In a plasma generated from a gas mixture, the excited noble gas can ionize the reactive gas by energy transfer (Penning ionization) via collision, resulting in a change in the discharge characteristics [25].

To enhance the reactive level of the zirconia surface during the plasma treatment, investigation of the electrical conductivity and quantitative ion concentration in terms of changes in surface electrochemistry should be conducted in an attempt to increase the bonding efficiency or osseointegration of zirconia implants. In a recent study, a new functional group was generated on the zirconia surface by carbon and nitrogen plasma ion implantation technology, resulting in the enhanced bioactivity and cytocompatibility of 3Y-TZP [14]. However, there has yet been no report on the plasma-zirconia interactions from the perspective of the role of gas compositions that are responsible for the kinetics of chemical reactions at the surface. Therefore, the present study highlights the effect of plasma gas compositions on the physicochemical surface modifications of 3Y-TZP to gain some insight into the plasma-generated ionic functionalities. In this study, He/O_2 mixture, N_2/Ar mixture, N_2, and Ar were provided as feed gases for plasma generation. Characterization methods such as contact angle, X-ray photoelectron spectroscopy (XPS), X-ray diffraction (XRD) and Rietveld analysis, confocal laser scanning microscopy (CLSM), and scanning electron microscopy (SEM) were used to identify any changes in surface energy, surface chemistry, phase composition, and morphology of 3Y-TZP. The null hypothesis tested in this study was that there would be no difference in the physicochemical surface properties among 3Y-TZP ceramics treated with various gas plasmas.

2. Results

2.1. Surface Energy Changes by Irradiation of Various Gas Plasmas

Figure 1 shows the contact angles with sessile drop images (A) and the values of γ^{total}, γ^{d}, and γ^{p} (B) in the zirconia specimens subjected to each plasma treatment. Table 1 summarizes contact angles measured on the specimens of each plasma group. A significant decrease in water contact angle was observed after plasma exposure in all plasma

groups with the lowest value of 69° in the N_2/Ar group. The diiodomethane contact angles remained roughly constant in all plasma groups except in the Ar group, presented in Figure 1A and Table 1. Total surface energy significantly increased after the plasma treatment in all plasma groups and these results were mainly consistent with an increase in γ^p. The largest value of γ^p was measured in the N_2/Ar group (Figure 1B).

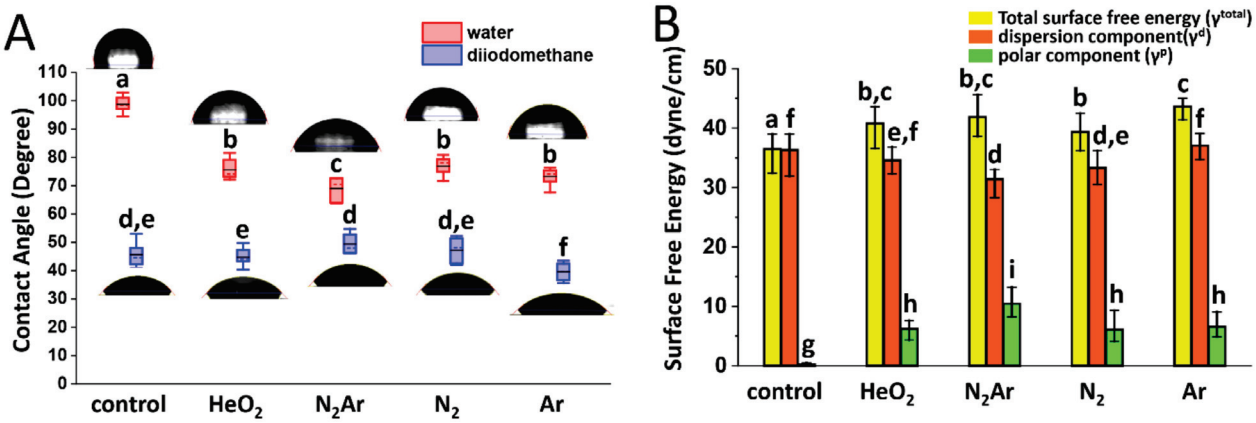


Figure 1. (**A**) Contact angles of water and diiodomethane; box plot showing the mean (black solid horizontal line), median (dashed horizontal line), interquartile range (box), and total range (whiskers) of the data set. (**B**) Values of the total surface free energy (γ^{total}), dispersion component (γ^d), and polar component (γ^p) in the zirconia specimens subjected to each plasma treatment. An identical letter within each value indicates no significant difference between each type of plasma gas ($p > 0.05$). The error bar represents the standard deviation.

Table 1. Contact angles for water and diiodomethane on the zirconia surfaces of each plasma group.

Plasma Group	Contact Angle (°)	
	Water	Diiodomethane
control	98.75 ± 2.70 ^{a}	45.66 ± 4.30 ^{d,e}
HeO_2	75.59 ± 3.38 ^{b}	44.72 ± 3.16 ^{e}
N_2Ar	69.00 ± 3.98 ^{c}	49.39 ± 3.33 ^{d}
N_2	76.86 ± 3.30 ^{b}	47.21 ± 4.14 ^{d,e}
Ar	73.22 ± 3.00 ^{b}	39.60 ± 3.19 ^{f}

Means with the same superscript letter in each column are not significantly different from each other based on Tukey's honest significant difference post hoc test ($p > 0.05$).

2.2. Surface Chemistry Changes by Irradiation of Various Gas Plasmas

Figure 2 shows the XPS C 1s, O 1s, N 1s, Y 3d, and Zr 3d core-level spectra, and Figure 3 shows the atomic percentages (at%) of these elements determined by XPS and the carbon/oxygen ratio in all groups. The nitrogen content on the zirconia surface increased after the plasma treatment in all plasma groups, but only to a few percent ranges (1–2%) as illustrated in Figure 3A,B. An increase in oxygen content and a decrease in carbon content were found in both N_2/Ar and He/O_2 groups, with the largest decrease in C content and the largest increase in O content in the N_2/Ar group (Figure 3A). As can be seen in Figure 3C, the lowest value of C/O ratio was observed in the N_2/Ar group. This would be related to the largest increase in the surface hydrophilicity in the N_2/Ar group, possibly by the production of a high level of oxygen-based radicals [26].

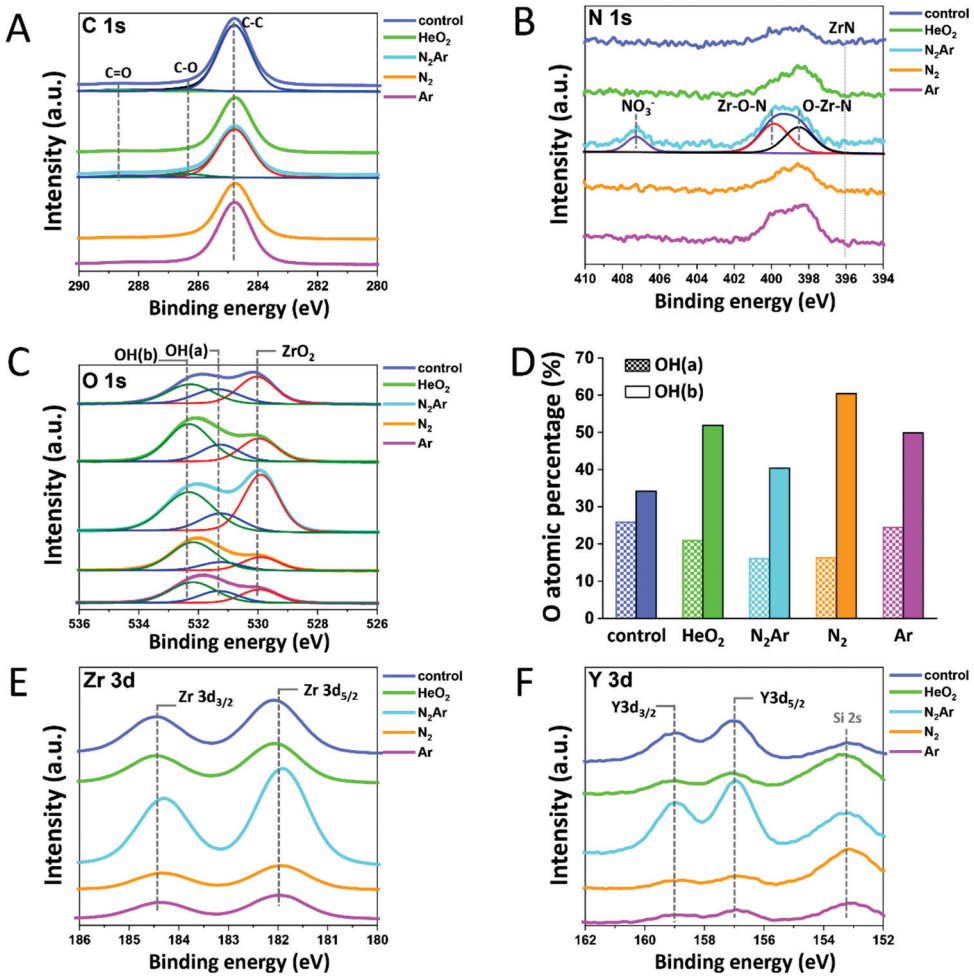


Figure 2. (**A**) C 1s; the carbon content was found to be a remarkable reduction in the N_2/Ar group compared to those in other groups. (**B**) N 1s; a new component appeared at a binding energy of 406.5 eV in the N_2/Ar group, which was associated with the presence of nitrate (NO_3^-) species. (**C**) O 1s XPS spectra; (**D**) Percentage areas of acidic hydroxyl OH(a) and basic hydroxyl OH(b) in O 1s spectra; (**E**) Zr 3d; and (**F**) Y 3d XPS spectra on outermost surfaces of zirconia with different plasma gases.

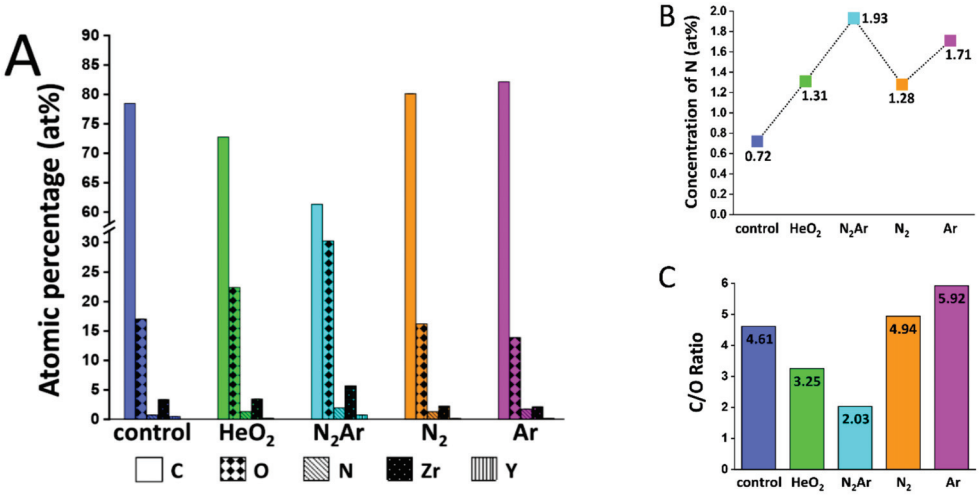


Figure 3. (**A**) Atomic percentage (at%) for each element detected in each plasma group; (**B**) Concentration of N in each plasma group; and (**C**) Carbon/oxygen ratio in each plasma group.

The N 1s photoelectron region, Figure 2B, showed a new component at a binding energy of 406.5 eV in the N_2/Ar group, which was associated with the presence of nitrate (NO_3^-) species [27]. This was due to the adsorption of a nitrogen atom (N) on the zirconia surface yielding N-containing functionalities [28]. A second component that appeared at a binding energy of around 399.1 eV was associated with the typical bonding states of N in zirconium oxynitride, or ZrO_xN_y which confirmed the introduction of nitrogen in the zirconia lattice [29,30]. The resulting N-doped zirconium oxynitride products were found in all tested groups without a direct N_2 feed, exhibiting the highest intensity in the N_2/Ar group (Figures 2C and 3B). This can be attributed to the fact that the surrounding air might have been involved in the interactions with zirconia surfaces during the plasma treatments [10].

Carbon content on the zirconia surface subjected to each plasma gas was shown in Figure 2A. The carbon content was found to be a remarkable reduction in the N_2/Ar group compared to those in other groups, indicating that the surface subjected to N_2/Ar plasma irradiation was less susceptible to carbon contamination during the subsequent handling in the air. During the plasma treatment, the remnant organic compounds at the surface were removed by breaking a C–C bond [31]. The surface oxidation occurred with a formation of new functional groups (C–O and C=O bonds) [32], thereby enhancing the surface hydrophilicity [33]. The O 1s spectra, as shown in Figure 2B, consisted of a broad feature that can be resolved into three components: the lattice oxygen in ZrO_2 (O_L) at around 530.0 eV, the oxygen in acidic hydroxyl OH(a) group at around 531.5 eV, and the oxygen in basic hydroxyl OH(b) group at around 532.5 eV [29]. The surface hydroxyls may be formed by the dissociation of the moisture in the air at the specimen's surface. Thus, the content of surface hydroxyls could increase when the surface provided the adsorption sites for H_2O, such as oxygen-deficient defects. The relatively high O_L-to-OH intensity ratio found in the N_2/Ar group indicated that the energy for dissociative adsorption of H_2O was relatively lower in the N_2/Ar group than those in other groups, probably resulting from the surface oxynitride formation in the N_2/Ar group (Figure 2B) through the partial nitridation of ZrO_2 [34]. However, all plasma groups showed increased OH(b) groups (Figure 2D), suggesting the plasma treatments left the surface more defective toward dissociative H_2O adsorption.

The XPS spectra of the Zr 3d spectra (Figure 2E) clearly revealed the two characteristic components of Zr $3d_{3/2}$ at 181.3 eV and of Zr $3d_{5/2}$ at 183.6 eV, which could be assigned to the zirconium in its Zr^{4+} state (ZrO_2) [35]. In the Y 3d spectra (Figure 2F), two components of Y3d ($Y3d_{3/2}$ and $Y3d_{5/2}$) for the oxidized yttrium in its $Y3^+$ state were identified. The pronounced Y3d exhibited in the N_2/Ar group could be considered a result of grain refinement on the microstructure [17].

2.3. Crystallinity Changes by Irradiation of Various Gas Plasmas

The percentage of the phase compositions and the lattice parameters for each plasma group were calculated and the results are presented in Table 2. Before plasma irradiation (control), the zirconia phases observed were a tetragonal phase (t-ZrO_2) as a major phase and a cubic phase (c-ZrO_2). However, the formation of a metastable tetragonal phase (t'-ZrO_2) was identified (up to 3 wt%) following the plasma treatments in all plasma groups.

The powder XRD patterns and W-H plots of each specimen are shown in Figure 4. All the detected peaks corresponded to tetragonal and cubic phases, while no obvious monoclinic phase was observed. On analyzing the XRD peaks, a slight broadening of the tetragonal peak was seen in the N_2/Ar group (Figure 4A,B), which was possible to deduce the contribution made by changes in the crystallite size and lattice strain [36,37]. By estimating from the slope and y-intercept of the W-H plot with Scherrer's equation [36,37], strain and particle size were compared. Since the positive slope indicates the tensile strain [15], the development of a compressive strain could be estimated from the flatter slope in the N_2/Ar group. A decrease in crystallite size, due to the lattice shrinkage and the occurrence of compressive strain in the N_2/Ar group, could contribute to the peak

broadening. The calculated crystallite sizes were 87.5 nm (control), 83.2 (He/O_2), 65.1 (N_2/Ar), 85.4 (N_2), and 85.5 (Ar).

Table 2. Rietveld analysis results for the phase compositions and the lattice parameters in each plasma group.

Plasma Group	Phase	Amount (wt%)	Lattice Parameters		
			a = b (Å)	c (Å)	*c*/*a* Ratio
control	t	62(2)	3.6069(2)	5.1777(4)	1.0151
	c	38(2)	5.1382(3)	5.1382(3)	
HeO_2	t	59(2)	3.6070(2)	5.1788(4)	1.0152
	t′	2(1)	3.625(2)	5.173(5)	1.0091
	c	39 (1)	5.1383(3)	5.1383(3)	
N_2Ar	t	67(2)	3.6098(2)	5.1808(4)	1.0148
	t′	3(1)	3.626(2)	5.175(5)	1.0092
	c	30(1)	5.1423(3)	5.1423(3)	
N_2	t	66(2)	3.6087(2)	5.1804(4)	1.0151
	t′	3(1)	3.626(1)	5.172(3)	1.0086
	c	31(1)	5.1407(3)	5.1407(3)	
Ar	t	60(2)	3.6075(2)	5.1779(4)	1.0149
	t′	2(1)	3.625(2)	5.173(6)	1.0091
	c	38(1)	5.1390(3)	5.1390(3)	

t: tetragonal zirconia (space group $P4_2/nmcS$); t′: metastable tetragonal zirconia (space group $P4_2/nmcZ$); c: cubic zirconia (space group $Fm\bar{3}m$); Values in parentheses correspond to the estimated standard deviation in the least significant figure to the left. c/a ratio = c (Å)/$\sqrt{2}$ a (Å).

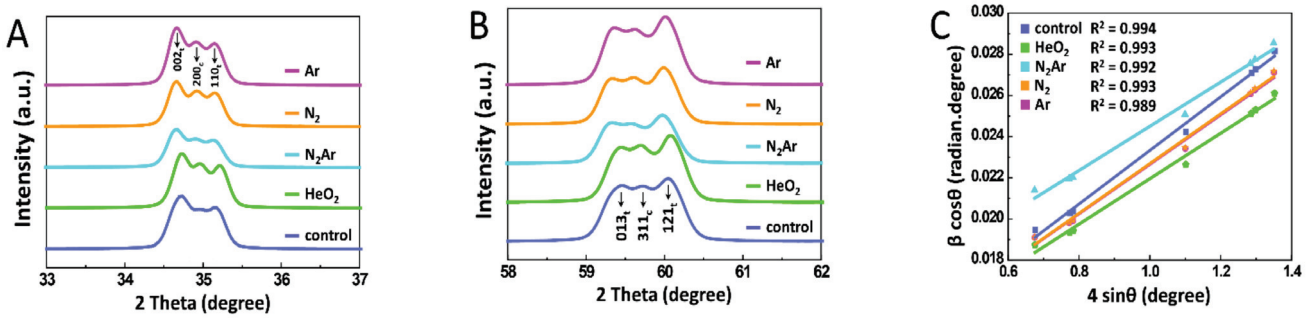


Figure 4. X-ray diffraction (XRD) patterns of zirconia specimens with each plasma gas (**A**) in the ranges of 2θ = 33–37°, (**B**) of 2θ = 58–62°, (**C**) Williamson-Hall (W-H) plot of ß cos θ against 4 sin θ of the tetragonal phases calculated from XRD spectra.

2.4. Surface Morphological Changes by Irradiation of Various Gas Plasmas

The magnified confocal images and SEM images of each plasma group are shown in Figure 5. The surface texture parameters (Sa, Sq, and Sv) measured from CLSM are given in Figure 6. With no significant morphological differences obtained, all specimens revealed relatively similar microstructures characterized by tetragonal symmetry integrated with large cubic crystals without relevant surface damages.

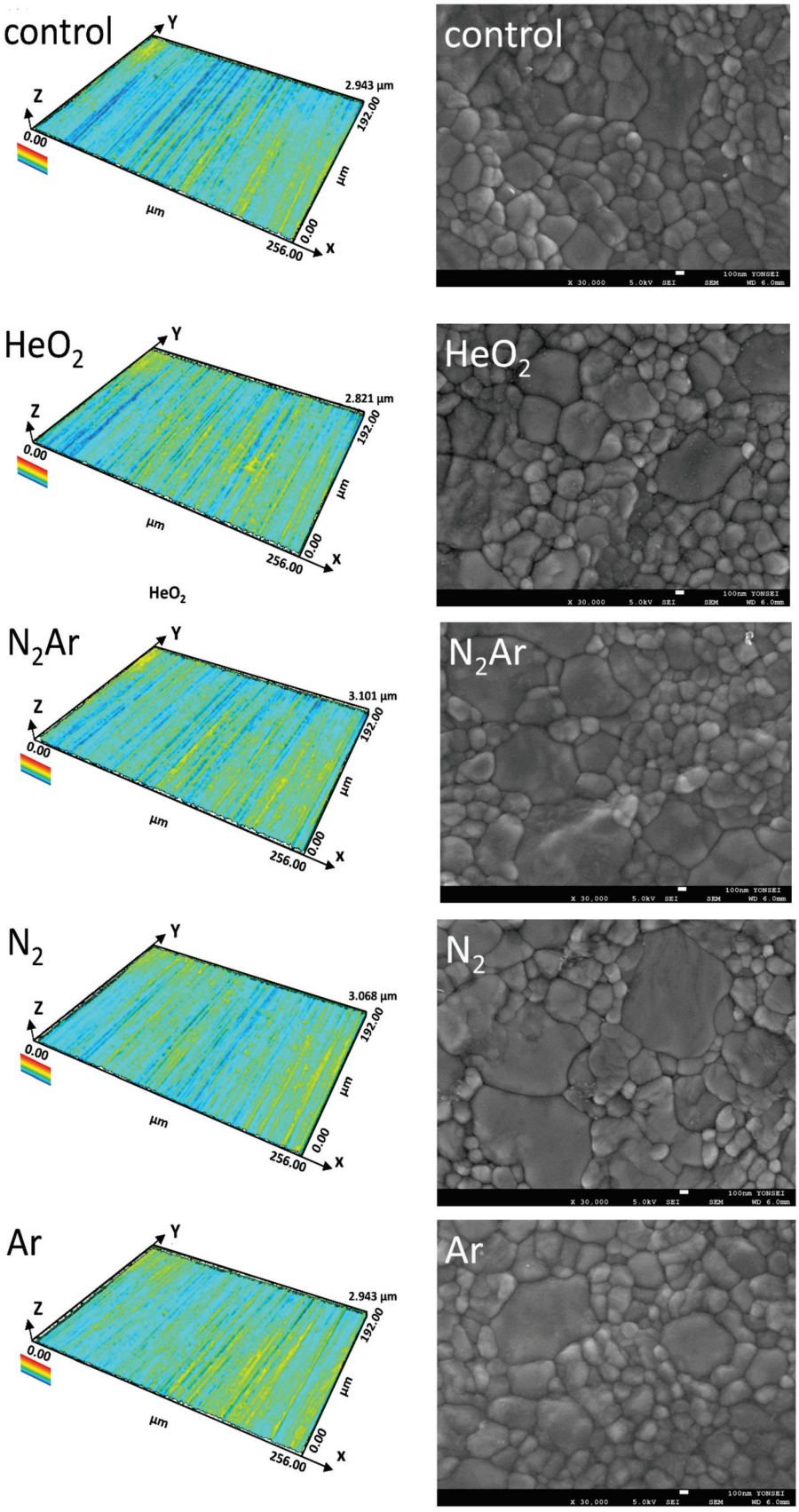


Figure 5. Representative three-dimensional images obtained by confocal laser-scanning microscopy (**left**) and scanning electron microscopic images at 30,000× magnification (**right**) of each group.

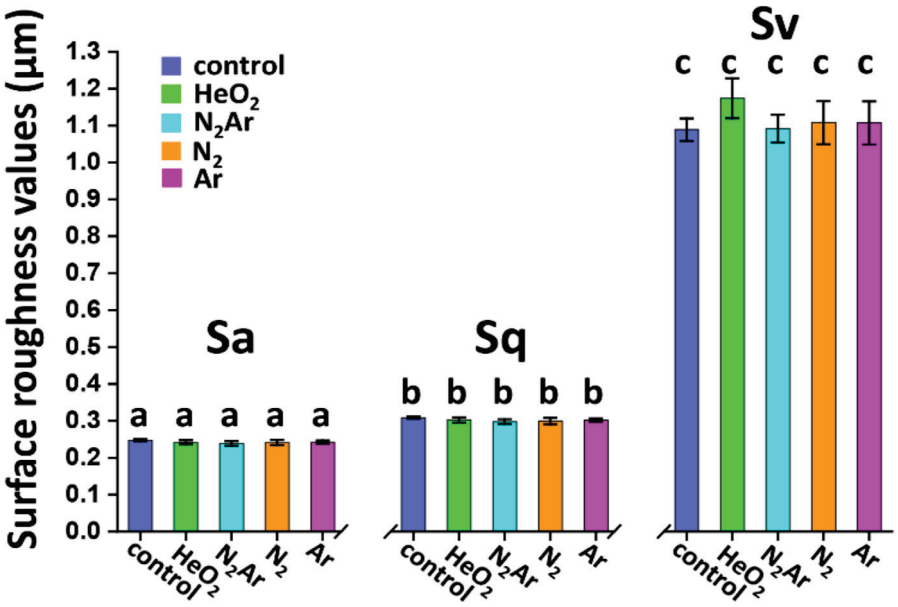


Figure 6. The surface texture parameters (Sa, Sq, and Sv) of each group. The identical letter shows no significant difference on Sa, Sq, and Sv values ($p > 0.05$).

3. Discussion

This study investigated the effect of plasma gas compositions on the physicochemical surface characteristics of 3Y-TZP. A CAP discharge was carried out by using four different feed gases (He/O_2 mixture, N_2/Ar mixture, N_2, and Ar) from an application distance of 10 mm for 60 s. According to the results of this study, the rate of decrease in water contact angle varied from 22.17% to 30.13%, while the rate of increase in surface free energy varied from 7.90% to 19.6%, depending on the plasma gas type. As previously reported [20], a lower contact angle indicated a more hydrophilic surface. In this study, a greater decrease in water contact angle was observed in the N_2Ar group than in other plasma groups. This result was supported by the results of the XPS analysis; the N_2Ar-specimen showed a lower carbon content and a higher oxygen content in comparison with the specimens subjected to other plasma gases. The dominant carbon species detected in XPS were generally associated with airborne carbon contaminants, which made the surface hydrophobic [38]. In the N_2Ar group, C-C bonds in the hydrocarbon were broken or excited to metastable states by the collision cross-sections [39] between N and Ar, resulting in the formation of new functional groups that could generate a hydrophilic surface. The N_2Ar-specimen had a greater amount of C-O species compared to other groups and this would be associated with the higher γ^p values in the N_2Ar group. Feng et al. [40] reported that γ^p component in the surface energy influenced the cellular interaction more importantly compared to γ^d component. Considering the most noticeable changes in contact angle and γ^p component observed in the N_2Ar group in this study, N_2Ar plasma could lead to higher bioactivity of the zirconia specimen compared to other plasma groups.

Partially stabilized zirconia, suitable for dental applications, is obtained by the addition of lower-valence oxide, such as 3 mol% (5.2 wt%) yttria. The oxygen vacancies, which are introduced to compensate for the charge imbalance, are responsible for the high ionic conductivity of the zirconia material [41]. In this study, the dissociation of water, which would create the OH(b) groups per vacancy, occurred in all plasma groups, resulting in more positive surface charges [40]. A greater increase in OH(b) was observed in the N_2 group than in other groups. A previous study reported that the OH(b) could play a more significant role than the OH(a) to enhance bioactivity of the substrate because the primary protein can be easily attracted to positively charged surfaces [16].

Unlike other plasma gases, N_2Ar plasma led to the formation of nitrate (NO_3^-) species on the zirconia surface, according to the results of the XPS analysis in this study. The nitrate

anion can produce a highly reactive nitrate radical ($^{\bullet}NO_3$), which can react with organic compounds due to high diffusivity into non-polar solvents [42]. Thus, this may enhance the bioactivity or bonding efficiency of 3Y-TZP. The ubiquitous formation of zirconium oxynitride (ZrO_xN_y) investigated in all plasma groups can be proposed as being associated with high oxygen concentration in the superficial regions of zirconia specimens. It has been reported that the zirconium oxynitride could be formed when the N concentration did not reach a critical value to transform it into the ZrN structure [29]. The plasma nitriding of zirconia could produce ZrN structures, which were characterized by high hardness, even harder than 3Y-TZP, high resistance to wear or corrosion, and high thermal stability [29]. Morisaki et al. [30] revealed that the nitridation of zirconia was generated by a replacement of oxides with nitrides, and the lattice structure of the zirconium oxynitride was slightly deformed from the ideal cubic structure. The results of this study are consistent with those obtained in Morisaki et al.'s study [30]. The Rietveld refinement showed a decrease in the cubic phase content and an increase in the metastable tetragonal (t') phase content in both N_2Ar and N_2 groups, suggesting the possible effects of the plasma nitriding on the lattice distortion [43]. The t' phase was formed in all plasma groups, which can be attributed to the induced oxygen atom displacements in the zirconia crystal structures [43] during the plasma irradiation. Considering the XRD peak broadening and the flatter slope from the W-H analysis obtained in the N_2Ar group, the plasma nitriding of 3Y-TZP would induce lattice strain through the crystal deformation [44]. This may play an important role in the enhancement of mechanical properties by increasing damage resistance [45]. A similar result was reported by Abbas et al. [46], who found the broadened XRD peaks in silicon samples subjected to N_2Ar plasma. They also concluded that the changes in crystallinity, crystallite sizes, residual stress, and surface morphology of Si samples were related to Ar concentration in N_2Ar plasma.

As mentioned, an admixture of molecular gas to a chemically inert noble gas, such as helium, neon, argon, etc., can change the plasma discharge kinetics, showing better biologic performance [23]. For N_2 plasma, its dissociation is very difficult because of the extremely strong triple bond between two N atoms [47]. A previous study revealed that the addition of argon to the N_2 plasma resulted in the enhanced generation of active species through Pennig excitation and ionization, depending on the Ar concentration in N_2Ar plasma [46]. Bravo et al. [47] reported that the metastable nitrogen molecules were produced utilizing a plasma gas mixture containing N_2 and Ar. Dyatko et al. [23] found that even a small amount of nitrogen addition (1%) to argon was responsible for a sharp decrease in the discharge voltage in N_2Ar plasma as compared to that in pure Ar gas. This behavior of the N_2Ar discharge involved the electron collision cross-section. This study used N_2Ar plasma containing 10% nitrogen, which was reported to be the most frequently used concentration for the application to surface treatments [47]. During the N_2Ar plasma irradiation on the zirconia surface, nitrogen atoms can be replaced by oxygen atoms and thus the zirconia surface tends to have more negative charges. The most suitable nitrogen concentration in N_2Ar plasma should be determined for the production of bioactive zirconia surface in further studies. Although helium plasma can easily give rise to a stable glow discharge with the addition of an active gas such as O_2, N_2, or CF_4, reactive oxygen species cannot easily reach the target material because helium is considerably lighter than air [48]. Contrary to helium, argon is denser than air and thus, the excited atomic oxygen can be easily transferred to the substrate [48]. According to the result of this study (Figure 3A), an increase in the reactive oxygen species upon adding nitrogen to argon was observed.

In this study, different plasma gas species produced different physicochemical surface interactions with 3Y-TZP, although the plasma treatments did not affect the surface morphology of zirconia as shown by SEM and CLSM analysis. Therefore, the null hypothesis was rejected. From a biomaterials perspective, biologic responses and, hence, the clinical function of 3Y-TZP can be enhanced by controlling the plasma gas type and the working gas composition. However, the interpretation of the present results should be done with caution since an aging effect such as a time-dependent hydrophobic recovery can occur at

the zirconia surface, which would act as a limiting factor on the efficiency of the plasma treatments [17]. Further investigations are required to identify the time scale for the hydrophobic recovery of the zirconia surface subjected to the plasma treatment with various gas species to determine the effective treatment time of plasma discharge to improve the bioactivity of zirconia surfaces.

4. Materials and Methods

4.1. Specimen Preparation and Plasma Surface Treatment

The 3Y-TZP (KATANA ML, Kuraray Noritake Dental, Osaka, Japan) sintered at 1500 °C for 2 h in air was used in this study. A total of 140 plate-shaped specimens (10.0 mm × 10.0 mm × 1.0 mm) were prepared and polished to a uniform finish with an 800 grit SiC paper. After ultrasonic cleaning for 20 min, the specimens were subjected to plasma irradiation at room temperature using a cold atmospheric pressure DBD plasma generator (PR-ATO-001, ICD Co., Anseong, Gyeonggi-do, Korea). The plasma was vertically applied to the specimen's surface from a distance of 10 mm [39] for 60 s. The schematic of the device is shown in Figure 7. All specimens were randomly allocated into five groups (n = 28), with four of them treated by plasmas with four different gases and one group untreated (control). As the feed gases, Ar, N_2, N_2/Ar mixture (10% nitrogen/90% argon) [7], and He/O_2 mixture (15% helium/85% oxygen) [8] were selected. The input voltage was fixed at 5 kV with a high voltage transformer, and the operation frequency was set to 25 kHz using a digital oscilloscope (MSO4032, Tektronix, Beaverton, OR, USA). A mass flow controller maintained a constant gas flow rate of 10 standard liters per minute (slm).

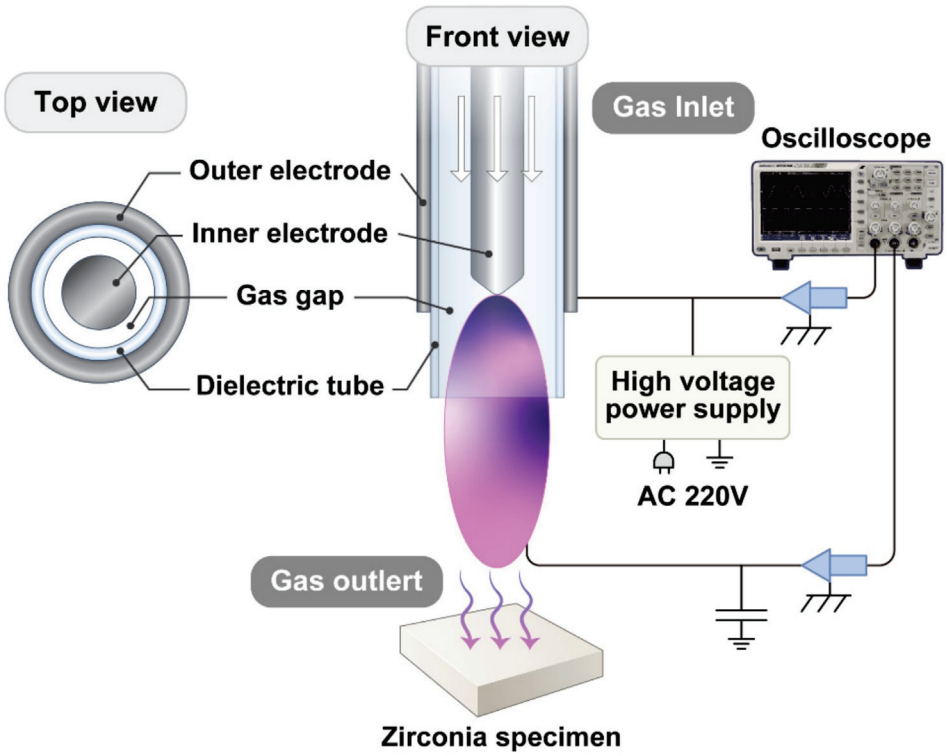


Figure 7. Schematic diagram of experimental setup for plasma surface treatments.

4.2. Surface Contact Angle and Surface Free Energy

The surface wettability of the specimen was characterized using a contact angle meter (Phoenix 300 Touch, S.E.O., Suwon, Gyeonggi-do, Korea). Contact angle measurements were performed by a sessile drop technique at room temperature and 60% relative humidity using two different test liquids, distilled water (n = 10) and non-polar diiodomethane (n = 10). All measurements were performed at the center of the specimen.

The surface free energy was calculated by measuring the contact angles of two test liquids according to the Owens–Wendt equation [49]. Total surface free energy (γ^{total}), including the dispersion component(γ^{d}) and polar component (γ^{p}), was calculated.

4.3. X-ray Photoelectron Spectroscopy (XPS) Measurement

The elemental composition of the specimen of each group was performed by using XPS (K-alpha, Thermo Fisher Scientific Inc., Waltham, MA, USA) with a monochromatic Al Kα X-ray source (1486.6 eV) at 12 kV and 3 mA (n = 1). Data acquisition and the processing of core-level spectra were performed using a software (Thermo Avantage v5.980, Thermo Fisher Scientific Inc., Waltham, MA, USA). All XPS spectra were calibrated with the C 1s peak at 284.6 eV [26].

4.4. X-ray Diffraction (XRD) and Rietveld Analysis

One specimen from each plasma group was submitted to determine the crystal structures and phase transformations. The X-ray powder diffraction (XRD) pattern was taken at room temperature in a DMAX-2200PC X-ray diffractometer (Rigaku, Tokyo, Japan) using monochromatic CuKα1 radiation (λ = 1.5406 Å). The data were collected in the 2θ range of 20–90 with a step size of 0.02 and a step time of 4 s/step. The quantitative phase analysis was obtained by Rietveld refinement implemented in the Fullprof program [15]. Especially, Williamson–Hall (W–H) analysis was used to determine the changes in the crystallite size and the lattice strain induced by the plasma treatment using the formula as given below [50]:

$$\beta_{hkl} \cos\theta = \frac{K\lambda}{D} + 4\varepsilon \sin\theta \quad (1)$$

where β is the integral breadth or the full width at half maxima, D is the crystallite size, K is a shape factor (0.9), and ε is the strain.

4.5. Surface Topography

Analyses of three-dimensional (3-D) surface characteristics were performed using a confocal laser scanning microscopy (CLSM; LEXT OLS3000, Olympus, Tokyo, Japan) at 50× magnification in a 256 × 192 μm^2 area (n = 5). The surface texture parameters, in particular the arithmetical mean height, Sa; the root mean square height, Sq; and the maximum pit height, Sv, were calculated in accordance with ISO 25,178 [51]. The surface analysis was independently carried out in 2 points at the center, and a total of 10 measurements was obtained for each plasma group.

The surface microstructures of the specimens were evaluated using a scanning electron microscope (SEM; JSM-7800F Prime, JEOL, Tokyo, Japan) at an accelerating voltage of 5.0 kV and a working distance (WD) of 6.0 mm at 3000×, 10,000×, and 30,000× magnifications (n = 1).

4.6. Statistical Analysis

The statistical significance of the data was assessed by a one-way analysis of variance (ANOVA) with Tukey's honesty significant difference (HSD) post hoc test at α = 0.05. All analyses were performed using statistical software (IBM SPSS Statistics, v25.0, IBM Corp., Chicago, IL, USA).

5. Conclusions

We have investigated the effect of plasma gas types on surface physicochemistry and surface topography of 3Y-TZP by contact angle, XPS, XRD, CLSM, and SEM analysis. With the limitation of this in vitro study, the following conclusions can be drawn:

1. Plasma processing of 3Y-TZP with He/O_2 mixture, N_2/Ar mixture, N_2, and Ar decreased the contact angle and increased the surface energy without changing its surface topography. In particular, the highest value of the polar component in the surface energy was obtained in the N_2/Ar group, which was probably related to the high interaction energy of the zirconia surface.

2. XPS revealed that a reduction in the surface C content along with an increase in O content was pronounced in the case of N_2/Ar compared to others, which was responsible for high hydrophilicity of the surface. XRD showed that the changes in crystallite size and microstrain due to oxygen atom displacements were observed in the N_2/Ar group.
3. Although further studies are required, promising findings obtained in this study show that N_2/Ar plasma treatment may contribute to enhancing the anti-microbial properties, the osseointegration capability, and the adhesion performance of 3Y-TZP by controlling the plasma-generated nitrogen functionalities.

Author Contributions: Conceptualization, H.-K.K., C.-H.K. and S.-U.K.; methodology, H.-K.K., C.-H.K., S.-U.K., Y.-K.K. and S.-J.K.; investigation, H.-K.K., C.-H.K., S.-U.K., Y.-W.Y., Y.-K.K. and S.-J.K.; formal analysis, H.-K.K., Y.-K.K. and S.-J.K.; data curation, S.-U.K. and C.-H.K.; software, H.-K.K., Y.-W.Y. and Y.-K.K.; writing–original draft preparation, S.-U.K. and H.-K.K.; writing–review and editing, S.-U.K., H.-K.K., C.-H.K., Y.-K.K. and S.-J.K.; funding acquisition, H.-K.K., C.-H.K., Y.-K.K. and S.-J.K. All authors have read and agreed to the published version of the manuscript.

Funding: This work was supported by the National Research Foundation of Korea (NRF) grant funded by the Korea government (MSIT: Ministry of Science and ICT) (Grant No. NRF-2019R1F1A1062112 and Grant No. NRF-2021R1A6A1A10044950); a grant of the Korea Health Technology R&D Project through the Korea Health Industry Development Institute (KHIDI), funded by the Ministry of Health & Welfare, Republic of Korea (Grant No. HR21C1003); and Basic Science Research Program through the National Research Foundation of Korea (NRF) funded by the Ministry of Science, ICT, and Future Planning (Grant No. 2018R1A2B3009008).

Institutional Review Board Statement: Not applicable.

Informed Consent Statement: Not applicable.

Data Availability Statement: The data presented in this study are available on request from the corresponding author.

Conflicts of Interest: The authors declare no conflict of interest.

References

1. Amani, H.; Arzaghi, H.; Bayandori, M.; Dezfuli, A.S.; Pazoki-Toroudi, H.; Shafiee, A.; Moradi, L. Controlling cell behavior through the design of biomaterial surfaces: A focus on surface modification techniques. *Adv. Mater. Interfaces* **2019**, *6*, 1900572. [CrossRef]
2. Babaeva, N.Y.; Naidis, G.V. Modeling of plasmas for biomedicine. *Trends Biotechnol.* **2018**, *36*, 603–614. [CrossRef]
3. Bárdos, L.; Baránková, H. Cold atmospheric plasma: Sources, processes, and applications. *Thin Solid Films* **2010**, *518*, 6705–6713. [CrossRef]
4. Liu, W.; Ma, C.; Zhao, S.; Chen, X.; Wang, T.; Zhao, L.; Li, Z.; Niu, J.; Zhu, L.; Chai, M. Exploration to generate atmospheric pressure glow discharge plasma in air. *Plasma Sci. Technol.* **2018**, *20*, 035401. [CrossRef]
5. Kang, S.U.; Choi, J.W.; Chang, J.W.; Kim, K.I.; Kim, Y.S.; Park, J.K.; Kim, Y.E.; Lee, Y.S.; Yang, S.S.; Kim, C.H. N_2 non-thermal atmospheric pressure plasma promotes wound healing in vitro and in vivo: Potential modulation of adhesion molecules and matrix metalloproteinase-9. *Exp. Dermatol.* **2017**, *26*, 163–170. [CrossRef] [PubMed]
6. Gentile, P.; Calabrese, C.; De Angelis, B.; Dionisi, L.; Pizzicannella, J.; Kothari, A.; De Fazio, D.; Garcovich, S. Impact of the different preparation methods to obtain autologous non-activated platelet-rich plasma (A-PRP) and activated platelet-rich plasma (AA-PRP) in plastic surgery: Wound healing and hair regrowth evaluation. *Int. J. Mol. Sci.* **2020**, *21*, 431. [CrossRef] [PubMed]
7. Park, J.K.; Kim, Y.S.; Kang, S.U.; Lee, Y.S.; Won, H.R.; Kim, C.H. Nonthermal atmospheric plasma enhances myoblast differentiation by eliciting STAT3 phosphorylation. *FASEB J.* **2019**, *33*, 4097–4106. [CrossRef]
8. Kim, C.H.; Kwon, S.; Bahn, J.H.; Lee, K.; Jun, S.I.; Rack, P.D.; Baek, S.J. Effects of atmospheric nonthermal plasma on invasion of colorectal cancer cells. *Appl. Phys. Lett.* **2010**, *96*, 243701. [CrossRef]
9. Yan, D.; Malyavko, A.; Wang, Q.; Lin, L.; Sherman, J.H.; Keidar, M. Cold atmospheric plasma cancer treatment, a critical review. *Appl. Sci.* **2021**, *11*, 7757. [CrossRef]
10. Yang, Y.; Zheng, M.; Yang, Y.; Li, J.; Su, Y.F.; Li, H.P.; Tan, J.G. Inhibition of bacterial growth on zirconia abutment with a helium cold atmospheric plasma jet treatment. *Clin. Oral Investig.* **2020**, *24*, 1465–1477. [CrossRef]
11. Brandenburg, R. Dielectric barrier discharges: Progress on plasma sources and on the understanding of regimes and single filaments. *Plasma Sources Sci. Technol.* **2017**, *26*, 053001. [CrossRef]
12. Zhang, Y.; Lawn, B.R. Novel zirconia materials in dentistry. *J. Dent. Res.* **2018**, *97*, 140–147. [CrossRef] [PubMed]
13. Valverde, G.B.; Coelho, P.G.; Janal, M.N.; Lorenzoni, F.C.; Carvalho, R.M.; Thompson, V.P.; Weltemann, K.D.; Silva, N.R. Surface characterisation and bonding of Y-TZP following non-thermal plasma treatment. *J. Dent.* **2013**, *41*, 51–59. [CrossRef] [PubMed]

14. Guo, S.; Liu, N.; Liu, K.; Li, Y.; Zhang, W.; Zhu, B.; Gu, B.; Wen, N. Effects of carbon and nitrogen plasma immersion ion implantation on bioactivity of zirconia. *RSC Adv.* **2020**, *10*, 35917–35929. [CrossRef]
15. Kim, H.K.; Yoo, K.W.; Kim, S.J.; Jung, C.H. Phase transformations and subsurface changes in three dental zirconia grades after sandblasting with various Al_2O_3 particle Sizes. *Materials* **2021**, *14*, 5321. [CrossRef]
16. Noro, A.; Kaneko, M.; Murata, I.; Yoshinari, M. Influence of surface topography and surface physicochemistry on wettability of zirconia (tetragonal zirconia polycrystal). *J. Biomed. Mater. Res. Part B* **2013**, *101B*, 355–363. [CrossRef]
17. Wu, C.C.; Wei, C.K.; Ho, C.C.; Ding, S.J. Enhanced hydrophilicity and biocompatibility of dental zirconia ceramics by oxygen plasma treatment. *Materials* **2015**, *8*, 684–699. [CrossRef]
18. Noro, A.; Kameyama, A.; Haruyama, A.; Takahashi, T. Influence of hydrophilic pre-treatment on resin bonding to zirconia ceramics. *Bull. Tokyo Dent. Coll.* **2015**, *56*, 33–39. [CrossRef]
19. Ahn, J.J.; Kim, D.S.; Bae, E.B.; Kim, G.C.; Jeong, C.M.; Huh, J.B.; Lee, S.H. Effect of non-thermal atmospheric pressure plasma (NTP) and zirconia primer treatment on shear bond strength between Y-TZP and resin cement. *Materials* **2020**, *13*, 3934. [CrossRef]
20. Huner, U.; Guler, H.A.; Damar Huner, I. Effect of gas type and application distance on atmospheric pressure plasma jet-treated flax composites. *J. Reinf. Plast. Compos.* **2017**, *36*, 1197–1210. [CrossRef]
21. Suenaga, Y.; Takamatsu, T.; Aizawa, T.; Moriya, S.; Matsumura, Y.; Iwasawa, A.; Okino, A. Influence of controlling plasma gas species and temperature on reactive species and bactericidal effect of the plasma. *Appl. Sci.* **2021**, *11*, 11674. [CrossRef]
22. Purevdorj, D.; Igura, N.; Ariyada, O.; Hayakawa, I. Effect of feed gas composition of gas discharge plasmas on *Bacillus pumilus* spore mortality. *Lett. Appl. Microbiol.* **2003**, *37*, 31–34. [CrossRef] [PubMed]
23. Dyatko, N.A.; Ionikh, Y.Z.; Meshchanov, A.V.; Napartovich, A.P.; Barzilovich, K.A. Specific features of the current-voltage characteristics of diffuse glow discharges in Ar: N_2 mixtues. *Plasma Phys. Rep.* **2010**, *36*, 1040–1064. [CrossRef]
24. Gupta, S.; Gangwar, R.K.; Srivastava, R. Diagnostics of Ar/N_2 mixture plasma with detailed electron-impact argon fine-structure excitation cross sections. *Spectrochim. Acta Part B* **2018**, *149*, 203–213. [CrossRef]
25. Dyatko, N.A.; Ionikh, Y.Z.; Napartovich, A.P. Influence of nitrogen admixture on plasma characteristics in a dc argon glow discharge and in afterglow. *Atoms* **2019**, *7*, 13. [CrossRef]
26. Barquete, C.G.; Simão, R.A.; Almeida Fonseca, S.S.; Elias, A.B.; Antunes Guimarães, J.G.; Herrera, E.Z.; Mello, A.; Moreira da Silva, E. Effect of cementation delay on bonding of self-adhesive resin cement to yttria-stabilized tetragonal zirconia polycrystal ceramic treated with nonthermal argon plasma. *J. Prosthet. Dent.* **2021**, *125*, 693.e1–693.e7. [CrossRef]
27. Jeon, B.; Kim, A.; Ricard, A.; Sarrette, J.P.; Yu, X.; Kim, Y.K. A study on selective surface nitridation of TiO_2 nanocrystals in the afterglows of N_2 and N_2-O_2 microwave plasmas. *Appl. Surf. Sci.* **2018**, *432*, 163–169. [CrossRef]
28. Lopez, L.C.; Belviso, M.R.; Gristina, R.; Nardulli, M.; d'Agostino, R.; Favia, P. Plasma-treated nitrogen-containing surfaces for cell adhesion: The role of the polymeric substrate. *Plasma Processes Polym.* **2007**, *4*, S402–S405. [CrossRef]
29. Milani, R.; Cardoso, R.P.; Belmonte, T.; Figueroa, C.A.; Perottoni, C.A.; Zorzi, J.E.; Soares, G.V.; Baumvol, I.J.R. Nitriding of yttria-stabilized zirconia in atmospheric pressure microwave plasma. *J. Mater. Res.* **2009**, *24*, 2021–2028. [CrossRef]
30. Morisaki, N.; Yoshida, H.; Matsui, K.; Tokunaga, T.; Sasaki, K.; Yamamoto, T. Synthesis of zirconium oxynitride in air under DC electic fields. *Appl. Phys. Lett.* **2016**, *109*, 83104. [CrossRef]
31. Ji, M.K.; Lee, J.T.; Yim, E.K.; Park, C.; Moon, B.K.; Lim, H.P. Effect of Atmospheric Pressure Plasma Treatment on Shear Bond Strength Between Zirconia and Dental Porcelain Veneer. *J. Nanosci. Nanotechnol.* **2020**, *20*, 5683–5685. [CrossRef] [PubMed]
32. Zhang, W.; Liu, J.; Shi, H.; Liu, N.; Yang, K.; Shi, L.; Gu, B.; Wang, H.; Ji, J.; Chu, P.K. Effects of plasma-generated nitrogen functionalities on the upregulation of osteogenesis of bone marrow-derived mesenchymal stem cells. *J. Mater. Chem. B* **2015**, *3*, 1856–1863. [CrossRef] [PubMed]
33. Kwon, S.; Choi, H.; Choi, W.; Kang, H. Wettability of CNW/ITO micro structure for modification of surface hydrophilicity. *Appl. Sci.* **2020**, *10*, 142. [CrossRef]
34. Katea, S.N.; Westin, G. Carbothermal nitridation of solution synthesised ZrO_2-carbon nanocomposites; phase-development from precursor to nitride. *Ceram. Int.* **2021**, *47*, 10828–10847. [CrossRef]
35. Smeacetto, F.; Salvo, M.; Ajitdoss, L.C.; Perero, S.; Moskalewicz, T.; Boldrini, S.; Doubova, L.; Ferraris, M. Yttria-stabilized zirconia thin film electrolyte produced by RF sputtering for solid oxide fuel cell applications. *Mater. Lett.* **2010**, *64*, 2450–2453. [CrossRef]
36. Shafi, P.M.; Bose, A.C. Impact of crystalline defects and size on X-ray line broadening: A phenomenological approach for tetragonal SnO2 nanocrystals. *AIP Adv.* **2015**, *5*, 057137. [CrossRef]
37. Deb, A.K.; Chatterjee, P. Estimation of lattice strain in alumina-zirconia nanocomposites by X-ray diffraction peak profile analysis. *J. Theor. Appl. Phys.* **2019**, *13*, 221–229. [CrossRef]
38. Vesel, A.; Mozetic, M.; Drenik, A.; Milosevic, S.; Krstulovic, N.; Balat-Pichelin, M.; Poberaj, I.; Babic, D. Cleaning of porous aluminium titanate by oxygen plasma. *Plasma Chem. Plasma Process.* **2006**, *26*, 577–584. [CrossRef]
39. Kim, M.C.; Song, D.K.; Shin, H.S.; Baeg, S.H.; Kim, G.S.; Boo, J.H.; Han, J.G.; Yang, S.H. Surface modification for hydrophilic property of stainless steel treated by atmospheric-pressure plasma jet. *Surf. Coat. Technol.* **2003**, *171*, 312–316. [CrossRef]
40. Feng, B.; Weng, J.; Yang, B.C.; Qu, S.X.; Zhang, X.D. Characterization of surface oxide films on titanium and adhesion of osteoblast. *Biomaterials* **2003**, *24*, 4663–4670. [CrossRef]
41. Chevalier, J.; Gremillard, L. The tetragonal-monoclinic transformation in zirconia: Lessons learned and future trends. *J. Am. Ceram. Soc.* **2009**, *92*, 1901–1920. [CrossRef]

42. Mezyk, S.P.; Cullen, T.D.; Rickman, K.A.; Mincher, B.J. The reactivity of the nitrate radical ($^{\bullet}NO_3$) in aqueous and organic solutions. *Int. J. Chem. Kinet.* **2017**, *49*, 635–642. [CrossRef]
43. Kim, H.K. Effect of a rapid-cooling protocol on the optical and mechanical properties of dental monolithic zirconia containing 3–5 mol% Y_2O_3. *Materials* **2020**, *13*, 1923. [CrossRef] [PubMed]
44. Feng, S.; Xu, Z. Strain characterization in two-dimensional crystals. *Materials* **2021**, *14*, 4460. [CrossRef] [PubMed]
45. Inokoshi, M.; Zhang, F.; Vanmeensel, K.; De Munck, J.; Minakuchi, S.; Naert, I.; Vleugels, J.; Van Meerbeek, B. Residual compressive surface stress increases the bending strength of dental zirconia. *Dent. Mater.* **2017**, *33*, e147–e154. [CrossRef]
46. Abbas, K.; Ahmad, R.; Khan, I.A.; Saleem, S.; Ikhlaq, U. Influence of Argon gas concentration in N_2-Ar plasma for the nitridation of Si in abnormal glow discharge. *Int. J. Mater. Metall. Eng.* **2016**, *10*, 858–870. [CrossRef]
47. Bravo, J.A.; Rincón, R.; Muñoz, J.; Sánchez, A.; Calzada, M.D. Spectroscopic characterization of argon-nitrogen surface-wave discharges in dielectric tubes at atmospheric pressure. *Plasma Chem. Plasma Process.* **2015**, *35*, 993–1014. [CrossRef]
48. Lim, J.P.; Uhm, H.S. Influence of oxygen in atmospheric-pressure argon plasma jet on sterilization of *Bacillus atrophaeous* spores. *Phys. Plasmas* **2007**, *6*, 912–922. [CrossRef]
49. Liber-Kneć, A.; Łagan, S. Surface testing of dental biomaterials-determination of contact angle and surface free energy. *Materials* **2021**, *14*, 2716. [CrossRef]
50. Mote, V.D.; Purushotham, Y.; Dole, B.N. Williamson-Hall analysis in estimation of lattice strain in nanometer-sized ZnO particles. *J. Theor. Appl. Phys.* **2012**, *6*, 6. [CrossRef]
51. Kim, H.K.; Ahn, B. Effect of Al_2O_3 sandblasting particle size on the surface topography and residual compressive stresses of three different dental zirconia grades. *Materials* **2021**, *14*, 610. [CrossRef] [PubMed]

International Journal of
Molecular Sciences

MDPI

Review

The Impact of Early Saliva Interaction on Dental Implants and Biomaterials for Oral Regeneration: An Overview

Marcel Ferreira Kunrath [1,2,*] and Christer Dahlin [1]

[1] Department of Biomaterials, Institute of Clinical Sciences, Sahlgrenska Academy, University of Gothenburg, P.O. Box 412, SE 405 30 Goteborg, Sweden; christer.dahlin@biomaterials.gu.se
[2] Department of Dentistry, School of Health and Life Sciences, Pontifical Catholic University of Rio Grande do Sul (PUCRS), P.O. Box 6681, Porto Alegre 90619-900, RS, Brazil
* Correspondence: marcel.kunrath@gu.se; Tel.: +46-0722063757

Abstract: The presence of saliva in the oral environment is relevant for several essential health processes. However, the noncontrolled early saliva interaction with biomaterials manufactured for oral rehabilitation may generate alterations in the superficial properties causing negative biological outcomes. Therefore, the present review aimed to provide a compilation of all possible physical–chemical–biological changes caused by the early saliva interaction in dental implants and materials for oral regeneration. Dental implants, bone substitutes and membranes in dentistry possess different properties focused on improving the healing process when in contact with oral tissues. The early saliva interaction was shown to impair some positive features present in biomaterials related to quick cellular adhesion and proliferation, such as surface hydrophilicity, cellular viability and antibacterial properties. Moreover, biomaterials that interacted with contaminated saliva containing specific bacteria demonstrated favorable conditions for increased bacterial metabolism. Additionally, the quantity of investigations associating biomaterials with early saliva interaction is still scarce in the current literature and requires clarification to prevent clinical failures. Therefore, clinically, controlling saliva exposure to sites involving the application of biomaterials must be prioritized in order to reduce impairment in important biomaterial properties developed for rapid healing.

Keywords: saliva; oral regeneration; interaction; biomaterials; bone regeneration

Citation: Kunrath, M.F.; Dahlin, C. The Impact of Early Saliva Interaction on Dental Implants and Biomaterials for Oral Regeneration: An Overview. *Int. J. Mol. Sci.* **2022**, *23*, 2024. https://doi.org/10.3390/ijms23042024

Academic Editor: Mary Anne Melo

Received: 20 January 2022
Accepted: 10 February 2022
Published: 11 February 2022

Publisher's Note: MDPI stays neutral with regard to jurisdictional claims in published maps and institutional affiliations.

Copyright: © 2022 by the authors. Licensee MDPI, Basel, Switzerland. This article is an open access article distributed under the terms and conditions of the Creative Commons Attribution (CC BY) license (https://creativecommons.org/licenses/by/4.0/).

1. Introduction

Saliva present in the oral cavity is recognized as the first liquid that interacts with materials or compounds coming from the external environment [1,2]. Furthermore, its presence is crucial in several basic food processes, such as lubrication, digestion and solubilization in the oral environment [2,3]. Saliva is predominantly water (99%); however, there is a high range of proteins, different minerals, dead cells and a large amount of bacteria associated with the composition [1,4]. The interaction of saliva and its compounds with biomaterials applied in oral rehabilitation or tissue regeneration is inherent, thus impacting the creation of small salivary pellicles [5,6] that may cause some chemical–physical–biological alterations in biomaterials.

Currently, biomaterials developed for oral rehabilitation and tissue regeneration, such as dental implants, membranes and bone substitutes, are made with extreme detailing of properties aimed at the best biological responses when interacting with oral tissues [7–9]. Alterations such as the micro- and nanotexturization of surfaces are developed with the aim of accelerated cellular response and high adhesion in contact with bone cells [7,10]; the porosity and mechanical strength are controlled in membranes and in bone substitutes for better tissue responses in guided bone regeneration [8,11,12]; and wetting properties are altered for superior physical–chemical interactions within surfaces and cells in oral tissues [13,14]. However, the early interaction with saliva can cause significant changes in these properties that can modify the desired effectiveness in biological terms.

A recent report showed the loss of hydrophilicity on dental implant surfaces after interaction with human saliva in vitro for 10 min, showing a negative outcome caused by the early interaction with saliva [14]. Additionally, surfaces with microroughness and high hydrophilicity showed greater adhesion of saliva proteins compared to smooth and less hydrophilic surfaces, suggesting that surface properties influence the interaction with saliva [15]. On the other hand, saliva shows some positive features against bacterial colonization due to its lubrication and viscosity properties; therefore, some investigations demonstrated greater bacterial colonization in static biomaterials without the presence of saliva compared with biomaterials embedded in saliva [16,17]. However, as a counterpoint against the beneficial characteristics, there are many reports showing the growth of bacterial biofilms in biomaterials applied in tissue regeneration after interaction with saliva, compromising properties and biocompatibility factors, normally caused by dysbiosis or imbalance in the superficial region, and generating an enrichment of substances suitable for pathogens [18–21].

It is well known that saliva has some influence on all biomaterials inserted in the oral environment, especially on those that are subjected to exposure for long periods of time such as dental implants and components for prosthetic rehabilitations [16,22]. However, the early influence of salivary interactions with biomaterials for oral regeneration remains poorly understood due to numerous innovative modifications in biomaterials and due to the difficulty of analyzing biomaterials directly after their application in the oral region. The aim of this review is to highlight the main early alterations caused in the physicochemical properties of biomaterials for oral regeneration exposed to saliva and to demonstrate their possible alterations in terms of biocompatibility and contamination when saliva interactions occur. The review will conclude with clinical considerations about possible effects derived from early salivary interaction with biomaterials for oral regeneration in the clinical environment.

2. Search Strategy

An electronic search in the PubMed Medline, Scopus and Google Scholar databases was conducted to identify in vitro, in vivo and clinical studies assessing the interaction of saliva with biomaterials for oral regeneration. The electronic search was carried out using key words and MeSH terms: “saliva” or “saliva contact” or “saliva interaction” or “saliva proteins” and “biomaterials” or “implants” or “dental implants” or “membranes” or “bone substitutes” or “bone regeneration” or “cells” or “bacteria”. The inclusion criteria for this study were as follows: (1) English written studies, (2) reviews, (3) meta-analyses, (4) clinical trials, (5) animal studies and (6) in vitro studies. The titles and abstracts were evaluated individually to find possible relevant studies for this review. The key studies (85) were then selected independently and analyzed to summarize the possible effects caused by the saliva interaction with biomaterials for bone regeneration.

3. Saliva Composition

Saliva is mainly secreted by the major glands (parotid, sublingual and submandibular) and minor glands such as labial, palatal and buccal glands [1,23]. The interaction of saliva with any substrate inserted in the oral environment results in the formation of a thin film with thickness measured in nanometers up to 1 h and in micrometers (approximately 1.3 μm) after 24 h [1,5].

The essential component of saliva is water (99%); however, inorganic elements such as NaCl, KCl, $NHCO_3$, HPO_4 and $CaCO_3$ and inorganic constituents such as proteins, mucin, serum albumin and globulin, enzymes, epithelial cells and lymphocytes are found [4,23]. In recent years, more than 1400 salivary proteins have been identified [24] and have specific actions in oral matter, such as lubrication, digestion, solubilization, defense, and remineralization. The most commonly identified proteins in saliva are shown in Table 1.

Table 1. Main groups of proteins found in human saliva and main functions.

Protein	Main Function	Percentages
Mucin	Protection, lubrication, bolus, inhibition of demineralization	~20%
Amylase	Digestion	~25%
bPRP (basic proline-rich proteins	Lubrication and remineralization	~20%
"S" Cystatins	Protection	~8%
aPRP (acidic proline-rich proteins)	Lubrication and remineralization	~12%
gPRP (glycosylated proline-rich proteins)	Lubrication and remineralization	~5%
Immunoglobulins	Protection	~5%

The absorption of proteins from saliva on certain substrates depends mainly on noncovalent interactions [1]. However, biomaterials used in oral regeneration, such as dental implants, membranes and bone substitutes, have different surface characteristics that aim for greater cellular interactions, such as hydrophilicity, porosity changes, greater roughness and high surface energy [25–27]. These superficial alterations can modify the interactions with saliva proteins, and the manufactured characteristics for better biological performance in these biomaterials can be affected after interaction with saliva (Figure 1).

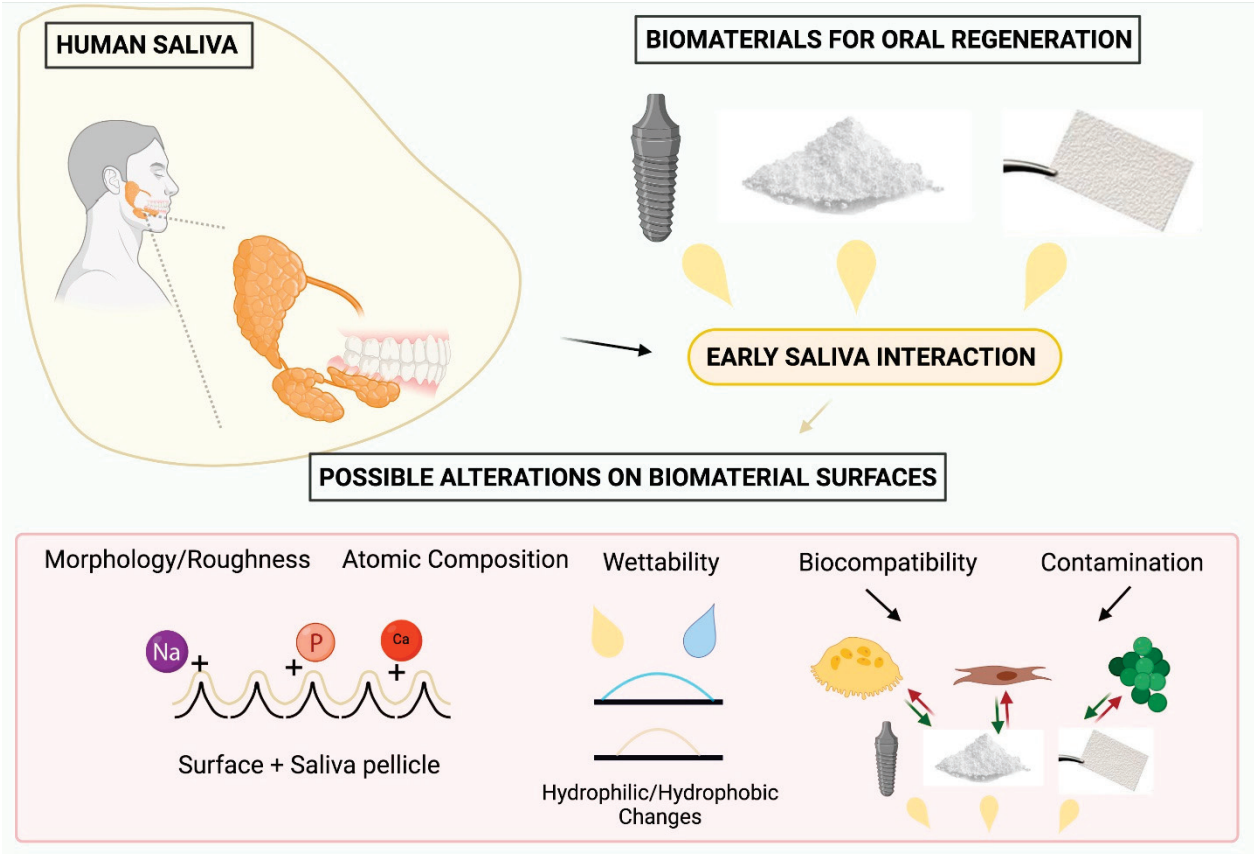


Figure 1. Scheme demonstrating the possible changes in biomaterials for oral regeneration after early saliva interaction. Saliva pellicle formation, wettability alterations and stimulation/repulsive responses for each type of cell were the most significant alterations. Created with BioRender.com.

4. Effects of Saliva Interaction on the Physical–Chemical Properties of Biomaterials for Oral Regeneration

4.1. Biomaterial Morphology/Roughness

Morphological characteristics and roughness measurements are essential features for biomaterials with rapid healing properties, with surface modifications being particularly important for dental implants and topographies for membranes [28,29]. Different morphologies have been proposed, aiming for immediate interactions at the micro- and nanoscale level with the extracellular membrane of cells [10,27,28]. Moreover, differences in roughness parameters have been reported to act on the adhesion properties of cells, as well as in the initial contact [30,31]. As described previously, saliva has the potential to create a thin layer over the substrate in a short period of time. In some cases, where specific nanotopographies or nanoroughness measurements are developed for biomaterials, this layer may affect or cause small alterations in these properties.

Normally, studies applying membranes for bone regeneration focus more on the investigation of biodegradation characteristics rather than early contact with saliva. After only 4 weeks of artificial saliva exposure, Liao et al. [32] observed some morphological differences or biodegradation in their specific carbonized hydroxyapatite/collagen/PLGA composite membrane. However, the literature is very scarce about the initial details that may cause possible changes in morphologies induced by the formation of a salivary pellicle. The current findings demonstrated only some adherence of impurities in dental implant surfaces after exposure for 10 min [14], thus suggesting a promising topic to be further investigated in dental biomaterials for oral rehabilitation.

Regarding roughness properties, some considerations are very clear within the studies done today. Substrates with high roughness parameters showed increased adhesion of saliva proteins compared with smooth surfaces; this statement is corroborated by diverse studies with different standards of roughness and different base materials applied [14,15,33]. Furthermore, specific saliva proteins, such as mucin glycoprotein 2 and lactoferrin, were reported as high-affinity proteins to rougher dental implant surfaces [33,34]. Additionally, Souza et al. [35] demonstrated changes in the proteomic profile of saliva protein adsorption to SLA (sand-blasted/acid-attacked) surfaces compared with machined surfaces. In contrast, the authors reported that roughness is not a parameter that creates specificity of adhered proteins because most proteins found on surfaces are similar, varying only in the quantification [15].

4.2. Biomaterial Surface Composition

The interaction with saliva may cause some specific adherence of different atomic elements present in saliva. Saliva in the natural state is composed of a large quantity of additional compounds present in the mouth. In addition to saliva proteins, minerals such as calcium and phosphate are easily found in saliva, ions from metals might be found in persons that have metallic devices in the oral environment and a wide number of impurities may be exhibited in the mouth due to the continuous process of feeding and digestion.

The discussion about early contact with saliva with biomaterials for oral rehabilitation and the possible atomic alterations caused by the interaction is another topic with few reports in the literature. Kunrath et al. [14] applied dental surfaces (machined, rougher and nanotexturized) to human saliva exposure for 10 min and 1 h. The results showed nonsignificant findings regarding the composition of the surfaces, only demonstrating that few impurities and minerals had adhered to the surfaces [14]. Moreover, other authors reported the stability of electrochemical and corrosion behavior after exposure (7 days) in artificial saliva of different commercial implant surfaces [36]. In contrast, another study demonstrated the influence of saliva pH on corrosion resistance using pure titanium and alloys for dental implants [37]. Lower pH values in saliva may represent an increased corrosion rate and kinetics [37,38].

For bone substitutes, only scarce information is available revealing a nonalteration in the atomic stability of granules derived from pork bone sludge after exposure for 60 days in

artificial saliva. The authors recommended further studies involving contaminated saliva to verify the differences with a real environment [39]. On the other hand, De Aza et al. [40] showed a material structural transformation (pseudowollastonite–α-tricalcium phosphate bioeutectic) internally and superficially after 30 days of exposure in human parotid saliva, creating a hydroxyapatite-like phase in the related bone substitute.

Studies reporting analyses in short periods of time were not found in the literature, and the understanding of the possible changes in biomaterials when in early interaction clinically with human saliva remains poorly investigated regarding the structure and surface composition.

4.3. Biomaterial Wettability

There is a consensus in the literature that hydrophobic solid surfaces are more attractive to saliva and their proteins [1,41,42]. On hydrophobic surfaces, saliva proteins adhere and group to the surface due to the process of not spreading under the entire substrate, thus managing to create a film. However, on hydrophilic surfaces, this process becomes more difficult due to the spacing and spreading of proteins when in contact with the surface with high surface energy [41,42]. Investigations have shown that hydrophilic surfaces provide the adhesion of specific saliva proteins, such as aPRP, bPRP, cystatin S and Statherin, but in less variety and quantity than hydrophobic surfaces [41,43]. Moreover, the interactions between saliva/substrate do not behave similarly to bacterial biofilm growth. The formation of the saliva pellicle is explained by the adhesion of a molecular film composed predominantly of saliva proteins [44]; thus, after the protein superposition over the entire surface, the chemical intercommunication between substrate/proteins decreases. Additionally, the saliva film creates properties of lubrication and viscosity derived mainly from the mucin protein, which complicate the film development at a higher thickness [44].

Schweikl et al. [45] reported the influence of wettability characteristics in applying different base materials used in dentistry, such as titanium, PTFE, PE and PMMA, regarding the adsorption of human saliva proteins. The authors showed slightly higher adsorption of saliva proteins to hydrophobic surfaces; moreover, most material surfaces with hydrophobic characteristics after saliva interaction had decreased measurements of surface angle contact due to the formation of the saliva pellicle [44]. Similarly, other studies found significantly higher adhesion of saliva proteins to hydrophobic surfaces on solid surfaces (Figure 2) [42,46].

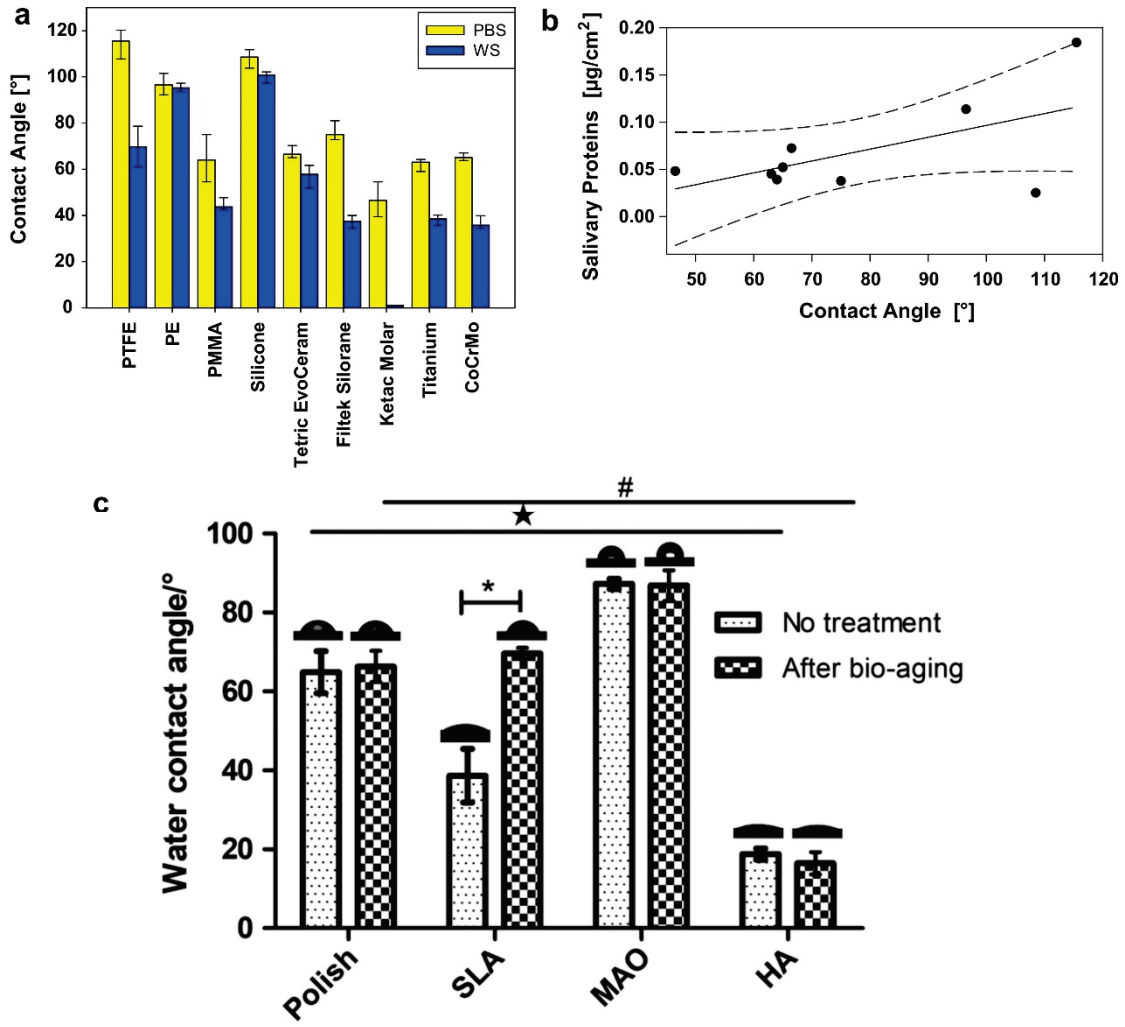


Figure 2. Reports about wettability characteristics and saliva protein adsorption (hydrophobic features demonstrated an increased level of saliva protein adsorption). (**a**) Different biomaterials and the corresponding contact angle after (WS) and before (PBS) saliva interaction, (**b**) followed by the level of protein adsorption for each different contact angle; images reproduced and adapted with permission from [45]. (**c**) Alterations in the measurements of contact angle after bioaging in human saliva for different surface treatments; saliva interaction affected hydrophilic properties in SLA treatment, * represent significance in the same group and # ★ represent significance between different groups; image reproduced and adapted with permission from [47].

Currently, there are huge numbers of publications referring to the advantages of hydrophilic surfaces for dental implants or for bone regeneration materials [48,49]. Hydrophilic surfaces provide improvement in some important behavior aspects for bone cells and soft tissue cells [48–50]; therefore, companies are developing biomaterials with superhydrophilic properties to achieve the best response possible when inserted in the desired oral environment. However, reports demonstrated that the early interaction of hydrophilic dental implant surfaces with human saliva showed the loss of this characteristic after interaction [14,47]. Additionally, Muller et al. [46] reported similar results that the saliva pellicle could change the hydrophobic/hydrophilic properties and vice versa.

5. Effects of Saliva Interaction on Biocompatibility Properties of Biomaterials

5.1. Biocompatibility

5.1.1. Dental Implants

Dental implants are usually placed with extreme accuracy associated with a free-contaminated environment during insertion in a planned site. However, controlling salivary production around the surgical site may be a complicated procedure. Normally, during implant insertion, the implant surface touches the bone tissue and/or the soft tissues that interact with saliva present in the mouth. Moreover, if the surgery is not assisted by surgical aspiration, saliva may touch the biomaterial due to normal saliva excretion by the major and minor salivary glands. To minimize the risk of contamination, authors reported techniques suggesting the use of a rubber dam during the placement of dental implants and sinus lift procedures in order to prevent saliva contamination in surgical sites [51].

The first interactions with oral tissues occur when the implant is inserted and are associated with blood protein adherence, pro-osteogenic cell adhesion and bone cell attachment; therefore, dental implant surfaces are designed to promote a beneficial response and attachment for these specific cells [7,10]. However, there are a huge number of reports showing the impairment of cell viability after saliva interaction with surfaces compared to surfaces without interaction [14,21,47,52]. The authors demonstrated that saliva interaction with biomaterials prior to cell culture impaired the behavior of the MC3T3-E1 osteoblast cell line [14], MG63 human osteoblasts [52] and bone marrow cells derived from Sprague-Dawley rats [21] (Figure 3); additionally, more reports showed the same problematic behavior for soft tissue cells such as human gingival fibroblasts (HGFs) [47,53]. On the other hand, Sun et al. [54] revealed that the addition of an isolated salivary protein (histatin-1) to a titanium surface improved the spread and some features of MC3T3-E1 osteoblast cells after culture for some days. Moreover, Caballe-Serrano et al. [55] demonstrated, using in vitro models, that bone tissue contaminated with saliva showed less osteoclast reabsorption and presented some differences in the immune response, which highlights the need for further investigation regarding the effects of saliva interaction in clinical or animal models.

Similarly, a study using animal models and implants contaminated with saliva prior to insertion showed osseointegration parameters with reduced values in comparison to implants not exposed to saliva, for example, lower bone-interface contact (BIC) [56]. Additionally, this specific report applied highly contaminated saliva collected from a patient with periodontitis, and the results could not determine whether saliva alone was responsible for the decreased results in terms of osseointegration. However, the study simulates a clinical reality that is the presence of high-contaminated saliva and the application of biomaterials in unhealthy patients.

5.1.2. Membranes and Bone Substitutes

As described in the previous chapter, the interaction with saliva has been studied with more emphasis in dental implants regarding the effects caused in the biological responses after saliva contamination. In the same way, a similar interaction may occur with biomaterials for guided bone regeneration, such as membranes, particulate bone substitutes, grafts and scaffolds. The clinical application of these biomaterials is normally aimed at the same sites where implants are placed, and the interaction with saliva is difficult to control.

Nevertheless, the literature is scarce regarding the early interaction with saliva in biomaterials for guided bone regeneration. Previous studies mostly employed cell cultures applying saliva to the substrate without any additional biomaterials, suggesting negative results for all the different types of cells applied, such as osteoblast-like cells or fibroblasts that interacted with the saliva [57–59].

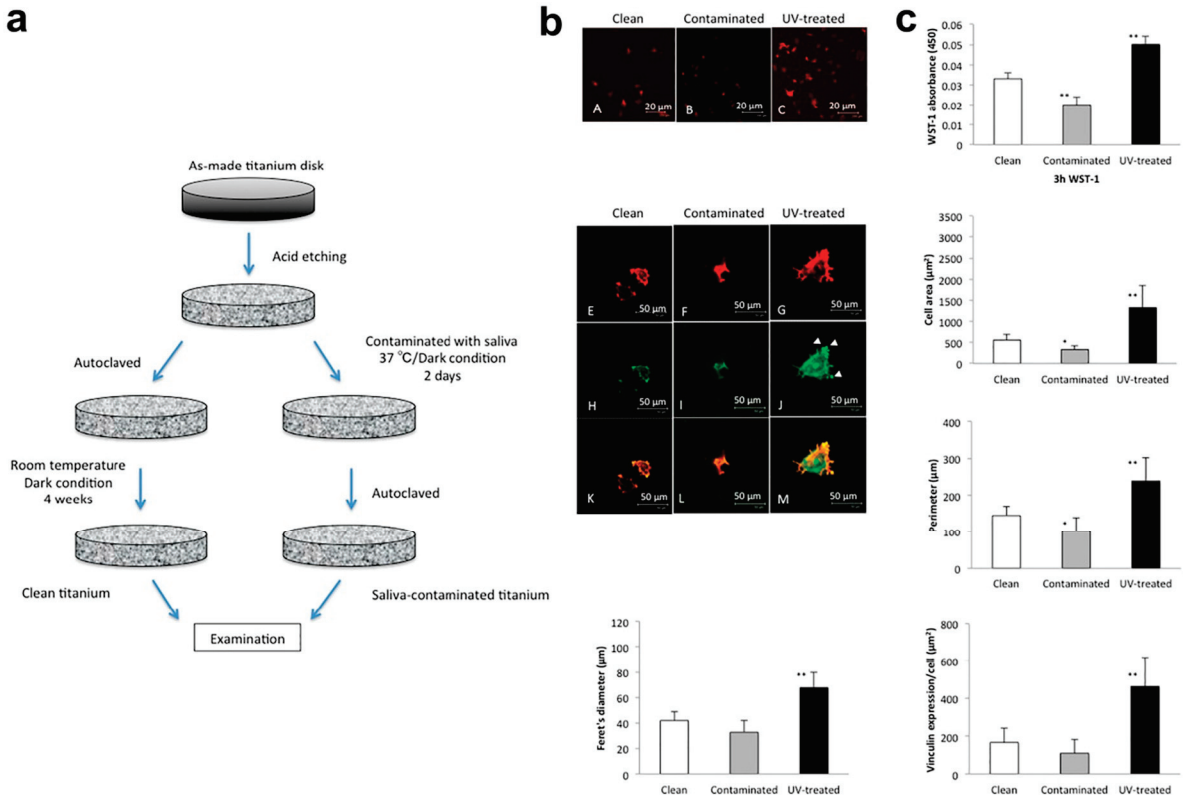


Figure 3. Osteoblast response after culture on saliva-contaminated surfaces for dental implants. Methodology for exposing surfaces to saliva (**a**); osteoblast morphology showing reduced spreading characteristics for contaminated surfaces (**b**); and significantly lower levels of important behavior features (Feret's diameter, WST-1 absorbance, cell area, perimeter and Vinculin expression) for osteoblasts seeded on contaminated surfaces with saliva (**c**); * $p < 0.05$, ** $p < 0.01$. Images reproduced and adapted with permission from Elsevier, reference [21].

Thus, consistent research about the early reactions of biomaterials for guided regeneration is still necessary to provide knowledge about the integrity and biocompatibility after possible saliva interactions in these biomaterials. Table 2 summarizes studies involving different cells and their reactions to contaminated substrates with saliva, suggesting in 100% of the studies that saliva impairs the behavior or proliferation of specific cells. The opposite is only revealed when studies propose the isolation of specific proteins (histatin-1) to adhere to the substrate and create a beneficial effect for the cells [54,60].

Table 2. Studies showing saliva interaction and biocompatibility responses in dental materials for bone regeneration.

Reference	Study Model	Cells or Animals Employed	Findings	Biomaterial Applied
Zhou et al. [47]	In vitro	HGFs cell seemed over the surfaces.	Decreased adhesion and proliferation of HGF cells after bioaging in saliva.	Dental implant surfaces.
Shams et al. [52]	In vitro	MG63 human osteoblasts.	Saliva contamination altered morphology and proliferation of osteoblasts.	Dental implant surfaces.
Kunrath et al. [14]	In vitro	Osteoblast cell line MC3T3-E1.	Saliva interaction reduced the viability of osteoblast cell line.	Dental implant surfaces.

Table 2. *Cont.*

Reference	Study Model	Cells or Animals Employed	Findings	Biomaterial Applied
Hirota et al. [21]	In vitro	Bone marrow cells from rats.	Saliva contamination impaired osteoblastic behavior.	Dental implant surfaces.
Zöller and Zentner [53]	In vitro	Human gingival fibroblasts-like cells.	Saliva contaminated surfaces had less fibroblast adhesion and proliferation.	Dental implant surfaces.
Sun et al. [54]	In vitro	Osteoblast cell line MC3T3-E1.	Histatin-1 was added to titanium surfaces promoting spreading of osteogenic cells.	Dental implant surfaces.
Jinno et al. [56]	In vivo	Sheep.	Contaminated saliva from a human with periodontitis was interacted (15s) with the implants before insertion. Osseointegration was prejudiced regarding BIC measurements by saliva contamination.	Dental implants.
Sun et al. [60]	In vivo	Sprague–Dawley rats.	The study proposed the addition of histatin-1 (saliva protein) to absorbable collagen sponge. The results showed high bone volume when the functionalized membrane was applied.	Membranes.
Proksch et al. [57]	In vitro	Murine MC3T3 osteoblasts.	Saliva interaction hampers the osteoblast behavior. Decreased level of proliferation, alkaline phosphatase and differentiation were verified in groups with saliva.	No biomaterial applied. Cells were exposed directly to culture mediums with or without saliva.
Heaney [58]	In vitro	Human gingival fibroblasts.	Saliva interaction decreased the cell adherence to the substrate.	No biomaterial applied. Cells were exposed directly to plastic wells with or without saliva.
Pourgonabadi et al. [59]	In vitro	Bone marrow cultures and RAW 264.7 mouse macrophages.	Saliva activated polarization into proinflammatory M1 macrophages.	No biomaterial applied. Cells were exposed directly to culture mediums with or without saliva.
Mi et al. [61]	In vitro and in vivo	Human umbilical vein endothelial cells.	The study proposed the application of saliva-derived exosomes in created skin wound in mouse. The results enhanced wound healing through promotion of angiogenesis.	Wound healing.

5.2. The Role of Saliva and Bacterial Contamination

5.2.1. Dental Implants

Biomaterial contamination in the initial stage of healing is one of the major causes of clinical failure and early loss of dental procedures [62,63]. The mouth is a human body area with an expressive quantity of bacteria, and saliva becomes an intraoral conductor for these different bacteria [64]. Associated with these characteristics, numerous unhealthy oral conditions, such as periodontitis, gingivitis, fungi and infections in adjacent teeth, may stimulate proliferation and the presence of more types of bacteria in contact with oral saliva.

Following these statements, dental implants inserted in contaminated patients with oral diseases or adjacent infections interacting with local saliva present a high risk of surface contamination. In addition, the conduction of bacterial cells to the bone tissue or to the intragingival tissue can occur from contamination with saliva. Surfaces developed for

dental implants contaminated with saliva were shown to stimulate the virulence of *Candida albicans* [65]; in addition, the salivary protein mucin was demonstrated to be a receptor for adhesion of *C. albicans* [66].

Other studies revealed that the salivary film formed over the surface could develop a favorable environment for bacterial nutrition and metabolism on the surface of implants [1,67] or teeth [1,68] (Figure 4). Rough surfaces provided greater adhesion of cells and proteins from saliva and likewise showed greater adhesion of the *S. oralis* bacteria to surfaces made with microscale roughness [14,67,69]. Surface physicochemical properties such as morphology, roughness and wettability can significantly alter the level of bacterial adhesion associated with saliva, suggesting that each substrate may differently influence the adhesion of contaminated saliva [70,71].

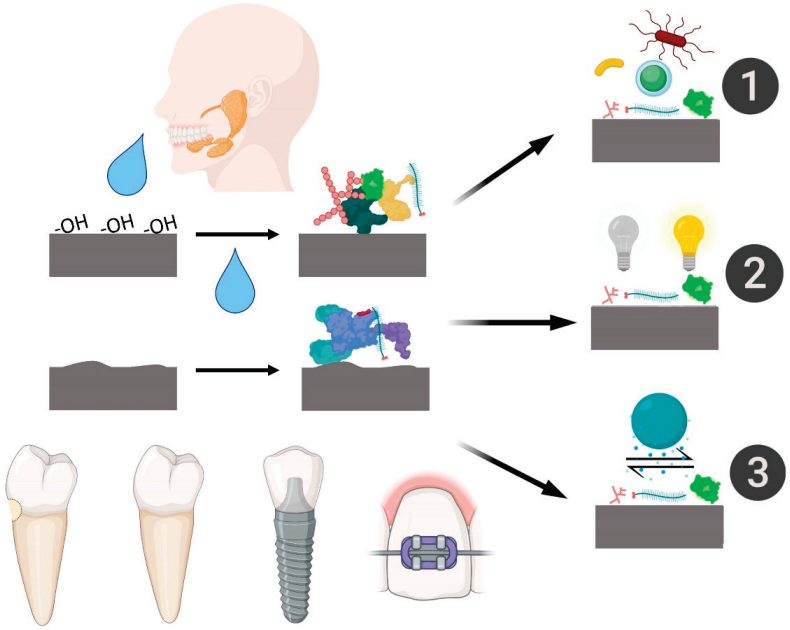


Figure 4. Scheme showing the diverse early effects of saliva contamination on different dental surface substrates. 1—Promotion of bacterial adhesion and colonization; 2—Promotion of surface staining; 3—Changes in the wettability, promoting different chemical interactions. Image reproduced with permission from Elsevier, reference [1].

Promising features for dental implant surfaces have been reported to control bacterial proliferation with the application of nanotexturizations or antibiotic-loaded surfaces [72,73], suggesting a protective coating for contaminated environments. However, preclinical and clinical studies are rare regarding assays with saliva-contaminated implants associated with innovative surface treatments. Jinno et al. [56] demonstrated the insertion of implants contaminated with human saliva derived from one patient with confirmed periodontitis; the results showed impairment in the osseointegration process for all contaminated implants compared to noncontaminated implants. Clinical studies revealed the presence of bacterial contamination that may promote peri-implant resorption around the implant–abutment interface, the region exposed to saliva, suggesting the requirement of special treatment (Chlorhexidine 0.20%) to improve the tissues response [74,75]. Therefore, the critical issue about the use of biomaterials close to contaminated saliva in oral sites should be confirmed with long-term clinical studies.

5.2.2. Membranes and Bone Substitutes

Equivalent results were shown for biomaterials manufactured for oral regeneration, such as modified membranes or hydroxyapatite substitutes [76–79]. The salivary film deposited over the biomaterial surface can mediate the adhesion of important bacteria present

in oral infections [68,78]. Moreover, organic biomaterials may promote a favorable environment for bacterial metabolism due to the degradation of specific molecules compared to inorganic biomaterials or synthetic biomaterials [76]. On the other hand, Lee et al. [79] revealed, using in vitro models, that their PMMA membranes possess antibacterial properties even after contamination with saliva. Studies applying saliva-contaminated biomaterials are scarce in the literature due to the associated negative effects, mainly in animal models and clinical models where the tissues can be damaged with these bacteria. Thus, it remains unclear how early saliva contact may impair healing around these biomaterials. Table 3 summarizes the main studies using biomaterials for bone regeneration with saliva and bacterial interactions.

Table 3. Studies showing saliva interaction with bacteria on different materials.

Reference	Study Model	Bacterial Information	Results	Biomaterial Applied
Gröbner-Schereiber et al. [80]	In vitro	*Streptococcus mutans*; *Streptococcus sanguis*	Saliva had no significant influence on the adherence of the specific strains.	Dental implant surfaces.
Mabboux et al. [70]	In vitro	*S. sanguinis*; *S. Constellatus*	Results showed that the physical–chemical properties of bacterial cells were influential on the bacterial adherence to surfaces with saliva contact.	Dental implant surfaces.
Hauser-Gerspach et al. [71]	In vitro	*S. sanguinis*	The bacterial vitality depends on the physical–chemical properties of the substrate.	Dental implant surface
Bürgers et al. [66]	In vitro	*Candida albicans*	Mucin protein serves as a receptor for *C. albicans* adherence and albumin may act as a blocker for this specific adhesion.	Dental implant surfaces.
Zhou et al. [47]	In vitro	*S. sanguinis*	Bacterial adhesion was promoted by bioaging in saliva.	Dental implant surface.
Dorkhan et al. [67]	In vitro	*S. oralis*	Saliva pellicle enhanced the bacterial metabolic activity.	Dental implant surfaces.
Dorkhan et al. [69]	In vitro	*S. oralis*	Saliva pellicle associated with rougher surfaces promoted high bacterial adherence.	Dental implant surfaces.
Cavalcanti et al. [65]	In vitro	*C. albicans*	Saliva contamination induced high virulence for *C. albicans*.	Dental implant surfaces.
Lima et al. [81]	In vitro	*S. mutans*; *Actinomyces naeslundii*	Saliva exposure did not create significant attachment of bacteria compared to noncontaminated surfaces with saliva.	Dental implant surfaces.
Li et al. [76]	In vitro	Natural saliva (wide number of microorganisms)	The substrate is significant to the proliferation of microorganisms. Biotic substrates promote rich environment for bacterial growth.	Different materials for oral regeneration (natural tissues, titanium and hydroxyapatite).
Mukai et al. [77]	Clinical	Human saliva (Wide number of microorganisms)	The study showed nonsignificance between the specificity of bacteria attached to each material. However, all materials demonstrated bacterial adhesion after contamination with saliva.	Different biomaterials for oral regeneration.
Carlen et al. [78]	In vitro	*P. gingivalis*; *F. nucleation*; *A. naeslundii*; *A. viscosuos*	The study suggested that the salivary pellicle could mediate the adhesion of bacteria present in gingivitis and periodontitis.	Hydroxyapatite beads.
Lee et al. [79]	In vitro	*E. coli* and *S. mutans*	Saliva pellicle did not promote bacterial proliferation. The material showed antibacterial properties even when saliva-coated.	Materials for oral rehabilitation (PMMA).
Turri et al. [82]	Clinical study	Biofilm oral flora; Investigation focused on *Staphylococcus spp.*	The membrane exposure to the oral cavity promoted a higher presence of bacteria compared to teeth surfaces exposed under the same conditions.	Membranes for guided oral regeneration (e-PTFE and d-PTFE).

6. Limitations of Studies Applying Saliva-Contaminated Biomaterials

In vitro or in vivo studies involving saliva may have some limitations when compared with clinical investigations. The first issue about laboratory studies with saliva is related to the use of human saliva or artificial saliva. The comparison between human and artificial saliva cannot be translated with complete accuracy; although the solution composition is almost the same, the presence of contaminants, impurities or cells cannot be created with precision in artificial saliva, as well as some exclusive properties of human saliva [44,83].

A second and determinant problem reported when applying human saliva in laboratory studies appears to be the methodology chosen to collect saliva from humans. Studies have applied different techniques to collect human saliva, such as collecting directly from the human mouth without storage or treatment, using techniques for saliva stimulation, filtering the saliva before application in the samples and application of different methodologies for storage and later investigation [14,15,35,56,84]. These different techniques need to be carefully understood to be able to compare the results with the different studies performed. Moreover, the clinical translation of some results applying different techniques for saliva collection requires attention by the readers due to the possibility of masking important saliva characteristics when compared to clinical human saliva, which may prevent some clinical conclusions.

From our point of view, the appropriate methodology to be applied in studies using saliva is focused on the search for maximum similarities to clinical human saliva, including all contaminants and impurities, and, if possible, should be associated with a direct application in the experiment without storage. On the other hand, several studies have demonstrated the stability of saliva composition and components using processes to store saliva at cold temperatures [14,84], and this alternative should be considered to develop and facilitate laboratory studies with scientific relevance.

7. Clinical Significance

The interaction between saliva and biomaterials is extremely difficult to control in the clinical setting. Normally, surgical procedures require "four hands" handling or more "hands" to create totally free-saliva environments applying good aspiration and perfect management. Restorative treatments are commonly employed with absolute isolation to prevent saliva contamination. In addition, the use of latex gloves by clinicians is often a factor for saliva stimulation in some patients.

Saliva is present on all tissues exposed to the oral environment, including blood when free in the mouth, soft tissues when accessed for gingival treatments and bone tissues when exposed for surgeries (Figure 5) [85]. Therefore, a minimal interaction with saliva is almost inherent. The formation of salivary pellicles over biomaterial substrates is quick and may change some specific properties, as mentioned in this review. Additionally, with intense biomaterial exposure to saliva, the positive biological response can be affected, reducing important cellular reactions [53,61]. In addition, saliva contamination can promote an environment for high bacterial metabolism and possible proliferation [68,78].

Thus, after removing the limitations of laboratory studies, clinical studies showed that saliva interaction must be controlled with the maximum of effort to prevent alterations in all types of biomaterials previously inserted in the oral environment. The early saliva interaction is not a clear factor that results in unsuccessful treatments; however, it is reported as a significant element that may impair positive properties developed for rapid healing in biomaterials applied in oral regeneration [14,21].

Additionally, this review has some limitations due to the compilation of results from different authors providing a wide visualization of all possible alterations caused by early saliva interaction investigated until the current moment, in addition, due to the narrative methodology. Therefore, studies applying preclinical and clinical investigations should be prioritized for clinical conclusions.

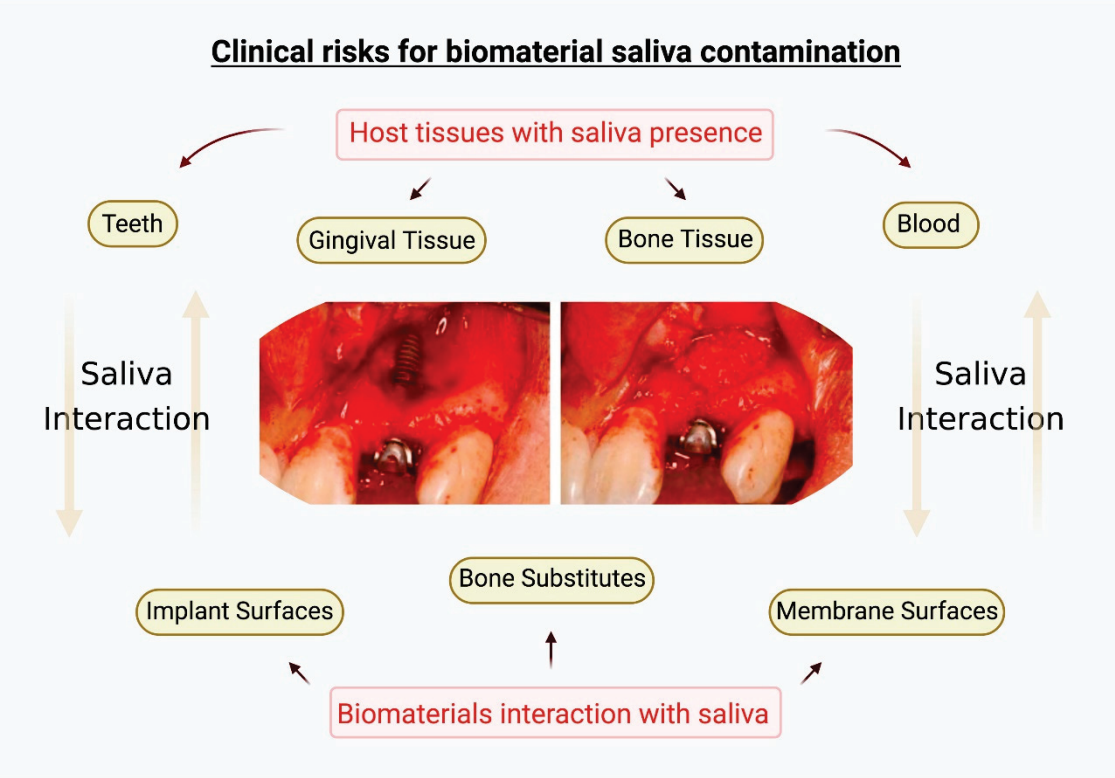


Figure 5. Scheme demonstrating the risks for biomaterial contamination with saliva in the oral environment when submitted to surgical procedures. Oral tissues are usually in constant contact with saliva, and the placement of biomaterials may generate early interactions. Created with BioRender.com.

8. Conclusions

Within the limitations of this critical review, different issues about the interaction between saliva and biomaterials for oral rehabilitation were clearly identified and elucidated. A constant tissue interaction and minimal biomaterial contact with saliva are almost inherent in surgical procedures involving dental implants, bone substitutes and membranes for guided regeneration. Therefore, some conclusions can be made after critical analysis of the investigations explored in this study:

1. Salivary pellicle formation over biomaterials is an extremely quick and natural process that occurs within the first minute of interaction with saliva. The pellicle thickness depends on the exposure time to saliva and on the physical–chemical properties of the substrate.
2. Accordingly to the physical–chemical studies explored, hydrophilic and hydrophobic characteristics are clearly altered by the interaction with saliva, causing substantial changes in biomaterials with surfaces designed for rapid healing. Moreover, rougher biomaterial surfaces showed high salivary protein adsorption.
3. Accordingly to the basic biological studies analyzed, biomaterial biocompatibility with different types of cells is significantly impaired after saliva interaction compared to biomaterials noncontaminated with saliva. In addition, salivary pellicle formation promoted specific conditions for bacterial adhesion and proliferation.
4. Clinically, there are no studies demonstrating that early saliva interaction is a factor for direct biomaterial rejections or infections. However, the saliva interaction can alter early biological responses at the surgical site that should be prevented. Efforts to control saliva invasion in surgical sites involving biomaterials for oral regeneration must be maximized to maintain all the basic physical–chemical–biological properties of the biomaterials.

Author Contributions: M.F.K. conceived the idea and contributed to review design, data acquisition, analysis and interpretation, and drafting and critical revision of the manuscript; C.D. contributed to analysis, drafting and revision of the manuscript. All authors have read and agreed to the published version of the manuscript.

Funding: This study was supported by the Osteology Research Scholarship (Osteology Foundation, Lucerne, Switzerland) to M.F.K. and the Area of Advance Materials of Chalmers and GU Biomaterials within the Strategic Research Area initiative launched by the Swedish Government.

Institutional Review Board Statement: Not applicable.

Informed Consent Statement: Not applicable.

Data Availability Statement: Not applicable.

Acknowledgments: The authors would like to thank Furqan A. Shah at the Department of Biomaterials, University of Gothenburg for fruitful discussions.

Conflicts of Interest: The authors declare no conflict of interest.

References

1. Fischer, N.G.; Aparicio, C. The salivary pellicle on dental biomaterials. *Colloids Surf. B Biointerfaces* **2021**, *200*, 111570. [CrossRef] [PubMed]
2. Mandel, I.D. The functions of saliva. *J. Dent. Res.* **1987**, *66*, 623–627. [CrossRef] [PubMed]
3. Laguna, L.; Fiszman, S.; Tarrega, A. Saliva matters: Reviewing the role of saliva in the rheology and tribology of liquid and semisolid foods. Relation to in-mouth perception. *Food Hydrocoll.* **2021**, *116*, 106660. [CrossRef]
4. Carpenter, G.H. The secretion, components, and properties of saliva. *Annu. Rev. Food Sci. Technol.* **2013**, *4*, 267–276. [CrossRef] [PubMed]
5. Hannig, M. Ultrastructural investigation of pellicle morphogenesis at two different intraoral sites during a 24-h period. *Clin. Oral Investig.* **1999**, *3*, 88–95. [CrossRef] [PubMed]
6. Rossetti, D.; Yakubov, G.E.; Stokes, J.R.; Williamson, A.M.; Fuller, G.G. Interaction of human whole saliva and astringent dietary compounds investigated by interfacial shear rheology. *Food Hydrocoll.* **2008**, *22*, 1068–1078. [CrossRef]
7. Kunrath, M.F.; Muradás, T.C.; Penha, N.; Campos, M.M. Innovative surfaces and alloys for dental implants: What about biointerface-safety concerns? *Dent. Mater.* **2021**, *37*, 1447–1462. [CrossRef]
8. Haugen, H.J.; Lyngstadaas, S.P.; Rossi, F.; Perale, G. Bone grafts: Which is the ideal biomaterial? *J. Clin. Periodontol.* **2019**, *46*, 92–102. [CrossRef]
9. Omar, O.; Elgali, I.; Dahlin, C.; Thomsen, P. Barrier membranes: More than the barrier effect? *J. Clin. Periodontol.* **2019**, *46*, 103–123. [CrossRef]
10. Kunrath, M.; dos Santos, R.; de Oliveira, S.; Hubler, R.; Sesterheim, P.; Teixeira, E. Osteoblastic cell behavior and early bacterial adhesion on macro-, micro-, and nanostructured titanium surfaces for biomedical implant applications. *Int. J. Oral Maxillofac. Implants* **2020**, *35*, 773–781. [CrossRef]
11. Li, J.J.; Dunstan, C.R.; Entezari, A.; Li, Q.; Steck, R.; Saifzadeh, S.; Sadeghpour, A.; Field, J.R.; Akey, A.; Vielreicher, M.; et al. A novel bone substitute with high bioactivity, strength, and porosity for repairing large and load-bearing bone defects. *Adv. Healthc. Mater.* **2019**, *8*, 1801298. [CrossRef] [PubMed]
12. De Santana, R.B.; de Mattos, C.M.L.; Francischone, C.E.; Van Dyke, T. Superficial topography and porosity of an absorbable barrier membrane impacts soft tissue response in guided bone regeneration. *J. Periodontol.* **2010**, *81*, 926–933. [CrossRef] [PubMed]
13. Hicklin, S.P.; Schneebeli, E.; Chappuis, V.; Janner, S.F.M.; Buser, D.; Brägger, U. Early loading of titanium dental implants with an intra-operatively conditioned hydrophilic implant surface after 21 days of healing. *Clin. Oral Implants Res.* **2016**, *27*, 875–883. [CrossRef] [PubMed]
14. Kunrath, M.F.; Hubler, R.; Silva, R.M.; Barros, M.; Teixeira, E.R.; Correia, A. Influence of saliva interaction on surface properties manufactured for rapid osseointegration in dental implants. *Biofouling* **2021**, *37*, 757–766. [CrossRef] [PubMed]
15. Zuanazzi, D.; Xiao, Y.; Siqueira, W.L. Evaluating protein binding specificity of titanium surfaces through mass spectrometry–based proteomics. *Clin. Oral Investig.* **2021**, *25*, 2281–2296. [CrossRef] [PubMed]
16. Mystkowska, J.; Niemirowicz-Laskowska, K.; Łysik, D.; Tokajuk, G.; Dąbrowski, J.R.; Bucki, R. The role of oral cavity biofilm on metallic biomaterial surface destruction–corrosion and friction aspects. *Int. J. Mol. Sci.* **2018**, *19*, 743. [CrossRef]
17. Dawes, C.; Pedersen, A.M.L.; Villa, A.; Ekström, J.; Proctor, G.B.; Vissink, A.; Aframian, D.; McGowan, R.; Aliko, A.; Narayana, N.; et al. The functions of human saliva: A review sponsored by the World Workshop on Oral Medicine VI. *Arch. Oral Biol.* **2015**, *60*, 863–874. [CrossRef]
18. Li, J.; Helmerhorst, E.J.; Leone, C.W.; Troxler, R.F.; Yaskell, T.; Haffajee, A.D.; Socransky, S.S.; Oppenheim, F.G. Identification of early microbial colonizers in human dental biofilm. *J. Appl. Microbiol.* **2004**, *97*, 1311–1318. [CrossRef]

19. Al-Ahmad, A.; Wiedmann-Al-Ahmad, M.; Carvalho, C.; Lang, M.; Follo, M.; Braun, G.; Wittmer, A.; Mülhaupt, R.; Hellwig, E. Bacterial and Candida albicansadhesion on rapid prototyping-produced 3D-scaffolds manufactured as bone replacement materials. *J. Biomed. Mater. Res. A* **2008**, *87A*, 933–943. [CrossRef]
20. Álvarez, S.; Leiva-Sabadini, C.; Schuh, C.M.A.P.; Aguayo, S. Bacterial adhesion to collagens: Implications for biofilm formation and disease progression in the oral cavity. *Crit. Rev. Microbiol.* **2021**, *48*, 83–95. [CrossRef]
21. Hirota, M.; Ikeda, T.; Sugita, Y.; Ishijima, M.; Hirota, S.; Ogawa, T. Impaired osteoblastic behavior and function on saliva-contaminated titanium and its restoration by UV treatment. *Mater. Sci. Eng. C* **2019**, *100*, 165–177. [CrossRef] [PubMed]
22. Kunrath, M.F.; Gupta, S.; Lorusso, F.; Scarano, A.; Noumbissi, S. Oral tissue interactions and cellular response zirconia implant-prosthetic components: A critical review. *Materials* **2021**, *14*, 2825. [CrossRef] [PubMed]
23. Humphrey, S.P.; Williamson, R.T. A review of saliva: Normal composition, flow, and function. *J. Prosthet. Dent.* **2001**, *85*, 162–169. [CrossRef] [PubMed]
24. Scarano, E.; Fiorita, A.; Picciotti, P.M.; Passali, G.C.; Calò, L.; Cabras, T.; Inzitari, R.; Fanali, C.; Messana, I.; Castagnola, M.; et al. Proteomics of saliva: Personal experience. *Acta Otorhinolaryngol. Ital.* **2010**, *30*, 125–130.
25. Amani, H.; Arzaghi, H.; Bayandori, M.; Dezfuli, A.S.; Pazoki-Toroudi, H.; Shafiee, A.; Moradi, L. Controlling cell behavior through the design of biomaterial surfaces: A focus on surface modification techniques. *Adv. Mater. Interfaces* **2019**, *6*, 1900572. [CrossRef]
26. Canullo, L.; Genova, T.; Rakic, M.; Sculean, A.; Miron, R.; Muzzi, M.; Carossa, S.; Mussano, F. Effects of argon plasma treatment on the osteoconductivity of bone grafting materials. *Clin. Oral Investig.* **2019**, *24*, 2611–2623. [CrossRef]
27. Kunrath, M.F.; Diz, F.M.; Magini, R.; Galárraga-Vinueza, M.E. Nanointeraction: The profound influence of nanostructured and nano-drug delivery biomedical implant surfaces on cell behavior. *Adv. Colloid Interface Sci.* **2020**, *284*, 102265. [CrossRef]
28. Marenzi, G.; Impero, F.; Scherillo, F.; Sammartino, J.C.; Squillace, A.; Spagnuolo, G. Effect of different surface treatments on titanium dental implant micro-morphology. *Materials* **2019**, *12*, 733. [CrossRef]
29. Bottino, M.C.; Thomas, V.; Schmidt, G.; Vohra, Y.K.; Chu, T.M.G.; Kowolik, M.J.; Janowski, G.M. Recent advances in the development of GTR/GBR membranes for periodontal regeneration—A materials perspective. *Dent. Mater.* **2012**, *28*, 703–721. [CrossRef]
30. Wennerberg, A.; Albrektsson, T. Effects of titanium surface topography on bone integration: A systematic review. *Clin. Oral Implants Res.* **2009**, *20*, 172–184. [CrossRef]
31. Anselme, K.; Bigerelle, M. Topography effects of pure titanium substrates on human osteoblast long-term adhesion. *Acta Biomater.* **2005**, *1*, 211–222. [CrossRef] [PubMed]
32. Liao, S.; Watari, F.; Zhu, Y.; Uo, M.; Akasaka, T.; Wang, W.; Xu, G.; Cui, F. The degradation of the three layered nano-carbonated hydroxyapatite/collagen/PLGA composite membrane in vitro. *Den. Mater.* **2007**, *23*, 1120–1128. [CrossRef] [PubMed]
33. Cavalcanti, Y.W.; Soares, R.V.; Assis, M.A.L.; Zenóbio, E.G.; Girundi, F.M.D.S. Titanium surface roughing treatments contribute to higher interaction with salivary proteins MG2 and lactoferrin. *J. Contemp. Dent. Pract.* **2015**, *16*, 141–146. [CrossRef] [PubMed]
34. Martínez-Hernández, M.; Hannig, M.; García-Pérez, V.I.; Olivares-Navarrete, R.; Fecher-Trost, C.; Almaguer-Flores, A. Roughness and wettability of titanium implant surfaces modify the salivary pellicle composition. *J. Biomed. Mater. Res. B Appl. Biomater.* **2021**, *109*, 1017–1028. [CrossRef]
35. Souza, J.G.S.; Bertolini, M.; Costa, R.C.; Lima, C.V.; Barão, V.A.R. Proteomic profile of the saliva and plasma protein layer adsorbed on Ti–Zr alloy: The effect of sandblasted and acid-etched surface treatment. *Biofouling* **2020**, *36*, 428–441. [CrossRef]
36. Mareci, D.; Ungureanu, G.; Aelenei, D.M.; Rosca, J.C.M. Electrochemical characteristics of titanium based biomaterials in artificial saliva. *Mater. Corros.* **2007**, *58*, 848–856. [CrossRef]
37. Barão, V.A.R.; Mathew, M.T.; Assunção, W.G.; Yuan, J.C.C.; Wimmer, M.A.; Sukotjo, C. Stability of cp-Ti and Ti-6Al-4V alloy for dental implants as a function of saliva pH—An electrochemical study. *Clin. Oral Implants Res.* **2011**, *23*, 1055–1062. [CrossRef]
38. Abey, S.; Mathew, M.T.; Lee, D.J.; Knoernschild, K.L.; Wimmer, M.A.; Sukotjo, C. Electrochemical behavior of titanium in artificial saliva: Influence of pH. *J. Oral Implantol.* **2014**, *40*, 3–10. [CrossRef]
39. Sobczak-Kupiec, A.; Olender, E.; Malina, D.; Tyliszczak, B. Effect of calcination parameters on behavior of bone hydroxyapatite in artificial saliva and its biosafety. *Mater. Chem. Phys.* **2018**, *206*, 158–165. [CrossRef]
40. De Aza, P. Reactivity of a wollastonite–tricalcium phosphate Bioeutectic® ceramic in human parotid saliva. *Biomaterials* **2000**, *21*, 1735–1741. [CrossRef]
41. Gibbins, H.L.; Yakubov, G.E.; Proctor, G.B.; Wilson, S.; Carpenter, G.H. What interactions drive the salivary mucosal pellicle formation? *Colloids Surf. B Biointerfaces* **2014**, *120*, 184–192. [CrossRef] [PubMed]
42. Vassilakos, N.; Arnebrant, T.; Glantz, P.O. Adsorption of whole saliva onto hydrophilic and hydrophobic solid surfaces: Influence of concentration, ionic strength and pH. *Eur. J. Oral Sci.* **1992**, *100*, 346–353. [CrossRef] [PubMed]
43. Svendsen, I.E.; Lindh, L. The composition of enamel salivary films is different from the ones formed on dental materials. *Biofouling* **2009**, *25*, 255–261. [CrossRef] [PubMed]
44. Sarkar, A.; Xu, F.; Lee, S. Human saliva and model saliva at bulk to adsorbed phases—Similarities and differences. *Adv. Colloid Interface Sci.* **2019**, *273*, 102034. [CrossRef] [PubMed]
45. Schweikl, H.; Hiller, K.A.; Carl, U.; Schweiger, R.; Eidt, A.; Ruhl, S.; Müller, R.; Schmalz, G. Salivary protein adsorption and Streptococccus gordonii adhesion to dental material surfaces. *Dent. Mater.* **2013**, *29*, 1080–1089. [CrossRef]

46. Müller, R.; Gröger, G.; Hiller, K.A.; Schmalz, G.; Ruhl, S. Fluorescence-based bacterial overlay method for simultaneous in situ quantification of surface-attached bacteria. *Appl. Environ. Microbiol.* **2007**, *73*, 2653–2660. [CrossRef]
47. Zhou, W.; Peng, X.; Zhou, X.; Li, M.; Ren, B.; Cheng, L. Influence of bio-aging on corrosion behavior of different implant materials. *Clin. Implant Dent. Relat. Res.* **2019**, *21*, 1225–1234. [CrossRef]
48. Kunrath, M.F.; Vargas, A.L.M.; Sesterheim, P.; Teixeira, E.R.; Hubler, R. Extension of hydrophilicity stability by reactive plasma treatment and wet storage on TiO(2) nanotube surfaces for biomedical implant applications. *J. R. Soc. Interface* **2020**, *17*, 20200650. [CrossRef]
49. Ikumi, R.; Miyahara, T.; Akino, N.; Tachikawa, N.; Kasugai, S. Guided bone regeneration using a hydrophilic membrane made of unsintered hydroxyapatite and poly(L-lactic acid) in a rat bone-defect model. *Dent. Mater. J.* **2018**, *37*, 912–918. [CrossRef]
50. Zigterman, B.G.R.; Van den Borre, C.; Braem, A.; Mommaerts, M.Y. Titanium surface modifications and their soft-tissue interface on nonkeratinized soft tissues—A systematic review (Review). *Biointerphases* **2019**, *14*, 040802. [CrossRef]
51. Checchi, V.; Generali, L.; Generali, P. Isolation through rubber dam to prevent COVID-19 exposure during flapless trans-crestal sinus lift procedures. *J. Oral Implantol.* **2021**, *47*, 407–409. [CrossRef] [PubMed]
52. Shams, N.; Ghasemi, M.; Sadatmansouri, S.; Bonakdar, S. Morphology and differentiation of MG63 osteoblast cells on saliva contaminated implant surfaces. *J. Dent.* **2015**, *12*, 424–429.
53. Zöller, G.O.; Zentner, A. Initial attachment of human gingival fibroblast-like cells in vitro to titanium surfaces oretreated with saliva and serum. *Clin. Oral Implants Res.* **1996**, *7*, 311–315. [CrossRef] [PubMed]
54. Sun, W.; Ma, D.; Bolscher, J.G.M.; Nazmi, K.; Veerman, E.C.I.; Bikker, F.J.; Sun, P.; Lin, H.; Wu, G. Human salivary histatin-1 promotes osteogenic cell spreading on both bio-inert substrates and titanium SLA surfaces. *Front. Bioeng. Biotechnol.* **2020**, *8*, 584410. [CrossRef]
55. Caballé-Serrano, J.; Cvikl, B.; Bosshardt, D.D.; Buser, D.; Lussi, A.; Gruber, R. Saliva suppresses osteoclastogenesis in murine bone marrow cultures. *J. Dent. Res.* **2015**, *94*, 192–200. [CrossRef]
56. Jinno, Y.; Johansson, K.; Stocchero, M.; Toia, M.; Galli, S.; Stavropoulos, A.; Becktor, J.P. Impact of salivary contamination during placement of implants with simultaneous bony augmentation in iliac bone in sheep. *Br. J. Oral Maxillofac. Surg.* **2019**, *57*, 1131–1136. [CrossRef]
57. Proksch, S.; Steinberg, T.; Keller, C.; Wolkewitz, M.; Wiedmann-Al-Ahmad, M.; Finkenzeller, G.; Hannig, C.; Hellwig, E.; Al-Ahmad, A. Human saliva exposure modulates bone cell performance in vitro. *Clin. Oral Investig.* **2011**, *16*, 69–77. [CrossRef]
58. Heaney, T.G. Inhibition of attachment of human gingival fibroblast-like cells in vitro by saliva and salivary-sulfated glycoprotein in the presence of serum. *J. Periodontol.* **1990**, *61*, 504–509. [CrossRef]
59. Pourgonabadi, S.; Müller, H.D.; Mendes, J.R.; Gruber, R. Saliva initiates the formation of pro-inflammatory macrophages in vitro. *Arch. Oral Biol.* **2017**, *73*, 295–301. [CrossRef]
60. Sun, P.; Shi, A.; Shen, C.; Liu, Y.; Wu, G.; Feng, J. Human salivary histatin-1 (Hst1) promotes bone morphogenetic protein 2 (BMP2)-induced osteogenesis and angiogenesis. *FEBS Open Bio* **2020**, *10*, 1503–1515. [CrossRef]
61. Mi, B.; Chen, L.; Xiong, Y.; Yan, C.; Xue, H.; Panayi, A.C.; Liu, J.; Hu, L.; Hu, Y.; Cao, F.; et al. Saliva exosomes-derived UBE2O mRNA promotes angiogenesis in cutaneous wounds by targeting SMAD6. *J. Nanobiotechnol.* **2020**, *18*, 68. [CrossRef] [PubMed]
62. Arciola, C.R.; Campoccia, D.; Montanaro, L. Implant infections: Adhesion, biofilm formation and immune evasion. *Nat. Rev. Microbiol.* **2018**, *16*, 397–409. [CrossRef] [PubMed]
63. Geurts, J.; Arts, J.J.C.; Walenkamp, G.H.I.M. Bone graft substitutes in active or suspected infection. Contra-indicated or not? *Injury* **2011**, *42*, S82–S86. [CrossRef] [PubMed]
64. De Jong, M.H.; Van Der Hoeven, J.S. The growth of oral bacteria on saliva. *J. Dent. Res.* **1987**, *66*, 498–505. [CrossRef]
65. Cavalcanti, Y.W.; Wilson, M.; Lewis, M.; Williams, D.; Senna, P.M.; Del-Bel-Cury, A.A.; Silva, W.J.D. Salivary pellicles equalise surfaces' charges and modulate the virulence of Candida albicans biofilm. *Arch. Oral Biol.* **2016**, *66*, 129–140. [CrossRef]
66. Bürgers, R.; Hahnel, S.; Reichert, T.E.; Rosentritt, M.; Behr, M.; Gerlach, T.; Handel, G.; Gosau, M. Adhesion of Candida albicans to various dental implant surfaces and the influence of salivary pellicle proteins. *Acta Biomater.* **2010**, *6*, 2307–2313. [CrossRef]
67. Dorkhan, M.; Svensäter, G.; Davies, J.R. Salivary pellicles on titanium and their effect on metabolic activity in Streptococcus oralis. *BMC Oral Health* **2013**, *13*, 32. [CrossRef]
68. Kolenbrander, P.E.; Palmer, R.J.; Periasamy, S.; Jakubovics, N.S. Oral multispecies biofilm development and the key role of cell–cell distance. *Nat. Rev. Microbiol.* **2010**, *8*, 471–480. [CrossRef]
69. Dorkhan, M.; Chávez de Paz, L.E.; Skepö, M.; Svensäter, G.; Davies, J.R. Effects of saliva or serum coating on adherence of Streptococcus oralis strains to titanium. *Microbiology* **2012**, *158*, 390–397. [CrossRef]
70. Mabboux, F.; Ponsonnet, L.; Morrier, J.J.; Jaffrezic, N.; Barsotti, O. Surface free energy and bacterial retention to saliva-coated dental implant materials—An in vitro study. *Colloids Surf. B Biointerfaces* **2004**, *39*, 199–205. [CrossRef]
71. Hauser-Gerspach, I.; Kulik, E.M.; Weiger, R.; Decker, E.M.; Ohle, C.V.; Meyer, J. Adhesion of Streptococcus sanguinis to dental implant and restorative materials in vitro. *Dent. Mater. J.* **2007**, *26*, 361–366. [CrossRef] [PubMed]
72. Kunrath, M.F.; Leal, B.F.; Hubler, R.; de Oliveira, S.D.; Teixeira, E.R. Antibacterial potential associated with drug-delivery built TiO_2 nanotubes in biomedical implants. *AMB Express* **2019**, *9*, 51. [CrossRef] [PubMed]
73. Kunrath, M.F.; Monteiro, M.S.G.; Gupta, S.; Hubler, R.; de Oliveira, S.D. Influence of titanium and zirconia modified surfaces for rapid healing on adhesion and biofilm formation of Staphylococcus epidermidis. *Arch. Oral Biol.* **2020**, *117*, 104824. [CrossRef] [PubMed]

74. Sinjari, B.; D'Addazio, G.; De Tullio, I.; Traini, T.; Caputi, S. Peri-implant bone resorption during healing abutment placement: The effect of a 0.20% Chrolhexidine gel vs. placebo—A randomized double blind controlled human study. *BioMed Res. Int.* **2018**, *2018*, 5326340. [CrossRef]
75. D'Ercole, S.; D'Addazio, G.; Di Ludovico, S.; Traini, T.; Di Giulio, M.; Sinjari, B. Porphyromonas Gingivalis load is balanced by 0.20% Chrolhexidine gel. A randomized, double-blind, controlled, microbiological and immunohistochemical human study. *J. Clin. Med.* **2020**, *9*, 284. [CrossRef]
76. Li, X.; Shang, L.; Brandt, B.W.; Buijs, M.J.; Roffel, S.; van Loveren, C.; Crielaard, W.; Gibbs, S.; Deng, D.M. Saliva-derived microcosm biofilms grown on different oral surfaces in vitro. *NPJ Biofilms Microbiomes* **2021**, *7*, 74. [CrossRef]
77. Mukai, Y.; Torii, M.; Urushibara, Y.; Kawai, T.; Takahashi, Y.; Maeda, N.; Ohkubo, C.; Ohshima, T. Analysis of plaque microbiota and salivary proteins adhering to dental materials. *J. Oral Biosci.* **2020**, *62*, 182–188. [CrossRef]
78. Carlén, A.; Rüdiger, S.G.; Loggner, I.; Olsson, J. Bacteria-binding plasma proteins in pellicles formed on hydroxyapatitein vitroand on teethin vivo. *Oral Microbiol. Immunol.* **2003**, *18*, 203–207. [CrossRef]
79. Lee, B.S.; Chen, Y.J.; Wei, T.C.; Ma, T.L.; Chang, C.C. Comparison of antibacterial adhesion when salivary pellicle is coated on both poly (2-hydroxyethyl-methacrylate)-and polyethylene-glycol-methacrylate-grafted poly (methyl methacrylate). *Int. J. Mol. Sci.* **2018**, *19*, 2764. [CrossRef]
80. Größner-Schreiber, B.; Griepentrog, M.; Haustein, I.; Müller, W.D.; Briedigkeit, H.; Göbel, U.B.; Lange, K.P. Plaque formation on surface modified dental implants. *Clin. Oral Implants Res.* **2001**, *12*, 543–551. [CrossRef]
81. Lima, E.M.C.X.; Koo, H.; Smith, A.M.V.; Rosalen, P.L.; Cury, A.A.D.B. Adsorption of salivary and serum proteins, and bacterial adherence on titanium and zirconia ceramic surfaces. *Clin. Oral Implants Res.* **2008**, *19*, 780–785. [CrossRef] [PubMed]
82. Turri, A.; Čirgić, E.; Shah, F.A.; Hoffman, M.; Omar, O.; Dahlin, C.; Trobos, M. Early plaque formation on PTFE membranes with expanded or dense surface structures applied in the oral cavity of human volunteers. *Clin. Exp. Dent. Res.* **2021**, *7*, 137–146. [CrossRef] [PubMed]
83. Baumann, T.; Kozik, J.; Lussi, A.; Carvalho, T.S. Erosion protection conferred by whole human saliva, dialysed saliva, and artificial saliva. *Sci. Rep.* **2016**, *6*, 34760. [CrossRef] [PubMed]
84. Rosa, N.; Marques, J.; Esteves, E.; Fernandes, M.; Mendes, V.M.; Afonso, Â.; Dias, S.; Pereira, J.P.; Manadas, B.; Correia, M.J.; et al. Protein quality assessment on saliva samples for biobanking purposes. *Biopreservation Biobanking* **2016**, *14*, 289–297. [CrossRef]
85. Avila, M.; Ojcius, D.M.; Yilmaz, O. The oral microbiota: Living with a permanent guest. *DNA Cell Biol.* **2009**, *28*, 405–411. [CrossRef]

MDPI
St. Alban-Anlage 66
4052 Basel
Switzerland
Tel. +41 61 683 77 34
Fax +41 61 302 89 18
www.mdpi.com

International Journal of Molecular Sciences Editorial Office
E-mail: ijms@mdpi.com
www.mdpi.com/journal/ijms







Academic Open
Access Publishing

www.mdpi.com

ISBN 978-3-0365-7724-1